Edited by
Thalappil Pradeep

ATOMICALLY PRECISE METAL NANOCLUSTERS

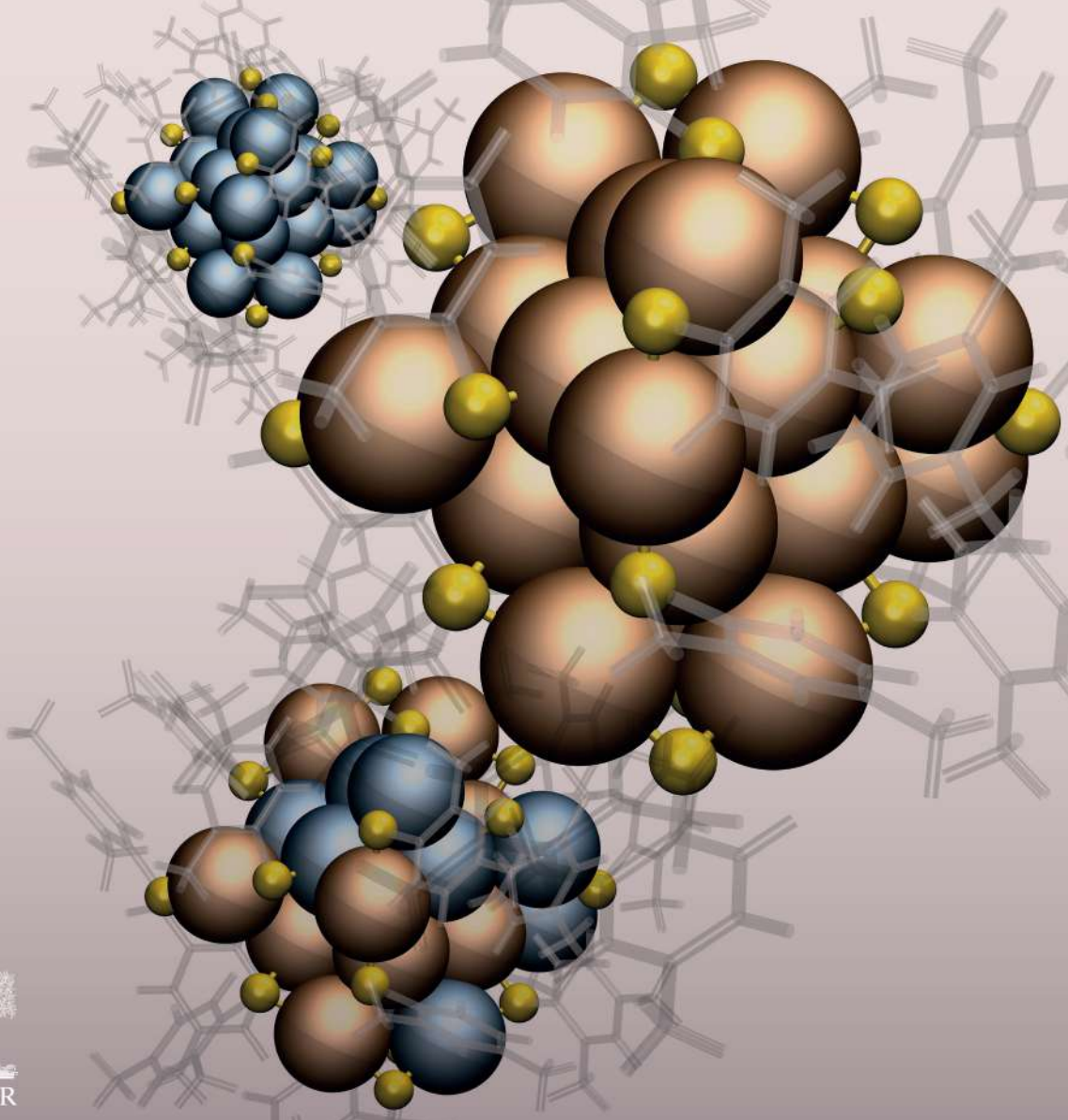

ELSEVIER

ATOMICALLY PRECISE METAL NANOCLUSTERS

ATOMICALLY PRECISE METAL NANOCLUSTERS

Edited by

Thalappil Pradeep
Deepak Parekh Institute Chair Professor and Professor of Chemistry,
Department of Chemistry, Indian Institute of Technology Madras,
Chennai, India

ELSEVIER

Elsevier

Radarweg 29, PO Box 211, 1000 AE Amsterdam, Netherlands
The Boulevard, Langford Lane, Kidlington, Oxford OX5 1GB, United Kingdom
50 Hampshire Street, 5th Floor, Cambridge, MA 02139, United States

Notices

Knowledge and best practice in this field are constantly changing. As new research and experience broaden our understanding, changes in research methods, professional practices, or medical treatment may become necessary.

Practitioners and researchers must always rely on their own experience and knowledge in evaluating and using any information, methods, compounds, or experiments described herein. In using such information or methods they should be mindful of their own safety and the safety of others, including parties for whom they have a professional responsibility.

To the fullest extent of the law, neither the Publisher nor the authors, contributors, or editors, assume any liability for any injury and/or damage to persons or property as a matter of products liability, negligence or otherwise, or from any use or operation of any methods, products, instructions, or ideas contained in the material herein.

ISBN: 978-0-323-90879-5

Publisher: Susan Dennis
Acquisitions Editor: Charles Bath
Editorial Project Manager: Howell Angelo M. De Ramos
Production Project Manager: Kumar Anbazhagan
Cover Designer: Christian J. Bilbow

Typeset by Aptara, New Delhi, India

Contents

14. Computational approaches for nanocluster science 313

Paulami Bose, Ganapati Natarajan and Thalappil Pradeep

15. Ag and Au nanoclusters 343

Udayabhaskararao Thumu and Thalappil Pradeep

Contributors

Ananya Baksi Technische Universität Dortmund Fakultät für Chemie und Chemische Biologie Anorganische Chemie Otto-Hahn-Straße 6, 44227 Dortmund, Germany

Mohammad Bodiuzzaman Postdoctoral Fellow Functional Nanomaterials Lab (FuNL) KAUST Catalysis Center (KCC) King Abdullah University of Science and Technology (KAUST), Thuwal, Kingdom of Saudi Arabia

Megalamane S. Bootharaju Senior researcher Seoul National University, South Korea

Paulami Bose DST Unit of Nanoscience (DST UNS) and Thematic Unit of Excellence (TUE), Department of Chemistry, Indian Institute of Technology Madras, Chennai, India

Amrita Chakraborty Department of Chemistry, Rice University, 6100 Main Street, Houston, Texas, USA

Papri Chakraborty DST Unit of Nanoscience (DST UNS) and Thematic Unit of Excellence (TUE), Department of Chemistry, Indian Institute of Technology Madras, Chennai, India

Indranath Chakraborty School of Nano Science and Technology, Indian Institute of Technology Kharagpur, Kharagpur, India

Wakeel Ahmed Dar Department of Science and Technology (DST) Unit of Nanoscience and Thematic Unit of Excellence, Department of Chemistry, Indian Institute of Technology (IIT) Madras, Chennai, India

Debasmita Ghosh ARNA Laboratory, Inserm U1212, CNRS5320, Université de Bordeaux, France

Arijit Jana DST Unit of Nanoscience (DST UNS) & Thematic Unit of Excellence (TUE), Department of Chemistry, Indian Institute of Technology Madras, Chennai, India

Madhuri Jash Postdoctoral Researcher, Department of Applied Physics, KTH - Royal Institute of Technology, Stockholm, Sweden

Anagha Jose DST Unit of Nanoscience and Thematic Unit of Excellence, Department of Chemistry, Indian Institute of Technology Madras, Chennai, India

Esma Khatun Department of Chemistry, DST Unit of Nanoscience (DST UNS) and Thematic Unit of Excellence (TUE), Indian Institute of Technology Madras, Chennai, India

Amoghavarsha R. Kini DST Unit of Nanoscience (DST UNS) and Thematic Unit of Excellence, Department of Chemistry, Indian Institute of Technology Madras, Chennai, India

Kumaranchira Ramankutty Krishnadas DST Unit of Nanoscience and Thematic Unit of Excellence, Department of Chemistry, Indian Institute of Technology Madras, Chennai, India

Ananthu Mahendranath DST Unit of Nanoscience and Thematic Unit of Excellence, Department of Chemistry, Indian Institute of Technology Madras, Chennai, India

Cheruvattil Koyitti Manju DST Unit of Nanoscience and Thematic Unit of Excellence, Department of Chemistry, Indian Institute of Technology Madras, Chennai, India

Abhijit Nag DST Unit of Nanoscience (DST UNS) and Thematic Unit of Excellence, Department of Chemistry, Indian Institute of Technology Madras, Chennai, India

Ganapati Natarajan International Centre for Clean Water, Block-B, 2nd Floor, IIT Madras Research Park, Taramani, Chennai, India

Thalappil Pradeep Deepak Parekh Institute Chair Professor and Professor of Chemistry,

Department of Chemistry, Indian Institute of Technology Madras, Chennai, India

Edakkattuparambil Sidharth Shibu Department of Nanoscience and Technology, University of Calicut, Kerala, India

Bhuvanachandran Nair Sreekala Sooraj Research Scholar, Department of Chemistry, Indian Institute of Technology, Madras, Chennai, India

Korath Shivan Sugi Institute of physical and theoretical chemistry, Eberhard Karls University of Tuebingen Auf der Morgenstelle 18 D-72076 Tuebingen, Germany

Udayabhaskararao Thumu, Institute of Fundamental and Frontier Sciences, University of Electronic Science and Technology of China, Chengdu, China

Preface

Matter at the nanoscale is becoming molecular. This implies precision in the constituent units of such matter, in composition, structure, and properties as in the case of a molecule, say benzene or hemoglobin. This transformation in matter is most evident in a class of materials referred to as nanoclusters (NCs) or atomically precise clusters (APCs) or even more specifically, atomically precise metal clusters (APMCs) or atomically precise metal nanoclusters (APMNCs). With 654 original papers and 103 reviews and a few books published in the area,[1] this subject has become prominent in materials science, with deep connections to chemistry, physics, and biology. We felt the need for writing a book with insights from the workbench, as it is where the subject blossoms. This will be possible only with the participation of graduating and fresh PhDs, postdocs, and early career faculty, who understand the nuances of this burgeoning field. Such insights are also essential for those who aspire to get into the area and make their hands dirty, so that the field expands further. This book is an attempt in this direction, although it has been visualized and directed by an older person.

The subject area of clusters has been explored intensely over many years. And the effort has expanded into atoms and molecules, like argon and water for example, as both make clusters. It has expanded into materials of every kind, oxides and, sulfides for example, as they too make clusters. As a result, the subject area of clusters is vast, and we are limiting ourselves to a smaller subtopic in this book. Most of the work in APMNCs is happening on noble metals, and especially gold, and the subject area may be termed more accurately as atomically precise noble metal nanoclusters (APNMNCs). Just to give an indication, of the over 773 papers (including reviews) published with "atomically precise cluster" in the title or abstract, 502 were on gold, 242 on silver (silver as the keyword), and 29 on other elements.[1] Among APMNCs of gold, the most studied is $Au_{25}L_{18}^{-}$, with ligands (L) such as glutathione and phenylethane thiol. Although an exact count of papers is uncertain, there should be about 800 papers published in the area.

A bond between two metal atoms would be the primary need of a metal cluster. Therefore, the entity, M_2 will be the smallest metal cluster. We could have M_2L as the first ligand-protected metal cluster and M_mL_l ($m = 2, 3, 4, \ldots$ and $l = 1, 2, 3\ldots$) as the general formula of such ligand-protected clusters. As clusters themselves could be composed of multiple metals (M, N, O…) and similar will be the diversity in ligands (L_1, L_2, L_3,…), and the clusters formed could be alloy clusters, protected with mixed ligands. Clusters could produce a range of nuclearities, and in fact there should be no restriction to limit their number, although at large m, clusters tend to become bulk materials in properties. The limiting factor in the study of such materials would be to make them with precision in composition and structure, and in quantities and to separate, isolate, and characterize closely lying clusters, especially at large m. Despite such limitations, clusters with thousands of atoms are being characterized these

[1] As on May 2, 2022, using Webofscience.

days. Obviously, isolation of such clusters presents the community with numerous opportunities on the exploration of properties.

This huge variety presented above speaks about both opportunities and limitations in the area. Starkly observable gaps in the current knowledge space include missing nuclearities, alloys, adducts, polymers, and assemblies. A somewhat deeper exploration of the literature reveals the absence of well-defined principles for synthesis for all nuclearities, precise structures, and methods of crystallization. Principles of growth and a detailed understanding of the building blocks, their self-organization and guiding principles for size evolution are much needed. One may see that cluster synthesis is still an art, with very little predictability, in comparison to established methods of synthesis, say, in organic chemistry.

While NCs can be formed by any kind of matter, greater efforts are needed to diversify into oxides, chalcogenides, pnictides, and others. These methods need a greater collection of synthetic methods, reagents, and conditions as reduction/oxidation of metal ions alone may not always work in such cases.

While the synthesis, identification, and structures of APMCs have been central aspects of research, their properties as individual clusters and assembled solids are becoming important in the recent past. Luminescence has been the most explored property, while mechanical, electrical, and magnetic properties are slowly gaining attention. Diversity in materials suggests diversity in properties and there is no limit to exploring properties in detail. With the discovery of superconductivity in K_3C_{60}, and greater understanding of transport properties of such materials, similar efforts are expected to intensify in APMNCs also. Similar is the interest in molecular magnetism.

When clusters become large, they may also become complex, in terms of structures, organization of core atoms, ligands, and interfaces. There is a possibility of different ligands with different binding geometries. All these result in complexities such as geometric, positional, and optical isomerism. These changes would lead to new properties, assemblies, polymers, and films. Such materials, their synthesis and characterization are likely to be complex.

The emerging complexity of clusters could make them similar to biological macromolecules like proteins and viruses. This would mean different structures, variation in structures with appropriate stimuli, self-organization, solvent dependence, etc. While noble metal clusters in protein and deoxy ribonucleic acid templates are known, clusters themselves resembling biological macromolecules in gases, solution, and solid states need greater research.

As we continue to synthesize more number of clusters and their variants, and as their properties are explored, better understanding of these materials evolve. These would need greater computational insights to derive better understanding and these lead to additional studies. However, as systems become larger, rigorous studies become difficult and approximate methods need to be used. Computational insights are needed not only to understand details of the structure in terms of catalytic sites, their geometries, accessible ligands, etc., they are also essential to understand molecular details of mechanisms of chemical transformations, physical properties of individual clusters, and their assemblies.

Developments in the area are supported by the tremendous advancements in instrumentation, introduction of methods for synthesis and characterization. The key to

understanding has been advanced mass spectrometry and soft ionization. Today, these developments have made it possible to measure clusters in the mega Dalton (MDa) mass range, with thousands of metal atoms. Such mass spectrometers can also do tandem mass spectrometry and mobility analyses, which provide greater insights on the structure of these entities. Mass spectrometers have also become instruments to measure photoelectron spectra, diffraction, luminescence, and infrared spectra of ions. While several of these measurements becoming possible in the case clusters, many others are yet to be developed.

In the coming years, clusters and their properties will become the central theme of many laboratories across the world. Magnetism, electrical conductivity, sensing, and mechanical properties will be explored for several cluster solids. They will also be explored in the solution for their chemistry, new catalysis, photophysics, and associated properties. From the current fascination of synthesis, purification, and crystal structure, the field will move to properties only if new applications are likely. Magnetism, catalysis, and sensing are likely to be the more impact making areas in this respect. For this, cluster materials need to be available in quantities for them to be explored in multiple laboratories across the world.

I am sure that many of these directions outlined above will be explored together, between research groups. For example, the emergence of cryoelectron microscopy and microelectron diffraction will make structure determination of clusters more collaborative. The introduction of new ligands such as alkynes, carbenes, and carboranes has expanded the area of APNMCs, which were till recently dominated by alkane and arene thiols, phosphines, and amines. A greater variety of ligands and synthetic methods using them will expand the area, both in terms of variety and ease of crystallization.

More cluster-based international linkages, conferences, discussion meetings, and special issues of journals are happening in the past few years. These efforts make the subject area more interdisciplinary. For anyone to initiate research in the area and those active to expand into other related areas, a concise summary of activities and unifying the various thoughts become essential. In this respect, the book is timely.

Finally, in any effort of this kind, there will be omissions and inaccuracies, although we have taken utmost care to eliminate them. Despite such efforts, there could still be a few lapses and let me take sole responsibility for the same. I must say that I will be glad to receive suggestions and constructive criticism for improvement.

Thalappil Pradeep
Chennai
April 30, 2022

Acknowledgments

This book was planned over 5 years ago while we were making a manuscript for Chemical Reviews on the same topic. Many of the topics we touched upon in the review needed more detailed attention and a book was thought to be most appropriate. However, diverse commitments kept me away from taking a plunge into it. Time was somewhat suitable during last year when Covid brought a stop to academic travels and there was more time to think about the delayed commitments. That is when a request came from Elsevier for publishing a book on this topic and that trigger restarted the effort.

For the book, I must thank my present and former group members who responded enthusiastically to the idea. I wanted the book to be written from the perspective of researchers at the workbench. This, I thought would give a deeper insight to the experimental details for anyone to reproduce the results. In many meetings, I had heard about the difficulties in making specific clusters, their purification, measuring their mass spectra, and obtaining well-defined crystals. We had faced these too in our group and therefore, I thought of writing the chapters including the lessons learned, to help the young researchers. For this purpose, we have also included a couple of videos (Video 1 and Video 2) on the synthesis and crystallization of clusters.

The period of writing was hard for most authors. Covid had upset the lab schedules, personal life, and some of the authors had also lost their relatives. With all these, they kept the commitment, managing multiple tasks. I thank them. In particular, I must acknowledge the additional efforts of Manju, Sooraj, Ananya, Papri, Indranath, Ananthu, Sugi, and Amoghavarsha for ensuring that the work was finished in time. A special word of appreciation for Manju for putting together the chapters and submitting them on the website and following up with the work routinely. Sooraj prepared the Appendix on all the clusters synthesized so far, with the assistance of Indranath and Esma. Sooraj also incorporated the suggestions of everyone.

I am grateful to note that the work presented here, and the knowledge accumulated are the result of a global effort. I thank all the players who contributed to building this marvelous edifice of cluster science. I am aware that the science has been built with the generous support of (mostly) public grants. In my laboratory, this support came from the Department of Science and Technology and Science and Engineering Research Board, which supported me generously.

I must thank the Indian Institute of Technology Madras for providing a healthy and vibrant academic environment for conducting such activities. For everything that is being done at the Institute, there is an invisible hand of goodness. I thank all my colleagues who contributed to building this environment over the years.

Finally, let me thank Elsevier and its staff who have done a meticulous job of completing the production in time. I must particularly thank Howell Angelo M. De Ramos, Editorial Project Manager at Elsevier for executing the work perfectly.

Thalappil Pradeep
May 3, 2022

CHAPTER

1

Atomically precise clusters of noble metals: An introduction

Thalappil Pradeep

Deepak Parekh Institute Chair Professor and Professor of Chemistry, Department of Chemistry, Indian Institute of Technology Madras, Chennai, India

Materials traditionally are infinite solids, where atomic linkages extend infinitely. Every chemical bond extends many, many times in each direction to make even a tiny piece of matter, which is typically composed of millions of atoms. However, a piece lying next to it could contain a different number of atoms. A macroscopic solid such as gold or silver or oxides such as alumina or silica is composed of millions of pieces, each with differing number of atoms, although the properties of each of those particles of one chemical species, will be the same. Thus, the idea of matter, built with atomically precise units making bulk materials, such as metals or ceramics, is not uncommon. However, such materials can cause tremendous interest in view of the likelihood of new properties that can arise in them and due to the curiosity to know where bulk properties emerge in matter. Research has explored both these aspects well over a century and such concerns were mostly on the variation in properties such as color and melting point with size of the object. As thickness of a gold foil is reduced to very small values, its color changes. This was seen in solution long ago, when gold particles or colloids were prepared, as observed by Faraday in 1857.[1] This is probably the very first example in scientific literature to show that properties of matter change drastically when constituent particles changed in size. In those early periods, there were no experimental methods to measure the dimensions of particles in the nanometer regime, although the particle sizes were thought to be in the range of nanometers. The variation in properties of gold or alloys of gold was used even centuries ago, as in Lycurgus cup, dated to 3500 BC, although the existence of nanometer-scale particles in them was proven only in 1990.[2]

Nanoparticles have been the subject of interest ever since Faraday's colloids. A more detailed study of them became possible after the Turkevich method,[3] which involved reducing gold or silver salts by trisodium citrate, making stable nanoparticles of the metals in water with citrate protection. Numerous studies became possible using this highly reproducible method. Stable nanoparticles of alkane/arene thiol protection became possible after the Brust method[4]

DOI: https://doi.org/10.1016/B978-0-323-90879-5.00008-1

where a phase transferred metal salt is reduced in presence of appropriate thiol. This method produced nanoparticles of a few nanometer in diameter, in organic solvents, exhibiting broad surface plasmon resonance and these particles could be dried and redissolved. The origins of atomically precise clusters can be traced to this synthetic method, by varying the metal:thiol ratio to reduce the cluster core size to 1-2 nanometer where the surface plasmon absorption disappears.

Atomic precision is typically the domain of molecules. The existence of hydrogen and oxygen in the water and the fact that water contains these elements in a definite ratio were probably the first demonstrations of atomic precision in matter.[5] Although the molecular nature of H_2O took some more time to get established,[6] molecules are recognized as atomically precise ever since the law of definite proportions.[7]

Atomic precision implies precise composition, well-defined molecular mass, and corresponding precision in structure. Precise composition and precise structure consequently suggest definite properties. Although several of these properties, such as melting and boiling points are yet to be established in atomically precise clusters, such entities are expected to have corresponding thermodynamic properties such as heat of formation and associated entropy and free energy. Although optical absorption and emission of several of the atomically precise clusters have been measured and in fact, these are the two properties examined more routinely in clusters prepared in solution state, many properties are yet to be known. For example, ionization potential of most of them as a molecular entity is unknown, although electron affinities were some of the earliest properties examined for naked clusters prepared in the gas phase.[8] The fact that many properties are yet to be known leaves adequate room for extensive studies. At present, atomic precision means a precise composition, mass, and structure. Intact structures upon melting and thermal evaporation are yet to be seen in this class of materials.

Atomic precision implies molecular behavior in matter. Important of these are chemical properties. Well-defined chemical reactions of atomically precise clusters are one of the manifestations of molecular behavior. These reactions will have corresponding energetics and thermodynamic parameters. Reactions would have kinetics and corresponding mechanisms. That would result in classifications of reactions to different categories.

One of the important classes of chemical reactions would be catalysis. In general, catalysis of clusters is investigated in the supported form. However, there is homogeneous catalysis too, often conducted in solution. This kind of reaction involves specific catalytic sites, interacting with reactants forming specific transition states.

A detailed understanding of these systems, their chemistry in particular, would need an acceptable nomenclature with which chemical processes involving them can be described. Such a nomenclature would allow a structurally precise name to be written for each of the clusters, specifying the location of atoms or groups, their connectivities, and relative orientations. Such a nomenclature would allow a detailed understanding of changes in atoms and their locations, in the course of chemical transformations. Ultimately, all of these would enable a detailed understanding of the complex processes happening in or using such systems, similar to the detailed knowledge possible in the case of ribosomes.

New materials are interesting in view of their properties. In the case of atomically precise clusters, the most fascinating property is their luminescence, particularly in the near-infrared region. The luminescence quantum yield is often large too, of the order of 25%. A particularly useful aspect is the >200 nm Stokes shift, which helps in detecting the emission without

being influenced by impurities or neighboring species. Luminescence is useful for biolabeling, environmental analysis, and sensing physical properties. Optical absorption, photophysical properties, carrier lifetime, etc., are also interesting too. The large extinction coefficient and absorption over an extended spectral widow have been used for new kinds of solar cells. Applications in the fields of catalysis, largely for simple oxidation process such as aldehyde of acid conversions, have been explored. Applications of clusters in metal ion sensing is another area of promise. Emerging properties of magnetism and electrical conductivity are beginning to be explored. The mechanical properties of cluster crystals are also becoming interesting and early reports have started appearing. Luminescent clusters protected with biomolecules such as proteins and DNA are more researched upon from the context of biological applications—imaging and delivery. They are stable and can be separated and powdered and are most importantly soluble in water.

Where do we go from here? Over 500 atomically precise clusters have been reported with nuclearity from 2 to 2000 and over 150 of them have been crystallized with M_2 to M_{279}.[9] Clusters of Au, Ag, Pt, and Cu are in this group in the pure form. Several alloys of each of these, especially of Au and Ag have been made with Pt, Ni, Pd, Ir, Cu, Cd, Hg, Ru, and Rh have been crystallized. A compendium of all the clusters prepared and crystallized so far with crystal structures determined are collected in the Appendix. Several of these clusters are known to exist in polymorphic forms. A list of alloy clusters known so far is also collected in Appendix. This shows a list of over 100 alloy clusters known so far with 70 of them being crystallized. The data presented makes it clear that there is much more to learn about clusters in general, in terms of their structures and properties.

Once such data are available, commonalities can be understood. Although molecular aspects of cluster systems are increasingly explored, it is unclear as to what makes a specific cluster system stable. We still do not have a unform methodology to make clusters of various nuclearities. We do not know what makes a given ligand form a specific cluster and why another cluster or nearly the same nuclearity is not made. All of these relate to the poor understanding of the steps involved in the formation of clusters. Choice of ligand–metal combinations, influence of starting materials used, synthetic conditions, reducing agents, counter ions, solvents, etc., are not clear in several cases. While clusters are made, the synthetic methodology is not optimized as in organic chemistry and yields are seldom reported.

The subject area will receive greater interest once certain uncommon and unusual properties are accomplished in these materials. Clusters will gain prominence if these properties can have economic value. Among those properties of intense interest are unusual magnetism, electrical conductivity including superconductivity, unusual catalysis, and novel mechanical properties.

Although the idea of creating matter with atomically precise building blocks has been an important motivation, research in the past few years has made the community realize that the matter produced is indeed way different from the bulk analogs of the principal constituent. For example, crystals of atomically precise gold clusters are fundamentally different from bulk gold; they are indeed a new class of materials. This is indeed the case with all the different types of clusters of single or multiple metals that we have made so far. From that perspective, we have expanded the scope of molecular materials through clusters. The variety this offers, however, is extremely large. For example, clusters not only self-assemble with themselves but also with other clusters, making cluster co-crystals. This leads to an infinite family of materials, A_nB_m, where A and B are clusters. Coupled with the kind of properties A and B can have, such

as magnetism in *A* and luminescence in *B*, new kinds of solids can be derived. This fascinating prospect in detail has not been realized yet, but directions along this path are available.

Clusters are in the size regime of biomolecules such as proteins or DNA. They also have structural complexity, similar to biomolecules, if we consider the ligand orientations and interactions possible. It is also possible to functionalize clusters to induce such flexibility. All of these would mean that clusters can arrange similar to biomolecules such as proteins or DNA. While arrangements similar to proteins are known to form, organizations similar to DNA are yet to be formed. If this happens, it will be another direction to pursue, and one may call this a new kind of nanobiochemistry or structural biology of nanoclusters. The properties these assemblies give and the possibilities such complex structures produce similar to DNA nanotechnology would be worth exploring.

With all these diverse possibilities, the expanding horizons of cluster science are bound to be rich.

References

1. Faraday MX. The Bakerian Lecture. —experimental relations of gold (and other metals) to light. *Philos Trans R Soc Lond*. 1857;147:145–181.
2. Barber DJ, Freestone IC. An investigation of the origin of the colour of the lycurgus cup by analytical transmission electron microscopy. *Archaeometry*. 1990;32:33–45.
3. Turkevich J, Stevenson PC, Hillier J. A study of the nucleation and growth processes in the synthesis of colloidal gold. *Discuss Faraday Soc*. 1951;11:55–75.
4. Brust M, Walker M, Bethell D, Schiffrin DJ, Whyman R. Synthesis of thiol-derivatised gold nanoparticles in a two-phase Liquid–Liquid system. *J Chem Soc Chem Commun*. 1994;0:801–802.
5. Cavendish HXIX. Three papers, containing experiments on factitious air. *Philos Trans R Soc Lond*. 1766;56:141–184.
6. Lavoisier AL. sur l'histoire naturelle et sur les arts. *Obs Sur la Phys*. 1783;23:452–455.
7. Proust JL. Research on prussian blue. *J Phys Chim d'Histoire Nat*. 1794;2:334–341.
8. Ray JR, Smalley LL. Spinning fluids in general relativity. *Phys Rev D Part Fields*. 1982;26:2619–2622.
9. Sakthivel NA, Theivendran S, Ganeshraj V, Oliver AG, Dass A. Crystal structure of faradaurate-279: Au279 (SPh-TBu)84 plasmonic nanocrystal molecules. *J Am Chem Soc*. 2017;139:15450–15459.

CHAPTER

2

Structure and chemical properties of clusters

Kumaranchira Ramankutty Krishnadas[a] *and Thalappil Pradeep*[b]

[a] DST Unit of Nanoscience and Thematic Unit of Excellence, Department of Chemistry, Indian Institute of Technology Madras, Chennai, India [b] Deepak Parekh Institute Chair Professor and Professor of Chemistry, Department of Chemistry, Indian Institute of Technology Madras, Chennai, India

2.1 Introduction

In this chapter, we present the chemical properties of ligand-protected atomically precise noble metal clusters. A brief overview of factors that makes nanoscale noble metals more reactive compared to their bulk counterparts is presented first, followed by a short account of historical developments that led to the *reactive* era of "noble" metal nanosystems. A detailed discussion on various types of chemical reactions of ligand-protected atomically precise noble metal clusters will be presented in the later sections. A few interesting examples of reactions wherein atomic precision has been achieved and also mechanistic insights available are also discussed. The chapter concludes with a summary and future directions.

2.2 Chemical reactivity at the nanoscale: Beyond surface to volume ratio

One of the prominent features of nanomaterials is their increased surface-to-volume ratios due to which a very large number of constituents (i.e., atoms, ions, or molecules) occupy the surface than the bulk. Increased number of constituents on the surface is often regarded as one of the main reasons for the enhanced chemical reactivity of nanomaterials. Though this is generally true, the complexities in the stability and chemical reactivity of nanomaterials cannot be explained by this factor alone. At the subnanometer size regime, quantum confinement effects and geometric factors play a major role in determining the chemical properties of nanomaterials.

DOI: https://doi.org/10.1016/B978-0-323-90879-5.00002-0

Noble metals, especially gold, in the bulk form are chemically inert and have been uninteresting to chemists. Relativistic effects play an important role in the reactivity of noble metals, in their smaller particulate forms.[1–3] Relativistic effects result in the contraction of the outer 6s orbitals and the expansion of the inner 5d orbitals of Au atom and therefore, Au has a higher electronegativity and smaller atomic radii compared to Hg and Ag. In addition to these, Au shows a variety of oxidation states such as Au^{+}, Au^{2+}, Au^{3+}, Au^{5+}, and Au^{-}. [4] All these factors contribute to its reactivity. Relativistic effects are extremely important in understanding the reactivity and physical properties of coordination compounds of Au, Ag, Cu, and Hg.[5–7]

2.3 Chemical reactivity at the nanoscale: A brief historical overview

Arnim Henglein's pioneering works provided early insights into the physical and chemical properties of small particles in solution, even before they were identified as nanomaterials.[8,9] Haruta and co-workers discovered that small particles of gold catalyzes the conversion of CO to CO_2 at very low temperatures.[10] This resulted in an explosion of activities that formed the basis of gold catalysis. Apart from catalysis, small clusters of gold were shown to be highly reactive. For example, small anionic gold clusters in the gas phase are known to react with oxygen.[11,12] Neutral and cationic gold clusters are also known for the conversion of CO to CO_2.[13] Effects of cluster geometry on catalytic activity of gold clusters have also been studied by various groups.[14,15] Silver clusters are known to be reactive toward oxygen.[16] The solution-phase chemistry of atomically precise gold clusters evolved from the studies of gold–phosphine coordination complexes.[17–19] Brust–Schiffrin method, reported in 1994, wherein thiolates can be used as protecting ligands to synthesize nanoparticles conveniently in solution is an important milestone in the chemistry of noble metal nanosystems.

2.4 Chemical properties of atomically precise metal clusters: Insights from gas phase studies

Bare or unprotected metal clusters in gas phase have been studied extensively by various tools. Mass spectrometry is one of the most essential tools for these studies[20] because it enables us to directly probe the composition, stability as well as reactivity of atomically precise clusters.[21] Gas-phase investigations of metal clusters using various tools such as mass spectrometry,[22] ion mobility spectrometry, photoelectron spectroscopy, vibrational spectroscopy,[23] etc., provided important insights into their chemical properties. The role of geometry and electronic structure of clusters on their reactivity were unveiled from these early investigations.

2.4.1 Geometric versus electronic stability in unprotected, gaseous phase metal clusters

Knight et al. and Walt de Heer observed that the mass spectra of bare, gas-phase clusters of Na show abundances for certain nuclearities, as shown in Fig. 2.1.[24,25] It was recognized that these nuclearities correspond to the clusters wherein the total number of valence electrons is equal to the number needed for closed electronic shells as in the case of noble gases. This concept of electronic shell closing or superatom theory has been useful in explaining the mass spectral abundances of naked Ag and Au clusters.[26–29] Further, this theory has been useful

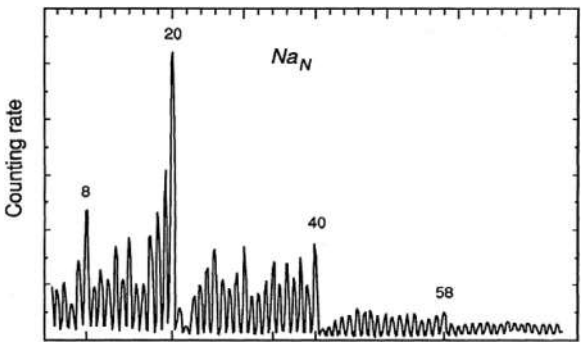

FIGURE 2.1 Mass spectra of Na_n clusters showing the abundance for $n = 8$, 20, 40, etc., which correspond to the clusters with the electronically closed shells (reproduced with permission from, ref.[24]).

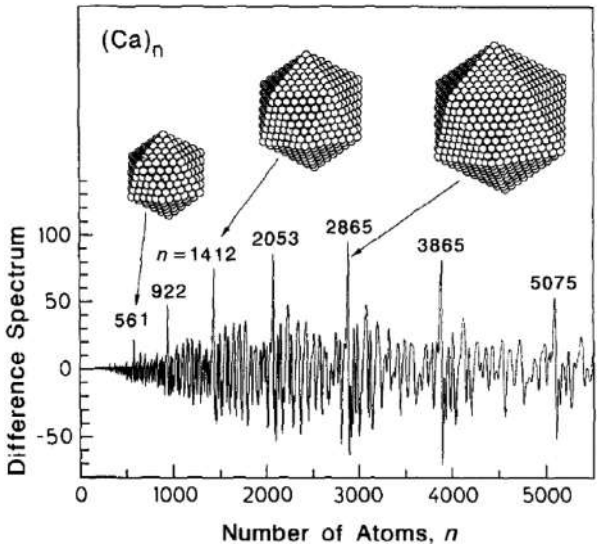

FIGURE 2.2 Mass spectra of Ca_n clusters. The peaks labeled in this mass spectrum are due to geometrically closed-shell clusters formed by the successive completion of icosahedral layers of metal atoms (reproduced with permission from ref.[37]).

in explaining the mass spectral abundances of small, ligand protected clusters, and metalloid clusters as well.[30,31]

Some of the metal clusters with closed electronic shells are also referred to as superatoms, a concept originally introduced by the pioneering work A. W. Castleman Jr., Puru Jena, and Shiv Khanna. For example, Khanna et al. showed that Al_{13}^- which has a magic number of 40 electrons exhibits special inertness toward gas-phase etching reactions.[32–34] The stability attained due to the electronic shell closing along with its compact geometry is considered as the basis for the extreme stability of such clusters.

Another type of shell closing that determines the stability of the metal clusters, van der Waals clusters of noble gases, etc., is the geometric shell closing.[35,36] Here, the stability is determined by the geometry of the cluster rather than the electronic shell closing. Mass spectral abundances are observed for the series of clusters in which each cluster is formed by successive addition of a geometrically complete layer of atoms, resulting in stable geometries, such as icosahedra. For example, clusters of alkaline earth metals possess icosahedral geometries, as shown in Fig. 2.2.[37] This is especially manifested in the case of large clusters containing a

few hundreds of atoms wherein the difference in electronic energy on the addition of every new atom is very small due to overlap of electronic bands. The principles of geometric and electronic shell closing are also applicable to several atomically precise, ligand-protected metal clusters as presented in a subsequent section.

Structure–activity relationship of these clusters can be more conveniently studied when the clusters are atomically precise in their composition and highly stable in solution. Ligand-protection is essential in order to impart stability to clusters in the solution phase. However, the presence of ligands creates some hurdles in clearly understanding the role of the sizes and geometries of these clusters. The protecting ligands often have a significant role in dictating the structure, physical properties as well as the chemical reactivity of clusters. In summary, small noble metal clusters and particles offer rich chemistry than the bulk form not only because of the smaller size but also due to the relativistic, morphological, charge state, and ligand effects. Some of these aspects are discussed in the following sections.

2.5 Molecule-like nature of ligand-protected atomically precise noble metal clusters

Almost all spectroscopic techniques and characterization tools that are commonly used in the chemistry of small molecules were also utilized for ligand-protected metal clusters. Techniques such as UV/Vis absorption, emission, NMR, electron paramagnetic resonance (EPR), and single-crystal X-ray diffraction, mass spectrometry, and electrochemistry have unambiguously proved molecule-like nature of atomically precise, ligand-protected noble metal clusters. Molecules are typically characterized by their well-defined molecular formulae, discrete electronic energy levels,[38] etc., and this is true for atomically precise ligand-protected metal clusters as illustrated for $Au_{25}(PET)_{18}$ (PET is 2-phenylethanethiolate) in Fig. 2.3. Ligand-protected, atomically precise clusters, typically in larger size regime, consist of two basic structural elements, that is, a well-defined core with a precise number of metal atoms and the outer metal-ligand oligomeric units, often referred to as staples, mounts, etc. For example, $Au_{25}(SR)_{18}$ contains an Au_{13} icosahedral core protected by six $Au_2(SR)_3$ staples, as presented in Fig. 2.4. In the following sections, we illustrate the molecule-like nature of these clusters revealed by various spectroscopic studies mentioned above. We also emphasize the fact that molecule-like nature of these clusters is reflected in their chemical reactivity as well.

The most important message of this chapter is that the ligand-protected noble metal clusters exhibit rich chemistry not only because of being too small but also due to the structure of the metal core, metal–ligand interfaces as well as the real structure of the ligands. Chemistry of $Au_{25}(SR)_{18}$, for example, is not because of being as small as Au_{25} but also due to the chemical reactivity of the metal–ligand interfaces in the form of $Au_2(SR)_3$ staples.

2.5.1 Superatom concept for ligand-protected noble metal clusters

In the previous section, it was mentioned that ligand-protected, atomically precise metal clusters possess well-defined molecular formulae and distinct charge states. Taking these aspects into account and also considering these clusters as metal-ligand complexes, the formula for calculating the shell closing free-electron count can be given as:

$$n^* = Nv_A - M - z,$$

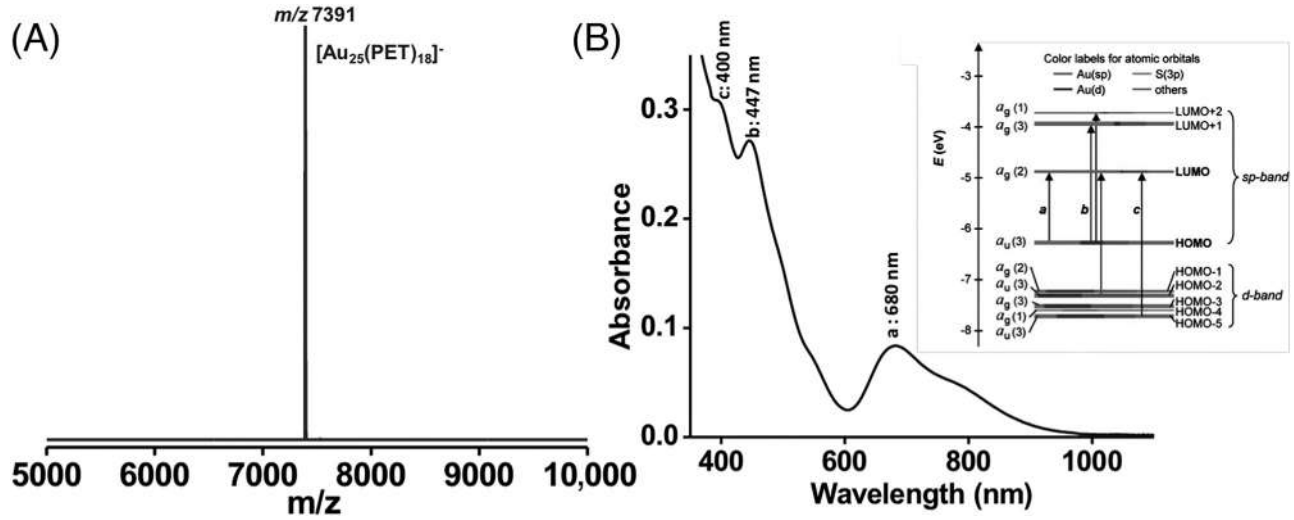

FIGURE 2.3 Negative ion mode ESI mass spectrum (A) and the UV/Vis absorption spectrum (B) of $Au_{25}(PET)_{18}$. PET is 2-phenylethanethiolate. Distinct absorption bands are marked in (B) which correspond to the electronic transitions shown in the inset. The inset in (B) is reproduced with permission from ref.[38].

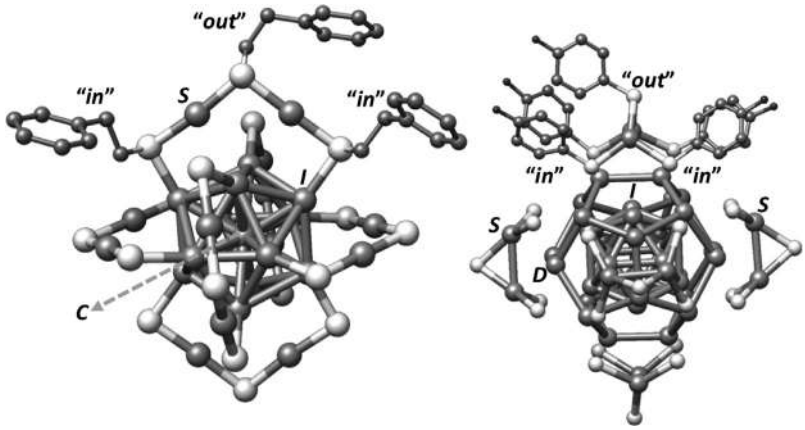

FIGURE 2.4 Schematic of the crystal structures of $Au_{25}(PET)_{18}$ (left) and $Ag_{44}(FTP)_{30}$ (right) showing various unique positions of metal atoms and ligands. PET is 2-phenylethanethiolate and FTP is 4-fluorothiophenolate. The unique metal atom positions are labeled *S* (staple), *I* (icosahedron), *C* (center), and *D* (dodecahedron). Color codes: Au, Ag (large gray spheres), S (white spheres), C (smaller gray spheres), F (smallest black spheres). The outward-projecting ligands are labeled "*out*" and the inner ligands are labeled "*in*." The aromatic ring structure of the ligands is not shown, only geometric structure is shown.

where n^* is the shell closing free-electron count, N is the number of metal atoms of element A, $v_A$is the atomic valence of atom A, M is the number of electron-localizing (or electron-withdrawing) ligands, and z is the overall charge of the cluster.[39] Stabilities of several ligand-protected metal clusters could be explained by the shell closing electronic configuration. For example, $[Au_{25}(SR)_{18}]^-$ correspond to an electronically closed-shell cluster with a shell closing free-electron count (or the magic number) of eight electrons ($N = 25$, $v_A = 1$, $M = 18$, $z = -1$). Here, thiolates act as strong, electron-localizing ligands. According to this concept, the free-electron count of $[Au_{25}(SR)_{18}]^-$ can be understood as follows (refer to Fig. 2.4 for the structure of $[Au_{25}(SR)_{18}]^-$): the valence (i.e., $6s^1$) electrons of the Au atoms in the six staples are localized by the thiolate ligands and therefore these atoms are in Au(I) oxidation state. Each of the sulfur atoms at the ends of the six staples is bound to one Au atom each of the Au_{13} icosahedron. However, each of these staples localizes the $6s^1$ electron of only one of the two icosahedral Au atoms to which the given staple is bound. Therefore, in effect, only six valence electrons (out of 12 in total) of the icosahedral Au atoms can be considered as "free." These six free electrons of the icosahedral core, one free $6s^1$ electron of the central atom (note that the central Au atoms is not bound to ligands and therefore its valence electron is free) and the single negative charge add up to a total of 8, which is a magic number.

Electronic shell closing has been considered to be an important factor that determines the feasibility of metal atom substitution reactions.[40] An example will be discussed in Section 2.9.2. However, note that this concept cannot explain the stability of several clusters such as $Au_{38}(SR)_{24}$ (which possess 14 free electrons, not a magic number). Therefore, electronic shell closing is not the only factor determining the stability and reactivity of ligand-protected clusters.[41]

2.6 Chemistry of ligand-protected atomically precise noble metal clusters: A structural view

As mentioned earlier, ligand-protected, atomically precise noble metal clusters consist of two basic structural elements, that is, metal atoms and the ligands. Therefore, the immediate chemical reaction that one can think of in these clusters is their substitution reactions, that is, the metal atoms and the ligands of a given cluster can be substituted or exchanged with a different metal atom and a different type of ligand. Ligand exchange reactions are one of the oldest reactions in the chemistry of monolayer protected clusters.[42,43] Crystal structures of $Au_{102}(SR)_{44}$,[44] and $Au_{25}(SR)_{18}$,[45,46] and other such clusters showed that the ligands exist as oligomeric, metal-thiolate complexes such as $Au(SR)_2$, $Au_2(SR)_3$, etc., as mentioned earlier. Moreover, there are different symmetry-unique locations for the ligands in a given cluster (see Fig. 2.4). For example, $Au_{25}(SR)_{18}$ contains an Au_{13} icosahedral core protected by six $Au_2(SR)_3$ staples, as mentioned earlier. In each of the staples, the twoterminal sulfur atoms are bound to two of the Au atoms of the Au_{13} core. Furthermore, among the 18 ligands, 12 are in a symmetry unique terminal or *in* positions and 6 are in symmetry unique bridging or *out* positions. NMR spectroscopic measurements proved that indeed this is the case. Similarly, various unique sites exist for an incoming metal atom. For example, there are three distinct positions available in $Au_{25}(SR)_{18}$ for a substituent metal atom. These positions are (1) the center of the icosahedron (C), (2) vertices of the icosahedron (I), and (3) the staple (S) positions, as depicted in Fig. 2.4. The availability of structural details of several clusters opens up the possibility to probe the site selectivity and specificity in metal atom and ligand exchange reactions. In the subsequent sections, we discuss these reactions in greater detail with a few examples.

2.6.1 Substitution of ligands

Consider the ligand exchange of $Au_{25}(PET)_{18}$. Ligand exchange reactions can be considered as nucleophilic attack of the substituent thiols/thiolates onto the Au atoms of the staple units. There are three distinct sites of attack available in $Au_{25}(SR)_{18}$ for an incoming thiol as a nucleophile. These sites are designated as A, B, and C, respectively, in Fig. 2.5A. Calculations of Aikens et al.[47] support this observation and also confirm the associative type mechanism proposed by Guo et al.[43] Even though the S–Au bond in site A is weaker than those in sites B and C, their calculations suggest that the attack of the incoming thiol at site B is preferred to sites A and C. However, selectivity to the core and terminal positions are dependent also on the bulkiness of the ligand's tail groups and the electronic factors of the incoming ligand, as observed by Pengo et al., who studied the ligand exchange reactivity by monitoring the evolution of the nuclear magnetic resonance (NMR) signals due to protons of the thiolate ligands (see Fig. 2.5B).[48] They found that the exchange of the outer thiolate ligand is more sensitive to the structure of the incoming thiol than the exchange of inner thiolate. In addition to the structure, the electron withdrawing/donating nature of the incoming ligand also plays a role in the kinetics and the site-specificity of ligand exchange.

Incomplete or partial ligand exchange results in a complex mixture of clusters with varying numbers of ligands. However, complete ligand exchange, retaining the core size, in presence of excess thiols has been reported by AbdulHalim et al., in the case of a p-mercaptobenzoic acid (MBA) protected cluster, $Ag_{44}(MBA)_{30}$.[49] For a cluster with a general

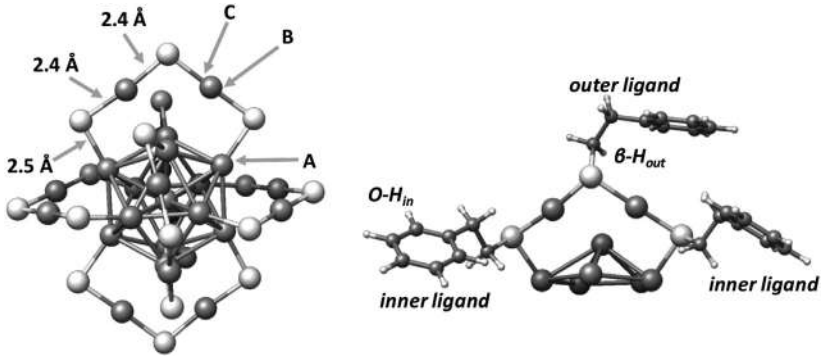

FIGURE 2.5 (A) $Au_{25}(SH)_{18}^-$ nanocluster with three distinct sites for nucleophilic attack by a thiol marked as A, B, and C. Bond distances (in Å) are shown. Color codes: Au (large dark gray spheres, S (large white spheres), C (small dark gray spheres), H (small white spheres). Hydrogens are not shown in (A). (B) Structure of the dimeric staple motif $Au_2(SR)_3$ (where –SR is 2-phenylethanethiolate) with indication of the distinct types of protons monitored in the kinetic analysis of the place exchange reaction (Figs 2.5A and B are redrawn from, ref.[47] and ref.[48], respectively).

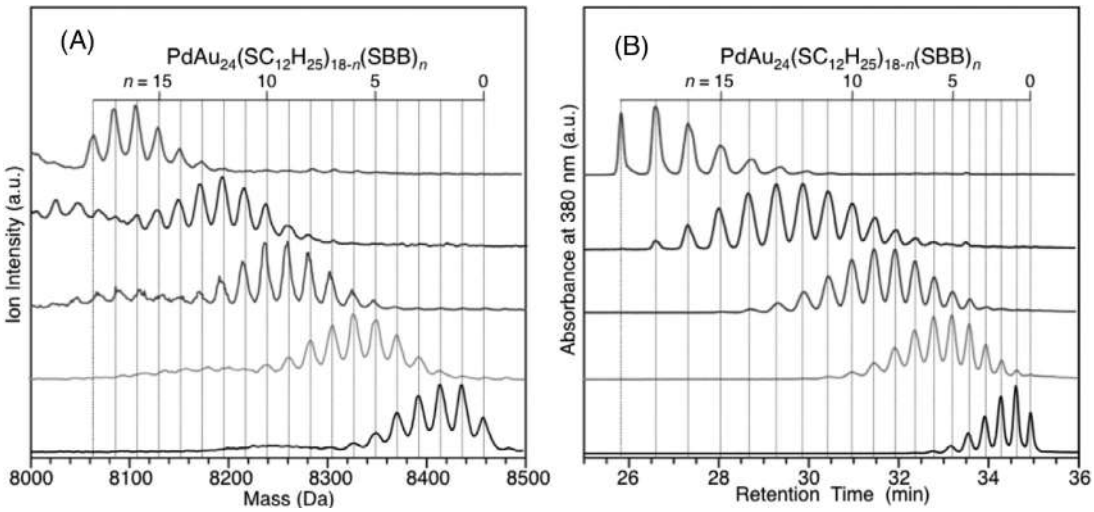

FIGURE 2.6 Comparison between (A) negative ion MALDI mass spectra and (B) HPLC chromatograms for $PdAu_{24}(SC_{12}H_{25})_{18-n}(SBB)_n$. The traces at the same heights in (A) and (B) correspond to the same sample (reproduced with permission from ref.[50]).

formula, $Au_{25}(SR)_{18-n}(SR^1)_n$, where SR and SR^1 are two different ligands, partial exchange generates a mixture of clusters with $n = 0$–18. Structural and stereoisomers possible for such partially ligand exchanged clusters increases the complexity of the ligand exchange chemistry. The separation of individual clusters in such a mixture is essential for meaningful investigation of ligand effects. For the first time, high-performance liquid chromatography (HPLC) was proven to be successful in separating a complex mixture of partially ligand exchanged $Au_{24}Pd_1$ clusters (see Fig. 2.6).[50] They have also succeeded in separating the structural isomers of $Au_{24}Pd(PET)_{18-n}(DDT)_n$ (DDT is 1-dodecanethiolate) formed during the reaction between

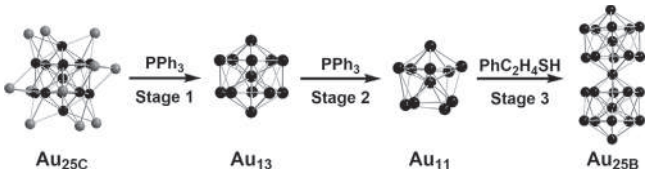

FIGURE 2.7 Schematic of the ligand-induced conversion of core-shell Au_{25} (Au_{25C}) to bi-icosahedral Au_{25} (Au_{25B}). (Reproduced with permission from ref.[53]).

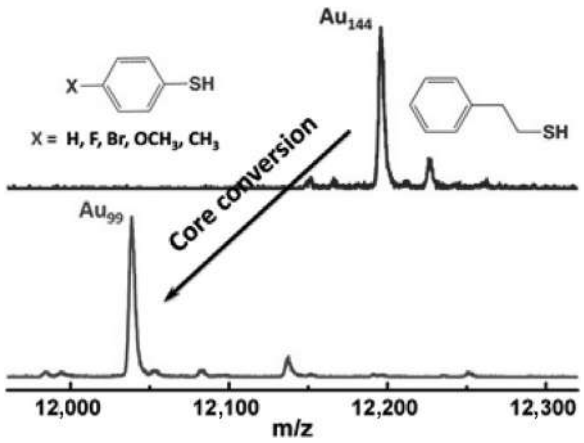

FIGURE 2.8 MALDI MS spectra showing the ligand-induced conversion of Au_{144} to Au_{99}. (Reproduced with permission from ref.[54]).

$Au_{24}Pd(PET)_{18}$ and DDT.[51] Applications of HPLC for such separations of monolayer protected clusters were outlined in a recent article.[51]

2.6.2 Ligand-induced structural transformations

Attempts to carry out ligand exchange also changes size of the clusters in some cases. For example, reaction of Au_{11} clusters with a different thiol results in the formation of Au_{25}.[52] Li et al. have shown that complete conversion of core-shell Au_{25} into bi-icosahedral Au_{25} is possible through ligand-induced transformations.[53] This conversion is a three-step process involving small clusters such as Au_{13}, Au_{11}, etc., as shown in Fig. 2.7.

When an excess amount of thiol is used, etching of the cluster core to smaller sizes is observed. An example is shown in Fig. 2.8.[54] Mechanistic aspects of the etching process are not known completely. However, Dreier and Ackerson have shown that oxygen or free radical initiator facilitates the etching process.[55]

It was shown that ligand exchange of $Ag_{35}(SG)_{18}$ in a biphasic liquid–liquid system leads to clusters with different cores depending on the nature of the ligand used. For example, when 4-fluorothiophenol (4-FTP) was used, $Ag_{35}(SG)_{18}$ was converted to $Ag_{44}(FTP)_{30}$.[56] Interestingly, this transformation was reversible with a slower kinetics than the forward reaction.

Mechanistic pathways of these chemical transformations have not been understood in detail. Ligand exchange strategy was adopted to transform $Ag_{44}(SR)_{30}$ into $Ag_{25}(SR)_{30}$, as shown in Fig. 2.9.[57]

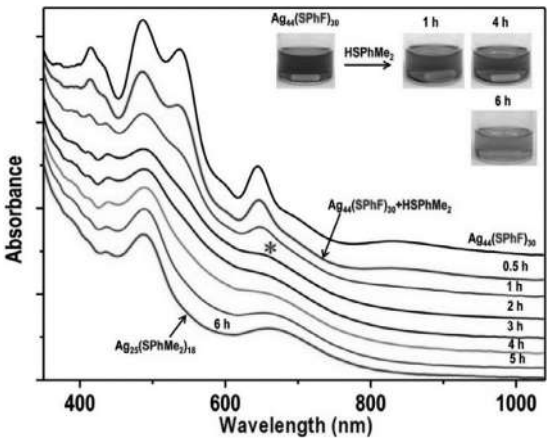

FIGURE 2.9 UV/Vis absorption spectra showing the ligand exchange of $Ag_{44}(SPhF)_{30}$ with $HSPhMe_2$. The asterisk on the spectrum for 2 h indicates the broadening and red-shifting of the 644 nm peak. (Reproduced with permission from, ref.[57]).

2.6.3 Substitution of metal atoms

Metal atom substitution can be achieved by reactions of clusters with a variety of heterometal atom sources such as simple metal ions, metal–ligand complexes, metal nanoparticles or clusters themselves, etc. One of the hurdles that limits our understanding of many of the alloy cluster systems such as $Au_{25-x}Ag_x(SR)_{18}$ and $Au_{38-x}Ag_x(SR)_{24}$ is their existence as a mixture. It is necessary to separate or isolate the mixture of alloy clusters into individual alloy clusters (containing precise numbers of metal atoms and ligands) for better understanding of their properties. Achieving the site-selective metal atom substitution in these reactions is still a big challenge. A few examples of successful site-selective metal atom substitution will be discussed in Sections 2.9.2, 2.10.2.1, 2.10.2.2, and 2.11.3. In the following sections, we outline various approaches to substitute or exchange metal atoms in a given cluster.

2.6.3.1 Substitution by coreduction

Earlier efforts to synthesize heterometallic clusters mainly utilized coreduction of individual precursor salt solutions. For example, Fields-Zinna et al. reported, for the first time, a heterometallic cluster, $Au_{24}Pd(SR)_{18}$, by coreducing a mixture of $HAuCl_4$ and $PdCl_2$ solutions using sodium borohydride in presence of suitable thiols.[58] Several bimetallic clusters such as $Au_{25-x}M_x(SR)_{18}$, $Au_{38-x}M_x(SR)_{18}$, $Au_{144-x}M_x(SR)_{60}$, (M = substituent metal atom), etc., have been synthesized using this method. Alloy clusters such as $Ag_{44-x}M_x(SR)_{30}$ (M = Au, Cu) and $Ag_{25-x}M_x(SR)_{18}$ (M = Au, Pt, Pd) were also reported. Li et al. have demonstrated that heavily doped $Au_{25-x}Ag_x$ clusters can be synthesized, wherein Ag atoms are located not only at the I positions but also at the S positions.[59] Now we discuss briefly the synthesis of heterometallic clusters using different types of heterometal atom sources.

2.6.3.2 Metal–ligand complexes as heterometal atom source

Substitution of metal atoms can be achieved by reactions of clusters with metal-thiolate and metal-phosphine complexes. Wang et al. have shown that the reaction between $Au_{25}(SR)_{18}$ and metal-thiolate complexes can be used to incorporate metal atoms such as Cu, Ag, Cd, and Hg, as shown in Fig. 2.10.[60]

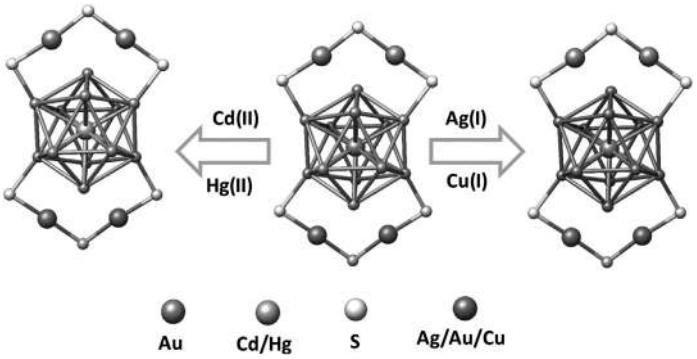

FIGURE 2.10 Metal exchange process of $Au_{25}(SR)_{18}$ using metal complexes with the metal core size preserved. Only part of the $Au_{25}(SR)_{18}$ structure is shown: the icosahedral Au_{13} core surrounded by two $Au_2(SR)_3$ motifs. (Reproduced with permission from, ref.[60]).

Trimetallic clusters have also been synthesized using a two-step metal exchange reaction. For example, $Au_{25}(SR)_{18}$ clusters were reacted with Ag(I)-thiolates to produce $Au_{25-x}Ag_x(SR)_{18}$ which was further reacted with Cd(II)- or Hg(II)-thiolates leading to trimetallic clusters, $Au_{24-x}Ag_xM_1(SR)_{18}$ (M_1=Cd/Hg).[61] Recently, Bootharaju et al. demonstrated that the reaction between $Ag_{25}(SR)_{18}$ and Au(III)-ligand complexes produced $Au_1Ag_{24}(SR)_{18}$.[62] This reaction will be discussed in detail in a later section.

2.6.3.3 *Metal ions as heterometal atom source*

Reaction of clusters with simple metal salts also results in substitution of metal atoms. For example, the addition of Ag(I) ions into a solution of anionic $Au_{25}(SR)_{18}$ resulted in the formation of $Au_{25-x}Ag_x(SR)_{18}$ clusters.[63] A redox model has been proposed for the reaction between the cluster and the Ag(I) ion. The neutral $Au_{25}(SR)_{18}$ has also been shown to be reactive with Ag(I) and Cu(II) ions.[64] These reactions resulted in a change in the oxidation state of these ions to Ag(0) and Cu(0) which indicate the occurrence of redox reaction between the atomically precise clusters and these metal ions. Liao et al. have shown that $Au_{24}Hg_1(PET)_{18}$ can be obtained exclusively by the reaction of $Au_{25}(PET)_{18}$ with Hg(II) salts.[65] Galvanic reduction reactions between clusters and metal ions also were utilized to synthesize alloy clusters. For instance, Udayabhaskararao et al. have synthesized Ag_7Au_6 cluster through the reaction between a mixture of $Ag_{7,8}$ clusters with $HAuCl_4$.[66] Reactions of clusters with metal ions have also been shown to simply add the heterometal atoms without substituting the metal atoms in the cluster. For example, Yao et al. recently demonstrated that $Au_{25}Ag_2(SR)_{18}$ could be synthesized by mixing acetonitrile solutions of $AgNO_3$ and $Au_{25}(SR)_{18}$.[67] Note that no Au was replaced in this reaction. Density functional theory (DFT) calculations suggest that probable location of Ag could be on the staples of the $Au_{25}(SR)_{18}$ and not in the Au_{13} core.

2.6.3.4 *Nanoparticles and clusters as heterometal atom source*

Metal nanoparticles or clusters themselves can also act as the source of heterometal atoms in metal atom substitution reactions. Xia et al. have shown that nanoparticles can be used as the source of heterometal atoms for substitution reactions.[68] In a similar attempt, Zhang et al. have shown that the reaction between $Au_{38-x}Ag_x$ and Au_{38} clusters results in the incorporation of Ag atoms into undoped Au_{38}.[69] These reactions, known as intercluster or interparticle reactions, will be discussed in greater detail in Section 2.9.

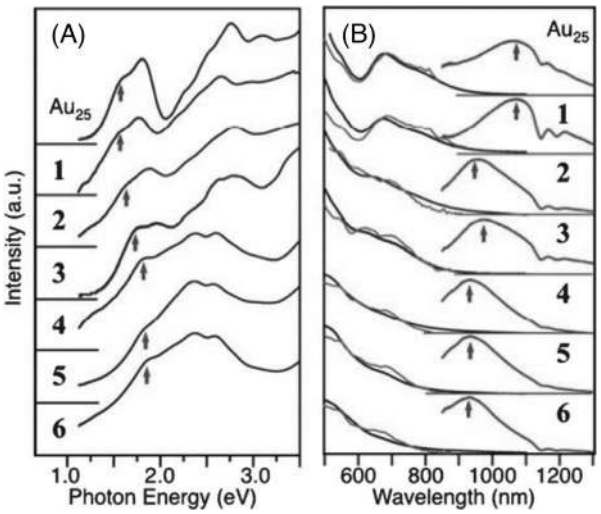

FIGURE 2.11 (A) Optical absorption spectra and a comparison (B) of optical absorption (dark gray, left), photoemission (dark gray, right), and photoexcitation (light gray, left) spectra of the toluene solutions of $Au_{25}(SC_{12}H_{25})_{18}$ and a mixture of alloy clusters of the general formula $Au_{25-n}Ag_n(SC_{12}H_{25})_{18}$ with values of $n = 1$. The numbers 1–6 in (A) and (B) correspond to mixtures of alloy clusters, of the above formula, containing 1, 4, 6, 7, 8, and 10 Ag atoms, respectively (reproduced with permission from ref.[74]).

2.6.3.5 *Metal atom substitution for tuning the properties*

In some cases, metal atom substitution in clusters results in enhancement of their stability[70,71] and their properties such as catalytic activity, photoluminescence,[72,73] etc. For example, Negishi et al. have shown that absorption and emission features of $Au_{25-x}Ag_x(SR)_{18}$ could be modulated by Ag doping, as shown in Fig. 2.11.[74]

2.7 Electrochemical properties of metal clusters

Electrochemistry provides an alternative tool (apart from absorption and emission spectroscopies) for visualizing systematic changes in electronic structure as a function of particle size and composition. Bulk electrodes of Ag and Au are commonly used in various electrochemical techniques. Electrodes were also modified with nanoparticles of these metals for various applications.[75–77] The redox potentials of the (bulk) Ag and Au electrodes correspond to the electronic structure of bulk metals. In this context, a few fundamental questions that arises are what would be the redox potentials when a bulk electrode is reduced to nanoscale dimensions? Or, can the nanoparticles or clusters be considered as nanoscale electrodes? These aspects have been described in a few reviews by Arnim Henglein.[8,78] His experiments demonstrated that the reactions that are not feasible in the bulk occur in the size regime of colloids. He also studied the size-dependent changes in the redox potentials of colloids in solutions.[8,9] Henglein's work showed that metal colloids in solution act as electron donors and acceptors.

One of the electrochemical signatures of particles at the nanosize regime is the appearance of quantized double layer charging, that is, the occurrence of distinct peaks in the voltammogram for every single addition or removal of electrons.[79–83] For example, differential pulse voltammogram of Au_{147} (upper panel of Fig. 2.12) shows a series of peaks.[84] These peaks correspond to the sequential redox processes of the cluster. Significant changes occur when the size of the particle is further reduced to the regime of atomically precise clusters. In this size regime of $\sim$2 nm, a few, well-separated peaks appear in the voltammogram compared to the multiple, equally spaced peaks observed in the case of the larger nanoparticles. This is shown in the

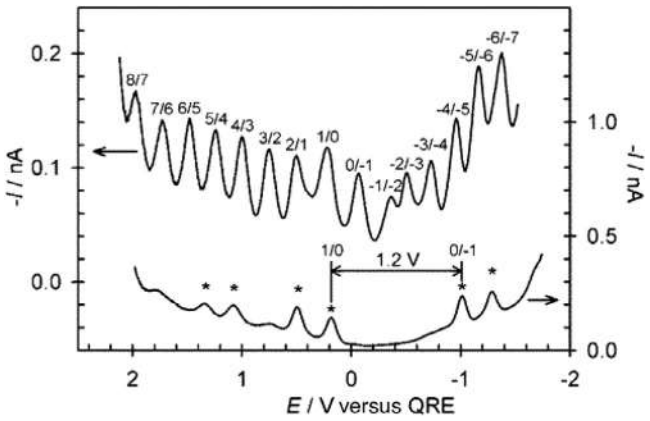

FIGURE 2.12 Differential pulse voltammogram (DPV) responses for solutions of hexanethiol-protecetd monolayer protected clusters of Au_{147} (upper) and Au_{38} (lower). The distinct HOMO–LUMO gap for the smaller cluster, Au_{38}, is marked. (Reproduced with permission from ref.[84]).

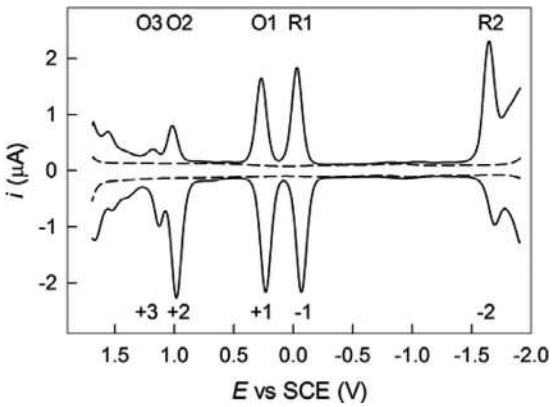

FIGURE 2.13 Differential pulse voltammogram (DPV) of neutral $Au_{25}(SR)_{18}$. The dashed lines show the corresponding background contribution. The peaks labeled (top) correspond to distinct charge states of the clusters as indicated (bottom) (reproduced with permission from ref. [85]).

lower panel of Fig. 2.12 which shows that for the smaller cluster, only a few redox states are possible. This difference arises due to further quantum confinement of the electronic energy levels in the clusters due to the molecular size of the clusters.

This confinement results in discrete electronic energy levels and distinct charges states, which cannot exist in larger nanoparticles. Thus, the monolayer protected clusters show distinct charge states. To give another example, $Au_{25}(SR)_{18}$ exist as cation, anion, and neutral species. Differential pulse voltammetry of this cluster shows distinct redox peaks for each of these charge states, as shown in Fig. 2.13.[85] Zhu et al. have shown that the anionic and neutral clusters can be reversibly converted from one charge state to the other by means of common oxidizing or reducing agents, as shown in Fig. 2.14.[86]

Electron transfer reactions[87–92] and electrogenerated chemiluminescence[93,94] of these clusters are also studied by various research groups.

Various charge states of these clusters have also been studied by EPR spectroscopy.[85,86] Redox processes of Au_{25} have been utilized to develop electrochemical sensors. For example, an Au_{25}-ZnO nanorod hybrid system was developed by Baek et al., for the electrochemical sensing of alkaline phosphatase using amperometric analysis.[95]

In the following three sections, we discuss two types of reactions wherein it is important to consider the redox properties of ligand-protected noble metal clusters.

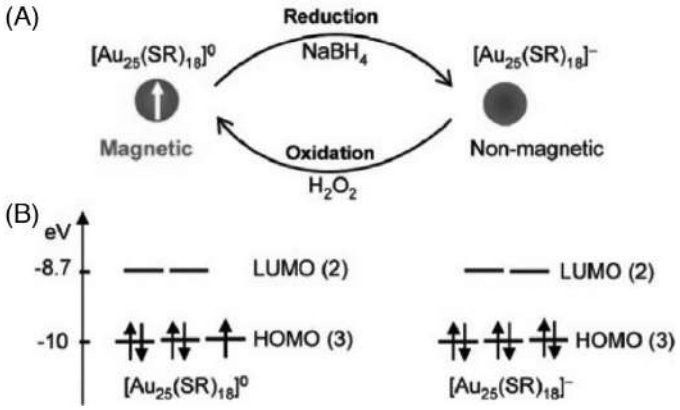

FIGURE 2.14 (A) Reversible conversion between the neutral and anionic $Au_{25}(SR)_{18}$. (B) DFT-calculated Kohn–Sham orbital energy level diagrams for the neutral and anionic clusters, respectively (reproduced with permission from ref.[86]).

2.7.1 Reactions with metal ions

In the previous section, it was mentioned that the redox properties of metals change with their size and as the size decreases to subnanometer size regime, distinct redox features appear. Now let us see what happens when an atomically precise noble metal cluster interacts with ions of reactive metals. Such interactions alter the absorption and emission features of the clusters. These changes have been utilized for the detection of toxic metal ions such as Hg(II), Cu(II), As(III), Cr(III), etc.[96–105]

Muhammed et al. observed, for the first time, that $Au_{25}(SG)_{18}$ reacts instantaneously with tetrachloroaurate anions leading to its decomposition.[106] Ions such as Ag(I), Fe(III), Cu(II), Ni(II), Cd(II), Zn(II), and Sr(II) also decomposed these clusters to Au-thiolates at a slower rate. X-ray photoelectron spectroscopic measurements showed that Hg(II), Hg(I), Pb(II), Cd(II), etc., interact with the core as well as the functional groups (such as –COOH, -OH, etc.) of the ligands protecting Ag NPs and Ag clusters.[107] Interaction with the core resulted in the reduction of Hg(II) and Hg(I) to Hg(0) while Cd(II) and Pb(II) did not undergo any reduction. Considering the standard reduction potentials which correspond to bulk metals, one may find that these reactions cannot occur. At the size regime of nanocrystals and clusters, electronic energy levels are significantly quantized, resulting in discrete electronic energy levels. This makes the redox properties of the metal clusters different from that of the bulk metal.

Chakraborty et al., have shown that $Ag_{25}(SG)_{18}$ selectively reacts with Hg(II) which decreases the intensity of the UV/Vis absorption features of the cluster, as shown in Fig. 2.15. The reaction resulted in the formation of alloys such as Ag_3Hg_2.[108] The shift or the decrease in the intensity of absorption spectral bands was quantitative *w.r.t.* the concentration of Hg(II), enabling its detection at the lowest limit of 1 ppb.

Metal ions can quench the fluorescence of the clusters by several mechanisms. Energy transfer mechanisms such as Förster resonance energy transfer and Dexter energy transfer as well as electron transfer can occur between the cluster and the metal ions causing fluorescence quenching. Metallophilic interactions, that is, weak, attractive interactions between electronically closed-shell species, also cause fluorescence quenching of clusters. These interactions are common in inorganic complexes.[109–111] Metallophilic interactions are rarely studied in the case of monolayer protected clusters. Theoretical calculations by Pykko et al. considered

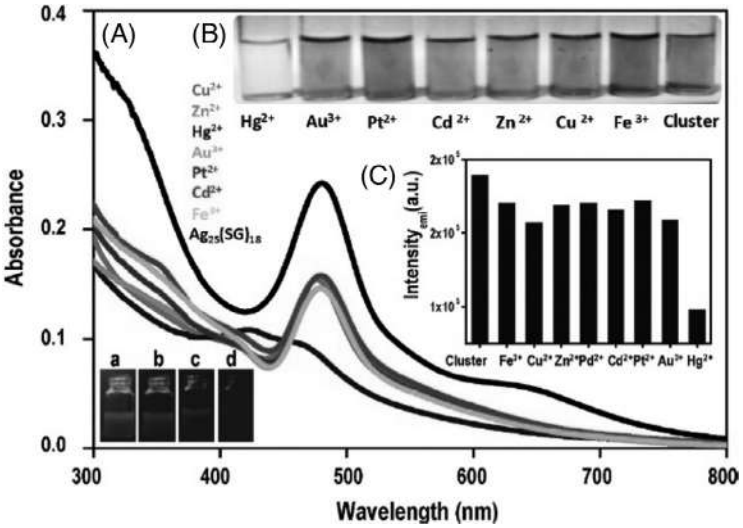

FIGURE 2.15 UV/Vis absorption spectra of various metal ions (10 ppm concentration) which are added to aqueous Ag_{25} cluster solution (A). Photographs of corresponding solutions under visible light (B). Effect of various metal ions (10 ppm) on the emission intensity of Ag_{25} cluster (C). Below the UV/Vis spectra, photographs (under UV excitation) depicting fluorescence quenching are given for the phase transferred cluster (a) upon addition of, 1 ppm (b), 2 ppm (c), and 10 ppm (d) solutions of Hg(II). (Reproduced with permission from, ref.[108]).

the possibility of such interactions between an Au_n cluster and closed-shell ions. This is of relevance to clusters such as $Au_{25}(SR)_{18}$ which has a Au_{13} core surrounded by Au(I)-SR (wherein Au(I) is a closed shell species) units. Also, as mentioned above, chemical changes of the core such as alloying (as in the previous example) or decomposition of clusters also affects their luminescence. Investigations of these interactions will provide insights about the metal ion-induced changes in absorption and emission and such changes also provide suggestions about their stability.

2.7.2 Reactions with halocarbons

Bulk silver electrodes have been used extensively to study dehalogenation of halocarbons in the context of electrocatalysis and heterogeneous electron transfer reactions.[112–117] High negative potentials are required for these reactions to occur on bulk Ag electrodes. As explained in the previous sections, it is interesting to see what happens when we use nanoparticles or atomically precise silver clusters for these reactions. Thiolate-protected Ag clusters and nanoparticles react spontaneously (without the application of an external voltage) in solution with halocarbons producing elemental carbon, AgCl, and Ag-thiolates.

Bootharaju et al. have shown that Ag_9 clusters react with CCl_4 in presence of isopropyl alcohol (IPA) to form AgCl, acetone and elemental carbon.[118] IPA is believed to play an important role in mediating the electron transfer between the cluster and the halocarbon. A schematic of the reaction is shown in Fig. 2.16.

Halogenated pesticides such as chlorpyrifos, etc., could also be decomposed readily by reaction with Ag nanoparticles.[119,120] It has been shown that reduced graphene-oxide silver (RGO@Ag) composite can be used to decompose γ-lindane, (hexachloro cyclohexane, a persistent pesticide) almost completely to AgCl and trichlorobenzenes.[121] RGO alone did not cause any decomposition of the pesticide. Control reactions with Ag@citrate NPs and elemental Ag showed very little degradation of this pesticide. These experiments showed that synergistic effect due to the RGO and the Ag in the composite is pivotal role in the decomposition.

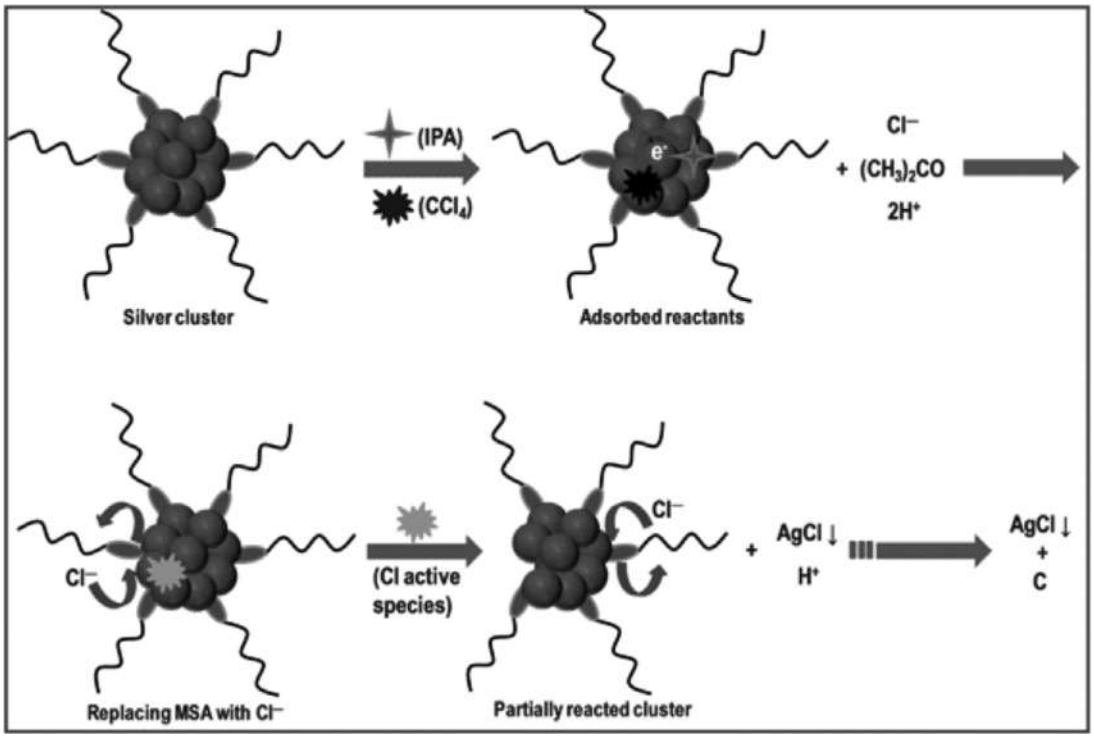

FIGURE 2.16 Schematic representation of the degradation of halocarbon, CCl_4, by silver clusters along with other chemical transformations. Some of the chemical species detected are not marked. (Reproduced with permission from ref.[118]).

2.8 Stereochemistry of ligand protected atomically precise metal clusters

Chirality is a fascinating phenomenon and a crucial factor determining the functions of biomolecules.[122,123] Chirality in nanomaterials has become an important aspect of nanoscience research.[124] Chirality in plasmonic nanomaterials is now an interdisciplinary field involving chemists, physicists, and biologists.[124–128]

Chirality in thiolate protected, atomically precise metal clusters has been theoretically predicted in many systems.[129,130] As mentioned earlier, these clusters possess a discrete metal core, and a metal–ligand interface consisting of metal–ligand oligomeric units and the tail groups of the protecting ligands. Chirality in such metal clusters arise from the various reasons associated with these structural components and some of these are briefly mentioned below.

2.8.1 Chirality due to the presence of chiral ligands

One of the strategies to synthesize chiral clusters is to use chiral protecting ligands. The use of a chiral ligand in order to induce chirality in ligand-protected clusters was experimentally demonstrated for the first time by Schaff et al., wherein glutathione was used as the ligand.[131]

Several other chiral ligands were used to synthesize chiral nanoclusters.[132–134] However, when a chiral molecule is used as the ligand, the chiroptical signatures of the metal core are believed to induce the transfer of chirality from the chiral ligand to the achiral metal core. This phenomenon is referred to as chirality induction. However, the exact mechanism of the chirality induction is not completely understood. In general, the induction of chirality in these systems can be argued as expected phenomena because of the presence of a chiral molecule on the metal core. In this context, achieving chirality in metal clusters or plasmonic nanosystems without the using achiral ligand or template has been considered challenging and inetersting.

2.8.2 Chirality due to the chiral arrangement of achiral ligands on achiral metal core

In 2007, Kornberg et al. reported the chirality of Au_{102} clusters, wherein no chiral ligand was used.[44] In this case, chirality resulted from the helical arrangement of the thiolate staple motifs. However, the separation of enantiomers of these clusters has not been achieved to date. The challenge of separating the enantiomers of the intrinsically chiral monolayer protected clusters was achieved for the first time by Dolamic et al.[41] They separated enantiomers of Au_{38} clusters using chiral HPLC. In this case also, the helical arrangement of the staple motifs on the cluster core is the reason for the overall chiral geometry of the clusters, as shown in Fig. 2.17.

The same group has shown that Au_{40} clusters are intrinsically achiral.[135] Zeng et al. reported intrinsic chirality of Au_{28} clusters which originates from the arrangement of staple motifs.[136] Enantiomers of this cluster were also separated by chiral HPLC. In many of the early examples, chirality of the monolayer protected clusters is believed to be originating from the chiral arrangement of the staple motifs than due to the inner metal core. However, vibrational circular dichroism measurements on $Au_{38}(PET)_{24}$ (Fig. 2.18) show that the metal core transfers chirality to the ligands.[137] This implies that an achiral molecule such as 2-PET adopts a chiral conformation, as shown in Fig. 2.18A. Note that the conformation of 2-PET molecule on the surface of $Au_{38}(SR)_{24}$ is chiral while the unbound 2-PET is an achiral molecule. This gives further evidence of the electronic interaction between ligands and metal atoms of the core. Circular dichroism measurements have been employed to probe the surface flexibility of these metal clusters. For example, measurements on the Au_{38} and its Ag-doped alloys, i.e., $Au_{38-x}Ag_x$, have shown that racemization of the enantiomers is faster for the alloys compared to the undoped clusters.[138] This shows that the surface of the Ag-doped Au_{38} is more flexible compared to that of undoped Au_{38}. In all of the above cases, chirality originates from the inherently chiral ligands or chiral arrangements of achiral ligands. However, chirality of the alloy clusters originating from a chiral metal core has not been reported so far. This is especially interesting since many unique positions are available (as mentioned earlier) for a substituent metal atom in these clusters. Chiroptical properties of metal clusters are promising considering the possibilities of chiral catalysis, enantioselective sensing, etc. In the future, synthetic methods for selective formation of the cluster enantiomers are also expected.

2.8.3 Chirality due to inherently chiral metal core

Noble metals such as Au and Ag possess achiral crystal structures in their bulk form. However, atomically precise clusters can have atomic packing which is different from their

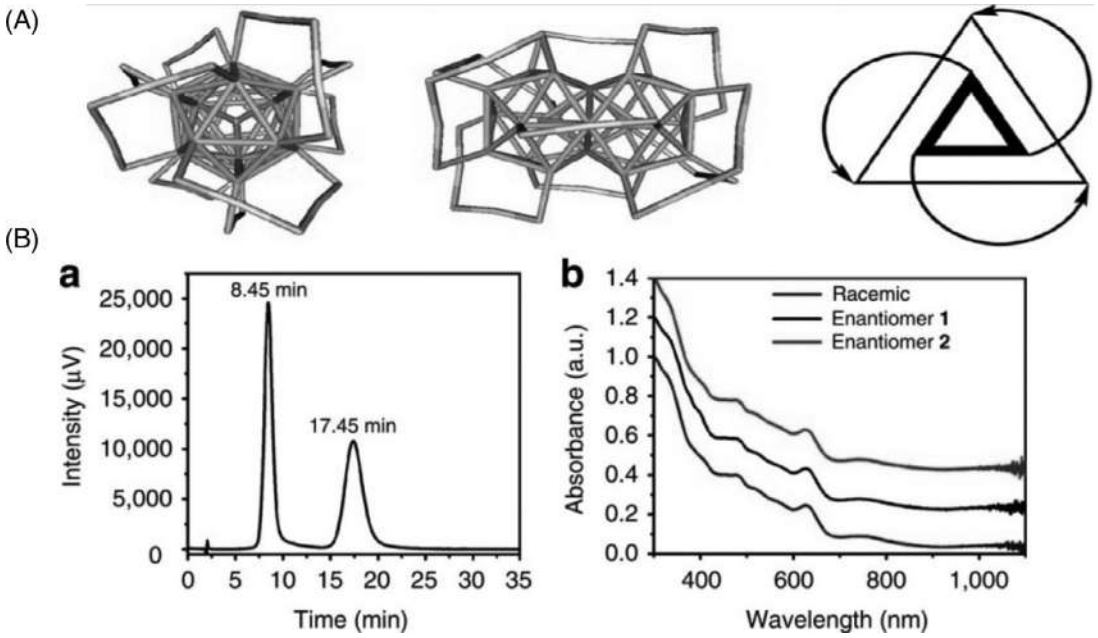

FIGURE 2.17 (A) Crystal structure of the left-handed enantiomer of $Au_{38}(SCH_2CH_2Ph)_{24}$. The -$CH_2CH_2Ph$ ligands are not shown for clarity. (left) Top view of the cluster; (middle) side-view; (right) schematic representation highlighting the handedness of the cluster. The top three core atoms in (A) binding to the long staples are shown by the inner triangle. The long staples are represented by arrows. The outer triangle represents the core Au atoms binding to the "end" of the staple. This representation is a top view along the C_3 axis, and the two triangles are not in one plane. (B) (**a**) HPLC-chromatogram of the enantioseparation of *rac*-$Au_{38}(SCH_2CH_2Ph)_{24}$ with the ultraviolet-visible detector at 380 nm. The peak at 8.45 min corresponds to enantiomer **1**; the second peak at 17.45 corresponds to enantiomer **2**. (**b**) Ultraviolet-visible spectra of enantiomers **1** (middle trace) and **2** (uppermost trace) and of the racemate (lowest trace). The well-known ultraviolet-visible signature of Au_{38} is perfectly reproduced in all spectra, showing that the two collected fractions are composed of $Au_{38}(SCH_2CH_2Ph)_{24}$. (Reproduced with permission from, ref.[41]).

bulk crystal structure. Even more interesting is the situation, wherein the atomic arrangement of the inner cores of ligand protected clusters has a chiral geometry. An example of such a cluster is presented in Fig. 2.19. Here, the inner Au_{20} core has a chiral geometry while the protecting ligands are achiral.[139]

2.8.4 Chirality due to encapsulation into chiral supramolecules or hosts

Chiroptical signatures in metal clusters can be induced by encapsulating them into macromolecules such as cyclodextrins.[140] For example, Ag_{15} clusters protected with glutathione entrapped in a cyclodextrin cavity show interesting chiroptical signatures (See Fig. 2.20). This supramolecular cluster exhibits intense circular dichroism which coincides with one of the optical absorption features of the cluster. This can be due to the metal-based electronic transitions in clusters.

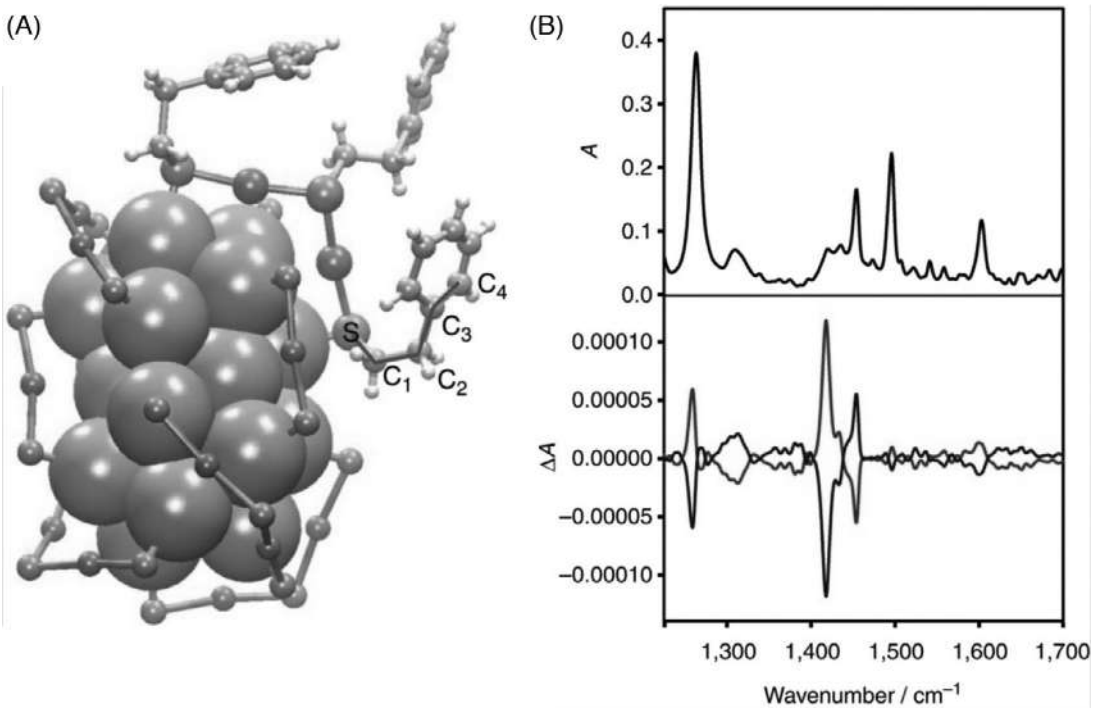

FIGURE 2.18 (A) Structure of the $Au_{38}(2\text{-PET})_{24}$ cluster. The 2-PET ligand is omitted for clarity except for one dimeric staple motif. For one 2-PET ligand the bonds relevant for the discussion of the 2-PET conformation are marked ($S–C_1–C_2–C_3–C_4$). Within the staple shown the center, 2-PET molecule adopts an anticonformation around the $C_1–C_2$ bond, whereas the other two molecules are in gauche conformation. (B) Infrared spectrum of A-$Au_{38}(2\text{-PET})_{24}$ (upper panel) and vibrational circular dichroism (VCD) spectra of enantiomer 1 (A-$Au_{38}(2\text{-PET})_{24}$, upward trace) and of enantiomer 2 (C-$Au_{38}(2\text{-PET})_{24}$, downward trace) (reproduced with permission from, ref.[137]).

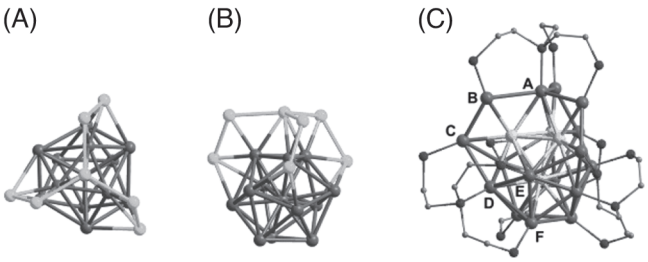

FIGURE 2.19 Top view (A), side view (B) and the bridging mode of PP_3 ligand (C) of the Au_{20} core structure in $[Au_{20}(PP_3)_4]^{4+}$. The phenyl groups have been omitted for clarity. Color codes: Au in Au_{13} icosahedron (dark gray), 7 Au atoms capping the Au_{13} icosahedron (light gray), P (smaller dark gray), C (smallest light gray). Note that the Au_{20} core structure in (A) is chiral. (Reproduced with permission from ref.[139]).

2.8.5 Chirality in metal clusters: structure-property correlations

The quantification of chirality of these clusters in terms of the contributions (to the chiroptical responses) of their structural components, that is, metal core, staples or mounts, and the organic tail groups of the ligands, can be addressed by Haussdorf–Chirality Measurement (HCM) values of these clusters.[141] This concept is based on Haussdorf's concept of distances

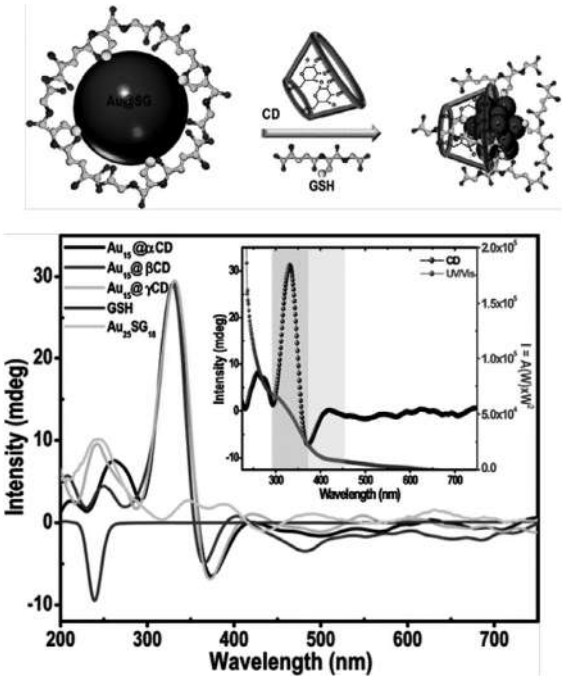

FIGURE 2.20 Schematic illustration of cyclodextrin (CD)-assisted one-pot synthesis of light-emitting gold quantum clusters (QCs) via the core etching reaction. Circular dichroism spectra of $Au_{15}@\alpha$CD, $Au_{15}@\beta$CD $Au_{15}@\gamma$CD clusters along with pure GSH and $Au_{25}SG_{18}$. The positive Cotton peak at ~330–380 nm and a negative Cotton peak at ~400–455 nm are attributed to the cluster core. Inset shows the combined plot of absorption and CD spectra of $Au_{15}@\alpha$CD, with one-to-one matching. (Reproduced with permission from, ref.[140]).

between two sets.[142] When this concept is applied to (chiral) molecules, the sets being considered are the atomic coordinates of the rigid molecular structures (enantiomers). In the context of ligand-protected metal clusters, this approach addresses the following questions: (1) is it possible to quantify and compare consistently the index or amount of chirality between different chiral clusters? And (2) is it possible to gain additional insights into the origin of chirality in terms of the atomic structure of a chiral cluster? The calculated HCM values of a few such clusters are shown in Fig. 2.21.

2.9 Intercluster reactions

In the previous sections, we mentioned that spectroscopic and mass spectrometric investigations unambiguously prove the molecule-like behavior of ligand-protected noble metal clusters. Can these clusters react just like common molecules? Can we understand these reactions just as we study the reactions using the common concepts of chemistry? These clusters indeed react with each other and a few examples of such intercluster reactions[143] are presented in the following sections.

2.9.1 Reaction between $Au_{25}(PET)_{18}$ and $Ag_{44}(FTP)_{30}$

Let us consider the reaction between $Au_{25}(PET)_{18}$ and $Ag_{44}(FTP)_{30}$.[144] A schematic of the crystal structures of these clusters is shown in Fig. 2.22. When the solutions of these clusters are mixed together, these clusters exchange their metal atoms, ligands, and metal–ligand

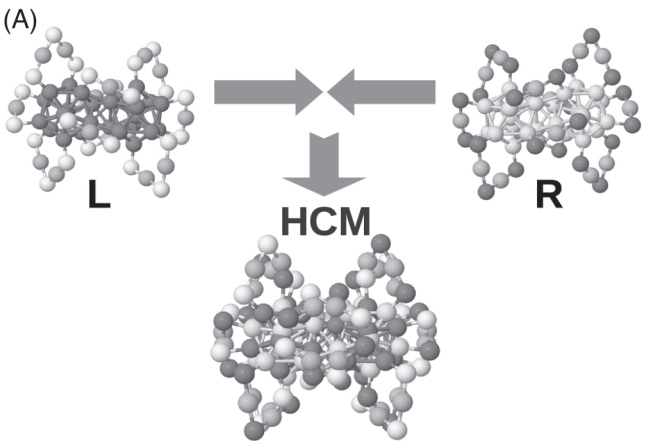

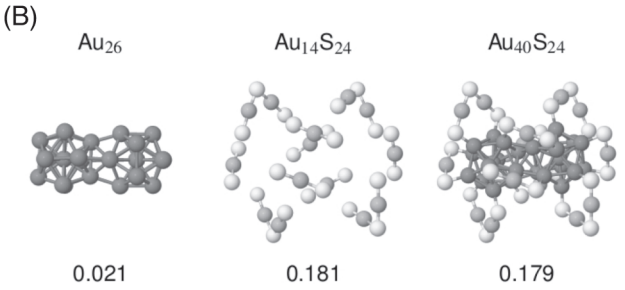

FIGURE 2.21 (A) Graphical representation of the Hausdorff Chirality Measure (HCM) of a ligand protected gold cluster: $Au_{40}S_{24}$. The left-handed and right-handed enantiomers of this clusters are labeled as L and R, respectively. The L and R structures are superimposed in the structure labeled as HCM. (B) HCM values of the the three structural units (Au_{26} core, $Au_{14}S_{24}$ shell and the complete $Au_{40}S_{24}$ framework) of $Au_{40}S_{24}$ cluster upon application of the divide and protect principle (core, ligands, complete system) ref.[141]).

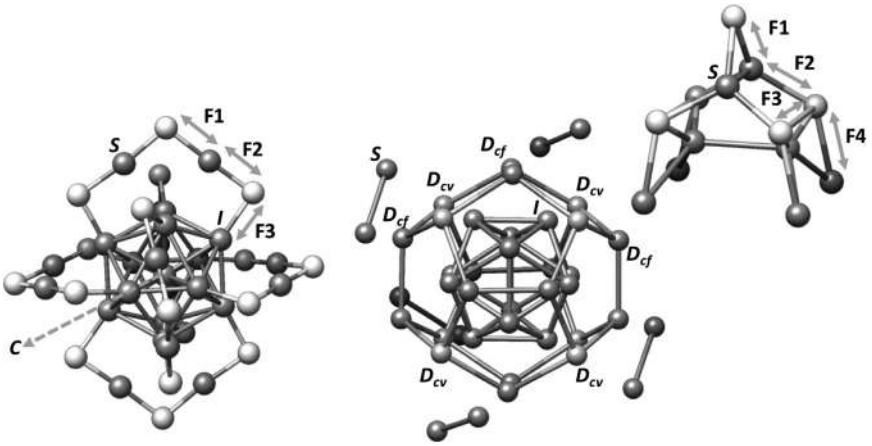

FIGURE 2.22 Schematic structures of the $Au_{25}(SR)_{18}$ (left) $Ag_{44}(SR)_{30}$ (right) showing symmetry-unique Ag and Au atom positions and Ag–S and Au–S bonds. Color codes and labels: Au/Ag: dark gray speheres, S: white speheres. Labels for unique metal atom positions: Au at the center of the Au_{13} icosahedron (C), Ag/Au in the icosahedral verteces (I), Ag at the vertices of the cube of the Ag_{20} dodecahedron (D_{cv}), Ag at the faces of the cube (D_{cf}). Ag (Au) in the mounts (staples) (S). F1–F4 are the distinct M–S (M = Ag or Au) bonds in $Au_{25}(SR)_{18}$ and $Ag_{44}(SR)_{30}$.

fragments to form alloy clusters. Fig. 2.23A and B shows ESI mass spectra of $Au_{25}(PET)_{18}$ and $Ag_{44}(FTP)_{30}$. Fig. 2.23C shows the mass spectra showing the products, that is, the alloy clusters formed from $Au_{25}(PET)_{18}$ by exchange of metal atoms (Au-Ag exchange), ligands (PET–FTP exchange), and metal–ligand fragments (Au-PET- Ag-DMBT exchange). Similarly, the Au atoms, PET ligand, and Au-PET fragments are also exchanged with $Ag_{44}(FTP)_{30}$ resulting in the formation of Ag-rich alloy clusters. (see Section 2.9.2 to see in detail what happens to $Ag_{44}(FTP)_{30}$ in such a reaction).

The most important aspect of this reaction is that the total number of metal atoms, ligands, the overall structural features, and the charge states of the clusters are preserved. Therefore, this reaction can be written as:

$$Au_{25}(PET)_{18} + Ag_{44}(FTP)_{30} = Au_{25-m}Ag_m(PET)_{18-n}(FTP)_n + Ag_{25-m}Au_m(PET)_{18-n}(FTP)_n$$

2.9.2 Reaction between $Au_{25}(FTP)_{18}$ and $Ag_{44}(FTP)_{30}$: Shell closing effects in intercluster reactions

In the previous section, we mentioned that the Au atoms, PET ligand, and Au-PET fragments are also exchanged with $Ag_{44}(FTP)_{30}$ when it is reacted with $Au_{25}(PET)_{18}$ resulting in the formation of Ag-rich alloy clusters. The mass difference between PET and FTP ligands is only 10 Da. The smaller mass difference of ligands makes the assignment of peaks due to ligand as well as fragment exchange complicated because of multiple charges states of $Ag_{44}(FTP)_{30}$ and alloys derived from it. Therefore, we consider now the reaction between $Au_{25}(FTP)_{18}$ and $Ag_{44}(FTP)_{30}$, with same ligands.[145] This allows us to clearly observe interesting effects due to the Au atom substitution into $Ag_{44}(FTP)_{30}$; exchange of ligands and metal–ligand fragments will not be detected because of the equal molecular masses of the ligands.

As we see in Fig. 2.24, substitution of Ag atoms by Au atoms into $Ag_{44}(SR)_{30}$ results in the formation of alloy clusters of the general formula, $[Ag_{44-x}Au_x(FTP)_{30}]^{4-}$. When the reaction is monitored in a time-dependent fashion, we see that $[Au_{12}Ag_{32}(FTP)_{30}]^{4-}$ appears to be the most abundant product in the 4^- region of the mass spectrum. Note that no such alloy clusters with more than 12 Au atoms, that is, clusters such as $[Au_{13}Ag_{31}(FTP)_{30}]^{4-}$, $[Au_{14}Ag_{30}(FTP)_{30}]^{4-}$, $[Au_{15}Ag_{29}(FTP)_{30}]^{4-}$, etc., were not detected.

An increase in the concentration of $Au_{25}(FTP)_{18}$ did not result in the formation of $[Au_xAg_{44-x}(FTP)_{30}]^{4-}$ with more than 12 Au atoms. These observations clearly show that $[Au_{12}Ag_{32}(FTP)_{30}]^{4-}$ is formed as the most abundant species because of its extraordinary stability. (Note that clusters with more than 12 Au atoms were formed in the 3- charge states, this is not discussed here, see ref.[145] for details). DFT calculations suggest that the 12 Au atoms are located in the innermost M_{12} icosahedron and therefore, the innermost Ag_{12} shell is completely substituted by an Au_{12} shell. Also note, that $[Au_{12}Ag_{32}(FTP)_{30}]^{4-}$ is an eight electron superatom, similar to the parent $[Ag_{44}\ (FTP)_{30}]^{4-}$. This shows that geometric shell closing (i.e., innermost M_{12} shell is occupied by the same type of metal atoms) and the electronic shell closing (i.e., attainment of the supertaomic electronic configuration) could be the reasons for the extraordinary stability of $[Au_{12}Ag_{32}(FTP)_{30}]^{4-}$. This reaction demonstrates that two closed-shell clusters, $[Ag_{44}(SR)_{30}]^{4-}$ and $[Au_{25}(SR)_{18}]^-$, produce another closed-shell alloy cluster, $[Au_{12}Ag_{32}(SR)_{30}]^{4-}$, with its overall geometrical structure, electronic configuration, and charge states preserved.[145]

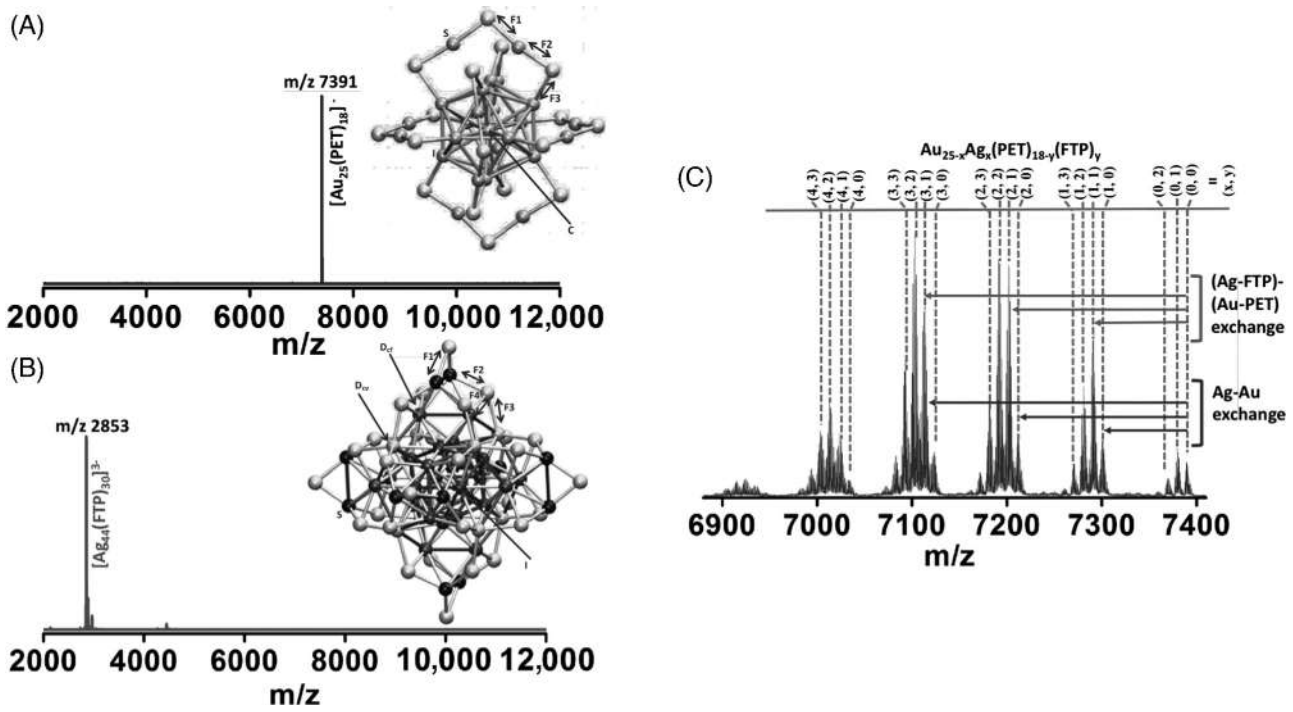

FIGURE 2.23 ESI mass spectra of (A) $Au_{25}(PET)_{18}$, (B) $Ag_{44}(FTP)_{30}$, and (C) a mixture of the two at $Au_{25}(PET)_{18}$:$Ag_{44}(FTP)_{30}$ molar ratio of 14.0:1.0 showing the formation of $Au_{25-x}Ag_x(PET)_{18-y}(FTP)_y$. Peaks at m/z 7391 in panel A and m/z 2853 in panel B are due to $[Au_{25}(PET)_{18}]^-$ and $[Ag_{44}(FTP)_{30}]^{3-}$, respectively. The numbers (x, y) of peak labels in (C) are according to the formula, $Au_{25-x}Ag_x(PET)_{18-y}(FTP)_y$. (Reproduced with permission from ref.[143]).

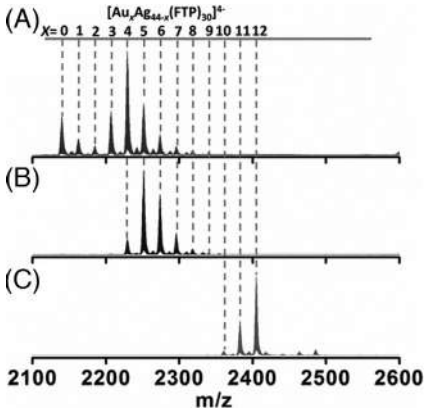

FIGURE 2.24 Mass spectra of the $[Au_xAg_{44-x}(FTP)_{30}]^{4-}$ clusters formed from $Ag_{44}(FTP)_{30}$ and $Au_{25}(FTP)_{18}$ at $Ag_{44}(FTP)_{30}$:$Au_{25}(FTP)_{18}$ molar ratios of 35.0:1.0 (A), 14.0:1.0 (B), and 5.0:1.0 (C). (Reproduced with permission from ref.[145]).

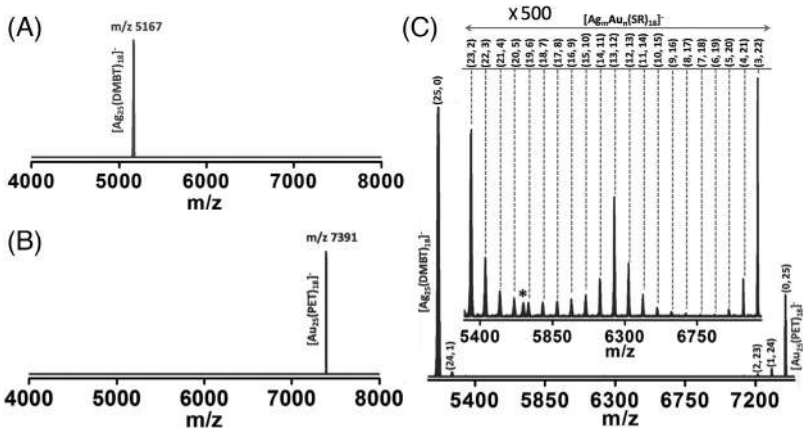

FIGURE 2.25 ESI mass spectra of $Ag_{25}(DMBT)_{18}$ (A), $Au_{25}(PET)_{18}$ (B), and a mixture of the two at a Ag_{25}:Au_{25} molar ratio of 0.3:1.0 measured within 2 min after mixing (C). The peak labels in (c) shown as numbers in red (m) and blue (n) in parentheses give the numbers of Ag and Au atoms, respectively, in the alloy clusters of formula $Ag_mAu_n(SR)_{18}$. The inset in (C) is the expanded region of the same mass spectrum between m/z 5.300 to 7.150. (c) and its inset shows that entire range ($n = 1$–24) of alloy clusters, $Ag_mAu_n(SR)_{18}$ ($m + n = 25$), are formed. The peak labeled with "*" in (c) is due to an unassigned dianionic species. (Reproduced with permission from ref.[146]).

2.9.3 Reaction between $Au_{25}(PET)_{18}$ and $Ag_{25}(DMBT)_{18}$

In the previous two reactions, the structure and composition of reacting clusters were different. Now let us consider two structurally and compositionally analogous clusters namely, $Au_{25}(PET)_{18}$ and $Ag_{25}(DMBT)_{18}$ wherein DMBT is 2,4-dimethylbenzenethiolate.[146] These two clusters possess common structural features, that is, M_{13} (Ag/Au) icosahedra, $M_2(SR)_3$ staple motifs. Fig. 2.25 shows the ESI mass spectra of these two clusters and the alloy clusters formed by the reaction between them. Similar to the previous examples, these clusters also exchange their metal atoms, ligands, and metal–ligand fragments to form alloy clusters. The molecular masses of PET and DMBT ligands are equal and therefore, features corresponding

to the exchange of ligands (PET-DMBT exchange) and the exchange of fragments (Au-PET–Ag-DMBT exchange) will not be observed in the mass spectrum. Therefore, this reaction can be written as:

$$Au_{25}(PET)_{18} + Ag_{25}(DMBT)_{18} = Au_{25-m}Ag_m(PET)_{18-n}(DMBT)_n + Ag_{25-m}Au_m(DMBT)_{18-n}(PET)_n$$

However, this is not a balanced chemical equation.

The number of metal atoms, ligands, and metal–ligand-fragments exchanged can be controlled simply by varying the concentrations of the two reactant clusters. Fig. 2.25C shows that within about 2 min of the reaction between these two clusters, alloy clusters with the entire range of $M_{25}(SR)_{18}$ compositions have been formed in solution. The most important aspect of this reaction is that the total number of metal atoms, ligands, the overall structural features (M_{13} icosahedral core, six $M_2(SR)_3$ staples) and the charge states of the clusters are preserved. Therefore, this reaction represents a unique example wherein the structure and the topology of the nanoparticle is conserved. This reaction will be discussed in detail later.

2.9.4 Dynamic nature of the clusters and intercluster reactivity

Various structural models have been proposed to understand the properties of atomically precise, ligand-protected metal clusters. One of the most popular models among them is the divide and protect model, wherein thiolate protected noble metal clusters, for example, have been viewed as consisting of a core of a definite number of metal atoms, protected with a well-defined shell of metal−ligand oligomeric complexes.[147] $Au_{25}(SR)_{18}$ wherein Au_{13} icosahedral core and the six $Au_2(SR)_3$ staples are present is the most popular example for this structural model. Electronic structure calculations show that the distinct electronic absorption features of these clusters (Fig. 2.3B inset) originate from various transitions between their discrete electronic energy levels. Therefore, crystallography and electronic structure calculations support this structural model of ligand-protected noble metal clusters. We need to address if these clusters really exist as distinct core and shell in solutions, or, are there any structural dynamics occurring in solution. Recent experiments unambiguously suggest that these clusters are highly dynamic in solutions. Therefore, this dynamicity could lead to intercluster reactivity. In order to understand the chemical reactivity of these clusters, it is necessary to consider other structural models which address the dynamic nature of metal–ligand interfaces of these clusters. We discuss some of these aspects in the following sections.

In this regard, the Borromean ring structural model of clusters is especially important.[148] According to this model, clusters such as $Au_{25}(SR)_{18}$ can be viewed as consisting of three interlocked $Au_8(SR)_6$ rings surrounding a central Au atom, ss, depicted in Fig. 2.26. The most important aspect of this model is the fact that the metal atoms (except that at the center) belong to a single structural unit, that is, metal-thiolate oligomeric rings. This is in contrary to the fact that according to the divide and protect model, metal atoms belong to two distinct structural units, that is, the innermost M_{13} icosahdedron and the six, outer $M_2(SR)_3$ staple units. The reason why this model has been named as Borromean ring model is due the fact that if one of these rings is broken, the other two becomes separated (which is the structural property of a Borromean ring construction). This implies that if one of the metal–sulfur bonds in any one

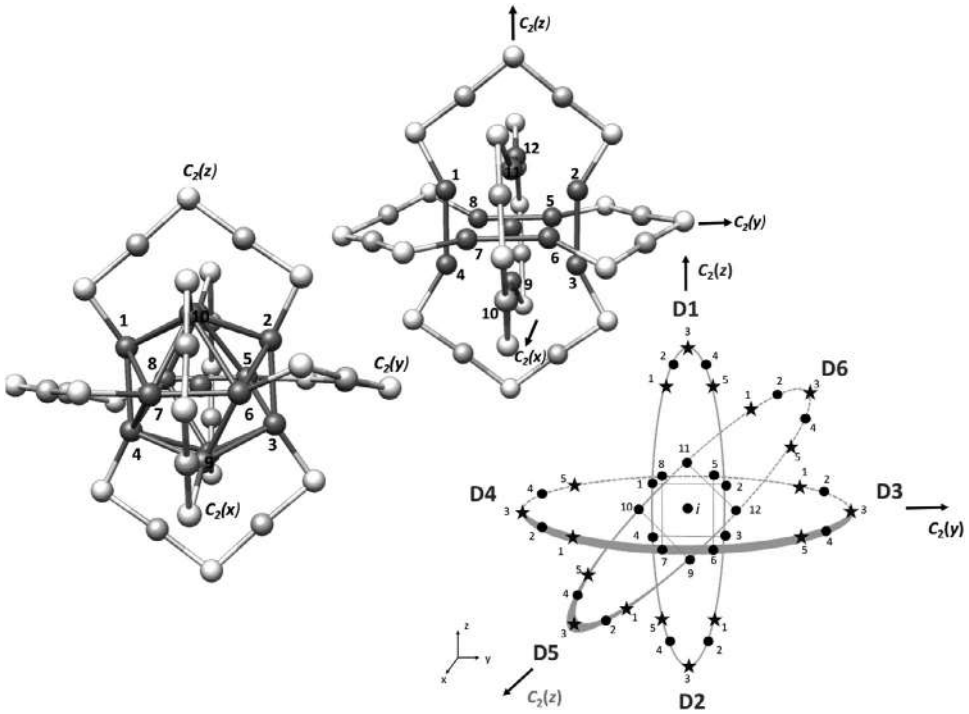

FIGURE 2.26 Borromean-rings diagram of $Au_{25}(S)_{18}$. The rings formed by pairs of coplanar staples are shown as ellipses. Gold atoms are shown by dots, and stars represent the S atoms of the ligands. The core Au atoms are numbered from 1 to 12, and the staple atoms are numbered clockwise from the end of the staple, from 1 to 5. The lines that join core Au atoms on opposite ends of the same staple are shown by the solid lines. The three perpendicular C2 axes are marked with the associated Cartesian axis direction in parentheses. The staple directions are labeled by the six staple locants D1–D6, marked in red. Inset (i) shows a 3D visualization of the ring structure of the core and staples of $Au_{25}(SR)_{18}$ aspicule, with each (Au_8S_6)-ring consisting of two coplanar staples and the core atoms that are bonded to these staples. The arrow indicates the angle of the anticlockwise rotation about the *y*-axis, needed to bring the icosahedron into a face-projected view of the face defined by the atoms 6, 7, and 9. (re-drawn from ref.[148]).

of these three rings is broken, the cluster can react easily with another cluster. Borromean ring model allows us to better address the intercluster reactivity in terms of the structural dynamics of the interlocked rings. This is discussed in more detail in one of the following sections.

When the metal atoms belong to a single structural unit, that is, the $M_8(SR)_6$ rings, we can ask the question: do the metal atoms (except the central atom) of $M_{25}(SR)_{18}$ (M=Ag/Au) are spectroscopically in the same environment? This question was addressed recently in the cases of $Ag_{25}(SR)_{18}$ and $Ag_{24}Au_1(SR)_{18}$ using ^{109}Ag NMR spectroscopy.[149] If the Ag atoms in $Ag_{25}(SR)_{18}$ existed distinctly as the central, icosahedral, and the staple ones, we expect three distinct features in the ^{109}Ag NMR spectrum. Surprisingly, only one feature was observed for $Ag_{25}(SR)_{18}$, as shown in Fig. 2.27. This indicates that the Ag atoms in the core and the staples are exchanged either in an intracluster fashion or in the intercluster fashion within the timescale of ^{109}Ag NMR measurements. The central Ag atom may not be able to exchange with others effectively, however, no other signal corresponding to the central Ag atom was observed.

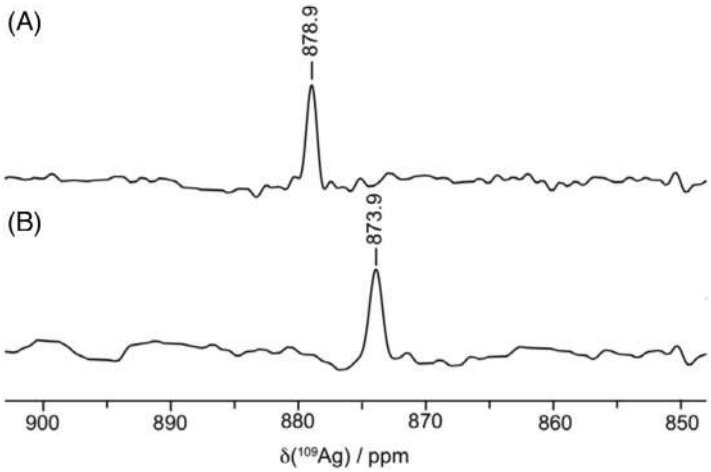

FIGURE 2.27 ^{109}Ag-NMR spectra acquired in DCM-d_2 at 298 K of $[Ag_{25}(DMBT)_{18}][TOA]$ (A) and (B) $[Ag_{24}Au(DMBT)_{18}]$ [TOA]. (Reproduced with permission from ref.[149]).

This could be due to the fact that ^{109}Ag NMR is a less sensitive technique and there is only one Ag atom per cluster and therefore, its feature may remain undetected in the experiment. Interestingly, the ^{109}Ag NMR spectrum of $Ag_{24}Au_1(SR)_{18}$ shows only one feature which again confirms the exchange of the Ag atoms. Notably, this peak shifted toward lower frequency by about 5 ppm. Such exchange in the interclsuter fashion is unlikely considering the difficulty in accessing the inner metal atoms by the other cluster. Therefore, it is more likely that the exchange occurs in the intracluster fashion.

2.9.5 What triggers intercluster exchange reactivity?—The role of metal–ligand interface

In the previous section, we presented a few examples of intercluster reactions and also the structural dynamics of these clusters facilitating intercluster reactions. Now we ask a very important question: what is the actual trigger for these reactions?[150] What happens when two clusters, $Au_{25}(SR)_{18}$ and $Ag_{25}(SR)_{18}$, for example, approach each other? Do these reactions proceed via collisions between these two clusters, just as common reactions in chemistry?

Let us consider the reaction between $Ag_{25}(SR)_{18}$ and $Au_{25}(SR)_{18}$. These clusters consist of a distinct M_{13} core protected by $M_2(SR)_3$ (M = Ag/Au) staples. According to the superatom theory, valence electrons of metal atoms in their staples are localized by polar covalent bonds with the sulfur atoms of the ligands. Furthermore, each of the $M_2(SR)_3$ staples localizes the valence electron of one of the metal atoms in the M_{13} core. Therefore, all of the metal atoms in the six $M_2(SR)_3$ staples and six of the metal atoms in the M_{13} core are considered to be in the +1 oxidation state. The remaining seven valence electrons of the M_{13} core and an acquired negative charge make the eight-electron superatom, $[M_{25}(SR)_{18}]^-$ M=Ag/Au. Charge neutrality is provided by the counter ions such as metal ions, ammonium ions, or phopsphonium ions.

The difference in the oxidation states of metal atoms in the core and the staples, as explained above, plays a crucial role in triggering the intercluster reactions.[150] Because of this difference

in oxidation states, redox-like reactions could occur between two clusters. Let us consider two such possibilities, taking the reaction between $Ag_{25}(SR)_{18}$ and $Au_{25}(SR)_{18}$ as an example. In the first case, an $Ag_{25}(SR)_{18}$ molecule reacts with the $Au_2(SR)_3$ staples of $Au_{25}(SR)_{18}$, wherein Au of $Au_2(SR)_3$ staples is in the +1 oxidation state. Redox reactions between silver clusters and Au(I) thiolates are known.[151] Alternatively, an $Au_{25}(SR)_{18}$ molecule reacts with the $Ag_2(SR)_3$ staples of $Ag_{25}(SR)_{18}$, wherein Ag of the $Ag_2(SR)_3$ staple is in the +1 oxidation state. Such reactions between $Au_{25}(SR)_{18}$ and Ag(I) thiolates are also known.[60] It remains unclear as to how the difference in oxidation states of metal atoms in the core and the staples contributes to the chemical reactivity of these clusters. Apart from these possibilities, it has also been intuitively suggested in the reaction between $Au_{25}(SR)_{18}$ and $Ag_{44}(SR)_{30}$, the interaction between these two intact clusters could result in the formation of small reactive fragments such as $Ag(SR)_2^-$, which react with the $Au_2(SR)_3$ staples of $Au_{25}(SR)_{18}$, resulting in an exchange of metal atoms, ligands, and M−L fragments. In this context, it is important to understand how much the chemistry of these clusters differ from that of the M−L complexes. In other words, do these clusters behave as unique entities in their reactions wherein the overall electronic structures of both of the reacting clusters need to be considered in order to explain their reactivity (rather than attributing their chemistry to the reaction between one of the clusters and the staples or the mounts of the other, as explained earlier)? In summary, the nature of the ligand and the bonding characteristics of the metal–ligand oligomeric units are extremely important to be considered in order to understand the stability[152] and chemical reactivity of these clusters.

2.9.6 Should the metal atoms be different for exchange reactivity: Isotope exchange between clusters

In the previous examples, the reactant clusters were of two different elements, that is, Ag and Au. We also discussed the possible roles of the differences in the oxidation states of metal atoms in various unique positions. This invokes the question that: Is it necessary that the two clusters are composed of different elements so as to react with each other? Or, is the metal atom exchange an inherent process occurring between clusters in solution? In order to address these questions, the reaction between isotopically pure $Ag_{25}(SR)_{18}$ clusters, that is, $^{107}[Ag_{25}(DMBT)_{18}]$and $^{109}[Ag_{25}(DMBT)_{18}]$ were investigated.[153] Surprisingly, the exchange of ^{107}Ag of $^{107}[Ag_{25}(DMBT)_{18}]^-$ with ^{109}Ag of $^{109}[Ag_{25}(DMBT)_{18}]^-$ was observed (see Fig. 2.28). This experiment shows that clusters of the same element also can undergo spontaneous metal atom exchange reactions in solutions. Most importantly, this study reveals that such spontaneous atom exchange reactions are an inherent chemical property of atomically precise pieces of metals. This dynamic situation of silver clusters can be analogous to the proton exchange between water molecules. However, the question that what actually triggers the chemical reactivity remains unanswered. Even though the clusters contain metal atoms of the same element, that is, silver, oxidation states of the Ag atoms in the staples and the core are different and redox process might occur even between the isotopically pure $Ag_{25}(SR)_{18}$ clusters, that is, the $^{109}[Ag_{25}(DMBT)_{18}]^-$ clusters might "see" the $^{107}Ag_2(DMBT)_3$ staples of in the Ag(I) oxidation state, and vice versa. In order to completely rule out such effects, experiments with isotopically pure, unprotected, and preferably, atomically precise metal clusters or nanoparticles should be carried out. In this reaction, the main contribution to the reaction-free energy is from the entropic factors due to the mixing of the two isotopically

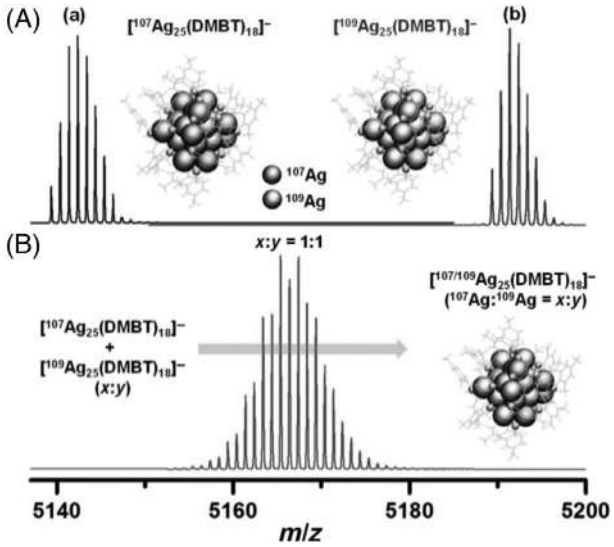

FIGURE 2.28 Mass spectra of the parent isotope clusters and the product of mixing. (A) ESI MS of the as-synthesized isotopically pure clusters, (a) $[^{107}Ag_{25}(DMBT)_{18}]^-$ and (b) $[^{109}Ag_{25}(DMBT)_{18}]^-$. (B) Mass spectral distribution of the product obtained by mixing the two isotopic clusters at 1:1 molar ratio. The spectrum was collected within 1 min after mixing the solutions of the clusters at room temperature. A representation of the clusters is shown. (Reproduced with permission from ref.[153]).

pure clusters. Entropic contribution is important in other reactions mentioned earlier as well because there are different combinations of unique metal atom positions between the clusters undergoing exchange reactivity.

2.10 Understanding the reaction mechanisms: Where are we?

Here, we discuss a few examples wherein some hints about reaction mechanisms are available.

2.10.1 Mechanistic insights into intercluster reactions

Experiments suggest that similar to commonly observed reactions in chemistry, collision between reacting clusters is necessary. For example, in the reaction between $Au_{25}(SR)_{18}$ and $Ag_{25}(SR)_{18}$, a dianionic adduct, $[Ag_{25}Au_{25}(DMBT)_{18}(PET)_{18}]^{2-}$, which could be one of the intermediates of the reaction was detected (see Fig. 2.29)[146]

Density functional theory (DFT) calculations revealed that this adduct could be formed through weak covalent bonding via interstaple metal−sulfur bonds (see Fig. 2.30). These calculations suggest that interactions between the M−L interfaces of the reacting clusters might occur in the initial stages of these reactions. It would be worthwhile to understand how these two clusters overcome the electrostatic repulsion while they approach each other. One of the reasons could be the fact that the overall negative charge of these clusters is not localized, instead it is diffused over the entire, large cluster molecule. In other words, these anionic clusters do not behave as point charges.

Recently, Zhang et al. attempted to detect such intermediates during the reaction between $Au_{38-x}Ag_x(SR)_{24}$ and $Au_{38}(SR)_{24}$ using in situ X-ray absorption fine structure

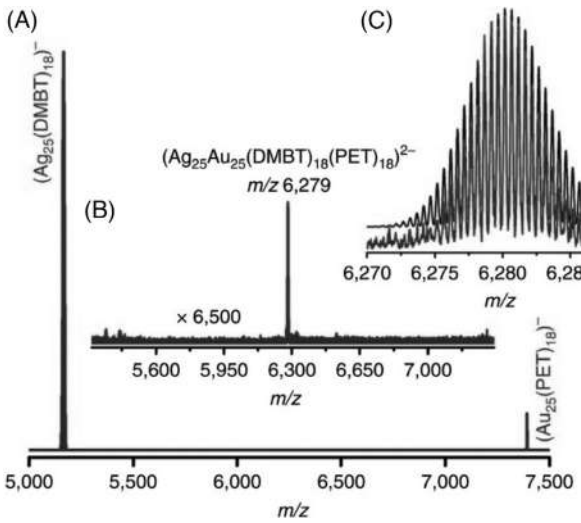

FIGURE 2.29 Full range electrospray ionization mass spectrum (ESI MS) of the mixture of $Ag_{25}(DMBT)_{18}$ (I) and $Au_{25}(PET)_{18}$ (II) at molar ratio (I:II) of 0.3:1.0 measured within 2 min after mixing (A), zoomed in region of panel a in the range between m/z 5.270 and 7.340 showing a feature due to the dianionic adduct, $(Ag_{25}Au_{25}(DMBT)_{18}(PET)_{18})^{2-}$ formed between I and II (B) and theoretical (upper) and experimental (lower) isotope patterns of the adduct features (C). DMBT is 2,4-dimethylbenzenethiol and PET is 2-phenylethanethiol. (Reproduced with permission from ref. [146]).

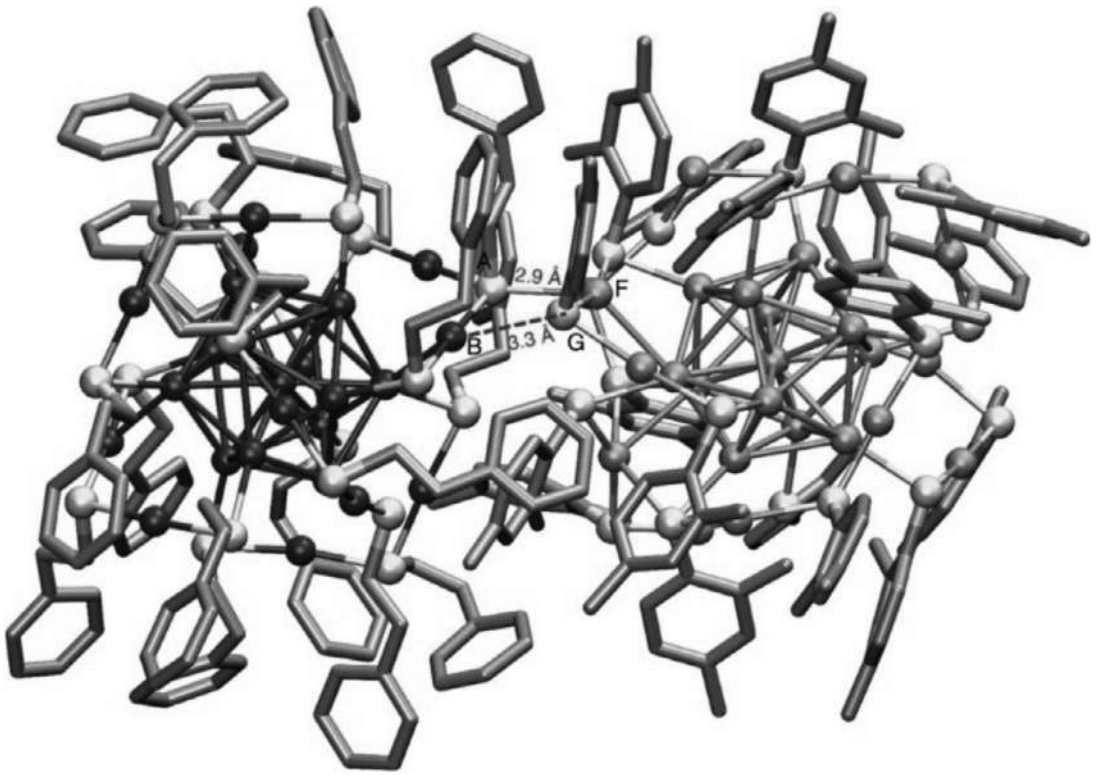

FIGURE 2.30 The geometry of $(Ag_{25}Au_{25}(DMBT)_{18}(PET)_{18})^{2-}$ adduct (with Ag_{25} on the left and Au_{25} on the right) obtained from DFT-optimization of the structure obtained from a force-field-based molecular docking simulation. The hydrogen atoms are omitted from the ligands for clarity. (Reproduced with permission from ref.[146]).

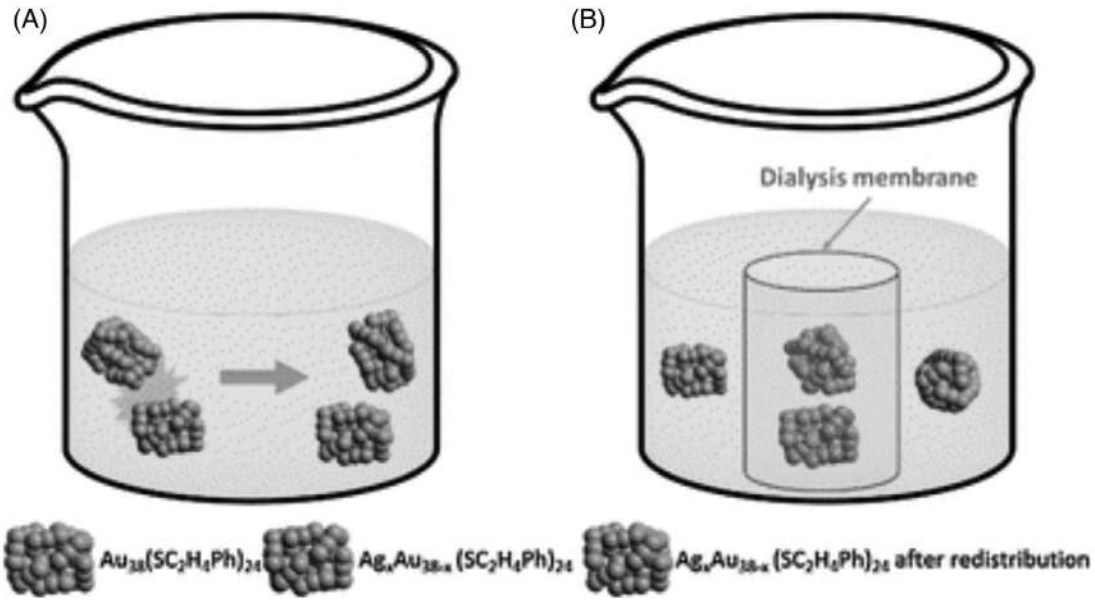

FIGURE 2.31 (A) Schematic of the reaction between $Au_{38}(SC_2H_4Ph)_{24}$ and $Ag_xAu_{38-x}(SC_2H_4Ph)_{24}$ that led to silver migration and consequent redistribution of silver atoms among the clusters. (B) Reaction in the presence of a dialysis membrane that prevent the direct physical contact between $Au_{38}(SC_2H_4Ph)_{24}$ and $Ag_xAu_{38-x}(SC_2H_4Ph)_{24}$. (Reproduced with permission from ref.[69]).

measurements.[154] However, the detection of exchanged Ag atoms in the staples was not successful, possibly due to a shorter residence time of the exchanged Ag atoms in the staples. They also demonstrated that when $Au_{38-x}Ag_x(SR)_{24}$ and $Au_{38}(SR)_{24}$clusters are separated using a dialysis membrane between them, no metal exchange occurs (see Fig. 2.31).[69] These experiments suggest that intercluster reactions require collisions between them, just like reaction between common, small molecules.

Due to the initial interactions between the two reacting clusters, the clusters could be destabilized due to possible reasons such as collisions, electron transfer, etc. A more detailed discussion on the mechanistic insights of these events are presented in the later sections. These rings in the destabilized clusters may undergo opening, and they become more flexible. They also could assume elongated conformations allowing the atoms at the free ends to interact more easily with the corresponding open rings on other cluster. A similar reorganization of the staples has been proposed (theoretically) earlier.[155] The ends of the open rings can interact more easily, exchanging the metal atoms, ligands, and the metal–ligand fragments. The Borromean ring model of $Au_{25}(SR)_{18}$ suggests that inclusion of Ag atoms into the Au_{13} core is not as significantly hindered, from the steric factors, as one would expect when this cluster is viewed as distinct core protected by distinct $Au_2(SR)_3$ staples.

Huang et al. performed detailed theoretical calculations in order to understand the mechanism of the intercluster exchange reaction between $Au_{25}(SR)_{18}$and $Ag_{25}(SR)_{18}$.[156] These studies also support the possibility of a dianionic dimer formed by these two clusters as an intermediate species. According to their calculations, the reaction proceeds via two-step

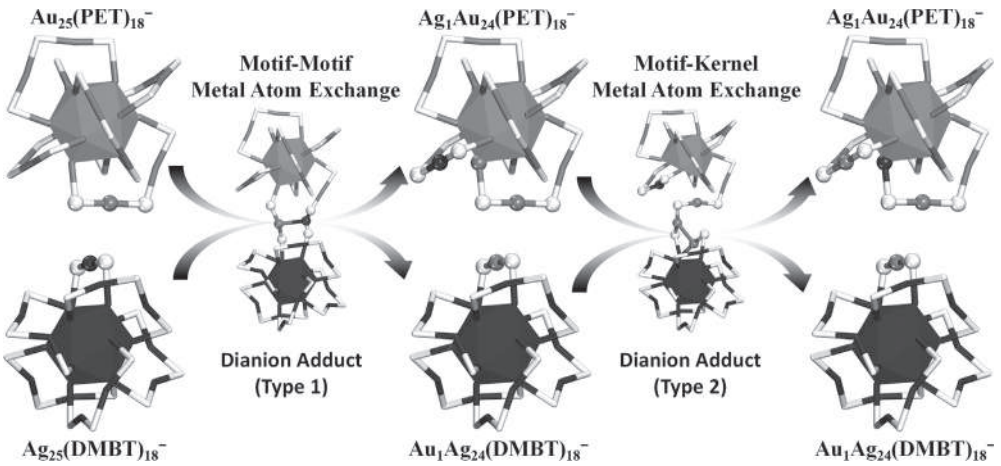

FIGURE 2.32 A schematic of the mechanism of the metal exchange reaction between the $[Au_{25}(PET)_{18}]^-$ and $[Ag_{25}(DMBT)_{18}]^-$ NCs. The R groups are removed for clarity, and the icosahedral M_{13} (M = Au/Ag) cores are represented by a polyhedron). (Reproduced with permission from ref.[156]).

mechanism, wherein the dianionic adduct is initially formed, then rearrangements in the metal–ligand staples occur, exchanging metal atoms in the staples. In the second stage, the substituted metal atoms in the staples swap with the metal atoms in their inner icosahedral cores. Snapshots of the mechanistic details evolved from this study are depicted in Fig. 2.32.

2.10.2 Mechanisms of metal atom substitution reactions

2.10.2.1 Shuttling of single metal atoms into and out of cluster to form alloy cluster

An interesting site-selective metal substitution reaction was demonstrated by Wang et al.[157] They showed that the Au atoms of the cluster $[Au_{24}(PPh_3)_{10}(SC_2H_4Ph)_5Cl_2]^+$ (referred to as Au_{24} hereafter, for convenience) can be substituted with other atoms such as Ag or Cu with high degree of site-selectivity. For example, the reaction of Au_{24} with Au(I)Cl in dichloromethane results in the formation of $[Au_{25}(PPh_3)_{10}(SC_2H_4Ph)_5Cl_2]^{2+}$(referred to as Au_{25} hereafter, for convenience), as shown in Fig. 2.33. The reaction of Au_{24} with CuCl or AgCl results in the formation of clusters such as $[Cu_1Au_{24}(PPh_3)_{10}(PET)_5Cl_2]^{2+}$and $[Ag_1Au_{24}(PPh_3)_{10}(PET)_5Cl_2]^{2+}$, respectively. X-ray crystallography reveals that the Cu atom occupies either the apex or the waist positions of the cluster and Ag atom occupy the apex position. Surprisingly, the central vacancy in both of these products is occupied exclusively by Au atoms, and not by the substituent Cu or Ag atoms. This observation shows that the substitution of Cu or Ag atoms in Au_{24} results in pushing one of the Au atoms into the central vacancy.

2.10.2.2 An illustration of superatom electron counting: Insights into the mechanism of Au doping in $[PdAg_{24}(SR)_{18}]^{2-}$

In a previous section, the superatom concept of thiolate-protected noble metal clusters has been mentioned. Here we present an example depicting the usefulness of this concept in

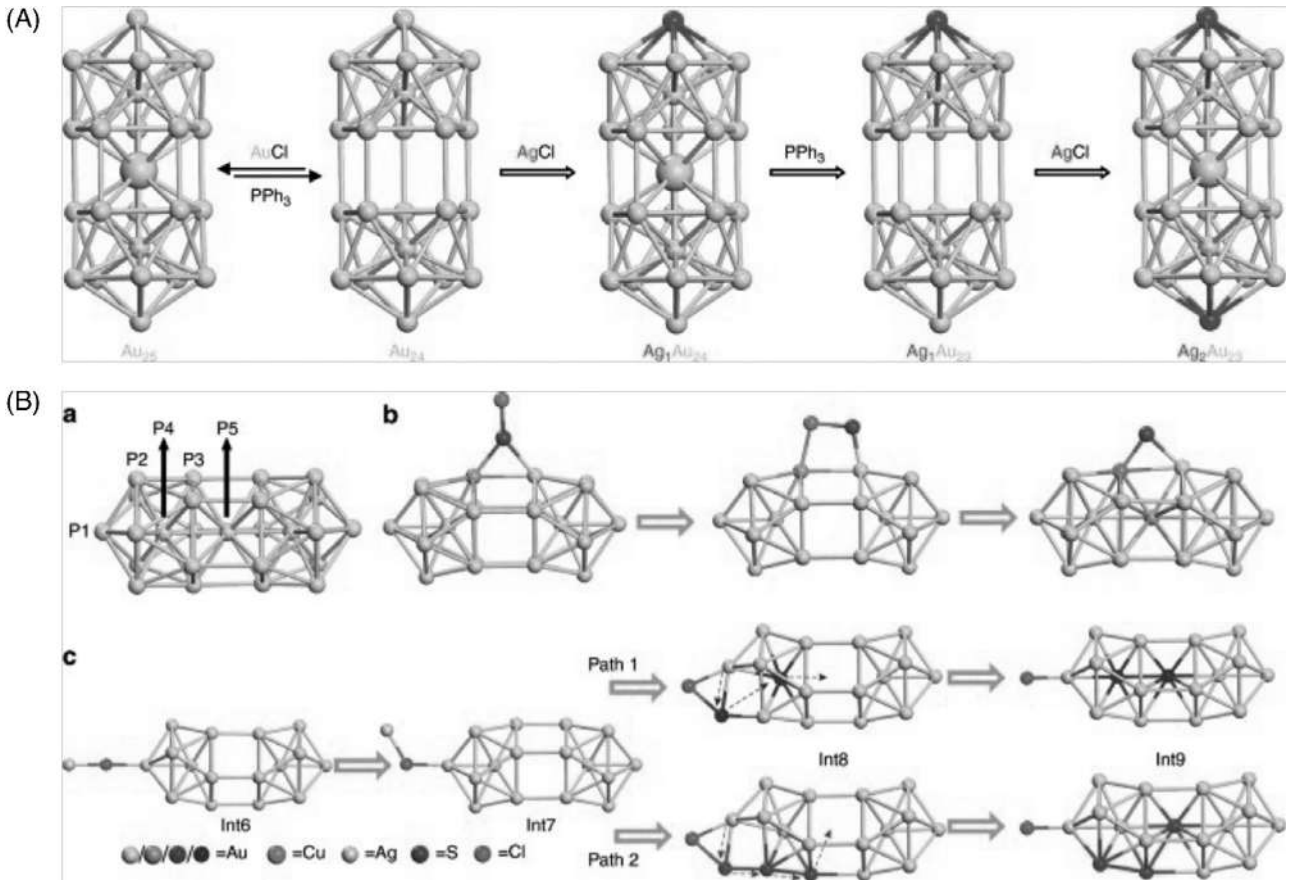

FIGURE 2.33 (A) Proposed mechanism of injecting two Ag atoms into the nanoparticle via the hollowing-refilling sequence: step 1, using PPh_3 to make a hole in the solid Au_{25} nanocluster; step 2, using AgCl to refill this hole and produce Ag_1Au_{24}; step 3, continue using PPh_3 to make a hole in the Ag_1Au_{24} nanocluster and form the hollow Ag_1Au_{23} nanocluster; step 4, using AgCl to refill the hole and yield the Ag_2Au_{23} nanocluster. (B) Mechanisms for the formation of doped MAu_{24} clusters based on DFT calculations. (a) Designation of sites P1–P5 in the Au_{25} structure. DFT-calculated mechanisms for MAu_{24} (M = Cu or Ag) formation with M at (b) waist and (c) apex positions. Only one Cl and S of the nanoparticle is presented. Other atoms and bonds are not shown for clarity. (Reproduced with permission from ref.[157]).

elucidating the mechanistic details of metal atom substitution reaction. The reaction considered here is the substitution of the Pd atom in $[PdAg_{24}(SR)_{18}]^{2-}$ by Au atom.[158] The reaction was monitored by time-dependent mass spectrometry. Fig. 2.34A shows that at 0 h, the mass spectral feature is only due to the parent cluster, $[PdAg_{24}(SR)_{18}]^{2-}$. After 2h, features due to clusters such as $[AuPdAg_{23}(SR)_{18}]^{2-}$and $[Au_2PdAg_{23}(SR)_{18}]^{2-}$along with the parent cluster, $[PdAg_{24}(SR)_{18}]^{2-}$, arise. After about 6h, all these features disappeared and the features due to the product clusters such as $[AuAg_{24}(SR)_{18}]^{-}$ and $[Au_2Ag_{23}(SR)_{18}]^{-}$ appears. The charge states of the parent cluster, $[PdAg_{24}(SR)_{18}]2^{-}$ changes from -2 to -1 in the product clusters. The parent cluster, $[PdAg_{24}(SR)_{18}]^{2-}$is an eight electron superatom (0+24-18-(-2) = 8). Crystal structure of $[PdAg_{24}(SR)_{18}]^{2-}$and the product clusters possess common structural features such an M13 icosahedron, and six $M_2(SR)_3$ staples. The Pd atom in $[PdAg_{24}(SR)_{18}]2^{-}$ is located at the center of the icosahedron. Notably, after about 2h of the reaction, clusters such as $[AuPdAg_{23}(SR)_{18}]^{2-}$and $[Au_2PdAg_{23}(SR)_{18}]2^{-}$ are formed without any change in the charge state. The Pd atom is not replaced at this stage of the reaction. This observation indicates that the substituted Au atoms in these clusters are located either in the outer staples or on the vertices of the icosahedron. However, the charge states of the final product clusters, $[AuAg_{24}(SR)_{18}]^{-}$ and $[Au_2Ag_{23}(SR)_{18}]^{-}$ changes to -1. Furthermore, the Pd atom is removed from these clusters. These two factors indicate that Au atoms moved from outer staples or the vertices of the icosahedron to the center of the icosahedrons (the second Au atom in $[Au_2Ag_{23}(SR)_{18}]^{-}$ will also be moved from the outer staples to the vertices of the icosahedron. This example shows that superatom concept is helpful to provide insights into the mechanistic details of metal atom substitution reactions.

2.11 Achieving atomic precision in cluster chemistry—A few examples

2.11.1 Single ligand exchange in a redox reaction

Cao et al. revealed an interesting single ligand exchange process during the reaction of $[Au_{25}SR_{18}]^{-}$ with molecular oxygen.[159] This reaction produces a new cluster, $[Au_{25}SR_{19}]^{0}$, by adding a single SR ligand. The reaction occurs in the reverse direction, that is, $[Au_{25}SR_{19}]^{0}$ generates $[Au_{25}SR_{18}]^{-}$, on reaction with CO. This example demonstrates that it is possible to precisely control the chemistry of the metal–ligand interfaces of these clusters. A summary of these reactions are shown schematically in Fig. 2.35.

2.11.2 Site-selective substitution of metal atoms *via* reaction with metal–thiolates and metal–phosphine complexes

A large number of alloy or heterometallic clusters are reported so far, however, most of them are synthesized as a mixture containing varying metal atom compositions. Therefore, it is challenging to achieve alloy or heterometalic clusters with precise compositions and with precisely controlled locations of heterometal atoms. This is especially true in the case of Ag–Au clusters because of their similar atomic radii and electronic configuration. For example, $Au_{25-x}Agx(SR)_{18}$ alloys were always synthesized as a mixture of clusters. Recently, Bootharaju et al. have successfully synthesized an atomically precise alloy cluster, $Ag_{24}Au_1(SR)_{18}$ by reacting $Ag_{25}(SR)_{18}$ with $AuClPPh_3$.[62] Attempts to produce the same cluster through coreduction route, that is, reducing a mixture of $HAuCl_4$ and $AgNO_3$ using $NaBH_4$, was unsuccessful as it

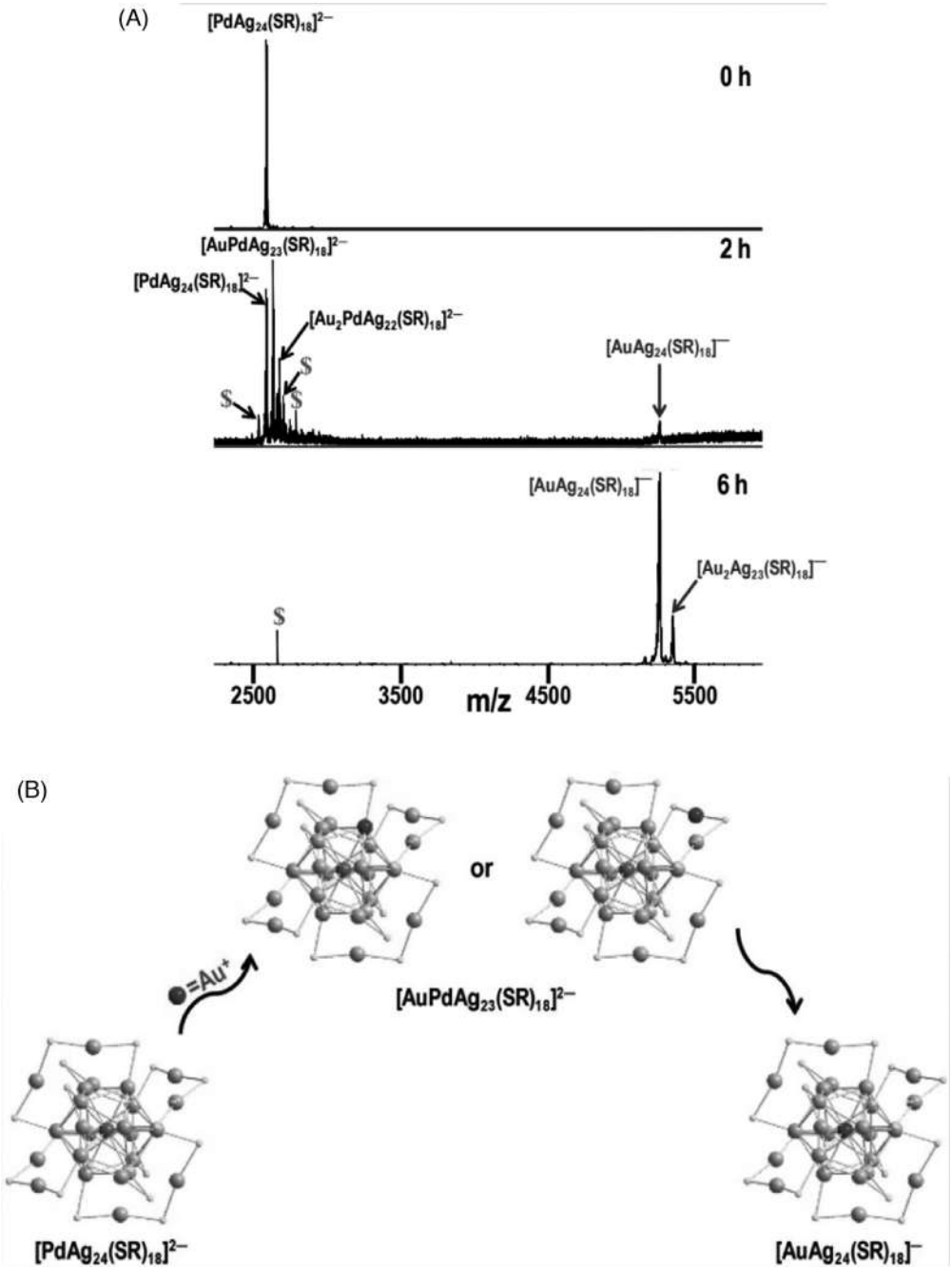

FIGURE 2.34 Time-dependent ESI MS of gold-doping of $[PdAg_{24}(SR)_{18}]2^-$ NCs. Peaks labeled with "$" sign are due to unidentified artifacts from the mass spectrometer (A) and mechanism of doping of $[PdAg_{24}(SR)_{18}]^{2-}$ NCs with gold. Ag: gray spheres, Pd: black sphere, S: small dots. (Reproduced with permission from ref.[158]).

(A) $[Au_{25}(SR)_{18}]^- + 1/2O_2 + HSR \rightarrow [Au_{25}(SR)_{19}]^0 + OH^-$ (1)

$[Au_{25}(SR)_{19}]^0 + CO + 2OH^- \rightarrow [Au_{25}(SR)_{18}]^- + HCO_3^- + HSR$ (2)

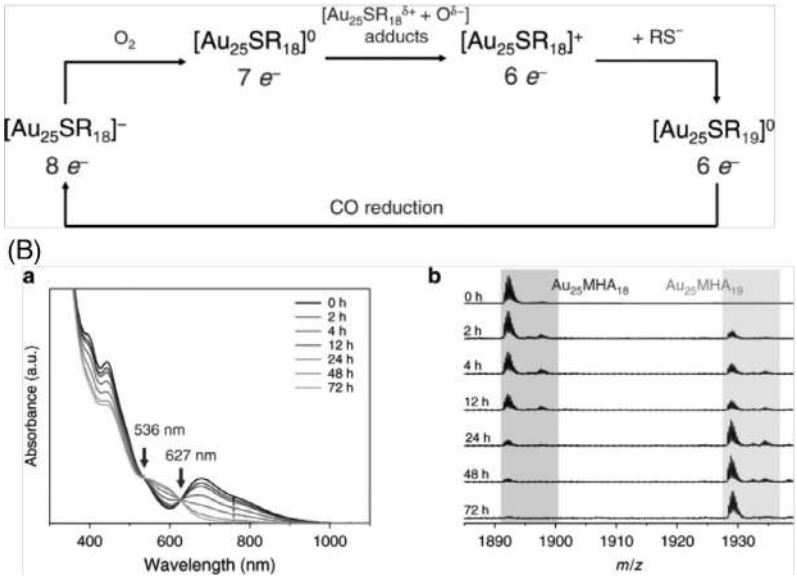

FIGURE 2.35 Schematic illustration of the addition/elimination reaction cycle between $[Au_{25}SR_{18}]^-$ and $[Au_{25}SR_{19}]^0$.(A) Time-course UV-Vis absorption spectra and (B) ESI-MS spectra in the transformation from $[Au_{25}MHA_{18}]$ species to $[Au_{25}MHA_{19}]^0$ (MHA is 6-mercaptohexanoic acid) after introducing excess thiol ligands. (Reproduced with permission from ref.[159]).

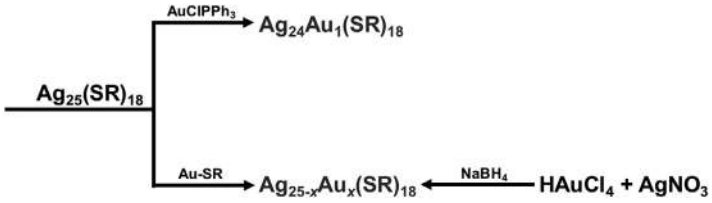

FIGURE 2.36 A schematic depicting the role of the heterometal atom source in dictating the product composition in metal atom substitution reaction.

produced a mixture of clusters of the general formula, $Ag_{25-x}Au_x(SR)_{18}$.Furthermore, the use of Au-SR complex as the heteroatom source also resulted in the formation of $Ag_{25-x}Aux(SR)_{18}$. These experiments reveal that the choice of the metal atom source, that is, whether it is a simple salt or a metal-phosphine and metal-thiolate complex, etc., is crucial in dictating the product composition. However, the mechanistic details of, and the reasons behind the selective formation of atomically precise alloys in these reactions remain unknown. These results are summarized in Fig. 2.36.

2.11.3 Site-selective Au atom substitution in $[Ag_{44}(p\text{-MBA})_{30}]^{4-}$

Let us now consider an example wherein site-selective metal atom substitution was achieved in the case of $Ag_{44}(p\text{-MBA})_{30}$, wherein *p*-MBA is *para*-mercaptobenzoic acid. As shown in Fig. 2.4, this cluster possesses four symmetry unique positions for Ag atoms. They are (1) innermost Ag_{12} icosahedron, (2) cube vertex (D_{cv}) positions (3) and cube face (D_{cf}) positions, and (4) the outermost mount positions. Yao et al. have shown that it is possible to selectively substitute 12 Ag atoms in the outermost mounts with twelve Au atoms. In order to achieve this, they reacted $Ag_{44}(p\text{-MBA})_{30}$ with Au-*p*-MBA complexes.[160] Au-*p*-MBA complexes were prepared by reacting a solution of $HAuCl_4$ with *p*-MBA in DMF. This reaction produced an alloy cluster, $[Ag_{32}Au_{12}(SR)_{30\text{-}b}Cl_b]$ where $b = 0$–2. Note that the Cl^- comes from the $HAuCl_4$ that was used to prepare Au-p-MBA complex. Mass spectrometric analysis, especially analyzing the fragmentation patterns of this cluster, shows that the substituent Au atoms preferably occupy the outermost mount positions rather than the other two inner positions. This is because, if the Au atoms in $[Ag_{32}Au_{12}(SR)_{30\text{-}b}Cl_b]$ were present in the inner positions, it is less likely to be present in the fragments. They carried out this reaction using $HAuCl_4$ and produced alloy clusters of similar molecular formula, $[Ag_{44\text{-}x}Au_x(L)_{30}]^{4-}$. However, fragments derived from these clusters did not contain any Au atom, which indicates that Au atoms in these clusters are likely to be present in the innermost icosahedral positions. Crystal structures of the alloy clusters prepared by these two methods were not obtained for unambiguously confirming the position of the substituent metal atoms. However, these experiments show that the choice of the source of the substituent metal atom is important in dictating the sites of the metal atom substitution.

In order to gain insights into the reaction mechanisms, it is necessary to understand what is the stoichiometry of Au-p-MBA complex that was reacted with $[Ag_{44}(SR)_{30}]^{4-}$. The mass spectrometric analysis of this complex shows $[Au_2(SR)_{3\text{-}b}Cl_b]^-$ ($b = 0$–2), and $[Au_2(SR)_2Cl]^-$. (Note that metal-thiolate complexes are generally polydipserse in nature and insoluble in most of the solvents, and therefore the fact that these two metal-thiolate complexes were detected by mass spectrometry imply that these are soluble). Considering one of these species, $[Au_2(SR)_2Cl]^-$, as the reacting metal-thiolate, they proposed a reaction as shown below:

$$[Ag_{44}(SR)_{30}]4- + [Au_2(SR')_2Cl]- \rightarrow [Ag_{43}Au(SR)_{28}(SR')_2]4- + [Au(SR)_2]- + AgCl$$

Based on these experimental results, they proposed a reaction mechanism, as depicted in Fig. 2.37. The interesting aspect of this mechanism is that this reaction involves only the exchange of the outer metal-thiolate fragments with the incoming metal-thiolate complex containing substituent metal atoms; it does not involve the inner metal atoms of the cluster and any galvanic reduction reaction by the cluster.

2.12 Summary and future perspectives

In summary, we discussed atomically precise, ligand-protected noble metal clusters are *molecules*, offering rich chemistry. However, further efforts are required to understand the structure–reactivity relations and reaction mechanism of these clusters. The factors that actually trigger their reaction, intercluster exchange reactions, for example, are yet to be understood. The dynamic nature of the metal–ligand interface plays a crucial role in these reactions.

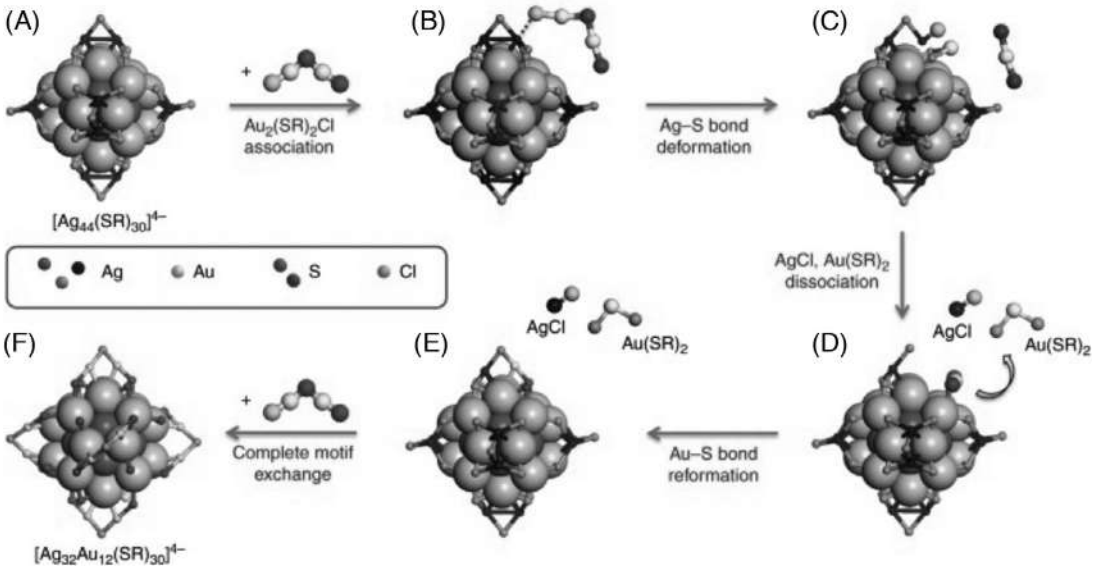

FIGURE 2.37 Schematic illustration of surface motif exchange reaction on Ag_{44} nanoclusters. (A) Pristine $[Ag_{44}(SR)_{30}]^{4-}$; (B) association of $[Au_2(SR')_2Cl]^-$ to $[Ag_{44}(SR)_{30}]^{4-}$; (C) Ag–S bond deformation in $[Au_2(SR')_2Cl]^-$ associated $[Ag_{44}(SR)_{30}]_{4-}$; (D) dissociation of AgCl and $[Au(SR)_2]^-$; (E) $[Ag_{43}Au(SR)_{28}(SR')_2]^{4-}$ formed by exchange of one SR–Ag(I)–SR motif; and (F) $[Ag_{32}Au_{12}(SR)_6(SR')_{24}]_{4-}$ produced by complete exchange of 12 SR–Ag(I)–SR motifs, where SR and SR′ denote pristine and foreign thiolate ligands, respectively. For an easy and clear presentation, the Ag atoms in Ag_{12} inner core and Ag_{20} external core are shown as large balls while the other atoms are shown as small dots. The hydrocarbon tails and carboxylic groups of the protecting ligands are omitted. (Reproduced with permission from ref.[160]).

List of abbreviation

CD	Cyclodextrin
DCM	Dichloromethane
DDT	1-Dodecanethiol
DFT	Density Functional Theory
DMBT	2,4-Dimethylbenzenethiolate
EPR	Electron Paramagnetic Resonance
ESI MS	Electrospray Ionization Mass spectrometry/spectrum
FTP	-4-fluorothiophenol
HCM	Haussdorf Chirality Measurement
HOMO	Highest Occupied Molecular Orbital
HPLC	High-Performance Liquid Chromatography
IPA	Isopropyl Alcohol
LUMO	Lowest Unoccupied Molecular Orbital
MALDI MS	Matrix-Assisted Laser Desorption Ionization Mass Spectrometry
MBA	4-mercaptobenzoic acid
MER	Metal Exchange Reaction
M-L	Metal–ligand
NMR	Nuclear Magnetic Resonance
PET	2-phenylethanethiolate
RGO	Reduced Graphene Oxide
SG	Glutathione
-SR	alkyl/aryl

TOA	Tetraoctyl Ammonium Bromide
UV/Vis	Ultraviolet/Visible

References

1. Pyykko P. Relativistic effects in structural chemistry. *Chem Rev*. 1988;88:563–594.
2. Bartlett N. Relativistic effects and the chemistry of gold. *Gold Bull*. 1998;31:22–25.
3. Schmidbaur H, Cronje S, Djordjevic B, Schuster O. Understanding gold chemistry through relativity. *Chem Phys*. 2005;311:151–161.
4. Schmidbaur H. The aurophilicity phenomenon: a decade of experimental findings, theoretical concepts and emerging applications. *Gold Bull*. 2000;33:3–10.
5. Schmidbaur H, Schier A. Argentophilic interactions. *Angew Chem Int Ed*. 2015;54:746–784.
6. Schmidbaur H, Schier A. Mercurophilic interactions. *Organometallics*. 2015;34:2048–2066.
7. Nitsch J, Lacemon F, Lorbach A, Eichhorn A, Cisnetti F, Steffen A. Cuprophilic interactions in highly luminescent dicopper(i)–NHC–picolyl complexes—fast phosphorescence or TADF? *Chem Commun*. 2016;52:2932–2935.
8. Henglein A. Small-particle research: physicochemical properties of extremely small colloidal metal and semiconductor particles. *Chem Rev*. 1989;89:1861–1873.
9. Henglein A. Physicochemical properties of small metal particles in solution: "microelectrode" reactions, chemisorption, composite metal particles, and the atom-to-metal transition. *J Phys Chem*. 1993;97:5457–5471.
10. Iizuka Y, Fujiki H, Yamauchi N, et al. Adsorption of CO on gold supported on TiO_2. *Catal Today*. 1997;36:115–123.
11. Huang W, Zhai H-J, Wang L-S. Probing the interactions of O_2 with small gold cluster anions (Au_n^-, $n = 1–7$): chemisorption vs physisorption. *J Am Chem Soc*. 2010;132:4344–4351.
12. Yoon B, Häkkinen H, Landman U. Interaction of O_2 with gold clusters: molecular and dissociative adsorption. *J Phys Chem A*. 2003;107:4066–4071.
13. Prestianni A, Martorana A, Labat F, Ciofini I, Adamo C. A DFT investigation of CO oxidation over neutral and cationic gold clusters. *J Mol Struct THEOCHEM*. 2009;903:34–40.
14. Li L, Gao Y, Li H, et al. CO oxidation on TiO_2 (110) supported subnanometer gold clusters: size and shape effects. *J Am Chem Soc*. 2013;135:19336–19346.
15. Wang J, Tan H, Yu S, Zhou K. Morphological Effects of gold clusters on the reactivity of ceria surface oxygen. *ACS Catalysis*. 2015;5:2873–2881.
16. Luo Z, Gamboa GU, Smith JC, et al. Spin accommodation and reactivity of silver clusters with oxygen: the enhanced stability of Ag_{13}. *J Am Chem Soc*. 2012;134:18973–18978.
17. Schmid G. The relevance of shape and size of Au_{55} clusters. *Chem Soc Rev*. 2008;37:1909–1930.
18. Teo BK, Shi X, Zhang H. Pure gold cluster of 1:9:9:1:9:9:1 layered structure: a novel 39-metal-atom cluster $[(Ph_3P)_{14}Au_{39}C_{16}]Cl_2$ with an interstitial gold atom in a hexagonal antiprismatic cage. *J Am Chem Soc*. 1992;114:2743–2745.
19. Schmid G, Pfeil R, Boese R, et al. $Au_{55}[P(C_6H_5)_3]_{12}CI_6$ — ein Goldcluster ungewöhnlicher Größe. 1981;114:3634–3642.
20. Bhat S, Chakraborty I, Baksi A, Narayanan RP, Pradeep T. Evolution of atomically precise clusters through the eye of mass spectrometry. In: *Nanoscience: Volume 3*. Cambridge, UK: The Royal Society of Chemistry; 2016:343–385.
21. Johnson GE, Laskin J. Understanding ligand effects in gold clusters using mass spectrometry. *Analyst*. 2016;141:3573–3589.
22. Chakraborty P, Pradeep T. The emerging interface of mass spectrometry with materials. *NPG Asia Materials*. 2019;11:48.
23. Gruene P, Rayner DM, Redlich B, et al. Structures of Neutral Au_7, <tex-math>Au_{19}</tex-math>, and <tex-math>Au_{20}</tex-math>Clusters in the Gas Phase. *Science*. 2008;321:674–676.
24. Knight WD, Clemenger K, de Heer WA, Saunders WA, Chou MY, Cohen ML. Electronic shell structure and abundances of sodium clusters. *Phys Rev Lett*. 1984;52:2141–2143.
25. de Heer WA. The physics of simple metal clusters: experimental aspects and simple models. *Rev Mod Phys*. 1993;65:611–676.
26. Walter M, Akola J, Lopez-Acevedo O, et al. A unified view of ligand-protected gold clusters as superatom complexes. 2008;105:9157–9162.

27. Castleman AW. From elements to clusters: the periodic table revisited. *J Phys Chem Lett*. 2011;2:1062–1069.
28. Häkkinen H. Atomic and electronic structure of gold clusters: understanding flakes, cages and superatoms from simple concepts. *Chem Soc Rev*. 2008;37:1847–1859.
29. Harkness KM, Tang Y, Dass A, et al. $Ag_{44}(SR)_{304}-$: a silver–thiolate superatom complex. *Nanoscale*. 2012;4:4269–4274.
30. Reveles JU, Khanna SN, Roach PJ, Castleman AW, Multiple valence superatoms. 2006;103:18405–18410.
31. Hartig J, Stößer A, Hauser P, Schnöckel H, A metalloid $[Ga_{23}\{N(SiMe_3)_2\}_{11}]$ cluster: the jellium model put to test. 2007;46:1658–1662.
32. Leuchtner RE, Harms AC, Jr. AWC, Thermal metal cluster anion reactions: behavior of aluminum clusters with oxygen. 1989;91:2753–2754.
33. Bergeron DE, Castleman AW, Morisato T, Khanna SN. Formation of Al13I-: evidence for the superhalogen character of Al13. 2004;304:84–87.
34. Khanna SN, Jena P. Atomic clusters: building blocks for a class of solids. *Phys Rev B*. 1995;51:13705–13716.
35. Echt O, Kandler O, Leisner T, Miehle W, Recknagel E. Magic numbers in mass spectra of large van der Waals clusters. *J Chem Soc, Faraday Trans*. 1990;86:2411–2415.
36. Echt O, Sattler K, Recknagel E. Magic numbers for sphere packings: experimental verification in free xenon clusters. *Phys Rev Lett*. 1981;47:1121–1124.
37. Martin TP. Shells of atoms. *Phys Rep*. 1996;273:199–241.
38. Zhu M, Aikens CM, Hollander FJ, Schatz GC, Jin R. Correlating the crystal structure of a thiol-protected Au_{25} cluster and optical properties. *J Am Chem Soc*. 2008;130:5883–5885.
39. Walter M, Akola J, Lopez-Acevedo O, et al. A unified view of ligand-protected gold clusters as superatom complexes. *Proc Natl Acad Sci*. 2008;105:9157–9162.
40. Jiang D-e, Dai S. From Superatomic $Au_{25}(SR)_{18}-$ to Superatomic $M@Au_{24}(SR)_{18}q$ core−shell clusters. *Inorg Chem*. 2009;48:2720–2722.
41. Dolamic I, Knoppe S, Dass A, Bürgi T. First enantioseparation and circular dichroism spectra of Au_{38} clusters protected by achiral ligands. *Nat Commun*. 2012;3:798.
42. Song Y, Murray RW. Dynamics and extent of ligand exchange depend on electronic charge of metal nanoparticles. *J Am Chem Soc*. 2002;124:7096–7102.
43. Guo R, Song Y, Wang G, Murray RW. Does core size matter in the kinetics of ligand exchanges of monolayer-protected Au clusters? *J Am Chem Soc*. 2005;127:2752–2757.
44. Jadzinsky PD, Calero G, Ackerson CJ, Bushnell DA, Kornberg RD. Structure of a thiol monolayer-protected gold nanoparticle at 1.1 Å resolution. 2007;318:430–433.
45. Heaven MW, Dass A, White PS, Holt KM, Murray RW. Crystal structure of the gold nanoparticle $[N(C_8H_{17})_4][Au_{25}(SCH_2CH_2Ph)_{18}]$. *J Am Chem Soc*. 2008;130:3754–3755.
46. Akola J, Walter M, Whetten RL, Häkkinen H, Grönbeck H. On the structure of thiolate-protected Au_{25}. *J Am Chem Soc*. 2008;130:3756–3757.
47. Fernando A, Aikens CM. Ligand exchange mechanism on thiolate monolayer protected $Au_{25}(SR)_{18}$ nanoclusters. *J Phys Chem C*. 2015;119:20179–20187.
48. Pengo P, Bazzo C, Boccalon M, Pasquato L. Differential reactivity of the inner and outer positions of $Au_{25}(SCH_2CH_2Ph)_{18}$ dimeric staples under place exchange conditions. *Chem Commun*. 2015;51:3204–3207.
49. AbdulHalim LG, Kothalawala N, Sinatra L, Dass A, Bakr OM. Neat and complete: thiolate-ligand exchange on a silver molecular nanoparticle. *J Am Chem Soc*. 2014;136:15865–15868.
50. Niihori Y, Matsuzaki M, Pradeep T, Negishi Y. Separation of precise compositions of noble metal clusters protected with mixed ligands. *J Am Chem Soc*. 2013;135:4946–4949.
51. Niihori Y, Kikuchi Y, Kato A, Matsuzaki M, Negishi Y. Understanding ligand-exchange reactions on thiolate-protected gold clusters by probing isomer distributions using reversed-phase high-performance liquid chromatography. *ACS Nano*. 2015;9:9347–9356.
52. Shichibu Y, Negishi Y, Tsukuda T, Teranishi T. Large-scale synthesis of thiolated Au_{25} clusters via ligand exchange reactions of phosphine-stabilized Au_{11} clusters. *J Am Chem Soc*. 2005;127:13464–13465.
53. Li M-B, Tian S-K, Wu Z, Jin R. Peeling the core–shell Au_{25} nanocluster by reverse ligand-exchange. *Chem Mater*. 2016;28:1022–1025.
54. Nimmala PR, Dass A. $Au_{99}(SPh)_{42}$ nanomolecules: aromatic thiolate ligand induced conversion of $Au_{144}(SCH_2CH_2Ph)_{60}$. *J Am Chem Soc*. 2014;136:17016–17023.

55. Dreier TA, Ackerson CJ, Radicals are required for thiol etching of gold particles. 2015;54:9249–9252.
56. Bootharaju MS, Burlakov VM, Besong TMD, et al. Reversible size control of silver nanoclusters via ligand-exchange. *Chem Mater*. 2015;27:4289–4297.
57. Bootharaju MS, Joshi CP, Alhilaly MJ, Bakr OM. Switching a nanocluster core from hollow to nonhollow. *Chem Mater*. 2016;28:3292–3297.
58. Fields-Zinna CA, Crowe MC, Dass A, Weaver JEF, Murray RW. Mass spectrometry of small bimetal monolayer-protected clusters. *Langmuir*. 2009;25:7704–7710.
59. Li Q, Wang S, Kirschbaum K, Lambright KJ, Das A, Jin R. Heavily doped Au_{25}–x$Ag_x(SC_6H_{11})_{18}$− nanoclusters: silver goes from the core to the surface. *Chem Commun*. 2016;52:5194–5197.
60. Wang S, Song Y, Jin S, et al. Metal exchange method using Au_{25} nanoclusters as templates for alloy nanoclusters with atomic precision. *J Am Chem Soc*. 2015;137:4018–4021.
61. Yang S, Wang S, Jin S, Chen S, Sheng H, Zhu M. A metal exchange method for thiolate-protected tri-metal $M_1Ag_xAu_{24}$−x$(SR)^{180}$ (M = Cd/Hg) nanoclusters. *Nanoscale*. 2015;7:10005–10007.
62. Bootharaju MS, Joshi CP, Parida MR, Mohammed OF, Bakr OM. Templated atom-precise galvanic synthesis and structure elucidation of a $[Ag_{24}Au(SR)_{18}]$−nanocluster. *Angew Chem Int Ed*. 2016;55:922–926.
63. Choi J-P, Fields-Zinna CA, Stiles RL, et al. Reactivity of $[Au_{25}(SCH_2CH_2Ph)_{18}]$1—nanoparticles with metal ions. *J Phys Chem C*. 2010;114:15890–15896.
64. Wu Z, Anti-galvanic reduction of thiolate-protected gold and silver nanoparticles. *Angew Chem Int Ed*. 2012;51:2934–2938.
65. Liao L, Zhou S, Dai Y, et al. Mono-MERCURY DOPING of Au_{25} and the HOMO/LUMO energies evaluation employing differential pulse voltammetry. *J Am Chem Soc*. 2015;137:9511–9514.
66. Udayabhaskararao T, Sun Y, Goswami N, Pal SK, Balasubramanian K, Pradeep T. Ag_7Au_6: a 13-atom alloy quantum cluster. *Angew Chem Int Ed*. 2012;51:2155–2159.
67. Yao C, Chen J, Li M-B, Liu L, Yang J, Wu Z. Adding two active silver atoms on Au_{25} nanoparticle. *Nano Lett*. 2015;15:1281–1287.
68. Xia N, Wu Z. Doping Au_{25} nanoparticles using ultrasmall silver or copper nanoparticles as the metal source. *J Mater Chem C*. 2016;4:4125–4128.
69. Zhang B, Salassa G, Bürgi T. Silver migration between $Au_{38}(SC_2H_4Ph)_{24}$ and doped $Ag_xAu_{38-x}(SC_2H_4Ph)_{24}$ nanoclusters. *Chem Commun*. 2016;52:9205–9207.
70. Negishi Y, Kurashige W, Niihori Y, Iwasa T, Nobusada K. Isolation, structure, and stability of a dodecanethiolate-protected Pd_1Au_{24} cluster. *Phys Chem Chem Phys*. 2010;12:6219–6225.
71. Negishi Y, Igarashi K, Munakata K, Ohgake W, Nobusada K. Palladium doping of magic gold cluster $Au_{38}(SC_2H_4Ph)_{24}$: formation of $Pd_2Au_{36}(SC_2H_4Ph)_{24}$ with higher stability than $Au_{38}(SC_2H_4Ph)_{24}$. *Chem Commun*. 2012;48:660–662.
72. Wang S, Meng X, Das A, Li T, Song Y, Cao T, Zhu X, Zhu M, Jin R, A 200-fold quantum yield boost in the photoluminescence of silver-doped Ag_xAu_{25-x} nanoclusters: the 13th silver atom matters. *Angew Chem Int Ed*. 2014;53:2376–2380.
73. Soldan G, Aljuhani MA, Bootharaju MS, et al. Gold doping of silver nanoclusters: a 26-fold enhancement in the luminescence quantum yield. *Angew Chem Int Ed*. 2016;55:5749–5753.
74. Negishi Y, Iwai T, Ide M. Continuous modulation of electronic structure of stable thiolate-protected Au_{25} cluster by Ag doping. *Chem Commun*. 2010;46:4713–4715.
75. Nantaphol S, Chailapakul O, Siangproh W. Sensitive and selective electrochemical sensor using silver nanoparticles modified glassy carbon electrode for determination of cholesterol in bovine serum. *Sens Actuators, B*. 2015;207:193–198.
76. Yang Z, Qi C, Zheng X, Zheng J. Sensing hydrogen peroxide with a glassy carbon electrode modified with silver nanoparticles, AlOOH and reduced graphene oxide. *Microchim Acta*. 2016;183:1131–1136.
77. Noor AaM, Shahid MM, Rameshkumar P, Huang NM. A glassy carbon electrode modified with graphene oxide and silver nanoparticles for amperometric determination of hydrogen peroxide. *Microchim Acta*. 2016;183:911–916.
78. Murray RW. Nanoelectrochemistry: metal nanoparticles, nanoelectrodes, and nanopores. *Chem Rev*. 2008;108:2688–2720.
79. Hicks JF, Miles DT, Murray RW. Quantized double-layer charging of highly monodisperse metal nanoparticles. *J Am Chem Soc*. 2002;124:13322–13328.

80. Miles DT, Murray RW. Temperature-dependent quantized double layer charging of monolayer-protected gold clusters. *Anal Chem*. 2003;75:1251–1257.
81. Chen S, Murray RW. Electrochemical quantized capacitance charging of surface ensembles of gold nanoparticles. *J Phys Chem B*. 1999;103:9996–10000.
82. Zamborini FP, Hicks JF, Murray RW. Quantized double layer charging of nanoparticle films assembled using carboxylate/(Cu^{2+} or Zn^{2+})/carboxylate bridges. *J Am Chem Soc*. 2000;122:4514–4515.
83. Wang D, Padelford JW, Ahuja T, Wang G. Transitions in discrete absorption bands of Au_{130} clusters upon stepwise charging by spectroelectrochemistry. *ACS Nano*. 2015;9:8344–8351.
84. Quinn BM, Liljeroth P, Ruiz V, Laaksonen T, Kontturi K. Electrochemical resolution of 15 oxidation states for monolayer protected gold nanoparticles. *J Am Chem Soc*. 2003;125:6644–6645.
85. Antonello S, Perera NV, Ruzzi M, Gascón JA, Maran F. Interplay of charge state, lability, and magnetism in the molecule-like $Au_{25}(SR)_{18}$ cluster. *J Am Chem Soc*. 2013;135:15585–15594.
86. Zhu M, Aikens CM, Hendrich MP, et al. Reversible switching of magnetism in thiolate-protected Au_{25} superatoms. *J Am Chem Soc*. 2009;131:2490–2492.
87. Liu Z, Zhu M, Meng X, Xu G, Jin R. Electron transfer between $[Au_{25}(SC_2H_4Ph)_{18}]-$TOA+ and oxoammonium cations. *J Phys Chem Lett*. 2011;2:2104–2109.
88. Chong H, Li P, Wang S, et al. Au_{25} clusters as electron-transfer catalysts induced the intramolecular cascade reaction of 2-nitrobenzonitrile. *Sci Rep*. 2013;3:3214.
89. Kawasaki H, Kumar S, Li G, et al. Generation of singlet oxygen by photoexcited $Au_{25}(SR)_{18}$ clusters. *Chem Mater*. 2014;26:2777–2788.
90. Antonello S, Hesari M, Polo F, Maran F. Electron transfer catalysis with monolayer protected Au_{25} clusters. *Nanoscale*. 2012;4:5333–5342.
91. Kauffman DR, Alfonso D, Matranga C, Li G, Jin R. Photomediated oxidation of atomically precise $Au_{25}(SC_2H_4Ph)_{18}-$ nanoclusters. *J Phys Chem Lett*. 2013;4:195–202.
92. Georganopoulou DG, Mirkin MV, Murray RW. SECM measurement of the fast electron transfer dynamics between Au_{38}^{1+} nanoparticles and aqueous redox species at a liquid/liquid interface. *Nano Lett*. 2004;4:1763–1767.
93. Hesari M, Workentin MS, Ding Z. Highly efficient electrogenerated chemiluminescence of Au_{38} nanoclusters. *ACS Nano*. 2014;8:8543–8553.
94. Swanick KN, Hesari M, Workentin MS, Ding Z. Interrogating near-infrared electrogenerated chemiluminescence of $Au_{25}(SC_2H_4Ph)_{18}+$ Clusters. *J Am Chem Soc*. 2012;134:15205–15208.
95. Baek G, Pandurangan P, Ko E, Mo Y, Lee D. Redox-active gold nanoclusters immobilized ZnO nanorod electrodes for electrochemical sensing applications. *RSC Adv*. 2014;4:10766–10769.
96. Chang H-C, Chang Y-F, Fan N-C, Ho J-aA. Facile preparation of high-quantum-yield gold nanoclusters: application to probing mercuric ions and biothiols. *ACS Appl Mater Interfaces*. 2014;6:18824–18831.
97. Chang H-Y, Chang H-T, Hung Y-L, Hsiung T-M, Lin Y-W, Huang C-C. Ligand effect on the luminescence of gold nanodots and its application for detection of total mercury ions in biological samples. *RSC Adv*. 2013;3:4588–4597.
98. Deng L, Zhou Z, Li J, Li T, Dong S. Fluorescent silver nanoclusters in hybridized DNA duplexes for the turn-on detection of Hg2+ ions. *Chem Commun*. 2011;47:11065–11067.
99. Wei H, Wang Z, Yang L, Tian S, Hou C, Lu Y. Lysozyme-stabilized gold fluorescent cluster: synthesis and application as Hg(2+) sensor. *Analyst*. 2010;135:1406–1410.
100. Wang C, Xu L, Wang Y, Zhang D, Shi X, Dong F, Yu K, Lin Q, Yang B, Fluorescent silver nanoclusters as effective probes for highly selective detection of mercury(II) at parts-per-billion levels. 2012;7:1652–1656.
101. Liu H, Zhang X, Wu X, Jiang L, Burda C, Zhu J-J. Rapid sonochemical synthesis of highly luminescent non-toxic AuNCs and Au@AgNCs and Cu (ii) sensing. *Chem Commun*. 2011;47:4237–4239.
102. Paramanik B, Bhattacharyya S, Patra A, Detection of Hg2+ and F− Ions by using fluorescence switching of quantum dots in an Au-cluster–CdTe QD nanocomposite. 2013;19:5980–5987.
103. Lan G-Y, Huang C-C, Chang H-T. Silver nanoclusters as fluorescent probes for selective and sensitive detection of copper ions. *Chem Commun*. 2010;46:1257–1259.
104. Roy S, Palui G, Banerjee A. The as-prepared gold cluster-based fluorescent sensor for the selective detection of AsIII ions in aqueous solution. *Nanoscale*. 2012;4:2734–2740.
105. Liu S, Lu F, Zhu J-J. Highly fluorescent Ag nanoclusters: microwave-assisted green synthesis and Cr3+ sensing. *Chem Commun*. 2011;47:2661–2663.

106. Muhammed H, A M, Pradeep T. Reactivity of Au_{25} clusters with Au_3+. *Chem Phys Lett*. 2007;449:186–190.
107. Bootharaju MS, Pradeep T. Investigation into the reactivity of unsupported and supported Ag_7 and Ag_8 clusters with toxic metal ions. *Langmuir*. 2011;27:8134–8143.
108. Chakraborty I, Udayabhaskararao T, Pradeep T. Luminescent sub-nanometer clusters for metal ion sensing: a new direction in nanosensors. *J Hazard Mater*. 2012;211-212:396–403.
109. Romanova J, Ranga Prabhath MR, Jarowski PD. Relationship between metallophilic interactions and luminescent properties in Pt(II) complexes: TD-DFT guide for the molecular design of light-responsive materials. *J Phys Chem C*. 2016;120:2002–2012.
110. Pyykkö P. Strong closed-shell interactions in inorganic chemistry. *Chem Rev*. 1997;97:597–636.
111. Hermann HL, Boche G, Schwerdtfeger P, Metallophilic interactions in closed-shell copper(I) compounds—a theoretical study. 2001;7:5333–5342.
112. Isse AA, Berzi G, Falciola L, Rossi M, Mussini PR, Gennaro A. Electrocatalysis and electron transfer mechanisms in the reduction of organic halides at Ag. *J Appl Electrochem*. 2009;39:2217.
113. Isse AA, Gennaro A, Lin CY, Hodgson JL, Coote ML, Guliashvili T. Mechanism of carbon−halogen bond reductive cleavage in activated alkyl halide initiators relevant to living radical polymerization: theoretical and experimental study. *J Am Chem Soc*. 2011;133:6254–6264.
114. Isse AA, Mussini PR, Gennaro A. New insights into electrocatalysis and dissociative electron transfer mechanisms: the case of aromatic bromides. *J Phys Chem C*. 2009;113:14983–14992.
115. Isse AA, Falciola L, Mussini PR, Gennaro A. Relevance of electron transfer mechanism in electrocatalysis: the reduction of organic halides at silver electrodes. *Chem Commun*. 2006:344–346.
116. Isse AA, Gottardello S, Maccato C, Gennaro A. Silver nanoparticles deposited on glassy carbon. Electrocatalytic activity for reduction of benzyl chloride. *Electrochem Commun*. 2006;8:1707–1712.
117. Fedurco M, Coppex L, Augustynski J. Ab initio and electrochemical studies on the reductive bond dissociation in Haloethanols. *J Phys Chem B*. 2002;106:2625–2633.
118. Bootharaju MS, Deepesh GK, Udayabhaskararao T, Pradeep T. Atomically precise silver clusters for efficient chlorocarbon degradation. *J Mater Chem A*. 2013;1:611–620.
119. Nair AS, Tom RT, Pradeep T. Detection and extraction of endosulfan by metal nanoparticles. *J Environ Monit*. 2003;5:363–365.
120. Bootharaju MS, Pradeep T. Understanding the degradation pathway of the pesticide, chlorpyrifos by noble metal nanoparticles. *Langmuir*. 2012;28:2671–2679.
121. Gupta SS, Chakraborty I, Maliyekkal SM. Simultaneous dehalogenation and removal of persistent halocarbon pesticides from water using graphene nanocomposites: a case study of Lindane. *ACS Sustain Chem Eng*. 2015;3:1155–1163.
122. Blackmond DG. The origin of biological homochirality. *Cold Spring Harb Perspect Biol*. 2010;2.
123. Bentley R Chirality in biology. In *Reviews in Cell Biology and Molecular Medicine*. 2006; 2nd Edition, Ed by: Robert A Meyers, Wiley-VCH Verlag GmbH & Co. KGaA, Weinheim.
124. Wang Y, Xu J, Wang Y, Chen H. Emerging chirality in nanoscience. *Chem Soc Rev*. 2013;42:2930–2962.
125. Valev VK, Baumberg JJ, Sibilia C, Verbiest T, Chirality and chiroptical effects in plasmonic nanostructures: fundamentals, recent progress, and outlook. 2013;25:2517–2534.
126. Yin X, Schäferling M, Michel A-KU, et al. Active Chiral Plasmonics. *Nano Lett*. 2015;15:4255–4260.
127. Li Z, Mutlu M, Ozbay E. Chiral metamaterials: from optical activity and negative refractive index to asymmetric transmission. *J Opt*. 2013;15.
128. Wang B, Zhou J, Koschny T, Kafesaki M, Soukoulis CM. Chiral metamaterials: simulations and experiments. *J Opt A: Pure Appl Opt*. 2009;11.
129. Lechtken A, Schooss D, Stairs JR, et al. Au_{34}−: A Chiral Gold Cluster? *Angew Chem Int Ed*. 2007;46:2944–2948.
130. Pei Y, Lin S, Su J, Liu C. Structure prediction of $Au_{44}(SR)_{28}$: a chiral superatom cluster. *J Am Chem Soc*. 2013;135:19060–19063.
131. Schaaff TG, Whetten RL. Giant gold−glutathione cluster compounds: intense optical activity in metal-based transitions. *J Phys Chem B*. 2000;104:2630–2641.
132. Yanagimoto Y, Negishi Y, Fujihara H, Tsukuda T. Chiroptical Activity of BINAP-Stabilized Undecagold Clusters. *J Phys Chem B*. 2006;110:11611–11614.
133. Knoppe S, Bürgi T. Chirality in thiolate-protected gold clusters. *Acc Chem Res*. 2014;47:1318–1326.

134. Nishida N, Yao H, Kimura K. Chiral functionalization of optically inactive monolayer-protected silver nanoclusters by chiral ligand-exchange reactions. *Langmuir*. 2008;24:2759–2766.
135. Knoppe S, Dolamic I, Dass A, Bürgi T, Separation of enantiomers and CD spectra of $Au_{40}(SCH_2CH_2Ph)_{24}$: spectroscopic evidence for intrinsic chirality. 2012;51:7589–7591.
136. Zeng C, Li T, Das A, Rosi NL, Jin R. Chiral structure of thiolate-protected 28-gold-atom nanocluster determined by x-ray crystallography. *J Am Chem Soc*. 2013;135:10011–10013.
137. Dolamic I, Varnholt B, Bürgi T. Chirality transfer from gold nanocluster to adsorbate evidenced by vibrational circular dichroism. *Nat Commun*. 2015;6:7117.
138. Zhang B, Bürgi T. Doping silver increases the $Au_{38}(SR)_{24}$ cluster surface flexibility. *J Phys Chem C*. 2016;120:4660–4666.
139. Wan X-K, Yuan S-F, Lin Z-W, Wang Q-M, A Chiral gold nanocluster Au_{20} protected by tetradentate phosphine ligands. *Angew Chem Int Ed*. 2014;53:2923–2926.
140. Shibu ES, Pradeep T. Quantum clusters in cavities: trapped Au_{15} in cyclodextrins. *Chem Mater*. 2011;23:989–999.
141. Pelayo JJ, Whetten RL, Garzón IL. Geometric quantification of chirality in ligand-protected metal clusters. *J Phys Chem C*. 2015;119:28666–28678.
142. Buda AB, Mislow K. A hausdorff chirality measure. *J Am Chem Soc*. 1992;114:6006–6012.
143. Krishnadas KR, Baksi A, Ghosh A, Natarajan G, Som A, Pradeep T. Interparticle reactions: an emerging direction in nanomaterials chemistry. *Acc Chem Res*. 2017;50:1988–1996.
144. Krishnadas KR, Ghosh A, Baksi A, Chakraborty I, Natarajan G, Pradeep T. Intercluster reactions between $Au_{25}(SR)_{18}$ and $Ag_{44}(SR)_{30}$. *J Am Chem Soc*. 2016;138:140–148.
145. Krishnadas KR, Baksi A, Ghosh A, Natarajan G, Pradeep T. Manifestation of geometric and electronic shell structures of metal clusters in intercluster reactions. *ACS Nano*. 2017;11:6015–6023.
146. Krishnadas KR, Baksi A, Ghosh A, Natarajan G, Pradeep T. Structure-conserving spontaneous transformations between nanoparticles. *Nat Commun*. 2016;7:13447.
147. Häkkinen H, Walter M, Grönbeck H. Divide and protect: capping gold nanoclusters with molecular gold−thiolate rings. *J Phys Chem B*. 2006;110:9927–9931.
148. Natarajan G, Mathew A, Negishi Y, Whetten RL, Pradeep T. A unified framework for understanding the structure and modifications of atomically precise monolayer protected gold clusters. *J Phys Chem C*. 2015;119:27768–27785.
149. Salassa G, Krishnadas KR, Pupier M, Viger-Gravel J, Bürgi T. Role of intercluster and interligand dynamics of $[Ag_{25}(DMBT)_{18}]-$ nanoclusters by multinuclear magnetic resonance spectroscopy. *J Phys Chem C*. 2021;125(4):2524–2530.
150. Krishnadas KR, Natarajan G, Baksi A, Ghosh A, Khatun E, Pradeep T. Metal–ligand interface in the chemical reactions of ligand-protected noble metal clusters. *Langmuir*. 2019;35:11243–11254.
151. Krishnadas KR, Udayabhaskararao T, Choudhury S, Goswami N, Pal SK, Pradeep T, Luminescent AgAu alloy clusters derived from Ag nanoparticles – manifestations of tunable AuI–CuI metallophilic interactions. 2014;2014:908–916.
152. Wang E, Xu WW, Zhu B, Gao Y, Understanding the chemical insights of staple motifs of thiolate-protected gold nanoclusters. *Small*. 2021;17:2001836.
153. Chakraborty P, Nag A, Natarajan G, Bandyopadhyay N, Paramasivam G, Panwar MK, Chakrabarti J, Pradeep T, Rapid isotopic exchange in nanoparticles. 2019;5:eaau7555.
154. Zhang B, Safonova OV, Pollitt S, et al. On the mechanism of rapid metal exchange between thiolate-protected gold and gold/silver clusters: a time-resolved in situ XAFS study. *Phys Chem Chem Phys*. 2018;20:5312–5318.
155. Liu C, Lin S, Pei Y, Zeng XC. Semiring chemistry of $Au_{25}(SR)_{18}$: fragmentation pathway and catalytic active site. *J Am Chem Soc*. 2013;135:18067–18079.
156. Huang B, Pei Y. On the mechanism of inter-cluster alloying reactions: two-stage metal exchange of $[Au_{25}(PET)_{18}]-$ and $[Ag_{25}(DMBT)_{18}]-$ clusters. *J Mater Chem A*. 2020;8:10242–10251.
157. Wang S, Abroshan H, Liu C, et al. Shuttling single metal atom into and out of a metal nanoparticle. *Nat Commun*. 2017;8:848.
158. Bootharaju MS, Sinatra L, Bakr OM. Distinct metal-exchange pathways of doped Ag_{25} nanoclusters. *Nanoscale*. 2016;8:17333–17339.
159. Cao Y, Fung V, Yao Q, et al. Control of single-ligand chemistry on thiolated Au_{25} nanoclusters. *Nat Commun*. 2020;11:5498.
160. Yao Q, Feng Y, Fung V, Yu Y, Jiang D-e, Yang J, Xie J. Precise control of alloying sites of bimetallic nanoclusters via surface motif exchange reaction. *Nat Commun*. 2017;8:1555.

CHAPTER

3

Nanocluster assembled solids

Arijit Jana[a] *and Thalappil Pradeep*[b]

[a]DST Unit of Nanoscience (DST UNS) & Thematic Unit of Excellence (TUE), Department of Chemistry, Indian Institute of Technology Madras, Chennai, India
[b]Deepak Parekh Institute Chair Professor and Professor of Chemistry, Department of Chemistry, Indian Institute of Technology Madras, Chennai, India

3.1 Introduction

Atomically precise noble metal nanoclusters (NCs) or aspicules are a new class of quantum materials having the core dimension of <3 nm, bridging the gap between atoms and nanoparticles. Closely spaced electronic orbitals and associated multiple electronic transitions, photoluminescence, chirality, semiconductivity, magnetism, etc., have rendered these materials unique in comparison to their bulk metallic counterparts.[1–3] The last decade witnessed the rapid exploration of different noble metal-based NCs of gold, silver, copper, their bimetallic and polymetallic counterparts protected by thiols, phosphines, proteins, DNAs, etc., which function as ligands. Metallic NCs and their compositions were studied in the gas phase as well as in the solution phase, using mass spectrometry. The study of NCs in the solid-state is lagging due to the difficulty in crystallizing them. Molecular complexity make their periodic packing difficult, resulting in amorphous solids. Intense efforts in this direction from various groups has eventually led to single crystals of different NCs. Single crystal structures solved using X-ray diffraction (XRD) and neutron diffraction helped us to elucidate their atomic arrangements in the solid-state. Along with single crystals, NC assembled gels and NCs in confined solids are also two different types of assembled solids wherein intercluster packing is relatively weak. In the first part of this chapter, we will discuss the limitation of crystallization and its remedy by applying modified crystallization techniques. Later part of the chapter discusses different types of assembled solids, such as cluster assembled gels, clusters in confined solids, etc., and their different properties.

3.2 Limitation of nanocluster solidification

After the discovery of C_{60}, metallic NCs in the gas phase have created tremendous interest. Different ionization techniques, such as laser-induced ionization, bombardment of metallic

DOI: https://doi.org/10.1016/B978-0-323-90879-5.00007-X

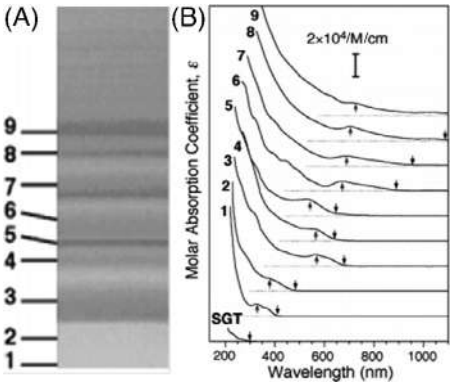

FIGURE 3.1 (A) Photographic image of the PAGE profile, where each color band indicates an individual nanocluster, (B) UV-vis spectral profile of the separated NCs with their characteristic features. Reproduced with permission from ref.[8]. Copyright 2005, American Chemical Society.

sources with inert gas ions, pulsed arc source and liquid metal ionization, etc., are used to prepare them in the gas phase. Baksi et al. prepared bare NCs of gold, such as Au_{25}^{+}, Au_{38}^{+}, and Au_{102}^{+} in the gas phase using laser desorption ionization of lysozyme-protected adducts.[4] The formation of a stable magic number of bare NCs in the gas phase is due to their electronic close shell structure. Similar to gold NCs, silver NCs are also prepared in the gas phase and their reactivity has been studied in the gas phase using mass spectrometry. Unsatisfied valences of the surface atoms make these gas-phase NCs highly reactive and they tend to form aggregated particles. Instability due to the reactivity limits their solidification in ambient condition. In monolayer-protected NCs, where the metallic core is protected by various surface ligands, reactivity is reduced. Most of the monolayer protected NCs have been synthesized in the solution phase by the reduction of metal thiolates using reducing agents. But crystallization of NCs always suffers from the complexity of a multiatomic environment. Although monolayer protected gold nanoparticles were prepared by Brust et al. in 1994, the first single crystals of gold NCs, that is, $[Au_{102}(p\text{-}MBA)_{44}]$ (where p-MBA = para-marcaptobenzoic acid) were made only in 2007.[5,6] In this section, we will discuss the limiting factors associated with the crystallization of monolayer protected NCs.

3.2.1 Synthetic limitations

Alchemists of the fourth century prepared gold, silver nanoparticles, and their alloys for imparting color and for medical purposes. In 1857, Faraday prepared colloidal gold by reducing $HAuCl_4$ using phosphorous.[7] The product was known as "potable gold." The transition from nanoparticles with particle dimension of 10–100 nm, to atomically precise nanoparticles with dimension of <3 nm began after the successful synthesis of gold nanoparticles by Brust et al. through the reduction of $HAuCl_4$ in two-phase (water and toluene) solvent mixture.[5] Monodispersed particle is the primary condition for obtaining quality crystals, but most of the solution-phase synthesis leads to polydispersed particles limiting their crystallization. Negishi et al. have shown the reduction of $HAuCl_4$ using $NaBH_4$ in presence of glutathione (GSH) as protecting ligands, which generates a mixture of Au NCs with varying nuclearity.[8] They separated all the NCs, that is, $[Au_{10}(SG)_{10}]$, $[Au_{15}(SG)_{13}]$, $[Au_{18}(SG)_{14}]$, $[Au_{22}(SG)_{16}]$, $[Au_{22}(SG)_{17}]$, $[Au_{25}(SG)_{18}]$, $[Au_{29}(SG)_{20}]$, $[Au_{33}(SG)_{22}]$, and $[Au_{39}(SG)_{24}]$ (shown in Fig. 3.1) using the polyacrylamide gel electrophoresis (PAGE) technique. These NCs were initially

identified using their characteristic UV-vis absorption features and further confirmed through mass spectrometric studies. They were unsuccessful in solving the structure due to the poor quality crystals.

Reducing agents have a profound role in solution-phase synthesis. Wu et al. presented the synthesis of $[Au_{19}(SR)_{13}]$ using a weaker reducing agent (borane-tetra butyl-amine complex), whereas strong reducing agents (sodium borohydride) resulted in $[Au_{25}(SR)_{18}]$.[9] Kinetic control of the product can be achieved based on the strength of the reducing agents, solvent mixtures, counter-ions, and the speed of stirring, whereas thermodynamic stability depends on their stability due to their magic number of closed-shell electrons. Size focusing is an approach to prepare monodispersed particles based on the thermodynamic stability.

The method is related to the better stability of a few gold NCs compared to other clusters. Size focusing of $[Au_{25}(SR)_{18}]$ upon prolonged aging leads to three characteristic UV-vis absorption features at 670, 450, and 400 nm. These peaks are the characteristic absorption features of Au_{25}. The size focusing process was further studied using matrix-assisted laser desorption ionization-mass spectrometric (MALDI-MS) measurements. Time-dependent measurements showed that just after the reaction, a mixture of NCs such as Au_{38}, Au_{44}, Au_{68}, and Au_{102} was formed along with Au_{25}. After 3 days of size focusing, Au_{25} survives as the end product due to its structural stability.

Other than the reduction of metal thiolate in the solution phase, ligand-exchange-induced structural transformation (LEIST) reactions have been used for synthesizing NCs. In this method, thiol-protected stable clusters have been synthesized from phosphine-protected labile clusters. Jana et al. showed the formation of Ag_{35} protected by 2-pyrene imine thiol and triphenylphosphine (TPP), using the LEIST reaction starting from the $[Ag_{18}(TPP)_{10}H_{16}]^{2+}$.[10] Cubical violet crystals of the NCs were grown using DCM/hexane layered crystallization. Due to the lack of intense diffraction spots, single-crystal structure was not resolved. Bodiuzzaman et al. prepared cocrystals of Ag_{40} and Ag_{46} NCs by following the LEIST reaction between the Ag_{18} and 2, 4-dimethylbenzene thiol (DMBT) ligand.[11] Crystallization of the reaction product leads to the formation of cocrystals of both the NCs in equal proportion within the lattice.

Apart from the traditional solution-phase synthesis, solid-state reaction by the mechanical grinding of metal precursors with ligands followed by the addition of reducing agents also results in NCs. Rao et al. reported the gram-scale synthesis of $[Ag_9(H_2MSA)_7]$ (where H_2MSA = mercapto succinic acid) using a solid-state synthesis.[12] Another report shows the solvent-free paste-based synthesis of $[Na_4Ag_{44}(p\text{-}MBA)_{30}]$, where the NC was formed by the reduction of a creamy white silver thiolate paste.[13] The characteristic UV-vis absorption spectrum and mass spectrometric studies confirm the formation of it. Although several reports showed the solid-state synthesis leading to NCs, homogeneous mixing of the reagents in their exact stoichiometric ratio is difficult. Kinetics of the atomic mobility is slow in comparison to solution-phase synthesis. Till today, there is no report of single-crystal structure of NC, prepared by solid-state methods.

3.2.2 Purification

The purity of monolayer-protected NCs is important for obtaining suitable quality crystals. The synthetic protocol mostly leads to polydisperse particles along with metallic complexes.

In earlier days, size-selected precipitation through ultracentrifugation was used extensively for purification. Carney et al. measured the sedimentation coefficients (S), namely 6.8, 9.6, and 27.1, for NCs $[Au_{25}(SR)_{18}]$, $[Au_{38}(SR)_{24}]$ and $[Au_{144}(SR)_{60}]$ (where SR = PET), respectively.[14] The S value increases upon increasing the molecular weight and hydrodynamic diameter of the NCs. Other purification methods, such as thin-layer chromatography (TLC), column chromatography, high-performance liquid chromatography (HPLC), polyacrylamide gel electrophoresis (PAGE), etc., were also used based on the principle of polarity differences. Using appropriate solvent is important for separation. Pradeep et al. have introduced the technique of TLC for the separation of NCs.[15–18] We have shown the TLC separation of mixed Ag_2S NCs using a THF/methanol (80: 20) mixture as the eluting solvent.[15] No separation was observed using 100% THF. Increasing the polarity upon the addition of methanol facilitates the separation. Another report demonstrated TLC separation of two Au_{25} NCs protected by hexane thiolate (HT) and butane thiolate (BT), using DCM/hexane solvent mixture. Even though the polarity difference between HT and BT is small, DCM/hexane solvent ratio of 40: 60, can separate them well.[16] This technique can also be used to remove excess thiol present during the course of the reaction. Not only the surface ligands, but also the inherent charge of the clusters promote the seperation. Sugi et al. have demonstrated the separation of Au_{25} NCs with different charge state, using reverse-phase HPLC technique by tuning the stationary phase of the column with alkyl and aryl functionality.[17] The weak van der Waals interaction between NCs with the stationary phase decides their separation. The high surface area of the stationary phase promotes selective absorption. Another report from this group showed precise separation of mixed thiolated alloy NCs, that is, $[PdAu_{24}(SR_1)_{18\text{-}n}(SR_2)_n]$, (where $n = 0, 1, 2,\ldots,18$) using HPLC technique.[18] During the separation, the mixture of clusters was adsorbed on the stationary phase by passing methanol. As clusters are insoluble in methanol, it promotes their adsorption in the column. In the second step, tetrahydrofuran (THF) was used as an eluting solvent. As the clusters are soluble in THF, it gradually eluted each clusters. There are a few reports on the separation of the mixture of gold NCs with limited success. Silver NCs are rarely separable using chromatography due to their comparable polarity and strong absorption by the stationary phase of the column. PAGE has been successful in separating two nearly similar silver NCs such as Ag_7 and Ag_8, protected by mercapto-succinic acid (MSA) ligands.[19] The Ag_7 NC separated by PAGE is bluish green-emitting, whereas Ag_8 NC is red-emitting.

3.2.3 Stability of nanoclusters

Metal NCs with dimension < 3 nm are reactive due to their high surface energy and intrinsic electronic structure. Several reports suggested that poor stability has limited their practical applications. The structural stability of NCs depends on the superatomic (close electronic cells such as 2, 8, 18 electrons) electronic configuration. NCs of nonsuperatomic configuration are relatively less stable. Unlike gold NCs, silver NCs are rarely reported due to their susceptibility toward oxidation. Silver NCs are light sensitive as well. Light-triggered interconversion from *ortho*-carborane 1, 2-dithiol protected Ag_{42} NC to Ag_{14} NC was observed through different intermediate NCs.[20] Formation of kernel-centered stable charge carriers was responsible for such type of interconversion.

3.3 Methods of nanocluster solidification

3.3.1 Crystallization

Crystallization of NCs is a phase transformation process, whereby an ordered phase forms from a disordered phase. The growth of crystals of a suitable size depends on two major processes, that is, nucleation and crystal growth. Nucleation is the primary process whereby NC aggregated among themselves and forms seed crystals. During the growth process, seed crystals transform to macro crystals. Purified NC of optimum concentration is required for the growth of suitable crystals. In this section, we discuss solvent-induced crystallization, wherein crystal growth occurs slowly inside suitable solvents. In addition to that, we will also discuss electro-crystallization of NCs, where millimeter size crystals are grown upon applying an electrical potential. There is no report so far of crystals of metal nanoparticles with dimension >5 nm.

3.3.1.1 Solvent-induced crystallization

Solvent-induced crystallization is the primary process of crystallization. More than 100 crystals have been grown by solvent-induced crystallization of gold, silver, copper, and alloy NCs. Various factors, such as choice of solvents, saturation limit, temperature and vapor pressure of the solvent control the quality and size of the crystals. Crystals are grown using different crystallization techniques, such as (1) solvent layering, (2) vapor diffusion, (3) hanging drop method, etc. In the solvent layering process, NCs solution in a "good" solvent is placed at the bottom of the crystallization tube and "bad" solvents are added as a layer on the top. The crystals form in the interface of the two solvents. Joshi et al. crystallized Ag_{25} by layering hexane on top of dichloromethane (DCM) at 4°C.[21] During the vapor diffusion process, solvents with high vapor pressure are placed outside the crystallization tube. The solvent vapor diffused into the seed solution and forms crystals. Crystals belonging to another crystal system were formed using the vapor diffusion of methanol into its DMF solution.[22] The slow evaporation of DMF leads to cubic crystals, whereas methanol vapor diffusion leads to trigonal crystals. In the hanging drop method, a large drop of a solution of cluster is exposed to the surrounding environment consisting of secondary solvents. Cerretani et al. have crystallized a NIR emitting Ag_{16} protected by DNA using the hanging drop method in an environment containing 3-(N-morpholino) propane sulfonic acid (pH 7), spermine, $Ca(NO_3)_2$ and polyethylene glycol at 293 K (Fig. 3.2).[23]

3.3.1.2 Electro-crystallization

Electro-crystallization is a fast crystallization technique by which crystals are grown on the electrode surface by applying low current, typically 50–200 nA. High-quality large crystals for applications in solid-state electronic devices are grown using this method. Recently, Antonello et al. reported the first crystals of clusters grown by electro-crystallization.[24] They have crystallized three different $[Au_{25}(SR)_{18}]^0$ NCs protected by organic thiols using this method. It may be noted that as synthesized $[Au_{25}(SR)_{18}]^-$ is diamagnetic in nature and its aerobic oxidation generates stable neutral paramagnetic $[Au_{25}(SR)_{18}]^0$ analog. Further oxidation of

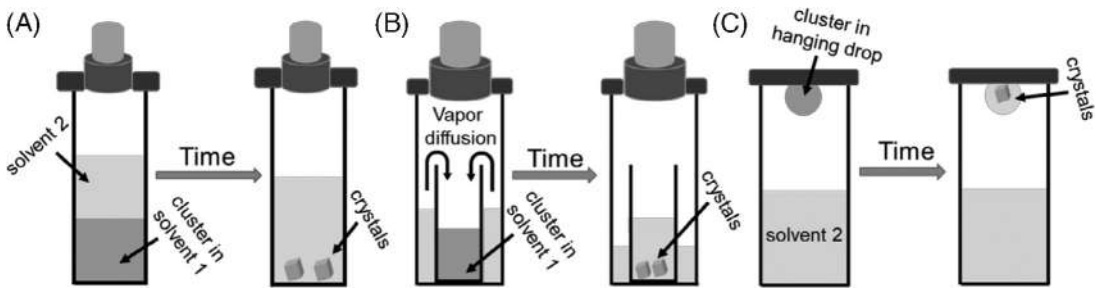

FIGURE 3.2 Schematic representation showing various solvent-induced crystallization techniques, that is, (A) layering, (b) vapor diffusion, and (C) hanging drop method.

the neutral species generates monocationic $[Au_{25}(SR)_{18}]^+$. Other higher charge state species are chemically labile. Multiscan cyclic voltammetry studies showed that neutral Au_{25} accumulates on the electrode surface and did not leave the diffusion layer, while anionic Au_{25} NCs diffuse toward electrodes, thereby accumulating increasing amount of clusters on the electrode surface. Fig. 3.3 shows optical images of the as grown millimeter size crystals on the gold electrode surface. The inherent electrical charge of the NC is the driving force for the potential driven intercluster packing. Not only the applied electrical potential, but also the deposition time, cluster concentration, nature of the electrode materials, and choice of solvent system are significant aspects during electro-crystallization.

3.3.2 Gelation

Gelation is the process by which NCs are linked to each other randomly through crosslinking and forms extended network solids. Generally, polymer materials such as poly-methyl methacrylate (PMMA), poly-vinylidene fluoride (PVDF), nylon, and poly-tetrafluoroethylene, with long hydrocarbon chains, are well known for their gelation property. Cluster assembled gels gained attention due to their composite properties. Three different methods were extensively used for gelation: (1) use of good and bad solvents, (2) use of polymer matrix as a gelation inducer, and (3) use of ions for induced gelation. Wu et al. showed the formation of self-assembled nanosheets of Ag_{15} NCs due to their hydrophobic interaction. The surface ligand, that is, 1-dodecanethiol promotes the intercluster assembly.[25] The same group have also shown the formation of multi-layered nanosheets due to dipole-induced intercluster interaction.[26]

3.4 Single crystal structure determination

The crystal structure of NCs was resolved using diffraction techniques carried out on suitable single crystals. XRD and electron diffraction (ED) are commonly used techniques for their structure determination. Although transmission electron microscope (TEM) can deduce the size and shape of the metallic core, interfacial ligands are not resolved using TEM. Several

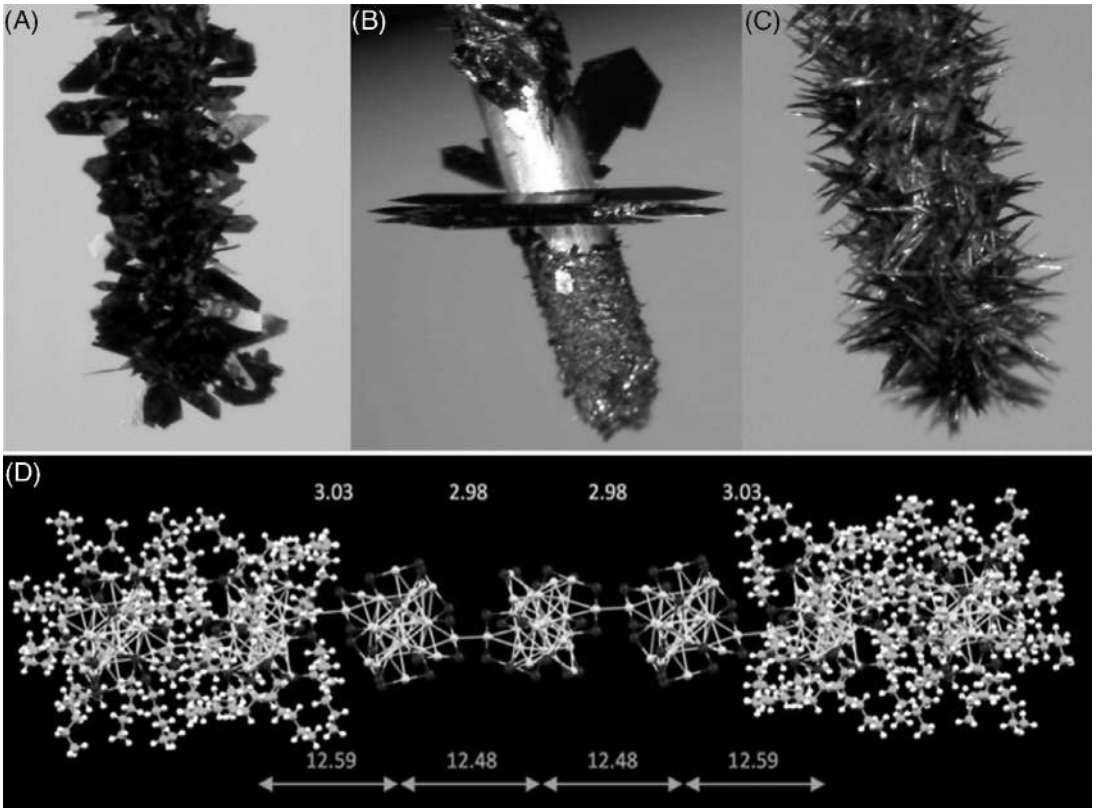

FIGURE 3.3 (A–C) Photographic images of the as grown Au_{25} crystals on the gold electrode surface. (D) Single-crystal molecular packing showing the linear packing of the Au_{25} cluster. Reproduced with permission from ref.[24]. Copyright 2017, American Chemical Society.

TEM measurements concludes the presence of an "amorphous layer" outside the metallic core. Single-crystal XRD resolved the atomic arrangements of the ligands as well as the metallic bonding of the kernel. The principle of the XRD technique is based on the interference of X-ray beam by the repetitive lattice arrangement of the atoms present in the crystals. The interference of X-ray with the crystals generates bright spots following the Bragg's law, that is, $n\lambda = 2d\sin\theta$, where n = integer, called the order of reflection, λ = wavelength of the X-ray beam, d = interlayer spacing, and θ = angle of incidence. The X-ray diffractometer used for structural determination consists of an X-ray source, goniometer, beam stopper, detector, and associated electronic components. A heated cathode-ray tube generates accelerated thermionic electrons, which collides with the target, typically made of Mo or Cu for X-ray generation. A filtered monochromatic X-ray beam is collimated before directing it to the crystals for diffraction. Although the resolution is higher in a normal lab X-ray diffractometer, a synchrotron X-ray diffractometer uses an intense X-ray source, which reduces the data collection time. Crystals are mounted on the goniometer to collect diffraction spots from all possible angles.

Different types of polymer mounting loops are used to place the crystals on the goniometer using a viscous oil. A beam stopper is placed opposite to the collimator to cut down the transmitted and small-angle diffraction spots, which prevents the burn out of the detector. Modern X-ray detectors used are charge-coupled devices and they convert X-ray photons into electrical signals for data processing. It records both the position and intensity of the diffraction peaks.

Structure solution of a crystal follows a few steps, such as (1) determination of unit cell and crystal system, (2) full-range data collection in all angles, (3) structural refinement and construction of the structure using different models. After positioning the crystal in the center, the initially collected set of diffraction frames determines the unit cell through auto-indexing. The orientation matrix of the unit cell inside the lattice is also calculated. The initial primitive unit cell and orientation matrix is further refined using the least square refinement method. After the refinement, full data collection in the possible 2θ range of 5–90° is carried out over 6–24 h based on crystal quality and the diffractometer. Each frame of diffraction spots is collected as a sphere and hemisphere upon increasing 0.1 to 0.3° range. Low-temperature data collections are performed based on sample quality. Data collections at low temperature reduce thermal ellipsoids, which helps to fix the electron density of individual atoms. After the collection of full data, structure solution was performed using different software packages. The information of unit cell, space group, reflection intensities, and the reflection phases are essential to calculate the electron density maps using the Fourier series. Anisotropic refinement parameters of the atoms are considered in the later stage of refinement due to the ellipsoid nature of the electron density of individual atoms in a chemical bond. Resolution of the crystals determines the bond length and it should be at least 1 Å. Generally, hydrogen atoms are not mapped due to their small electron density, so they are inherently included in the respective position. For the specific interest of hydrogens, neutron diffraction experiments are carried out for accurate positioning. The major problem of structural determination of NCs is the formation of microcrystals and polycrystals having multiple domains.

Structural determination of NCs using electron diffraction (ED) is an alternative approach. Low-dose electron beam is used for obtaining diffraction spots in this technique. Azubel et al. structurally resolved Au_{68} using this method.[27] The use of low-dose electron beam reduced the beam-induced damage of the crystals. Subsequently, image averaging was performed to improve the signal-to-noise ratio. A three dimensional reconstruction strategy was employed to get electron density maps. The ED structure was further verified by small angle X-ray scattering (SAXS), infrared absorption, and density functional theory (DFT) studies.

3.5 Different types of nanocluster assembled solids

NAS are packed NCs with varying order of intermolecular packing. As compared to amorphous or powder-like solid materials, crystalline materials have a long-range of inter-cluster ordering, which is called lattice. Different types of intermolecular interactions such as electrostatic interaction, CH–π interaction, π–π stacking, aurophilic interaction, etc., lead to crystallization. Structure determination of a single crystal through XRD correlates with their properties (Fig. 3.4).

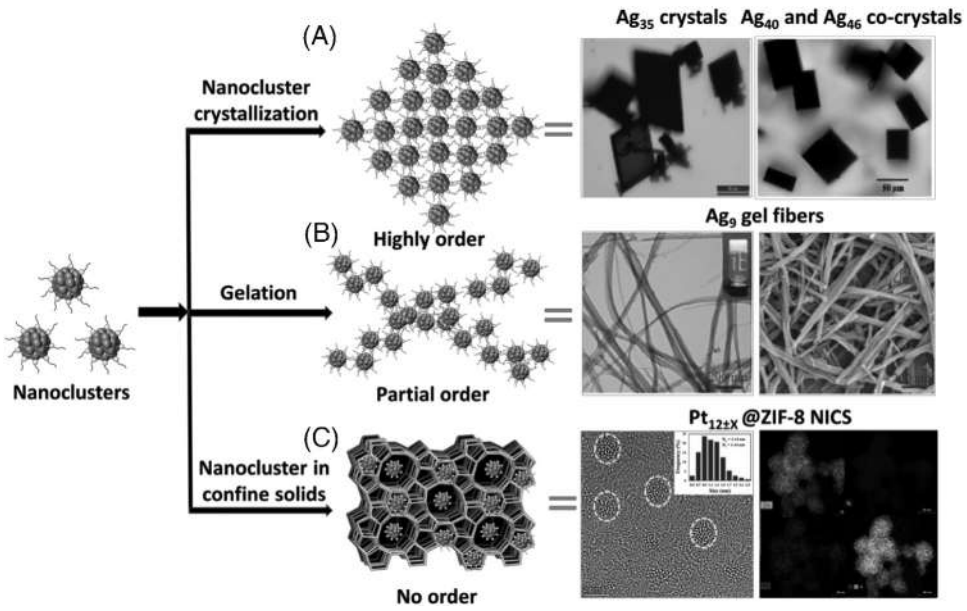

FIGURE 3.4 Overview of different types of assembled solids: (A) crystals, (B) gel fibers, and (C) NCs in confined solids. Optical and SEM images of these materials are shown here. Reproduced with permission from refs.[10,11,45,48]. Copyright 2020 Royal Society of Chemistry, copyright 2019 Wiley-VCH, copyright 2019, 2020 American Chemical Society.

3.5.1 Nanocluster crystals

3.5.1.1 Homocluster crystals

Homocluster crystals have only one type of NCs inside the unit cell. Sometimes, counter ions or solvent molecules are also packed inside the unit cell with different favorable intermolecular interactions. NCs having counter ions or solvent molecules belong to the group of homocluster crystals. Here we will discuss gold, silver and alloy homocluster crystals.

3.5.1.1.1 Gold nanocluster crystals

Among different metal NCs, gold NCs lead the field due to the facile synthetic protocol as well as stable products. In the year of 2007, Jadzinsky et al. successfully resolved the structure of $[Au_{102}(p\text{-}MBA)_{44}]$ NC using single-crystal XRD technique.[6] The NC has a decahedron-shaped gold core, which was further surrounded by a shell of Au atoms. The p-MBA ligands protected the gold atoms through Au-S bonds. Later in 2008, Heaven et al. resolved the structure of $[Au_{25}(SCH_2CH_2Ph)_{18}]^-$, composed of an Au_{13} icosahedral core with a central atom and a shell of 12 gold atoms connected as six Au_2S_3 staples, positioned in the 12 face of the icosahedron.[28] Qian et al. determined total structure of $[Au_{38}(SC_2H_4Ph)_{24}]$ nanoparticles.[29] The core of the NC is composed of two face-fused Au_{23} biicosahedra, which is further capped by three monomeric and six dimeric silver sulfide staples. Generally, it was observed that the crystal system of gold metals and nanoparticles is face-centered cubic (fcc), so it is interesting

to understand the atomic arrangement of the gold core of NCs. Depending on the binding of ligands, the packing style of the gold core is of diverse types, including fcc, body-centered cubic (bcc) and hexagonal close packing (hcp). Au NCs having bcc type arrangement were first observed in $[Au_{38}S_2(SR)_{20}]$, where SR is adamentane thiolate. The conversion from fcc type $[Au_{38}(SR)_{24}]$ to bcc type in $[Au_{38}S_2(SR)_{20}]$ is due to ligand-induced core transformation.

Although gold NCs with small nuclearity (<150 atoms) are molecular in nature, with multiple UV-vis absorption features, increasing the nuclearity imparts them with metallic character. A handful of structurally resolved large gold NCs, such as $[Au_{191}(SR)_{66}]$, $[Au_{246}(SR)_{80}]$, etc., showed molecular to plasmonic transition. The Au_{191} has a singly twined Au_{155} core, protected by a shell of 24 monomeric (–S–Au–S–) and s dimeric (–S–Au–S–Au–S–) staples. The Au_{155} core is further made up of Au_{89} inner core and 66 surface Au atoms. The inner core is made up of layered Au_3 inner triangle, protected by Au_{23} hexagonally packed close shell kernel and a shell of 63 Au atoms.

3.5.1.1.2 Silver nanocluster crystals

The first structurally resolved single crystal of silver NC, $[Ag_{44}(p\text{-}MBA)_{30}]^{4-}$ was reported in 2013. The cluster has a dodecahedral Ag_{32} core, made up of Ag_{12} icosahedron encapsulated by Ag_{20} dodecahedron. The Ag_{32} core is further protected by six Ag_2S fragments. AbdulHalim et al. structurally resolved the crystal structure of $[Ag_{29}(BDT)_{12}(TPP)_4]$ (where BDT = 1, 3 benzene dithiol and TPP = triphenylphosphine), in 2015.[30] The NC has a central icosahedron (Ag_{13} core) surrounded by $Ag_{16}S_{24}P_4$ shell. Fig. 3.5 shows the structural anatomy of the Ag_{29}. It was observed that 12 silver atoms on the shell form four trigonal prisms and are oriented in a tetrahedral fashion. The same group structurally resolved $[Ag_{25}(DMBT)_{18}]^-$ having a centered icosahedral (Ag_{13}) core, connected by nonicosahedral Ag_{12} atoms through 18 sulfide linkages as six Ag_2S_3 staples.[21] DFT studies showed that their molecular like multiple UV-vis absorption features are due to electronic transitions from triply degenerate HOMO to doubly degenerate LUMO orbitals. The same group also prepared a box-shaped $[Ag_{67}(SPhMe_2)_{32}(PPh_3)_8]^{3+}$.[31] Structural anatomy showed that it has an Ag_{23} core and a box-like $Ag_{44}S_{32}P_8$ shell. As formed Ag_{23} core is composed of several fused cuboctahedra, which is distinctly different from the commonly formed icosahedral core. The absorption spectrum showed molecular features.

In comparison to the thiolate-protected silver NCs, the protein, dendrimer-protected NCs are rarely solved using SC-XRD, due to difficulty in crystallization. Several DNA-based silver NCs have been synthesized and studied through mass spectrometric studies. The first report of structurally resolved green-emitting DNA-protected Ag_8 was made in 2019.[32] The flexibility of the encapsulating 5′-AACCCC-3′ nucleotide determines the shape of Ag_8. The Ag_8 has a trapezoidal Ag_5, of which four silver atoms are coplanar, while the fifth silver atom is ~12° out of the plane. The remaining three silver atoms have a zipper-like arrangement. Later, Cerretani et al. synthesized a NIR emitting DNA-protected Ag_{16} and solved its single crystal structure.[23] Fig. 3.6 shows the single-crystal structure of the NC. Two DNA decamer fragments of 5′-CACCTAGCGA-3′ protected the Ag_{16} core in a horse-shoe like conformation. The diameter and height of each decamer fragment is 7 Å and 15 Å and they are bonded to silver core through silver mediated interactions and a few hydrogen bonds. The Ag–Ag bond distance of 2.7–2.8 Å indicates strong metallic bonding.

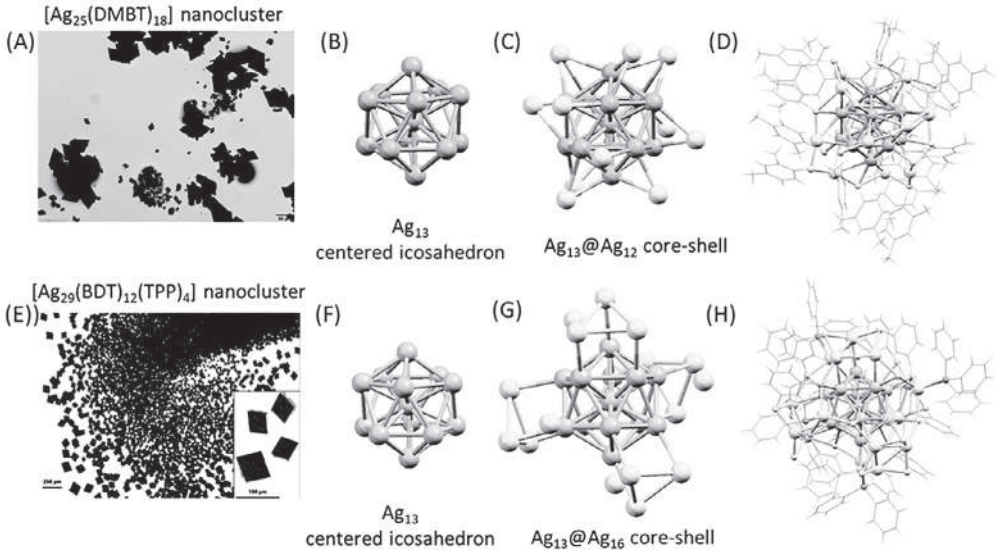

FIGURE 3.5 (A,E) Optical microscopic images of Ag_{25} and Ag_{29} crystals, respectively. (B,F) Both the NCs have Ag_{13} centered icosahedral core. (C,G) The Ag_{13} core is further protected by twelve independent Ag atoms which creates a $Ag_{13}@Ag_{12}$ core-shell geometry for Ag_{25} NCs, whereas four Ag_3 units capped the Ag_{13} core in a tetrahedral fashion along with four Ag atoms creates a $Ag_{13}@Ag_{16}$ core-shell geometry in Ag_{29}. (D,H) Total structure of the Ag_{25} and Ag_{29} NCs, respectively. Reproduced with permission from refs.[21,30]. Copyright 2015, 2015 American Chemical Society.

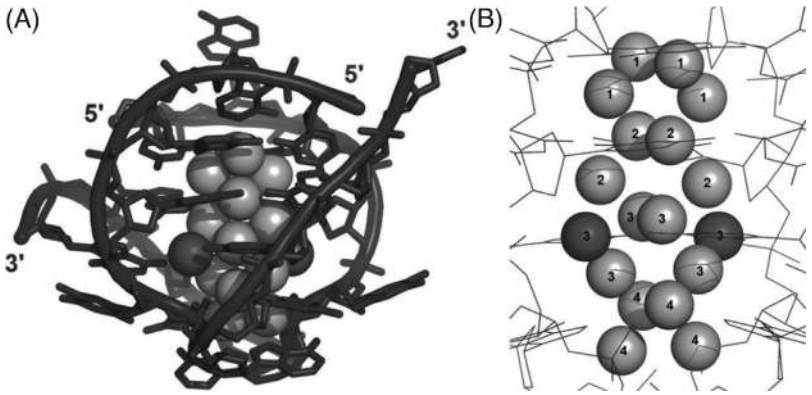

FIGURE 3.6 (A) Total structure of Ag_{16} protected by two DNA stands, (B) four layer-like core arrangements of silver atoms. Reproduced with permission from ref.[23]. Copyright 2019, Wiley VCH.

3.5.1.1.3 Alloy nanocluster crystals

Alloy NCs have more than one metal in their metal core. Alloy NCs are generally of two types, (1) doped alloy NCs, wherein a few (<5) of heteroatoms are present, (2) bimetallic alloy NCs, where heteroatoms are present in large number (>5) and stay in specific core or shell of

the NCs. Murray et al. first prepared the palladium doped alloy NC, that is, $[PdAu_{24}(SR)_{18}]$.[33] They confirmed the cluster composition through mass spectrometric studies. Single-crystal structure reveals that Pd atom is localized at the centroid of the Au_{12} icosahedron. They also observed that the shorter Pd-Au bonds as compared to Au-Au bonds causes enhanced stability. Heteroatom doping drastically alters their electronic structure. According to DFT calculations, $[Au_{25}(SR)_{18}]^-$ has a 8e system, which is converted to $[Pd(Au_{24}(SR)_{18}]^0$ with 6e. The HOMO-LUMO band gap (0.33 eV) of Pd doped alloy cluster in significantly smaller than the Au_{25} (1.35 eV). Not only palladium, other monometallic Au_{25} NCs such as $[Au_{24}Pt(PET)_{18}]$, $[Au_{24}Cd(SC_2H_4)_{18}]$, $[Au_{24}Cu(PET)_{18}]$, and $[Au_{24}Hg(SC_2H_4Ph)_{18}]$ have been synthesized using different strategies and some of them were structurally elucidated using single-crystal XRD.

Similar to doped gold NCs, doped silver NCs are also reported by various groups. Yang et al. prepared $[Au_{12}Ag_{32}(SR)_{30}]$ bimetallic alloy NCs, analogous to the $[Ag_{44}(SR)_{30}]$.[34] The bimetallic alloy NC has a double-shell like $Au_{12}@Ag_{20}$ core, protected by six $Ag_2(SR)_5$ units on the surface. The inner core of the cluster consists of an Au_{12} hollow icosahedral cage, protected by a dodecahedral Ag_{20} shell. Another bimetallic alloy NC of $[Au_{80}Ag_{30}(C{\equiv}CPh)_{42}Cl_9]$ has also been reported with four-shell metallic core arrangement as, $Au_6@Au_{35}@Ag_{30}Au_{18}@Au_{21}$. The chloride ligands bonded in μ_2 mode are significant to stabilize the NC. Yang et al. prepared a bimetallic Ag-Cu alloy NC, $[Ag_{40.13}Cu_{13.87}S_{19}(^tBuS)_{20}(^tBuSO_3)_{12}]$ having sulfonate ligands.[35] The cluster consists of a $Cu_{10}Ag_2S_7$ core surrounded by $M_{42}(^tBuS)_{20}(^tBuSO_3)_{12}$ shell. A few bare sulfur atoms connect the core with the shell and the surface of the cluster is protected by oxygen atoms of $^tBuSO_3$ and S atoms of ^tBuS ligands.

3.5.1.2 *Heterocluster crystals and cocrystals*

Heterocluster crystals are a new type of crystals having more than one cluster packed inside the unit shell. Huang et al. prepared peanut like silver thiolate NC encapsulated by the polyoxomolybdate anion. This heterocluster crystal has a $[Mo_{20}O_{66}]^{12-}$ core, surrounded by $[Ag_{62}(S^tBu)_{40}]^{22+}$ shell.[36] The $[Mo_{20}O_{66}]^{12-}$ core is made up of two $[Mo_7O_{24}]^{6-}$ heptamolybdenum anions, which are connected by a bridging $[Mo_6O_{18}]$ unit. Oxygen ligands are connected to each other and forms the $[Mo_{20}O_{66}]^{12-}$ unit. The silver thiolate shell is stabilized by Ag–S covalent bond and Ag···Ag argentophilic interactions. The absorption spectrum showed absorption bands up to the near IR region, owing to the charge transfer from $[Mo_{20}O_{66}]^{12-}$ donor to $[Ag_{62}(S^tBu)_{40}]^{22+}$ acceptors. This type of near IR edge was not observed for silver NCs. Similarly, Liu et al. reported heterocluster crystals of Ag clusters having 90 silver atoms encapsulated by a $W_5O_{19}^{8-}$ unit.[37] Structural anatomy reveals that the structure is similar to a dumbbell, with two $W_5O_{19}@Ag_{38}$ heads connected by a narrow $(SO_4)_2Ag_{14}$ waist. The material showed strong near-infrared emission upon cooling down to 93 K.

Cocrystallization is a new approach for preparing crystals having more than one NC in a single lattice. Cocrystallized NCs have superior physiochemical properties as compared to their individual components. Although there is no report of gold-based cocrystals, different pairs of silver NCs such as Ag_8–Ag_{12}, Ag_{16}–Ag_{17}, Ag_{40}–Ag_{46}, Ag_{210}–Ag_{211}, etc., were reported recently by various groups.[38] The exchange reaction between $[Ag_{18}(PPh_3)_{10}H_{16}]$ and $HSPhMe_2$ ligands spontaneously cocrystallized $[Ag_{40}(SPhMe_2)_{24}(PPh_3)_8]$ and $[Ag_{46}(SPhMe_2)_{24}(PPh_3)_8]$ NCs with the same number of surface ligands but different core atoms.[11] Inside the lattice, both clusters are symmetrically packed in the same proportion. The main difference between these

clusters is that Ag_{40} has an Ag_8 simple cubic kernel, whereas Ag_{46} has an Ag_{14} fcc kernel. The presence of a common shell, $[Ag_{32}(SR)_{24}(PPh_3)_8]$ causes their packing. Intercluster interaction of similar surface ligands is the driving force behind the binary packing.

3.5.1.3 *Isomeric and polymorphic crystals*

Isomeric NCs are a pair of NCs with the same molecular formula but different geometric structures. Polymorphism is the property of NCs whereby identical clusters crystallize in different crystal structures. Pseudo-polymorphism occurs when a compound exhibits different crystalline structures, of which a structure has a host of solvent molecules. The structural variation could be due to: (1) variation of ligands, (2) effect of solvents during crystallization, (3) presence of counter ions, etc., We will discuss some examples of isomorphic and polymorphic crystals.

There was no report on structural isomerism of NCs, until 2013. In 2014, two gold NCs, $[Au_{24}(SCH_2Ph\text{-}^tBu)_{20}]$ and $[Au_{24}(SePh)_{20}]$ have the same number of Au atoms with thiol or selenol ligands, respectively, are considered as an example of core isomerism. Structural anatomy of these NCs revealed that both have an Au_8 inner kernel, composed of bi- Au_4 tetrahedra. The outer kernel of $[Au_{24}(SCH_2Ph\text{-}^tBu)_{20}]$ is composed of four $Au_4(SR)_5$ staples, whereas two trimeric $[Au_3(SeR)_4]$ and two pentameric $[Au_5(SeR)_6]$ staples construct the outer kernel of $[Au_{24}(SePh)_{20}]$. The difference in their kernel structure leads to different UV-vis optical absorption features. As the ligands are not identical, they are not isomers. However, kernel structure variation was revealed for these clusters, which manifest in optical properties. Tian et al. reported a pair of structural isomers of $[Au_{38}(PET)_{24}]$ (Au_{38T}) with earlier reported structure (Au_{38Q}) having the same ligand.[39] Structural analysis reveals that Au_{38Q} (Q for Qian) has a Au_{23} core, composed of two icosahedral Au_{13} units formed through the Au_3 face sharing. The Au_{23} core is further protected by six dimeric (Au_2S_3) and three monomeric (AuS_2) staples. However, Au_{38T} (T for Tian) has an Au_{23} core with a single Au_{13} icosahedron and Au_{12} capping with Au_2 sharing. The core is further surrounded by three Au_2S_3, two Au_3S_3, three AuS_2, and one free sulfide protection. These isomers exhibit distinctly different optical properties as well as structural stability. Au_{38T} is less stable in comparison to Au_{38Q} and irreversible thermal transformation from Au_{38T} to Au_{38Q} was observed.

Tuning of surface ligands is also significant in core isomerism. Jin et al. reported $[Au_{28}(SR)_{20}]$ NC protected by two different thiolates, that is, tertiary butyl benzene thiol (TBBT) and cyclohexane thiolate (CHT).[40,41] They prepared TBBT-protected Au_{28} by ligand exchange reaction of $[Au_{25}(PET)_{18}]$ using excess TBBT ligand. They synthesized $[Au_{28}(CHT)_{20}]$ by ligand exchange reaction of $[Au_{28}(TBBT)_{20}]$. It has also been observed that the conversion is reversible. X-ray crystallographic studies reveal that both the NCs have FCC penetrated bicuboctahedral Au_{20} core. Surface packing showed that $[Au_{28}(CHT)_{20}]$ was protected by two trimeric and two monomeric units, whereas $[Au_{28}(TBBT)_{20}]$ was protected by four dimeric units (presented in Fig. 3.7). Distortion of packing in both the Au_{20} core and gold–sulfur interface was observed.

We have reported a polymorphic $[Ag_{29}(BDT)_{12}(TPP)_4]$ having cubic and trigonal forms with variable luminescence.[22] Crystallization of $[Ag_{29}(BDT)_{12}(TPP)_4]$ by dropcasting in DMF solution leads to cubic crystals, whereas vapor diffusion of methanol in DMF leads to trigonal crystals. Although molecular structure of both the forms is exactly the same, the unit cell molecular packing indicates eight NCs packed together inside the unit cell for cubic crystals, whereas six NCs are packed for trigonal crystals. We have also observed that cubic crystals

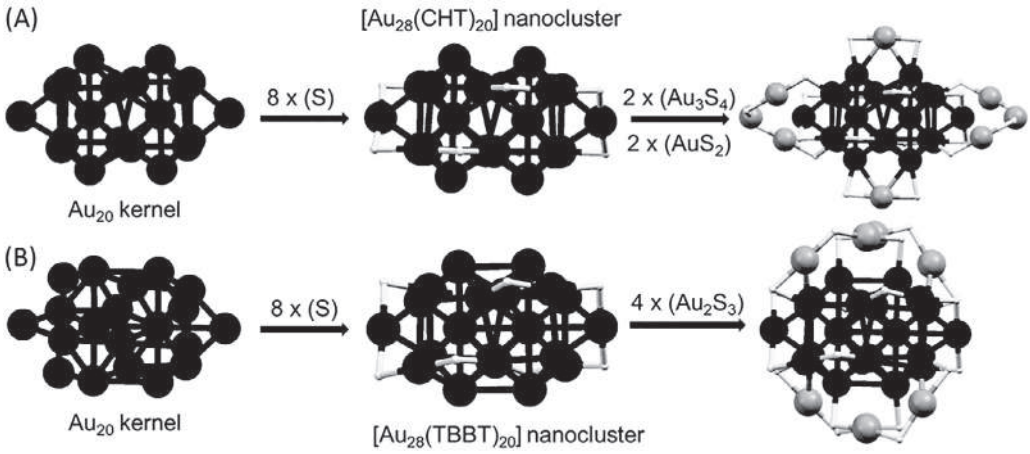

FIGURE 3.7 Structural anatomy of (A) $[Au_{28}(CHT)_{20}]$ and (B) $[Au_{28}(TBBT)_{20}]$ NCs having an Au_{20} kernel and different sulfide staples. Different interatomic bonding was observed in these structures. Reproduced with permission from refs.[40,41]. Copyright 2013, 2016 American Chemical Society.

are more luminous compared to trigonal crystals. Secondary ligand shell of Ag_{29} influences intercluster packing. Single-crystal XRD showed that several CH–π interactions of the secondary ligands is the driving force for better rigidity of the cubic crystals. The higher rigidity of cubic crystals imparts them enhanced luminescence as compared to trigonal crystals.

3.5.2 Nanocluster assembled gels

NC assembled gels are semi-crystalline solids, that retain chemical properties of the individual NC. NC protected by hydrophilic ligands such as 2-marcaptobenzoic acid (MBA), 2-mercaptonicotinic acid (MNA), etc., has a tendency to form hydrogels. Xie et al. studied the gelation tendency of water soluble $[Ag_9(MBA)_9](NH_4)_9]$ (shortly Ag_9) NC, which formed fibers in presence of an antisolvent (Fig. 3.8).[42]

The gelation of NCs was achieved by intercluster argentofilic interactions and several other noncovalent interactions such as π–π stacking, hydrogen bonding, CH–π interaction, etc., Photoluminescence studies ascertained their emission enhancement from solution state to the gel state, owing to the transition from loosely organized assemblies to confined gel fibers. Time-resolved lifetime measurements confirm the average lifetime (T_{ave}) of 400 ns in the gel state in comparison to the lifetime of 3 ns in solution. The 144 times enhancement of the lifetime indicates the switching from fluorescence to phosphorescence. NC assembled gels are mostly irreversible in nature, due to their strong chemical bonding with each other. Another study carried out by Shen et al. showed the morphological evolution of the as grown self-assembled Ag_6.[43] Protonated Ag_6 (Ag_6-H) forms spherical vesicals in polar aprotic solvents such as dimethylsufoxide and acetonitrile, whereas they form fibers in polar protic solvents, that is, ethylene glycol, methanol, etc., The nanowires form hydrogels in aqueous

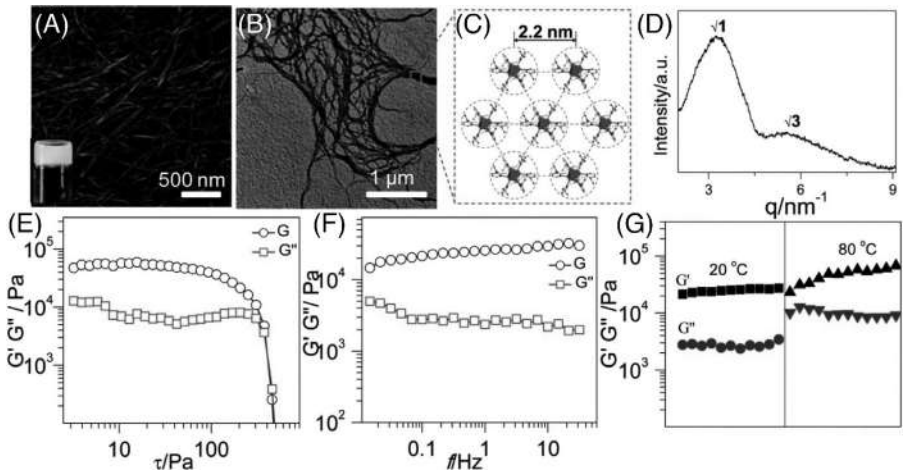

FIGURE 3.8 (A) The SEM micrograph of Ag_6 hydrogel (inset, photographic image of the gel), (B) TEM image of the same gel, (C) schematic representation of assembly, and (D) SAXS pattern of the hydrogel. Rheological measurements of (E) stress sweep test, (F) frequency test, and (G) frequency test at 20°C and 80°C. Reproduced with permission from ref.[43]. Copyright 2017, Royal Society of Chemistry.

medium. Intercluster $\pi-\pi$ stacking and solvent-mediated hydrogen bonding are key to their morphological evolution.

External gelling agents, such as cellulose nanocrystals (CNC), chitosan, amino acid, etc., have been used to promote gelation. Zhao et al. observed that 4-mercapto benzoic acid protected water-soluble Ag_9 forms gels due to extensive hydrogen bonding, in presence of CNC.[44] Hydrogen bonding of CNC with surface ligands of NCs enhance their gelation behavior. Sunlight mediated gelation of silver NCs protected by amino acids occurs where amino acid and gelatine matrix act as mediator for the synthesis as well as protecting ligand, respectively. The red-emitting NC showed remarkable stability up to 4 months. Similarly, another report by Sun et al. showed the 2-mercaptobenzoic acid protected Ag_9 NC gels upon interaction with succinic acid.[45] The orange red-emitting gel showed aggregation induced emission (AIE) behavior and acts as a white light emitter.

3.5.3 Nanoclusters in confined solid

Instability of NCs due to their higher reactivity limits their practical applications. Creating crystals and gels are also synthetically challenging. NCs confined in stable matrices can overcome this issue. Several organic matrices such as fullerenes, cyclodextrins, curcumin, porphyrins, crown ethers, and organometallic matrices such as polyoxometalates (POMs), oxides, zeolites, silica and metal organic frameworks (MOFs), etc., can be used as templates. These confined solids show higher stability and catalytic activity as compared to the free NC.

Luo et al. showed the encapsulation of $[Au_{25}(SG)_{18}]$ in zeolite imidazolate framework (ZIF-8) matrices through Zn-carboxylate linkages.[46] High angle annular dark-field scanning

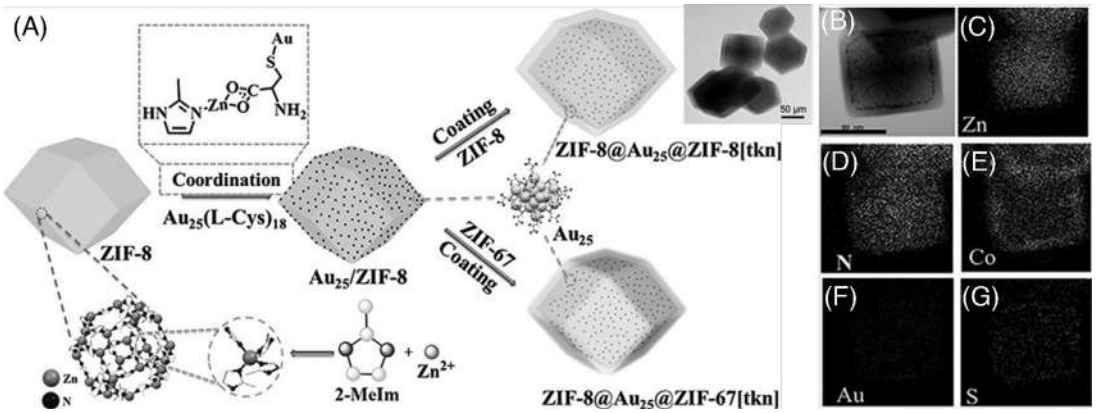

FIGURE 3.9 (A) Schematic illustration of the synthesis of sandwich-like NC MOFs (inset shows the TEM image of ZIF-8@Au_{25}@ZIF-67). (B–G) The EDS elemental profile indicating the existence of C, Zn, N, Co, Au, and S in the structure. Reproduced with permission from ref.[47]. Copyright 2020, American Chemical Society.

tunneling electron microscopy (HADFF-STEM) confirms that the [$Au_{25}(SG)_{18}$] NCs are mostly distributed on the outer surface of the composite. Thermogravimetric analysis confirms their enhanced thermal stability. They observed a large fluorescence variation based on the distribution of the NC inside and outside of the ZIF-8 crystals. The composite materials displayed catalytic activity toward nitrobenzene reduction. Similarly, Yun et al. prepared sandwich-type composite of ZIF-8@Au_{25}@ZIF-67, which catalyzed terminal alkyne carboxylation reaction at room temperature.[47] The ultrathin surface shell enhanced its catalytic activity and selectivity as compared to Au_{25}@ZIF-8 NICS materials (Fig. 3.9). Kratzl et al. prepared a small platinum NC ($Pt_{12\pm x}$) confined in ZIF-8 matrix.[48] They prepared the materials by thermal decarbonylation of an inclusion compound $[NBu_4]_2[\{Pt_3(CO)_6\}_4]$@ZIF-8. As synthesized platinum NCs are uniformly distributed in the pores of ZIF-8. They have shown that the material acts as an effective catalyst for oxygen reduction reaction (ORR).

Different carbon-based materials such as graphene, carbon nanotube, $C_{60,}$ and C_{70} trapped NCs have potential applications in drug delivery, sensors, catalysis, etc. Chandrasekar et al. prepared covalently functionalized glutathione-protected silver NC with graphene.[49] Glutathione functionalization was carried out following the carbodiimide crosslinking coupling reaction between the terminal –COOH groups of graphene with the amine groups of glutathione ligand. Glutathione functionalized graphene was used during the NC synthesis. Interestingly, the composite materials retained the red luminescence of the NC.

3.6 Properties of nanocluster assembled solids

Solidification of the NC leads to various properties such as photoluminescence, conductivity, magnetism, catalysis and hypergolic activity, etc. In comparison to the solution phase properties, here we will mostly discuss the properties of NC crystals, gels and confined solids.

3.6.1 Photoluminescence

NCs have emerged as an efficient solid-state luminescence material and the luminescence can be tuned by tuning the atomic number, core arrangements, and ligand environment. Reports have shown ultraviolet, visible, and NIR emission from them. Generally, they have short emission quantum yields (<10%) than conventional luminophores. Sometimes, their luminescence in solution state quenches significantly. Aggregation of clusters in the solid-state reduces rotation and vibrational energy loss due to rigidfication, which significantly enhances their luminescence by opening (increasing the probability of relaxation through) the radiative path. Here, we will discuss different solid-state emission pathways, such as crystallization induced emission (CIE), crystallization induced enhanced emission (CIEE), AIE, self-assembly induced emission, etc., for NCs.

CIE and CIEE are the most important pathway, whereby nonemissive clusters become strong emitters in the solid-state. Khatun et al. reported that dimethyl benzene thiol (DMBT) protected Ag_{22} emits strongly after crystallization.[50] It must be noted that the same clusters are nonemissive in solution state and faintly emissive in the amorphous state. Detailed analysis of the single-crystal structure reveals that different CH–π and π–π interactions are responsible for their solid-state emission. Another report showed that bimetallic $[Au_4Ag_{13}(DPPM)_3(SR)_9]$ emits strongly in the crystalline state due to CIEE effect.[51] The NC exhibits strong luminescence at 695 nm in solid crystalline states, in comparison to the weak emission in amorphous as well as in solution states. Single crystal analysis confirmed that restriction of different C–H$\cdot\cdot\pi$ interaction of triangular rotor-like structure facilitates enhanced emission in the crystalline state.

AIE is a phenomena when nonemissive NCs become highly emissive upon aggregation in the solution or in the solid state. Luo et al. presented the aggregation of Au(I)-thiolate complexes over the Au(0) core and as formed Au(0)@Au(I)-thiolate core-shell NCs emitting strong orange-yellow emission.[52] Aggregation of the Au(I)-thiolate increases the emission property. They have observed mixed solvent-induced aggregation of Au(I)-thiolate complex upon addition of more amount of ethanol in an aqueous solution of the NC. Sequential addition of ethanol gradually increases the aggregation which leads to the formation of dense aggregates with more emission. Gold NCs are weakly emitting and mostly their emission quenches by the surrounding environment. It has been observed that protein and polymer based gold NCs are highly emitting than the thiolate-based gold NCs. Surface coordination of the NC with specific linkers will also leads to cluster based network solids due to aggregation. Kuppan et al. showed emission tuning of marcaptopropionate protected gold NC, after preparing Zn^{2+} assisted self-assembled networks.[53] The intercluster assembly was achieved by the coordination of Zn^{2+} through the carboxylic chain of the ligand. The yellow emitting NCs ($\lambda_{max} = 580$ nm) with a quantum yield of 6% were transformed to a highly ordered green emitting ($\lambda_{max} = 500$ nm) assembled network with quantum yield of 20%. Atomic packing inside the core also has tremendous effect on the luminescence property. Chen et al. noticed discrete luminescence of $[Au_{28}(SR)_{20}]$ NCs with two different thiols having the same core but different shell structure.[54] They have termed it as "isomerization-induced luminescence." They observed that $[Au_{28}(CHT)_{20}]$ (where, CHT = cyclohexane thiolate) exhibited 15 times more emission quantum yield as compared to the $[Au_{28}(TBBT)_{20}]$ (where, TBBT = *p*-tert butylbenzene thiolate). Femtosecond pump probe transient absorption measurements confirm the nature of charge transfer from the metal core to the ligand shell. The outward hanging

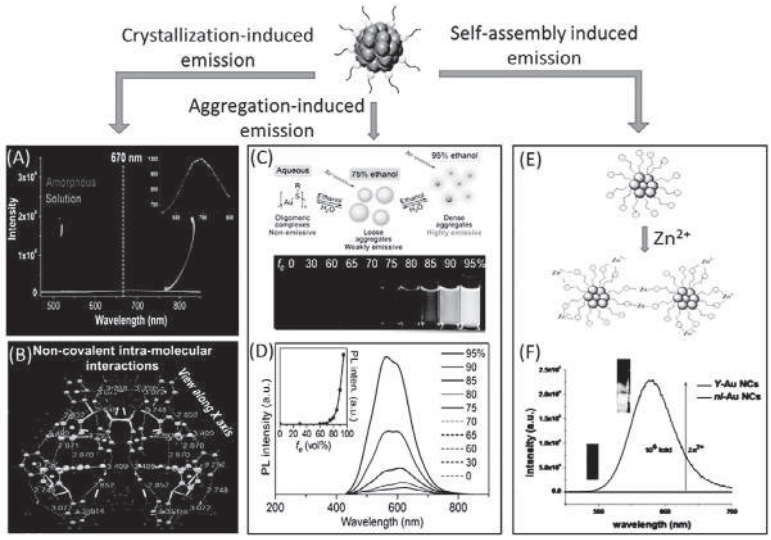

FIGURE 3.10 Different pathways of luminescence enhancement of the NCs due to their aggregation. (A and B) Crystallization-induced emission of Ag_{22}. (C and D) Aggregation-induced emission of gold thiolate cluster. (E and F) Self-assembly induced emission enhancement of gold NC. Reproduced with permission from refs.[50,52,53]. Copyright 2019, 2012 American Chemical Society, copyright 2017 Royal Society of Chemistry.

staples of $[Au_{28}(CHT)_{20}]$ reduces the interaction with staples, which slow down the dumping of excitation energy.

Physical parameters such as temperature, pressure, solvent vapors of the external environment affect emission tuning in the solid state. Kang et al. monitored the effect of temperature for two different NCs, that is, $[Ag_{29}(BDT)_{12}(TPP)_4]$ and $[Pt_1Ag_{28}(S\text{-}Adm)_{18}(TPP)_4]$.[55] They noticed two-step emission enhancement of Ag_{29}: (1) first 25 fold emission enhancement upon decreasing the temperature from 293 K to 251 K and (1) 280 fold emission jump on further cooling to 107 K. First step is associated with 22.5-fold enhancement of emission quantum yield, whereas the second step is associated with 100-fold enhancement of quantum yield. In contrast, Pt_1Ag_{28} showed one step emission enhancement of 20-fold (quantum yield of 100-fold) upon decreasing the temperature to 125 K. Decreasing the temperature supresses the dissociation-aggregation of TPP ligands on the cluster surface, which enhances the luminescence. Various reports on Au_8, Ag_{44}, Ag_{50}, Ag_{52}, Ag_{64}, Ag_{73}, Ag_{80}, and Ag_{90} NCs from Sun group have presented emission enhancement upon cooling the crystals.[3] For these NCs, small change in emission wavelength was observed. While for Ag_{18} and Ag_{180} NCs, emission enhancement along with wavelength variation was observed. For Ag_{18}, tuning of emission from red (λ_{max} = 700 nm) to yellow (λ_{max} = 550 nm) was observed upon cooling from 296 K to 77 K. Li et al. reported pressure-induced luminescence enhancement of a series of gold NCs, that is, Au_{21}, Au_{28}, Au_{24}, $Au_{14}Cd$, and $Au_{28}Pt$.[56] They also observed that the pressure-induced red shifting of absorption maxima is due to the structural distortion of the excited state (Fig. 3.10).

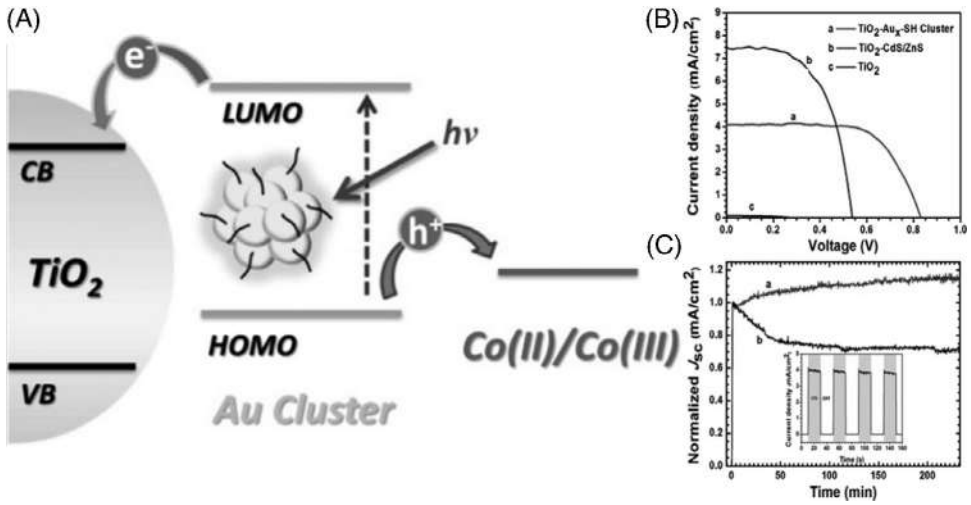

FIGURE 3.11 (A) Schematic representation of the working principle of a NC-sensitized solar cell. (B) The current-voltage (I–V) plot indicates comparable current density of NC-based solar cell with quantum dot-based solar cell. (C) Stability of photocurrent of two types of solar cells (inset showed reversible on-off current density using light illumination). Reproduced with permission from ref.[60]. Copyright 2013, American Chemical Society.

3.6.2 Conductivity

Metals are electrically conductive, due to the presence of free electrons. Thiolated metal NCs behave as semiconducting materials, due to their metallic core and sulfide staples. They are also redox-active. Intercluster molecular packing, ligand shells, and counter ions inside the crystal lattice influence their electrical transport. Literature reports showed that conductivity of silver NCs are comparable with silver-thiolate coordinating frameworks. Wang et al. demonstrated Ag_{88} protected by *p*-tert-butylthiacalix[4]arene has a better photocurrent response (0.20 $\mu A/cm^2$) than its silver thiolate precursors (0.16 $\mu A/cm^2$).[57] The band gap of 1.48 eV for Ag_{88} NC is lower in comparison to 2.19 eV band gap of metal thiolates, which correlates with their photoresponse behavior. Aggregation of silver atoms in the clusters broadens the absorption edge and reduces the band gap (Fig. 3.11).

Yuan et al. studied anisotropic electrical conductivity of a single crystal of mixed 34 atom gold and silver NC protected by twenty 1-ethynyladamantane ligands.[58] They observed that the average electrical conductivity of 1.49×10^{-5} S/m along the c axis, which is 1800 fold enhanced conductivity than other axes (a and b axes). The intercluster interaction through –Ag–Au–Ag– bond along the c axis enhances electrical conductivity along the polymerization axis. Insulating adamantane ligands, perpendicular to the polymerization axis, reduces conductivity along with a and b directions. Counter ions also affect the electrical conductivity of NC assembled solids. Li et al. measured electrical transport properties of two different types of single crystals of Au_{21} protected by two different counter ions, that is, $AgCl_2^-$ and Cl^-.[59] Electrical conductivity measurements showed that $Au_{21}@AgCl_2^-$ crystals have an average electrical conductivity ($\sigma = 1.44 \times 10^{-8}$ S/m), which is approximately two orders of magnitude

lower than $Au_{21}@Cl^-$ ($\sigma = 2.38 \times 10^{-6}$ S/m) crystals. The average centre-to-centre distances of neighboring Au_{21} NC with $[AgCl_2]^-$ and Cl^- counter ions are 16.80 and 16.39 Å, respectively. Reducing the intercluster bond distance increases their electrical conductivity.

Efficient harnessing solar energy in the form of electrical energy is a challenge. Along with silicon solar cells, different types of materials, such as organic luminophores, cadmium telluride, perovskites, gallium arsenide, copper indium gallium selenide, and hybrid materials are extensively studied to improve the light harvesting efficiency of solar cell devices. Metal NCs are also used as sensitizers in solar cells. Although bulk gold do not exhibit any light-harvesting activity due to the overlap between valence band and conduction band, gold NCs with molecule-like multiple absorption features can be utilized in light-harvesting applications. Discrete electronic energy levels and excited-state lifetimes up to few microsecond make Au NCs as effective materials for solar cells. Chen et al. used glutathione-protected gold NC as a sensitizer material.[60] They observed a stable photocurrent of 3.96 mA/cm^2 using gold NC linked with mesoscopic TiO_2 films. The redox activity of Au(0)@core and Au(I)@thiolate shell promotes electron injection into TiO_2, which leads to higher photovoltage along with high power conversion efficiency (>2%). Silver NCs are not preferred for solar light harvesting application, due to their intrinsic instability and short carrier lifetimes. It was observed that aggregation of NCs upon tuning pH increases the stability of the NC film as well as its semiconducting ability.

3.6.3 Magnetic property

Gold, silver, and copper are diamagnetic. Their size reduction to a few atomic NCs produces unpaired electrons, which generates paramagnetism or even ferromagnetism. Single gold atom is paramagnetic due to the presence of 6s unpaired electrons. Atomic NCs with odd number of atoms are paramagnetic due to the unpaired electron, although there are a few exceptions to the magnetic characteristics in particles with dimension of 1–5 nm as observed in different ultra-small gold nanoparticles. Zhu et al. in 2009 first observed paramagnetism in $[Au_{25}(SR)_{18}]$ NCs.[61] They observed that the charge state of NC reversibly switched their magnetic behavior. The neutral charge state of Au_{25} NC is paramagnetic, while anionic Au_{25} NC is diamagnetic. DFT calculations revealed that the delocalized unpaired electron in icosahedral Au_{13} core contributes to paramagnetism. Additional removal of electrons from these super atomic orbitals may render the clusters to be super-atom paramagnet (Fig. 3.12).

Further, the same group also studied the effect Ag doping in Au_{25} NC and tuning of its magnetic properties. A series of Ag doped Au_{25} NCs, that is, $[Au_{25-x}Ag_x(SR)_{18}]^o$, where x varies from 1 to 9 were studied to understand the doping effects.[62] With increasing Ag doping, the linear decrease of axial EPR signal indicates the spin pairing of Ag inside the Au_{25} core. Zhou et al. showed the spin pairing effect of the same NC after Mn doping.[63] According to their quantum mechanical calculation, the position of Mn doping in icosahedral Au_{12} surface has a great influence on their spin pairing. Doping of different magnetic elements such as Fe, Ni, Co can increase the magnetic nature of gold NCs. McCoy et al. observed that $[Au_{102}(p\text{-MBA})_{44}]$ NC (where p-MBA is *para*-mercapto benzoic acid), being a magic number series of electronically close-shell gold super atoms, behaves as a paramagnetic substance and it gets heated after treatment with a radiofrequency pulse.[64]

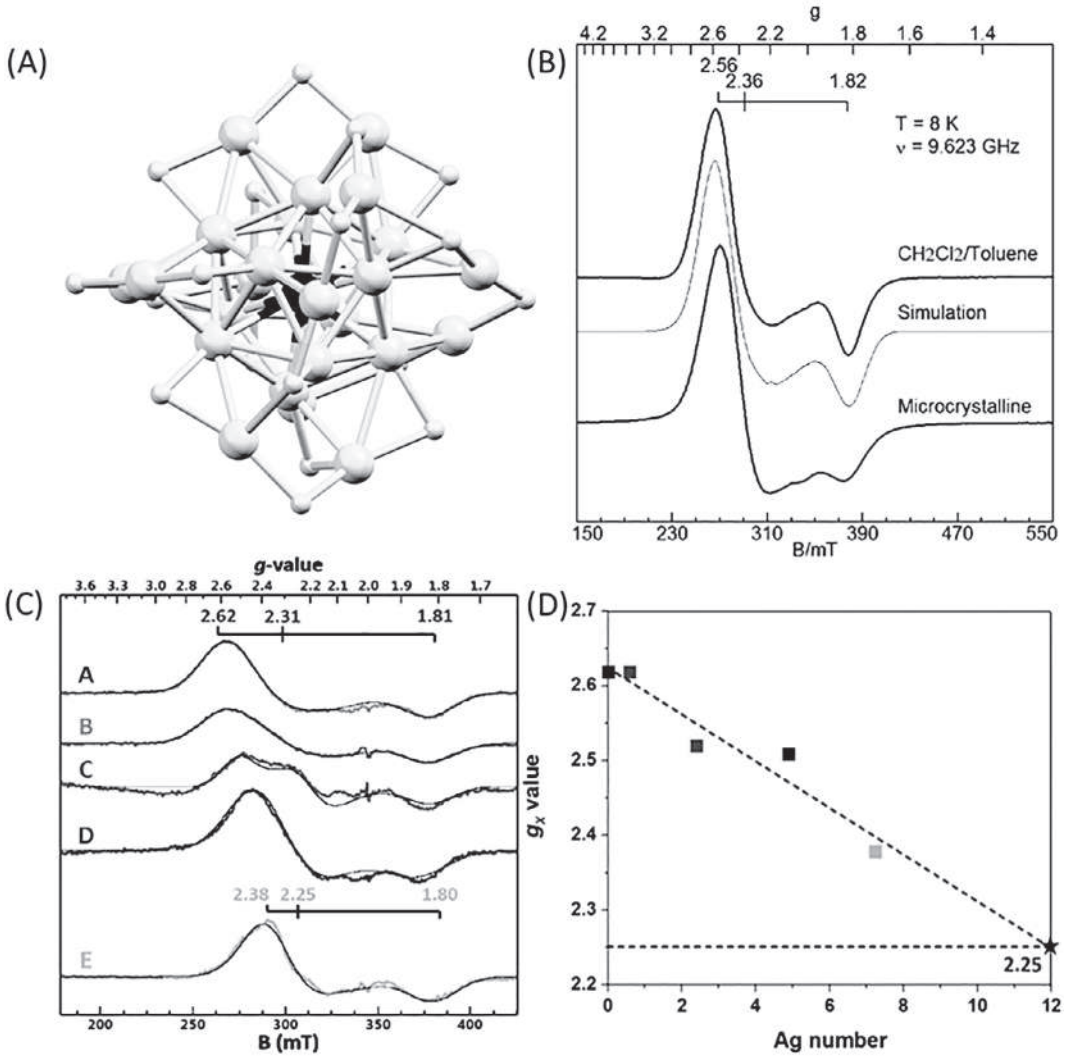

FIGURE 3.12 (A) The kernel structure of $[Au_{25}(SR)_{18}]$ having a Au_{13} centered-icosahedron surrounded by $Au_{12}S_{18}$ fragments. (B) EPR spectra of $[Au_{25}(SR)_{18}]^{\circ}$ in its different forms. (C) X-band EPR spectra of $[Au_{25-x}Ag_x(PET)_{18}]^{\circ}$ where, $x = 0$ (A), 0–2 (B), 0–6 (C), 3–7 (D), 5–9 (E). (D) Plot of g_x values indicates linear decrease of g_x upon increasing Ag doping. Reproduced with permission from refs.[61,62]. Copyright 2009, 2020, American Chemical Society.

Ji et al. reported that $[Ni_{39}(SC_2H_4Ph)_{24}]$ and $[Ni_{41}(SC_2H_4Ph)_{25}]$ NCs exhibit better ferromagnetic hysteresis in the temperature range of 300 to 1.8 K as compared to their metallic state.[65] The saturation magnetization (M_s) and coercivity (H_c) of NCs at 300 K are 0.088 emu/g and 345 Oe, respectively, whereas, bulk nickel at 300 K has a M_s and H_c of 55 emu/g and 0.7 Oe, respectively. The lower saturation magnetization and higher coercivity indicate better

ferromagnetic behavior. The cluster size, shape, surface and aggregated structure contributes to ferromagnetism.

3.6.4 Mechanical property

Mechanical properties of cluster assembled solids is the key to understand intercluster packing in its different forms. Strong metallic bonding makes metals rigid, whereas metallic NCs show polymer-like mechanical property. For sizes of <3 nm, there is no report of mechanical property of individual NC. Single crystal of μm or mm size has been used for studying mechanical properties in crystalline state. Nano indentation experiments were performed on crystals using a nm size tip. We have designed single crystals of $[Ag_{29}(DBT)_{12}(TPP)_4]$ (where BDT = 1, 3 benzene dithiol and TPP = triphenyl phosphine) with Young's modulus (E) of 4.48 and hardness (H) of 0.285 GPa, which indicates polymer-like nature as compared to bulk metals.[66] The capping ligands outside the metallic core imparts them with polymer-like mechanical properties. Another study showed the mechanical property of polymorphic crystals of Ag_{29} NC having identical structure but with different packing arrangements.[67] The Ag_{29} NCs crystallized in two crystal systems, that is, cubic and trigonal. Young's modulus of the trigonal crystal is higher than that of the cubic crystal. Intercluster CH–π, π–π interaction and difference in their intercluster packing affects their mechanical properties. We have also studied the mechanical properties of homocluster and heterocluster crystals. Indentation measurements confirmed that Young's modulus of trigonal homocluster crystals of Ag_{46} is lower than that of monoclinic cocrystals of $Ag_{40}@Ag_{46}$. Both showed metal-like stiffness and polymer-like damping characteristics. All the studies proved that in addition to molecular packing, size of the metallic core and surface ligands affect mechanical properties.

Recently, an interesting report by Sun et al. showed visible color tuning of the crystals of $[Ag_{50}S_7(SC_6H_4F)_{36}(dppp)_6]$, on application of pressure.[68] They observed that orange red crystals gradually change their color to dark red upon increasing pressure from 1 atm to 7.5 Gpa and the color tuning is reversible. Although there is no phase transition, Raman spectra indicate that the pressure-induced blue shift of vibrational peaks is due to the reduction of Ag–Ag bond distance. The same study also confirms the flexible nature of the metallic core. Rheological stress-strain measurements were carried out to get an insight into the mechanical properties of crosslinked gel fibers. Xia et al. have studied mechanical and self-healing property of water-soluble Ag_6 protected by six mercaptonicotinate ligands. Both the strain sweep and frequency sweep tests indicate that the storage modulus (G′) is higher than the loss modulus (G″) (Fig. 3.8). Another stress–strain measurement at a fixed frequency (1 Hz) showed high yield stress (τ, 300 Pa), which indicates slow gel to quasi-liquid phase transition. Thermogravimetric analysis showed thermal stability up to 80°C, which further indicates the stability of these fibers. Another report showed Ag_9 protected by nine mercaptobenzoic acid exhibits elastic modulus of about 600 Pa with viscosity modulus of 100 Pa and a yield stress of 80 Pa, suggesting their solid-state mechanical stability (Fig. 3.13).

3.6.5 Catalytic property

Metallic NCs consisting of few atoms to several thousand atoms are used as an effective catalyst for different catalytic reactions. Ultra-small size, shape, large surface area, available active sites, and electronic properties determine their catalytic activity. Metallic

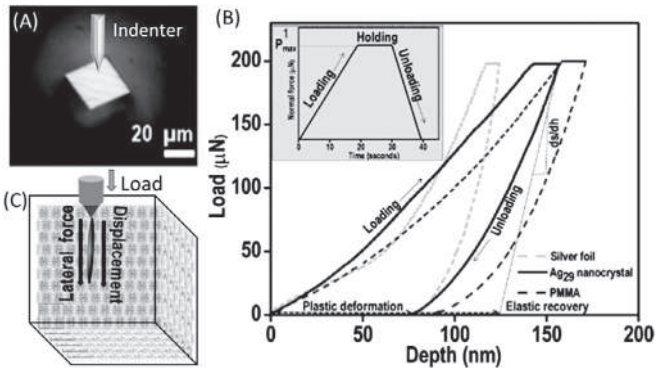

FIGURE 3.13 (A) Optical image of a cuboid Ag_{29} crystals used for indentation experiments. A nm size indenter used for the measurements. (B) The load-displacement graph of the same crystals as compared to silver foil and PMMA. It indicates polymer-type elasticity of the NC crystals. (C) The effect of direction of the applied load on the molecular packing of the cluster. Reproduced with permission from ref.[66]. Copyright 2018 Wiley-VCH.

nanoparticles are also used for catalysis, but due to the lack of structural details, factors affecting their catalytic activity are still unknown. On the other hand, structural details enable understanding atom-specific catalytic activity of NCs. DFT calculations are also extensively used to understand the selectivity and binding sites for catalysis reactions. In this section, we discuss different types of catalytic reactions of NCs, such as (1) organic catalysis, (2) photocatalysis, and (3) electrocatalysis.

3.6.5.1 *Organic catalysis*

Metallic gold is not considered as an active catalyst due to its chemical inertness. The demonstration of CO oxidation using colloidal gold nanoparticles as catalysts has led to numerous research efforts in this area. There are several reports of organic catalysis reactions such as oxidation, reduction, hydrogenation, and coupling reaction using various metal NCs. To increase the activity of NCs, different supports such as metal oxide, carbon nanotube, polyvinylpyrrolidone, graphitic materials, etc., were used. Thermal calcination at 200–900°C was also carried out to remove surface ligands.

Here, we discuss oxidation reactions such as styrene oxidation, hydrocarbon oxidation, glucose oxidation, etc., using NCs as a catalyst. Li et al. showed $[Au_{25}(SR)_{18}]$ catalyzed styrene oxidation using oxidizing agents such as TBHP (*tert*-butyl hydroperoxide) and O_2.[69] The oxidant initially formed peroxyformate (Au_{25}–O_{2ad}) and hydroperoxides, which eventually got converted to superoxides ($O_2^{\cdot}$). The side on connection of the superoxides through Au–O bond on gold surface forms a low energy barrier transition state, which promotes epoxidation. The partial positive charge ($\delta^+ = 0.3$) on Au_{12} shell outside the Au_{13} centered icosahedral kernel electrostatically attracts nucleophiles (–CH=CH_2), which facilitates the reaction. Another study by the same group showed the effect of heteroatom doping on the styrene oxidation. They observed enhanced catalytic activity of monoplatinum doped Au_{25} (Pt_1Au_{24}) as compared to Au_{25}.[70] Smaller energy gap of $E_g = 0.8$ eV due to a broad NIR absorption peak at 1100 nm of Pt_1Au_{24} renders higher catalytic activity. Numerous reports from various groups showed different selectivity and yield of the products (Fig. 3.14).

Hydrocarbon oxidation is one of the most important reactions having industrial importance. Zhang et al. studied aerobic oxidation of cyclohexane to cyclohexanol and cyclohexanone using $[Au_{38}(SC_2H_4Ph)_{24}]$ supported on Al_2O_3 and CeO_2.[71] Thermal calcination at 300°C removes the surface ligands, thereby activating the catalyst. They observed higher catalytic activity in CeO_2 supported clusters due to the presence of cationic gold species, which is

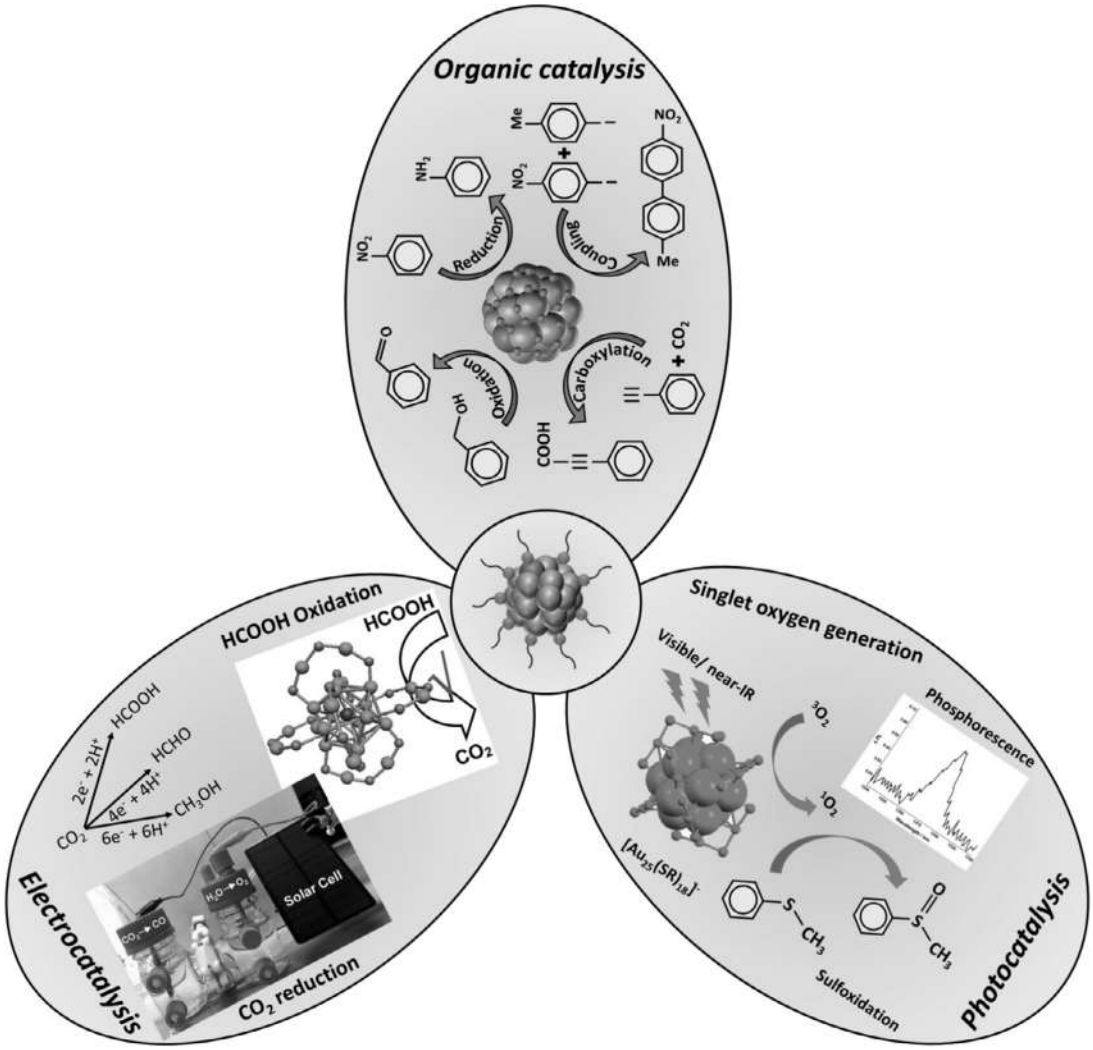

FIGURE 3.14 (A) Schematic representation showing different types of NC-based catalysis reactions, that is, (A) organic catalysis, (B) photocatalysis, and (C) electrocatalysis. Reproduced with permission from the refs.[82,85,86]. Copyright 2014, 2015 American Chemical Society, 2018 Elsevier.

not present in Al_2O_3 supports. Wang et al. showed phenyl alkynyl protected $[Au_{34}Ag_{28}(C{\equiv}C\text{-}Ph)_{34}]$ showed better hydrolytic oxidation of organosilanes to silanols as compared to partially or completely removed surface ligands.[72] The untreated catalyst showed nearly 100% conversion efficiency as compared to below 3% for 200°C heat treated samples. Zhang et al. studied aerobic oxidation of glucose to gluconic acid using active carbon supported gold NCs, that is, $[Au_{25}(PET)_{18}]$ (1.2 nm), $[Au_{38}(PET)_{24}]$ (1.5 nm), $[Au_{144}(PET)_{60}]$ (1.9 nm), parentheses give the diameters.[73] They observed size-dependent reactivity in the order, $Au_{144}{>}Au_{38}{>}Au_{25}$.

In addition to oxidation, various reduction reactions such as nitro reduction, alkyne semi hydrogenation, α, β-unsaturated ketones, etc., have been studied. Yamamoto et al. showed the reduction of 4-nitrophenol to 4-aminophenol catalyzed by N, N-dimethylformamide stabilized gold NCs using $NaBH_4$ as reducing agents.[74] The pseudo-first order catalytic reaction depends on the penetration of the reagents into the metallic core, which is protected by a layer of DMF. The hydrogenation reaction is a metal catalytic reaction where alkynes (–C≡C–) are converted to olefins (–C=C–) in presence of hydrogen. Li et al. noticed high conversion efficiency (>99%) of alkyne, using TiO_2 supported $[Au_{25}(SR)_{18}]$.[75] DFT calculation reveals that the outer surface Au_3 triangle acts as an active catalytic surface. They also carried out the enantioselective synthesis of Z-alkene isomer using bare NCs. Another report shows chemoselective hydrogenation of nitrobenzaldehyde to nitrobenzyl-alcohol using $[Au_{99}(SPh)_{42}]$ on oxide support. The most interesting fact is that the same reaction condition promotes nitro group reduction using gold nanoparticles as a catalyst.

Gold NCs have been extensively studied for different heterogeneous carbon-carbon bond formation reactions such as Ullmann coupling, Sonogashira coupling, Suzuki coupling, etc. Oxide supported $[Au_{25}(PET)_{18}]$ NCs exhibited Ullmann type homogeneous catalytic conversion of aryl iodides to biaryl derivatives with catalytic conversion efficiency up to 99.8%. They studied the template effects of various oxide supports such as TiO_2, CeO_2, SiO_2, and observed almost negligible contribution from them. The proposed mechanism of the catalysis reaction is that, at first, aryl iodide adsorbs the active sites of Au surface through [Au···I] interaction. Subsequent oxidative addition of multiple iodides and reductive elimination leads to biaryl products. Li et al. showed an efficient Sonogashira cross-coupling reaction of phenylacetylene (Ph-C≡CH) and phenyl iodide (Ph-I) using $[Au_{25}(SR)_{18}]$ NCs leads to biphenyl-acetylene (Ph-C≡C-Ph).[76] Theoretical calculations indicated that two open Au_3 facets behave as an active surface for binding both the reactants. To further investigate the effect of individual atoms, Li et.al studied coupling reactions between p-iodoanisole (CH_3O-Ph-I) and phenylacetylene using bimetallic $[M_xAu_{25-x}(SR)_{18}]$, where M = Cu, Ag, and Pt.[77] They observed that $[Ag_xAu_{25-x}(SR)_{18}]$ exhibits comparable selectivity as that of sonogashira cross-coupling with $[Au_{25}(SR)_{18}]$, while centrally doped $[PtAu_{24}(SR)_{14}]$ has reduced catalytic activity. Interestingly, $[Cu_xAu_{25-x}(SR)_{18}]$ NCs prefer Ullmann type homocoupling reactions and they lead to 4,4′-dimethoxy-1,1′-biphenyl as a predominant product. The carboxylation reaction of terminal alkyne with CO_2 leads to the formation of propiolic acid through C–C bond formation. Liu et al. showed the effect of monoatomic doping of Au, Pd, and Pt in Ag_{25} toward the carboxylation reaction.[78]

3.6.5.2 *Photocatalysis*

NCs with multiple optical absorption features and closely spaced molecular orbitals behave as an active catalysts for different photocatalytic reactions such as, photo-electrochemical water splitting, degradation of pollutants, singlet oxygen generation, etc. Photo-electrochemical water splitting involves three primary steps: (1) formation of excitons after light absorption, (2) e^--h^+ pair separation, and (3) formation of H_2 or O_2 after the redox reaction. Negishi et al. prepared a composite photocatalyst of Au_{25}@GSH and $BaLa_4Ti_4O_{15}$, following the surface adsorption and thermal calcination method.[79] The material promotes water splitting to H_2 and O_2 upon white light illumination and its efficiency is higher than conventional gold nanoparticles. Similarly, Du et al. studied the photocatalytic effect of monoplatinum doped

Ag_{25} ($PtAg_{24}$) and primitive Ag_{25}.[80] They prepared a composite of each NC in graphitic carbon nitride (g-C_3N_4) matrix. $PtAg_{24}$@g-C_3N_4 showed fourfold enhanced photocatalytic hydrogen generation than Ag_{25}@g-C_3N_4. They observed light absorption capacity of g-C_3N_4 after NC deposition. It was observed that Ag atoms poorly transfer its interfacial charge due to the availability of trapped electron. Pt doping facilitates energy state mixing and promotes interfacial charge transfer. The formation of stable excited state charge carriers with long lifetime also increases the catalytic activity.

Photocatalytic reduction of pollutants depends on the formation of active radicals and ions. Yu et al. showed photocatalytic degradation of methyl orange using $Au_{25}(SR)_{18}$ and TiO_2 nanocomposite materials.[81] The composite material absorbs light and generates electron and hole pair (e^--h^+). As formed e^- interacts with dissolved oxygen and forms superoxide radical anion ($O_2^{\cdot -}$), whereas h^+ oxidizes H_2O and forms hydroxyl radicals (·OH). These active species are responsible for the pollutant decomposition. The formation of highly reactive singlet oxygen species ($^1O_2$) has importance in various applications in the area of photodynamic therapy, catalytic oxidation, etc. According to the report by Kawasaki et al. $[Au_{25}(SR)_{18}]^-$ NCs acts as photosensitizer under visible/near-IR (532, 650, and 808 nm) illumination.[82] They detected the formation of singlet oxygen species through its emission maximum at 1276 nm. The stable triplet excited state and the optical band gap of 1.3 eV for $[Au_{25}(SR)_{18}]^-$ as compared to the bandgap of 0.97 eV for $^1O_2$ promotes efficient energy transfer. Singlet oxygen also promotes the catalytic oxidation of organic sulfide to sulfoxide. Both the anionic and neutral Au_{25} NCs efficiently produced singlet oxygen.

3.6.5.3 Electrocatalysis

Electrocatalytic CO_2 reduction to various useful products such as methanol, methane, formic acid, and acetylene is an active area of research due to environmental effects of greenhouse gases. Chemical stability of CO_2 make it highly inert to reduction reactions. Electrocatalytic CO_2 reduction involves complex multistep interfacial electron transfer process, which is associated with high over-potential. Molecule-like multiple electronic orbitals and surface charge on NCs facilitate CO_2 reduction process. Jin et al. studied electrochemical reduction of CO_2 to CO using negatively charged Au_{25} within 90 mV thermodynamic potential.[83] They observed nearly 100% conversion efficiency at -1V (vs RHE) potential. Similar UV-vis absorption features after the reduction reaction indicates the stability of the NC. Theoretical calculation showed small charge redistribution on the cluster surface upon CO_2 adsorption. To better understand the effect of charge state of the NC, they studied the catalytic activity of Au_{25}^-, Au_{25}°, and Au_{25}^+ having the same size, shape, and surface structure.[84,85] They observed identical catalytic products, onset potential, and Tafel slopes for all three NCs, which indicate same type of reaction path. However, Au_{25}^- has higher cathodic current density and faradic efficiency than the other two clusters, which confirm that negative surface charge facilitates CO_2 binding. Similar to the CO_2 reduction, formic acid oxidation is an important electrocatalytic process. Chen et al. have shown that Pt doped $Au_{24}Pt_1$ deposited on a multwall carbon nanotube behaves as an active catalyst for oxidation reaction.[86] DFT calculation predicts the favorable binding of HCOOH to the cluster staples through binding with carbon centers. The formation of the active *COOH intermediate through an energetically favorable pathway is the rate-determining step for the formation of CO_2 as an end product.

Catalytic conversion of chemical energy to electrical energy in fuel cell is an important direction for pollution-free energy generation. Energy generation is associated with two different consecutive reactions, such as fuel (H_2) oxidation and oxygen reduction. Atomically precise NCs behave as an active catalyst for $2e^-$ and $4e^-$ ORR. Fuel oxidation is rarely reported using NCs. Platinum and gold NCs are widely used as catalysts for ORR.[87] Yamamoto et al. studied ORR of phenylazomethine dendrimer protected Pt NC having varying nuclearity.[88] They observed four electron reduction over Pt NC leading to water as an end product. A large irreversible cathodic current in presence of surrounding oxygen manifests ORR. The rise of the current density upon increasing the loading of the catalyst confirms their catalytic activity. Particle size controls the kinetics of the reaction. Ye et al. investigated ORR kinetics of different Pt NC protected by hydroxyl-terminated poly-(amidoamine) dendrimers, having approximate nuclearity of 55, 100, 147, 200 and 240 atoms.[89] The results showed that large particles exhibit highest catalytic activity. Although contradictory reports from Wang et al. suggest that decreasing the size of the particles increases the catalytic activity.[90] Among these Au NCs, that is, Au_{25}, Au_{38} and Au_{144}, they observed that Au_{25} exhibits best catalytic activity having positive onset potential comparable to commercially available 20% Pt/C electrode. The catalytic activity not only depends on the size of the NCs but also on the uncoordinated surface atoms and metal oxygen binding energy. Theoretical calculation suggests that d-electron density increases upon decreasing the size of the particles.[91] Further, for smaller particles, d band becomes narrower and is shifted to the Fermi level, which facilitates the adsorption of oxygen.

3.6.6 Hypergolic property

Hypergolic activity is the property of materials to ignite spontaneously upon exposure to an oxidizer. Different types of hypergolic materials, such as borane derivatives, hydrazine, etc., can be used as a prominent component in rocket fuels. Recently it has been shown that *ortho*-carborane-based NC exhibits efficient hypergolic property. Fig. 3.15 shows the hypergolic behavior of the Ag_{14} NC. In view on the huge demand of high energy combustion materials for rocket fuels, there is a global effort to obtain effective hypergolic materials, which can ignite spontaneously in presence of an oxidizer. Metal NCs protected with alkylated carborane emerged as safe hypergolic materials for combustion in presence of fumed nitric acid as an oxidizer under ambient conditions. Mak et al. demonstrated Ag_{14}@CBA and Cu_6Ag_8@CBA (where CBA is *ortho*-carboranealkynyl) NCs protected by *ortho*-carborane alkenyl ligands showed hypergolic activity.[92] Although carboranes are hypergolically inert, they become an active hypergolic material in metal NCs due to metal-ligand interaction. Fig. 3.15 showed photographic images of the hypergolic activity of NCs with varying ignition time. It may be further noted that these NCs are remarkably inert toward temperature, friction, impact and electrostatic discharge, ensuring safety in their handling and storage.

3.7 Summary and future perspective

In this chapter, we have presented an area of NAS materials such as single-crystals, clusters in confined solids, gels, and their solid-state structures, properties, and applications. The

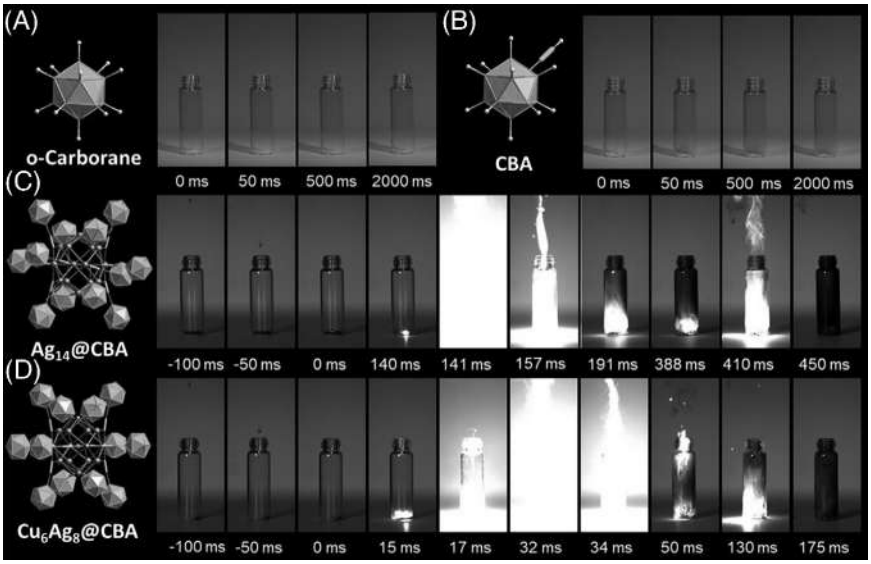

FIGURE 3.15 Photographic images of the ignition process of (A) o-carborane, (B) CBA, (C) Ag_{14}@CBA, and (D) Cu_6Ag_8@CBA, in presence of fuming nitric acid as an oxidizer. No hypergolic activity was observed for o-carborane and CBA molecules. But both NCs showed hypergolic activity with varying sensitivity. Reproduced with permission from ref.[92]. Copyright 2020 American Chemical Society.

efforts of different research group leads to the success of achieving atomic-level understanding of various cluster solids. Atom-specific functional properties of these solids are correlated using their structures. Despite this growth, there remains a gap of detailed understanding of cluster nucleation and associated atomic arrangements. New observations are emerging in this direction using transmission electron microscopy in the liquid state. Not only cluster crystals, but also their amorphous crystalline gels have useful properties. Tuning the cluster core by doping, surface ligand engineering and controlling the gelation behavior, can enable synthesis of quantum materials for future applications. The area is expanding rapidly. We note that this chapter was completed with the literature search carried out up to October 2021.

List of abbreviation

Adm	Adamentane
AIE	Aggregation induced emission
bcc	body-centered cubic
BDT	Benzene dithiol
BT	Butane thiol
CBA	*ortho*-Carboranealkynyl
CHT	Cyclohexane thiol
CIE	Crystallization-induced emission
CIEE	Crystallization-induced enhanced emission
CNC	Cellulose nanocrystal
DCM	Dichloromethane

DFT	Density functional theory
DMBT	Dimethylbenzene thiol
DMF	N, N-Dimethylformamide
DNA	Deoxyribonucleic acid
DPPM	Diphenyl phosphino methane
DPPP	Diphenyl phosphino propane
ED	Electron diffraction
fcc	face-centered cubic
GSH	Glutathione
H_2MSA	Mercapto succinic acid
HADFF-STEM	High angle annular dark field scanning tunnelling electron microscopy
hcp	hexagonal close packing
HOMO	Highest occupied molecular orbital
HPLC	High performance liquid chromatography
HT	Hexane thiol
LEIST	Ligand exchange induced structural transformation
LUMO	Lowest unoccupied molecular orbital
MALDI	Matrix-assisted laser desorption ionization
MNA	Mercaptonicotinic acid
MOF	Metal organic framework
NAS	Nanocluster assembled solid
NC	Nanocluster
NICS	Nanocluster in confined solid
NIR	Near infrared
ORR	Oxygen reduction reaction
PAGE	Polyacrylamide gel electrophoresis
PET	Phenyl ethane thiol
p-MBA	*para*-Mercaptobenzoic acid
PMMA	Poly-methyl methacrylate
POM	Polyoxometalate
SAXS	Small angle X-ray scattering
SEM	Scanning electron microscope
TBBT	Tertiary butyl benzene thiol
TBHP	tert-Butyl hydroperoxide
TEM	Transmission electron microscope
THF	Tetrahydrofuran
TLC	Thin layer chromatography
TPP	Triphenylphosphine
XRD	X-ray diffraction
ZIF	Zeolite imidazole framework

References

1. Jin R, Zeng C, Zhou M, Chen Y. Atomically precise colloidal metal nanoclusters and nanoparticles : fundamentals and opportunities. *Chem Rev*. 2016;116:10346–10413.
2. Chakraborty I, Pradeep T. Atomically precise clusters of noble metals : emerging link between atoms and nanoparticles. *Chem Rev*. 2017;117:8208–8271.
3. Kang X, Zhu M. Tailoring the photoluminescence of atomically precise nanoclusters. *Chem Soc Rev*. 2019;48:2422–2457.
4. Baksi A, Pradeep T, Yoon B, Yannouleas C, Landman U. Bare clusters derived from protein templates: Au_{25}^{+}, Au_{38}^{+} and Au_{102}^{+}. *Chem Phys Chem*. 2013;14:1272–1282.
5. Brust M, Walker M, Bethell D, Schiffrin DJ, Whyman R. Synthesis of Thiol-derivatised Gold Nanoparticles in a two-phase liquid-liquid system. *J Chem Soc, Chem Commun*. 1994:801–802.

6. Jadzinsky PD, Calero G, Ackerson CJ, Bushnell DA, Kornberg RD. Structure of a thiol monolayer–protected gold nanoparticle at 1.1 Å resolution. *Science (80-.)*. 2007;318:430–434.
7. Faraday M. Experimental relations of gold (and other Metals) to Light. *Phil Trans R Soc*. 1857;147:145–181.
8. Negishi Y, Nobusada K, Tsukuda T. Glutathione-protected gold clusters revisited: bridging the gap between gold(I)-thiolate complexes and thiolate-protected gold nanocrystals. *J Am Chem Soc*. 2005;127:5261–5270.
9. Wu Z, MacDonald MA, Chen J, Zhang P, Jin R. Kinetic control and thermodynamic selection in the synthesis of atomically precise gold nanoclusters. *J Am Chem Soc*. 2011;133:9670–9673.
10. Jana A, Chakraborty P, Dar A, et al. Dual emitting Ag_{35} nanocluster protected by 2-pyrene imine thiol. *Chem Commun*. 2020;56:12550–12553.
11. Bodiuzzaman M, Ghosh A, Sugi KS, Nag A, Khatun E. Camouflaging structural diversity : co-crystallization of two different nanoparticles having different cores but the same shell. *Angew Chemie - Int Ed*. 2019;58:189–194.
12. Rao TUB, Nataraju B, Pradeep T. Ag_9 quantum cluster through a solid-state route. *J Am Chem Soc*. 2010;132:16304–16307.
13. Bhattarai B, Chakraborty I, Conn BE, Atnagulov A, Pradeep T, Bigioni TP. High-yield paste-based synthesis of thiolate-protected silver nanoparticles. *J Phys Chem C*. 2017;121:10964–10970.
14. Carney RP, Kim JY, Qian H, et al. Determination of nanoparticle size distribution together with density or molecular weight by 2D analytical ultracentrifugation. *Nat Commun*. 2011;2:1–8.
15. Manju CK, Mohanty JS, Sarkar D, Chennu S, Pradeep T. Towards atomically precise luminescent Ag_2S clusters separable by thin layer chromatography. *J Mater Chem C*. 2018;6:5754–5759.
16. Ghosh A, Hassinen J, Pulkkinen P, Tenhu H, Ras RHA, Pradeep T. Simple and efficient separation of atomically precise noble metal clusters. *Anal Chem*. 2014;86:12185–12190.
17. Sugi KS, Bhat S, Nag A, Ganesan P, Mahendranath A, Pradeep T. Ligand structure and charge state-dependent separation of monolayer protected Au_{25} clusters using non-aqueous reversed-phase HPLC. *Analyst*. 2020;145:1337–1345.
18. Niihori Y, Matsuzaki M, Pradeep T, Negishi Y. Separation of precise compositions of noble metal clusters protected with mixed ligands. *J Am Chem Soc*. 2013;135:4946–4949.
19. Udaya Bhaskara Rao T, Pradeep T. Luminescent Ag_7 and Ag_8 clusters by interfacial synthesis. *Angew Chemie - Int Ed*. 2010;49:3925–3929.
20. Jana A, Jash M, Poonia AK, et al. Light-activated intercluster conversion of an atomically precise silver nanocluster. *ACS Nano*. 2021;15:15781–15793.
21. Joshi CP, Bootharaju MS, Alhilaly MJ, Bakr OM. $[Ag_{25}(SR)_{18}]^-$: The "golden" silver nanoparticle. *J Am Chem Soc*. 2015;137:11578–11581.
22. Nag A, Chakraborty P, Bodiuzzaman M, Ahuja T, Antharjanam S, Pradeep T. Polymorphism of $Ag_{29}(BDT)_{12}(TPP)_4^{3-}$ cluster: interactions of secondary ligands and their effect on solid state luminescence. *Nanoscale*. 2018;10:9851–9855.
23. Cerretani C, Kanazawa H, Vosch T, Kondo J. Crystal structure of a NIR-emitting DNA-stabilized Ag_{16} nanocluster. *Angew Chemie - Int Ed*. 2019;58:17153–17157.
24. Antonello S, Dainese T, Pan F, Rissanen K, Maran F. Electrocrystallization of monolayer-protected gold clusters: opening the door to quality, quantity and new structures. *J Am Chem Soc*. 2017;139:4168–4174.
25. Wu Z, Dong C, Li Y, et al. Self-assembly of Au_{15} into single-cluster-thick sheets at the interface of two miscible high-boiling solvents. *Angew Chemie - Int Ed*. 2013;52:9952–9955.
26. Wu Z, Liu J, Li Y, et al. Self-Assembly of Nanoclusters into Mono-, Few- and Multilayered Sheets *via* Dipole-Induced Asymmetric van der Waals Attraction. *ACS Nano*. 2015;9:6315–6323.
27. Azubel M, Koivisto J, Malola S, et al. Electron microscopy of gold nanoparticles at atomic resolution. *Science (80-.)*. 2014;345:909–912.
28. Heaven MW, Dass A, White PS, Holt KM, Murray RW. Crystal structure of the gold nanoparticle $[N(C_8H_{17})_4][Au_{25}(SCH_2CH_2Ph)_{18}]$. *J Am Chem Soc*. 2008;130:3754–3755.
29. Qian H, Eckenhoff WT, Zhu Y, Pintauer T, Jin R. Total structure determination of thiolate-protected Au_{38} nanoparticles. *J Am Chem Soc*. 2010;132:8280–8281.
30. AbdulHalim LG, Bootharaju MS, Tang Q, et al. $Ag_{29}(BDT)_{12}(TPP)_4$: a tetravalent nanocluster. *J Am Chem Soc*. 2015;137:11970–11975.
31. Alhilaly MJ, Bootharaju MS, Joshi CP, et al. $[Ag_{67}(SPhMe_2)_{32}(PPh_3)_8]^{3+}$: synthesis, total structure and optical properties of a large box-shaped silver nanocluster. *J Am Chem Soc*. 2016;138:14727–14732.

32. Huard DJE, Demissie A, Kim D, et al. Atomic structure of a fluorescent Ag_8 cluster templated by a multistranded DNA scaffold. *J Am Chem Soc*. 2019;141:11465–11470.
33. Fields-zinna CA, Crowe MC, Dass A, Weaver JEF, Murray RW. Mass spectrometry of small bimetal monolayer-protected clusters. *Langmuir*. 2009;25:7704–7710.
34. Yang H, Wang Y, Huang H, et al. All-thiol-stabilized Ag_{44} and $Au_{12}Ag_{32}$ nanoparticles with single-crystal structures. *Nat Commun*. 2013;4:1–8.
35. Yang S, Chai J, Chong H, Song Y, Yu H, Zhu M. Sulfonate, sulfide and thiolate ligands into an ultrasmall nanocluster: $[Ag_{40.13}Cu_{13.87}S_{19}(^tBuS)_{20}(^tBuSO_3)_{12}]$. *Chem Commun*. 2018;54:4314–4316.
36. Huang RW, Xu QQ, Lu HL, et al. Self-assembly of an unprecedented polyoxomolybdate anion $[Mo_{20}O_{66}]^{12-}$ in a giant peanut-like 62-core silver-thiolate nanocluster. *Nanoscale*. 2015;7:7151–7154.
37. Liu JW, Su HF, Wang Z, et al. A giant 90-nucleus silver cluster templated by hetero-anions. *Chem Commun*. 2018;54:4461–4464.
38. Kang X, Zhu M. Cocrystallization of atomically precise nanoclusters. *ACS Mater Lett*. 2020;2:1303–1314.
39. Tian S, Li YZ, Li MB, et al. Structural isomerism in gold nanoparticles revealed by X-ray crystallography. *Nat Commun*. 2015;6:1–6.
40. Zeng C, Li T, Das A, Rosi NL, Jin R. Chiral structure of thiolate-protected 28-gold-atom nanocluster determined by X-ray crystallography. *J Am Chem Soc*. 2013;135:10011–10013.
41. Chen Y, Liu C, Tang Q, et al. Isomerism in $Au_{28}(SR)_{20}$ nanocluster and stable structures. *J Am Chem Soc*. 2016;138:1482–1485.
42. Xie Z, Sun P, Wang Z, et al. Metal–organic gels from silver nanoclusters with aggregation- induced emission and fluorescence-to-phosphorescence switching. *Angew Chemie*. 2020;59:9922–9927.
43. Shen J, Wang Z, Sun D, et al. Self-assembly of water-soluble silver nanoclusters: superstructure formation and morphological evolution. *Nanoscale*. 2017;9:19191–19200.
44. Zhao T, Zhang S, Bi Y, et al. Development and characterization of multi-form composite materials based on silver nanoclusters and cellulose nanocrystals. *Colloids Surfaces A*. 2020;603.
45. Sun P, Wang Z, Bi Y, et al. Self-assembly-driven aggregation-induced emission of silver nanoclusters for light conversion and temperature sensing. *ACS Appl. Nano Mater*. 2020;3:2038–2046.
46. Luo Y, Fan S, Yu W, et al. Fabrication of $Au_{25}(SG)_{18}$–ZIF-8 nanocomposites: a facile strategy to position $Au_{25}(SG)_{18}$ nanoclusters inside and outside ZIF-8. *Adv Mater*. 2018;30:1–9.
47. Yun Y, Sheng H, Bao K, et al. Design and remarkable efficiency of the robust sandwich cluster composite nanocatalysts ZIF-8@Au_{25}@ZIF-67. *J Am Chem Soc*. 2020;142:4126–4130.
48. Kratzl K, Kratky T, Günther S, et al. Generation and stabilization of small platinum clusters $Pt_{12\pm x}$ inside a metal-organic framework. *J Am Chem Soc*. 2019;141:13962–13969.
49. Chandrasekar A, Pradeep T. Luminescent silver clusters with covalent functionalization of graphene. *J Phys Chem C*. 2012;116:14057–14061.
50. Khatun E, Bodiuzzaman M, Sugi KS, et al. Confining an Ag_{10} core in an Ag_{12} shell: a four-electron superatom with enhanced photoluminescence upon crystallization. *ACS Nano*. 2019;13:5753–5759.
51. Chen T, Yang S, Chai J, et al. Crystallization-induced emission enhancement: a novel fluorescent Au-Ag bimetallic nanocluster with precise atomic structure. *Sci Adv*. 2017;3:1–8.
52. Luo Z, Yuan X, Yu Y, et al. From aggregation-induced emission of Au(I)−thiolate complexes to ultrabright Au(0)@Au(I)−thiolate core−shell nanoclusters. *J Am Chem Soc*. 2012;134:16662–16670.
53. Kuppan B, Maitra U. Instant room temperature synthesis of self-assembled emission-tunable gold nanoclusters: Million-fold emission enhancement and fluorimetric detection of Zn^{2+}. *Nanoscale*. 2017;9:15494–15504.
54. Chen Y, Zhou M, Li Q, Gronlund H, Jin R. Isomerization-induced enhancement of luminescence in $Au_{28}(SR)_{20}$ nanoclusters. *Chem Sci*. 2020;11:8176–8183.
55. Kang X, Wang S, Zhu M. Observation of a new type of aggregation-induced emission in nanoclusters. *Chem Sci*. 2018;9:3062–3068.
56. Li Q, Mosquera MA, Jones LO, et al. Pressure-induced optical transitions in metal nanoclusters. *ACS Nano*. 2020;14:11888–11896.
57. Wang Z, Su HF, Gong YW, et al. A hierarchically assembled 88-nuclei silver-thiacalix[4]arene nanocluster. *Nat Commun*. 2020;11:1–8.
58. Yuan P, Zhang R, Selenius E, et al. Solvent-mediated assembly of atom-precise gold–silver nanoclusters to semiconducting one-dimensional materials. *Nat Commun*. 2020;11:1–8.

59. Li Q, Russell JC, Luo TY, et al. Modulating the hierarchical fibrous assembly of Au nanoparticles with atomic precision. *Nat Commun*. 2018;9:1–7.
60. Chen YS, Choi H, Kamat PV. Metal-cluster-sensitized solar cells. A new class of thiolated gold sensitizers delivering efficiency greater than 2%. *J Am Chem Soc*. 2013;135:8822–8825.
61. Zhu M, Aikens CM, Hendrich MP, et al. Reversible switching of magnetism in thiolate-protected Au_{25} superatoms. *J Am Chem Soc*. 2009;131:2490–2492.
62. Li Y, Biswas S, Luo T-Y, et al. Doping effect on the magnetism of thiolate-capped 25-atom alloy nanoclusters. *Chem Mater*. 2020;32:9238–9244.
63. Zhou M, Cai YQ, Zeng MG, Zhang C, Feng YP. Mn-doped thiolated Au_{25} nanoclusters: atomic configuration, magnetic properties and a possible high-performance spin filter. *Appl Phys Lett*. 2011;98.
64. McCoy RS, Choi S, Collins G, Ackerson BJ, Ackerson CJ. Superatom paramagnetism enables gold nanocluster heating in applied radiofrequency fields. *ACS Nano*. 2013;7:2610–2616.
65. Ji J, Wang G, Wang T, You X, Xu X. Thiolate-protected Ni_{39} and Ni_{41} nanoclusters: synthesis, self-assembly and magnetic properties. *Nanoscale*. 2014;6:9185–9191.
66. Sugi KS, Mallikarjunachari G, Som A, Ghosh P. Probing the mechanical response of luminescent dithiol-protected $Ag_{29}(BDT)_{12}(TPP)_4$ cluster crystals. *Chem Nano Mat*. 2018;4:1–9.
67. Sugi KS, Bandyopadhyay P, Bodiuzzaman M, et al. Manifestation of structural differences of atomically precise cluster-assembled solids in their mechanical properties. *Chem Mater*. 2020;32:7973–7984.
68. Sun Q-Q, Li Q, Li H-Y, et al. Thermochromism and piezochromism of an atomically precise high-nuclearity silver sulfide nanocluster. *Chem Commun*. 2021;57:2372–2375.
69. Li G, Jin R. Atomic level tuning of the catalytic properties: Doping effects of 25-atom bimetallic nanoclusters on styrene oxidation. *Catal Today*. 2016;278:187–191.
70. Qian H, Jiang DE, Li G, et al. Monoplatinum doping of gold nanoclusters and catalytic application. *J Am Chem Soc*. 2012;134:16159–16162.
71. Zhang B, Kaziz S, Li H, et al. Modulation of active sites in supported $Au_{38}(SC_2H_4Ph)_{24}$ cluster catalysts: effect of atmosphere and support material. *J Phys Chem C*. 2015;119:11193–11199.
72. Wang Y, Wan X-K, Ren L, et al. Atomically precise alkynyl-protected metal nanoclusters as a model catalyst: observation of promoting effect of surface ligands on catalysis by metal nanoparticles. *J Am Chem Soc*. 2016;138:3278–3281.
73. Zhang J, Li Z, Huang J, et al. Size dependence of gold clusters with precise numbers of atoms in aerobic oxidation of d-glucose. *Nanoscale*. 2017;9:16879–16886.
74. Yamamoto H, Yano H, Kouchi H, Obora Y, Arakawa R, Kawasaki H. N,N-Dimethylformamide-stabilized gold nanoclusters as a catalyst for the reduction of 4-nitrophenol. *Nanoscale*. 2012;4:4148–4154.
75. Li G, Jin R. Gold nanocluster-catalyzed semihydrogenation: A unique activation pathway for terminal alkynes. *J Am Chem Soc*. 2014;136:11347–11354.
76. Li G, Jiang DE, Liu C, Yu C, Jin R. Oxide-supported atomically precise gold nanocluster for catalyzing Sonogashira cross-coupling. *J Catal*. 2013;306:177–183.
77. Li Z, Yang X, Liu C, Wang J, Li G. Effects of doping in 25-atom bimetallic nanocluster catalysts for carbon–carbon coupling reaction of iodoanisole and phenylacetylene. *Prog Nat Sci Mater Int*. 2016;26:477–482.
78. Liu Y, Chai X, Cai X, et al. Central doping of a foreign atom into the silver cluster for catalytic conversion of CO_2 toward C−C bond formation. *Angew Chemie*. 2018;130:9923–9927.
79. Negishi Y, Mizuno M, Hirayama M, et al. Enhanced photocatalytic water splitting by $BaLa_4Ti_4O_{15}$ loaded with ~1 nm gold nanoclusters using glutathione-protected Au_{25} clusters. *Nanoscale*. 2013;5:7188–7192.
80. Du XL, Wang XL, Li YH, et al. Isolation of single Pt atoms in a silver cluster: Forming highly efficient silver-based cocatalysts for photocatalytic hydrogen evolution. *Chem Commun*. 2017;53:9402–9405.
81. Yu C, Li G, Kumar S, Kawasaki H, Jin R. Stable $Au_{25}(SR)_{18}/TiO_2$ composite nanostructure with enhanced visible light photocatalytic activity. *J Phys Chem Lett*. 2013;4:2847–2852.
82. Kawasaki H, Kumar S, Li G, et al. Generation of singlet oxygen by photoexcited $Au_{25}(SR)_{18}$ clusters. *Chem Mater*. 2014;26:2777–2788.
83. Kauffman DR, Alfonso D, Matranga C, Qian H, Jin R. Experimental and computational investigation of Au_{25} clusters and CO_2: a unique interaction and enhanced electrocatalytic activity. *J Am Chem Soc*. 2012;134:10237–10243.

84. Kauffman DR, Alfonso D, Matranga C, et al. Probing active site chemistry with differently charged Au_{25}^{q} nanoclusters (q = -1, 0, +1). *Chem Sci*. 2014;5:3151–3157.
85. Kauffman DR, Thakkar J, Siva R, et al. Efficient electrochemical CO_2 conversion powered by renewable Energy. *ACS Appl Mater Interfaces*. 2015;7:15626–15632.
86. Lu Y, Zhang C, Li X, et al. Significantly enhanced electrocatalytic activity of Au_{25} clusters by single platinum atom doping. *Nano Energy*. 2018;50:316–322.
87. Du Y, Sheng H, Astruc D, Zhu M. Atomically precise noble metal nanoclusters as efficient catalysts: a bridge between structure and properties. *Chem Rev*. 2020;120:526–622.
88. Yamamoto K, Imaoka T, Chun WJ, et al. Size-specific catalytic activity of platinum clusters enhances oxygen reduction reactions. *Nat Chem*. 2009;1:397–402.
89. Ye H, Crooks JA, Crooks RM. Effect of particle size on the kinetics of the electrocatalytic oxygen reduction reaction catalyzed by Pt dendrimer-encapsulated nanoparticles. *Langmuir*. 2007;23:11901–11906.
90. Wang L, Tang Z, Yan W, Yang H, Wang Q, Chen S. Porous carbon-supported gold nanoparticles for oxygen reduction reaction: effects of nanoparticle size. *ACS Appl Mater Interfaces*. 2016;8:20635–20641.
91. Van Bokhoven JA, Miller JT. d electron density and reactivity of the d band as a function of particle size in supported gold catalysts. *J Phys Chem C*. 2007;111:9245–9249.
92. Wang Q, Wang J, Wang S, et al. *o* -Carborane based and atomically-precise metal clusters as hypergolic materials. *J Am Chem Soc*. 2020;142:12010–12014.

CHAPTER

4

Optical properties of metal clusters

Bhuvanachandran Nair Sreekala Sooraj[a] *and Thalappil Pradeep*[b]

[a]Research Scholar, Department of Chemistry, Indian Institute of Technology, Madras, Chennai, India [b]Deepak Parekh Institute Chair Professor and Professor of Chemistry, Department of Chemistry, Indian Institute of Technology Madras, Chennai, India

4.1 Introduction

Atomically precise noble metal nanoclusters (NCs) are an exciting area of material science research due to their wide range of applications as well as tunable optical and electronic properties. This chapter will discuss the optical absorption spectra, evolution such properties with size, their fluorescence, excited-state phenomena, and nonlinear optical properties of these systems. The methods used for computing optical properties will be discussed toward the end of the chapter.

Extensive electronic and optical properties of metal NCs mainly arise from the electrons present in orbitals of the partially filled conduction band and such electronic states are delocalized throughout the metal nanostructure.[1] These properties are controlled by the size, symmetry of crystal lattice, morphology, and surface structure of the clusters. When the size is sufficiently small, the continuous optical spectra (with plasmonic behavior) give way to discrete electronic transitions among quantized levels, each associated with a delocalized orbital spread across the NC.[1]

4.2 Optical absorption spectroscopy

Optical absorption is one of the best tools to identify NCs since monolayer-protected ultrasmall metal clusters (with diameter < 2.2 nm) exhibit prominent quantum confinement.[2] The conversion of the electronic band structure to distinct energy levels leads to well-defined optical bands in the absorption spectra. Due to molecule-like HOMO–LUMO transition, the optical absorption spectra of metal clusters exhibit step-like features with spectral broadening,

Atomically Precise Metal Nanoclusters.
DOI: https://doi.org/10.1016/B978-0-323-90879-5.00010-X

and the absence of the plasmon resonance peaks confirms the formation of clusters. As the number of atoms increases in the metal cluster over a size range of above 2 nm, the plasmon band intensifies, and the optical spectra resemble that of the bulk metal. Average core diameters range from 1.5 to 5.2 nm in this window, implying that the transition from molecular to metallic behavior can occur at smaller core sizes.[3]

The absorption spectra of NCs show broad bands which appear like a hump, and are often difficult to distinguish them from distinct peaks. In order to distinguish between the peaks and humps, a unit conversion is done from wavelength to energy while plotting the spectra. The conversion is done using the formula,

$$E = hc/\lambda \tag{4.1}$$

The recorded signal as a function of wavelength f(λ) has to be converted to a function of energy.

$$f(E)dE = f(\lambda)d\lambda \tag{4.2}$$

From the above two equations, we get

$$f(E) = f(\lambda)(d\lambda/dE) = f(\lambda)(d/dE)(hc/E)$$

$$f(E) = -f(\lambda)\left(hc/E^2\right) \tag{4.3}$$

The factor (hc/E^2), known as the Jacobian factor, which is used to scale the signal values along with wavelength conversion [wavelength (in nm) = 1239.8/(energy (in eV)].[4] To see the application of this equation, see Fig. 4.2.

4.3 Optical spectroscopy of archetypal clusters

4.3.1 Au_{25} and Ag_{25}

In our discussion, clusters are described in terms of their core sizes (M_n), although they have a specific number of ligands and appropriate charges. The optical absorption spectra of $Au_{25}(SR)_{18}$ (R = Phenylethanethiol) cluster in toluene show multiple molecule-like transitions, consisting of at least three well-defined bands at 1.8, 2.75, and 3.1 eV in the UV-vis spectrum (Fig. 4.1A). This is fundamentally different from the optical behavior of gold nanocrystals (>3 nm), which typically shows surface plasmon resonance (SPR) (collective electron excitation) at ~2.4 eV for spherical particles (3–30 nm in diameter). It is evident from the optical absorption spectra that quantum size effects dominate the $Au_{25}(SR)_{18}$ cluster.

The correlation between geometric structure and optical properties of clusters was studied by TDDFT calculations, by calculating the optical absorption spectrum and electronic structure of a model cluster, $Au_{25}(SH)_{18}^-$.[5] The Kohn-Sham orbital energy diagram (Fig. 4.1B) clearly explains the molecular orbitals (MOs), contributions of various atomic orbitals (AOs), and energy of transition. Analysis of the electronic structure of $Au_{25}(SH)_{18}^-$ reveals that the highest occupied molecular orbital (HOMO) and the three lowest unoccupied molecular orbitals (LUMOs) are mainly composed of 6sp AOs of gold, which constitutes the sp band (Fig. 4.1B). The orbitals, HOMO-1 to HOMO-5 are mainly constructed from the 5d[10] AOs of gold and thus

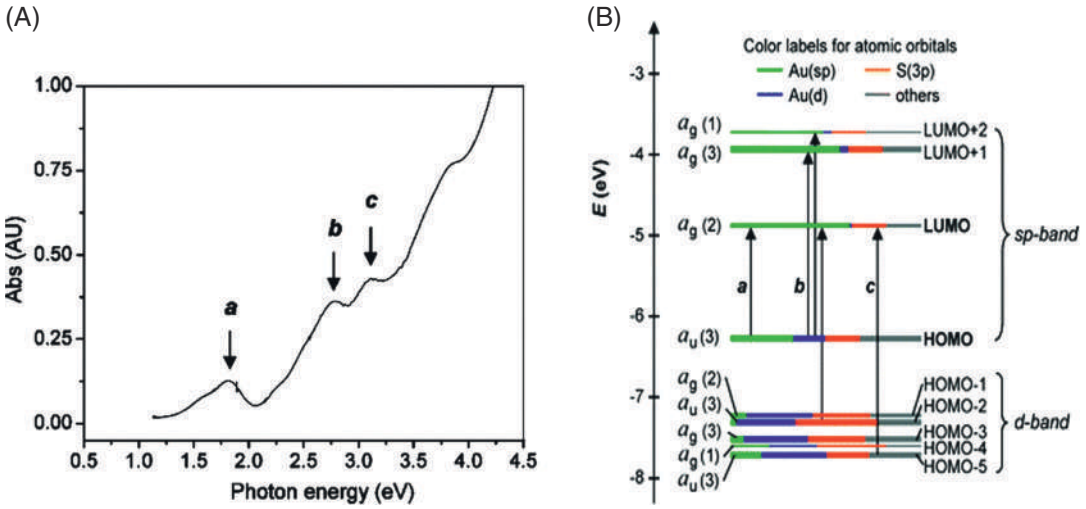

FIGURE 4.1 (A) The UV-vis spectrum of $Au_{25}(SR)_{18}$ clusters. (B) Kohn–Sham orbital energy level diagram for a model cluster $Au_{25}(SH)_{18}^{-}$.[5] "Reprinted with permission from ref.[5]. Copyright {2008} American Chemical Society."

constitute the d-band. A significant degree of S(3p) character is present in both HOMO and LUMO orbitals. Besides that, the HOMO and LUMO levels are triply and doubly degenerate, respectively.[5]

In the $Ag_{25}(SH)_{18}^{-}$ cluster, the HOMO–LUMO transition is calculated to be present at 1.64 eV.[6] In contrast to the $Au_{25}(SH)_{18}^{-}$ cluster, the strong peak at 2.33 eV arises from the HOMO to LUMO+1 transition. Even though the HOMO–LUMO gap is almost the same for both $Au_{25}(SH)_{18}^{-}$ and $Ag_{25}(SH)_{18}^{-}$, the energy level splitting between the LUMO and LUMO+1 is about 0.3 eV smaller for $Ag_{25}(SH)_{18}^{-}$; thus, enabling the transition from HOMO to LUMO+1 to occur at lower energy for this cluster. The peak at 2.49 eV arises from the HOMO-1 to LUMO transition, while the peak at 2.65 eV corresponds to the HOMO to LUMO+3 transition.[6]

4.3.2 Ag_{44} and analogous clusters

The UV-vis spectra of $[Ag_{44}(SR)_{30}]^{4-}$ cluster (where SR = SPhF, $SPhF_2$, or $SPhCF_3$) in water exhibits six apparent peaks (at 833, 641, 535, 483, 411, and 374 nm) and two shoulder peaks (at 689 and 590 nm).[7a] The optical energy gap for the $[Ag_{44}(SR)_{30}]^{4-}$ cluster is estimated to be 1.2 eV with absorption tailing up to 1050 nm. The optical studies performed by varying the surface thiolates do not exhibit any change in absorption bands, indicating a negligible influence of thiolate ligands on the absorption of metal clusters.

The substitution of Ag_{12} in the first shell of $[Ag_{44}(SR)_{30}]^{4-}$ cluster by Au_{12} results in the formation of analogous alloy clusters. $[Au_{12}Ag_{32}(SPhF_2)_{30}]^{4-}$ and $[Au_{12}Ag_{32}(SPhCF_3)_{30}]^{4-}$ clusters have two distinct peaks at 490 and 390 nm and three weak shoulders at 728, 620 and 576 nm. But for $[Au_{12}Ag_{32}(SPhF)_{30}]^{4-}$, the two major peaks are red-shifted to 508 and 403 nm. The significant difference in the optical absorption of $[Ag_{44}(SR)_{30}]^{4-}$ from

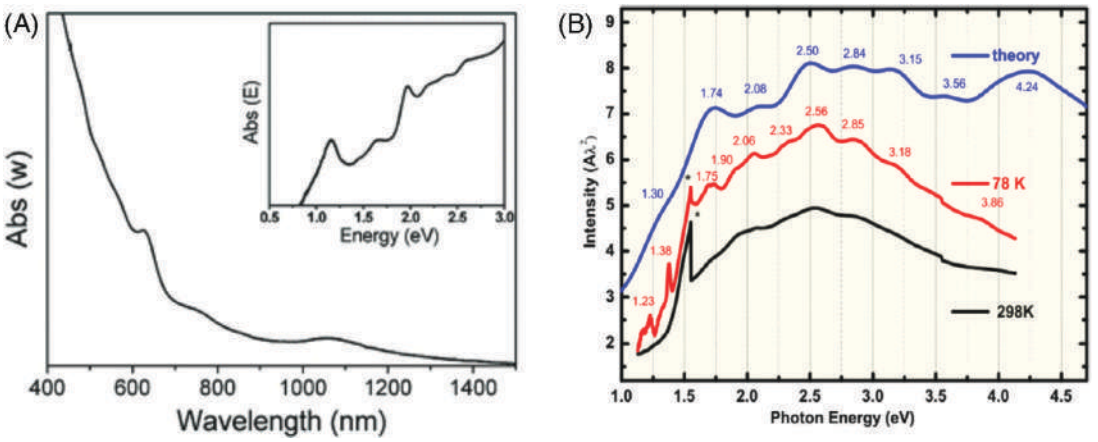

FIGURE 4.2 (A) The UV-vis spectrum of $Au_{38}(SC_2H_4Ph)_{24}$ clusters. (The inset shows the spectrum in the energy scale);[9] "Reprinted with permission from ref.[9]. Copyright {2009} American Chemical Society." (B) UV−vis−NIR absorption spectra of $Au_{102}(SPh)_{44}$ in 3-methyltetrahydrofuran at 298 K, 78 K, and the simulated spectrum.[10] "Reprinted with permission from ref.[10]. Copyright {2015} American Chemical Society."

$[Au_{12}Ag_{32}(SPhF_2)_{30}]^{4-}$ clearly indicates a significant contribution of the core metal atoms to the optical properties of these clusters.[7a] The optical spectrum of selenolate protected Ag_{44} closely resembles that of the thiolate protected cluster.[7b]

4.3.3 Au_{38}, Au_{102}, and larger clusters

For the $Au_{38}L_{24}$ ((L = SC_2H_4Ph) cluster, the UV-vis-NIR spectrum is shown in Fig. 4.2A. The absorption spectra show a series of peaks at 490, 520, 560, 620, 750, and 1050 nm.[8] The absorption spectrum is converted to energy scale using the equation, wavelength (in nm) = 1239.8/energy (in eV), which is explained in Section 4.2. The corresponding peaks in energy scale are 2.53, 2.39, 2.21, 2.00, 1.66, and 1.18 eV.[8] The most distinct peak at 2.00 eV is the characteristic feature of Au_{38} clusters. These absorption peaks resemble those of $Au_{38}(SC_{12}H_{25})_{24}$ cluster, which indicates that the optical absorption of these is rarely influenced by the 'R' groups of the thiolate.[9] The bandgap energy is determined to be 0.92 eV by tauc plot, which is close to 0.9 eV for $Au_{38}(SC_{12}H_{25})_{24}$ cluster.[9] Tauc plot consists of $h\nu$ (photon energy) on the x-axis and $(\alpha h\nu)^{1/2}$ on the y-axis, where α is the absorption coefficient. Extrapolating this linear graph to the x-axis yields the bandgap energy of the material.

The UV-vis-NIR absorption spectra of $Au_{102}(SPh)_{44}$ at two different temperatures (298 K and 78 K) are shown in Fig. 4.2B.[10] A temperature-dependent study of the absorption spectra of $Au_{102}(SPh)_{44}$ shows an increase in absorption intensities without any shift in the peaks. In Fig. 4.2B, absorption intensity is plotted against photon energy displays around ten distinct peaks between 3.86 eV and 1.23 eV and two peaks in the low energy region. In the absorption spectra, there is a rapid increase in intensity up to 1.75 eV, a maximum around 2.50 eV, and a decrease in intensity for higher energies beyond 3.50 eV. In the range of above 3.50 eV, the intensity of simulated spectra drops less rapidly than the experimental one. The broad band

centerd at 4.24 eV observed in the simulated spectrum is beyond the limits of experimental measurements.[10] In Fig. 4.2B, the experimental spectra at low temperature (78 K) are in good agreement with the simulated spectrum.

The absorption spectra of larger Au clusters, $Au_{133}(TBBT)_{52}$, $Au_{191}(TBBT)_{66}$, and $Au_{279}(TBBT)_{84}$ (TBBT - 4-tert-butylbenzenethiolate), were studied by Amala Dass and coworkers.[11] $Au_{133}(TBBT)_{52}$ exhibits broad, a strong absorption feature at 510 nm and minor features at 430 and 710 nm. The $Au_{191}(TBBT)_{66}$ cluster shows discrete features at 450 and 520 nm. The broader peak at 520 nm is due to SPR. The $Au_{279}(TBBT)_{84}$ cluster exhibits metal like SPR at 510 nm.[12]

4.3.4 Size evolution and metallicity

The optical properties of NCs are highly dependent on their size. The metallic-state AuNPs, with a size range of 5–100 nm mainly show SPR,[13] whereas those smaller than 2.2 nm exhibit distinct quantum confinement effects.[14] The extensive work by Whetten et al. on gold nanomolecules (AuNMs) reveals an approximate range of core size at which the molecular to metallic transition occurs.[15] Tsukuda and coworkers reported the evolution of photoluminescence and absorption spectra of a series of glutathione-protected AuNCs.[16] They observed that the HOMO–LUMO gap (*E*g) reduces with an increase in the size of NCs, while the PL emission position remains the same. Recently, Zhou et al. reported that the decrease of Eg in thiolate-protected AuNCs, with the size, is not a smooth evolution.[14] Detailed investigations on the emergence of plasmonic response in AuNMs have revealed that plasmonic features appear in the specific size range between 200 and 400 Au atoms. However, the mechanism and precise size range of molecular to metallic transition are still unclear. Time-resolved transient absorption (TA) measurements are powerful to characterize and differentiate molecule-like and plasmon-like transitions in AuNMs. Plasmonic gold NCs show a prominent bleach near 530 nm and exhibit power-dependent transient decay.[15] On the other hand, NCs with molecular behavior show single-particle transitions with excited-state absorption (ESA) characteristics and power-independent transient decay (Fig. 4.3).[15]

Amala Dass and coworkers have reported a new $Au_{279}(TBBT)_{84}$ cluster and studied its optical properties using steady-state and TA measurements to probe its metallic nature.[12] This cluster was the smallest gold nanocrystal to exhibit SPR, with a peak at 510 nm in the absorption spectra. The faradaurate plasmonic nanomolecule F-279 (a name introduced by Dass et al.) is a critical size in the transition from molecule to metallic state in AuNMs with a core size of 2.2 nm.[12] The cluster $Au_{246}(S\text{-}C_6H_4\text{-}CH_3)_{80}$ has a core size of 2.2 nm but exhibits a molecule nature with optical absorptions at 400, 470, and 600 nm.[18] The gold NCs with core sizes larger than F-279 are all plasmonic: F-329 (2.2 nm), F-500 (2.4 nm), and F-940 (3 nm). Thus, the nature of ligand (bulky, aromatic, aliphatic) has a crucial role in producing discrete and stable sizes in the molecule-to-metallic regime. Xu et al. have predicted that the evolution from the molecule-to-metal transition in AuNMs might occur at ~263 Au atoms by interpolating the trend between bandgap and the number of Au atoms for known NMs.[19]

Zhou et al. mapped the evolution in excited-state dynamics and steady-state optical properties of thiolate-protected AuNCs ranging from Au_{23} to Au_{246}.[14] Steady-state absorption spectra combined with transient absorption spectroscopy (TAS) revealed that the optical properties of AuNCs could be classified into three stages: (1) nonscalable (when

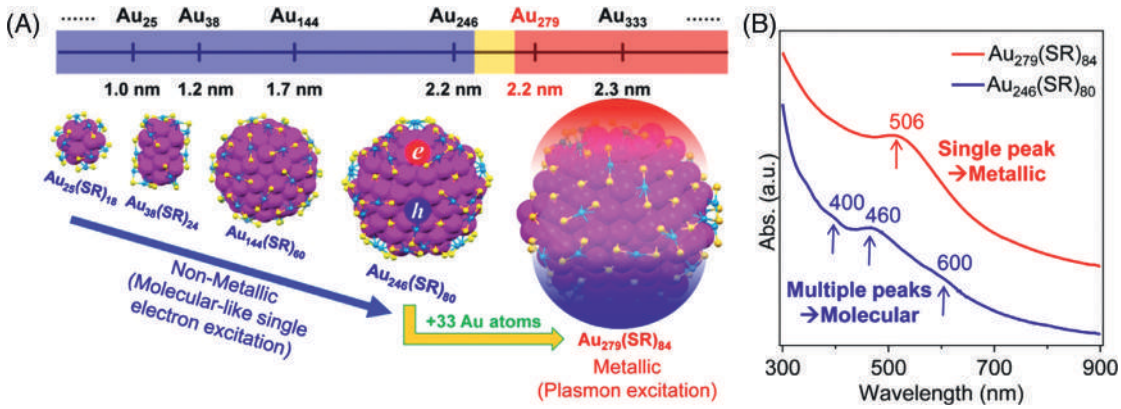

FIGURE 4.3 The size dependence of the electronic and optical properties in atomically precise gold nanoparticles. (A) Sharp transition from nonmetallic Au_{246} (bandgap Eg > 0) to metallic Au_{279} (Eg = 0); (B) Manifestation of the nonmetal-to-metal transition in optical absorption spectra.[17] "Reprinted with permission from ref.[17]. Copyright {2021} Springer Nature."

n<~50 atoms), (2) intermediate (~50–100 atoms), and (3) scalable (>100 atoms). For non-scalable clusters smaller than Au_{52}, the atomic structure determines the optical absorption spectra and excited-state lifetimes rather than the core size (n). Also, the excited-state lifetime is only weakly affected by bandgap (Eg). In medium-sized NCs (Au_{64}, Au_{92}, and Au_{99}), the size and structure together determine their absorption spectra and excited-state lifetimes. The structural effect is negligible for scalable NCs (Au_{103}, Au_{130}, Au_{133}, Au_{144}, and Au_{246}), and core size exclusively determines the optical properties.[14]

The optical excitation mechanisms are different for metallic and nonmetallic states. In metallic state AuNCs, optical excitation collectively excites the electrons in the conduction band and heats those electrons to a very high temperature (>1000 K).[20] Then the energy is dissipated from electrons to the lattice vibration via electron–phonon (e–p) coupling. Finally, the lattice releases the energy to the environment through phonon–phonon interaction. Therefore, the initial pump fluence determines the electronic temperature and the e–p coupling time, making the electron dynamics exhibit fluence dependence.[20] In nonmetallic state AuNCs, photoexcitation generates a single-electron transition from the ground state to the excited state; the initial pump fluence determines only the excited-state population.[21] Hence the fluence dependence of excited-state relaxation can be utilized for probing nonmetallic to metallic transition in larger AuNCs.[21]

Excitation dynamics of molecular and metallic AuNMs were studied in detail and best revealed using ultrafast TA measurements. Molecule-like single-particle excitations show broad positive ESA and pump power independent kinetics. In contrast, pump-power-dependent kinetics and strong plasmonic bleach are the hallmarks of electron dynamics in metallic AuNMs. A recent report of $Au_{191}(TBBT)_{66}$ cluster exhibits optical absorption features at 450 and 520 nm with an emergent plasmonic-like response, whereas its neighboring sized clusters, $Au_{133}(TBBT)_{52}$ and $Au_{279}(TBBT)_{84}$, show molecule-like and metal-like characteristics, respectively.[11] TA studies revealed that $Au_{191}(TBBT)_{66}$ exhibits molecule-like long-lived excited states

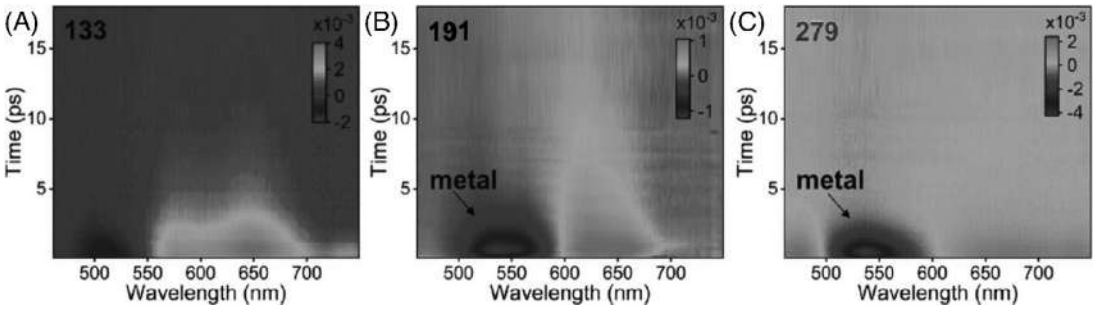

FIGURE 4.4 Measured transient absorption surfaces, are shown in (A) Au_{133}, (B) Au_{191}, and (C) Au_{279} clusters from 0.1 to 18 ps at 115 $\mu J/cm^2$ fluence.[11] "Reprinted with permission from ref.[11]. Copyright {2020} American Chemical Society."

and metal-like electron–phonon relaxation dynamics.[11] The $Au_{191}(TBBT)_{66}$ TA data show a negative bleach with a maximum at 540 nm and a positive excited state absorption (ESA) on either side of the bleach. This positive ESA grows with time until a delay of 820 fs, implying electron–electron thermalization processes in metallic Au NPs. The bleach recovers with time at a longer time delay and gives rise to a broad featureless ESA. The bleach recovery is attributed to e–p relaxation. These are characteristic features of metallic AuNPs with bleach arising from plasmonic absorption.

The TA map for the Au_{191} cluster compared to Au_{133} and Au_{279} (Fig. 4.4) reveals the transition from molecule to metallic nature. At 0.5 ps time delay, the Au_{133} cluster displays two positive ESA features at 580 and 650 nm and small bleach at 510 nm, while the Au_{191} and Au_{279} clusters exhibit plasmon bleach at 540 nm. The transition from molecule to metallic nature is governed by various aspects, including symmetry, interactions between core-gold and surface-gold, anisotropic atomic structure, electronic structure, and extended conjugation in the ligand shell.

4.4 Photoluminescence of clusters

Emission spectroscopy (photoluminescence) is another optical property of NCs, which arises from the transition between HOMO and LUMO levels. The bulk metal and metallic particles have a continuous band, and their fast nonradiative relaxation process makes it inefficient for photoluminescence. The density of states can be decreased by reducing the particle size of NCs, resulting in a larger gap between adjacent energy levels, thus enhancing photoluminescence. Photoluminescence of NCs is highly dependent on solvents and protecting ligands.

In our earlier work on photoluminescence, the reported quantum yields (QYs) of NCs were very low.[22] Wang et al. recently reported that by using dithiols, QY could be improved.[23] Water-soluble thiolate-protected gold NCs have relatively stronger QY compared to organic-soluble ones.[24] But the PL is stronger in the near-infrared (NIR) region for both these types of gold NCs, whereas the visible luminescence is weak at room temperature.[25] Time-resolved

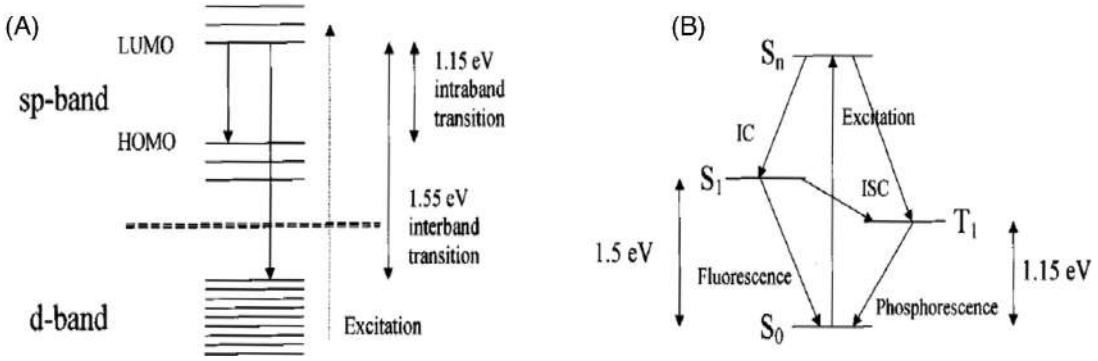

FIGURE 4.5 (A) Model for the origin of the two luminescence bands: The high energy band at 1.55 eV is proposed to be due to radiative interband recombination between the sp- and d-bands, while the low energy band at 1.15 eV is thought to originate from intraband radiative transitions within the sp-band, across the HOMO–LUMO gap. (B) Molecular model for the origin of the two luminescence bands.[28] "Reprinted with permission from ref.[28]. Copyright {2002} American Chemical Society."

fluorescence studies reveal that visible and NIR luminescence of gold NCs originates from the metal core state and surface state, respectively.[26] Most of the $Au_n(SR)_m$ NCs have lower fluorescence QYs (<1%). But a few NCs such as $Au_{24}(SCH_2Ph\text{-}tBu)_{20}$, $Au_{22}(SG)_{18}$, $Au_{18}(SG)_{14}$, $Au_{15}(SG)_{13}$, etc., exhibit higher QYs (5%−10%) (Fig. 4.5).[27]

Some gold clusters are not luminescent in the visible region under UV light exposure, but they can show emission in the NIR region. Bigioni et al. reported an $Au_{25}(SR)_{18}$ cluster, whose QY ($QY = (4.4 \pm 1.5) \times 10^{-5}$) was five orders of magnitude more than that of bulk gold, due to intraband (sp to sp) transitions.[22] The $Au_{25}(SR)_{18}$ cluster shows a strong emission ($QY = \sim 1 \times 10^{-3}$) in the near infra-red (NIR) region and a weaker emission ($QY = \sim 10^{-6}$–10^{-7}) in the visible region (Fig. 4.6).[28] The origin of luminescence of $Au_{25}(SR)_{18}$ cluster is attributed to its electronic structure. The $Au_{25}(SR)_{18}$ cluster has a core-shell structure where the core consists of 13 gold atoms, and the shell is a semiring made of six $Au_2(SR)_3$ staples, which is responsible for its luminescence.

The luminescence of gold NCs can be enhanced by employing various strategies, such as (1) modifying the core size or doping the core with other metal atoms, (2) capping the core surface with different types of ligands, and (3) exploiting aggregation-induced emission (AIE).[29] The surface ligands influence the luminescence of clusters in two different ways: (1) ligands to metal cluster core charge transfer (i.e., LMCCCT) through the Au−S bonds, (2) direct donation of delocalized electrons of electron-rich atoms or groups of the ligands to the metal core.[24] Jiang et al. increased the QY of a lipoic acid-capped Au_{22} cluster from 1% to 10% through an oxidation treatment, suggesting that increasing the positivity of the charge state of NCs can also increase the QY.[30]

Yu et al. proposed an AIE mechanism to explain the high QY (QY = 8%) of a luminescent $Au_{22}(SG)_{18}$ cluster.[31] Xie and coworkers have done a lot of work on AIE (AIE) in metal NCs.[32] Thiolate-protected metal NCs have a core−shell structure with Au(I)−thiolate motifs in the surface shell. These longer Au(I)−thiolate motifs emit stronger luminescence through the mechanism of AIE. The degree of aggregation determines both the luminescence intensity

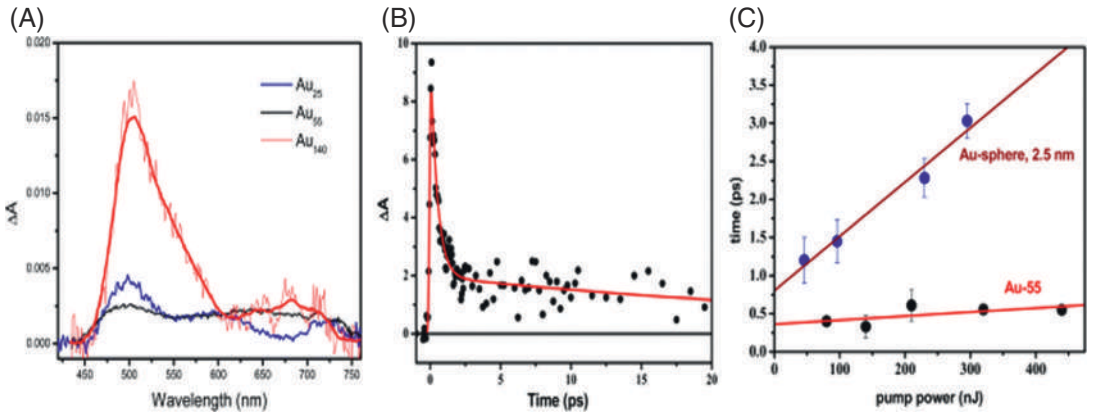

FIGURE 4.6 (A) Transient absorption spectra of Au_{25}, Au_{55}, and Au_{140} at 550 fs; (B) kinetic trace from transient absorption for Au_{55} at 640 nm; (C) Pump power dependence against average lifetime for Au_{55} cluster and a 2.5 nm nanoparticle.[37] "Reprinted with permission from ref.[37]. Copyright {2013} American Chemical Society."

and color. Xie and coworkers utilized the AIE principle to obtain a luminescent cluster with a QY of 15% by controlling the aggregation of Au(I)−thiolate complexes onto in situ generated Au(0) cores to form core−shell NCs. The $Au_{24}(SCH_2Ph\text{-}tBu)_{20}$ cluster with long motifs (i.e., tetrameric staples) is observed to have ~5% QY, which suggests that long oligomeric Au(I)−thiolate motifs enhance the luminescence.[33]

Shibu et al. have examined the solid-state emission of $Au_{25}(SG)_{18}$ cluster, in the temperature range of 80–300 K.[34] The emission intensity (a broad peak around 670 nm) increases gradually with increase in temperature. A strong enhancement in intensity occurs beyond 160 K. The peak position does not change with temperature, confirming that the $Au_{25}(SG)_{18}$ structure is intact.[35] In contrast to $Au_{25}(SR)_{18}$, the $Au_{38}(SR)_{24}$ cluster exhibits a different behavior at very low temperatures. Van Wijngaarden et al. have studied the solution phase temperature dependence of the emission spectra of $Au_{38}(SR)_{24}$ clusters between 4 and 300 K.[36] At low temperatures, emission bands with fine structures exist in the near-infrared region. As the temperature increases, the fine structures overlap and form broad emission peaks, which are characteristics of metal clusters. The lowest energy emission peak is assigned to a transition between HOMO and LUMO energy levels, whereas the higher energy peaks are assigned to emission from higher excited states, where the nonradiative relaxation competes with radiative decay.

Fluorescence measurements were carried out for silver NCs, where the clusters formed in acrylates exhibit a single emission band in the region of 550–650 nm. When mercaptosuccinic acid was incorporated as the ligand, Ag_7 and Ag_8NCs were reported to exhibit luminescence. The NCs exhibit two emission bands at 440 and 650 nm corresponding to Ag_7 and Ag_8, respectively.[15] Pradeep and coworkers recently reported the luminescence enhancement of Ag_{29} clusters via the secondary ligand, PPh_3.[9] They studied the luminescence in polymorphic structures (cubic and trigonal) of $[Ag_{29}(BDT)_{12}(PPh_3)_4]^{3-}$ and revealed the effect of secondary ligands on enhancing the luminescence. The C–H$\cdots\pi$ interactions present in the cluster restrict the intramolecular rotations and vibrations, thus enhancing radiative transition in the crystalline state.[9]

4.5 Dynamics of excited states

4.5.1 Common methods and examples

Ultrafast electron dynamics, including relaxation time scales, radiative emission, and e–p coupling, are essential for understanding the electronic structure and practical applications of gold NCs.[37] Various techniques such as TA, femtosecond time-resolved fluorescence up-conversion etc., were extensively used to understand the correlation between electron dynamics and structures of NCs.[21,26]

Relaxation dynamics of electrons and holes occur in the time scale of subpicoseconds to microseconds. These processes can be probed by various time-resolved spectroscopy techniques, including TAS and time-resolved PL. Nanosecond time-resolved PL was used to probe the emission lifetime and energy transfer, whereas ultrafast PL spectroscopy was used to investigate the core and surface states of NCs. Determination of accurate excited-state lifetime using time-resolved PL is difficult for NCs with low PL QY. However, the TAS technique probes the difference between absorption of ground and excited states as a function of the time delay. This method does not require the sample to be luminescent. Thus, TAS in femtosecond scale is a powerful tool to study the energy flow in NCs. In TAS, the system is first excited by a pump pulse, and ESA is measured using the probe pulse and then compared with ground state absorption. TA of a large variety of NCs and nanoparticles has been studied.[18,43] Goodson group has performed a comparative study of TA for Au_{25}, Au_{55}, and Au_{140} clusters (Fig. 4.6A).[37] The characteristic SPR at 530 nm was absent for these three clusters. The ESA signals were observed at 500 and 675 nm (Fig. 4.6A).

Analysis of transient dynamics of Au_{25} NC shows that the ESA signal near 670 nm can bleach after 1 ns, which corresponds to the HOMO–LUMO transition in the metal core.[26] These studies have revealed a positive correlation between the core size and absorption, related to the quantum size effect. The kinetic trace at 640 nm for the Au_{55} cluster (Fig. 4.6B) shows a fast initial relaxation to the intermediate state, followed by a slow decay to the ground state. This observation indicates a HOMO–LUMO charge transfer (~1 ps) in the metal core, followed by a core-shell charge transfer (>1 ns).[9] Analysis of TA spectra showed that ground state bleaching (GSB) is observed at ~670 nm, corresponding to a HOMO–LUMO absorption peak. The bleach observed at 550 nm is attributed to another ground state of the Au_{25} cluster.[18]

Besides TA, pump power dependence is another method to understand the electron–phonon and electron–electron relaxation processes. Electron–phonon relaxation corresponds to the energy transfer from the electronic state to the lattice, which strongly depends on the pump power.[18] Electron–electron relaxation in nanoparticles is attributed to the sharing of energy by excited electrons, followed by thermal relaxation. This process is weakly dependent on pump power. However, both of these phenomena are not observed in NCs because of their discrete energy levels.[18]

Recently, Wang et al. reported a study of ultrafast excited-state dynamics of the largest alkynyl-protected fcc gold NC, Au_{110}. ESA of the Au_{110} cluster was observed at 518 and 630 nm in the TA spectra.[36] The GSB overlaps with the broad ESA in the visible range; no negative signal is observed. Broad ESA bands indicate that excited states in Au_{110} are densely packed. From the pump power measurements, the decay constants of the cluster

were calculated as 10 ps and 1 ps, which is comparable to the time scales of phonon–phonon coupling and electron–phonon coupling in plasmonic gold nanoparticles.[37]

Link et al. explored the excited-state relaxation of $Au_{25}(SG)_{18}$ cluster and have shown that subpicosecond and nanosecond decays are independent of the laser power.[38] TA of gold NCs exhibits strong ESA, while that of large gold nanoparticles is dominated by strong bleaching due to SPR. Miller et al. proposed a core−shell relaxation model to unravel the excited-state relaxation process of $[Au_{25}(SR)_{18}]^{-}$.[39] They observed ultrafast relaxation within the Au metal core (<200 fs) and strong core-shell coupling (1.2 ps) between the orbitals of the Au_{13} kernel and surface motifs. Zhou et al. identified the solvation dynamics and charge transfer in thiol protected as well as phosphine-protected Au_{20}NCs.[40,41] The charge transfer [ligand-to-metal charge transfer (LMCT)] between surface ligands and metal core was confirmed by the solvent-dependent oscillation in the kinetic traces. Yi et al. and Mustalahti et al. studied the pump power-dependent electron dynamics of $Au_{144}(SR)_{60}$ cluster, which indicated the traces of metallic behavior.[42,43] A recent work by Jin et al. reported pump-power-independent electron dynamics in $Au_{133}(SR)_{52}$ cluster.[21] Stamplecoskie and Kamat investigated small $Au_n(SG)_m$ NCs ($n = 10$, 15, 18, 25) by femtosecond TAS and revealed that the excited-state behavior is dominated by LMCT.[44]

4.6 Nonlinear processes

4.6.1 Two-photon absorption and emission

Two-photon absorption (TPA) is a nonlinear absorption phenomenon involving a direct transition from the ground state to high energy states by the simultaneous absorption of two photons. Two successive single-photon excitations are difficult to differentiate from direct TPA since the net result is similar. But in the high-intensity regime, two-photon transitions are prominent and exhibit saturation.[45] In saturable absorption, the simultaneous absorption of two photons promotes a large number of electrons into a finite number of higher energy states. Thus the low-level state gets depleted, and the absorption cannot increase further with incident light intensity. The phenomenon of reverse saturable absorption (RSA), including ESA, can counteract the saturation process. Thus the incident photons get absorbed by the excited states when their population becomes large enough. The incident photon intensity as well as the incident frequency is critical and may lead to different behaviors depending on the resonant or nonresonant character of the transitions involved.[45]

The nonlinear absorption coefficient, $\alpha(I)$, where "I" is the incident intensity, can be described by the following general expression:

$$\alpha(I) = \frac{\alpha_0}{1 + I/I_s} + \beta I \tag{4.4}$$

where α_0, I_s, β are the linear absorption coefficient, saturation intensity, and TPA coefficient, respectively. The Z-scan theory was used to fit the experimental data to derive the values of β and I_s, where α_0 is the linear absorption.[55]

The evolution of nonlinear optical properties of nanoparticles, from molecular to the plasmonic regime, has been studied in the case of gold and silver NCs.[45,46] For gold NCs with approximately less than 150 gold atoms, a nonsaturated TPA is observed at 532 nm excitation

wavelength. The saturation intensity for gold NCs is much larger than the typical value of 108 W/cm^2. For plasmonic nanoparticles, a strong TPA is observed with clear saturation of linear absorption as well as RSA.[45] Ramakrishna et al. observed that $Au_{25}(SR)_{18}$ cluster has a reasonable luminescence efficiency ($\sim 2.5 \times 10^{-4}$) in the NIR region which can be used for two-photon imaging with infrared light.[10] Patel et al. studied three water-soluble silver clusters emitting at 660, 680, and 710 nm and determined a large two-photon cross-section of ~5000 GM.[47]

The relatively strong emission under single-photon excitation for Au clusters led to studies on the possibility of two-photon excited emission. Goodson and coworkers made the first report on two-photon excited emission with Au_{25} cluster under 1290 nm excitation, with an emission peak at 830 nm.[10] They measured the two-photon fluorescence excited at 800 nm and showed that the TPA cross-section increases as the size of gold clusters increases from 1.1 to 4.0 nm. The two-photon absorption cross-section for the Au_{25} cluster is 427,000 GM, which is much larger than the typical value of approximately 1000 GM at 800 nm for organic macromolecules. The emission wavelength maxima for both NCs and nanoparticles are dependent on size. The emission is in the range of 500 to 535 nm for NCs, while nanoparticles emit around 550 nm. The difference in the emission wavelengths results from the different energy gaps between HOMO and LUMO and is affected by the size.[37]

4.6.2 Second-order processes

Knoppe et al. reported that $[Au_{25}(capt)_{18}]^-$ exhibits second harmonic generation (SHG) due to the loss of the center of inversion by the inclusion of chiral captoril ligand.[48] An SHG response is observed at 800 nm for $[Au_{25}(capt)_{18}]^-$, along with a weak signal around 1100 nm. The weak signal at 1100 nm reveals that a second harmonic is generated under nonresonant conditions. In their study, SHG was observed for $[Au_{25}(capt)_{18}]^-$, but not for $[Au_{25}(2\text{-PET})_{18}]^-$, which affirms the importance of molecular symmetry in SHG. The molecular symmetry appears to be the main factor for efficient SHG in Au: thiolate clusters, although resonance enhancement is present. The same group has studied the $Au_{38}(SCH_2CH_2Ph)_{24}$ cluster, which is noncentrosymmetric and exhibits a significant SHG response. $Au_{38}(SCH_2CH_2Ph)_{24}$ cluster also shows two-photon fluorescence at 800 nm excitation.[48]

Another report from Knoppe et al. revealed the second-order nonlinear optical scattering properties of phosphine-protected Au_{20} clusters.[49] The first hyperpolarizability of $[Au_{20}(PP_3)_4]Cl_4$ is smaller than thiolate-protected gold clusters of similar size and inherent chirality. The value of the first hyperpolarizability (β) at the fundamental wavelengths 1300 nm and 1064 nm were calculated as $(55 \pm 5.5) \times 10^{-30}$ esu and $(93 \pm 9.3) \times 10^{-30}$ esu, respectively.[49]

4.6.3 Third-order processes

Jing et al. have reported a study of the third-order optical properties of the two gold nanoparticles (BPCP-AuNPs and DHCD-AuNPs) using the *Z*-scan technique.[50] The *Z*-scan technique is a sensitive single-beam technique for measuring the nonlinear refractive index and nonlinear absorption coefficient of many materials. The optical nonlinearities are measured by detecting the far-field sample transmittance of a focused Gaussian beam as a function

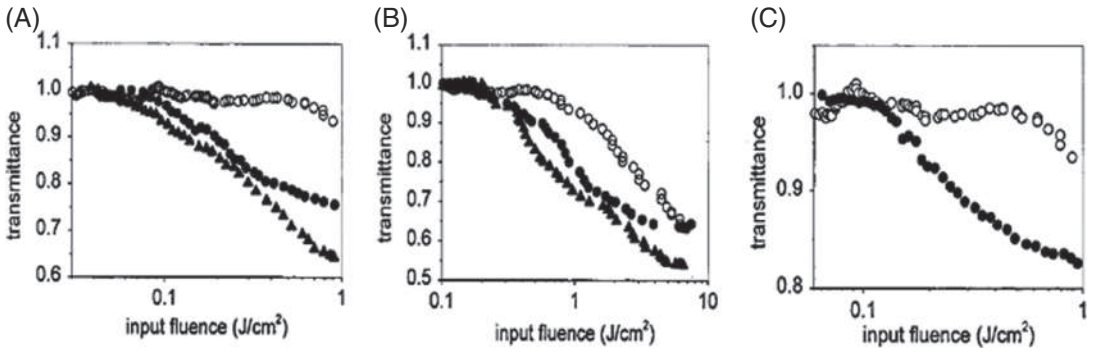

FIGURE 4.7 Optical limiting of the clusters (A) Ag, (B) Au, and (C) $AuAg_{0.75}$, dissolved in toluene. Open circles show limiting in pure toluene. Solid circles are for ODT capped clusters, while triangles are for OT capped clusters.[52] "Reprinted with permission from ref.[52]. Copyright {2000} American Physical Society."

of sample position (z). Jing et al. have measured the nonlinear refraction as 0.09, using Z-scan under 4 ns laser pulses. From the theoretical fitting of Z-scan data, they calculated a third-order nonlinear refractive index, γ as 4.2×10^{-17} m^2/W and 2.19×10^{-17} m^2/W for BPCP-AuNPs and DHCD-AuNPs, respectively.[50] The stronger nonlinear optical effect in BPCP-AuNPs is attributed to the extensive π-conjugated system in the BPCP ligand.

Banska et al. studied the third-order nonlinear optical properties of $Au_{25}(Capt)_{18}$ clusters by Z-scan technique with a femtosecond laser excitation in a broad range of wavelengths.[51] Philip et al. studied the nonlinear processes in a wide variety of gold clusters such as $Au_{25}SR$, $Au_{38}SR$, $Au_{144}SR$ clusters, and the TPA coefficients were calculated as 2.0×10^{-10}, 3.5×10^{-10}, and 7.5×10^{-10} m/W, respectively.[47] Ramakrishna et al. studied larger gold clusters such as Au_{140}, Au_{309}, Au_{976}, Au_{2406}, and measured the two-photon absorption cross-sections as 871×10^3 GM, 1476×10^3 GM, 905×10^3 GM, 3452×10^3 GM, respectively.[10]

4.6.4 Optical limiting

Optical limiting is the phenomenon of reducing the optical transmission of a material with increasing laser fluence. This property is desirable for the protection of human eyes and sensors from intense laser radiation. Sandhyarani et al. reported an optical limiting study using the Z-scan technique by 35 ps pulses at 532 nm on silver, gold and alloy clusters.[52] The technique of Z-scan involves moving the sample through the focus of a laser. As a result, the sample experiences various laser intensities along the z-axis. Ag and Au clusters exhibit almost the same efficiency for optical limiting, but the alloy clusters are less efficient in optical limiting.

Fig. 4.7A depicts the nonlinear transmittance plotted as a function of the input laser fluence for solutions of octanethiol (OT) and octadecanethiol (ODT) capped AgNCs in toluene. The octanethiol capped Ag clusters show a better optical limiting than octadecanethiol capped Ag clusters. Similarly, Fig. 4.7B shows the limiting behavior of gold clusters, AuOT and AuODT in toluene. Comparative study of these clusters reveals that Ag clusters exhibit a

better limiting capability than AuNCs because of their early onset of limiting and larger reduction in transmittance. Fig. 4.7C shows the optical limiting obtained for alloy cluster $AuAg_{0.75}$, and the limiting efficiency is observed to be less than that of pure Ag and Au clusters.[52]

4.7 Computational methods and optical properties

Understanding the structure and dynamics of molecular systems from the optical absorption spectra requires detailed and dynamically accurate molecular models.[53] Different types of computational methods are used to compute linear and nonlinear optical spectra. Some of the standard methods are (1) linearized semiclassical method; (2) semiclassical forward–backward initial-value representation (FB-IVR) method; (3) Standard second-order cumulant (2OC) approximation which is based on the ground-state equilibrium frequency–frequency correlation function; (4) Alternative second-order cumulant (2OCa) approximation which can account for nonequilibrium dynamics on the excited state potential surface.[53]

The quantum-mechanical expressions for the one- and two-dimensional spectra are explained below. A two-state system is considered with the following field-free Hamiltonian:

$$\hat{H} = |\mathrm{g}\rangle\hat{H}_{\mathrm{g}}\langle\mathrm{g}| + |\mathrm{e}\rangle\hat{H}_{\mathrm{e}}\langle\mathrm{e}|$$

Here, $|\mathrm{g}\rangle$ and $|\mathrm{e}\rangle$ are the adiabatic ground and excited states, and $\hat{\mathrm{H}}_{\mathrm{g/e}} = V_{\mathrm{g/e}}(Q) + T(P)$ are the corresponding adiabatic Hamiltonians where $V_{\mathrm{g/e}}(Q)$ is potential energy, and $T(P)$ is kinetic energy.

The measurement of one-dimensional (1D) spectra is based on detecting the time-resolved linear response of the system to a single impulsive pulse at time t=0. The assumption is that the system is in its equilibrium ground state before the arrival of the pulse. Using the Condon approximation, the signal can be expressed as proportional to the following linear optical response function (ORF).[54]

$$J(t_1) = |\mu_{\mathrm{ge}}|^2 \mathrm{Tr}\left[e^{i\hat{H}_{\mathrm{g}}t_1/\hbar}e^{-i\hat{H}_{\mathrm{e}}t_1/\hbar}\hat{\rho}_{\mathrm{g}}\right]$$

Here, μ_{ge} is the transition dipole moment, and $\hat{\rho}_g = \mathrm{e}^{-\beta Hg}/\mathrm{Tr}^{[\mathrm{e}-\beta Hg]}$ is the equilibrium ground state density operator, with $\beta = 1/k_{\mathrm{B}}T$. Then the linear absorption spectrum can be defined as the frequency-domain analogue of $J(t_1)$:[54]

$$I(\omega_1) = \mathrm{Re}\int_0^\infty \mathrm{d}t_1 e^{-i\omega t_1} J(t_1)$$

The two-dimensional (2D) spectra are measured based on detecting the time-resolved nonlinear response of the system to three sequential impulsive pulses with wave vectors $\mathbf{k}_a$, $\mathbf{k}_b$, and $\mathbf{k}_c$. The time delay between pulses a and b is denoted as t_1, while that of pulses b and c are denoted as t_2. The signal field is detected at a time interval t_3 after pulse c, in the background-free directions, $\mathbf{k}_{\mathrm{nr}} = \mathbf{k}_a$ - $\mathbf{k}_b + \mathbf{k}_c$ and, $\mathbf{k}_{\mathrm{r}} = -\mathbf{k}_a + \mathbf{k}_b + \mathbf{k}_c$, corresponding to the *nonrephasing* and *rephasing* signals, respectively.[55] It is again assumed that the system is in its equilibrium ground state before the arrival of the first pulse, and using the Condon approximation, the

nonrephasing and rephasing signals can be expressed as proportional to the following third-order ORFs:[54]

$$R_{\mathrm{nr}}(t_3, t_2, t_1) = R_1(t_3, t_2, t_1) + R_4(t_3, t_2, t_1)$$

$$R_{\mathrm{r}}(t_3, t_2, t_1) = R_2(t_3, t_2, t_1) + R_3(t_3, t_2, t_1)$$

The 2D spectrum at a given value of t_2 is defined as the frequency-domain analogue, with respect to t_1 and t_3, of $R_{\mathrm{nr}}(t_3,t_2,t_1)$ and $R_{\mathrm{r}}(t_3,t_2,t_1)$:

$$I(\omega_3, t_2, \omega_1) \equiv \mathrm{Re} \int_0^\infty \mathrm{d}t_1 \int_0^\infty \mathrm{d}t_3 \{e^{i(\omega_1 t_1 + \omega_3 t_3)} R_{\mathrm{nr}}(t_3, t_2, t_1) + e^{i(-\omega_1 t_1 + \omega_3 t_3)} R_{\mathrm{r}}(t_3, t_2, t_1)\}$$

Other approaches using frequency-dependent polarizability and linear-response time-dependent density functional theory (TDDFT) are utilized to study the optical properties. The most widely used approach is linear-response TDDFT.[56] TDDFT is an extension of density functional theory (DFT) to the time-dependent domain. The conceptual and computational foundations of TDDFT are analogous to DFT.[57] TDDFT can be viewed as an exact reformulation of time-dependent quantum mechanics, where the fundamental variable is no longer the many-body wave function but the density. With the development of Casida's equations[58] or random-phase approximation, it was possible to rapidly and efficiently determine the TDDFT solution for molecules.[59] Currently, TDDFT is a popular approach for modeling the structures, energies, and electronic properties of excited states (ES). It is widely used to determine vibrationally resolved optical spectra, excited-state structures, emission wavelengths, and in the simulation of photochemical reactions.[57] To see more details on computational methods, refer to Chapter 14.

4.8 Summary and future perspectives

The various aspects of optical properties of atomically precise NCs are discussed above. The optical properties of clusters are dependent on the size, shape, composition, and structure. The correlation between structure and optical properties has been explored by both experimental and theoretical methods. The excited-state dynamics, as well as luminescence of clusters, make them potential candidates for various applications. Further exploration of the excited-state relaxation dynamics of metal NCs will be helpful in understanding molecule to metallic transition. Also, a deeper understanding of the structure-dependent relaxation pathways and decay lifetimes can improve the potential of NCs as to energy storage and conversion devices. Extensive studies on the nonlinear optical properties of NCs will help to elucidate the structural correlation and benefit the applications of such materials. Many of the phenomena observed can be modeled computationally, and accurate results comparable with the experiments can be obtained. Overall, the study of optical properties of NCs will reveal their beauty and mystery, which will broadly impact nanoscience.

List of abbreviation

AuNM	gold nanomolecule
AuNP	gold nanoparticle
Capt	captoril
DOF	degrees of freedom
DFT	density functional theory
ESA	excited-state absorption
FB-IVR	forward-backward Initial value representation
FRET	Förster resonance energy transfer
GM	Goeppert-Mayer
GSB	ground state bleaching
HOMO	highest occupied molecular orbital
LMCCCT	ligands to metal cluster core charge transfer
LUMO	lowest unoccupied molecular orbital
NC	nanocluster
NIR	near infrared region
ORF	optical response function
PET	phenylethanethiol
PL	photoluminescence
QY	quantum yield
RSA	reversible saturable absorption
SHG	second harmonic generation
SPR	surface plasmon resonance
TAS	transient absorption spectroscopy
TBBT	4-tert-Butylbenzenethiol
TDDFT	time-dependent density functional theory
THG	third harmonic generation
TPA	two-photon absorption
TRPL	time–resolved photoluminescence
UV-vis	ultraviolet−visible spectroscopy
2OC	second-order cumulant
2Oca	alternative second-order cumulant

References

1. Gregory Schaaff T, Whetten RL. Giant gold-glutathione cluster compounds: intense optical activity in metal-based transitions. *J Phys Chem B*. 2000;104:2630–2641.
2. Chakraborty I, Pradeep T. Atomically precise clusters of noble metals: emerging link between atoms and nanoparticles. *Chem Rev*. 2017;117:8208–8271.
3. Hostetler MJ, Wingate JE, Zhong CJ, et al. Alkanethiolate gold cluster molecules with core diameters from 1.5 to 5.2 Nm: core and monolayer properties as a function of core size. *Langmuir*. 1998;14:17–30.
4. Mooney J, Kambhampati P. Correction to "Get the basics right: jacobian conversion of wavelength and energy scales for quantitative analysis of emission spectra". *J Phys Chem Lett*. 2014;5:3497−3497.
5. Zhu M, Aikens CM, Hollander FJ, Schatz GC, Jin R. Correlating the crystal structure of a thiol-protected Au_{25} cluster and optical properties. *J Am Chem Soc*. 2008;130:5883–5885.
6. Aikens CM. Origin of discrete optical absorption spectra of $M_{25}(SH)$ 18- nanoparticles (M = Au, Ag). *J Phys Chem C*. 2008;112:19797–19800.
7. (a) Yang H, Wang Y, Huang H, et al. All-thiol-stabilized Ag_{44} and $Au_{12}Ag_{32}$ nanoparticles with single-crystal structures. *Nat Commun*. 2013;4:1–8; (b) Chakraborty I, Kurashige W, Kanehira K, et al. $Ag_{44}(SeR)_{30}$: a hollow cage silver cluster with selenolate protection. *J Phys Chem Lett*. 2013;4:3351–3355.
8. Qian H, Zhu Y, Jin R. Size-focusing synthesis, optical and electrochemical properties of monodisperse $Au_{38}(SC_2H_4Ph)_{24}$ nanoclusters. *ACS Nano*. 2009;3:3795–3803.

9. Qian H, Zhu M, Andersen UN, Jin RF. Large-scale synthesis of dodecanethiol-stabilized Au_{38} clusters. *J Phys Chem A*. 2009;113:4281–4284.
10. Rambukwella M, Sementa L, Barcaro G, Fortunelli A, Dass A. Organosoluble $Au_{102}(SPh)_{44}$ nanomolecules: synthesis, isolation, compositional assignment, core conversion, optical spectroscopy, electrochemistry, and theoretical analysis. *J Phys Chem C*. 2015;119:25077–25084.
11. Sakthivel NA, Shabaninezhad M, Sementa L, et al. The missing link: $Au_{191}(SPh\text{- }tBu)_{66}$ janus nanoparticle with molecular and bulk-metal-like properties. *J Am Chem Soc*. 2020;142:15799–15814.
12. Sakthivel NA, Stener M, Sementa L, Fortunelli A, Ramakrishna G, Dass A. $Au_{279}(SR)_{84}$: the smallest gold thiolate nanocrystal that is metallic and the birth of plasmon. *J Phys Chem Lett*. 2018;9:1295–1300.
13. Hartland GV. Optical studies of dynamics in noble metal nanostructures. *Chem Rev*. 2011;111:3858–3887.
14. Zhou M, Higaki T, Li Y, Zeng C, Li Q. Three-stage evolution from nonscalable to scalable optical properties of thiolate-protected gold nanoclusters. *J Am Chem Soc*. 2019;141:19754–19764.
15. Kumara C, Zuo X, Ilavsky J, Cullen D, Dass A. Atomic structure of $Au_{329}(SR)_{84}$ faradaurate plasmonic nanomolecules. *J Phys Chem C*. 2015;119:11260–11266.
16. Negishi Y, Nobusada K, Tsukuda T. Glutathione-protected gold clusters revisited: bridging the gap between gold(I)-thiolate complexes and thiolate-protected gold nanocrystals. *J Am Chem Soc*. 2005;127:5261–5270.
17. Jin R, Higaki T. Open questions on the transition between nanoscale and bulk properties of metals. *Commun Chem*. 2021;4:28.
18. Zhou M, Zeng C, Song Y, et al. On the non-metallicity of 2.2 Nm $Au_{246}(SR)_{80}$ nanoclusters. *Angew Chemie - Int Ed*. 2017;56:16257–16261.
19. Xu WW, Gao Y. Unraveling the atomic structures of the $Au_{68}(SR)_{34}$ nanoparticles. *J Phys Chem C*. 2015;119:14224–14229.
20. Arbouet A, Voisin C, Christofilos D, Langot P, Fatti ND. Electron-phonon scattering in metal clusters. *Phys Rev Lett*. 2003;90.
21. Zeng C, Chen Y, Kirschbaum K, Appavoo K, Sfeir MY, Jin R. Structural patterns at all scales in a nonmetallic chiral $Au_{133}(SR)_{52}$ nanoparticle. *Sci Adv*. 2015;1.
22. Bigioni TP, Whetten RL, Dag Ö. Near-infrared luminescence from small gold nanocrystals. *J Phys Chem B*. 2000;104:6983–6986.
23. Tang Z, Xu B, Wu B, Robinson DA, Bokossa N, Wang G. Monolayer reactions of protected Au nanoclusters with monothiol tiopronin and 2,3-dithiol dimercaptopropanesulfonate. *Langmuir*. 2011;27:2989−2996.
24. Wu Z, Jin R. On the ligand's role in the fluorescence of gold nanoclusters. *Nano Lett*. 2010;10:2568−2573.
25. Wang G, Guo R, Kalyuzhny G, Choi J-P, Murray RW. NIR luminescence intensities increase linearly with proportion of polar thiolate ligands in protecting monolayers of Au_{38} and Au_{140} quantum dots. *J Phys Chem B*. 2006;110:20282–20289.
26. Devadas MS, Kim J, Sinn E, Lee D, Goodson T, III, Ramakrishna G. Unique ultrafast visible luminescence in monolayer-protected Au_{25} clusters. *J Phys Chem C*. 2010;114:22417–22423.
27. Shichibu Y, Negishi Y, Tsunoyama H, Kanehara M, Teranishi T, Tsukuda T. Extremely high stability of glutathionate-protected Au_{25} clusters against core etching. *Small*. 2007;3:835–839.
28. Link S, Beeby A, FitzGerald S, El-Sayed MA, Schaaff TG, Whetten RL. Visible to infrared luminescence from a 28-atom gold cluster. *J Phys Chem B*. 2002;106:3410–3415.
29. Conroy CV, Jiang J, Zhang C, et al. Enhancing near Ir luminescence of thiolate Au nanoclusters by thermo treatments and heterogeneous subcellular distributions. *Nanoscale*. 2014;6:7416−7423.
30. Jiang J, Conroy CV, Kvetny MM, et al. Oxidation at the core−ligand interface of Au lipoic acid nanoclusters that enhances the near-IR luminescence. *J Phys Chem C*. 2014;118:20680–20687.
31. Yu Y, Luo Z, Chevrier DM, et al. Identification of a highly luminescent $Au_{22}(SG)_{18}$ nanocluster. *J Am Chem Soc*. 2014;136:1246−1249.
32. Goswami N, Yao Q, Luo Z, Li J, Chen T, Xie J. Luminescent metal nanoclusters with aggregation-induced emission. *J Phys Chem Lett*. 2016;7:962−975.
33. Luo Z, Yuan X, Yu Y, et al. From aggregation-induced emission of Au(I)−thiolate complexes to ultrabright Au(0)@Au(I)−thiolate core−shell nanoclusters. *J Am Chem Soc*. 2012;134:16662–16670.
34. Shibu ES, Pradeep T. Photoluminescence and temperature-dependent emission studies of Au_{25}clusters in the solid state. *Int J Nanosci*. 2009;2:223–226.

35. Shibu ES, Muhammed MAH, Tsukuda T, Pradeep T. Ligand exchange of $Au_{25}SG_{18}$ leading to functionalized gold clusters: spectroscopy, kinetics, and luminescence. *J Phys Chem C*. 2008;112:12168–12176.
36. Wijngaarden JT, Van, Toikkanen O, Liljeroth P, Quinn BM, Meijerink A. Temperature-dependent emission of monolayer-protected Au_{38} clusters. *J Phys Chem C*. 2010;114:16025–16028.
37. Yau SH, Varnavski O, Goodson III T. An ultrafast look at Au nanoclusters. *Acc Chem Res*. 2013;46:1506−1516.
38. Link S, El-Sayed MA, Schaaff TG, Whetten RL. Transition from nanoparticle to molecular behavior: a femtosecond transient absorption study of a size-selected 28 atom gold cluster. *Chem Phys Lett*. 2002;356:240−246.
39. Miller SA, Fields-Zinna CA, Murray RW, Moran AM. Nonlinear optical signatures of core and ligand electronic states in $Au_{24}pd_{118}$. *J Phys Chem Lett*. 2010;1:1383−1387.
40. Zhou M, Vdović S, Long SR, et al. Intramolecular charge transfer and solvation dynamics of thiolate-protected $Au_{20}(SR)_{16}$ clusters studied by ultrafast measurement. *J Phys Chem A*. 2013;117:10294–10303.
41. Zhou M, Long S, Wan X, et al. Ultrafast relaxation dynamics of phosphine-protected, rod-shaped Au_{20} clusters: interplay between solvation and surface trapping. *Phys Chem Chem Phys*. 2014;16:18288–18293.
42. Yi C, Tofanelli MA, Ackerson CJ, Knappenberger KL. Optical properties and electronic energy relaxation of metallic $Au_{144}(SR)_{60}$ nanoclusters. *J Am Chem Soc*. 2013;135:18222–18228.
43. Mustalahti S, Myllyperkiö P, Lahtinen T, et al. Ultrafast electronic relaxation and vibrational cooling dynamics of $Au_{144}(SC_2H_4Ph)_{60}$ nanocluster probed by transient mid-IR spectroscopy. *J Phys Chem C*. 2014;118:18233–18239.
44. Stamplecoskie KG, Kamat PV. Size-dependent excited state behavior of glutathione-capped gold clusters and their light-harvesting capacity. *J Am Chem Soc*. 2014;136:11093–11099.
45. Reyna AS, Russier-Antoine I, Bertorelle F, et al. Nonlinear refraction and absorption of Ag_{29} nanoclusters: evidence for two-photon absorption saturation. *J Phys Chem C*. 2018;122:18682–18689.
46. Yang H, Wang Y, Huang H, et al. All-thiol-stabilized Ag_{44} and $Au_{12}Ag_{32}$ nanoparticles with single-crystal structures. *Nat Commun*. 2013;4:1–8.
47. Qian H, Y Sfeir M, Jin R. Ultrafast relaxation dynamics of $[Au_{25}(SR)_{18}]$ nanoclusters: effects of charge state. *J Phys Chem C*. 2010;114:19935–19940.
48. Knoppe S, Vanbel M, Van Cleuvenbergen S, Vanpraet L, Bürgi T, Verbiest T. Nonlinear optical properties of thiolate-protected gold clusters. *J Phys Chem C*. 2015;119:6221–6226.
49. Knoppe S, Zhang QF, Wan XK, Wang QM, Wang LS, Verbiest T. Second-order nonlinear optical scattering properties of phosphine-protected Au_{20} clusters. *Ind Eng Chem Res*. 2016;55:10500–10506.
50. Lv J, Jiang L, Li C, et al. Large third-order optical nonlinear effects of gold nanoparticles with unusual fluorescence enhancement. *Langmuir*. 2008;24:8297–8302.
51. Patel SA, Richards CI, Hsiang JC, Dickson RM. Water-soluble Ag nanoclusters exhibit strong two-photon-induced fluorescence. *J Am Chem Soc*. 2008;130:11602–11603.
52. Reji P, Ravindra Kumar G, Sandhyarani N, Pradeep T. *Phys Rev B*. 2000;62:13160–13166.
53. McRobbie PL, Geva E. A benchmark study of different methods for calculating one- and two-dimensional optical spectra. *J Phys Chem A*. 2009;113:10425–10434.
54. Silbey RJ. Principles of Nonlinear Optical Spectroscopy By Shaul Mukamel (University of Rochester). Oxford University Press: New York. 1995. xviii + 543 pp. $65.00. ISBN 0-19-509278-3. *J Am Chem Soc*. 1996;118:12872.
55. Varnavski O, Ramakrishna G, Kim J, Lee D, Goodson T. Critical size for the observation of quantum confinement in optically excited gold clusters. *J Am Chem Soc*. 2010;132:16–17.
56. Kurth S, Stefanucci G, Almbladh CO, Rubio A, Gross EKU. Time-dependent quantum transport: a practical scheme using density functional theory. *Phys Rev B - Condens Matter Mater Phys*. 2005;72:1–13.
57. Laurent AD, Jacquemin D. TD-DFT benchmarks: a review. *Int J Quantum Chem*. 2013;113:2019–2039.
58. Casida ME, Chong D. Recent advances in density functional methods. *Comput Chem: Rev Curr Trends*. 1995;1: 10–30.
59. Stratmann RE, Scuseria GE, Frisch MJ. An efficient implementation of time-dependent density-functional theory for the calculation of excitation energies of large molecules. *J Chem Phys*. 1998;109:8218–8224.

CHAPTER

5

Supramolecular chemistry of nanoclusters

Abhijit Nag[a] *and Thalappil Pradeep*[b]

[a]**DST Unit of Nanoscience (DST UNS) and Thematic Unit of Excellence, Department of Chemistry, Indian Institute of Technology Madras, Chennai, India**

[b]**Deepak Parekh Institute Chair Professor and Professor of Chemistry, Department of Chemistry, Indian Institute of Technology Madras, Chennai, India**

5.1 Introduction to supramolecular chemistry

Supramolecular chemistry is one of the most emerging and impactful fields of chemistry which highlights chemistry "beyond the molecule" or "the chemistry of molecular assemblies and of the intermolecular bond."[1] In general, traditional chemistry emphasizes on covalent bonding (along with other strong bonds), while supramolecular chemistry focuses on weak noncovalent interactions. Being highly interdisciplinary in nature, it attracts not only chemists but also biologists, physicists, environmental scientists, theoreticians, biochemists, and crystallographers. Supramolecular chemistry involves phenomena such as protein folding, molecular self-assembly, molecular recognition, mechanically interlocked molecular architectures, host–guest chemistry, and dynamic covalent chemistry. The study of supramolecular chemistry focuses on the specific noncovalent interactions between molecules, like dipole-dipole, ion-dipole, hydrogen bonding, van der Waals (vdWs) forces, metal coordination, π–π interactions, hydrophobic forces, and electrostatic interactions. These phenomena are vital in biological processes, such as enzyme action, genetic information processing, molecular transport, protein assembly, etc. In 1987, Jean-Marie Lehn, Donald J. Cram, and Charles J. Pedersen shared the Nobel Prize in chemistry for the recognition of their research on "host–guest" assemblies. In 2016, Fraser Stoddart, Jean-Pierre Sauvage, and Ben Feringa were awarded the Nobel Prize in chemistry for their work on the design and synthesis of tiny molecular machines. This chapter will highlight recent advances in the supramolecular chemistry of nanoclusters (NCs) and their applications.

As mentioned in earlier chapters, the metal core of NCs is surrounded by staple motifs, which are further protected by a monolayer of ligands, such as thiolates, phosphines, etc.[2,3] As these protected ligands consist of aliphatic and aromatic hydrocarbons and various

Atomically Precise Metal Nanoclusters.
DOI: https://doi.org/10.1016/B978-0-323-90879-5.00021-4

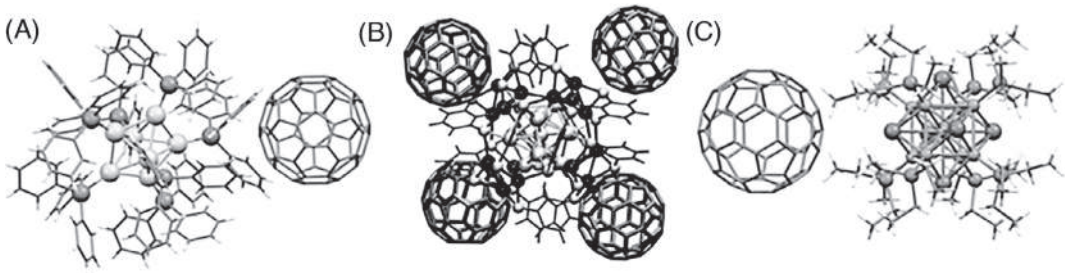

FIGURE 5.1 (A) Crystal structure of $[Au_7(PPh_3)_7]C_{60}$. Reproduced with permission.[8] (B) DFT optimized structure of $[Ag_{29}(S_2R)_{12}(C_{60})_4]^{3-}$. Reproduced with permission.[10] (C) Crystal structure of $[Ni_9Te_6(PEt_3)_8][C_{60}]$. Reproduced with permission.[9]

functional groups, possibilities of supramolecular interactions of such ligands with other suitable molecules always exist.[4,5] In the context of NCs, we have categorized the topic into the following parts: supramolecular molecular chemistry of NCs with (1) fullerenes, (2) cyclodextrins (CDs), (3) cucurbiturils (CBs), and (4) crown ethers.

5.2 Fullerenes

Fullerenes[6] are well established in supramolecular chemistry because of their size, shape, π-electron structure, and electron-accepting properties.[7] The first crystal structure of fullerides with gold NCs was studied by Martin Schulz-Dobrick et al. in 2008. Single crystals were achieved via the layering method.[8] The slow interdiffusion of $[Au_8(PPh_3)_8](NO_3)_2$ in acetonitrile and KC_{60} in THF gave rise to black crystals containing gold NCs and fullerides. Two different single crystals, $[Au_7(PPh_3)_7]C_{60}$·THF (Fig. 5.1A) and $[Au_8(PPh_3)_8](C_{60})_2$ were obtained using this approach. Negatively charged fullerides interacted with positively charged NCs via electrostatic interactions. Such electrostatic attractions and intermolecular interactions gave rise to intercluster building blocks. This kind of intercluster hybrid materials could exhibit highly exciting electron-transport properties.

Likewise, the binary assembly of transition metal NCs with fullerenes was demonstrated by Xavier Roy et al.[9] Two equivalents of C_{60} and $[Co_6Se_8(PEt_3)_6]$ were dissolved in toluene. Single crystals of $[Co_6Se_8(PEt_3)_6][C_{60}]_2$ were achieved by keeping the resulting solution for 12 h for crystallization. Similarly, mixing $[Cr_6Te_8(PEt_3)_6]$, and two equivalents of C_{60} gave rise to $[Cr_6Te_8(Pet_3)_6][C_{60}]_2$.

Both $[Cr_6Te_8(PEt_3)_6][C_{60}]_2$ and $[Co_6Se_8(PEt_3)_6][C_{60}]_2$ resulted in a superatomic structure that is similar to the structure of cadmium iodide (CdI_2). Such hybrid materials of transition metal NCs with fullerenes exhibited activated electronic transport property with activation energies in the range of 100 to 150 millielectron volts. Similarly, the interdiffusion of $Ni_9Te_6(PEt_3)_8$ and C_{60} gaves rise to black crystals of $[Ni_9Te_6(PEt_3)_8][C_{60}]$ (Fig. 5.1C) at -30° after 2 weeks. $[Ni_9Te_6(PEt_3)_8][C_{60}]$ complex showed a structure similar to rock salt. The charge transfer from $Ni_9Te_6(PEt_3)_8$ to fullerene was more compared to the other transition metal NCs as the former

is more reducible. These hybrid materials of transition metal NCs with fullerenes exhibited magnetic properties at low temperatures.

Recently, supramolecular functionalization of silver NCs with fullerenes was studied by Chakraborty et al.[10] Mixing of $Ag_{29}(S_2R)_{12}^{3-}$ NC in DMF and C_{60} in toluene at room temperature gave rise to to $[Ag_{29}(S_2R)_{12}(C_{60})_n]^{3-}$ (n = 1–9) (S_2R = 1,3-benzenedithiolate). $[Ag_{29}(S_2R)_{12}(C_{60})_n]^{3-}$ (n = 1–4) adducts were confirmed using electrospray ionization mass spectrometry (ESI MS) when four equivalent of C_{60} in toluene was added to the NC solution. The cavity created by the aromatic ligand surfaces of the NC allowed the π-electron surface of fullerenes to interact. Structural compatibility was one of the main reasons for the generation of such complexes. Molecular docking and density functional theory (DFT) calculations were employed to elucidate structures of $[Ag_{29}(S_2R)_{12}(C_{60})_n]^{3-}$ (n = 1–4) adducts (Fig. 5.1B). The close-up view of the optimized structures revealed that the $\pi\cdots$H-C, $\pi\cdots\pi$ and vdWs interactions between the aromatic rings of S_2R of the NC and the π surface of the fullerene gave rise to the formation of such adducts. Another fullerene, C_{70} was used to support the results where also similar results were obtained. In a subsequent study, fullerene (C_{60} and C_{70})-induced complexation of $[M_{25}(SR)_{18}]^-$ (M = Ag or Au and -SR= thiolate ligand) was confirmed using ESI MS.[11] Multiple fullerenes were attached to the ligand surface of a single NC in case of $[Ag_{29}(S_2R)_{12}]^{3-}$ whereas the attachment of multiple NCs was noticed on the surface of a fullerene in the case of $[M_{25}(SR)_{18}]^-$. So, the nature of such hybrid materials in the case of $[M_{25}(SR)_{18}]^-$ was different compared to the fullerene adducts of $[Ag_{29}(S_2R)_{12}]^{3-}$.

5.3 Cyclodextrins

CDs[12] are cyclic oligosaccharides connected by α-1,4 glycosidic bonds. They contain a hydrophobic central cavity and hydrophilic outer surface. Due to their molecular structure, size, and shape, they exhibit an exceptional ability to encapsulate molecular species into its internal cavity, termed as a host–guest complex. There are three commonly used CDs, α-CD (connected by six glucose subunits), β-CD (connected by seven glucose subunits), and γ-CD (connected by eight glucose subunits). In this chapter, we will mainly focus on the host–guest complexes of CDs with NC.

Pradeep and coworkers investigated the host–guest interaction between β-CDs and $[Au_{25}(SR)_{18}]$ (SR = 4-(t-butyl)benzyl mercaptan).[13] Most of the investigations were carried out by ESI MS, which revealed that a maximum of four CDs were attached to the surface of NC by encapsulating SBB ligands (Fig. 5.2A). A schematic representation of the resulted adducts of β-CDs and $[Au_{25}(SR)_{18}]$ is provided in Fig. 5.2B. Such supramolecular interactions are facilitated by the narrower rim of the β-CD and were confirmed by optimizing the structure of HSBB∩CD. The four β-CDs interacted with the NC in a tetrahedral symmetry, reducing steric hindrance among β-CDs. The DFT optimized structure revealed that vdW interactions between β-CDs and the SBB ligand were accountable for attaching β-CDs on the surface of the NC. Such supramolecular interactions between SBB and β-CD gave rise to an enhancement of luminescence and stability of the NC.

Similarly, Yan et al. functionalized the surface of $[Au_{38}S_2(SR)_{20}]$ NC (SR = 1-adamantanethiolate) with α-, β-, and γ-CDs.[14] Most of the studies were carried out using UV-Vis and mass-spectrometry techniques. β-CD, among all the CDs selectively interacted

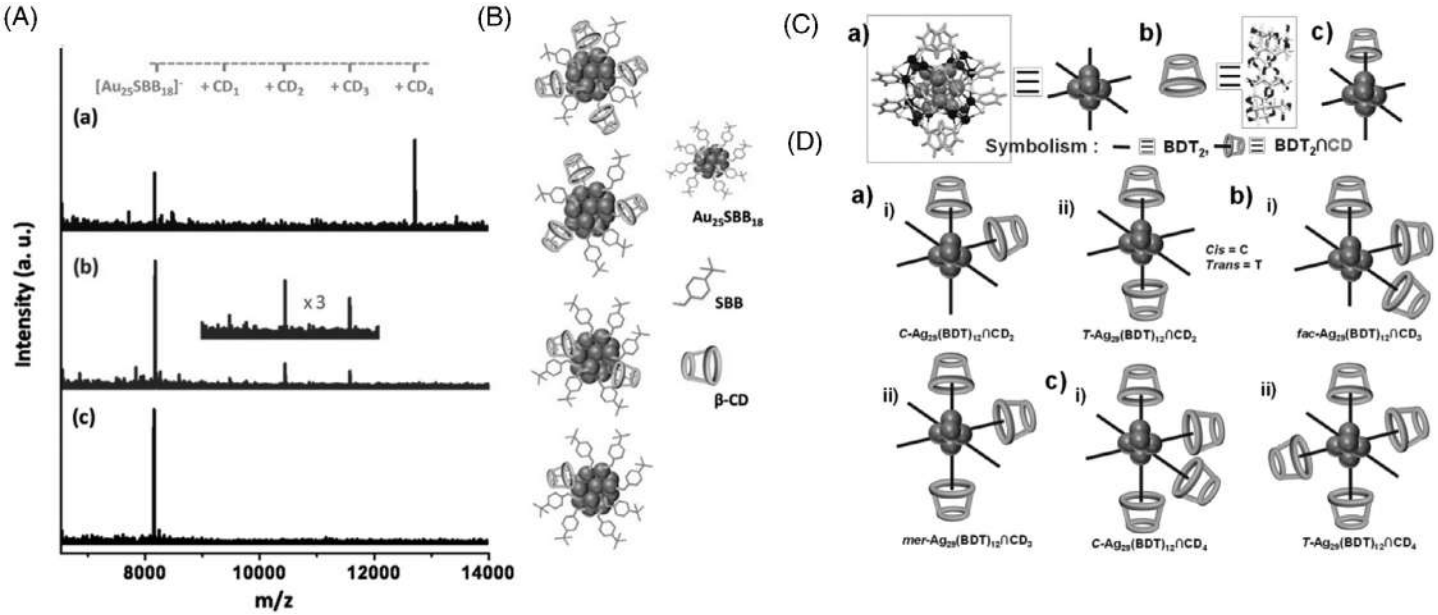

FIGURE 5.2 (A) ESI MS of the $[Au_{25}SBB_{18}\cap CD_n]$ (n = 1–4) adducts. (B) Schematic presentation of $[Au_{25}(SBB)_{18}\cap(\beta\text{-CD})_n]$ (n = 1–4) adducts. Reproduced with permission.[13] (C) Schematic presentation of (a) $[Ag_{29}(S_2R)_{12}]$ where S_2R is 1,3-benzenedithiolate and (b) β-CDs. (D) Simple presentation of the isomers of $[Ag_{29}(S_2R)_{12}\cap(CD)_n]$ (n = 2–3). Reproduced with permission.[21]

with the NC surface which resulted in $Au_{38}S_2(SR)_{20}\cap(\beta\text{-CD})_1$ and $[Au_{38}S_2(SR)_{20}\cap(\beta\text{-CD})_2]$ complexes. Molecular dynamics simulations were carried out to obtain the structure of these complexes, wherein two β-CDs remained at the two corners of the Au_{38} NC which minimized the mutual steric hindrance. The attachment of β-CDs on the NC surface lead to enhanced stability.

Isomerism of NCs is a very interesting area of research.[15–20] In this context, host–guest adducts of $[Ag_{29}(S_2R)_{12}\cap(CD)_n]$ (n = 1–6) (termed as I) were produced by mixing the as-prepared $[Ag_{29}(S_2R)_{12}]$ with α-, β-, and γ-CDs in DMF.[21] ESI MS and nuclear magnetic resonance (NMR) study established the formation of supramolecular adducts. A molecular docking study and DFT computation were performed to achieve the lowest energy structures of $[Ag_{29}(S_2R)_{12}\cap(CD)_n]$ (n = 1–6) adducts. The lowest energy structures revealed that CD encapsulated a pair of S_2R ligands. Non-covalent interactions like C-H$\cdots\pi$, hydrogen bonding, and vdWs interactions, and weak ionic Ag$\cdots$O played a crucial role in the formation of such host–guest adducts. More importantly, the special geometry of these complexes resulted in a system that resembled the octahedral complexes of transition metals which are composed of various isomers. Simple illustrations of these isomers are provided in Fig. 5.2D. These isomers of I (n = 2–4) were detected using ion mobility mass spectrometry (IM MS).

5.4 Cucurbiturils

CBs[22] are macrocyclic containers consisting of glycoluril (=$C_4H_2N_4O_2$=) monomers linked by methylene bridges (-CH_2-). The molecular structure of CB contains a partly enclosed cavity wherein oxygen atoms are placed along the edges and tilted inwards. The name of the molecule is given by its similarity to a pumpkin that belongs to Cucurbit family. CBs are usually expressed as cucurbit[n]uril, where n represents the number of glycoluril (=$C_4H_2N_4O_2$=) units. Two basic acronyms are CB[n] and CB_n. They are well-known as suitable hosts for a vast series of guest molecules having a wide range of cavity sizes through non-covalent and cation-dipole interactions. Here, we will mainly focus on the host–guest complexes of CBs with NC.

Recently, Tao Jiang et al. first reported a method for illuminating and improving the emission of AuNC, $[Au_{22}(FGGC)_{18}]$ (FGGC = N-terminal Phe-Gly-Gly-Cys peptide) in a reversible way, using a host–guest complexation strategy between CB[n] (n = 7, 8) and FGGC peptides in water (Fig. 5.3A).[23] The supramolecular complexation approach has indeed improved the emission of AuNCs through the rigidification of the NC surface. This resulted in the effective elimination of nonradiative transition and promotion of the radiative transition, as confirmed by an ultrafast spectroscopy study. Such host–guest interactions between AuNCs and CBs gave rise to a high (Quantum yield) QY of 39% for CB[8] and 51% for CB[7] in water at ambient temperature, respectively. It is one of the highest red emitting AuNCs in water at ambient temperature. $[Au_{22}(FGGC)_{18}]$ recorded a relatively low QY of 7.5% under the same circumstances.

In a subsequent study, Nag et al. studied the host–guest complexation of $[Ag_{29}(LA)_{12}]$ (LA = α-lipoic acid) with cucurbit[7]uril (CB[7]) in an aqueous medium at ambient temperature.[24] The experimental findings were supported with molecular docking analysis and DFT optimizations (Fig. 5.3B). This research demonstrated that CB[7] encapsulated one of the NC's

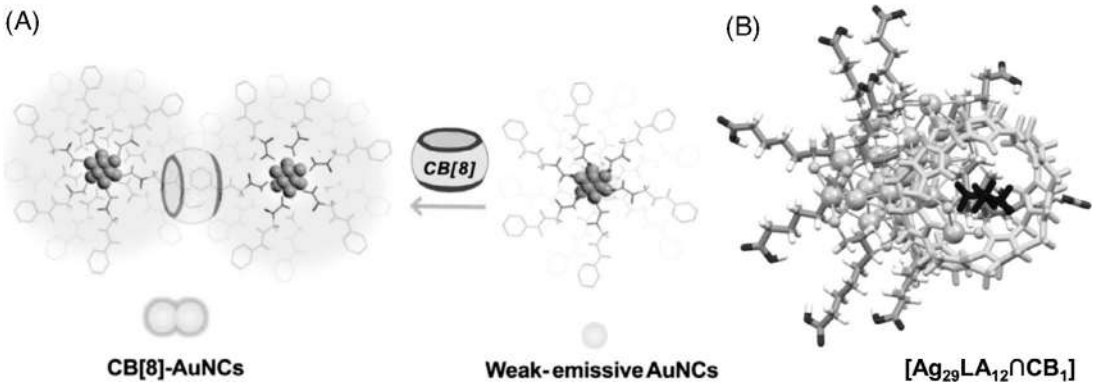

FIGURE 5.3 (A) Supramolecular interactions of CB[8] with AuNCs resulted in enhancement in luminescence. Reproduced with permission.[23] (B) DFT optimized structure of $[Ag_{29}(LA)_{12}CB[7]_1]$. Reproduced with permission.[24]

LA ligands. In this case too, host–guest interactions increased luminescence about 1.25 times compared to the parent NC.

5.5 Crown ethers

Crown ethers[25] are heterocyclic compounds with multiple ether groups. They are widely used in the formation of host–guest complexes. The hydrophilic cavity formed by ether oxygen atoms is extremely effective in capturing alkali and alkaline earth metal ions. The cavity size is highly specific to a particular metal ion. The molecules, 18-crown-6, 15-crown-5, and 12-crown-4, for example, have a high affinity for potassium, sodium, and lithium cations, respectively. Crown ethers are well-known for their ion transport mechanism as well as in phase-transfer catalysis. They are used to construct supramolecular assemblies. In the following, we will mainly focus on the supramolecular complexes of crown ethers with NCs.

Pradeep and coworkers investigated the first crystal structure of a supramolecular-assembly red luminescent $[Ag_{29}(S_2R)_{12}(TPP)_4]^{3-}$ (Ag_{29}) with dibenzo-18-crown-6 (DB18C6) (Fig. 5.4).[26] In the crystal lattice of the trigonal Ag_{29} ($Ag_{29}T$) cluster, the crystal-induced auto arrangement of DB18C6 molecules formed a hexameric cage-like structure. The anisotropic expansion of the $Ag_{29}T$ lattice along the z-axis led to the insertion of hexameric cages into the crystalline grid. The main reason for such self-organized assemblies was the intermolecular C-H$\cdots\pi$ interactions between $DB18C6Na^+$ and the ligands triphenylphosphine (TPP) and S_2R of the NC, and the electrostatic interaction of 3 $DB18C6Na^+$ and negatively charged Ag_{29} NC. This structure is similar to a new family of complexes called "lattice inclusion" in NCs. Such supramolecular interactions gave rise to a luminescence enhancement of 3.5 fold more than the parent crystals of $Ag_{29}T$. This study offers a new concept for the development of enhanced luminescent cluster-assembled functional materials.

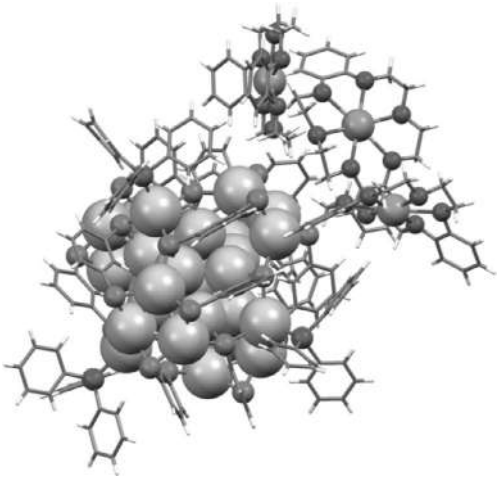

FIGURE 5.4 (A) Total structure of $[Ag_{29}(S_2R)_{12}(TPP)_4]^{3-}$ with 3 dibenzo-18-crown-6 (DB18C6). Reproduced with permission.[26]

5.6 Properties of supramolecular complexes of NCs

Specific properties of supramolecular complexes should include the following:

1. **Structural complementarity:** The host and guest are mutually complementary with respect to their geometric structure and electronic properties. Complementarity allows the host to select guests of a particular structure. In supramolecular chemistry, this phenomenon is called "molecular recognition."
2. Due to a large number of noncovalent interactions, supermolecular complexes have a high degree of structural organization.
3. Self-assembled structures may result from supramolecular interactions. Small molecular species interact spontaneously and lead to much larger and more complex assemblies. The entropy of the system therefore diminishes, $\Delta S < 0$. However, it is a spontaneous process and the change of Gibbs energy is negative: $\Delta G = \Delta H - T\Delta S < 0$, this must be true if $\Delta H < 0$ and $|\Delta H| > |T\Delta S|$. As a result, during self-assembly, heat is released.

Apart from these fundamental aspects, supramolecular complexes of NCs exhibit a variety of additional properties, which are discussed below.

Luminesce: NCs can become more luminescent as a result of supramolecular complexation. When cucurbituls, CDs, and crown ethers form supramolecular adducts with NCs, their luminescence is enhanced.[24,26] The entire structure becomes extremely rigid due to the existence of strong noncovalent interactions between the host and the guest. As a result, the whole system becomes extremely luminescent.

Charge transfer: When there is a difference in an electronic property, there may be a charge transfer between a guest and a host. This was demonstrated in the case of $[Ag_{29}(S_2R)_{12}(C_{60})_n]^{3-}$, where NC has three negative charge states.[10] The NC appears to have transferred an electron to C_{60}, as collision-induced dissociation analysis forms a C_{60}^- species. Similarly, it is known that the reducing NC $[Ni_9Te_6(PEt_3)_8]$ forms a charge-transfer complex with the fullerene.[9]

Magnetism: A very recent emerging field is the magnetic properties of the NC. More information on the magnetic properties of NCs will be covered in the previous chapter. Such properties of supramolecular complexes of NCs could be improved via noncovalent interactions. At low temperatures, binary assemblies of fullerenes with $[Ni_9Te_6(PEt_3)_8]$ NCs exhibited magnetic properties.[9]

5.7 Applications of supramolecular complexes of NCs

The following are some of the applications of supramolecular complexes of NCs:

Sensing: One of the most fundamental applications of NCs is sensing. Supramolecular complexes of $[Ag_{29}LA_{12}]$ with CDs emit a bright red light under UV.[24] Nag et al. developed a method to detect dopamine at a concentration of about 10 nM using $[Ag_{29}LA_{12}@CD_n]$ ($n = 1$–3), where @ denotes the supramolecular adduct.[24] The vacant cavity of CD encapsulated dopamine molecules, resulting in quenching.

Cell imaging: One of the fascinating applications of NC-supramolecular complexes is live-cell imaging. Because of their excellent optical properties, supramolecular complexes of $[Au_{22}(FGGC)_{18}]$ with CB[7] demonstrated exceptional luminescence imaging of cancer A549 cells.[23]

Photocatalytic activity: Xie and his colleagues developed a hybrid material composed of per-6-thio-cyclodextrin (SH-CD) protected gold nanoparticles and TiO_2 nanoparticles (NPs).[27] This hybrid material demonstrated superior photocatalytic performance compared to TiO_2 NPs alone. As a result, the photocatalytic decomposition of organic pollutants via host–guest complexation was enhanced by this hybrid material. When compared to only TiO_2 NPs (47%), the hybrid TiO_2 system had a higher efficiency (98%).

Catalytic activity: Zhao et al. recently created a hybrid material with adamantanethiolate-protected $[Au_{40}(S\text{-}Adm)_{22}]$ and γ-CD-MOF.[28] This hybrid material outperformed parent $[Au_{40}(S\text{-}Adm)_{22}]$ NCs in terms of water solubility and catalytic activity. The horseradish peroxidase (HRP)-mimicking catalysis was enabled using this water-soluble hybrid material.

5.8 Summary and future perspectives

This chapter provided a concise discussion of various supramolecular interactions of NCs with molecules such as (1) fullerenes, (2) CDs, (3) CBs, and (4) crown ethers. The structural compatibility of NCs with other molecules such as fullerenes, CDs, CBs, and crown ethers promotes the formation of host–guest complexes. Supramolecular interactions may result in luminesce enhancement. Although some supramolecular complexes were identified as a mixture of adducts in the solution and gas phases, isolation of these complexes in the solid-state can lead to the formation of new classes of cluster-assembled solids. Furthermore, due to different binding modes to the NCs, it is difficult to separate the isomers of supramolecular complexes. Such isomerism could lead to the emergence of novel properties such as chirality, self-assembly, and so on. The supramolecular complexes of NCs including cluster-assembled solids of metal-organic frameworks have a wide range of applications. Such supramolecular complexes could lead to the development of new magnetic, conducting, and luminescent

materials. Supramolecular complexes of NCs with CDs and CBs have the potential to be used as drug delivery vehicles and bioimaging agents.

List of abbreviation

Ag_{29}	$[Ag_{29}(S_2R)_{12}(TPP)_4]^{3-}$
$Ag_{29}T$	Trigonal Ag_{29}
CdI_2	Cadmium iodide
CBs	Cucurbiturils
CB[7]	Cucurbit[7]uril
CDs	Cyclodextrins
DFT	Density functional theory
DB18C6	Dibenzo-18-crown-6
ESI MS	Electrospray ionization mass spectrometry
FGGC	N-terminal Phe-Gly-Gly-Cys peptide
HRP	Horseradish peroxidase
IM MS	Ion mobility mass spectrometry
LA	α-lipoic acid
NMR	Nuclear magnetic resonance
NCs	Nanoclusters
NPs	Nanoparticles
S_2R	1,3-benzenedithiolate
SR	4-(t-butyl)benzyl mercaptan
SH-CD	Thio-cyclodextrin
TPP	Triphenylphosphine
vdWs	van der Waals

References

1. Huang F, Anslyn EV. Introduction: Supramolecular chemistry. *Chem Rev*. 2015;115:6999–7000.
2. Chakraborty I, Pradeep T. Atomically precise clusters of noble metals: Emerging link between atoms and nanoparticles. *Chem Rev*. 2017;117:8208–8271.
3. Jin R, Zeng C, Zhou M, Chen Y. Atomically precise colloidal metal nanoclusters and nanoparticles: Fundamentals and opportunities. *Chem Rev*. 2016;116:10346–10413.
4. Chakraborty P, Nag A, Chakraborty A, Pradeep T. Approaching materials with atomic precision using supramolecular cluster assemblies. *Acc Chem Res*. 2019;52:2–11.
5. Nonappa, Ikkala O. Hydrogen bonding directed colloidal self-assembly of nanoparticles into 2D crystals, capsids, and supracolloidal assemblies. *Adv Funct Mater*. 2018;28.
6. Kroto HW, Heath JR, O'Brien SC, Curl RF, Smalley RE. C_{60} : Buckminsterfullerene. *Nature*. 1985;318:162–163.
7. Diederich F, Gómez-López M. Supramolecular fullerene chemistry. *Chem Soc Rev*. 1999;28:263–277.
8. Schulz-Dobrick M, Jansen M. Intercluster compounds consisting of gold clusters and fullerides: $[Au_7(PPh_3)_7]C_{60}\cdot THF$ and $[Au_8(PPh_3)_8](C_{60})_2$. *Angew Chem Int Ed*. 2008;47:2256–2259.
9. Roy X, Lee C-H, Crowther AC, et al. Nanoscale atoms in solid-state chemistry. *Science*. 2013;341:157.
10. Chakraborty P, Nag A, Paramasivam G, Natarajan G, Pradeep T. Fullerene-functionalized monolayer-protected silver clusters: $[Ag_{29}(BDT)_{12}(C_{60})_n]^{3-}$ (n = 1–9). *ACS Nano*. 2018;12:2415–2425.
11. Chakraborty P, Nag A, Mondal B, Khatun E, Paramasivam G, Pradeep T. Fullerene-mediated aggregation of $M_{25}(SR)_{18}^-$ (M = Ag, Au) nanoclusters. *J Phys Chem C*. 2020;124:14891–14900.
12. Crini G. Review: A history of cyclodextrins. *Chem Rev*. 2014;114:10940–10975.
13. Mathew A, Natarajan G, Lehtovaara L, et al. Supramolecular functionalization and concomitant enhancement in properties of Au_{25} Clusters. *ACS Nano*. 2014;8:139–152.
14. Yan C, Liu C, Abroshan H, Li Z, Qiu R, Li G. Surface modification of adamantane-terminated gold nanoclusters using cyclodextrins. *Phys Chem Chem Phys*. 2016;18:23358–23364.

15. Chen Y, Liu C, Tang Q, et al. Isomerism in $Au_{28}(SR)_{20}$ nanocluster and stable structures. *J Am Chem Soc*. 2016;138:1482–1485.
16. Kang X, Zhu M. Structural isomerism in atomically precise nanoclusters. *Chem Mater*. 2021;33:39–62.
17. Xu WW, Zeng XC, Gao Y. The structural isomerism in gold nanoclusters. *Nanoscale*. 2018;10:9476–9483.
18. Matus MF, Malola S, Kinder Bonilla E, Barngrover BM, Aikens CM, Häkkinen H. A topological isomer of the $Au_{25}(SR)_{18}^-$ nanocluster. *Chem Commun*. 2020;56:8087–8090.
19. Qin Z, Zhang J, Wan C, et al. Atomically precise nanoclusters with reversible isomeric transformation for rotary nanomotors. *Nat Commun*. 2020;11:6019.
20. Baksi A, Ghosh A, Mudedla SK, et al. Isomerism in monolayer protected silver cluster ions: an ion mobility-mass spectrometry approach. *J Phys Chem C*. 2017;121:13421–13427.
21. Nag A, Chakraborty P, Paramasivam G, Bodiuzzaman M, Natarajan G, Pradeep T. Isomerism in supramolecular adducts of atomically precise nanoparticles. *J Am Chem Soc*. 2018;140:13590–13593.
22. Barrow SJ, Kasera S, Rowland MJ, del Barrio J, Scherman OA. Cucurbituril-based molecular recognition. *Chem Rev*. 2015;115:12320–12406.
23. Jiang T, Qu G, Wang J, Ma X, Tian H. Cucurbiturils brighten Au nanoclusters in water. *Chem Sci*. 2020;11:3531–3537.
24. Nag A, Chakraborty P, Thacharon A, et al. Atomically precise noble metal cluster-assembled superstructures in water: Luminescence enhancement and sensing. *J Phys Chem C*. 2020;124:22298–22303.
25. Gokel GW, Leevy WM, Weber ME. Crown ethers: Sensors for ions and molecular scaffolds for materials and biological models. *Chem Rev*. 2004;104:2723–2750.
26. Chakraborty P, Nag A, Sugi KS, Ahuja T, Varghese B, Pradeep T. Crystallization of a supramolecular coassembly of an atomically precise nanoparticle with a crown ether. *ACS Mater. Lett*. 2019;1:534–540.
27. Zhu H, Goswami N, Yao Q, et al. Cyclodextrin–gold nanocluster decorated TiO2 enhances photocatalytic decomposition of organic pollutants. *J Mater Chem A*. 2018;6:1102–1108.
28. Zhao Y, Zhuang S, Liao L, et al. A dual purpose strategy to endow gold nanoclusters with both catalysis activity and water solubility. *J Am Chem Soc*. 2020;142:973–977.

CHAPTER

6

Nanocluster–nanoparticle coassemblies

Amrita Chakraborty[a] *and Thalappil Pradeep*[b]

[a]Department of Chemistry, Rice University, 6100 Main Street, Houston, Texas, USA
[b]Deepak Parekh Institute Chair Professor and Professor of Chemistry, Department of Chemistry, Indian Institute of Technology Madras, Chennai, India

6.1 Introduction

Faraday initiated research on metal nanoparticles (NPs) in the 19th century. Precisely, he obtained a sol of gold by systematic reaction between aqueous $HAuCl_4$ and phosphorous. Since then, colloidal NPs of metals, especially gold, have gained tremendous attention, owing to their vivid colors and extraordinary physical and chemical stability. Moreover, due to enhanced light-matter interactions at the surface of metal NPs, they exhibit electronic, optical, magnetic, and catalytic properties that are dependent on their size, shape, and composition.[1] Advancement of nanoscience has made synthesis of NPs of various size, shape, pattern, composition, and functionalities feasible,[2] enabling highly tunable physicochemical properties. Further, NPs placed in close vicinity of each other, show enhanced and unprecedented properties due to plasmonic coupling. Hierarchical structures constituting carefully arranged metal NPs exhibit collective properties that have potential applications in biodiagnostics,[3a] ultrasensitive chemical and metal ion detection,[3b] photovoltaics,[4] etc. Therefore, researchers have investigated various methods to assemble NPs extensively, especially of noble metals, into hybrid structures to obtain desired functionalities. Though intrasystem assemblies were the early examples of composite nanomaterials,[6] assembling prefabricated NPs of different size regime,[7] or different metals[8] have proved to be of greater utility in biosensing, multimodal imaging, and advanced optical communication. Nanoclusters (NCs) are strictly monodisperse in size and precise in composition. Their surface ligands are capable of exhibiting rich chemical interactions, making them potential building blocks of hierarchical nanostructures. Chapter 20 presents instances of intercluster assemblies. In this chapter, we discuss the coassemblies of NCs with noble metal NPs producing precise nanocomposites, which show emerging physicochemical properties in a few cases.

DOI: https://doi.org/10.1016/B978-0-323-90879-5.00019-6

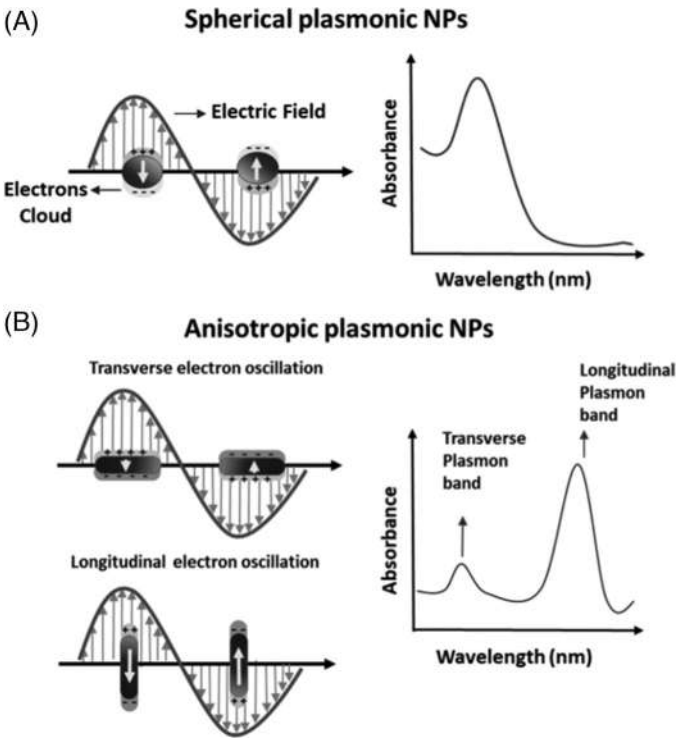

FIGURE 6.1 Schematic representation of surface plasmon resonance (SPR) band in (A) spherical and (B) rod-shaped plasmonic NPs. Reproduced with permission from reference 9b. Copyright 2019, Springer.

6.2 Importance of colloidal assembly

Owing to high surface-to-volume ratio, metallic NPs show unique optoelectronic properties. For example, the delocalized conduction band electrons of metals oscillate when perturbed by the electric field of an incident electromagnetic radiation. When the frequency of the incident light is in-phase with that of the inherent oscillation of the electron clouds at the surface of a conductor, a resonant condition, distinctly different from the respective bulk oscillation, is achieved, known as SPR. In the case of metallic NPs of dimension comparable to the incident wavelength, SPR is confined to the surface of the particle, and is termed as localized surface plasmon resonance (LSPR) (Fig. 6.1). The resonance frequency of colloidal nanocrystals is highly specific to its size, shape, composition, and dielectric environment.[9] In the case of small spherical NPs, the entire charge distribution associated with it oscillates uniformly, showing a single sharp absorbance band at the LSPR frequency. This band appears around 520 nm in the case of AuNPs of ~10 nm dimension, and around 390 nm in case of Ag NPs. With increase in particle size, the absorption maximum shifts toward the longer wavelength. However, in the case of nonspherical particles such as rods, ellipsoids, triangular prisms, etc., nature of the LSPR band is determined by the particle morphology, and its position is highly sensitive to the size, dielectric constant of the surrounding medium, presence of neighboring particles, etc. (Fig. 6.2).[10,11] Due to differential surface curvature of these NPs, the localization of SPR leads to an inhomogeneous distribution of electromagnetic field along

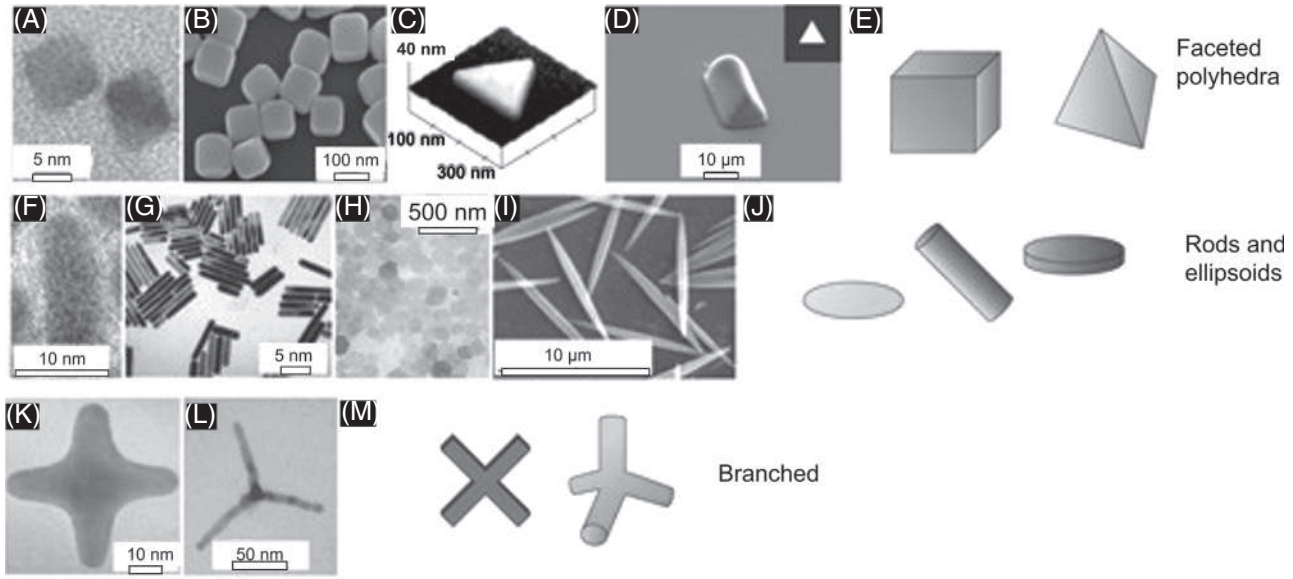

FIGURE 6.2 Electron microscopic images of various kinds of nanomaterials and corresponding cartoon representation: Cubes of PbSe (A) and silver (B); prisms of gold (C) and a polymer (D), which are examples of faceted polyhedral particles (E). Rods and ellipsoids of CdSe (F), gold (G), gibbsite (H), and polymer latex (I) are shown along with their graphical representations (J). Gold (K) and CdTe tetrapods (L) are included as branched particles (M) (adapted from Glotzer et al.,2007). Reproduced with permission from reference 10. Copyright 2007, Nature Publishing Group.

their surface. As a result, particles with sharp protrusions work as efficient nanoprobes for surface-enhanced spectroscopic techniques such as Raman,[12] fluorescence,[13] and infrared spectroscopies.[14]

In addition, coupling between the plasmons associated with neighboring NPs lead to collective properties that have encouraged studies of their assemblies into hierarchical structures. While assemblies of spherical, homogeneous particles are useful to understand the underlying principles of colloidal assembly, directional interactions between nonspherical, or "anisotropic" NPs are likely to result in more complex hierarchical structures. For example, metallic NPs of suitable shape, size, and composition have been assembled in an end-to-end or side-to-side fashion by using mediator or chemical linkers such as polymers, dithiols, macromolecules, DNA strands, etc.[15] In some cases, external magnetic or electric fields have been employed to arrange NPs in a desired geometry.[16] Another popular approach is template-mediated assemblies, whereby 1D metallic or nonmetallic nanostructures, 2D chemically patterned substrates, 3D molecular frameworks, DNA origami, etc., extensively guide the self-assembly of NPs.[17] In such assembled structures, near-field coupling between the surface plasmons often result in confinement of electromagnetic energy, showing extraordinary enhancement in SERS signal.[18] Optimum interparticle distance in plasmonic NP-luminescent semiconductors QD composite structures leads to PL enhancement due to plasmon-exciton coupling.

6.3 NCs in colloidal assembly

Self-assembly of micro- and nano-structures has gained attention as sensors, photonic crystals, and in energy harvesting applications. Owing to their easily achievable size and shape monodispersity, plasmonic NPs are used as building blocks to create hierarchical nanostructures, that exhibit collective optoelectronic properties. Nanogaps in such assembled structures are known to act as plasmonic hot spots such that analytes placed in these gaps show multifold enhancement in their SERS signal. Even a subtle change in the dimension of nanogaps significantly alters the intensity of electromagnetic field localized in the gaps. These gaps are determined by the position, orientation, and surface curvature of the participating NPs. Hence, success of self-assembly is strictly guided by the size and shape-uniformity of the building blocks, and their placement in a well-defined structure with precision. Unfortunately, despite significant advancements in the field of NP synthesis, none of the synthetic protocols assure atomic precision of the nanostructures. NCs, the new class of nanomaterials, can overcome this issue. Their atomically precise composition results in high size-uniformity. Moreover, crystal structures of noble metal NCs (NMNCs) have been helpful in understanding the distribution and orientation of their surface ligands, which can provide functionalities for necessary chemical interactions. These two factors encouraged researchers to explore NCs as colloidal building blocks along with plasmonic NPs. Depending on various factors such as the nature of inter-system and intrasystem interaction, NP–NC interface, size, and composition of the two nanosystems, there are three different outcomes when NPs and NCs form colloidal assemblies:

Mild interaction allowing the components to retain their identities.

Moderate interaction leading to emerging physical properties.
Strong interaction causing chemical modification of the components.

The following sections include instances of NP–NC assemblies classified in the above three categories.

6.3.1 NP–NC assembly leading to precise hierarchical structures

Due to their ultrasmall size, it is possible to load NCs on alumina, silica particles, graphene sheets, SnO_2 nanowire networks, etc. In most of these cases, NCs retain their identities. Plasmonic NPs are inherently stabilized by surfactant molecules which can be easily replaced by suitable ligands to initiate specific chemical interactions between two similar or different nanosystems. Therefore, assembling NCs protected by suitable ligands on plasmonic NPs through chemical interactions is a straightforward method to create novel composite nanostructures.

6.3.1.1 H-bonding mediated assembly at liquid–air interface

Organization of colloidal building blocks into 2D or 3D superlattices are important in creating functional nanomaterials. One of the most versatile and experimentally simple approaches is solvent evaporation-mediated self-assembly of the NPs at liquid–air interface. As suggested by Murray's group, the basic principle involves evaporation of a high-boiling point solvent, such that the assembly process is slow enough for the systematic arrangement of NPs.[19] This approach has been successfully utilized to coassemble two different types of nanocrystals into binary nanocrystal superlattices. Assembly of NPs at liquid–air interface can be spontaneous,[20] as well as guided by a specific interaction.[21] As mentioned earlier, nonspherical nanocrystals are more attractive as the building blocks of hierarchical nanocomposites due to their ability to form directional assembly. 1D nanostructures such as Ag NWs,[22] GeNWs,[23] ZnSeNWs[24] PbS NWs,[25] carbon nanotubes,[26] etc. organize at the air–liquid surface keeping their long axis parallel to each other. Tellurium nanowires (TeNWs) dispersed in 1-butanol also organize into a similar monolayer assembly. $Ag_{44}(pMBA)_{30}$ NC (abbreviated here as Ag_{44}) can be anchored on the surface of TeNWs through the -COO^- group of pMBA ligands. When Ag_{44}-treated TeNWs, dissolved in 1-butanol, are subjected to slow evaporation of the solvent, they form a crossed bilayer assembly.[27] Surprisingly, due to the structural precision of Ag_{44} NCs, the two subsequent layers assemble with a precise 81° angle between themselves to ensure maximum H-bonding interaction (Fig. 6.3).

When another NC with the same surface ligand, that is, $Au_{102}(p\text{MBA})_{44}$ (abbreviated as Au_{102}) is used in place of Ag_{44} in the similar way, a similar TeNWs array is formed but with greater distance between the two neighboring TeNWs and a smaller (~77°) angle between the two successive layers. The greater inter-TeNW distance can be attributed to the larger diameter of Au_{102} than Ag_{44}, and the smaller interlayer angle to the difference in geometrical arrangement of *p*MBA ligands in the two NCs. These observations validate the role of sandwiched NC between two TeNWs to guide the overall assembly.

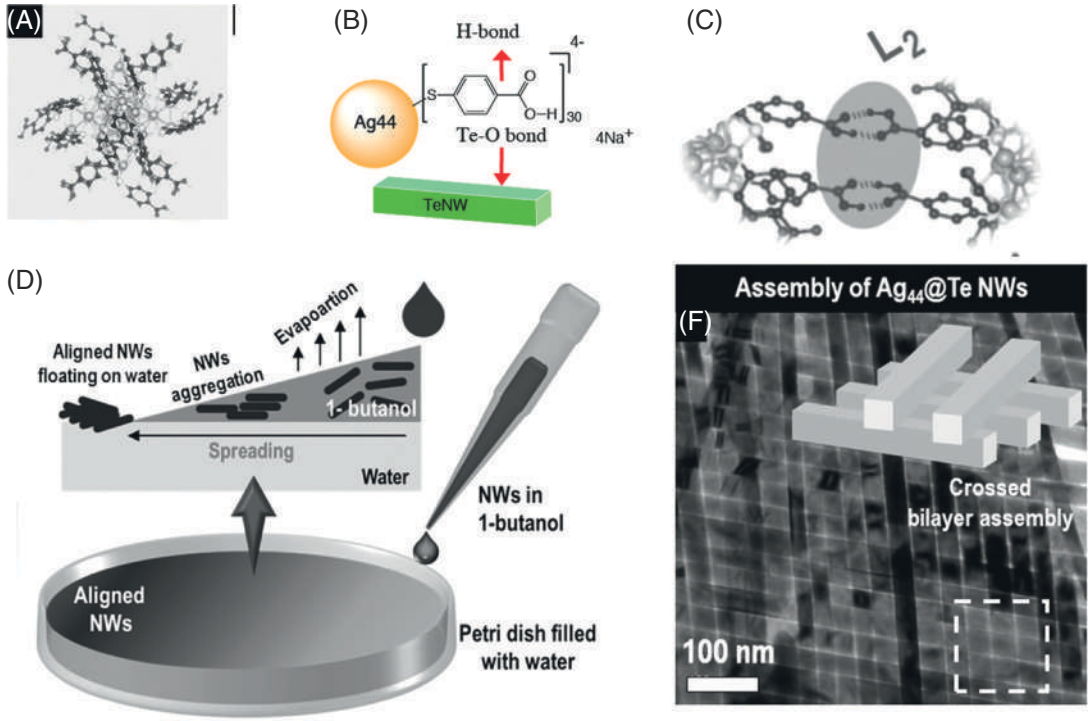

FIGURE 6.3 (A) Crystal structure of Ag_{44}, schematic illustrations of (B) Ag_{44} anchored TeNWs, (C) H-bonding between two adjacent Ag_{44}-fuctionalized TeNWs, (D) solvent evaporation-driven assembly of TeNW at the liquid–air interface, and (E) TEM image of the bilayer, Ag_{44}@TeNWs placed at 81° angle (inset shows the cartoon representation of the same). Reproduced with permission from reference 27. Copyright 2016, John Wiley and Sons.

6.3.1.2 H-bonding mediated assembly in solution

Solution phase assemblies of 1D, 2D, and 3D NPs of noble metals are extensively used to form functional hybrid nanostructures as they find applications in the field of nanomedicines and optically active metamaterials. The exceptional stability of gold NPs (AuNPs), along with facile surface modifications and easy shape control has made them the most studied systems. Gold nanorods (AuNRs), besides forming end-to-end[28] and sidewise assemblies[29] within themselves, act as an excellent templates for assembling other entities from small dye molecules[30] to quantum dots (QDs).[7a] The resulting nanocomposites often give rise to unique structures and novel physicochemical properties. Dimension of the NCs reside between that of molecules and QDs. Therefore, attempts have been made to use them as building blocks along with AuNRs in colloidal assemblies.[31] The previous section shows that pMBA-protected NCs assemble with other nanostructures via H-bonding. As-synthesized AuNRs reside in micelles formed by cetyl trimethyl ammonium bromide (CTAB) in their aqueous solution. In order to facilitate their interaction with the NCs, the surface of AuNRs is functionalized with pMBA under controlled pH. To this, pMBA-functionalized AuNRs (denoted as AuNR@pMBA), dispersed in DMF, Ag_{44} was added and mixed by inversion. TEM and STEM studies reveal

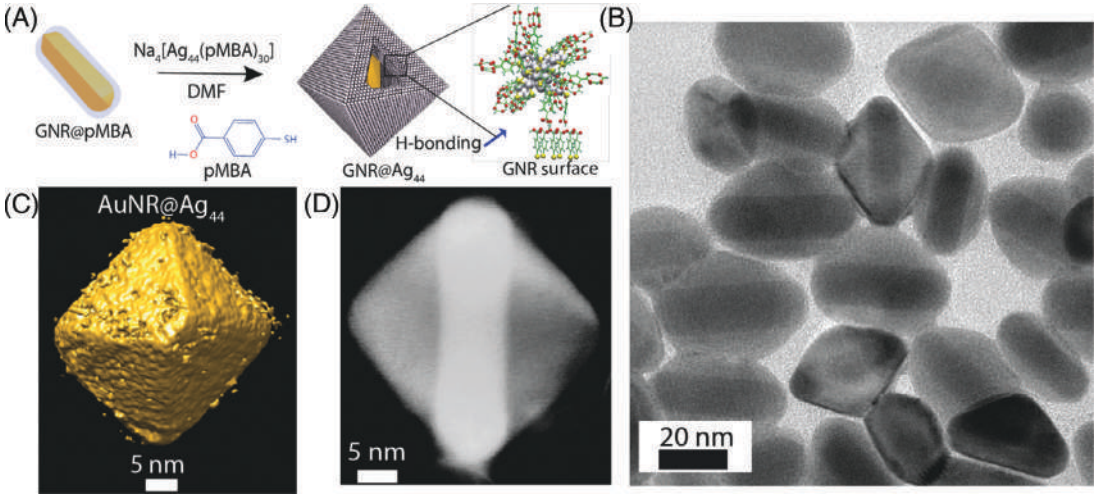

FIGURE 6.4 (A) Schematic illustration of Ag_{44} attachment on pMBA-functionalized AuNRs, (B) TEM image of the AuNT@Ag_{44} composites, (C) 3D tomographic reconstruction of AuNT@Ag_{44} showing octahedral geometry, and (D) STEM tomographic reconstruction of a single particle clearly showing underlying AuNR. Reproduced with permission from reference 31. Copyright 2018, John Wiley and Sons.

that the Ag_{44} moieties assemble in multiple layers surrounding individual AuNRs through H-bonding between their surface ligands, leading to a unique AuNR core-Ag_{44} shell structure (Fig. 6.4). Tomographic reconstructions reveal that preferential adsorption of the NCs on either (110) or (100) surface facets of AuNRs resulted in an octahedral shell, encapsulating each AuNRs. However, in case of pMBA-protected Au_{102} and Au_{250} NCs, such assembly does not produce a similar compact shell. Rather, in aqueous medium, the Au NCs assemble in a single or a few layers encapsulating AuNRs. This is because pMBA molecules of the NCs have to be partially protonated to be dispersed in water, which in turn reduces the extent of H-bonding possible among the NCs. Spontaneous encapsulation of individual AuNRs by another nanosystem with such high precision has been challenging for a long time, which was made possible due to the atomically precise size and composition of NCs and the definite arrangements of their ligands, allowing systematic assembly.

6.3.2 Assemblies leading to enhanced or emerging properties

6.3.2.1 Luminescent NCs assembled on plasmonic microstructures for sensing applications

Typically, even a very low concentration of toxic or heavy metal ions,[32] important chemicals,[33] small biomolecules such as cysteine,[34] biothiols,[35] proteins, etc., quench PL intensity of luminescent Au and Ag NCs, partially or fully, making them useful in chemical and biomolecule sensing. However, when placed at an optimum distance from a plasmonic NP, PL intensity of conventional fluorophores enhance due to plasmon-induced PL enhancement.[17] If NCs behaved in a similar way, they could attain a lower detection limit for PL-based sensing. With this motivation, Mathew et al. grew a silica shell around gold mesoflowers (MFs) and

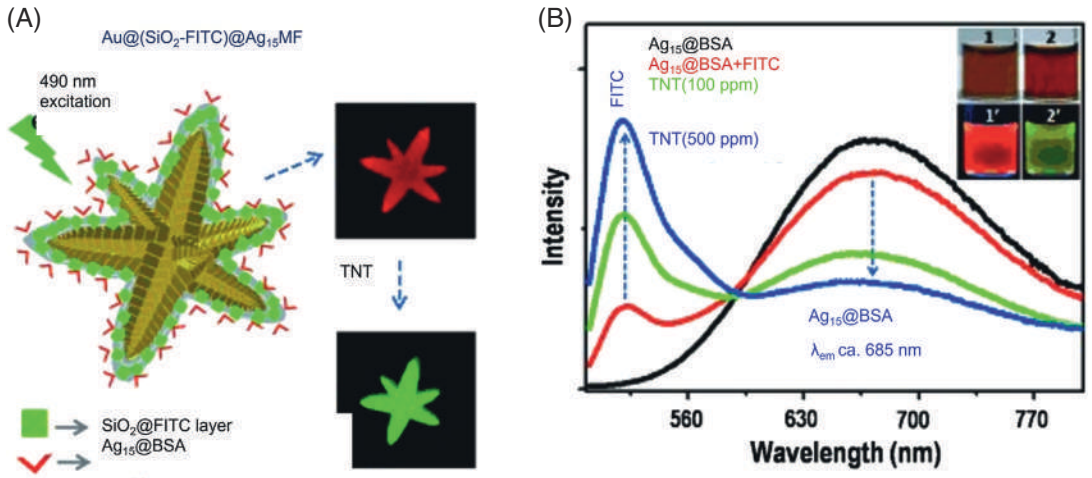

FIGURE 6.5 (A) Schematic representation of the composite: Au@SiO_2-FITC@Ag_{15} MF, Fluorescence images (ca. 490 nm excitation) taken using a dark field fluorescence microscope. Insets show the optical images corresponding to the fluorescence images; scale bars are 3 mm. Reproduced with permission from reference 36. Copyright 2012, John Wiley and Sons. This figure is also given as a color print elsewhere in the book.

anchored BSA-protected Ag_{15} NC to it.[36] Au MF is a unique anisotropic mesostructure with fivefold symmetric stem and has surface enhancing nanoscale features. These particles are several micrometres in dimension, and their shape can be identified using optical microscopes. The resulting nanocomposite was termed as Au@SiO_2@Ag_{15} MFs, whereby the bright red luminescence of the parent NC was retained. However, when exposed to 2,4,6- trinitrotoluene (TNT), PL intensity of the material was quenched due to the Meisenheimer complex formation through the chemical interaction between TNT and the free amino groups of BSA (Fig. 6.5). This quenching of luminescence associated with single particles was detected using dark-field fluorescence microscopy, which lowered the detection limit of TNT to one part per trillion (ppt), whereas that using bulk Ag_{15}-BSA NC was 10 ppm. Further, upon functionalizing the silica-coated MF with a green emissive dye, namely fluorescein isothiocyanate (FITC) prior to anchoring Ag_{15}-BSA, the visual detection was made easier. Initially, the green luminescence was suppressed by the red luminescence of the NC, but upon adding 10 ppb TNT, red luminescence due to Ag_{15}-BSA was selectively quenched and the particles showed green luminescence under a dark-field fluorescence microscope.

6.3.2.2 Assembling NCs on plasmonic NPs for bioimaging and therapeutics

Owing to their high biocompatibility and easy conjugation to drugs through AuNPs have been successfully employed for intracellular drug delivery and other therapeutic applications.[37] Ag NPs are known to generate reactive oxygen species which causes apoptosis of cells by damaging the DNA.[38] On the other hand, a large variety of NMNCs show bright photoluminescence. Their ultrafine size, large stokes shift, excellent photostability, and low environmental toxicity have provided an attractive alternative to organic dyes and many of the common QDs in biomedical applications such as fluorescence-based bioimaging, detection,

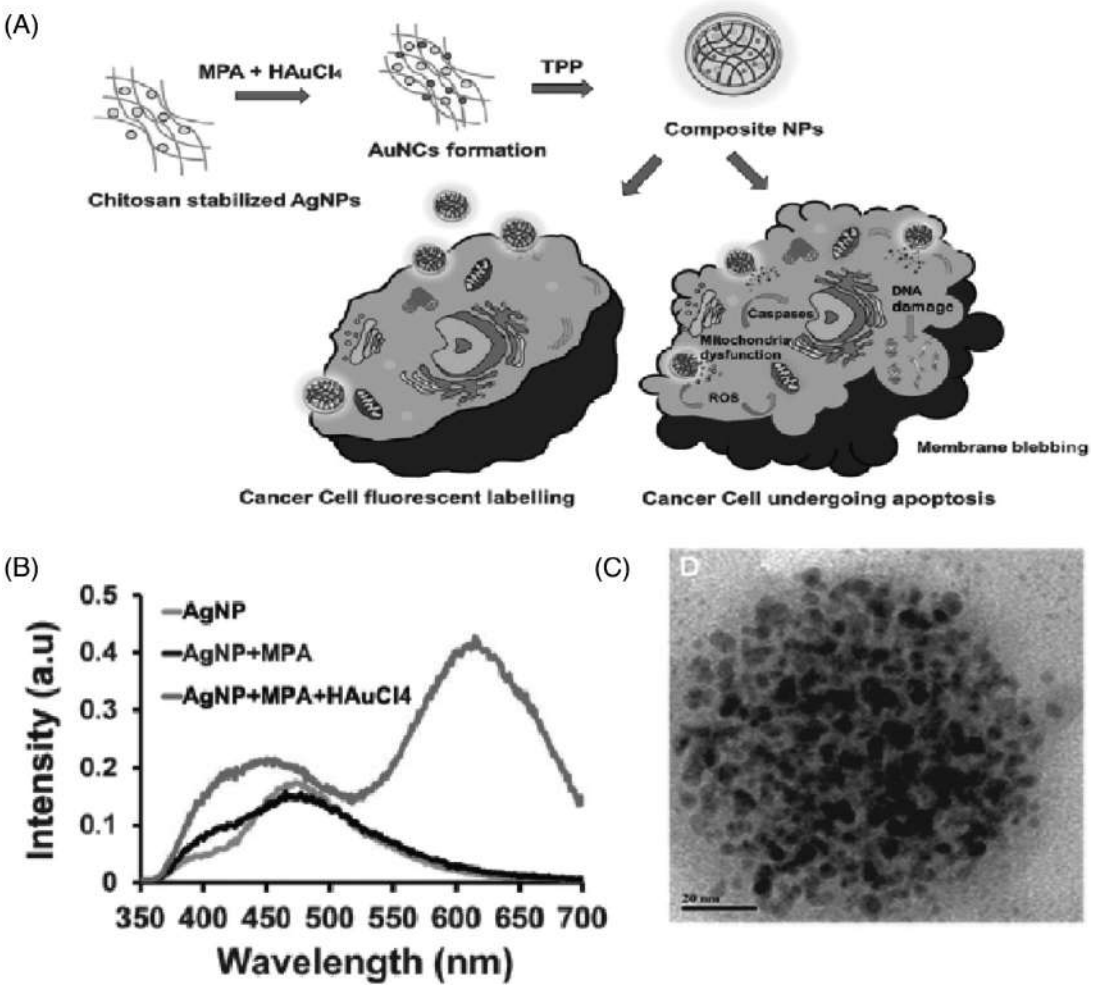

FIGURE 6.6 (A) Schematic of the synthesis and delivery of AgNP–AuNC nanocomposite for bioimaging and initiation of apoptosis in cancer cells, (B) emission spectra of the nanocomposite showing emission peak at 620 nm (upon excitation at 300 nm), and (C) TEM image of it. Reproduced with permission from reference 41. Copyright 2018, The Royal Society of Chemistry.

and therapy.[39] As the tissues show little fluorescence contrast in the NIR region, Au NCs with excitation and emission both in NIR region can serve as ideal probes for two photons in vivo imaging.[40] Therefore, efforts have been made to combine luminescent NCs and AgNPs as in vitro as well as in vivo nanoprobes in bioimaging. Using chitosan, a natural polymer as the stabilizer and template for synthesis of AgNPs, and subsequently synthesizing luminescent Au NCs by galvanic replacement reaction using $HAuCl_4$ and mercapto propionic acid as the ligand, a theranostic nanocomposite was formed (Fig. 6.6). The right size and surface charge has facilitated uptake of AgNP–AuNC nanocomposite by HeLa cells.[41] Subsequently, the red

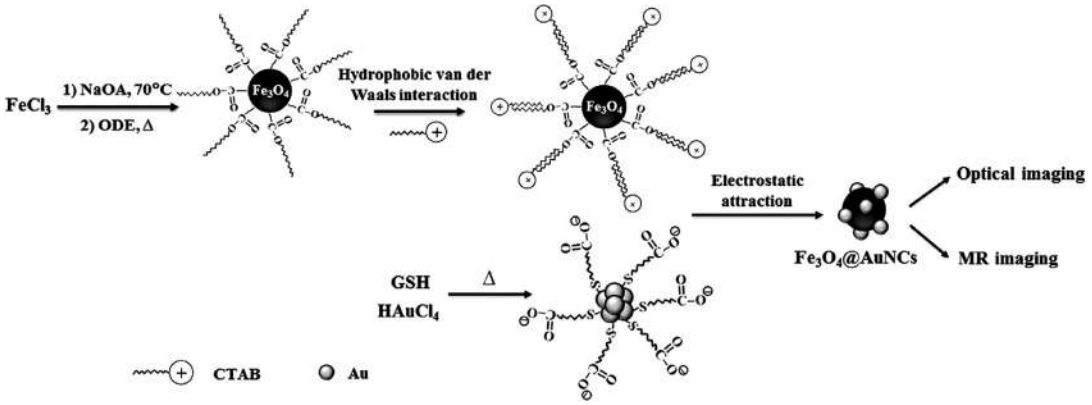

FIGURE 6.7 The synthetic procedure of Fe_3O_4@AuNCs for multimodal FI/MRI nanoprobes. Reproduced with permission from reference 44. Copyright 2015, The Royal Society of Chemistry.

luminescent Au NC allows imaging of cells, and the anti-cancer activity of AgNPs enable successful killing of cancer cells through apoptosis.

6.3.2.3 Luminescent NCs assembled on magnetic NPs for dual-mode imaging

Individual imaging technologies such as fluorescent imaging (FI), ultrasound imaging, magnetic resonance imaging (MRI), X-ray computed tomography have specific strengths and limitations. But combining two or more of them suitably serve as more efficient tools for diagnoses. For example, nano-sized iron oxide particles exhibit excellent permeability and unique superparamagnetism, showing great potential in sensors, immunoassay, bioimaging, etc. But they tend to aggregate and precipitate easily, which prevents their utility in biomedicine. However, conjugation of semiconductor QDs to magnetic NPs produces popular dual-mode MRI/FI nanoprobes.[42] Recently, it is found that fluorescent Au NCs, functionalized with reactive groups can conjugate drugs through amide or Au-S covalent bond formation for efficient drug delivery.[43] Glutathione (GSH), due to its excellent metal-chelating property, acts as one of the most popular ligands to various Au NCs. Besides, it has been effective in easy release of drugs inside cells. Hence, GSH-protected Au NCs are being used in these systems instead of QDs to avoid instability and aggregation of the composite materials. With the aim to synthesize a nanocomposite that simultaneously possesses bright red luminescence, cytocompatibility and superparamagnetic property, iron oxide NPs and glutathione-protected Au NC have been combined. For this, inherently hydrophobic Fe_3O_4 magnetic NPs are made hydrophilic by either functionalizing them with CTAB,[44] or growing a silica shell around them,[45] and then suitable luminescent Au NCs are anchored to the composite material through electrostatic attraction. The resulting nanocomposite, termed as Fe_3O_4-AuNC, shows attraction toward a magnet placed in close proximity, proving their magnetic property (Fig. 6.7). They can be redispersed in aqueous medium instantly upon removal of the magnet. In the dispersed state, they show bright red luminescence under UV excitation. With the help of MTT assay and apoptosis assay, the cytotoxicity of the composite nanoprobe was determined.

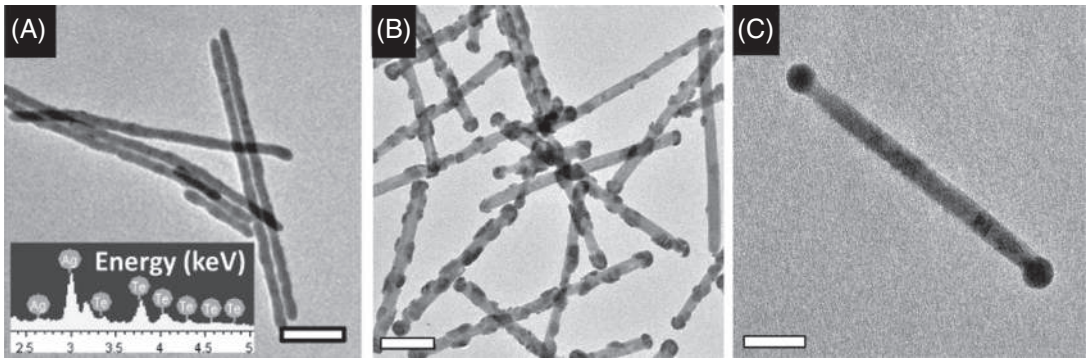

FIGURE 6.8 (A) TEM image of TeNWs treated with Ag^+, along with corresponding EDS spectrum in inset that shows the presence of Ag and Te along the NWs. (B) TEM image of NWs decorated with nodules obtained through Ag cluster reaction with Te NW. (C) TEM image of a single Ag-Te-Ag NW obtained after heating NWs shown in (B). Reproduced with permission from reference 48. Copyright 2014, American Chemical Society.

6.4 NP–NC assembly leading to chemical modifications

6.4.1 Unique reactivity of silver NC toward TeNW

Au and Ag NCs of less than 2 nm dimension, not only show molecule-like optoelectronic properties, but also exhibit profound chemical reactivity. Upon reacting with salts such as tetraoctylammonium halide and sodium halide, $[Au_{25}(SCH_2CH_2Ph)_{18}]^0$ spontaneously converts to its anionic form, $[Au_{25}(SCH_2CH_2Ph)_{18}]^-$.[46] Mercaptosuccinic acid (MSA) protected silver NC, Ag_9MSA_7, reacts with chlorocarbons at room temperature producing silver chloride and amorphous carbon. A mixture of Ag_7 and Ag_8, protected by MSA, participates in galvanic exchange reaction in presence of $HAuCl_4$, resulting in AuAg alloy NCs.[47] These observations encouraged researchers to explore chemical reactivity of NMNCs with NPs. Indeed, GSH-protected silver NC $Ag_{32}SG_{19}$ is observed to react with TeNW quite differently compared to Ag^+ ion and AgNP.[48] Both Ag and Ag NPs convert TeNWs to silver telluride nanowires, whereas $Ag_{32}SG_{19}$ coalesces on the surface of TeNWs, decorating them with silver nodules (Fig. 6.8). Similar to the mobility of Ag NCs on graphite surface observed earlier,[49] here $Ag_{32}SG_{19}$ NCs first anchored to the TeNW surface, and due to the lattice strain between silver and tellurium, they eventually start diffusing across the surface. In this process, neighboring NCs encounter themselves and coalesce to form aggregates. Further, when heated at 60°C, these Ag nodules started to move toward the tip of the TeNWs and coalesce with themselves, finally giving a Ag-tip-Te NW nanodumbbell. These studies have opened a new direction toward the chemistry between nanosystems of various kinds.

6.4.2 Atom exchange between Au NCs and Ag NPs

Understanding of chemical reactivity of Ag NCs toward other nanomaterials such as graphite, TeNW, and GNRs, was mostly limited to the coalescence or assembly of the

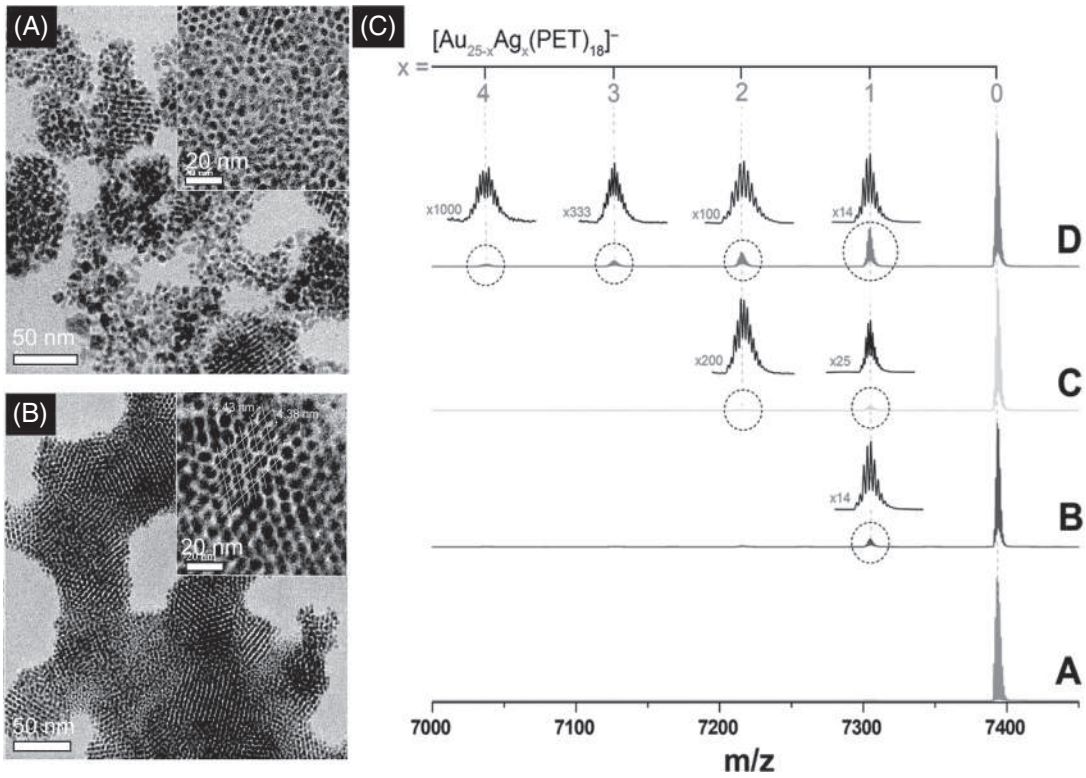

FIGURE 6.9 HRTEM micrographs of (A) 4 nm silver NPs protected by 2-PET, and (B) spontaneously assembled NPs after the parent NPs reacted with the $Au_{25}(PET)_{18}$ NC. (C) Size-dependent reactivity monitored using ESI MS: Spectra monitored after 2 min of reaction with (B) 8 nm, (C) 4 nm, and (D) 3 nm particles, and the extent of exchange was compared with the spectrum of the parent (A) $Au_{25}(PET)_{18}$ NC. Reproduced with permission from reference 51. Copyright 2020, The Royal Society of Chemistry.

NCs on their surfaces for a long time. In 2016, a remarkable study showed that thiol-protected Au and Ag NCs, namely, $Au_{25}(PET)_{18}$ and $Ag_{44}(FTP)_{30}$ (where PET and FTP refer to 2-phenylethanethiol and 4-fluorothiophenol, respectively) rapidly exchanged metal atoms as well as metal-thiolate fragments in the solution phase.[50] Subsequently, many other inter-NC reactions were studied, which gave valuable insights into the chemical properties of the NC family (these are discussed in detail in Chapter 2). The study was then extended to reacting NCs with plasmonic NPs, which belong to a different size regime on the nanoscale. Surprisingly, ultrasmall, thiol-protected Ag NPs too, took part in similar atom-exchange reactions with PET-protected Au_{25} NCs.[51] Under ambient conditions, the NC reacted with polydisperse Ag-PET NPs (of average diameter 4 nm) and an alloy cluster of formula $Au_{25-x}Ag_x(PET)_n$ was formed as a transient intermediate (Fig. 6.9). Subsequent metal and ligand exchange between the two reactant nanosystems caused digestive ripening of the polydisperse Ag NPs, finally producing alloy NPs of uniform dimension. Such a reaction is highly dependent on the nature of the ligand protecting the NC and the NP. Reactivity of Ag NPs toward the same NC is found to decrease significantly with increase in size of the plasmonic NP. In the case of Ag NPs of

8 nm core-size, the value of x of the intermediate, $Au_{25-x}Ag_x(PET)_n$ was limited to 1, whereas in the case of 4 nm Ag NPs, it could be up to 4.

6.5 Summary and future perspective

Chemical interaction between NCs and plasmonic NPs are of two categories:

Weak interactions assembling the NCs with NPs result in a composite nanostructure, wherein identities of both constituents are preserved. Such assemblies form spontaneously, either in solution or in liquid–air interface, and yet lead to hybrid nanostructures of precise morphology. This strategy can be used to combine unique optoelectronic properties of both, the NC and the NP, producing a nanoprobe of more complex structure and improved functionalities.

a. Strong chemical interactions that modify chemical composition of the nanoscale constituents. This often leads to exchange of metal atoms between the NCs and the NPs, which serve as an alternative strategy of controlled doping of foreign metals into the monometallic parent structure.

Assembly of colloidal NPs into complex nanostructures can bridge the nanoscopic and microscopic worlds and thereby meet many technological needs as described above. Combining different nanosystems in single structures show synergistically improved optoelectronic properties. The studies discussed in this chapter expand the chemistry of NMNCs and prove their efficiency as building blocks of heterogeneous nanocomposites. However, a library of noble metal NPs are now known and many of them can be combined to form plasmonic nanosystems of diverse size, shape, and composition to achieve unprecedented optoelectronic properties. For example,

a. Using the surface chemistry of respective ligands, luminescent NCs can be combined to NPs of the same composition, but diverse shape. Thus, effect of shape anisotropy on plasmon-enhanced luminescence of NCs can give interesting insights that might help to design advanced nanoprobes for fluorescence-based applications.

b. Alloy NPs show modified electronic properties than their monometallic counterparts. Additionally, anisotropic alloy NPs are fascinating in terms of tip-specific enhancement in properties. However, bottom-up synthesis of such particles is limited by poor size and shape uniformity. Since atom exchange takes place between NC and spherical NPs in solution, the former can act as the source of foreign metal atoms to create alloy NPs of nonspherical geometry.

Thus, chemistry between NCs and NPs holds great promise in designing new hybrid nanomaterials that are difficult to achieve otherwise.

List of abbreviation

AgNP	silver nanoparticle
AuNP	gold nanoparticle
AuNR	gold nanorod
CTAB	cetyl trimethyl ammonium bromide

DNA	deoxyribonucleic acid
FI	fluorescent imaging
FITC	fluorescein isothiocyanate
FTP	4-fluorothiophenol
LSC	linearized semiclassical
LSPR	localised surface plasmon resonance
LUMO	lowest unoccupied molecular orbital
MRI	magnetic resonance imaging
MSA	mercaptosuccinic acid
NC	nanocluster
NMNC	noble metal nanocluster
NP	nanoparticle
PET	phenylethanethiol
PET	2-phenylethanethiol
PL	photoluminescence
pMBA	para-mercapto benzoic acid
QD	quantum dot
SERS	surface enhanced Raman scattering
TNT	2,4,6- trinitrotoluene
GSH	glutathione
TeNW	tellurium nanowire
UI	ultrasound imaging

References

1. (a) Kamat PV. Photophysical, photochemical and photocatalytic aspects of metal nanoparticles. *J Phys Chem B*. 2002;106:7729–7744; (b) Roduner E. Size matters: why nanomaterials are different. *Chem Soc Rev*. 2006;35:583–592; (c) Bowker M. A prospective: surface science and catalysis at the nanoscale. *Surf Sci*. 2009;603:2359–2362; (d) Talapin DV, Lee J-S, Kovalenko MV, Shevchenko EV. Prospects of colloidal nanocrystals for electronic and optoelectronic applications. *Chem Rev*. 2010;110:389–458; (e) He X, Song X, Qiao W, et al. Phase- and size-dependent optical and magnetic properties of CoO nanoparticles. *J Phys Chem C*. 2015;119:9550–9559.
2. (a) Lu X, Rycenga M, Skrabalak SE, Wiley B, Xia Y. Chemical synthesis of novel plasmonic nanoparticles. *Annu Rev Phys Chem*. 2009;60:167–192; (b) Grzelczak M, Pérez-Juste J, Mulvaney P, Liz-Marzán LM. Shape control in gold nanoparticle synthesis. *Chem Soc Rev*. 2008;37:1783–1791; (c) Bhol P, Bhavya MB, Swain S, Saxena M, Samal AK. Modern chemical routes for the controlled synthesis of anisotropic bimetallic nanostructures and their application in catalysis. *Front Chem*. 2020;8:357.
3. (a) Rosi NL, Mirkin CA. Nanostructures in biodiagnostics. *Chem Rev*. 2005;105:1547–1562; (b) Stewart ME, Anderton CR, Thompson LB, et al. Nanostructured plasmonic sensors. *Chem Rev*. 2008;108:494–521.
4. (a) Atwater HA, Polman A. Plasmonics for improved photovoltaic devices. *Nat Mater*. 2010;9:205–213; (b) Ferry VE, Munday JN, Atwater HA. Design considerations for plasmonic photovoltaics. *Adv Mater*. 2010;22:4794–4808.
5. (a) Lal S, Link S, Halas NJ. Nano-optics from sensing to waveguiding. *Nat Photonics*. 2007;1:641–648; (b) Maier SA, Brongersma ML, Kik PG, Meltzer S, Requicha AAG, Atwater HA. Plasmonics—a route to nanoscale optical devices. *Adv Mater*. 2001;13:1501–1505.
6. Grzelczak M, Vermant J, Furst EM, Liz-Marzán LM. Directed self-assembly of nanoparticles. *ACS Nano*. 2010;4:3591–3605.
7. (a) Nepal D, Drummy LF, Biswas S, Park K, Vaia RA. Large scale solution assembly of quantum dot–gold nanorod architectures with plasmon enhanced fluorescence. *ACS Nano*. 2013;7:9064–9074; (b) Trotsiuk L, Muravitskaya A, Kulakovich O, et al. Plasmon-enhanced fluorescence in gold nanorod-quantum dot coupled systems. *Nanotechnology*. 2019;31; (c) Lu G, Yang Z, Zheng K, et al. Metal-enhanced fluorescence of interlaminar composite film with self-assembled quantum Dots/Au@SiO2 microarchitecture. *Org Electron*. 2020;77.
8. (a) Locatelli E, Ori G, Fournelle M, Lemor R, Montorsi M, Comes Franchini M. Click chemistry for the assembly of gold nanorods and silver nanoparticles. *Chem - Eur J*. 2011;17:9052–9056; (b) Muhammed MAH, Döblinger M,

Rodríguez-Fernández J. Switching plasmons: gold nanorod–copper chalcogenide core–shell nanoparticle clusters with selectable metal/semiconductor NIR plasmon resonances. *J Am Chem Soc*. 2015;137:11666–11677.
9. (a) Kelly KL, Coronado E, Zhao LL, Schatz GC. The optical properties of metal nanoparticles: the influence of size, shape, and dielectric environment. *J Phys Chem B*. 2003;107:668–677; (b) Alba-Molina D, Giner-Casares JJ, Cano M. Bioconjugated plasmonic nanoparticles for enhanced skin penetration. *Top Curr Chem*. 2019;378:8.
10. Glotzer SC, Solomon MJ. Anisotropy of building blocks and their assembly into complex structures. *Nat Mater*. 2007;6:557–562.
11. Ogarev VA, Rudoi VM, Dement'eva OV. Gold nanoparticles: synthesis, optical properties, and application. *Inorg Mater Appl Res*. 2018;9:134–140.
12. (a) Dieringer JA, McFarland AD, Shah NC, et al. Surface enhanced Raman spectroscopy: new materials, concepts, characterization tools, and applications. *Faraday Discuss*. 2006;132:9–26; (b) Nalbant Esenturk E, Hight Walker AR. Surface-enhanced Raman scattering spectroscopy via gold nanostars. *J Raman Spectrosc*. 2009;40:86–91.
13. (a) Camacho SA, Aoki PHB, Albella P, Oliveira ON, Constantino CJL, Aroca RF. Increasing the enhancement factor in plasmon-enhanced fluorescence with shell-isolated nanoparticles. *J Phys Chem C*. 2016;120:20530–20535; (b) Sultangaziyev A, Bukasov R. Review: applications of surface-enhanced fluorescence (SEF) spectroscopy in bio-detection and biosensing. *Sens Biosens Res*. 2020;30.
14. Neubrech F, Huck C, Weber K, Pucci A, Giessen H. Surface-enhanced infrared spectroscopy using resonant nanoantennas. *Chem Rev*. 2017;117:5110–5145.
15. (a) Tan SF, Anand U, Mirsaidov U. Interactions and attachment pathways between functionalized gold nanorods. *ACS Nano*. 2017;11:1633–1640; (b) Nie Z, Fava D, Rubinstein M, Kumacheva E. Supramolecular" assembly of gold nanorods end-terminated with polymer "pom-poms": effect of pom-pom structure on the association modes. *J Am Chem Soc*. 2008;130:3683–3689; (c) Lukach A, Liu K, Therien-Aubin H, Kumacheva E. Controlling the degree of polymerization, bond lengths, and bond angles of plasmonic polymers. *J Am Chem Soc*. 2012;134:18853–18859; (d) Shibu Joseph ST, Ipe BI, Pramod P, Thomas KG. Gold nanorods to nanochains: mechanistic investigations on their longitudinal assembly using α,ω-alkanedithiols and interplasmon coupling. *J Phys Chem B*. 2006;110:150–157; (e) Lin H, Lee S, Sun L, et al. Clathrate colloidal crystals. *Science*. 2017;355:931.
16. Wang K, Jin S-M, Xu J, et al. Electric-field-assisted assembly of polymer-tethered gold nanorods in cylindrical nanopores. *ACS Nano*. 2016;10:4954–4960.
17. Mezour MA, Perepichka II, Zhu J, Lennox RB, Perepichka DF. Directing the assembly of gold nanoparticles with two-dimensional molecular networks. *ACS Nano*. 2014;8:2214–2222.
18. Nam J-M, Oh J-W, Lee H, Suh YD. Plasmonic nanogap-enhanced raman scattering with nanoparticles. *Acc Chem Res*. 2016;49:2746–2755.
19. Dong A, Chen J, Vora PM, Kikkawa JM, Murray CB. Binary nanocrystal superlattice membranes self-assembled at the liquid–air interface. *Nature*. 2010;466:474–477.
20. Sánchez-Iglesias A, Grzelczak M, Pérez-Juste J, Liz-Marzán LM. Binary self-assembly of gold nanowires with nanospheres and nanorods. *Angew Chem Int Ed*. 2010;49:9985–9989.
21. Kim JY, Kwon SJ, Chang J-B, Ross CA, Hatton TA, Stellacci F. Two-dimensional nanoparticle supracrystals: a model system for two-dimensional melting. *Nano Lett*. 2016;16:1352–1358.
22. Tao A, Kim F, Hess C, et al. Langmuir−Blodgett silver nanowire monolayers for molecular sensing using surface-enhanced raman spectroscopy. *Nano Lett*. 2003;3:1229–1233.
23. Wang D, Chang Y-L, Liu Z, Dai H. Oxidation resistant germanium nanowires: bulk synthesis, long chain alkanethiol functionalization, and langmuir−blodgett assembly. *J Am Chem Soc*. 2005;127:11871–11875.
24. Acharya S, Panda AB, Belman N, Efrima S, Golan Y. A Semiconductor-nanowire assembly of ultrahigh junction density by the Langmuir–Blodgett technique. *Adv Mater*. 2006;18:210–213.
25. Patla I, Acharya S, Zeiri L, Israelachvili J, Efrima S, Golan Y. Synthesis, two-dimensional assembly, and surface pressure-induced coalescence of ultranarrow PbS nanowires. *Nano Lett*. 2007;7:1459–1462.
26. Li X, Zhang L, Wang X, et al. Langmuir−Blodgett assembly of densely aligned single-walled carbon nanotubes from bulk materials. *J Am Chem Soc*. 2007;129:4890–4891.
27. Som A, Chakraborty I, Maark TA, Bhat S, Pradeep T. Cluster-mediated crossed bilayer precision assemblies of 1D nanowires. *Adv Mater*. 2016;28:2827–2833.
28. Abtahi SMH, Burrows ND, Idesis FA, Murphy CJ, Saleh NB, Vikesland PJ. Sulfate-mediated end-to-end assembly of gold nanorods. *Langmuir*. 2017;33:1486–1495.

29. Kumar J, Thomas R, Swathi RS, Thomas KG. Au nanorod quartets and Raman signal enhancement: towards the design of plasmonic platforms. *Nanoscale*. 2014;6:10454–10459.
30. (a) Zhao L, Ming T, Chen H, Liang Y, Wang J. Plasmon-induced modulation of the emission spectra of the fluorescent molecules near gold nanorods. *Nanoscale*. 2011;3:3849–3859; (b) Abadeer NS, Brennan MR, Wilson WL, Murphy CJ. Distance and plasmon wavelength dependent fluorescence of molecules bound to silica-coated gold nanorods. *ACS Nano*. 2014;8:8392–8406.
31. Chakraborty A, Fernandez AC, Som A, et al. Atomically precise nanocluster assemblies encapsulating plasmonic gold nanorods. *Angew Chem Int Ed*. 2018;57:6522–6526.
32. (a) Chakraborty I, Udayabhaskararao T, Pradeep T. Luminescent sub-nanometer clusters for metal ion sensing: A new direction in nanosensors. *J Hazard Mater*. 2012;211-212:396–403; (b) Liu H, Zhang X, Wu X, Jiang L, Burda C, Zhu J-J. Rapid sonochemical synthesis of highly luminescent non-toxic AuNCs and Au@AgNCs and Cu (ii) sensing. *Chem Commun*. 2011;47:4237–4239.
33. (a) Shiang Y-C, Huang C-C, Chang H-T. Gold nanodot-based luminescent sensor for the detection of hydrogen peroxide and glucose. *Chem Commun*. 2009:3437–3439; (b) Jin L, Shang L, Guo S, et al. Biomolecule-stabilized Au nanoclusters as a fluorescence probe for sensitive detection of glucose. *Biosens Bioelectron*. 2011;26:1965–1969.
34. Shang L, Dong S. Sensitive detection of cysteine based on fluorescent silver clusters. *Biosens Bioelectron*. 2009;24:1569–1573.
35. Han B, Wang E. Oligonucleotide-stabilized fluorescent silver nanoclusters for sensitive detection of biothiols in biological fluids. *Biosens Bioelectron*. 2011;26:2585–2589.
36. Mathew A, Sajanlal PR, Pradeep T. Selective visual detection of TNT at the sub-zeptomole level. *Angew Chem Int Ed*. 2012;51:9596–9600.
37. Yang W, Liang H, Ma S, Wang D, Huang J. Gold nanoparticle based photothermal therapy: development and application for effective cancer treatment. *Sustain Mater Technol*. 2019;22:e00109.
38. (a) Lee Y-H, Cheng F-Y, Chiu H-W, et al. Cytotoxicity, oxidative stress, apoptosis and the autophagic effects of silver nanoparticles in mouse embryonic fibroblasts. *Biomaterials*. 2014;35:4706–4715; (b) Hsin Y-H, Chen C-F, Huang S, Shih T-S, Lai P-S, Chueh PJ. The apoptotic effect of nanosilver is mediated by a ROS- and JNK-dependent mechanism involving the mitochondrial pathway in NIH_3T_3 cells. *Toxicol Lett*. 2008;179:130–139.
39. (a) Su Y, Xue T, Liu Y, Qi J, Jin R, Lin Z. Luminescent metal nanoclusters for biomedical applications. *Nano Res*. 2019;12:1251–1265; (b) Xiao Y, Wu Z, Yao Q, Xie J. Luminescent metal nanoclusters: Biosensing strategies and bioimaging applications. *Aggregate*. 2021;2:114–132.
40. Kaur N, Aditya RN, Singh A, Kuo T-R. Biomedical applications for gold nanoclusters: recent developments and future perspectives. *Nanoscale Res Lett*. 2018;13:302.
41. Dutta D, Sahoo AK, Chattopadhyay A, Ghosh SS. Bimetallic silver nanoparticle–gold nanocluster embedded composite nanoparticles for cancer theranostics. *J Mater Chem B*. 2016;4:793–800.
42. Park J-H, von Maltzahn G, Ruoslahti E, Bhatia SN, Sailor MJ. Micellar hybrid nanoparticles for simultaneous magnetofluorescent imaging and drug delivery. *Angew Chem Int Ed*. 2008;47:7284–7288.
43. (a) Zhang Y, Wu M, Dai W, et al. High drug-loading gold nanoclusters for responsive glucose control in type 1 diabetes. *J Nanobiotechnol*. 2019;17:74; (b) Li Q, Pan Y, Chen T, et al. Design and mechanistic study of a novel gold nanocluster-based drug delivery system. *Nanoscale*. 2018;10:10166–10172.
44. Wang C, Yao Y, Song Q. Gold nanoclusters decorated with magnetic iron oxide nanoparticles for potential multimodal optical/magnetic resonance imaging. *J Mater Chem C*. 2015;3:5910–5917.
45. Binaymotlagh R, Hajareh Haghighi F, Aboutalebi F, Mirahmadi-Zare SZ, Hadadzadeh H, Nasr-Esfahani M-H. Selective chemotherapy and imaging of colorectal and breast cancer cells by a modified MUC-1 aptamer conjugated to a poly(ethylene glycol)-dimethacrylate coated Fe_3O_4–AuNCs nanocomposite. *New J Chem*. 2019;43:238–248.
46. Zhu M, Chan G, Qian H, Jin R. Unexpected reactivity of $Au_{25}(SCH_2CH_2Ph)18$ nanoclusters with salts. *Nanoscale*. 2011;3:1703–1707.
47. Udayabhaskararao T, Sun Y, Goswami N, Pal SK, Balasubramanian K, Pradeep T. Ag_7Au_6: A 13-atom alloy quantum cluster. *Angew Chem Int Ed*. 2012;51:2155–2159.
48. Som A, Samal AK, Udayabhaskararao T, Bootharaju MS, Pradeep T. Manifestation of the difference in reactivity of silver clusters in contrast to its ions and nanoparticles: the growth of metal tipped Te nanowires. *Chem Mater*. 2014;26:3049–3056.
49. Goldby IM, Kuipers L, Issendorff Bv, Palmer RE. Diffusion and aggregation of size-selected silver clusters on a graphite surface. *Appl Phys Lett*. 1996;69:2819–2821.

50. Krishnadas KR, Ghosh A, Baksi A, Chakraborty I, Natarajan G, Pradeep T. Intercluster reactions between $Au_{25}(SR)_{18}$ and $Ag_{44}(SR)_{30}$. *J Am Chem Soc*. 2016;138:140–148.
51. Bose P, Chakraborty P, Mohanty JS, et al. Atom transfer between precision nanoclusters and polydispersed nanoparticles: a facile route for monodisperse alloy nanoparticles and their superstructures. *Nanoscale*. 2020;12:22116–22128.

CHAPTER

7

Cluster-based metal–organic frameworks

Wakeel Ahmed Dar[a] *and Thalappil Pradeep*[b]

[b]Department of Science and Technology (DST) Unit of Nanoscience and Thematic Unit of Excellence, Department of Chemistry, Indian Institute of Technology (IIT) Madras, Chennai, India [b]Deepak Parekh Institute Chair Professor and Professor of Chemistry, Department of Chemistry, Indian Institute of Technology Madras, Chennai, India

7.1 Introduction

Research interest in metal nanoparticles has grown tremendously in recent years due to their importance in basic science and their potential applications in catalysis, biological imaging, optics, chemical sensing, nanomedicine, etc.[1–3] Among the nanomaterials, nanoclusters (NCs) are a recent addition to the exotic class of materials. NCs are composed of just a few to tens of metal atoms with a definite ligand shell, forming molecules of discrete composition and having sizes similar to the Fermi wavelength of electrons.[1–3] Silver metal NCs stabilized by different thiols and co-protected by ancillary ligands have been widely studied.[4–7] The properties of NCs can be controlled by ligands (mostly thiols) that can alter their structural and electronic properties. Because of their unique dimensions (<3 nm), NCs behave as molecules and serve as a bridge between atoms and nanoparticles.[1] Molecular behavior of NCs is inherent because of their precise composition and structure leading to discrete energy levels, interparticle reactions, etc.[1,2] In determining the structure, stability of NCs plays an important role. Many NCs have been crystallized[4–18] and they exhibit fascinating structures. Most of the silver NCs exhibit limited stability as they are prone to decomposition at room temperatures which restrict their use for a wide range of applications.[19,20]

Various methods have been developed to create novel materials with the desirable features of NCs. For example, substrate anchoring of NCs,[21,22] host–guest interactions[23], etc. were used to synthesize one-dimensional (1D) alignment of NCs. 2D and 3D NC arrays have been created using Langmuir-Blodgett and adsorption techniques.[24] However, these approaches have limitations since the NCs are not placed in a regular pattern and their assembly requires a wide area, both of which have a direct impact on their properties. NCs were crystallized to

DOI: https://doi.org/10.1016/B978-0-323-90879-5.00005-6

address this problem, and a regular pattern of metal NCs was observed during crystallization. 1D, 2D, and 3D structural arrays of NCs have been created using this approach. Strong bonds have been found in these structures involving metal–metal or metal–non-metal interactions, such as Au–Au, Au–Ag, Ag–O, Ag–Cl, Ag–N, etc. To create next-generation materials with the astonishing properties of NCs, methods for assembling metal NCs to a size that makes them simple to handle must be developed. Similar to regular metal–organic frameworks (MOFs), NCs were transformed into MOFs utilizing suitable organic linkers. There have been many efforts to design and synthesize novel functional porous materials.[25–34] The study on MOFs or coordination polymers has grown at an unprecedented rate in recent decades, and it is unquestionably one of the most intriguing research fields in material and coordination chemistry. The coordination polymers were first reported in 1950s[35] and early 1960s,[36–40] but Robson and co-workers,[41,42] followed by Kitagawa et al.,[43,44] Yagi and coworkers,[45] and Ferey et al.[46] rediscovered it and lead the field to the advanced level. In 2017, Zang et al.[47] reported the first silver NC-based MOF in which NC units were interconnected using a bidentate organic linker such as bpy. MOFs enriched with NC nodes lead to a substantial increase in their stability as compared to the pristine cluster. Successful integration of NCs and organic linkers have been demonstrated in MOFs recently.[47] Because of the integration of properties from both organic and inorganic (NC) components into a single material, such MOFs have received a lot of interest. The study of MOFs is still in its early stage and many MOFs have been reported recently using different organic linkers such as bpy, pyz, bpyNH_2, bpe, bpa, *o-*, *m-*, *and p*-pch, tppa, tpp, bpb, cppp, tppe[47–59] (a list of these acronyms are included at the end of this Chapter). As a result, not only the geometrical structure of metal NCs, but also the geometrical structure of NC-based MOFs, can now be controlled.

This chapter will focus on the synthesis, structure, properties, and applications of the recently reported silver cluster-based MOFs. These are associated with metal-rich cluster nodes interconnected with each other *via o*rganic linkers. MOFs have gained importance due to their stability, porous nature, and more efficient luminescence compared to the pristine silver NCs.

7.2 Synthesis approaches for silver metal-based MOFs

NC-based MOFs can be understood by simply deconstructing them into their constituent metal-rich NC nodes and corresponding organic linkers. Appropriate chemical equivalents are combined. A primary need for designing MOFs is adequate knowledge of NCs and organic ligands that act as connectors such as N-donor ligands (bpy, pyz, bpyNH_2, bpe, bpa, *o-*, *m-*, and *p*-pch, tppa, tpp, bpb, bpy, cppp, tppe). These organic connectors provide firm support in connecting the NCs, incorporating rigidity and ideally resulting in large porous materials. Structural design of MOFs can be obtained using simple approaches such as (1) the ligand-exchange approach, and (2) the one-pot approach.

1. **Ligand-exchange approach:** In this reaction methodology, MOFs were prepared by the reaction between already synthesized NCs and organic linker(s). For example, for the synthesis of $[Ag_{12}(TBT)_8(TFA)_4(bpy)_4]$ denoted as Ag_{12}bpy MOF, initially Ag_{12} NC ($[(Ag_{12}(TBT)_6(TFA)_6(CH_3CN)_6]\cdot CH_3CN$) was synthesized using a standard procedure. The

TABLE 7.1 List of nanocluster-based MOFs, including cluster nodes and organic linkers reported.

	Nanocluster node	Organic linker	Code	References
1D	$[Ag_{14}(C_2B_{10}H_{10}S_2)_6]$	pyz	Ag_{14}pyz	48
	$[Ag_{18}(PhPO_3)(TBT)_{10}(TFA)_2(PhPO_3H)_4]$	3-bpyNH$_2$	Ag_{18}bpyNH$_2$	49
	$[Ag_{15}Cl(TBT)_8(TFA)_{5.67}(NO_3)_{0.33}(DMF)_2]$	bpy	Ag_{15}bpy	50
	$[Ag_{10}(TFA)_4(TBT)_6(CH_3CN)]$	*p*-pch	Ag_{10}pch-*p*	51
	$[Ag_{10}(TFA)_4(TBT)_6(CH_3CN)_2]$	*o*-pch	Ag_{10}pch-*o*	51
	$[Cd_6Ag_4(SPh)_{16}(DMF)_3(CH_3OH)]$	bpe	Cd_6Ag_4bpe	52
2D	$[Ag_{12}(TBT)_6(TFA)_6]$	bpy	Ag_{12}bpy	53
	$[Ag_{14}(C_2B_{10}H_{10}S_2)_6]$	dpd	Ag_{14}dpd	48
	$[Ag_{12}(TBT)_6(TFA)_6]$	tppa	Ag_{12}tppa	54
	$[Ag_{12}(TBT)_6(TFA)_3]$	tpp	Ag_{12}tpp	55
	$[Ag_{14}Cl(TBT)_8(TFA)_5(DMF)]$	bpy	Ag_{14}bpy	50
	$[Ag_{10}(TFA)_4(TBT)_6(CH_3CN)_4]$	*m*-pch	Ag_{10}pch-*m*	51
	$[Ag_{12}(TBT)_6(TFA)_6(CH_3CN)_6]$	bpzNH$_2$	Ag_{12}bpzNH$_2$	56
3D	$[Ag_{12}(TBT)_8(TFA)_4]$	bpy	Ag_{12}bpy	47
	$[Ag_{14}(C_2B_{10}H_{10}S_2)_6]$	bpb	Ag_{14}bpb	48
	$[Ag_{14}(C_2B_{10}H_{10}S_2)_6]$	bpy	Ag_{14}bpy-dc	48
	$[Ag_{10}(TBT)_6(TFA)_2(PhPO_3H)_2]$	bpy	Ag_{10}bpy	57
	$[Ag_{12}(TBT)_6(TFA)_6]$	cppp	Ag_{12}cpp	58
	$[Ag_{12}(TBT)_6(TFA)_6][Ag_8(TBT)_4(TFA)_4]$	tppe	$Ag_{12}Ag_8$tppe	59
	$[Ag_{12}(TBT)_8(TFA)_4]$	bpyNH$_2$	Ag_{12}bpyNH$_2$	72

Ag_{12} NC and bpy were then added to a solution of acetonitrile and ethanol, resulting in the formation of Ag_{12}bpy MOF.[47]

2. **One-pot approach:** In this case, MOFs were synthesized in a single-step reaction. For example, Ag_{12}bpy MOF was synthesized by adding Ag(TBT)$_n$, TFA, and bpy to a solution of acetonitrile and ethanol.[47] Similarly, Ag_{12}bpa,[60] Ag_{12}bpe,[60] Ag_{10}bpy,[57] Ag_{14}bpy,[50] and Ag_{15}bpy[50] (as listed in Table 7.1) MOFs were synthesized using one-pot approach.

7.3 Structural features

The structure of atomically precise NCs determines their properties and applications. We recently discovered that structure-property control is not just restricted to NCs, but also to 1D,

2D, and 3D MOF structures. The development of new methods will result in the formation of novel materials for many applications such as oxygen sensing, solvent recognition, etc. Coordinated 1D, 2D, and 3D metal NC structures have been widely explored[61] and are discussed below.

7.3.1 One-dimensional coordinated structures

1D coordinated structures of atomically precise NCs were obtained through different types of interactions such as (1) direct metal–metal bonding, (2) metal–oxygen (Ag–O) bonding, (3) regulation of counter ions, or (4) incorporation of organic linkers.

(i) Direct metal–metal bonding

In this case, 1D coordinated structures of NCs are formed through direct metal–metal bonds. For example, unusual behavior was observed in $[Au_{25}(SBu)_{18}]$ NC in solution as it exists as a monomer and is paramagnetic. However, in the solid-state, a polymeric chain of $[Au_{25}(SBu)_{18}]_n$ was obtained in which Au–Au bonds are formed between adjacent NC units, as visualized from the single-crystal X-ray diffraction and is antiferromagnetic. This type of polymeric behavior in the solid-state leads to the formation of molecular gold nanowires.[62] Similarly, direct metal–metal bonding was also observed in $Au_{25}(S\text{-}nC_5H_{11})_{18}$,[63] $Au_{24}Hg(SBu)_{18}$, and $Au_{24}Cd(SBu)_{18}$.[64] In alloy cluster such as $(AuAg)_{34}(adm)_{20}$, heterometallic Ag–Au–Ag bonding was observed between adjacent NCs.[65]

(ii) Metal–oxygen bonding

In this type, metal atoms of NCs are coordinated through oxygen atoms of the counter ion. For example, in $[Ag_{20}(TBT)_{10}(TFA)_8(DMF)_2(CO_3)]$ cluster, CO_3^{2-} anion acts as a template for the formation of Ag–O–Ag bonding between the adjacent clusters, which results in the formation of 1D coordinated structures.[66] Similar type of M–O–M bonding was also observed in $[Ag_{18}(TBT)_{10}(NO_3)_6(DMF)_4(CO_3)]$.[67]

(iii) Regulation of counterions

1D coordinated structures are also assisted by counter ions of the NC. The site-specific tailoring of counter ions determines the formation of 1D-coordinated structures. For example, in $[Au_{21}(SC_6H_{11})_{12}(DPPM)_2]^+[AgCl_2]^-$ and $[Au_{21}(SC_6H_{11})_{12}(DPPM)_2]^+[Cl]^-$, counter ions such as $[AgCl_2]^-$ and $[Cl]^-$ assist in the formation of a 1D coordinated structure by π–π, anion–π, and aryl C–H···Cl interactions, *via* site-specific surface hooks.[68] $[Ag_{29}(BDT)_{12}(PPh_3)_4]^{3-}$ NC, (BDT = 1,3-Benzenedithiol), can also be converted into 1D chain by employing Cs^+ ion as a counter ion that results in the formation of 1D assembly of $[Cs_3Ag_{29}(BDT)_{12}(PPh_3)_4]$. It has been observed that Cs−S and Cs···π interactions exist in this system.[69]

(iv) Insertion of organic linkers

The conversion of NCs into 1D structures, besides the methods discussed above, can be controlled using suitable organic linkers having bidentate connectivity such as pyrazine, bpy, $bpyNH_2$, etc. For example, $[Ag_{14}(C_2B_{10}H_{10}S_2)_6(CH_3CN)_8]\cdot 4CH_3CN$ NC upon treatment with pyrazine (an organic linker) was converted into a 1D polymeric chain, namely, $\{[Ag_{14}(pyz)_{6.5}(DMAc)(CH_3CN)_{0.5}]\cdot 2DMAc\}_n$.[48] The 1D structure of $[Ag_{18}(PhPO_3)(TBT)_{10}$

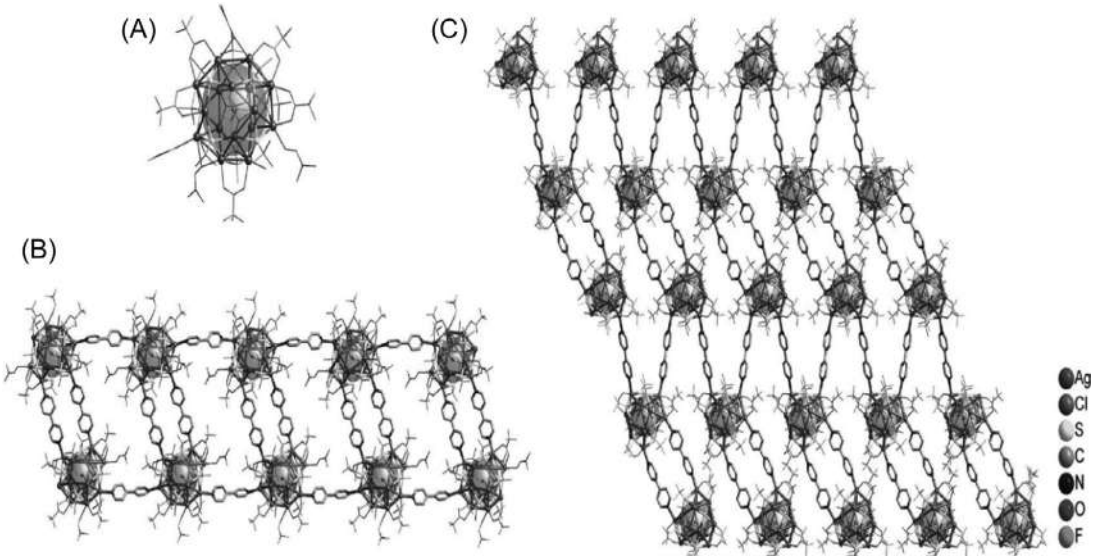

FIGURE 7.1 Crystal structures corresponding to (A) $[Ag_{16}Cl(TBT)_8(TFA)_7(DMF)_4(H_2O)]$ (0D NC); (B) Ag_{15}bpy (1D MOF); and (C) Ag_{14}bpy (2D MOF). Reproduced with permission from ref.[50]. Copyright 2019 American Chemical Society.

$(TFA)_2(PhPO_3H)_4]$ NC units coordinated by $bpyNH_2$ as organic linker was also reported.[49] In another example, bpy insertion in $[Ag_{15}Cl(TBT)_8$ $(TFA)_{5.67}(NO_3)_{0.33}(DMF)_2]$ denoted as Ag_{15} NC results in the 1D-polymeric chain of $[Ag_{15}Cl(TBT)_8(TFA)_{5.67}(NO_3)_{0.33}(DMF)_2(bpy)_4]_n$ denoted as Ag_{15}bpy, in which each Ag_{15} NC node is coordinated to four units of bpy resulting in a ladder-shaped 1D structure (Fig. 7.1).[50] In another case, *para- and ortho*-pyridine carboxylic hydrazide, independently, upon reaction with $[Ag_{12}(TBT)_6(TFA)_6(CH_3CN)_6]$ resulted in the formation of a 1D coordinated structure containing $[Ag_{10}(TFA)_4(TBT)_6$ $(CH_3CN)_2]$ and $[Ag_{10}(TFA)_4(TBT)_6(CH_3CN)]$ cluster nodes. In both cases, the carboxylate ion acts as a bridge between the two NCs.[51] $[Cd_6Ag_4(SPh)_{16}(DMF)(H_2O)]$ NC was also converted to 1D structure by *trans*-1, 2-bis(4-pyridyl)ethylene. Coordination occurs between the Cd of the NC and nitrogen atom of the linker in this bimetallic cluster, but there is no coordination between the Ag atoms.[52]

7.3.2 Two- and three-dimensional coordinated structures

Metal–oxygen bonding and the insertion of organic linkers can be used to create 2D and 3D coordinated silver NC structures which are discussed below.

(i) Metal–oxygen bonding

The introduction of ligands such as TFA, NO_3^-, $PhSO_3^-$, etc., that encourage the formation of Ag–O bonding has resulted in the formation of two-dimensional (2D) silver cluster-based

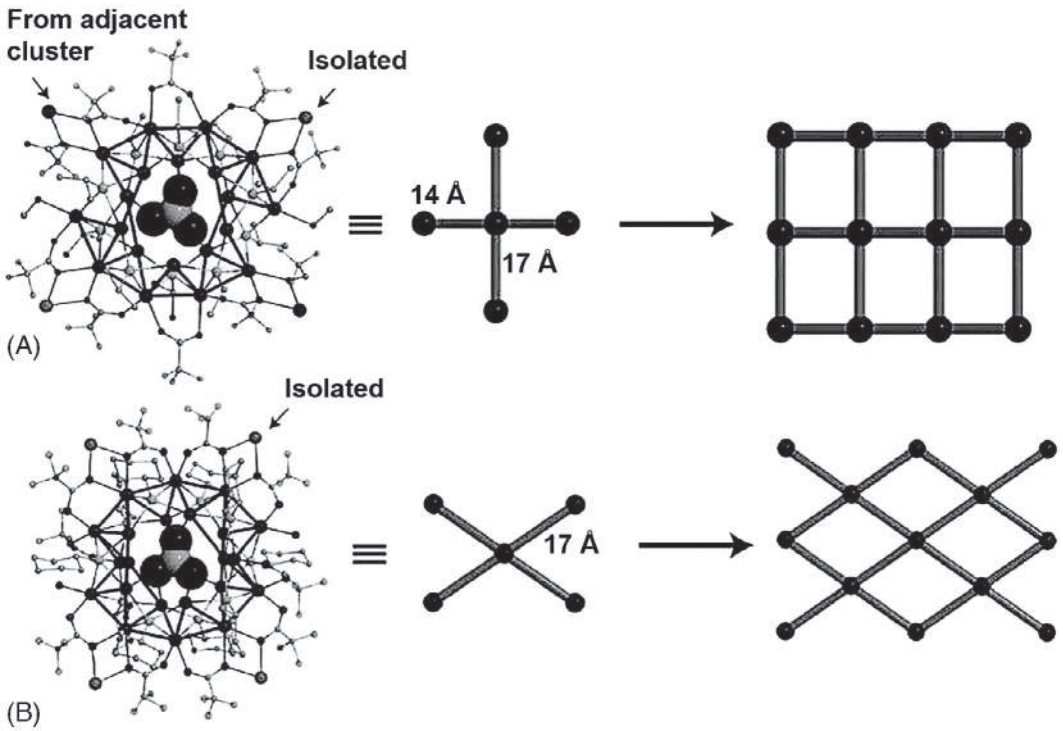

FIGURE 7.2 Crystal structure of (A) $AgAg_{20}$ MOF and (B) Ag_2Ag_{20} MOF. Reproduced with permission from refe.[67]. Copyright 2017, John Wiley and Sons.

frameworks. For example, TFA ligand helps in the formation of the 2D framework structures in $\{Ag[Ag_{20}(S^iPr)_{10}(TFA)_9(CF_3COOH)(CH_3OH)_2(CO_3)]\}_n$, denoted as $AgAg_{20}$ MOF, and $\{Ag_2[Ag_{20}(SCy)_{10}(TFA)_{10}(CF_3COOH)_2(H_2O)_2(CO_3)]\cdot(H_2O)_3(CH_3OH)_3\}_n$, denoted as Ag_2Ag_{20} MOF, facilitated by Ag–O bonding between adjacent clusters and CO_3^{2-} ion acts as a template, sitting at the center of each core. In these 2D frameworks, the NC units are connected to four adjacent NC units resulting in the formation of a layered 2D framework structure. Two types of bonding exist in $AgAg_{20}$ MOF: (1) one in which adjacent clusters are joined by oxygen atoms of TFA ligands with Ag–O bond distance of 14 Å and (2) another due to trapping of the isolated silver atom between oxygen atoms of TFA ligands of adjacent cluster units, with a bond distance of 17 Å. The second type of bonding also exists in all the intercluster linkages of Ag_2Ag_{20} MOF. This could be due to the presence of bulkier thiolate groups such as cyclohexyl thiolate in Ag_2Ag_{20} MOF that prevents direct metal–metal bonding in it (Fig. 7.2).[67]

The 2D framework structure was also found in $[Ag_{46}(V_{10}O_{28})(SEt)_{23}(PhSO_3)_{15}(CO_3)]$, denoted as $Ag_{46}V_{10}$, in which adjacent cluster units are joined through oxygen atoms of $PhSO_3^-$ ligand through Ag–O bonding (Fig. 7.3B).[70] Similar type of Ag–O bonding is observed in $[Ag_{11}Cl(amt)_8(TFA)_2\cdot 2CHCl_3]$, $[Ag_{11}Cl(amt)_8(NO_3)_2\cdot 2CHCl_3]$, and $[Ag_{11}Cl(amt)_8(CF_3SO_3)_2\cdot 2CHCl_3]$, in these cases TFA^-, NO_3^-, and $CF_3SO_3^-$ ions act as bridging ligands.[71] Metal–oxygen bonding can also be used to create 3D coordinated

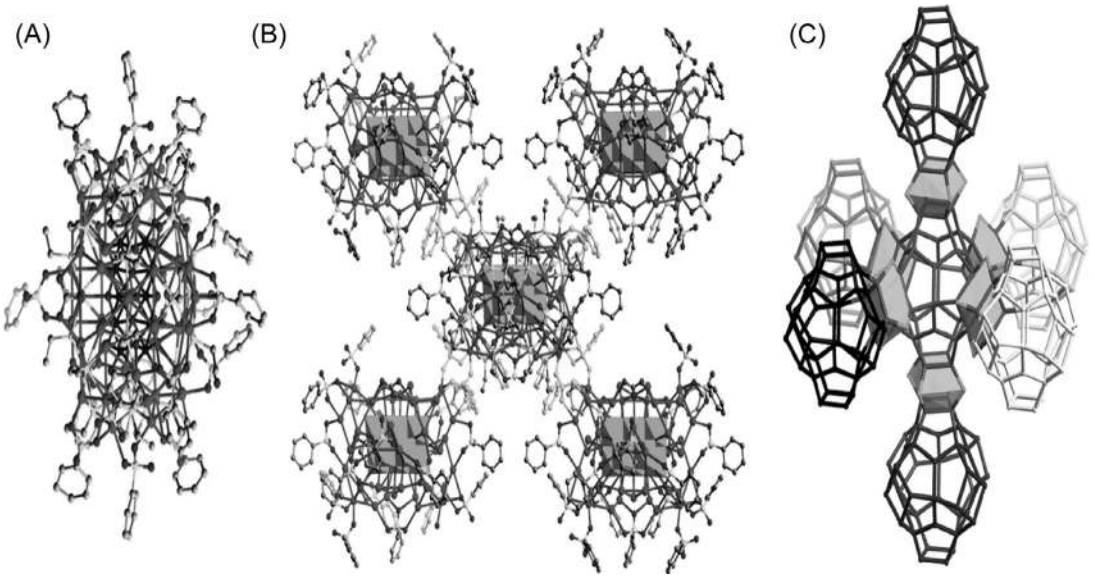

FIGURE 7.3 Crystal structure of (A) $Ag_{46}V_{10}$ unit and (B) its extended 2D structure. (C) 3D structure of $[Mo_6O_{19}@Ag_{44}(EtS)_{24}(SCl_4)_3]_n$. Reproduced with permission from ref.[70]. Copyright 2009, The Royal Society of Chemistry.

structures. For example, $[Ag_{14}(S^iPr)_6(TFA)_{11}(H_2O)_3(CH_3OH)]$ represents a covalent 3D MOF system and in this case, each cluster moiety is coordinated to six adjacent clusters through O–Ag–O linkage facilitated by oxygen atoms of TFA ligands.[67] Ag–Cl and Ag–S bonding between adjacent clusters can also result in 3D coordinated structures. For example, $[Ag_{44}(Mo_6O_{19})(SEt)_{24}(SCl_4)_3]_n$, exists as a 3D structure *via* Ag–Cl and Ag–S bonding and $Mo_6O_{19}^{2-}$ acts as an anion template (Fig. 7.3C).[70]

(ii) Insertion of linker molecules

The 2D and 3D coordinated frameworks can be easily synthesized using bidentate organic linkers such as bpy, bpa, bpe, etc. Zang et al. were the first to report the formation of a 3D framework structure of silver clusters, namely, $[Ag_{12}(TBT)_8(TFA)_4(bpy)_4]_n$, denoted as $Ag_{12}bpy$.[47] In their study, $[Ag_{12}(TBT)_8(TFA)_4]$ NC nodes were coordinated to adjacent NC nodes through bpy organic linker resulting in a long polymeric structure, also called the silver NC-based framework (MOF). This was the first study that revealed the formation of silver MOFs and has greatly influenced many new studies. These MOFs enriched with metal-rich nodes are associated with novel properties arising from the integration of both NC nodes and organic linkers.[47] The same group synthesized 2D–MOFs, namely, $[Ag_{12}(TBT)_6(TFA)_6(bpy)_3{\cdot}(DMAc_xtoluene_y)]_n$. In this study, $[Ag_{12}(TBT)_8(TFA)_4(bpy)_4]_n$, a 3D MOF with tetragonal geometry was converted into a 2D MOF, namely, $[Ag_{12}(TBT)_6(TFA)_6(bpy)_3{\cdot}(DMAc_xtoluene_y)]_n$ with trigonal geometry at the NC node induced by solvents such as toluene and DMAc and led to a new phenomenon of structural isomerism in MOFs (Fig. 7.4).[53] This study suggests that the solvent has a significant role in the NC node transformation in MOFs.

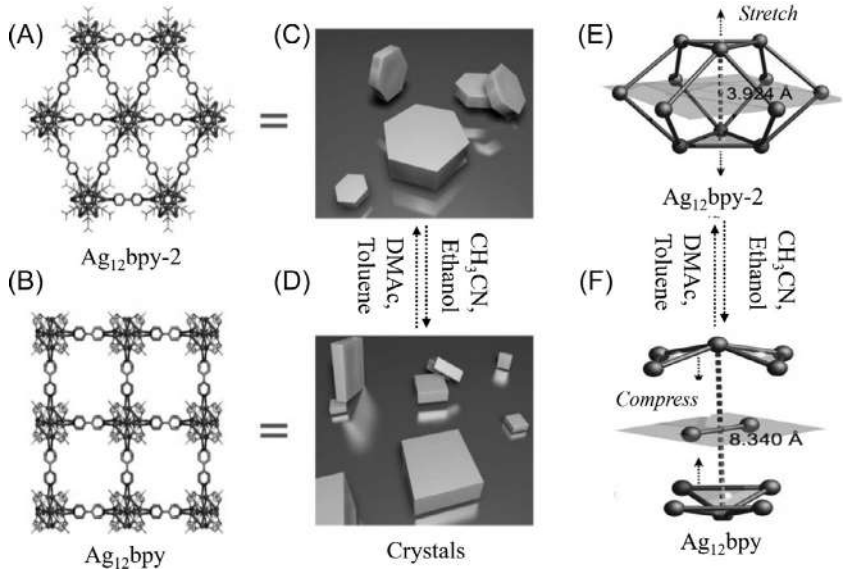

FIGURE 7.4 Structure transformation induced by the solvent in Ag_{12}bpy and Ag_{12}bpy-2. Reproduced with permission from ref.[53]. Copyright 2018, John Wiley and Sons.

A 2D coordinated framework structure containing $[Ag_{14}(C_2B_{10}H_{10}S_2)_6(CH_3CN)_4]$ with nodes linked together by bidentate dpd ligand was synthesized.[48] Zang et al. reported 2D structures made up of $[Ag_{12}(TBT)_6(TFA)_6]$ cluster nodes, joined by tppa linker. In this, DMAc solvent got trapped between the 2D layers during formation. This 2D structure shows a breathing mechanism in which layers get close to each other upon solvent removal and move away when solvent gets incorporated between the layers.[54] This lead to the change in their emission properties. A 2D MOF namely, $[Ag_{12}(TBT)_6(TFA)_3(tpp)]_n$, denoted as Ag_{12}tpp, was synthesized and can be used as efficient catalysts for mustard gas detoxification.[55] A 2D MOF containing $[Ag_{14}Cl(TBT)_8(TFA)_5(DMF)]$ nodes linked together by bpy ligand was reported. The Cl^- ion was found at the center of the Ag_{14} node and acts as a template for its formation (Fig. 7.1B).[50] Another similar entity, $[Ag_{10}(TFA)_4(TBT)_6(CH_3CN)_4(m\text{-pch})_4]$ was synthesized.[51] The use of *m*-pch linker results in a 2D MOF, whereas *o*- and *p*-pch linkers result in the formation of 1D coordinated structures, namely, $[Ag_{10}(TFA)_4(TBT)_6(p\text{-pch})_2(CH_3CN)_2]_n$ and $[Ag_{10}(TFA)_4(TBT)_6(o\text{-pch})_4(CH_3CN)]_n$.[51] Although 2D MOFs are associated with improved stability and efficient luminescence, their low solubility limits their use in optoelectronic devices. To address this issue, Zang et al. fabricated a 2D MOF, $[Ag_{12}(TBT)_6(TFA)_6(bpzNH_2)_3]_n$, denoted as $Ag_{12}bpzNH_2$, for device applications *via* self-assembly. An amino group substituted linker was used in this case, which helps in the functionalization of MOF with polymer-based materials. Using post-synthetic modification, size-limited crystals of MOF, functionalized with $–NH_2$ group on the linker, were treated with MA to yield methacrylamide group functionalized MA–$Ag_{12}bpzNH_2$ nanoparticles. Photo-induced free radical polymerization of MA–$Ag_{12}bpzNH_2$ nanoparticles with acrylate monomers (BMA and TEGDMA) results in a well-developed $Ag_{12}bpzNH_2$ thin film for device applications. MA is useful for anchoring

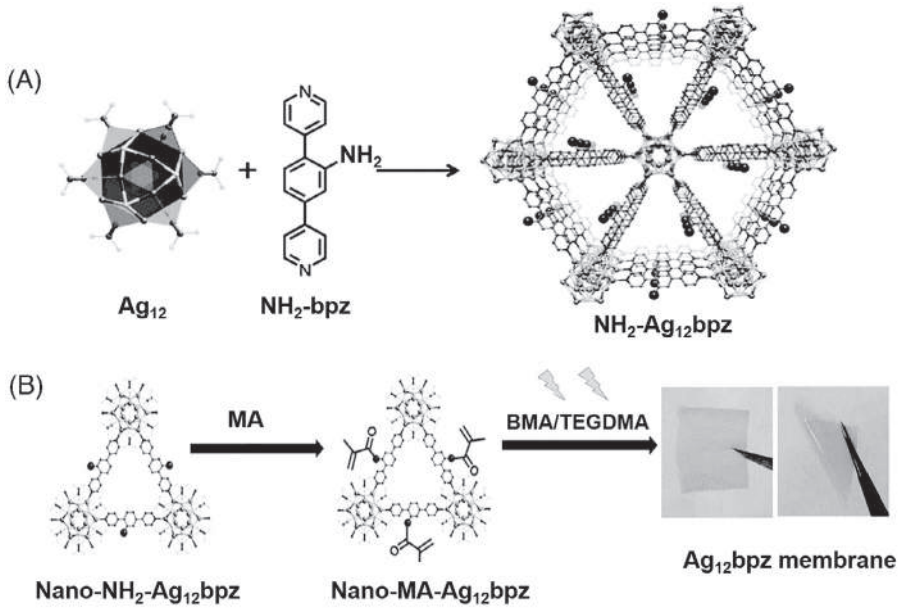

FIGURE 7.5 (A) Crystal structure of $Ag_{12}bpzNH_2$. (B) Schematic of the fabrication process of the silver clusters-based thin film. Reproduced with permission from ref.[56]. Copyright 2009, The Royal Society of Chemistry.

MOF in this case, BMA acts as a cross-linker, providing the membrane with consistent mechanical strength, and TEGDMA increases the membrane's flexibility due to its long carbon chains (Fig. 7.5).[56]

A $[Ag_{12}(TBT)_8(TFA)_4(bpy)_4]_n$ MOF was first synthesized and the framework shows 3D structural arrangement in which $[Ag_{12}(TBT)_8(TFA)_4]$ cluster units were linked by bpy linkers in a bilayer fashion. This Ag_{12}bpy MOF shows enhanced stability and is more luminescent than Ag_{12} NC (Fig. 7.6).[47] In another example, $[Ag_{14}(C_2B_{10}H_{10}S_2)_6(bpy)_8]$, denoted as Ag_{14}bpy-dc, a 3D coordinated structure was synthesized in which eight vertices of Ag_{14} NC units are coordinated to adjacent NC units *via* bpy ligand, resulting in the formation of a 3D MOF.[48] In another example,[48] bpb ligand was used as a linker, and a 3D Ag_{14}bpb MOF was obtained, with $Ag_{14}(C_2B_{10}H_{10}S_2)_6$ NC as a cluster node, and is topologically similar to Ag_{14}bpy MOF.[50] For the same cluster unit, bpb linker induces more stability than bpy in the framework structure. This could be due to the interwoven and tight packing of adjacent layer (Fig. 7.7).[48]

A new isostructural complex, $[Ag_{12}(TBT)_8(TFA)_4(bpyNH_2)_4]_n$, denoted as $Ag_{12}bpyNH_2$, was synthesized using functionalized bpy such as 3-amino-4,4′-bipyridine ($bpyNH_2$) as a linker. The incorporation of amino groups in bpy ligand gives rise to (i) a blue sub–nanosecond fluorescence component centered at ~456 nm and (ii) a yellow phosphorescence component at 556 nm. Through the incorporation of NH_2 functionalized bpy, $Ag_{12}bpyNH_2$ behaves as a single component fluorescence-phosphorescence ratiometric sensor for the detection of oxygen (Fig. 7.8).[72] In another case, a 2D MOF, namely, $[Ag_{10}(TBT)_6(TFA)_2(PhPO_3H)_2(bpy)_2]$, denoted as Ag_{10}bpy, appears as a 3D coordinated structure in the crystalline phase due to the

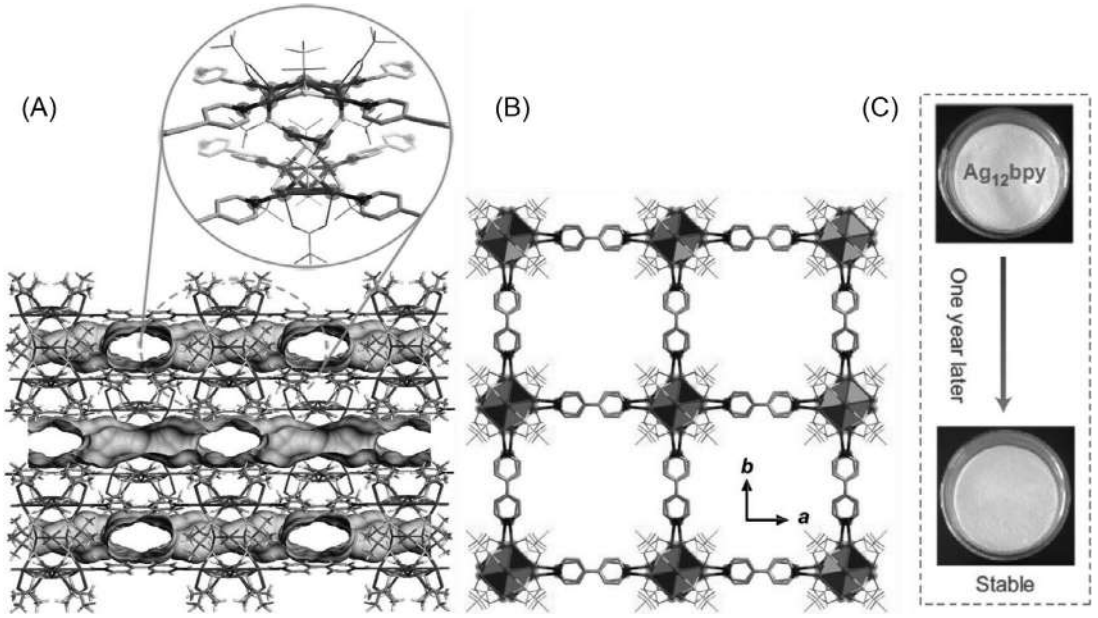

FIGURE 7.6 (A) Crystal structure of $[Ag_{12}(TBT)_8(TFA)_4(bpy)_4]$ MOF, (B) structure of its single layer, and (C) photograph of Ag_{12}bpy powder. Reproduced with permission from ref.[47]. Copyright 2017, Springer Nature.

stacking of 2D layers on top of each other. The layers are held together by weak hydrogen bonding (O···H–O and O···H–C) interactions resulting in 3D coordinated structures. The weak interactions between the 2D layers are responsible for the structural changes in the 3D coordinated structures upon interaction with solvent molecules (Fig. 7.9).[57]

In another example, $[Ag_{12}(TBT)_6(TFA)_6(cppp)_2(DMAc)_{12}]_n$, denoted as Ag_{12}cpp, a 3D MOF was synthesized, in which the organic linker is tetradentate with two pyridyl and two nitrile donor sites. This is the first example showing coordination through nitrile groups. This 3D MOF shows greater rigidity and efficient fluorescence with a quantum yield of 61%.[58] All examples discussed above demonstrate the presence of only one type of silver cluster at the nodes of a specific structure. Tang et al. reported a 3D MOF, namely, $\{[Ag_{12}(TBT)_6(TFA)_6]_{0.5}[Ag_8(TBT)_4(TFA)_4](tppe)_2(DMAc)_{10}\}_n$ denoted as $Ag_{12}Ag_8$tppe, with two different silver cluster nodes such as $\{[Ag_{12}(TBT)_6(TFA)_6]$ and $[Ag_8(TBT)_4(TFA)_4]$, joined together by a tetradentate tppe linker. In this case, three units of Ag_8 and one Ag_{12} cluster are coordinated to the N-donor sites of tppe (Fig. 7.10).[59]

7.4 Properties of nanocluster frameworks

7.4.1 Stability

Silver NCs have drawn tremendous research interest due to their fascinating structures and exotic properties. However, the use of silver NCs for a wide range of applications is

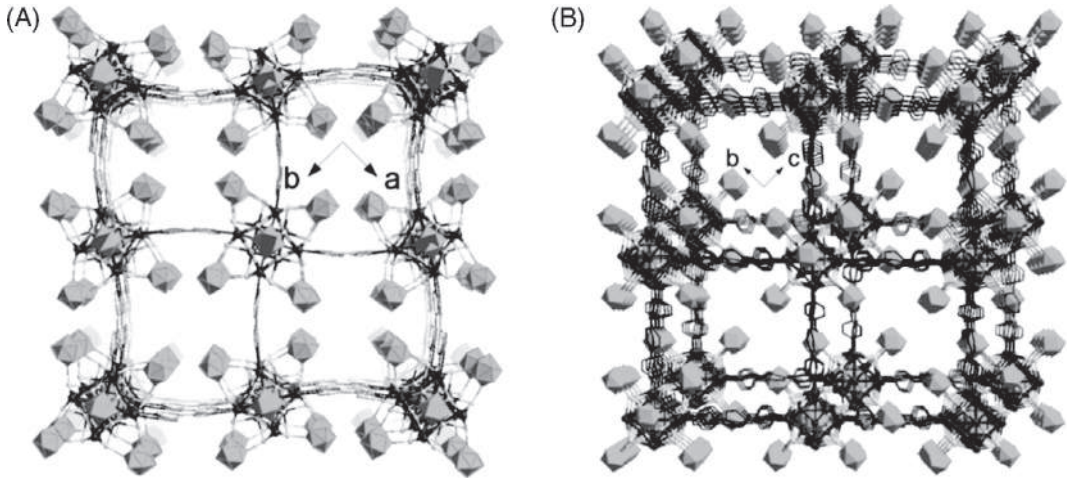

FIGURE 7.7 Crystal structure of 3D porous framework of (A) $[Ag_{14}(C_2B_{10}H_{10}S_2)_6(bpy)_8]$ and (B) $[Ag_{14}(C_2B_{10}H_{10}S_2)_6(bpb)_8]$ MOF. Reproduced with permission from ref.[48]. Copyright 2018, American Chemical Society.

limited due to their inherent instability. Silver chalcogenide clusters exhibit very poor or no emission at room temperatures. The maximum luminescence quantum yield for such clusters was found to be 1.4%.[73,74] The stability and associated properties of silver clusters usually depend on the metallic core, stabilizing ligand, and the surrounding environment.[74–76] Thus, there is a need to develop a mechanism to increase the stability of silver NCs so that they can be developed into functional materials. Zang et al. first demonstrated increased stability of silver chalcogenide clusters from 30 minutes to one year by coordinating silver NCs to adjacent NCs using organic linkers such as bpy.[47] The coordination of silver NC and organic linkers lead to their integration into a new material with enhanced stability. An increase in the stability upon the transformation of pristine Ag_{12} NC into Ag_{12}bpy MOF is also accompanied by an increase in its luminescence quantum yield (~60 folds). The increment in the stability of the MOFs could be due to the formation of a rigid coordination framework incorporated by organic linkers. Thus, the conversion of silver NCs into MOFs overcomes their stability. Recently, many MOFs have been reported with enhanced stability.[47–59] However, wide use of MOFs is limited due to their solubility issues. To overcome the solubility and processability of MOFs, Zang et al. developed a new strategy in which MOFs were embedded into a polymer matrix that maintains the unique properties of the framework in the matrix, which lead to their use in device applications.[56] In this method, MOFs were anchored to a polymeric flexible membrane (Fig. 7.5B). A functionalized organic linker such as NH_2bpz was chosen for the synthesis of MOF, namely, $[Ag_{12}(TBT)_6(TFA)_6(NH_2bpz)_3]_n$, denoted as $Ag_{12}bpzNH_2$. In the post-synthetic modification, the amino group on the linker facilitates MOF anchoring on the polymeric substrate *via* inter-crosslinking. The functionalized $Ag_{12}bpzNH_2$ was treated with acrylate monomers to yield a novel MOF thin film through photo-induced free radical polymerization. The fabricated Ag_{12}bpz thin film exhibits a significant improvement in its physical and chemical properties as compared to MOF.[56,77] This has opened up new areas for the practical applications of the MOFs.

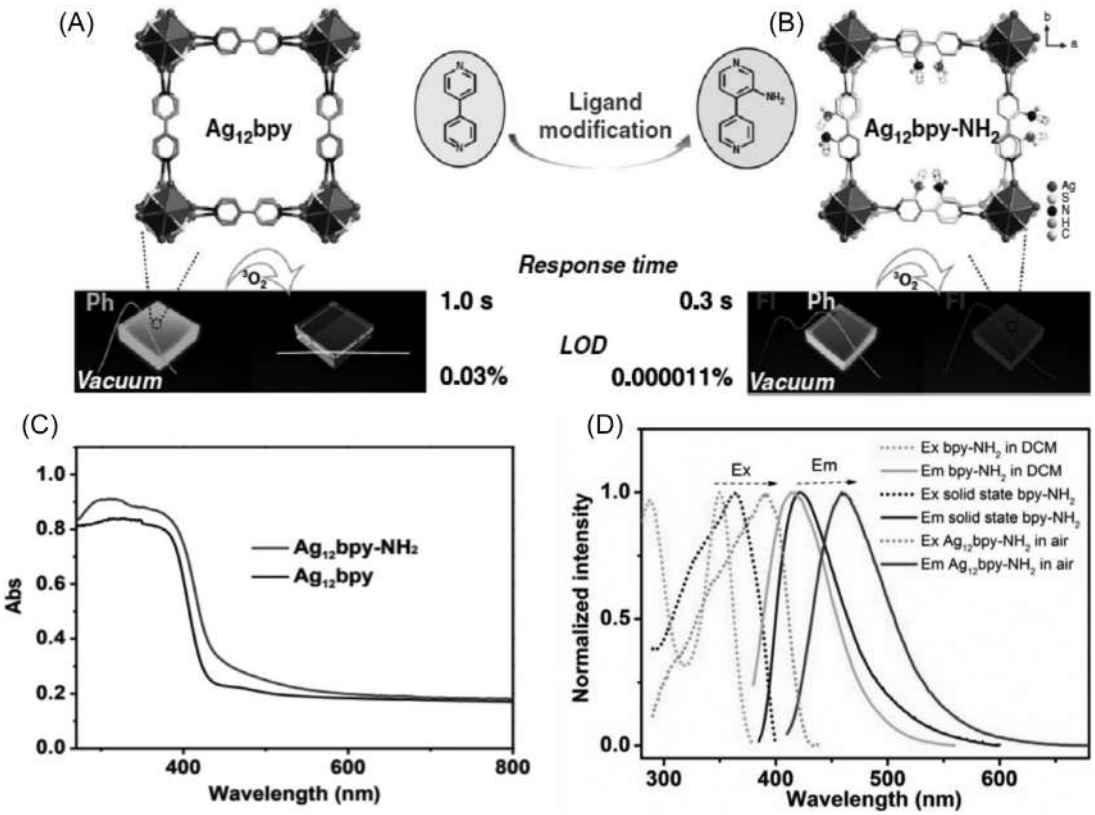

FIGURE 7.8 Crystal structure of (A) $Ag_{12}bpy$ and (B) $Ag_{12}bpyNH_2$. (C) UV-vis absorption of $Ag_{12}bpy$ and $Ag_{12}bpyNH_2$. (D) Emission and excitation spectra of $Ag_{12}bpyNH_2$ (air) and $bpyNH_2$ (in solid and DCM). Reproduced with permission from ref.[72]. Copyright 2020, Springer Nature.

7.4.2 Structure transformation

The structure of a particular MOF depends on the ligands, solvent, and synthetic methodology employed. In a few cases, unusual single-crystal-to-single-crystal structural transformations have also been reported in MOFs. In one of the examples reported recently, $[Ag_{12}(TBT)_6(TFA)_6(bpa)_3(DMAc)_{12}]_n$ and $[Ag_{12}(TBT)_6(TFA)_6(bpe)_3(DMAc)_{14.7}]_n$, denoted as $Ag_{12}bpa$ and $Ag_{12}bpe$, respectively, gets transformed into the new structures upon treatment with mixed solvents denoted as the solution-immersion method. When crystals of $Ag_{12}bpa$ MOF were immersed in acetonitrile, the structure (1) of the NC node gets distorted and the linker bpe gets rearranged to a new structure (2) with a different packing arrangement (Fig. 7.11). However, when the crystals of $Ag_{12}bpe$ were treated with acetonitrile, Ag_{12} node gets converted into Ag_{10} node, resulting in the formation of a new $Ag_{10}bpe$ MOF. These observations suggest that acetonitrile triggers structural transformations in both $Ag_{12}bpe$ and $Ag_{12}bpa$ MOFs (Fig. 7.12).[60] In another report, tetragonal ($[(Ag_{12}(TBT)_8(TFA)_4(bpy)_4)]_n$) denoted as $Ag_{12}bpy$ MOF gets transformed into a trigonal $[Ag_{12}(TBT)_6(TFA)_6(bpy)_3]_n$ denoted as

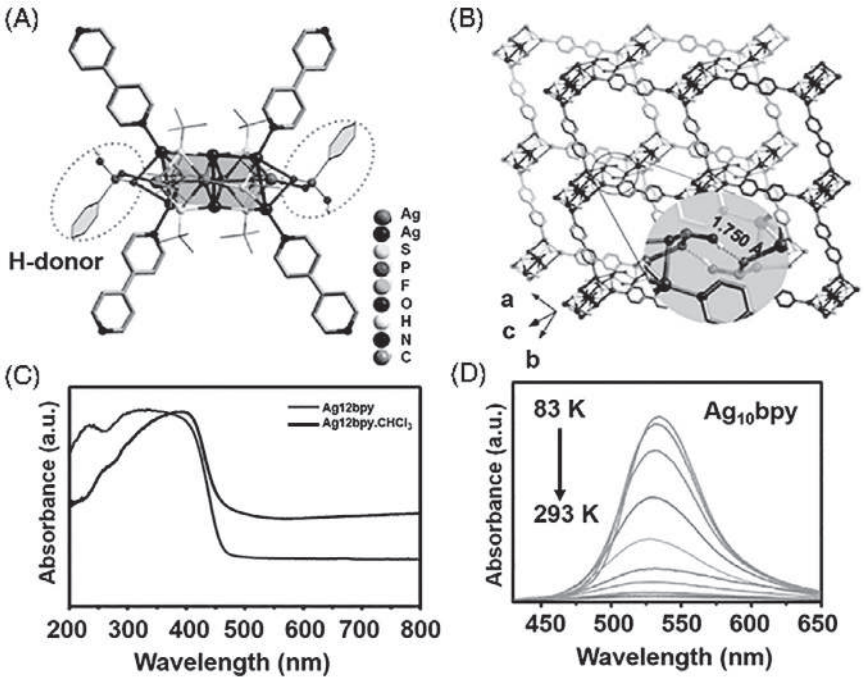

FIGURE 7.9 (A) Crystal structure of core in Ag_{10}bpy MOF. (B) Layering in Ag_{10}bpy MOF; (C) absorption spectra of Ag_{12}bpy and Ag_{12}bpy.$CHCl_3$. (D) Photoluminescence spectra of Ag_{10}bpy at an excitation of 365 nm excitation. Reproduced with permission from ref.[57]. Copyright 2018, American Chemical Society.

Ag_{12}bpy-2 MOF triggered by a mixed solvent (acetonitrile and ethanol) at room temperature. Surprisingly, the mixed solvent DMAc and toluene triggered the reverse transformation of the MOFs. Ag_{12}bpy MOF (3D) having a separate silver core gets converted into Ag_{12}bpy MOF (2D) of hollow cuboctahedron by acetonitrile and ethanol. A reversible cluster node isomerization from 2D to 3D MOFs was reported in this case (Fig. 7.4C–F). Through this structural transformation at a cluster node, a single-emissive Ag_{12}bpy MOF gets converted into a dual-emissive Ag_{12}bpy-2 MOF.[53]

7.4.3 Absorption properties

The appearance of guest molecule-modulated optical properties in MOF materials is an intriguing feature. The guest molecules trapped in MOFs directly affect their absorption properties. Furthermore, the presence of a functional group at a specific position in the organic linker such as 3-amino-4,4′-bipyridine also influences the absorption properties.[72] Bakr et al. reported the optical absorption spectra of $[Ag_{14}Cl(TBT)_8(TFA)_5(bpy)_2(DMF)]\cdot 2(DMF)$ and $[Ag_{15}Cl(TBT)_8(TFA)_{5.67}(NO_3)_{0.33}(bpy)_2(DMF)_2]\cdot 4.3(DMF)$, these MOFs display the absorption bands in the UV region followed by a shoulder peak at 420 nm. The peak at 420 nm was assigned to the trapped DMF molecules in the framework. When these materials are dried, this band nearly disappears, confirming the solvent (DMF) peak in this case (Fig. 7.13A and B).[50]

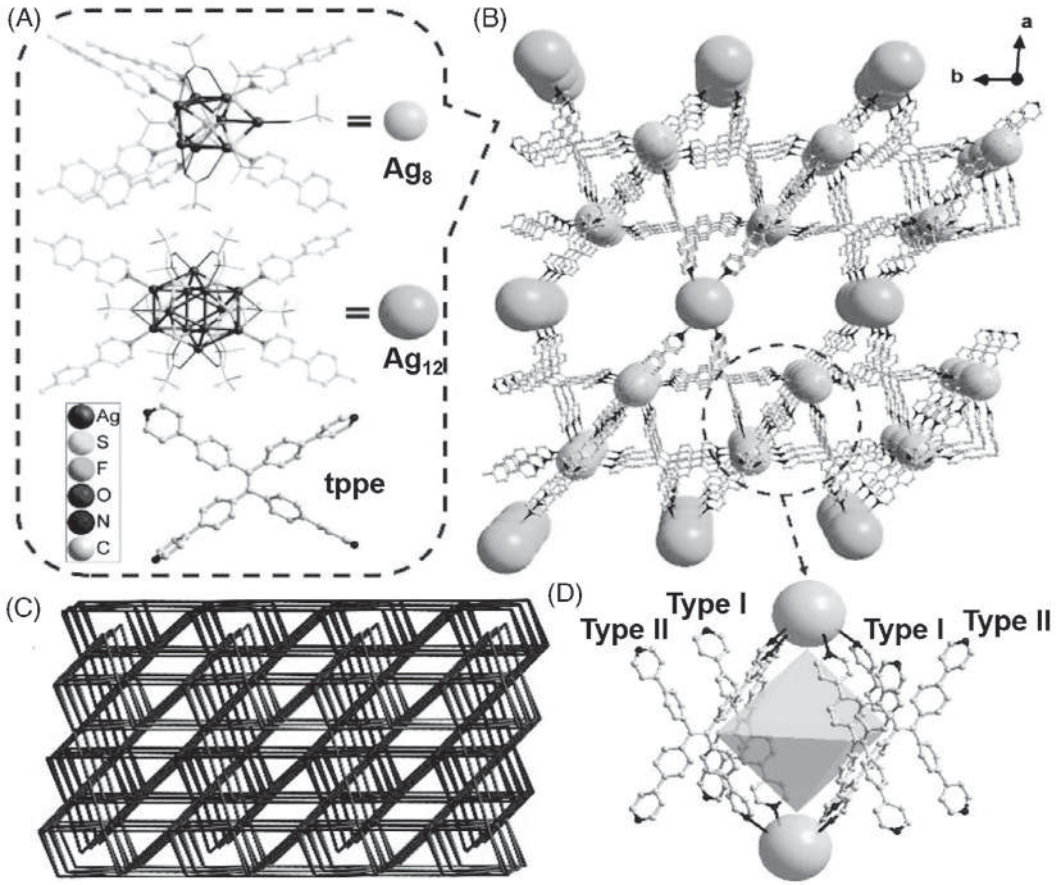

FIGURE 7.10 (A) Total structure of the $[Ag_8(TBT)_4(TFA)_4]$ cluster, $[Ag_{12}(TBT)_6(TFA)_6]$cluster, and tppe linker, and (B) crystal structure of $[Ag_{12}(TBT)_6(TFA)_6]_{0.5}[Ag_8(TBT)_4(TFA)_4](tppe)_2(DMAC)_{10}$ MOF, (C) mixed MOF with twofold interpenetrated topology, and (D) an octahedral cavity enclosed by four type ligands and two Ag_8 clusters. Reproduced with permission from ref.[59]. Copyright 2018, John Wiley and Sons.

In another case, a solvent-induced bathochromic shift was observed in the diffuse reflectance UV-vis spectrum of $Ag_{10}bpy{\cdot}CHCl_3$ compared to the solvent-free $Ag_{10}bpy$ (Fig. 7.9C).[57] In $[Ag_{12}(TBT)_8(TFA)_4(bpyNH_2)_4]_n$, UV-vis absorption intensity increases below 600 nm and gets red-shifted, extending to 680 nm compared to $[Ag_{12}(TBT)_8(TFA)_4(bpy)_4]$. This change in the UV-vis spectra can be attributed to a new $n\rightarrow\pi^*$ transition due to the presence of $-NH_2$ group in the organic linker in $Ag_{12}bpyNH_2$ (Fig. 7.8C).[72] Furthermore, anchoring of $Ag_{12}bpzNH_2$ MOF with polymer substrates such as methacrylamide (MA) exhibits broader absorption bands compared to pristine $Ag_{12}bpzNH_2$ MOF. This could be attributed to the extensive conjugation of π-electrons from amine to amide in this system (Fig. 7.14A).[56] To summarize, all MOFs exhibit UV absorption bands, however, the change in optical properties is modulated by solvent, the functional group on the linkers, or polymer substrates.

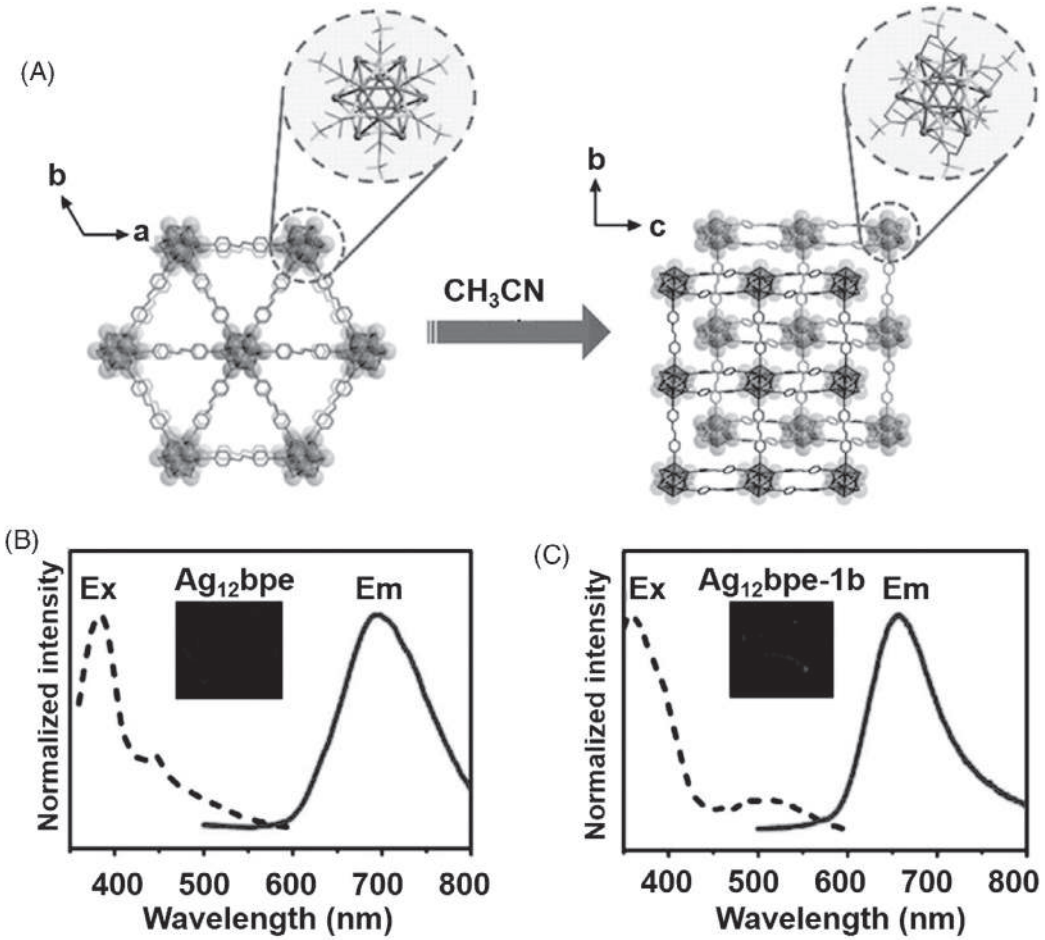

FIGURE 7.11 (A) Structural conversion of $[Ag_{12}(TBT)_6(TFA)_6(bpa)_3(DMAc)_{12}]_n$ to $[Ag_{12}(TBT)_6(TFA)_6(bpe)_3(DMAc)_{14.7}]_n$ (TFA, TBT, and H atoms are omitted for clarity). The insets are structures of $Ag_{12}S_6$ units. (B) Photoluminescence spectra of (a) and (b) MOFs at 83 K. Insets: photographs of the crystals. Reproduced with permission from ref.[60]. Copyright 2019, John Wiley and Sons.

7.4.4 Luminescence properties

Silver NCs are usually associated with poor or no luminescence at room temperature. For example, Ag_{12} NC shows weak luminescence with an emission quantum yield of 0.2% and the emission vanishes within minutes on exposure to air. However, when $[(Ag_{12}(TBT)_6(TFA)_6(CH_3CN)_6]\cdot CH_3CN$ NC is transformed into $[(Ag_{12}(TBT)_8(CF_3COO)_4(bpy)_4)]_n$, denoted as Ag_{12}bpy MOF, the emission quantum yield increases up to 60 fold (Fig. 7.15).[47] The synthesis of new MOF materials is progressing, and numerous reports have been published.

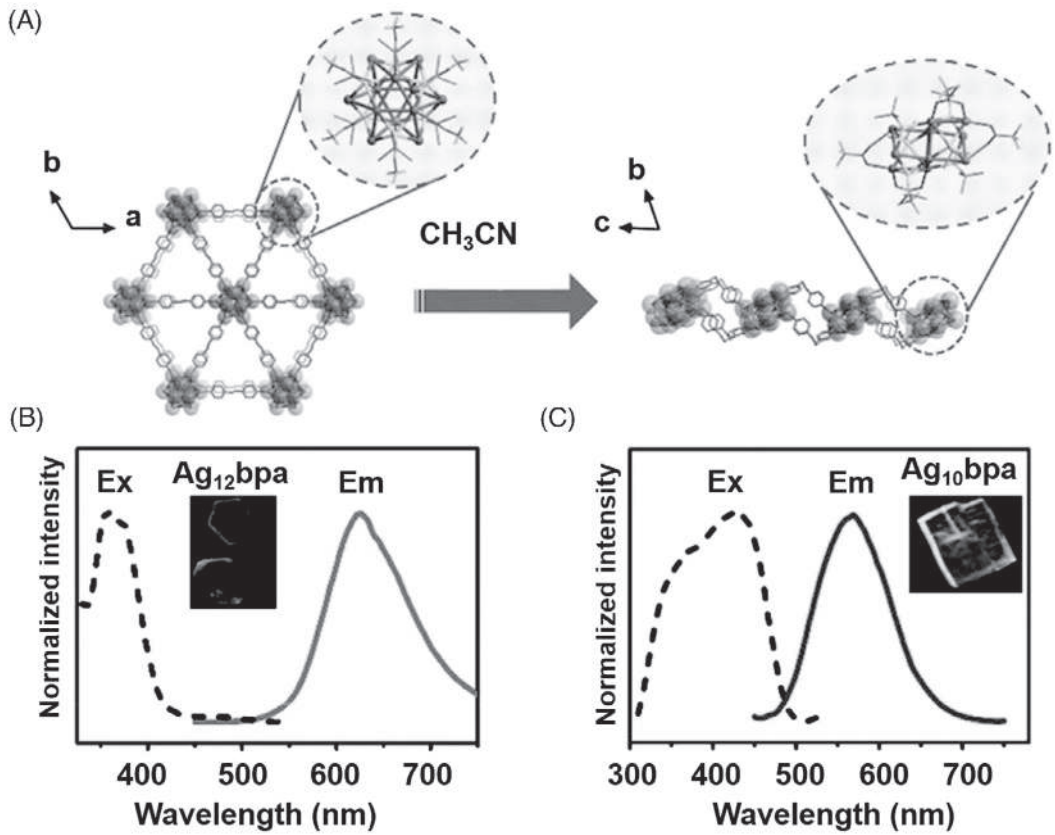

FIGURE 7.12 (A) Structural conversion of a 2D Ag_{12}bpa into 1D Ag_{10}bpa MOF. The structure of $Ag_{12}S_6$ core is shown in insets. Photoluminescence spectra of (B) Ag_{12}bpa and (C) Ag_{10}bpe. Photographs of the crystals are shown in insets. Reproduced with permission from ref.[60]. Copyright 2019, John Wiley and Sons.

Luminescence in these framework structures could be due to metal-to-ligand charge transfer (MLCT), ligand-to-metal charge transfer (LMCT), or metal-centered transitions. The trapped guest molecule may also alter the luminescence in these materials. Density functional theory (DFT) calculations were used to determine the origin of the emission transitions in MOFs. DFT calculations indicate that in Ag_{12} NC emission transitions arise from the combination of metal-centered and LMCT. However, the emission transitions in Ag_{12}bpy MOF arise from Ag(I)-to-ligand (bpy) (MLCT) along with some contributions from ligands (sulfur from thiols and oxygen from trifluoroacetate) to bpy indicating ligand-to-ligand charge transfer (LLCT).[47] Efficient emission in these MOFs could be attributed to their orderly positioned chromophores and rigid structural framework, which prevents nonradiative energy dissipation.[47] From the lifetime measurements of Ag_{12}bpy, it is evident that the excited state exhibits triplet state character which is responsible for luminescence in it.[47] The intense fluorescence of Ag_{12}bpy MOF compared to Ag_{12} NC suggests that bpy ligand is responsible for the modulation of the excited state in

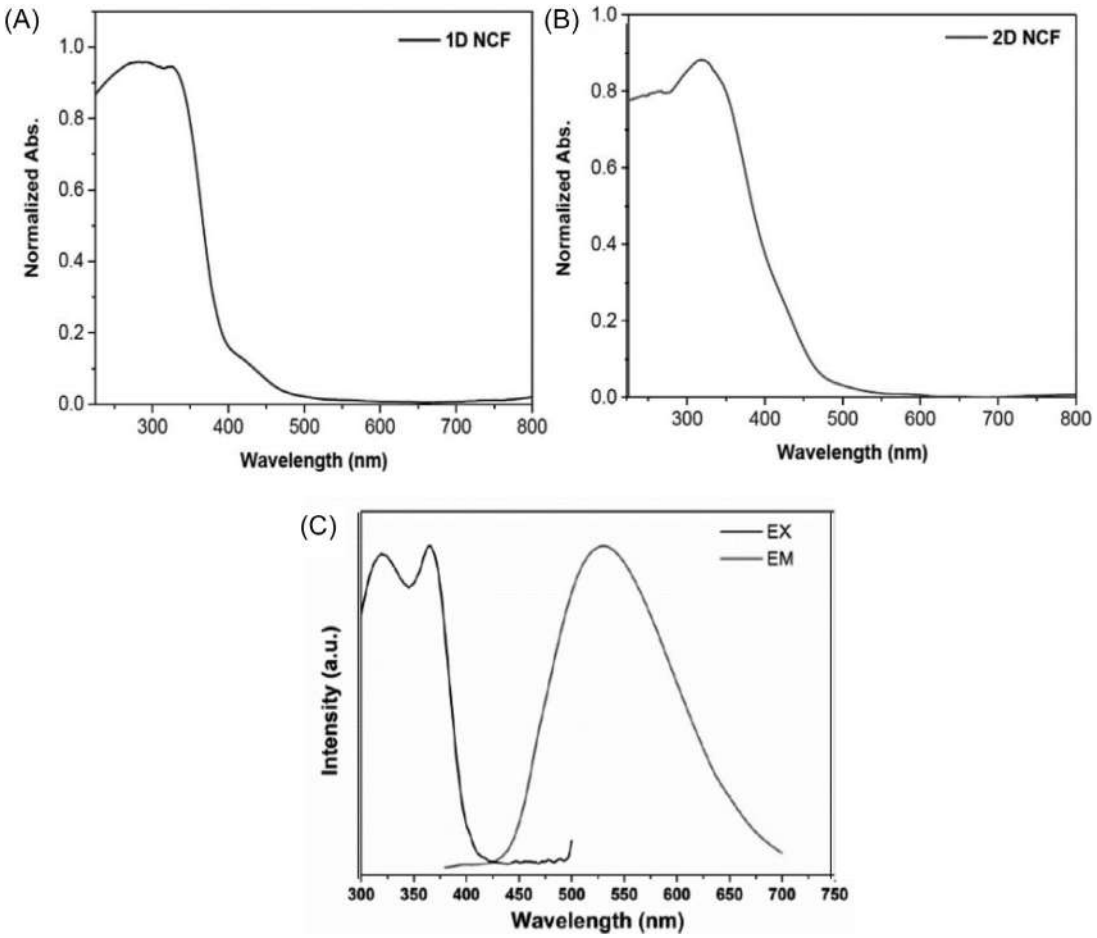

FIGURE 7.13 UV-visible absorption spectra of (A) $[Ag_{15}Cl(TBT)_8(TFA)_{5.67}(NO_3)_{0.33}(bpy)_2(DMF)_2]$ (1D) and (B) $[Ag_{14}Cl(TBT)_8(TFA)_5(bpy)_2(DMF)]$ (2D). (C) Room temperature excitation (365 nm) and emission spectra of 2D MOF. Reproduced with permission from ref.[50]. Copyright 2019 American Chemical Society.

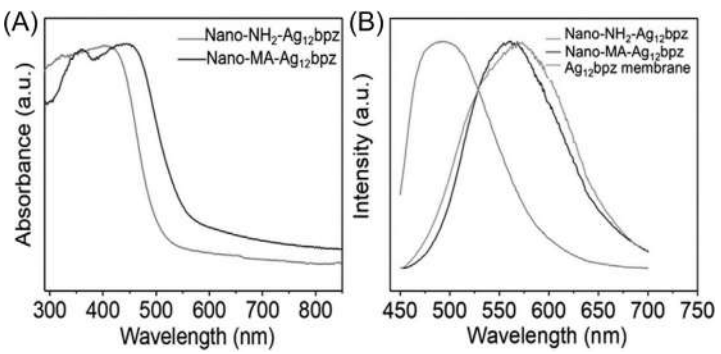

FIGURE 7.14 UV-vis absorption spectra of $Ag_{12}bpzNH_2$ MOF and MA-$Ag_{12}bpzNH_2$. (D) PL spectra of $Ag_{12}bpzNH_2$ MOF, MA-$Ag_{12}bpzNH_2$, and $Ag_{12}bpz$ thin film. Reproduced with permission from ref.[56]. Copyright 2009, The Royal Society of Chemistry.

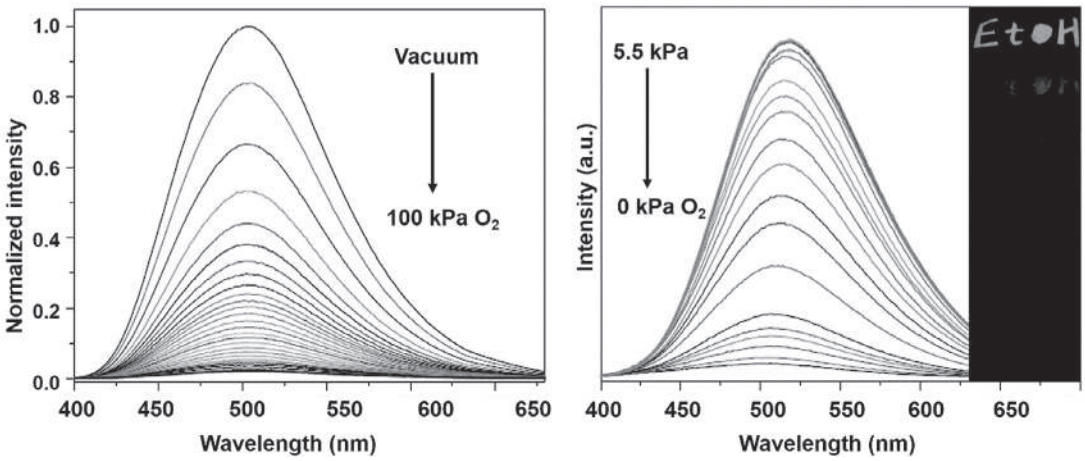

FIGURE 7.15 (A) Photoluminescence of Ag_{12}bpy under vacuum and in presence of various pressures of oxygen. (B) PL profiles Ag_{12}bpy upon exposure to various partial pressures of ethanol. Inset: tracking picture record of EtOH escaping into the air in 1 min. Reproduced with permission from ref.[47]. Copyright 2017, Springer Nature.

the former case. However, for $[(Ag_{12}(TBT)_6(TFA)_6(bpy)_3)]_n$ denoted as Ag_{12}bpy-2 MOF, emission spectra show group peaks. The luminescence in this MOF originates from ligand-to-metal–metal charge transfer, S → Ag (LMMCT) in combination with metal-centered (ds/dp) transitions (Fig. 7.16).[53] The MOFs of $[Ag_{12}(TBT)_6(TFA)_6(bpa)_3(DMAc)_{12}]_n$ and $[Ag_{12}(TBT)_6(TFA)_6(bpe)_3(DMAc)_{14.7}]_n$, denoted as Ag_{12}bpa and Ag_{12}bpe, respectively, display no room-temperature luminescence. However, luminescence increases with a decrease in temperature and shows a maximum at 83K (Figs. 7.11–7.12).[60] In both cases, the emission was attributed to LMCT (S→Ag) excited state along with the mixing of metal-centered (ds/dp) transitions.[60] A 2D MOF namely, $[Ag_{14}Cl(TBT)_8(TFA)_5(bpy)_2(DMF)]\cdot 2(DMF)$, shows a green emission at room temperature with λ_{max} at 530 nm upon excitation at λ_{ex} 365 nm. However, a weak luminescence at low temperature was observed in a 1D structure of $[Ag_{15}Cl(TBT)_8(TFA)_{5.67}(NO_3)_{0.33}(bpy)_2(DMF)_2]\cdot 4.3(DMF).H_2O$.[50] The luminescence in the above systems arises from the ligand-to-cluster charge transfer. In another example, Ag_{10}bpy displays emission with λ_{max} at 518 nm upon excitation at λ_{ex} 365 nm at low temperature and decreases with an increase in temperature (Fig. 7.9D). The energy transfer mechanism shows that emission transitions arise from MLCT and cluster-to-ligands transitions.[57] In $Ag_{12}bpyNH_2$ MOF the linker contains $–NH_2$ group at 3-position of bpy and displays an emission band at λ_{em} 556 nm upon excitation at λ_{ex} 370 nm at room temperature. The emission from this MOF is similar to $bpyNH_2$ group but showed a band shift to a longer wavelength (Fig. 7.8D).[72] In another example, MOF was functionalized with a polymer methacrylamide (MA). The luminescence of the MOF, namely, $[Ag_{12}(TBT)_6(TFA)_6(NH_2bpz)_3]_n$ embedded in a polymer substrate (MA) was recorded with a λ_{max} 562 nm compared to pristine MOF with λ_{max} 489 nm upon excitation a λ_{ex} at 430 nm (Fig. 7.14B).[56] The functionalized MOF shows a red shift. The emission color changes from green to yellow upon functionalization. The methacrylamide groups are responsible for this effect. The emission quantum yield was 14.8%, which was much higher than normal MOFs. The embedding or cross-linking of MOF with

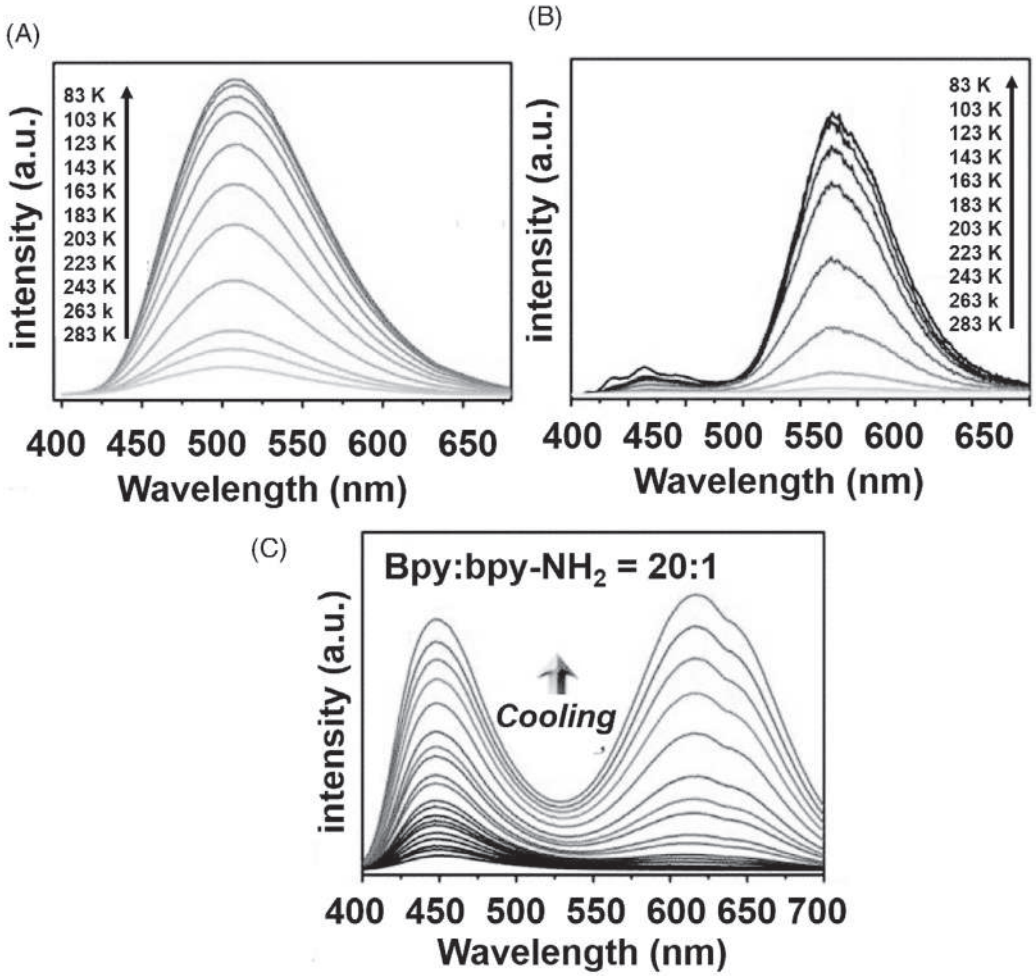

FIGURE 7.16 Photoluminescence spectra of (A) Ag_{12}bpy at λ_{ex} 365 nm and (B) Ag_{12}bpy-2 at λ_{ex} 280 nm. (C) Temperature-dependent PL profiles of the Ag_{12}bpy-2:NH_2 mixture. Reproduced with permission from ref.[53]. Copyright 2018, John Wiley and Sons.

polymer substrate results in a rigid structure that prevents molecular vibrations and thereby prevents nonradiative energy loss. The enhanced stability and efficient luminescence of MOFs will allow them to be used in a variety of applications, including sensors, catalysis, and so on.

7.4.5 Single-to-dual emission transformation

Dual-emissive luminescent materials are potential candidates for sensing applications due to their internal ratiometric signals. MOFs are promising in this regard and have not been explored fully. The transformation or isomerism of silver cluster nodes would enable us to achieve dual-emissive MOFs and allow us to understand their structure-property relationships. As we have mentioned in section 7.4.2, solvent plays an important role in the transformation or isomerization of a core in MOFs from one geometry to another.[53] In such cases, single-to-dual emission transformation was evident. In one of the examples, $[Ag_{12}(TBT)_8(TFA)_4(bpy)_4]_n$, denoted as Ag_{12}bpy MOF shows a single-emission behavior at a particular λ_{ex} at 365 nm; however, when this MOF was treated with solvent, a dual-emissive product $[(Ag_{12}(TBT)_6(TFA)_6(bpy)_3)]_n$, denoted as Ag_{12}bpy-2 MOF was obtained, *via* cluster-node rearrangement or isomerization. When crystals of Ag_{12}bpy were dissolved in a mixture of DMAc and toluene, entirely new hexagonal crystals of Ag_{12}bpy-2 were obtained. However, a reversible rearrangement was observed when the crystals of Ag_{12}bpy-2 were dissolved in a mixture of acetonitrile and ethanol. The dissolution and recrystallization lead to the reversible transformation of one MOF into another. This structural change at the cluster nodes led to a change in luminescence associated with these MOFs, and single-to-dual emission was observed. This study shows that this transformation is reversible and depends on the choice of the solvent(s). This structural rearrangement of the core triggered by solvent(s) is directly responsible for a substantial change in their emission properties. Therefore, a solvent-triggered single green emission of Ag_{12}bpy gets converted into a dual red-blue emission from Ag_{12}bpy-2 at low temperature (Fig. 7.16).[53] Furthermore, the crystals of Ag_{12}bpy-2 were dissolved in a solution of DMAc and toluene (3:1) containing bpy-NH_2 to ascertain whether a linker exchange is possible or not. Structural analysis after crystallization of the product showed that mixed linker MOF, namely, Ag_{12}bpy-2/NH_2 was obtained. The mixed linker MOF is isoreticular with Ag_{12}bpy-2. The bpyNH_2 linker has a strong influence on the blue emission component. In Ag_{12}bpy/NH_2, different molar ratios of linkers were used and an optimized concentration of 20:1 (bpy to bpyNH_2) was employed in which the emission intensity increases in both blue and red regions upon excitation at 365 nm, and the temperature was varied between 83–293 K (Fig. 7.16C).[53] These results demonstrate that by incorporating mixed linkers in the same framework in various molar ratios, modulation of the emission can occur even when one of the linkers is in trace quantities. In this way, single-crystal to single-crystal transformation results in a single-to-dual emission transformation.

The organic linker plays an important role in tuning the electronic properties of MOFs.[47–59] In a recent study, the incorporation of a functional group in the organic linker was realized to alter the electronic properties in MOFs.[72] For example, Ag_{12}bpy was sensitive to oxygen; however, replacing bpy with bpyNH_2 linker modulates the emission of this system, wherein a ratiometric oxygen sensing was achieved with greater sensitivity (Fig. 7.8D). This is the first report of fluorescence-phosphorescence dual-emissive MOF which provides an outstanding

limit of detection and response speed. This indicates that introduction of the $–NH_2$ group tunes the electronic properties. To further understand the functional substitution on the organic linker, electron-donating ($–CH_3$) and electron-withdrawing (–F) groups on the organic linker were used independently in the MOF construction. A single phosphorescence emission was observed in both $–CH_3$ and –F organic linkers containing MOFs due to the absence of fluorescence in these linkers. In $Ag_{12}bpyNH_2$, luminescence increases considerably by over 4-fold compared to $Ag_{12}bpy$. This could be due to the $–NH_2$ group substitution which may alter the electronic properties of MOF and induces intersystem crossing from the singlet to the triplet state.[72] The efficient luminescence and well-organized cluster arrangement in the MOFs could enable these assembled materials useful for various applications like sensing, catalysis, etc.

7.4.6 Computational studies

DFT calculations were performed to understand the mechanism of the energy transfer process in silver cluster-based MOFs. In $[(Ag_{12}(TBT)_6(TFA)_6(CH_3CN)_6]\cdot CH_3CN$ NC, DFT calculation shows that a weak luminescence arises due to the combination of LMCT and metal-centered transitions. In $[Ag_{12}(TBT)_8(TFA)_4(bpy)_4]_n$, the luminescence originates from MLCT (Ag(I)→bpy) excited state along with LLCT (ligand (S, O)–to–ligand (bpy) charge transfer) followed by intersystem crossing (ISC).[47] DFT calculations were also performed to understand the structure-luminescence relationship in substituted linkers such as $Ag_{12}bpyNH_2$. In $Ag_{12}bpy$, a single luminescent peak was observed; however, in $Ag_{12}bpyNH_2$ dual luminescent peaks at 463 nm and 620 nm were observed. These emission peaks originated from two triplet excited states (T_1 and T_2) mainly due to cluster-centered transitions (a mixture of LMCT and metal-center transitions) and intra-ligand transitions as shown in Fig. 7.17.[53] From the results, changing the structure of the cluster provides an efficient pathway to tune the electronic structure and luminescence of MOFs. Therefore, introducing the $–NH_2$ group into the linker (bpy) considerably helps in modulating the molecular energy levels.

7.5 Applications

7.5.1 Sensing

MOFs are potential sensing candidates. $Ag_{12}bpy$ MOF senses oxygen and ethanol vapor. The crystals of this material on exposure to O_2/air rapidly quench their luminescence. It was studied that MOF shows a short response time, hypersensitivity, good stability, and reproducibility that indicates its outstanding performance for oxygen sensing. This material may be useful for many practical applications such as chromogenic oxygen indicators in food processing, anaerobic conditions, etc.[47] $Ag_{12}bpy$ also shows real-time sensing of ethanol traces in air or breath of individuals on consuming alcohol. $Ag_{12}bpy$ was found to be stable and retains morphology and crystallinity after exposure to O_2/air, ethanol traces, etc.[47] In another example, luminescence studies of $Ag_{10}bpy$ MOF show interesting features in distinguishing chloromethanes such as dichloromethane, chloroform, and tetrachloromethane. This material shows its stability even after ten cycles.[57] In another example, $Ag_{12}bpz$ MOF was embedded

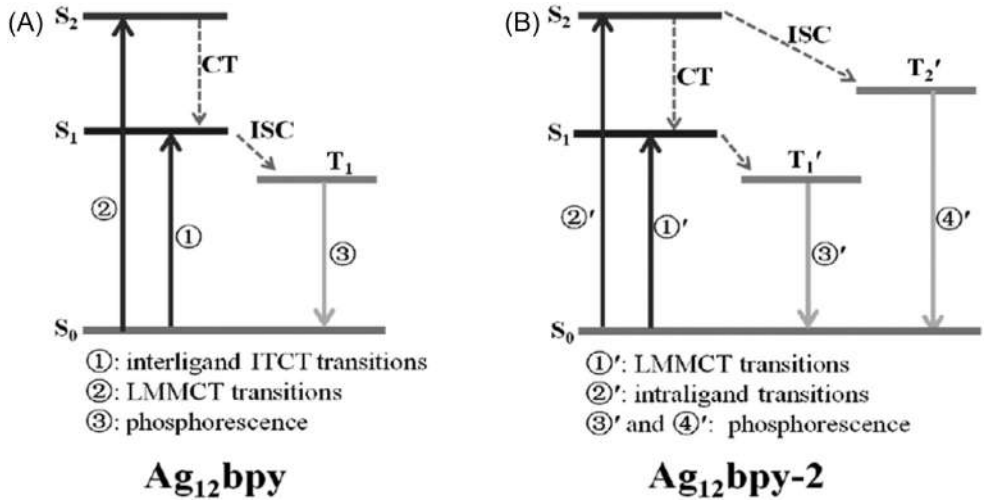

FIGURE 7.17 Schematic representation of energy transfer of (A) Ag_{12}bpy and (B) Ag_{12}bpy-2, respectively. Acronyms: ISC intersystem crossing; CT charge transfer; S_0 ground state and the subscript in each singlet (S) or triplet (T) is nonspecific. Reproduced with permission from ref.[53]. Copyright 2018, John Wiley and Sons.

into polymer substrates which lead to the increase in stability and efficient luminescence. Ag_{12}bpz polymerized membrane shows rapid and cyclic detection of nitrobenzene (NB).[56] To summarize, the applications of MOFs are emerging and open up a new area in stable silver cluster-based materials.

7.5.2 Dual-function luminescence switching

In Ag_{12}bpy MOF, ultrafast dual-function luminescent switching was observed, which could be attributed to rigid open channels and electronic properties associated with the system. Upon exposure to O_2, the luminescence of Ag_{12}bpy MOF switches off. However, the same MOF shows multicolor luminescence upon exposure to volatile organic compounds (VOCs). The host–guest relationship in this system can be attributed to the stable open channels which can be used for a wide range of applications. Switching-off luminescence upon exposure to O_2 and switching-on luminescence (multicolor) upon exposure to VOCs offer unique ultrafast dual-functioning in this system. The green luminescence of Ag_{12}bpy quenches upon exposure to air/O_2 (turn-off) and exhibits multicolor emission upon exposure to VOCs (turn-on) and the MOF behaves as an ultrafast dual-function switch (Fig. 7.15). These properties of Ag_{12}bpy could be useful for real-time sensing.[47]

7.6 Summary and future perspectives

In this chapter, we discussed the recent developments in the design, synthesis, and characterizations of 1D long chain structures of NCs and, 2D and 3D NC-based MOFs, and

their applications. NC-based MOFs are a novel class of solids associated with metal-rich nodes, and exhibit the integrated properties of component NCs and organic linkers. NC-based MOFs gained importance due to their enhanced stability, rigid structure, porous nature, and efficient luminescence as compared to the pristine silver NCs. Many of these MOFs have been successfully embedded in a polymer matrix and the properties of the frameworks in the matrix were retained, which could lead to their use in optoelectronic devices. A few MOFs have shown an interesting feature in terms of flexibility and dynamic behaviour in the framework structure upon solvent interaction. The properties of the frameworks are directly controlled by the structure and number of metal atoms in NC nodes, as well as the nature of the organic linkers. To summarise, we highlighted the various synthetic approaches for the formation of 1D long-chain structures of NCs, as well as 2D and 3D NC-based MOFs with rich architectural diversity, metal rich nodes, and concomitant properties, paving the way for the fabrication of rigid 2D and 3D framework solids for advanced applications. We believe that this new field encourages more scientists to explore this area.

List of abbreviation

ACN	Acetonitrile,
adm	1-Ethynyladamantane,
amt	2-Acetamido-5-methyl-1,3,4- thiadiazole,
bpy	4,4'-Bipyridine,
BDT	1,3-Benzenedithiol,
BMA	Butyl methacrylate,
bpb	1,4-Bis(4- pyridyl)benzene,
bpe	*Trans*-1,2-bis(4-pyridyl)ethylene)],
$bpyNH_2$	3-Amino-4,4′-bipyridine,
bpa	1,2-Bis(4-pyridyl)ethane,
$bpzNH_2$	1,4-Bis (pyrid-4-yl)benzenamine,
CH_3OH	Methanol,
CH_3CN	Acetonitrile,
$C_2B_{10}H_{10}S_2$	1,2-Dithiolate-o-carborane,
$CF_3SO_3^-$	Trifluromethane sulfonate,
cppp	2,5-Bis(4-cyanophenyl)-1,4-bis(4-(pyridine-4-yl)-phenyl)-1,4-dihydropyrrolo[3,2-*b*]pyrrole,
dpd	Dipyridin-4-yl-diazene,
DMF	Dimethylformamide,
DMAc	N, N-dimethylethanamide,
DPPM	Bis(diphenylphosphinomethane),
EtOH	Ethanol,
NO_3^-	Nitrate ion,
pyz	Pyrazine,
o-pch	2-Pyridine carboxylic hydrazide,
m-pch	3-Pyridine carboxylic hydrazide,
p-pch	4-Pyridine carboxylic hydrazide,
PPh_3	Triphenylphosphine,
$PhSO_3H$	Benzenesulfonic acid,
SBu	n-Butanethiolate,
S^iPr	Isopropyl thiolate,
SCy	Cyclohexyl thiolate,
SEt	Ethanethiolate,
SPh	Benzenethiol,

S-nC_5H_{11}	1-Pentanethiol,
SC_6H_{11}	Cyclohexanethiolate,
TBT	Tertiarybutylthiolate,
TFA	Trifluoroacetate,
tppa	Tris(4-pyridylphenyl)-amine,
tpp	5,10,15,20-Tetra(4-pyridyl)porphyrin,
tppe	1,1,2,2-tetrakis(4-(pyridin-4-yl)phenyl)-ethene,
TEGDMA	Triethylene glycol dimethacrylate

References

1. Chakraborty I, Pradeep T. Atomically precise clusters of noble metals: emerging link between atoms and nanoparticles. *Chem Rev*. 2017;117:8208–8271.
2. Du Y, Sheng H, Astruc D, Zhu M. Atomically precise noble metal nanoclusters as efficient catalysts: a bridge between structure and properties. *Chem Rev*. 2018;120:526–622.
3. Chakraborty P, Nag A, Chakraborty A, Pradeep T. Approaching materials with atomic precision using supramolecular cluster assemblies. *Acc Chem Res*. 2019;52:2–11.
4. Li B, Huang RW, Qin JH, et al. Thermochromic luminescent nest-like silver thiolate cluster. *Chem - A Eur J*. 2014;20:12416–12420.
5. Pradeep T, Mohammad B, Ghosh A, et al. Camouflaging structural diversity: co-crystallization of two different nanoparticles having different cores but the same shell. *Angew Chemie Int Ed*. 2018;58:189–194.
6. Fenske D, Anson CE, Eichhöfer A, et al. Syntheses and crystal structures of $[Ag_{123}S_{35}(S^tBu)_{50}]$ and $[Ag_{344}S_{124}(S^tBu)_{96}]$. *Angew Chemie - Int Ed*. 2005;44:5242–5246.
7. Anson CE, Eichöfer A, Issac I, et al. Synthesis and crystal structures of the ligand-stabilized silver chalcogenide clusters $[Ag_{154}Se_{77}(Dppxy)_{18}]$, $[Ag_{320}(S^tBu)_{60}S_{130}(Dppp)_{12}]$, $[Ag_{352}S_{128}(S^tC_5H_{11})_{96}]$, and $[Ag_{490}S_{188}(S^tC_5H_{11})_{114}]$. *Angew Chemie - Int Ed*. 2008;47:1326–1331.
8. Wang ZY, Wang MQ, Li YL, et al. Atomically precise site-specific tailoring and directional assembly of superatomic silver nanoclusters. *J Am Chem Soc*. 2018;140:1069–1076.
9. Yang H, Wang Y, Zheng N. Stabilizing subnanometer Ag(0) nanoclusters by thiolate and diphosphine ligands and their crystal structures. *Nanoscale*. 2013;5:2674–2677.
10. Dar WA, Bodiuzzaman M, Ghosh D, et al. Interparticle reactions between silver nanoclusters leading to product cocrystals by selective cocrystallization. *ACS Nano*. 2019;13:13365–13373.
11. Li Y-L, Wang Z-Y, Ma X-H, Luo P, Du C-X, Zang S-Q. Distinct photophysical properties in atom-precise silver and copper nanocluster analogues. *Nanoscale*. 2019;11:5151–5157.
12. Dhayal RS, Lin YR, Liao JH, et al. $[Ag_{20}\{S_2P(OR)_2\}_{12}]$: a superatom complex with a chiral metallic core and high potential for isomerism. *Chem A Eur J*. 2016;22:9943–9947.
13. Dhayal RS, Liao JH, Liu YC, et al. $Ag_{21}\{S_2P(O^iPr)_2\}_{12}]^+$: an eight-electron superatom. *Angew Chemie - Int Ed*. 2015;54:3702–3706.
14. Joshi CP, Bootharaju MS, Alhilaly MJ, Bakr OM. $[Ag_{25}(SR)_{18}]^-$: The "Golden" silver nanoparticle. *J Am Chem Soc*. 2015;137:11578–11581.
15. Khatun E, Bodiuzzaman M, Sugi KS, et al. Confining an Ag_{10} core in an Ag_{12} shell: a four-electron superatom with enhanced photoluminescence upon crystallization. *ACS Nano*. 2019;13:5753–5759.
16. AbdulHalim LG, Bootharaju MS, Tang Q, et al. $\{Ag_{29}(BDT)_{12}(TPP)_4\}$: a tetravalent nanocluster. *J Am Chem Soc*. 2015;137:11970–11975.
17. Jana A, Chakraborty P, Dar WA, et al. Dual emitting ag_{35} nanocluster protected by 2-pyrene imine thiol. *Chem Commun*. 2020;56:12550–12553.
18. Yang H, Wang Y, Huang H, et al. All-thiol-stabilized Ag_{44} and $Au_{12}Ag_{32}$ Nanoparticles with single-crystal structures. *Nat Commun*. 2013;4:2422.
19. Desireddy A, Conn BE, Guo J, et al. Ultrastable silver nanoparticles. *Nature*. 2013;501:399–402.
20. Wang QM, Lin YM, Liu KG. Role of anions associated with the formation and properties of silver clusters. *Acc Chem Res*. 2015;48:1570–1579.
21. Teranishi T, Sugawara A, Shimizu T, Miyake M. Planar array of 1D gold nanoparticles on ridge-and-valley structured carbon. *J Am Chem Soc*. 2002;124:4210–4211.

22. Yonezawa T, Onoue SY, Kimizuka N. Metal coating of DNA molecules by cationic, metastable gold nanoparticles. *Chem Lett*. 2002;12:1172–1173.
23. Yuichi N, Hironori T, Yasushi Y, Tatsuya T. Subnanometer-sized gold clusters with dual molecular receptors: synthesis and assembly in one-dimensional arrangements. *Chem Lett*. 2005;34:1638–1639.
24. Yokoyama T, Hirata N, Tsunoyama H, Negishi Y, Nakajima A. Characterization of floating-gate memory device with thiolate-protected gold and gold-palladium nanoclusters. *AIP Adv*. 2018;8.
25. Jones CW, Tsuji K, Davis ME. Organic-functionalized molecular sieves as shape-selective catalysts. *Nature*. 1998;393:52–54.
26. Furukawa H, Cordova KE, O'Keeffe M, Yaghi OM. The chemistry and applications of metal-organic frameworks. *Science*. 2013;341 1230444-1-12.
27. Zhou HC, Long JR, Yaghi OM. Introduction to metal-organic frameworks. *Chem Rev*. 2012;112:673–674.
28. Li JR, Sculley J, Zhou HC. Metal-organic frameworks for separations. *Chem Rev*. 2012;112:869–932.
29. Horcajada P, Gref R, Baati T, et al. Metal-organic frameworks in biomedicine. *Chem Rev*. 2012;112:1232–1268.
30. James SL. Metal-organic frameworks. *Chem Soc Rev*. 2003;32:276–288.
31. Allendorf MD, Bauer CA, Bhakta RK, Houk RJT. Luminescent metal-organic frameworks. *Chem Soc Rev*. 2009;38:1330–1352.
32. Zhou HCJ, Kitagawa S. Metal-organic frameworks (MOFs). *Chem Soc Rev*. 2014;43:5415–5418.
33. Furukawa H, Ko N, Go YB, et al. Ultrahigh porosity in metal-organic frameworks. *Science*. 2010;329:425–428.
34. Schneemann A, Bon V, Schwedler I, Senkovska I, Kaskel S, Fischer RA. Flexible metal-organic frameworks. *Chem Soc Rev*. 2014;43:6062–6096.
35. Kinoshita Y, Matsubara I, Higuchi T, Saito Y. The crystal structure of bis(Adiponitrilo)copper(I) nitrate. *Bull Chem Soc Jpn*. 1959;32:1221–1226.
36. Block BP, Rose SH, Schaumann CW, Roth ES, Simkin J. Coordination polymers with inorganic backbones formed by double- bridging of tetrahedral elements. *J Am Chem Soc*. 2002;84:3200–3201.
37. Berlin AA, Matveeva NG. Polymeric chelate compounds. *Russ Chem Rev*. 1960;29:119.
38. Knobloch FW, Rauscher WH, Knobloch FW, Rauscher WH. Coordination polymers of Copper(II) prepared at liquid-liquid interfaces. *J Polym Sci*. 1959;38:261–262.
39. Kubo M, Kishita M, Kuroda Y. Polymer molecules involving coordination links in the crystals of cupric oxalate and related compounds. *J Polym Sci*. 1960;48:467–471.
40. Tomic EA. Thermal stability of coordination polymers. *J Appl Polym Sci*. 1965;9:3745–3752.
41. Batten SR, Hoskins BF, Robson R. Two interpenetrating 3D networks which generate spacious sealed-off compartments enclosing of the order of 20 solvent molecules in the structures of $Zn(CN)(NO_3)(Tpt)_{2/3}$.Cntdot.Solv (Tpt = 2,4,6-Tri(4-Pyridyl)-1,3,5-Triazine, Solv = .Apprx.3/4C2H2Cl4.Cntdot.3/4CH3OH or .Apprx.3/2$CHCl_3$. Cntdot.1/3CH_3OH). *J Am Chem Soc*. 1995;117:5385–5386.
42. Hoskins BF, Robson R. Design and construction of a new class of scaffolding-like materials comprising infinite polymeric frameworks of 3D-linked molecular rods. a reappraisal of the zinc cyanide and cadmium cyanide structures and the synthesis and structure of the diamond-related frameworks $[N(CH_3)_4][CuIZnII(CN)_4]$ and CuI[4,4′,4″,4‴-Tetracyanotetraphenylmethane]BF_4.$XC_6H_5NO_2$. *J Am Chem Soc*. 1990;112:1546–1554.
43. Kitagawa S, Kawata S, Nozaka Y, Munakata M. Synthesis and crystal structures of novel copper(I) co-ordination polymers and a Hexacopper(I) Cluster of Quinoline-2-Thione. *J Chem Soc Dalt Trans*. 1993:1399–1404.
44. Kitagawa S, Matsuyama S, Munakata M, Emori T. Synthesis and crystal structures of novel one-dimensional polymers, $[\{M(Bpen)_X\}_\infty][M = CuI, X = PF_6, M = AgI, X = ClO_4^-$, Bpen =trans-1,2-Bis(2-Pyridyl)Ethylene] and $[\{Cu(Bpen)(CO)(CH_3CN)(PF_6)\}_\infty]$. *J Chem Soc Dalt Trans*. 1991:2869–2874.
45. Yaghi OM, Li H. Hydrothermal synthesis of a metal-organic framework containing large rectangular channels. *J Am Chem Soc*. 1995;117:10401–10402.
46. Riou D, Férey G. Hybrid open frameworks (MIL_n). Part 3 crystal structures of the HT and LT forms of MIL-7: a new vanadium propylenediphosphonate with an open-framework. Influence of the synthesis temperature on the oxidation state of vanadium within the same structural type. *J Mater Chem*. 1998;8:2733–2735.
47. Huang RW, Wei YS, Dong XY, et al. Hypersensitive dual-function luminescence switching of a silver-chalcogenolate cluster-based metal-organic framework. *Nat Chem*. 2017;9:689–697.
48. Wang ZY, Wang MQ, Li YL, et al. Atomically precise site-specific tailoring and directional assembly of superatomic silver nanoclusters. *J Am Chem Soc*. 2018;140:1069–1076.

49. Ma XH, Wang JY, Guo JJ, Wang ZY, Zang SQ. Reversible wide-range tuneable luminescence of a dual-stimuli-responsive silver cluster-assembled material. *Chin J Chem*. 2019;37:1120–1124.
50. Alhilaly MJ, Huang R-W, Naphade R, et al. Assembly of atomically precise silver nanoclusters into nanocluster-based frameworks. *J Am Chem Soc*. 2019;141:9585–9592.
51. Lu SH, Li Y, Yang SX, et al. Three silver coordination polymers with diverse architectures constructed from pyridine carboxylic hydrazide ligands. *Inorg Chem*. 2019;58:11793–11800.
52. Wang ZK, Sheng MM, Qin SS, et al. Assembly of discrete chalcogenolate clusters into a one-dimensional coordination polymer with enhanced photocatalytic activity and stability. *Inorg Chem*. 2020;59:2121–2126.
53. Huang RW, Dong XY, Yan BJ, et al. Tandem silver cluster isomerism and mixed linkers to modulate the photoluminescence of cluster-assembled materials. *Angew Chemie - Int Ed*. 2018;57:8560–8566.
54. Du XS, Yan BJ, Wang JY, Xi XJ, Wang ZY, Zang SQ. Layer-sliding-driven crystal size and photoluminescence change in a novel SCC-MOF. *Chem Commun*. 2018;54:5361–5364.
55. Cao M, Pang R, Wang QY, et al. Porphyrinic silver cluster assembled material for simultaneous capture and photocatalysis of mustard-gas simulant. *J Am Chem Soc*. 2019;141:14505–14509.
56. Wang YM, Zhang JW, Wang QY, et al. Fabrication of silver chalcogenolate cluster hybrid membranes with enhanced structural stability and luminescence efficiency. *Chem Commun*. 2019;55:14677–14680.
57. Dong XY, Huang HL, Wang JY, Li HY, Zang SQ. A flexible fluorescent SCC-MOF for switchable molecule identification and temperature display. *Chem Mater*. 2018;30:2160–2167.
58. Wei Z, Wu XH, Luo P, Wang JY, Li K, Zang SQ. Matrix coordination induced emission in a three-dimensional silver cluster-assembled material. *Chem A Eur J*. 2019;25:2750–2756.
59. Wu XH, Luo P, Wei Z, et al. Guest-triggered aggregation-induced emission in silver chalcogenolate cluster metal–organic frameworks. *Adv Sci*. 2019;6.
60. Wang JY, Huang RW, Wei Z, Xi XJ, Dong XY, Zang SQ. Linker flexibility-dependent cluster transformations and cluster-controlled luminescence in isostructural silver cluster-assembled materials (SCAMs). *Chem – A Eur J*. 2019;25:3376–3381.
61. Kang X, Zhu M. Intra-cluster growth meets inter-cluster assembly: the molecular and supramolecular chemistry of atomically precise nanoclusters. *Coord Chem Rev*. 2019;394:1–38.
62. De Nardi M, Antonello S, Jiang DE, et al. Gold nanowired: a linear $(Au_{25})_n$ polymer from Au_{25} molecular clusters. *ACS Nano*. 2014;8:8505–8512.
63. Antonello S, Dainese T, Pan F, Rissanen K, Maran F. Electrocrystallization of monolayer-protected gold clusters: opening the door to quality, quantity, and new structures. *J Am Chem Soc*. 2017;139:4168–4174.
64. Fei W, Antonello S, Dainese T, et al. Metal doping of $Au_{25}(SR)_{18}^-$ clusters: insights and hindsights. *J Am Chem Soc*. 2019;141:16033–16045.
65. Yuan P, Zhang R, Selenius E, et al. Solvent-mediated assembly of atom-precise gold–silver nanoclusters to semiconducting one-dimensional materials. *Nat Commun*. 2020;11:1–8.
66. Zhou K, Qin C, Wang XL, Shao KZ, Yan LK, Su ZM. Unexpected 1D self-assembly of carbonate-templated sandwich-like macrocycle-based Ag20S10 luminescent nanoclusters. *Cryst Eng Comm*. 2014;16:7860–7864.
67. Chen ZY, Tam DYS, Zhang LLM, Mak TCW. Silver thiolate nano-sized molecular clusters and their supramolecular covalent frameworks: an approach toward pre-templated synthesis. *Chem An Asian J*. 2017;12:2763–2769.
68. Li Q, Russell JC, Luo TY, et al. Modulating the hierarchical fibrous assembly of au nanoparticles with atomic precision. *Nat Commun*. 2018;9:1–7.
69. Wei X, Kang X, Yuan Q, et al. Capture of cesium ions with nanoclusters: effects on inter- A Nd intramolecular assembly. *Chem Mater*. 2019;31:4945–4952.
70. Wang Z, Sun YM, Qu QP, et al. Enclosing classical polyoxometallates in silver nanoclusters. *Nanoscale*. 2019;11:10927–10931.
71. Li X-Y, Su H-F, Xu J. A 2D layer network assembled from an open dendritic silver cluster Cl@Ag 11 N 24 and an N-Donor ligand. *Inorg Chem Front*. 2019;6:3539–3544.
72. Dong XY, Si Y, Yang JS, et al. Ligand engineering to achieve enhanced ratiometric oxygen sensing in a silver cluster-based metal-organic framework. *Nat Commun*. 2020;11:1–9.
73. Fuhr O, Dehnen S, Fenske D. Chalcogenide Clusters of Copper and Silver from Silylated Chalcogenide Sources. *Chem Soc Rev*. 2013;42:1871–1906.
74. Yam VWW, Au VKM, Leung SYL. Light-emitting self-assembled materials based on D_8 and D_{10} transition metal complexes. *Chem Rev*. 2015;115:7589–7728.

75. Chen Y, Liu C, Tang Q, et al. Isomerism in $Au_{28}(SR)_{20}$ nanocluster and stable structures. *J Am Chem Soc*. 2016;138:1482–1485.
76. Abdulhalim LG, Bootharaju M, Siddaramappa, et al. $Ag_{29}(BDT)_{12}(TPP)_4$: a tetravalent nanocluster. *J Am Chem Soc*. 2015;137:11970–11975.
77. Shultz AM, Sarjeant AA, Farha OK, Hupp JT, Nguyen ST. Post-synthesis modification of a metal-organic framework to form metallosalen-containing MOF materials. *J Am Chem Soc*. 2011;133:13252–13255.

CHAPTER

8

Synthesis of atomically precise clusters

Amoghavarsha R. Kini[a] *and Thalappil Pradeep*[b]

[a]DST Unit of Nanoscience (DST UNS) and Thematic Unit of Excellence, Department of Chemistry, Indian Institute of Technology Madras, Chennai, India
[b]Deepak Parekh Institute Chair Professor and Professor of Chemistry, Department of Chemistry, Indian Institute of Technology Madras, Chennai, India

8.1 Introduction

It has been an intense desire of chemists worldwide to precisely control nanoparticles at the atomic level and establishes structure-property relations. To achieve this objective, a method of synthesizing monodisperse nanoparticles was the need of the hour. However, the synthesis of nanoparticles with atomic precision seemed impractical until the discovery of Buckminsterfullerene (C_{60}), a ~1 nm diameter particle, in 1985 by Kroto et al.[1] Since then, many nanomaterials have been synthesized with exciting properties using simple equipment and chemicals.

Nanoclusters (NCs) are nanoparticles that have a few tens to a few hundred atoms in them. The size of NCs ranges from 1 to 3 nm, which is in between that of molecules and nanoparticles.[2] This is the size range where the transition of physical and chemical properties of materials occurs from a molecule-like behavior to more bulk-like behavior. Therefore, NCs are believed to bridge the gap in our knowledge at the transition state between molecules and bulk materials. So far, numerous NCs have been synthesized composed of different metals, of which gold (Au) and silver (Ag) NCs are notable ones. This chapter will discuss some of the commonly used techniques to synthesize NCs of Au and Ag.

8.2 Synthesis techniques of gold and silver nanoclusters

Noble metal NCs are generally synthesized using a suitable metal precursor, a protecting ligand, and a reducing agent to reduce metals to the desired size. Usually used protecting ligands are phosphines and thiols, but other ligands are also being explored, like alkynyl ligands.[3–6] Careful selection of the precursor, ligand, solvent, reducing agent, purification

Atomically Precise Metal Nanoclusters.
DOI: https://doi.org/10.1016/B978-0-323-90879-5.00013-5

methods, and separation techniques must be made to obtain pure clusters with high yield. There are other methods as well to synthesize NCs which will be discussed further in this section.[2]

8.2.1 Brust–Schiffrin method

Brust–Schiffrin method, commonly known as Brust method, is the first method used for synthesizing NCs using thiol ligands. Earlier, phosphines were used as protecting ligands to synthesize metal NCs. However, the NCs would slowly agglomerate in the solution phase, thereby losing their dispersibility. Brust et al., for the first time in 1994, synthesized Au NCs, using thiols as protecting ligands, that were stable in both solution and solid-state. They synthesized Au NCs using dodecanethiol ($C_{12}H_{25}SH$) as the protecting ligand and $NaBH_4$ as the reducing agent.[7]

Brust method is a two-phase synthesis using water and toluene as two solvent phases and tetraoctylammonium bromide as a phase transfer agent. An aqueous solution of hydrogen tetrachloroaurate ($HAuCl_4$) (30 mL, 30 mmol dm^{-3}) is mixed with a solution of tetraoctylammonium bromide in toluene (80 mL, 50 mmol dm^{-3}) and vigorously stirred until $AuCl_4^-$ is completely transferred into the organic layer. To this organic phase, 170 mg of dodecanethiol ligand was added. After some time, freshly prepared aqueous solution of $NaBH_4$ (25 mL, 0.4 mol dm^{-3}) was added to the organic phase with vigorous stirring. This reaction was let to stir for another 3 h, and the organic phase was separated and it was reduced to 10 mL by evaporating the solvent in a rotary evaporator. To this 10 mL solution, 400 mL ethanol was added (to remove excess thiol) and was kept at -18°C for 4 h. The brown precipitate formed was filtered and washed with ethanol, redissolved in 10 mL toluene, mixed with 400 mL ethanol, and kept at -18°C. The steps of filtration and washing of the precipitate with ethanol were repeated.[7] The overall reaction can be summarized in the following two equations:

$$AuCl_4\,(aq) + N(C_8H_{17})_4{}^+ + C_6H_5Me \rightarrow N(C_8H_{17})_4{}^+AuCl_4\,(C_6H_5Me)$$

$$m AuC1_4{}^-(C_6H_5Me) + nC_{12}H_{25}SH(C_6H_5Me) + 3me^- \rightarrow 4mCl^-(aq) + (Au_m)(C_{12}H_{25}SH)_n(C_6H_5Me)$$

This technique is used to synthesize many different clusters like $Au_{25}(SC_6H_{13})_{18}$, $Au_{38}(SC_{12}H_{25})_{24}$[8]. Brust synthesis method of NCs has become the basis for the synthesis of a plethora of clusters and has played an important role in developing modified synthetic approaches.

8.2.2 Modified Brust methods

Many groups worldwide have modified this technique to synthesize NCs of small size and tailor them to meet their needs. Variations have used new ligands, metal:ligand ratios, addition of co-ligands and varying synthetic conditions. One of the most studied gold clusters is Au_{25} NC, protected by a wide range of thiol ligands. This NC is primarily synthesized using a modified Brust method. Jin et al. have synthesized Au_{25} NC using 2-phenylethanethiol (PET) as the protecting ligand.[9] The procedure is as follows:

Around 62.0 mg (0.16 mmol) of $HAuCl_4 \cdot 3H_2O$ was dissolved in 4.4 mL of THF in a three-necked flask. This solution was cooled to 0°C in an ice bath for ~30 mins. The stirring was reduced to a very slow speed (~60 rpm), and 112 µL of PET (5 equivalents of the moles of Au) was slowly added to the gold solution. The yellow solution so formed was kept for stirring overnight, and the solution turned colorless. The stirring speed was increased to >1000 rpm, and an aqueous solution of 60 mg (10 equivalents of the moles of Au) $NaBH_4$ freshly dissolved in 1.5 mL ice-cold Millipore water was added rapidly in one shot. The reaction was then allowed to stir for another ~3h in ice-cold temperature. After 3h, the ice bath was removed, and the solution was warmed to room temperature in which it was stirred for over 60 h, which is the aging process of the cluster (performed to size focus the cluster). Some of the by-products of the reaction are then removed by simple centrifugation, and the supernatant so obtained is thoroughly washed with ethanol several times to purify the cluster. The cluster was then characterized, and the composition was determined to be $Au_{25}(PET)_{18}$.[9]

This technique with slight modifications has been used to synthesize various NCs, including Ag NCs. Like $Ag_{25}(DMBT)_{18}$,[10] $Ag_{29}(BDT)_{12}(TPP)_4$[11] and $Ag_{44}(DFBT)_{30}$ [12] (where, DMBT—2,4 dimethylbenzene thiol, BDT—1,3 benzene dithiol, TPP—triphenylphosphine and DFBT—3,4 difluorobenzenethiol) are some of the examples of Ag clusters synthesized by various modified Brust methods. Principally, in all these methods, varying metal:ligand ratios and solvents are used but the reducing agent, $NaBH_4$ is kept constant.

8.2.3 Ligand exchange induced structural transformation (LEIST)

Ligand exchange is a technique to alter an NC by mixing it with a different protecting ligand. It is a post-synthetic approach for obtaining new NCs. This technique may or may not result in a change in the core size of the NC, but there occurs either partial (yielding mixed ligand protected NC) or complete ligand exchange.[2,13] The starting material required for this reaction is just a pure sample of NC and a protecting ligand different from the one used for the NC. The ratio of cluster/thiol should be carefully selected, as a larger concentration of thiol will lead to the decomposition of the cluster, and a smaller concentration of thiol will result in incomplete exchange leading to the formation of clusters with mixed ligand shell.[14]

Hutchison group was the first to utilize this technique to replace phosphine ligands in undecagold (Au_{11}) with thiols without affecting the core size. The procedure followed by Hutchison group is as follows:

$Au_{11}(PPh_3)_8Cl_3$ **(1)**, the precursor for ligand exchange reaction, was synthesized as reported by Bartlett et al., in a type of modified Brust method. Ligand exchange occurs when **1** is stirred with excess thiol in a single organic phase or a biphasic system (Scheme 8.1). Hutchison et al. have performed ligand exchange of undecagold cluster with three different thiol ligands. Ligands used are octadodecanethiol (path a in Scheme 8.1), leading to the formation of **2**, (N,N-dimethylamino)ethanethiol hydrochloride (path b in Scheme 8.1), leading to the formation of **3** and 2-mercaptoethanesulfonate (MESA) (path c and d in Scheme 8.1), leading to the formation of **4** with a mixed ligand shell which upon treatment with excess MESA will yield **5**. The products formed are then dried and purified by precipitation or column chromatography.[14]

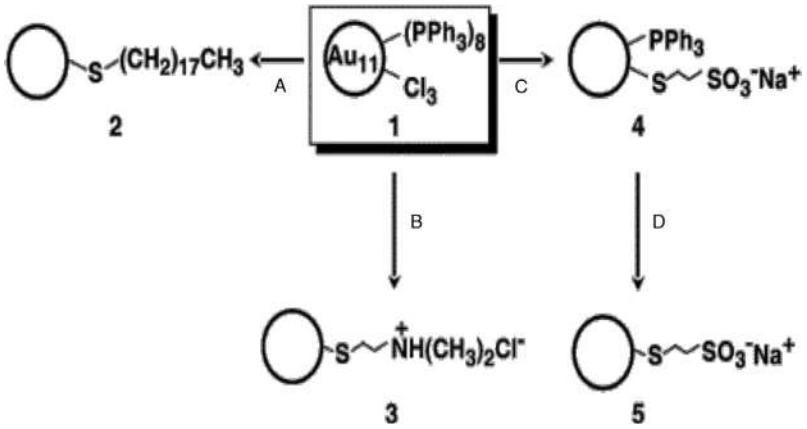

SCHEME 8.1 (A) ligand exchange of 1 in $CHCl_3$ at 55°C with excess octadecanethiol produces the thiol-stabilized particle **2**; (B) interfacial ($CHCl_3/H_2O$) ligand exchange of **1** at 55°C with (N,N-dimethylamino)ethanethiol hydrochloride produces the cationic thiol stabilized particle **3** in a single step; (C) interfacial ($CHCl_3/H_2O$) ligand exchange of **1** at 55°C with sodium 2-mercaptoethanesulfonate (MESA) produces the anionic particle **4**, which contains mixed ligand shell; (D) treatment of **4** with excess MESA in 1:1 THF/H_2O yields particle **5** containing only MESA in the ligand shell. Adapted with permission from ref [14]. Copyright 2002, American Chemical Society.

Similarly, many other clusters can undergo LEIST reactions reported by Pradeep et al.,[15–17] Niihori et al.,[18] Shichibu et al.,[19] and others. This technique is significant because it can synthesize clusters that cannot be efficiently synthesized by conventional techniques.

8.2.4 Solid-state synthesis

This method of synthesis of NCs was conceived by Pradeep et al. It is different from the conventional solution-phase synthesis because it reduces the diffusion of reactants during the reaction as they are mixed in the solid-state. Pradeep et al. synthesized the Ag_9 cluster protected by mercaptosuccinic acid (H_2MSA) with the composition, $Ag_9(H_2MSA)_7$ using the solid-state route.[20] The procedure is as follows:

$AgNO_3$ and H_2MSA (1:5 molar ratio) were ground thoroughly using a mortar until the color changes from colorless to orange. This reaction is feasible because of the strong affinity between silver and sulfur, and the product formed is a silver thiolate. Then sodium borohydride (five times the moles of $AgNO_3$) was added in the solid form, and the mixture was thoroughly ground, resulting in the formation of a brownish-black powder. The particle growth was controlled because of the lack of a protic solvent (which facilitates faster reduction to form metallic particles). To this mixture, around 15 mL of water was added slowly for 1 min, forming a cluster solution with strong effervescence due to the release of H_2 gas. The cluster solution was precipitated by adding excess ethanol, and the residue was washed with ethanol with repeated centrifugation and dispersion. The images taken at each step during the synthesis of the cluster are shown in Fig. 8.1.

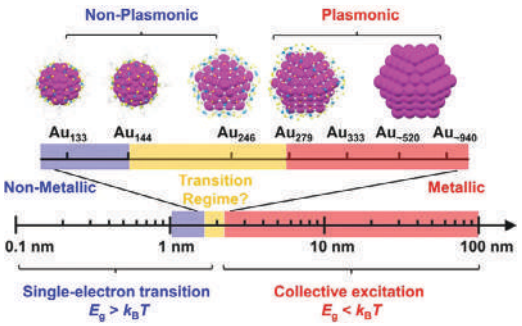

FIGURE 8.1 Images taken at different stages of the synthesis of Ag_9 cluster by the solid-state route. Adapted with permission from ref.[20]. Copyright 2010, American Chemical Society.

After washing with alcohol, a fine reddish-brown powder of cluster was obtained by solvent evaporation. The obtained product was identified to be a mixture of nanoparticles and Ag_9 clusters, separated by PAGE and was characterized by UV-Vis and Mass spectrometry.[20] Some of the other clusters synthesized with this technique are Ag_{44},[59] Ag_{55},[60] and Ag_{152} [61].

8.2.5 High-temperature synthesis

Pradeep et al. reported the synthesis of atomically precise NCs at relatively high temperatures (>80°C). This technique opens new avenues for high-temperature cluster research as these clusters are very stable at temperatures normally detrimental to the stability of samples prepared by other low-temperature techniques.[21] Clusters synthesized by this technique have the composition of $Ag_{75}(SG)_{40}$, as confirmed by MALDI MS supported by SEM/EDAX data. The Ag:S ratio is 1.83:1, and agrees well with the composition stated above.

Pradeep et al. followed the following procedure to synthesize $Ag_{75}(SG)_{40}$: A 20 mL aqueous solution of 5.88 mM $AgNO_3$ was mixed with a 20 mL aqueous solution of 2.034 mM glutathione ligand (GSH) and stirred for 5 min at 70°C. Then a 20 mL solution of 0.0112 mM formic acid in water was added to the above solution in stirring conditions. Formic acid acts as a reducing agent for the formation of the cluster. The temperature was kept constant throughout the reaction. With time, the color of the solution changed, indicating nucleation and growth of clusters. The reaction showed no color change after 3 h of stirring at 70°C, which indicated the completion of the reaction at 3 h. The cluster solution formed was reddish-brown, and the sample was characterized by mass spectrometry and UV-Visible spectroscopy. This cluster was reported to be stable even after several months. Continuous exposure to heat (70°C) did not affect the optical spectra of the cluster, contrary to other silver clusters, which are generally not stable above 50°C,[21] although certain stable clusters have been reported recently.[57]

8.2.6 Other notable techniques

In addition to the techniques mentioned above, several other methods are available to synthesize metal NCs. The principle of all the techniques is similar, that is, the metal precursor is reduced using a reducing agent to form clusters in presence of a ligand. Some of the techniques are mentioned below.

Microemulsion technique is a method for synthesizing very small NCs of the type Ag_n ($n < 10$), developed by Quintela et al.[22] These clusters were synthesized in water-in-oil microemulsions containing silver nitrate and sodium hypophosphite monohydrate as a mild reducing agent. A mixture of water/sodium bis(2-ethylhexyl) sulfosuccinate (AOT) in the molar ratio of 1:6, respectively, was used to prepare the microemulsion. The concentration of AOT was maintained at 0.1 M based on the overall volume of the microemulsion, and the concentrations of metal ion and the reducing agent were maintained at 0.1 M and 1 M, respectively, based on the volume of the aqueous phase used in the reaction. One of these microemulsions contains metal ions ($AgNO_3$), and the other contains reducing agent ($NaH_2PO_2.H_2O$). Silver microemulsions are then added slowly at room temperature over the sodium hypophosphite microemulsion under stirring. The transparent solution gradually changes from transparent, light yellow to dark brown, indicating the formation of clusters.

Sonochemical synthesis of silver NCs was conceived by Suslick et al.[23] This technique uses sonication to reduce Ag^+ ions. A polymer, PMAA [poly(methacrylic acid)], was used as a capping agent to prevent the aggregation of Ag NCs from forming large Ag nanoparticles. PMAA has carboxylic acid groups that have a strong affinity toward Ag ions, which is an excellent template for synthesizing Ag NCs. Suslick et al. reported this technique for synthesizing water-soluble fluorescent Ag NCs and also emphasized the importance of stoichiometry of PMMA and Ag^+ ions in the synthesis of these clusters. The clusters were synthesized as follows: 30 mL solution of PMMA-Ag^+ with different carboxylate/Ag^+ ratios were prepared using 45 mg of $AgNO_3$ in 5 mL water and 25 mL PMAA solution of different concentrations. The pH of this solution was then adjusted to 4.5 using 0.1 M HNO_3 or NaOH. The mixture was then purged with argon gas in a sealed vessel for 2 h at 20°C. The vessel containing the reaction mixture was then sonicated using an ultrasonic horn for around 180 min under argon flow.[23] The clusters thus obtained were cleaned and characterized for their quantum yield.

Electrochemical synthesis was used by Serra et al. for the synthesis of copper NCs.[24] These clusters were synthesized in galvanostatic conditions. It is based on reducing Cu ions produced during electrolysis from the soluble Cu anode at 25 mA/cm^2 current. The experiment was performed in a thermostated three-electrode electrochemical cell. The supporting electrolyte used here was 0.1 M tetrabutylammonium nitrate (TBAN) because of its stability under reaction conditions up to -1.8 V (vs Ag/AgCl). A Cu sheet was used as an anode, a Pt sheet of the same size was used as a cathode, and Ag/AgCl electrode was used as a reference. The working electrode (Cu) and counter electrode (Pt) were carefully cleaned and polished (using aluminum oxide for Pt electrode and sandpaper for Cu electrode) before synthesis. Both the electrodes were then sonicated with water in an ultrasonic bath. Additionally, electrochemical polishing was carried out on the Pt electrode by repeated cyclic voltammetry in 1M sulfuric acid. The cell was maintained under a nitrogen atmosphere (to remove oxygen and avoid oxidation), it was magnetically stirred and kept at a constant temperature of 25.0 ± 0.1°C during the whole process. The suspension formed was centrifuged at 8000 rpm for 10 min to separate the yellow solid and the colorless supernatant. The supernatant was discarded, and the residue is washed with water by continuous redispersion and centrifugation to eliminate TBAN and Cu ions. Finally, the obtained clusters were dissolved in a suitable solvent and were characterized. LDI-TOF mass spectrometry of the obtained cluster solution shows that the cluster had a composition of $[Cu_3Bu_3N_2]^-$ (at m/z value around 390) and $Cu_{14}Bu_2N(OH)_2]^-$ (at m/z of ~1050).[24]

There are many other methods for the synthesis of NCs like template mediated synthesis,[25,26] radiolytic synthesis,[27,28] microwave-assisted synthesis,[29] slow reduction process,[30] photoreduction[31,32] and many more which are not commonly used. These are some of the notable techniques with which we can synthesize homometallic NCs. The next section of this chapter will be focused on the synthesis of alloy NCs.

8.3 Synthetic techniques of gold and silver alloy nanoclusters

Alloy NCs comprise of two or more different metals in their core or the staples and show distinct properties compared to their homometallic counterparts. There are several approaches to synthesize alloy NCs, but all of them require at least two metal precursor salts, ligand, and a reducing agent.[13,33,34] Synthetic methods of alloy NCs include coreduction, metal exchange, galvanic and antigalvanic reduction, intercluster reactions, and LEIST techniques, which are discussed in greater detail in Chapter 16.

8.3.1 Coreduction method

The coreduction method involves the simultaneous reduction of 2 or more metals in presence of a ligand. When metals and ligands are mixed in a suitable solvent, they form metal–ligand complexes, which are then reduced to form clusters by adding an appropriate amount of reducing agent. This method was used during the initial trials to synthesize alloy NCs. Coreduction usually results in the formation of a mixture of different clusters. These mixtures can be separated using preparative thin-layer chromatography, column chromatography, electrophoretic separation, solvent extraction, etc.[13] Several types of alloy NCs have been synthesized by this method, one of the examples being $[NiAg_{24}(DMBT)_{18}]^{2-}$ ($NiAg_{24}$), whose synthesis will be discussed here.

Approximately 10 mg of $AgNO_3$ and 10 mg of $Ni(OAc)_2$ (nickel acetate) were dissolved in 5 mL MeOH, and 9 mL of DCM was added to the mixture. The reaction was cooled to 0°C and stirred at 900 RPM for 5 min. About 10 µL of 2,4-DMBT (2,4-dimethyl benzenethiol) was added while stirring the solution, which forms yellow-colored metal thiolates. This was followed by the addition of 10 mg of PPh_4Br, resulting in the formation of Ag-Ni-phosphine-thiolates. The reaction mixture was then stirred for 20 min before adding $NaBH_4$ (40 mg in 0.5 mL of ice-cold water), reducing the phosphine-thiolates to form $NiAg_{24}$ cluster. About 50 µL of triethylamine was added to stabilize the reaction. The reaction was then stirred at 0°C overnight, and the product was washed with water and methanol to remove excess thiols and unreacted $NaBH_4$.[35] This procedure can be adopted to synthesize many other clusters like, $MAu_{24}(SR)_{18}$ and $MAg_{24}(SR)_{18}$ (M = Ni/Pd/Pt), $Au_xAg_{44-x}(SR)_{30}$, $Au_xAg_{29-x}(BDT)_{12}(PPh_3)_4$, etc.[13,36]

8.3.2 Metal exchange method

In this method, an already synthesized cluster is used and a hetero metal is doped into it by reacting it with appropriate metal thiolates. The main disadvantage of the coreduction method is that we cannot usually synthesize alloy NCs of metals with significant differences in their electrochemical reduction potentials by chemical methods, but using this method, such NCs

can also be made. This method involves the reaction of an NC with a hetero metal thiolate which results in the exchange of metal atoms (either from the core or surface staple of the NC) with the hetero metal thiolate.[13] There are two principles in which metal exchange reactions work: the galvanic exchange and the antigalvanic exchange. These principles are discussed in more detail in Chapter 16.

Galvanic exchange is a type of metal exchange method for the synthesis of alloy NCs, wherein a metal ion of higher reduction potential will replace a metal atom (with lower reduction potential) from a cluster by reducing it. An example is the replacement of Ag atoms from $PtAg_{24}(SR)_{18}$ NC with Au ions furnished by $AuPPh_3Cl$, as reported by Bootharaju et al.[37] The procedure followed by them is as follows: $[PtAg_{24}(SR)_{18}]^{2-}$ NC was synthesized using coreduction method and was dissolved in DCM to form a solution with a concentration 5 mg/mL. About 10 μL of $AuPPh_3Cl$ solution (8 mg/mL in DCM) was added to the cluster solution and stirred for a desired amount of time. The formed product was dried and washed with methanol to remove unreacted materials and then dissolved in DCM for further characterization. Thereafter, several reactions like this were reported and a sequence of metal activity was introduced based on their reduction potentials: Fe > Cd >Co > Ni > Cu > Hg > Ag > Pd > Pt > Au. This sequence gave a hint as to which metal ions can be doped into which metal clusters.[13]

Some of the metal atoms like Cu and Ag, even though cannot reduce Au as such by galvanic theory, still replace Au atoms from their clusters to form alloy NCs. This technique of forming alloy NCs by adding metal ions with lower reduction potential than the metal atoms in the cluster is called an antigalvanic exchange. Wu showed that when an Au NC is reacted with Ag or Cu ions, the Au atoms would be replaced by Ag or Cu, forming alloy NCs.[38] He reacted $Au_{25}(SC_2H_4Ph)_{18}$ NC with $AgNO_3$ in the ratio 5.2:1 by which he synthesized Ag-doped Au NCs. For Cu doping, he reacted the Au_{25} NC with $Cu(NO_3) \cdot 3H_2O$ (ratio 11.0:1). After studying such reactions, he included Au NCs in the metal activity sequence signifying that NCs have different redox activity than their bulk counterparts. The reason for this is the size regime of NCs, where quantum effects are more pronounced. The modified metal activity sequence is Fe > Cd > Co > Ni > Pb > Au NCs > Cu > Hg > Ag > Pd > Pt > Au.[13]

8.3.3 Ligand exchange method

As previously discussed in this chapter, this technique is the reaction of a ligand with an already synthesized cluster, which results in a whole new cluster with either the same or different metal composition. Chapter 16 has a detailed account on the principles and examples of ligand exchange technique. The typical procedure for this method is synthesizing an NC and mixing it with the ligand of choice, which induces transformation in the NC and produces alloy NCs with desired properties.[13]

Bootharaju et al. reported the conversion of $[Pt_2Ag_{23}Cl_7(TPP)_{10}]$ NC to $[PtAg_{28}(BDT)_{12}(TPP)_4]4^-$ by addition of BDT (1,3-benzene dithiol), which brought about a structural transformation in the NC.[39] The $[Pt_2Ag_{23}Cl_7(TPP)_{10}]$ NC was synthesized using a coreduction technique using $Na_2PtCl_6 \cdot 6H_2O$ and $AgNO_3$ as the metal precursors and TPP (triphenylphosphine) as the protecting ligand. Then 175 mg of this NC was dissolved in 15 mL of acetone, and about 12 μL of BDT ligand was added to it under stirring condition. The solution was stirred for 12 h, after which the precipitate was collected by centrifugation. The residue was then

washed several times with methanol to remove excess ligands and finally it was dissolved in DMF. The solution was then characterized, and the composition of the cluster was found to be $[PtAg_{28}(BDT)_{12}(TPP)_4]^{4-}$.[39]

Another notable example of this ligand exchange method was reported by Zhu et al.[40] They reported the conversion of $[Pt_2Ag_{23}Cl_7(TPP)_{10}]$ NC to $[Pt_1Ag_{24}(SPhMe_2)_{18}](PPh_4)_2$ and then converted this NC to $[Pt_1Ag_{12}(dppm)5(SPhMe_2)_2]^{2+}$ NC. $[Pt_2Ag_{23}Cl_7(TPP)_{10}]$ was synthesized by the coreduction method, and 10 mg of this cluster was reacted with 200 µL of $SPhMe_2$ ligand in 10 mL DCM. About 10 mg of PPh_4Br was also added to provide the counter ion. The reaction was then stirred at room temperature for 30 min, and the solution obtained was dried by evaporating the solvent. The dried residue containing the $[Pt_1Ag_{24}(SPhMe_2)_{18}](PPh_4)_2$ cluster was washed with excess methanol several times, and a pure cluster was obtained by recrystallization. About 10 mg of this cluster was then redissolved in 10 mL DCM, and 30 mg of dppm (diphenylphosphinomethane) ligand was added under vigorous stirring condition. The reaction was continued for 15–20 min, and the solvent was evaporated to obtain a crude, dry product. $[Pt_1Ag_{12}(dppm)5(SPhMe_2)_2]^{2+}$ cluster was extracted from the crude product using 20 mL methanol, and this solution was allowed to age for 24 h in a freezer. The yellow solution so obtained was then centrifuged to remove the by-products of the reaction in the residue, and the supernatant was dried to get the pure $[Pt_1Ag_{12}(dppm)5(SPhMe_2)_2]^{2+}$ NC.[40]

Many other NCs have been synthesized by bringing about the structural transformation from the already synthesized clusters using ligand exchange. However, the procedures have to be optimized to obtain a better yield and improve the quality of clusters. The essential factors are the reaction time, reaction temperature, and aging time.

8.3.4 Metal deposition method

The metal deposition technique, also known as intramolecular metal exchange, is a technique where an alloy cluster is synthesized by the metal exchange method.[13,41] The foreign metal atom diffuses within the structure, responding to an external factor forming a new alloy cluster. Li et al. reported metal exchange reaction when Au_{25} NC was reacted with $AgNO_3$.[41] PET protected Au_{25} was synthesized as discussed previously in this Chapter. Around 10 mg of Au_{25} NC was dissolved in 10 mL of MeCN, and 0.67 mg of $AgNO_3$ (dissolved in MeCN) was added to the solution under stirring condition. The color of the solution changed from brown to dark green, and $[Ag_2Au_{25}(PET)_{18}]^+$ NC precipitated out. The mixture was then dried and washed several times with MeCN to remove unreacted $AgNO_3$ and other by-products of the reaction. In the Ag_2Au_{25} cluster, the Ag atoms occupy the surface staple position, and this cluster was used to carry out intramolecular metal exchange. This transformation occurs in two steps: self-metal exchange and the metal stripping. Fig. 8.2 shows how the two steps progress after an alloy cluster was synthesized.

In the first step of the reaction, one of the metal atoms doped onto the surface staples will diffuse into the cluster's core, and then Ag and Au atoms are stripped away from the surface staple producing the final product, $AgAu_{24}(SR)_{18}$. The transformation is brought about by dissolving around 2 mg of Ag_2Au_{25} NC in 10 mL of CH_2Cl_2 and adding 0.1 mL of PET ligand. This excess ligand stimulates the reaction, which slowly turns the green-colored solution to brown. After about 70 min, the reaction was stopped whereby all the Ag_2Au_{25} clusters were

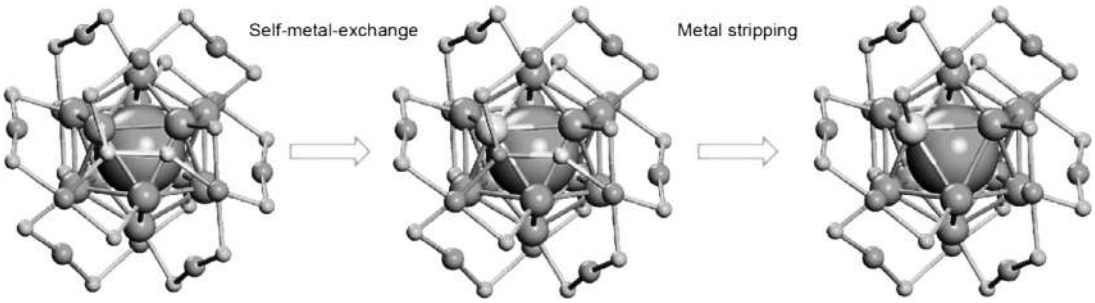

FIGURE 8.2 Proposed mechanism for the intramolecular metal exchange reaction in $[Ag_2Au_{25}(PET)_{18}]^+$ nanocluster. Adapted with permission from ref.[41]. Copyright 2018, Nanomaterials.

converted to $Ag_xAu_{25-x}(SR)_{18}^-$ ($x = 0$–2).[41] The same method was also reported by Wang et al.[42] in a hollow bi-icosahedral $Au_{24}(PPh_3)_{10}(SC_2H_4Ph)_5Cl_2$ NC to convert it into nonhollow $MAu_{24}(PPh_3)_{10}(SC_2H_4Ph)_5Cl_2$ ($M = Ag/Cu$) NC and also by Zheng et al. for the synthesis of $AuAg_{24}(MHA)_{18}$ (MHA—6-mercaptohexanoic acid) NC by reacting $Ag_{25}(MHA)_{18}$ NCs with Au-MHA complexes.[43]

8.3.5 Intercluster reactions

The intercluster reaction is one of the easiest techniques to obtain bi and trimetallic alloy NCs by mixing two NCs under suitable conditions. Krishnadas et al. investigated this phenomenon by mixing Ag_{44} and Au_{25} protected by 4-fluorothiophenol (FTP).[13,44] $Au_{25}(FTP)_{18}$ was synthesized by a ligand exchange method by adding FTP ligand to $Au_{25}(n\text{-BuS})_{18}$ (*n*-BuS—1-butanethiol), and $Ag_{44}(FTP)_{30}$ was synthesized using the solid-state route. These two clusters were then dissolved in CH_2Cl_2 to prepare the stock solution, and required volumes of both clusters were added to a reaction bottle containing 1 mL CH_2Cl_2. The solution was mixed with a pipette and not magnetically stirred. The color change was immediately observed after mixing the two clusters, and the reaction was monitored using MALDI MS and ESI MS. The reaction product is $Au_xAg_{44-x}(SR)_{30}$, but the main product is $Au_{12}Ag_{32}(FTP)_{30}$. This reaction was carried out at around ~30°C.[44]

Esma et al. reported the formation of a trimetallic alloy NC by mixing an alloy NC with a homometallic NC.[35] They studied the reaction between MAg_{28} (M–Ni/Pd/Pt) and Au_{25}, resulting in a trimetallic MAu_xAg_{28-x} cluster. The synthetic protocols followed by them are as follows: $MAg_{24}(DMBT)_{18}$ NC was synthesized using the coreduction method, which was then transformed to $MAg_{28}(BDT)_{12}(PPh_3)_4$ through ligand exchange by mixing with the required amounts of BDT and PPh_3 ligands and $Au_{25}(PET)_{18}$ was synthesized using modified the Brust method. MAg_{28} NC was taken in DMF and mixed with DCM solution of Au_{25}, and excess DMF was added. The solution was mixed using a pipette and not stirred.[35] The product formed was characterized (at regular time intervals to study the course of reaction) using absorption spectroscopy and mass spectrometry.

The methods mentioned above are the most commonly used techniques for the synthesis of alloy NCs. More information on the principles of synthesis of alloy NCs is provided in Chapter 16.

8.4 Synthesis of nanoclusters with larger core (>100 metal atoms)

NCs with larger cores are of great interest because they form a bridge between NCs and nanoparticles. The samples show plasmonic features like that of bulk metal when the core becomes bigger, as the size-dependent quantum confinement effect will be lost.[45,46] The synthesis of such large clusters is similar to the modified Brust method (discussed earlier in this chapter), which will be followed by size focusing to obtain stable clusters. These clusters are better characterized by mass spectrometry and single-crystal XRD as UV/Vis spectrum shows only one feature of surface plasmons and no molecular features are observable.

The section below will discuss the synthesis of different clusters with the increasing number of metal atoms.

8.4.1 Au_{102}(*p*-MBA)$_{44}$

Kalisman et al. reported the synthesis of Au_{102} NC and characterized it by MALDI TOF MS, TGA, XPS, UV/Vis spectroscopy and electron microscopy.[47] The synthesis was done by mixing aqueous solutions of *p*-MBA (para-mercaptobenzoic acid), NaOH, and $HAuCl_4$ to give a solution with 9 mM *p*-MBA and 3 mM $HAuCl_4$. Methanol was added to the solution to make it 48% (v/v). The mixture was kept for ~1 h at room temperature on a rocking platform to mix the solution thoroughly. A freshly prepared solution of 150 mM $NaBH_4$ in ice-cold water was added to the above solution, and the rocking was continued for about 5 h. The solution turned black, indicating the formation of Au NCs. The product was precipitated by adding either 80 mM ammonium acetate or 10 mM NaCl, then adding methanol (to 80%) to the solution. The solution was then centrifuged at around 13,000 g for 10 min. The pellet formed was dried in the air overnight and was redissolved in a minimum amount of water. The obtained supernatant was again treated with ammonium acetate and methanol (to 60%—to remove contaminants) and again centrifuged at 13,000 g for 10 min to precipitate the contaminants **(0)**. The supernatant obtained was repeatedly centrifuged to check for no further precipitation and then treated with ammonium acetate and methanol (to 80%) to separate the cluster **(1)**. The pellet **(0)** was then redispersed in water to improve the yield and then again treated with methanol (to 60%) and ammonium acetate to remove the contaminants. The supernatant was treated with methanol (to 80%) and centrifuged at 13,000 g for 10 min to precipitate the cluster **(2)**. The pellets **(1)** and **(2)** were dissolved in a minimum quantity of water and mixed.[47] This solution was then used to characterize the Au_{102}(*p*-MBA)$_{44}$ cluster. The formed NC particles had a mean diameter of 13.3Å with a standard deviation of 0.7Å, shown in Fig. 8.3**.**

8.4.2 Au_{191}(TBBT)$_{66}$

The synthesis of this cluster was reported by Amala Dass et al. They used MALDI MS and ESI MS along with single crystal XRD and UV/Vis spectroscopy to characterize this cluster.[48] The cluster was synthesized by mixing 500 mg of $HAuCl_4 \cdot 3H_2O$ and 700 mg of TOABr (tetraoctyl ammonium bromide, which acts as both phase transfer agent and stabilizing agent) in 50 mL ethyl acetate in a round bottom flask. The solution was stirred vigorously for 2 h, and 0.6 mL of TBBT (4-tert-butylbenzenethiol) ligand was added. The solution was stirred

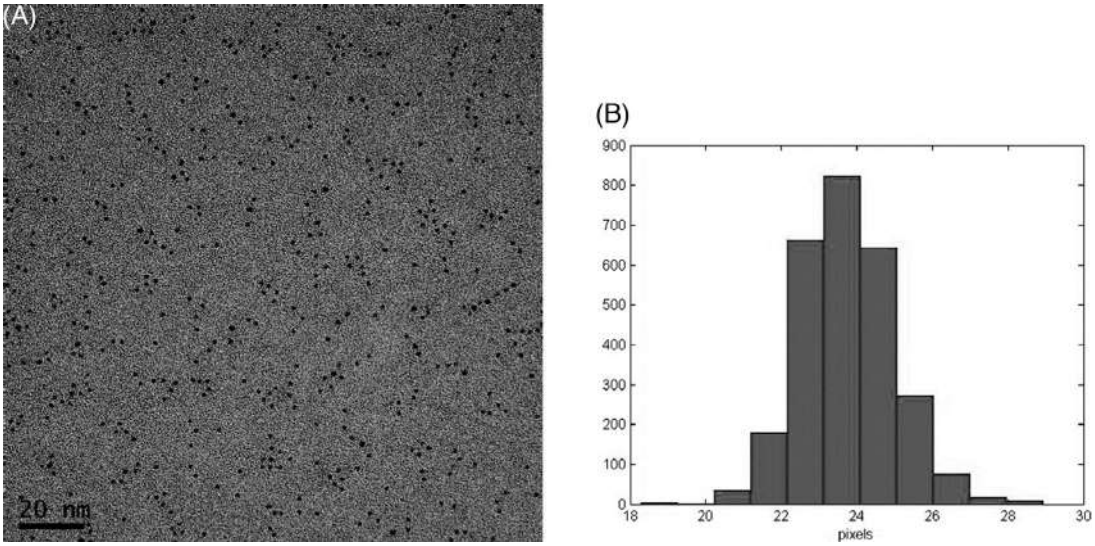

FIGURE 8.3 (A) Transmission electron micrograph of Au_{102} cluster. (B) Histogram showing number of particles (on *y*-axis) with diameters in number of pixels (on *x*-axis, 1 pixel = 0.56 Å. Adapted with permission from ref.[47]. Copyright 2011, American Chemical Society.

for another 4 h to form the metal–ligand complexes. The reaction was then reduced by adding 480 mg of $NaBH_4$ dissolved in 10 mL ice-cold water. The reaction was run for 24 h with constant stirring, and the solvent was removed by rotary evaporation. The dry product was washed with water and methanol to remove excess thiol. The product was then dissolved in toluene, and size focusing was carried out by mixing the cluster with excess TBBT ligand and heated to 90°C for ~18 h. The product was then precipitated by adding methanol and water and centrifuged at 4400 rpm for 5 min. The residue was then washed with water and methanol several times to remove excess thiols and other by-products. The product obtained was then dissolved in DCM and used for characterization.[48]

8.4.3 Au_{246}(*p*-MBT)$_{80}$

R. Jin et al. synthesized this NC to study the transition from molecular to plasmonic behavior in metal nanoparticles.[45] This cluster shows a nonmetallic character which was confirmed by the presence of a small bandgap. This cluster was synthesized by following a two-step size focusing method as previously described. About 1 mmol of $HAuCl_4$ was dissolved in 5 mL H_2O, and 1.16 mmol of TOABr (dissolved in 10 mL toluene) was added. This mixture was vigorously stirred for a few minutes, and the aqueous phase was removed. The $HAuCl_4$ is now transferred to the toluene phase by the action of TOABr. About 4 mmol *p*-MBT (para methylbenzene thiol) was added to the solution under stirring conditions. After 30 min of stirring, 10 mmol $NaBH_4$ dissolved in 5 mL ice-cold H_2O was added in one go. The color of the solution changed immediately to black. After about 10 min, the aqueous phase was again removed, and the toluene phase was dried by rotary evaporation. The residue obtained after evaporation is washed with methanol several times to remove excess thiol and other

by-products of the reaction. The product obtained was dissolved in CH_2Cl_2, which contained mixed size NCs, $Au_x(p\text{-MBT})_y$ and the solution was dried.

The mixed-size NCs were mixed with 1 mL *p*-MBT and 1 mL toluene, and the solution was heated to about 80°C and stirred at slow rpm. The reaction was carried out for another 10 h. The product obtained was washed with methanol to remove excess thiol, and the cluster was extracted with CH_2Cl_2. The Au_{246} clusters obtained were ~90% pure, but further purification was carried out by solvent fractionation using toluene/methanol to remove smaller nanoparticles. The product obtained after purification was used for subsequent characterization and crystallization.[45]

8.4.4 $Au_{\sim 2000}(SR)_{\sim 290}$

This cluster is around ~3.8 nm diameter reported by Sandra Vergara et al.[49] The synthesis is similar to previously discussed large clusters, which involves synthesizing the cluster followed by thermochemical etching, otherwise known as size focusing. About 30 mmol of $HAuCl_4$ was dissolved in 15 mL of H_2O and the mixture was mixed with 36.7 mmol TOABr in 15 mL toluene and it was stirred for 30 min leading to the phase transfer of Au salt into toluene forming an orange-colored organic layer. The aqueous phase was removed, and around ~0.1 mmol hexanethiol ligand was added to the organic layer with constant stirring for another 1 h. Then, 2.5 M $NaBH_4$ dissolved in 2mL ice-cold water was added to the reaction mixture and stirred for another 2 h. The brown-colored organic layer was then decanted and dried by rotary evaporation. The product was washed with methanol several times, and the final product formed was dissolved in toluene.

About 100 mg of the product was treated with 1mL hexanethiol ligand and thermochemically etched by heating to ~90°C for ~14 days. The product obtained was rewashed with methanol to remove excess thiol. The cleaned product was extracted using toluene for several days by adding 10 mL of toluene to the solid product and leaving it undisturbed overnight. The Au_{2000} cluster slowly diffused from the solid phase to the toluene phase making it sightly red. This process was repeated several times to increase the yield of the product. After extraction, solvent fractionation was performed using toluene/methanol in 3:2 ratio to obtain pure clusters.[49]

Large clusters are of great interest as they can be studied to understand the transition between a molecular cluster and a plasmonic nanoparticle. Recently, R. Jin et al. reported the critical number of Au atoms for this transition, which falls between Au_{246} and Au_{279}, as shown in Fig. 8.4.

Clusters with other cores such as Au_{110}, Au_{133}, Au_{144}, Au_{191}, Au_{279}, Au_{329}, $Au_{\sim 500}$, $Au_{\sim 900}$, $Au_{\sim 1400}$, etc., have also been reported.[48,50–57]

In Tables 8.1 and 8.2, we present a concise summary of various synthetic processes which are commonly used in NC literature.

8.5 Summary and future perspectives

This chapter dealt with the synthetic techniques for some notable clusters which are commonly used for various studies. But reliable protocols to obtain clusters of the desired

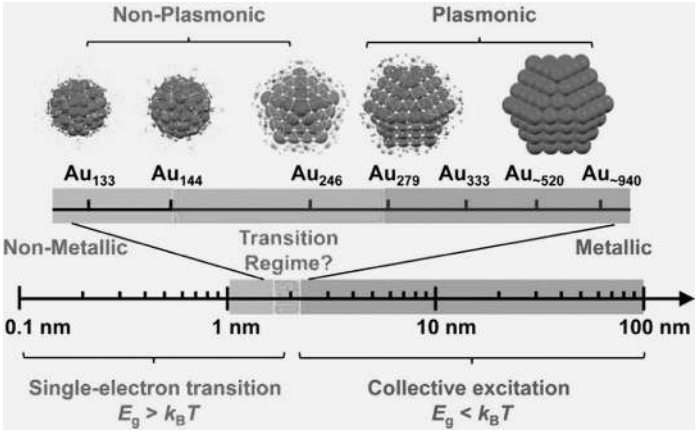

FIGURE 8.4 Schematic showing the transition of clusters of large metalcore from nonmetallic state to metallic state. Adapted with permission from ref.[46]. Copyright 2021, American Chemical Society.

size with high purity are limited. Engineering ligands by altering the positions of functional groups through organic reactions could be a promising approach to synthesize new clusters. Exploring diverse types of ligands like alkynes and carborane thiols is also an approach to fulfilling this vision. Alloy NC synthesis can be performed by mixing metal salts and ligands or a homometallic cluster with metal thiolates. These clusters have been shown to exhibit altered properties as compared to their homometallic counterparts. New synthetic approaches should be designed to synthesize alloy NCs composed of more than three metals, resulting in high entropy alloy NCs. These NCs could be employed in catalysis, biomedicine, bioimaging, sensing, etc.[2,13] New synthetic approaches that can facilitate control over the number of atoms doped in a cluster and even the position where it gets doped will help enhance properties being explored.

Metal clusters with larger cores have been extensively studied in the case of Au, but other notable metals which form clusters like Ag are not studied. Ag can be used to synthesize large clusters, and their properties can be studied. These studies can even be extended toward the synthesis of large alloy NCs.

List of abbreviation

1,3-BDT	1,3-benzenedithiol
2,4-DMBT	2,4-dimethylbenzenethiol
3,4-DFBT	3,4-difluorobenzenethiol
DCM	dichloromethane
EDAX	Energy dispersive X-ray analysis
H_2MSA	Mercaptosuccinic acid
LDI-TOF MS	Laser desorption ionization – time of flight mass spectrometer
LEIST	Ligand exchange induced structural transformation
MALDI-MS	Matrix assisted laser desorption ionization – mass spectrometer
MeCN	acetonitrile
MESA	mercaptoethanesulphonate
NCs	Nanoclusters
PAGE	Poly-acrylamide gel electrophoresis
PET	2-phenylethanethiol
PMAA	Poly(methacrylic acid)

TABLE 8.1 Showing common homometallic clusters and their synthetic processes.

Method of synthesis	Cluster	Precursor salt/cluster	Ligand	References
Brust method and Modified Brust method	$Au_{25}(PET)_{18}$	$HAuCl_4{\cdot}3H_2O$	2-phenylethanethiol	9
	$Au_{25}(SG)_{18}$	$HAuCl_4{\cdot}3H_2O$	Glutathione	9
	$Ag_{25}(DMBT)_{18}$	$AgNO_3$	2,4-dimethylbenzenethiol	10
	$Ag_{29}(BDT)_{12}(TPP)_4$	$AgNO_3$	1,3 benzenedithiol and triphenylphosphine	11
LEIST	$Au_{36}(TBBT)_{24}$	$Au_{38}(PET)_{24}$	4-*tert*-butylbenzene thiol	58
	$Au_{28}(TBBT)_{20}$	$Au_{25}(PET)_{18}$	4-*tert*-butylbenzene thiol	58
	$Au_{133}(TBBT)_{52}$	$Au_{144}(PET)_{60}$	4-*tert*-butylbenzene thiol	58
Solid-state synthesis	$Ag_9(H_2MSA)_7$	$AgNO_3$	Mercaptosuccinic acid	20
	$Ag_{44}(SePh)_{30}$	$AgNO_3$	Benzeneselenol	59
	$Ag_{55}(BBS)_{31}$	$AgNO_3$	4-(tertbutyl) benzyl mercaptan	60
Solid-state synthesis	$Ag_{152}(PET)_{60}$	$AgNO_3$	2-phenylethanethiol	61
High-temperature synthesis	$Ag_{75}(SG)_{40}$	$AgNO_3$	Glutathione	21

TABLE 8.2 Showing common alloy nanoclusters and their synthetic processes.

Method of Synthesis	Cluster	Precursor salt/cluster	Ligand	References
Coreduction method	$Au_xAg_{44-x}(SPhF_2)_{30}$	$AuPPh_2PyCl + AgNO_3$	3,4-difluorobenzenethiol	62
	$MAg_{24}(DMBT)_{18}$ (M= Ni/Pd/Pt)	$AgNO_3 + Ni(OAc)_2/Pd(OAc)_2/K_2PtCl_4$	2,4-dimethylbenzenethiol	35
	$Au_xAg_{29-x}(BDT)_{12}(PPh_3)_4$	$AgNO_3$ + C18H15AuClP	1,3-benzenedithiol + Triphenylphosphine	36
LEIST	$[PtAg_{28}(BDT)_{12}(TPP)_4]$	$[Pt_2Ag_{23}Cl_7(TPP)_{10}]$	1,3-benzene dithiol	39
	$[Pt_1Ag_{24}(SPhMe_2)_{18}](PPh_4)_2$	$[Pt_2Ag_{23}Cl_7(TPP)_{10}]$	2,4-dimethylbenzenethiol	40
	$[Pt_1Ag_{12}(dppm)5(SPhMe_2)_2]$	$[Pt_1Ag_{24}(SPhMe_2)_{18}](PPh_4)_2$	Diphenylphosphino-methane	40
Metal exchange	$[Au_xPtAg_{24-x}(DMBT)_{18}]$	$[PtAg_{24}(DMBT)_{18}] + AuPPh_3Cl$	2,4-dimethylbenzenethiol	37
	Galvanic exchange			
	$Au_{23}Ag_2S_{12}$	$Au_{25}(PET)_{18} + AgNO_3$	2-phenylethanethiol	38
	Antigalvanic exchange			
Metal deposition method	$[Ag_2Au_{25}(PET)_{18}]$	$Au_{25}(PET)_{18} + AgNO_3$	2-phenylethanethiol	41
Intercluster reactions	$Au_{12}Ag_{32}(FTP)_{30}$	$Ag_{44}(FTP)_{30} + Au_{25}(FTP)_{18}$	4-fluorothiophenol	44
	$NiAu_{12}Ag_{16}(BDT)_{12}(TPP)_4$	$NiAg_{28}(BDT)_{12}(TPP)_4 + Au_{25}(PET)_{18}$	1,3-benzenedithiol + Triphenylphosphine + 2-phenylethanethiol	35

p-MBA	*para*-mercaptobenzoic acid
p-MBT	*para*-methylbenzenethiol
SEM	Scanning electron microscope
TBAN	Tetrabutyl ammonium nitrate
TBBT	4-tert butylbenzenethiol
THF	tetrahydrrofuran
TOABr	tetraoctylammoniumbromide
TPP	triphenylphosphine
XRD	X-ray diffraction

References

1. Kroto H, Heath J, O'Brien S, et al. C_{60}: Buckminsterfullerene. *Nature*. 1985;318:162–163.
2. Chakraborty I, Pradeep T. Atomically precise clusters of noble metals: emerging link between atoms and nanoparticles. *Chem Rev*. 2017;117:8208–8271.
3. Wang Y, Wan X-K, Ren L, et al. Atomically precise alkynyl-protected metal nanoclusters as a model catalyst: observation of promoting effect of surface ligands on catalysis by metal nanoparticles. *J Am Chem Soc*. 2016;138:3278–3281.
4. Yuan S-F, Li P, Tang Q, et al. Alkynyl-protected silver nanoclusters featuring an Anticuboctahedral kernel. *Nanoscale*. 2017;9:11405–11409.
5. Lei Z, Wan X-K, Yuan S-F, Wang J-Q, Wang Q-M. Alkynyl-protected gold and gold–silver nanoclusters. *Dalton Trans*. 2017;46:3427–3434.
6. Lei Z, Wan X-K, Yuan S-F, Guan Z-J, Wang Q-M. Alkynyl approach toward the protection of metal nanoclusters. *Acc Chem Res*. 2018;51:2465–2474.
7. Brust M, Walker M, Bethell D, Schiffrin DJ, Whyman R. Synthesis of thiol-derivatized gold nanoparticles in a two-phase liquid–liquid system. *J Chem Soc Chem Commun*. 1994;0(7):801–802.
8. Gaur S, Miller JT, Stellwagen D, Sanampudi A, Kumar CSSR, Spivey JJ. Synthesis, characterization, and testing of supported au catalysts prepared from atomically-tailored Au_{38} $(SC_{12}$ $H_{25})_{24}$ clusters. *Phys Chem Chem Phys*. 2012;14:1627–1634.
9. Wu Z, Suhan J, Jin R. One-pot synthesis of atomically monodisperse, thiol-functionalized Au_{25} nanoclusters. *J Mater Chem*. 2009;19:622–626.
10. Joshi CP, Bootharaju MS, Alhilaly MJ, Bakr OM. $[Ag_{25}$ $(SR)_{18}]^{-}$: the "Golden" silver nanoparticle. *J Am Chem Soc*. 2015;137:11578–11581.
11. AbdulHalim LG, Bootharaju MS, Tang Q, et al. Ag_{29} $(BDT)_{12}$ $(TPP)_4$: a tetravalent nanocluster. *J Am Chem Soc*. 2015;137:11970–11975.
12. Yang H, Wang Y, Huang H, et al. All-thiol-stabilized Ag_{44} and $Au_{12}Ag_{32}$ nanoparticles with single-crystal structures. *Nat Commun*. 2013;4:2422.
13. Khatun E, Pradeep T. New routes for multicomponent atomically precise metal nanoclusters. *ACS Omega*. 2021;6:1–16.
14. Woehrle GH, Warner MG, Hutchison JEL. Exchange reactions yield subnanometer, thiol-stabilized gold particles with defined optical transitions. *J Phys Chem B*. 2002;106:9979–9981.
15. Shibu ES, Muhammed MAH, Tsukuda T, Pradeep T. Ligand exchange of $Au_{25}SG_{18}$ leading to functionalized gold clusters: spectroscopy, kinetics, and luminescence. *J Phys Chem C*. 2008;112:12168–12176.
16. Habeeb Muhammed M, Ramesh S, Sinha S, Pal S, Pradeep T. Two distinct fluorescent quantum clusters of gold starting from metallic nanoparticles by pH-dependent ligand etching. *Nano Res*. 2008;1:333–340.
17. Muhammed H, A M, Pradeep T. Aqueous to organic phase transfer of Au_{25} clusters. *J Cluster Sci*. 2009;20:365–373.
18. Niihori Y, Matsuzaki M, Pradeep T, Negishi Y. Separation of precise compositions of noble metal clusters protected with mixed ligands. *J Am Chem Soc*. 2013;135:4946–4949.
19. Shichibu Y, Negishi Y, Tsukuda T, Teranishi T. LargeScale synthesis of thiolated Au_{25} clusters via ligand exchange reactions of phosphine-stabilized Au11 clusters. *J Am Chem Soc*. 2005;127:13464–13465.
20. Rao TUB, Nataraju B, Pradeep T. Ag_9 quantum cluster through a solid-state route. *J Am Chem Soc*. 2010;132:16304–16307.

21. Chakraborty I, Udayabhaskararao T, Pradeep T. High temperature nucleation and growth of glutathione protected ~Ag_{75} clusters. *Chem Commun*. 2012;48:6788.
22. Ledo-Suárez A, Rivas J, Rodríguez-Abreu CF, et al. Facile synthesis of stable subnanosized silver clusters in microemulsions. *Angew Chem Int Ed*. 2007;46:8823–8827.
23. Xu H, Suslick KS. Sonochemical synthesis of highly fluorescent Ag nanoclusters. *ACS Nano*. 2010;4:3209–3214.
24. Vilar-Vidal N, Blanco MC, López-Quintela MA, Rivas J, Serra C. Electrochemical synthesis of very stable photoluminescent copper clusters. *J Phys Chem C*. 2010;114:15924–15930.
25. Mathew A, Sajanlal PR, Pradeep T. A fifteen atom silver cluster confined in bovine serum albumin. *J Mater Chem*. 2011;21:11205–11212.
26. Shichibu Y, Negishi Y, Tsunoyama H, Kanehara M, Teranishi T, Tsukuda T. Extremely high stability of glutathionate protected Au_{25} clusters against core etching. *Small*. 2007;3:835–839.
27. Ershov BG, Henglein A. Time-resolved investigation of early processes in the reduction of Ag^+ on polyacrylate in aqueous solution. *J Phys Chem B*. 1998;102:10667–10671.
28. Linnert T, Mulvaney P, Henglein A, Weller H. Long-lived nonmetallic silver clusters in aqueous solution: preparation and photolysis. *J Am Chem Soc*. 1990;112:4657–4664.
29. Liu T, Su Y, Song H, Lv Y. Microwave-assisted green synthesis of ultrasmall fluorescent water-soluble silver nanoclusters and its application in chiral recognition of amino acids. *Analyst*. 2013;138:6558–6564.
30. Ghosh A, Udayabhaskararao T, Pradeep T. One-step route to luminescent $Au_{18}SG_{14}$ in the condensed phase and its closed shell molecular ions in the gas phase. *J Phys Chem Lett*. 2012;3:1997–2002.
31. Chakraborty I, Udayabhaskararao T, Deepesh GK, Pradeep T. Sunlight mediated synthesis and antibacterial properties of monolayer protected silver clusters. *J Mater Chem B*. 2013;1:4059–4064.
32. Zheng J, Dickson RM. Individual water-soluble dendrimer-encapsulated silver nanodot fluorescence. *J Am Chem Soc*. 2002;124:13982–13983.
33. Kang X, Li Y, Zhu M, Jin R. Atomically precise alloy nanoclusters: syntheses, structures, and properties. *Chem Soc Rev*. 2020;49:6443–6514.
34. Kawawaki T, Imai Y, Suzuki D, et al. Atomically precise alloy nanoclusters. *Chem – Eur J*. 2020;26:16150–16193.
35. Khatun E, Chakraborty P, Jacob BR, et al. Intercluster reactions resulting in silver-rich trimetallic nanoclusters. *Chem Mater*. 2020;32:611–619.
36. Soldan G, Aljuhani MA, Bootharaju MS, et al. Gold doping of silver nanoclusters: a 26-fold enhancement in the luminescence quantum yield. *Angew Chem Int Ed*. 2016;55:5749–5753.
37. Bootharaju MS, Sinatra L, Bakr OM. Distinct metal-exchange pathways of doped Ag_{25} nanoclusters. *Nanoscale*. 2016;8:17333–17339.
38. Wu Z. Anti-Galvanic reduction of thiolate-protected gold and silver nanoparticles. *Angew Chem Int Ed*. 2012;51:2934–2938.
39. Bootharaju MS, Kozlov SM, Cao Z, et al. Direct versus ligand-exchange synthesis of $[PtAg_{28}(BDT)_{12}(TPP)_4]^{4-}$ nanoclusters: effect of a single-atom dopant on the optoelectronic and chemical properties. *Nanoscale*. 2017;9:9529–9536.
40. Kang X, Xiong L, Wang S, Pei Y, Zhu M. De-assembly of assembled Pt_1Ag_{12} units: tailoring the photoluminescence of atomically precise nanoclusters. *Chem Commun*. 2017;53:12564–12567.
41. Li Y, Chen M, Wang S, Zhu M. Intramolecular metal exchange reaction promoted by thiol ligands. *Nanomaterials*. 2018;8:1070.
42. Wang S, Abroshan H, Liu C, et al. Shuttling single metal atom into and out of a metal nanoparticle. *Nat Commun*. 2017;8:848.
43. Zheng K, Fung V, Yuan X, Jiang DE, Xie J. Real time monitoring of the dynamic intracluster diffusion of single gold atoms into silver nanoclusters. *J Am Chem Soc*. 2019;141:18977–18983.
44. Krishnadas KR, Baksi A, Ghosh A, Natarajan G, Pradeep T. Manifestation of geometric and electronic shell structures of metal clusters in intercluster reactions. *ACS Nano*. 2017;11:6015–6023.
45. Zhou M, Zeng C, Song Y, et al. On the non-metallicity of 2.2 Nm $Au_{246}(SR)_{80}$ nanoclusters. *Angew Chem Int Ed*. 2017;56:16257–16261.
46. Zhou M, Du X, Wang H, Jin R. The critical number of gold atoms for a metallic state nanocluster: resolving a decades-long question. *ACS Nano*. 2021;15(9):13980–13992.
47. Levi-Kalisman Y, Jadzinsky PD, Kalisman N, et al. Synthesis and characterization of Au_{102} (*p*-MBA)$_{44}$ Nanoparticles. *J Am Chem Soc*. 2011;133:2976–2982.

48. Sakthivel NA, Shabaninezhad M, Sementa L, et al. The missing link: Au_{191} (SPh- *t* Bu)$_{66}$ Janus nanoparticle with molecular and bulk-metal-like properties. *J Am Chem Soc*. 2020;142:15799–15814.
49. Vergara S, Santiago U, Kumara C, et al. Synthesis, mass spectrometry, and atomic structural analysis of $Au_{\sim 2000}(SR)_{\sim 290}$ nanoparticles. *J Phys Chem C*. 2018;122:26733–26738.
50. Wang J-Q, Shi S, He R-L, et al. Total structure determination of the largest alkynyl-protected Fcc gold nanocluster Au_{110} and the study on its ultrafast excited-state dynamics. *J Am Chem Soc*. 2020;142:18086–18092.
51. Dass A, Theivendran S, Nimmala PR, et al. Au_{133} (SPh- *t* Bu)$_{52}$ nanomolecules: x-ray crystallography, optical, electrochemical, and theoretical analysis. *J Am Chem Soc*. 2015;137:4610–4613.
52. Sakthivel NA, Theivendran S, Ganeshraj V, Oliver AG, Dass A. Crystal structure of faradaurate-279: Au_{279} (SPh-*t* Bu)$_{84}$ plasmonic nanocrystal molecules. *J Am Chem Soc*. 2017;139:15450–15459.
53. Kumara C, Zuo X, Ilavsky J, Cullen D, Dass A. Atomic structure of Au_{329} (SR)$_{84}$ faradaurate plasmonic nanomolecules. *J Phys Chem C*. 2015;119:11260–11266.
54. Kumara C, Zuo X, Ilavsky J, Chapman KW, Cullen DA, Dass A. Super-stable, highly monodisperse plasmonic faradaurate-500 nanocrystals with 500 gold atoms: $Au_{\sim 500}(SR)_{\sim 120}$. *J Am Chem Soc*. 2014;136:7410–7417.
55. Kumara C, Zuo X, Cullen DA, Dass A. Faradaurate-940: synthesis, mass spectrometry, electron microscopy, high-energy x-ray diffraction, and x-ray scattering study of $Au_{\sim 940\pm 20}$ (SR)$_{\sim 160\pm 4}$ nanocrystals. *ACS Nano*. 2014;8:6431–6439.
56. Kumara C, Hoque MM, Zuo X, Cullen DA, Whetten RL, Dass A. Isolation of a 300 KDa, $Au_{\sim 1400}$ gold compound, the standard 3.6 Nm capstone to a series of plasmonic nanocrystals protected by aliphatic-like thiolates. *J Phys Chem Lett*. 2018;9:6825–6832.
57. Jana A, Jash M, Poonia AK, et al. Light-activated intercluster conversion of an atomically precise silver nanocluster. *ACS Nano*. 2021;15(10):15781–15793.
58. Zeng C, Chen Y, Das A, Jin R. Transformation chemistry of gold nanoclusters: from one stable size to another. *J Phys Chem Lett*. 2015;6:2976–2986.
59. Chakraborty I, Kurashige W, Kanehira K, et al. $Ag_{44}(SeR)_{30}$: a hollow cage silver cluster with selenolate protection. *J Phys Chem Lett*. 2013;4:3351–3355.
60. Chakraborty I, Mahata S, Mitra A, De G, Pradeep T. Controlled synthesis and characterization of the elusive Thiolated Ag_{55} cluster. *Dalton Trans*. 2014;43:17904–17907.
61. Chakraborty I, Govindarajan A, Erusappan J, et al. The superstable 25 KDa monolayer protected silver nanoparticle: measurements and interpretation as an icosahedral Ag_{152} (SCH_2 CH_2 Ph)$_{60}$ cluster. *Nano Lett*. 2012;12:5861–5866.
62. Yang H, Wang Y, Huang H, et al. All-thiol-stabilized Ag_{44} and $Au_{12}Ag_{32}$ nanoparticles with single-crystal structures. *Nat Commun*. 2013;4:2422.

CHAPTER

9

Chromatography and separation in nanocluster science

Korath Shivan Sugi[a] *and Thalappil Pradeep*[b]

[a] **Institute of physical and theoretical chemistry Eberhard Karls University of Tuebingen Auf der Morgenstelle 18 D-72076 Tuebingen Germany** [b] **Deepak Parekh Institute Chair Professor and Professor of Chemistry, Department of Chemistry, Indian Institute of Technology Madras, Chennai, India**

9.1 Introduction

The synthesis of atomically precise metal NCs using various synthetic protocols often results in a mixture of NCs with diverse cores along with various side products and excess ligands. Hence, it is essential to isolate NCs in their pure form with respect to composition. Molecular purity/monodispersity is a crucial factor in the context of crystallization. Hence, to obtain monodisperse NCs, several purification and separation methods were explored.[1] NCs are effectively isolated using fractional precipitation, polyacrylamide gel electrophoresis (PAGE), high-performance liquid chromatography (HPLC), and thin-layer chromatography (TLC) techniques, which has enabled an in-depth understanding of the composition and the properties of NCs.[1b,2] Apart from isolation, high-resolution techniques are also used to track and evaluate product distribution.

In this chapter, we have discussed various separation techniques to isolate atomically precise nanoclusters. The upcoming sections outline the brief history, basic principles, instrumentation, and experimental procedure of various NC separation techniques. A detailed discussion of modifications brought about in each technique to isolate atomically precise NCs with high-resolution and reproducibility is presented. The final section summarizes the chapter and provides future directions.

9.2 Various techniques used for the separation of NCs

Atomically precise NCs can be broadly classified into hydrophilic and hydrophobic NCs depending on the protecting ligands.[2] NCs that are synthesized with hydrophilic ligands are known to display high quantum yields and are biocompatible.[2] Their properties can be altered

DOI: https://doi.org/10.1016/B978-0-323-90879-5.00009-3

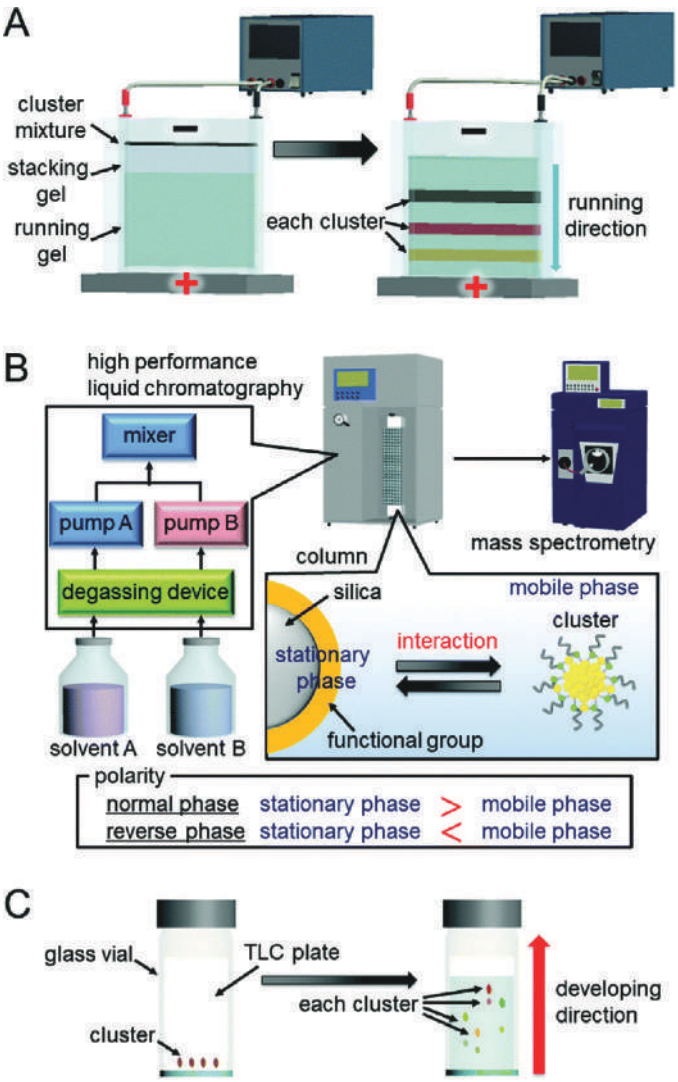

FIGURE 9.1 Schematic diagram of (A) PAGE, (B) HPLC, and (C) TLC separation techniques. Reproduced with permission from ref.[1b]. Copyright 2020, Royal Society of Chemistry.

by replacing the metal core or surface ligands with hetero atoms or hetero ligands. Unlike hydrophobic NCs, hydrophilic NCs are investigated to a limited extent due to their complex mass distributions. The majority of synthetic protocols yield NCs bearing hydrophobic ligands.[2] In order to correlate the structure-property relationship of NCs, monodispersity, and molecular purity is essential. In general, atomically precise NCs are isolated using techniques such as PAGE, HPLC, and TLC (Fig. 9.1).[1b] The hydrophilic NCs are mainly isolated using techniques such as PAGE, hydrophilic interaction liquid chromatography (HILIC), gel filtration chromatography (GFC), and ion pair chromatography. The century-old chromatographic techniques such as HPLC, gel permeation chromatography (GPC), and TLC are used to separate hydrophobic NCs. Further details of these techniques will be discussed subsequently.

Reversed-phase HPLC methods are widely used to separate NCs due to their solubility in nonpolar solvents. Nowadays integrated HPLC-ESI-MS, which uses both reversed-phase and ion-pairing methods, are actively used for the separation of NCs.[3] A concise pictorial summary of these techniques is presented in Fig. 9.2. We will discuss specific details subsequently.

9.2.1 Brief history of PAGE

The electrophoresis principle dates back to as early as 1853 when Hittorf studied the movement of ions in an electric field.[4] The studies by W.B. Hardy and Leonor Michaelis in the 20th century established that many biologically important molecules show electrophoretic mobilities.[5] Later, in 1931, the use of electrophoresis technique for molecular separation and chemical analysis began with the work of Arne Tiselius, who developed the "Tiselius apparatus" for moving boundary electrophoresis.[6] In the late 1940s, the shortcomings of moving boundary electrophoresis were addressed by new methods, wherein solid or gel matrices were employed to separate compounds into different zones or bands. In 1955, Oliver Smithies introduced starch gel as an electrophoretic substrate, which enabled the widespread use of this method in biochemistry.[7] The use of gels such as starch gel or polyacrylamide enabled the effective separation of biomolecules with minute differences.[5a,8] In 1959, Ornstein and Davis introduced discontinuous electrophoresis (colloquially, disc electrophoresis), which used polyacrylamide gels for the separation of protein mixtures.[9] This method was further improved by the work of Raymond and Weintraub.[8b] In the following years, several developments such as the use of agarose gel,[10] denaturing agents such as SDS,[11] and two dimensional gels[12] improved the efficiency of the electrophoresis technique.

In 1984, David C. Schwartz and Charles Cantor introduced alternating voltage gradient to the standard protocol, which enabled high-resolution separation of larger molecules and is known as pulsed-field gel electrophoresis.[13] During the same period, capillary electrolysis (CE) method gained attention. The pioneering work on CE was carried out by Hjerten[14] in 1967, although separations were carried out using tubes of 3 mm I.D., and the instrument was quite large. The potential of this technique was investigated thoroughly by Jorgenson's group, which resulted in high-resolution analyte separations employing both electrophoresis and electroosmotic flow.[15] Since then, diverse electrophoresis methods, such as, affinity electrophoresis,[16] electrophoretic mobility shift assay,[17] isotachophoresis,[18] and preparative electrophoresis[19] have been developed.

9.2.2 Brief history of chromatography

The liquid chromatography separation technique had its origin in the 19th century. Runge's work on the separation of dye using paper was considered as the precursor of chromatography.[20] Also, in 1861, Goppelsroeder used a form of paper chromatography, called capillary analysis, to separate colored pigments, which is considered as the real beginning of chromatographic separation.[21] In 1903, Mikhail Tswett, who was influenced by the work of Goppelsroder, separated plant pigments using a column filled with calcium carbonate and petroleum ether as a mobile phase.[22] This process was known as chromatography. The word chromatography has Greek roots; chroma means "color," and Graphein means "to write," which refers to color writing. After the discovery of the chromatography concept by Tswett,

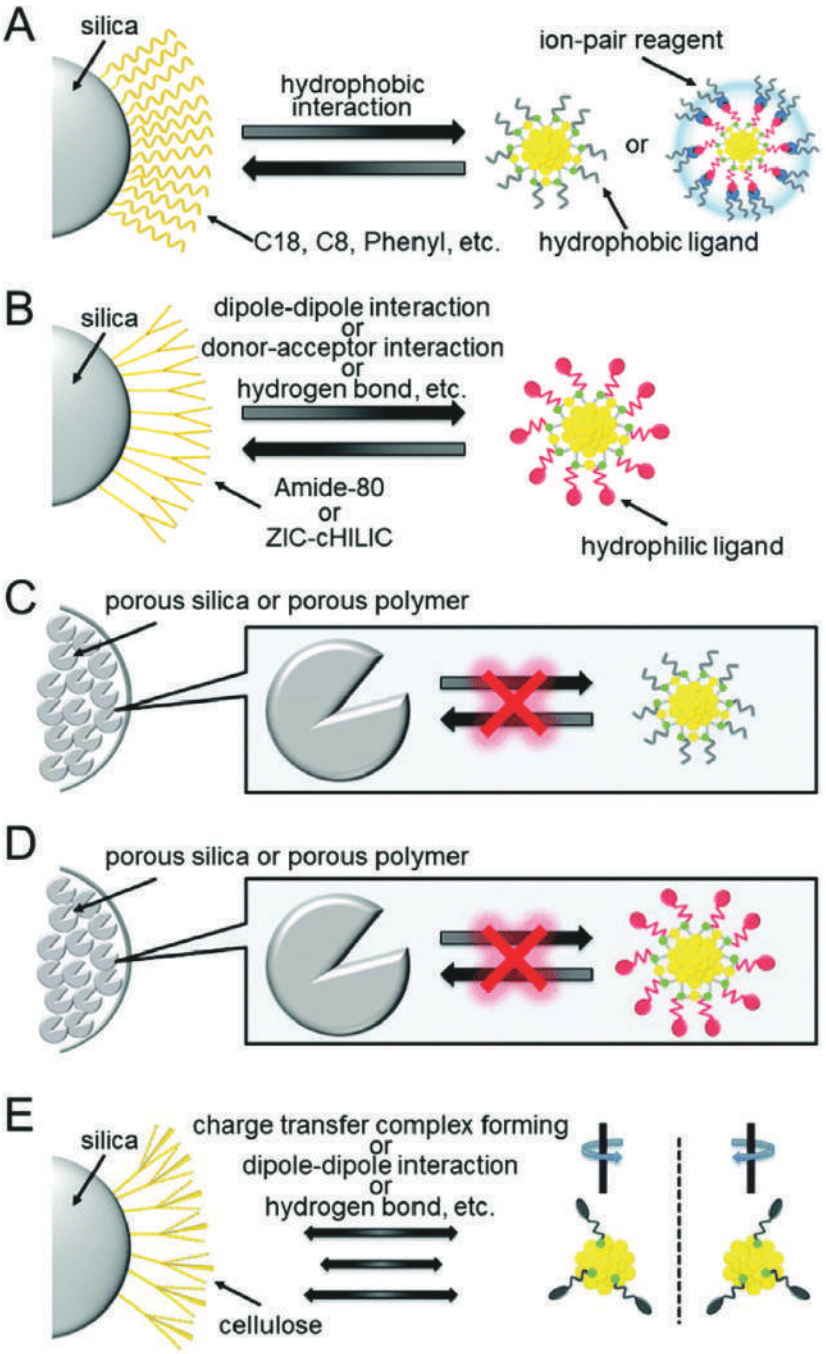

FIGURE 9.2 Schematic illustration of the stationary phase used in different chromatographic techniques such as (A) RP partition and ion-pair chromatography, (B) HILIC, (C) GPC, (D) GFC, and (E) chiral chromatography. Reproduced with permission from ref.[1b]. Copyright 2020, Royal Society of Chemistry.

the technique did not receive much attention for more than two decades. At the beginning of the 20th century, this technique was used to purify small quantities of pigments for spectroscopic characterization. Kuhn and Lederer in 1930 demonstrated the preparative scale chromatographic separation of α and β carotene from carrots.[23] In the mid-1940s, Spedding et al. purified rare earth elements using ion-exchange chromatography.[24]

In 1941, A. J. P. Martin and Richard Synge successfully separated amino acids using a column packed with impregnated silica gel in a glass tube and chloroform as a mobile phase. The amino acids were separated based on their partition coefficients, and the process was known as partition chromatography.[25] They were awarded the Nobel prize in 1952 for this work. In 1944, Martin and James developed gas chromatography, wherein the analyte was vaporized and separated.[26] Helium gas was used as the mobile phase.

The paper-based separation of pigments or analytes dates back to the 19th century. The first report on the use of thin layer for separation is by N. A. Izmailov and M. S. Shraiber in 1938.[27] They separated plant extracts on a 2-mm thick layer of aluminum oxide. In 1956, Egon Stahl promoted TLC by using silica gel as a sorbent layer.[27]

In 1956, Grant Lathe and Colin Ruthven demonstrated the size-dependent separation of mixed proteins in columns with starch gel matrix, resulting in size exclusion chromatography (SEC). [28] This technique was widely used in polymer science. In 1965, Cal Giddings and Josef Huber predicted that the liquid chromatography could be operated with high efficiency by reducing the particle size of the stationary phase and increasing the mobile phase velocity by applying pressure.[29] The first HPLC was constructed by Csaba Horvath at Yale University.[30] In 1962, Ernst Klesper demonstrated the use of fluid above its critical point as a mobile phase to separate thermally labile metal porphyrins, which at that time was known as high-pressure gas chromatography (HPGC), and later came to be known as supercritical fluid chromatography.[31] Strain et al. demonstrated that applying an electric field across columns can result in higher selectivity due to the combination of electrophoretic and chromatographic separation.[32] This resulted in the capillary electrochromatography technique (CEC). Jorgenson and Lukacs demonstrated the use of packed capillary columns for CEC in 1981.[33] The chromatographic principles are used in various ways to create advanced chromatographic techniques, resulting in improved separation of molecules. Nowadays, chromatography is extended to all branches of science.

9.3 Principle, instrumentation, and procedure of various separation techniques

9.3.1 Poly acrylamide gel electrophoresis (PAGE)

In PAGE, the separation of analyte is based on the electrophoresis principle, wherein when current flows through an analyte solution, the charged analyte move toward an oppositely charged electrode. The running layer and the stacking layer consist of polyacrylamide gel prepared in different concentrations. The analyte is introduced at the upper end of the gel with the aid of glycerol and electrophoresis is performed. The analyte is separated into different bands depending on the mobility of its constituents. Each separate band of analyte is collected and dissolved in a respective solvent for further characterization.

The PAGE technique and device are simple and inexpensive, wherein the separation of analyte can be visually detected.

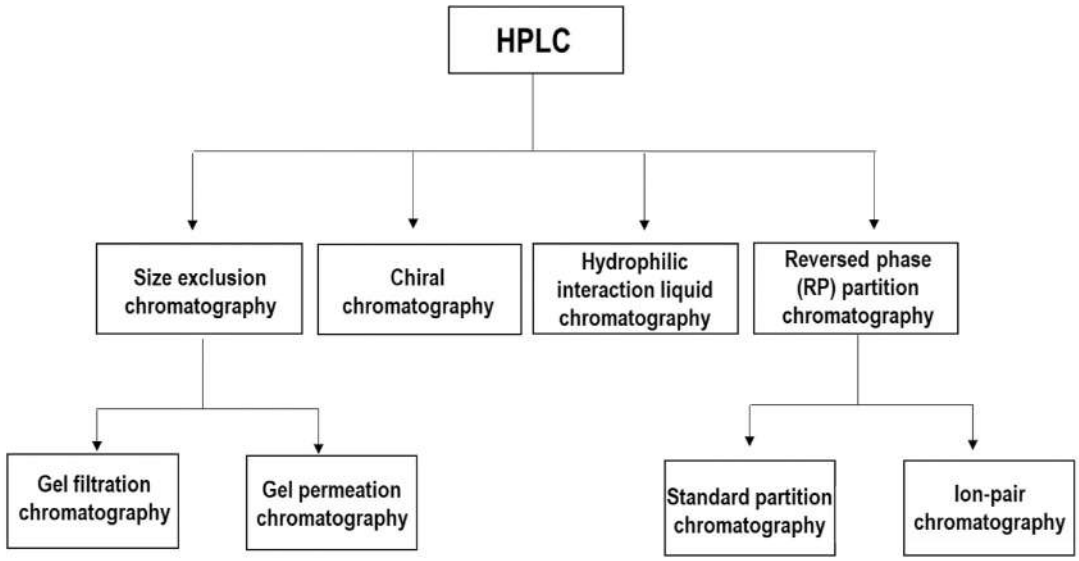

FIGURE 9.3 Classification of various liquid chromatographic techniques.

9.3.2 High-performance liquid chromatography

Chromatography is a separation technique used to isolate the analytes depending on the extent of interaction between the analyte and the stationary phase. In liquid chromatography, the mobile phase used is liquid. Open column chromatography is a method widely used by organic chemists to isolate compounds. In this technique, the analyte is loaded onto the upper end of the column packed with a stationary phase. Then the mobile phase is passed through the open column, which separates the analyte. In the case of NCs, this technique is widely used to separate excess thiolates owing to its simplicity.

HPLC is a widely used separation technique with improved resolution and sensitivity. In this technique, high pressure is applied, enabling the mobile phase to flow through the column at a high flow rate, thereby reducing the time that the analyte stays in the stationary phase. Depending upon the separation mechanism, they are classified into four categories: size exclusion, ion exchange, partition, and adsorption (Fig. 9.3). Based on the polarity of the stationary phase, the separation condition is broadly divided into normal-phase and reversed-phase chromatography. In the normal-phase, the polarity of the stationary phase is higher than that of the mobile phase, whereas the stationary phase has lower polarity than the mobile phase in reversed-phase chromatography. The HPLC separation of NCs involves adsorption, size exclusion, and partition separation mechanism.

An HPLC instrument consists of a mobile phase reservoir, degasser unit, high-pressure liquid pump, autosampler/injector, column, and detector. Depending upon the characteristics of the analyte, either isocratic mode or gradient mode is used for the separation. The analyte is injected into the system, and the mobile phase is allowed to pass through the column. The separation occurs depending on the interaction of the analyte with the stationary phase and polarity of the mobile phase, which is evident from their corresponding chromatogram.

9.3.3 Thin layer chromatography (TLC)

TLC is similar to paper chromatography, wherein a planar surface is used as a stationary phase. The stationary phase of choice is coated on a glass/aluminum/plastic plate. The separation mechanism is similar to HPLC. In TLC separation, the analyte is spotted on the lower end of the TLC plate using a micropipette or capillary tube. The TLC plate containing the analyte is carefully placed in a sealed container containing mobile phase/solvent. The solvent rises due to capillary action, which facilitates the separation of the analyte. The TLC is a less expensive technique, and the separation of analytes can be visually confirmed.

9.4 Earlier studies on the separation of atomically precise nanoclusters

The separation of compounds from their mixture plays a vital role in the analysis and characterization of compounds. Fractional precipitation is one of the earliest methods which is still used to isolate NCs from the mixture. The NCs are isolated depending on their solubility in different solvents. Generally, the solubility of NCs decreases with an increase in size.[1a] Whetten et al. isolated a series of gold NCs protected with dodecanethiolate using this method.[34] The mass of the separated fractions was obtained from laser desorption/ionization mass spectrometry (LDI-MS) measurements. Several hexyl, dodecyl, and octadecyl-protected gold nanocrystals were isolated by gradually adding a poorer solvent to precipitate NCs (9.4A).[35]

Murray and his colleagues used the solvent selective extraction protocol to isolate alkane thiol-protected gold NCs from a mixture of NCs.[36] In this method, NCs are extracted with ethanol.[37] To date, the solvent fractionation method is widely used to purify and isolate monodisperse NCs from the as-synthesized crude mixture. The well-celebrated $Au_{25}(SR)_{18}$ NCs were isolated from the crude by fractional precipitation using methanol.[38] The excess reactants, such as tetraoctylammoniumbromide (TOAB) and thiol, were removed in the course of separation. After precipitation with methanol, the NCs were extracted in acetone to remove the larger insoluble $Au_{144}(SR)_{18}$ NCs. In 2012, Choi and coworker's developed a facile protocol to isolate pencillamine-protected gold NCs by sequential size-selective precipitation.[39] Schematic illustration of the isolation process is presented in Fig. 9.4B. In this method, different volume fractions of acetone were added to the supernatant, which facilitated the extraction of four different fractions of NCs. The compositions of the extracted fractions were determined as Au_{11}, Au_{18}, Au_{28}, and Au_{38}. The fractional precipitation method is still widely used due to its simplicity, rendering large-scale purification of NCs possible. Despite these merits, this method has significant drawbacks, such as it is tedious and ineffective in the case of longer chain alkanethiol protected NCs and hydrophilic NCs.

9.5 Separation of hydrophilic nanoclusters

9.5.1 PAGE

9.5.1.1 Separation based on number of constituent atoms

The gel electrophoresis[8b] technique is widely used for the separation of macromolecules and bioproteins based on their charge and size. In nanocluster science, hydrophilic NCs are

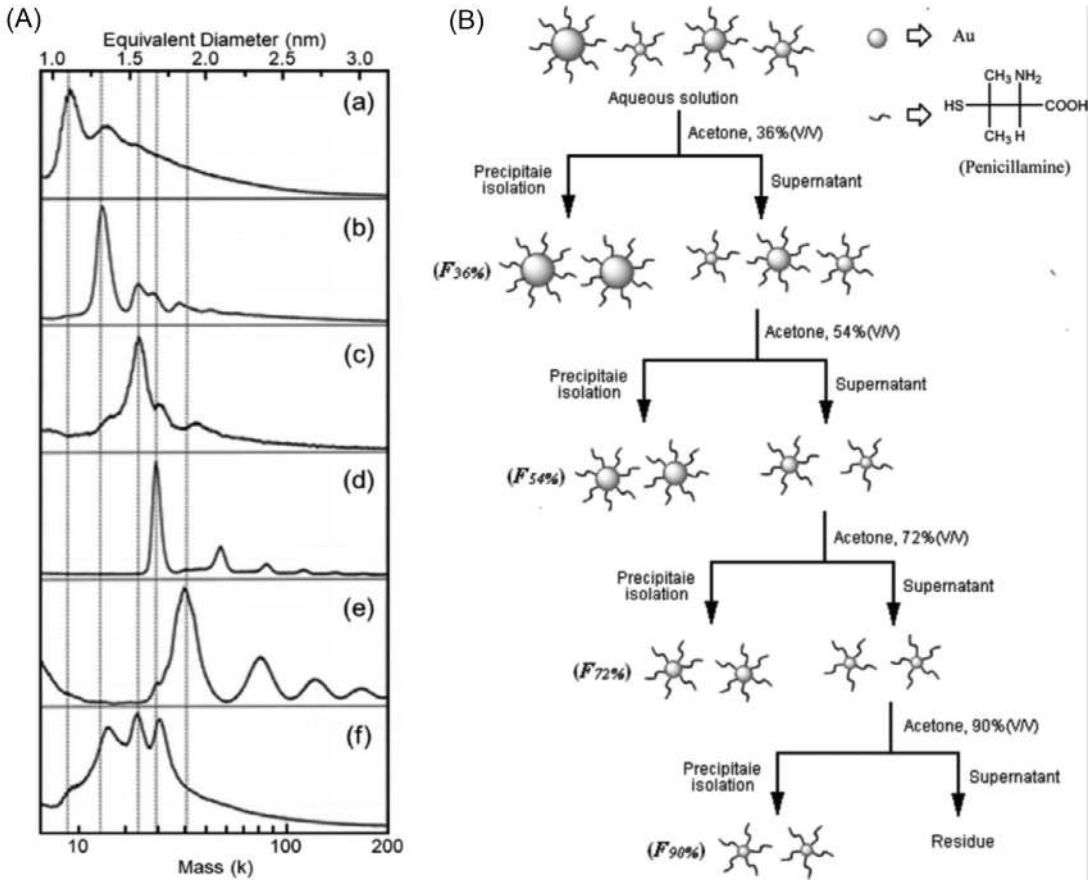

FIGURE 9.4 (A) Low-resolution mass spectra, plotted as abundance versus $(\text{mass})^{1/3}$, of size-separated NCs (b–e) and (a) and (f) are unseparated samples. The R groups used in the preparation of the samples shown are (a) C_{12}, (b) C_{18}, (c–e) C_6, (f) C_{12}. (B) Schematic diagram of sequential size-selective precipitation (SSSP) of penicillamine protected gold NC mixture. Reproduced with permission from refs[35,39]. Copyright 1997 and 2012, respectively, American Chemical Society.

isolated using this method. In gel electrophoresis, the NCs are moved through polyacrylamide in an electric field in the electrophoresis chamber. The mobility of smaller metal NCs is higher than that of more massive NCs. Such mobility differences enables the separation of NCs in the form of bands when they move across the gel. The use of PAGE technique in nanocluster science began in 1998, when Schaaf and Whetten et al. separated $Au_n(SG)_m$ NCs (SG = glutathione) into different bands.[40] Later on, using this technique, they isolated a series of glutathione protected gold NCs.[41] Negishi and Tsukuda et al. further extended this method for the isolation of a mixture of gold NCs, and their corresponding chemical composition was evaluated using ESI MS.[42] A few larger glutathione protected NCs such as Au_{43} and $Au_{\sim 56}$, were separated by Kimura et al. and Dass et al., and their chemical composition was confirmed by ESI MS.[42b,43] This technique was also used for the separation of other hydrophilic ligands such as tiopronin and mercaptosuccinic acid protected gold NCs (Fig. 9.5).[44] Isolation

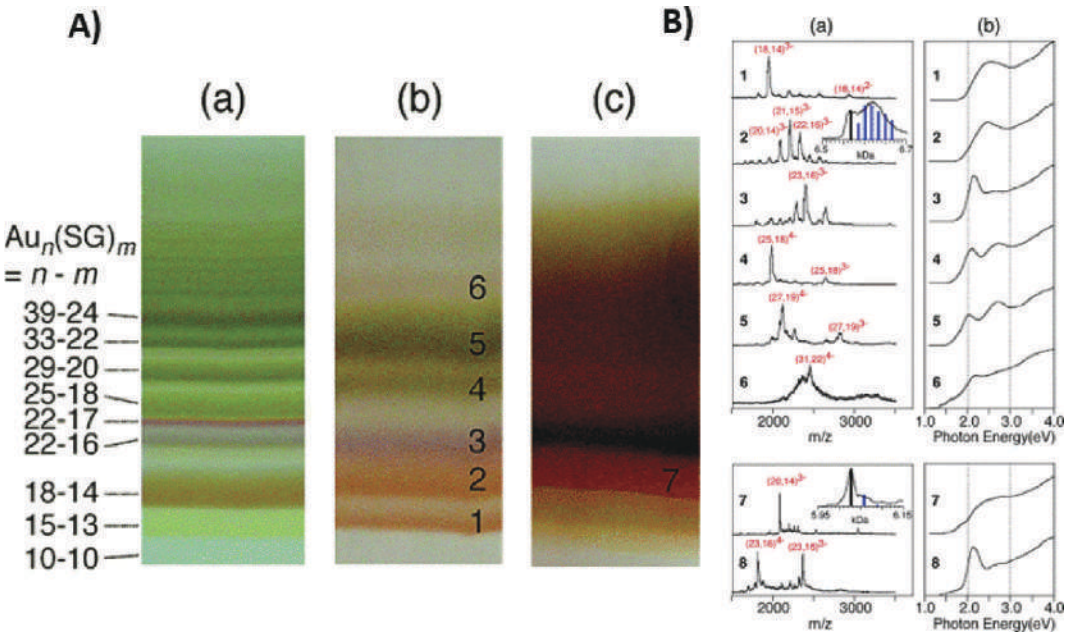

FIGURE 9.5 (A) PAGE separation of (a) $Au_n(SG)_m$, (b) $Au_n(S(PG))_m$, and (c) $Au_n(S(SA))_m$ NCs. (B) Negative-ion ESI MS (a) and UV-vis spectra (b) of Au:S(PG) (1–6) and Au:S(SA) (7 and 8) NCs. Deconvoluted spectra of the main peaks of 2 and 7 are shown in the insets of panel a. Reproduced with permission from ref.[44]. Copyright 2006, American Chemical Society.

of NCs using the PAGE technique has been extended to other metal NCs as well. Bigioni et al. separated glutathione-protected silver NCs using PAGE and suggested that the composition of glutathione-protected silver and gold NCs might be different.[45]

Isolation of NCs using PAGE helped in procuring further insight into their composition, stability, and physical properties.

9.5.1.2 *Monitoring NC reaction using PAGE technique*

The isolation of NCs using PAGE enables a visual detection of the separation process. This aspect of the PAGE technique is used to monitor the formation process and track the chemical composition of the products. The reaction between triphenylphosphine-protected gold clusters and glutathione was optimized and monitored using PAGE separation, and the separated products were further characterized using ESI-MS.[46] The role of radical initiator in the synthesis of mercaptobenzoic acid-protected Au_{102} NCs was examined using the PAGE technique.[47] This study revealed that O_2 was required for radical generation during synthesis. The degradation of glutathione-protected silver NCs under various conditions was monitored using PAGE.[48] The structural changes in NCs and the reaction intermediates during NC synthesis can be monitored using this technique.[49]

PAGE technique is also used to identify luminescent NCs.[50] The crude NCs that are isolated into distinct bands using PAGE are subjected to ultraviolet (UV) irradiation to distinguish between non-emitting and emitting NCs.

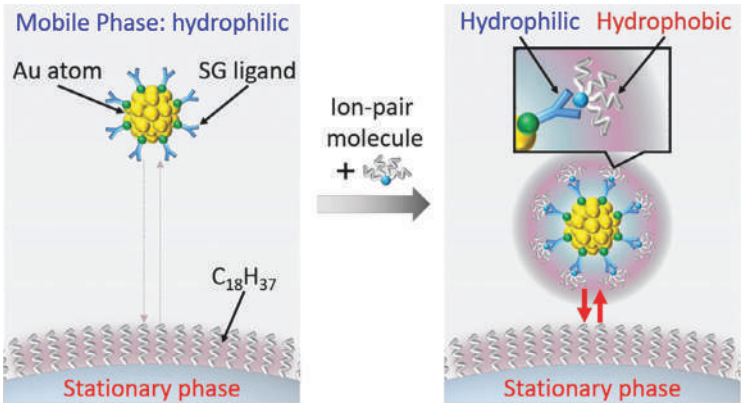

FIGURE 9.6 Schematic illustration displaying the separation of hydrophilic gold NCs by ion-pair chromatography. Reproduced with permission from ref.[54]. Copyright 2017, American Chemical Society.

9.5.1.3 Separation of NCs using SDS-PAGE

Sodium dodecyl sulfate (SDS) PAGE separation is used frequently in the purification of proteins. The charge state of the analytes is known to affect mobility. In order to exclude the effect of the charge state, SDS was added to the sample and electrophoresis solutions. The binding efficiency of mixed ligand (maleimide and mercaptobenzoic acid) protected Au_{102} NCs is demonstrated using the SDS-PAGE technique.[51]

9.5.2 Ion-pair chromatography

Hydrophilic NCs are also separated using RP-chromatography, where the separated NCs can be analyzed using LC/MS. In order to isolate hydrophilic NCs using RP-chromatography, the surface of NC is modified using an ion-pair reagent to make them hydrophobic (Fig. 9.6). Murray et al. first reported the separation of $Au_n(NALC)_m$ (NALC=N-acetyl-L-cysteine) and $Au_n(S(PG))_m$ (S(PG)=N-(2-mercaptopropionyl)glycine) using C18 column and tetrabutylammonium fluoride as ion-pair reagent.[52] The NCs were separated based on their core size. Choi et al. also attempted to separate $Au_n(NALC)_m$ NCs using similar experimental conditions and analyzed the fractions using MALDI MS. Dong and Choi et al. extended this method to separate other NCs such as N-acetyl-L-cysteine-protected palladium NCs.[53] Later, Nihori et al. achieved high-resolution separation of glutathione-protected gold NCs.[54] The presence of nonvolatile ion-pairing reagent $(C_4H_9)_4N^+$ in the separated fractions limits the LC-MS analysis. Whetten et al. resolved this issue by replacing the nonvolatile $(C_4H_9)_4N^+$ with volatile triethylamine, and they achieved both isolation and determination of the chemical composition of mercaptobenzoic acid (MBA) protected gold NCs by LC-MS.[3,55]

9.5.3 Hydrophilic interaction liquid chromatography (HILIC)

The complications of using ion-pair reagent can be resolved using a HILIC column, to separate the hydrophilic NCs which can be efficiently integrated to the mass spectrometer.[56] This technique is considered as a variant of normal phase liquid chromatography and is used to separate polar compounds. In HILIC, the stationary phase is polar and the mobile phases generally used are aprotic solvents, miscible in water. The commonly used polar phases are

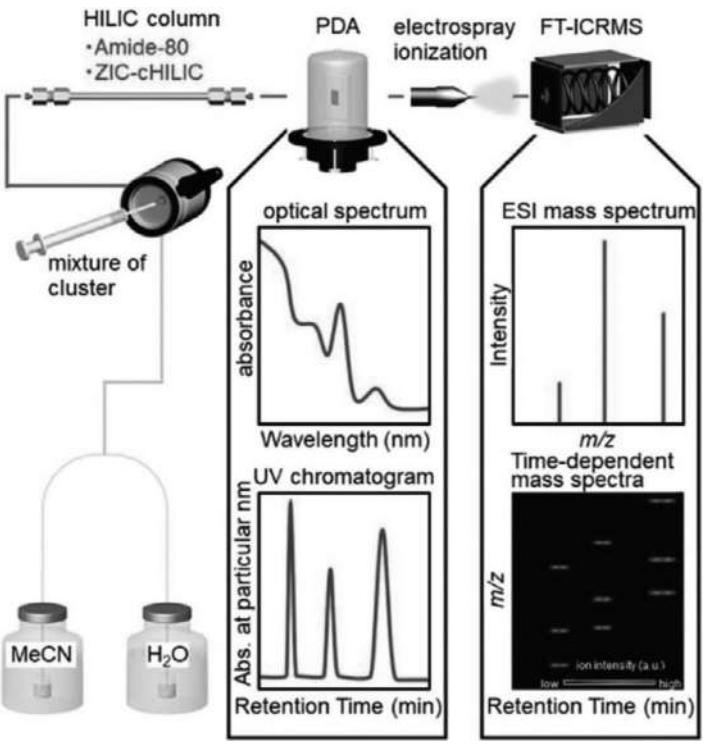

FIGURE 9.7 Schematic representation of chromatograms and the corresponding ESI mass spectra of glutathione protected alloy NCs separated by HILIC columns. Reproduced with permission from ref.[57]. Copyright 2017, Royal Society of Chemistry.

amino, amide, cationic, and zwitterion bonded phases. The elution process starts with low polar organic solvent, and the analytes are separated with increasing aqueous content. Niihori et al. attempted to isolate and analyze glutathione-protected gold NCs and their alloys by LC-MS using a HILIC column (Fig. 9.7).[57] They used two columns, an Amido-80 column, and ZIC-cHILIC. The high-resolution separation of glutathione-protected gold NCs allowed them to detect new NCs. The $Au_{n-x}M_x(SG)_m$ alloy NCs were separated depending on the number of constituent atoms in HILIC columns. Stamplecoskie et al. isolated the glutathione protected silver NCs using an amide column.[58]

9.6 Separation of hydrophobic NCs

9.6.1 Reversed phase-high performance liquid chromatography (RP-HPLC)

The variant of RP-HPLC, such as ion-pair chromatography and HILIC, are already discussed above. RP partition chromatography is extensively used to separate hydrophobic metal NCs due to the availability of several stationary phases and cluster-friendly mobile phases for separation. The mobile phases used in RP-chromatography are suitable for ESI MS, enabling identification of the chemical composition of the isolated NCs. Unlike the normal phase, the polarity of the stationary phase used in RP chromatography is lower than that of the mobile phase (Fig. 9.8). The analyte separation depends on the difference in the partition coefficient.

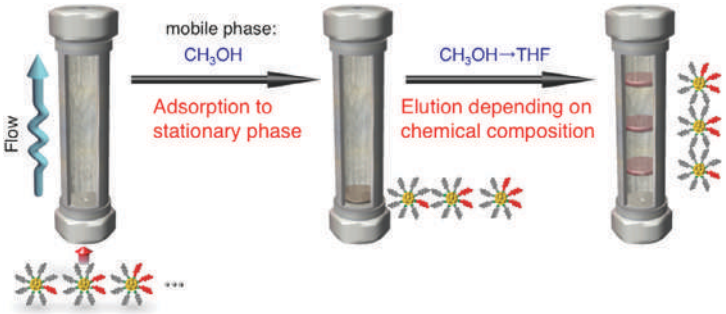

FIGURE 9.8 Schematic representation of the linear gradient separation method. Reproduced with permission from ref.[66]. Copyright 2013, American Chemical Society.

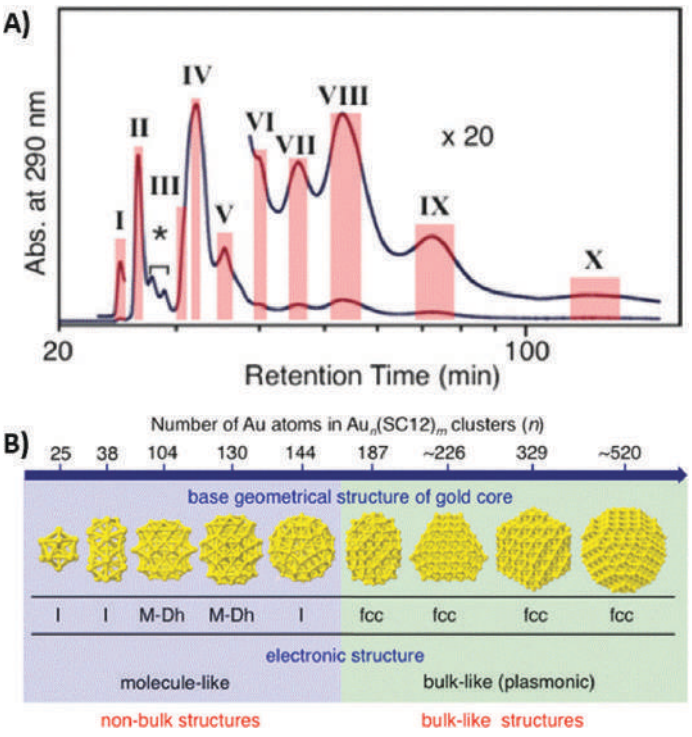

FIGURE 9.9 (A) Chromatogram of the as-prepared dodecanethiol protected gold NCs separated using C8 and Ph columns. (B) Evolution of electronic and geometrical structures of isolated $Au_n(SC_{12}H_{25})_m$ NCs. Reproduced with permission from ref.[61]. Copyright 2015, American Chemical Society.

9.6.1.1 Separation based on the number of constituent atoms

The separation of NCs using RP-HPLC was first demonstrated by Murray et al. with hexane thiolate-protected gold NCs.[59] The separated fractions of NCs were characterized using electrochemical measurements and UV-vis spectroscopy.[60] Later, Negishi et al. successfully isolated dodecanethiol-protected Au_{130} and Au_{180} NCs by connecting columns in series.[61] They also succeeded in developing a method to isolate a wide range of dodecanethiol-protected gold NCs, from $Au_{38}(DDT)_{24}$ to $Au_{\sim 520}(DDT)_{\sim 130}$ (Fig. 9.9). Knoppe et al. further investigated the high-resolution separation of dodecanethiol-protected Au_{25} and Au_{38} NCs.[62] They further studied the effect of the alkyl chain length of the protecting ligands on the

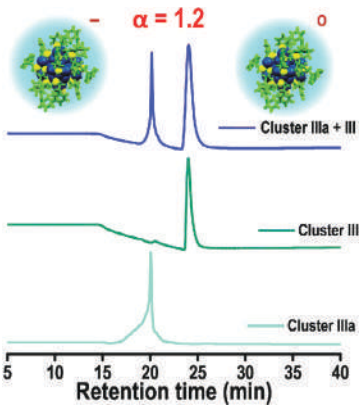

FIGURE 9.10 High-resolution separation of anionic and neutral PET thiol protected Au_{25} NCs using phenyl-hexyl column.

retention time. The isolation of phenylethanethiol (PET) protected gold NCs was carried out using a capillary C18 column, and the eluted NC sample was directly analyzed by ESI MS.[63] This method was further extended to other phenylethanethiol protected NCs such as Au_{104}, Au_{130}, Au_{137}, and Au_{144}.[63]

9.6.1.2 *Separation based on charge state of the NCs*

The NCs are eluted due to differences in their partition coefficient in RP-liquid chromatography. The charge state of the NCs can alter the partition coefficient, thereby facilitating charge state-dependent separation of NCs. Negishi et al. first reported the charge state-dependent separation of NCs.[64] In their study, they observed that the retention time of neutral and anionic dodecanethiol-protected Au_{25} NCs are different. With this insight, they successfully elucidated the unknown charge state of $Au_{24}Pd(DDT)_{18}$ NCs. Sugi et al. also demonstrated the charge state separation of PET-protected Au_{25} NCs using phenyl-hexyl column (Fig. 9.10).[65]

9.6.1.3 *Separation based on heteroligands*

It is well known that ligand engineering strategies are employed to tune the physical/chemical properties of NCs. Synthesis of NCs by substituting different ligands on the same NC or ligand exchange reactions yield products having a wide distribution of ligand combinations. Such products can be isolated with high-resolution using RP-liquid chromatography. Niihori et al. demonstrated the separation of NCs with different ligand combinations.[66] In their study, they isolated the ligand exchanged products of $Au_{24}Pd(DDT)_{18}$ with SBB (4-tert- butyl benzyl thiolate) using RP liquid chromatography. In the initial phase, NCs were adsorbed on the stationary phase, and by controlling the polarity of the mobile phase using a gradient program, the NCs were separated. Here, along with the partition coefficient, their ability to interact with/adsorb on the stationary phase plays a major role in the separation of NCs. They further extended the method to isolate $Au_{24}Pd(SR1)_{m-x}(SR2)_x$ NCs with two types of ligands (SRs) (Fig. 9.11).[67] This improved isolation was achieved by introducing the step gradient method instead of the linear-gradient method. This advanced method was used to isolate NCs having two types of ligands with equivalent molecular weights. Further, Niihori et al. separated the ligand exchanged coordination isomers using different mobile phases used in previous investigations, that is, methanol-THF was replaced by acetonitrile-acetone.[68] This

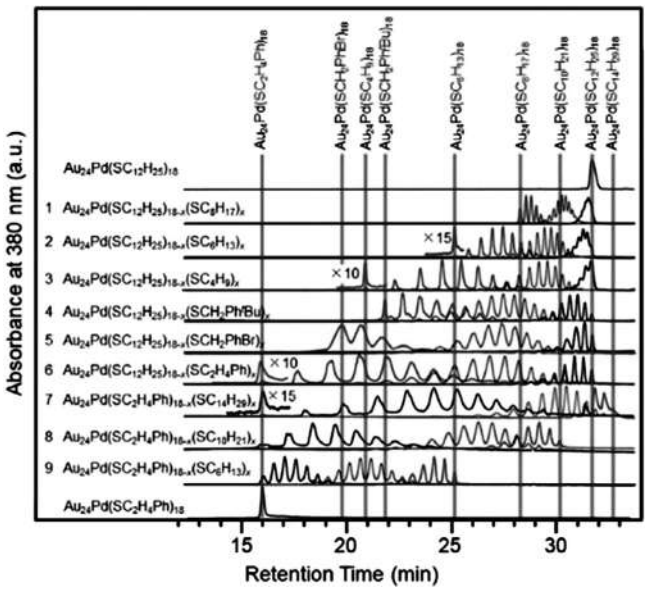

FIGURE 9.11 Chromatograms of $Au_{24}Pd(SR1)_{18-x}(SR2)_x$ NCs. Reproduced with permission from ref.[67]. Copyright 2014, Royal Society of Chemistry.

isolation provided further insight into the ligand exchange position and mechanism in the case of NCs (Fig. 9.12).

9.6.1.4 Separation based on the heteroatoms in the core of the NCs

Apart from separating ligand exchanged products, RP partition chromatography is also used to separate heteroatom-containing NCs. Niihori et al. successfully separated the alloys of butanethiolate protected gold NCs using core-shell type stationary phase, enabling high-resolution separation of structural isomers of $Au_{25-x}Ag_x(SC_4H_9)_{18}$ ($x = 1$–4) NCs.[69] This study revealed that the isomer distribution varies depending on the synthesis method and has established a precise correlation between the chemical composition of NCs and their corresponding electronic structure. This method was further extended to isolate $[Au_{38-x}Ag_x(SR)_{24}]^0$ NCs synthesized via cluster–metal complex reaction or antigalvanic reaction.[70]

9.6.2 Size exclusion chromatography

In SEC, NCs are separated according to their physical size. Here, unlike RP partition chromatography, the analyte and stationary phase do not interact. SEC is classified into two types, GPC and GFC. They differ from each other in terms of the mobile phase used. In GPC, an organic solvent is used as a mobile phase, whereas, in GFC, an aqueous solvent is used. As the separation depends on the physical size, the larger NCs are eluted first, followed by the smaller ones.

9.6.2.1 Gel permeation chromatography

In 2000, Wilcoxon et al. tried to separate gold NCs using GPC; the stationary phase was porous organics.[71] The precise chemical composition of gold NCs was difficult to obtain, so in their study, they synthesized NCs with the same metal core but varied the chain length

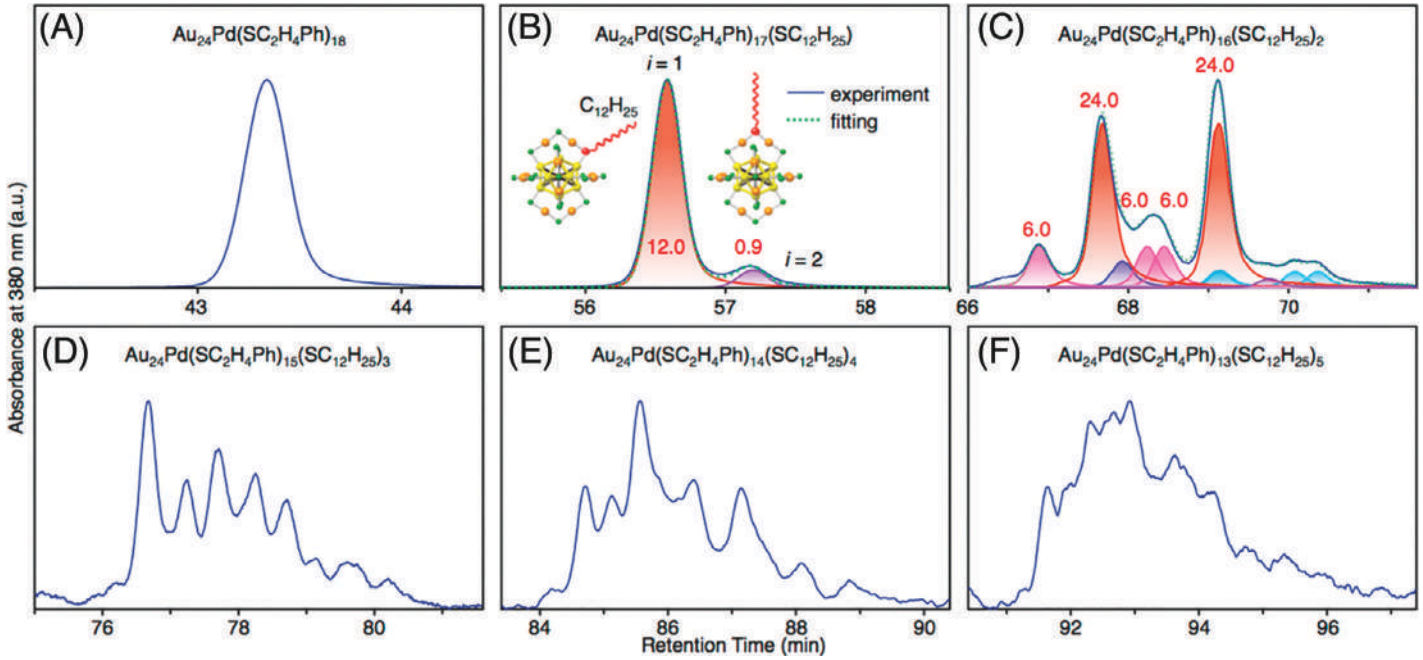

FIGURE 9.12 Chromatograms of (A) $Au_{24}Pd(SC_2H_4Ph)_{18}$, (B) $Au_{24}Pd(SC_2H_4Ph)_{17}(SC_{12}H_{25})$, (C) $Au_{24}Pd(SC_2H_4Ph)_{16}(SC_{12}H_{25})_2$, (D) $Au_{24}Pd(SC_2H_4Ph)_{15}(SC_{12}H_{25})_3$, (E) $Au_{24}Pd(SC_2H_4Ph)_{14}(SC_{12}H_{25})_4$, and (F) $Au_{24}Pd(SC_2H_4Ph)_{13}(SC_{12}H_{25})_5$. Reproduced with permission from ref.[68]. Copyright 2015, American Chemical Society.

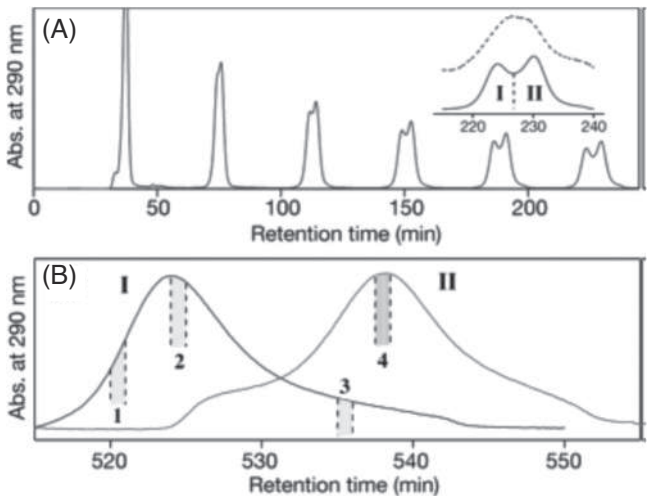

FIGURE 9.13 (A) GPC chromatogram of $Au_n(ODT)_m$. (B) GPC chromatograms of fractions I and II. Reproduced with permission from ref.[74]. Copyright 2006, American Chemical Society.

of the protecting thiol. By comparing the retention time, they examined the thickness of the ligand layer. Later, Tsukuda et al. performed such studies on $Pd_n(SC_lH_{2l+1})_m$ NCs (l=10, 12, 14, 16, or 18) by GPC.[72] Wilcoxon et al. further performed the size-dependent separation of $Au_n(SC_lH_{2l+1})_m$ and $Ag_n(DDT)_m$ NCs,[73] which affirmed a correlation between particle size and electronic structure. Later Tsukuda et al. accomplished the separation of $Au_n(ODT)_m$ NCs with higher resolution by recycling (Fig. 9.13).[74] They also isolated the Au_{55} metal core cluster with high purity, and the chemical composition of this cluster was further revealed by Jin et al. using ESI MS.[75]

Further, Jin et al. successfully separated $Au_{38}(PET)_{24}$ and $Au_{40}(PET)_{24}$ NCs using GPC.[76]

Besides separation, GPC is also employed for tracking NC reactions. The growth of SBB-protected silver NCs was traced by Negishi et al. using GPC.[77] The size-selective synthesis method used for the synthesis of several NCs such as PET protected Au_{19}, Au_{20}, and Au_{24} were discovered using GPC, which tracks the size evolution of NCs.[78]

9.6.3 Chiral chromatography

Chiral chromatography is used to separate analytes into their optical isomers using the chiral stationary phase. A chiral compound functionalized silica gel is used as the stationary phase. The mechanism of separation of analytes into optical isomers is proposed to follow the "three-point bond model."[79] According to this model, the analyte interacts with the chiral stationary phase to form a diastereomeric aggregate. Various interactions that result in such aggregate formation are supramolecular interactions, hydrogen-bond formation, complex formation, ion-pair formation, etc. The binding energy of such aggregates varies with optical isomers, and is reflected in their retention time.

Deciphering the first crystal structure of $Au_{102}(p\text{-}MBA)_{44}$ revealed the possibility of optical isomers in atomically precise NCs.[80] Chirality of NCs is extensively studied using chiral chromatography. Burgi and coworkers reported the first study on the separation of NCs into chiral isomers in 2010.[81] They separated PET-protected Au_{38} NCs using cellulose-based

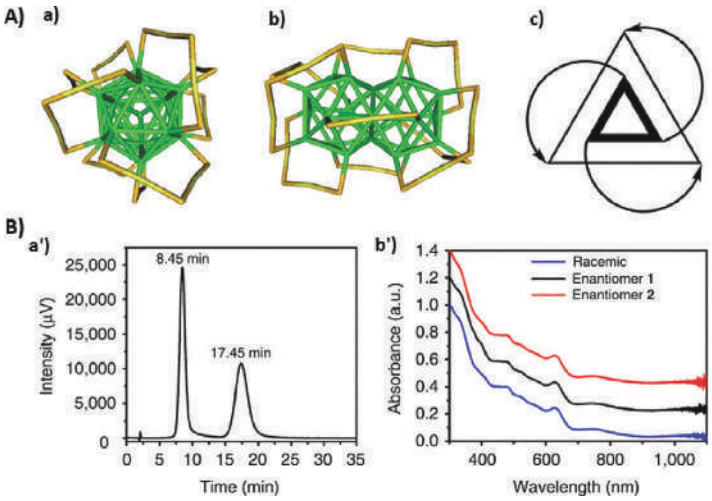

FIGURE 9.14 The crystal structure of the left-handed enantiomer of PET protected Au_{38} NC. (a) and (b) Top and side view. (c) Schematic representation handedness of the Au_{38} NC. (a′) HPLC chromatogram of the enantioseparation of rac- $Au_{38}(SC_2H_4Ph)_{24}$. The peak at 8.45 min corresponds to enantiomer 1; the second peak at 17.45 min corresponds to enantiomer 2. (b′) Optical absorbance spectra of enantiomers 1,2, and of the racemate. Reproduced with permission from ref.[81]. Copyright 2012, Springer Nature.

chiral stationary phase (Fig. 9.14). This investigation unveiled the distinct properties of NC isomers.

Besides separation, chiral chromatography is also used to monitor the ligand exchange reactions of Au_{38} NCs. The ligand exchange reaction between enantiopure 1,1′-binaphthyl-2,2′-dithiol (BINAS) and racemic Au_{38} NCs was studied by Knoppe et al. using a cellulose-based chiral column.[82] This study revealed that the ligand exchange is diastereoselective, and the exchange is four times faster in the case of a particular enantiomer with 60% diastereomeric excess. The ligand exchange reaction between enantiopure planar chiral [2.2] paracyclophane-4-thiol-1 (PCP-4-SH) and gold NC was also studied using chiral chromatography.[83] Several investigations on the separation of isomers and ligand exchanged products of chiral NCs, and their corresponding alloys were carried out using chiral chromatography.[84]

9.6.4 Thin layer chromatography (TLC)

TLC is a facile separation technique used for the preliminary analysis of a crude mixture. The stationary phase is often a thin sheet of plastic/aluminum foil/glass coated with a layer of silica gel, cellulose, or alumina as adsorbent material. Depending on the properties of the stationary phase, various solvents are used as the mobile phase, and they move by capillary action through the stationary phase. In NC science, TLC is mainly used to separate NCs based on their charge state and size. In 2014, Pradeep et al. separated a mixture of $Au_{25}(PET)_{18}$ and $Au_{144}(PET)_{60}$ NCs using TLC.[85] They have successfully separated $Au_{25}(PET)_{18}$ and $Au_{25}(SC_4H_9)_{18}$ NCs with different ligand combinations, and butane thiol protected neutral and anionic Au_{25} NCs using TLC (Fig. 9.15). TLC still serves as a low-cost and straightforward technique in the separation and purification of atomically precise NCs. Subsequently, TLC has been used in the separation of a variety of cluster mixtures.

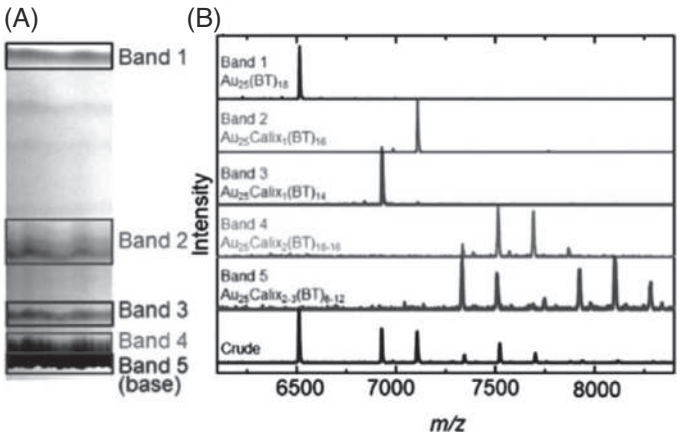

FIGURE 9.15 (A) Photograph of the TLC plate having different bands of mixed ligand protected $Au_{25}(calix)_{0\text{-}3}(BT)_{6\text{-}18}$ NCs and (B) corresponding MALDI-MS. Reproduced with permission from ref.[85]. Copyright 2014, American Chemical Society.

9.7 Toward preparative scale separation of atomically precise nanoclusters

9.7.1 Preparative scale size exclusion chromatography (PSEC)

The separation techniques mentioned above are mostly restricted to analytical traces. Large-scale production of monodisperse NCs is inevitable for their applications in catalysis, sensing and to create NC assembled solids via crystallization. In 2011, Burgi et al. separated gold NCs in a semipreparative scale using a gravity flow SEC set up.[86] They used charge-neutral styrene-divinylbenzene beads as the stationary phase in a glass column and THF as mobile phase, with ~40 mg of analyte loading. Repeated cycles of separation resulted in the isolation of Au_{38}, Au_{40}, and other large NCs. Their studies indicate that such a packed column can be reused more than 20 times without any loss in the separation efficiency.

Preparative scale separation was further extended to octanethiol-protected platinum NCs by size-exclusion chromatography.[87] Monodisperse platinum NCs with different ring sizes were obtained through 25 recycling processes. This large-scale isolation enabled preparative scale catalysis using the separated NCs. Recently, Sakthivel et al. demonstrated the versatility of the gravity flow SEC technique in isolating a wide range of NCs with similar sizes and different protecting ligands (Fig. 9.16).[88] They successfully isolated $Au_{137}(SR)_{56}$ from a mixture of $Au_{329}(SR)_{84}$, $Au_{144}(SR)_{60}$, $Au_{137}(SR)_{56}$, and $Au_{130}(SR)_{50}$ NCs. They further extended this protocol to isolate phenylethanethiolate, thiophenolate, 4-tert-butylbenzene thiolate, and tert-butyl thiolate protected gold NCs. The monodispersity of the separated NCs is further improved by performing multiple cycles. Their study concluded that the resolution of the separation can be improved by varying the column length. The isolated fractions of NCs were further characterized using MALDI MS. Such preparative scale separation of NCs with ease of use can contribute to large-scale production of monodisperse NCs.

9.7.2 Preparative thin layer chromatography (PTLC)

The TLC separation technique was extensively used to separate NCs due to low cost and ease of use. Wu's group introduced the preparative scale TLC (PTLC), wherein they

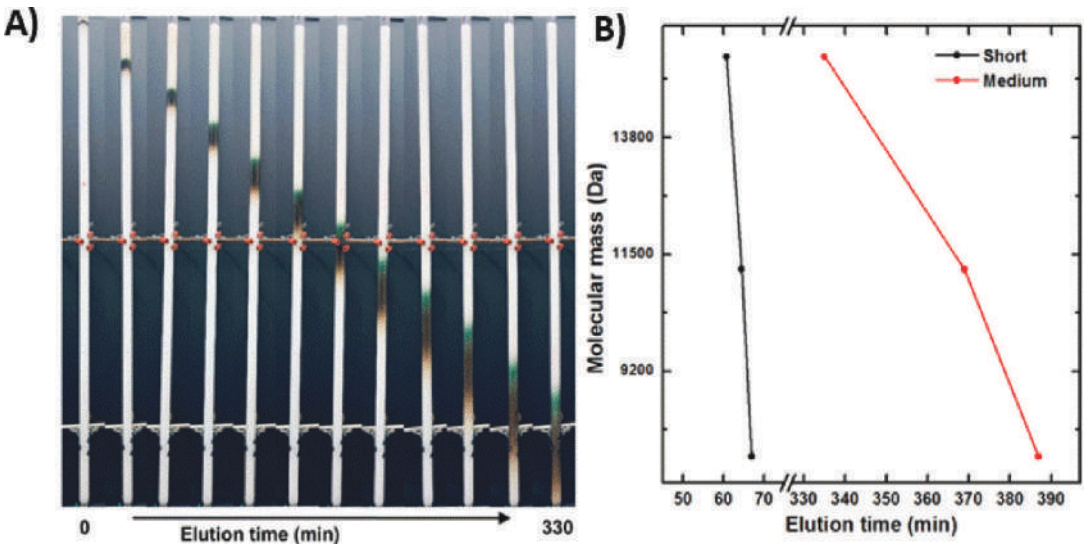

FIGURE 9.16 (A) Photograph of the SEC band during elution. (B) Plot of molecular weight vs elution time. Reproduced with permission from ref.[88]. Copyright 2021, American Chemical Society.

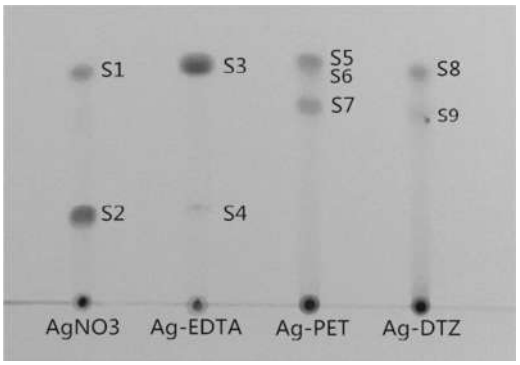

FIGURE 9.17 Photograph of the isolation of silver NCs in TLC plate with different metal precursors. Reproduced with permission from ref.[89]. Copyright 2015, Royal Society of Chemistry.

used TLC plates of ~10 cm × 20 cm dimension to isolate NCs. They used PTLC to isolate the ion-precursor and ion-dose-dependent antigalvanic reduction products of gold NCs (Fig. 9.17).[89] The structural isomers of $Au_{38}(PET)_{24}$ NCs were successfully separated by Jin et al. using PTLC.[90] Chen et al. successfully isolated the homologous series of phenylethanethiolate protected Pd clusters using PTLC.[91] Till date, PTLC is extensively used to optimize NC synthesis protocols, to separate structural isomers, chiral NCs, NC reaction products, and monodisperse NCs from the crude mixture.[92]

9.8 Summary and future perspectives

The various synthetic protocols used for NC synthesis mainly result in NCs of different core sizes. The effective use of the separation techniques renders monodisperse NCs, and

an in-depth understanding of the properties of atomically precise NCs. It is important to obtain monodisperse NCs in preparative scale for applications including catalysis, transport properties, and sensing. The various chromatographic techniques can be effectively modified for high-resolution separation of NCs. The methods so far developed can only separate gold NCs and their alloys. The separation of silver NCs has remained unsuccessful due to their poor stability. Recent studies of intercluster reactions and ligand exchange reactions indicate the dynamic nature of molecular NCs, which impedes the isolation of such molecular NCs. It is important to develop new methods that can be extended to other metal NCs. The integration of HPLC with MS can result in a better separation of NCs. The isolation of supramolecular assemblies of NCs by HPLC-MS studies can help gain more information. The high-throughput procedures such as integrated capillary HPLC and ion-pairing reversed-phase chromatography can enable the isolation of nanoclusters which might be difficult to resolve using standard separation techniques. Furthermore, the use of two and three-dimensional HPLC can unravel new insights in NC separation.

List of abbreviation

BINAS	1,1′-binaphthyl-2,2′-dithiol
CE	Capillary electrophoresis
CEC	Capillary electro chromatography technique
DCM	Dichloromethane
DDT	1-Dodecanethiol
DMBT	2,4-Dimethylbenzenethiolate
ESI MS	Electrospray ionization mass spectrometry/spectrum
FTP	4-fluorothiophenol
GFC	Gel filtration chromatography
HPGC	High-pressure gas chromatography
HPLC	High-performance liquid chromatography
HILIC	Hydrophilic interaction liquid chromatography
LC-MS	Liquid chromatography-mass spectrometry
LDI-MS	Laser desorption/ionization mass spectrometry
MALDI MS	Matrix-assisted laser desorption ionization mass spectrometry
MBA	4-mercaptobenzoic acid
NALC	N-acetyl-L-cysteine
NC	Nanocluster
ODT	1-octadecanethiol
PAGE	Polyacrylamide gel electrophoresis
PCP-4-SH	[2.2] Paracyclophane-4-thiol
PET	2-phenylethanethiolate
PSEC	Preparative size exclusion chromatography
PTLC	Preparative thin layer chromatography
SBB	4-tert- butylbenzylthiolate
SDS	Sodium dodecyl sulfate
SEC	Size exclusion chromatography
SG	Glutathione
S(PG)	2-mercaptopropionyl glycine
-SR	alkyl/aryl
SSSP	Sequential size-selective precipitation
THF	Tetrahydrofuran
TLC	Thin layer chromatography
TOAB	Tetraoctylammoniumbromide
UV/Vis	Ultraviolet/visible

References

1. (a) Tsukuda T, Häkkinen H. Protected Metal Clusters: From Fundamentals to Applications. Elsevier Science, Amsterdam; 2015; (b) Negishi Y, Hashimoto S, Ebina A, Hamada K, Hossain S, Kawawaki T. Atomic-level separation of thiolate-protected metal clusters; 2020 *Nanoscale.* 12:8017–8039; (c) Niihori Y, Uchida C, Kurashige W, Negishi Y. High-resolution separation of thiolate-protected gold clusters by reversed-phase high-performance liquid chromatography; 2016 *Phys Chem Chem Phys.* 18:4251–4265.
2. Niihori Y, Yoshida K, Hossain S, Kurashige W, Negishi Y. Deepening the understanding of thiolate-protected metal clusters using high-performance liquid chromatography. *Bull Chem Soc Jpn*. 2019;92:664–695.
3. Black DM, Hoque MM, Plascencia-Villa G, Whetten RL. New evidence of the bidentate binding mode in 3-MBA protected gold clusters: analysis of aqueous 13–18 kDa gold-thiolate clusters by HPLC-ESI-MS reveals special compositions Aun(3-MBA)p, (n = 48–67, p = 26–30). *Nanomaterials*. 2019;9:1303.
4. Hittorf W. Ueber die Wanderungen der Ionen während der Elektrolyse. *Ann Phys*. 1853;165:177–211. https://doi.org/10.1002/andp.18531650602.
5. (a) Vesterberg O. History of electrophoretic methods. *J Chromatogr A*. 1989;480:3–19; (b) Hardy WB. Colloidal solution. The globulins. *J Physiol*. 1905;33:251–337.
6. Tiselius A. A new apparatus for electrophoretic analysis of colloidal mixtures. *Trans Faraday Soc*. 1937;33:524–531.
7. Smithies O. Zone electrophoresis in starch gels: group variations in the serum proteins of normal human adults. *Biochem J*. 1955;61:629–641.
8. (a) Raymond S, Weintraub L. Acrylamide gel as a supporting medium for zone electrophoresis. *Science*. 1959;130:711; (b) Raymond S, Nakamichi M, Aurell B. Acrylamide gel as an electrophoresis medium. *Nature*. 1962;195:697–698.
9. (a) Ornstein L. Disc electrophoresis. I. Background and theory. *Ann NY Acad Sci*. 1964;121:321–349; (b) Davis BJ. Disc electrophoresis. II. Method and application to human serum proteins. *Ann NY Acad Sci*. 1964;121:404–427.
10. (a) Hjertén S. A new method for preparation of agarose for gel electrophoresis. *Biochim Biophys Acta*. 1962;62:445–449; (b) Brishammar S, Hjertén S, Hofsten Bv. Immunological precipitates in agarose gels. *Biochim Biophys Acta*. 1961;53:518–521.
11. Shapiro AL, Viñuela E, V Maizel J. Molecular weight estimation of polypeptide chains by electrophoresis in SDS-polyacrylamide gels. *Biochem Biophys Res Commun*. 1967;28:815–820.
12. (a) Smithies O. Zone electrophoresis in starch gels and its application to studies of serum proteins. In: Anfinsen CB, Anson ML, Bailey K, Edsall JT, eds. *Adv Protein Chem.*, Vol. 14, Academic Press, Amsterdam; 1959:65–113; (b) Dale G, Latner AL. Isoelectric focusing of serum proteins in acrylamide gels followed by electrophoresis; 1969 Clinica chimica acta, international journal of clinical chemistry; 24:61–68; (c) O'Farrell PH. High resolution two-dimensional electrophoresis of proteins; 1975 *J Biol Chem.* 250:4007–4021.
13. Schwartz DC, Cantor CR. Separation of yeast chromosome-sized DNAs by pulsed field gradient gel electrophoresis. *Cell*. 1984;37:67–75.
14. Hjertén S. Free zone electrophoresis. *Chromatogr Rev*. 1967;9:122–219.
15. Jorgenson JW, Lukacs KD. Capillary zone electrophoresis. *Science*. 1983;222:266–272.
16. Heegaard NHH, Kennedy RT. Identification, quantitation, and characterization of biomolecules by capillary electrophoretic analysis of binding interactions. *Electrophoresis*. 1999;20:3122–3133.
17. Hellman LM, Fried MG. Electrophoretic mobility shift assay (EMSA) for detecting protein–nucleic acid interactions. *Nat Protoc*. 2007;2:1849–1861.
18. Everaerts FM, Geurts M, Mikkers FEP, Verheggen TPEM. Analytical isotachophoresis. *J Chromatogr A*. 1976;119:129–155.
19. Bier M. [3]Preparative electrophoresis. *Methods in Enzymology*, Vol. 5, Academic Press, Amsterdam; 1962:33–50.
20. Runge FF. Bildungstrieb der Stoffe: Veranschaulicht in selbständig gewachsenen Bilder, (Fortsetzung der Musterbilder)/von Friedlieb Ferdinand Runge. Oranienburg: Selbstverlag des Verfassers; 1855.
21. (a) von Krempelhuber A. Verhandlungen der Naturforschenden Gesellschaft in Basel, Vol. Bd. 3, Basel; 1861:1861–1863; (b) Farradane J. History of chromatography; 1951 *Nature.* 167:120.
22. Tswett M. Adsorptionsanalyse und Chromatogra-phische Methode. Anwendung auf die Chemie des Chlorophylls. *Ber deutsch bot Ges*. 1906;24:384–393.
23. Kuhn R, Lederer E. Fraktionierung und Isomerisierung des Carotins. *Naturwissenschaften*. 1931;19:306.
24. Spedding FH, Voigt AF, Gladrow EM, et al. The separation of rare earths by ion exchange.1,2 II. Neodymium and praseodymium. *J Am Chem Soc*. 1947;69:2786–2792.

25. Martin AJ, Synge RL. A new form of chromatogram employing two liquid phases: a theory of chromatography. 2. Application to the micro-determination of the higher monoamino-acids in proteins. *Biochem J*. 1941;35:1358–1368.
26. James AT, Martin AJP. Gas-liquid partition chromatography: the separation and micro-estimation of volatile fatty acids from formic acid to dodecanoic acid. *Biochem J*. 1952;50:679–690.
27. Stahl E. History of the development of thin-layer chromatography. In: Stahl E, ed. Thin-Layer Chromatography: A Laboratory Handbook. Berlin and Heidelberg: Springer; 1965:1–4.
28. Lathe GH, Ruthven CRJ. The separation of substances and estimation of their relative molecular sizes by the use of columns of starch in water. *Biochem J*. 1956;62:665–674.
29. (a) Dynamics of Chromatography, Part I: Principles and Theory. New York, NY: Marcel Dekker, Incorporated; 1965; (b) Huber JFK. High efficiency, high speed liquid chromatography in columns; 1969 *J Chromatogr Sci*.;7:85–90.
30. Horvath CG, Lipsky SR. Peak capacity in chromatography. *Anal Chem*. 1967;39:1893.
31. Klesper K. High pressure gas chromatog raphy above critical temperatures. *J Org Cher*. 1962;27:700–701.
32. (a) Rathore AS, Horváth C. Chapter 1 - migration of charged sample components and electroosmotic flow in packed capillary columns. In:Deyl Z, Švec F, eds. *J Chromatogr Lib*., Vol. 62, Elsevier, Amsterdam; 2001:1–38; (b) Strain HH. On the combination of electrophoretic and chromatographic adsorption methods; 1939 *J Am Chem Soc*. 61:1292–1293; (c) Strain H, Sullivan uJ. Analysis by electromigration plus chromatography; 1951 *Anal Chem*. 23:816–823.
33. Jorgenson JW, Lukacs KD. High-resolution separations based on electrophoresis and electroosmosis. *J Chromatogr A*. 1981;218:209–216.
34. Whetten RL, Khoury JT, Alvarez MM, et al. Nanocrystal gold molecules. *Adv Mater*. 1996;8:428–433.
35. Schaaff TG, Shafigullin MN, Khoury JT, et al. Isolation of smaller nanocrystal Au molecules: robust quantum effects in optical spectra. *J Phys Chem B*. 1997;101:7885–7891.
36. Hicks JF, Templeton AC, Chen S, et al. The monolayer thickness dependence of quantized double-layer capacitances of monolayer-protected gold clusters. *Anal Chem*. 1999;71:3703–3711.
37. Tracy JB, Kalyuzhny G, Crowe MC, Balasubramanian R, Choi J-P, Murray RW. Poly(ethylene glycol) ligands for high-resolution nanoparticle mass spectrometry. *J Am Chem Soc*. 2007;129:6706–6707.
38. (a) Negishi Y, Chaki NK, Shichibu Y, Whetten RL, Tsukuda T. Origin of magic stability of thiolated gold clusters: a case study on $Au_{25}(SC_6H_{13})_{18}$. *J Am Chem Soc*. 2007;129:11322–11323; (b) Parker JF, Weaver JEF, McCallum F, Fields-Zinna CA, Murray RW. Synthesis of Monodisperse $[Oct_4N^+][Au_{25}(SR)_{18}^-]$ Nanoparticles, with Some Mechanistic Observations. *Langmuir*. 2010;26:13650–13654.
39. Yang X, Su Y, Paau MC, Choi MMF. Mass spectrometric identification of water-soluble gold nanocluster fractions from sequential size-selective precipitation. *Anal Chem*. 2012;84:1765–1771.
40. Schaaff TG, Knight G, Shafigullin MN, Borkman RF, Whetten RL. Isolation and selected properties of a 10.4 kDa Gold:glutathione cluster compound. *J Phys Chem B*. 1998;102:10643–10646.
41. Schaaff TG, Whetten RL. Giant Gold−Glutathione cluster compounds: intense optical activity in metal-based transitions. *J Phys Chem B*. 2000;104:2630–2641.
42. (a) Negishi Y, Takasugi Y, Sato S, Yao H, Kimura K, Tsukuda T. Magic-numbered Aun clusters protected by glutathione monolayers (n = 18, 21, 25, 28, 32, 39): isolation and spectroscopic characterization. *J Am Chem Soc*. 2004;126:6518–6519; (b) Negishi Y, Nobusada K, Tsukuda T. Glutathione-protected gold clusters revisited: bridging the gap between Gold(I)−Thiolate complexes and thiolate-protected gold nanocrystals. *J Am Chem Soc*. 2005;127:5261–5270.
43. Kothalawala N, Lee West Iv J, Dass A. Size-dependent molecule-like to plasmonic transition in water-soluble glutathione stabilized gold nanomolecules. *Nanoscale*. 2014;6:683–687.
44. Negishi Y, Takasugi Y, Sato S, Yao H, Kimura K, Tsukuda T. Kinetic stabilization of growing gold clusters by passivation with thiolates. *J Phys Chem B*. 2006;110:12218–12221.
45. Kumar S, Bolan MD, Bigioni TP. Glutathione-stabilized magic-number silver cluster compounds. *J Am Chem Soc*. 2010;132:13141–13143.
46. Shichibu Y, Negishi Y, Tsukuda T, Teranishi T. Large-scale synthesis of thiolated au25 clusters via ligand exchange reactions of phosphine-stabilized Au_{11} Clusters. *J Am Chem Soc*. 2005;127:13464–13465.
47. Dreier TA, Compel WS, Wong OA, Ackerson CJ. Oxygen's role in aqueous gold cluster synthesis. *J Phys Chem C*. 2016;120:28288–28294.

48. Desireddy A, Kumar S, Guo J, Bolan MD, Griffith WP, Bigioni TP. Temporal stability of magic-number metal clusters: beyond the shell closing model. *Nanoscale*. 2013;5:2036–2044.
49. Bootharaju MS, Burlakov VM, Besong TMD, et al. Reversible size control of silver nanoclusters via ligand-exchange. *Chem Mater*. 2015;27:4289–4297.
50. (a) Yu Y, Luo Z, Chevrier DM, et al. Identification of a highly luminescent $Au_{22}(SG)_{18}$ nanocluster. *J Am Chem Soc*. 2014;136:1246–1249; (b) Udaya Bhaskara Rao T, Pradeep T. Luminescent Ag_7 and Ag_8 clusters by interfacial synthesis. *Angew Chem Int Ed*. 2010;49:3925–3929.
51. Stark MC, Baikoghli MA, Lahtinen T, et al. Structural characterization of site-modified nanocapsid with monodispersed gold clusters. *Sci Rep*. 2017;7:17048.
52. Choi MM, Douglas AD, Murray RW. Ion-pair chromatographic separation of water-soluble gold monolayer-protected clusters. *Anal Chem*. 2006;78:2779–2785.
53. Zhang L, Hu Q, Li Z, et al. Chromatographic separation and mass spectrometric analysis of N-acetyl-l-cysteine-protected palladium nanoparticles. *Anal Methods*. 2017;9:4539–4546.
54. Niihori Y, Kikuchi Y, Shima D, et al. Separation of glutathionate-protected gold clusters by reversed-phase ion-pair high-performance liquid chromatography. *Ind Eng Chem Res*. 2017;56:1029–1035.
55. Black DM, Alvarez MM, Yan F, et al. Triethylamine solution for the intractability of aqueous gold–thiolate cluster anions: how ion pairing enhances ESI-MS and HPLC of aq-Au_n(pMBA)p. *J Phys Chem C*. 2017;121:10851–10857.
56. Buszewski B, Noga S. Hydrophilic interaction liquid chromatography (HILIC)—a powerful separation technique. *Anal Bioanal Chem*. 2012;402:231–247.
57. Niihori Y, Shima D, Yoshida K, et al. High-performance liquid chromatography mass spectrometry of gold and alloy clusters protected by hydrophilic thiolates. *Nanoscale*. 2018;10:1641–1649.
58. Ramsay H, Simon D, Steele E, Hebert A, Oleschuk RD, Stamplecoskie KG. The power of fluorescence excitation–emission matrix (EEM) spectroscopy in the identification and characterization of complex mixtures of fluorescent silver clusters. *RSC Adv*. 2018;8:42080–42086.
59. Jimenez VL, Leopold MC, Mazzitelli C, Jorgenson JW, Murray RW. HPLC of monolayer-protected gold nanoclusters. *Anal Chem*. 2003;75:199–206.
60. (a) Song Y, Jimenez V, McKinney C, Donkers R, Murray RW. Estimation of size for 1−2 nm nanoparticles using an HPLC electrochemical detector of double layer charging. *Anal Chem*. 2003;75:5088–5096; (b) Song Y, Heien MLAV, Jimenez V, Wightman RM, Murray RW. Voltammetric detection of metal nanoparticles separated by liquid chromatography. *Anal Chem*. 2004;76:4911–4919.
61. Negishi Y, Nakazaki T, Malola S, et al. A critical size for emergence of nonbulk electronic and geometric structures in dodecanethiolate-protected Au clusters. *J Am Chem Soc*. 2015;137:1206–1212.
62. Knoppe S, Vogt P. HPLC of monolayer-protected gold clusters with baseline separation. *Anal Chem*. 2019;91:1603–1609.
63. Black DM, Bhattarai N, Bach SB, Whetten RL. Selection and identification of molecular gold clusters at the Nano(gram) scale: reversed phase HPLC-ESI-MS of a mixture of Au-Peth MPCs. *J Phys Chem Lett*. 2016;7:3199–3205.
64. Negishi Y, Kurashige W, Niihori Y, Iwasa T, Nobusada K. Isolation, structure, and stability of a dodecanethiolate-protected Pd_1Au_{24} cluster. *Phys Chem Chem Phys*. 2010;12:6219–6225.
65. Sugi KS, Bhat S, Nag A, Ganesan P, Mahendranath A, Pradeep T. Ligand structure and charge state-dependent separation of monolayer protected Au_{25} clusters using non-aqueous reversed-phase HPLC. *Analyst*. 2020;145:1337–1345.
66. Niihori Y, Matsuzaki M, Pradeep T, Negishi Y. Separation of precise compositions of noble metal clusters protected with mixed ligands. *J Am Chem Soc*. 2013;135:4946–4949.
67. Niihori Y, Matsuzaki M, Uchida C, Negishi Y. Advanced use of high-performance liquid chromatography for synthesis of controlled metal clusters. *Nanoscale*. 2014;6:7889–7896.
68. Niihori Y, Kikuchi Y, Kato A, Matsuzaki M, Negishi Y. Understanding ligand-exchange reactions on thiolate-protected gold clusters by probing isomer distributions using reversed-phase high-performance liquid chromatography. *ACS Nano*. 2015;9:9347–9356.
69. Niihori Y, Koyama Y, Watanabe S, et al. Atomic and isomeric separation of thiolate-protected alloy clusters. *J Phys Chem Lett*. 2018;9:4930–4934.

70. Niihori Y, Hashimoto S, Koyama Y, Hossain S, Kurashige W, Negishi Y. Dynamic behavior of thiolate-protected gold–silver 38-atom alloy clusters in solution. *J Phys Chem C*. 2019;123:13324–13329.
71. Wilcoxon JP, Provencio PP. Heterogeneous growth of metal clusters from solutions of seed nanoparticles. *J Am Chem Soc*. 2004;126:6402–6408.
72. Murayama H, Narushima T, Negishi Y, Tsukuda T. Structures and stabilities of alkanethiolate monolayers on palladium clusters As studied by gel permeation chromatography. *J Phys Chem B*. 2004;108:3496–3503.
73. (a) Wilcoxon JP, Martin JE, Provencio P. Optical properties of gold and silver nanoclusters investigated by liquid chromatography. *J Chem Phys*. 2001;115:998–1008; (b) Wilcoxon JP, Provencio P. Etching and aging Effects in nanosize Au clusters investigated using high-resolution size-exclusion chromatography. *J Phys Chem B*. 2003;107:12949–12957.
74. Tsunoyama H, Negishi Y, Tsukuda T. Chromatographic isolation of "Missing" Au_{55} clusters protected by alkanethiolates. *J Am Chem Soc*. 2006;128:6036–6037.
75. (a) Tsunoyama R, Tsunoyama H, Pannopard P, Limtrakul J, Tsukuda T. MALDI mass analysis of 11 kDa gold clusters protected by octadecanethiolate ligands. *J Phys Chem C*. 2010;114:16004–16009; (b) Qian H, Jin R. Synthesis and electrospray mass spectrometry determination of thiolate-protected $Au_{55}(SR)_{31}$ nanoclusters. *Chem Commun*. 2011;47:11462–11464.
76. Qian H, Zhu Y, Jin R. Isolation of ubiquitous $Au_{40}(SR)_{24}$ clusters from the 8 kDa Gold clusters. *J Am Chem Soc*. 2010;132:4583–4585.
77. Negishi Y, Arai R, Niihori Y, Tsukuda T. Isolation and structural characterization of magic silver clusters protected by 4-(tert-butyl)benzyl mercaptan. *Chem Commun*. 2011;47:5693–5695.
78. (a) Wu Z, MacDonald MA, Chen J, Zhang P, Jin R. Kinetic control and thermodynamic selection in the synthesis of atomically precise gold nanoclusters. *J Am Chem Soc*. 2011;133:9670–9673; (b) Zhu X, Jin S, Wang S, et al. One-pot synthesis of phenylmethanethiolate-protected $Au_{20}(SR)_{16}$ and $Au_{24}(SR)_{20}$ nanoclusters and insight into the kinetic control. *Chemistry, an Asian journal*. 2013;8:2739–2745.
79. Dalgliesh CE. The optical resolution of aromatic amino-acids on paper chromatograms. *J Chem Soc. (Resumed)*. 1952;756:3940–3942.
80. Jadzinsky PD, Calero G, Ackerson CJ, Bushnell DA, Kornberg RD. Structure of a thiol monolayer-protected gold nanoparticle at 1.1 Å resolution. *Science*. 2007;318:430–433.
81. Dolamic I, Knoppe S, Dass A, Bürgi T. First enantioseparation and circular dichroism spectra of Au_{38} clusters protected by achiral ligands. *Nat Commun*. 2012;3:798.
82. Knoppe S, Dharmaratne AC, Schreiner E, Dass A, Bürgi T. Ligand exchange reactions on Au_{38} and Au_{40} clusters: a combined circular dichroism and mass spectrometry study. *J Am Chem Soc*. 2010;132:16783–16789.
83. Beqa L, Deschamps D, Perrio S, Gaumont A-C, Knoppe S, Bürgi T. Ligand exchange reaction on $Au_{38}(SR)_{24}$, separation of $Au_{38}(SR)_{23}(SR')_1$ regioisomers, and migration of thiolates. *J Phys Chem C*. 2013;117:21619–21625.
84. (a) Zhang B, Bürgi T. Doping silver increases the $Au_{38}(SR)_{24}$ cluster surface flexibility. *J Phys Chem C*. 2016;120:4660–4666; (b) Barrabés N, Zhang B, Bürgi T. Racemization of Chiral $Pd_2Au_{36}(SC_2H_4Ph)_{24}$: DOPING INCREASES THE FLEXIBILITY OF THE CLUSTER Surface. *J Am Chem Soc*. 2014;136:14361–14364; (c) Kazan R, Zhang B, Bürgi T. $Au_{38}Cu_1$(2-PET)$_{24}$ nanocluster: synthesis, enantioseparation and luminescence. *Dalton Trans*. 2017;46:7708–7713; (d) Jin S, Xu F, Du W, et al. Isomerism in Au–Ag Alloy nanoclusters: structure determination and enantioseparation of $[Au_9Ag_{12}(SR)_4(dppm)_6 \times 6]3+$. *Inorg Chem*. 2018;57:5114–5119.
85. Ghosh A, Hassinen J, Pulkkinen P, Tenhu H, Ras RHA, Pradeep T. Simple and efficient separation of atomically precise noble metal clusters. *Anal Chem*. 2014;86:12185–12190.
86. Knoppe S, Boudon J, Dolamic I, Dass A, Bürgi T. Size exclusion chromatography for semipreparative scale separation of $Au_{38}(SR)_{24}$ and $Au_{40}(SR)_{24}$ and larger clusters. *Anal Chem*. 2011;83:5056–5061.
87. Imaoka T, Akanuma Y, Haruta N, et al. Platinum clusters with precise numbers of atoms for preparative-scale catalysis. *Nat Commun*. 2017;8:688.
88. Sakthivel NA, Jupally VR, Eswaramoorthy SK, et al. Size exclusion chromatography: an indispensable tool for the isolation of monodisperse gold nanomolecules. *Anal Chem*. 2021;93:3987–3996.
89. Tian S, Yao C, Liao L, Xia N, Wu Z. Ion-precursor and ion-dose dependent anti-galvanic reduction. *Chem Commun*. 2015;51:11773–11776.
90. Tian S, Li Y-Z, Li M-B, et al. Structural isomerism in gold nanoparticles revealed by X-ray crystallography. *Nat Commun*. 2015;6:8667.

91. Chen J, Liu L, Weng L, et al. Synthesis and properties evolution of a family of tiara-like phenylethanethiolated palladium nanoclusters. *Sci Rep*. 2015;5:16628.
92. (a) Gan Z, Lin Y, Luo L, et al. Fluorescent gold nanoclusters with interlocked staples and a fully thiolate-bound kernel. *Angew Chem Int Ed*. 2016;55:11567–11571; (b) Liao L, Chen J, Wang C, et al. Transition-sized Au_{92} nanoparticle bridging non-fcc-structured gold nanoclusters and fcc-structured gold nanocrystals. *Chem Commun*. 2016;52:12036–12039; (c) Liao L, Zhuang S, Yao C, et al. Structure of chiral $Au_{44}(2,4\text{-DMBT})_{26}$ nanocluster with an 18-electron shell closure. *J Am Chem Soc*. 2016;138:10425–10428; (d)Liao L, Yao C, Wang C, Tian S, Chen J, Li M-B, Xia N, Yan N, Wu Z, Quantitatively monitoring the size-focusing of Au nanoclusters and revealing what promotes the size transformation from $Au_{44}(TBBT)_{28}$ to $Au_{36}(TBBT)_{24}$. Anal Chem 2016;88:11297–11301; (e) Xia N, Yuan J, Liao L, et al. Structural oscillation revealed in gold nanoparticles. *J Am Chem Soc*. 2020;142:12140–12145; (f) Wu Z, Dong J, Gan Z, et al. Synthesizing photoluminescent $Au_{28}(SCH_2Ph\text{-}tBu)_{22}$ nanoclusters with feature structures by using a joint method. *Angew Chem Int Ed*. 2022;n/a; (g) Li Y, Zhou M, Song Y, Higaki T, Wang H, Jin R. Double-helical assembly of heterodimeric nanoclusters into supercrystals. *Nature*. 2021;594:380–384.

CHAPTER

10

Mass spectrometry of atomically precise clusters

Papri Chakraborty[a] *and Thalappil Pradeep*[b]

[a]DST Unit of Nanoscience (DST UNS) and Thematic Unit of Excellence (TUE), Department of Chemistry, Indian Institute of Technology Madras, Chennai, India
[b]Deepak Parekh Institute Chair Professor and Professor of Chemistry, Department of Chemistry, Indian Institute of Technology Madras, Chennai, India

10.1 Introduction

Mass spectrometry (MS) is an analytical technique used to study ions. MS measures mass/charge (m/z) ratio of gaseous ions. In 1912, Thomson introduced this technique by measuring m/z values for ions in the gas phase.[1] Since then, this technique has advanced tremendously. A mass spectrometer mainly consists of three essential components: source, analyzer, and detector.[2] In the early days, MS was mainly useful for the analysis of organic molecules but was later applied for the analysis of proteins and macromolecules as well.[3] This became possible due to advancements in methods of ionization, and improvements in instrumentation that helped achieve higher resolution and higher mass ranges for detection. MS has also found applications in material science. Fullerene, C_{60}, was discovered by MS.[4] MS was also used to characterize gas-phase clusters of Na, like Na_n ($n = 4$–100).[5] Bare Au and Ag NCs, synthesized in the gas phase, were also characterized by MS.[6,7] Recently, MS was used extensively in the study of ligand protected atomically precise NCs.[8–10] These ligand-protected NCs are made of noble metals like Au and Ag and are mostly protected by monolayers of thiols and phosphines. These NCs are synthesized in the solution phase and many of them have been crystallized. Chemical composition and charge states of NCs can be deduced from the isotopic distribution of peaks observed in MS. Various methods of ionization are used to ionize these NCs into the gas phase. Soft ionization techniques like electrospray ionization (ESI) and matrix assisted laser desorption ionization (MALDI) are particularly useful in transferring the intact molecular ions from solution phase to the gas phase. A variety of bare and ligand-protected NCs have been characterized by MS till date.[8] MS has emerged as an important tool in understanding the chemical reactivity and transformation of NCs. Tandem MS involves dissociation of mass-selected ions and provides additional structural details of

Atomically Precise Metal Nanoclusters.
DOI: https://doi.org/10.1016/B978-0-323-90879-5.00022-6

gas-phase ions. MS when coupled to other techniques like ion mobility (IM) can be used to understand structural changes/isomerism in the gaseous ions. Such studies have also helped to understand the gas-phase structures of the NCs. Several other hyphenated techniques like, liquid-chromatography (LC) MS helped to analyze and separate NCs from their mixtures in solution. Spectroscopy of mass-selected ions has opened up yet another huge area of interest on atomically precise NCs.

In this chapter, a comprehensive discussion on MS to characterize atomically precise NCs is presented. The use of MS in the characterization of gold, silver, other metal NCs and their alloys, protected by ligands like thiols and phosphines, is discussed. Various methods of ionization and the advancement in mass spectrometric instrumentation that has enabled such studies are discussed. This chapter also discusses tandem MS and IM MS to understand structures of NCs. The use of MS in characterizing NCs prepared in macromolecular templates like proteins is also discussed. The chapter concludes with future perspectives on the use of spectroscopic techniques coupled to MS for studying isolated NC ions and expanding MS techniques for analyzing megadalton-sized particles.

10.2 Various techniques for ionization of NCs

Various methods of ionization, used in mass spectrometers, involve ionizing neutral molecules or transferring charged molecules from the solution or condensed phase into the gas phase.[11] The ionization of the neutral molecules occurs by processes such as electron capture or ejection, protonation or deprotonation, cationization, etc. In the 1980s, electron ionization (EI) was primarily used as the ionization technique in mass spectrometers.[12] However, this technique was limited to the ionization of small molecules. Gradually, other ionization techniques like MALDI,[13] and ESI[14] were developed. MALDI and ESI are soft ionization techniques that have evolved into the most widely used techniques for mass analysis of larger molecules and offer excellent results in terms of sensitivity and mass range. For the analysis of NCs also, MALDI and ESI are the most promising ionization techniques today. A brief overview of these two techniques is presented below.

10.2.1 Matrix-assisted laser desorption ionization (MALDI)

The technique of MALDI MS was developed in the late 1980s by Tanaka, Karas, and Hillenkamp[15,16] and since then it has been a powerful technique for the analysis of large biomolecules and has found enormous applications in the ionization of noble metal NCs. A schematic of the MALDI MS process is presented in Fig. 10.1. In this technique, the analyte is mixed with a large excess of the matrix. Weak organic acids such as sinapinic acid, 2,5-dihydroxy benzoic acid, α-cyano-4-hydroxycinnamic acid, etc., that are good absorbers of UV irradiation, are usually chosen as the matrix. Lasers of fixed wavelength (commonly used is 337 nm nitrogen laser) are used for ionization. When the analyte-matrix mixture is irradiated by a laser, the matrix absorbs the radiation and is vaporized into the gas phase carrying the analyte molecules along with it. Thus, the matrix protects the analyte from direct UV irradiation. Lasers with pulse widths in the range of 1–100 ns are used and the MALDI source generates pulsed ions. When the matrix along with the analyte is released from the MALDI target or sample plate, cation/proton exchange occurs between the sample and the analyte leading to the formation of charged analyte molecules. Singly charged molecular ions are

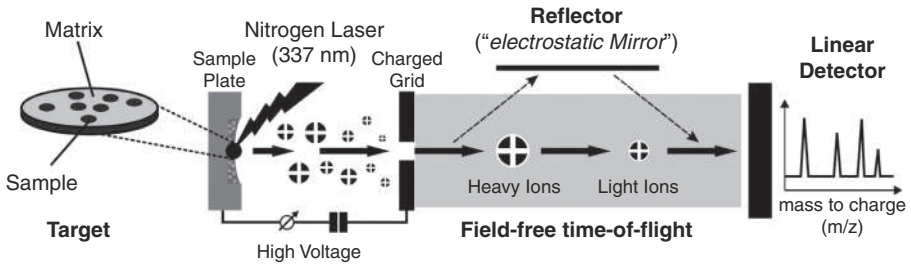

FIGURE 10.1 Scheme showing the process involved in MALDI-TOF MS.[17]

predominantly formed. The charged ions are accelerated by an electric field and after passing through charged grids, the ions drift through a field-free space. After traversing through this time-of-flight (TOF) tube, ions reach the detector and the mass spectrum is collected. The length of TOF determines the resolution of the mass spectrum. For similar charges, ions with low mass reach the detector faster than the ions with higher mass. The detector records the signal as a function of time (t) and from this t, the value of m/z is given by the equation:

$$\frac{m}{z} = 2\,E_{kin}\frac{t^2}{s^2}$$

where E_{kin} is the kinetic energy of the ion and s is the length of the flight tube. The resolution of the MALDI mass spectrum can be increased by increasing the length of the path tube or by increasing the travel path of the ions using reflectors or electrostatic mirrors in the TOF analyzer, as shown in Fig. 10.1.

10.2.2 Electrospray ionization

The technique of ESI was first developed by Dole et al. in the late 1960s.[18] John Fenn further developed this technique for ionizing large macromolecules[14] and was awarded the Nobel prize in chemistry in 2002. ESI is also a softer ionization technique and produces multiple-charged ions from solution with minimum fragmentation. ESI has emerged to be a powerful technique for ionizing intact NCs into the gas-phase. A schematic of the ESI process is presented in Fig. 10.2. The analyte solution is sprayed from a capillary or needle, on the application of a potential. In the presence of this strong electric field, the solution is electrosprayed in the form of charged droplets. Heat/dry gas is used to assist the evaporation of solvent from the droplets. As the size of the droplets decreases, the surface charge density increases and finally the droplets reach the "Rayleigh limit." At this point, the repulsion between the like charges overcomes the surface tension holding the droplet together causing the larger droplet break into a number of smaller droplets by a process known as "Coulomb fission." The newer droplets are also subjected to further desolvation and coulomb fission and finally, the charged ions enter the vacuum of the mass spectrometer.

10.3 Instrumentation

The major components of a mass spectrometer comprise an ionization source, a mass analyzer, and an ion detector. The state-of-the-art mass spectrometers are well-equipped with ionization sources like EI, atmospheric pressure chemical ionization (APCI), ESI, MALDI, fast

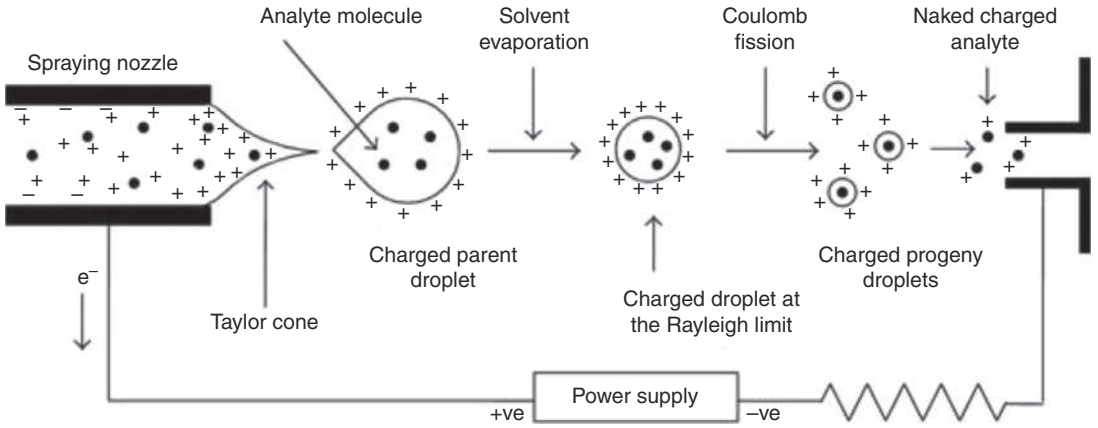

FIGURE 10.2 Scheme showing the process involved in ESI MS.[19]

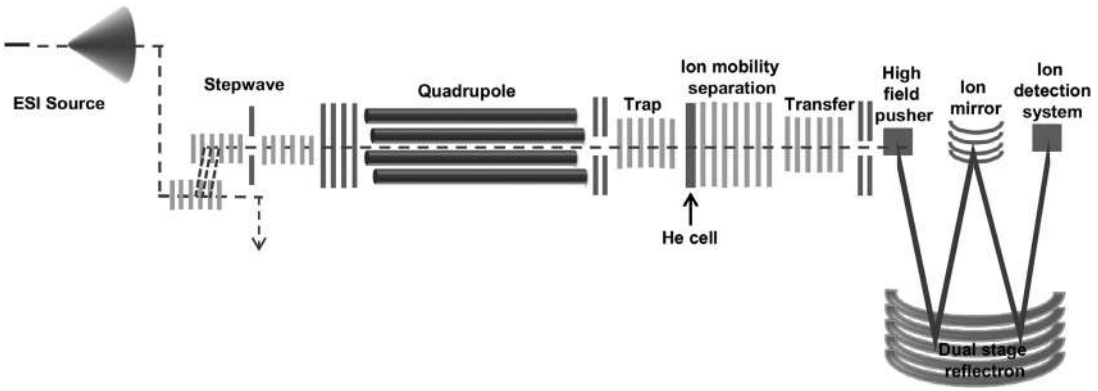

FIGURE 10.3 Schematic of a high-resolution mass spectrometer.[8]

atom bombardment, etc. For analysis of NCs, soft ionization sources like ESI and MALDI, as discussed above, are commonly used. Mass analyzers are used to separate the ions. TOF is one such mass analyzer where the ions are allowed to pass through flight tubes and their flight time is measured. Ion separation is achieved by the interaction of the ions with electrostatic or magnetostatic fields. After the separation in the mass analyzer, the ions finally reach the detector. Moreover, modern mass spectrometers include additional instrumentation to couple techniques like tandem mass spectrometry (MS/MS), IM or LC with MS. Over the years, advancement in instrumentation has helped improve the resolution of mass spectral measurements and a resolution ($m/\Delta m$) of $\sim$ 30,000–50,000 is achievable in modern-day mass spectrometers. Such high resolution has also enabled to precisely determine the composition of atomically precise NCs. Schematic of a high-resolution mass spectrometer is presented in Fig. 10.3. This shows the coupling of an ESI source to a mass spectrometer. Such mass spectrometers also use additional ion guides called "stepwaves" to filter neutral contaminants

before the ions enter the quadrupole and increase the sensitivity of detection. Quadrupole mass analyzers are used to select ions of particular m/z values that are further subjected to fragmentation by collision with gases like Ar by a process known as collision-induced dissociation (CID). IM or surface-induced dissociation (SID) devices are also coupled to mass spectrometers to obtain additional information on the structure and properties of NCs. This will be discussed in detail in the upcoming sections. In the TOF analyzer, the path of the ions can be increased by the use of ion mirrors and reflectors, thereby increasing resolution of the mass spectrum. Finally, the ions reach the detector, and the mass spectrum is obtained which is a plot of the ion intensity vs the m/z value of the ion. Further details on the analysis of a mass spectrum, especially of NCs, is discussed in the subsequent sections.

10.4 Mass spectrometry of ligand-protected metal NCs

MS can determine the exact composition of the metal NCs, that is, the number of metal atoms and ligands in the NCs. Whetten et al. first applied laser desorption ionization (LDI) for characterizing gold NCs protected by dodecanethiolate.[20] A Nd:YAG laser (532 nm, 5 ns) was used to irradiate NCs in a TOF mass spectrometer. A solution containing NCs of mixed core sizes was separated through fractional crystallization and each fraction was monitored using LDI MS. From their studies, the number of Au atoms in the core of the NC was determined. Tsukuda et al. also characterized poly(N-vinyl-2-pyrrodidone) stabilized gold NCs using LDI MS.[21] In yet another study on alkanethiolate protected gold NCs by Arnold and Reilly, it was found that LDI can cause cleavage of all C–S bonds and the resulting mass spectrum of the NC showed a series of peaks that differed by mass of 197 or 32 corresponding to the loss of Au or S atoms.[22] Thus, it was evident that LDI was not an effective technique to determine the composition of metal NCs. Gradually, the use of MALDI evolved in analyzing metal NCs, wherein the use of suitable matrices could significantly reduce the fragmentation upon exposure to UV laser, and hence the accurate molecular formula of the NCs could be determined. Gold NCs have been most extensively studied due to their high stability. Other metal NCs composed of silver, copper, platinum, etc. and their alloys have also been studied through MS. The analysis of ligand-protected other metal NCs is discussed in detail in the following sections. MS is equally important in analyzing bare metal NCs as well and is discussed separately in Chapter 17.

10.4.1 Gold NCs

A wide variety of ligand-protected Au NCs has been synthesized and characterized till date. Although crystal structures of many such gold NCs are available, MS is also a promising technique to determine their precise composition. In the family of ligand-protected gold NCs, the most studied NC is $Au_{25}(SR)_{18}$ where SR is a thiolate ligand.[23,24] In 2008, Dass et al. successfully measured MALDI MS of intact $Au_{25}(PET)_{18}$ NCs.[25] The authors demonstrated that the use of trans-2-[3-(4-tert-butylphenyl)-2-methyl-2-propenylidene] malononitrile (DCTB) matrix could effectively reduce the fragmentation as shown in Fig. 10.4A. Low energy laser pulses were used to reduce fragmentation. Intact molecular ion of $Au_{25}(PET)_{18}$ was observed at m/z 7391 in the presence of DCTB matrix. The m/z value of 7391 corresponds to the single charged molecular ion which consists of 25 Au atoms and 18 PET ligands, i.e. 25 × mass

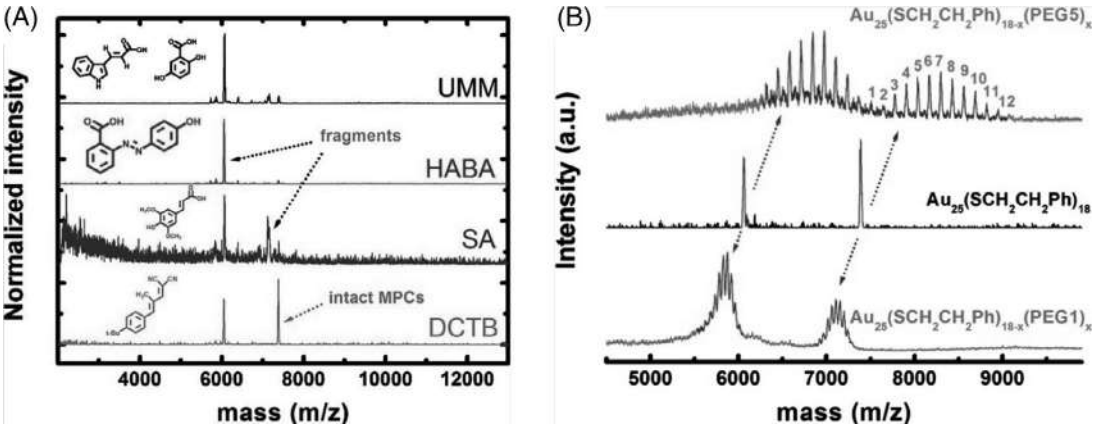

FIGURE 10.4 (A) MALDI MS of $Au_{25}(PET)_{18}$ in different matrices, (B) MALDI MS showing exchange of PET ligands of $Au_{25}(PET)_{18}$ with PEG5 and PEG1.[25]

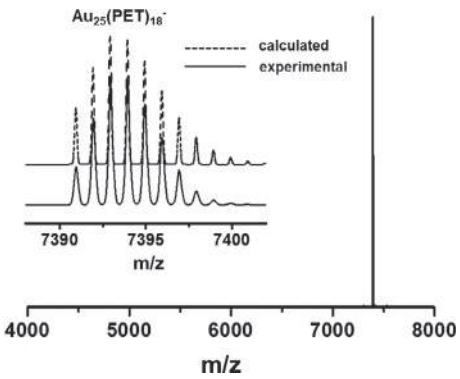

FIGURE 10.5 HR MS of $Au_{25}(PET)_{18}^-$. Inset shows the comparison of experimental and calculated isotopic patterns of $Au_{25}(PET)_{18}^-$.

of an Au atom (197) + 18 × mass of PET (137) = 7391. The molecular ion peak at m/z 7391 was observed in both positive and negative ion modes corresponding to the NC in 1+ and 1- charged states, respectively. Fragmented peaks corresponding to $Au_{21}(PET)_{14}$ were also observed. Ligand exchange of the NC was also performed to prepare mixed-monolayer protected NCs. Ligand exchange was performed with $CH_3(OCH_2CH_2)_5SH$ (PEG5-SH), which is heavier than PET by 130 Da, and with $CH_3(OCH_2CH_2)SH$ (PEG1-SH), which is lighter than PET by 46 Da.[25] In both cases, the mixedmonolayer protected NCs could be precisely analyzed by MS, as shown in Fig. 10.4B. When PEG5-SH was used, the peaks appeared on the higher mass side of $Au_{25}(PET)_{18,}$ and peaks corresponding to the exchanges of PET by PEG5-S was observed. Similarly, when PEG1-SH was used, peaks corresponding to the exchanges of PET by PEG1-S were observed on the lower mass side of $Au_{25}(PET)_{18}$. The isotopic resolution of the peaks were obtained from MALDI and agreed well with the simulated isotopic patterns. The isotopic patterns are resolved better in modern-day high-resolution mass spectrometers, which is shown in Fig. 10.5 and will be discussed in the following section. ESI MS has also been used for the characterization of gold NCs. Different methods were introduced to improve ionization of organic soluble gold

NCs like ligand exchange with ionizable ligands,[26] use of ionization enhancers like caesium acetate, etc. Over the years, mass spectrometric instrumentation has improved. A mass spectrum of $Au_{25}(PET)_{18}^-$, measured in a high-resolution ESI mass spectrometer, is shown in Fig. 10.5. Under the soft ionization conditions of ESI, no fragmentation of the NC was observed and a single peak was observed at $m/z \sim 7391$. The isotopic pattern of this peak is also presented in the inset of Fig. 10.5. Au has only one isotope, so the isotopic pattern originates due to the contribution of the isotopes of C, H, and S present in the ligand moeity. The experimental isotopic pattern was in agreement with the simulated patterns, which further confirmed the composition. Each of the peaks of this isotopic distribution are separated by m/z value of 1, which suggests a charge state of 1. For a doubly and triply charged ion, this difference would be 0.5 and 0.33, respectively. Thus, the charge state of the NC can also be accurately deduced from the mass spectrum. Thus, an analysis of the m/z value and isotopic distribution of the peaks help in confirming the molecular composition and charge state of the NCs. Several other gold NCs have been characterized using the techniques of MALDI and ESI. Gold NCs like $[Au_{23}(SC_6H_{11})_{16}]^-$,[27] $[Au_{24}(PPh_3)_{10}(SC_2H_4Ph)_5X_2]^+$,[28] $[Au_{19}(PhC{\equiv}C)_9(Hdppa)_3]^{2+}$,[29] $[Au_{20}(PPh_3)_4]^{4+}$,[30] $Au_{24}(SAdm)_{16}^{2+}$,[31] etc. were characterized by ESI MS. Some NCs like $Au_{25}(SG)_{18}$,[32] $Au_{25}(MHA)_{18}$[33] were ionized in multiple charged states in ESI MS due to the nature of their ligands. Ionization of some gold NCs were achieved using CsOAc, for e.g. $Au_{18}(SC_6H_{11})_{14}$ ionized as $[Au_{18}(SC_6H_{11})_{14}Cs]^+$.[34] Similarly, $Au_{28}(TBBT)_{20}$ ionized as $[Au_{28}(TBBT)_{20}{+}2Cs]^{2+}$ and $[Au_{28}(TBBT)_{20}{+}Cs]^+$ on using CsOAc during ESI MS.[35] MALDI is more effective than ESI in ionizing larger gold NCs. $Au_{133}(SPh\text{-}^tBu)_{52}$ shows the molecular ion peak in MALDI MS.[36] In ESI MS too, it is ionized in +2 and +3 charged states. Similarly, another larger NC, $Au_{329}(SCH_2CH_2Ph)_{84}$ is ionized in +1 state in MALDI and 2-, 3-, 4-, 5-charged states in ESI.[37] Thus, both MALDI and ESI have developed into powerful techniques in characterizing gold NCs and in most cases, the composition obtained from MS studies has been in accordance with the crystal structure data of these NCs.

10.4.2 Silver NCs

MS has been powerful in characterizing silver NCs as well. Due to the reduced stability and light sensitivity of Ag, characterization of Ag NCs by MS has remained challenging. As silver has two isotopes (^{107}Ag and ^{109}Ag), silver NCs usually show broader isotopic distributions compared to analogous gold NCs with identical metal and ligand composition. This can be clearly observed in the ESI MS of $Ag_{25}(DMBT)_{18}^-$ (DMBT is 2,4-dimethyl benzene thiol) NC,[38] presented in Fig. 10.6A. $Ag_{25}(DMBT)_{18}^-$ is the structural analogue of the gold NC, $Au_{25}(PET)_{18}^-$ (PET is 2-phenyl ethane thiol). The ligands PET and DMBT have identical formulas ($C_8H_{10}S$) and hence the difference in the isotopic patterns is solely due to the difference in the isotopes of Au and Ag. Similarly, several other silver NCs have also been characterized by ESI MS, for e.g., $Ag_{44}(SR)_{30}$ NC which ionizes in both 4- and 3- charged states[39,40] as shown in Fig. 10.6B. The charge states of the NCs can be accurately defined from the isotopic distribution which shows a difference of 0.25 and 0.33 for 4- and 3- charged states, respectively. Several other Ag NCs like $[Ag_{21}[S_2P(O^iPr)_2]_{12}]^+$,[41] $[Ag_{67}(SPhMe_2)_{32}(PPh_3)_8]^{3+}$,[42] $[Ag_{29}(BDT)_{12}(TPP)_4]^{3-}$,[43] etc., were also characterized by ESI MS. Ionization enhancers like CsOAc are also effective in ionizing certain Ag NCs, for example, $Ag_{55}(BBS)_{31}$ is ionized as

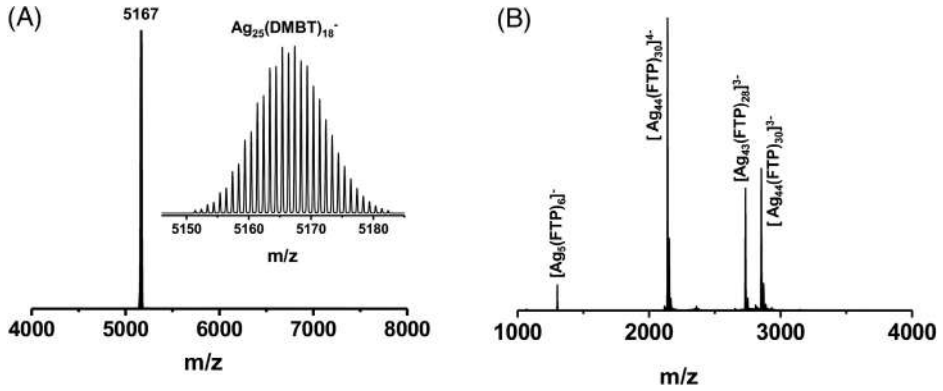

FIGURE 10.6 (A) ESI MS of $Ag_{25}(DMBT)_{18}^-$. Inset shows the experimental isotopic distribution of the molecular ion peak at 5167. (B) ESI MS of $Ag_{44}(FTP)_{30}$ (FTP is fluoro-thiophenol) ionized in both 4- and 3- charge states.[39]

$[Ag_{55}(BBS)_{31}(Cs)_x]^{3-}$ ($x = 1$–3).[44] MALDI has also been used for the ionization of several silver NCs like $Ag_{68}(SBB)_{34}$[45] and $Ag_{152}(SCH_2CH_2Ph)_{60}$.[46]

10.4.3 Other metal NCs

Apart from Au and Ag NCs, the other metal NCs that are thoroughly investigated by MS include NCs of platinum (Pt), palladium (Pd), copper (Cu), etc. Pt NCs such as $Pt_5(MBT)_7$ (MBT is 2-mercapto-benzothiazole),[47] $Pt_{11}(BBS)_8$ (BBSH is 4-(tert-butyl)benzyl mercaptan),[48] etc., which were characterized using MALDI and ESI MS. As Pt has five isotopes (^{192}Pt, ^{194}Pt, ^{195}Pt, ^{196}Pt, and ^{198}Pt), the isotopic distribution of the peaks is much broader compared to analogous NCs of Au which has only one isotope. CsOAc was effectively used for the ionization of Pt NCs as well. $Pt_{11}(BBS)_8$ was ionized as $[Pt_{11}(BBS)_8Cs(H_2O)]^+$ in the positive ion mode.[48] Negishi et al. characterized CO protected Pt NCs such as $[Pt_{17}(CO)_{12}(PPh_3)_8]^{n+}$ ($n = 1$, 2) by MALDI and ESI MS.[49] Although Pd NCs have been investigated by MS to a lesser extent, a few NCs such as a series of tiara-like $Pd_n(SR)_{2n}$ ($5 \leq n \leq 20$) NCs were characterized by Chen et al. using MALDI MS.[50] On the other hand, Cu NCs are also widely investigated using MS. Benzotriazolate (BTA) protected $Cu_n(BTA)_m$ NCs were characterized by ESI MS.[51] MALDI MS was also used to determine the composition of $\sim Cu_{38}(PET)_{25}$ NCs which showed a single peak around $m/z \sim 5800$ in the negative ion mode.[52] The composition of a hydride-protected $Cu_{20}H_{11}(S_2P(O^iPr)_2)$ NC was determined using ESI MS which was consistent with the results from XRD.[53] Recently, Sun et al. also characterized $[Cu_{25}H_{10}(SPhCl_2)_{18}]^{3-}$ by ESI MS.[54] Isotopic distribution of the peak was broad, akin to Ag NCs due to the two natural isotopes of Cu, that is, ^{63}Cu and ^{65}Cu. Several other Cu NCs like $[Cu_{61}(S^tBu)_{26}S_6Cl_6H_{14}]^+$,[55] $[Cu_{81}(PhS)_{46}(^tBuNH_2)_{10}(H)_{32}]^{3+}$,[56] $[Cu_{23}(PhSe)_{16}(Ph_3P)_8(H)_6]^+$,[57] etc., are also well-characterized by ESI MS and their molecular formulae determined from MS were in accordance with the formulae deduced from their crystal structures. Thus, MS has proved to be a powerful tool for characterizing NCs of metals apart from gold and silver.

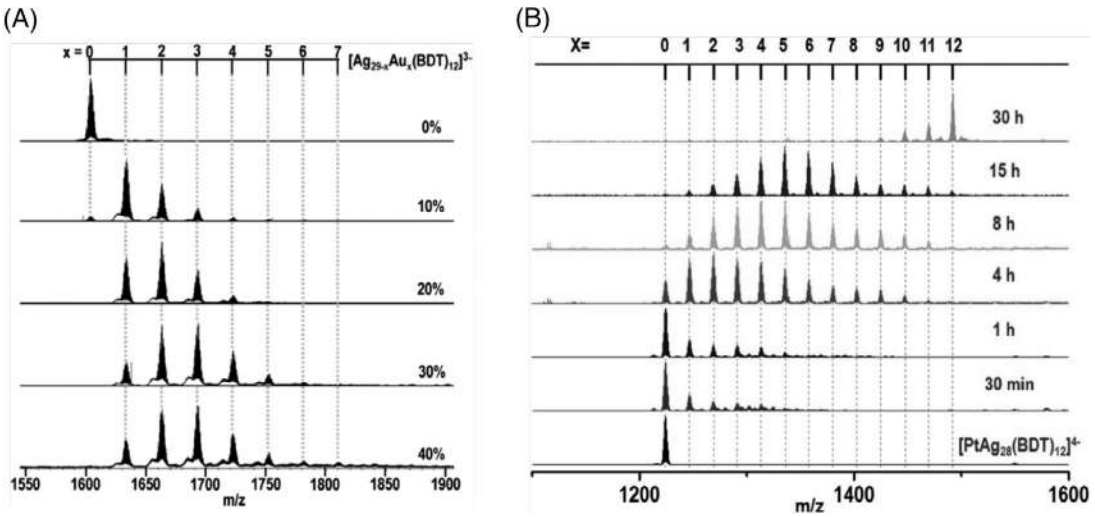

FIGURE 10.7 (A) ESI MS showing Au exchange in $[Ag_{29}(BDT)_{12}]^{3-}$ at various concentration of Au and hence formation of the alloy NCs, $[Ag_{29-x}Au_x(BDT)_{12}]^{3-}$.[59] (B) ESI MS showing Au doping in bimetallic $[PtAg_{28}(BDT)_{12}]^{4-}$ and formation of trimetallic $[PtAg_{28-x}Au_x(BDT)_{12}]^{4-}$ alloy NCs.[60]

10.4.4 Alloy NCs

MS is also used for determining the exact composition of alloy NCs. Doping one Au atom in $Ag_{25}(DMBT)_{18}^-$ forms $Ag_{24}Au(DMBT)_{18}^-$ which can be accurately studied by MS.[58] $Ag_{25}(DMBT)_{18}^-$ ionizes at m/z 5167 and when a single Ag atom is exchanged with Au, the m/z value of $Ag_{24}Au(DMBT)_{18}^-$ changes to 5257. So, for each exchange of an Ag atom by an Au atom, the mass of the alloy NC increases by 90, concurrent with the difference in the masses of Ag and Au atom. Similarly, when Au atoms of $Au_{25}(SR)_{18}^-$ are exchanged with Ag, the mass of the alloy NC decreases by 90 for each exchange. The compositions are also reflected in the isotopic distribution of the peaks. Similarly, doping of other metals like Pt and Pd in parent Au or Ag NCs can also be determined. Such doping can be accompanied by a change in charge state of the parent NCs and can be determined using MS. Thus, it has been possible to characterize bimetallic or trimetallic alloy NCs using MS. Fig. 10.7A shows the ESI mass spectra of alloy NCs $[Ag_{29-x}Au_x(BDT)_{12}]^{3-}$ where $x = 1$–7.[59] Number of Ag–Au exchanges in the parent NC can be controlled by controlling reaction conditions and can be accurately determined using MS. As the alloy NCs are in 3^- charge state, the m/z value changes by 30 for each Au-Ag exchange. Similarly, trimetallic alloy NCs were also accurately characterized, as shown in Fig. 10.7B.[60] Doping of a Pt atom in $[Ag_{29}(BDT)_{12}]^{3-}$ results in the formation of $[Ag_{28}Pt(BDT)_{12}]^{4-}$ which gives a single peak at m/z 1224 as shown in Fig. 10.7B. Further doping of Au in $[Ag_{28}Pt(BDT)_{12}]^{4-}$ results in a series of trimetallic NCs, $[PtAg_{28-x}Au_x(BDT)_{12}]^{4-}$ which are characterized by ESI MS.[60] Thus, from mass spectrometric studies it is clearly observed that Au atoms exchanges with the Ag atoms of the NC and the central Pt atom remains unexchanged. Thus, precise composition of alloy NCs has also been determined using MS and this has enabled an extensive study of intercluster reactions of NCs.[61,62]

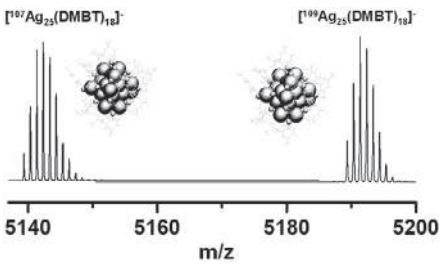

FIGURE 10.8 HR ESI MS of isotopically pure NCs, $^{107}Ag_{25}(DMBT)_{18}^{-}$, and $^{109}Ag_{25}(DMBT)_{18}^{-}$.[63]

10.4.5 Isotopically pure NCs

As discussed in the previous sections, the isotopic abundance of constituent elements of the NCs is reflected in their isotopic distributions that is essential in determining their accurate composition. Silver NCs exhibit broader isotopic patterns due to the two natural isotopes of Ag (^{107}Ag and ^{109}Ag). MS is also employed to characterize isotopically pure NCs. The ESI MS of $Ag_{25}(DMBT)_{18}^{-}$ NC,[38] made from naturally abundant Ag, was presented in Fig. 10.6A. Fig. 10.8 shows ESI MS of $Ag_{25}(DMBT)_{18}^{-}$ made from isotopically pure Ag, that is, ^{107}Ag and ^{109}Ag. The peaks for $^{107}Ag_{25}(DMBT)_{18}^{-}$ and $^{109}Ag_{25}(DMBT)_{18}^{-}$ appear at m/z 5142 and 5192, respectively, as shown in Fig. 10.8.[63] The peaks for these two isotopic NCs differ by m/z 50 due to the change in 25 atoms of Ag with the respective isotopes. Isotopic distribution of the peaks for $^{107}Ag_{25}(DMBT)_{18}^{-}$ and $^{109}Ag_{25}(DMBT)_{18}^{-}$ are narrower compared to the isotopic distribution of $Ag_{25}(DMBT)_{18}^{-}$ consisting of naturally abundant Ag. Other isotopic silver NCs like $^{107}Ag_{29}(BDT)_{12}^{3-}$ and $^{109}Ag_{29}(BDT)_{12}^{3-}$ have also been characterized by high-resolution ESI MS.[63] Reactions between isotopic silver NCs was also studied using ESI MS, wherein NCs with varying ^{107}Ag/^{109}Ag abundances were identified.[63,64]

10.5 Mass spectrometry of adducts of NCs

Apart from the characterization of the parent NCs, MS is also powerful in detecting adducts of NCs. Such adducts include dimers, adducts of NCs with gases, metal ions and other molecules. Bhat et al. characterized adducts of $Au_{25}(SR)_{18}^{-}$ with oxygen gas using ESI MS. The adducts $[Au_{25}(SR)_{18}(O_2)_n]^{-}$ ($n = 1$–3) were confirmed from their m/z positions and isotopic patterns in ESI MS.[65] Adducts of $[Ag_{29}(BDT)_{12}]^{3-}$ with protons and alkali metal ions were also characterized by ESI MS.[66] Baksi et al. detected dimers and trimers of $[Au_{25}(SR)_{18}]^{-}$ by using ESI MS.[67] Here, the dimers, $[Au_{25}(SR)_{18}]_2^{2-}$ and the trimers, $[Au_{25}(SR)_{18}]_3^{3-}$ could be identified from their isotopic distributions. Monomer, dimer, and trimer ionize at the same m/z position i.e., ~7391 but the peaks of their isotopic distribution are separated by 1, 0.5, and 0.33, respectively, which helps in the successful characterization of the adducts of the NCs. This is shown in Fig. 10.9A. Also, heterodimers of adducts of NCs could be detected using ESI MS. Fig. 10.9B, shows the mass spectrum of a heterodimer, $[Au_{25}(SR)_{18}Ag_{25}(SR)_{18}]^{2-}$.[62] Adducts of NCs with other molecules like fullerenes,[68,69] cyclodextrins,[70] crown ethers,[71] cucurbiturils,[72] etc., were also studied by MS which has helped to expand the field of supramolecular chemistry of NCs (refer to Chapter 5 for a detailed discussion on this topic).

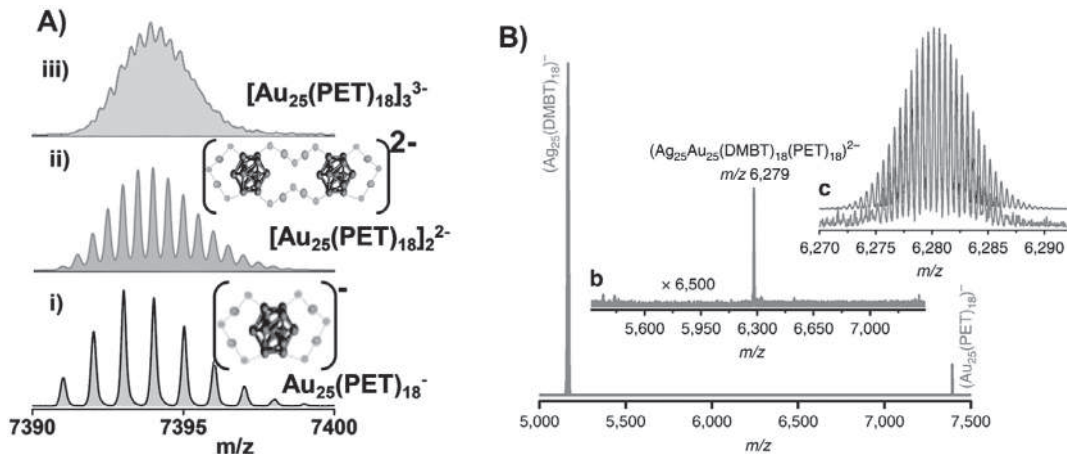

FIGURE 10.9 (A) ESI MS of i) monomer $[Au_{25}(PET)_{18}]^-$, ii) dimer $[Au_{25}(PET)_{18}]_2^{2-}$, and iii) trimer $[Au_{25}(PET)_{18}]_3^{3-}$.[67] (B) ESI MS of a dimeric adduct of NCs, $[Ag_{25}Au_{25}(DMBT)_{18}(PET)_{18}]^{2-}$.[62]

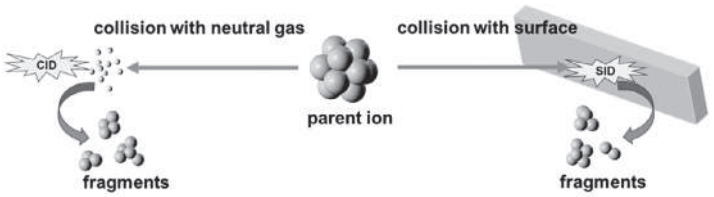

FIGURE 10.10 Schematic of the tandem MS process of collision-induced dissociation and surface-induced dissociation.

10.6 Tandem mass spectrometry of NCs

In tandem MS, ions of interest are subjected to fragmentation by collision with gases, surfaces or by activation with light. The fragmentation pattern of ions reveals important information on the structure of ions. Such studies have also been helpful for understanding structures of atomically precise NCs. Different types of tandem mass spectrometric techniques are used for characterization of NCs such as CID, SID, electron transfer dissociation, and ultraviolet photodissociation (Fig. 10.10). These are discussed separately in the following sections.

10.6.1 Collision-induced dissociation

10.6.1.1 Principle and instrumentation

CID is used to induce fragmentation of gas-phase ions. Here, mass-selected ions are accelerated by applying suitable electric potential and collided with neutral gasses like He, N_2, or Ar. Activation of the ions occurs during this collision process and some part of the kinetic energy is converted into the internal energy of the ions resulting in their fragmentation. CID can be performed at low energies (<1 keV) in tandem quadrupole and ion trap instruments and at high energies in tandem sector and TOF instruments. CID has remained one of the most common methods of ion activation and has also been used in characterizing noble metal NCs

in the gas phase. The parent NC ions are usually mass-selected using a quadrupole mass filter and then collided with neutral gases in a collision cell.

10.6.1.2 CID of metal NCs

CID of metal NCs reveals important structural information. Fields-Zinna et al. reported CID on $Na_xAu_{25}(SC_2H_4Ph)_{18-y}(S(C_2H_4O)_5CH_3)_y$ which revealed that fragmentation involved the $Au_2(SR)_3$ semirings of the staples of the NCs.[73] Angel et al. also studied fragmentation of $Au_{25}(SR)_{18}$ using HR ESI MS.[74] This study revealed that the major fragments of $Au_{25}(SR)_{18}^{\mp}$ were $Au_{21}(SR)_{14}^{\mp}$, and $Au_{17}(SR)_{10}^{\mp}$ formed due to successive losses of $Au_4(SR)_4$ fragments. The electron counts of the fragments $Au_{21}(SR)_{14}^{\mp}$, and $Au_{17}(SR)_{10}^{\mp}$ are 8 and 6 in negative and positive ions, respectively, suggesting that geometric factors have a greater influence compared to the electronic factors. Black et al. performed CID studies on large NCs like $Au_{144}(SR)_{60}$ which ionizes in the gas phase in multiple charged states.[75] Their studies revealed that CID of NC ions is also specific to their charge states. Similarly, fragmentation of silver NCs has also been studied which also showed systematic thiolate losses. $Ag_{29}(S_2R)_{12}$ showed systematic losses of $Ag_5(S_2R)^-$ thiolates.[39] The fragmentation process is presented in Fig. 10.11. Similarly, $Ag_{25}(SR)_{18}^-$ or $Ag_{44}(SR)_{30}^{4-}$ showed systematic losses of smaller thiolate fragments during CID.[39] Fragmentation of alloy NCs has also been carried out to identify the position of heterometals in the NC, for example, CID of $Cu_xAg_{29-x}(S_2R)_{12}^{3-}$ showed Cu to be associated with the smaller thiolate fragments supporting their doping into staples of the NCs.[76] Moreover, CID on $[Ag_{18}(TPP)_{10}H_{16}]^{2+}$ (TPP is triphenyl phosphine) resulted in sequential desorption of dihydrogen from the NC and formation of a bare NC, Ag_{17}^+ in the gas phase.[77] CID has also been performed on aggregates of NCs like dimers or supramolecular complexes of NCs.[67,68] CID resulted in dissociation of NC dimers into their respective monomers providing valuable information on the nature of their interaction.[67] Also, CID on supramolecular adducts of NCs with other molecules like fullerenes[68,69] and cyclodextrins[70] helped to understand the binding modes of such host-guest complexes of NCs.

10.6.1.3 Stability and energetics of NCs

CID of metal NCs has also been used to understand their energetics. Survival yield analysis studies the relative abundance of the parent as well as the fragment ions as a function of the applied collision energy and helps to understand the stability of the ions in the gas-phase. The energy required for 50% dissociation of the parent ions is considered as a characteristic of the stability of an ion under the given experimental conditions. Using this approach, Chakraborty et al. revealed the gas-phase stability order of a few silver NCs as $[Ag_{29}(SR)_{12}]^{3-} > [Ag_{25}(SR)_{18}]^- > [Ag_{44}(SR)_{30}]^{3-}$ which was comparable to their solution-phase stabilities.[39] Such studies were also used to understand stabilities of supramolecular complexes of NCs with alpha, beta and gamma cyclodextrins.[70] Thus, CID has been used not only to understand structures of NCs but also their stabilities in the gas phase.

10.6.2 Surface-induced dissociation

10.6.2.1 Principle and instrumentation

SID is an alternative technique of ion activation. In this technique, precursor ions are collided with surfaces which leads to their dissociation. Several types of surfaces have been

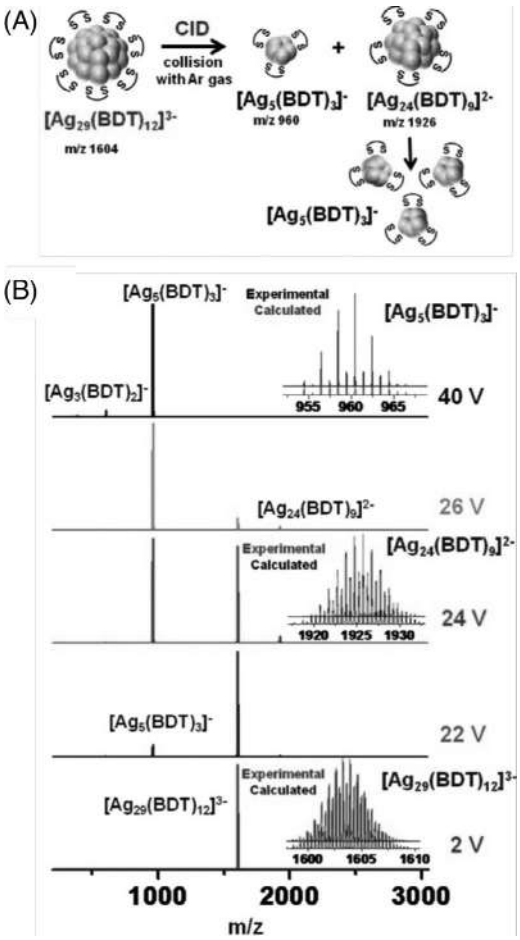

FIGURE 10.11 (A) Scheme showing the fragmentation channel of $Ag_{29}(BDT)_{12}^{3-}$. (B) CID MS of $Ag_{29}(BDT)_{12}^{3-}$ at varying collision energies. The comparison of the experimental and theoretical isotopic patterns of the parent and fragment ions is presented as insets.[39]

used for this purpose, the most common being gold surfaces, protected by self-assembled monolayers of $CF_3(CF_2)_{10}CH_2CH_2S$-. SID has been particularly useful in studying quaternary structures of proteins in comparison to ordinary collision with gases in CID. This technique of SID has also been effectively used in understanding structure and energetics of NCs.

10.6.2.2 SID of metal NCs

Johnson et al. studied SID of small gold NCs like $Au_7(TPP)_6^{2+}$, $Au_8(TPP)_6^{2+}$, $Au_8(TPP)_7^{2+}$, and $Au_9(TPP)_7^{2+}$.[78] Comparison of the stabilities of these NCs as obtained from SID is presented in Fig. 10.12. Compared to CID, SID has been more effective in understanding the energetics of the NCs. The technique was used to determine the activation entropies and also kinetics of dissociation of NCs. SID also helped to estimate the microcanonical rate constants for different fragmentation channels of the NCs and identify the kinetically and thermodynamically favored channels.[78] Baksi et al. compared both CID and SID on $Ag_{11}(SG)_7^-$

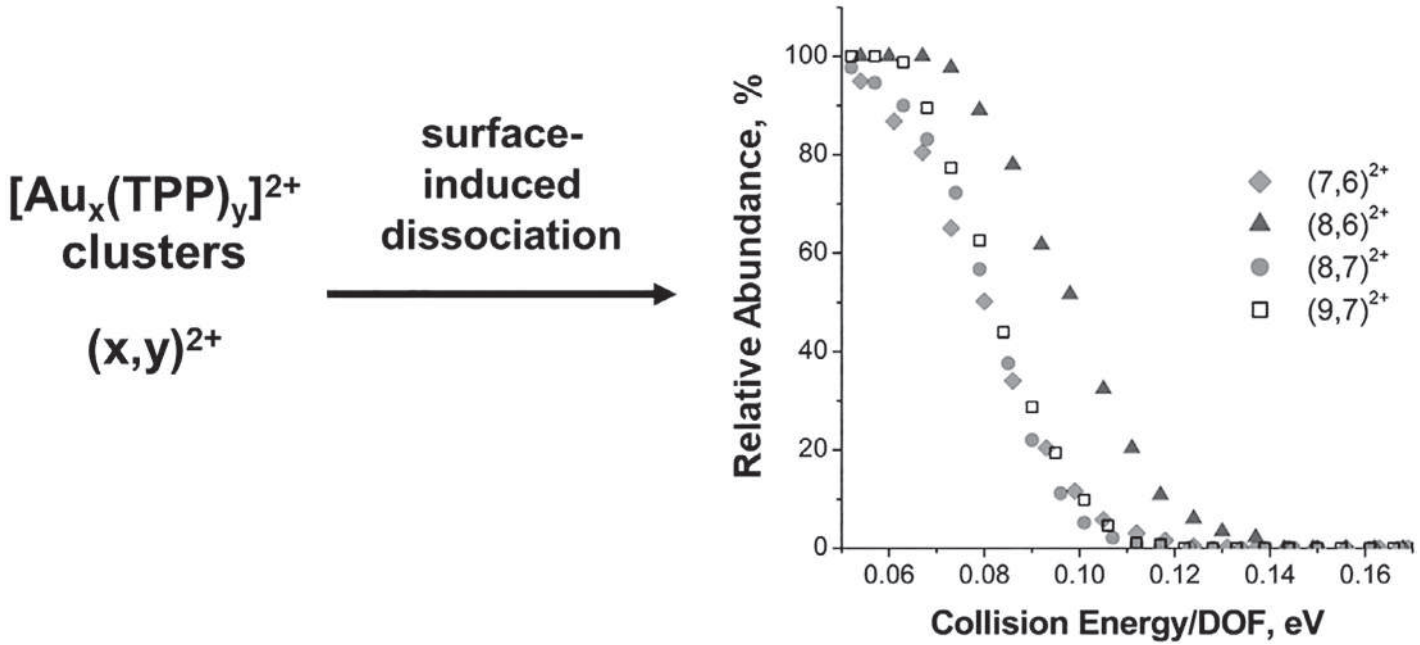

FIGURE 10.12 Survival curves for SID on Au NCs shown as a function of collision energy/degree of freedom (DOF). The NCs are denoted as (*x*,*y*) where *x* denotes the number of Au atoms and *y* denotes the number of triphenyl phosphine (TPP) ligands in the NC.[78]

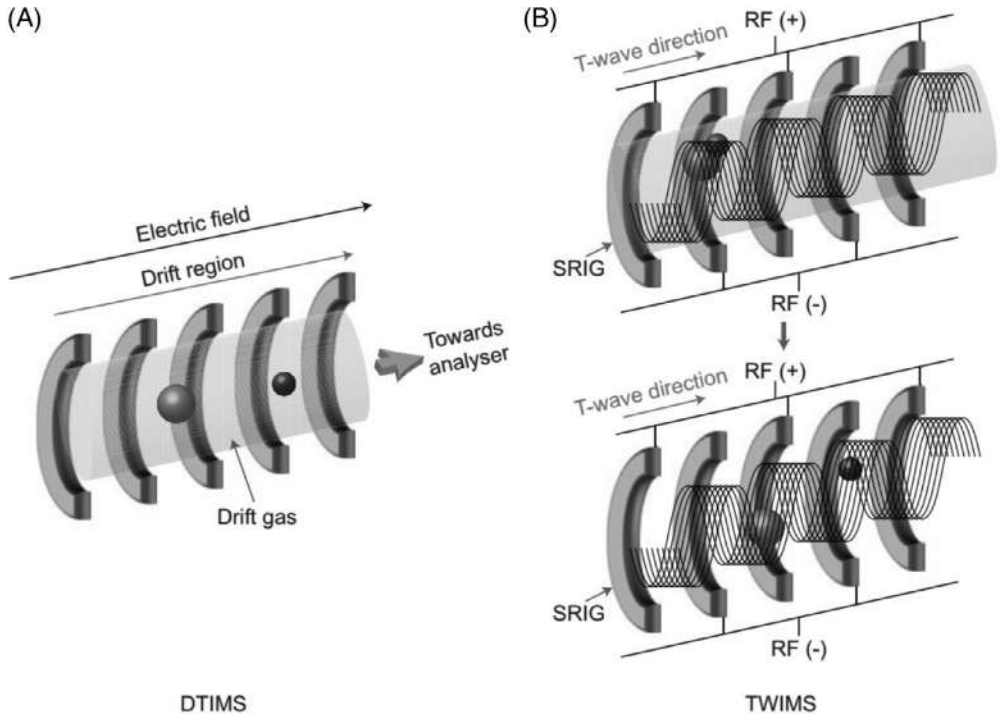

FIGURE 10.13 Schematic of (A) drift tube ion mobility spectrometry (DTIMS) and (B) traveling wave ion mobility spectrometry (TWIMS).[81]

NCs and showed that SID resulted in greater extent of fragmentation compared to CID and SID also resulted in charge stripping of the ions.[79]

10.7 Ion mobility mass spectrometry of NCs

10.7.1 Principle and instrumentation

IM when coupled with MS allows the separation of species with the same m/z values but with different size and shape.[80,81] IM MS helps to understand structures and conformational dynamics in a system. It can separate isomers of molecules as well as distinguish different conformers of proteins and other macromolecules. The separation occurs due to differences in the mobility of ions of different structures while traversing through the buffer gas. Different types of IM techniques are coupled to mass spectrometers like a drift tube (DT) and traveling wave (TW) IMS. These techniques are presented schematically in Fig. 10.13. In DTIMS, ions pass through DTs filled with buffer gas like He or N_2. The ions travel under the influence of static electric field and are separated based on the difference in their arrival time. Usually smaller and compact structures travel faster through the DT compared to larger or extended structures. The drift times of the ions also help to calculate the collision cross-section (CCS)

according to the Mason–Schamp equation:

$$\Omega = \frac{3ze}{16N}\left(\frac{2\pi}{\mu k_B T}\right)^{\frac{1}{2}}\frac{1}{K_o}$$

where Ω is CCS of ion, z is the charge state of ion, e is elementary charge, N is number density of the buffer gas, k_B is Boltzmann constant, T is temperature of the gas, and K_o is reduced mobility. These experimentally obtained CCS can be compared with the calculated CCS of structures obtained from X-ray, NMR or DFT calculations. Usually, CCS values are calculated using the projection approximation, trajectory method or exact hard-sphere scattering methods. In TWIMS, a series of ring electrodes are stacked together and opposite phases of radiofrequency voltages are applied to adjacent electrodes. While this field radially confines the ions, a DC voltage is also applied to propel the ions axially. Under the influence of these two fields, a TW is created in the device where smaller or compact ions move faster with the wave whereas the ions with larger or extended structures roll over the waves and take longer time to traverse through the device. Thus, due to the difference in their drift times, the ions can be separated. However, as the electric field constantly change in case of a TWIMS, the direct relationship between Ω and K_o is no longer valid and hence in the case of a TWIMS, CCS values of ions are determined by calibration with ions of known CCS (determined from DTIMS), under same experimental conditions. While these are the most commonly used types of IMS devices coupled to mass spectrometers, other types are also available such as trapped ion mobility spectrometry (TIMS), Field-asymmetric IMS, etc. TIMS is a relatively new development. TIMS can be accepted as an excellent alternative to DTIMS. Its working principle is the reversal of DTIMS. Here, the ions are held stationary against the moving gas and the ions are eluted depending on the electric field applied. TIMS can reach a resolution of about 300. Other types are not discussed here as they have not yet been largely used in characterizing NCs.

10.7.2 Separation of gas-phase isomers and aggregates of NCs

IM MS has been effective in separating isomers of the atomically precise NCs. Four isomers of $Ag_{44}(FTP)_{30}^{4-}$ NCs were separated using IM in the gas phase though NC showed only one stable form in condensed phase.[82] The mobilograms showing the separation of the four isomers of $Ag_{44}(FTP)_{30}^{4-}$ is presented in Fig. 10.14. The number of isomers in the gas phase was also dependent on the charge state of the NC. $Ag_{44}(FTP)_{30}^{3-}$ showed two isomers. IM MS was also used to identify isomerism in $[Ag_{11}(SG)_7]^-$ NCs.[79] A topological isomer of $Au_{25}(PET)_{18}$ was also detected in the gas phase by IM MS.[83] The experimental CCS obtained from IM MS agreed well with the calculated structure of $Au_{25}(PET)_{18}$ wherein there was rotation of the core of the NC without the cleavage of any Au-S bond.[84] This isomer was observed in the gas-phase by collisional activation. IM MS was also used to separate aggregates of NCs. Monomers, dimers, and trimers of $Au_{25}(SR)_{18}$ were separated in the gas phase.[67] Here, the monomer $Au_{25}(SR)_{18}^-$, dimer $[Au_{25}(SR)_{18}]_2^{2-}$ and trimer $[Au_{25}(SR)_{18}]_3^{3-}$ showed the same m/z value but could be separated by IM MS based on the difference in their drift times through the buffer gas. Thus, IM MS is used extensively in understanding various isomers and aggregates of NCs.

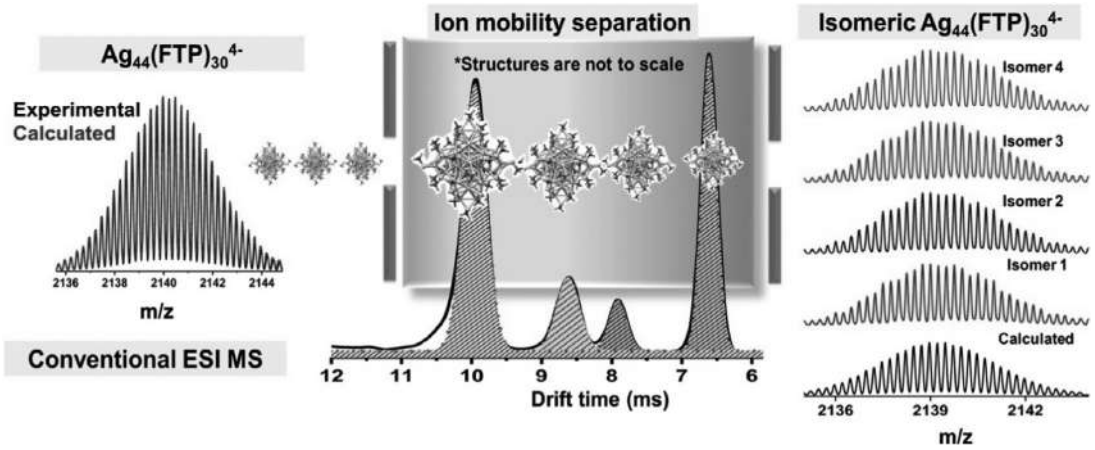

FIGURE 10.14 Ion mobility separation of the isomers of $Ag_{44}(FTP)_{30}^{4-}$.[82]

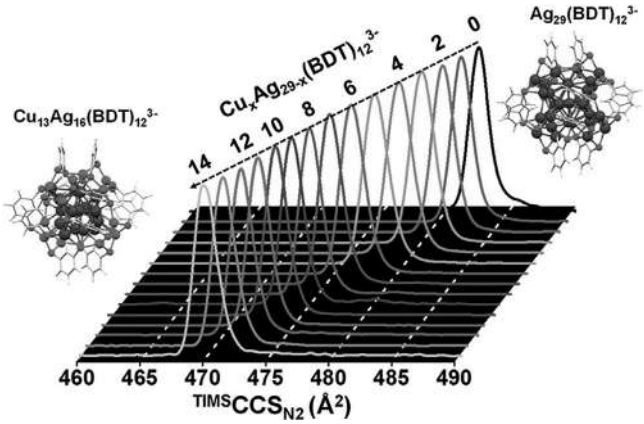

FIGURE 10.15 Ion mobility traces of $Cu_xAg_{29-x}(BDT)_{12}^{3-}$ showing a linear decrease in the collision cross sections with increase in the number of Cu doping in the NC.[76]

10.7.3 Determining structures of NCs from IM MS

IM is also used to understand the inherent structures of NCs. The CCS values of NCs obtained from IM MS gives valuable insights on their structures. Daly et al. studied IM MS on $[Ag_{14}(C{\equiv}C^tBu)_{12}Cl]^+$, $[Ag_{14}(C{\equiv}C^tBu)_{12}Br]^+$, $[Ag_8Cu_6(C{\equiv}C^tBu)_{12}Cl]^+$, and $[Ag_8Cu_6(C{\equiv}C^tBu)_{12}Br]^+$ and compared the CCS values obtained from IM MS with the CCS values calculated from their crystal structures, which suggested that the condensed-phase structure was retained in the gas phase too.[85] The arrival times of the heterometallic NCs were smaller compared to that of the homometallic ions which were consistent with crystal structures. This approach was also helpful in understanding structures of the alloy NCs, $Cu_xAg_{29-x}(BDT)_{12}^{3-}$ ($x = 1$–14). IM MS studies showed that the CCS values of the alloy NCs decreased linearly with increase in the number of doped Cu atoms in $Ag_{29}(BDT)_{12}^{3-}$, as shown in Fig. 10.15.[76] Further, comparison of the CCS values with the CCS values of DFT optimized structures also revealed that Cu doping occurred mainly in the staples of the NCs. Thus, IM MS is used as a powerful technique in determining structures of NCs, in the absence of the

crystal structure as well. Moreover, IM MS is also accepted as a technique for understanding structures or determining sizes of NCs like other techniques, such as X-ray powder diffraction (XRPD) and time-resolved fluorescence anisotropy (TRFA).[86] This was tested by performing all the three studies; XRPD, TRFA, and IM MS on glutathione protected Au NCs and comparing the sizes obtained from three different techniques. IM MS can also detect changes in structures that are induced by ligand exchange or other such modifications in the structure of the NC. Ligare et al. performed ligand exchange on $[Au_8(PPh_3)_7]^{2+}$ and $[Au_{11}(PPh_3)_9H]^{2+}$ NCs with $MePPh_2$ and studied this phenomenon using IM MS.[87] The changes in the structure due to ligand exchange could be identified by IM MS.

10.8 Mass spectrometry of metal NCs in macromolecular templates

Apart from thiol and phosphine-protected NCs, MS is largely used to characterize NCs prepared in macromolecular templates like proteins, DNA and dendrimers. Such NCs are especially important because of their applications in biology. These NCs exhibit interesting properties like luminescence. Proteins like bovine serum albumin (BSA), human serum albumin (HSA), lysozyme, lactoferrin, insulin, etc. have been commonly used as templates for making noble metal NCs.[88,89] Apart from Au and Ag NCs, Cu, Fe, and Pt NCs have also been synthesized in protein templates. Till date, crystallization of such protein-protected NCs has not been achieved and MS remains as one of the most efficient techniques in characterizing protein-protected NCs. However, protein-protected NCs have been mainly characterized using MALDI MS. ESI MS of such NCs is still challenging. The formation of the NCs is usually characterized by analyzing the mass shifts with respect to the proteins and hence calculating the number of metal atoms in the NC. In MALDI MS, mostly the parent single charged NC peak is observed and MALDI MS of protein-protected NCs are performed using matrices such as α-cyano-4-hydroxy cinnamic acid , sinapinic acid, etc. Some of the commonly studied protein-protected gold NCs are Au_{25} and Au_{38} NCs protected by BSA, denoted as Au_{25}@BSA[90] and Au_{38}@BSA.[91] The MALDI MS spectra registered a shift corresponding to 25 and 38 Au atoms and thus the atomicity of the NCs was assigned. Au NCs protected by smaller proteins like lysozyme (Lyz) have also been characterized by MALDI MS. Baksi et al. reported Au_{QC}@Lyz and characterized it by MALDI MS.[92] Although most of the reports are on Au NCs in protein templates, there are few reports of protein protected Ag NCs as well. Recently, Ghosh et al. reported Ag_{18}@BSA which was synthesized by a unique method employing phosphine and hydride co-protected Ag_{18} as precursor.[93] The authors studied the time evolution of the Ag_{18}@BSA NC by MALDI MS, as shown in Fig. 10.16.

10.9 Mass spectrometry of larger NCs

The advancement in mass spectrometric techniques has made the characterization of larger NCs feasible using a combination of LDI, ESI and MALDI techniques. MS has been successfully used to determine the composition of large NCs such as Au_{333},[94] $Au_{\sim 500}$,[95] $Au_{\sim 940}$,[97] etc. MS can determine the composition of large plasmonic particles like $Au_{\sim 1400}$[98] and $Au_{\sim 2000}$.[96] Fig. 10.17 shows the MALDI MS of $Au_{\sim 2000}(SC_6H_{13})_{\sim 290}$ nanoparticles having a mass of

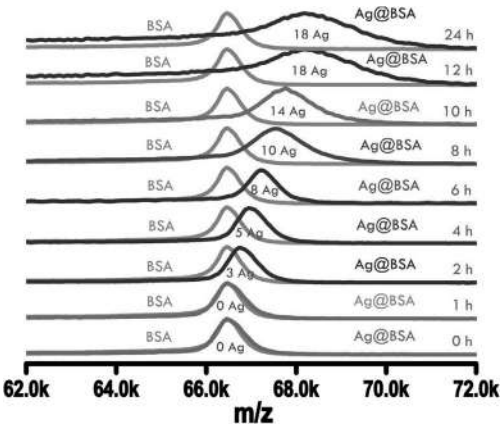

FIGURE 10.16 MALDI MS showing the time-dependent evolution of Ag_{18}@BSA NC.[93]

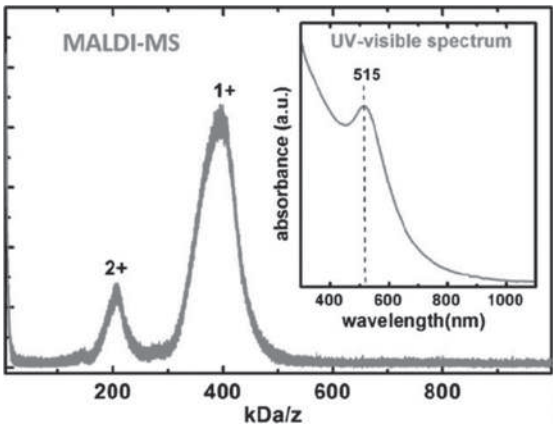

FIGURE 10.17 MALDI MS of $Au_{\sim 2000}(SC_6H_{13})_{\sim 290}$ nanoparticles. Inset shows optical absorption spectrum of the nanoparticles.[96]

~400 kDa.[96] The optical absorption spectra presented in the inset clearly shows the plasmonic nature of the particles.

10.10 Summary and future perspectives

The chapter discusses the application of MS to characterize atomically precise NCs. This chapter focused on the various methods of ionization of NCs, determination of the composition of the NCs from MS and the use of various tandem MS and IM MS studies in understanding structures of NCs. The use of MS in understanding NCs is expected to expand further in the future. Due to the capabilities of MS methods, gas-phase studies on NCs are gaining importance. MS analysis transfers the NC ions into the gas phase and enables further studies on isolated ions like photoelectron spectroscopy, electron detachment spectroscopy, etc. Such studies can probe the energy levels of the NCs in the absence of solvents. IR spectroscopy on isolated ions can reveal further information on their structures. IR can help in understanding the nature of interactions in the gas-phase aggregates of NCs. Spectroscopy of trapped ions in mass spectrometers also enables studies such as electron diffraction, which

can determine the structure of the ions in the gas phase. Techniques like trapped ion laser-induced fluorescence can study the gas-phase emission of NCs. Isomer-specific spectroscopic properties of the NCs can also be studied in the gas phase by coupling an IM cell and a spectroscopic technique successively to the mass spectrometer. Moreover, catalysis of isolated NC ions and ion soft-landing of mass-selected NC ions are expected to develop into active areas of research in the near future. On the other hand, mass spectrometric instrumentation is also improving and approaching the megadalton range to characterize large particles.

List of abbreviation

MS	mass spectrometry
ESI	electrospray ionization
MALDI	matrix assisted laser desorption ionization
IM	ion mobility
EI	electron ionization
TOF	time-of-flight
APCI	atmospheric pressure chemical ionization
LC	Liquid chromatography
CID	collision-induced dissociation
SID	surface-induced dissociation
LDI	laser desorption ionization
DMBT	2,4-dimethyl benzene thiol
PET	2-phenyl ethane thiol
MBT	2-mercapto-benzothiazole
BBSH	4-(tert-butyl)benzyl mercaptan
DTIMS	Drift tube ion mobility spectrometry
TWIMS	Traveling wave ion mobility spectrometry
TIMS	Trapped ion mobility spectrometry
XRPD	X-ray powder diffraction
TRFA	Time-resolved fluorescence anisotropy

References

1. Thomson JJ. Bakerian lecture:-rays of positive electricity. *Proc R Soc Lond A*. 1913;89:1–20.
2. Hossain M. The mass spectrometermass spectrometers and its components. Selected reaction monitoring mass spectrometry (SRM-MS) in proteomics: a comprehensive view, Cham, Springer International Publishing; 2020:17–52.
3. McLafferty FW. A century of progress in molecular mass spectrometry. *Annu Rev Anal Chem (Palo Alto Calif)*. 2011;4:1–22.
4. Kroto HW, Heath JR, O'Brien SC, Curl RF, Smalley RE. C_{60}: buckminsterfullerene. *Nature*. 1985;318:162–163.
5. Knight WD, Clemenger K, de Heer WA, Saunders WA, Chou MY, Cohen ML. Electronic shell structure and abundances of sodium clusters. *Phys Rev Lett*. 1984;52:2141–2143.
6. Furche F, Ahlrichs R, Weis P, et al. The structures of small gold cluster anions as determined by a combination of ion mobility measurements and density functional calculations. *J Chem Phys*. 2002;117:6982–6990.
7. Lechtken A, Neiss C, Kappes MM, Schooss D. Structure determination of gold clusters by trapped ion electron diffraction: $Au_{14}-$–$Au_{19}-$. *Phys Chem Chem Phys*. 2009;11:4344–4350.
8. Chakraborty P, Pradeep T. The emerging interface of mass spectrometry with materials. *NPG Asia Mater*. 2019;11:48.
9. Harkness KM, Cliffel DE, McLean JA. Characterization of thiolate-protected gold nanoparticles by mass spectrometry. *Analyst*. 2010;135:868–874.
10. Chen T, Yao Q, Nasaruddin RR, Xie J. Electrospray ionization mass spectrometry: a powerful platform for noble-metal nanocluster analysis. *Angew Chem Int Ed*. 2019;58:11967–11977.
11. Wang Y, Sun J, Qiao J, Ouyang J, Na N. A "Soft" and "Hard" ionization method for comprehensive studies of molecules. *Anal Chem*. 2018;90:14095–14099.

12. Watson JT. Encyclopedia of Analytical Chemistry. Electron ionization mass spectrometry. John Wiley & Sons, Ltd; 2006.
13. Hillenkamp F, Karas M, Beavis RC, Chait BT. Matrix-assisted laser desorption/ionization mass spectrometry of biopolymers. *Anal Chem*. 1991;63:1193A–1203A.
14. Fenn J, Mann M, Meng C, Wong S, Whitehouse C. Electrospray ionization for mass spectrometry of large biomolecules. *Science*. 1989;246:64–71.
15. Tanaka K, Waki H, Ido Y, Akita S, Yoshida Y, Yoshida T, Matsuo T. Protein and polymer analyses up to m/z 100 000 by laser ionization time-of-flight mass spectrometry. *Rapid Commun Mass Spectrom*. 1988;2:151–153.
16. Karas M, Bachmann D, Bahr U, Hillenkamp F. Matrix-assisted ultraviolet laser desorption of non-volatile compounds. *Int J Mass Spectrom Ion Processes*. 1987;78:53–68.
17. Schiller J, Süss R, Arnhold J, et al. Matrix-assisted laser desorption and ionization time-of-flight (Maldi-Tof) mass spectrometry in lipid and phospholipid research. *Prog Lipid Res*. 2004;43:449–488.
18. Dole M, Mack LL, Hines RL, Mobley RC, Ferguson LD, Alice MB. Molecular beams of macroions. *J Chem Phys*. 1968;49:2240–2249.
19. Banerjee S, Mazumdar S. Electrospray ionization mass spectrometry: a technique to access the information beyond the molecular weight of the analyte. *Int J Anal Chem*. 2012;2012.
20. Whetten RL, Khoury JT, Alvarez MM, Murthy S, Vezmar I, Wang ZL, Stephens PW, Cleveland CL, Luedtke WD, Landman U. Nanocrystal gold molecules. *Adv Mater*. 1996;8:428–433.
21. Tsunoyama H, Negishi Y, Tsukuda T. Chromatographic isolation of "Missing" Au_{55} clusters protected by alkanethiolates. *J Am Chem Soc*. 2006;128:6036–6037.
22. Arnold RJ, Reilly JP. High-resolution time-of-flight mass spectra of alkanethiolate-coated gold nanocrystals. *J Am Chem Soc*. 1998;120:1528–1532.
23. Zhu M, Aikens CM, Hollander FJ, Schatz GC, Jin R. Correlating the crystal structure of a thiol-protected Au_{25} cluster and optical properties. *J Am Chem Soc*. 2008;130:5883–5885.
24. Heaven MW, Dass A, White PS, Holt KM, Murray RW. Crystal structure of the gold nanoparticle $[N(C_8H_{17})_4][Au_{25}(SCH_2CH_2Ph)_{18}]$. *J Am Chem Soc*. 2008;130:3754–3755.
25. Dass A, Stevenson A, Dubay GR, Tracy JB, Murray RW. Nanoparticle MALDI-TOF mass spectrometry without fragmentation: $Au_{25}(SCH_2CH_2Ph)_{18}$ and mixed monolayer $Au_{25}(SCH_2CH_2Ph)_{18-X}(L)_X$. *J Am Chem Soc*. 2008;130:5940–5946.
26. Tracy JB, Kalyuzhny G, Crowe MC, Balasubramanian R, Choi J-P, Murray RW. Poly(Ethylene Glycol) ligands for high-resolution nanoparticle mass spectrometry. *J Am Chem Soc*. 2007;129:6706–6707.
27. Das A, Li T, Nobusada K, Zeng C, Rosi NL, Jin R. Nonsuperatomic $[Au_{23}(SC_6H_{11})_{16}]^-$ nanocluster featuring bipyramidal Au_{15} kernel and trimeric $Au_3(SR)_4$ motif. *J Am Chem Soc*. 2013;135:18264–18267.
28. Das A, Li T, Nobusada K, Zeng Q, Rosi NL, Jin R. Total structure and optical properties of a phosphine/thiolate-protected Au_{24} nanocluster. *J Am Chem Soc*. 2012;134:20286–20289.
29. Wan X-K, Tang Q, Yuan S-F, Jiang D-e, Wang Q-M. Au_{19} nanocluster featuring a V-shaped alkynyl–gold motif. *J Am Chem Soc*. 2015;137:652–655.
30. Chen J, Zhang Q-F, Williard PG, Wang L-S. Synthesis and structure determination of a new Au_{20} nanocluster protected by tripodal tetraphosphine ligands. *Inorg Chem*. 2014;53:3932–3934.
31. Crasto D, Barcaro G, Stener M, Sementa L, Fortunelli A, Dass A. $Au_{24}(SAdm)_{16}$ nanomolecules: X-ray crystal structure, theoretical analysis, adaptability of adamantane ligands to form $Au_{23}(SAdm)_{16}$ and $Au_{25}(SAdm)_{16}$, and its relation to $Au_{25}(SR)_{18}$. *J Am Chem Soc*. 2014;136:14933–14940.
32. Shichibu Y, Negishi Y, Tsukuda T, Teranishi T. Large-scale synthesis of thiolated Au_{25} clusters via ligand exchange reactions of phosphine-stabilized Au_{11} clusters. *J Am Chem Soc*. 2005;127:13464–13465.
33. Yao Q, Yuan X, Yu Y, Yu Y, Xie J, Lee JY. Introducing amphiphilicity to noble metal nanoclusters via phase-transfer driven ion-pairing reaction. *J Am Chem Soc*. 2015;137:2128–2136.
34. Chen S, Wang S, Zhong J, et al. The structure and optical properties of the $[Au_{18}(SR)_{14}]$ nanocluster. *Angew Chem Int Ed*. 2015;54:3145–3149.
35. Zeng C, Li T, Das A, Rosi NL, Jin R. Chiral structure of thiolate-protected 28-gold-atom nanocluster determined by X-ray crystallography. *J Am Chem Soc*. 2013;135:10011–10013.
36. Dass A, Theivendran S, Nimmala PR, et al. $Au_{133}(SPh\text{-}tBu)_{52}$ nanomolecules: X-ray crystallography, optical, electrochemical, and theoretical analysis. *J Am Chem Soc*. 2015;137:4610–4613.
37. Kumara C, Zuo X, Ilavsky J, Cullen D, Dass A. Atomic structure of $Au_{329}(SR)_{84}$ faradaurate plasmonic nanomolecules. *J Phys Chem C*. 2015;119:11260–11266.

38. Joshi CP, Bootharaju MS, Alhilaly MJ, Bakr OM. $[Ag_{25}(SR)_{18}]-$: the "Golden" silver nanoparticle. *J Am Chem Soc*. 2015;137:11578–11581.
39. Chakraborty P, Baksi A, Khatun E, Nag A, Ghosh A, Pradeep T. Dissociation of gas phase ions of atomically precise silver clusters reflects their solution phase stability. *J Phys Chem C*. 2017;121:10971–10981.
40. Desireddy A, et al. Ultrastable silver nanoparticles. *Nature*. 2013;501:399–402.
41. Dhayal RS, Liao J-H, Liu Y-C, et al. $[Ag_{21}\{S_2P(OiPr)_2\}_{12}]+$: an eight-electron superatom. *Angew Chem Int Ed*. 2015;54:3702–3706.
42. Alhilaly MJ, et al. $[Ag_{67}(SPhMe_2)_{32}(PPh_3)_8]^{3+}$: synthesis, total structure, and optical properties of a large box-shaped silver nanocluster. *J Am Chem Soc*. 2016;138:14727–14732.
43. AbdulHalim LG, Bootharaju MS, Tang Q, et al. $Ag_{29}(BDT)_{12}(TPP)_4$: a tetravalent nanocluster. *J Am Chem Soc*. 2015;137:11970–11975.
44. Chakraborty I, Mahata S, Mitra A, De G, Pradeep T. Controlled synthesis and characterization of the elusive thiolated Ag_{55} cluster. *Dalton Trans*. 2014;43:17904–17907.
45. Ghosh A, Pradeep T. Synthesis of atomically precise silver clusters by using the miscibility principle. *Eur J Inorg Chem*. 2014;2014:5271–5275.
46. Chakraborty I, Govindarajan A, Erusappan J, et al. The Superstable 25 KDa monolayer protected silver nanoparticle: measurements and interpretation as an icosahedral $Ag_{152}(SCH_2CH_2Ph)_{60}$ cluster. *Nano Lett*. 2012;12:5861–5866.
47. Kawasaki H, Yamamoto H, Fujimori H, Arakawa R, Inada M, Iwasaki Y. Surfactant-free solution synthesis of fluorescent platinum subnanoclusters. *Chem Commun*. 2010;46:3759–3761.
48. Chakraborty I, Bhuin RG, Bhat S, Pradeep T. Blue emitting undecaplatinum clusters. *Nanoscale*. 2014;6:8561–8564.
49. Nair LV, et al. $[Pt_{17}(CO)_{12}(PPh_3)_8]^{n+}$ (n = 1, 2): synthesis and geometric and electronic structures. *J Phys Chem C*. 2017;121:11002–11009.
50. Chen J, Pan Y, Wang Z, Zhao P. The fluorescence properties of tiara like structural thiolated palladium clusters. *Dalton Trans*. 2017;46:12964–12970.
51. Salorinne K, Chen X, Troff RW, Nissinen M, Häkkinen H. One-pot synthesis and characterization of subnanometre-size benzotriazolate protected copper clusters. *Nanoscale*. 2012;4:4095–4098.
52. Ganguly A, Chakraborty I, Udayabhaskararao T, Pradeep T. A copper cluster protected with phenylethanethiol. *J Nanopart Res*. 2013;15:1522.
53. Dhayal RS, Liao J-H, Lin Y-R, et al. A nanospheric polyhydrido copper cluster of elongated triangular ortho-bicupola array: liberation of H_2 from solar energy. *J Am Chem Soc*. 2013;135:4704–4707.
54. Sun C, Mammen N, Kaappa S, et al. Atomically precise, thiolated copper–hydride nanoclusters as single-site hydrogenation catalysts for ketones in mild conditions. *ACS Nano*. 2019;13:5975–5986.
55. Ghosh A, Huang R-W, Alamer B, et al. $[Cu_{61}(StBu)_{26}S_6C_{16}H_{14}]^+$: a core–shell superatom nanocluster with a Quasi-J_{36} Cu_{19} Core and an "18-Crown-6" metal-sulfide-like stabilizing belt. *ACS Mater Lett*. 2019;1:297–302.
56. Huang R-W, Yin J, Dong C, et al. $[Cu_{81}(PhS)_{46}(^tBuNH_2)_{10}(H)_{32}]^{3+}$ reveals the coexistence of large planar cores and hemispherical shells in high-nuclearity copper nanoclusters. *J Am Chem Soc*. 2020;142:8696–8705.
57. Huang R-W, Yin J, Dong C, et al. $[Cu_{23}(PhSe)_{16}(Ph_3P)_8(H)_6]\cdot BF_4$: atomic-level insights into cuboidal polyhydrido copper nanoclusters and their quasi-simple cubic self-assembly. *ACS Mater Lett*. 2021;3:90–99.
58. Bootharaju MS, Joshi CP, Parida MR, Mohammed OF, Bakr OM. Templated atom-precise galvanic synthesis and structure elucidation of a $[Ag_{24}Au(SR)_{18}]^-$ nanocluster. *Angew Chem Int Ed*. 2016;55:922–926.
59. Soldan G, Aljuhani MA, Bootharaju MS, AbdulHalim LG, Parida MR, Emwas A-H, Mohammed OF, Bakr OM. Gold doping of silver nanoclusters: a 26-fold enhancement in the luminescence quantum yield. *Angew Chem Int Ed*. 2016;55:5749–5753.
60. Khatun E, Chakraborty P, Jacob BR, et al. Intercluster reactions resulting in silver-rich trimetallic nanoclusters. *Chem Mater*. 2020;32:611–619.
61. Krishnadas KR, Ghosh A, Baksi A, Chakraborty I, Natarajan G, Pradeep T. Intercluster reactions between $Au_{25}(SR)_{18}$ and $Ag_{44}(SR)_{30}$. *J Am Chem Soc*. 2016;138:140–148.
62. Krishnadas KR, Baksi A, Ghosh A, Natarajan G, Pradeep T. Structure-conserving spontaneous transformations between nanoparticles. *Nat Commun*. 2016;7:13447.
63. Chakraborty P, Nag A, Natarajan G, et al. Rapid isotopic exchange in nanoparticles. *Sci Adv*. 2019;5:eaau7555.
64. Tang L, Kang X, Wang X, Zhang X, Yuan X, Wang S. Dynamic metal exchange between a metalloid silver cluster and silver(I) thiolate. *Inorg Chem*. 2021;60:3037–3045.

65. Bhat S, Narayanan RP, Baksi A, et al. Detection of $[Au_{25}(PET)_{18}(O_2)n]^-$ (n = 1, 2, 3) species by mass spectrometry. *J Phys Chem C*. 2018;122:19455–19462.
66. Chakraborty P, Baksi A, Mudedla SK, et al. Understanding proton capture and cation-induced dimerization of $[Ag_{29}(BDT)_{12}]^{3-}$ clusters by ion mobility mass spectrometry. *Phys Chem Chem Phys*. 2018;20:7593–7603.
67. Baksi A, Chakraborty P, Bhat S, Natarajan G, Pradeep T. $[Au_{25}(SR)_{18}]_2^{2-}$: a noble metal cluster dimer in the gas phase. *Chem Commun*. 2016;52:8397–8400.
68. Chakraborty P, Nag A, Paramasivam G, Natarajan G, Pradeep T. Fullerene-functionalized monolayer-protected silver clusters: $[Ag_{29}(BDT)_{12}(C_{60})n]^{3-}$ (n = 1–9). *ACS Nano*. 2018;12:2415–2425.
69. Chakraborty P, Nag A, Mondal B, Khatun E, Paramasivam G, Pradeep T. Fullerene-mediated aggregation of $M_{25}(SR)_{18}^-$ (M = Ag, Au) nanoclusters. *J Phys Chem C*. 2020;124:14891–14900.
70. Nag A, Chakraborty P, Paramasivam G, Bodiuzzaman M, Natarajan G, Pradeep T. Isomerism in supramolecular adducts of atomically precise nanoparticles. *J Am Chem Soc*. 2018;140:13590–13593.
71. Chakraborty P, Nag A, Sugi KS, Ahuja T, Varghese B, Pradeep T. Crystallization of a supramolecular coassembly of an atomically precise nanoparticle with a crown ether. *ACS Mater Lett*. 2019;1:534–540.
72. Nag A, Chakraborty P, Thacharon A, et al. Atomically precise noble metal cluster-assembled superstructures in water: luminescence enhancement and sensing. *J Phys Chem C*. 2020;124:22298–22303.
73. Fields-Zinna CA, Sampson JS, Crowe MC, et al. Tandem mass spectrometry of thiolate-protected Au nanoparticles $Na_xAu_{25}(SC_2H_4Ph)_{18-Y}(S(C_2H_4O)_5CH_3)_Y$. *J Am Chem Soc*. 2009;131:13844–13851.
74. Angel LA, Majors LT, Dharmaratne AC, Dass A. Ion mobility mass spectrometry of $Au_{25}(SCH_2CH_2Ph)_{18}$ nanoclusters. *ACS Nano*. 2010;4:4691–4700.
75. Black DM, Bhattarai N, Whetten RL, Bach SBH. Collision-induced dissociation of monolayer protected clusters Au_{144} and Au_{130} in an electrospray time-of-flight mass spectrometer. *J Phys Chem A*. 2014;118:10679–10687.
76. Baksi A, Schneider EK, Weis P, et al. Linear size contraction of ligand protected Ag_{29} clusters by substituting Ag with Cu. *ACS Nano*. 2020;14:15064–15070.
77. Ghosh A, Bodiuzzaman M, Nag A, Jash M, Baksi A, Pradeep T. Sequential dihydrogen desorption from hydride-protected atomically precise silver clusters and the formation of naked clusters in the gas phase. *ACS Nano*. 2017;11:11145–11151.
78. Johnson GE, Priest T, Laskin J. Size-dependent stability toward dissociation and ligand binding energies of phosphine ligated gold cluster ions. *Chem Sci*. 2014;5:3275–3286.
79. Baksi A, Harvey SR, Natarajan G, Wysocki VH, Pradeep T. Possible isomers in ligand protected Ag_{11} cluster ions identified by ion mobility mass spectrometry and fragmented by surface induced dissociation. *Chem Commun*. 2016;52:3805–3808.
80. Cumeras R, Figueras E, Davis CE, Baumbach JI, Gràcia I. Review on ion mobility spectrometry. Part 1: current instrumentation. *Analyst*. 2015;140:1376–1390.
81. Lanucara F, Holman SW, Gray CJ, Eyers CE. The power of ion mobility-mass spectrometry for structural characterization and the study of conformational dynamics. *Nat Chem*. 2014;6:281–294.
82. Baksi A, Ghosh A, Mudedla SK, et al. Isomerism in monolayer protected silver cluster ions: an ion mobility-mass spectrometry approach. *J Phys Chem C*. 2017;121:13421–13427.
83. Kalenius E, Malola S, Matus MF, Kazan R, Bürgi T, Häkkinen H. Experimental confirmation of a topological isomer of the ubiquitous $Au_{25}(SR)_{18}$ cluster in the gas phase. *J Am Chem Soc*. 2021;143:1273–1277.
84. Matus MF, Malola S, Kinder Bonilla E, Barngrover BM, Aikens CM, Häkkinen H. A topological isomer of the $Au_{25}(SR)_{18}-$ nanocluster. *Chem Commun*. 2020;56:8087–8090.
85. Daly S, et al. Gas-phase structural and optical properties of homo- and heterobimetallic rhombic dodecahedral nanoclusters $[Ag_{14-n}Cu_n(C{\equiv}CtBu)_{12}X]^+$ (X = Cl and Br): Ion Mobility, VUV and UV spectroscopy, and DFT calculations. *J Phys Chem C*. 2017;121:10719–10727.
86. Soleilhac A, Bertorelle F, Comby-Zerbino C, et al. Size characterization of glutathione-protected gold nanoclusters in the solid, liquid and gas phases. *J Phys Chem C*. 2017;121:27733–27740.
87. Ligare MR, Baker ES, Laskin J, Johnson GE. Ligand induced structural isomerism in phosphine coordinated gold clusters revealed by ion mobility mass spectrometry. *Chem Commun*. 2017;53:7389–7392.
88. Xavier PL, Chaudhari K, Baksi A, Pradeep T. Protein-protected luminescent noble metal quantum clusters: an emerging trend in atomic cluster nanoscience. *Nano Rev*. 2012;3:14767.
89. Meng X, Zare I, Yan X, Fan K. Protein-protected metal nanoclusters: an emerging ultra-small nanozyme. *WIREs Nanomed Nanobiotechnol*. 2020;12.

90. Xie J, Zheng Y, Ying JY. Protein-directed synthesis of highly fluorescent gold nanoclusters. *J Am Chem Soc*. 2009;131:888–889.
91. Habeeb Muhammed MA, Verma PK, Pal SK, et al. Luminescent quantum clusters of gold in bulk by albumin-induced core etching of nanoparticles: metal ion sensing, metal-enhanced luminescence, and biolabeling. *Chem Eur J*. 2010;16:10103–10112.
92. Baksi A, Xavier PL, Chaudhari K, Goswami N, Pal SK, Pradeep T. Protein-encapsulated gold cluster aggregates: the case of lysozyme. *Nanoscale*. 2013;5:2009–2016.
93. Ghosh D, Bodiuzzaman M, Som A, et al. Internalization of a preformed atomically precise silver cluster in proteins by multistep events and emergence of luminescent counterparts retaining bioactivity. *J Phys Chem C*. 2019;123:29408–29417.
94. Qian H, Zhu Y, Jin R. Atomically precise gold nanocrystal molecules with surface plasmon resonance. *Proc Natl Acad Sci*. 2012;109:696–700.
95. Kumara C, Zuo X, Ilavsky J, Chapman KW, Cullen DA, Dass A. Super-stable, highly monodisperse plasmonic faradaurate-500 nanocrystals with 500 gold atoms: $Au_{\sim 500}(SR)_{\sim 120}$. *J Am Chem Soc*. 2014;136:7410–7417.
96. Vergara S, Santiago U, Kumara C, et al. Synthesis, mass spectrometry, and atomic structural analysis of $Au_{\sim 2000}(SR)_{\sim 290}$ nanoparticles. *J Phys Chem C*. 2018;122:26733–26738.
97. Kumara C, Zuo X, Cullen DA, Dass A. Faradaurate-940: synthesis, mass spectrometry, electron microscopy, high-energy x-ray diffraction, and x-ray scattering study of $Au_{\sim 940\pm 20}(SR)_{\sim 160\pm 4}$ nanocrystals. *ACS Nano*. 2014;8:6431–6439.
98. Kumara C, Hoque MM, Zuo X, Cullen DA, Whetten RL, Dass A. Isolation of a 300 KDa, $Au_{\sim 1400}$ gold compound, the standard 3.6 nm capstone to a series of plasmonic nanocrystals protected by aliphatic-like thiolates. *J Phys Chem Lett*. 2018;9:6825–6832.

CHAPTER

11

Spectroscopy of gas phase cluster ions

Ananya Baksi[a] *and Thalappil Pradeep*[b]

[a] Technische Universität Dortmund Fakultät für Chemie und Chemische Biologie Anorganische Chemie Otto-Hahn-Straße 6, 44227 Dortmund, Germany [b] Deepak Parekh Institute Chair Professor and Professor of Chemistry, Department of Chemistry, Indian Institute of Technology Madras, Chennai, India

11.1 Introduction

Nanoclusters have distinct structures and properties in condensed and in the gas phase when compared with their bulk counterpart.[1] Most of the interesting properties of nanoclusters arise from their precise structures where a change in one atom is enough to make large changes.[2] Besides, this can also result in several isomers.[3] The strong size-dependence of such nanoclusters is important for fundamental studies for a detailed understanding of properties such as their catalytic activity.[2b,4] Several properties of nanoclusters can be understood from their equilibrium geometric structure, which often deviate from the bulk lattice, making structure determination an important step in understanding the properties of nanoclusters.[5] While complete structural information can be achieved by single-crystal X-ray diffraction,[1a,5,6] such possibilities do not exist in the gas phase, although there is constant effort to determine structures in the gas phase, such as gas phase electron diffraction.[7] Palmer and group found effective ways to deposit size selected nanoclusters and study them using electron microscopy.[8] Matrix isolation spectroscopy is used to freeze the ions during their structure determination in the gas phase.[9]

The following methods discussed in this chapter are generally used for gas phase structure and property determination. In most cases, a specific property is compared with several theoretically modeled isomeric structures to confirm the occurrence of one or multiple conformers in the specified experimental condition. We will limit our discussion on only noble metal nanoclusters here, to make the discussion shorter. The synthesis and characterization of bare and protected clusters discussed here are covered in other chapters of this book.

Atomically Precise Metal Nanoclusters.
DOI: https://doi.org/10.1016/B978-0-323-90879-5.00001-9

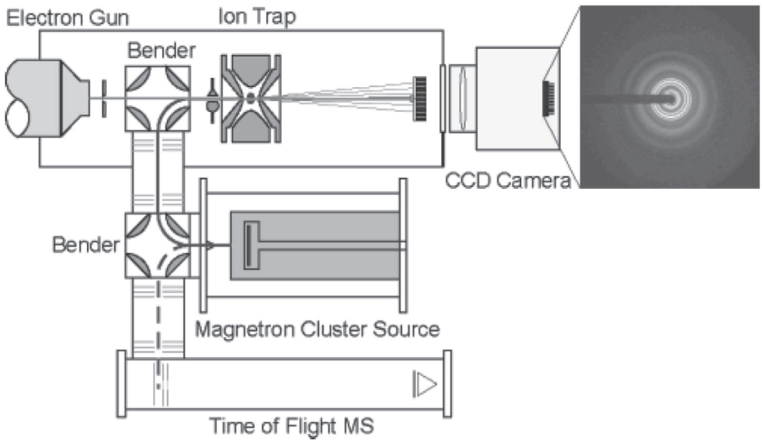

FIGURE 11.1 Schematic diagram of TIED set up. Reproduced with permission[12].

11.2 Trapped ion electron diffraction

11.2.1 Theory and instrumentation

Trapped ion electron diffraction (TIED) was first introduced by Park and group for the structure determination of C_{60}^{+}.[10] In general, the basic setup comprised of a cluster source, an ion trap wherein size selected clusters are trapped and allowed to interact with the electron beam and the diffracted electrons are mapped on a phosphor screen as Debye-Scherrer rings similar to powder diffraction.[11] Depending on the structure and orientation, the diffraction pattern is analyzed and specific structural information is obtained.

Component of the TIED system used by Schoos and Kappes et al. is shown in Fig. 11.1.[12] A magnetron cluster source is used for the production of bare clusters which are mass-selected by quadrupole ion trap. Temperature of the trapped ions can be controlled in the range 90–450 K by the heating and cooling assembly attached to the trap electrodes. A well-collimated electron beam of 40 keV kinetic energy and 0.5 mm diameter is generated from a long focal length electron gun, which pass through the trap via 1.5 mm diameter holes in the end cap. This creates a scattering angle of 7.7° and maximum scattering vector 14.5 $Å^{-1}$. The diffracted electrons are detected on a phosphor screen assembly, imaged on a liquid nitrogen cooled CCD camera situated outside the UHV chamber. About 10^5 ions are captured from the ion beam, mass-selected, thermalized in a He bath at 10^{-3} mbar and the electron cloud is irradiated by the electron beam at 10^{-9} mbar for 30 s. All the fragments are carefully removed for proper size selection. A reference measurement is performed under similar conditions with the cluster ion beam and the data is used for background subtraction. The scattering pattern is processed mathematically and is fit to a modeled geometry (the process is detailed elsewhere).[12,13]

11.2.2 Structure determination

First report on the structures of small gold nanoclusters anions was reported by Landman and Park et al. following experimental TIED data compared with theoretically modeled

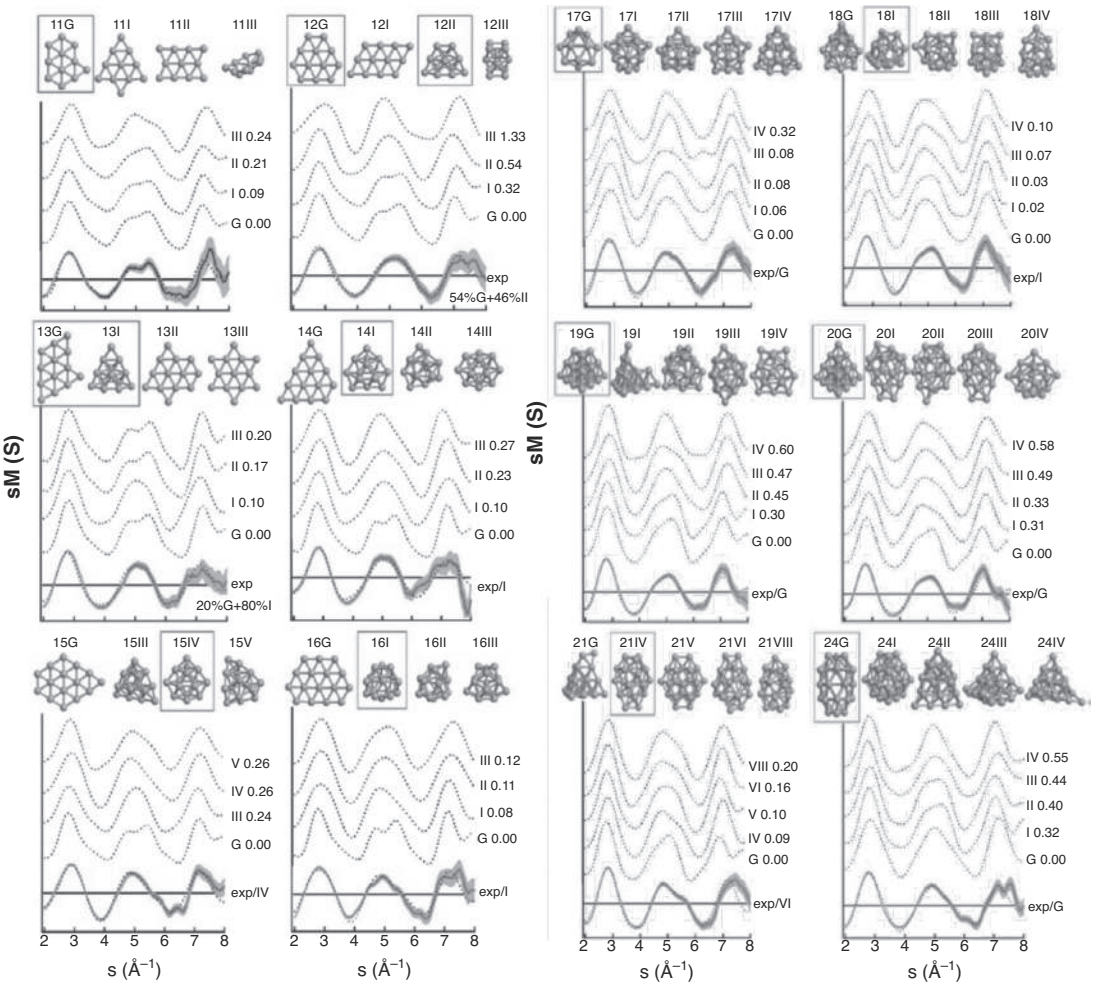

FIGURE 11.2 Calculated isomer structures for Au_n^- clusters with $11 \leq n \leq 24$ are shown at the top of each panel with corresponding diffraction patterns depicted below dotted curve The energy of the isomer above that of the ground state (GS) is shown on the right for each isomer. The diffraction intensity has arbitrary units. The isomers that constitute the best fit are marked by a frame in each panel. Reproduced with permission.[14]

isomers of Au_{11}^- to Au_{24}^- as shown in Fig. 11.2.[14] They found structural evolution of 2D planar (Au_{11}^-) to 3D structures (Au_{12}^-–Au_{14}^-) to hollow cages (Au_{16}^-–Au_{17}^-) followed by emergence of tetrahedral (Au_{20}^-) and ultimately highly symmetric tube like structure (Au_{24}^-). Representative scattering spectra of each cluster ion along with the theoretically calculated scattering patterns of several possible isomers are shown in Fig. 11.2. The structures of Au_{14}–Au_{19}^- were revisited by Schoos et al. with improved low temperature TIED experiment. While hollow cage structures are preferred for Au_{16}–Au_{18}^- flat 3D structures were observed for Au_{14}–Au_{15}^- and Au_{19}^- had a tetrahedral structures.[15]

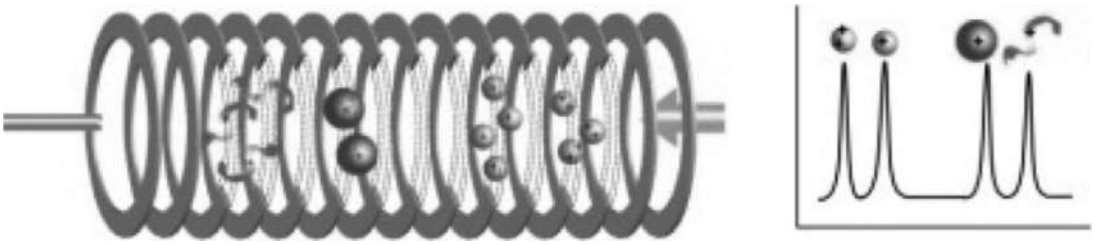

FIGURE 11.3 Schematic representation of a drift tube where high electric field is applied. TWIMS have almost similar configuration but is a low pressure a small drift tube where potential is applied which travels across the length and that way pushes the ions forward. Reproduced with permission.[26]

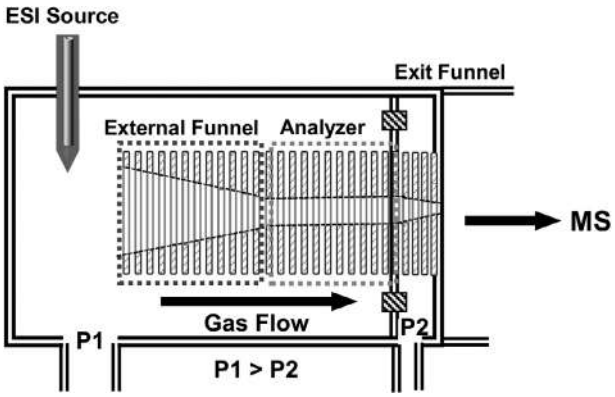

FIGURE 11.4 Schematic representation of the TIMS tunnel. Here ions are hold against the gas flow.

Structure of Au_n^+ ($n = 11$–20) were studied by TIED as well. While experimentally observed structure of Au_{11}^+–Au_{13}^+ resemble their predicted structure, layered structure was found for $Au_{14\text{-}17}^+$. Appearance of cage like structure was observed from Au_{18}^+ onwards with Au_{20}^+ possessing two isomers. Structure of these nanoclusters highly depend on the constituent metal atoms and their charge, as observed for $(Au/Ag/Cu)_{20}^{+/0/-}$.[16] While both $Cu_{20}^{+/-}$ adopt icosahedral structure, strong deviation was observed for the $Ag_{20}^{+/-}$ case, wherein Ag_{20}^- had strongly distorted icosahedral structure unlike icosahedral Ag_{20}^+. Interestingly, Au_{20}^- is not icosahedral rather a tetrahedral structure was confirmed from the TIED experiment and is different from the Au_{20}^+, which is a mixture of distorted icosahedral and tetrahedral structures (Fig. 11.3). A mixture of enantiomers was observed experimentally and surface reconstruction was proposed for such isomerization for Au_{34}^- nanoclusters in a different study by Schoos and colleague.[17] They have also reported structures of cationic Ag_n^+ clusters ($19 \leq n \leq 79$) specifically for Ag_{19}, Ag_{38}, Ag_{55}, Ag_{59}, Ag_{75}, and Ag_{79} cluster cations by TIED at 100 K. In this case, they found a more spherical double icosahedron with one missing atom instead of a regular double icosahedron. Ag_{38}^+ has an icosahedral motif with decahedral structure. Ag_{55}^+ is an example of ideal Mackay icosahedron and other clusters are based on icosahedron structure (Fig. 11.4).[13]

In another study, several 55 atom 3d and 4d transition metal nanoclusters' structures resemble their corresponding bulk lattice morphology.[18] The structures can be divided into 4 groups.

Anionic Sc_{55}, Co_{55}, Ni_{55}, Cu_{55}, Pd_{55}, and Ag_{55} have high symmetry Mackay icosahedron structure comprising of 13 atom core and 42 atom-shell. This structure can also be considered as a typical multiply twinned particle (MTP) type geometry with 20 tetrahedra stacked in fcc fashion. While fcc metals Ni_{55}^-, Cu_{55}^-, and Ag_{55}^- possess MTP geometry with sphere-like structure having rounded corners and edges, platonic icosahedral structure with planar facets was observed for hcp Co_{55}^- and much longer core-shell bond distance was found for hcp Sc_{55}^-. Pd_{55}^- is an exception as it relaxes into a C_i from I_h symmetry structure. All bcc metals (in the bulk) V_{55}^-, Cr_{55}^-, Mn_{55}^-, Fe_{55}^-, Nb_{55}^-, and Mo_{55}^- adopt polytetrahedral geometry forming locally icosahedral coordination shell. The Fe_{55}^- has reduced sphericity and higher number of surface atoms due to four interpenetrating 19-atom double icosahedra. The hcp Ti_{55}^- and Zr_{55}^- have irregular icosahedral structures and can be interpreted as a combination of the two above-mentioned groups. Ru_{55}^- and Rh_{55}^- comprise segments resembling bulk hcp or fcc structure pointing toward icosahedral—bulk transition for 55 atom clusters. Such bulk transition was observed for Pd_{90}^- and larger nanoclusters. While Pd_{55}^- and Pd_{65}^- are icosahedral in nature, mixture of icosahedral (86%) and closed pack (14%) structure was found for Pd_{75}^-. Fraction of fcc component gradually increases for Pd_{85}^- to Pd_{105}^- and becomes maximum for Pd_{147}^-.[19]

11.3 Ion mobility spectrometry (IMS)

While TIED considers molecular scattering for structure determination, ion mobility (IM) considers collision cross-section for identification of size and shape of the ion.[20] When combined with mass spectrometry, the technique is called ion mobility spectrometry (IMS) and has been used by several groups to understand the structures of both bare and protected nanoclusters. Here, we briefly discuss the fundamentals and modern adaptation of IMS in the context of nanoclusters.

11.3.1 Instrumentation and fundamentals

The history of ion mobility can be traced back to Rutherford in the 1890s and was combined with magnetic sector mass spectrometer in 1960 by McDaneil. ESI was coupled with IM in 1968 and laser ionization in 1982. First differential mobility analyzer was commercialized by Thermo in 1975. In 1989, Blanchard described the tandem ion mobility (IM/IM). In 1990, portable IM spectrometers were commercialized. In the same year, field asymmetric ion mobility spectrometry (FAIMS) and differential mobility analyzer (DMS) were introduced. Bower developed MALDI-based IM–MS in 1995. In 1996, Jarold built a high-resolution drift tube IM spectrometer. Traveling wave IM–MS was commercialized by Waters in 2006. In 2011, high resolution trapped ion mobility was coupled with MS by Bruker. Drift tube based commercial IM–MS was introduced in 2014 by Agilent. In the following section, working principle of different IMS techniques are briefly discussed.[2a,21,22]

Theory. When ions are subjected to electric field, they travel along the field. But when the field is applied in presence of a buffer gas, the trajectory of the ions becomes complicated due to collisions with the buffer gas in random directions. However, in uniform weak electric filed the ions will drift through the buffer gas with constant velocity and in line with the field. If

electric field, E is applied and the ions drift velocity is v, then

$$v = K \times E, \text{ where Kisthei on mobility} \tag{11.1}$$

The acceleration of the ion and its mobility is proportional to its charge, z. Additionally, the deceleration of the ions is inversely proportional to the number density (N) of the buffer gas. Larger ions undergo more interaction compared to smaller ions, and hence mobility is inversely proportional to the collision cross-section, σ. A quantitative relation among these parameters can be made using momentum transfer theory which accounts for the ion charge, momentum gained in the electric field, and loss resulting from friction with buffer gas as follows:

$$K = \left(\frac{3}{16N}\right)\left(\frac{2\pi}{kT}\right)^{0.5}\frac{z}{\sqrt{\mu}\sigma} \tag{11.2}$$

where μ is the reduced mass of the ion and the buffer gas, k the Boltzmann's constant, T the temperature in Kelvin.[23]

Modeling. Collision cross-section is a measure of size of the ion. However, here size is determined by the ion-buffer gas interaction potential in three dimensions.[3] Depending on the buffer gas, this interaction potential may consist of charge–dipole, charge-induced dipole, dipole–dipole as well as van der Waals interactions. To get the full essence of the IMS experimental result, one has to consider the geometric-structure of the ions and calculate CCS. In this context, He is a wiser choice as buffer gas. Since it is monoatomic, it has no dipole moment and polarizablity is often very low and hence interaction of the ions with He can therefore be approximated well as elastic scattering of hard spheres. If the atoms of nanoclusters ions with specific geometry are replaced with hard spheres with element-specific radius then CCS of the overall ion can be determined by averaging over several projection. This method is known as projection approximation (PA) method. PA is valid for ions with convex geometry. For concave structures, several collisions have to be considered as the scattered buffer gas can collide with another part of the cluster ion. This is considered in exact hard-sphere scattering model developed by Jarold and group.[24] For structure independent modeling, trajectory method is found to be more accurate for calculating CCS of any ion where trajectory of the interacting buffer gas molecule is considered. The gas molecules start interacting at a random starting point with a Maxwell–Boltzmann-distributed initial velocity and a given the trajectory is corrected after definite time intervals according to the interaction between the gas molecule and the ion. In a regular trajectory method calculation, only the Lennard–Jones interaction and the charge induced dipole moment of the gas are included. For N_2 based IMS measurements often, quadrupole moment of N_2 needs to be considered owing to its considerable polarizablity. Charge distribution on the ion also is important to get the clearer structural information from the model. Most often Mulikken, natural population analysis, and natural bond order are considered for the effective overall charge distribution of the constituent ions. A specific structure can be confirmed to be present if the calculated CCS is within 2% error of the experimentally observed CCS and is often a trial and error method to confirm the exact structure.

Various IMS instruments. As described above several IMS methods are known and are used in combination with different mass spectrometric techniques. In the following different techniques are briefed.[20a,22,25]

Drift tube ion mobility spectrometry (DT-IMS). This is the most commonly used IMS method for the nanoclusters structure analysis. Briefly, ions travel through a drift tube maintained in a uniform electric field. Buffer gas is passed in the opposite direction to the ion flow. Depending on the size of the ions they take different time to drift through the drift cell and are analyzed as per their arrival time distribution. This method works on the first principle and do not need any calibration. CCS can be directly obtained from the experimental parameters and are often used as the reference CCS during calibration in other techniques. Considering Eq. 11.1, drift velocity of the ion v_d

$$vd = K \times E = L/td = K \times E/L \tag{11.3}$$

$$\text{Therefore, } K = L2/E \times td \tag{11.4}$$

where L is the length of the drift tube, td is the drift time of the ion of interest. CCS can be directly calculated from Eq. 11.2. DT-IMS is mostly used for early structure determination of bare nanoclusters (see below).[26]

Traveling wave ion mobility spectrometry (TWIMS). This is a variant of conventional drift tube IMS.[27] Unlike a uniform high electric field applied in DT, a small electrical potential is applied in this low-pressure drift tube which pushes the ions through the tube creating a wave pushing. This setup does not require very high voltage like DT but cannot determine the CCS directly without calibration. This concept is commercialized by Waters' in the form of Synapt HDMS in 2006. Further modifications of this technique includes structure for lossless ion manipulation (SLIM) and cyclic TWIMS both of which offer very high resolution.

Trapped ion mobility spectrometry (TIMS). Briefly, in trapped IMS, an electric field gradient holds the ions in a flow of drift gas and the field is lowered over time thus eluting the ions with increasing mobilities in sequence.[28] The source of this flow is a pressure difference between the entrance and the exit of the TIMS-tunnel. The ions are being held by an electric field gradient (EFG) against a constant N_2 flow. The flow is a pressure difference between the entrance and exit of the TIMS-tunnel. Lowering the EFG results in the elution of the analyte according to its inverse mobility (1/K). Depending on the difference between start-EFG and end-EFG (ΔEFG) as well as the duration of this reduction (ramp time $= t_r$), high resolutions can be achieved. The lower the rate at which the electric field gradient is decreased and higher the pressure difference (P1-P2) the higher is the mobility resolution. Resolutions of 250 and more have been reported. In front of the trap part of the TIMS- tunnel, a second ramp accumulates the ions for a given period of time (accumulation time $= t_a$). This technique also requires calibration to get the CCS.

Differential mobility analyzer (DMA), Field asymmetric ion mobility spectrometry (FAIMS), structure for lossless ion manipulation (SLIM) are also used for different molecules which are beyond the scope of this book.

11.3.2 IMS of bare nanoclusters

Several pure and doped fullerenes were studied by IMS and their structures were deduced using a combination of experiment and DFT calculation by several groups. Similarly structures of other transition metals and semiconductor clusters like Al, In, Ge, Si, Pb, Sn, Bi, Ru, etc., have been studied using IMS. Here, we will explain the method for coinage metal nanoclusters.

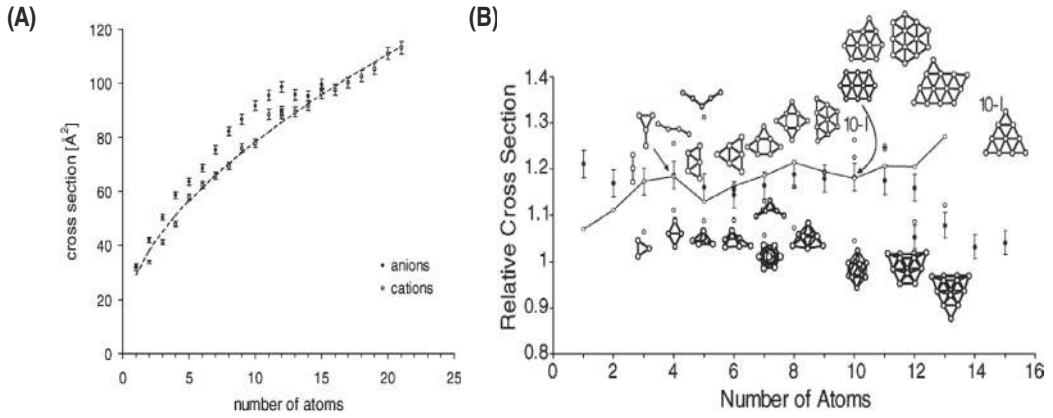

FIGURE 11.5 (A) Experimental drift tube CCS (in He) of Ag_n^+ ($n = 1$–25).[29] (B) Relative collision cross-sections of the silver cluster cations, comparison of the experimental data with quantum chemically computed structures. The line connects the collision cross-sections of the global minima calculated at MP2 level.[3] Reproduced with permission.[3,29]

Most of the clusters described here are prepared by laser vaporization of the respective metal target.

11.3.2.1 Ag nanoclusters

Several silver cluster cations have been studied using IMS and their structures have been confirmed through a comparison of experimental and calculated collision cross-section.[29] The structure of coinage metal clusters is relatively easier to calculate due to the filled d-orbitals resulting in the participation of only the outermost s-electron in bonding. Weis et al. have shown that the CCS of the Ag_n^+ ($n = 1$–25) increases monotonically with the number of atoms raised to the power of 2/3, as expected for quasi-spherical clusters (Fig. 11.5).[3] However, the deviation from the quasispherical geometry is stronger for the smaller clusters compared to the larger clusters. They also calculated several possible isomeric structures of the clusters theoretically and tried to find the most possible isomer from the experiment.[29] For Ag_3^+, only one isomeric structure, which is an isosceles triangle, was found. As the calculated CCS matches exactly with the experiment, and hence possibility of other isomers was ruled out. Similarly, for Ag_4^+, among three possible isomers (diamond shape (lowest energy), square, and Y shape), the diamond shape was found to be the most probable in terms of both energy and calculated CCS. Beyond Ag_6^+, three-dimensional structures were predicted. CCS in N_2 for Ag_5^+ – Ag_{17}^+ is also reported by Baksi et al. which were produced from collision-induced dissociation (CID) of Ag_{17}^+.[30]

11.3.2.2 Cu nanoclusters

Cationic Cu clusters follow a similar CCS trend as silver clusters; however, the experimental CCS of the Cu clusters is much smaller due to size difference between Ag and Cu. In both cases, the main structural motif was found to be triangular which is very important for both planar and 3D structures. For Cu_3^+ and Cu_4^+, similar triangular and diamond shape geometry was

found. For Cu_5^+, 5 different isomers were calculated using DFT among which the W-shaped isomer (energy minima) was found to be the best fit as per experimental CCS. This structure is different than Ag_5^+ which was found to be X-type geometry. 3D structures were observed from Cu_6^+ onwards.[3]

11.3.2.3 Cationic Au nanoclusters

Compared to silver and copper, Au clusters show stronger deviation in their experimental CCS especially for $Au_{6\text{-}9}^+$ and Au_{11}^+ clusters.[31] Both Au_3^+ and Au_4^+ have similar structure to Ag and Cu. The pentamer has similar X-type geometry as seen for Ag. The trigonal bipyramidal structure is higher in energy and also do not fit experimentally. For both Au_6^+ and Au_7^+, unlike Ag and Cu, planar structure was found experimentally. Until this point both DFT and MP2 methods matches with the experimentally observed structures. For, Au_8^+, DFT predicts a planar structure while MP 2 predicts a 3D structure. However, experimentally 3D structure was confirmed but this was not the lowest energy isomer predicted by both methods. From Au_9^+ onwards, 3D structure is predicted as well as experimentally observed. The unusual large CCS of Au_{11}^+ is not due to the planar geometry rather, it is an open 3D structure with D_{3h} symmetry. However, in this case, all the atoms are in the surface and no atom is actually inside and the calculated CCS of this isomer fits exactly with the experimentally observed one (Scheme 11.1).[32]

Although one major isomer is predicted from the experiment at room temperature, the data do not really confirm the absence of other fast converting isomers. If other isomers are interconverting faster than the average arrival time (drift time), their presence will not be seen unless the interconversion rate is reduced at lower temperature. As shown in Fig. 11.6B, upto Au_8^+, only one peak was observed in the arrival time distribution at 77K. However, Au_9^+ showed two peaks confirming presence of a second isomer.[32] Fragmentation of Au_{10}^+ into Au_9^+ also resulted similar bimodal distribution confirming that these isomers are not due to energetic aggregation. The bimodal distribution changes significantly when the temperature was raised slowly. Upto 120 K, similar bimodal distribution was observed, but beyond 140 K, the pattern disappears and a broad Gaussian distribution was found. The broadness decreased with increasing temperature (Fig. 11.7).

11.3.2.4 Anionic Au nanoclusters

Others studies on structural identification of gold cluster anions suggest considerable different structures compared to their cationic analogue.[2a,33] The same is true for the CCS of such cluster anions as the experimental CCS of anionic clusters are larger compared to the cationic clusters of same nuclearity (up to 20% difference). Larger size of anions can be understood from the simple concept of extended electron clouds which interact strongly with the drift (buffer) gas and hence the size is larger. But this difference should diminish with increasing size of the clusters as the effect of an additional electron will be stronger for smaller size clusters. Such convergence toward cationic cluster CCS can be observed up to Au_5^- and Au_6^- but the size increases again beyond this size (Fig. 11.8). The other reason can be the structure of cationic and anionic clusters are entirely different. From DFT optimized structures and experimental CCS, Au_3^- has a linear structure compared to the triangular structure of the Au_3^+. Similarly, a Y-shaped structure over a diamond shape was experimentally found for Au_4^-. For the Au_5^-, W shape structure, for Au_6^-, an isosceles triangle, for Au_7^- and Au_8^-

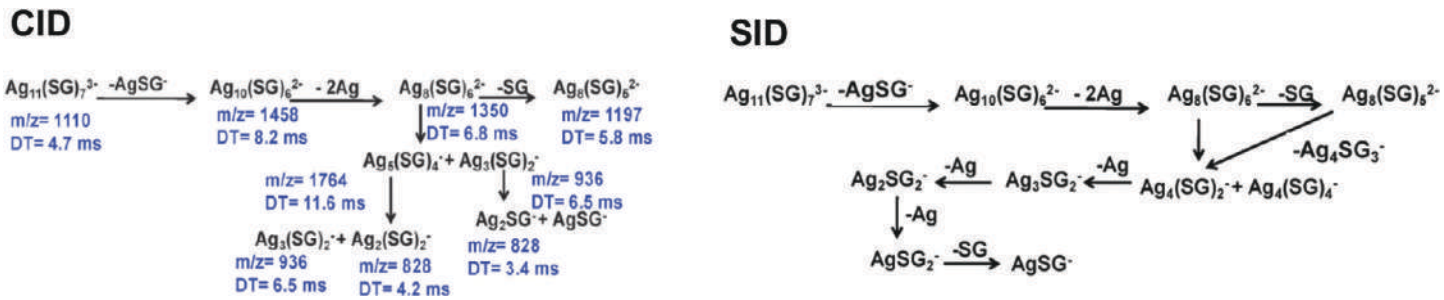

SCHEME 11.1 Fragmentation pattern of $Ag_{11}(SG)_7^{3-}$ by CID and SID are compared. SID showed charge stripping and different fragmentation pattern than CID.[38]

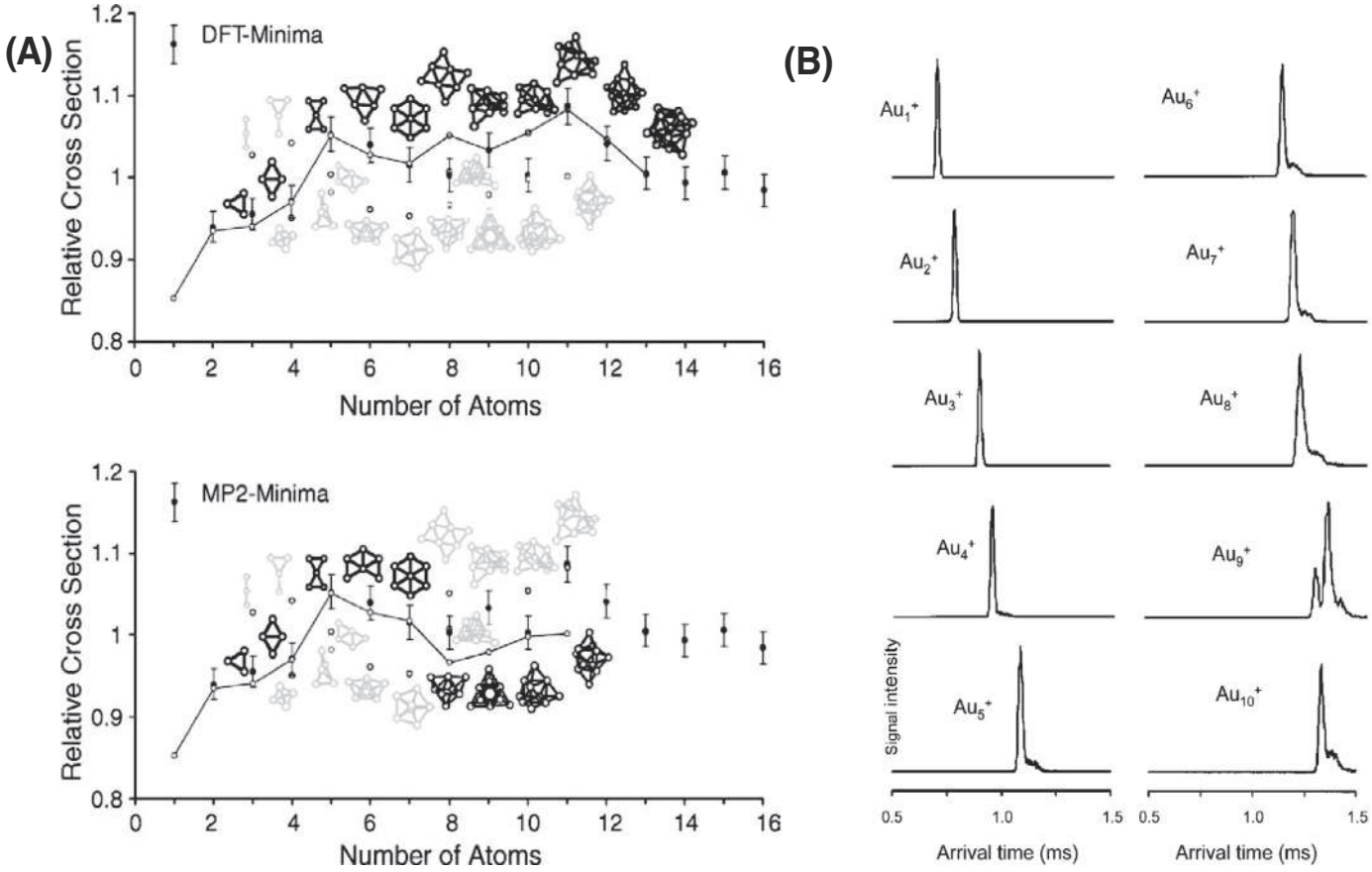

FIGURE 11.6 (A) Optimized structures of Au_n^+ clusters ($n = 1$–16) using DFT and MP2. (B) Arrival time distribution of Au_n^+ ($1 \leq n \leq 10$) at 77 K showing single isomer expect for Au_9^+ which shows a bimodal distribution, indicating the presence of two isomeric species. Reproduced with permission.[3,32]

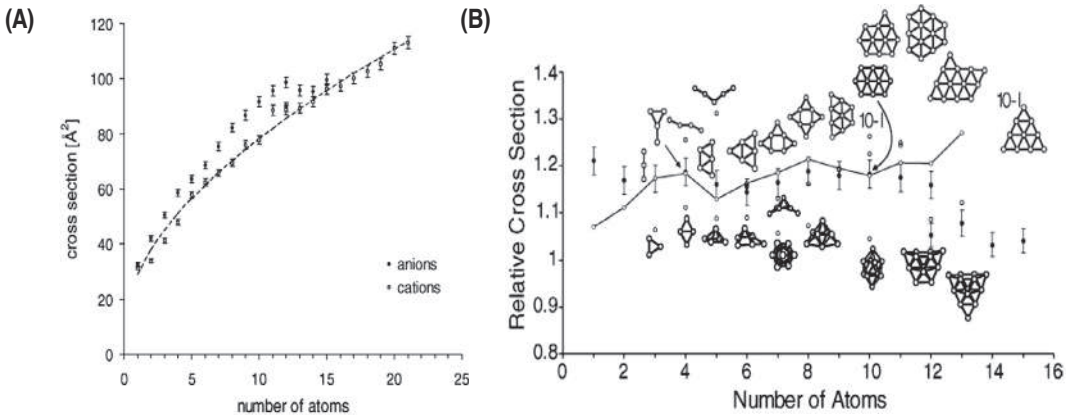

FIGURE 11.7 (A) Experimental CCS of the cationic and anionic Au clusters. (B) Relative CCS of the anions is compared with the CCS of the calculated structures. The line connects the CCS of the respective global minima (except Au_4^- and Au_{10}^-) shown in the upper part of the figure which are mostly planar structures. The local minima of the 3D structures are shown in the lower part of the figure which energetically less favorable (three-dimensional) and have much lower CCS compared to experiment. Reproduced from with permission.[3]

a central Au_4 square was found. Larger clusters also contain Au_7 ring except for Au_{10}^- and Au_{13}^-. Although a triangle with 4 atoms per edge is favored for Au_{10}^- by DFT, the calculated CCS was found to be larger compared to the experimental CCS. The planar structure though slightly higher in energy matches perfectly with the experiment. For Au_{12}^-, two distinct peaks were observed pointing toward the presence of two isomeric structures one of which is planar and the other a 3D structure. The size decrease from Au_{12}^- to Au_{13}^- can be associated with the transition from planar to 3D structure. Therefore, smaller Au_n clusters, irrespective of their charges, prefer planar structure ($n = 7$ and beyond for cations and $n = 12$ and beyond for anions) because of the lowering of the 6S orbital due to relativistic effect which enables more s-d hybridization and larger number of metal-metal bonds leading to planar structure. Generally, it takes a larger number of atoms to create metallic bodings to take over.

11.3.2.5 Mixed coinage metal nanoclusters

While silver prefers 3D structure and Au prefers planar structure, alloys of Au and Ag have not been studied so much. For dimers, the CCS of $Au–Ag^+$, is much larger than the average of Ag_2^+ and Au_2^+. Similar trend is observed for $Au–Cu^+$ but not for $Ag–Cu^+$. This anomaly cannot be understood from the bond length rather can be realized from nonuniform charge distribution as Au–Ag and Au–Cu bonds are polar where Ag/Cu carries a larger portion of the charge. Considering this effect during CCS calculation, an exact match with the experimental CCS was found. Similar anomaly can also be understood for triangular $(AuAg)_3^+$ clusters. From the experimental CCS values, Ag_3Au^+ has a Y-shaped structure while the other $(AuAg)_4^+$ clusters are diamond-shaped. The pentamers mostly show a single isomer except $Ag_3Au_2^+$ which shows a bimodal arrival time distribution which is found to be trigonal bipyramidal and X-shape structure.[3]

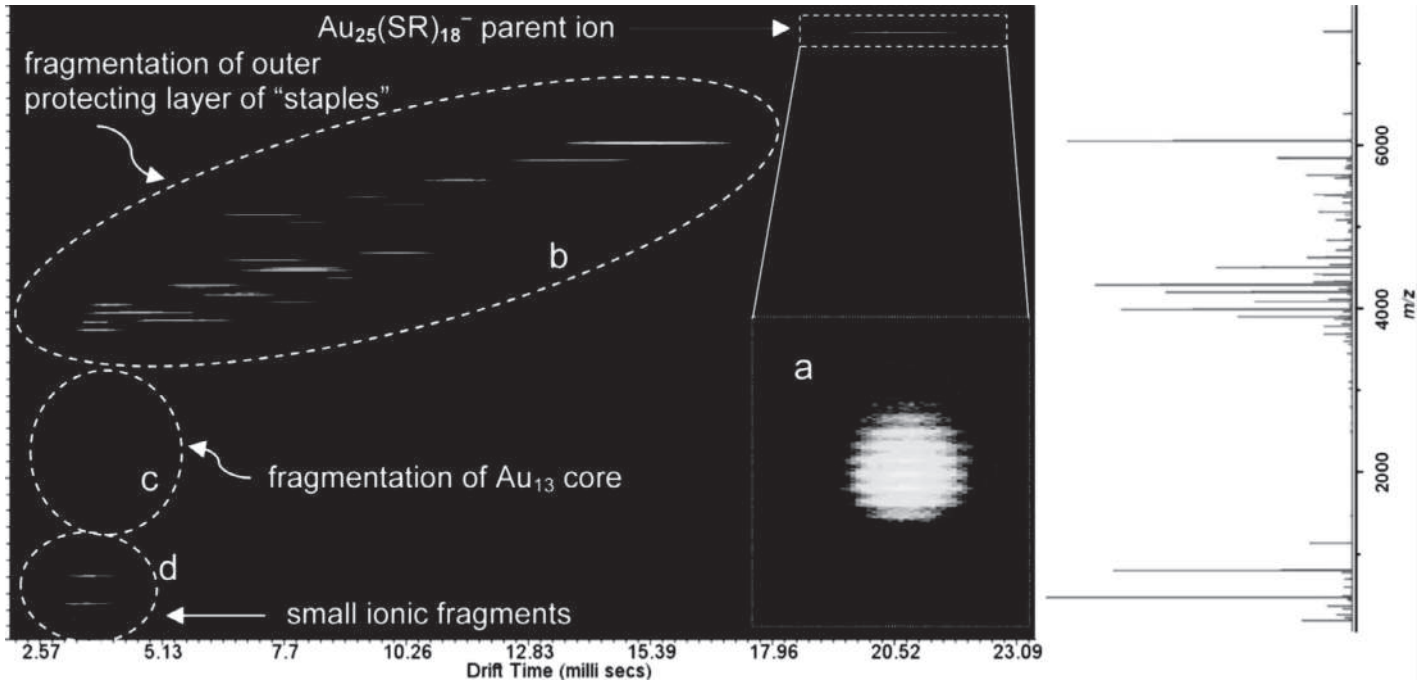

FIGURE 11.8 TWIMS of $Au_{25}(PET)_{18}^-$ showing a single isomer in the inset (A). The fragments (due to CID) were found to form eight different band shown in (B) which are due to fragmentation from the staple. Fragments from the Au_{13} core are in the region marked (C) and small anionic fragments are found in region (D). Reproduced with permission.[34]

11.3.3 IMS of protected nanoclusters

11.3.3.1 IMS of protected Au nanoclusters

Understanding structure of the bare cluster is tricky as they do not have any known crystal structure. This problem is solved to certain extent for the protected nanoclusters as many such clusters have known crystal structure. However, with growing interest in the structure and reactivity of the protected clusters, it is becoming more important to know their solution and gas phase structure along with their condensed phase geometry. In many cases, these two differ significantly. In the following, the use of IMS in the context of structure, dynamics of individual clusters, and during reaction will be explained.

The first reported IMS of monolayer protected cluster was on $Au_{25}(PET)_{18}^-$ cluster by Ackerson and group where the cluster was fragmented and the fragments from the core and the staple aligned in different regions which enabled to differentiate between such fragments (from Au_{13} core and $Au_{12}PET_{18}$ shell). They also found presence of only one isomer of $Au_{25}(PET)_{18}^-$ from the experimental condition.[34]

11.3.3.1.1 Isomeric clusters via core conversion

Recently, Hakkinen and coworkers predicted from theory that if the Au_{13} core of the $Au_{25}(PET)_{18}^-$ is rotated, it could generate a topologically connected isomer that is connected to the known crystal structure by a low-barrier collective rotation of the icosahedral Au_{13} core as shown in Fig. 11.9A.[35] This conversion does not affect the Au-S staple structures but shows a completely different optical absorption feature compared to the known crystal structure. They also predicted from CCS calculation that these two isomers will be very different in their CCS and could be separated by IMS study. Later they found experimentally by drift tube IMS measurement that this is indeed true. The topological isomer has a much larger CCS (581 $Å^2$ compared to 454 $Å^2$ for the isomers of known crystal structure), as shown in Fig. 11.9B. The core conversion can also be done manually by activating the clusters in-source.[36]

11.3.3.1.2 Isomeric clusters via charge heterogeneity

Isomerism evolved due to charge distribution when $Au_{25}(MBA)_{18}$ cluster was studied using IMS. In this study, Chirot and coworkers used a custom-built drift tube IMS-IMS-MS set up to study how the charge is distributed in the ligands and the core.[37] They used o-, m-, and p-MBA to confirm their findings. Due to –COOH groups in MBA, there are several charged species (-3 to -7) seen in the mass spectrum. For higher charge (-7) in both m- and p-, the core did not possess any charge and is entirely distributed on the ligands. However, the scenario changes as they went from -7 toward -3 charge state where the core possess -1 (77.5% for o-, 96% for m- and 90% for p-) with about 14.5% o- had -2 charge on the core. From the high-resolution arrival time distribution of $Au_{25}(m\text{-}MBA)_{18}^{5-}$ shown in Fig. 11.10, clearly three peaks are observable. Extracted mass spectrum from each of these regions surprisingly resulted into different species where x is the net charge possessed by the core and the rest is due to deprotonation of the –COOH groups. They also found that the population of x can be changed by collisional activation of the clusters where $Au_{25}(o\text{-}MBA)_{18}^{5-}$ tends to possess +1 charge in the core, $Au_{25}(m\text{-}MBA)_{18}^{5-}$ and $Au_{25}(p\text{-}MBA)_{18}^{5-}$ had 0 and −1, respectively, at higher collision voltage.

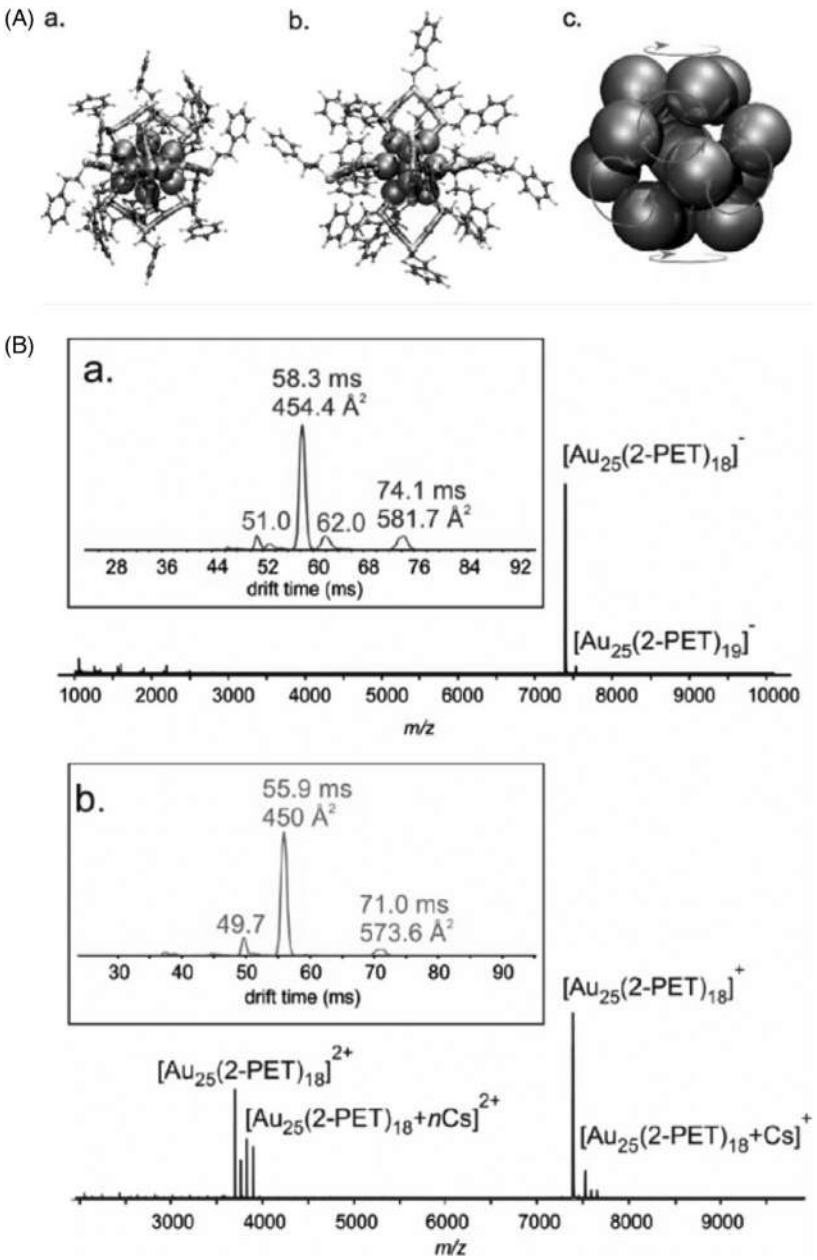

FIGURE 11.9 (A) Representation of the crystal structure (major isomer) and DFT optimized minor isomer in a and b, respectively. The Au_{13} core conversion is shown in c. (B) Drift tube IMS of $Au_{25}(PET)_{18}^-$ and $Au_{25}(PET)_{18}^+$ is shown in a and b, respectively. For $Au_{25}(PET)_{18}^-$, the major isomer corresponding to the crystal structure is found at 58.3 ms with experimental CCS of 454.4 Å^2 and the minor isomer is found at 74.1 ms with CCS 581.7 Å^2. For $Au_{25}(PET)_{18}^+$, the major and minor isomers were found at 55.9 and 71.0 ms, respectively.[36] Reproduced with permission.[36] See for further details https://pubs.acs.org/doi/10.1021/jacs.0c11509 and further permissions related to the material excerpted should be directed to the ACS.

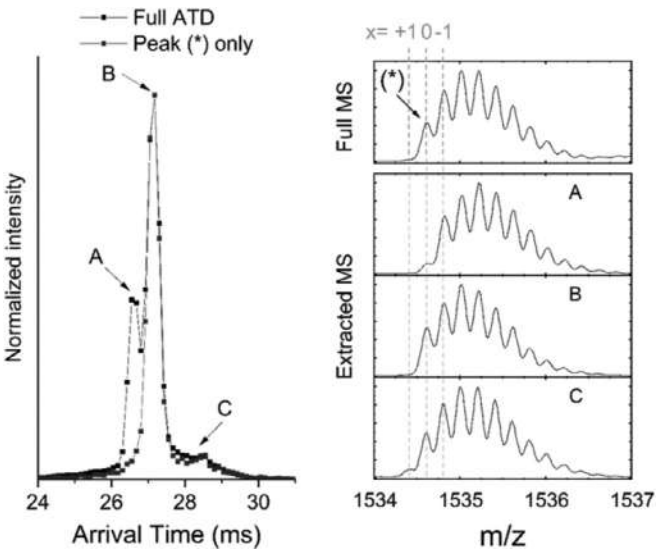

FIGURE 11.10 High resolution DT-IMS of $Au_{25}(m\text{-}MBA)_{18}^{5-}$ showing three peaks in the arrival time distribution. The extracted mass spectra from the region A, B, and C correspond to the different isotope pattern due to charge heterogeneity in the core and the ligands. Reproduced with permission.[37]

11.3.3.2 IMS of protected Ag nanoclusters

11.3.3.2.1 Isomeric clusters via ligand rearrangement

The first observation of isomerism in Ag clusters was found for $Ag_{11}(SG)_7^{3-}$ nanoclusters.[38] This cluster has a Ag_7 core and one $Ag_2(SG)_3$ and 2 $Ag(SG)_2$ units in the staple.[39] When this cluster was analyzed with TWIMS, it showed two clear peaks at 4.7 and 5.6 ms, respectively. The population of these two peaks vary slightly with different number of Na attached to the ligands as shown in Fig. 11.11B. For $Ag_{11}(SG)_7Na_3^{3-}$, the highest intense peak is 83% populated while for $Ag_{11}(SG)_7Na_4^{3-}$, it is 87% populated. From the DFT optimized structure, the cluster has flexible staples that can rearrange in another isomeric form (slightly higher energy isomer), as the activation barrier is rather small. But due to this different orientation of the ligand layer, the size change is considerable and hence the coexistence of the isomers can be justified. Other factors, such as hydrogen bonding, Coulomb repulsion between two adjacent clusters may also give rise to isomerism. DT-IMS of small glutathione-protected clusters ($Au_{10\text{-}12}SG_{10\text{-}12}$) showed a rather catenane type of structure in opposed to the core-shell structure of $Ag_{11}(SG)_7$ cluster.[40]

Another example of ligand rearrangement was observed for a well-studied $Ag_{44}(SR)_{30}$ clusters.[41] In the condense phase, all the ligands are somehow fixed and they cannot have lot of dynamics unlike in solution and in gas phase. This cluster does not show any isomerism in the condensed phase (as seen from the respective crystal structure). However, the cluster when studied using TWIMS showed different number of isomers depending on the protecting ligand or charge state. For example, $Ag_{44}(4\text{-}FTP)_{30}^{4-}$ showed four isomers with 33%, 7%, 12%, and 48% population, the same cluster at 3-charge state had only two isomers with 16% and 84% population. With other protecting agents like $Ag_{44}(SPhF_2)_{30}^{4-}$, only two isomers with 71% and 29% population were observed. For the MBA-protected clusters, $Ag_{44}(p\text{-}MBA)_{30}^{4-}$ and $Ag_{44}(p\text{-}MBA)_{30}^{3-}$ showed 3 and 5 isomers, respectively (Figs 11.12–11.18).

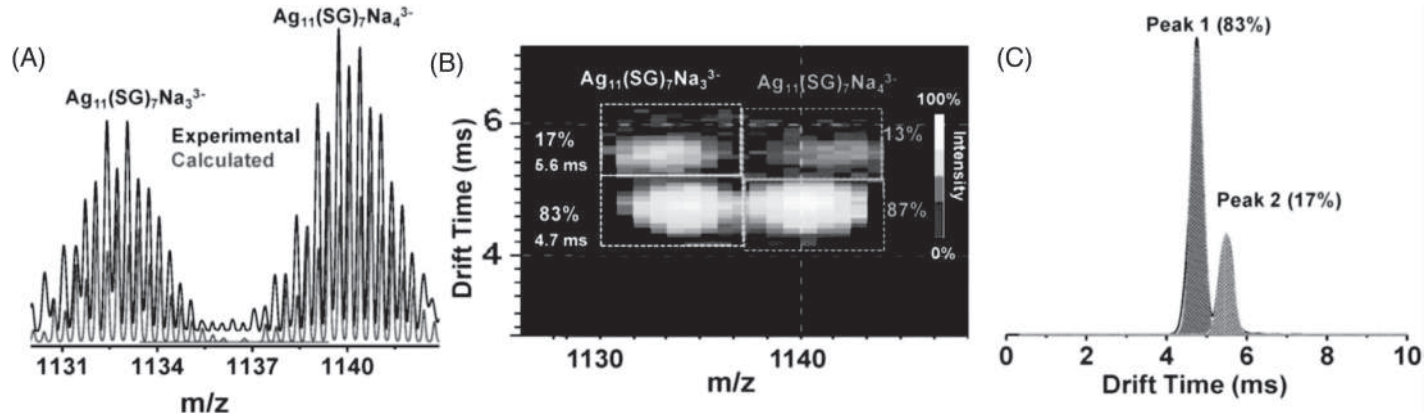

FIGURE 11.11 (A) ESI–IM–MS of $Ag_{11}(SG)_7$ showing 3- charged ion with three and four Na attachments. Extracted ion mobility drift time versus m/z shown in (B) confirms the presence of two isomeric species. Drift profile of $Ag_{11}(SG)_7Na_3^{3-}$ is shown in (C) showing two peaks with varying population calculated from the area under the curve. Reproduced with permission.[38]

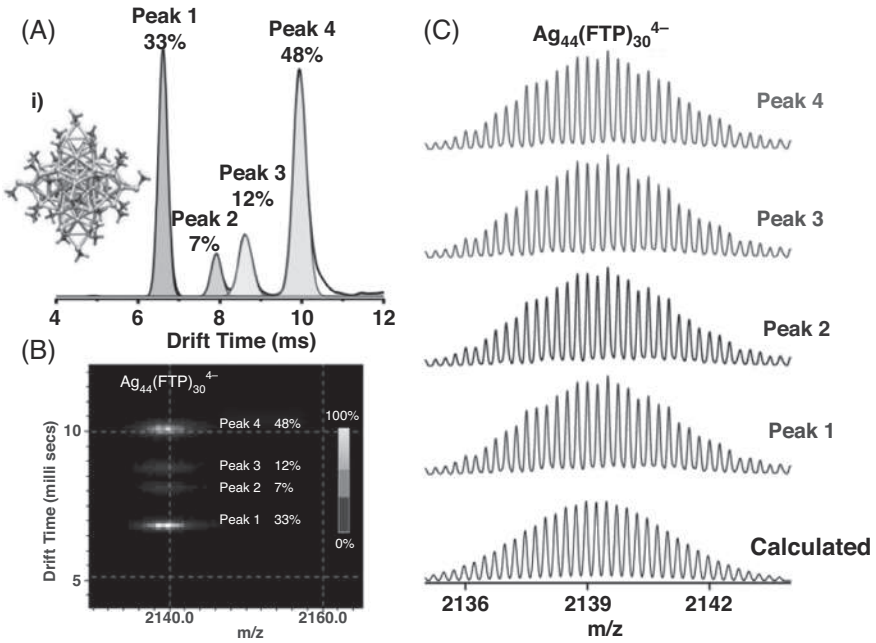

FIGURE 11.12 (A) Drift time distribution of $Ag_{44}(FTP)_{30}^{4-}$ showing four isomeric peaks with relative abundances of 33%, 7%, 12%, and 48%, respectively (calculated from area under the peak). (B) Four well-defined spots observed in 2D contour plot. Extracted mass spectrum from each of the four peaks is exactly same confirming the isomers. Reproduced with permission.[41]

Even the solvation medium affects the number of isomers as seen for $Ag_{44}(4\text{-FTP})_{30}^{4-}$ when electrosprayed from DCM, DMF, and ACN. In DCM, four isomers were found, while in both DMF and ACN only two isomers were seen. This anomaly can be understood from the different viscosity and surface tension of the spraying solvent which lead to different degree of deformity in the clusters in the gas phase and hence they show different number of isomers. To understand the origin of isomerism in this case, staple opening was predicted. Looking closely to the staple structure of the cluster, it consists of 6 $Ag_2(SR)_5$ units wherein one SR is bridged to two Ag and is not directly bonded to any of the core atoms (intermediate 20 dodecahedron shell). Considering no core rearrangement possible, if one or two such bridging ligands are opened, it does not affect the overall structure but will result in 4 isomers, namely, intact (without any SR opening), one SR opened, and cis and trans SR opened in 2 SR opened case.

11.3.3.3 Cluster dimers

The ligand dynamics in solution and gas phase may give rise to another situation where two or more adjacent clusters come close to each other and they form dimers, trimmers, or higher oligomers. In most of the cases, due to mass spectrometric parameters used, such oligomers may dissociate into monomeric units without being detected. This is true for widely studied $Au_{25}(SR)_{18}$ cluster, where no dimers or higher oligomers were seen in regular

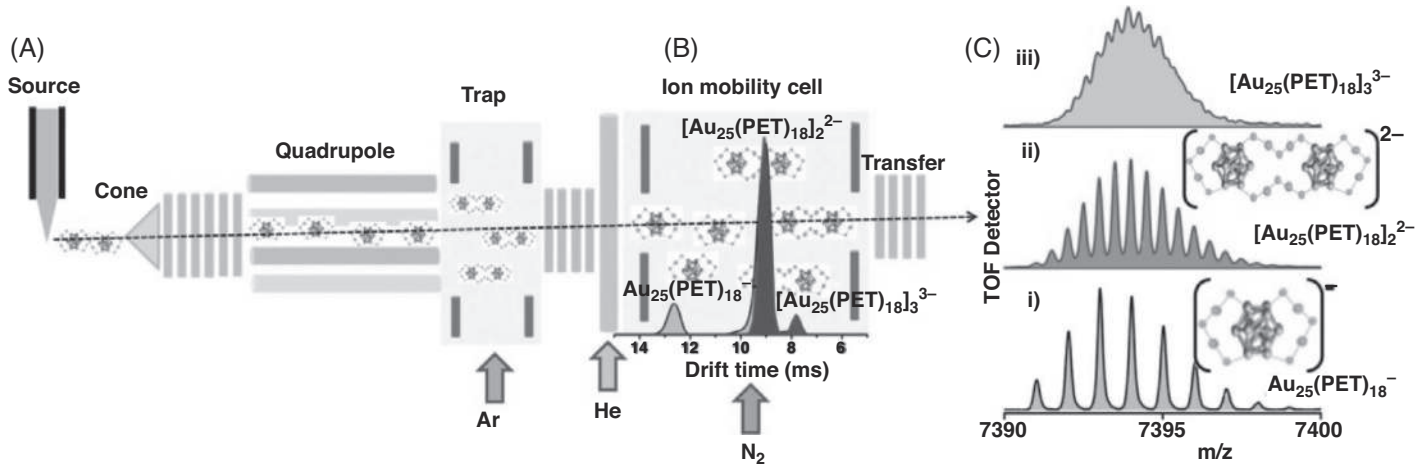

FIGURE 11.13 (A) Schematic representation of the experimental set up to find the cluster oligomers. The monomer (1-), dimer (2-), and trimer (3-) being the same mass are difficult to identify by regular mass are well separated when passed through the TWIMS cell as shown in (B). Extracted mass from the highest to lowest drift time is shown in i) to iii) in (C) which clearly show the presence of monomer, dimer and trimer. Reproduced with permission.[42]

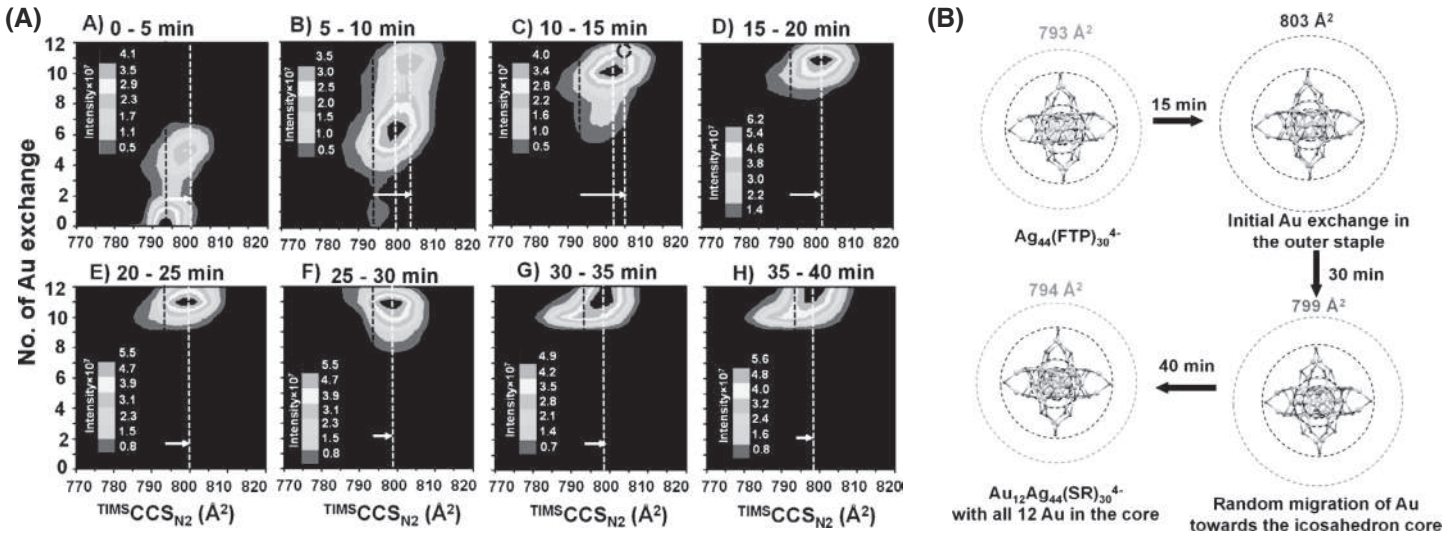

FIGURE 11.14 (A) Contour plot of time dependent CCS change of $Au_xAg_{44-x}(FTP)_{30}^{4-}$ ($x = 0$–12). The CCS increases with each Au exchange and after 12 Au exchange the reaction stops (15–20 min). Then the product $Au_{12}Ag_{32}(FTP)_{30}^{4-}$ starts rearranging and the size decreases until reaches the reactant $Ag_{44}(FTP)_{30}^{4-}$. The mechanism is schematically explained in (B). Reproduced with permission.[43]

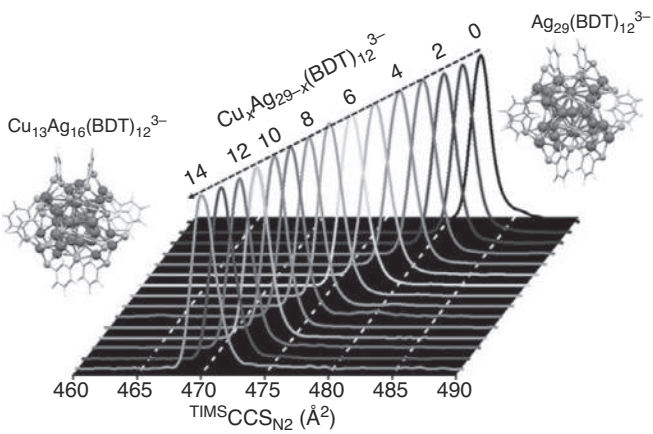

FIGURE 11.15 CCS of $Cu_xAg_{29-x}(BDT)_{12}^{3-}$ ($x = 0$–14) decreases lineally with each Cu exchange. DFT optimized structure of $Ag_{29}(BDT)_{12}^{3-}$ and $Cu_{13}Ag_{16}BDT)_{12}^{3-}$ are shown alongside the plot. Reproduced with permission.[44]

mass spectrometric conditions. However, when the same cluster was passed through ion mobility cell after careful adjustment of several parameters, cluster dimer, trimmers were easily observable. The ratio of $Au_{25}(SR)_{18}$ monomer (1-): dimer (2-): trimer (3-) can easily be tuned by tuning the trap gas flow and He flow (curtain gas to reduce excess heating of the ions before entering the IMS cell). It is even possible to see only dimers and trimers without monomers which can then be dissociated to monomers by CID. The data suggests that such oligomers are indeed present but are probably weakly bound and can be missed in presence of extra potential.

When $Au_{25}(SR)_{18}$ was ligand exchanged with a few dodecanethiol (DDT) to form $Au_{25}(PET)_{18-x}(DDT)_x$ ($x = 0$–3), six mixed dimers and nine mixed trimmers formed. Mixed tetramers were also observed, although, at much lower population. Ligand exchange with DDT facilitated inter-digitization of the long-chain alkane and leading to the formation of stronger dimers. To understand the structure of the dimers, longer Au–SR chain was considered which is known to be present in Au-thiolates. The stronger aurophilic interaction can also result in dimer formation. Similar assembly is also seen in the condensed phase in the context of linear polymers of $Au_{25}(SBu)_{18}$.

11.3.3.4 Structural change during reaction

IMS is a powerful tool to understand the reaction mechanism by following associated structural changes, although such studies are limited. Baksi et al. have studied inter-cluster reaction between $Ag_{44}(FTP)_{30}^{4-}$ and $Au_{25}(SR)_{18}^{-}$ using TIMS and monitored the size change of the reactant and the products over a 40 min time scale.[43] As Ag and Au are isomorphous, also their comparable bond length and bond angle with the thiolates makes it difficult to follow such reaction without high-resolution IMS instrument. In this study, a resolution over 160 was achieved which was sufficient to notice minor structural changes. From previous studies, it was known that such reaction lead to $Au_{12}Ag_{32}(SR)_{30}^{4-}$ formation where 12 Au atoms occupy the central icosahedron position. However, considering the cluster structure the Ag_{12} core is protected with a 20 atom dodecahedron shell and $Ag_{12}(SR)_{30}$ staple. Therefore, direct exchange of Ag/Au in the core is not possible. From the time-dependent study, the CCS of the parent

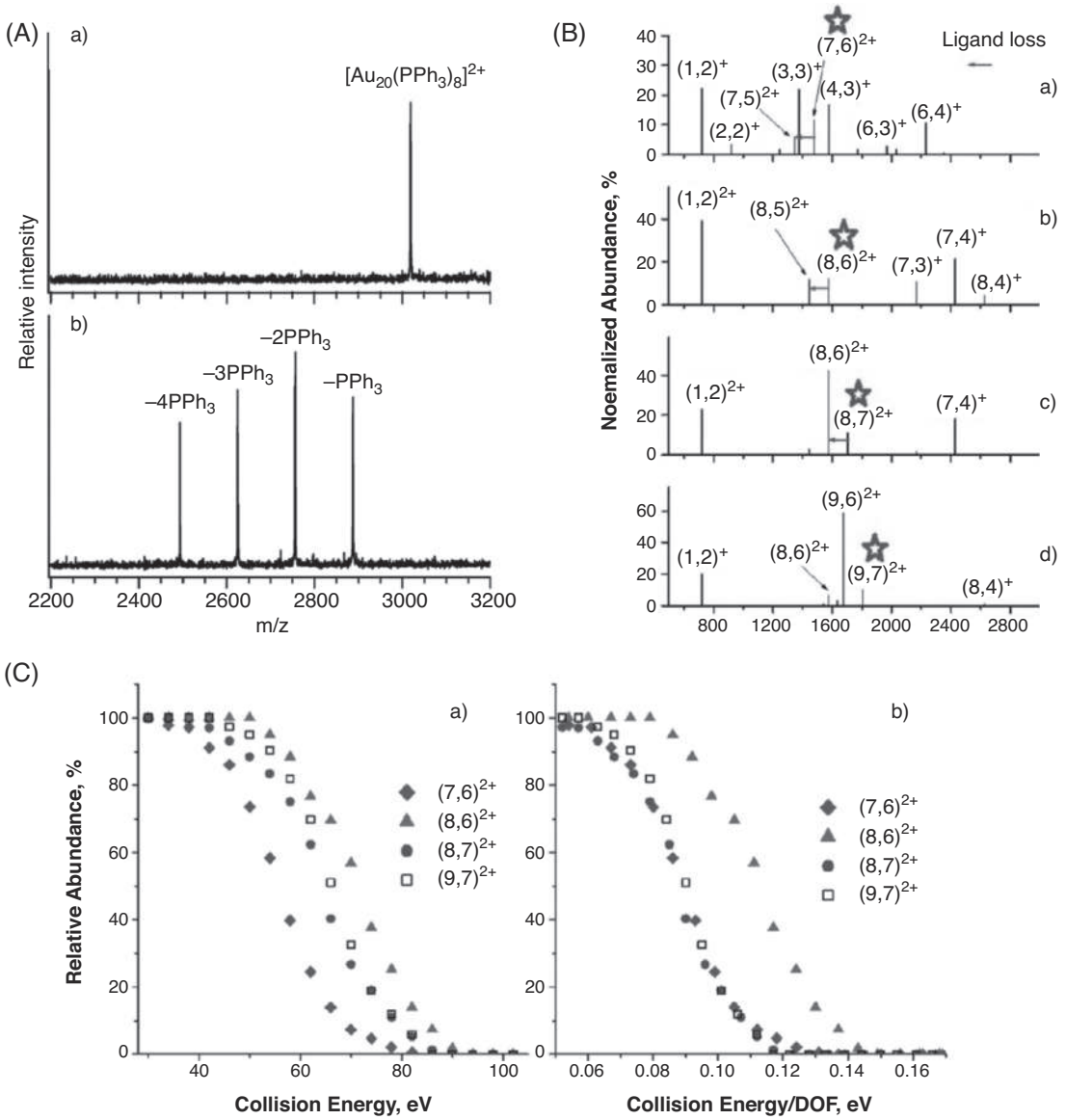

FIGURE 11.16 (A) (a) ESI and (b) CID mass spectra of $[Au_{20}(PPh_3)_8]^{2+}$ showing successive ligand loss (90% fragmentation) when collided with benzene at an average collision energy of ~0.64 eV.[49] (B) Representative positive-mode FT-ICR-MS mass spectra of SID fragments for (a) $[Au_7(PPh_3)_6]^{2+}$ (b) $[Au_8(PPh_3)_6]^{2+}$, (c) $[Au_8(PPh_3)_7]^{2+}$, and (d) $[Au_9(PPh_3)_7]^{2+}$ The red arrows indicate loss of neutral PPh_3.[50] (C) Survival curves plotted as a function of (a) collision energy and (b) collision energy per vibrational degree of freedom obtained for mass-selected clusters shown in B.[50] Reproduced with permission[49,50]

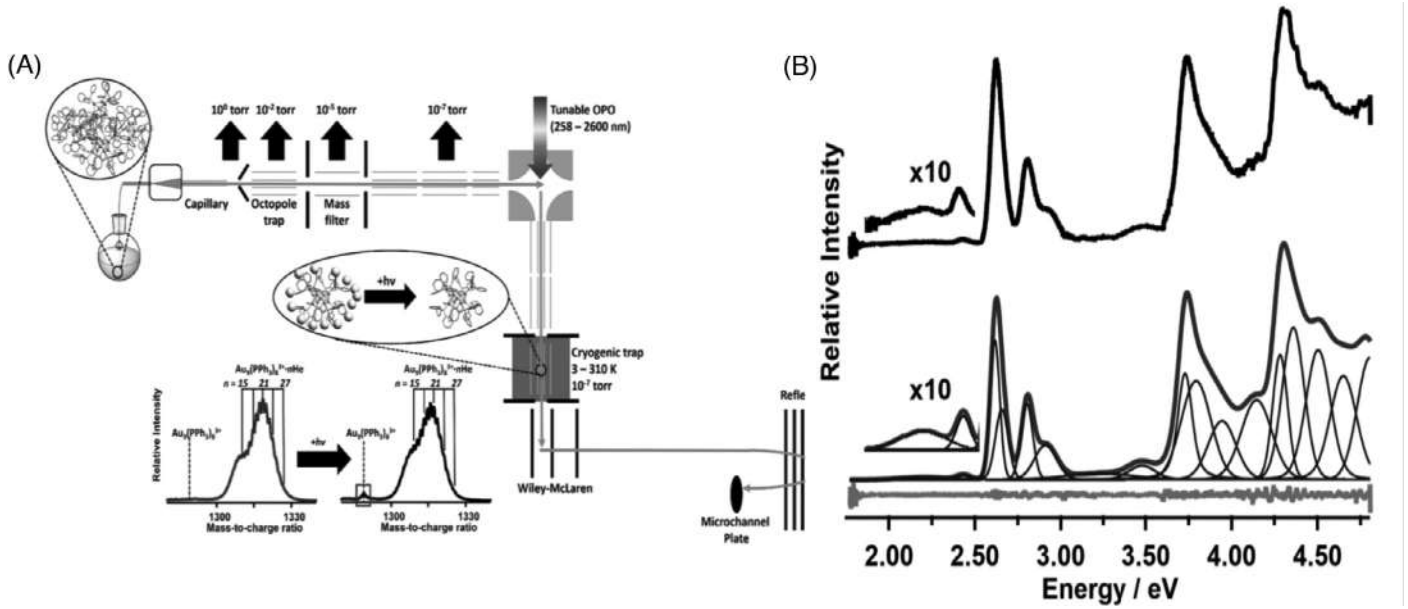

FIGURE 11.17 (A) Schematic diagram of the mass-selective photofragmentation spectrometer with tunable laser source and cryogenic trap. (B) Measured mass-selective UV/vis spectrum of He-tagged $Au_6(PPh_3)_6^{2+}$ (top) and the cluster's fitted UV/vis spectrum (bottom) using a linear combination of 17 Voigt bands. Reproduced with permission.[59b]

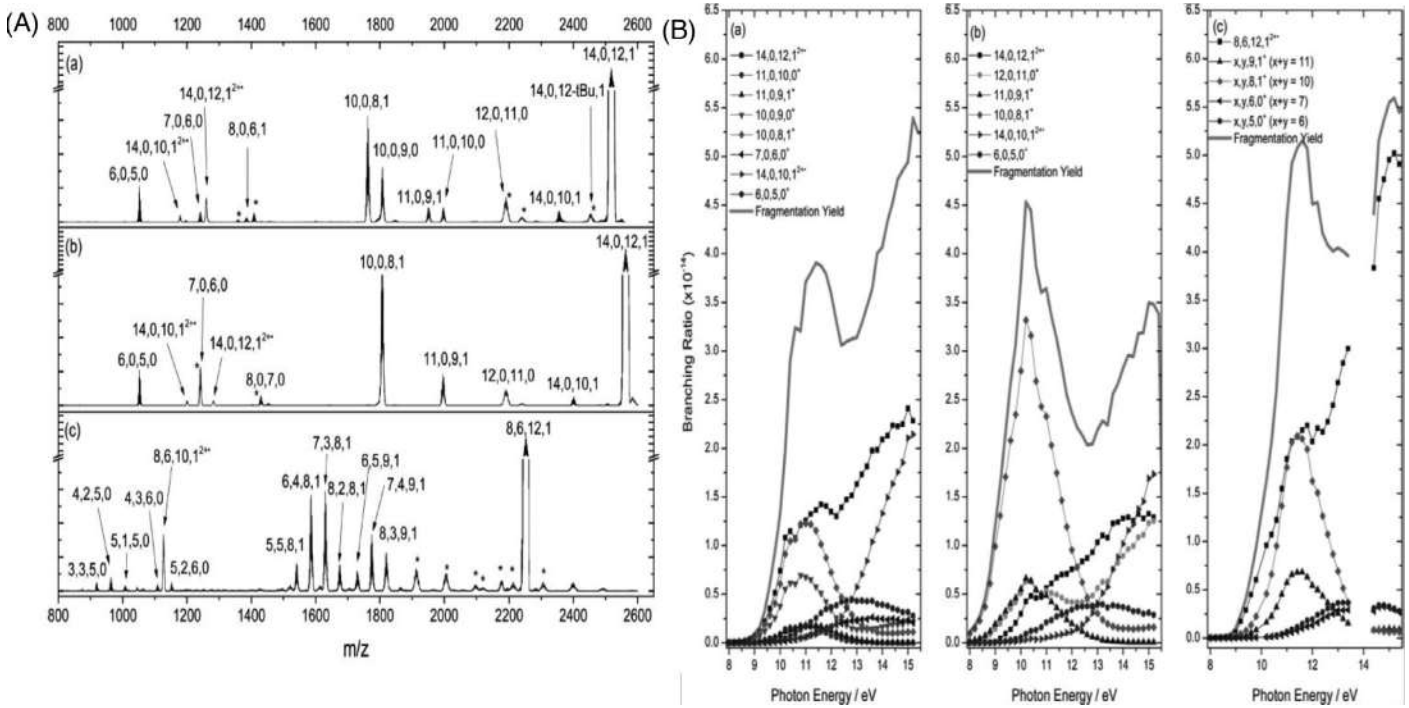

FIGURE 11.18 (A) Tandem mass spectrometry (MS/MS) (a) $[Ag_{14}(C{\equiv}CtBu)_{12}Cl]^+$ b) $[Ag_{14}(C{\equiv}CtBu)_{12}Br]^+$ and $[Ag_8Cu_6(C{\equiv}CtBu)_{12}Cl]^+$ which were irradiated at 11 eV for a period of 200 ms. (B) Product ion yields as a function of the VUV irradiation energy, which was varied from 8 to 15.5 eV. Reproduced with permission.[62]

cluster increases with time and 12 Au exchange is complete within around 15–20 min. At this stage the size increases from 793 to 803 Å^2. After that, the reaction is stopped and the Au atoms moves toward the core in a nanogymnastic fashion via a randomly distributed structure where Au atoms occupy all three layers and the size decreases to 799 Å^2. At about 40 min, all the 12 Au atoms occupy the center position and the size do not change any further. The final size of $Au_{12}Ag_{32}(SR)_{30}^{4-}$ is 794 Å^2 which is identical with $Ag_{44}(FTP)_{30}^{4-}$ (794 Å^2) as the interacting N_2 molecules do not see the core atoms whether they are Au or Ag the size remained same. The mechanism was established by calculating the CCS of the total structure keeping all the ligands and considering three isomers of $Au_{12}Ag_{32}(SR)_{30}^{4-}$ (in outer staple, statistically distributed and in the core).

Such rearrangement of the atoms may not occur always. In specific cases, the exchanged heteroatoms may occupy the initially exchanged outer shell position without moving toward the core (no nanogymnastic). This was observed when reaction of $Ag_{29}(BDT)_{12}^{3-}$ was reacted with $Cu_{12}S_6(DPPPT)_4$ (DPPPT = bis-(diphenylphosphino)pentane) cluster.[44] About 50% of the Ag atoms got exchanged with Cu. Surprisingly with each Cu exchange the size of the cluster $Cu_xAg_{29-x}(BDT)_{12}^{3-}$ ($x = 0$–14) decreases linearly from 482.6 to 469.9 Å^2 with 0.9 Å^2 decrease per Ag/Cu exchange. There are three different types of Ag atoms present in $Ag_{29}(BDT)_{12}^{3-}$ which lead to four isomers when a single Ag is exchanged with Cu. After calculating the CCS of all four isomers and comparing with the experimental data, the Cu atoms were found to be on the outer staple. Similarly, for 2 Cu exchanges, 19 isomers were considered among which again outer shell occupancy of the Cu atoms are both energetically favorable as well as in best agreement with the experiment. For 3 and 4 Cu exchanges, 6 isomers for each were considered which also follow the outer Cu occupancy from the experimental data. For $Cu_{13}Ag_{16}(BDT)_{12}^{3-}$, among 11 possible isomers, the one with all 12 Cu occupying the staple and one occupying the free Ag position (attached to PPh_3) was found to be the best match although this isomer was not the lowest energy isomer but the second-lowest with 0.14 eV higher in energy which is considerably small considering the size of the cluster.

11.4 Dissociation mass spectrometry

Most common way to gain structural information from mass spectrometry is to use activation methods to induce fragmentation of the desired cluster ion. Most of the commercial mass spectrometers are equipped with CID where the cluster ions are activated via collision with kinetically energized gas molecules (mostly N_2, Ar, or other rare gases). Such ions can also be dissociated on surface and the process is known as surface-induced dissociation (SID). Multiply charged cluster ions have the possibility to dissociate via electron capture or by electron-induced dissociation. When laser-based activation sources are used the process is called photo dissociation (PD). The ions undergo dissociation via the electronically excited state upon photoabsorption of UV-vis light. A unique feature of PD-MS is that the energy deposited on the clusters is tuned precisely and can be larger than that by CID. As a result, the PD with the UV light results in richer fragmentation patterns compared to those by the CID method. In SID-MS, Au/Ag MPCs are allowed to collide with the solid surface. It is demonstrated that ~10% of the collisional energy can be deposited into a projectile by collision

with a solid surface on a timescale of femtoseconds, collision with the surface can impart much larger energy than that by PD and CID and promote further fragmentation.

11.4.1 Dissociation of bare cluster ions

Gold cluster cations Au_n^+ ($2 \leq n \leq 23$) when collided with rare gases, they undergo dissociation by single Au atom loss.[45] Two atoms loss occurs mostly occur through the loss of dimer rather than sequential dissociation. The following are the mostly observed fragmentation pathway for both cationic and anionic clusters.[46]

$$(Au_n)^z \rightarrow (Au_{n-1})^z + Au$$

$$(Au_n)^z \rightarrow (Au_{n-2})^z + Au_2$$

$$(Au_n)^z \rightarrow (Au_n)^{z+1} + e^-$$

The minimum kinetic energy of clusters required to induce dissociation exhibit a pronounced odd–even effect. Clusters with an even number of delocalized electrons are more stable than those with an odd number. For Au_n^+ ($13 \leq n \leq 23$), monomer loss is the main fragmentation channel suggesting that the binding energies of all the cluster cations lie above the dimer binding energy.[47] Using energy-resolved dissociation, the bond dissociation energies of small anionic gold clusters Au_n^- ($2 \leq n \leq 7$) could be estimated.[48] In all the cases, single Au atom loss was observed which is favored for odd electron anions and the extracted dissociation energy shows strong odd–even effect. In the following, several fragmentation methods used and the key observations from the studies are summarized, separately for cationic and anionic Au clusters. Similar observation was seen for silver clusters as well.

11.4.2 Dissociation of ligated cluster ions

CID and SID of ligated clusters is detailed in Chapter 10. Here a summary of the studies is given. PD of ligated clusters is detailed here. One of the early CID reported for ligated clusters was on phosphine-protected tetrahedral and un-coordinated $Au_{20}(PPh_3)_8^{2+}$ cluster by Wang et al. This cluster fragments via PPh_3 loss.[49]

Compared to CID, core fission was not observed. Unlike to CID, SID of multiply charged phosphine protected Au clusters $[Au_7(PR_3)_6]^{2+}$, $[Au_8(PR_3)_6]^{2+}$, $[Au_8(PR_3)_7]^{2+}$, and $[Au_9(PR_3)_7]^{2+}$ were in strong contrast where the parent cluster ion underwent fission rather than only neutral PPR_3 loss as seen in CID.[49]

$$\left[Au_7(PR_3)_6\right]^{2+} \rightarrow \left[Au_6(PR_3)_4\right]^{+} + \left[Au_1(PR_3)_2\right]^{+}$$

Bordbelt and group have studied SID of phosphine-protected clusters in details. They compared the size and ligand-dependent stability of $Au_x(PPh_3)_y^{2+}$ ($x = 7, 8, 9$; $y = 6, 7$) and found that in all cases, along with neutral ligand loss, fission occurs. They have also calculated the stability with respect to collision energy and found that $Au_8(PPh_6)_y^{2+}$ is the most stable one among the examined species.[50]

Multiply charged clusters provide the opportunity to study fragmentation via electron loss/capture channel.[50,51] Three types of reaction channel was seen for DPPM protected Au clusters as follows:

$[Au_xL_y]^{n+} + e^- \rightarrow [Au_xL_y]^{(n-1)+}$ …….. charge reduction
$[Au_xL_y]^{n+} + e^- \rightarrow [Au_xL_{y-1}]^{(n-1)+} + L$ ……..charge reduction and ligand loss
$[Au_xL_y]^{n+} + e^- \rightarrow [Au_xL_{y\text{-}1}\ (CH_2PPh_2)]^{(n-1)+} + Ph_2P^+$ …….. charge reduction and ligand activation.

Interesting observation was recorded when hydride-rich $Ag_{18}H_{16}(PPh_3)_{10}^{2+}$ was fragmented by CID. Along with PPh_3 loss, sequential H_2 loss was also observed leading to $Ag_{17}H_{14}^+$ and Ag_{17}^+ cluster. Similar observation was found for other phosphine protected clusters.[30]

Fragmentation pattern of the thiolate protected clusters are different where along with thiolate ligand loss, M_xL_y fragments are also seen.[52] In general, Au clusters fragment via $Au_4(SR)_4$ loss as seen both by CID as well as by laser activation during MALDI MS measurement.[53] For example, first fragmentation of $Au_{25}(SR)_{18}^-$ ($8e^-$) is always by loss of neutral $Au_4(SR)_4$ ring and the fragment ion $Au_{21}(SR)_{14}^-$ still retains the $8e^-$.[54] With higher CE, another $Au_4(SR)_4$ loss was also observed. Calculation predicts that $Au_{25}(SR)_{18}^- \rightarrow Au_{21}(SR)_{14}^- + Au_4(SR)_4$ is exothermic only by 0.82 eV and the product undergoes complex structural rearrangement. In contrast to $Au_{25}(SR)_{18}^-$, analogous $Ag_{25}(SR)_{18}^-$ fragments via $Ag_3(SR)_3$ loss. In general, all silver clusters fragments via $Ag_1(SR)_2$, $Ag_2(SR)_3$, $Ag_3(SR)_3$, $Ag_5(SR)_6$, or $Ag_3(S_2R)_3$ loss.[55] SID of $Ag_{11}(SG)_7^{3-}$ was distinctly different than CID. When collided on fluorocarbon coated Au surface, $Ag_{11}(SG)_7^{3-}$ underwent charge stripping and formed $Ag_{11}(SG)_7^{2-}$ and $Ag_{11}(SG)_7^-$.[38,39] See Chapter 10 for CID and SID of thiolate protected clusters in detail.

11.5 Spectroscopic methods

Several spectroscopic methods have been employed to understand structure of gas-phase cluster ions. In some cases, interaction with laser causes fragmentation and the process is called PD. As much higher and more precise energy can be provided for the fragmentation, PD generally results into richer fragmentation pattern compared to other dissociation process. Several groups have tried to understand gas phase absorption and emission spectroscopy of the cluster ions in custom-built instruments which includes UV-vis spectroscopy, IR spectroscopy, Photoelectron spectroscopy (PES) to name a few. In the following, each of these techniques are mentioned in the context of bare and protected clusters.

11.5.1 Photo-dissociation (PD) and UV-vis spectroscopy

Fragmentation pattern and the key observation from PD of bare gold and silver cluster ions are tabled in Section 8.3. Here PD of ligated clusters are shown. Brodbelt and Whetten reported the first ultra-violet PD (UVPD) of AU_{25}(p-MBA)$_{18}$ and Au_{36}(p-MBA)$_{24}$ cluster using 193 nm laser.[56] The richer fragmentation pattern obtained just by single pulse of 193 nm resulted in Au-S and C-S bond cleavage. Initial fragmentation occurred via ammonia loss while at multipulse process, partly the ligand layer was removed via C-S bond cleavage. Lower number of laser pulses resulted primarily in fragmentation pathways that led to near complete removal of the protecting monolayer but retained the total number of gold atoms resulting in $Au_{25}S_{12}$ formation. Monomer evaporation was also observed (like bare clusters) at high number of laser pulse resulting in Au_4-Au_{20} species. These types of fragmentation

point toward a much larger photon absorption cross-section of the noble metal nanoclusters compared to biomolecules.

Among the ligand-protected clusters, early PD experiments were performed with phosphine-protected gold clusters.[57] Johnson and coworkers performed cryogenic absorption spectroscopy of $[Au_9(PR_3)_9]^{3+}$ and tagged the ions with He and N_2.[58] Interestingly, such tagging freezes the internal motion of the Au_8 core. The tags can be removed completely when UV laser radiation is absorbed. The action spectroscopy resulted in absorption spectra of the ion showed sharp signals due to diminishing thermal broadening effect and the spectra could be directly compared with the calculated absorption pattern. In a different study with $[Au_9(PPh_3)_9]^{3+}$, the group studied the effect of surface hydride, chloride, and bromide and found that these anions have similar effect on the absorption spectra and hence behave as either metallic or ligand like.[57,59]

While gas phase UV-vis absorption spectra of base clusters have been reported 20 years ago for Au_n (n = 7, 9, 11, 13) and Au_n^+ (n= 6–13), very little structural information was obtained. The authors reported odd-even effect and only Au_{13} data confirmed the icosahedron structure.[60] First gas phase UV-vis absorption spectrum of $Au_{25}(SG)_{18}^-$ was reported by Dugourd and group.[61] They trapped $[Au_{25}(SG)_{18\text{-}6H}]^{7-}$ and excited the ions with 260 and 500 nm laser and studied the laser-induced dissociation. In contrast to CID, after photo-excitation the anions were relaxed by electron emission. Following electron detachment at variable wavelength they were able to produce the UV-vis absorption spectra of the ion in the gas phase which mostly resemble the absorption spectrum recorded in solution. In another study, Dogourd and O'Hair studied the structure and gas phase property of $[Ag_{14}(C{\equiv}CtBu)_{12}Cl]^+$ and $[Ag_8Cu_6(C{\equiv}CtBu)_{12}Cl]^+$ by IM, vacuum ultraviolet (VUV), and ultraviolet (UV) spectroscopy along with DFT calculations.[62] Combination of IM and DFT calculation confirms the cluster retains its condensed phase structure in the gas phase as well. The VUV exhibited richer fragmentation pattern as well as photoionization. They have examined the onset of ionization of these two clusters with Cl^- and Br^- and found that the templating anion does not have any effect. The vertical and adiabatic ionization energies also showed similar trend.

11.5.2 Photoelectron spectroscopy

11.5.2.1 Bare clusters

PES of bare clusters revealed several interesting feature in their PES. In the 1990s although several PES of bare clusters were reported due to poor resolution, enough structural information was not attained. Wang et al. worked extensively on the PES of the bare clusters.[7a] A schematic diagram of the instrumental setup is shown in Fig. 11.19A.[63] A laser vaporization source was used for the cluster generation with a Nd:YAG laser (532 nm). A tunable laser Nd:YAG Nd:YAG laser- 355 nm (3.496 eV) and 266 nm (4.661 eV), and a 193 nm (6.424 eV) from an ArF excimer laser was used for the photo-detachment experiments. For small clusters like Au_4^- a Y-shaped structure as predicted from DFT was the best match from the experiment. For n = 5, 6, 8, and 10, the lowest energy 2D structure was assigned as the major isomer for each case based on their simulated PES spectra.[64] For n = 7, 9, 11, and 13, satisfactory agreement between experimental and theoretical PES spectra was not achieved. The PES of Au_{12}^- showed evidence for the coexistence of multiple isomers, and a mixture of 3D and 2D structures was assigned, consistent with the IMS observation as discussed in Section 8.2. Beyond n = 14, 3D structures are seen in the experiment, although those are not the lowest

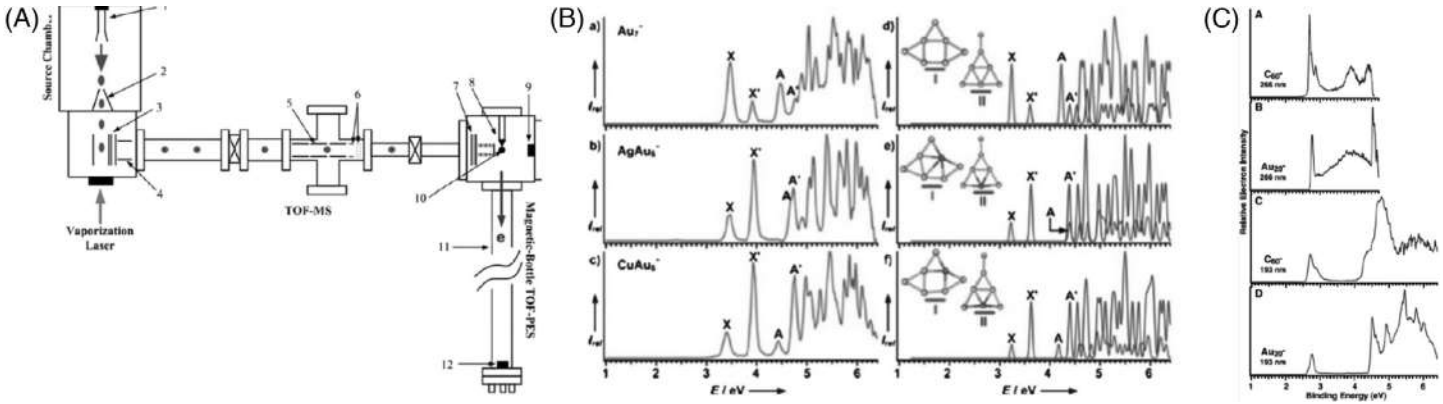

FIGURE 11.19 (A) Experimental setup with laser based cluster source and tunable laser for PES.[63] (B) PES of Au_{20}^- and C_{60}^- at 193 nm and 266 nm. (C) 193 nm photoelectron spectra of (a) Au_7^-, (b) $AgAu_6^-$, and (c) $CuAu_6^-$, compared with the simulated spectra for corresponding structures in (D–F), respectively.[7a] Reproduced from with permission.[63]

energy isomers. As discussed in Sections 8.1 and 8.2, the 2D to 3D transition occurs at n =12. Several isomers are possible for smaller clusters and in many cases, it is difficult to predict which isomer is experimentally observed. For example, Au_{10}^- PES shows strong anomaly compared to other even number clusters as it does not have any energy gap suggesting open shell structure.[64b] Along with the D3h symmetry a weak feature is observed at the lower binding energy suggesting a minor isomer. The peaks corresponding to the minor isomer was gradually titrated out in presence of small amount of O_2 in the carrier gas leaving clean signal corresponding to D3h isomer.[65]

When isoelectronic substitution was made on the MAu_n^- clusters (n = 7–15, M = Cu, Ag), the PES features did not change significantly.[66] But the clusters with multiple possible isomers showed change in the isomeric population on hetero-metal substitution. Comparative PES of Au_7^-, $AgAu_6^-$, and $CuAu_6^-$ is shown in Fig. 11.19C. From n = 7–15, isomeric structures were well resolved systematically with isoelectronic substitution. While Au_8^- has two isomers, Au_9^- has only one isomer. For Au_{10}^-, four isomeric structures were resolved from PES. For Au_{11}^-, the major species corresponds to C_S structure with minor contribution from D_{2h} isomer. The C_{2v} structure of Au_{13}^- was seen before in TIED and IMS study but the C_{3v} isomer with almost equal population was not reported before. Similarly only C_2 symmetry structure of Au_{14}^- was observed in PES although a second C_{2v} structure was seen in previous experiments. Major isomer for Au_{15}^- was found to be of C_{2v} symmetry with minor contribution of C_1 structure. All these structures (n = 13–15), have similar shell-like flat cage structure as grown from Au_{12}^- motif.

Cage to pyramid transition occurs in the range n = 16–19. The Au_{16}^- is highly symmetric cage with tetrahedral (T_d) as seen by PES.[67] The spectra is quite simple due to its high symmetry and have a high vertical detachment energy (VDE) and does not have any energy gap breaking the odd-even alteration observed in the size range. This is in agreement with open-shell structure with two unpaired electrons as discussed for Au_{10}^-. This high VDE can be explained in terms of electronic shell closing model as Au_{16}^- is just one electron less from being $18e^-$ ($1S^21P^61D^{10}$) which led to a perfect Td with 18 –electron Au_{16}^{2-}. Also, it was found that Au_{16}^{2-} has 3 16-center-2-electron (16c-2e) bonds occupied by 6 globally delocalized electrons giving rise to spherical aromaticity like fullerenes and is responsible for the unique hollow cage structure of Au_{16}^{2-} and Au_{16}^-. Both Au_{17}^- and Au_{18}^- evolved from this T_d structure with C_{2v} symmetry by adding one and two Au atoms on the top. Au_{16}^- –Au_{18}^- are the first example of golden cage which are experimentally confirmed by PES and TIED. Doping of heteroatoms in the Au_{16}^- cage with Cu, Ag, Zn, In all resulted in the central atom doping which did not distort the geometric and electronic structure significantly and hence their PES spectra were essentially similar with minor difference in the isomer intensity. Doping with magnetic elements like Fe, Co, Ni distorted the T_d structure but retain elemental magnetism.

For n > 18 like Au_{19}^- has only one isomer and Au_{20}^- is a golden cluster. PES revealed that Au_{20}^- has an extremely large energy gap even greater than that of C_{60}, and an electron affinity comparable with that of C_{60} suggesting that the Au_{20}^- should be highly stable and chemically inert. From DFT, Au_{20}^- possesses a T_d structure, which is a fragment of the FCC lattice of bulk gold with a small structural relaxation (Table 11.1). That's why Au_{20}^- is a unique cluster with atomic packing similar to that of bulk gold but with very different properties.[68]

From PES of Au_{21}^- to Au_{25}^-, Au_{21}^- showed dominant T_d based pyramidal structure as seen in Au_{20}^-.[69] For Au_{22}^- and Au_{23}^- a pyramidal and double-layer structures are found and

TABLE 11.1 Fragmentation pattern of Au cluster cations.

Cluster	*n*	Method	Observation
Au_n^+	2–23	CID	CID for $n \leq 15$ results in dimer loss. For $n > 15$ clusters fragment via monomer loss
Au_n^+	2–23	CID	Binding energy for the dissociation. Odd even effect, even number clusters are more stable
Au_n^{2+}	15	CID	Fragments into the complimentary ion pairs
Au_n^{2+}	12	CID	Fragmentation into the complimentary ions pairs
Au_n^{2+}	7–35	CID	Fission occurs for small clusters at $n \leq 15$ Larger clusters undergo gold atom evaporation
Au_n^{3+}	19–35	CID	Fission occurs for small clusters at $n \leq 25$ and larger clusters exhibit gold atom evaporation
Au_n^{2+}	7–35	CID	Odd–even effect disappears for $n < 11$
Au_n^{3+}	19–35	CID	The dissociation energy as a function of cluster size is smaller than Au_n^{2+}. No odd–even effect
Au_n^+	12–72	EID	Odd–even effects. For larger clusters magic numbers are observed
Au_n^+	3–23	PD	Undergo dimer evaporation
Au_n^+	9, 21	PD	Determination of dissociation energies
Au_n^+	7–15	PD	The energy dependence for monomer and dimer evaporation has been calculated for the size-selected clusters decay pathway
Au_n^+	2–27	PD	Au_9^+ shows anomalous behavior due to electron shell closing at $n = 8$
Au_n^+	14,16	PD	Determination of dissociation energies
Au_n^+	14–24	PD	Determination of dissociation energies
Au_n^+	9, 11, 13, 15	PD	Determination of dissociation energy via dimer evaporation
Au_n^+	17–21	PD	Excitation energies far above the clusters dissociation thresholds have been used to induce multisequential fragmentation by the evaporation of neutral monomers
Au_n^+	3–21	PD	Fragmentation pathways monitored as a function of cluster size
Au_n^+	5, 8, 12	PD	Isomers can be distinguished by their distinct decay rates
Au_n^+	30	PD	The determination of relative dissociation energies
Au_n^+	7–27	PD	The monomer-dimer branching ratios as a function of the excitation energy and dissociation energy were determined

a tubular structure was observed for Au_{24}^-. Interestingly, Au_{25}^- has a core-shell structure with a single atom core and 24 atom-shell suggesting a structural transition from tubular to core-shell geometry between n= 24 and 25. Au_{32} was predicted to be "a 24-carat-gold-fullerene" which is a highly stable icosahedral (I_h) symmetry like C_{60} but such high-symmetry hollow cage structure is unexpected for such cluster size.[70] From PES, it was found that this cluster

TABLE 11.2 Fragmentation of gold cluster anions.

Cluster	*n*	Method	Observation
Au_n^-	2–21	CID	Neutral monomer and dimer evaporation
Au_n^-	2–7	CID	Determination of dissociation energies
Au_n^{2-}	21–31	CID	Fragmentation via electron loss
Au_n^-	16–30	EID	Electron capture to form dianion with strong odd–even
Au_n^-		EID	Production of dianionic and trianionic clusters
Au_n^-	25	EID	Threshold for production of Au_{25}^{2-} is determined
Au_n^-	6,7	PD	Determination of dissociation energies
Au_n^-	7	PD	Using a green laser pointer shows decay into Au_6^- and Au_5^-
Au_n^{2-}	29	PD	Decay observed by PD
Au_n^{2-}	29	PD	Dissociation products determined
Au_n^-	14, 17	PD	Study of decay rates
Au_n^{2-}	35, 40, 45, 50	PD	Neutral loss and electron emmission
Au_n^-	11–40, 51–70	Low energy electrons	Production of dianions and trianions

possess a low-symmetry C_1 core-shell structure with a triangular three atom core (Table 11.2). The next shell closing electron structure is observed for 34-electron system, a neutral Au_{34} which has a very high HOMO-LUMO gap.[71] The anionic Au_{34}^- possess a chiral structure with C_3 symmetry. It has a core-shell structure with a four atom tetrahedral core as seen by PES. Nine well-resolved spectral features up to 5.5 eV were observed in PES which was reproduced very well in the simulation confirming unequivocally the C_1 global minimum structure. By attaching one atom to the surface of Au_{34}^- also has the C_1 structure.

The next Mackay icosahedron is with 55 atom and is expected to be highly symmetric but from all other experiments it was found that Au_{55}^- rather possess a low symmetry amorphous structure. PES of Cu_{55}^-, Ag_{55}^-, and Au_{55}^- revealed that both Ag_{55}^- and Cu_{55}^- have similar well-resolved peaks leading to high symmetry I_h structure while the same of Au_{55}^- was a broad peak with several fine structures confirming presence of several low symmetry structures due to relativistic effect. PES of M_n^- (M = Cu, Ag, Au and $n = 53, 55, 57$, and 58) are shown in Fig. 11.20B.[73] Combined PES and DFT of Au_n^- (n= 55-66) provided mechanism of how the relativistic effect leads to low-symmetry structure of Au_{55}^-.[74] The structure of Au_{58}^- is a highly spherical core-shell structure and the other structures till Au_{64}^- can be formed just by adding new atoms on the surface of Au_{58}^-.

11.5.2.2 Protected clusters

11.5.2.2.1 Electron affinity

PES of thiolate protected cluster was reported very recently by Tsukuda group.[75] They have used a custom built instrument for the study. Briefly, $Au_{25}(SC_{12}H_{25})_{18}^-$ clusters were electrosprayed at 120°C and were accelerated by a 10 Hz pulsed voltage for 200 μs (upto

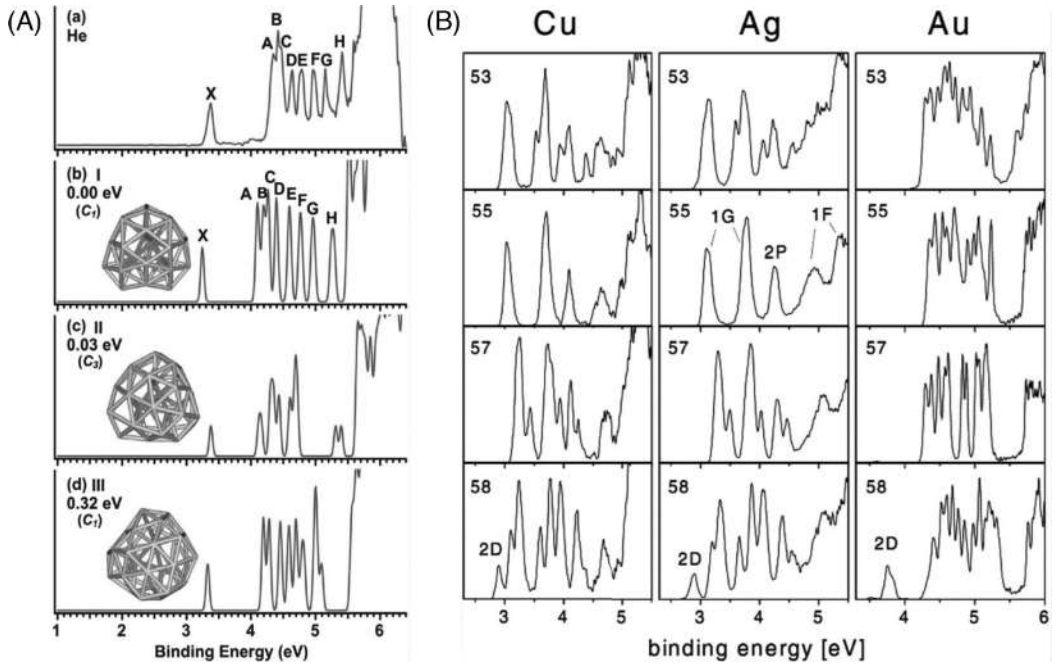

FIGURE 11.20 (A) PES spectrum of Au_{34}^- compared with simulated spectra of candidate structures.[72] (B) Photoelectron spectra of Cu_n^-, Ag_n^-, and Au_n^- (n = 53, 55, 57, 58) obtained at a photon energy of 6.424 eV.[7a,73] Reproduced with permission.[72,73]

12.8 keV) applied to Wiley–McLaren acceleration grid. The ions were detected by a TOF MS. The mass selected cluster ion beams were irradiated with a nanosecond pulse Nd:YAG (355 nm, 1.5 mJ per pulse) as shown in Fig. 11.21A. The photoelectrons generated in this process were collected by an inhomogeneous electric field. The electron kinetic energies were determined using a magnetic bottle PES (MB-PES) and the data were calibrated using iodide ion. Typical PES of $Au_{25}(SC_{12}H_{25})_{18}^-$ is shown in Fig. 11.21B where the spectrum was recorded for 20,000 laser shots and were averaged over three neighboring data points. For an electron with 1 eV kinetic energy, a resolution of about 110 meV was achieved in this work. A typical PES of $Au_{25}(SC_{12}H_{25})_{18}^-$ shows two bands labeled as A and B and are attributed to electron detachment from the 1P superatomic orbital and Au 5d orbital localized on the Au atoms of the core, respectively. The energies of the top (E_{top}) and onset of the band (E_{th}) were found to be 2.5 and 2.2 eV. Although DFT predicted splitting of the band A, it did not split due to spin-orbit coupling in the neutral state. The E_{top} is associated with the VDE which is the energy required to remove an electron while retaining the geometric structure. The experimental adiabatic electron affinity (AEA) from the E_{th} was found to be 2.2 eV which is significantly lower than the calculated AEA.

11.5.2.2.2 Thermionic emission

PES of $[Ag_{25}(SPhMe_2)_{18}]^-$ and $[Au_{25}(SC_2H_4Ph)_{18}]^-$ were performed at 355 nm and their AEA were found to be similar 2.02 and 2.36 eV, respectively.[76] When the clusters were

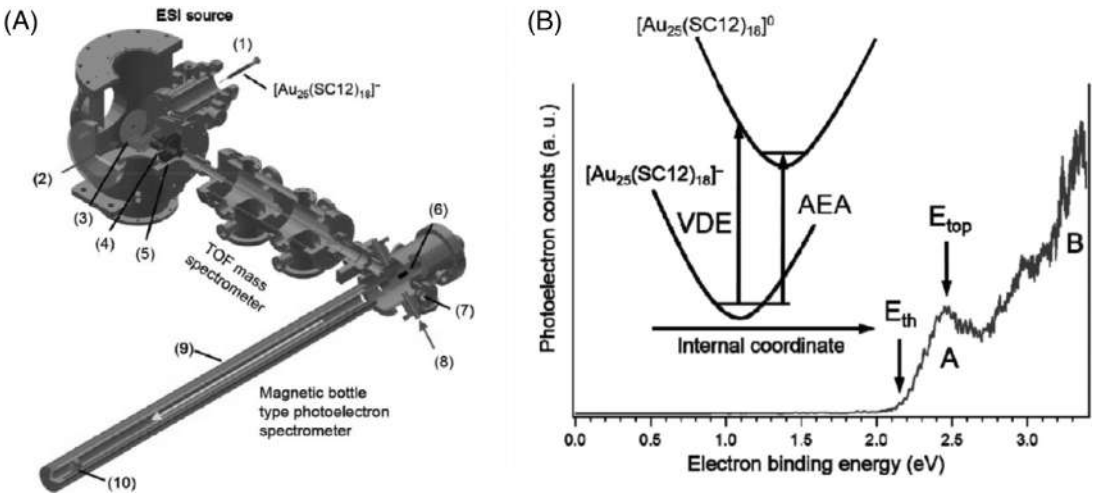

FIGURE 11.21 (A) Experimental set up used for PES and the resulted PES of $Au_{25}(SC_{12}H_{25})_{18}^-$ is shown in (B). Reproduced with permission.[75]

irradiated at 266 nm (4.66 eV), instead of electron detachment, slow electron emission was found to be the major process supressing electron detachment and photo fragmentation. It was proposed that the electron emission is a thermionic process from the vibrationally hot (vibration temperature 1600 K) M_{13} core through an electronically excited state $[M_{25}(SR)_{18}]^{-*}$. This state is embedded in the electron detachment continuum and quickly interconvert to vibrationally excited $[M_{25}(SR)_{18}]^-$ following thermionic emission leaving the internal energy in the remaining neutral $[Au_{25}(SC_2H_4Ph)_{18}]^0$. Although at such high photon energy photodissociation is expected but was completely supressed. Probably the rigid $M_2(SR)_3$ ligands protects the rigid M_{13} core such that the IC is feasible but the nuclear motion is retarded toward dissociation.

11.5.2.2.3 Heteroatom doping effect on repulsive Coulomb barrier

Effect of heteroatoms in the electronic structure was further monitored by PES taking $MAg_{24}(SPhMe_2)_{18}$ (M = Ag, Au, Pd, and Pt) as examples.[77] These clusters have super atomic core $[Au/Ag@Ag_{12}]^{5+}$ or $[Pd/Pt@Ag_{12}]^{5+}$ with I_h symmetry. The PES were measured at 266, 355, and 532 nm except for $[Au/AgAg_{24}(SPhMe_2)_{18}]^-$ as the detachment threshold energy of $[Au/AgAg_{24}(SPhMe_2)_{18}]$ is very close to 532 nm (2.32 eV). The PES of $[Ag_{25}(SPhMe_2)_{18}]^-$ at 355 nm looks very similar to the one of $[Au_{25}(SC_{12}H_{25})_{18}]^-$ and the extracted AEA which was found to be 2.02 eV is also similar to analogous $[Au_{25}(SC_{12}H_{25})_{18}]^-$ (2.2 eV) and $[Au_{25}(SC_2H_4Ph)_{18}]^-$ (2.36 eV). Similarly PES of $[Ag_{25}(SPhMe_2)_{18}]^-$ and $[AuAg_{24}(SPhMe_2)_{18}]^-$ at 355 nm also looks similar with AEA of $[AuAg_{24}(SPhMe_2)_{18}]^-$ to be 2.08 compared to 2.02 for $[Ag_{25}(SPhMe_2)_{18}]^-$ suggesting Au substitution do not change the electronic structure so much (Fig. 11.22A). In contrast, when Pd and Pt are in the central position of the Ag_{13} icosahedron, the AEA of $[Ag_{25}(SPhMe_2)_{18}]^0$, $[AuAg_{24}(SPhMe_2)_{18}]^0$, $[PdAg_{24}(SPhMe_2)_{18}]^-$, and $[PtAg_{24}(SPhMe_2)_{18}]^-$ were found to be 2.02, 2.08, 0.61, and 0.60 eV, respectively. While Au in the center does not change the superatomic orbitals, in presence of Pd or Pt the orbitals were

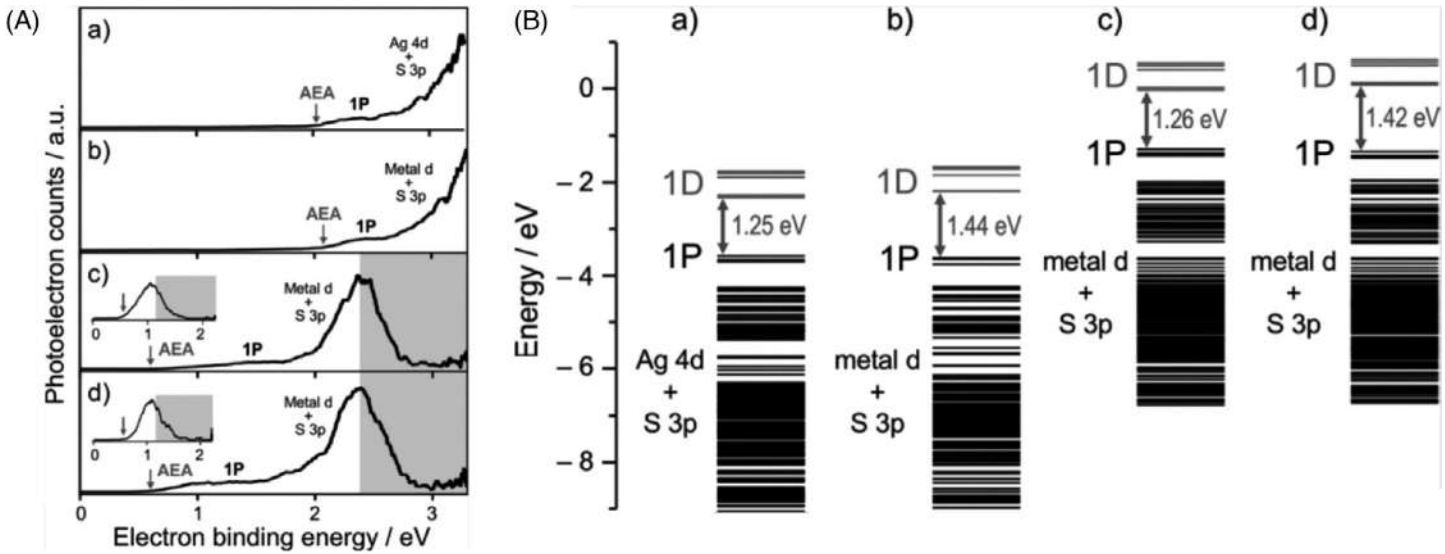

FIGURE 11.22 (A) PES of a) $[Ag_{25}(SMe)_{18}]^{-}$, b) $[AuAg_{24}(SMe)_{18}]^{-}$, c) $[PdAg_{24}(SMe)_{18}]^{2-}$, and d) $[PtAg_{24}(SMe)_{18}]^{2-}$ at 355 nm. (B) Orbital energies for a) $[Ag_{25}(SMe)_{18}]^{-}$, b) $[AuAg_{24}(SMe)_{18}]^{-}$, c) $[PdAg_{24}(SMe)_{18}]^{2-}$, and d) $[PtAg_{24}(SMe)_{18}]^{2-}$, calculated using the PBE functional. Orbital energies are given with reference to the calculated VDE. Reproduced with permission.[77]

shifted up about 1.4 eV (Fig. 11.22B). This upward shift is attributed to the presence of repulsive Coulomb barrier (RCB).

In a recent study, Tsukuda and Hakkinen found that $Ag_{44}(SR)_{30}^{4-}$ is energetically metastable with respect to electron detachment and AEA of $Ag_{44}(SR)_{30}^{4-}$ is negative.[78] The RCB was found to be 2.7 eV from PES study at 266 and 355 nm. However, the ion was stable and no electron detachment was seen under regular CID condition. The energy barrier associated with electron detachment due to the RCB is much higher than the energy required for fragmentation.

11.5.2.2.4 Time resolved pump-probe spectroscopy

To understand the emission from dithiol protected $[Ag_{29}(BDT)_{12}(PPh_3)_4]$ cluster, Kapees and coworkers studied pump-probe spectroscopy of isolated $[Ag_{29}(BDT)_{12}]^{3-}$ in absence of solvent.[79] They used femtosecond time-resolved PES. The cluster ion was excited using several wavelength (265, 295, 325 nm) and the third electron affinity, EA (3) was found to be 0.9±0.1 eV. The RCB height was found to be 1.7 ± 0.1 eV. The RCB height is in contrast to the classical metallic sphere model of charge delocalization and was concluded that the cluster ion cannot be well described using classical metallic sphere as the charge is not uniformly distributed throughout the ligand stabilized cluster.

When PES was measured at 490 nm, two components were observed and can be fitted with two-component Gaussian. With varying laser intensity these two peaks were found to be centered at 2.66 eV and 3.42 eV manifesting two-photon intensity dependence and the two different electron kinetic energy is attributed to two separate electronic states. To further investigate the two photon process, time resolved pump-probe spectroscopy with 490 nm (2.53 eV) pump and 800 nm (1.55 eV) probe was used. Contour plot of electron signal versus electron kinetic energy as a function of pump-probe delay indicated ultrafast decay in an average time scale of less than 100 fs. This is associated with a decrease in electron kinetic energy from 3.0 to 2.1 eV. A long-lived state of 2.1 eV remained populated even after 100 ps. Considering EA(3), the excitation energy relative to the trianion ground state is 1.45 eV. During excitation, one or more states get populated with significant charge transfer from the shell to the core. These CT states relax over several hundred femtoseconds via charge recombination to yield either a vibrationally excited singlet state (IC) or a long-lived triplet state (ISC). The process is described by Jablonski diagram in Fig. 11.23B.

11.5.3 IR spectroscopy

Another spectroscopic method that has gained interest over the years for structure identification is IR spectroscopy, although so far most of the studies were performed on the bare clusters.[80] In many cases, reactivity of the neutral and anionic clusters toward gas molecules was used to elucidate their structure in the gas phase. Fielecke et al. pioneered this topic and have performed most of the experiments. They studied geometric structure of several small neutral gold clusters by IR spectroscopy in the range of 47 and 220 wavenumber. They have studied IR spectra of neutral Au_7, Au_{19}, and Au_{20} cluster as Kr complex.[81] Experimental IR spectra of Au_7-Kr spectra is compared with calculated spectra of 4 low lying isomers among which Isomer 1 (plannar with C_S symmetry) matches best. The main peaks at 165, 186, and

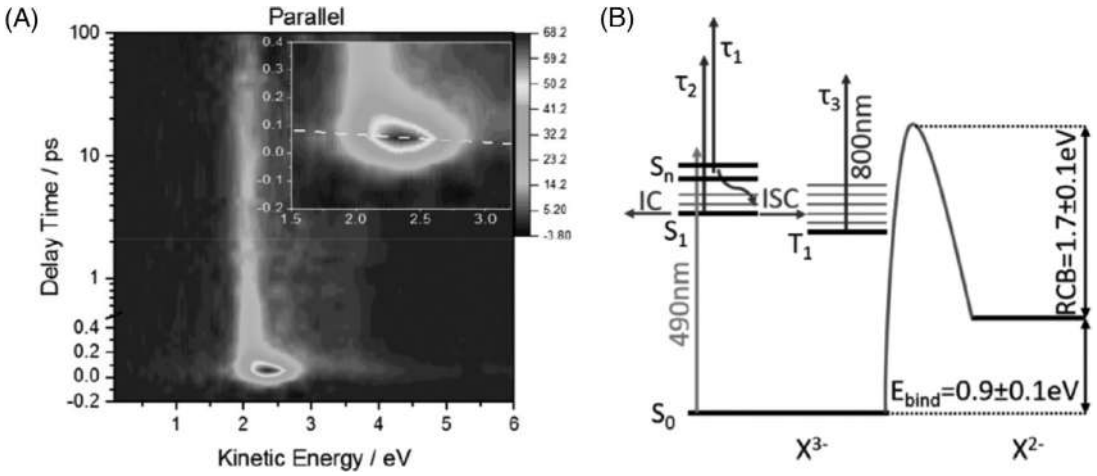

FIGURE 11.23 (A) Time resolved pump (490 nm)-probe (800 nm) measurement recorded at parallel laser polarization. The contour plots of the transient photoelectron counts *vs* electron kinetic energy and pump−probe delay. The dynamics during first 400 fs is expanded in the inset. (B) Jablonski diagram is showing the proposed relaxation mechanism. Reproduced with permission.[79]

201 cm^{-1} were reproduced considering Isomer 1, only the relative intensities of the peaks do not match completely. As discussed in other sections, Au_{20} is known to have a highly symmetric T_d structure. The far IR-multi photon dissociation (FIR-MPD) was very simple with only peak at 148 cm^{-1} suggesting toward high symmetric structure. The peak corresponds to a triply degenerate vibration (t_2) in T_d bare Au_{20}. If one corner atom is removed from the T_d structure of Au_{20}, the symmetry is reduced from T_d to C_{3v} and as a consequence the degeneracy in the t_2 level is lifted resulting in doubly degenerate (e) and a nondegenerate (a_1) level in Au_{19}. This splitting was reflected in the IR spectrum of Au_{19}-Kr where the e lies at 149 cm^{-1} and the a_1 vibration was seen at 167 cm^{-1}.

Smaller clusters structures were resolved in presence of O_2 as ligand by measuring the O–O stretching frequency. Both $Au_4{}^0$ (1502 cm^{-1}) and $Au_4{}^-$ (1060 cm^{-1}) showed 2D distorted Y-shaped structure but the peak positions differ considerably.[82] This is due to two distinct motifs one being O–O stretching of superoxo $O_2{}^-$ (1060 cm^{-1}) and the other around 1500 cm^{-1} due to slightly activated O_2 species. All the odd-sized clusters showed the superoxo stretch bands suggesting similar level of activation. Two vibrational bands for Au_7O_2 suggested the presence of two isomers either in the parent cluster or formed after binding to O_2. Similar observation was found for $Au_{12}O_2$ for which IR spectra is broader compared to lighter clusters suggesting isomeric species while $Au_{11}O_2$ and Au_9O_2 do not show any such broadening suggesting presence of only one isomer. Goldsmith et al. have studied the planar to 3D transition of small Kr tagged gold clusters by this method. They found that the critical size for the transition is Au_{11} at 100 K. At 100 K, Au_{11} was found to have capped trigonal prism with D_{3h} symmetry. However, at room temperature (300 K), 3D isomers can coexist from Au_8 onwards. The experimental data are shown in Fig. 11.24.[83]

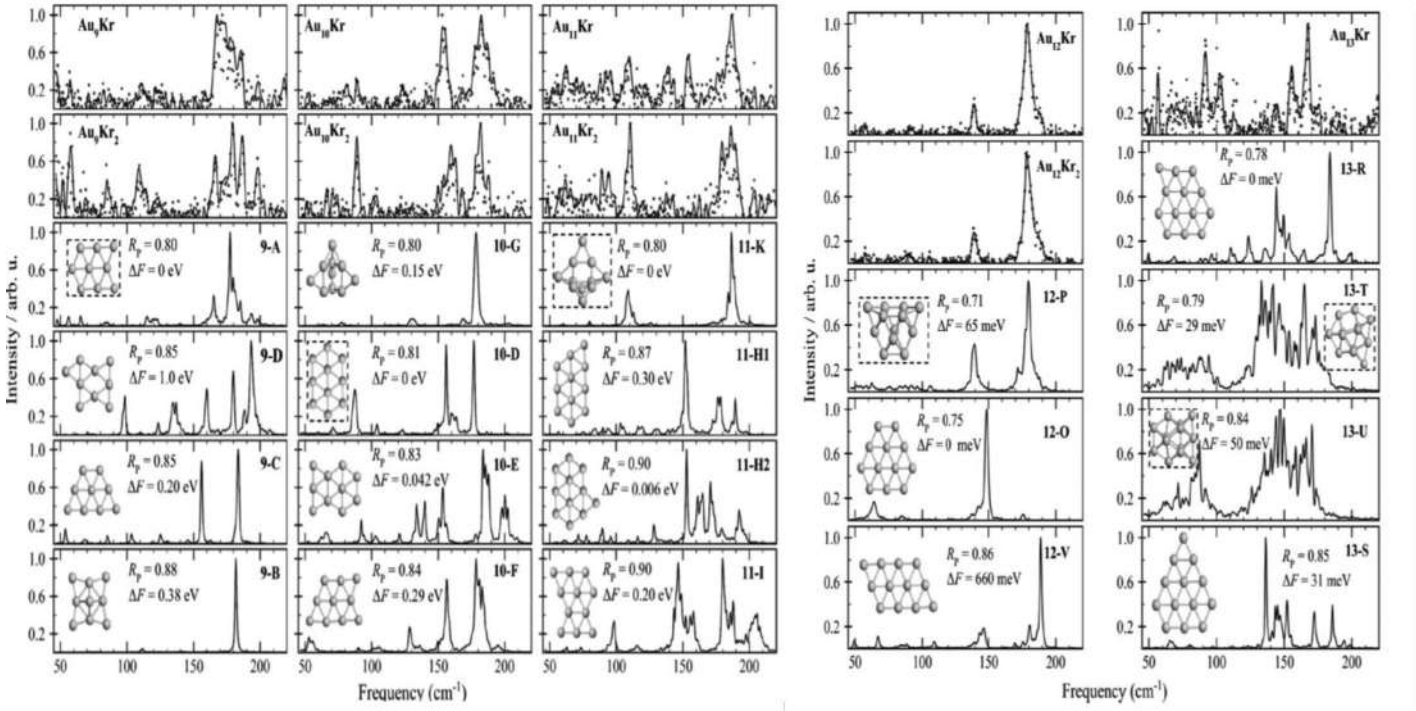

FIGURE 11.24 FIR-MPD of Au_9-Au_{13} at 100 K. Reproduced from For Au_9-Au_{12}, upper two panels are experimental data with 1 and 2 Kr complexes, respectively. For Au_{13} (right column) only experimental data for only Au_{13}-Kr is shown. Calculated spectra of several isomers are compared with the experimental data in the lower panels. All free energy calculations were done at 100 K. The experimentally observed structure is shown with dashed box in each case. Reproduced with permission.[83]

11.6 Summary and future perspectives

Starting from the infancy till today, gas phase spectroscopic studies have shown potential to unravel structure, property and reactivity of bare clusters (metal, semiconductor, molecular etc.). Along with advancement in synthetic methods and instrumentation, structural determination has always been of importance as the cluster reactivity depends highly on the structure. Each additional atom has influence in structure and reactivity as discussed through TIED, IMS, dissociation mass spectrometry and several other spectroscopic methods. TIED is in combination with theoretical calculation proven to be a good choice for bare clusters as discussed in Section 11.1.

Alongside bare clusters gas phase property determination of protected clusters is gaining increasing interest in recent times as many clusters show distinctly different properties in the gas phase compared to condensed phase. The structures determined by TIED were also confirmed (in many cases) from IMS of the bare cluster ions. Mass spectrometric methods allow to understand the cluster size and nuclearity in the gas phase which is considered to be the reflection of solution phase property as discussed in Section 11.2. The introduction of IMS for the protected clusters opened new avenues in the context of isomers, oligomers and even reaction monitoring. Isomers due to collisional activation, charge heterogeneity, ligand arrangements, etc., offered in depth understanding of the gas phase behavior of the protected clusters. Structures obtained during mass spectrometric analysis and IMS are known to reflect their solution phase structures. Therefore properties of the protected clusters could be better understood combining their condensed phase and gas phase structures.

Dissociation mass spectrometry offers structural information of the parent cluster as well as the fragments produced in that process. Clusters ions can be fragmented by collisional activation with neutral gas or by colliding on the surface. When the ions interact with light in the gas phase absorb the incident light, the action may result in PD as discussed in Section 11.3.

Several gas phase PES and PD studies show potential to gain more information on the electronic and geometric structure of the protected cluster ions as discussed in Section 11.4. PES can reveal structural information, structural transition from 2D to 3D, presence of isomers, ligand-binding site and can offer valuable information for cluster-based catalysis. Although number of such studies are still limited for protected clusters, information such as electron affinity, RCB, etc., can be obtained which help in deeper understanding of the cluster structure in the gas phase.

Looking ahead, with large number of protected clusters of known condensed phase structure and many unsolved problems in the bare clusters, gas phase spectroscopy is expected to shine light on the structure, property, and reactivity of both bare and ligated clusters. Mass spectrometry has always been and will continue to be an indispensable tool with advanced instrumentation, improved ionization methods, higher resolution, high mass range, integrated IMS, additional laser source along with CID. Mass spectrometric techniques for cluster synthesis is expected to be popular technique as many metastable clusters can be generated by this process and gas phase spectroscopic methods will be useful to understand these clusters in detail. Integration of spectroscopic methods will help in understanding the structure and reactivity of the protected clusters alongside bare clusters. The introduction of polarized light could be interesting as many clusters are known to be chiral in nature. How

chirality is affected in the gas phase would be very interesting to study by gas phase circular dichroism or by using chiral medium in the IMS.

Abbreviation

AEA	Adiabatic electron affinity
BDT	Benzene dithiol
CCD	Charge-coupled device
CCS	Collision cross section
CID	Collision induced dissociation
CT	Charge transfer
DDT	Dodecanethiol
DFT	Density functional theory
DMS	Differential mobility analyzer
DMBT	Dimethyl benzene thiol
DT-IMS	Drift tube ion mobility spectrometry
EA	Electron affinity
EFG	Electric field gradient
ESI	Electrospray ionization
FAIMS	Field asymmetric ion mobility spectrometry
FT ICR	Fourier-transformed ion cyclotron resonance
FTP	Fluorothiophenol
HV	High vacuum
IC	Internal conversion
IMS	Ion mobility spectrometry
ISC	Inter system crossing
MALDI	Matrix assisted laser desorption ionization
MBA	Mercaptobenzoic acid
MPD	Multi photon detachment
MP2	Møller–Plesset
MS	Mass Spectrometry
PA	Projection approximation
PD	Photo dissociation
PET	Phenylethanethiol
PES	Photoelectron spectroscopy
RCB	Repulsive Coulomb barrier
SID	Surface induced dissociation
SLIM	Structure for lossless ion manipulation
TIED	Trapped ion electron diffraction
TIMS	Trapped ion mobility spectrometry
TWIMS	Travelling wave ion mobility spectrometry
UHV	Ultra-high vacuum
VDE	Vertical detachment energy

References

1. (a) Chakraborty I, Pradeep T. Atomically precise clusters of noble metals: emerging link between atoms and nanoparticles. *Chem Rev (Washington, DC, US)*. 2017;117:8208–8271; (b) Pradeep T, Baksi A, Xavier PL. Noble metal clusters in protein templates. *RSC Smart Mater*. 2014;7:169–225; (c) Bhat S, Chakraborty I, Baksi A, Narayanan RP, Pradeep T. Evolution of atomically precise clusters through the eye of mass spectrometry. *Nanoscience (Cambridge, U.K.)*. 2016;3:343–385.
2. (a) Zavras A, Khairallah GN, O'Hair RAJ. Gas phase formation, structure and reactivity of gold cluster ions. In: Mingos DMP, ed. *Gold Clusters, Colloids and Nanoparticles II*. Cham: Springer International Publishing;

2014:139–230; (b) Luo Z, Castleman AW, Khanna SN. *Reactivity of metal clusters*; 2016 *Chem Rev (Washington, DC, US)*;116:14456–14492.
3. Weis P. Structure determination of gaseous metal and semi-metal cluster ions by ion mobility spectrometry. *Int J Mass spectrom*. 2005;245:1–13.
4. Sanchez A, Abbet S, Heiz U, et al. When gold is not noble: nanoscale gold catalysts. *J Phys Chem A*. 1999;103:9573–9578.
5. Jena P, Castleman Jr AW. Clusters: a bridge across the disciplines of physics and chemistry. *Proc Natl Acad Sci. USA*. 2006;103:10560–10569.
6. Jin R, Zeng C, Zhou M, Chen Y. Atomically precise colloidal metal nanoclusters and nanoparticles: fundamentals and opportunities. *Chem Rev. (Washington, DC, US)*. 2016;116:10346–10413.
7. (a) Wang L-M, Wang L-S. *Probing the electronic properties and structural evolution of anionic gold clusters in the gas phase*; 2012 *Nanoscale*;4:4038–4053; (b) *[In: The Chemical Physics of Solid Surfaces, 2007; 12]*. Elsevier B. V.; 2007.
8. Li ZY, Young NP, Di Vece M, et al. Three-dimensional atomic-scale structure of size-selected gold nanoclusters. *Nature*. 2008;451:46–48.
9. Bondybey VE, Smith AM, Agreiter J. New developments in matrix isolation spectroscopy. *Chem Rev. (Washington, D. C.)*. 1996;96:2113–2134.
10. Maier-Borst M, Cameron DB, Rokni M, Parks JH. Electron diffraction of trapped cluster ions. *Phys Rev A: At Mol Opt Phys*. 1999;59:R3162.
11. Kruckeberg S, Schooss D, Maier-Borst M, Parks JH. Diffraction of trapped (CsI)nCs+: the appearance of bulk structure. *Phys Rev Lett*. 2000;85:4494–4497.
12. Schooss D, Blom MN, Parks JH, von Issendorff B, Haberland H, Kappes MM. The structures of Ag_{55}+ and Ag_{55}-: trapped ion electron diffraction and density functional theory. *Nano Lett*. 2005;5:1972–1977.
13. Blom MN, Schooss D, Stairs J, Kappes MM. Experimental structure determination of silver cluster ions (Agn+,19≤n≤79). *J Chem Phys*. 2006;124.
14. Xing X, Yoon B, Landman U, Parks JH. Structural evolution of Au nanoclusters: from planar to cage to tubular motifs. *Phys Rev B: Condens Matter Mater Phys*. 2006;74.
15. (a) Lechtken A, Neiss C, Kappes MM, Schooss D. Structure determination of gold clusters by trapped ion electron diffraction: Au_{14}– Au_{19}. *Phys Chem Chem Phys*. 2009;11:4344–4350; (b) Wang L-M, Bai J, Lechtken A, et al. Magnetic doping of the golden cage cluster M@Au_{16}- (M=Fe,Co,Ni). *Phys Rev B: Condens Matter Mater Phys*. 2009;79.
16. Lechtken A, Neiss C, Stairs J, Schooss D. Comparative study of the structures of copper, silver, and gold icosamers: influence of metal type and charge state. *J Chem Phys*. 2008;129.
17. Lechtken A, Schoos D, Stairs JR, et al. Au_{-34}: a chiral gold cluster? *Angew Chem Int Ed*. 2007;46:2944.
18. Rapps T, Ahlrichs R, Waldt E, Kappes MM, Schooss D. On the structures of 55-atom transition-metal clusters and their relationship to the crystalline bulk. *Angew Chem Int Ed*. 2013;52:6102–6105.
19. Kohaut S, Rapps T, Fink K, Schooss D. Structural evolution of palladium clusters Pd55–Pd147-: transition to the bulk. *J Phys Chem A*. 2019;123:10940–10946.
20. (a) Eiceman GA, Karpas Z. Ion Mobility Spectrometry. 2nd Edition. CRC; 2004; (b) Lapthorn C, Pullen F, Chowdhry BZ. Ion mobility spectrometry-mass spectrometry (IMS-MS) of small molecules: separating and assigning structures to ions. *Mass Spectrom Rev.* 2013;32:43–71.
21. (a) Eiceman GA. Advances in ion mobility spectrometry: 1980-1990. *Crit Rev Anal Chem*. 1991;22: 471; (b) Collins DC, Lee ML. Developments in ion mobility spectrometry-mass spectrometry. *Anal Bioanal Chem*. 2002;372:66–73.
22. Hill Jr HH, Siems WF, Louis St, R H. Ion mobility spectrometry. *Anal Chem*. 1990;62:1201A.
23. Gabelica V, Marklund E. Fundamentals of ion mobility spectrometry. *Curr Opin Chem Biol*. 2018;42:51–59.
24. Shvartsburg AA, Jarrold MF. An exact hard-spheres scattering model for the mobilities of polyatomic ions. *Chem Phys Lett*. 1996;261:86–91.
25. Kanu AB, Dwivedi P, Tam M, Matz L, Hill Jr HH. Ion mobility-mass spectrometry. *J Mass Spectrom*. 2008;43:1–22.
26. Jiang W, Chung NA, May JC, McLean JA, Robinson RAS. Ion mobility–mass spectrometry. In: *Encyclopedia of Analytical Chemistry*; 2019:1–34. https://onlinelibrary.wiley.com/doi/10.1002/9780470027318.a9292.pub2.
27. Shvartsburg AA, Smith RD. Fundamentals of traveling wave ion mobility spectrometry. *Anal Chem. (Washington, DC, U. S.)*. 2008;80:9689–9699.
28. Michelmann K, Silveira JA, Ridgeway ME, Park MA. Fundamentals of trapped ion mobility spectrometry. *J Am Soc Mass Spectrom*. 2015;26:14–24.

29. Weis P, Bierweiler T, Gilb S, Kappes MM. Structures of small silver cluster cations (Agn+, n < 12): ion mobility measurements versus density functional and MP2 calculations. *Chem Phys Lett*. 2002;355:355–364.
30. Baksi A, Jash M, Bag S, et al. Mechanistic elucidation of the structure and reactivity of bare and hydride-protected Ag_{17}+ clusters. *J Phys Chem C*. 2019;123:28494–28501.
31. Gilb S, Weis P, Furche F, Ahlrichs R, Kappes MM. Structures of small gold cluster cations (Aun+, n < 14): Ion mobility measurements versus density functional calculations. *J Chem Phys*. 2002;116:4094–4101.
32. Weis P, Bierweiler T, Vollmer E, Kappes MM. Au_9+: rapid isomerization reactions at 140 K. *J Chem Phys*. 2002;117:9293–9297.
33. Furche F, Ahlrichs R, Weis P, et al. The structures of small gold cluster anions as determined by a combination of ion mobility measurements and density functional calculations. *J Chem Phys*. 2002;117:6982–6990.
34. Angel LA, Majors LT, Dharmaratne AC, Dass A. Ion mobility mass spectrometry of $Au_{25}(SCH_2CH_2Ph)_{18}$ nanoclusters. *ACS Nano*. 2010;4:4691–4700.
35. Matus MF, Malola S, Bonilla K, et al. A topological isomer of the $Au_{25}(SR)_{18}$-nanocluster. *Chem Commun (Cambridge, UK)*. 2020;56:8087–8090.
36. Kalenius E, Malola S, Matus MF, Kazan R, Burgi T, Hakkinen H. Experimental confirmation of a topological isomer of the ubiquitous $Au_{25}(SR)_{18}$ cluster in the gas phase. *J Am Chem Soc*. 2021;143:1273–1277.
37. Comby-Zerbino C, Bertorelle F, Dugourd P, Antoine R, Chirot F. Structure and charge heterogeneity in isomeric $Au_{25}(MBA)_{18}$ nanoclusters - insights from ion mobility and mass spectrometry. *J Phys Chem A*. 2020;124:5840–5848.
38. Baksi A, Harvey SR, Natarajan G, Wysocki VH, Pradeep T. Possible isomers in ligand protected Ag_{11} cluster ions identified by ion mobility mass spectrometry and fragmented by surface induced dissociation. *Chem Commun (Cambridge, UK)*. 2016;52:3805–3808.
39. Baksi A, Bootharaju MS, Chen X, Hakkinen H, Pradeep T. $Ag_{11}(SG)_7$: a new cluster identified by mass spectrometry and optical spectroscopy. *J Phys Chem C*. 2014;118:21722–21729.
40. Comby-Zerbino C, Bertorelle F, Chirot F, Dugourd P, Antoine R. Structural insights into glutathione-protected gold $Au_{10–12}(SG)_{10–12}$ nanoclusters revealed by ion mobility mass spectrometry. *Eur Phys J D*. 2018;72:1–5.
41. Baksi A, Ghosh A, Mudedla SK, et al. Isomerism in monolayer protected silver cluster ions: an ion mobility-mass spectrometry approach. *J Phys Chem C*. 2017;121:13421–13427.
42. Baksi A, Chakraborty P, Bhat S, Natarajan G, Pradeep T. $[Au_{25}(SR)_{18}]_{22-}$: a noble metal cluster dimer in the gas phase. *Chem Commun (Cambridge, UK)*. 2016;52:8397–8400.
43. Baksi A, Schneider EK, Weis P, et al. Nanogymnastics: visualization of intercluster reactions by high-resolution trapped ion mobility mass spectrometry. *J Phys Chem C*. 2019;123:28477–28485.
44. Baksi A, Schneider EK, Weis P, et al. Linear size contraction of ligand protected Ag_{29} clusters by substituting Ag with Cu. *ACS Nano*. 2020;14:15064–15070.
45. (a) Becker S, Dietrich G, Hasse HU, et al. Fragmentation pattern of gold clusters collided with xenon atoms. *Comput Mater Sci*. 1994;2:633; (b) Becker S, Dietrich G, Hasse HU, et al. Fragmentation of gold clusters stored in a Penning trap. *Rapid Commun Mass Spectrom*. 1994;8:401; (c) Schweikhard L, Beiersdorfer P, Bell W, et al. Production and investigation of multiply charged metal clusters in a Penning trap. *Hyperfine Interact*. 1996;99:97–104; (d) Schweikhard L, Dietrich G, Kruckeberg S, Lutzenkirchen K, Walther C, Ziegler J. Collision induced dissociation of doubly charged stored metal cluster ions. *Rapid Commun Mass Spectrom*. 1997;11:1592–1595; (e) Weidele H, Vogel M, Herlert A, et al. Decay pathways of stored metal-cluster anions after collisional activation. *Eur Phys J D*. 1999;9:173–177; (f) Ziegler J, Dietrich G, Kruckeberg S, Lutzenkirchen K, Schweikhard L, Walther C. Multicollision-induced dissociation of multiply charged gold clusters, Aun_{2+}, n = 7-35, and Aun_{3+}, n = 19-35. *Int J Mass spectrom*. 2000;202:47–54; (g) Vogel M, Hansen K, Herlert A, Schweikhard L. Energy dependence of the decay pathways of optically excited small gold clusters. *Appl Phys B: Lasers Opt*. 2001;73:411–416; (h) Vogel M, Hansen K, Herlert A, Schweikhard L. Decay pathways of small gold clusters. The competition between monomer and dimer evaporation. *Eur Phys J D*. 2001;16:73–76; (i) Vogel M, Hansen K, Herlert A, Schweikhard L. Model-free determination of dissociation energies of polyatomic systems. *Phys Rev Lett*. 2001;87; (j) Vogel M, Hansen K, Herlert A, Schweikhard L. Dimer dissociation energies of small odd-size clusters Au+n. *Eur Phys J D*. 2002;21:163–166; (k) Vogel M, Hansen K, Herlert A, Schweikhard L. Multisequential photofragmentation of size-selected gold cluster ions. *Phys Rev A: At Mol Opt Phys*. 2002;66; (l) Vogel M, Herlert A, Schweikhard L. Photodissociation of small group-11 metal cluster ions: fragmentation pathways and photoabsorption cross sections. *J Am Soc Mass Spectrom*. 2003;14:614–621; (m) Vogel M, Hansen K, Schweikhard L.

Signature of cluster isomers in time-resolved photodissociation experiments. *Int J Mass spectrom*. 2004;233:117–123; (n) Schweikhard L, Hansen K, Herlert A, Herraiz Lablanca MD, Vogel M. Photodissociation of stored metal clusters. *Eur Phys J D*. 2005;36:179–185.

46. (a) Ziegler J, Dietrich G, Kruckeberg S, Lutzenkirchen K, Schweikhard L, Walther C. Dissociation pathways of doubly and triply charged gold clusters. *Hyperfine Interact*. 1998;115:171–179; (b) Herlert A, Kruckeberg S, Schweikhard L, Vogel M, Walther C. Electron impact ionization/dissociation of size selected gold cluster cations. *J Electron Spectrosc Relat Phenom*. 2000;106:179–186; (c) Yannouleas C, Landman U, Herlert A, Schweikhard L. Trianionic gold clusters. *Eur Phys J D*. 2001;16:81–85; (d) Yannouleas C, Landman U, Herlert A, Schweikhard L. Multiply charged metal cluster anions. *Phys Rev Lett*. 2001;86:2996–2999.
47. (a) Walther C, Becker S, Dietrich G, et al. Photofragmentation of metal clusters stored in a penning trap. *Z Phys D: At Mol Clusters*. 1996;38:51–58; (b) Lindinger M, Dasgupta K, Dietrich G, et al. Time resolved photofragmentation of Aun+ and Agn+ clusters (n = 9, 21). *Z Phys D: At Mol Clusters*. 1997;40:347–350.
48. (a) Spasov VA, Shi Y, Ervin KM. Time-resolved photodissociation and threshold collision-induced dissociation of anionic gold clusters. *Chem Phys*. 2000;262:75–91; (b) Herlert A, Schweikhard L, Vogel M. Photoinduced dissociation of anionic and electron detachment of dianionic gold clusters by use of a laser pointer. *Int J Mass spectrom*. 2002;213:157–161; (c) Herlert A, Schweikhard L. Production of dianionic and trianionic noble metal clusters in a Penning trap. *Int J Mass spectrom*. 2003;229:19–25; (d) Herlert A, Schweikhard L. First observation of delayed electron emission from dianionic metal clusters. *Int J Mass spectrom*. 2006;252:151–156; (e) Herlert A, Schweikhard L. Delayed neutral-atom evaporation of photoexcited anionic gold clusters. *Int J Mass spectrom*. 2006;249/250:215–221; (f) Herlert A, Schweikhard L. Two-electron emission after photoexcitation of metal-cluster dianions. *New J Phys*. 2012;14; (g) Schweikhard L, Herlert A, Kruckeberg S, Vogel M, Walther C. Electronic effects in the production of small dianionic gold clusters by electron attachment on to stored Aun-, n = 12-28. *Philos Mag B*. 1999;79:1343–1352.
49. Zhang H-F, Stender M, Zhang R, Wang C, Li J, Wang L-S. Toward the solution synthesis of the tetrahedral Au20 cluster. *J Phys Chem B*. 2004;108:12259–12263.
50. Johnson GE, Laskin J. Understanding ligand effects in gold clusters using mass spectrometry. *Analyst (Cambridge, UK)*. 2016;141:3573–3589.
51. Tomihara R, Hirata K, Yamamoto H, Takano S, Koyasu K, Tsukuda T. Collision-induced dissociation of undecagold clusters protected by mixed ligands $[Au_{11}(PPh_3)_{8X2}]^+$ (X = Cl, CCPh). *ACS Omega*. 2018;3:6237–6242.
52. Fields-Zinna CA, Sampson JS, Crowe MC, et al. Tandem mass spectrometry of thiolate-protected Au nanoparticles $NaxAu_{25}(SC_2H_4Ph)_{18}$-y($S(C_2H_4O)_5CH_3$)y. *J Am Chem Soc*. 2009;131:13844–13851.
53. Koyasu K, Tsukuda T. Gas-phase studies of chemically synthesized Au and Ag clusters. *J Chem Phys*. 2021;154.
54. Liu C, Lin S, Pei Y, Zeng XC. Semiring chemistry of $Au_{25}(SR)_{18}$: fragmentation pathway and catalytic active site. *J Am Chem Soc*. 2013;135:18067–18079.
55. Chakraborty P, Baksi A, Khatun E, Nag A, Ghosh A, Pradeep T. Dissociation of gas phase ions of atomically precise silver clusters reflects their solution phase stability. *J Phys Chem C*. 2017;121:10971–10981.
56. Black DM, Crittenden CM, Brodbelt JS, Whetten RL. Ultraviolet photodissociation of selected gold clusters: ultraefficient unstapling and ligand stripping of $Au_{25}(pMBA)_{18}$ and $Au_{36}(pMBA)_{24}$. *J Phys Chem Lett*. 2017;8:1283–1289.
57. Fagan JW, Weerawardene KLDM, Cirri A, Aikens CM, Johnson CJ. Toward quantitative electronic structure in small gold nanoclusters. *J Chem Phys*. 2021;155.
58. Cirri A, Morales Hernandez H, Kmiotek C, Johnson CJ. Systematically tuning the electronic structure of gold nanoclusters through ligand derivatization. *Angew Chem Int Ed*. 2019;58:13818–13822.
59. (a) Cirri A, Hernandez HM, Johnson CJ. Hydride, chloride, and bromide show similar electronic effects in the $Au_9(PPh_3)_{83+}$ nanocluster. *Chem Commun (Cambridge, UK)*. 2020;56:1283–1285; (b) Cirri A, Hernandez HM, Johnson CJ. High Precision electronic spectroscopy of ligand-protected gold nanoclusters: effects of composition, environment, and ligand chemistry. *J Phys Chem A*. 2020;124:1467–1479.
60. Collings BA, Athanassenas K, Lacombe D, Rayner DM, Hackett PA. Optical absorption spectra of Au_7, Au_9, Au_{11}, and Au_{13}, and their cations: gold clusters with 6, 7, 8, 9, 10, 11, 12, and 13 s-electrons. *J Chem Phys*. 1994;101:3506.
61. Hamouda R, Bellina B, Bertorelle F, et al. Electron emission of gas-phase $[Au_{25}(SG)_{18\text{-}6}H]7$- gold cluster and its action spectroscopy. *J Phys Chem Lett*. 2010;1:3189–3194.
62. Daly S, Choi CM, Zavras A, et al. Gas-Phase structural and optical properties of homo- and heterobimetallic rhombic dodecahedral nanoclusters $[Ag_{14}$-nCun$(CCtBu)_{12}X]+$ (X = Cl and Br): ion mobility, VUV and UV spectroscopy, and DFT calculations. *J Phys Chem C*. 2017;121:10719–10727.

63. Wang L-S, Cheng H-S, Fan J. Photoelectron spectroscopy of size-selected transition metal clusters: Fen-, n = 3-24. *J Chem Phys*. 1995;102:9480.
64. (a) Haekkinen H, Yoon B, Landman U, Li X, Zhai H-J, Wang L-S. On the electronic and atomic structures of small AuN- (N = 4-14) clusters: a photoelectron spectroscopy and density-functional study. *J Phys Chem A*. 2003;107:6168–6175; (b) Huang W, Wang L-S. Au10-: isomerism and structure-dependent O_2 reactivity. *Phys Chem Chem Phys*. 2009;11:2663–2667.
65. Stolcic D, Fischer M, Gantefoer G, Kim YD, Sun Q, Jena P. Direct observation of key reaction intermediates on gold clusters. *J Am Chem Soc*. 2003;125:2848–2849.
66. Pal R, Wang L-M, Huang W, Wang L-S, Zeng XC. Structure evolution of gold cluster anions between the planar and cage structures by isoelectronic substitution: Aun- (n = 13-15) and MAun- (n = 12-14, M = Ag, Cu). *J Chem Phys*. 2011;134.
67. Bulusu S, Li X, Wang L-S, Zeng XC. Evidence of hollow golden cages. *Proc Natl Acad Sci USA*. 2006;103:8326–8330.
68. Li J, Li X, Zhai H-J, Wang L-S. Au_{20}: a tetrahedral cluster. *Science (Washington, DC, US)*. 2003;299:864–867.
69. Bulusu S, Li X, Wang L-S, Zeng XC. Structural transitions from pyramidal to fused planar to tubular to core/shell compact in gold clusters: Aun- (n = 21–25). *J Phys Chem C*. 2007;111:4190–4198.
70. Ji M, Gu X, Li X, Gong X, Li J, Wang L-S. Experimental and theoretical investigation of the electronic and geometrical structures of the Au_{32} cluster. *Angew Chem Int Ed*. 2005;44:7119–7123.
71. Gu X, Bulusu S, Li X, et al. Au_{34}-: a fluxional core-shell cluster. *J Phys Chem C*. 2007;111:8228–8232.
72. Shao N, Huang W, Gao Y, et al. Probing the structural evolution of medium-sized gold clusters: Aun- (n = 27-35). *J Am Chem Soc*. 2010;132:6596–6605.
73. Hakkinen H, Moseler M, Kostko O, Morgner N, Hoffmann MA, von Issendorff B. Symmetry and electronic structure of noble-metal nanoparticles and the role of relativity. *Phys Rev Lett*. 2004;93.
74. Huang W, Ji M, Dong C-D, et al. Relativistic effects and the unique low-symmetry structures of gold nanoclusters. *ACS Nano*. 2008;2:897–904.
75. Hirata K, Yamashita K, Muramatsu S, et al. Anion photoelectron spectroscopy of free $[Au_{25}(SC_{12}H_{25})_{18}]$. *Nanoscale*. 2017;9:13409–13412.
76. Hirata K, Kim K, Nakamura K, et al. Photoinduced thermionic emission from $[M_{25}(SR)_{18}]^-$ (M = Au, Ag) revealed by anion photoelectron spectroscopy. *J Phys Chem C*. 2019;123:13174–13179.
77. Kim K, Hirata K, Nakamura K, et al. Elucidating the doping effect on the electronic structure of thiolate-protected silver superatoms by photoelectron spectroscopy. *Angew Chem Int Ed*. 2019;58:11637–11641.
78. Tasaka Y, Nakamura K, Malola S, et al. Electron binding in a superatom with a repulsive coulomb barrier: the case of $[Ag_{44}(SC_6H_3F_2)_{30}]_4$- in the gas phase. *J Phys Chem Lett*. 2020;11:3069–3074.
79. Veenstra AP, Monzel L, Baksi A, et al. Ultrafast intersystem crossing in isolated $Ag_{29}(BDT)_{123}$- probed by time-resolved pump-probe photoelectron spectroscopy. *J Phys Chem Lett*. 2020;11:2675–2681.
80. Gruene P, Butschke B, Lyon JT, Rayner DM, Fielicke A. Far-IR spectra of small neutral gold clusters in the gas phase. *Z Phys Chem (Muenchen, Ger)*. 2014;228:337–350.
81. Gruene P, Rayner DM, Redlich B, et al. Structures of Neutral Au_7, Au_{19}, and Au_{20} Clusters in the Gas Phase. *Science (Washington, DC, US)*. 2008;321:674–676.
82. Woodham AP, Meijer G, Fielicke A. Charge separation promoted activation of molecular oxygen by neutral gold clusters. *J Am Chem Soc*. 2013;135:1727–1730.
83. Goldsmith BR, Florian J, Liu J-X, et al. Two-to-three dimensional transition in neutral gold clusters: the crucial role of van der Waals interactions and temperature. *Phys Rev Mater*. 2019;3.

CHAPTER

12

Structure by single crystal X-ray diffraction

Mohammad Bodiuzzaman[a] *and Thalappil Pradeep*[b]

[a]Postdoctoral Fellow Functional Nanomaterials Lab (FuNL) KAUST Catalysis Center (KCC) King Abdullah University of Science and Technology (KAUST), Thuwal, Kingdom of Saudi Arabia [b]Deepak Parekh Institute Chair Professor and Professor of Chemistry, Department of Chemistry, Indian Institute of Technology Madras, Chennai, India

12.1 Introduction

Atomic precision in nanoscience has applications in various fields.[1,2] Atomically precise nanoclusters (NCs) are a recent addition to the class of fascinating materials. NCs are composed of just a few to tens of metal atoms with a definite ligand shell, forming molecules of precise composition and having sizes similar to the Fermi wavelength of electrons. NCs have been utilized in areas ranging from electronics, catalysis, sensing to nanomedicine.[3–10] The massive excitement in precise materials is that it is possible to manipulate their properties with atomicity. In this chapter we focus on the developments of atomic structures of gold and silver NCs by single crystal X-ray diffraction (SC-XRD).

12.1.1 Importance of crystal structures

Single-crystal X-ray crystallography is a widely accepted method for structural analysis. To quote Francis Crick, "If you want to understand the function, study structure." Single-crystal X-ray (SC-XRD) is essential to understand the complete structure of NCs which confirms the precision of the materials.[11] Crystal structure determination enables us to understand the cluster core and ligand orientation. It is of great significance for analyzing their structural evolution, ligand metal interface, reactivities, unique properties among others.

12.1.2 Challenges

Single crystals are the "holy grail" of cluster science. Single crystal X-ray methods require good quality single crystals. Here, good quality crystals mean which give enough diffraction

Atomically Precise Metal Nanoclusters.
DOI: https://doi.org/10.1016/B978-0-323-90879-5.00023-8

spots to resolve the structure. All crystals do not diffract as they are not ordered sufficiently in the resolution of atomic scale. There are a couple of major reasons for the limited success in crystallizing NCs.

(i) The limitation in synthetic methods and lack of purity of materials are the principal reasons for not getting good quality single crystals. These are discussed in detail in cluster assembled solids chapter.
(ii) Due to high complexity of the surface structure and dynamic nature of polyatomic structures inhibits the ordered packing often resulting in amorphous materials.

12.1.3 Developments

The development of new synthetic methods has set the approach to design new atomically precise monodisperse NCs. Such highly pure NCs have enabled crystallization and elucidation of their total crystal structures. Recently, several structures of metal NCs have been resolved by X-ray diffraction, and numerous issues have been addressed. Kornberg et al., in 2007, provided breakthrough by crystallizing $Au_{102}(SR)_{44}$, the first-ever crystal of a thiolated protected NC.[12] This was followed by reports on icosahedral $Au_{25}(PET)_{18}$ and bi-icosahedral $Au_{38}(PET)_{24}$ in 2008 and 2010, respectively.[13,14] Thereafter, structures of many noble metal NCs have been solved. In the subsequent discussions, we will present crystallization methods and different structural aspects of NCs.

12.2 Crystallization

It is a method of precipitation in which crystals are formed by precipitating from a solution or deposition from gas. Crystallization has two important steps. The first one is the process of nucleation, the emergence of a crystalline phase in the supersaturated solvent. The second one is crystal growth, in which the size of particles increases and leads to a crystal. Common methods of crystallization are described below.

12.2.1 Slow evaporation

It is the easiest method for samples that are not sensitive to air. Here, a concentrated solution (close to saturation) is dissolved in a solvent then allowed to evaporate in a vial that has pores in the cap. The size of the aperture depends on the nature of the solvent used. Another variation in this method is to keep the vial inclined so that some of the crystals can grow on the inner surface of the vial. This helps to remove sensitive crystals without any damage. Crystals of Ag_{16} and Ag_{17} were grown by this method.[15]

12.2.2 Solvent diffusion

This method is suitable where milligram quantities of samples are available. A less dense solvent is carefully added to the top of the sample solution to form a distinct layer. A good solvent combination is $CHCl_3$ or CH_2Cl_2 with hexane or toluene where the sample is soluble in

$CHCl_3$ or CH_2Cl_2 and almost insoluble in the hexane or toluene. Crystals grow at the interface of the two solvents. $Ag_{25}(SPhMe_2)_{18}$ was crystallized by this method.[16]

12.2.3 Vapor diffusion

This method is similar to the previous method of solvent diffusion and also applicable to milligram quantities of sample. In this case the sample is dissolved in a good solvent in a small sample tube. Then, it is placed in a larger tube containing a bad solvent and this tube is then sealed. Good solvent dissolves the materials and bad solvent works as a precipitant. The method works best if the good solvent is less volatile and thus predominately the bad solvent diffuses into the sample solution. Polymorphic crystals of $Ag_{29}BDT_{12}(PPh_3)$ were obtained by this method.[17]

12.2.4 Solvothermal

Solvothermal reaction is evolving as an important strategy for crystallization of metal NCs. It is performed in a sealed system at elevated temperature and pressure to initiate a chemical transformation. It is applied to aqueous and nonaqueous solvents. In this method, precursors are mixed together in a solvent and sealed in autoclave. Then, autoclave is heated at higher temperature and as it is sealed the pressure of the mixture increases which helps in crystallization. Crystallization depends on nature of the precursors and solvent system. Single crystals of $Cd_8S_4(SPhMe\text{-}3)_{14}$ and $Cd_{17}S_4(SPhMe\text{-}3)_{26}$ were obtained by this method.[18]

12.3 Basic core structural building blocks

12.3.1 Face-centered cubic structures

An important question is if the face-centered cube (fcc) structure intrinsic to bulk gold can be preserved in the case of very small nanoparticles. The unit cell of a fcc consists of 14 atoms, 8 corners, and 6 face centers. However, this Au_{14} structure is not observed so far, its modified form, that is, cuboctahedron is reported. It retains all symmetry elements of fcc, as illustrated in Fig. 12.1A. An FCC unit cell can be seen as it is made of three layers containing five and four atoms in an alternate manner (5+4+5). Jin et al. have shown the transformation of an FCC unit cell to a cuboctahedron by simple operations.[2] Firstly, an Au_{14} structure (5+4+5) is extended to another layer of 4 atoms (5+4+5+4) and the left layer is removed. These operations connecting Au–Au bonds will convert noncentered Au_{14} to a centered Au_{13} framework (Fig. 12.1A). This framework is called as cuboctahedron. It exhibits cubic close packing (ccp) and C_2, C_3, and C_4 rotational axes of symmetry. It contains eight triangular facets and six square facets. Furthermore, if it is viewed from C_3 axis, a sequence of 3:7:3 layer is visible. This sequence is similar to the a/b/c stacking of fcc structures.

$Au_{36}(t\text{-}BuSPh)_{24}$ was the first report of an fcc-structured gold NC.[19] The crystal structure anatomy showed the presence of an Au_{28} FCC kernel which exhibited a/b/c stacking (Fig. 12.1B). The appearance of fcc kernel in a small size regime was unexpected, and a substantial finding was that the stabilizing ligand was key to protecting the NC. Cuboctahedra arrangement was observed in the $[Au_{23}(SC_6H_3)_{16}]$ NC.[20] It consisted of a cuboctahedral kernel protected by two trimeric $Au_3(SR)_4$ staples with one on the top and the other at the bottom.

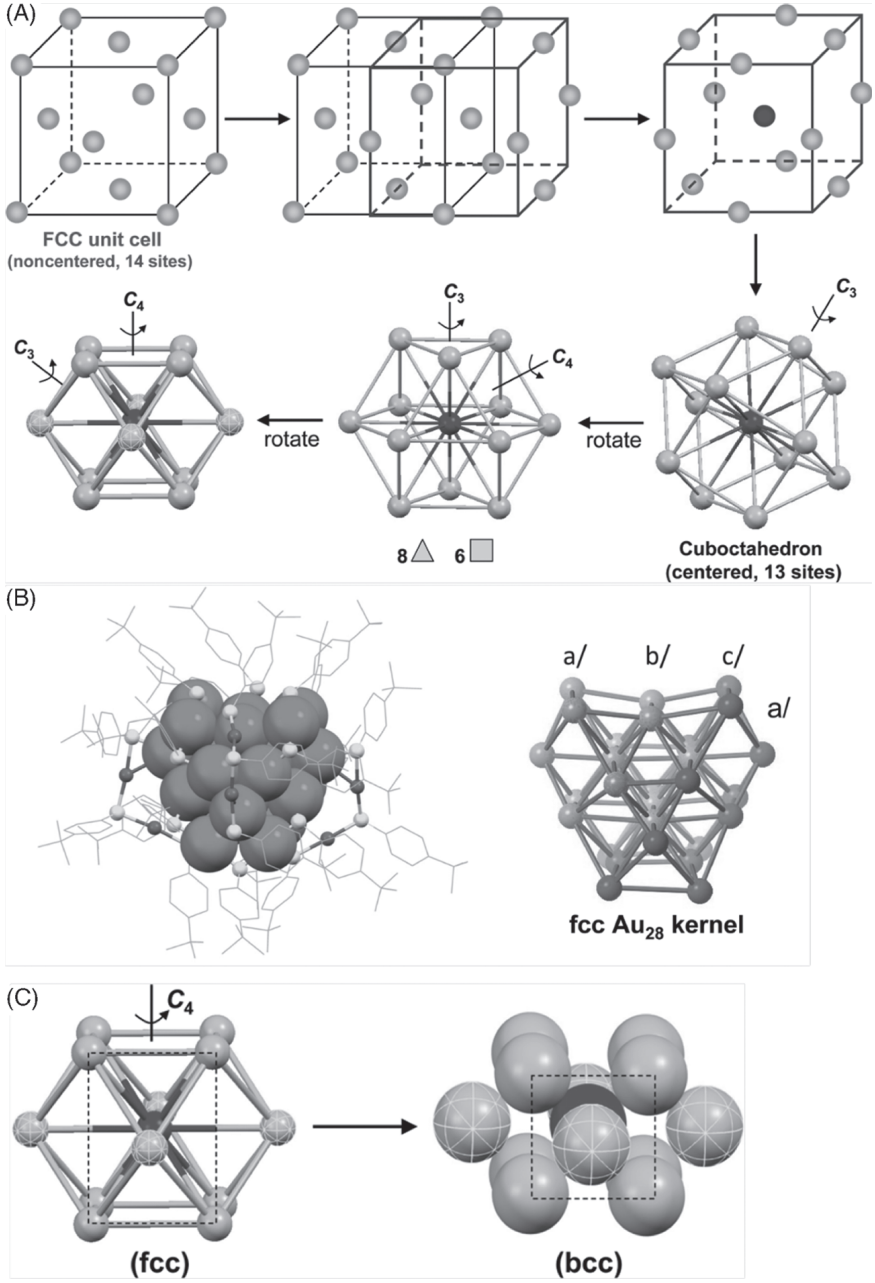

FIGURE 12.1 (A) Transformation of fcc unit cell to cuboctahedron by extending a half-cell toward right and dropping the left half-cell. (B) Left side presents the crystal structure of $Au_{36}(SPh\text{-}tBu)_{24}$. Right side shows an Au_{28} kernel structure with a/b/c stacking of gold atoms. (C) Construction of a bcc structure from an fcc structure by compression along C_4 axis. The dashed rectangular framework on the left side transforms into a square on right side. Marked atoms become body center of bcc structure. Adapted from references[2,19] with permission. Copyright {2016} American Chemical Society. Copyright {2012} WILEY VCH.

12.3.2 Body-centered cubic structures

Jin group reported $Au_{38}S_2(S\text{-}Adm)_{20}$ NC which exhibits a bcc arrangement.[21] This framework is different from the fcc structure of gold. Transformation of an fcc to bcc structure is shown in Fig. 12.1C. This occurs via compression of the structure along C_4 axis, and the marked rectangle became a square which resulted in the formation of a bcc. Seemingly, the compressing force is generated by supramolecular interactions in the ligand shell.

12.3.3 Hexagonal structures

HCP arrangement is quite common in gold nanoparticles, however, in the case of NCs it was reported in 2015.[22] $Au_{18}(HT)_{14}$ (HT = hexanethiolate) was reported to have Au_9 kernel which displayed an a/b/a structure.[22,23] Other examples of HCP structures are phosphine protected Au_{39} NC.[24]

12.3.4 Icosahedron

It is the most commonly reported structure of NC. Icosahedron can be constructed from cuboctahedron. Cuboctahedron is composed of three layers of gold like—Au_3, Au_6, and Au_3. Contraction of the middle layer results in a chair like conformation of cyclohexane.[2] This compression removes six square faces and generates twelve triangular faces. A comparison of volume and surface area of icosahedra and cuboctahedra is presented in Fig. 12.2A. In terms of stability of both structures, I_h is more stable as it is having a greater number of Au–Au bonds at the periphery. Jin group has demonstrated the conversion of a cuboctahedron to an icosahedron structure by doping.[27] One of the well-known NCs, $Au_{25}(SR)_{18}$, was observed to possess a centered icosahedral core.[26] The Au atom in the center of the icosahedra has a coordination number of 12 and this atom is not bound to any sulfur atoms of the ligand shell. Each of 12 gold atoms of the icosahedral core is bound to one of the terminal sulfur of Au_2SR_3 staples (Fig. 12.2B). There are six such staples present in the structure and hence, $Au_{25}(SR)_{18}$ can alternatively be written as $Au@Au_{12}[Au_2SR_3]_6$. Zhu group reported that Au_{60} consists of five centered icosahedral Au_{13}, and Au_{13} building blocks are adjoined by sharing a vertex atom (i.e., five vertex gold atoms in total $5 \times 13-5=60$).[28]

12.3.5 Tetrahedron

Earlier calculations predicted Au_4 as building block for several NCs. In $Au_{20}(SR)_{16}$ structure (R = Ph-tBu), a bi-tetrahedral Au_7 framework was observed. Here, two Au_4 building blocks were connected by a shared vertex. Another bi-tetrahedral structure in an antiprismatic manner, Au_8, was seen in $Au_{24}(SR)_{20}$ nanoNC.[29] Later, perfect tetrahedral structures were solved for Au_{40} and Au_{52} NCs and will be discussed later.

12.3.6 Decahedron

The pioneering work of Kornberg and coworkers resolved the structure of $Au_{102}(MBA)_{44}$ and gold-thiolate layer of $Au_{23}(MBA)_{44}$, where Au atoms are in Au(I) oxidation state. $Au_{23}(MBA)_{44}$ is composed of 19 units of $Au(SR)_2$ and 2 units of $Au_2(SR)_3$. Later, a bigger NC, Au_{130} was observed with decahedral structure with a perfect 5-fold symmetry.[30]

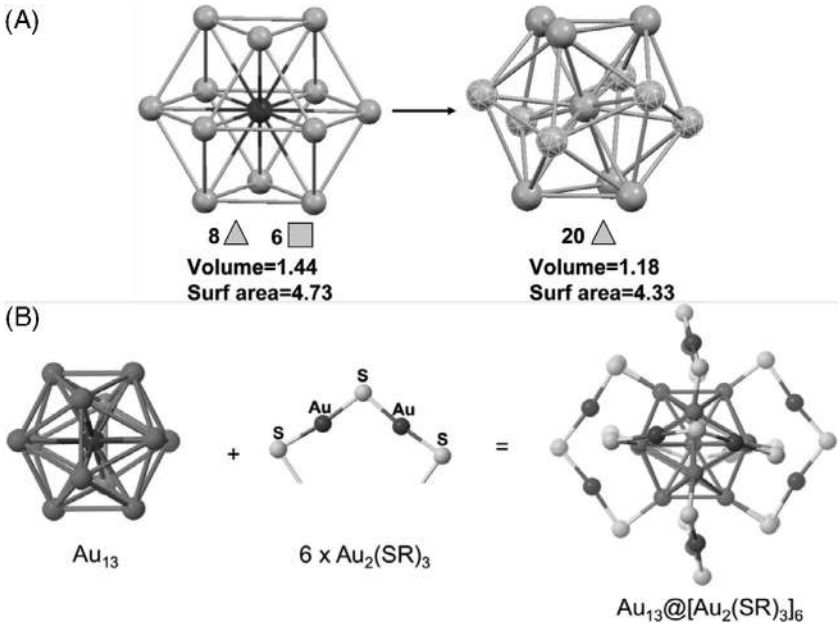

FIGURE 12.2 (A) Transformation of a cuboctahedron to an icosahedron. Cuboctahedron is a mixture of square and triangular facets, whereas icosahedron contains only triangular facets. Volume and surface area of both are shown below for respective structures. (B) Structural dissection of $Au_{25}(SR)_{18}$ NC. Au_{13} is a centered icosahedron and is protected by six staple units to form the complete structure. Adapted from references[25,26] with permission. Copyright {2008} American Chemical Society.

12.4 Growth of building blocks

As discussed in the previous section, among basic structural building blocks of the kernel, the Au_{13} cuboctahedron, icosahedron, and decahedron are predominant. In the subsequent discussion, we have mentioned the modes that are frequently observed in crystal structures. It is worth noting that the following discussions are based on crystal structures and these growth modes might not be the same particle growth mechanism observed in the solution phase.

12.4.1 Fusion

This growth occurs in a series of rod-shaped NCs namely, Au_{13}, Au_{25}, and Au_{37}.[14,31,32] Here, icosahedral units are connected by sharing of vertex to form rod-shaped NCs. It is worth noting that Au_{25} NC exhibit two structures, namely, monoicosahedra (discussed in Fig. 12.2B), and bi-icosahedra (Fig. 12.3B). Structure of tri-icosahedral $[Au_{37}(PH_3)_{10}(SCH_3)_{10}Cl_2]$ was predicted earlier by Takeshi group.[33] Au_{38} has an Au_{23} kernel composed of two Au_{13} icosahedra. Two icosahedra are fused by sharing an Au_3 face, as shown in Fig. 12.3A.

12.4.2 Layer by layer

An interesting growth along [001] direction was observed in fcc NCs, having composition, $Au_{8n+4}(TBBT)_{4n+4}$ (TBBT = *t*-butyl benzenethiol). Here, *n* varies from 3 to 6, denoting the

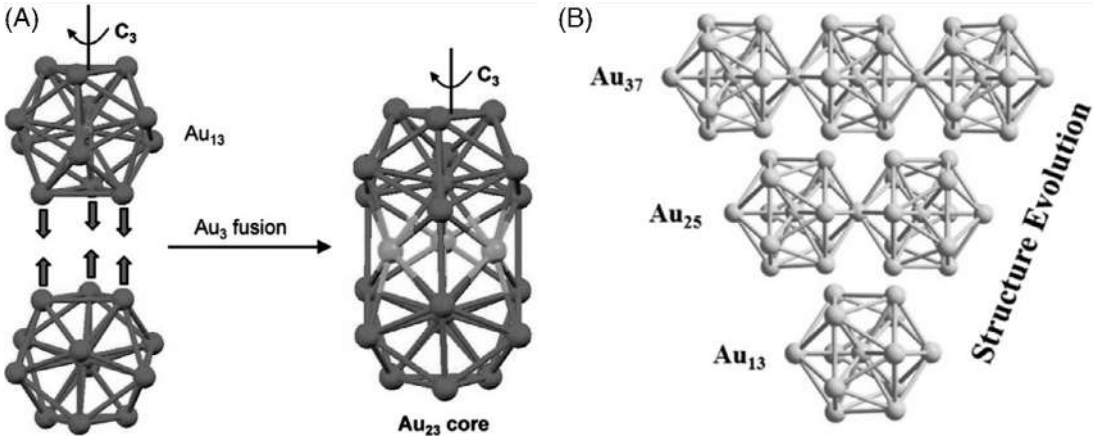

FIGURE 12.3 (A) Formation of Au_{23} core by fusion of Au_3 units of icosahedra in Au_{38} NCs. Shared Au_3 faces are shown by arrows. (B) Assembly of icosahedral building blocks to form rod like NCs. Structural evolution from mono-icosahedral Au_{13} to tri-icosahedral Au_{37} NCs. Adapted with permission from references.[31,32,34] Copyright {2011} and {2015} American Chemical Society.

number of layers along [001] direction with a constant $Au_8(TBBT)_4$ spacing between successive layers. This family of NCs includes growth of NCs from $Au_{28}(TBBT)_{20}$ to $Au_{52}(TBBT)_{32}$. $Au_{52}(TBBT)_{32}$ (i.e., $n = 6$) has Au_{48} core consisting of six 4×4 fcc layers along the [001] direction.

12.5 Surface structure

Study of NCs offers an opportunity to explore surface structure at the atomic level. The surface structure though an important aspect, was the most difficult to characterize in the case of NCs. The interface of metal-thiolate has been studied for more than two decades,[35,36] but the atomic arrangements of Self Assembled Monolayer (SAM) is not understood completely. The success at structure elucidation of NCs gives atomic-level insights of structure of SAM.[37] The surfaces of noble metal NCs are mostly covered by oligomeric $M_x(SR)_{x+1}$ motifs. Generally, higher the number of the atomicity of NCs, tendency to form smaller chain length, as in - $Au_{102}(SR)_{44}$, $Au_{130}(SR)_{50}$ - monomeric staple units (–SR–Au–SR) have been observed.[12,30] Smaller NCs are protected by long staples as in $Au_{25}(SR)_{18}$, dimeric staple motifs (–SR–Au–SR–Au–SR–) are present. Here, the bond angle of –S–Au–S is 180° and Au-S-Au is close to 100°. Tri, tetra, and pentameric staple motifs are also identified in $Au_{23}(SR)_{16}$, $Au_{18}(SR)_{14}$, and $Au_{24}(SeR)_{20}$, respectively.[20,22,38] In $Au_{20}(TBBT)_{16}$, staple motifs coil to form an eight-membered ring of AuSR. This macrocyclic ring covers the Au_7 inner core.[39] Jiang et al., introduced the idea of "staple fitness" to understand the surface structures. This concept tells us that when the staple motifs protect a high-symmetry core, they tend to find the most stable configuration. It explains staple structures of $Au_{25}(SR)_{18}$ and $Au_{38}(SR)_{24}$ and was able to interpret other small $Au_n(SR)_m$ sizes.[40] A summary of surface structures is presented in Fig. 12.4.

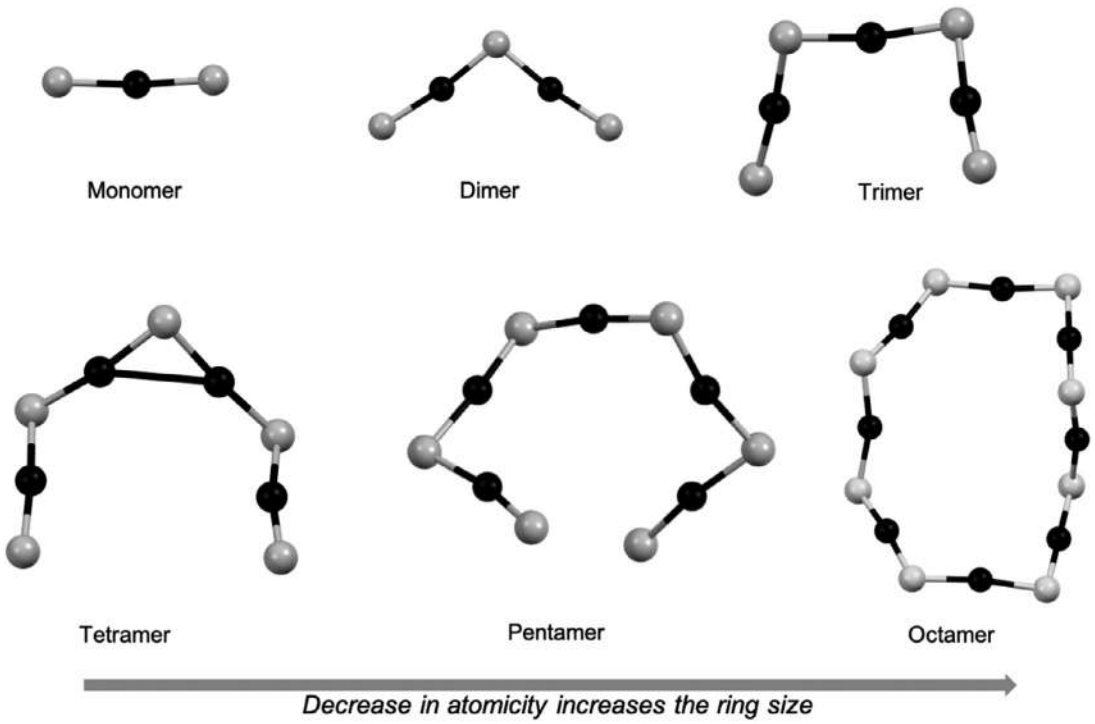

FIGURE 12.4 Structures of surface protecting motifs in NCs. As the atomicity of nanoclusters decreases, longer is the motif $Au_x(SR)_{x+1}$ structure, monomer evolves into an octameric ring. This octameric macrocycle was observed in the case of $Au_{20}(SR)_{16}$ NCs.

12.6 Crystal structures of archetypal nanoclusters

12.6.1 Gold nanoclusters

Vapor diffusion method is commonly employed to crystallize gold NCs. The first report on SC-XRD of a thiolate protected NC, Au_{102}(p-MBA)$_{44}$, was made in 2007.[12] Structural analysis showed that the NCs have a truncated Au_{49} kernel passivated by a unit of 15-atoms each the at top and bottom resulting in the formation Au_{79} kernel. This kernel is surrounded by five monomeric staples at the top and bottom, along with nine monomers and two dimeric staples at the waist. Thirteen gold atoms are arranged such that it destroys the fivefold symmetry of Au_{102}, imparting chirality to the molecule.

Research groups led by Murray and Jin solved the structure of $Au_{25}(SC_2H_4Ph)_{18}$, composed of an icosahedral core protected with six –SR-Au-SR-Au-SR- staple units in 2008. Later in 2010, crystal structure of $Au_{38}(SC_2H_4Ph)_{24}$ was reported by Qian et al.[14] It is consisted of a bi-icosahedral inner core with three -SR-Au-SR- and six –SR-Au-SR-Au-SR- staple units. This structure was predicted earlier, in 2008 from density functional theory.

Later, Jin et al. reported Au_{40} and Au_{52} NCs with high level of structural complexity.[41] Here, gold atoms in the NC first segregated into four-atom tetrahedral units which then

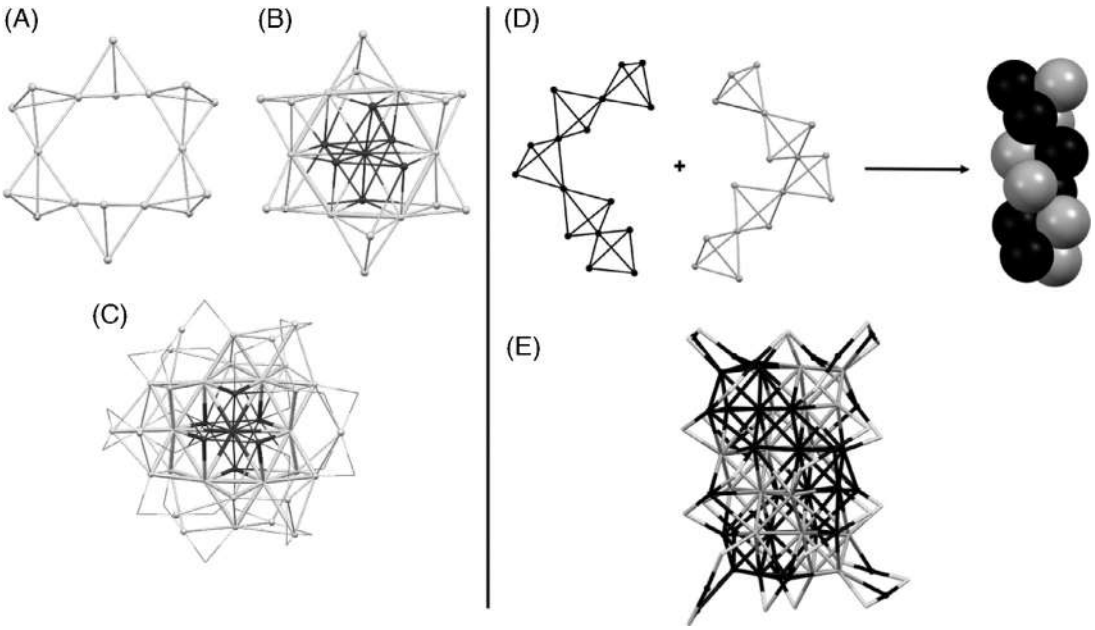

FIGURE 12.5 (A) Six tetrahedral units are connected to each other to form a hexagon like benzene. (B) Au_7 bi-tetrahedron is surrounded by five tetrahedral units to form Au_{25} kernel. (C) Au_{25} kernel is protected by six AuS_2 and three Au_3S_4 units to give $Au_{40}S_{24}$ structure. (D) Five pentatetrahedral units are connected to form a double stranded DNA like kernel of Au_{32}. (E) Au_{32} kernel is protected by four AuS_2 and eight Au_2S_3 units to create $Au_{52}S_{32}$.

coiled into a Kekulé-like ring in the Au_{40} NC and a DNA-like double helix in Au_{52}. Structural analysis of Au_{40} shows a kernel of 25 atom (Fig. 12.5B) and is protected by nine staples (Fig. 12.5C). It is important to note that kernel gold atoms form eight tetrahedral Au_4 building blocks, as indicated by the different Au–Au bond distances. Out of eight tetrahedral units, two constitute central antiprism, and remaining six units assemble to form a Kekulé-like ring, wherein tetrahedra are arranged alternatively in up-and-down manner. The ring is protected by six units of –SR–Au–SR– staples and the central antiprism is surrounded by three –SR–Au–SR–Au-SR-Au-SR– (Au_3SR_4) units. Similar partitions of tetrahedral units to form artistic superstructures are seen in Au_{52} NCs. These instances manifest a generality of molecular complexity in NCs. Anatomy of Au_{52} displays a kernel of 32 gold atoms divided into ten tetrahedral units. These units are brought together to form like a double-stranded DNA (Fig. 12.5D). The double helix is surrounded by eight dimeric Au_2SR_3 and four monomeric $AuSR_2$ staples.

Obtaining single crystal structure of Au_{144} was quite challenging. It was identified by mass spectrometry long ago (in 2001) and the structure was predicted in 2009. Several groups tried to crystallize these NCs, however, good quality crystals required for structure determination were not available. Finally, Jin and Wu provided the structure of the long pursued material.[42] Crystal structure showed that the crystal of $Au_{144}(SCH_2Ph)_{60}$ is of trigonal crystal family and belongs to the space group of *P*-31*c*. Authors have mentioned the role of ligand and inter and intraparticle interactions are crucial in the growth of good quality crystals. Au_{144}

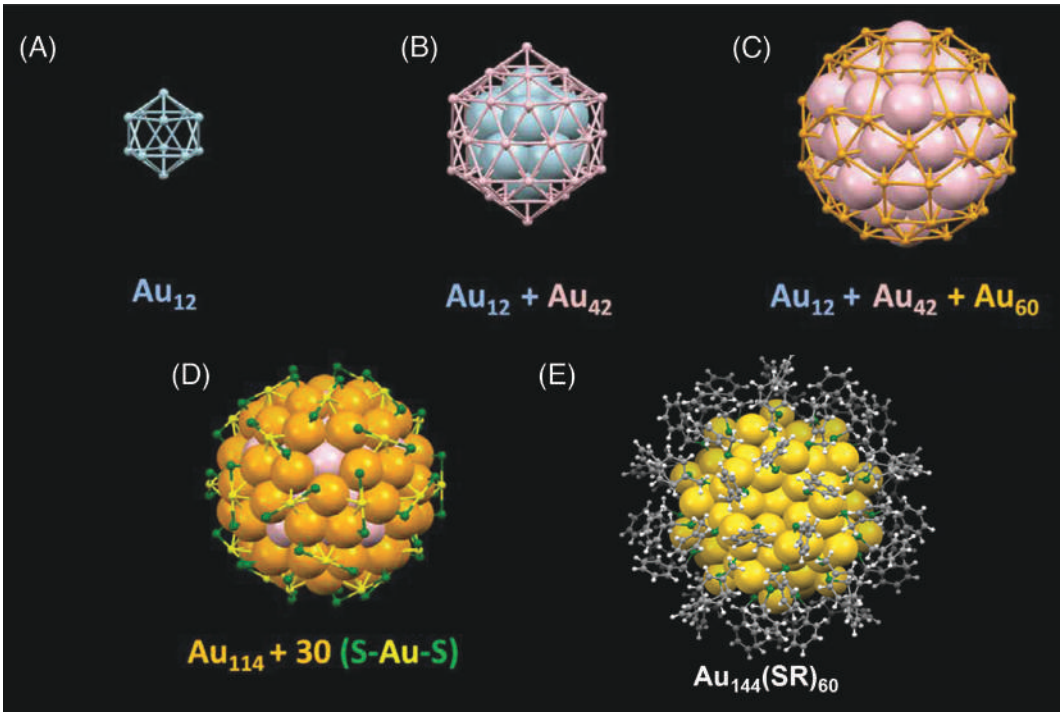

FIGURE 12.6 Structural anatomy of $Au_{144}(SCH_2Ph)_{60}$. (A) Inner icosahedral core of 12 gold atoms. (B) Kernel structure of Au_{54} (Au_{12} + Au_{42}). Au_{12} icosahedron is shown in space fill model. Au_{42} core is presented in ball-stick model. (C) Structure of Au_{114} (Au_{54} + Au_{60}) kernel. Au_{60} is presented in ball-stick model and is called rhombicosidodecahedron shell. (D) Au_{114} is protected by thirty units of $AuSR_2$. (E) Full structure of $Au_{144}(SCH_2Ph)_{60}$.

exhibits a highly symmetric packing similar to Au_{60}. The entire NC is 2.9 nm, which is close to previous studies. We note that as per literature, large NCs often form triclinic or monoclinic crystals. Structural analysis revealed that it contains two enantiomers in the unit cell as a racemic pair. Au_{144} exhibits 6 C_5, 10 C_3, and 15 C_2 rotational symmetry axes. It is close to the structure of Pd_{145} reported by Dahl group in 2000.[43] However, there are differences between the two systems: (1) the vacancy at the central position makes the metal count 144 in the case of Au_{144} from 145 in the case of Pd_{145} and (2) the chirality at the outer shell in Au_{144}. The structure of Au_{144} was predicted by Whetten and Lopez-Lozano et al., which showed a remarkable agreement with experimentally derived crystal structure.[44] Structural analysis showed that the inner core is a hollow icosahedron. This was the first experimentally observed hollow icosahedron in thiolate-protected gold NCs (Fig. 12.6A). However, a similar hollow icosahedron was reported earlier for silver and alloy NCs.[45] The average bond length in hollow icosahedra is 2.7 Å, much shorter than that of other reported gold NCs. The second shell is composed of 42 Au atoms to form a Au_{54} icosahedral structure (Fig. 12.6B). This structure is encapsulated by a 60-atom shell to form rhombicosidodecahedron (Fig. 12.6C), which was seen earlier in case of Pd_{145}. This architecture contains twelve pentagons and twenty triangular

faces. The vertices of these faces form thirty parallelograms which are protected by thirty $AuSR_2$ staples to form $Au_{144}SR_{60}$ (Au_{12}+Au_{42}+Au_{60}+30$AuSR_2$) (Fig. 12.6C and D).

Wang and coworker reported the crystal structures of alkyne-protected gold NCs.[46,47] They reported crystal structures of $[Au_{19}L_9(PPR)_3]^{2+}$, $[Au_{23}L_9(PR)_6]^{2+}$, and $[Au_{24}L_{14}(PR)_4]^{2+}$ NCs (where L represents C_2Ph). Similar to the thiol protected NCs, metal core is surrounded with alkynyl monomeric and dimeric staple motifs. In $[Au_{19}L_9(PPR)_3]^{2+}$, the Au_{13} icosahedra is protected by three V-shaped PhC_2-Au-C_2(Ph)-Au-C_2Ph motifs (Au_2L_3 motifs). This motif is identical to dimeric SR-Au-SR-Au-SR motif staples. In case of $[Au_{23}L_9(PR)_6]^{2+}$, the Au_{17} kernel is protected by three dimeric staple and six phosphine ligands.[46] A rod like structure is observed in $[Au_{24}L_{14}(PR)_4]^{2+}$, unlike the above two structures. Au_{22} kernel is protected with two monomeric staple units (PhC_2-Au-C_2Ph).[48] Alkynyl protected Au_{144} was reported by Lei et al.[49] Both the NCs have a similar structure of kernel but different surface structure, due to difference in ligand molecules. Alkynyl protected Au_{144} NC showed no icosahedral symmetry due to asymmetry in the ligand shell. Optical properties of both NCs are different. $Au_{144}L_{60}$ is a new material and was not observed earlier.

Large NC crystals nowadays can be studied by single-crystal diffraction. Measurements on some of the larger NCs were possible with synchrotron radiation. Here, we have presented structural aspects of a few NCs to get the essence of really large NCs. Crystal structure of large NCs explores the hierarchical structural complexities and their assembly. Jin group showed that NC self-assembly can display the same level of hierarchy, complexity, and accuracy as biomolecules. They crystallized a NC namely, $Au_{246}(MBT)_{80}$ having a diameter of 2.2 nm.[50] Single-crystal analysis resolved the packing of metals, ligands, and NCs. This study presents the role of ligands in assembling simple building units into complex structure. Dass group reported crystal structure of a plasmonic nanocrystal, $Au_{279}SR_{84}$.[51] It has a core-shell structure with a truncated octahedral core. The geometry of Au_{279} revealed the presence of magic number of shells, Au@Au_{12}@Au_{42}@Au_{92}@Au_{54}. These shells were protected by six units of Au_2SR_3, eighteen $AuSR_2$, and 30 bridging ligands.

12.6.2 Silver nanoclusters

Crystallizing silver NCs was difficult compared to the gold NCs because of their reduced stability or higher reactivity, aerial oxidation, light sensitivity, and lesser purity. Most of the silver NCs were crystallized using liquid–liquid diffusion method. Nanfeng et al., reported phosphine and thiol, mixed ligand protected Ag_{14} NCs and the complete structure was determined by SCXRD.[52] Recently, benzene dithiol and carborane thiol protected Ag_{14} were reported. In all Ag_{14} structures, the basic core structure is cubic. It consists of an octahedral Ag_6^{4+} inner core surrounded by eight units of $[Ag^+(SC_6H_3F_2^-)_2PPh_3]$ in a tetrahedral fashion sharing one corner. It is worth noting that all thiolates are connected to three silver and no staple units are present, whereas staple units were common in gold NCs.

Successively, single crystal structures of other mixed ligand-protected NCs like Ag_{16} and Ag_{32} were also resolved.[53] Following these initial crystallization experiments of Ag NCs, single crystal structures of all thiol protected Ag_{44}(p-MBA)$_{30}$ and Ag_{44}(p-FTP)$_{30}$ were determined.[45,54] The composition of Ag_{44} NC was unknown till 2012, might be due to the lack of poor ionization of the molecular peak in the mass spectrum. In 2009 Bakr et al., reported a silver nanoparticle with multiple absorption peaks which was assigned as $[Ag_{44}(SR)_{30}]^{4-}$ from ESI

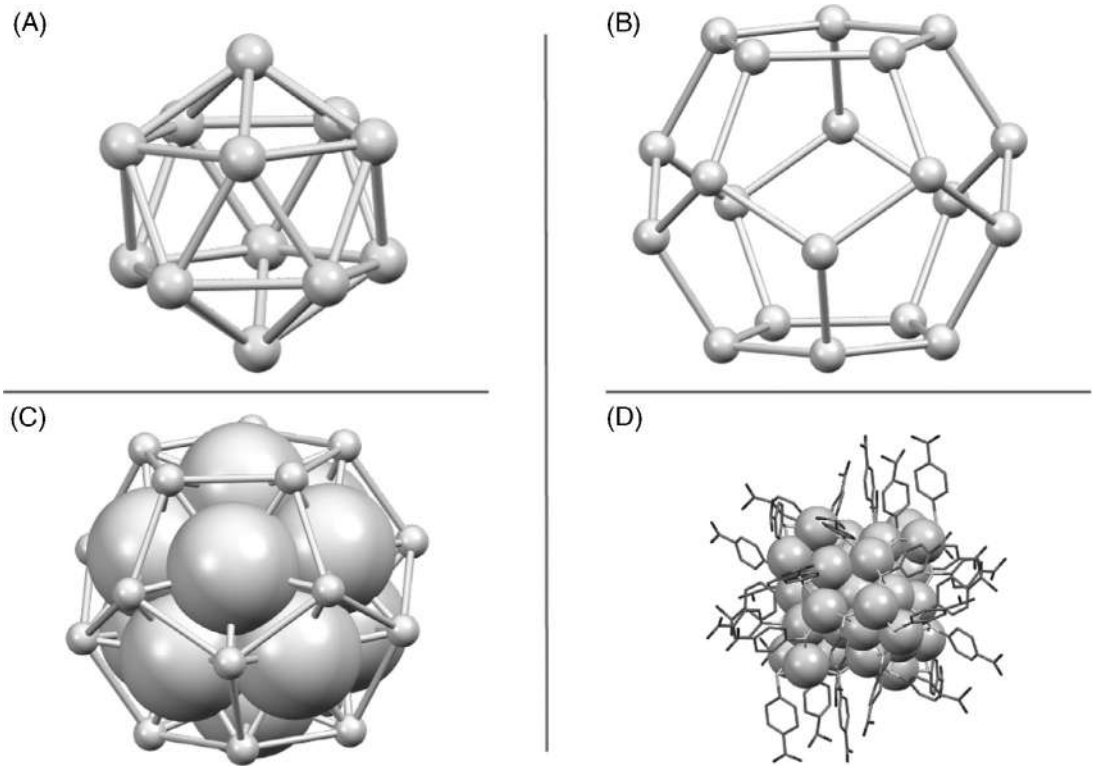

FIGURE 12.7 (A) Ag_{12} hollow icosahedron (B) Ag_{20} kernel structure. Shared pentagonal faces are connected to form this kernel. (C) Ligands and staples are removed to draw Ag_{32} (Ag_{12} + Ag_{20}) kernel structure. It's a union of Ag_{12} and Ag_{20}. (D) Full structure of Ag_{44}(p-MBA)$_{30}$ where metals are in space fill model and ligands are in stick model.

MS in 2012.[55] The structure of $Ag_{44}(FTP)_{30}$ NC is provided in Fig. 12.7D. This NC has a distinct hollow cage structure. It is made up of an icosahedral 12 Ag atom hollow cage enclosed by 20 Ag atoms forming a keplerate structure (Fig. 12.7A–C). This core is surrounded by the six $Ag_2(SR)_3$ staple motifs in an octahedral fashion. A 25 atom Ag NC with a similar structure as that of the $Au_{25}(SR)_{18}$, $Ag_{25}(DMBT)_{18}$ where DMBT is 2,4-dimethylbenzene thiol, was crystallized.[16] It has a centered icosahedral Ag_{13} core encapsulated by six dimeric staples of $Ag_2(SR)_3$.

Another well-known mixed ligand protected NC, namely $Ag_{29}(BDT)_{12}(TPP)_4$, (BDT = 1,3 benzenedithiol and TPP = triphenylphosphine) has an icosahedral core structure protected by $Ag_{16}S_{24}P_4$ unit (Fig. 12.8). SCXRD analysis reveals that the $[Ag_{29}(BDT)_{12}TPP)_4]^{3-}$ contains a centered icosahedral inner core (Fig. 12.8A), which is protected by four tetrahedral, AgS_3P and Ag_3S_6 motifs. Here, silver atoms of Ag_3S_6 motifs protect 13 Ag atoms of the centered icosahedral core to form tetrahedrally aligned prisms (Fig. 12.8B and C). Silver atoms of AgS_3P structure surround the Ag_{13} inner core at tetrahedral points.[17]

A box-like crystal structure of Ag_{67} was reported by Bakr group.[56] It is protected by a mixed ligand shell of thiolate ($SPhMe_2$) and phosphine (PPh_3). Crystal structure contains an inner core of Ag_{23}, covered by a box-like shell of $Ag_{44}S_{32}P_8$ (Fig. 12.9E and F). It was protected by tetrahedral AgS_3P and AgS_2 motifs. The shell Ag_{44} consists of an Ag_{36} cuboid-like box

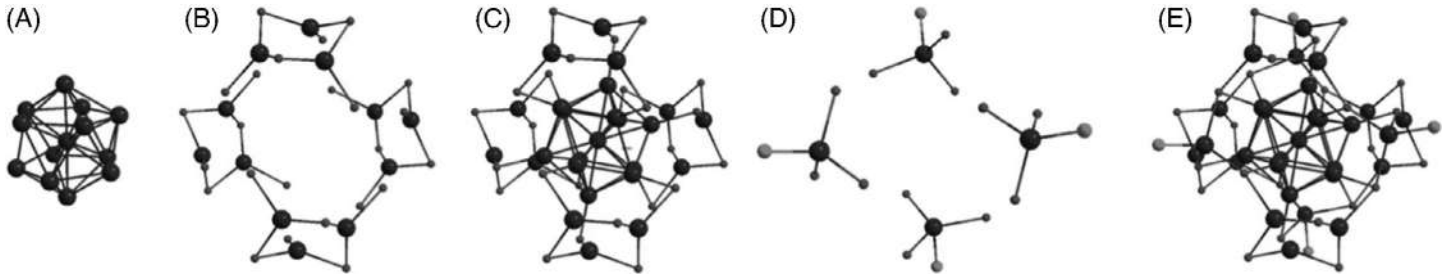

FIGURE 12.8 (A) Crystal structure of centered Ag_{13} icosahedron. (B) Cyclohexane like structure of the shell, Ag_3S_3. (C) Structure of $Ag_{25}S_{12}$. (D) Structure of tetrahedral AgS_3P. (E) Overall structure of $Ag_{29}S_{24}P_4$. Carbon and hydrogen atoms are omitted for simplicity. Adapted from ref.[17] with permission. Copyright {2015} American Chemical Society.

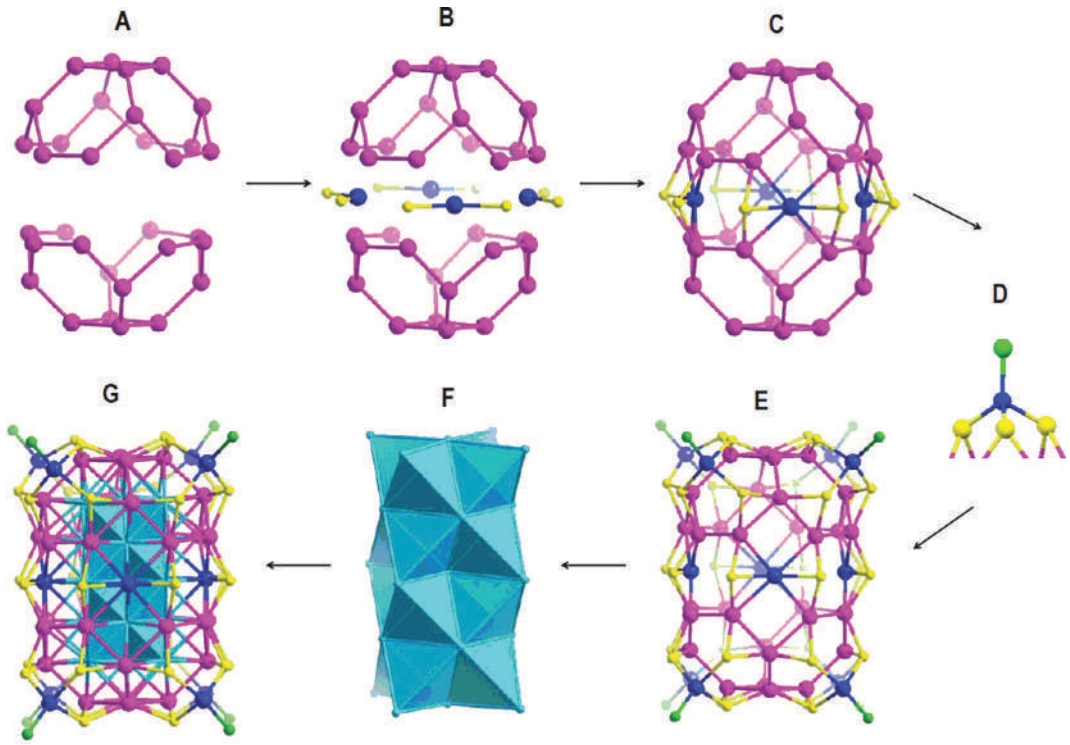

FIGURE 12.9 Construction of total structure of Ag_{67} NC. (A) Two Ag_{16} bowls. (B) Connection between two Ag_{16} bowls by four units of linear AgS_2 to create a closed $Ag_{36}S_8$, that is, (C). (D) Tetrahedral AgS_3P ligand motifs. (E) Eight AgS_3P motifs situated on eight hexagonal faces of C to form the structure of $Ag_{44}S_{32}P_8$. (F) Ag_{23} metal core. (G) Ag_{23} core encapsulated by E to form the total structure $Ag_{67}S_{32}P_8$. Adapted from ref.[56] with permission. Copyright {2016} American Chemical Society.

as shown in Fig. 12.9C. The box, Ag_{36} is made of planar and nonplanar hexagons and squares. The construction of Ag_{36} is shown in Fig. 12.9A and B. The inner core, Ag_{23} is composed of uncommon centered cuboctahedron, rather than centered icosahedron geometry. The NC was protected by tetrahedral AgS_3P and AgS_2 motifs (Fig. 12.9G).

A unique pair of silver nanoscale pieces, $Ag_{46}(SR)_{24}(PPh_3)_8$, and $Ag_{40}(SR)_{24}(PPh_3)_8$ was reported by our group.[57] This pair is composed of a common shell, $Ag_{32}S_{24}P_8$ akin to fullerenes. It comprises of Ag_{24} outer core, covered by 8 units of AgS_3P. The Ag_{24} outer core consists of shared hexagons. $Ag_{32}S_{24}P_8$ shell covers the fcc core, Ag_{14} and a simple cubic, Ag_8 to form Ag_{46} and Ag_{40} NCs, respectively.[57,58]

Zhu and Jin came up with the protocol for large-scale synthesis and crystallization of a large silver NC.[59] X-ray diffraction of the crystals was carried out to determine the composition of the material, which was found to be Ag_{146} with space group of $P\bar{1}$. Total structure of the NC resembles a "flying saucer" and diameters from top and side view are 2.9 nm and 1.4 nm, respectively (Fig. 12.10A). Structural investigation reveals that Ag_{146} contains a Ag_{51} core and $Ag_{95}S_{80}Br_2$ shell, as shown in Fig. 12.10B and 12.10C. Further structural anatomy of Ag_{146} revealed that the inner core Ag_{51} contains three shells. The first shell is made of Ag_7,

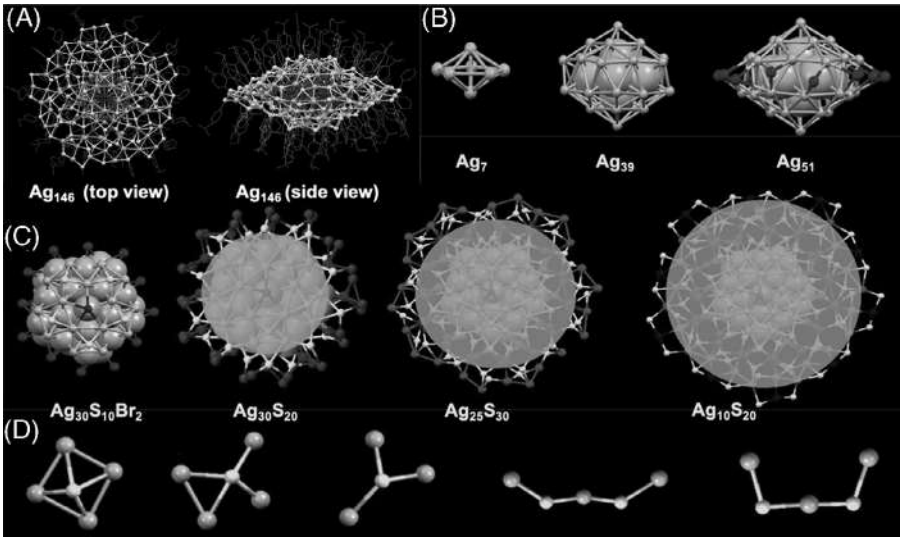

FIGURE 12.10 (A) Full structure of Ag_{146} at top and side view. (B) Core structures of Ag_7, Ag_{39}, and Ag_{51}. (C) Surface structures of Ag_{146}. Structures of $Ag_{30}S_{12}Br_2$, $Ag_{30}S_{20}$, $Ag_{25}S_{30}$, and $Ag_{10}S_{20}$. (D) Structure of various Ag-S staples. Adapted from ref.[59] with permission. Copyright {2018} American Chemical Society.

a decahedron having a D_{5h} symmetry. The average Ag–Ag bond distances of Ag_{146} is 2.78 Å. Ag_7 exhibited a pentagonal bipyramid where the pentagon is at waist of the decahedron. This is encapsulated by a shell of Ag_{32} and forms a quasi-decahedral structure of Ag_{39}. It is not a perfect decahedral, as pentagons at top and bottom are not at eclipsed position. Ag_{39} shell is capped by Ag_{12} ring to form Ag_{51} decahedron. The average Ag-Ag distances are larger than the other two shells due to the rotation of the pentagons in Ag_{39}. Surface structure of Ag_{146} can be divided by four parts, $Ag_{30}S_{10}Br_2$, $Ag_{30}S_{20}$, $Ag_{25}S_{30}$, and $Ag_{10}S_{20}$. It is protected by various Ag-S staples, like Ag_4S (square pyramid and tetrahedral), Ag_3S and Ag_3S_2, as shown in Fig. 12.10D.

Nanfeng group was able to capture the embryonic growth of fcc silver NCs. They have crystallized NCs, namely, $Ag_{38}(SR)_{26}(PR')_8$ and $Ag_{63}(SR)_{36}(PR')_8$ which resembled Nichol's cubes, as shown in Fig. 12.11.

Here, the main elementary unit in the cube, another fcc silver NC, Ag_{14} was reported by the same group.[60] Metal framework structure of Ag_{38} and Ag_{63} is comprised of four (2^2) $(2 \times 2 \times 1)$ and eight (2^3) $(2 \times 2 \times 2)$ cubes (the importance of powers of 2 is not apparent) of Ag_{14}, respectively. This is illustrated in Fig. 12.11. This kind of growth suggests that the nanosized molecular materials might be the beginning of an evolution of a series from 1, 2^2, 2^3 to n^3 of silver cubes.[60] Here, four fcc units in Ag_{38} forms a square with shared faces. The lengths of edges are 9.6 and 5.0 Å and average Ag-Ag bond distances are 3.51 Å, shorter than that in Ag_{14}. In Ag_{63}, eight fcc units form a cube with shared faces. It can be viewed as two Ag_{38} units merged with sharing of two faces. Here, the lengths of edges are 9.5 Å, shorter than Ag_{38}. The average Ag−Ag bond length in Ag_{63} is 3.0 Å, much shorter than that of basic building block (Ag_{14}) and Ag_{63}. Due to short Ag–Ag bond distance, the edge length in Ag_{63} is short.

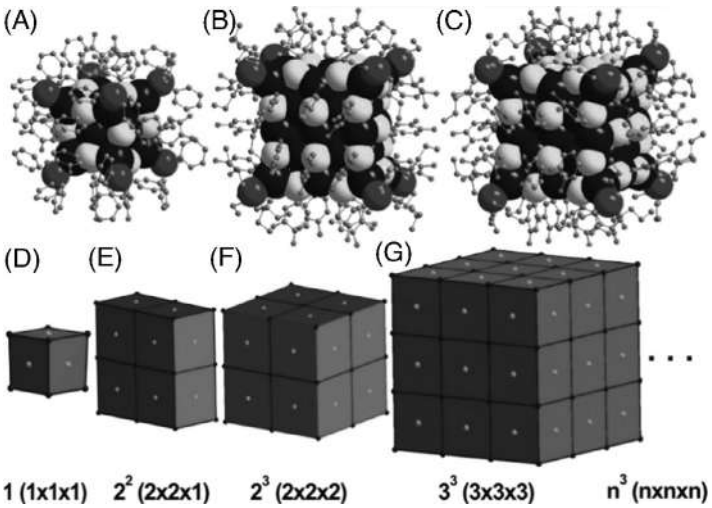

FIGURE 12.11 Crystal structures of silver NC cubes and their corresponding models: (A) $[Ag_{14}(SR)_{12}(PPh_3)_8]$ (1); (B) $[Ag_{38}(SR)_{26}(PR')_8]$ (2^2); (C) $[Ag_{63}(SPhF_2)_{36}(PR')_8]^+$ (2^3) NCs. (d–g) Ideal fcc packing growth series of 1 to 3^3 cubes. Number of metal cubes are shown below the model. Adapted from ref.[60] with permission. Copyright {2017} American Chemical Society.

Structures of these metal framework are shown in Fig. 12.11. A summary of crystal structures of silver and gold NCs up to 2020 are presented in Table 12.1.

12.7 Cocrystals

Cocrystallization is a process whereby two or more different species coexist in a lattice, through intermolecular interactions. It includes the study of bi-, tri-component crystalline materials along with their construction rules. Various intermolecular interactions in the assembled materials enrich the multicomponent solid with unique properties that are different from their individual constituents. Cocrystal engineering is significant for the formulation of functionalized materials like energetic materials and pharmaceuticals.[61–64] Cocrystallization of atomically precise NCs is a relatively new research area. It presents enormous possibilities in the field of atomically precise solids. Recently, we have summarized this in the Concept article.[65] There are five distinct classes of cocrystals of NCs. A summary of these classes is shown in Fig. 12.12. These are described below.

(1) Crystals consisting of different cores encapsulated by the same shell. A unique pair of Ag_{40} and Ag_{46} was cocrystallized with this strategy. Ag_{40} and Ag_{46} were composed of inner cores, simple cubic (Ag_8) and face-centered cubic (Ag_{14}), respectively. These inner cores are protected by a common shell of $Ag_{32}S_{24}P_8$.[57]

(2) The second kind of cocrystal is opposite to the kind (1). Here, NCs possessing the same core were protected by different shell. A large metallic core, $Ag_{19}@Ag_{52}@Ag_{45}@Ag_{89}$ (Ag_{205}) was covered by the Ag_6 and Ag_5 crystallized together.[66]

(3) Another way of creating cocrystals is via homometallic interparticle reactions.[15] In this case the precursor NCs, Ag_{12} and Ag_{18} were allowed to react at ambient temperature to form Ag_{16} and Ag_{17}. The single crystal structure showed the coexistence of both the NCs in the lattice. An interesting observation is that the concentration of Ag_{16} and Ag_{17} in the

TABLE 12.1 Crystal structures of gold and silver nanoclusters.

Number	Atomicity	Ligand	Composition	Reference
1	Au_2	Bis(diphenylphosphino)methane	$[Au(Ph_2P)_2CH]_2$	69
2	Au_4	Tri-phenylphosphine, iodide	$Au_4(\mu\text{-}I)_2(PPh_3)_4$	70
3	Au_5	Bis(diphenylphosphino)methane	$Au_5(dppmH)_3(dppm)$	71
4	Au_6	Tri-phenylphosphine	$Au_6(PPh_3)_6$	72,73
5	Au_7	Tri-phenylphosphine	$Au_7(PPh_3)_7$	74
6	Au_8	Tri-phenylphosphine	$[Au_8(PPh_3)_8](PF_6)_2$	75
7	Au_8	Tri-phenylphosphine	$[Au_8(PPh_3)_8](NO_3)_2$	76
8	Au_8	Bis(diphenylphosphino)methane	$Au_8(dppm)_4S_2$	77
9	Au_9	Tris-p-methylphenylphosphine, chloride/bromide	$Au_9(P(C_6H_4\text{-}p\text{-}Me)_3)_8X_3$	78
10	Au_9	Tris-p-methylphenylphosphine	$[Au_9(P(C_6H_4\text{-}p\text{-}Me)_3)_8]\ [BF_4]_3$	79
11	Au_{10}	Dicyclohexylphenylphosphine, chloride	$[Au_{10}Cl_3(PCy_2Ph)_6](NO_3)$	80
12	Au_{11}	Tri-phenylphosphine	$Au_{11}(PPh_3)_{10}(SCN)_3$	81
13	Au_{11}	Tris-p-chlorophenylphophi ne, iodide	$Au_{11}I_3[P(C_6H_4\text{-}p\text{-}Cl)_3]_7$	82
14	Au_{11}	Tris-p-flurophenylphophine, iodide	$Au_{11}I_3[P(C_6H_4\text{-}p\text{-}F)_3]_7$	83
15	Au_{11}	N-heterocyclic carbene	$Au_{11}(PPh_3)_6(NHC)_2Cl_2$	84
16	Au_{11}	Tri-phenylphosphine, iodide	$Au_{11}(PPh_3)_7I_3$	85
17	Au_{11}	Bisphenyl ether	$Au_{11}(DPEphos)_4Cl_2$	86
18	Au_{11}	4,5-Bis(diphenylphosphino)-9,9-dimethylxanthene	$Au11(Xantphos)_4Cl_2$	86
19	Au_{13}	Dimethylphenylphosphine, chloride	$Au_{l3}(PMe_2Ph)_{10}Cl_2$	87,88
20	Au_{13}	Bis(diphenylphosphino)methane	$Au_{13}(dppm)_6$	77
21	Au_{13}	Bis-N-heterocyclic Carbene	$Au_{13}(bisNHC)_5Cl_2$	87
22	Au_{14}	Tri-phenylphosphine, nitrate	$Au_{14}(PPh_3)_8(NO_3)_4$	89
23	Au_{18}	Cyclohexylthiol	$Au_{18}(SC_6H_{11})_{14}$	23
24	Au_{19}	N,N-bis(diphenylphosphino)amine), Phenylalkyne	$Au_{19}(PhC{\equiv}C)_9(Hdppa)_3$	46
25	Au_{20}	4-*t*-butylbenzenethiol	$Au_{20}(TBBT)_{16}$	39
26	Au_{20}	tris(2-(diphenylphosphino)ethyl)phosphine	$Au_{20}(PP_3)_4$	90
27	Au_{20}	2-carboxythiophenol	$Au_{20}(PPh_3)_{12}H_2(2\text{-}COOH\text{-}PhS)$	91
28	Au_{21}	Adamentanethiol	$Au_{21}(S\text{-}Adm)_{15}$	92

(*continued on next page*)

TABLE 12.1 Crystal structures of gold and silver nanoclusters—cont'd

Number	Atomicity	Ligand	Composition	Reference
29	Au_{22}	1,8-bis-(diphenylphosphinooctane)	$Au_{22}(L)_6$	93
30	Au_{22}	3,3-Dimethyl-1-butyne	$Au_{22}(tBuC{\equiv}C)_{18}$	94
31	Au_{23}	2-mercaptobenzoxazole, tri-phenylphosphine	$Au_{23}(SR)_4(PPh_3)_9$	95
32	Au_{23}	Cyclohexanethiol	$Au_{23}(SC_6H_{11})_{16}$	20
33	Au_{23}	3,3-Dimethyl-1-butyne	$Au_{23}(C{\equiv}CBu^t)_{15}$	96
34	Au_{24}	Phenylethanethiol and tri-phenylphosphine	$Au_{24}(PPh_3)_{10}(SC_2H_4\ Ph)_5X_2$	29
35	Au_{24}	Benzeneselenol	$Au_{24}(SePh)_{20}$	38
36	Au_{24}	Adamentanethiol	$Au_{24}(SAdm)_{16}$	97
37	Au_{25}	Phenylethanethiol	$Au_{25}(SCH_2CH_2Ph)_{18}$	25
38	Au_{28}	4-tert-butylbenzenethiol	$Au_{28}(TBBT)_{20}$	98
39	Au_{30}	tert-butanethiol	$Au_{30}S(S\text{-}t\text{-}Bu)_{18}$	99
40	Au_{30}	1-adamantanethiolate	$Au_{30}(S\text{-}Adm)_{18}$	100
41	Au_{32}	Tri-*n*-butylphosphine	$Au_{32}(^nBu_3P)_{12}Cl_8$	101
42	Au_{36}	4-tert-butylbenzenethiol	$Au_{36}(SPh\text{-}tBu)_{24}$	19
43	Au_{36}	3,5-dimethylbenzenethiol	$Au_{36}(DMBT)_{24}$	102
44	Au_{38}	Phenylethanethiol	$Au_{38}(SCH_2CH_2Ph)_{24}$	34
45	Au_{39}	Tri-phenylphosphine	$Au_{39}Cl_6(Ph_3P)_{14}$	24
46	Au_{40}	o-methylbenzenethiol	$Au_{40}(o\text{-}MBT)_{24}$	41
47	Au_{40}	Ethynylbenzene	$Au_{40}(PhCC)_{20}(dppm)_4$	103
48	Au_{44}	Ethynylbenzene	$Au_{44}(PhC{\equiv}C)_{28}$	104
49	Au_{44}	4-tert-butylbenzenelthiol,	$Au_{44}(TBBT)_{28}$	105
50	Au_{44}	2,4-dimethylbenzenethiol	$Au_{44}(2,4\text{-}DMBT)_{26}$	106
51	Au_{48}	m-methylbenzenethiol	$Au_{48}(m\text{-}MBT)_{26}$	107
52	Au_{49}	2,4-dimethylbenzenethiol	$Au_{49}(2,4\text{-}DMBT)_{27}$	108
53	Au_{52}	4-tert-butylbenzenethiol	$Au_{52}(TBBT)_{32}$	41
54	Au_{56}	4-tert-butylbenzenethiol	$Au_{56}(TBBT)_{34}$	109
55	Au_{60}	Tri-phenylphosphine, benzeneselenol	$Au_{60}Se_2(Ph_3P)_{10(}SeR)_{15}$	28
56	Au_{67}	Phenylmethanethiol	$Au_{67}(SCH_2Ph)_{35}$	110
57	Au_{67}	3,5-bis(trifluoromethyl)-phenylacetylide	$Au_{67}L_{32}Cl_4$	111
58	Au_{92}	4-tert-butylbenzenethiol	$Au_{92}(TBBT)_{44}$	112

(*continued on next page*)

TABLE 12.1 Crystal structures of gold and silver nanoclusters—cont'd

Number	Atomicity	Ligand	Composition	Reference
59	Au_{102}	p-Mercaptobenzoic acid	$Au_{102}(p\text{-}MBA)_{44}$	12
60	Au_{103}	2-Thionaphthol	$Au_{103}S_2(S\text{-}Nap)_{41}$	113
61	Au_{106}	3,5-bis(trifluoromethyl)-phenylacetylide	$Au_{106}L_{40}Cl_{12}$	111
62	Au_{110}	4-(Trif luoromethyl)phenylacetylene	$Au_{110}(p\text{-}CF3C6H4C{\equiv}C)_{48}$	114
63	Au_{130}	4-methylbenzenethiol	$Au_{130}(p\text{-}MBT)_{50}$	30
64	Au_{133}	4-tert-butylbenzenethiol	$Au_{133}(SPh\text{-}tBu)_{52}$	115
65	Au_{144}	2-phenylethanethiol	$Au_{144}(SCH_2CH_2Ph)_{60}$	42
66	Au_{144}	2-fluorophenylacetylene	$Au_{144}(C{\equiv}CAr)_{60}$	49
67	Au_{146}	p-mercapto benzoic acid	$Au_{146}(p\text{-}MBA)_{57}$	116
68	Au_{246}	p-methylbenzenethiol	$Au_{246}(SR)_{80}$	50
69	Au_{279}	4-tert-butylbenzenethiolate	$Au_{279(}SPh\text{-}tBu)_{84}$	51
70	Ag_8	Perfluoroglutaric acid	$Ag_8(pfga)_6$	117
71	Ag_{14}	3,4-difluoro-benzenethioland Tri-phenylphosphine	$Ag_{14}(SC_6H_3F_2)_{12}(PPh_3)_8$	52
72	Ag_{16}	1,2-bis(diphenylphosphino)ethane, and 3,4-difluorothiophenol	$Ag_{16}(DPPE)_4(SC_6H_3F_2)_{14}$	53
73	Ag_{17}	tert-butylthiol, trifluoroacetate	$Ag_{17}(TBT)_8(TFA)_7(CH_3CN)_3Cl$	15
74	Ag_{21}	Dithiophosphate	$Ag_{21}[S_2P(OiPr)_2]_{12}$	118
75	Ag_{23}	2-phenyletahnethiol	$Ag_{23}(PPh_3)_8(SC_2H_4Ph)_{18}$	119
76	Ag_{25}	2,4-dimehylbenzenethiol	$Ag_{25}(DMBT)_{18}$	16
77	Ag_{29}	1,3-benzenedithiol	$Ag_{29}(BDT)_{12}(TPP)_4$	17
78	Ag_{30}	Closo-carborane and Bis(diphenylphosphino)methane	$Ag_{30}(C2B10H9S3)_8Dppm_6$	120
79	Ag_{31}	*t*butylthiol and trifluoroacetate	$Ag_{31}S_3(StBu)_{17}(CF_3COO)_7$	121
80	Ag_{32}	1,2-bis(diphenylphosphino)ethane and 4-(trifluoromethyl)thiophenol	$Ag_{32}(DPPE)_5(SC_6H_3F_2)_{24}$	53
81	Ag_{33}	2-phenylethanethiol and triphenylphosphine	$Ag_{33}(SCH_2CH_2Ph)_{24}(PPh_3)_4$	122
82	Ag_{38}	p-Flurothiophenol and 3,4-difluorothiophenol	$Ag_{38}(SPhF_2)_{26}(PR'_3)_8$	60
83	Ag_{40}	2-4-dimethylbenzenethiol, triphenylphosphineand hydride	$Ag_{40}(DMBT)_{24}(PPh_3)_8H_{12}$	123
84	Ag_{40}	2-4-dimethylbenzenethiol, triphenylphosphine	$Ag_{40}(DMBT)_{24}(PPh_3)_8$	58

(*continued on next page*)

TABLE 12.1 Crystal structures of gold and silver nanoclusters—cont'd

Number	Atomicity	Ligand	Composition	Reference
85	Ag_{42}	^{t}butylthiol	$Ag_{42}(SBu^{t})_{24}$	124
86	Ag_{44}	4-Mercaptobenzoic acid	$Na_4Ag_{44}(MBA)_{30}$	45,54
87	Ag_{44}	2-ethylbenzenethiolate and triphenylphosphine	$Ag_{44}(EBT)_{26(}TPP)_4$	125
88	Ag_{46}	2-4-dimethylbenzenethiol, triphenylphosphine	$Ag_{46}(SPhMe_2)_{24}(PPh_3)_8$	58
89	Ag_{46}	2-4-dimethylbenzenethiol	$Ag_{46}S_7(SPhMe_2)_{24}$	126
90	Ag_{47}	3,3-dimethyL-1-butyne and D-valine	$Ag_{47}L_{12}(C{\equiv}CtBu)_{16}$	127
91	Ag_{50}	4-tert-butylbenzyl mercaptan	$Ag_{50}(Dppm)_{6(}SR)_{30}$	128,129
92	Ag_{50}	Fluorothiophenol and 1,3-bis(diphenylphosphino)propane	$Ag_{50}S_7(SC_6H_4F)_{36(}dppp)_6$	128
93	Ag_{63}	p-Flurothiophenol and 3,4-difluorothiophenol	$Ag_{63}(SPhF_2)_{36}(PR'_3)_8$	60
94	Ag_{61}	Cyclohexanethiol	$\mathbf{Ag_{61}}(SC_6H_{11})_{40}Cl$	124
95	Ag_{66}	isopropyl thiol	$Ag_{66}(MoO_4)_9(^{i}PrS)_{28}(PhCOO)_{18}$	130
96	Ag_{67}	2-4-dimethylbenzenethiol, triphenylphosphine	$Ag_{67}(SPhMe_2)_{32}(PPh_3)_8$	56
97	Ag_{78}	Bis(diphenylphosphino)methane	$Ag_{78}(iPrPhS)_{30}(dppm)_{10}Cl_{10}$	131
98	Ag_{136}	4-tert-butylbenzenethiolate	$Ag_{136}(SR)_{64}Cl_3Ag_{0.45}$	132
99	Ag_{146}	4-isopropylbenzenethiolate	$Ag_{146}Br_2(SR)_{80}$	59
100	Ag_{210}	*i*propylbenzenethiol	$Ag_{210}(iPrPhS)_{71}$	66
101	Ag_{211}	*i*propylbenzenethiol	$Ag_{211}(iPrPhS)_{71}(Ph_3P)_6Cl$	66

reaction mixture is almost equal, but partial encapsulation occurred in the crystal (Ag_{16}: $Ag_{17} = 1{:}2$).

(4) The other type of cocrystal is the giant vs small NC. A giant $(AuAg)_{267}$ and small $(AuAg)_{45}$ NCs, assembled into a bi-component hierarchical structure.[67] In this category of cocrystals, a unique growth was observed. One component, $AuAg_{267}$ was stabilized by magic sizes, and another component, $AuAg_{45}$ contained magic electron configuration. In a single lattice, two particles with different origin of stability existed through strong intermolecular forces which includes C–H…π, π…π and H…H interactions.

(5) In this category of cocrystal, a double ionic NC system was reported by He et al. Combination of $[Ag_{26}Au(SR)_{18}(PPh_3)_6]^+$ and $[Ag_{24}Au(SR)_{18}]^-$ was synthesized in an in-situ growth mechanism.[68] Single-crystal X-ray analysis revealed the presence of alternate layers of both the NCs in a systematic way.

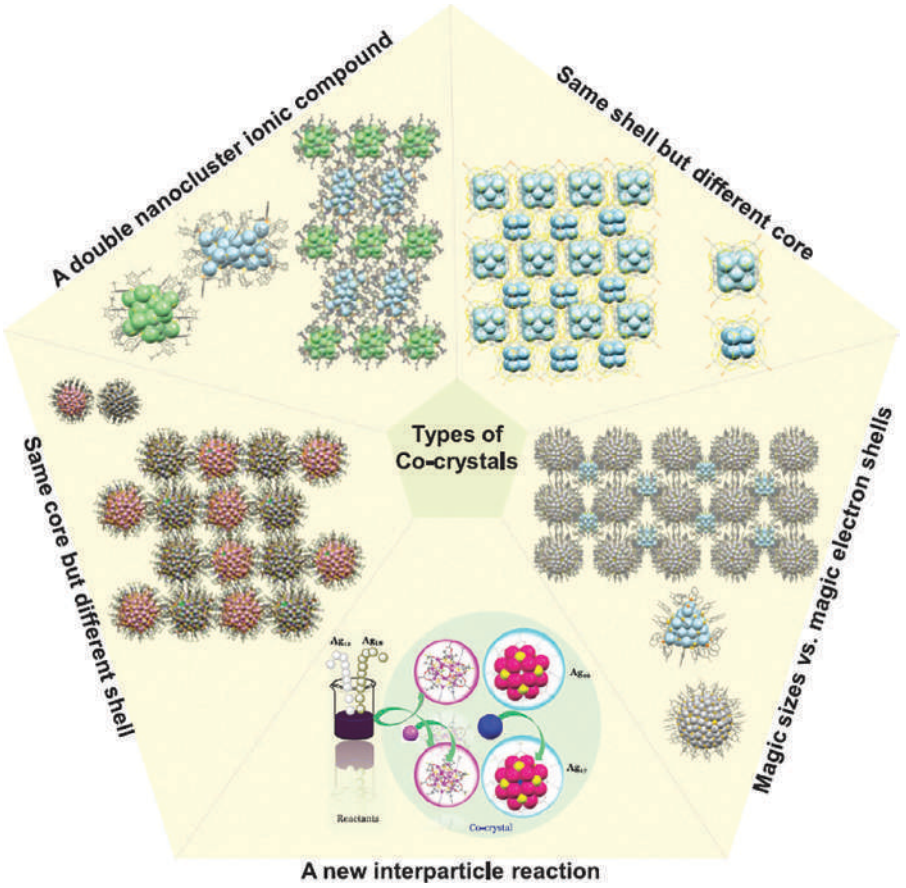

FIGURE 12.12 Cocrystallization in metal atomically precise NCs. Five different approaches are shown. Reproduced from refs[15,65] with permission. Copyright {2021} WILEY VCH. Copyright 2019 American Chemical Society.

Collectively, the cocrystallization of heterogeneous NCs has come up as a new "growth point" in NC science because it helps in understanding of both intracluster structures and intercluster packing modes. In addition, the NC cocrystallized systems are anticipated to show exceptionally different physicochemical properties compared to individual component NCs.

12.8 Summary and future perspectives

In this chapter, we have presented major development witnessed in the field of atomically precise NCs in the determination of atomic structures by SC-XRD. We have discussed basic building block and their assembly to create new molecular materials. Several NCs have been crystallized but many of them are still in the medium range (e.g., atomicity < 100). Giant NCs are expected to show unique patterns in the core and complexity on surface. This can provides

size-dependent structural rules and provide crucial insights about NC stability. It will also be interesting to investigate the transition of NCs into nanocrystals. New methodologies are needed to tackle the limitation of getting quality crystals. This is applicable not only to large NCs, but even toward plasmonic metal nanoparticles. Atomic precision in larger particles (> 3 nm) and their structure determination is a way forward to create new horizons in NC science.

List of abbreviation

BINAS	1,1′-binaphthyl-2,2′-dithiol
BDT	1,3-benzenedithiol
DCM	Dichloromethane
DDT	1-Dodecanethiol
DMBT	2,4-Dimethylbenzenethiolate
ESI MS	Electrospray ionization mass spectrometry/spectrum
FTP	4-fluorothiophenol
MBA	4-mercaptobenzoic acid
NC	Nanocluster
ODT	1-octadecanethiol
PCP-4-SH	[2.2] Paracyclophane-4-thiol
PET	2-phenylethanethiolate
SAM	Self Assembled Monolayer
SBB	4-tert- butylbenzylthiolate
SC-XRD	Single crystal X-ray diffraction
SG	Glutathione
-SR	alkyl/aryl
TBBT	*t*-butyl benzenethiol
THF	Tetrahydrofuran
TOAB	Tetraoctylammoniumbromide
UV/Vis	Ultraviolet/visible

References

1. Chakraborty I, Pradeep T. Atomically precise clusters of noble metals: Emerging link between atoms and nanoparticles. *Chem Rev*. 2017;117:8208.
2. Jin R, Zeng C, Zhou M, Chen Y. Atomically precise colloidal metal nanoclusters and nanoparticles: fundamentals and opportunities. *Chem Rev*. 2016;116:10346.
3. Chen W, Chen S. Oxygen electroreduction catalyzed by gold nanoclusters: strong core size effects. *Angew Chem Int Ed*. 2009;48:4386–4389.
4. Kitahara H, Sakurai H. Gold nanoclusters as a catalyst for intramolecular addition of primary amines to unactivated alkenes under aerobic conditions. *Chem Lett*. 2010;39:46–48.
5. Chakraborty I, Udayabhaskararao T, Pradeep T. Luminescent sub-nanometer clusters for metal ion sensing: a new direction in nanosensors. *J Hazard Mater*. 2012;211:396–403.
6. Choi S, Dickson RM, Yu J. Developing luminescent silver nanodots for biological applications. *Chem Soc Rev*. 2012;41:1867–1891.
7. Mathew A, Pradeep T. Noble metal clusters: applications in energy, environment, and biology. *Part Part Syst Charact*. 2014;31:1017–1053.
8. Du Y, Sheng H, Astruc D, Zhu M. Atomically precise noble metal nanoclusters as efficient catalysts: a bridge between structure and properties. *Chem Rev*. 2020;120(2):526–622.
9. Chen T, Xu S, Zhao T, et al. Gold nanocluster-conjugated amphiphilic block copolymer for tumor-targeted drug delivery. *ACS Appl Mater Interfaces*. 2012;4:5766–5774.
10. Chen L-Y, Wang C-W, Yuan Z, Chang H-T. Fluorescent gold nanoclusters: recent advances in sensing and imaging. *Anal Chem*. 2015;87:216–229.
11. Ghosh A, Mohammed OF, Bakr OM. Atomic-level doping of metal clusters. *Acc Chem Res*. 2018;51:3094–3103.

12. Jadzinsky PD, Calero G, Ackerson CJ, Bushnell DA, Kornberg RD. Structure of a thiol monolayer-protected gold nanoparticle at 1.1 Å resolution. *Science*. 2007;318:430–433.
13. Zhu M, Aikens CM, Hollander FJ, Schatz GC, Jin R. Correlating the crystal structure of a thiol-protected Au_{25} cluster and optical properties. *J Am Chem Soc*. 2008;130:5883.
14. Qian H, Eckenhoff WT, Bier ME, Pintauer T, Jin R. Crystal structures of Au_2 complex and Au_{25} nanocluster and mechanistic insight into the conversion of polydisperse nanoparticles into monodisperse Au_{25} nanoclusters. *Inorg Chem*. 2011;50:10735–10739.
15. Dar WA, Bodiuzzaman M, Ghosh D, et al. Interparticle reactions between silver nanoclusters leading to product cocrystals by selective cocrystallization. *ACS Nano*. 2019;13:13365–13373.
16. Joshi CP, Bootharaju MS, Alhilaly MJ, Bakr OM. $[Ag_{25}(SR)_{18}]-$: the "golden" silver nanoparticle. *J Am Chem Soc*. 2015;137:11578–11581.
17. AbdulHalim LG, Bootharaju MS, Tang Q, et al. $Ag_{29}(BDT)_{12}(TPP)_4$: a tetravalent nanocluster. *J Am Chem Soc*. 2015;137:11970–11975.
18. Zhang Q, Bu X, Zhang J, Wu T, Feng P. Chiral semiconductor frameworks from cadmium sulfide clusters. *J Am Chem Soc*. 2007;129:8412–8413.
19. Zeng C, Qian H, Li T, et al. Total structure and electronic properties of the gold nanocrystal $Au_{36}(SR)_{24}$. *Angew Chem Int Ed*. 2012;51:13114.
20. Das A, Li T, Nobusada K, Zeng C, Rosi NL, Jin R. Nonsuperatomic $[Au_{23}(SC_6H_{11})_{16}]-$ nanocluster featuring bipyramidal Au_{15} kernel and trimeric $Au_3(SR)_4$ Motif. *J Am Chem Soc*. 2013;135:18264–18267.
21. Liu C, Li T, Li G, et al. Observation of body-centered cubic gold nanocluster. *Angew Chem Int Ed*. 2015;54:9826–9829.
22. Das A, Liu C, Byun HY, et al. Structure determination of $[Au_{18}(SR)_{14}]$. *Angew Chem Int Ed*. 2015;54:3140–3144.
23. Chen S, Wang S, Zhong J, et al. The structure and optical properties of the $[Au_{18}(SR)_{14}]$ nanocluster. *Angew Chem Int Ed*. 2015;54:3145–3149.
24. Teo BK, Shi X, Zhang H. Pure gold cluster of 1:9:9:1:9:9:1 layered structure: a novel 39-metal-atom cluster $[(Ph_3P)_{14}Au_{39}C_{l6}]C_{l2}$ with an interstitial gold atom in a hexagonal antiprismatic cage. *J Am Chem Soc*. 1992;114:2743–2745.
25. Heaven MW, Dass A, White PS, Holt KM, Murray RW. Crystal structure of the gold nanoparticle [N(C8H17)4] $[Au_{25}(SCH_2CH_2Ph)_{18}]$. *J Am Chem Soc*. 2008;130:3754–3755.
26. Zhu M, Aikens CM, Hollander FJ, Schatz GC, Jin R. Correlating the crystal structure of a thiol-protected Au_{25} cluster and optical properties. *J Am Chem Soc*. 2008;130:5883–5885.
27. Li Q, Wang S, Kirschbaum K, Lambright KJ, Das A, Jin R. Heavily doped $Au_{25}–xAgx(SC_6H_{11})_{18}-$ nanoclusters: silver goes from the core to the surface. *Chem Commun*. 2016;52:5194–5197.
28. Song Y, Fu F, Zhang J, et al. The magic Au_{60} nanocluster: a new cluster-assembled material with five Au_{13} building blocks. *Angew Chem Int Ed*. 2015;54:8430–8434.
29. Das A, Li T, Li G, et al. Crystal structure and electronic properties of a thiolate-protected Au_{24} nanocluster. *Nanoscale*. 2014;6:6458–6462.
30. Chen Y, Zeng C, Liu C, et al. Crystal structure of barrel-shaped chiral Au_{130}(p-MBT)$_{50}$ nanocluster. *J Am Chem Soc*. 2015;137:10076–10079.
31. Shichibu Y, Negishi Y, Watanabe T, Chaki NK, Kawaguchi H, Tsukuda T. Biicosahedral gold clusters $[Au_{25}(PPh_3)_{10}(SCnH_2n+1)5Cl2]2+$ (n = 2−18): a stepping stone to cluster-assembled materials. *J Phys Chem C*. 2007;111:7845–7847.
32. Jin R, Liu C, Zhao S, et al. Tri-icosahedral gold nanocluster $[Au_{37}(PPh_3)_{10}(SC_2H_4Ph)_{10} \times 2]+$: linear assembly of icosahedral building blocks. *ACS Nano*. 2015;9:8530–8536.
33. Nobusada K, Iwasa T. Oligomeric gold clusters with vertex-sharing bi- and triicosahedral structures. *J Phys Chem C*. 2007;111:14279–14282.
34. Qian H, Eckenhoff WT, Zhu Y, Pintauer T, Jin R. Total structure determination of thiolate-protected Au_{38} nanoparticles. *J Am Chem Soc*. 2010;132:8280–8281.
35. Grönbeck H, Häkkinen H, Whetten RL. Gold−thiolate complexes form a unique c(4 × 2) structure on $Au_{(111)}$. *J Phys Chem C*. 2008;112:15940–15942.
36. Hakkinen H. The gold-sulfur interface at the nanoscale. *Nat Chem*. 2012;4:443–455.
37. Burgi T. Properties of the gold-sulphur interface: from self-assembled monolayers to clusters. *Nanoscale*. 2015;7:15553.

38. Song Y, Wang S, Zhang J, et al. Crystal structure of selenolate-protected $Au_{24}(SeR)_{20}$ nanocluster. *J Am Chem Soc*. 2014;136:2963–2965.
39. Zeng C, Liu C, Chen Y, Rosi NL, Jin R. Gold–thiolate ring as a protecting motif in the $Au_{20}(SR)_{16}$ nanocluster and implications. *J Am Chem Soc*. 2014;136:11922–11925.
40. Jiang D-e. Staple fitness: a concept to understand and predict the structures of thiolated gold nanoclusters. *Chemistry – A European Journal*. 2011;17:12289–12293.
41. Zeng C, Chen Y, Liu C, Nobusada K, Rosi NL, Jin R. Gold tetrahedra coil up: Kekulé-like and double helical superstructures. *Sci Adv*. 2015;1.
42. Yan N, Xia N, Liao L, et al. Unraveling the long-pursued Au_{144}structure by x-ray crystallography. *Sci Adv*. 2018;4:eaat7259.
43. Tran NT, Powell DR, Dahl LF. Nanosized Pd(145)(CO)(x)(PEt(3))(30) containing a capped three-shell 145-atom metal-core geometry of pseudo icosahedral symmetry This research was supported by the National Science Foundation (CHE-9729555). The CCD area detector system was purchased in part in 1995 with a NSF grant (CHE-9310428). Color figures were made with Crystal Maker, Interactive Crystallography for MacOS (David Palmer). Dedicated by L.F.D. to Professor Dr. Heinrich Vahrenkamp, an exceptional Inorganic Chemist and special friend, at the Festkolloquium (May 19, 2000) at the University of Freiburg. *Angew Chem Int Ed Engl*. 2000;39:4121–4125.
44. Lopez-Acevedo O, Akola J, Whetten RL, GroÌˆnbeck H, HaÌˆkkinen H. Structure and bonding in the ubiquitous icosahedral metallic gold cluster $Au_{144}(SR)_{60}$. *J Phys Chem C*. 2009;113:5035–5038.
45. Desireddy A, Conn BE, Guo J, et al. Ultrastable silver nanoparticles. *Nature*. 2013;501:399–402.
46. Wan X-K, Tang Q, Yuan S-F, Jiang D-e, Wang Q-M. Au_{19} nanocluster featuring a V-shaped alkynyl–gold motif. *J Am Chem Soc*. 2015;137:652–655.
47. Wan X-K, Yuan S-F, Tang Q, Jiang D-e, Wang Q-M. Alkynyl-protected Au_{23} nanocluster: a 12-electron system. *Angew Chem Int Ed Engl*. 2015;54:5977–5980.
48. Wan X-K, Xu WW, Yuan S-F, Gao Y, Zeng X-C, Wang Q-M. A near-infrared-emissive alkynyl-protected Au_{24} nanocluster. *Angew Chem Int Ed*. 2015;54:9683–9686.
49. Lei Z, Li J-J, Wan X-K, Zhang W-H, Wang Q-M. Isolation and total structure determination of an all-alkynyl-protected gold nanocluster Au_{144}. *Angew Chem Int Ed*. 2018;57:8639–8643.
50. Zeng C, Chen Y, Kirschbaum K, Lambright KJ, Jin R. Emergence of hierarchical structural complexities in nanoparticles and their assembly. *Science*. 2016;354:1580–1584.
51. Sakthivel NA, Theivendran S, Ganeshraj V, Oliver AG, Dass A. Crystal structure of faradaurate-279: Au_{279}(SPh-tBu)$_{84}$ plasmonic nanocrystal molecules. *J Am Chem Soc*. 2017;139:15450–15459.
52. Yang H, Lei J, Wu B, et al. Crystal structure of a luminescent thiolated Ag nanocluster with an octahedral Ag_6^{4+} core. *Chem Commun*. 2013;49:300–302.
53. Yang H, Wang Y, Zheng N. Stabilizing subnanometer Ag(0) nanoclusters by thiolate and diphosphine ligands and their crystal structures. *Nanoscale*. 2013;5:2674–2677.
54. Yang H, Wang Y, Huang H, et al. All-thiol-stabilized Ag_{44} and $Au_{12}Ag_{32}$ nanoparticles with single-crystal structures. *Nat Commun*. 2013;4:2422.
55. Harkness KM, Tang Y, Dass A, et al. $Ag_{44}(SR)_{30}^4$: a silver-thiolate superatom complex. *Nanoscale*. 2012;4:4269.
56. Alhilaly MJ, Bootharaju MS, Joshi CP, et al. [$Ag_{67}(SPhMe_2)_{32}(PPh_3)_8$]3+: synthesis, total structure, and optical properties of a large box-shaped silver nanocluster. *J Am Chem Soc*. 2016;138:14727–14732.
57. Bodiuzzaman M, Ghosh A, Sugi KS, et al. Camouflaging structural diversity: co-crystallization of two different nanoparticles having different cores but the same shell. *Angew Chem Int Ed*. 2019;58:189–194.
58. Chai J, Yang S, Lv Y, et al. A unique pair: Ag_{40} and Ag_{46} nanoclusters with the same surface but different cores for structure–property correlation. *J Am Chem Soc*. 2018;140:15582–15585.
59. Song Y, Lambright K, Zhou M, et al. Large-scale synthesis, crystal structure, and optical properties of the Ag_{146}Br2$(SR)_{80}$ nanocluster. *ACS nano*. 2018;12:9318–9325.
60. Yang H, Yan J, Wang Y, et al. Embryonic growth of face-center-cubic silver nanoclusters shaped in nearly perfect half-cubes and cubes. *J Am Chem Soc*. 2017;139:31–34.
61. Perumalla SR, Shi L, Sun CC. Ionized form of acetaminophen with improved compaction properties. *CrystEngComm*. 2012;14:2389–2390.
62. Griffini G, Brambilla L, Levi M, Castiglioni C, Del Zoppo M, Turri S. Anthracene/tetracene cocrystals as novel fluorophores in thin-film luminescent solar concentrators. *RSC Adv*. 2014;4:9893–9897.

63. Wang J-R, Yu Q, Dai W, Mei X. Drug–drug co-crystallization presents a new opportunity for the development of stable vitamins. *Chem Commun*. 2016;52:3572–3575.
64. Zhang J, Gu P, Long G, et al. Switching charge-transfer characteristics from p-type to n-type through molecular "doping" (co-crystallization). *Chem Sci*. 2016;7:3851–3856.
65. Bodiuzzaman M, Dar WA, Pradeep T. Cocrystals of atomically precise noble metal nanoclusters. *Small*. 2021;17:2003981.
66. Liu J-Y, Alkan F, Wang Z, et al. Different silver nanoparticles in one crystal: $Ag_{210}(iPrPhS)_{71}(Ph_3P)_5Cl$ and $Ag_{211}(iPrPhS)_{71}(Ph_3P)_6Cl$. *Angew Chem Int Ed*. 2019;58:195–199.
67. Yan J, Malola S, Hu C, et al. Co-crystallization of atomically precise metal nanoparticles driven by magic atomic and electronic shells. *Nat Commun*. 2018;9:3357.
68. He L, Gan Z, Xia N, Liao L, Wu Z. Alternating array stacking of $Ag_{26}Au$ and $Ag_{24}Au$ nanoclusters. *Angew Chem Int Ed*. 2019;58:9897–9901.
69. Briant CE, Hall KP, Mingos DMP. Unusual degradation reaction of icosahedral cluster compounds of gold with chelating diphosphanes and the x-ray structure of di[bis(diphenylphosphino)methanido]digold(I), [Au(Ph2P)2CH]2. *J Organomet Chem*. 1982;229:C5–C8.
70. Demartin F, Manassero M, Naldini L, Ruggeri R, Sansoni M. Synthesis and x-ray characterization of an iodine-bridged tetranuclear gold cluster, di-μ-iodo-tetrakis(triphenylphosphine)-tetrahedro-tetragold. *J Chem Soc Chem Commun*. 1981:222–223.
71. Van der Velden JWA, Bour JJ, Vollenbroek FA, Beurskens PT, Smits JMM. Synthesis of a new pentanuclear gold cluster by metal evaporation. Preparation and x-ray structure determination of [tris{bis(diphenylphosphino) methane}][bis(diphenylphosphino)methanido]pentagold dinitrate. *J Chem Soc Chem Commun*. 1979:1162–1163.
72. Briant CE, Hall KP, Mingos DMP. Synthesis and structural characterization of $[Au_6(PPh_3)_6](NO_3)2.3CH_2Cl_2$, an edge-shared bitetrahedral gold cluster. *J Organomet Chem*. 1983;254:C18–C20.
73. Briant CE, Hall KP, Mingos MP, Wheeler AC. Synthesis and structural characterization of hexakis (triphenylphosphine)hexagold(2+) nitrate and related clusters with edge-sharing bitetrahedral geometries. *J Chem Soc Dalton Trans*. 1986:687–692.
74. Van der Velden JWA, Beurskens PT, Bour JJ, et al. Intermediates in the formation of gold clusters. Preparation and x-ray analysis of $[Au_7(PPh_3)_7]$+ and synthesis and characterization of $[Au_8(PPh_3)_6I]PF6$. *Inorg Chem*. 1984;23:146–151.
75. Vollenbroek FA, Bosman WP, Bour JJ, Noordik JH, Beurskens PT. Reactions of gold-phosphine cluster compounds. Preparation and x-ray structure determination of octakis(triphenylphosphine)octagold bis(hexafluorophosphate). *J Chem Soc Chem Commun*. 1979:387–388.
76. Van der Velden JWA, Bour JJ, Bosman WP, Noordik JH. Synthesis and x-ray crystal structure determination of the cationic gold cluster compound $[Au_8(PPh_3)_7](NO_3)_2$. *J Chem Soc Chem Commun*. 1981:1218–1219.
77. Zhang S-S, Feng L, Senanayake RD, et al. Diphosphine-protected ultrasmall gold nanoclusters: opened icosahedral Au_{13} and heart-shaped Au_8 clusters. *Chem Sci*. 2018;9:1251–1258.
78. Bellon PL, Cariati F, Manassero M, Naldini L, Sansoni M. Novel gold clusters. Preparation, properties, and X-ray structure determination of salts of octakis(triarylphosphine)enneagold, $[Au_9L_8]X_3$. *J Chem Soc D*. 1971:1423–1424.
79. Hall KP, Theoblad BRC, Gilmour DI, Mingos DMP, Welch AJ. Synthesis and structural characterization of [Au9{P(p-C6H4OMe)3}8](BF4)3, a cluster with a centred crown of gold atoms. *J Chem Soc Chem Commun*. 1982:528–530.
80. Briant CE, Hall KP, Wheeler AC, Mingos DMP. Structural characterisation of $[Au_{10}Cl_3(PCy_2Ph)_6](NO_3)$ (Cy = cyclohexyl) and the development of a structural principle for high nuclearity gold clusters. *J Chem Soc Chem Commun*. 1984:248–250.
81. McPartlin M, Mason R, Malatesta L. Novel cluster complexes of gold(0)–gold(I). *J Chem Soc D*. 1969:334.
82. Albano VG, Bellon PL, Manassero M, Sansoni M. Intermetallic pattern in metal-atom clusters. Structural studies on $Au_{11} \times 3(PR3)7$ species. *J Chem Soc D*. 1970:1210–1211.
83. Bellon P, Manassero M, Sansoni M. Crystal and molecular structure of triiodoheptakis[tris(p-fluorophenyl) phosphine]undecagold. *J Chem Soc Dalton Trans*. 1972:1481–1487.
84. Narouz MR, Osten KM, Unsworth PJ, et al. N-heterocyclic carbene-functionalized magic-number gold nanoclusters. *Nat Chem*. 2019;11:419–425.
85. Smith RK, Nanayakkara SU, Woehrle GH, et al. Spectral diffusion in the tunneling spectra of ligand-stabilized undecagold clusters. *J Am Chem Soc*. 2006;128:9266–9267.

86. Huang T-H, Zhao F-Z, Hu Q-L, et al. Bisphosphine-stabilized gold nanoclusters with the crown/birdcage-shaped Au_{11} cores: structures and optical properties. *Inorg Chem*. 2020;59:16027–16034.
87. Yi H, Osten KM, Levchenko TI, et al. Synthesis and enantioseparation of chiral Au_{13} nanoclusters protected by bis-N-heterocyclic carbene ligands. *Chem Sci*. 2021;12:10436–10440.
88. Briant CE, Theobald BRC, White JW, Bell LK, Mingos DMP, Welch AJ. Synthesis and x-ray structural characterization of the centered icosahedral gold cluster compound $[Au_{13}(PMe_2Ph)_{10}Cl_2](PF_6)_3$, the realization of a theoretical prediction. *J Chem Soc Chem Commun*. 1981:201–202.
89. Gutrath BS, Oppel IM, Presly O, et al. $[Au_{14}(PPh_3)_8(NO_3)_4]$: an example of a new class of $Au(NO_3)$-ligated superatom complexes. *Angew Chem Int Ed*. 2013;52:3529–3532.
90. Chen J, Zhang Q-F, Williard PG, Wang L-S. Synthesis and structure determination of a New Au_{20} nanocluster protected by tripodal tetraphosphine ligands. *Inorg Chem*. 2014;53:3932–3934.
91. Yuan S-F, Li J-J, Guan Z-J, Lei Z, Wang Q-M. Ultrastable hydrido gold nanoclusters with the protection of phosphines. *Chem Commun*. 2020;56:7037–7040.
92. Chen S, Xiong L, Wang S, et al. Total structure determination of $Au_{21}(S\text{-}Adm)_{15}$ and geometrical/electronic structure evolution of thiolated gold nanoclusters. *J Am Chem Soc*. 2016;138:10754–10757.
93. Chen J, Zhang Q-F, Bonaccorso TA, Williard PG, Wang L-S. Controlling gold nanoclusters by diphospine ligands. *J Am Chem Soc*. 2014;136:92–95.
94. Han X-S, Luan X, Su H-F, et al. Structure determination of alkynyl-protected gold nanocluster $Au_{22}(tBuC{\equiv}C)_{18}$ and its thermochromic luminescence. *Angew Chem Int Ed*. 2020;59:2309–2312.
95. Li S, Sun Y, Wu C, et al. Distinct structure assembly driven by metal–ligand binding in Au_{23} nanoclusters and its relation to photocatalysis. *Chem Commun*. 2021;57:2176–2179.
96. Guan Z-J, Hu F, Li J-J, Wen Z-R, Lin Y-M, Wang Q-M. Isomerization in alkynyl-protected gold nanoclusters. *J Am Chem Soc*. 2020;142:2995–3001.
97. Crasto D, Barcaro G, Stener M, Sementa L, Fortunelli A, Dass A. $Au_{24}(SAdm)_{16}$ nanomolecules: X-ray crystal structure, theoretical analysis, adaptability of adamantane ligands to form $Au_{23}(SAdm)_{16}$ and $Au_{25}(SAdm)_{16}$, and its relation to $Au_{25}(SR)_{18}$. *J Am Chem Soc*. 2014;136:14933–14940.
98. Zeng C, Li T, Das A, Rosi NL, Jin R. Chiral structure of thiolate-protected 28-gold-atom nanocluster determined by X-ray crystallography. *J Am Chem Soc*. 2013;135:10011–10013.
99. Crasto D, Dass A, Gold G. $Au_{30}(S\text{-}t\text{-}C_4H_9)_{18}$ molecules. *J Phys Chem C*. 2013;117:22094–22097.
100. Higaki T, Liu C, Zeng C, et al. Controlling the atomic structure of Au_{30} nanoclusters by a ligand-based strategy. *Angew Chem Int Ed*. 2016;55:6694–6697.
101. Fetzer F, Maier A, Hodas M, et al. Structural order enhances charge carrier transport in self-assembled Au-nanoclusters. *Nat Commun*. 2020;11:6188.
102. Liu X, Xu WW, Huang X, et al. De novo design of $Au_{36}(SR)_{24}$ nanoclusters. *Nat Commun*. 2020;11:3349.
103. Wang T, Zhang W-H, Yuan S-F, Guan Z-J, Wang Q-M. An alkynyl-protected Au_{40} nanocluster featuring PhCC–Au–P^P motifs. *Chem Commun*. 2018;54:10367–10370.
104. Wan X-K, Guan Z-J, Wang Q-M. Homoleptic alkynyl-protected gold nanoclusters: $Au_{44}(PhC{\equiv}C)_{28}$ and $Au_{36}(PhC{\equiv}C)24$. *Angew Chem Int Ed*. 2017;56:11494–11497.
105. Zeng C, Chen Y, Iida K, et al. Gold quantum boxes: on the periodicities and the quantum confinement in the Au_{28}, Au_{36}, Au_{44}, and Au_{52} Magic Series. *J Am Chem Soc*. 2016;138:3950–3953.
106. Liao L, Zhuang S, Yao C, et al. Structure of chiral $Au_{44}(2,4\text{-}DMBT)_{26}$ nanocluster with an 18-electron shell closure. *J Am Chem Soc*. 2016;138:10425–10428.
107. Zhou Y, Liao L, Zhuang S, et al. Traceless removal of two kernel atoms in a gold nanocluster and its impact on photoluminescence. *Angew Chem Int Ed*. 2021;60:8668–8672.
108. Liao L, Zhuang S, Wang P, et al. Quasi-dual-packed-kerneled $Au_{49}(2,4\text{-}DMBT)_{27}$ nanoclusters and the influence of kernel packing on the electrochemical gap. *Angew Chem Int Ed*. 2017;56:12644–12648.
109. Liao L, Wang C, Zhuang S, et al. An unprecedented kernel growth mode and layer-number-odevity-dependent properties in gold nanoclusters. *Angew Chem Int Ed*. 2020;59:731–734.
110. Gu W, Zhao Y, Zhuang S, et al. Unravelling the structure of a medium-sized metalloid gold nanocluster and its filming property. *Angew Chem Int Ed*. 2021;60:11184–11189.
111. Li J-J, Guan Z-J, Yuan S-F, Hu F, Wang Q-M. Enriching structural diversity of alkynyl-protected gold nanoclusters with chlorides. *Angew Chem Int Ed*. 2021;60:6699–6703.
112. Zeng C, Liu C, Chen Y, Rosi NL, Jin R. Atomic structure of self-assembled monolayer of thiolates on a tetragonal Au_{92} nanocrystal. *J Am Chem Soc*. 2016;138:8710–8713.

113. Higaki T, Liu C, Zhou M, Luo T-Y, Rosi NL, Jin R. Tailoring the structure of 58-electron gold nanoclusters: $Au_{103}S2(S\text{-}Nap)41$ and its implications. *J Am Chem Soc*. 2017;139:9994–10001.
114. Wang J-Q, Shi S, He R-L, et al. Total structure determination of the largest alkynyl-protected fcc gold nanocluster Au_{110} and the study on its ultrafast excited-state dynamics. *J Am Chem Soc*. 2020;142:18086–18092.
115. Dass A, Theivendran S, Nimmala PR, et al. $Au_{133}(SPh\text{-}tBu)_{52}$ Nanomolecules: X-ray crystallography, optical, electrochemical, and theoretical analysis. *J Am Chem Soc*. 2015;137:4610–4613.
116. Vergara S, Lukes DA, Martynowycz MW, et al. MicroED structure of $Au_{146(}p\text{-}MBA)_{57}$ at subatomic resolution reveals a twinned FCC cluster. *J Phys Chem Lett*. 2017;8:5523–5530.
117. Liu K-G, Gao X-M, Liu T, Hu M-L, Jiang D-e. All-carboxylate-protected superatomic silver nanocluster with an unprecedented rhombohedral Ag_8 core. *J Am Chem Soc*. 2020;142:16905–16909.
118. Dhayal RS, Liao J-H, Liu Y-C, et al. $[Ag_{21}\{S2P(OiPr)2\}12]+$: an eight-electron superatom. *Angew Chem Int Ed*. 2015;54:3702–3706.
119. Liu C, Li T, Abroshan H, et al. Chiral Ag_{23} nanocluster with open shell electronic structure and helical face-centered cubic framework. *Nat Commun*. 2018;9:744.
120. Huang J-H, Wang Z-Y, Zang S-Q, Mak TCW. Spontaneous resolution of chiral multi-thiolate-protected Ag_{30} nanoclusters. *ACS Central Science*. 2020;6:1971–1976.
121. Feng Y-H, Lin Z-S, Liu S-Q, et al. A stably discrete 31-nuclearity silver(i) thiolate nanocluster luminescent thermometer supported by DMF auxiliary ligands. *New J Chem*. 2020;44:663–667.
122. Tian F, Chen R. Pd-mediated synthesis of Ag_{33} chiral nanocluster with core–shell structure in T point group. *J Am Chem Soc*. 2019;141:7107–7114.
123. Yuan X, Sun C, Li X, et al. Combinatorial identification of hydrides in a ligated Ag_{40} nanocluster with noncompact metal core. *J Am Chem Soc*. 2019;141:11905–11911.
124. Chen T, Yang S, Song Y, et al. All-thiolate-stabilized Ag_{42} nanocluster with a tetrahedral kernel and its transformation to an Ag_{61} nanocluster with a bi-tetrahedral kernel. *Chem Commun*. 2020;56:7605–7608.
125. Bootharaju MS, Lee S, Deng G, et al. $Ag_{44}(EBT)_{26}(TPP)_4$ nanoclusters with tailored molecular and electronic structure. *Angew Chem Int Ed*. 2021;60:9038–9044.
126. Liu X, Chen J, Yuan J, et al. A silver nanocluster containing interstitial sulfur and unprecedented chemical bonds. *Angew Chem Int Ed*. 2018;57:11273–11277.
127. Liu W-D, Wang J-Q, Yuan S-F, Chen X, Wang Q-M. Chiral superatomic nanoclusters Ag_{47} induced by the ligation of amino acids. *Angew Chem Int Ed*. 2021;60:11430–11435.
128. Sun Q-Q, Li Q, Li H-Y, et al. Thermochromism and piezochromism of an atomically precise high-nuclearity silver sulfide nanocluster. *Chem Commun*. 2021;57:2372–2375.
129. Du W, Jin S, Xiong L, et al. $Ag_{50}(Dppm)_6(SR)_{30}$ and its homologue $AuxAg_{50}–x(Dppm)_6(SR)_{30}$ alloy nanocluster: seeded growth, structure determination, and differences in properties. *J Am Chem Soc*. 2017;139:1618–1624.
130. Wang Z, Yang F-L, Yang Y, Liu Q-Y, Sun D. Hierarchical multi-shell 66-nuclei silver nanoclusters trapping subvalent Ag_6 kernels. *Chem Commun*. 2019;55:10296–10299.
131. Zhang W-J, Liu Z, Song K-P, et al. A 34-electron superatom Ag_{78} cluster with regioselective ternary ligands shells and its 2D rhombic superlattice assembly. *Angew Chem Int Ed*. 2021;60:4231–4237.
132. Yang H, Wang Y, Chen X, et al. Plasmonic twinned silver nanoparticles with molecular precision. *Nat Commun*. 2016;7:12809.

CHAPTER

13

Electron microscopy of clusters

Ananthu Mahendranath[a] *and Thalappil Pradeep*[b]

[a]DST Unit of Nanoscience and Thematic Unit of Excellence, Department of Chemistry, Indian Institute of Technology Madras, Chennai, India [b]Deepak Parekh Institute Chair Professor and Professor of Chemistry, Department of Chemistry, Indian Institute of Technology Madras, Chennai, India

13.1 Introduction

Atomically precise noble metal nanoclusters (NCs) have emerged as the all-important material to understand structure–property correlation at the nanoscale.[1] Precise determination of the atomic structure of NCs becomes vital in this respect. The foremost technique that has revealed the structure of most thiolate protected NCs in solution is single-crystal X-ray diffraction (SCXRD).[2–8] But this technique is limited to materials that can be crystallized to diffractable single crystals. Even when crystals give diffraction spots, minute structural details are often lost. Also weak scattering of X-rays by lower elements often leads to missing them in the final structure.

Furthermore, X-ray diffraction does not apply to NCs that exist in the gas phase. Many NCs had been characterized by other techniques like mass spectrometry and UV/Vis spectroscopy, but whose structure at the atomic level is unknown.[9] These necessitated the search for novel approaches and techniques beyond SCXRD to understand the structural aspects of NCs. Electron microscopy is a preeminent tool used for the routine characterization of nanoparticles. Advancements in this technique, especially over the last decade, have demonstrated the emergence of electron microscopy as an effective alternative method to SCXRD.

This chapter will discuss significant advancements concerning the understanding of NCs and imaging them using electron microscopy, the challenges involved, and briefly on other related techniques.

13.2 Microscopy of naked clusters

NCs prepared in the gas phase are often naked, meaning without ligands. These "bare" clusters are devoid of protecting ligands and hence are highly reactive. More about these clusters are dealt with in Chapter 17. Some of the earlier attempts to image clusters using

Atomically Precise Metal Nanoclusters.
DOI: https://doi.org/10.1016/B978-0-323-90879-5.00014-7

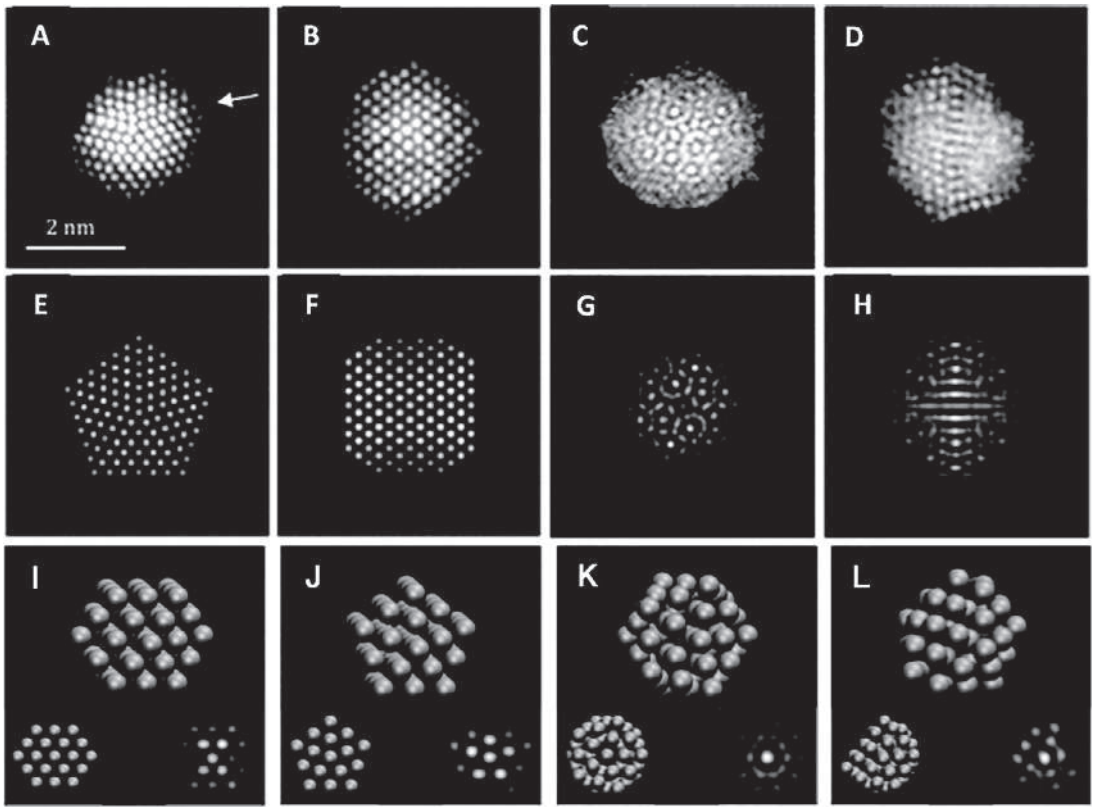

FIGURE 13.1 (A - H) Typical HAADF-STEM images and the corresponding simulations of size-selected Au_{923} clusters. (I–L) Atomic models and multislice simulations of Au_{55} clusters. Adapted with permission from ref.[10] and ref.[11] Copyright 2012 American Chemical Society and Copyright 2012 by the American Physical Society.

electron microscopy were done on such mass-selected (bare) gold clusters. Wang et al.[10] employed a single-shot high-angle annular dark-field (HAADF) scanning transmission electron microscopy (STEM) intensity map approach, combined with STEM simulations to determine the 3D structure of Au NCs within size range of 100–1000 atoms. HAADF detectors made it possible to record electrons that are incoherently scattered to higher angles by the specimen. Au NCs in this size range typically arrange in three atomic configurations: icosahedron (Ih), dodecahedron (Dh), and face-centered. Fig. 13.1(A–D) depicts the experimental HAADF images for (A) a decahedron along a fivefold axis, (B) fcc polyhedron along the <110> axis, (C and D) icosahedron along a fivefold axis and a twofold axis, respectively, for size-selected Au_{923} clusters. The geometric structures of these NCs as illustrated in Fig. 13.1(E–H) were arrived at using atomic resolution, single-shot HAADF imaging combined with simulations employing multislice electron scattering method on the standard atomic models of Ino-Dh, cuboctahedron, and Ih. It is to be noted that 923 is a magic number for Ino-Dh, cuboctahedron,

and Ih configurations. The arrow in Fig. 13.1(A) marks the edge where no reentrant structure is present.

Using a similar approach, coupling aberration-corrected STEM coupled with systematic multislice electron scattering simulations, the structure of a size-selected Au_{55} cluster, soft-landed on amorphous carbon, was reported.[11] It had a fluctuating chiral structure, unlike high-symmetry configurations like face-centered cubic polyhedron, icosahedron, or decahedron. Fig. 13.1(I–L) represents atomic models of cuboctahedral, Ino-decahedral, icosahedral, and chiral Au_{55} clusters, respectively. The insets on the right of Fig. 13.1(I–L) show the simulations along particular orientations shown on the left, specifically, the ⟨110⟩ axis, fivefold axis, fivefold axis, and $\theta = 20°/\alpha = 90°$.

fThis method was extended to image adatoms and small clusters on size-selected, truncated octahedral gold clusters, $Au_N(N = 923 \pm 23)$.[12] Fig. 13.2(c and d), shows a truncated octahedral Au_{923} cluster projected along the ⟨110⟩ axis with six facets clearly visible; the uppermost and lowermost are {100} and the others are {111} (.). Individual adsorbates are labeled in (c) and (d).

In our earlier attempts to image thiolate-protected NCs, the strategy adopted was to introduce a cryogenic (cryo) stage to reduce the expected beam-induced thermal heating of NCs. In one such study, hexanethiolate protected Au_{38} was imaged using a C_s corrected HAADF-STEM.[13] In this approach, under optimized imaging conditions, a series of images were recorded with an acquisition speed of 0.2 s/frame for each cluster as depicted in Fig. 13.3. The images often appeared blurred and they also indicated structural fluctuation in consecutive frames. Their approach showed that most of the Au_{38} clusters had a prolate projected shape which was consistent with calculations based on a low-energy biicosahedral gold core. In Fig. 13.3, panels (a–c) show cluster A (approximately spherical), with an approximately circular projected shape; panels (d–f) show cluster B, with an approximately elliptical projected shape. The insert in (b) displays the corresponding raw image. In some cases single Au atoms can be seen around the clusters, as indicated by the arrows in (c) and (c). Also shown in (b) and (e) are the best-fit ellipses used to obtain the aspect ratios.

13.3 Imaging structures using C_s corrected—TEM and single particle reconstruction

It was a long-standing challenge to image biological specimens without undergoing changes during preparation for electron microscopy. For particles in solution, one of the challenges was to save them from damages caused by dehydration, which tend to distort their structure. High contrast images generally require a higher e-beam intensity. But this often lead to damage of specimens from beam interaction. Hence, to image specimens as it is, was another challenge. Modern structural biology has extensively relied upon cryo-electron microscopy and computational 3D reconstruction for understanding biological macromolecular assemblies. To minimize the damage caused by the electron beam, a minimal electron dose is employed. However, at such a low dose, the images recorded often have higher noises and low contrast. Nevertheless, this issue has been addressed using an averaging technique, whereby multiple images of identical specimens are collected and averaged.

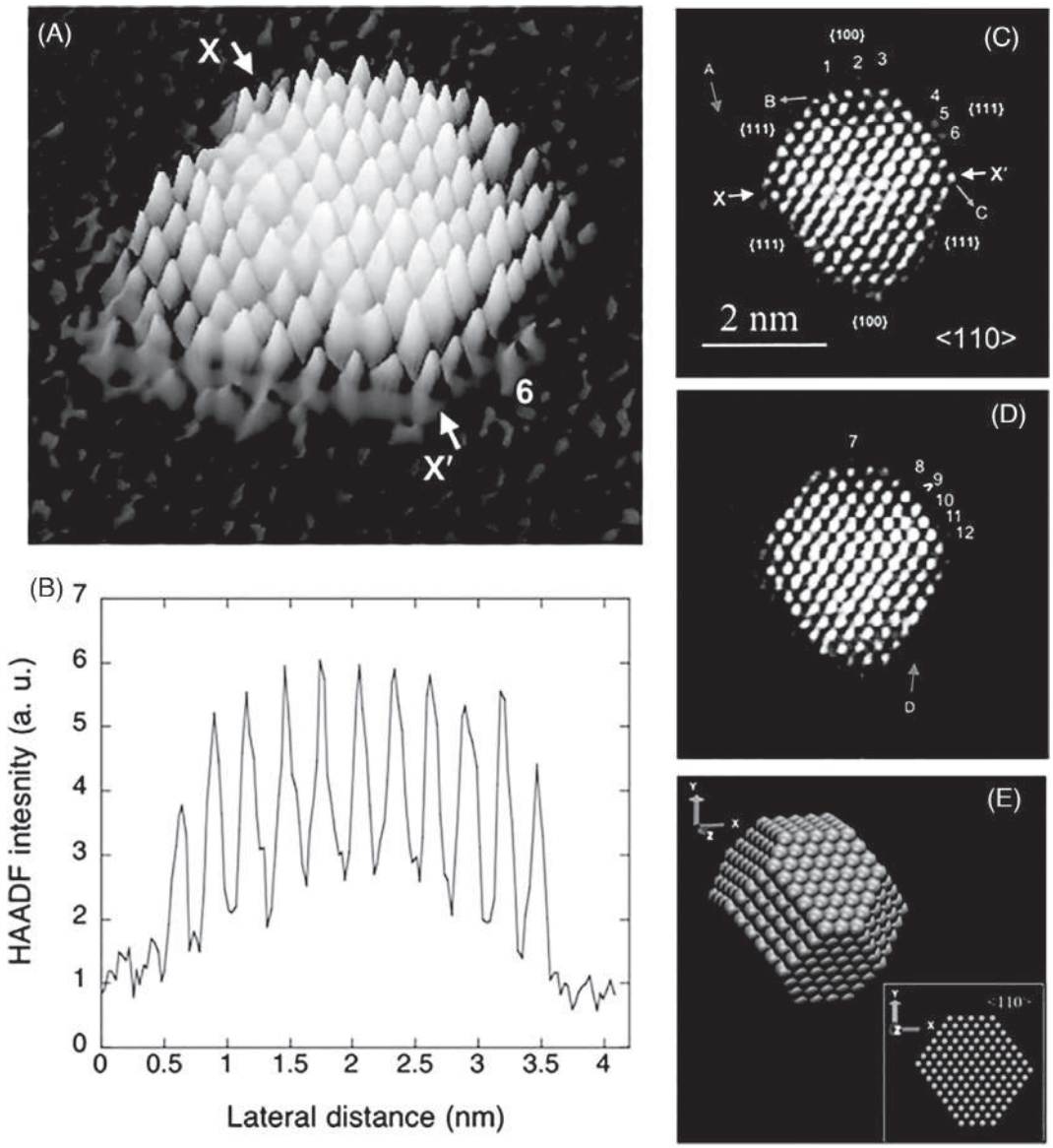

FIGURE 13.2 (a) A 3D intensity plot of a truncated octahedral Au_{923} cluster obtained by HAADF-STEM imaging. (b) Intensity profile along the line $X-X'$ in (A) in which 3 pixels (0.028 nm/pixel) are binned. (c) A false color display of the same HAADF image as (a). Panel (d) is the next frame after (c) in a series of HAADF-STEM images obtained with a speed of 6 s/frame. The images are processed using a smoothing kernel (averaging 3×3 neighboring pixels). Panel (e) shows an atomic model of a truncated-octahedral Au_{923} cluster, based on the images above. The electron beam direction is along the Z-axis. The inset is the $\langle 110 \rangle$ view of this model. Note that the atomic model is not an exact 3D reconstruction from the experimental images (c) or (d) and does not include the surface adatoms.Adapted with permission from ref.[12] Copyright 2012 American Chemical Society.

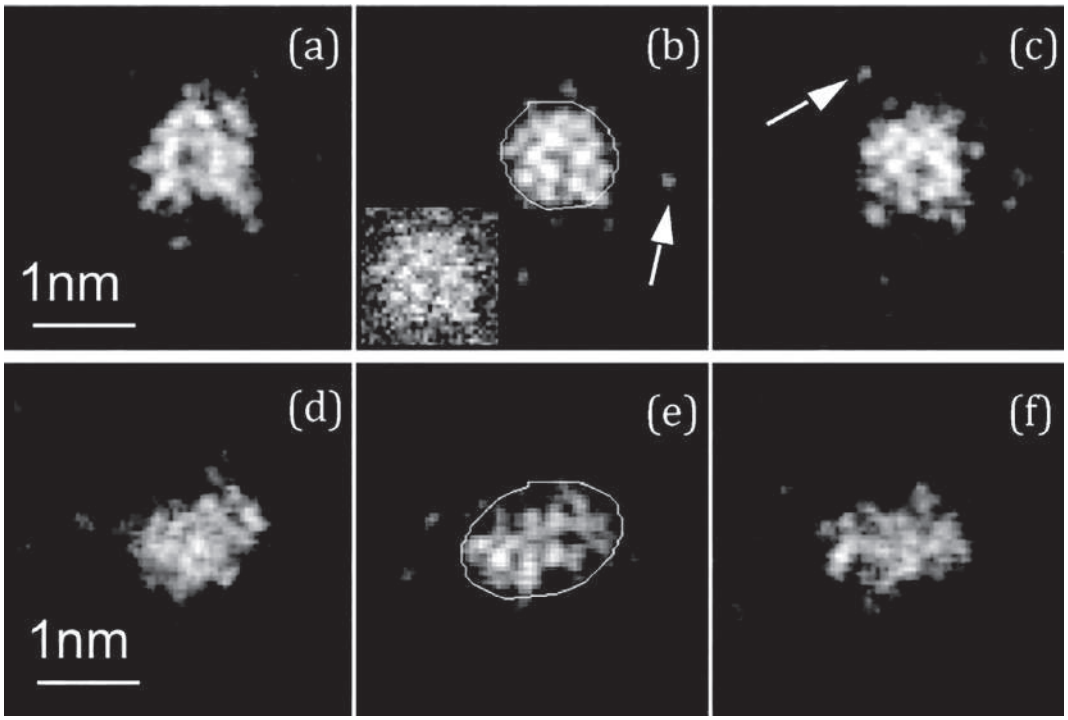

FIGURE 13.3 Representative series of HAADF-STEM images (0.2 s/frame) of MP–Au_{38} clusters under optimized imaging conditions. The images are slightly smoothed. Reprinted with permission from ref. 13. Copyright 2011 John Wiley and Sons.

Recently, Maia Azubel et al. employed the advancements in biological TEM and computational 3D reconstruction and successfully determined the crystal structure of a water soluble gold cluster consisting of 68 Au atoms protected by 3-mercaptobenzoic acid (3-MBA).[14] Single-particle reconstruction requires that all possible orientations of the particle are looked at. For the flexible structure of proteins, more data are collected, and that has to be sorted between different conformations. However, in the case of metal NCs, the rigid structure and the precise composition made them an ideal choice of sample for these experiments. The cluster samples were very sensitive to radiation damage, and hence the low dose strategy was chosen for data collection. This approach limits the number of electrons used for recording the image. They also made sure that the field of particles to be imaged is exposed to the e-beam for the shortest time as possible. This was achieved by first scanning the grid at low magnification, so as to identify the area of interest, followed by focusing at two spots very near to this area. Once beam correction is done for these spots, the beam or stage is moved in order to expose the area of interest. It is necessary to use a flat grid for these experiments. This was because the range of acceptable defocus values for resolving individual atoms, was limited to 1.5–2.5 nm. The accurate extrapolation of defocus values from adjacent areas required that the grids are truly flat.

Various steps involved in single-particle reconstruction of Au_{68} is shown in Fig. 13.4. The electron density map in Fig. 13.4(B) shows 68 peaks corresponding to the gold atoms. The overall structure consists of a 13-gold atom cuboctahedron with a central gold atom, surrounded by 24 atoms in fcc-like arrangement and 31 atoms that do not obey fcc packing. The positions of sulfur atoms were assigned from density functional theory (DFT) calculations. Overall, when we compare the structures of water soluble Au_{102} and Au_{68}, the latter has a lesser symmetry and an incompletely filled electronic shell.

The structure of 3-MBA protected Au_{144} nanocluster was also resolved by the same approach.[15] The structure was arrived at by collecting information from nearly 4300 particles. An electron dose of $\sim 800\ e^{-}/Å^2$ at a magnification of 320,000 (pixel size 0.32 Å) was employed for recording the images. This study revealed that most of the gold atoms in Au_{144} were arranged in fcc packing, but there were local variations, especially on the surface and clear deviation from a regular shape of the particle. The evidence for 40 ligands was arrived at using a combination of mass spectrometry, XPS, and TGA. Resuls from this study are depicted in Fig. 13.5.

These studies demonstrate that low electron dose aberration-corrected electron microscopy and single-particle analysis serve two critical purposes in one shot. First, it is a very reliable technique instead of X-ray diffraction, especially when good diffraction crystals are unavailable. Second, this will serve as a powerful technique for understanding the structure and homogeneity of NCs in solution. To better put it in context, consider the crystals of Au_{102}(4-MBA)$_{44}$. This was initially formed during a gold nanoparticle synthesis, and subsequently, its structure was solved using X-ray diffraction. So the structure of other particles formed in that methodology was unknown. But contrary to this, the structures of the Au_{68} and Au_{144} particles would be a representative of the majority, as it was derived through an algorithm that averaged structures from a huge number of particles (nearly 1000). So this method, in a way, confirms the structural uniformity of the crystals and rules out the possibility of the existence of any structural isomers.

13.4 Electron micro-diffraction and nanobeam electron diffraction

Electron micro-diffraction (MicroED) is an electron crystallography technique introduced primarily for determining high-resolution protein structures.[16] This technique is carried out in a cryo-electron microscope. MicroED made it possible to collect more diffraction data from a single protein 3D crystals leading to their structure determination. MicroED provides an advantage of collecting diffraction data from smaller crystals (up to six magnitude smaller), compared to SCXRD. This method underwent major improvement with the introduction of a continuous-rotation data collection method, leading to more accurate diffraction data.[17]

NCs that lie in the transition size range between smaller clusters having distinct HOMO–LUMO gap and larger clusters that exhibit plasmonic resonance are of particular interest. MicroED revealed the crystal structure of one such cluster, Au_{146}(p-MBA)$_{57}$ (p-MBA: para-mercaptobenzoic acid) up to a subatomic resolution of 0.85 Å against 1.3 Å from SCXRD.[18] The atomic structure revealed that the 119 core gold atoms are arranged in a twinned FCC structure, and the 27 surface gold atoms follow a C2 rotational symmetry about an axis

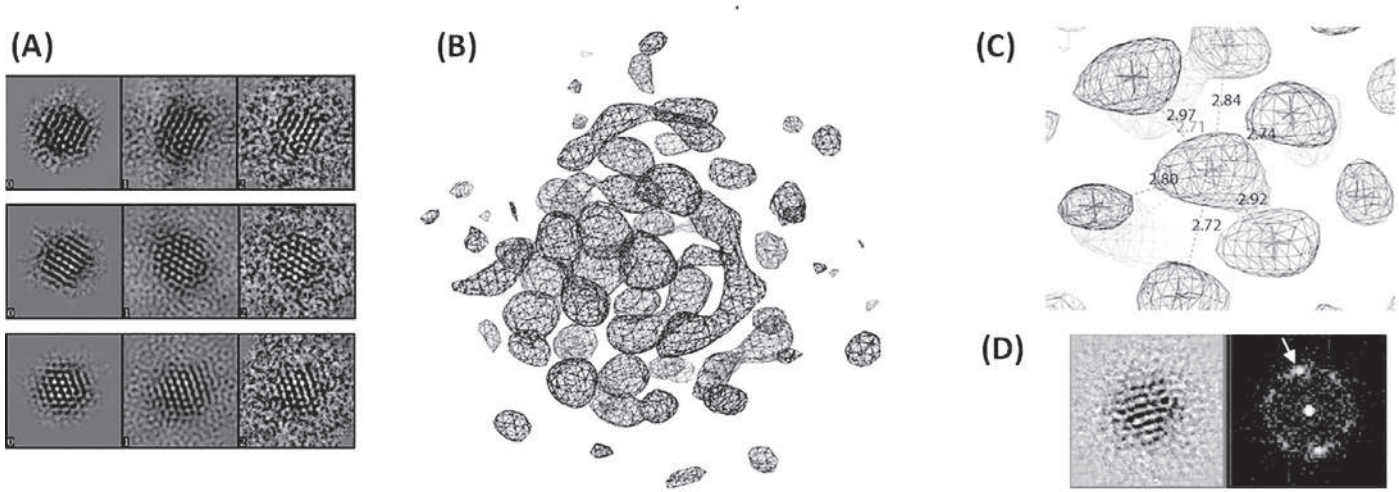

FIGURE 13.4 (A–D) Three-dimensional (3D) reconstruction of Au_{68} NP structure from electron micrographs. (A) Representative components of the reconstruction. (Left) Back projection from the reconstruction; (middle) corresponding class average of the EM images; (right) EM images. (B and C) Electron density map, mesh. Stars in (B) and (C) show the position of atomic coordinates for gold atoms. (C) Region of the electron density map surrounding the central atom. Dashed lines show coordination of the central atom; numbers indicate gold–gold distances in angstroms. (D) A cross section of the 3D reconstruction (left) and its Fourier transform (right). The arrow indicates spots at 2.4 Å resolution. Adapted from ref.[14].

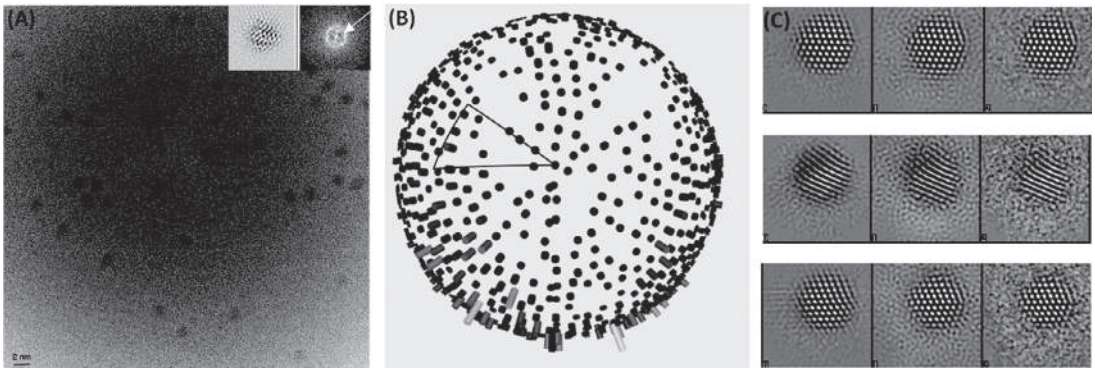

FIGURE 13.5 (A) Aberration-corrected transmission electron micrograph of the presumptive $Au_{144}(3\text{-MBA})_x$ particle. Inset shows a cross section of the 3D reconstruction (left panel) and its Fourier transform (right panel). Arrow indicates spots at 2.4 Å resolution. (B) Distribution of 2D projections of images in Euler space. The height of each point or bar is proportional to the number of particles assigned to that projection. (C) Representative Euler space points of the reconstruction. Left panel, back projection; middle panel, class average; right panel, raw data. Adapted with permission from ref.[15]. Copyright 2017 American Chemical Society.

bisecting the twinning plane. Interestingly this structure was in stark contrast from the structure of $Au_{144}(SCH_2Ph)_{60}$,[19] an important cluster in this transition size regime (Fig. 13.6).

Nanobeam electron diffraction (NBD) was a derivate of combining STEM imaging with nanoarea parallel beam diffraction on a TEM with Koehler illumination. Even though the initial design allowed only parallel beam of 80 nm in diameter to perform NBD, further developments in this area created beam diameters as low as 1 nm. Bahena et al.[20] employed NBD combined with HAADF-STEM at reduced voltages to determine the structure of thiolate protected chiral-icosahedral $Au_{144}(SCH_2CH_2Ph)_{60}$. They generated the diffraction pattern using 80 kV voltage. Using NDB they could acquire images for nearly 20 s before irreversible damage occurred. The final structure was solved in combination with experimental and theoretical models derived using DFT (Fig. 13.7).

13.5 Challenges and precautions in measurements

NCs belong to the class of materials that are extremely sensitive under electron beam. Irradiation with intense electron beam, even for a very short duration, can trigger aggregation of NCs.[21] This leads to fusion of such clusters, resulting in formation of nanoparticles. This possesses a major challenge for imaging these clusters as such. The rule of thumb is to keep the beam energy low (around 200 keV or less) and provide as low exposure as possible while imaging NCs. Even though this is the case, imaging clusters at atomic resolution would require even lower beam intensities.

Exempting the case of Au_{68}, only the structures of bigger clusters (greater than 100 atoms) have been solved using electron microscopy. Apart from the extended exposure damages that occur, induced and intrinsic mobility, the requirement to sample many nonequivalent orientations, and the need to measure a statistically significant number of equivalent structures limits the employability of electron microscopy in structure determination of smaller nanoclusters.

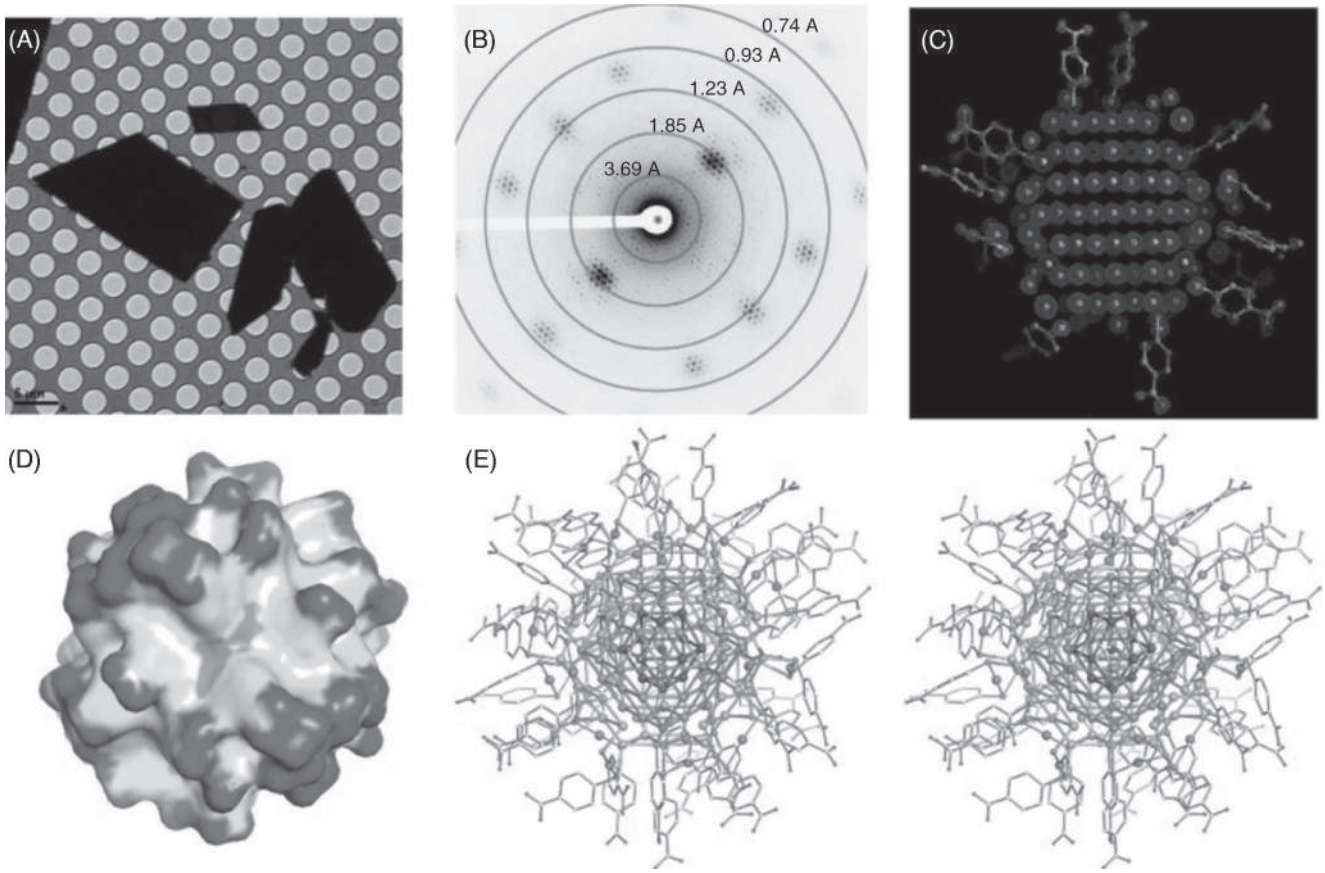

FIGURE 13.6 MicroED and X-ray determination of the crystal structure of Au_{146}(p-MBA)$_{57}$. (A) Transmission electron micrograph of Au_{146}(p-MBA)$_{57}$ crystals and (B) typical MicroED data extending well beyond 1 Å. (C) MicroED density map (2Fo-Fc, contoured at 2σ), shown as red mesh, identifies atomic positions of Au (white spheres) and S (yellow spheres) atoms. Ligands (p-MBA) are shown as blue framework. (D) Surface representation of the cluster with oxygen in red, carbon in white, sulfur in cyan, and gold in green. The full set of p-MBA ligands was determined using X-ray data. (E) Stereoscopic representation of the cluster including all gold atoms and p-MBA ligands. Reprinted with permission from ref.[18]. Copyright 2017 American Chemical Society.

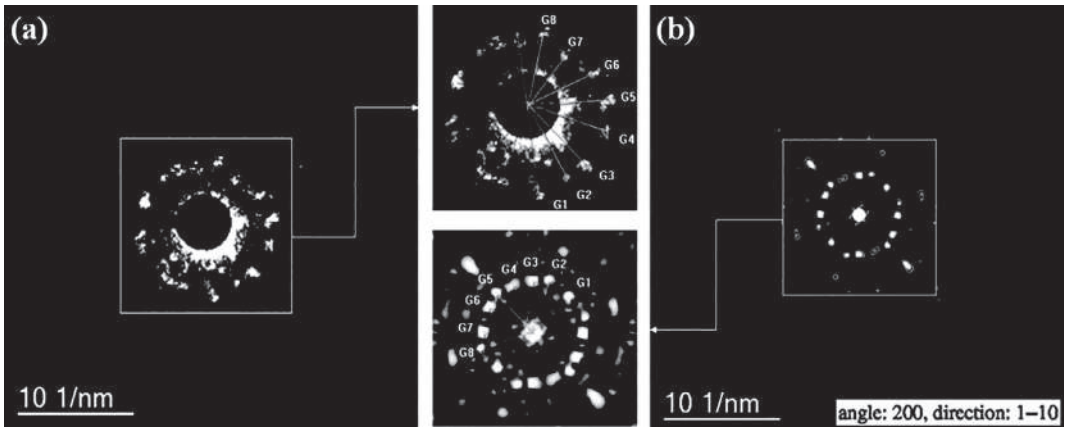

FIGURE 13.7 Comparison between experimental and theoretical electron diffraction patterns. In these patterns, a projection with 16 reflections is observed. (A) Experimental NBD pattern and (B) simulated electron diffraction pattern. Reprinted with permission from ref.[20]. Copyright 2017 American Chemical Society.

13.6 Analytical procedures for improved data collection

Overcoming the beam-induced damages is a major challenge while using electron microscopy to image or understand the structure of NCs. One of the solutions to this, especially in the case of thiolate protected clusters, is to use an electron beam of low intensity while imaging. Doing so will enable the capture of images directly from the crystallites, before the onset of damage. This approach using a conventional TEM would give a time window of approximately 60s for imaging before significant alterations happen to the sample, even without cooling. This has been used to successfully image various lattice planes in $Ag_{29}(BDT)_{12}(TPP)_4$ at 100 kV in a conventional TEM,[23] as depicted in Fig. 13.8. A TEM with a higher acquisition rate would enable more images with this strategy before the samples get damaged.

For this methodology to work, it is also essential that the crystallites are within a thickness range where electron beam can transmit. One safe method to achieve this is by grinding the crystallites using a mortar and pestle. Techniques like focused ion beam (FIB) can be used to cut very thin pieces from NC crystals. Still, the incident high-energy ion beam usually leaves a lot of debris on the sample surface, making it difficult to further analyze it in a TEM. Depending on the nature and stability of NCs, the crystalline structure may also get distorted to some extend while employing techniques like FIB.

13.7 Beyond electron microscopes

Beyond electron microscopy, other techniques should also be looked at to understand the structural details of NCs. One of the first techniques to image atoms was field ion microscopy (FIM). NCs have not been studied using FIM. A possible reason that prevented this might be the extreme experimental conditions involved in sample preparation and subsequent

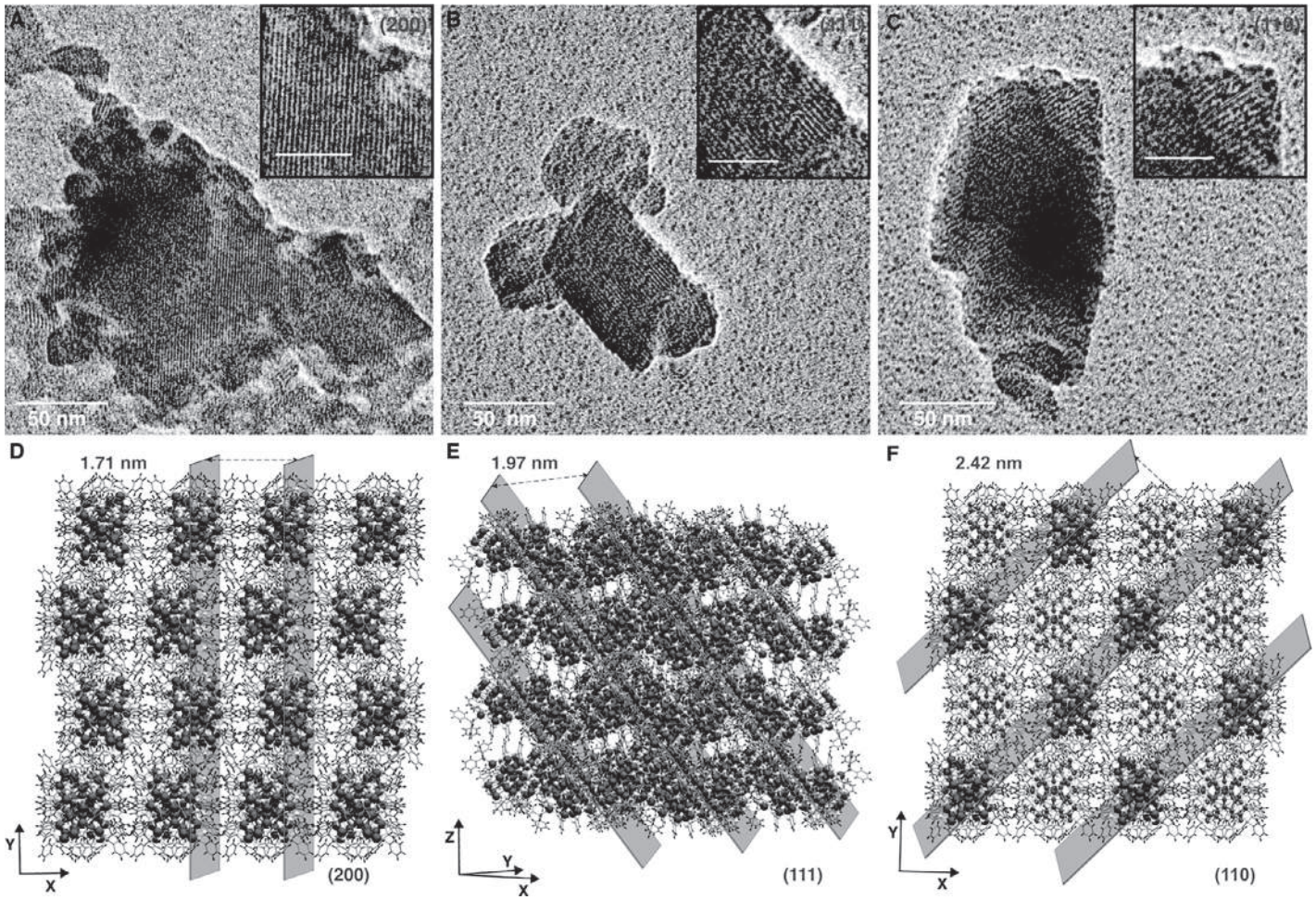

FIGURE 13.8 TEM images of $Ag_{29}C$ crystallites representing various lattice planes (A–C). The insets show expanded views of the corresponding lattice planes. (D)–(F) are representative images of a $2 \times 2 \times 2$ unit cell of $Ag_{29}C$. Scale bars in insets are 25 nm. Early signs of beam-induced damage are seen in B.

measurements. NC samples are in general fragile and may not withstand such an environment. But with new exotic clusters with increased stability being reported, the possibility does open up to characterize these nanoclusters using FIM. FIM also paved for another advanced characterization technique, atom probe tomography (APT), which has become prominent in metallurgy. APT is a technique that gives both 3D imaging and the chemical identity of atoms in a sample. In a recent study Ji et al.[22] employed APT in understanding the structure of a multivariate metal–organic framework (MOF) crystal, revealing some important structural aspects that were previously unknown. The structure of MOF-74 that was used in this study was previously solved using SCXRD. This might have an important implication in cluster science as well. The use of APT to understand single crystals of nanoclusters might shed deeper insights into their structures.

13.8 Summary and future perspective

There is a clear necessity for looking beyond SCXRD to understand structural details of NCs. Recent advancements have shown that electron microscopy can be an effective technique to address many of these issues. HAADF-STEM imaging has revealed the structure of many naked clusters. Applying a method like single-particle reconstruction from structural biology has made important advancements in cluster science. With the application of techniques like FIM, APT, electron tomography, etc., which are generally not employed to study clusters, novel structural aspects may be revealed. Traditional TEM itself can be used to understand cluster crystals by modified sample preparation protocols.

List of abbreviation

APT	atom probe tomography
C_s	spherical aberration
DFT	density functional theory
FIB	focused ion beam
FIM	field ion microscopy
HAADF	high-angle annular dark-field
MicroED	electron micro-diffraction
MOF	metal–organic framework
NBD	nanobeam electron diffraction
SCXRD	single crystal X-ray diffraction
STEM	scanning transmission electron microscopy
TEM	transmission electron microscopy
UV/Vis	ultraviolet/visible

References

1. Chakraborty I, Pradeep T. Atomically precise clusters of noble metals: emerging link between atoms and nanoparticles. *Chem Rev.* 2017;117(12):8208–8271. https://doi.org/10.1021/acs.chemrev.6b00769.
2. Jadzinsky PD, Calero G, Ackerson CJ, Bushnell DA, Kornberg RD. Structure of a thiol monolayer-protected gold nanoparticle at 1.1 Å resolution. *Science*. 2007;318:430–433. https://doi.org/10.1126/science.1148624.
3. Bodiuzzaman M, Ghosh A, Sugi KS, et al. Camouflaging structural diversity: co-crystallization of two different nanoparticles having different cores but the same shell. *Angew Chem Int Ed*. 2019;58:189–194. https://doi.org/10.1002/ANIE.201809469.

4. Crasto D, Malola S, Brosofsky G, Dass A, Häkkinen H. Single crystal XRD structure and theoretical analysis of the chiral $Au_{30}S(S\text{-}t\text{-}Bu)_{18}$ cluster. *J Am Chem Soc*. 2014;136:5000–5005. https://doi.org/10.1021/JA412141J.
5. Heaven MW, Dass A, White PS, Holt KM, Murray RW. Crystal structure of the gold nanoparticle $[N(C_8H_{17})_4][Au_{25}(SCH_2CH_2Ph)_{18}]$. *J Am Chem Soc*. 2008;130:3754–3755. https://doi.org/10.1021/JA800561B.
6. AbdulHalim LG, Bootharaju MS, Tang Q, et al. $Ag_{29}(BDT)_{12}(TPP)_4$: a tetravalent nanocluster. *J Am Chem Soc*. 2015;137:11970–11975. https://doi.org/10.1021/JACS.5B04547.
7. Li Y, Jin R. Seeing ligands on nanoclusters and in their assemblies by X-ray crystallography: atomically precise nanochemistry and beyond. *J Am Chem Soc*. 2020;142:13627–13644. https://doi.org/10.1021/JACS.0C05866.
8. Joshi CP, Bootharaju MS, Alhilaly MJ, Bakr OM. $[Ag_{25}(SR)_{18}]$-: the "golden" silver nanoparticle silver nanoparticle. *J Am Chem Soc*. 2015;137:11578–11581. https://doi.org/10.1021/jacs.5b07088.
9. Chakraborty P, Pradeep T. The emerging interface of mass spectrometry with materials. *NPG Asia Mater*. 2019;11:1–22. https://doi.org/10.1038/s41427-019-0149-3.
10. Wang ZW, Palmer RE. Determination of the ground-state atomic structures of size-selected Au nanoclusters by electron-beam-induced transformation. *Phys Rev Lett*. 2012; 108:245502. https://doi.org/10.1103/PhysRevLett.108.245502.
11. Wang ZW, Palmer RE. Experimental evidence for fluctuating, chiral-type Au_{55} clusters by direct atomic imaging. *Nano Lett*. 2012;12:5510–5514. https://doi.org/10.1021/nl303429z.
12. Wang ZW, Palmer RE. Mass spectrometry and dynamics of gold adatoms observed on the surface of size-selected Au nanoclusters. *Nano Lett*. 2012;12:91–95. https://doi.org/10.1021/nl2037112.
13. Wang ZW, Toikkanen O, Quinn BM, Palmer RE. Real-space observation of prolate monolayer-protected Au_{38} clusters using aberration-corrected scanning transmission electron microscopy. *Small*. 2011;7:1542–1545. https://doi.org/10.1002/smll.201002168.
14. Azubel M, Koivisto J, Malola S, et al. Electron microscopy of gold nanoparticles at atomic resolution. *Science*. 2014;345:909–912. https://doi.org/10.1126/science.1251959.
15. Azubel M, Koh AL, Koyasu K, Tsukuda T, Kornberg RD. Structure determination of a water-soluble 144-gold atom particle at atomic resolution by aberration-corrected electron microscopy. *ACS Nano*. 2017;11:11866–11871. https://doi.org/10.1021/acsnano.7b06051.
16. Shi D, Nannenga BL, Iadanza MG, Gonen T. Three-dimensional electron crystallography of protein microcrystals. *Elife*. 2013;2:e01345. https://doi.org/10.7554/ELIFE.01345.
17. Nannenga BL, Shi D, Leslie AGW, Gonen T. High-resolution structure determination by continuous-rotation data collection in MicroED. *Nat Methods*. 2014;11:927–930. https://doi.org/10.1038/nmeth.3043.
18. Vergara S, Lukes DA, Martynowycz MW, et al. MicroED structure of Au_{146}(p-MBA)$_{57}$ at subatomic resolution reveals a twinned FCC cluster. *J Phys Chem Lett*. 2017;8:5523–5530. https://doi.org/10.1021/ACS.JPCLETT.7B02621.
19. Yan N, Xia N, Liao L, et al. Unraveling the long-pursued Au_{144} structure by X-ray crystallography. *Sci Adv*. 2018;4:eaat7259. https://doi.org/10.1126/sciadv.aat7259.
20. Bahena D, Bhattarai N, Santiago U, et al. STEM electron diffraction and high-resolution images used in the determination of the crystal structure of the $Au_{144}(SR)_{60}$ cluster. *J Phys Chem Lett*. 2013;4:975–981. https://doi.org/10.1021/jz400111d.
21. Shibu ES, Muhammed MAH, Tsukuda T, Pradeep T. Ligand exchange of $Au_{25}SG_{18}$ leading to functionalized gold clusters: spectroscopy, kinetics, and luminescence. *J Phys Chem C*. 2008;112:12168–12176. https://doi.org/10.1021/jp800508d.
22. Ji Z, Li T, Yaghi OM. Sequencing of metals in multivariate metal-organic frameworks. *Science (80-.)*. 2020;369:674–680. https://doi.org/10.1126/science.aaz4304.
23. Mahendranath Ananthum et al. *Chemical Communication*. 2022;58(12):1906–1909. https://doi.org/10.1039/D1CC05643C.

CHAPTER

14

Computational approaches for nanocluster science

Paulami Bose[a], *Ganapati Natarajan*[b] *and Thalappil Pradeep*[c]

[a]DST Unit of Nanoscience (DST UNS) and Thematic Unit of Excellence (TUE), Department of Chemistry, Indian Institute of Technology Madras, Chennai, India [b]International Centre for Clean Water, Block-B, 2nd Floor, IIT Madras Research Park, Taramani, Chennai, India [c]Deepak Parekh Institute Chair Professor and Professor of Chemistry, Department of Chemistry, Indian Institute of Technology Madras, Chennai, India

14.1 Importance of computational approach in cluster science

The computational approach to chemistry allows properties of molecules and molecular materials to be understood in unprecedented detail with insights at the molecular scale. Computational chemistry contributes to the study of the fundamental properties of atoms, molecules, and chemical reactions, using mathematical and computational algorithms, statistics, and large databases to integrate chemical theory and modeling with experimental observations. With advancement in visualization software, it is possible to illustrate complex atomistic systems in an understandable form. Computational chemistry has applications to nearly all areas of chemistry including drug delivery, energy storage, cluster science, molecular dynamics, cheminformatics, and others.

One striking example of the usefulness of computational methods in MPCs is in assigning the peaks in the optical spectrum at specific wavelengths to specific transitions between molecular orbitals of the clusters, a task which requires an understanding of the electronic structure and symmetries of the orbitals, involved which is only found from the solution the underlying quantum-mechanical Hamiltonian by computational algorithms. A second common example is in structural prediction, where only mass-spectral data for the composition of a cluster is known and precise structural information from X-ray diffraction is lacking. Here, the predictive power of simulations enables one to generate the most likely structural models for the MPCs at the atomic and nanoscale. Computer simulations are complementary to that

Atomically Precise Metal Nanoclusters.
DOI: https://doi.org/10.1016/B978-0-323-90879-5.00018-4

of experiments: a more complete understanding of the structure and any desired properties of MPCs can be gained, since the details of the atomic scale structural and electronic mechanisms occurring in these quantum-confined MPCs are mostly unobservable being at the limits of experimental resolution.

Computational chemistry has a long history beginning with initial efforts to solve the Schrödinger equation for ions and molecules using numerical methods, but is now a standard component of any chemical investigation in the literature, and several awards have recognized the importance of computational methods. In 1995, Paul Crutzen, Mario Molina, and F. Sherwood Rowland were awarded the Nobel Prize in Chemistry for creating mathematical models using thermodynamic and chemical laws to explain the formation and decomposition of ozone in the atmosphere. In 1998, Walter Kohn and John Pople won the Noble Prize in Chemistry for their work on density functional theory (DFT) and computational methods in quantum chemistry. And finally with the 2013 Nobel Prize in Chemistry win by Martin Karplus, Michael Levitt, and Arieh Warshel for their work in 1970 which laid the foundations for today's computer models that combine principles of classical (Newtonian) physics and quantum physics to better replicate the fine details of chemical processes. With the ongoing technical advancements, such as those in machine learning and artificial intelligence, there is a tremendous boost to the field of computational chemistry.

This chapter begins with the basic computational methods followed by the electronic structure and its underlying concepts and models, such as, superatoms. Next, the methods used for understanding and predicting the structure of nanoclusters are discussed. Then the application of computational techniques to calculate properties, such as optical, catalytic, magnetic, is addressed briefly.

14.2 Basics of computational methods and models

The core principle of computational chemistry is that the properties of any molecule or solid, including its chemical bonding and structure are ultimately derived from the properties of the electrons and nuclei, which are based on the theory of quantum mechanics. In principle, all chemical properties, including the structure, valency, and chemical bonding of atoms and molecules, and condensed matter, such as liquids and solids, can be predicted by quantum mechanical concepts and calculations.

Computational chemistry was original founded as an approach which attempted to practically compute the predictions of quantum mechanics for molecules, thereby leading to predictions and explanations for their structure, bonding, spectroscopic properties, reactivity, and so on.

At the quantum level, molecular and chemical behavior, such as optical properties, bonding or reactivity of any assembly of atoms or molecules containing N_n nuclei and N_e electrons is governed by the Schrödinger equation, which in its nonrelativistic time-dependent form is given as below:

$$i\hbar\frac{d}{dx}\left|\Psi(\{R_n\},\{r_n\}),t\right\rangle = \hat{H}\left|\left|\Psi(\{R_n\},\{r_n\}),t\right\rangle\right. \tag{14.2.1}$$

where $\boldsymbol{R}_n$ and $\boldsymbol{R}_e$ stand for the all the N_n nuclear and all N_e electron coordinates, and the Hamiltonian, $\hat{H}$, is given by:

$$\hat{H} = -\sum_{I=1}^{N_n} \frac{\hbar^2}{2M_I}\nabla_I^2 - \sum_{i=1}^{N_e} \frac{\hbar^2}{2m}\nabla_i^2 + \frac{e^2}{2}\sum_{I=1}^{N_n}\sum_{J\neq I}^{N_n} \frac{Z_I Z_J}{|R_I - R_J|} + \frac{e^2}{2}\sum_{i=1}^{N_n}\sum_{j\neq i}^{N_n} \frac{Z_I Z_J}{|r_i - r_j|} + e^2 \sum_{I=1}^{N_n}\sum_{j\neq I}^{N_n} \frac{Z_I}{|R_I - r_j|} \tag{14.2.2}$$

where Z stands for the nuclear charge, M denotes the nuclear mass, and m the electron mass. The subscripts I and J run over the nuclei and subscripts i and j run over the electrons.

Computer simulation results can provide crucial insights needed in interpreting experimental measurements, predicting material properties, and in designing new compounds. Many software packages, such as CP2K, GPAW, LAMMPS, GROMACS, Quantum espresso to name but a few, are now available providing powerful tools for atomistic simulations.[1] Some of these packages combine a variety of methods such as DFT, ab initio or DFT-based molecular dynamics (MD), Monte Carlo (MC), and Ehrenfest dynamics. We now present the various methods used in molecular modeling in the following section.

14.2.1 Density functional theory

DFT is a theory of electronic ground-state structure, expressed in terms of the electronic density distribution $n(\mathbf{r})$ for many electron systems.[2] DFT contributes to the understanding and calculation of the ground-state density, $n(\mathbf{r})$, and energy, E, of any system consisting of nuclei and electrons, such as, molecules, solids, liquids, and nanoclusters, etc., with or without applied *static* perturbations. The electron density is a one-electron quantity that is easier to compute since it with approximations than the complicated ground-state many-body electronic wavefunction which depends on the coordinates of all the electrons, and this leads to elegant simplification of the electronic part of the quantum-mechanical many-body structure problem of Eq. (14.2) above, in terms of a variational principle involving only the electron density. The choice of computational method depends on the number of atoms in the system (N_{at}) and on the level of accuracy acceptable. DFT as well as traditional wavefunction-based methods such as coupled-cluster and quantum Monte Carlo are preferred for few-atom systems ($N_{at} \sim 5$–10) with high accuracy while the DFT and semiempirical methods are suitable choice for large-atom systems ($N_{at} \sim 10$–1000) with modest accuracy, where quantum effects are important.[2] The central quantities of a DFT method are the electron density $n(\mathbf{r})$ and the fictitious Kohn–Sham single-particle orbitals ψ_i, and their energies, ε_i.

In 1964, Hohenberg and Kohn developed the DFT[3] based on the proof of their two theorems. According, to their first theorem, for an arbitrary number of N electrons in a box subjected to an external potential $v(\boldsymbol{r})$ and with the mutual electron–electron Coulomb repulsion, the external potential is in one-to-one correspondence with the resulting electron density, $n(\mathbf{r})$, and is also unique functional of the electron density. The second Hohenberg–Kohn theorem states that the total energy of the ground state may be expressed as a functional of the ground-state electron density, $n(\mathbf{r})$. The energy functional of the electrons in the system with a nondegenerate ground state is written as,

$$E[n] = F[n] + V[n], \tag{14.2.2.1}$$

where $F[n]$ is a *universal functional* of the charge density, $n(\mathbf{r})$, in the sense of being independent of the details of the atomic or molecular system, and is given by,

$$F[n] = T[n] + U[n], \tag{14.2.2.2}$$

where $T[n]$ is the kinetic-energy functional and $U[n]$ is the potential-energy functional of the interacting electron system, respectively.

However, the precise mathematical expressions of T and U functionals are unknown, unlike that for the external potential functional V, and this will have an important consequence. Now, for a given potential $v(r)$, the total energy E_v can be defined as the functional of electron density $n(\boldsymbol{r})$,

$$E_v[n(r)] = \int v(r)n(r)dr + F[n(r)] \tag{14.2.2.3}$$

Here, the charge density is defined only in the terms of wave functions of the occupied states,

$$n(r) = \sum_{i=1}^{N} \left|\psi_i(r)\right|^2 \tag{14.2.2.4}$$

Hohenberg and Kohn established that the functional $E_v[n(r)]$ in Eq. (14.2.2.3) attains its minimum for the ground state $n(\boldsymbol{r})$, subject to the constraint of constant number of particles (N),

$$N[n] = \int n(r)\, dr = N \tag{14.2.2.5}$$

Hohenberg and Kohn proved a variational principle in their paper which may be quoted as,

> *"It is well known that for a system of N particles, the energy functional $E_v[n']$ of Ψ' has a minimum at the '**correct**' ground state Ψ, relative to **arbitrary variations of Ψ'** in which the total number of particles is kept constant."*

$$E_v[\Psi'] = \langle\Psi'|V|\Psi'\rangle + \langle\Psi'|T + U|\Psi'\rangle \tag{14.2.2.6}$$

The next crucial step in the proof involves a density $n'(\boldsymbol{r})$, associated with another potential $v'(\boldsymbol{r})$ that leads to the energy that is higher than the one obtained for the ground state density $n(\boldsymbol{r})$ of the system. The following inequality was established, also known as the DFT variational principle,

$$E_v[\Psi'] = \int v(r)n'^{(r)}dr + F[n'], > E_v[\Psi] = \int v(r)n(r)\, dr + F[n] \tag{14.2.2.7}$$

The energy functional of Eq. (14.2.2.3) cannot be minimized s the exact form of the universal functional $F[n]$ is unknown, and we only have the form of the external potential functional $V[n]$. The achievement of Kohn and Sham was to rearrange and regroup the terms of Eq. (14.2.2.3) by introducing a reference system of non-interacting electrons making possible to use an approximation for the interacting part of the potential. The Kohn–Sham method put the energy functional into a form which was possible to minimize by the solution of a single-particle Schrödinger equation, now known by their name.

Kohn and Sham introduced the local-density approximation (LDA) as an approximation to the interacting part of F[n] and then the energy functional equation was given as,

$$E = \int v(r)n(r)dr + \frac{1}{2}\int\int \frac{n(r)n(r')}{|r-r'|}drdr' + T_s[n] + E_{xc}[n] \tag{14.2.2.8}$$

where $T_s[n]=\sum_{i=1}^{N} \Psi_i| - \frac{1}{2}\nabla_i^2|\Psi_i$ represents the kinetic energy of a non-interacting reference system of electrons with density $n(\boldsymbol{r})$ and $E_{xc}[n]$ is the exchange-correlation (XC) energy. The functional, $E_{xc}[n]$ is expressed in terms of the exchange-correlation energy per electron ($\in_{xc}(n(\boldsymbol{r}))$ of a uniform electron gas having density of $n(\boldsymbol{r})$,

$$E_{xc}[n] = \int n(r)\in_{xc}(n(r))dr \tag{14.2.2.9}$$

where, in the LDA approximation, $E_{xc}[n] = -\frac{3}{4}\left(\frac{3}{\pi}\right)^{1/3}\int n(r)^{4/3}$

Finally, writing the Euler–Lagrange equation for stationary E leads to a self-consistent single-electron equation called Kohn–Sham equation,

$$\left\{-\frac{1}{2}\nabla^2 + \left[v(r) + \int \frac{n(r')}{|r-r'|}dr' + \mu_{xc}(n(r))\right]\right\}\psi_i(r) = \varepsilon_i\psi_i(r) \tag{14.2.2.10}$$

where $\mu_{xc}(n(\boldsymbol{r}))$ is the exchange correlation contribution to the chemical potential of a uniform gas of density $n(\boldsymbol{r})$, and is known as the Kohn–Sham potential,

$$\mu_{xc}(n(r)) = \frac{\delta E_{xc}[n(r)]}{\delta n(r)}. \tag{14.2.2.11}$$

The solution of the Kohn–Sham equation leads to a set of energy eigenvalues ε_i and orbitals $\psi_i(r)$ known as the Kohn–Sham orbitals. Thus the ground-state density and energy from DFT are composed of sums of single-particle quantities, and it is advantageous to ascribe meaning to these constituent single-particle quantities. While it is unclear what is the exact physical meaning for the Kohn–Sham eigenvalues is, they are widely used to calculate the EDOS and the orbitals, in order to visualize how the density is distributed for each electron in the spectrum of states, for example, the band-gap states in a metal nanocluster, or semiconducting quantum dot. The computational solution of the Kohn–Sham equations depends on the choice of basis-set functions and exchange-correlation functional which are known as the level of theory.

Improvements to the LDA XC functional are possible such as the generalized gradient approximation (GGA) functionals and these give improved results for properties such as binding energies, vibrations, and energy gaps. Hybrid XC functionals which use an exact exchange part from Hartree–Fock theory, such as B3LYP and van der Waals functionals are also widely used. Magnetic or spin-polarized systems with unpaired electrons are treated by decomposing the electron density into a sum of up-spin and down-spin densities, and in this case the LDA approximation is known as the LSDA (local spin-density approximation).

DFT, especially when all-electron calculations are considered is an ab initio method which does not require the use of empirical data from experiments but only the atom element types or their positions in space to solve the equations. In practice, information from experiments is sometimes used to calibrate the calculations; many DFT methods use pseudopotentials for reasons of efficiency to replace the effects of core electrons, and in some cases fitting of

DFT calculations is done with reference to experimental results in level of theory studies, for example.

The key consideration in the solution of the Kohn–Sham equation is the choice of basis set and XC functional to be used, and this will often depend on the types of atoms, and their number and whether higher accuracy required. A multitude of basis sets such as gaussian, atomic orbital, real-space grid functions, and wavelets are in use, and generally the more basis functions are included the more accurate the calculation becomes. Depending on the molecular system, for atomic orbital or Gaussian orbital basis sets, different types of functions such as radial, split-valence, polarization, and diffuse functions may be included providing an improved description of bonding and molecular properties. In cases where a more approximate property calculation is sufficient, which is sometimes the case for larger molecular systems, efficiency is the prime consideration and a minimal basis set may be used. In chemical systems, a more accurate description of the valence electrons, rather than the core electrons, is often needed and the treatment of the core electrons may be approximated using effective-core potentials or pseudopotentials.

14.2.2 Total energy and force methods

Applying the Born–Oppenheimer approximation to decouple the electron–nuclear systems, the forces on the nuclei may be calculated from the ground-state wavefunction and the Hamiltonian derivative matrix, using the Hellmann–Feynman theorem,[4]

$$F_i = -\left\langle \psi \left| \frac{\partial}{\partial R_i} \hat{H} \right| \psi \right\rangle \tag{14.2.3.1}$$

where ψ is the many electron ground-state function and the derivative acts on the parts of the Hamiltonian which depend on the atomic positions, namely, the nuclei–nuclei interaction potential and electron–nuclear interaction potential. The utility of the Hellman–Feynman theorem is that it enables us to calculate the forces on the atoms without having to evaluate derivatives by finite differences, which is a computationally expensive procedure requiring $6N$ energy evaluation for N atoms. Instead, only a single expectation value need be evaluated for each atom.

The core algorithm of ab initio optimization and dynamics relies on the computation of the total energy also known as the interatomic potential, or potential energy surface.[5] The value of the interatomic potential, for a fixed configuration of nuclei, $V(\mathbf{R}1,\ldots,\mathbf{R}N)$ is obtained as the total energy of the system which is the sum of the KS energy functional E_v, defined above, and the repulsive potential energy functional of the nuclei–nuclei interaction V_{nn}. Hence, after the solution of the electronic part of the Hamiltonian by the KS equation, the interatomic potential, or total energy function, may be calculated, and by applying the Hellman–Feynman theorem the forces on each atom may also be computed. Finding the optimal geometry of a molecular system is then equivalent to local minimization of the potential energy surface and is effected by algorithms in which the nuclear positions may be moved according to an optimization scheme which lowers the total energy until its minimum is found. Alternatively, the interatomic potential computed ab initio may be used to simulate the time evolution of nuclear positions using the classical molecular dynamics scheme described in the next section.

14.2.3 Force fields, classical molecular dynamics, and Monte Carlo methods

A force field (FF) is a mathematical expression relating the energy of the system to its particle coordinates. The force field methods are designed to overcome the scaling issues in ab initio methods by expressing the electronic energy as a parameterized function.[6] Typically, the parameters are fitted to either experiments or high level ab initio calculations. The total energy (E_{FF}) expression takes into account the contribution of the bonding and nonbonding interactions,

$$E_{FF} = E_{str} + E_{bend} + E_{tors} + E_{vdw} + E_{el} + E_{cross} \tag{14.2.2.1}$$

Here, the stretching (*str*), bending (*bend*), and torsion (*tors*) modes contribute to the bonding interactions. Electrostatic (*el*) and van der Waals (*vdw*) forces contribute to the nonbonding interactions, while, E_{cross} corresponds to the coupling between the other five energy terms. Dreiding[7] and universal[8] force fields (UFF) are methods that contain parameters for all the atom in the periodic table. Other popular force fields, with more specialized purposes such as biomolecules and liquids, are CHARMM,[9] AMBER,[10] GROMOS,[11] OPLS,[12] and COMPASS.[13]

The primary objective of a classical Monte Carlo (MC) simulation is to generate an ensemble of representative configurations by applying random perturbations, for a complex macromolecular system under specific thermodynamics conditions.[14] Although the Monte Carlo simulations do not provide any information on the time evolution, instead they provide conformations from which probabilities and relevant thermodynamic observations such as free energy may be calculated. Monte Carlo simulations also play a fundamental role in designing complex and hybrid molecular dynamic (MD) algorithms.[15]

On the other hand, molecular dynamics studies the time evolution, called the trajectory, of the coordinates and the state of a macromolecular structure. A typical trajectory is solved using Newton's equations, and it is important to interpret time-dependent observables, molecular surface accessibility, molecular interactions, antibody–antigen interaction, and others. An MD calculation requires a set of initial positions and velocities for all atoms, the forces acting between the particles, and a definition of the boundary conditions. The trajectory is obtained by solving the classical equation of motion,

$$m_i \frac{d^2 r_i}{dt^2} = f_i = \frac{\partial}{\partial r_i} U(r_1, r_2, \ldots, r_N) \tag{14.2.2.2}$$

where $U(r_1,r_2,\ldots,r_N)$ is the potential energy of N particles at its coordinates. The initial position and velocity of each particle can be obtained from the crystallographic file and Maxwellian distribution data, respectively. The force (f_{ij}) exerted by atom j on atom i could be calculated, for example, from the Lennard–Jones potential,

$$f_{ij} = -\frac{\partial y}{\partial x}\left\{4\epsilon\left[\left(\frac{\sigma}{r_{ij}}\right)^{12} - \left(\frac{\sigma}{r_{ij}}\right)^{6}\right]\right\} = \frac{48\epsilon}{\sigma^2}\left[\left(\frac{\sigma}{r_{ij}}\right)^{14} - \frac{1}{2}\left(\frac{\sigma}{r_{ij}}\right)^{8}\right] r_{ij}, \tag{14.2.2.3}$$

where σ is the distance at the potential well minimum and ϵ is the well depth. The periodic boundary condition is finally defined depending on the system in consideration.

14.2.4 QM/MM and multiscale methods

Warshel and Levitt introduced a hybrid QM/MM (quantum mechanics/molecular mechanics) approach to the molecular simulation method.[16] In this method, the system is categorized into a chemically active part and an inert environment and then treated by quantum mechanics (QM) and classical molecular mechanics methods (MM). This method is known for providing accurate structural and free energy changes in solution at an affordable computational cost. The energy of the system can be calculated using additive energy scheme[17]:

$$E(S) = E_{QM} + E_{MM} + E_{QM/MM} \tag{14.2.2.1}$$

where E_{QM} is the QM energy of the QM region and E_{MM} is the MM energy of the MM region. $E_{QM/MM}$ represents the interaction energy between the two systems which are based on electrostatic and van der Waals interaction described by Lennard–Jones potential,

$$E_{QM/MM} = \hat{H}_{QM-MM} + E_{ij}, \tag{14.2.2.2}$$

$$\hat{H}_{QM-MM} = -\sum_{i,m} \frac{q_m}{r_{im}} + \sum_{A,m} \frac{Z_A q_m}{R_{Am}}. \tag{14.2.2.3}$$

The first two terms represent the interaction between the classical charges of the MM region and the total charge density in the QM region. Here, q_m represents the charges of MM atoms, Z_A is the atomic number of QM atoms, i runs over the QM electrons, A over the QM atoms including link atoms, and m over the MM atoms. The van der Waals interaction (E_{ij}) is usually described by Lennard–Jones potential, is given by the equation,

$$n(r) = \sum_{i=1}^{N} \left|\psi_i(r)\right|^2 \tag{14.2.2.4}$$

where i and j run over the QM and MM atoms, respectively, and σ and ϵ are constants already defined in Eq. (14.2.2.3) above which depending on the atom types.

Such methods have applications in modeling the structure of cluster–biomolecule interactions such as protein protected nanoclusters, or nanoclusters in solution where the nanocluster is treated by quantum methods and the solvent classically.

14.2.5 Transition states and reaction pathways

In 1935, theory of reaction rates, now known as conventional transition state theory, was proposed simultaneously by Henry and Eyring[18] and by Evans and Polanyi.[19] Transition state theory is primarily a theory for electronically adiabatic reactions, in other words, reactions occurring on a single Born–Oppenheimer potential energy surface. The transition state theory can predict the intermediates, chemical reaction mechanisms, and also the reaction rates.

Upon solving the time-dependent Schrödinger equation of Eq. (14.2.6.1), one can obtain exact rates of reactions.

$$i\hbar \frac{\partial \Psi(R_n, R_e, t)}{\partial t} = \hat{H}_{tot} \Psi(R_n, R_e, t), \tag{14.2.6.1}$$

$$\text{where, } \hat{H}_{tot} = \hat{K}_n + \hat{K}_e + \hat{V}_{nn} + \hat{V}_{ee} + \hat{V}_{ne}. \tag{14.2.6.2}$$

The total Hamiltonian of Eq. (14.2.6.2) is given as the sum of nuclear (K_n) and electronic kinetic energies (K_e) and the internuclear (Kn_n), nuclear–electron (K_{ee}), and electron–electron interactions (V_{ne}).

The wave function can be defined in terms of the basis functions depending on the nuclear coordinates, $\psi_\mu(R_n,t)$:

$$\Psi(R_n, R_e, t) = \sum_\mu \chi_\mu(R_e; R_n)\psi_\mu(R_n, t), \tag{14.2.6.3}$$

Substituting in Eq. (14.2.6.1) gives,

$$i\hbar\frac{\partial\psi_v}{\partial t} = \left[\hat{K}_n + \hat{V}_{nn}\right]\psi_v + \sum_\mu \chi_v\left|\hat{K}_e + \hat{V}_{ee} + \hat{V}_{ne}\right|\chi_\mu\psi_\mu + \sum_\mu C_{v\mu}\psi_\mu, \tag{14.2.6.4}$$

$$\text{where, } C_{v\mu} = \left\langle \sum_i \frac{1}{m_i}\chi_v|\nabla_i|\chi_\mu\nabla_i + \frac{1}{2}\chi_v\left|\nabla^2{}_i\right|\chi_\mu \right\rangle. \tag{14.2.6.5}$$

Here, the Born–Oppenheimer approximation comes into play, $C_{v\mu}$ =0, and the electronic problem is assumed to be solved by,

$$\hat{K}_e + \hat{V}_{nn} + \hat{V}_{ee} + \hat{V}_{ne}\left|\chi_v(R_e; R_n)\right\rangle = \varepsilon_v(R_n)\left|\chi_v(R_e; R_n)\right\rangle. \tag{14.2.6.6}$$

The final equation with decoupled electronic and nuclear degrees of freedom where the nuclei can move on a single potential energy surface, $\varepsilon_v(\boldsymbol{R}_n)$,

$$i\hbar\frac{\partial\psi_v(R_n, t)}{\partial t} = \left[\hat{K}_n + \varepsilon_v(R_n)\right]\psi_v(R_n, t). \tag{14.2.6.7}$$

The transition state theory presented above is based on four assumptions, (1) classical nuclear dynamics, (2) nuclear dynamics occur on a single potential energy surface, (3) thermal equilibrium at the reactant valley, and (4) no re-crossing of the transition state potential energy surfaces. The electronic problem can be solved using ab initio, DFT, semiempirical model potentials, and others.

14.2.6 TD-DFT and excited state methods

In 1984, Runge and Gross proposed the extension of DFT to the time-dependent domain, called as TD-DFT.[20] With the development of an effective linear response (LR) formalism for TD-DFT, known as Casida's equations[21] or random-phase approximation it was possible to rapidly and efficiently determine the solution of the TD-DFT equations for molecules.[22] Today, TD-DFT is a popular approach for modeling the structures, energies, and electronic properties of excited states (ES). TD-DFT finds application in the determination of ES structures and emission wavelengths, in vibrationally resolved optical spectra, estimation of atomic point charges and dipole moments, and also in the simulation of photochemical reactions.[23]

An extensive review of TD-DFT was published by Gross and Kohn followed by papers by Casida. Here, the simpler solution to the TD-DFT as published by Stratmann and Scuseria by excluding the spin variables is presented.[22]

Assuming, the charge density $\rho(\boldsymbol{r},\boldsymbol{t})$ of the interacting system is defined as,

$$\rho(r,t) = \sum_{i=1}^{N} \left|\psi_i(r,t)\right|^2 \tag{14.2.7.1}$$

The time-dependent Kohn–Sham equation is,

$$\left[-\frac{1}{2}\nabla^2 + v_{eff}(r,t)\right]\psi(r,t) = i\frac{\partial}{\partial t}\psi(r,t) \tag{14.2.7.2}$$

where $v_{\mathit{eff}}(\boldsymbol{r},t)$ is the potential for a noninteracting system with orbitals $\psi(\boldsymbol{r},t)$ yielding a charge density $\rho(\boldsymbol{r},t)$ and we have used atomic units. The time-dependent effective Kohn–Sham potential is:

$$v_{eff}(r,t) = v(t) + v_{SCF}(r,t) \tag{14.2.7.3}$$

where $v(t)$ is a perturbation applied as a time-varying external potential and the self-consistent field potential, the potential seen on average by one electron in the presence of all others, v_{SCF}, comprises the time dependence of the Hartree and exchange-correlation potential, as given below.

$$v_{SCF}(r,t) = \int \frac{\rho(r,t)}{|r-r'|}dr' + v_{xc}(r,t) \tag{14.2.7.4}$$

where v_{xc} is the exchange-correlation potential defined as the functional derivative of the exchange-correlation action A_{xc},

$$v_{xc}[\rho](r,t) = \frac{\delta A_{xc}[\rho]}{\delta\rho(r,t)} \approx \frac{\delta E_{xc}[\rho_t]}{\delta\rho_t(r,t)} = v_{xc}[\rho](r) \tag{14.2.7.5}$$

Here, the functional A_{xc} of ρ over both space and time is approximated by E_{xc}, exchange-correlation functional of time-independent Kohn–Sham theory, by integrating out the explicit time dependence of A_{xc}. E_{xc} is becomes a functional of ρ over space at a fixed time, t. This approximation is known as the adiabatic approximation of TD-DFT. The solution of the TD-DFT Kohn–Sham equation may be obtained efficiently using linear-response methodology, without needing to fully solve the Kohn–Sham equations as in time-independent DFT.

The linear response to a weak and time-dependent perturbation, such as spatially uniform electric field oscillating with a frequency (ω), provides information related to the optical absorption of the molecule due to electronic excitations. An electric field ($\delta v(t)$) is applied as a perturbation into the Kohn–Sham (or the Hartree–Fock) Hamiltonian to a system already in the ground state.

$$\delta v_{eff}(r,t) = \delta v(t) + \delta v_{SCF}(r,t) \tag{14.2.7.6}$$

where $\delta v_{SCF}(t)$ corresponds to the linear response arising from the change in charge density.

The outputs of a linear response TD-DFT calculation are a set of excitation energies, or frequencies, and oscillator strengths of the lowest energy excitations. Hybrid functionals like B3LYP, HSE06, and PBE0, and long-range corrected functionals such as ωLC-PBE, LC-BLYP, CAM-B3LYP, and ωB97X-D are now routinely used in the excitation-energy calculations of molecules due to their higher accuracy.

Time-dependent Hartree–Fock (TD-HF) and configuration-interaction singles are also less accurate but more computationally efficient methods which are often used by computational chemists.

14.3 Electronic structure of monolayer protected nanoclusters from DFT

In nanometer-sized metal particles, the fundamental physical concept of quantum confinement and symmetry arises from the fermion shell structure. The Nobel Prize of Physics in 1963 went to the concept of fermion shell making it a significant discovery in the history of science. The most stable monolayer-protected metal nanoclusters essentially have an electronic structure with a large HOMO (highest occupied molecular orbital) and LUMO (lowest unoccupied molecular orbital) energy gap, and the free-electron behavior is responsible for the overall electronic properties, like optical excitations and chemical reactivity. Extensive literature is already available on theoretical and experimental work of the monolayer protected nanoclusters.[24] This section is specifically dedicated to a popular concept of "superatoms."

14.3.1 Electronic stability of nanoclusters

The periodic arrangement and properties of elements in the Mendeleev's periodic table can be fully explained in terms of the electronic theory of atoms and the universal *Aufbau* sequence of electrons in a centrosymmetric Coulombic potential. Similarly, the stability and chemical properties of simple metal nanoclusters and nanoparticles can be predicted using the *superatom electronic theory*.[25] For most of the gold nanoclusters, the 6s atomic orbitals mainly contributes to the delocalized orbitals having 6s-character and closer to the Fermi level.[26] The exceptional stability in nanoclusters is associated with a total electron count (n^*).

$$n^* = 2, 8, 18, 34, 58, 92, 138, \ldots. \tag{14.3.1.1}$$

The n^* are known as magic numbers that correspond to a strong electron shell closure configuration in an anharmonic mean-field potential. Similarly, in an atom–ligand complex, superatoms tend to get electronically stabilized by adsorption of ligands. Here, the ligands can either withdraw electrons from the metal core or get attached as a weak Lewis base (L) ligand and hence coordinate to the metal core via a dative bond. An electronically closed-shell superatom having an empirical formula, $(L_s \cdot A_N X_M)^z$ has an electron count,

$$n^* = N_{v_A} - M - z \tag{14.3.1.1}$$

where the shell-closing electron count (n^*) of the metal core needs to satisfy the magic number. The n^* is calculated from the superatomic number (product of number (N) of atoms in the metal core, A, and their atomic valence, v_A), number (M) of electron-localizing or electron-withdrawing ligands, and overall charge on the complex (z). Weak ligands, L_s, coverage is required for steric protection of the metallic core.

14.3.2 Superatom model

For a nanocluster of atoms, the concept of electronic states being analogous to an atom or a nucleus is proposed on the basis of similarity of shell structure in the electronic energy

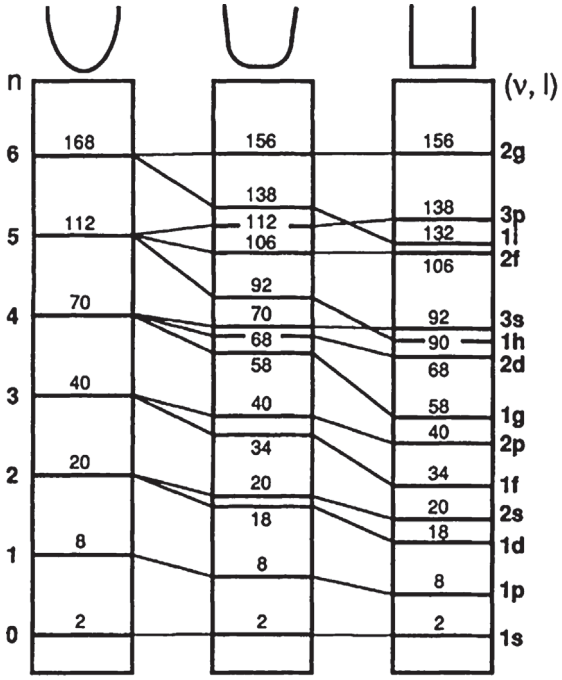

FIGURE 14.1 Noninteracting electrons occupying energy levels in spherical 3D infinite, harmonic, intermediate, and squared, potential wells, shown respectively from left to right. Reproduced with permission from ref.[28b]. Copyright 1993, The American Physical Society.

levels which arise from the spherically-symmetric central potentials which are common to all three situations. The superatom model explains the enhanced stability of nanoclusters by their electronic shell closure configuration. In 1984, Knight et al. observed the mass spectra of gas phase Na clusters containing 2, 8, 20, 40, …, atoms per nanocluster and their enhanced stability can be explained by the *nuclear shell model*.[27] The electrons are nearly free in a Na nanocluster as they are in its bulk state. Based on this assumption, Knight proposed a simple Jellium model where the Na ions are replaced by a uniform spherical potential well. According to the Jellium model, the valence electrons in a metallic nanocluster are treated as an electron gas in a continuous potential box of square-well, parabolic, or rounded square radial dependence, which represents the attractive Coulomb potential of the positive core as shown in Fig. 14.1.[28] Later theoreticians developed a similar model for other metal nanoclusters, such as that proposed by Nilsson, where the *s* and *p* valence electrons are delocalized over the entire nanocluster in a spherically-symmetric square potential well.[29] Solving the Schrödinger equation gives rise to a new set of molecular orbitals with the same symmetry as normal atomic orbitals, and this was called the *superatom model*. Based on *Aufbau* filling of the electronic shells, new superatomic orbitals appear as $|1S^2|$, $|1S^21P^6|$, $|1S^21P^61D^{10}2S^2|$, $|1S^21P^61D^{10}2S^21F^{14}2P^6|$,….which correspond to electron counts of 2, 8, 20, 40, …, respectively.

14.3.3 Valence electron count and models for the shell-closing number

Walther et al. introduced the concept of the alternate *superatom model* for monolayer-protected metal nanoclusters (MPCs) of gold.[30] The electron count rule slightly varies for metal

MPCs compared to the gas phase NCs. In the case of metal MPCs, the protecting ligands can delocalize electrons through ionic, covalent, or even dative bonds. In 2008, the estimation of the total free valence electron count (n_e) in gold-containing MPCs protected by ligands, like thiolates and/or phosphines, denoted by $[Au_m(SR)_n]^q$, was proposed using a simple formula:

$$n_e = m - n - q \tag{14.3.1}$$

where m, n, and q are the number of metal atoms, ligands, overall charge, respectively.

14.3.4 Projection of orbitals onto superatomic states (PDOS)

The density of states is defined by,

$$\rho(\varepsilon) = \sum_n \langle \psi_n | \psi_n \rangle \delta(\varepsilon - \varepsilon_n) \tag{14.3.2}$$

where ε_n is the eigenvalue of the eigenstate $|\,|\psi_n\rangle$.

The above equation can be rewritten with the complete orthonormal basis,

$$\rho(\varepsilon) = \sum\nolimits_i \rho_i(\varepsilon), \;\; \rho_i(\varepsilon) = \sum\nolimits_n \langle \psi_n | i \rangle \langle i | \psi_n \rangle \delta(\varepsilon - \varepsilon_n) \tag{14.3.3}$$

$$\rho(\varepsilon) = \int dr \rho(r, \varepsilon), \; \rho(r, \varepsilon) = \sum\nolimits_n \langle \psi_n | r \rangle \langle r | \psi_n \rangle \delta(\varepsilon - \varepsilon_n) \tag{14.3.4}$$

Using that $1 = \sum_i |i\rangle\langle i|$ and $1 = \int dr |r\rangle\langle r|$.

where $\rho_i(\varepsilon)$ and $\rho(r, \varepsilon)$ refer to projected density of states (PDOS) and local density of states (LDOS).

The electron density can be calculated by energy integration of LDOS multiplied by a Fermi distribution,

$$\int d\varepsilon n_F(\varepsilon) \rho(r, \varepsilon) = n(r) \tag{14.3.5}$$

Summation of PDOS over i returns the spectral weight of orbital i.

Molecular orbital PDOS is the projection of the Kohn–Sham eigenstates $|\,|\psi_n\rangle$ over a set of orthonormal states $|\,|\psi_{n'}\rangle$. The solution of the KS equations can be computed using real-space DFT code GPAW (grid-based projector-augmented wave method).[31]

In case of gold nanoclusters, *6s* atomic orbitals mainly contribute to the superatomic orbitals over *p* and *d* atomic orbitals.[32] Jiang et al. reported a DFT-based calculations considering a spherical core-shell Au_{13}, hexagonal planar Au_7 and nanotube segment of Au_{35} systems representing zero-, two-, and one-dimensional cases, respectively. The geometry and orbital morphology influence the configuration of the superatomic orbitals. Fig. 14.2 illustrates the plots corresponding the Au *6s* atomic orbitals in the before mentioned systems with total density of states (DOS) and partial density of states. The dominant contribution from the Au *6s* orbitals can be found from the emergence of the *6s* PDOS peaks at the energy levels corresponding to its plotted superatomic orbitals. The superatomic orbitals contribute to the frontier orbitals for all the structures. The spherical Au_{13} has a regular superatomic configuration of $1S^21P^61D^5$, while two-dimensional planar Au_7 lacks the out-of-plane *1P* orbital in $1S^21P^41D^1$. Au_{35}, due to compatibility between orbital morphology and its tubular geometry, shows modulations in energy level of the occupied superatomic orbitals resulting in less intuitive configuration of $1S^21P^61D^{10}1F^{10}1G^61H^1$.

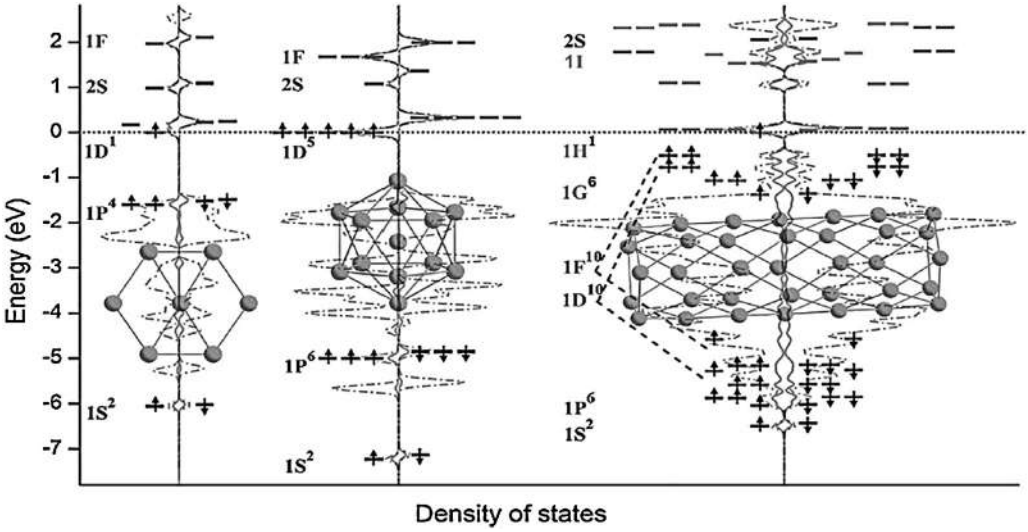

FIGURE 14.2 Superatomic orbital diagram of Au_7, Au_{13}, and Au_{35} illustrating the dominance of Au 6s atomic orbital and density of states. Adapted with permission from the ref.[32] Copyright 2017, The Springer Nature Group.

Similarly for silver nanoclusters, the linear combination of Au *5s* atomic orbitals contributes to the frontier orbitals and finally to its electronic properties.[33]

Most popular computation route for superatomic structures of noble metal nanoclusters involve geometrical optimization using DFT with BP86 functional and a double-ζ (DZ) Slater type basis set.[34] The calculation setup also requires approximations, like, frozen-core for the noble metal orbitals, and zeroth-order regular (ZORA) for incorporating relativistic effects.[35] Excited states are usually computed using the TD-DFT method with SOAP functional[36] and TZP all-electron basis set.

14.3.5 Nonsuperatomic nanoclusters

Superatom model can treat only nanoclusters with a spherical core, while the theory fails to explain the stability of nanoclusters with a nonspherical core. The classical example of nanocluster with a nonspherical core is $Au_{38}(SR)_{24}$ which is composed of a face-fused bi-icosahedral Au_{23} core.[37] $Au_{28}(TBBT)_{20}$ (where, TBBT refers to 4-*tert*-butylbenzenethiolate) is another example of nonsuperatomic rod-like Au_{20} kernel nanocluster composed of two interpenetrating cuboctahedra.[38] Cyclohexanethiolate-capped $[Au_{23}(SR)_{16}]^-$ nanocluster is a 8e system that is composed of a Au_{13} cuboctahedron-based bipyramidal Au_{15} kernel.[39] The "superatom" $Au_{25}(SR)_{18}]^q$ ($q = -1, 0$) nanocluster is a well-studied nanocluster system, while another Au_{25}-based system was reported but which showed nonsuperatomic electronic properties. The nonsuperatomic nanocluster is a rod-like $[Au_{25}(PPh_3)_{10}(SePh)_5Cl_2]^q$ ($q = +1$ or $+2$) nanocluster having two icosahedral Au_{13} units sharing a Au-atom vertex and five bridging Au–Se(S)–Au motifs.[40]

14.4 Structural prediction of nanoclusters

The general solution of the structure prediction of atomic, molecular, and crystalline systems is one of the difficult problems in computational chemistry and condensed matter physics, and hence computational approaches have been adopted to apprehend the vast combinatorial, structural, and topological complexity leading to the diverse structures of crystals, glasses, molecules, proteins, nanoclusters, and so on, seen in nature. The structure-prediction problem may be stated simply as: given a chemical composition find its associated structural phase diagram which also includes the ground-state structure.[41]

Nanocluster structure prediction so far has concentrated only on the prediction of the molecular nanocluster motif rather than its crystalline or superlattice arrangement, not least to avoid the complexities of this formidable multiscale prediction problem. For nanoclusters, this may be the gas-phase molecular structure or the nanocluster or molecular unit prediction, and also the crystalline structure for a particular composition of metal and ligand atoms. Due to the variety of nanocluster motifs, core-structures which are also ligand dependent, it is desirable that more general methods be developed, both within each class of metal (e.g., Au and Ag) and ligand type (e.g., thiolates, phosphines, alkynyls, *N*-heterocyclic carbenes, etc.) and between different ones (e.g., Ag–Au alloy nanoclusters, and mixed-ligand alloy nanoclusters), rather than using specific models for each particular class of nanocluster such as silver-thiolate, gold-phosphine, and so on. The following are the approaches used for nanocluster structure prediction.

(i) Brute force or combinatorial trial isomer approach
(ii) Phenomenological and heuristic models for prediction
(iii) Global optimization methods
(iv) Data-driven methods such as machine learning

(i) Combinatorial isomer approach

The simplest method of structural prediction relies on creating a guess structure is based on physical, or chemical intuition, data from previously known experimental structures, computing its energy and geometry minimum using DFT and then calculating its properties such as optical absorption, HOMO–LUMO gaps, and comparing these with experimental data. The putative low-energy isomers are constructed by assuming a high-symmetry core polyhedral shell with a varying surface arrangement of motifs.

The structural prediction of metal nanoclusters is complicated due to the structural diversity manifested as varying core shapes and sizes with an equally bewildering variety of surface motif structures and their bonding. The search for the lowest energy structure or global minimum requiring the use of accurate DFT methods and global optimization techniques is prohibitively expensive due to large number of degrees of freedom. Hence, it is desirable to develop computational methods which can efficiently predict the structure and it has led to recent breakthroughs in machine-learning based methods.[42]

The relationship between the geometry of a molecule and its energy is contained in the potential energy surface (PES). PES is a central and unifying concept in computational

chemistry, as both molecular structure and dynamics can be understood from it. The Born–Oppenheimer equation decouples the nuclear and electron degrees of freedom, so that the nuclei are stationary compared to the electrons.

This enables the internuclei potential to be defined containing both the nuclear–nuclear repulsion and mutual attraction of nuclei for the electron cloud and this results in the standard potential energy surface or curve such as for a diatomic molecule. The most stable equilibrium structures are found at the minimum of the PES and the search for the set of nuclear coordinates for which the energy is minimum forms the basis for any structural prediction.

Very often experimental data on structure or similar structures, combined with physical or chemical intuition, symmetry considerations, etc., are used to create an initial guess geometry which may be geometry optimized using a chosen interatomic potential or ab initio method.

The resulting minimization may be either local minimum or global minimum, however, it cannot be ascertained to be the latter, and based on the results of multiple trial isomer structures where few structures are found to be lower in energy, than the others, and of these one is the lowest energy isomer, we may suppose at best that it is a good guess for the global minimum. Supposing one has a very accurate potential energy surface such as one from an ab initio method, in this case the global minimum will coincide with the stable ground state structure observed in experiments, which provides additional verification that it is the global minimum.

The trial isomer method utilizing different core shapes and arrangement of surface staples has been applied to successfully predict the structures of many gold thiolate NCs, such as $Au_{25}(SR)_{18}$[43] and $Au_{38}(SR)_{24}$[44] for example.

(ii) Phenomenological models of structure prediction

The inherent structure model as well as the GUM model provides a method for generating trial structure for DFT optimization. These have been described in detail elsewhere in the book.

(iii) Global optimization methods

Any collection of atoms, a molecule, a nanocluster, or a solid can be characterized by its potential energy surface which is the $3N$-dimensional hypersurface which represents the interatomic interactions between the atoms. The most stable ground state structure is the global minimum of the PES, and therefore the prediction of the structure of a nanocluster may be understood as the search for the global minimum of its PES. Genetic algorithms are evolutionary in nature and are used for global optimization of the potential energy surface of a collection of atoms or molecules. In each successive step of the algorithm, a new generation is created by combining traits, which are distinctive structural patterns, from different parent structures and a fitness function is calculated which is the energy. However, to apply global optimization for structure prediction requires an accurate and efficient interatomic potential for nanoclusters and the data-driven method to obtain these is described in the next section.

(iv) Machine learning methods

Finally, data-driven methods such as machine learning potentials may be developed by training a neural network potential to predict the energy of an arbitrary arrangement of metal and surface atoms. The accuracy of such potentials is very high when they are trained on structures and energies obtained from DFT calculations based on X-ray diffraction structures.

This enables one to use efficiently global-optimization methods to predict the nanocluster structure where the potential may be computed by some analytical expression, which though not easily physically interpreted due to the complexity of the parameterized expression, it can nevertheless be computed at a similar efficiency to a classical molecular dynamics potential, rather than using a DFT-based potential. Jindal et al. have developed a machine-learning potential based on a single artificial neural network (ANN) for any number of chemical species in a molecular system which they have applied to gold–silver nanoalloys and thiol protected gold nanoclusters.[45] Chiriki et al. have applied this potential for gold thiolate nanoclusters on the $Au_N(SR)_M$ ($N = 10,\ldots, 38$) and shown that the predicted structures optical absorption.[46] Malola et al. developed a distance-based machine learning method for finding the surface arrangement of staples on a gold nanoparticle.[47]

14.5 Spectroscopic property calculations

With the advancement in high-level computing, today it is possible to calculate the spectral properties of metal nanoclusters. In recent times, DFT has evolved as a powerful tool in the computation of spectroscopic properties. DFT method using quantum-chemical computational programs is capable of calculating molecular and electronic structures of ground state systems and various spectral parameters related to nuclear magnetic resonance (NMR), electron spin resonance (ESR), optical absorption spectroscopy (UV–Vis), and infrared spectroscopy (IR).

14.5.1 Optical absorption spectroscopy

With the commercially available software packages, time-dependent DFT calculations can be efficiently utilized to compare the experimental spectra with the calculated ones. The *linear response* TD-DFT calculation involves a computation of the response to a weak external field treated as perturbation.[48] Later, Yabana and Bertsh introduced an alternate approach called time-evolution formalism that can be used for systems with strong-field perturbations without restricting it to the linear regime only.[49] To calculate a linear response optical spectrum, a perturbation needs to be chosen which is weak enough to ensure the linear dependence between the perturbation and response.[50]

The optical absorption spectral calculation involves a series of steps, and the atomic or molecular system is assumed to be much smaller (~1–10 nm) than the wavelength of the perturbing electric field, for example, a laser ($\lambda \sim 600$ nm).

Step 1: Calculation of induced dipole moment, $\mu(t)$, which can be approximated from the permanent dipole moment, $V(\boldsymbol{r},t)$, on its interaction with a field in z-direction,

$$V(r,t) = ezE(t)\hat{e}_z \tag{14.5.1}$$

Total induced dipole, $\mu(t)$, is assumed to be parallel to $\boldsymbol{E}(t)$,

$$\mu(t) = \int_{-\infty}^{\infty} dt' \alpha\left(t - t'\right) E\left(t'\right) \tag{14.5.2}$$

where α represents the dynamic polarizability of the system.

Step 2: The dynamic polarizability, $\alpha(\omega)$, can be finally computed by applying a Fourier transform.

$$\mu(\omega) = \alpha(\omega)E(\omega) \tag{14.5.3}$$

Step 4: The dynamic polarizability can be expressed in the form of sum-over-states (SOS),

$$v_{applied}(r,t) = \varepsilon(t).\, r \tag{14.5.4}$$

$$\mu(t) = -e \int rn(r.t)rd \tag{14.5.6}$$

$$\alpha(\omega) = \mu(\omega)/E(\omega) \tag{14.5.7}$$

$$\alpha(\omega) = \sum\nolimits_{I\neq 0} \frac{f_I}{\omega_I^2 - \omega^2} \tag{14.5.8}$$

where ω_I and f_I represent the vertical excitation energies and conforming oscillator strength, respectively.

The final spectrum, $S(\omega)$, can be calculated using the equation known as Lorentzian broadened stick spectrum,

$$S(\omega) = \frac{2\omega}{\pi} Im\alpha(\omega + i\eta) \tag{14.5.9}$$

The optical properties of monolayer-protected noble metal nanoclusters came into prominence only after the X-ray crystal structures of $Au_{102}(SR)_{44}$ and $Au_{25}(PET)_{18}$ were solved. Zhu et al. explored the electronic structure of the $Au_{25}(PET)_{18}$ nanocluster using DFT method.[51] Combining the X-ray crystallographic studies and Kohn–Sham calculation method, the model $Au_{25}(PET)_{18}$ nanocluster was explained (Fig. 14.3). The highest occupied molecular orbital (HOMO) and lowest unoccupied molecular orbitals (LUMO) mainly comprised of *sp*-band with contribution from 6*sp* atomic orbitals. The HOMO-1 to HOMO-5 was composed of *d*-band with contribution from $5d^{10}$ atomic orbitals. Furthermore, both the HOMO and LUMO orbitals have a significant contribution from S(3*p*) atomic orbitals. Also, the HOMO and LUMO are triply and doubly generate, respectively. It is worth noting that the 13 Au atom icosahedron core only contributes to the HOMO, LUMO, and other orbitals, like HOMO − 1 and LUMO + 1. Fig. 14.3B shows the optical absorption spectrum of $Au_{25}(PET)_{18}$ nanocluster which was computed using linear response TD-DFT. At 1.52 eV, the first transition (peak a, Fig. 14.3B) corresponds to a LUMO ← HOMO intraband (*sp* ← *sp*) transition. Then, at 2.63 eV the second transition (peak b, Fig. 14.3B) arises from mixed transitions, intraband (*sp* ← *sp*) and interband (*sp* ← *d*) transitions. The third transition occurs at 2.91 eV (peak c, Fig. 14.3B) arises from another interband (*sp* ← *d*) transition. From the structural point of view, the first transition at 1.52 eV arises entirely from the icosahedral Au_{13} core.

14.5.2 Emission and luminescence spectra

Metal nanoclusters are a collection of a few to hundreds of atoms with a core size nearing the Fermi wavelength of an electron (~0.5 nm in case Au and Ag). Hence, smaller nanoclusters possess a discrete molecular-like electronic energy levels resulting in intense absorption and emission transitions.

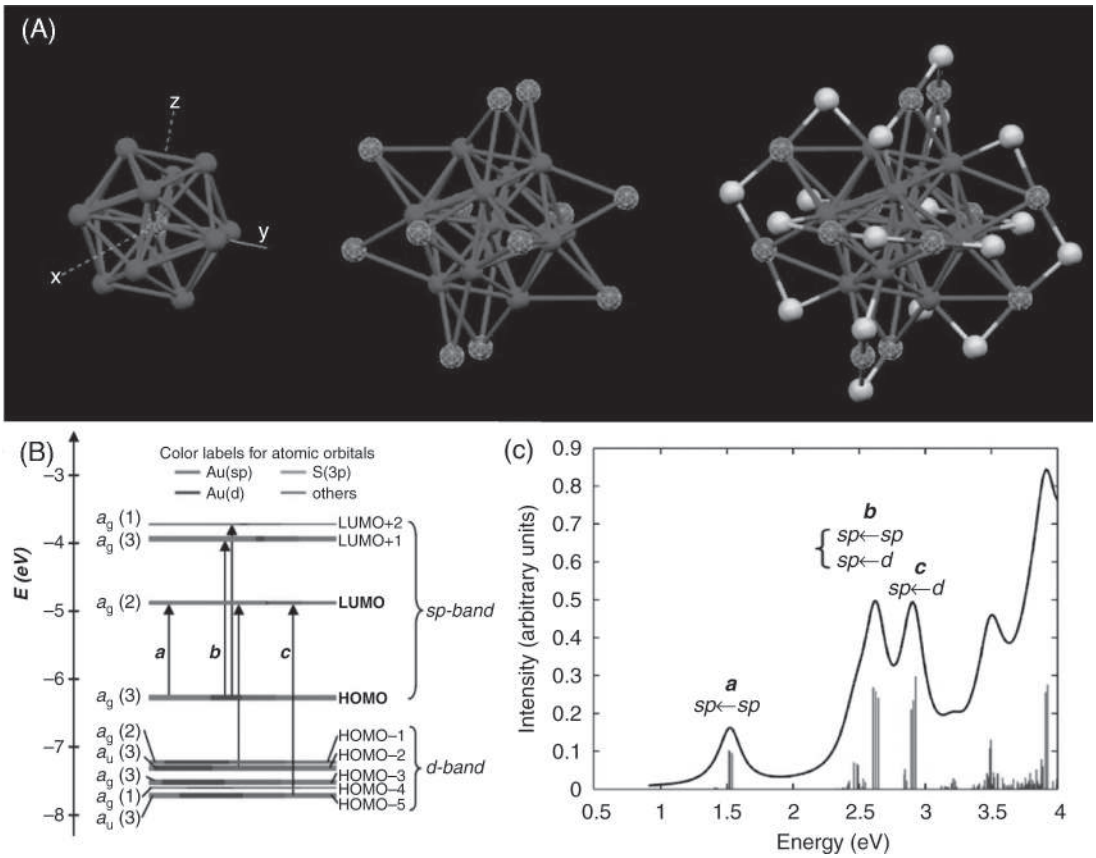

FIGURE 14.3 (A) Crystal structure, (B) Kohn–Sham orbital energy level diagram, and (C) theoretical absorption spectrum of the $Au_{25}(PET)_{18}$ nanocluster. Reproduced with permission from the ref[51]. Copyright 2008, The American Chemical Society.

The reason behind the emergence of photoluminescence can be explained by following points,

1. Intraband ($sp \leftarrow sp$) and interband ($sp \leftarrow d$) transitions.
2. Charge transfer on interaction between the protecting groups and the metal core, further classified as ligand-to-metal charge transfer (LMCT) and metal-to-ligand charge transfer (MLCT).

The absorption spectral calculation requires estimating the transition bands from an optimized nanocluster geometry using the most popular TD-DFT method. For example, most of the geometric optimization involves DFT as implemented in grid-based projector augmented wave (GPAW) method.[31a, 52] The energies of the electron transition and its corresponding transition dipole moments were obtained from the calculation. The final calculation of spectral

line intensities involve solving the Gaussian function,

$$I(\lambda) = \sum_i f_i \exp\left[-\frac{1}{2}\left(\frac{\lambda - \lambda_i}{\sigma}\right)^2\right] \tag{14.5.10}$$

Likewise, the emission spectral calculation primarily involves the estimation of the Stokes shift. Initially, the first excited state has to be calculated for the optimized geometry using popular methods, like, TD-B3LYO/LANL2DZ.

14.5.3 Mechanism of luminescence and its enhancements

The integrated luminescence intensity method is the most popular method to determine the luminescence quantum yield of nanoclusters which requires a comparative study based on photoluminescence emission.[53]

Luminescence of a sample can be written as,

$$F = K\varphi C\sigma lI \tag{14.5.11}$$

where K and φ are terms for the instrumental parameter and quantum yield, respectively. While the terms F, C, σ, l, and I refer to the photoluminescence quantum yield of the sample, sample concentration, photon absorption cross section, path length, and flux of incident photon (photons cm^2/s), respectively.

Finally, the quantum yield is calculated using the experimental parameters related to the nanocluster (in terms of "s") and reference (in terms of "r"), and absorption of the sample ($C\sigma$), respectively.

$$\varphi_s = \frac{F_s}{C_s\sigma_s} \times \frac{C_r\sigma_r}{F_r} \times \varphi_r \tag{14.5.12}$$

Upon quantifying the extent of luminescence enhancement, the theoretical investigation on the nanocluster structure sheds light on the reason for luminescence and its enhancement.

14.5.4 Vibrational circular dichroism spectra

Like differential spectroscopy, vibrational circular dichroism (VCD) spectra provide extra information on each electronic transition of a molecule. VCD measurements can help in understanding chirality transfer from an intrinsically chiral metal particle or nanocluster to adsorbed achiral molecules. Since some of the thiolate-protected metal nanoclusters are known to be chiral, VCD has evolved as a powerful technique to probe the conformation of chiral molecules by differential absorption of a circularly polarized light.[54] As reported by Whetten et al. glutathione protected Au nanoclusters showed a strong chiroptic activity[44] in the metal-based electronic transitions.[55] X-ray studies have proved that the gold nanoclusters are composed of SR–Au–SR–Au–SR (where SR = thiolates) staple motifs arranged in a chiral manner on the surface of the symmetrical metal core.

For example, calculations were performed on the isolated 2-PET as well as on a Au_4(2-PET)$_4$ model.[56] The vibrational frequencies, IR absorption, and VCD intensities were calculated using DFT for geometry-optimized structures. For the gold atoms, an effective core potential

was used. The calculations were performed using the B3PW91functional and a LANL2DZ basis set for Au and a 6-31G(d,p) basis set for all other atoms. Frequencies were scaled by a factor of 0.97. IR absorption and VCD spectra were constructed from calculated dipole and rotational strengths assuming Lorentzian band shape with a half-width at half maximum of 5 cm^{-1}. All calculations were performed using Gaussian09, Revision C.01.

14.5.5 Raman spectra

The Raman intensity of the kth vibrational mode is calculated using the following equation,

$$I_k = \frac{d\sigma}{d\Omega} = \frac{\pi^2}{\varepsilon_0^2}(\tilde{\nu}_1 - \tilde{\nu}_2)^4 \frac{h}{8\pi^2 c\tilde{\nu}_k}(S_k/45)\frac{1}{1-\exp(hc\tilde{\nu}_k/k_BT)'}. \quad (14.5.10)$$

Here, S_k refers to the scattering factor ($Å^4$/amu) evaluated using the polarizability gradient method as implemented by Gaussian 09.

$$S_k = 45\left(\frac{d\alpha}{dQ_k}\right)^2 + 7\left(\frac{dy}{dQ_k}\right)^2. \quad (14.5.10)$$

The most common approach is to subject a DFT-optimized nanocluster geometry is to an all-electron DFT calculation using B3LYP/6-31+G(d) basis set, as implemented in Gaussian 09 package.

14.5.6 Surface plasmon

A quantized collective oscillation of electron on the surface of a metal crystal and nanoparticle surface is referred to as a surface plasmon. The effect of a surface plasmon can be estimated by calculating the induced local polarizabilities inside the metal nanocluster and then the Maxwell equation is solved to obtain the enhanced local electric fields. The discrete dipole approximation (DDA) and finite-difference time-domain (FDTD) method are popular methods in computation of local electric fields.[57] The emergence of localized surface plasmon resonance for gold nanoclusters was demonstrated for Au_{266} and $Au_{314}(SH)_{96}$ with core sizes between 1.5 nm and 2 nm using linear response time-dependent density functional perturbation theory (TD-DFPT).[58]

14.6 Catalysis and other property calculations

Metal nanoparticle-based heterogeneous catalysis is gaining prominence in the chemical industry. The conventional nanocatalysts are composed of supported polydisperse nanoparticles and the polydispersity is a major drawback to its catalytic performance. Other drawbacks of polydisperse nanocatalysts are their poorly defined surface and its unknown surface composition which interferes with our understanding of the catalytic mechanism. To overcome these major hurdles, the atomically precise metal nanoclusters are highly desirable to study the fundamental studies of catalysis.

14.6.1 Catalytic mechanisms

A thiol-capped noble metal nanocluster with atomic precision is an interesting and exciting candidate for newer generation of nanocatalysts to elucidate mechanisms and also establish structure–reactivity correlations. DFT studies on these nanoclusters can shed light on the catalytic process mechanism by identifying the cluster–support interactions and the corresponding charge delocalization. The activated O_2 molecule mediated oxidation and Langmuir–Hinshelwood (LH) mechanism is widely accepted for the oxidation of CO on free gold nanoclusters.[59] In one of the studies on catalytic application of nanoclusters, diphosphine-capped $Au_{22}(L^8)_6$ (Fig. 14.4) was computationally studied for its ability to oxidize CO.[60] Using DFT calculations, the reactivity of a diphosphine-protected $Au_{22}(L^8)_6$ nanocluster was investigated where oxygen activation and CO oxidation were the testing probes. Calculations suggest that the cus Au at the interface shows a strong adsorption and activation toward oxygen, thereby promoting the dissociation of two O_2 molecules into fully oxidized $Au_{22}(L^8)_6O_4$ nanoclusters with a activation barrier of 0.6–0.7 eV. The additional O_2 gets preferentially adsorbed at the terminal Au_{11} unit around the Au–P framework. Also, the $Au_{22}(L^8)_6$ nanocluster shows high activity with low activation barrier (0.51 eV) for CO oxidation. Fig. 14.4C, D shows the structures (initial reactants, transition states, intermediates, and final products) and its corresponding energies for the minimum catalytic reaction pathway for O_2 activation and CO oxidation on $Au_{22}(L^8)_6$. The coadsorbed CO^* and $O_2{}^*$ initiates $OOCO^*$ formation, with a calculated activation barrier of 0.51 eV (TS1). For the subsequent dissociation of $OOCO^*$, the barrier height decreases to 0.11 eV (TS2). After generation of the first CO_2, the adsorbed O^* can be preferably attacked by another adsorbed CO^* with a small energy gap of 0.40 eV (TS3). This suggests that the highly active species for the oxidation reaction is the dissociative O^* on the $Au_{22}(L^8)_6$ nanocluster. The spontaneous dissociation of the O–O bond via the formation of an $OOCO^*$ intermediate can be accounted to for the lower energy barrier (0.11 eV) for the cleavage of an O–O bond of the $OOCO^*$ versus dissociation of pure O_2 (0.6–0.7 eV). Also, the small rate-determining energy gap (0.51 eV for $OOCO^*$ formation) concludes that the in situ CO oxidation can be effectively catalyzed by the uncoordinated Au of $Au_{22}(L^8)_6$ nanocluster. Such a catalytic ability of gold nanoclusters makes it a promising candidate as a nanocatalyst for important practical applications (Fig. 14.4).

14.6.2 Magnetic properties

It is already known that gas phase and surface-supported monatomic gold MPCs are paramagnetic due to the unpaired 6s electrons, whereas gold in its bulk form is diamagnetic. There are evidences for the size-dependent magnetism in gold nanoparticles ranging in the size of 1–5 nm.[61] Manzhou Zhu and coworkers reported a reversible and switchable paramagnetism in $Au_{25}(SR)_{18}$, where R refers to phenylethyl.[62] The origin of the magnetism in Au_{25} nanocluster was explained through a DFT computation. Calculations reveal that the both neutral and anionic nanoclusters are approximately triply and doubly degenerate at the Kohn–Sham highest occupied molecular orbital (HOMO) and lowest occupied molecular orbital (LUMO) levels (Fig. 14.5B). The origin of the paramagnetism can be understood from the electronic configuration corresponding to a HOMO of the neutral nanocluster $(au)^2(au)^2(au)^2$. The

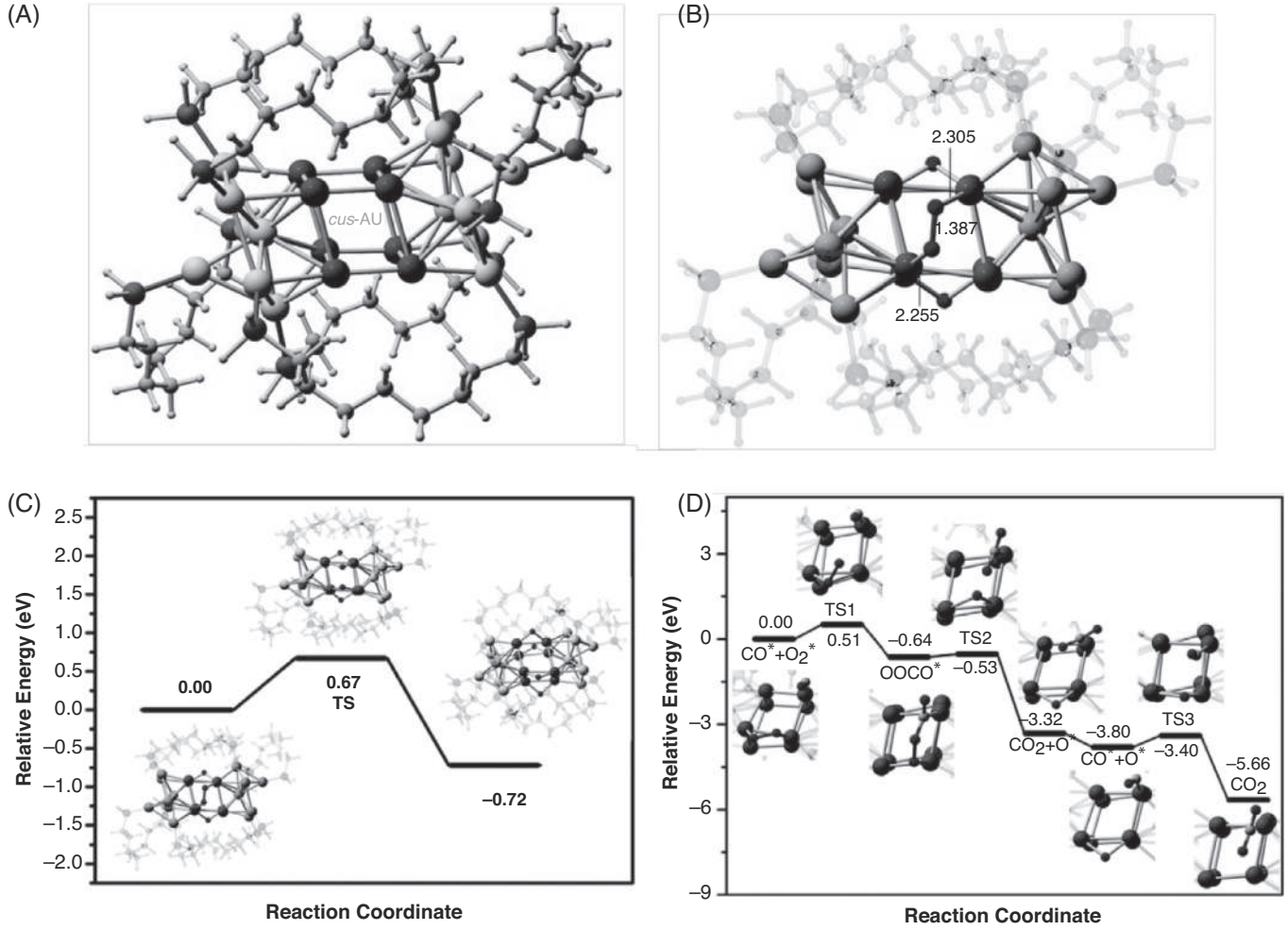

FIGURE 14.4 Optimized structure of the (A) $Au_{22}(L^8)_6$ nanocluster, and (B) $Au_{22}(L^8)_6O_2$ cluster. Preferable reaction pathway for the (C) second O_2 molecule activation and (D) CO oxidation at the *cus* Au sites of the diphosphine-capped Au_{22} nanocluster. Adapted with permission from the ref.[60]. Copyright 2019, The Royal Society of Chemistry.

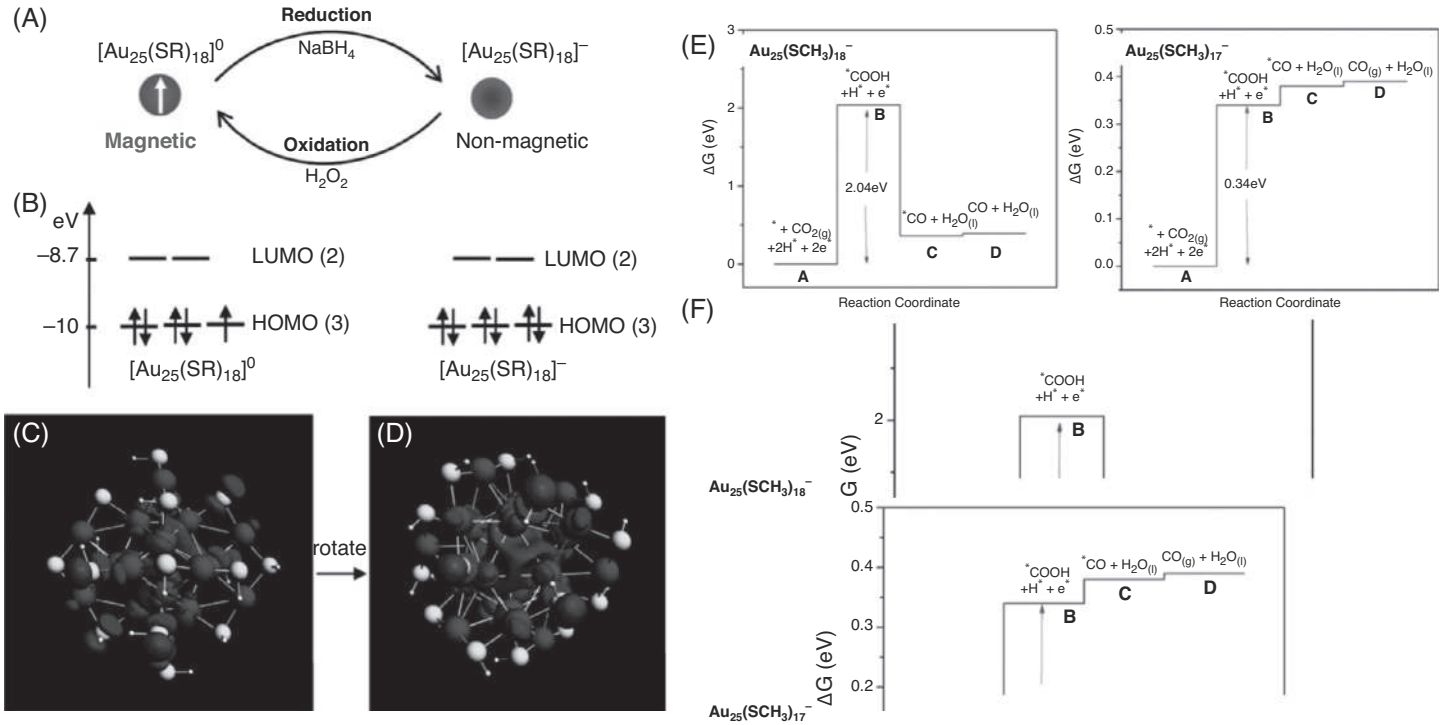

FIGURE 14.5 (A) Switching magnetism between the neutral and anionic $Au_{25}(SR)_{18}$ nanocluster. (B) Calculated Kohn–Sham orbital energy y-level representation for the neutral and anionic nanocluster. (C–D) Kohn–Sham HOMO projected for the neutral species. (E) Free energy diagram for the conversion of CO_2 to CO over fully protected $Au_{25}(SR)_{18}$ and singly dethiolated $Au_{25}(SR)_{17}$ nanoclusters, and (F) the proposed mechanism. Reproduced with permission from the refs.[62] and [63]. Copyright 2009, The American Chemical Society. Copyright 2016, The AIP Publishing.

presence of a single unpaired electron at the HOMO is in agreement with the paramagnetism observed in both the EPR and SQUID measurements. While for the $[Au_{25}(SR)_{18}]^-$ nanocluster, a totally filled three quasi-degenerate Kohn–Sham orbitals was calculated with an electronic configuration of $(au)^2(au)^2(au)^2$ (Fig. 14.5B). The absence of any unpaired electrons at the HOMO was experimentally confirmed with the disappearance of the EPR signal for the anionic nanocluster. DFT calculations further reveal that the unpaired spin is majorly distributed over the Au_{13} metal core and thereby exhibits an axial character. The anionic $[Au_{25}(SR)_{18}]^-$ nanocluster is composed of eight electrons delocalized over an icosahedral core. The triply degenerate HOMO when projected on the spherical harmonics predicts that the HOMO states have a P-character and the electronic shell configuration of $1S^21P6$. Calculations suggest that the anionic $[Au_{25}(SH)_{18}]^0$ nanocluster has an electronic configuration of $1S^21P5$, hence the unified P-shell exhibits an axial symmetry (Fig. 14.5C, D).

14.6.3 Electrochemical properties

Recently, electrochemistry of atomically precise metal nanoclusters, especially gold nanoclusters, is gaining prominence for their plausible application in the field of electrocatalysis and electrochemical sensing.[64] Voltammetry is a useful tool to investigate the electronic structure of metal nanoclusters, especially HOMO and LUMO energy levels. Heteroatom doping is an excellent strategy for atomic level alteration of the optical and electrochemical properties of metal nanoclusters. Although superatom theory successfully predicts the eight-electron configuration for $[Au_{25}(SR)_{18}]^-$ nanocluster and many of its doped counterparts, due to occurrence of the Jahn–Teller distortion, a contrasting electronic structure was observed in optical spectra and voltammogram for the Pt- and Pd-doped counterparts, $[PtAu_{24}(SR)_{18}]^0$ and $[PdAu_{24}(SR)_{18}]^0$. Further, heteroatom doping is also capable of altering the surface properties as well as redox potentials. Metal nanoclusters due to its atomic precision can be suitably engineered to attain high electrochemical activity as well as selectivity toward electrocatalytic applications.

Computational design of solid catalyst for hydrogen evolution reaction (HER) from water shows the importance of the hydrogen adsorption free energy (ΔG_H) for an active HER catalyst. When the catalytic activities for a wide range of catalyst materials are plotted against ΔG_H, it typically gives a volcano relationship, suggesting a catalyst with $\Delta G_H = 0$ shows the highest catalytic activity. This concept is in agreement with Sabatier principle where an active catalyst must have a moderate binding to the reaction intermediates. Bimetallic nanoclusters like, $PtAu_{24}(SC_6H_{13})_{18}$ were the first example of an HER electrocatalyst.[65] From the mechanistic studies, the H-binding on the nanocluster is a thermodynamically neutral step followed by a Pt–H chemical bond formation, suggesting the dopant playing the key role in HER. In contrast to HER, the CO_2 reduction reaction (CO_2RR) is a multielectron and multiproton process with the involvement of multiple surface-bound intermediates.[66] Kaffaman et al. reported CO_2 conversion to CO, electrocatalyzed by the $Au_{25}(PET)_{18}$ nanocluster.[67] Extensive reviews on CO_2 by gold and silver nanoclusters are already available.[68] Mechanistic studies on the CO_2 electroreduction using DFT were reported by Alfonso et al. where the fully-capped $Au_{25}(SR)_{18}$ and dethiolated $Au_{25}(SR)_{17}$ nanoclusters were energetically compared for CO_2RR.[63] Fig. 14.5E and F shows the energy difference required for the formation of intermediate COOH and

the proposed mechanism for CO_2 reduction to CO in fully protected Au_{25} and $Au_{25}(SR)_{17}$ nanoclusters, respectively.

In conclusion, metals nanoclusters can serve as unique electrocatalysts for water splitting and CO_2 reduction with excellent activity and selectivity. Such materials are also perfect models for parallel experimental and theoretical studies.

14.6.4 Thermodynamic and vibrational properties of nanoclusters

The thermodynamic properties of nanoclusters including their melting point, and molecular dynamics simulations are used to understand the effects of temperature on the structure and vibrational properties of the nanoclusters. Other structural properties such as the stiffness of bonds may be studied using elastic calculations. The thermal properties of metal clusters are believed to originate from the bond stiffness.[69] For example, in case of thiolate-protected, icosahedral-shaped gold nanoclusters $Au_{25}(PET)_{18}$, $Au_{38}(PET)_{24}$, and $Au_{144}(PET)_{60}$, the Au–Au bonds have different stiffnesses depending on their lengths. Longer the Au–Au bond (as located at the core surface), more will be the flexibility compared to that of the bulk metal. While the shorter Au–Au bonds, eventually stiffer than those of the bulk metal, are mainly distributed along the radial direction and forms a cyclic structural backbone with the rigid Au–SR oligomers.

14.7 Summary and future perspectives

In this chapter, we presented an overview of the theory behind the computational approaches that underpin many of the simulations in nanocluster science such as DFT, QM-MM, force fields, and TD-DFT. The applications of computational approaches to fundamental aspects such as the electronic structure and stability of nanoclusters and their structural prediction were described with emphasis on general methods being employed. We provided examples to illustrate the remarkable success of computations in nanocluster property calculations aimed at unraveling the microscopic mechanisms involved in applications such as catalysis, spectroscopy, electrochemistry, magnetism, and thermodynamic properties. With the advent of data-driven methods, all aspects of synthesis, structure and property prediction of nanoclusters will be revolutionized, leading to efficient synthesis of nanoclusters with specific target properties.

List of abbreviation

Ω-B97X-D	long-range-corrected Becke 97
AMBER	assisted model building with energy refinement
ANN	artificial neural network
B3LYP	Becke, 3-parameter, Lee–Yang–Parr
CAM-B3LYP	Coulomb-attenuating method Becke, 3-parameter, Lee–Yang–Parr
CHARMM	chemistry at Harvard macromolecular mechanics
COMPASS	condensed-phase optimized molecular potentials for atomistic simulation studies
DDA	discrete dipole approximation
DFT	density functional theory
DOS	density of states
EDOS	electronic density of states

ESR	electron spin resonance
FDTD	finite-difference time-domain
FF	force field
GCA	generalized gradient approximation
GGA	generalized gradient approximation
GPAW	grid-based projector-augmented wave method
GROMOS	GROningen molecular simulation
GUM	grand unified model
HER	hydrogen evolution reaction
HF	Hartree–Fock
HOMO	highest occupied molecular orbital
HSE	Heyd–Scuseria–Ernzerhof
KS	Kohn–Sham
LAMMPS	large-scale atomic/molecular massively parallel simulator
LANL2DZ	Los Alamos National Laboratory 2 Double-Zeta
LC	long-range-corrected
LDA	local-density approximations
LH	Langmuir–Hinshelwood
LMCT	ligand-to-metal charge transfer
LR	linear response
LSDA	local spin density approximation
LUMO	lowest unoccupied molecular orbital
MC	Monte Carlo
MD	molecular dynamics
ML	machine learning
MLCT	metal-to-ligand charge transfer
MM	molecular mechanics
MPC	monolayer-protected metal nanocluster
NMR	nuclear magnetic resonance
OPLS	optimized potentials for liquid simulations
PBE	Perdew–Burke–Ernzerhof
PDOS	projected density of states (on superatomic orbitals)
PES	potential energy surface
PET	phenylethanethiol
QM	quantum mechanics
QM/MM	quantum mechanics/molecular mechanics
SOAP	statistical averaging of orbital potentials
SQUID	superconducting quantum interference device
TBBT	4-*tert*-butylbenzenethiolate
TD-DFT	time-dependent density functional theory
TDHF	time-dependent Hartree–Fock
UFF	universal force field
UV–Vis	optical absorption spectroscopy
VCD	vibrational circular dichroism
XC	exchange-correlation functional
ZORA	zeroth-order regular approximation

References

1. Hutter J, Iannuzzi M, Schiffmann F, Vandevondele J. Cp2k: Atomistic simulations of condensed matter systems. *Wiley Interdiscip Rev: Comput Mol Sci*. 2014;4:15–25.
2. Kohn W, Becke AD, Parr RG. Density functional theory of electronic structure. *J Phys Chem*. 1996;100:12974–12980.
3. Hohenberg P, Kohn W. Inhomogeneous electron gas. *Phys Rev*. 1964;136:B864–B871.

4. Feynman RP. Forces in molecules. *Phys Rev*. 1939;56:340–343.
5. Payne MC, Teter MP, Allan DC, Arias TA, Joannopoulos JD. Iterative minimization techniques for ab initio total-energy calculations: molecular dynamics and conjugate gradients. *Rev Mod Phys*. 1992;64:1045–1097.
6. Xu P, Guidez EB, Bertoni C, Gordon MS. Perspective: ab initio force field methods derived from quantum mechanics. *J Chem Phys*. 2018;148.
7. Mayo SL, Olafson BD, Goddard WA. DREIDING: a generic force field for molecular simulations. *J Phys Chem*. 1990;94:8897–8909.
8. Rappe AK, Casewit CJ, Colwell KS, Goddard WA, Skiff WM. UFF, a full periodic table force field for molecular mechanics and molecular dynamics simulations. *J Am Chem Soc*. 1992;114:10024–10035.
9. MacKerell AD, Bashford D, Bellott M, et al. All-atom empirical potential for molecular modeling and dynamics studies of proteins. *J Phys Chem B*. 1998;102:3586–3616.
10. Cornell WD, Cieplak P, Bayly CI, et al. A second generation force field for the simulation of proteins, nucleic acids, and organic molecules. *J Am Chem Soc*. 1995;117:5179–5197.
11. Oostenbrink C, Villa A, Mark AE, Van Gunsteren WF. A biomolecular force field based on the free enthalpy of hydration and solvation: the GROMOS force-field parameter sets 53A5 and 53A6. *J Comput Chem*. 2004;25:1656–1676.
12. Jorgensen WL, Maxwell DS, Tirado-Rives J. Development and testing of the OPLS all-atom force field on conformational energetics and properties of organic liquids. *J Am Chem Soc*. 1996;118:11225–11236.
13. Sun H. COMPASS: an ab initio force-field optimized for condensed-phase applicationsoverview with details on alkane and benzene compounds. *J Phys Chem B*. 1998;102:7338–7364.
14. Fichthorn KA, Weinberg WH. Theoretical foundations of dynamical Monte Carlo simulations. *J Chem Phys*. 1991;95:1090–1096.
15. Duane S, Kennedy AD, Pendleton BJ, Roweth D. Hybrid Monte Carlo. *Phys Lett B*. 1987;195:216–222.
16. Warshel A, Levitt M. Theoretical studies of enzymic reactions: dielectric, electrostatic and steric stabilization of the carbonium ion in the reaction of lysozyme. *J Mol Biol*. 1976;103:227–249.
17. Salahub DR, de la Lande A, Goursot A, Zhang R, Zhang Y. Recent progress in density functional methodology for biomolecular modeling. In: Putz MV, Mingos DMP, eds. *Applications of Density Functional Theory to Biological and Bioinorganic Chemistry*. Berlin, Heidelberg: Springer Berlin Heidelberg; 2013:1–64.
18. Eyring H. The activated complex in chemical reactions. *J Chem Phys*. 1935;3:107–115.
19. Evans MG, Polanyi M. Some applications of the transition state method to the calculation of reaction velocities, especially in solution. *Trans Farad Soc*. 1935;31:875–894.
20. Runge E, Gross EKU. Density-functional theory for time-dependent systems. *Phys Rev Lett*. 1984;52:997–1000.
21. Casida ME, Chong D. Time-Dependent Density Functional Response Theory for Molecules. In Recent Advances in Density Functional Methods. *Comput Chem: Rev Curr Trends*. 1995:155–192.
22. Stratmann RE, Scuseria GE, Frisch MJ. An efficient implementation of time-dependent density-functional theory for the calculation of excitation energies of large molecules. *J Chem Phys*. 1998;109:8218–8224.
23. Laurent AD, Jacquemin D. TD-DFT benchmarks: a review. *Int J Quant Chem*. 2013;113:2019–2039.
24. (a) Jin R, Zeng C, Zhou M, Chen Y. Atomically precise colloidal metal nanoclusters and nanoparticles: fundamentals and opportunities. *Chem Rev*. 2016;116:10346–10413; (b) Chakraborty I, Pradeep T. Atomically precise clusters of noble metals: emerging link between atoms and nanoparticles. *Chem Rev*. 2017;117:8208–8271.
25. (a) Khanna SN, Jena P. Assembling crystals from clusters. *Phys Rev Lett*. 1992;69:1664–1667; (b) Ball P. A new kind of alchemy. *New Sci*. 2005;186:30–33.
26. (a) Walter M, Häkkinen H. A hollow tetrahedral cage of hexadecagold dianion provides a robust backbone for a tuneable sub-nanometer oxidation and reduction agent via endohedral doping. *Phys Chem Chem Phys*. 2006;8:5407–5411; (b) Yoon B, Koskinen P, Huber B, et al. Size-dependent structural evolution and chemical reactivity of gold clusters. *Chem Phys Chem*. 2007;8:157–161.
27. Knight WD, Clemenger K, de Heer WA, Saunders WA, Chou MY, Cohen ML. Electronic shell structure and abundances of sodium clusters. *Phys Rev Lett*. 1984;52:2141–2143.
28. (a) Polozkov RG, Ivanov VK, Verkhovtsev AV, Korol AV, Solov'yov AV. New applications of the Jellium model for the study of atomic clusters. *J Phys: Conf Ser*. 2013;438; (b) de Heer WA. The physics of simple metal clusters: experimental aspects and simple models. *Rev Mod Phys*. 1993;65:611–676.
29. Nilsson L, Karplus M. Empirical energy functions for energy minimization and dynamics of nucleic acids. *J Comput Chem*. 1986;7:591–616.

30. Walter M, Akola J, Lopez-Acevedo O, et al. A unified view of ligand-protected gold clusters as superatom complexes. *Proc Natl Acad Sci*. 2008;105:9157.
31. (a) Mortensen JJ, Hansen LB, Jacobsen KW. *Real-space grid implementation of the projector augmented wave method*; 2005 *Phys Rev B*. 71; (b) Häkkinen H. Chapter 8 – Electronic structure: shell structure and the superatom concept. In: Tsukuda T, Häkkinen H, eds. *Frontiers of Nanoscience*. Elsevier; 2015:189–222.
32. Jiang W, Gao Y, Xu D, Liu F, Wang Z. Structural influence on superatomic orbitals of typical gold nanostructure building blocks. *J Electron Mater*. 2017;46:3938–3941.
33. Yumura T, Kumondai M, Kuroda Y, Wakasugi T, Kobayashi H. Utilizing super-atom orbital ideas to understand properties of silver clusters inside ZSM-5 zeolite. *RSC Adv*. 2017;7:4950–4959.
34. (a) Becke AD. Density-functional exchange-energy approximation with correct asymptotic behavior. *Phys Rev A*. 1988;38:3098–3100; (b) Perdew JP. Density-functional approximation for the correlation energy of the inhomogeneous electron gas. *Phys Rev B*. 1986;33:8822–8824.
35. van Lenthe E, Snijders JG, Baerends EJ. The zero-order regular approximation for relativistic effects: the effect of spin–orbit coupling in closed shell molecules. *J Chem Phys*. 1996;105:6505–6516.
36. Gritsenko OV, Schipper PRT, Baerends EJ. Approximation of the exchange-correlation Kohn–Sham potential with a statistical average of different orbital model potentials. *Chem Phys Lett*. 1999;302:199–207.
37. Qian H, Eckenhoff WT, Zhu Y, Pintauer T, Jin R. Total structure determination of thiolate-protected Au_{38} nanoparticles. *J Am Chem Soc*. 2010;132:8280–8281.
38. Zeng C, Li T, Das A, Rosi NL, Jin R. Chiral structure of thiolate-protected 28-gold-atom nanocluster determined by X-ray crystallography. *J Am Chem Soc*. 2013;135:10011–10013.
39. Das A, Li T, Nobusada K, Zeng C, Rosi NL, Jin R. Nonsuperatomic $[Au_{23}(SC_6H_{11})_{16}]-$nanocluster featuring bipyramidal Au_{15} kernel and trimeric $Au_3(SR)_4$ motif. *J Am Chem Soc*. 2013;135:18264–18267.
40. Song Y, Jin S, Kang X. How a single electron affects the properties of the "non-superatom" Au_{25} nanoclusters. *Chem Mater*. 2016;28:2609–2617.
41. Narasimhan S. A handle on the scandal: data driven approaches to structure prediction. *APL Mater*. 2020;8.
42. Behler J. Perspective: machine learning potentials for atomistic simulations. *J Chem Phys*. 2016;145.
43. Akola J, Walter M, Whetten RL, Häkkinen H, Grönbeck H. On the structure of thiolate-protected Au_{25}. *J Am Chem Soc*. 2008;130:3756–3757.
44. Pei Y, Gao Y, Zeng XC. Structural prediction of thiolate-protected Au_{38}: a face-fused Bi-icosahedral Au core. *J Am Chem Soc*. 2008;130:7830–7832.
45. Jindal S, Bulusu SS. A transferable artificial neural network model for atomic forces in nanoparticles. *J Chem Phys*. 2018;149.
46. Chiriki S, Jindal S, Singh P, Bulusu SS. Correlation of structure with UV-visible spectra by varying SH composition in Au-SH nanoclusters. *J Chem Phys*. 2018;149.
47. Malola S, Nieminen P, Pihlajamäki A, Hämäläinen J, Kärkkäinen T, Häkkinen H. A method for structure prediction of metal-ligand interfaces of hybrid nanoparticles. *Nat Commun*. 2019;10:3973.
48. (a) Onida G, Reining L, Rubio A. Electronic excitations: density-functional versus many-body Green's-function approaches. *Rev Mod Phys*. 2002;74:601–659; (b) Casida ME, Time-dependent density functional response theory for molecules. In Recent Advances in Density Functional Methods, Part I, edited by D.P. Chong (Singapore, World Scientific, p. 155.
49. Yabana K, Bertsch GF. Time-dependent local-density approximation in real time. *Phys Rev B*. 1996;54:4484–4487.
50. Yao C, Chen J, Li M-B, Liu L, Yang J, Wu Z. Adding two active silver atoms on Au_{25} nanoparticle. *Nano Lett*. 2015;15:1281–1287.
51. Zhu M, Aikens CM, Hollander FJ, Schatz GC, Jin R. Correlating the crystal structure of a thiol-protected Au_{25} cluster and optical properties. *J Am Chem Soc*. 2008;130:5883–5885.
52. Enkovaara J, Rostgaard C, Mortensen JJ, et al. Electronic structure calculations with GPAW: a real-space implementation of the projector augmented-wave method. *J Phys: Condensed Matter*. 2010;22.
53. Khatun E, Ghosh A, Chakraborty P, et al. A thirty-fold photoluminescence enhancement induced by secondary ligands in monolayer protected silver clusters. *Nanoscale*. 2018;10:20033–20042.
54. Nafie LA, Keiderling TA, Stephens PJ. Vibrational circular dichroism. *J Am Chem Soc*. 1976;98:2715–2723.
55. Schaaff TG, Whetten RL. Giant gold−glutathione cluster compounds: intense optical activity in metal-based transitions. *J Phys Chem B*. 2000;104:2630–2641.

56. Dolamic I, Knoppe S, Dass A, Bürgi T. First enantioseparation and circular dichroism spectra of Au_{38} clusters protected by achiral ligands. *Nat Commun*. 2012;3:798.
57. Morton SM, Silverstein DW, Jensen L. Theoretical studies of plasmonics using electronic structure methods. *Chem Rev*. 2011;111:3962–3994.
58. Malola S, Lehtovaara L, Enkovaara J, Häkkinen H. Birth of the localized surface plasmon resonance in monolayer-protected gold nanoclusters. *ACS Nano*. 2013;7:10263–10270.
59. Manzoor D, Pal S. Hydrogen atom chemisorbed gold clusters as highly active catalysts for oxygen activation and CO oxidation. *J Phys Chem C*. 2014;118:30057–30062.
60. Li F, Tang Q. An $Au_{22}(L_8)_6$ nanocluster with in situ uncoordinated Au as a highly active catalyst for O_2 activation and CO oxidation. *Phys Chem Chem Phys*. 2019;21:20144–20150.
61. (a) Crespo P, Litrán R, Rojas TC, et al. Permanent magnetism, magnetic anisotropy, and hysteresis of thiol-capped gold nanoparticles. *Phys Rev Lett*. 2004;93; (b) Hori H, Teranishi T, Nakae Y, Seino Y, Miyake M, Yamada S. Anomalous magnetic polarization effect of Pd and Au nano-particles. *Phys Lett A*. 1999;263:406–410; (c) Hori H, Yamamoto Y, Iwamoto T, Miura T, Teranishi T, Miyake M. Diameter dependence of ferromagnetic spin moment in Au nanocrystals. *Phys Rev B*. 2004;69; (d) Negishi Y, Kurashige W, Niihori Y, Iwasa T, Nobusada K. Isolation, structure, and stability of a dodecanethiolate-protected Pd_1Au_{24} cluster. *Phys Chem Chem Phys*. 2010;12:6219–6225; (e) Negishi Y, Tsunoyama H, Suzuki M, et al. X-ray magnetic circular dichroism of size-selected, thiolated gold clusters. *J Am Chem Soc*. 2006;128:12034–12035.
62. Zhu M, Aikens CM, Hendrich MP, et al. Reversible switching of magnetism in thiolate-protected Au_{25} superatoms. *J Am Chem Soc*. 2009;131:2490–2492.
63. Alfonso DR, Kauffman D, Matranga C. Active sites of ligand-protected Au_{25} nanoparticle catalysts for CO_2 electroreduction to CO. *J Chem Phys*. 2016;144.
64. Kwak K, Lee D. Electrochemistry of atomically precise metal nanoclusters. *Acc Chem Res*. 2019;52:12–22.
65. Kwak K, Choi W, Tang Q, et al. A molecule-like $PtAu_{24}(SC_6H_{13})_{18}$ nanocluster as an electrocatalyst for hydrogen production. *Nat Commun*. 2017;8:14723.
66. Seh ZW, Kibsgaard J, Dickens CF, Chorkendorff I, Nørskov JK, Jaramillo TF. Combining theory and experiment in electrocatalysis: insights into materials design. *Science*. 2017;355:eaad4998.
67. Kauffman DR, Alfonso D, Matranga C, Qian H, Jin R. Experimental and computational investigation of Au_{25} clusters and CO_2: a unique interaction and enhanced electrocatalytic activity. *J Am Chem Soc*. 2012;134:10237–10243.
68. Zhao S, Jin R, Jin R. Opportunities and challenges in CO_2 reduction by gold- and silver-based electrocatalysts: from bulk metals to nanoparticles and atomically precise nanoclusters. *ACS Energy Lett*. 2018;3:452–462.
69. Yamazoe S, Takano S, Kurashige W, et al. Hierarchy of bond stiffnesses within icosahedral-based gold clusters protected by thiolates. *Nat Commun*. 2016;7:10414.

CHAPTER

15

Ag and Au nanoclusters

Udayabhaskararao Thumu[a] *and Thalappil Pradeep*[b]

[a] Institute of Fundamental and Frontier Sciences, University of Electronic Science and Technology of China, Chengdu, China [b] Deepak Parekh Institute Chair Professor and Professor of Chemistry, Department of Chemistry, Indian Institute of Technology Madras, Chennai, India

15.1 Introduction

Mankind's interests toward gold (Au) and silver (Ag) metals are bizarre due to their beautiful surface luster. The earlier scientific community had tremendous attention on these inert metals for their superior conductivity properties. The study of these metals at 2–100 nm size range is greater attractive in the later years (1980 to till now). In the past decade, nanoparticle research has taken a great leap toward further downscaling them at their atomic level; at these sizes, they are called nanoclusters (≤2 nm). There are drastic changes in their band structure while this transformation from bulk-to-nanoparticles (NPs)-to-nanoclusters (NCs) (Fig. 15.1), they bridge the gap between single atoms and nanoparticles. NCs can behave like atoms with the potential capability to manipulate light, advantageous in comparison to atoms as these can be available in material form. Ag and Au NCs display unique properties that combine the aspects of well-known functional materials: semiconductor quantum dots and organic semiconductors. Like colloidal quantum dots, they exhibit quantum confinement and decent stability. On the other hand, like organic semiconductors, they are atomically precise with a well-defined number of atoms in their structures.

A chapter on Ag and Au nanocluster systems (Ag/Au NCs) is essential since research findings on these systems has been at the forefront and they set benchmark for other metal NC research. Over the years, numerous studies have been conducted on these systems. Few examples include- the size-focusing synthetic methods, crystal structure elucidation, physicochemical properties (optics, chirality, electrochemistry, and magnetism), practical applications (catalytic and biological fields), composite materials (such as graphene, semiconductors, and metal-organic frameworks), cluster alloying, doping, and internanocluster reactions. These concepts can also be extended to other metal NCs (Cu, Pd, Pt, and Ir). Due to the wide scope of this area, this chapter provides only an overview of the fundamental developments in the field of Ag/Au NCs. The topics listed above are available as separate chapters.

Atomically Precise Metal Nanoclusters.
DOI: https://doi.org/10.1016/B978-0-323-90879-5.00017-2

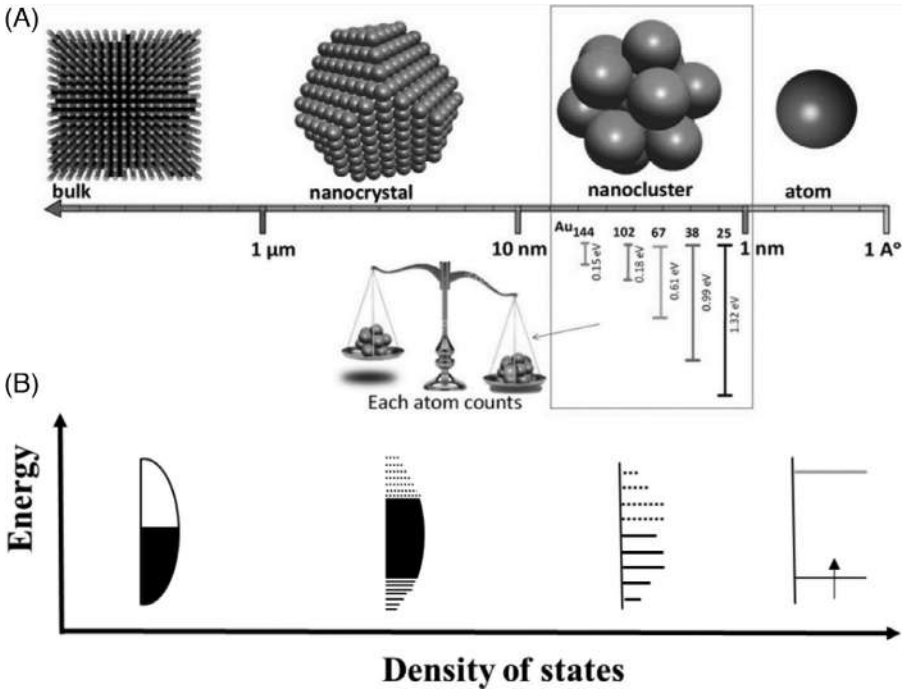

FIGURE 15.1 (A) Schematic representation of Au metal at different size scales and their respective changes in band structure is depicted in (B). Bulk metal and the NPs possess a continuous band of energy levels. Few-atom NCs exhibit discrete energy levels due to their quantum confinement. It facilitates the interaction between light and matter results the novel absorption and emission due to electron transitions between quantized energy levels.

The field of metal NCs emerged as an extension of two major research areas, namely, phosphate-protected metal clusters and plasmonic nanoparticles. The field of phosphine-protected NCs began in mid-19th century.[1] Even though the phosphate-protected cluster's research was much earlier to thiolated-NCs research, the latter research field has not taken considerable advantage from it. Instead, thiolated-NC research has grown independently by a massive curiosity to scale down the Ag and Au NP sizes via their size-separation techniques[2] followed by their spectroscopic studies such as electrochemistry, mass spectrometry, and optical properties.[3,4] In the later years, this study of down scaling the NPs had evolved into major research area, and very recently, the thiolated-NCs research benefited from mixed ligand (thiolate and phosphene) approaches.

15.2 Journey from bulk to atomically precise nanoclusters

15.2.1 The color difference in bulk Ag/Au metals

Bulk Au has an orange–yellow color whereas silver is not, even though both lie in the same group of the periodic table. Fig. 15.2 shows the fundamental optical transitions and reflectance

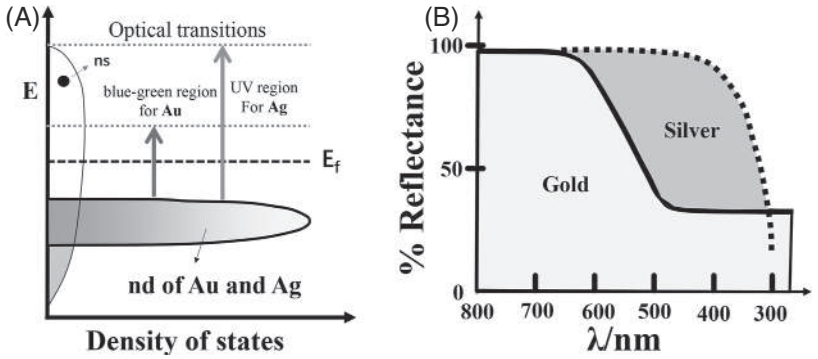

FIGURE 15.2 (A) Electron transitions of gold and silver metals, absorption take place in blue–green region for Au and required UV energy in Ag. (B) Comparison of optical reflectance spectrum of bulk Au and Ag. Gold has low reflectivity at lower wavelengths and preferentially higher reflectivity in yellow to red region whereas silver reflects majority of the visible wavelengths results nearly white or silvery color.

properties of bulk Ag and Au. They differ in their light reflectance properties due to the difference in interactions of light with the surface electrons. Briefly, the color of these metals arises due to the differences in the energy gap of the outermost $nd^{10}ns^1$ sublevels.[5] When light falls on the bulk gold, it has strong absorption band in the blue–green region as a result of electronic transitions from d band to the s/p conduction band (Fig. 15.2A, optical transitions in Au). Since the absorption is in blue–green region, the gold appears its complementary wavelength that is orange–yellow color (Fig. 15.2B). When light falls on silver metal, it absorbs high-energy ultraviolet photons to excite electrons because of the higher energy gap between d band and the s/p conduction band (Fig. 15.2A, optical transitions in Ag). As a result, all of the lower-energy photons in the visible region (300–700 m) therefore are reflected (Fig. 15.2B). Thus, it exhibits a typical silvery color.

15.2.2 Color tunability in Ag/Au nanoparticles (3–100 nm)

In thin Ag/Au films, the electron gas on the surface of the metal is highly sensitive to dielectric medium, such as air, glass, and water (Fig. 15.3A). For example, in contrast to yellow appearance of bulk gold, Au thin films appear blue by transmitted light due to the light absorption in yellow and red region. The optical properties are highly depending on the energy transfer between incident light and the surface electron wave (or surface plasmons, SP) present on a NPs. Surface plasmons are the oscillation of electrons in a free electron gas on a metal surface and they are quantized. The surface electron wave can propagate in all the directions such as height, depth and lateral direction (Fig. 15.3B). When a light ($\lambda = 500$ nm) exposed on an Au surface, the height of SP from the metal surface is about ≈250–1000 nm, its depth is about ≈5 nm and the traveling distance in lateral direction is about ≈2–20 um. If the lateral dimension is smaller than the surface plasmon wave, the plasmon is called localized surface plasmon resonance (LSPR) (Fig. 15.3C and D). Interestingly, the color differences seen in the Ag (silvery) and Au (orange yellow) metals differs at their nanoscale and both systems exhibit tunable colors in the visible region. The reason for the new physical properties are due to the

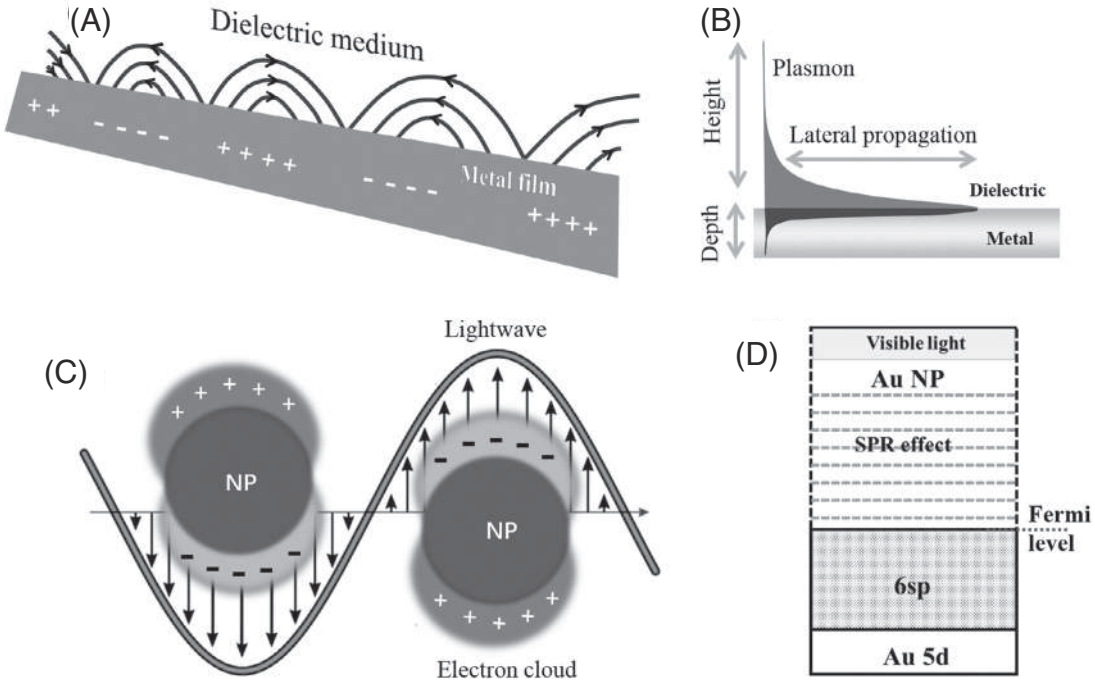

FIGURE 15.3 (A) The valence electrons in metals films are free electrons (refer Fig. 15.7 for further details) that are delocalized in a constant potential field with respect to the surrounding dielectric medium. (B) three-dimensional propagation (height, depth, and lateral) of plasmon on a metal film. (C) Representation of LSPR on a NC surface. The free electron gas on the NC surface undergoes a charge separation with respect to the positive ionic lattice and creates a dipole. The formed dipole undergoes the oscillation around the NC due to the interaction with accelerating electric component of the incident light. (D) Band structure representation of collective oscillation conduction band 6SP electrons responsible for surface plasmon wave. In a nanoparticle, this surface wave is in resonance with the oscillating electric field of incident light resulting the phenomenon of SPR.

collective oscillation of surface electrons in the conduction band also called LSPR at nanoscale.[6] Absorption of light by the surface electrons occurs at a particular frequency (usually, blue–green region) and gives rise to various complementary colors in the visible region (brownish yellow, ruby red) for Ag/Au NPs.

The SPR properties of spherical particles can be well-studied by the Mie scattering theory and provides analytical solution for light scattering characteristics of the NPs. It predicts size, shape, optical constants of the NPs, concentration, chemical composition, surrounding medium's dielectric properties, and spatial distribution of the NCs. Mie scattering is basically the elastic scattered light by particles with size similar to or larger than the wavelength of the incident light. Mie signal is proportional to the square of the particle diameter. Based on the size of the NPs this theory can be classified into two parts.[7] In the first case, optical responses from large Au and Ag NPs (Radius > Wavelength of light, λ). In these large NP systems, the interaction of external electromagnetic fields of light is influenced by the surface free electron density and, therefore, they exhibit bulk-like dielectric function relative to that

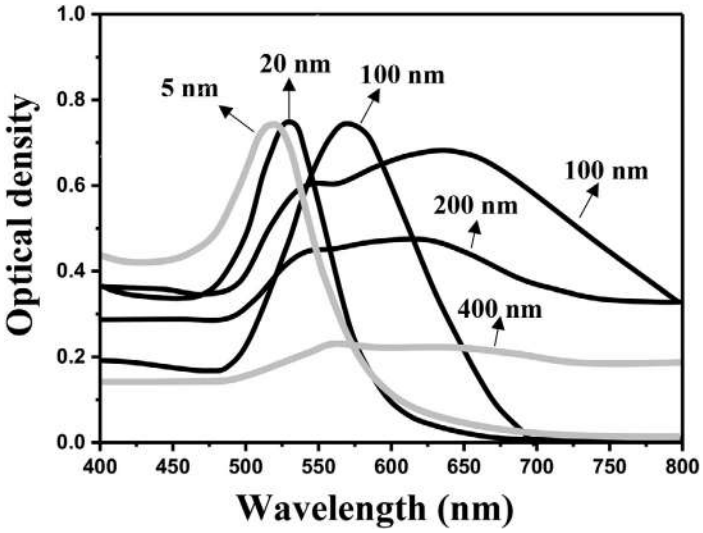

FIGURE 15.4 UV–visible spectra of Au NPs of different sizes (5–400 nm) in aqueous medium. The sizes are labeled next to the spectra, indicated by arrows. The trend of absorbance of the incident light has changed with increase in the NP size. As the particle grows larger, the absorption spectrum becomes closer to a continuous spectrum similar to the absorption of the bulk gold. Data were redrawn and adapted from Sigma Aldrich.

of the surrounding medium (see the absorption spectrum of Au NPs of size 200–400 nm, Fig. 15.4). The optical properties can be quantitatively described with Mie theory. In the second case, when particle size approaches the electron mean free path (~50 nm for Ag and Au), the dielectric function and refractive indices become strongly depends on size. At this size regimes also Mie theory still provides a solution for the system. As per the SPR principle, the Au NPs exhibit color change from brilliant red color to a pale brownish-yellow color when the size decreases from 5 nm to 3 nm. The color tunability is due to variation in the interaction of light and the SP on a NP surface. The next section will discuss the optical properties of NPs below 3 nm.

The oscillation frequency, and hence the color, depends on the size and shape of the particle as well as the dielectric constant of the surrounding medium. When particle size increases, the wavelength of surface plasmon resonance shifts to longer wavelengths, resulting in the absorption of red wavelength, and reflection of blue (Fig. 15.4). The shift in the SPR is specific to surroundings and often used these NPs for biomolecules and environmental sensors.

15.2.3 Color exhibition in Ag/Ag NCs (1–3 nm)

The principle of SPR is not applicable below a specific particle size and the Mie theory does not provide an adequate solution for these systems. In this case, the particle size is less than the electron mean free path. That means the size approaches the Fermi wavelength of an electron also called De Broglie's wavelength of an electron at the Fermi energy. The Fermi wavelength of an electron for gold and silver is ~0.5 nm. All of the thermodynamic, electronic, optical, and chemical properties of NCs are significantly different from the above two plasmonic-size regimes. Moreover, new properties such as multiple absorption bands, photoluminescence (PL), electrochemiluminescence, chirality, nonlinear optical properties, ultrafast electron dynamics, etc. emerges at this size scale.

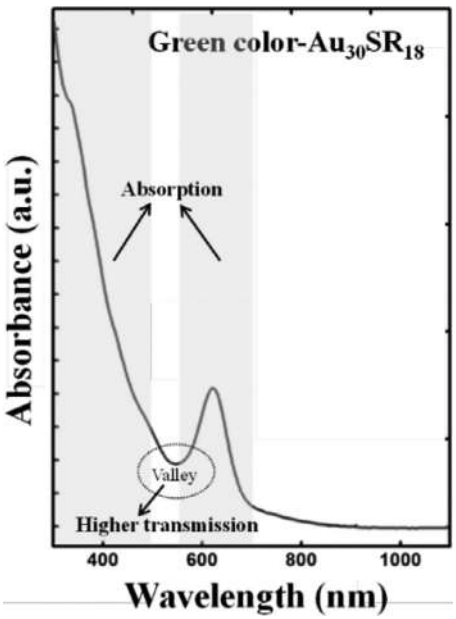

FIGURE 15.5 Absorption spectrum collected from Au_{30} clusters. It has a sharp peak at 620 nm which decays into a valley in the range of 520–570 nm and again rises exponentially in the lower wavelength region, with shoulders at 484 and 337 nm. Reproduced with permission from ref.[8]. Copyright 2013 American Chemical Society.

Even in the case of NCs, the color displayed is vivid based on their absorption properties, for example, $Au_{25}SR_{18}$ system (SR = alkane thiolate), Au_{25}^{-}, Au_{25}^{0}, and Au_{25}^{+} (ligands are omitted for simplicity) solutions appear in pale brown to greenish and to pale yellow, respectively. Au_{38} solutions exhibit brownish color; however, $Au_{30}SR_{18}$ has a distinct green color, though in both cases ligands are colorless.[8] The optical absorption spectrum of Au_{30} is shown in Fig. 15.5, which is similar to chlorophyll absorption spectrum. Au_{30} molecule has increased transmission in the green color region (a valley at ~545 nm) as a result of strong absorptions in the red (630–740 nm) and blue (440–490 nm) regions.

Another fundamental difference among NPs and NCs is that, the clusters are dominant absorbers while NPs (above 5 nm) tend to show scattering contributions along with absorption contribution. Scattering property is related to the surface area to volume ratio of the particle, while the absorption is related to concentration. Solutions of Ag/Au NCs are often pale colors and transparent because the scattering efficiency is negligible.

15.2.4 Melting properties of bulk to nanoclusters via nanoparticles

Bulk gold shows excellent chemical stability against oxidation, with a high melting point (1064°C). In this regards it is appropriate to recall an old Chinese idiom, "True gold fears no fire," which is attributed to the fact that bulk gold stays intact and shiny when placed over wood fires (600–1000°C), whereas most other metals (such as copper, zinc, and nickel and their alloys) would melt and/or tarnish in these conditions. However, nanoscience offers different ways to change behavior of gold at different temperatures while preserving its special characteristics. NPs show a melting temperature depression with decreasing size due to influence of surface energy. Melting of NPs can be observed in a transmission electron microscope, and gold NPs have been found to melt at 27°C compared to the bulk melting

temperature of 1064°C.[9,10] The surface energy increases as the size of a crystal becomes smaller. Thermodynamics predicts a lowering in the melting temperature, if the surface energy of the solid is higher than that of the liquid. Most of the melting behavior studies have been carried out on gold NPs in absence of any stabilization by surface ligands. So, there are no sufficient experimental evidences on melting point of NCs. Typically, gold NCs stabilized by thiolated ligands in practice, lowers the surface energy of the NPs and gives a different melting behavior compare to bare Au NPs. It should be noted that below 2 nm, the melting point function breaks down and the packing structure of the Au atoms is usually different from FCC. Thus, it is expected to exhibit an entirely different melting behavior.

15.2.5 Magnetic properties of bulk to nanoclusters via nanoparticles

The noble metals (Au, Ag, and Cu) are all excellent conductors, and each has a single unpaired electron in its valence s-orbitals that generate the free electrons in the conduction band. It is known that single gold atom is paramagnetic because of the unpaired $6s^1$ electron, while bulk gold is diamagnetic.[11] The single electron cannot induce magnetism in these bulk metals. This is because they are dominated by closed-shell core electrons (core diamagnetism). This diamagnetic contribution is several times larger than that of paramagnetic contribution produced by the unpaired electron. At the nanoscale, ferromagnetic behavior was observed for both films formed from bare Au clusters and Au NPs embedded in films of titania.[12] Nevertheless, there is no general rule that the size reduction always brings about magnetism in these metals. For example, bare gold films deposited on glasses at 300 K was observed to be more diamagnetic than bulk gold, but the same sample placed at low temperatures (5K) shows magnetism.[13] Magnetism in gold NPs has been attributed to a surface effect, especially, surface bound molecules provide significant orbital contribution to the magnetic moment. Zhang and sham proposed the increase of density of unoccupied d-state holes, as a result of metal–ligand bonds, is the reason for magnetism in thiolated NPs.[14] It has also been observed that, depending on ligands and experimental conditions, the NP (~2 nm) may exhibit ferromagnetism, paramagnetism, and diamagnetism.[15] Several research groups have studied magnetism in monolayer-protected Au NCs, but the results were often contradictory, and thus, a clear understanding of this phenomenon is still missing. For example, for the similar type of Au NCs (around 1.5–2 nm), Crespo et al. observed ferromagnetism,[16] whereas Yamamoto and Hori detected both superparamagnetism and Pauli paramagnetism.[17] Greget et al. concluded that 1.9 nm NPs were diamagnetic, whereas larger particles (4.4 nm) were ferromagnetic.[18] Munoz-Marquez et al. observed ferromagnetism in 2.1 nm clusters and diamagnetism in smaller clusters (1.4 nm).[19]

The reason for the limited understanding of the magnetic properties of Ag/Au NPs is the lack of atomic precision and undetermined charge state, and lack of synthetic control over NPs crystalline habit; it influences the magnetic anisotropy. A little change in these properties can switch the NPs from being magnetic to nonmagnetic. It is known that thiolated-Au NPs can carry multiple surface charges depending on the synthetic parameters. It is worth noting that the removal or addition of electrons can be triggered by oxygen or a mild reductant yields different magnetic states.

NCs have added advantage due to its controlled atomically precise structure. One such example is of $Au_{25}(SR)_{18}$ given here. Electron paramagnetic resonance (EPR) studies on

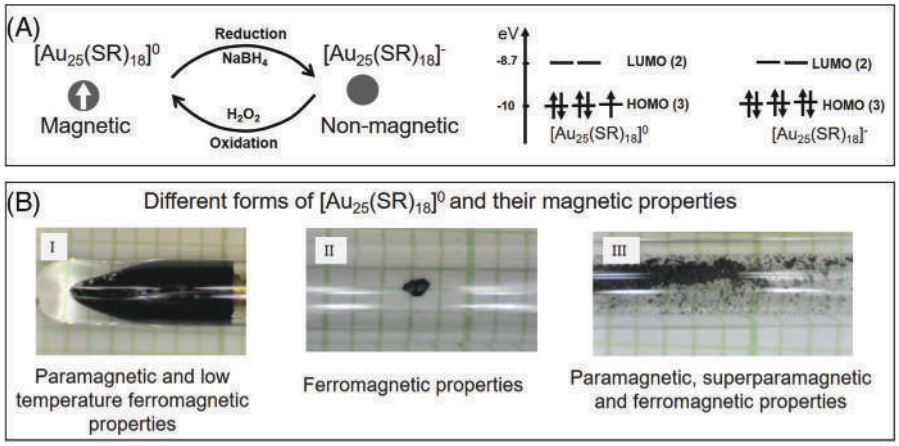

FIGURE 15.6 (A) Reversible conversion between the neutral and anionic $Au_{25}(SR)_{18}$ NCs. DFT-calculated Kohn–Sham orbital energy level diagrams for the neutral and anionic NCs, respectively. Reproduced with permission from ref.[20] Copyright 2009 American Chemical Society. (B) I, II, and III photographs of $[Au_{25}(SR)]^0$ amorphous film, one single crystal collection of microcrystals, show different magnetic behaviors at room and low temperature. Reproduced with permission from ref.[21] Copyright 2017 American Chemical Society.

precise structures of anionic to neutral $Au_{25}(SR)_{18}$ showed transition from diamagnetism to paramagnetism, respectively (Fig. 15.6A).[20] As shown in Fig. 15.6B, the paramagnetism of neutral $[Au_{25}(SR)_{18}]^0$ is due to the open shell electronic structure (i.e., seven delocalized Au valence electrons distributed in the superatomic orbitals, $1s^21p^5$). The odd number of electrons leads to one unpaired electron. When the unpaired electron is removed from neutral NCs by oxidation to form $[Au_{25}(SR)_{18}]^+$ (6e), or is paired with an electron via chemical reduction to give $[Au_{25}(SR)_{18}]^-$ (8e), in both cases the NC becomes diamagnetic.

The magnetic behaviors are highly depending on various crystalline forms of NCs.[21] For example, the $[Au_{25}(SR)_{18}]^0$ has taken in different forms such as 1. as a thin film, 2. single crystals, 3. collection of smaller crystals (microcrystals). These forms representing a range of crystallographic orders. Though all of them are composed of same material $[Au_{25}(SR)_{18}]^0$, they exhibit the different magnetic behaviors reveal the discrepancy seen in the earlier studies on Au NP systems (Fig. 15.6B I, II and III). In case of films, $[Au_{25}(SR)_{18}]^0$ exhibits a paramagnetic behavior, but at low temperature, ferromagnetic interactions are detected. In the case of single crystals, interestingly, orientation dependent hysteresis experiments showed that the free single crystals undergo reorientation with respect to the applied field and exhibit ferromagnetism. In the third case, a large collection of microcrystals is magnetic even at room temperature and shows distinct paramagnetic, superparamagnetic, and ferromagnetic behavior. Simulated electron paramagnetic resonance spectra reveals that both spin–orbit coupling and crystal distortion are important to explain the observed magnetic behaviors. Magnetism in Ag/Au NCs is thus demonstrated to be the outcome of a very delicate balance of various factors. To obtain reproducible results, the NC samples must be (i) pure atomic precise Ag/Au NCs, (ii) of known charge state, and (iii) well-defined in terms of crystallinity and experimental conditions.

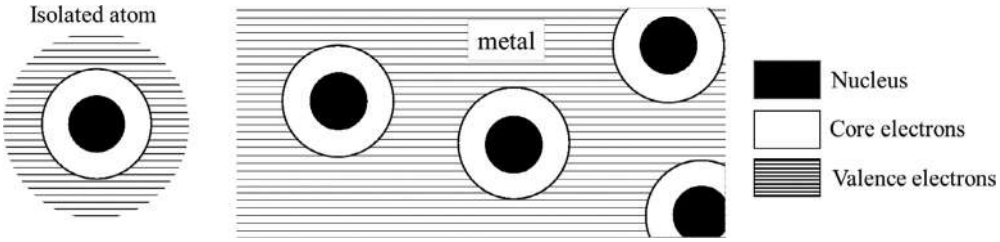

FIGURE 15.7 The valence electrons of metals are free electrons to delocalize in constant potential field.

15.2.6 Transformation of crystal structures from bulk-to-nanoparticles-to-nanoclusters

It is well known that in the bulk as well as at nanoscale (above 2 nm diameter) the Ag/Au exhibits FCC structure. However, NCs often have non-FCC structures. This has been successfully validated by synthesis of Au/Ag NCs of other crystal types (icosahedral, BCC, HCP) too along with FCC structure. Research in the field of atomically precise gold-thiolate NCs first revealed noncrystallographic (not a typical BCC, HCP, and FCC structures) structures such as decahedral,[22] icosahedral,[23] and bi-icosahedral[24] structures in $Au_{102}(SR)_{44}$ and $Au_{25}(SR)_{18}$ and $Au_{38}(SR)_{24}$ nanoclusters, respectively. These structures are novel as such packing modes are not observed in bulk gold. After these initial reports, it was assumed that these noncrystallographic structures would be predominant in $Au_n(SR)_m$ NCs. Recently, the crystallographic structures such as $Au_{36}(SR)_{24}$ - FCC,[25] $Au_{30}(SR)_{18}$ (HCP),[26] and $Au_{38}S_2(SR)_{20}$ (BCC)[27] are reported. A detailed description on the crystal structures is presented in Chapter 12. Similar to the Au NCs, the Ag NCs also exhibit various non-FCC structures. For example, $Ag_{44}(SR)_{30}$[28] and $Ag_{25}(SR)_{18}$[29] crystal structures are similar to $Au_{25}SR_{18}$.

15.2.7 Variation of band structures from bulk to nanoclusters

The density free electrons in the conduction band of Ag and Au metals are very high which is in the range of 6×10^{22} per cm^3. These electronic states are densely spaced, forming quasi-continuous bands (e.g., 6s or 6sp band and 5d bands). Drude developed a theory in 1900, also called the free electron theory, that provides approximate estimation of band structures of metals. This model is an application of kinetic theory of dilute gases but the electron densities are almost 100 times of typical gas density. This theory considers substantial reduction of attractive forces of nucleus on the valence electrons due to the presence of inner-shell electrons (strong electron screening effects). As a result, the valence electrons in metals are free electrons and are delocalized in a constant potential field provided by the positively charged cores, throughout the bulk. Moreover, these electrons are not bound to any specific metal atom (Fig. 15.7).

The major difference between the Drude model and kinetic theory is that the energy levels of a gas are not quantized while they are quantized in metal atoms due to the Pauli exclusion principle. Therefore, a simple particle in a box model can be used to describe the energies of the free electrons in few-nm and smaller-sized metals. This simple model sheds light on how

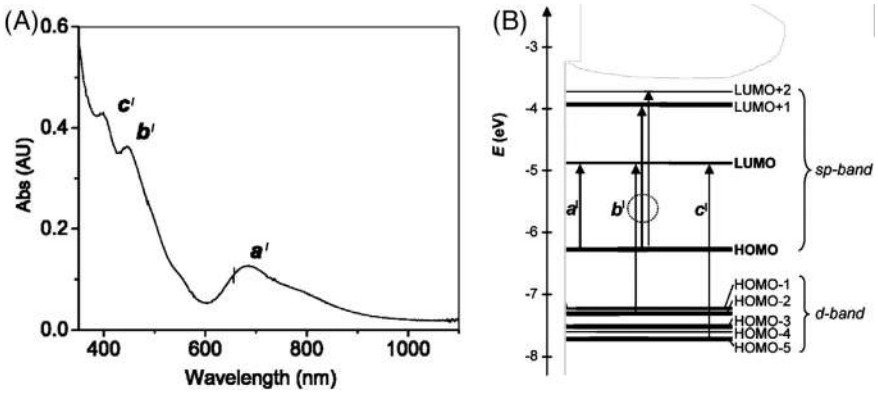

FIGURE 15.8 (A) Optical absorption spectrum of $[Au_{25}(SR)_{18}]^-$ NCs, their prominent electronic transitions are labeled as a′, b′, and c′. (B) Kohn–Sham orbital energy level diagram for a model compound $Au_{25}(SH)_{18}$, corresponding experimental transitions (a′, b′, and c′) are marked. Each KS orbital is composed of the relative contributions of the atomic orbitals of Au (6sp), Au (5d), S (3p). Reproduced with permission from ref.[30] Copyright 2008 American Chemical Society.

free electrons arrange in metals, as governed by level multiplicities within this approximately harmonic confinement potential at small cluster size. The top most filled level corresponds to the highest electron energy of a given metal, called the Fermi energy E_f, and is independent of the metal size.

In NPs, the metals possess a metallic core with free electrons and conduction band consists of quasi-continuous energy levels (band structure of NPs in Fig. 15.1). On the NP surface there exists a attractive force between electrons and positive charges. The displacement of free electron gas in NPs with respect to the force exerted by the electric field of light gives rise to polarization changes at the NP surface (Fig. 15.3C). Thus, light can collectively excite these electrons to give plasmonic responses.

In NCs, the 5d electrons of gold are more tightly bound to the nucleus than 6s electrons, thereby producing a large energy gap (more than thermal energy, k_{BT}) between the s and d bands.[30] For example, the $[Au_{25}(SR)_{18}]^-$ exhibit multiple molecular-like absorption bands (Fig. 15.8A), and the results are in good agreement with time-dependent density functional theory calculations (Fig. 15.8B). The absorption spectrum shows multiple bands at 670 nm, 450 nm, and 400 nm (Fig. 15.8A). Density functional theory calculation predicts excellent solution for these optical transitions in NCs. The characteristic electronic transition at a wavelength 670 nm (peak a′ in Fig. 15.8B) originates from the (LUMO ← HOMO) transition, which is basically an intraband ($sp \leftarrow sp$) transition. The absorption band at 450 nm (peak b′) composed of both intraband ($sp \leftarrow sp$) and interband ($sp \leftarrow d$) transitions. The transition at 400 nm (peak c′) corresponds to the interband ($sp \leftarrow d$) transition. Similarly, the molecule-like multiple absorption bands in exhibited in other NCs are due to single-electron transitions between quantized electronic energy levels.

On the other hand, a brief history of quantization in metals is provided in this section. Discreteness of electronic energy levels in few-atom NCs was first discussed by Frohlich (1937). Later, this problem was popularized by Kubo (Kubo, 1962) and Kawabata (1966).[31]

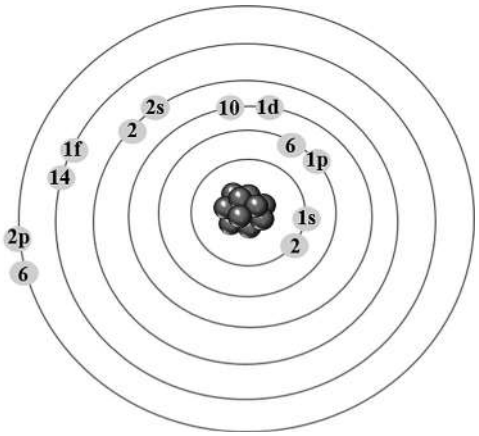

FIGURE 15.9 Jellium model electronic shell in nanoclusters mimicking the atomic structures. Nanoclusters with valence electrons 8, 18, 20, 34, 40, 58 are considered closed electronic shells configuration treated as electronic stability to a cluster.

Kubo produced quantitative predictions of the electronic structure of very small metal clusters whereby the energy level spacing between adjacent levels for an N-atom particle is of the order of E_f/N, where E_f is the Fermi energy of the bulk metal. The relative difference between the energy level spacing and thermal energy has become a criterion to distinguish metallic and nonmetallic behavior. If the energy level spacing is smaller than k_{BT} can create mobile electron-hole pairs in the metals, and current can flow. However, if energy level spacing is much larger than available thermal energy, free electrons in metal clusters are confined to discrete energy levels. Thus, the metal NCs are often considered to be nonmetallic, even though they may exhibit free electron scaling behavior. Although Kubo et al. predicted some properties of metal cluster electronic structure, quantitative correlation of electronic structures with the number of metal atoms was not elucidated until 1984, when W. Ekardt employed time dependent local-density approximations within the frame of the self-consistent spherical jellium model.[32]

In contrast to classical electromagnetic theory such as Mie theory for plasmonic systems, jellium model, and time-dependent density functional theory have been successful in explaining properties of NCs. Fundamentally, jellium model is the Drude free electron model and contains the same assumptions, which originates from nuclear physics. In this model, a metal cluster is modeled as uniform, positively charged spheres with electronic shells filled with free electrons (Fig. 15.9). These free electrons are provided by the valence electrons of the individual metal atom constituents of the clusters which delocalizes and forms orbitals surrounding the positively charged core. The free electrons are considered to move freely in the orbital without any electron–electron and electron–ion interactions due to strong electron screening effects in noble metal atoms. This structure is similar to the electronic structure of single atom and is subjected to the Pauli exclusion principle, as a result these metal NCs are often referred to as "multielectron" artificial atoms. Greater details on electronic stability of NCs through jellium model is available in Chapter 2.

15.2.8 Calculation of transformation of plasmonic to nanoclusters

The transition from plasmonic behavior to the molecule-like features of NCs is an ongoing research area.[33] From theoretical point of view, it is helpful to estimate the size of gold NPs at

which they exhibit quantum size effect. One can use the previously discussed discrete energy level theory to find the approximate quantum size regime.

$$a^3 = \frac{4\pi^2}{\delta}\left(\frac{\hbar}{2m}\right)^{\frac{3}{2}} E^{\frac{-1}{2}}$$

where $\delta = k_B T$, $k_B = 1.38 \times 10^{-23}$ J/K at temperature 298 K, $\bar{h} = 1.05 \times 10^{-34}$ m^2 Kg/s, E is Fermi level, 5.5 eV = 8.8×10^{-19} J, m is the mass of electron, 9.1×10^{-31} Kg, the corresponding particle volume (a^3) is 5×10^{-27} m^3 and equivalent particle size 1.7 nm. This gives the critical particle size at which electronic energy quantization will become important.

The average spacing (δ) or Kubo gap of electronic energy levels follows this relation:

$$\delta \approx \frac{E_f}{N}$$

where E_f is the Fermi energy and N is the number of gold atoms. N is in the scale of particle volume (nm^3). Thus, the spacing is inversely proportional to the cube of particle size. The spacing δ substantially increases with decreasing NCs size, and this will affect the physicochemical properties of small particles. If one uses the thermal energy ($k_B T$) at room temperature (~298 K) as a criterion, electronic energy quantization becomes distinct when δ is larger than $k_B T$.

$$\delta \geq k_B T \tag{15.2}$$

Substituting the Fermi energy of gold or silver ($E_f = 5.5$ eV) into the equations, one obtains the critical number of gold atoms to be ~200–300 or the equivalent diameter ~1.8–2.1 nm (roughly 2 nm).

Each gold atom in the cluster donates one 6s valence electron. The net number of gold atoms in the FCC unit cell is 4. Thus, the valence electron density of gold also equal to the number density of gold atoms can be calculated using

$$N = \frac{4}{(0.408\,\text{nm})^3} \approx 59\,\text{nm}^{-3}$$

From the above calculation the quantization occurs when the number of valence electrons is about 280.

$$\text{Volume} = \frac{\text{Number of atoms} = 280}{\text{number density} = 59\ \text{nm}^{-3}} \approx 5\,\text{nm}^3 \approx (1.7\,\text{nm})^3$$

that is, particle size 1.7 nm, identical to the above estimation of critical cluster size. Thus, around ~2 nm size, electronic energy quantization will become important, and below this size the collective plasmon mode cannot be supported. Recent experimental findings agree with the theoretically estimated sizes, the molecular NCs to plasmonic NPs transformation occurred around 200–300 Au atom region. Calculated values are in agreement with the experimental results as shown in Fig. 15.10. The Au_{279} showed plasmon resonance peak, whereas Au_{133} possessed still a molecular structure.[34]

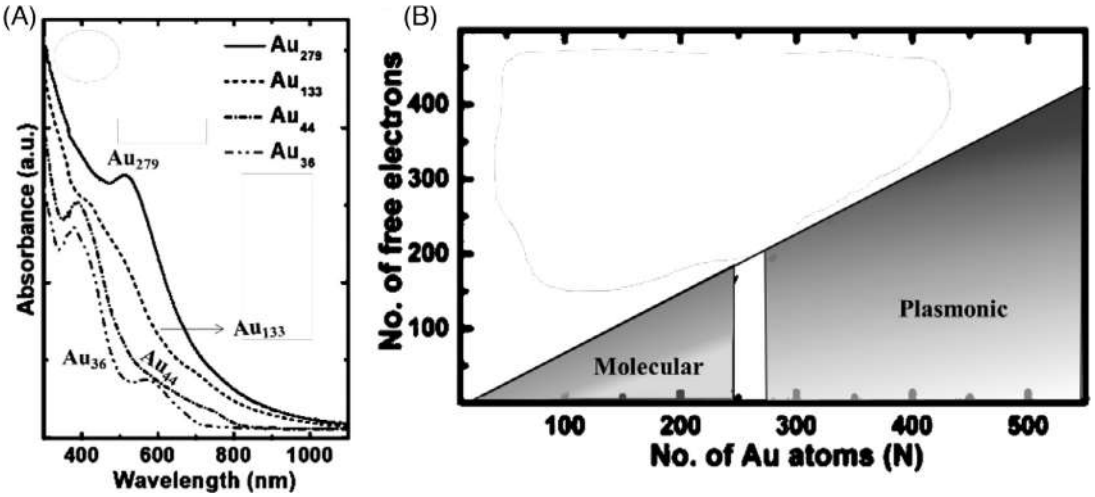

FIGURE 15.10 Au_{279} is the smallest identified AuNPs to exhibit surface plasmon resonance, which is at 510 nm, the others Au_{133} and lower sizes possess discrete optical absorption, molecular nature. The transformation from molecular to plasmon occurs in between ~200–300 atom. Reproduced with permission from ref.[34] Copyright 2018 American Chemical Society.

15.2.9 Quantum confinement in thiolated-Ag and Au nanoclusters

The transition from NPs to NCs is accompanied by a change of band structure from continuous energy states to discrete energy states. In NCs, typically, separation between the discrete energy levels decreases (lower band gap) with increase in particle size, which causes absorption and emission to redshift. Fig. 15.11 shows the changes in the optical absorption profiles of different sizes of Au NCs, including $Au_{25}(SR)_{18}$, $Au_{38}(SR)_{24}$, and other compositions, to illustrate the quantum size effects.

Chakraborty et al.[36] demonstrated the emergence of metallicity in Ag NCs ($Ag_{44}(SR)_{30}$, $Ag_{55}(SR)_{31}$, ~$Ag_{75}(SR)_{40}$, ~$Ag_{114}(SR)_{46}$, $Ag_{152}(SR)_{60}$, ~$Ag_{202}(SR)_{70}$, ~$Ag_{423}(SR)_{105}$, and ~$Ag_{530}(SR)_{100}$) by comparing their absorption profiles. A systematic appearance of a plasmon-like optical absorption feature with increase in NCs size was observed in these systems. Up to ~Ag_{114}, multiple absorption features were seen in the absorption spectra of these NCs, resembling a quantized system till this size regime. For Ag_{152} and larger clusters, the plasmonic feature corresponding to a single peak at ~460 nm evolved pointing to the emergence of metallicity in Ag NCs composed of ~150 metal atoms. Yang et al.[37] in their recent report solved crystal structures of plasmonic twinned Ag NPs with composition $[Ag_{136}(SR)_{64}Cl_3Ag_{0.45}]^-$ and $[Ag_{374}(SR)_{113}Br_2Cl_2]$, respectively. Ag_{136} and Ag_{374} clusters consists of fivefold twinned cores enclosed within related structurally distinctive Ag−SR complex shells.

However, these NCs do not follow a systematic band gap trend, that is, decrease of band gap with increase in size. For example, the optical bandgap of $Au_{36}(SR)_{24}$ NC is 2.1 eV, which is higher than the 2.0 eV bandgap of $Au_{28}(SR)_{25}$ NC.[38] These abnormalities further proposes that the other factors such as crystal structure of a NCs influence the trend in band gap. It is found that the size effect in a particular crystal structure (FCC, HCP, and BCC) shows a similar

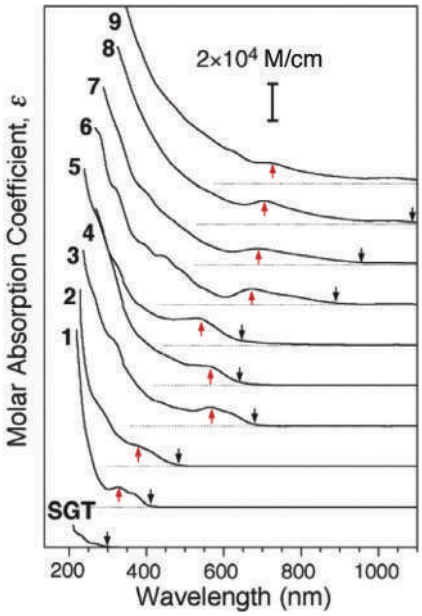

FIGURE 15.11 Optical absorption spectra of aqueous solutions of 1–9 and sodium Au(I) thiomalate at ambient temperature. 1–9 are $Au_{10}(SG)_{10}$, $Au_{15}(SG)_{13}$, $Au_{18}(SG)_{14}$, $Au_{22}(SG)_{16}$, $Au_{22}(SG)_{17}$, $Au_{25}(SG)_{18}$, $Au_{29}(SG)_{20}$, $Au_{33}(SG)_{22}$, and $Au_{39}(SG)_{24}$. Reproduced with permission from ref.[35] Copyright 2005 American Chemical Society.

trend in band gap trend. In other words, NCs belongs to a FCC crystal group shows systematic trend in relation to size to energy gap (NCs with FCC series are listed in Section 15.4.7). Based on the optical properties (steady-state absorption, bandgap, transient absorption, as well as carrier dynamics) of Au NCs, comprising tens to hundreds of gold atoms, Jin et al. classified the NCs in three groups[39]: (i) NCs with less than 50 Au atoms; these are nonscalable as their optical properties are strongly dependent on the structure rather than size; (ii) NCs with 50–100 Au atoms; show both size- and structure-dependent optical properties; and (iii) NCs with more than 100 Au atoms; exhibit optical properties solely dependent on size, and the structure effect is negligible.

15.3 Types of Ag and Au nanoclusters based on surface coverage

Generally, there are two main strategies for preparing metal NCs. The first approach relies on the use of specific capping agents, for example, alkanethiols as ligands, which interact strongly with the metal surface to form ultrasmall NCs protected by a monolayer of ligands. The second approach is the template-assisted synthesis. Here, biomolecules, dendrimers, and polymers are used as a template to direct the formation of Ag/Au NCs. The nature of the capping agent determines not only the size of NCs, but also their optical properties. The following few subsections focus on the Ag/Au NCs stabilized by various surface forces, including, unprotected gas phase NCs, NCs stabilized by emulsions and protected by ligands such as polymers, biomolecules, and small molecules.

15.3.1 Gas phase clusters

The early days of investigation dealt with successful creation of few-atom naked-metal clusters in gas matrices at low temperature. The precise determination of atomic number in

a NC along with absorption and emission properties were carried out by mass spectrometry coupled with optical spectroscopy.[40] These studies have successfully provided well-defined gas phase Ag_n ($n = 2$–5) clusters in argon matrix whose optical properties reveal an important link between Ag atoms and Ag NCs. Marcus and Schwentner first reported that gold dimers yield UV and visible emission in 1987[41]. Harbich et al. used a similar method to prepare Au_2 and Au_3 embedded in argon matrices and studied their UV and visible photophysics at low temperature.[42,43] Collings et al. also investigated the gas phase visible and UV absorption spectra of gold clusters Au_n ($n = 7$, 9, 11, 13) using photodepletion spectroscopy.[44] Similarly, several silver clusters Ag_2, Ag_3, Ag_4, Ag_5, and Ag_8 and their optical properties were reported by several groups. In general, all these few-atom naked clusters exhibit absorption and emission in the range of 200–400 nm.

In a typical process, silver atoms are sputtered from a silver target hit by an individual projectiles of gas ions or pulsed lasers.[45] The surface atoms of Ag/Au target are indeed at relatively higher energy state than the atoms at the core. The surface atoms are highly reactive because they have a higher degree of freedom due to the missing atoms above or below the surface. When the surface atoms impacted by these individual projectiles, some of the atoms gets experience an impact which will have an energy that can overcome the binding energy of the atom on the surface. This impact allows few atoms to get detached from the surface. When this process happens, one can see number of such atoms from the target surface to come out. These sputtered gas phase atoms or molecules undergo nucleation leading to the formation of cluster nucleus. Nucleation can be either homogeneous or heterogeneous. Heterogeneous nucleation occurs between foreign objects, inert gases, etc. Note that inert gases are used to cool the clusters through collision and deactivation process. Dimer formation occurs when a nucleated ions involved in the collision process, which removes excess internal energy as kinetic energy. The dimer acts as a seed for further condensation and growth process. Size-selected clusters can be soft landed on an inert substrate (such as graphite, silicon, and oxides), or trapped in rare gas matrices.[46–50]

$A + A + A\ (KE_1, \text{kinetic energy}) \rightarrow A_2 + A\ (KE_2 > KE_1)$ Homogeneous nucleation
$A + A + B\ (KE_1) \rightarrow A_2 + B\ (KE_2 > KE_1)$ Heterogeneous nucleation

During the cluster growth analysis, certain clusters have higher mass intensity than others. Interestingly, the mass spectra of ionized Ag_n clusters showed numerous high and low intensity peaks composed of odd–even silver atom patterns. In mass spectrometry, clusters must be charged in order to separate them according to their size. Charge on the NCs be achieved by electron impact ionization or photoionization. The ionization potential as well as electron affinity values also altars based on odd-even silver atom patterns. Even number-atom Ag_n clusters exhibit higher ionization potential and electron affinity values in compare to the next odd atom Ag_n clusters.[51] The changes in the properties are associated with their stability. Some of the gas phase clusters are highly stable than the others, the number of constituent atoms in stable clusters are generally called as magic numbers, such as 8, 20, 34, 40, and 48. The stability of clusters and the reason for the even–odd alternation can be well understood by the spherical jellium model (more details in Chapter 2).

They find applications in energy storage and catalysis. Silver clusters are well-known for their catalytic properties,[52] for example, in the production of formaldehyde from methanol and in the production of ethylene oxide from ethylene.[53] Goodman et al. reported in the late 1990s that Au clusters supported on titanium dioxide (TiO_2) were able to catalyze the

oxidation of carbon monoxide (CO) under low temperature and the catalytic reaction was strongly dependent to quantum size effect of the Au clusters.[54]

In in 2001, Dickson et al. demonstrated another approach to produce naked few atom fluorescent Ag NCs. They were generated by the photoreduction of nanoscale silver oxide (Ag_2O).[55] They can serve as a novel class of information storage medium, wherein data could be readily written on thin Ag_2O films with a blue light (<520 nm) and nondestructively readiable with the intense red fluorescence upon excitation by green light (>520 nm).

15.3.2 Nanoclusters in inorganic templates

In 1970s–1980s, NCs with well-defined number of atoms were successfully stabilized in solid matrices such as inorganic glasses and zeolites. Zeolites are crystalline, highly porous materials with a negatively charged aluminosilicate framework, and serve as an excellent template to produce Ag NCs.[56] Zeolite hosts were extensively used to produce Ag NCs (Ag_n, $n = 3$–100) compared to Au NCs due to the following reasons:

(1) Ag^+ is the only noble monopositive cation that forms a mononuclear species with appreciable stability in water. No hydrolysis occurs. Of all the noble metals, only Ag^+ ions can be exchanged, easily and completely the cation contents present in the zeolites. Stoichiometric ion exchange, impossible to achieve for most cations, is frequently observed for Ag^+.
(2) The reversible oxidation–reduction of silver in zeolites provides an excellent model system for studying the mechanism of formation of noble metal NCs within zeolite channels and cavities. These are excellent models for studying the mechanism of catalysis for the dehydrogenation of hydrocarbons.
(3) Hydrated silver zeolites are light-sensitive materials. It was proposed that silver zeolites incorporated into membrane electrodes to photocatalytic water splitting.

In general, synthesis of silver NCs in glasses/zeolites is a two-step process. The preparation of Ag^+-doped glasses/zeolites either by melting $AgNO_3$ together with other glass forming materials, or by immersion of a glass slide in a molten salt bath containing the silver salt, so that Ag^+ replaces Na^+ in an ion exchange reaction, or by ion implantation. Second step includes the reduction of Ag^+ to Ag^0 and following the formation of Ag_n^+ NCs within a zeolite. Several reduction pathways were available, including heat treatment,[57,58] UV light excitation,[59] and two-photon excitation[60] laser irradiation,[61,62] synchrotron irradiation,[63] thermal annealing or controlled quenching of the melt.[64] During activation, the silver ions reduce to form NCs, they grow only to oligomeric size due to the limited cage dimensions. Electron paramagnetic resonance spectroscopy was used to determine the charge state of silver in zeolite.[65] The Ag NCs within a zeolite exhibit high ambient stability against photobleaching with a decent quantum yield (up to 20%). The glass matrix is transparent and therefore these fluorescent glasses and their thin films, and fibers could find applications as optical components. Furthermore, direct laser writing on the Ag^+-doped glass enables fabrication of 3D fluorescent structures at the nanometer scale, opening up applications in optical data storage and nanophotonics.[62,66] The recorded images do not photobleach and are claimed to have tolerance toward temperature, ageing, and humidity. Growing a well-designed Ag NCs in glasses is useful for perennial storage of images over many centuries.[66] For example, Ag NCs with submicron resolution in the 3D space of a giant zeolite crystal were created using a two-photon activation process.[60]

Results show that high writing resolutions down to the diffraction limit are obtained. An excellent readability due to the positive contrast imaging, brightness and stability of the emissive clusters were seen in these materials (Fig. 15.12). This material has been potential applications for fluorescent lamps and biocompatible labels.

15.3.3 Monolayer protected nanoclusters

Various aspects (synthesis, characterization, properties, applications) of water soluble thiolated Ag/Au NCs are discussed in various chapters of this book. The efforts on the precise control of the sizes of Au NCs dates back to 1970s–1980s, a series of Au NCs (Au_5, Au_8, Au_{10}, Au_{11}, Au_{13}, and Au_{55}) protected by weakly bound ligands (e.g., phosphine) were synthesized and characterized. Investigation of thiol-protected gold NCs has given a deeper insight into this cluster research. Over 100 molecules of this kind with formulas, such as $Au_{18}(SR)_{14}$, $Au_{20}(SR)_{16}$, $Au_{23}(SR)_{16}$, $Au_{24}(SR)_{16}$, $Au_{25}(SR)_{18}$, $Au_{28}(SR)_{20}$, $Au_{30}S(SR)_{18}$, $Au_{36}(SR)_{24}$, $Au_{38}(SR)_{24}$, $Au_{40}(SR)_{24}$, $Au_{52}(SR)_{32}$, $Au_{92}(SR)_{44}$, $Au_{102}(SR)_{44}$, $Au_{130}(SR)_{50}$, $Au_{133}(SR)_{52}$, are synthesized.[67] In addition, several atomically precise AuNCs also have been synthesized, with hardly any information on crystal structures. There have been continuous improvements in the synthetic protocols to prepare precise structures that can be made soluble either in organic or aqueous medium depending on the rational design of ligand functionality and structure.

15.3.3.1 Solubility of nanoclusters

One of the primary physical properties of Ag/Au NCs is solubility in a specific solvent (Table 15.1). Solubility of Ag/Au NCs depends on the behavior solvent such as its permanent dipole moment and polarizability of a solvent. The parameters such as size, shape, ligands, the charge state, and the presence of counterions on NCs, should be major factors that determines the solubility properties of Ag/Au NCs. Neutral Au NCs such as $Au_{38}(SR)_{24}$ are soluble in toluene and DCM. These structures generally exhibit a dipole moment of 1.5−4.5 D and anisotropy above 35 $Å^3$. The anionic $Au_{25}(PET)_{18}$ (PET = phenylethanethiolate) was found to have a high dipole moment due to the presence of the TOA^+ counterion. The large dipole moment explains why the NC can dissolve in the polar acetonitrile. Au_{30}(S-Adm)$_{18}$ NC with unusual solubility was observed. This cluster is nonpolar and has extremely low anisotropy, and cannot dissolve in organic solvents such as DCM, toluene, etc. Neutral $Au_{25}(PET)_{18}$ was also found to be nonpolar, however, it exhibits high anisotropy. This suggests that dipole can be induced in the NC, enabling its dissolution in common solvents such as toluene and DCM.

15.3.3.2 Aqueous-soluble nanoclusters

Thiolate groups in alkanethiols had strong affinity toward Au/Ag surfaces, so they are most commonly adopted stabilizers for metal NCs. Among these, glutathione (GSH) is shown to be an excellent stabilizer and other thiols such as tiopronin, captopril, thiolate cyclodextrin, captopril, mercaptosuccinic acid, 3-mercaptopropionic acid, and zwitterionic thiolates have also been reported to stabilize fluorescent Ag/Au NCs. In 1998–2000, Whetten et al. synthesized a class of glutathione (GSH) coated Au NCs with core sizes ranging from 4 kDa to 14 kDa and observed the core-size-dependent optical properties from these water-soluble Au clusters. The subsequent classic work by the Tsukuda group in 2004–2005 led to the electrophoretic

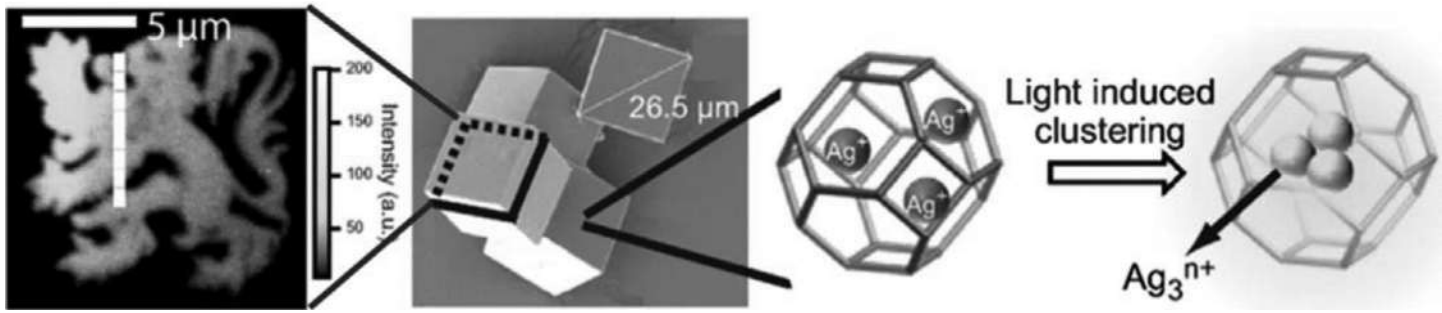

FIGURE 15.12 Photoactivated silver-exchanged zeolite enables writing of submicron scale fluorescent patterns and the schematic representation of silver clusters in zeolites. Reproduced with permission from ref.[60] Copyright 2010 John Wiley and Sons.

TABLE 15.1 Experimental stability and solubility of Au NCs. Tol, toluene; Ben, benzene; DCM, dichlorobenzene; ACN, acetonitrile; THF, tetrahydrofuran; and other commonly used solvents. Reproduced with permission from ref.[68] Copyright 2019 American Chemical Society.

Name	Solvent	Nonsolvent
$Au_{21}(S\text{-}Adm)_{15}$	Tol, DCM	MeOH, CAN
$Au_{25}(PET)_{18}$	Ben, Tol, DCM	EtOH, ACN
$[Au_{25}(PET)_{18}]^{-}$ TOA^{+}	Ben, Tol, DCM, ACN	EtOH
$AU_{28}(TBBT)_{20}$	Tol, DCM	MeOH, EtOH
$Au_{30}(S\text{-}Adm)_{18}$	Ben	Tol, Chloroform, DCM, THF, MeOH, ACN, Acetone
$Au_{30}(S\text{-}^{t}But)_{18}$	Tol, DCM, THF	MeOH, EtOH
$AU_{36}(TBBT)_{24}$	Tol, DCM	EtOH
$Au_{38}S_2(S\text{-}Adm)_{20}$	Tol, DCM	MeOH
$Au_{40}(o\text{-}MBT)_{24}$	Tol, DCM	MeOH
$Au_{52}(TBBT)_{32}$	Tol, DCM	MeOH
$Au_{133}(TBBT)_{52}$	Tol, DCM, THF	MeOH, EtOH, ACN

isolation and electrospray mass spectrometric identification of a series of water-soluble nanoclusters, including $Au_{15}(SG)_{13}$, $Au_{18}(SG)_{14}$, $Au_{22}(SG)_{16}$, $Au_{22}(SG)_{17}$, $Au_{25}(SG)_{18}$, $Au_{29}(SG)_{20}$, $Au_{33}(SG)_{22}$, and $Au_{39}(SG)_{24}$, and among these species $Au_{25}(SR)_{18}$ received the most extensive attention.[35] Ag NCs covered with L- or D-form penicillamine,[69] mercptosuccinincacid, 3-mercaptophenylboronic acid,[70] dihydrolipoic acid, captopril, etc., are known as water soluble Ag NCs. Chiral-thiol covered silver clusters exhibit strong optical activity (obtained anisotropy factor is in the order of 1×10^{-3} to 1×10^{-5}) in circular dichroism spectrum, which can be attributed to metal-based electronic transitions. Anisotropy factor gradually increases with decreasing cluster diameter, however, a steep rise was observed when the diameter was less than ~1.5 nm. The chiroptical response of Ag NCs is several-fold higher than that of Au NCs containing the same ligand. The intense optical activity is due to the dissymmetric field as well as an intrinsically chiral-core. Jin and coworkers reported the synthesis of monodisperse $Ag_7(DMSA)_4$ (DMSA is dimercaptosuccinicacid),[71] with two distinct peaks at 480 and 620 nm in its absorption profile. Dihydrolipoic acid (DHLA) water-soluble dithiol-protected Ag NCs[72] show excellent optical properties, including narrow emission profile with a large Stokes shift (more than 200 nm) and good photostability. The large Stokes shift eliminates spectral overlap between absorption and emission which reducing interference between these signals and eliminates quenching of fluorescence leads a stronger signal which are looked-for the biological imaging.

A variety of NCs such as A_7, Ag_8, and Ag_9 protected with mercaptosuccinic acid[73] are characterized by MS but their crystal structures are not available. However, it is worth mentioning that yielding the chemical composition of Ag NCs is quite challenging. This is because during the MS characterization the ionized clusters may undergo undesirable fragmentation, so the end results are not corresponding to the original clusters. Glutathione

and captopril (Capt) have shown excellent protecting capabilities for Ag NCs, with their combination NCs with well-resolved absorption features (350, 480, 500, and 650 nm)[74] and a bright red luminescencent Ag_{15} was found.

Fluorescent Ag/Au NCs with carboxyl, hydroxyl surface functional groups could be transferred from aqueous medium to organic medium by phase transfer molecules. For example, Habeeb et al.[75] developed a method to transfer glutathione protected Au_{25} clusters from aqueous to toluene phase using tetraoctylammonium bromide (TOA^+Br^-) while keeping the cluster core intact. The phase transfer is possible due to charge neutralization of hydrophilic carboxylate anion of the glutathione ligand on the Au_{25} surface by the electrostatic attraction of hydrophobic tetraoctylammonium cation in the toluene phase. In aqueous solutions, pH plays a crucial role in controlling the size of NCs. For example, Pradeep et al.[76] found the synthesis of Au_{25} and Au_8, from mercaptosuccinic acid (MSA)-protected Au NPs of 4–5 nm core diameter by etching with excess GSH. While etching at pH ~3 yield Au_{25}, while that at pH 7–8 yield Au_8. Xie et al.[77] developed a NC synthesis method using gaseous carbon monoxide (CO) as a mild reducing agent at selected pH conditions.

Water soluble AuNCs find applications as sensors for biological systems, metal ions (Fe^{3+}, Hg^{2+}, Cu^{2+}, etc…) and identifying anions (I^- and CN^-). Size dependent interactions of NCs with biological system has been very unique property of these NCs, due to these surprising biological interactions occurs for ultrasmall Au NCs. Water-soluble $Au_{25}(capt)_{18}^-$ clusters were explored to efficiently generate singlet oxygen upon photoexcitation for cytocompatibility and photodynamic activity toward cancer cells.[78] Overall, the creation of water-soluble fluorescent Au NCs with high quantum yields and tunable emission offers an opportunity to develop new generation energy materials or optoelectronic materials, and biocompatible fluorophores as biological labels.[79]

15.3.3.3 Organic-soluble nanoclusters

Typical organic soluble NCs are protected by the thiolate ligands such as, n-alkane thiol, tertiary and secondary alkane thiols, benzene, cyclohexane, adamantane, naphthalene substituted thiols. It took a long time to achieve the true monodisperse Ag/Au NCs at the atomic level. Whetten et al. (since mid-1990s) isolated a series of narrow size distributed NPs in the range of 1.0 to 3.5 nm by solvent fractionation (isolating NC mixture based on their different solubilities). Few years later the synthetic developments, the initial crystallization was reported on water soluble Au_{102} nanocluster. However, later on major progress and structural determination have been seen in case of organic soluble Ag/Au NCs.

Initial efforts to stabilize well-defined silver clusters were developed by Murray and coworkers, whereby they synthesized $Ag_{140}SSB_{53}$ (BBS = thiolate of 4-tert-butylbenzyl mercaptan (BBSH)).[80] Negishi et al. also attempted to synthesize the BBS protected-Ag clusters. In this report, small silver clusters of average size ~1.2 nm were synthesized.[81] Ag_{44} silver cluster with high molar extinction coefficients were reported by Bakr et al.[82] with emission spectrum in the IR region centered around 1375 nm. Ag_{44} NCs tend to be magic clusters because of their closed electronic shell ($44e^- - 30e^- + 4e^- = 18\,e^-$). Synthesis, crystal structures and properties of various NCs (Ag_{14}, Ag_{25}, Ag_{29}, Ag_{48}, Ag_{62}, etc.) are discussed in relevant chapters.

15.3.4 Polymer protected nanoclusters

Polymers with abundant carboxylic acid groups are identified as promising templates for the synthesis of Ag NCs due to the strong affinity between silver surfaces and the carboxylic acid groups. The most notable literature on polymer encapsulated NCs is related to water soluble Ag NCs because of easier preparation methods of Ag NCs comparing with Au NCs. In addition, Ag NCs formation could be benefacted by the photoreduction activity of silver ions, that means UV-light illumination is sufficient to activate the reduction silver ions. This process does not require any additional reducing agents. This photoreduction activity of silver had also used to produce highly fluorescent Ag NCs encapsulated in dendrimers, biological scaffolds. The resulting emissive NCs exhibit good photostability, excitation-dependent emission and a stimuli-responsive properties.

Initially, Prof. Henglein had succeeded in stabilizing intermediate clusters, wherein the synthesis involves the radiolytic reduction of Ag^+ ions in the presence of sodium polyphosphate. Later, sodium polyphosphate was replaced by sodium polyacrylate to improve the stability of NCs. The polymer radicals are produced upon the illumination of suitable light. These radicals reduces the Ag^+ to Ag^0. The formed atomic Ag, rapidly reacts with Ag^+ to produce a diatomic cluster, $Ag_2{}^+$, which then grows into a stable polyatomic cluster. The clusters are attached to the polymer chains through the interaction with their functional groups. The coulombic repulsion between chains prevent clusters from coming closer. This reaction process could be stopped upon the removal of light supply, thus this process allows to investigate the chemical and physical properties of intermediate clusters. Few widely used polymer templates for the fluorescent Ag NCs preparation are polyelectrolyte, poly (methacrylic acid) (PMAA) as a template, hyperbranched polyethylenimine (PEI), copolymers of 2-(methacrylamido) glucopyranose (MAG), methacrylic acid (MAA), microgels (poly N-isopropylamide-acrylic acid-2 hydroxyethyl acrylate, (poly NIPAM-AA-HEA)), hydrogels (composed of multiarm star polyglycerol-block-poly(acrylic acid) copolymers), with modular ligands made of lipoic acid (LA), a functional group (–OCH_3) and a polyethylene glycol (PEG) segment.[83]

Luminescent PMAA-Ag NCs have also been synthesized via convenient sonochemical,[84] and microwave-assisted approaches,[85] and poly(N-vinylpyrrolidone) (PVP) protected Au NCs by electrochemical method.[86] Qu et al. reported an interesting finding in the synthesis of (hyperbranched polyethylenimine) PEI-templated Ag NCs.[87]

In the presence of PEI, Ag NPs were first formed, followed by transformation from NPs to NCs as time passed. The average diameter changed from 5.3 nm to 3.9 nm and finally to 1.0–2.0 nm during the course of 168 h of reaction, which was ascribed to the role of PEI. Ras et al. reported PMAA-Ag NCs prepared by the photoactivation under visible light. These NCs exhibited novel electrochemiluminescent and solvatochromic properties.[88] PMAA-AgNCs as well as other clusters had been used for sensing applications. For example, deficiency of Cys will lead to hematopoiesis decrease, leukocyte loss and psoriasis. Hcy is a risk factor for cardiovascular diseases and Alzheimer's disease. A simple fluorescence method for both Cys and Hcy selective detection of α-amino acids has been developed based on PMAA-Ag NCs. Regarding Au NCs, an electrochemical method is developed which is based on the anodic dissolution of a gold electrode in the presence of PVP and subsequent electroreduction of the Au-PVP complexes to PVP-Au NCs. Zhu's group fabricated a new hyperstar−$Au_{25}(SR)_{18}$

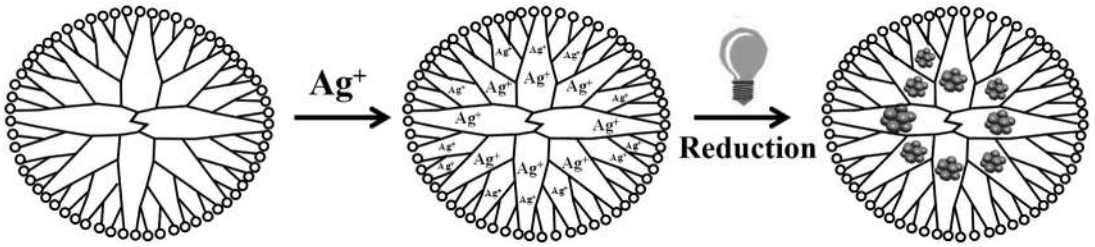

FIGURE 15.13 Schematic representation of Ag NCs formation in dendrimer cavities.

nanocomposite by ligand exchange between thiolates of $Au_{25}(SR)_{18}$ NCs and disulfide groups of hyperstar polymers.[89]

Dendrimer templates, a unique category of branched polymers with well-defined molecular weights, employed to encapsulate ultrasmall Au NCs. In the dendrimer-based synthesis, metal ions (e.g., Cu^{2+}, Pd^{2+}, and Pt^{2+}) first penetrate into the interior of dendrimer, and then the resulting nanocomposite is reduced to yield a dendrimer-encapsulated, zerovalent NCs (Fig. 15.13). This process is normally driven by strong association of metal ions with intradendrimer groups. Poly (amidoamine) (PAMAM) and poly (propyleneimine) (PPI) have been frequently utilized as macromolecule templates to produce NCs based on the capability to sequester metal ions from aqueous or methanol solutions. Zheng et al. reported a stable aqueous dispersion of fluorescent Ag NCs with an OH-terminated dendrimer as scaffold in 2002.[90] Later, they further applied PAMAM dendrimers to synthesize Au NCs and the dendrimer-stabilized Au_8 NCs.[91] Possible applications of such NCs are as sensors for biomolecules. Triulzi et al. developed immunoassay based identification of human IgG antigen by Au QD–PAMAM-antihuman IgG complexes.[92]

15.3.5 Biological scaffold templated nanoclusters

Irrespective of the diverse absorption and emission properties of thiolate protected Ag/Au NCs, these materials exhibit only weak emission. Thiolates connect to the gold surface with stronger covalent bonds, however, for higher emission intensity weakly coordinating ligands are preferred. Nevertheless, it is known that the weaker ligands are incapable of effective synthesis of pure and monodisperse clusters. Encapsulation by amine-based dendrimers has produced NCs that are extremely bright and photostable. Yet, they cause agglomeration at higher concentrations or required introduction of buffer, thereby quenching the emission. Therefore, it is essential to balance the ligand–core interactions versus brighter emissions. In this scenario, the electron-rich binding of biomolecules such as peptide, oligonucleotide and protein scaffolds are used to fabricate stable bright emissive Ag/Au NCs.

Typically, some biomolecules have high affinities for noble metal ions. Silver and gold ions have different affinities toward biomolecules. For example, the photoactivation of gold and silver ions incubated with NIH-3T3 cellular matrices showed that silver and gold NCs were generated at different cellular organelles.[93] Silver ions were reported to bind biological molecules through functional groups such as thiols, carboxylates and amines. However, the

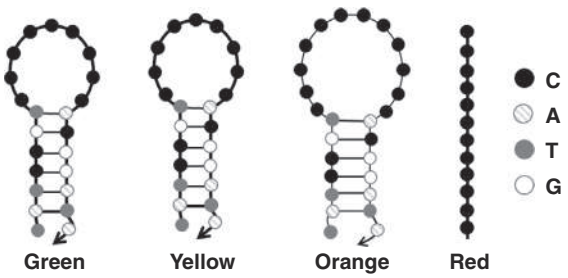

FIGURE 15.14 Nucleobases present in single stranded DNA (or RNA) templates and its variants in terms of type (A, T, G, or C). Redrawn and reproduced with permission from ref.[96] Copyright 2020 American Chemical Society.

binding of gold ions to biological molecules was studied only to limited extend. A few investigations indicate that gold ions have high affinity for albumin and red blood cells.[94] The binding sites for gold ions are expected to be sulfur or nitrogen, depending on the oxidation state of gold.

15.3.5.1 DNA scaffold

DNA oligonucleotides act as good stabilizers for Ag NCs because of the high affinity of Ag^+ toward cytosine bases of single-stranded DNA. Raman and recent NMR studies demonstrated that the nitrogen in nucleobases could coordinate to metal ions. Initially, Dickson and coworkers prepared the Ag(I) ions in oligonucleotide complex with the help of cytosine-rich sequences, followed by chemical reduction process (usually, sodium borohydride) creates Ag NCs in DNA scaffolded.[95] In a biochemical reaction, the end product is highly dependent on the sequence of the DNA. In the same way, the type of DNA scaffolded-Ag NCs and their optical properties are encoded in the original oligonucleotide sequence. Nucleobases (A, T, G, or C) present in single stranded DNA (or RNA) templates and their variants includes, sequences, lengths, and structures or environmental factors (such as buffer, pH, metal ions, macromolecular polymers, and small molecules) offers bright, tunable DNA-encapsulated Ag_n NCs ($n = 5$–11) with emission ranging from visible-to-near-IR (Fig. 15.14). It is important to note that double-stranded DNAs (or RNAs) are not suitable for Ag NCs formation where free nucleobases are not available to protect NC.

Apart from single oligonucleotide, mismatched double-stranded DNA (dsDNA), loop-dependent synthesis of fluorescent Ag NCs on DNA hairpins with 3–12 cytosines in the loop was also reported.[97] Somoza et al. developed novel oligonucleotides substituted in a benzene ring for preparing a highly fluorescent Ag NCs. The emission exhibited by these derivatives is 60 times higher than that obtained with a single strand.[98]

Unlike Ag NCs, DNA encapsulated Au NCs have limited reports. This possibly owing to the weak association between the negatively charged DNA and the commonly used precursor, $AuCl_4^-$. Chen et al. introduced an etching approach to prepare atomically monodisperse Au_8 NCs from Au NPs with the assistance of biomolecules including amino acids, proteins, and DNA under sonication.[99] The mechanism for this reaction was proposed to be a nitrogen-atom-activated surface reaction, indicating the dual function of amines as both stabilizing adsorbates and efficient etching agents.

DNA-Ag NCs have been reported for detecting different targets (e.g., nucleic acids, small molecules, proteins, metal ions, germ, and cells) and cell imaging. To summarize the current

research, analyzing the target via the fluorescent "on–off" mechanism can be achieved in the following four ways:

1. using the fluorescence of the Ag NCs directly,
2. using strand hybridization (structural transformation or G-rich proximity) to increase or decrease the fluorescence,
3. using electron transfer to realize a change in the fluorescence signal,
4. quenching the fluorescence using a reactive quencher.

These methods fully demonstrate the significant potential of Ag NCs as fluorescent signals in analytical detection.

15.3.5.2 Nanoclusters in peptides and proteins

By sunlight irradiation of silver ions embedded in short peptide-based hydrogel, Ag NCs are made inside hydrogels.[100] Peptides often possess diverse in their binding sequences. Thus, the preparation of peptide encapsulated Ag NCs requires tedious trial-and-error optimization of reaction conditions to find a higher quantum yield conditions. Moreover, peptides are moderately stable at room temperature (chemical lifetime of 3 days). The peptides with short length likely to oxidize NCs through oxygen and chloride ions in aqueous solution. Typically, peptides are distinguished from proteins by their shorter length. Narayanan and Pal reported a synthesis of luminescent Ag QCs in α-chymotrypsin and studied the cluster protein interaction using time resolved fluorescence and reported that the conformation and activity of the enzyme is affected considerably by reaction conditions.[101] The synthesis involves the usage of reducing agent ($NaBH_4$), it could have modified the conformation and the activity of the protein. Few reports are available on specific cluster-core-containing proteins such as Ag_{15}@BSA[102] and Ag_8@BSA,[103] where BSA is bovine serum albumin. Ag_{15}@BSA, in combination with mesoporous gold nanostars, could be used in the visible detection of TNT, down to zeptomolar concentrations.[104] Attachment of a protein to a Ag NCs could substantially influence the biological response. For example, Ag NCs:DHLA (DHLA:α-6,8-dithiooctanoic acid) with human serum albumin had excellent uptake by HeLa cells. In fluorescence microscopy, intense fluorescence emission from protein connected Ag NCs:DHLA was observed from inside the cells, in contrast to the pronounced uptake of Ag NCs:DHLA.[105]

Compared with Ag NCs, protein-stabilized Au NCs are more common. A "pioneering green" synthetic approach was developed by Ying's group in 2009[106] for the preparation of Au NCs with red emission. Notably, the reason of BSA being an excellent scaffold for fluorescent Au NCs might result from the combination of Au–S bonding with the protein (via the 35 Cys residues in BSA), and the steric protection due to the bulkiness of the protein. As a matter of fact, the process is similar to the biomineralization behavior of organisms in nature.

Inspired by this finding, researchers tried to explore other proteins as efficient bioscaffolds for preparing Au NCs such as chicken egg-white, trypsin, and lysozyme. Besides their known roles as reductants and capping agents, proteins can also function as etching agents for the synthesis of Au NCs. BSA can be the scaffold for not only Au NCs formation, but also in the synthesis of fluorescent Ag and Cu NCs. Arakawa et al. reported for the first time a pH dependent synthesis of Au NCs with blue (Au_5 and Au_8), green (Au_{13}), and red (Au_{25}) fluorescent emission using porcine pepsin.[107] In Zhang's research, horseradish peroxidase (HRP) was used as a model functional template to direct the synthesis of fluorescent Au

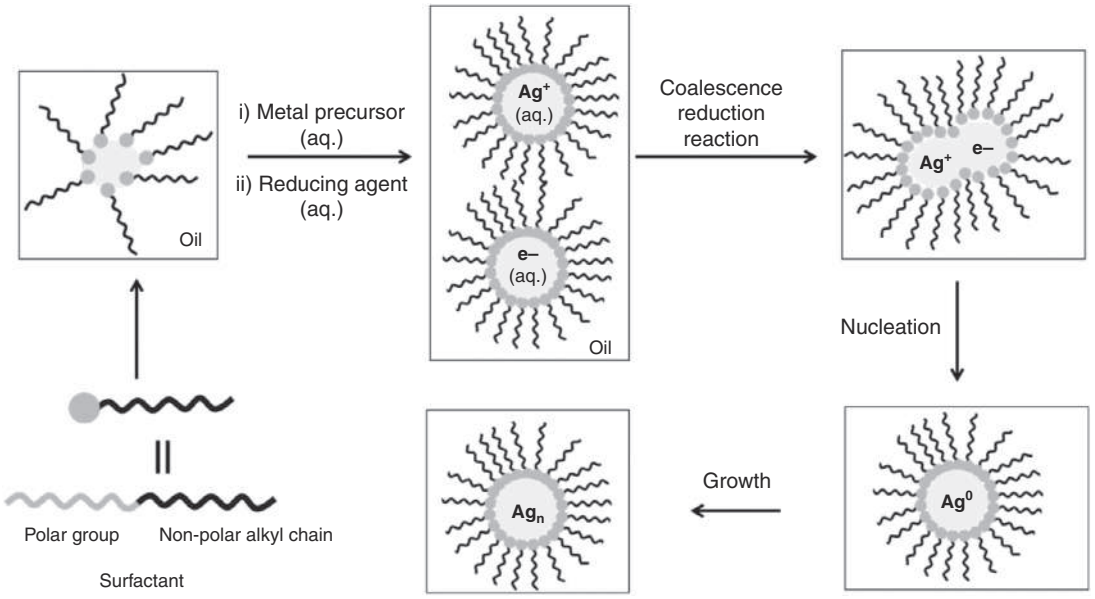

FIGURE 15.15 Silver clusters in microemulsions.

NCs:HRP bioconjugates. Experimental data indicated that the obtained bioconjugates remain both fluorescence of Au NCs and catalytic activity of HRP enzyme.[108] Biological scaffold templated NC has similarly been anticipated for various applications detecting the molecules, nanomedicine, and bioimaging. For more details, readers can refer to the chapter dedicated to biological application of NCs.

15.3.6 Nanoclusters in emulsions

Nanoclusters that fulfill the conditions of bare surfaces with excellent solubility in solutions offer promising applications in catalysis. Such unique possibilities have been provided using microemulsions. These are isotropic, transparent, and thermodynamically stable liquid dispersions of water and oil. They contain a special liquid core-shell structure due to either water dispersed in oil or oil dispersed in water. Especially in reverse microemulsions nanosized water droplets spontaneously formed within the micelles act as "nanoreactors," within which chemical reactions can be performed leading to the formation of NCs (Fig. 15.15). Random collisions between droplets allow exchange of contents via rapid fusion/fission transient processes, but the size of the exchanged species can be drastically reduced using appropriate rigid surfactant films. In this way the formation of relatively monodisperse nanoparticles can be achieved.

Lopez-Quintela and coworkers reported the synthesis of Ag_n clusters ($n \leq 10$) in microemulsions using the kinetic control method.[109] Scanning tunneling microscope shows that the clusters organize into one atom-high nanoislands when they are deposited over a substrate. Certain surfactants, such as anionic surfactant-sodium bis(2-ethylhexyl) sulfosuccinate,

dissolved in hydrocarbons, can form reverse micelles having nanometer-sized water cores (droplets) stabilized by surfactant molecules. As this arrangement allows a variety of polar and ionic species to be dissolved into the water core. These clusters exhibit novel properties, such as wide bandgaps (ca. 2.3 eV), fluorescence and paramagnetic molecular-like behavior that could lead promising applications in the area of catalysis.

15.3.7 Nanoclusters with hydrides and sulfides

Hydrides are considered as electron withdrawing ligands (similar to thiols), and therefore, the numbers of free electrons for the three NCs, ($[Ag_{18}H_{16}(TPP)_{10}]^{2+}$, $[Ag_{25}H_{22}(DPPE)_8]^{3+}$, and $[Ag_{26}H_{22}(TFPP)_{13}]^{2+}$), are 0 (18 − 16 − 2), 0 (25 − 22 − 3), and 2 (26 − 22 − 2), respectively; since the phosphines were not involved in the free electron count.[110] The phosphines used here are triphenylphosphine (TPP), 1,2-bis(diphenylphosphino)ethane [DPPE], and tris(4-fluorophenyl)phosphine [TFPP]. The $[Ag_{26}H_{22}(TFPP)_{13}]^{2+}$ NC completes the electron-shell closing rule which explains its higher stability, whereas for the first two cases stability comes from the geometry. Discovery of such hydride-rich metal clusters shows that smaller ligands can also act as protecting ligands, and many clusters can be revisited to see the existence of hydride in the clusters, as in most of the cases $NaBH_4$ was used as the reducing agent.

Monolayer protected silver sulfide NCs (similar to the quantum dots) are another class of material, also treated as silver chalcogenide clusters, which have properties similar to those of the noble metal NCs (detailed discussion within chapter 18). Li et al. deciphered the single crystal structure of an atomically precise silver sulfide NCs, $[Ag_{62}S_{13}(SBut)_{32}](BF_4)_4$,[111] which also exhibited luminescence. The thiol acts not only as a protecting agent but also as a source of S_2^- by the cleavage of the −C−S bond. The cluster displayed unique UV/visible features (bands in the UV regions and a low energy band at 543 nm) along with a sharp emission at 621 nm (when excited at 497 and 591 nm). The single crystal data suggested that the cluster possessed a core/shell geometry. The thiolates can coordinate to three surface silver atoms or to one subsurface and two surface silver atoms. In another work, Li et al. have reported a nest-like structure for the $[Ag_{33}S_3(SR)_{16}(RCOO)_9(NO_3)(RCN)_2](NO_3)$ cluster.[112] Few examples of silver sulfide clusters are $Ag_{56}S_{12}(SR)_{20}$],[113] $[Ag_{70}S_{20}(SPh)_{28}(dppm)_{10}]^-(CF_3CO_2)_2$, $[Ag_{123}S_{35}(SBut)_{50}]$, $[Ag_{262}S_{100}(SBut)_{62}(dppp)_6]$,[114] $[Ag_{344}S_{124}(SBut)_{96}]$,[115] etc. Recently Manju et al. reported a highly luminescent $Ag_{56}Se_{13}S_{15}$ cluster which shows Hg^{2+} detection at 1 ppb concentration.[116]

The observation of a BCC structure in $Au_{38}S_2(S\text{-}Adm)_{20}$ is surprising because no other thiolate-protected gold NCs (or larger NPs) has ever shown such a packing structure.[27] The formation of this novel structure can be explained due to the bulky carbon tail of S-Adm and/or sulfido atoms. The sulfido group is considered to stabilize the core as confirmed by DFT calculations.

15.4 Stability of atomically precise thiolate-protected Ag/Au NCs

The stability of NCs is lower than that of both, thiolated Au-complexes and NPs. Typically, most of the NCs are sensitive to the ambient conditions such as temperature, metal ions, solvents, pH, ligands, and external surroundings. Few NCs, such as Au_{25}, Au_{38}, Au_{144} etc., are

robust and can be preserved for several months in both solid and solution states. The number of surface exposed Ag/Au atoms increases markedly during the course of size reduction below 1.5 nm. Thus, the role of the of Au core-thiolate staple motifs (typically RS–Au–SR and RS–Au–S–Au–SR) too dominates to stabilize the cluster core. Indeed, the experimental and theoretical studies on these clusters reveal that the thiolate staple motif exerts direct influence on geometric and electronic structures. The influences include charge transfer at the Au–S interface and deformation of the core structures, thus influencing the stability. The factors influence the stability of a NCs will be discussed in next few sections.

15.4.1 Decomposition pathways: fission or fusion

The process of transformation of NCs to thiolate complexes or to their aggregates is called decomposition. In a metastable cluster, a subtle change in the surrounding medium or aerial oxidation causes "decomposition." Decomposition can occur via fission/etching (breaking into smaller component pieces) or fusion (agglomerative growth of particles). Fission is an established pathway occurs through the release of protected staple motifs that results in the formation of Au-thiolates complexes and complete or partial disruption of the NC geometry. Etching represents a type of fission that is widely used in the synthesis of metal nanostructures and is highly dependent on the presence of oxygen.[117] The concept of decomposition is not merely bad. It is advantageous for the size focusing of polydisperse NC mixture to monodisperse NCs. Such reactions are very common in ligand-exchange-induced transformation of making particular $Au_n(SR)_m$ NCs. A few examples include the transformations of $Au_{25}(SR)_{18}$ to $Au_{28}(SR)_{20}$,[118] $Au_{38}(SR)_{24}$ to $Au_{36}(SR)_{24}$,[25] and $Au_{144}(SR)_{60}$ to $Au_{133}(SR)_{52}$.[119]

15.4.2 Comparison of stability of Ag/Au NCs

Even though Ag and Au belong to the same group in the periodic table, they show distinctly different properties in many cases. Ag in zerovalent state is less stable and is reactive toward aerial oxidation, in comparison to Au. So, it is difficult to stabilize the clusters as well as difficult to obtain pure diffractable Ag single crystals to explore their properties. Stabilization of Ag NCs require proper scaffold design to minimize their aggregation or etching pathways. A few reports are known for mixed ligand (phosphine and thiol) and complete thiol protected Ag NCs. For example, $Ag_{14}(SR)_{12}(PPh_3)_8$, Ag_{16}, and Ag_{32} clusters $Ag_{29}(BDT)_{12}(TPP)_4$ [BDT, benzenedithiol], and $Ag_7(DMSA)_4$ (DMSA = dimercaptosuccinic acid). In addition to them fully thiolated Ag_{32}, Ag_{44}, and Ag_{152} are also prepared.[67]

15.4.3 Effect of e-beam

It is important to note that TEM, a major characterization technique for a typical nanomaterial fails to resolve the atomic packing of the NCs. High voltage electron beam interacts with the NCs and induces permanent damage (Fig. 15.16). General process is coalescence of neighboring NCs followed by the formation of aggregates.[120] Thus, critical characterization techniques for obtaining a single crystal structure of protected noble metal NCs are very difficult primarily because of stability and sensitivity issues. It is worth noting that the advanced electron microscopy techniques are employed to view the NCs at atomic resolution. For example, Azubel et al.[121] have determined the structure of Au_{68}, with atomic resolution

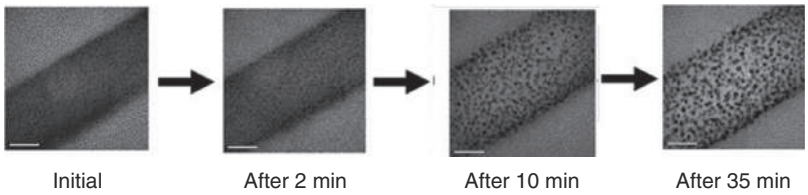

FIGURE 15.16 Formation of gold nanoparticles due to the exposure of the Au_{25}NCs anchored on a dipeptide tube to the electron beam. The scale bars correspond to 20 nm. Reproduced with permission from ref.[120] Copyright 2009 Royal Society of Chemistry.

by a new approach employing aberration-corrected transmission electron microscopy with minimal electron dose and electron density mapping.

15.4.4 Solvent polarity

Solvent nature is a deciding factor in stabilizing a particular NCs. This solvent polarity had direct influence on designing a synthetic method to make a selected cluster. For example, in a given synthetic process the reaction in toluene yields a mixed-size clusters along with the desired $Au_{25}SR_{18}$. The reason for the higher polydispersity in this case is due to the long-term stability of different size-mixed clusters in toluene. However, when the same reaction performed in THF also produces mixture of NCs, initially, such as Au_{25}, Au_{38}, Au_{44}, Au_{68}, and Au_{102}, but those NCs eventually transforms to single Au_{25} NCs over time. Majority of the NCs in THF undergoes decomposition/etching process followed by the transformation to pure Au_{25} clusters. This whole cluster transformation process was understood by a systematic mass spectral investigation.

In order to realize the decomposition pathway of NCs under the influence of solvent polarity, Ackerson et al. performed a systematic study on $Au_{25}SR_{18}$ NCs dissolved in solution. These results reveals that the nature of solvent plays a significant role on NC lifetimes.[122] Fig. 15.17 shows the effect of solvent on the life time of $[Au_{25}PET_{18}]^0$ NCs dissolved in organic solvents. NCs in toluene exhibit excellent stability compared to other selected solvents, it proofs the influence of solvent polarity index on cluster lifetimes. From the Fig. 15.17, it is also observed that higher polarity of a solvent promotes faster decomposition and it follows a trend in relation to the polarity index. Note that the polarity index provides the degree of interaction with a test solute, from Burdick & Jackson solvents.

As discussed earlier, the decomposition of a suspended NCs could be either of two process (i) fusion of two NCs to a larger component or (ii) fission of a single NCs into smaller components. This decomposition process could be understood by time-dependent absorption studies of the $Au_{25}(SR)_{18}$ in a selected solvent in air. A careful study of disappearance of characteristic peaks of Au_{25} or emerging new peaks can provide the kinetics of a NC reaction. These processes have distinct kinetics, the fission pathways following zeroth order kinetics and fusion pathways following first order kinetics. Lower polarity solvents favor zeroth order decay (fission) pathways and higher polarity solvents favor first order decay (fusion). This suggests that the higher polarity solvents may be driving aggregation of particles capped by nonpolar ligands.

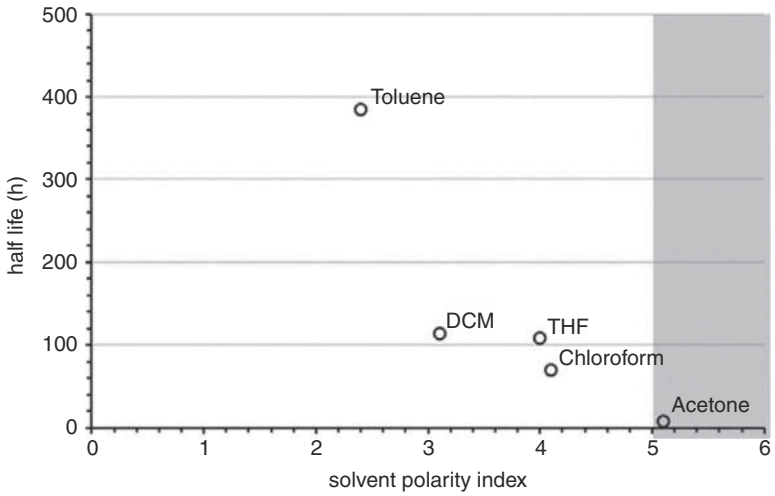

FIGURE 15.17 $Au_{25}(PET)_{18}^{0}$ half-lives in toluene, DCM, THF, chloroform, and acetone in air. The black overlay represents regions of polarity solvent polarity where fusion mechanisms are (increasingly) observed. Reproduced with permission from ref.[122] Copyright 2011 Royal Society of Chemistry.

In case of water soluble NCs, the instability occurs through agglomerative growth pathways. This process is well-established for water-soluble NPs. Theoretically, colloidal stability is attributed to a combination of van der Waals attraction, electrostatic double layer repulsion, and steric terms, described classically in DLVO theory.[123] For water soluble NCs, manipulation of ligand shell charge had appear to improve NC stability which will be discussed in the following sections.[124]

It is worth noting that $Au_{30}(Adm)_{18}$ shows[26] peculiar, and different solubility in organic solvents compared to other NCs; it is highly soluble in benzene, slightly soluble in toluene and chloroform, but insoluble in dichloromethane—which is widely used solvent for thiolate-protected NCs including other-Adm protected Au NCs. Our understanding about the relationship between solubility of NCs and cluster morphology, the role of the ligands (incredibly bulky thiolates) remains unclear.

15.4.5 Surface effects

NCs are also sensitive to the external nanosurfaces. For example, in an experiment, chemically synthesized reduced graphene oxide in water was mixed with $Au_{25}SR_{18}$ in THF. Within few minutes a completely new, larger NC, was formed at the liquid–liquid interface.[125] The presence of larger NCs was analyzed by TEM as was as mass spectrometry. The energy gain due to the reduction of the graphene oxide surface curvature might have been the driving force to trap the smaller Au_{25} NCs, leading to their coalescence.

15.4.6 Electronic stability

The stability in electronic terms has been explained by the superatom model which is based on the "jellium" model of electrons confined within a spherically symmetric potential well of

the metal core. If the number of free electrons falls in the "magic" number series of 2, 8, 18, 20, 34, 58, …, the cluster shows high stability. Greater details are provided in Chapter 2. For example, thiolate protected $Ag_{152}(SR)_{60}$, $Ag_{44}(SR)_{30}$ $Ag_{25}(SR)_{18}$ are stable. The high stability of these NCs is due to its closed shell configuration. The stability of $Ag_{152}(SR)_{60}$ system can be attributed to the presence of the magic number of electrons (152−60 = 92) that results in a closed shell electronic structure. The relative importance of geometric and electronic stabilization of discrete-sized, thiolate-stabilized Au NCs in general has yet to be fully clarified. For example, $Au_{25}(SR)_{18}{}^{0}$ and $Au_{38}(SR)_{24}$ are stable, though they are of non-magic-number NCs. Their stability could be explained by geometric stability.

15.4.7 Geometric stability

Geometric stability of naked clusters is explained by the theory of "full-shell clusters." The smallest full-shell cluster atomic number is 13 (first magic number). It can be viewed as a central metal atom which is surrounded by 12 other atoms of the same size in a cubic or hexagonal close packed manner. Forty-two atoms form a second full shell around the first 12 atoms, yielding the second full-shell cluster 55 (second magic number). The total number of atoms for one-shell cluster is 1 + 12 = 13 and 13 + 42 = 55 for two shell cluster, etc. The number of atoms per shell equals to $10n^2 + 2$, where n is shell number. This way, the stability of Au_{13} and Au_{55} can be explained. This theory is well explained the geometric stability of gas phase clusters but have limitations to provide the reasons for the stability of thiolated-NCs.

In general, Ag/Au NCs adopt different crystalline phases FCC, HCP, and BCC irrespective of similarity in their sizes; for example, $Au_{36}(SR)_{24}$, $Au_{30}(SR)_{18}$, and $Au_{38}S_2(SR)_{20}$ crystallize in FCC, HCP, and BCC, respectively. Smaller as well as larger NCs are available with FCC structures such as Au_{40} and Au_{52}, but now larger clusters are found in HCP or BCC.[126] In case of FCC-type AuNCs, a set of magic series had found recently. The series include $Au_{28}(SR)_{20}$, $Au_{36}(SR)_{24}$, $Au_{44}(SR)_{28}$, and $Au_{52}(SR)_{32}$. They are well separated by spacing of $Au_8(SR)_4$ and one-direction layer by layer growth in their structure. The HOMO–LUMO energy gap (E_g) followed an inverse square law between E_g and the size trend in the magic series. The existence of HCP and BCC magic series and the separation $Au_m(SR)_n$ units are still remains to be addressed. Further studies are required on systematic control over crystalline phases of NCs, that could explain the geometric stability in greater detail. Additional contribution to the geometric stability of NCs comes from thiolate ligands. For example, in the size-focusing synthesis using methanol as the reaction solvent, using cyclohexanethiol (HS-c-C_6H_{11}) gives rise to FCC $[Au_{23}(S\text{-}c\text{-}C_6H_{11})_{16}]^-$,[127] whereas adamantanethiol (S-Adm) leads to HCP Au_{30}(S-Adm)$_{18}$.[26,128] The next section focuses on the role of ligands on the geometric stability of NCs.

15.4.8 Steric stability

The ligands had strong influence even from the early stages (nucleation and growth) of synthetic process. Subsequently, they had impact on electronic, geometric, solubility properties of NCs. The first strategy to enhance the firmness of NCs is to select ligands that have stronger interaction with Ag/Au. For example, Kurashige et al.[128] applied selenolates as protecting ligands for Au_{25} NCs, resulting in better stability in solution than of Au_{25} NCs protected by

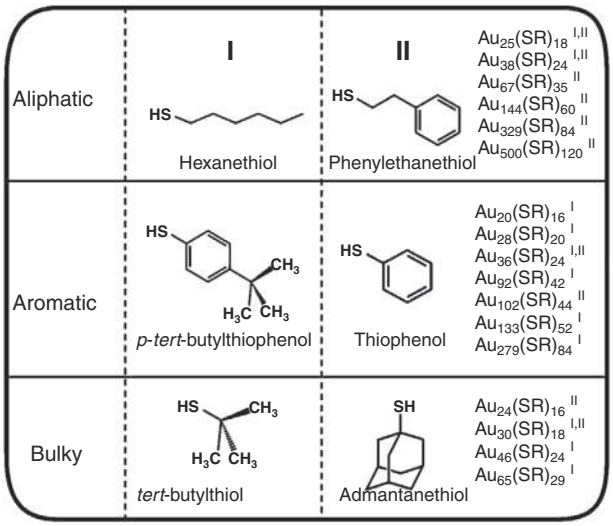

FIGURE 15.18 Influence of ligand on the final composition of nanocluster. Reproduced with from ref.[132]

thiolates. In another synthetic procedure for the preparation of $Au_{144}(SR)_{60}$, by replacing PET with cyclohexanethiol leads to the formation of another NCs, $Au_{64}(S\text{-}c\text{-}C_6H_{11})_{32}$.[129] Effect of ligand on the final composition of NCs is listed in Fig. 15.18.

The compactness of the ligand shell on NC is usually dictated by several factors.

15.4.8.1 Hydrophobic interactions on NCs

In case of regular ligands generally three types of ligand effects have been recognized.

(a) The bulky carbon site from the sulfur head: The α-carbon bulkiness has a straightforward effect since the α-position is the closest to the anchoring sulfur atom on gold. By changing primary thiol ($-S-CH_2$) to a secondary ($-S-CH$) and tertiary thiols ($-S-C$), different sizes and structures can be obtained.[126,130,131] For example, with primary 2-PET or alkanethiolates, Au_{20}, Au_{24}, Au_{25}, Au_{38}, Au_{40}, Au_{55}, Au_{67}, Au_{130}, Au_{137}, and Au_{144} have been synthesized; with secondary cyclohexanethiolate, Au_{18}, Au_{23}, Au_{28}, and Au_{64} were prepared, and with tertiary tert-butylthiolate or adamantanethiolate, Au_{24}, Au_{30}, and Au_{38} were obtained. This effect bears some similarity with the well-known concept of "cone angle" invoked in early research on phosphine-protected metal clusters, but has taken entire ligand into consideration rather than a specific site of the ligand.

(b) The positions (ortho, meta, and para) of functional groups ($-CH_3$, $-COOH$, etc.): Fig. 15.19 presents the classification of ligands based on substituent group next to the thiolates. Surprisingly, adjusting the position of the methyl group from para- to meta- to ortho-, the nanocluster size changes from Au_{130} to Au_{104} to Au_{40}, respectively.[54] This effect indicates that the Au NCs structure is quite sensitive to a subtle change in rigidity in the thiolate ligands. PET has a methylene group next to thiol group which cause the formation of $Au_{38}PET_{24}$ whereas a new BCC $Au_{36}(SR)_{24}$ formed by cyclopentanethiolate have bulkier groups at the α-position.[133] The new structure $Au_{36}(TBBT)_{24}$ (tert-butyl

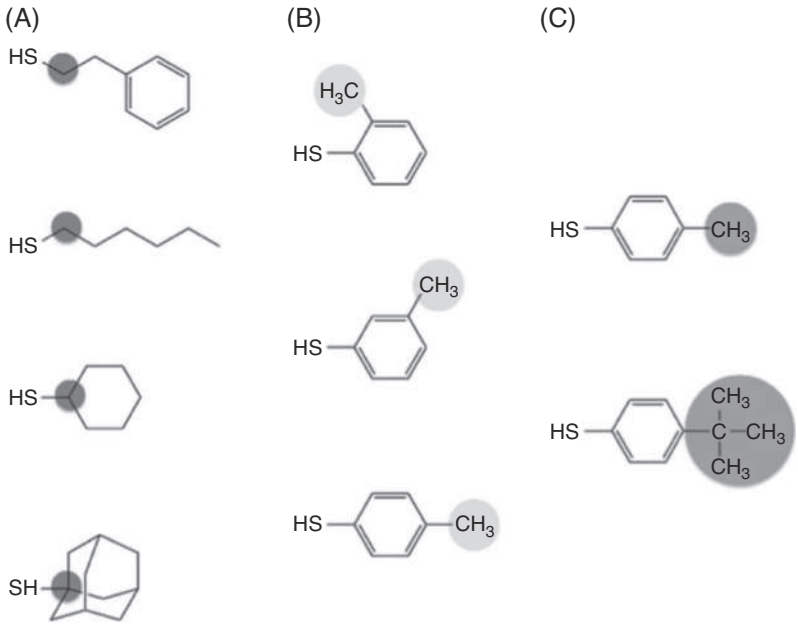

FIGURE 15.19 Classification of ligands based on substituent group next to the thiolates. Reproduced with permission from ref.[130] Copyright 2015 American Chemical Society.

benzenethiol = TBBT) can also be prepared with another thiol having bulkier group in α-position. This shows the carbon tail structure at the α-position of the thiolate could play an important role in the size and structural transformation.

(c) Size of the substituent group at the para-position of benzenethiol: The para-position is distant from the Au–S interface of a NC; therefore, one can expect no major effect from pare substitutes on the NC composition during a synthesis. However, interestingly, when the para group is methyl (i.e., p-methylbenzenethiol, abbreviated as p-MBT), $Au_{130}(p\text{-}MBT)_{50}$ was obtained as the product.[134] In contrast, if the para group is tert-butyl, $Au_{133}(TBBT)_{52}$ was obtained.[135] By comparing the atomic structures of Au_{130} and Au_{133}, the curvature of the NC seems correlated to the bulkiness of the para group on benzenethiol, that is, the p-TBBT prefers to assemble on the highly curved spherical structure, while the p-MBT selected the less curved, barrel shaped core structure.[134] It is worth noting that the TBBT ligand has been utilized to create a novel series of $Au_n(SR)_m$ NCs, including Au_{20}, Au_{28}, Au_{36}, Au_{44}, Au_{52}, and also Au_{133}.

15.4.8.2 Electrostatic interaction between functional groups of neighboring ligands

Even the most widely studied metal NC, that is, $Au_{25}(SR)_{18}$, exhibits relatively poor stability in realistic biological media due to the presence of differently charged species (OH^-, H^+, metal ions, complexes, etc.). In aqueous media, stable metal NCs can be obtained by selecting ligands with longer carbon chains and stronger hydrophobic interactions within the ligand shell.[124] In the case of short-chain, NCs exhibit poor stability, for example, $Au_{25}(MPA)_{18}$

(MPA = mercaptopropionic acid). However, the van der Waals forces of attraction between the neighboring hydrocarbon chain favors the protection of the Au core, but the electrostatic repulsion between the deprotonated carboxyl groups (i.e., $–COO^–$; pKa value is 4.3 for carboxyl group) of MPA ligands weakens the protection of the ligand shell for the Au core. Moreover, the short molecular length of MPA implies a thin protection shell (i.e., short penetration path for foreign species), which could enable the penetration of subversive species (e.g., free ligands such as MPA, ions such as $Cl^–$, and dissolved oxygen) into the shell of the MPA ligand, subsequently decomposing the Au NCs. Compared with C_3 chain thiol, C_6 chain are relatively longer and thus has a stronger hydrophobic interaction between neighboring ligands, which could minimize the negative effect of the electrostatic repulsion of carboxyl groups of C_6 chains, forming a strengthened protection shell for the Au cores. Another advantage of the long-chain ligands is they have considerable swing flexibility in an aqueous solution, which could partially diminish the possibility of the diffusion of subversive species into the ligand shell.

Another approach to improve the stability is to use two types of thiolate ligands with similar chain length but opposite charges (e.g., $–COO^–$ and $–NH_3^+$) to form a pseudocage-like ligand shell on the NC surface via electrostatic attraction. For example, MHA containing one carboxyl group (e.g., –COOH) and cystine containing one amine group (e.g., $–NH_2$, pKa value is 10.75 for amine) can be used as protecting ligands, which could coordinate together via inter-ligand electrostatic interaction (i.e., $–COO^–\cdots NH_3^+$ bond).

15.4.8.3 Bulkiness (i.e., steric hindrance) of the ligand

Bulky ligands (BLs) are routinely employed for synthesizing many kinds of NPs, which suggests that steric effects are important and often beneficial to stabilize a NP. In addition to the geometric and electronic effects, the energetic balance between high-ligand density and steric overlap has an important role in determining the molecular formulas and structures of discrete-sized NPs. Two common BLs are trioctylphosphine and trioctylphosphine oxide, other bulky phosphines have been routinely used for stabilizing semiconductor quantum dots, metal chalcogenide NPs, and anisotropic nanostructures.

Murray et al.[136] followed by Tracy et al.[137] and various groups have reported that the use of bulky thiols in the synthesis of Au NCs, influences the core sizes dramatically than the typical non-bulky thiols. Water-soluble thiols too showed that thiols with different bulky nature gave different NP size distributions; for example, glutathione produced Au_{25} whereas other thiols could not produce the same cluster always.

Study of self-assembled monolayers (SAMs) on Au surfaces had provided useful insights to understand the NCs. For example, Weiss and coworkers[138] study of admantanethiolate (-SAdm) SAMs on Au surfaces revealed following details for BL versus non-BL protected NCs:

(a) The steric hindrance of BLs is much more significant than non-BLs. BL NPs are predicted to typically have smaller sizes than non-BLs because steric overlap of BLs increases as the NP size (radius of curvature) increases. The steric hindrance provided by the ligand shell could protect the metal core and efficiently minimize the possibility of the penetration of subversive species (e.g., etching molecules) that could decompose the metal core into the ligand shell.

(b) The numerical density of ligands in the monolayer is lower for BLs than for non-BLs; for example, the surface density of thiolate bonds in -SAdm self-assembled monolayers on Au surfaces is reduced to about 55% of that of linear alkanethiolates. The absence of $Au_{25}(SAdm)_{18}$ indicates that the $Au_{25}(SR)_{18}$ structure would be too compact for -SAdm ligands. The steric bulkiness of the S-Adm ligand enables the formation of the structurally weaker $Au_{16}(S\text{-}Adm)_{12}$. Upon ligand exchange with a sterically less hindered cyclohexanethiol, more thiolates are accommodated, and thus $Au_{16}(SAdm)_{12}$ easily changes to Au_{18}.[154]

(c) The interstitial spaces in BL monolayers are more prominent than in non-BL monolayers. Steric overlap between ligands within different staples might force greater spacing between the staples. The steric overlap could also occur within the same staple, resulting in a strained conformation, thereby modifying (most likely, increasing) the distance between the anchor points to the core. Alternatively, the steric overlap between neighboring -SAdm ligands might be severe enough to prevent the formation of staples. A recent study of SAdm SAMs showed that -SAdm binds only one surface Au adatom (one Au atom that lies on a crystal surface), whereas nonbulky thiolates bind to two adatoms. Each of these possibilities would expand the volume of the Au core.

15.4.9 Thermal stability

In general, it is a standard practice to store NCs in refrigerator at 4°C. Depending on the sensitivity of NC toward oxidation, the solutions can be stored either in inert or ambient conditions. Up to certain temperature range, the NCs show tunable optical and electrical properties. For example, Pradeep and coworkers,[139] Miles and Murray[140,141] have reported temperature dependence of optical and electrochemical properties in $Au_{25}(SR)_{18}$. These findings show that the band gap in NCs is increased with decrease in temperature. In another example, the NCs switches among two isomers based on the applied temperature. A completely reversible temperature-responsive conformational isomers (NC based rotary nanomotor) is found in biicosahedral $[Au_{13}Ag_{12}(PPh_3)_{10}Cl_8]SbF_6$ NCs, composed of two icosahedral Au_7Ag_6 units by sharing one common Au vertex.[142]

There were also a few studies attempted to know the effect of temperatures (above 100°C) on these NCs. The NCs in solution undergoes decomposition in fission/fusion pathways leading to Ag/Au thiolate complexes or bigger NPs upon rise in temperature. In a comparative study, polyamide polymer-embedded $Au_{25}SR_{18}$ and Au NPs were subjected them to gradual rise of temperature from 150 to 450 °C.[143] In case of $Au_{25}SR_{18}$ NCs, they tend to grow ≈NP aggregates of 30–100 nm whereas much bigger aggregates of size 250 nm have seen in case of heating Au NPs. Note that these experiments are performed in presence of polymer. So, the aggregation is process might be different than that of solution as well as in solid state.

The effect of temperature on NCs in solid state could be understood from thermogravimetry analysis. In case of the thiolate self-assembled monolayers on gold surface, the Au−S bond was stable up to 100−150 °C. Pradeep and coworkers demonstrated a systematic decomposition of $Au_{25}(SG)_{18}$ NCs by TGA.[139] The TGA graph shows a little mass-loss below 200 °C which is attributed to residual water. Unlike the NPs and other organic soluble NCs, $Au_{25}(SG)_{18}$ exhibit two-step mass-loss in the range of 200–700 °C. The first mass-loss, around 18%, centered around 250 and 400 °C, correspond to the six thiolates bridge between two Au(I)

centers, [RS−Au−RS−Au−SR] and the second mass-loss, ~36%, correspond to 12 thiolates, [RS−Au−RS−Au−SR] connected to the icosahedral Au_{13} core. Total weight % of thiolates are 54% (18% + 36%). The remaining mass, of 46%, is associated with gold/gold sulfide after all the organics are decomposed.[139] The observed theoretical value of weight percent of gold and thiolates is 47% and 48% in $Au_{25}SG_{18}$, which is in good agreement with the experimentally observed values. Similarly, TG analysis of organic soluble $Au_{25}(SR)_{18}$, $Au_{38}(SR)_{24}$, and $Au_{144}(SR)_{60}$ NCs leaves the respective metal/metal sulfide content as residual after the TGA analysis in the temperature range of 200–600 °C (Fig. 15.20A).

In other studies, a comparison of thermal stability of $Au_{25}(SR)_{18}$ at all three different oxidation states (−1, 0, +1) were carried out using differential scanning calorimetry (DSC). The electron configuration of −1, 0, and +1 states of $Au_{25}(SR)_{18}$ are $1s^21p^6$, $1s^21p^5$, and $1s^21p^4$, respectively.[144] Among this $1s^21p^6$ (with the noble-gas-like superatomic electron configuration) is the stable electron configuration. Thus, this state is treated as superatomic electron configuration. In this analysis, a major thermal event was attributed to the ligand shell desorption, followed by the decomposition of the NCs. It is considered that this thermal event represents the thermal stability of the desired cluster, that is, higher the thermal decomposition value more the thermal stability. A careful and repeated thermal measurement on these three samples revealed that the thermal decomposition events for the three charge states occurred at 227.5 °C, 221 °C, and 209 °C for −1, 0, +1 respectively. From these values, $[Au_{25}(SR)_{18}]^-$ had higher decomposition temperature. Hence, it is more stable than the $[Au_{25}(SC_6H_{13})_{18}]^0$ radical, which in turn is more stable than the $[Au_{25}(SC_6H_{13})_{18}]^+$ superatomic diradical (Fig. 15.20B). Removal of one additional electron from $[Au_{25}(SC_6H_{13})_{18}]^-$ causes approximately 10 °C of destabilization.

The ligand symmetry environment of $Au_{144}(SC_6H_{13})_{60}$ appears to change reversibly upon the oxidation and reduction of $Au_{144}(SC_6H_{13})_{60}$ cluster. Because of complex factors, such as changeable counterion, charge-dependent thermal stability, ligand-steric factor and the apparent breakdown of symmetry in some oxidation states, leads to structural, electronic, and thermal stability of these clusters are unpredictable .

In addition to the charge state, the ligand steric size had substantial influence on the thermal stability of $Au_{25}(SR)_{18}$. The thermal stability of a similar set of clusters with different steric sized ligands was determined by differential scanning calorimetry. The decomposition temperatures of NCs protected by ethanethiol, butanethiol, phenylethane thiol, and hexanethiol are shown in Fig. 15.21. Among the PET protected Au_{25} NCs could be recognized as highest thermally stable over others due to a more sterically demanding ligand, by virtue of its branched nature. The thermal decomposition trend of NCs shows a strong correlation with sterically larger ligands on NC surface pointing toward greater thermal stability. Compare to the straight chain alkanethiols, the branched alkyl chains provides a larger "cluster cone angle" could explain the reason for enhancement in their stability.

15.4.9.1 Thermal stability in solution

In solution, NCs undergo decomposition with increasing temperatures through fusion process. Remya et al.[146] illustrated the thermal stability of glutathione protected Ag NCs in aqueous solutions. With increase in temperature, the clusters undergo thiolate desorption and heterolytic bond cleavage, resulting the formation of Ag_2S NPs at 80 °C. The cluster initially dissociates into thiolates (Ag-SR) which can follow two possible cleavage

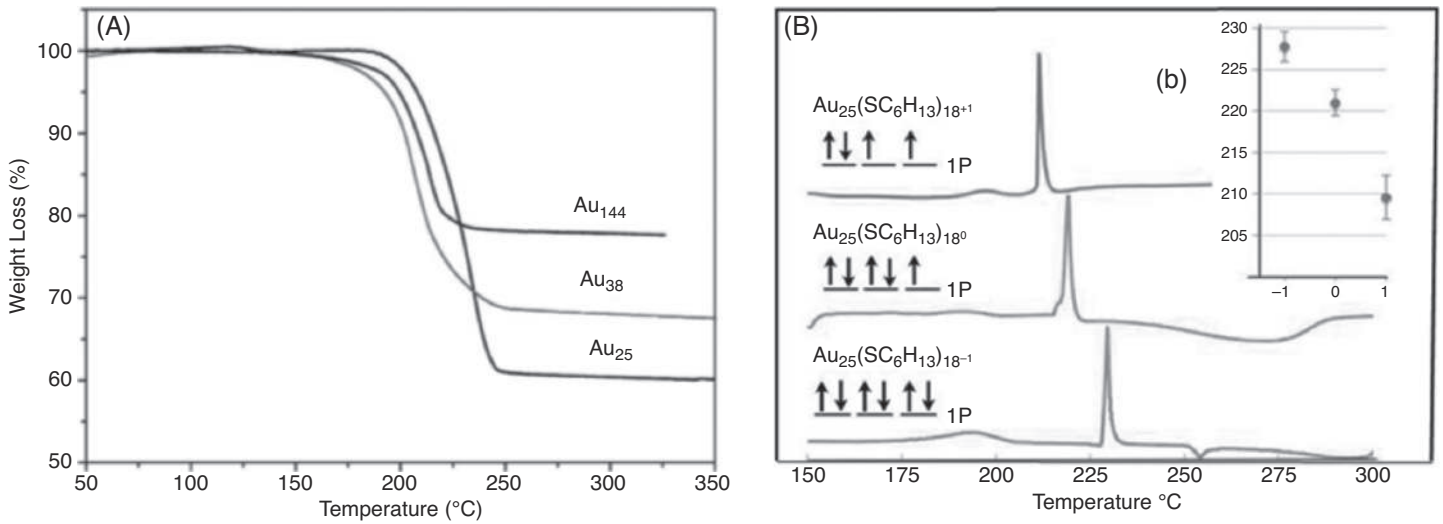

FIGURE 15.20 (A) Thermogravimetric analysis of $Au_{25}(SR)_{18}$, $Au_{38}(SR)_{24}$, and $Au_{144}(SR)_{60}$ NCs ($R = CH_2CH_2Ph$). Reproduced with permission from ref.[145] Copyright 2010 John Wiley and Sons. (B) DSC curves for the −1, 0, and +1 charge states of $Au_{25}(SC_6H_{13})_{18}$. The temperatures of the corresponding thermal decomposition events for the three charge states (227.5°C, 221°C, and 209°C) are plotted in the inset. Reproduced with permission from ref.[144] Copyright 2012 American Chemical Society.

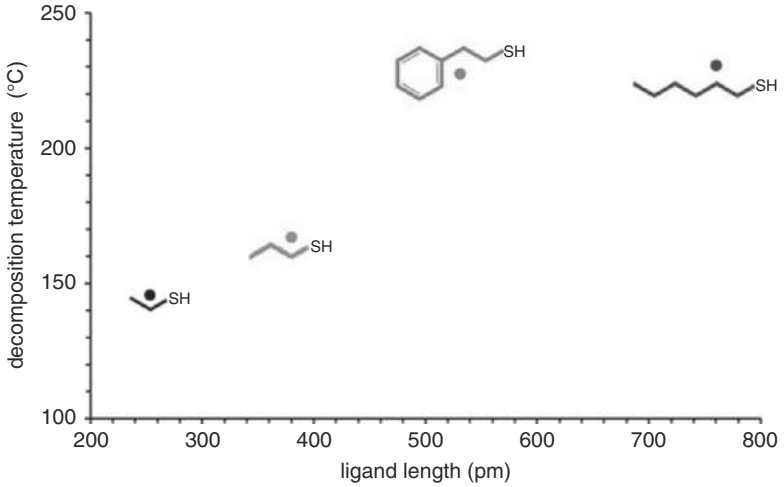

FIGURE 15.21 Effect of ligand chain on the stability of nanoclusters. Reproduced with permission from ref.[122] Copyright 2017 Royal Society of Chemistry.

mechanisms.

$$2R-S-Ag \rightarrow 2Ag + R-S-S-R \quad \text{(a)}$$

$$2R-S-Ag \rightarrow 2AgS + (R-S-R)_2 \quad \text{(b)}$$

Among these, reaction (b) was seen thermodynamically favorable as ΔH is more negative. This is a low temperature route (80 °C) to make Ag_2S NPs than that of traditional Ag_2S NPs synthesis heat-treated at ~200 °C. In another study, Bakr et al.[82] have shown nonplasmonic to plasmonic transformation of monolayer-protected AgNCs at ~90 °C.

The stability of Au_{25} NCs in aqueous solutions also highly dependent on ligand structure. For example, temperature stability of water-soluble $Au_{25}(SG)_{18}$ is compared with that of $Au_{25}(Capt)_{18}$ (Capt, captopril).[147] Both samples were maintained at equal optical density, and their stability was monitored by absorption spectra, while heating the solutions at 80 °C. The absence of decomposition signatures in $Au_{25}(Capt)_{18}$, showed that the stability of $Au_{25}(Capt)_{18}$ is much higher than that of the $Au_{25}(SG)_{18}$. The solutions were further heated for 24 h and the absorption spectra were recorded. During this time period the $Au_{25}(Capt)_{18}$ showed no sign of degradation, while glutathione capped Au_{25} showed a completely featureless spectrum.

15.4.10 Oxidation state

The stability of NCs also depends on overall charge present on a NC. Regarding $Au_{25}(SR)_{18}$, as it has been mentioned above that the changes in charge states can induce significant differences in the structures as well as physicochemical properties of Au_{25}NCs. For example, typically, Au_{25}NCs available in three charge states, they are $[Au_{25}(PET)_{18}]^-$, $[Au_{25}(PET)_{18}]^0$ and $[Au_{25}(PET)_{18}]^+$. Among $[Au_{25}(PET)_{18}]^0$ temporal stability is high due to its stable geometry. Note that the temporal stability is the stability observed based on absorption profile collected in air, contrary to the thermal stability which is observed through DSC or rise in

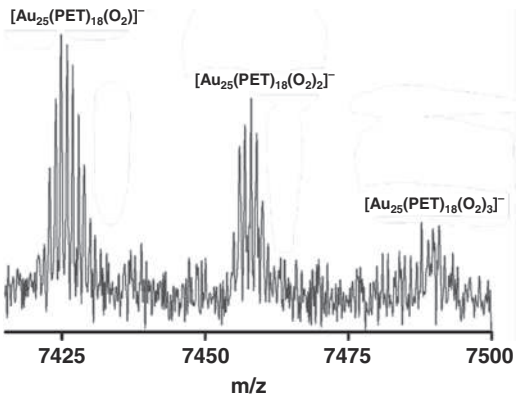

FIGURE 15.22 ESI-MS spectra of $[Au_{25}(PET)_{18}]^-$ in DCM after introducing O_2. The O_2 atmosphere was created using an O_2-filled balloon. Reproduced with permission from ref.[148] Copyright 2018 American Chemical Society.

temperature. $[Au_{25}(PET)_{18}]^+$ is the least durable among the three systems, and it decomposes completely to thiolates on addition of excess thiols or rise of temperature.

The charge state is highly related to the presence of O_2 in a desired solvent. Stability experiments such as storing the $[Au_{25}(SR)_{18}]^-$ NC solutions in argon endures for long period of time compared to that of the NCs placed under ambient atmosphere. Pradeep et al. studied the interaction between $[Au_{25}(SR)_{18}]^-$ and molecular O_2 in solution using electrospray ionization mass spectrometry and absorption spectroscopy.[148] Up to three O_2 attachments to $[Au_{25}(SR)_{18}]^-$ were detected in the mass spectrometry (Fig. 15.22). This gives direct evidence of the interaction of $[Au_{25}(SR)_{18}]^-$ with molecular O_2. Mass spectral study reveals the adduct formation between $[Au_{25}(SR)_{18}]^-$ and O_2 was observed only in the case of DCM and not in toluene. This explains the more stability of NCs in toluene then the other selected solvents. Oxygen attachment to the NCs leads to its decomposition to a polymer-like products.

In another experiment, the lifetime of NCs in stabilized-THF and nonstabilized THF solvents are studied through absorption spectra. Note that the stabilized-THF contained a radical inhibitor butylated hydroxytoluene. Due to the presence of radical inhibitor in the former THF, the $[Au_{25}(SR)_{18}]^-$ NCs exhibit longer lifetimes than the nonstabilized THF. Overall, the argon atmosphere and radical inhibitor contributes to NC stability or cluster decomposition process which is strongly dependent on the dissolved oxygen level. Typically, decomposition occurs through an oxygen dependent etching process. In fact, the influence of oxidation state of NC in solid state is different than that of solvated NCs. In solid state, it is related to electronic stability or superatom model and steric nature that determines the lifetime of the NCs.

There is also correlation between thermal stability verses different charged NCs carrying various steric structured ligands. Fig. 15.23 shows the observed decomposition temperatures for Au_{25} clusters protected by ethanethiol, propanethiol, hexanethiol, and phenylethanethiol in the -1, and 0 oxidation states. As discussed in the earlier section, increasing the oxidation state of the clusters, deviating from a full superatomic electron shell generally decreases their thermal stability. However, in case of PET protection this trend is reversed (0 is more stable than -1 charged NCs) due to the domination of steric hindrance of ligand that provides a larger contribution than oxidation state to its practical thermal stability.

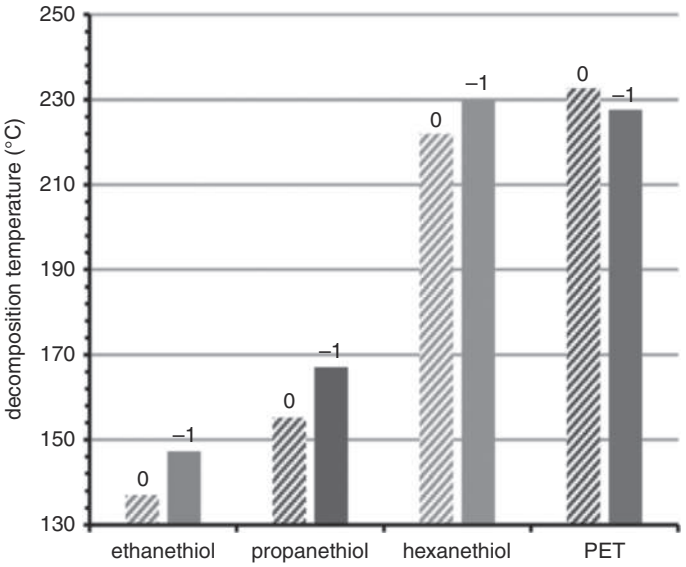

FIGURE 15.23 Relative stability of $Au_{25}SR_{18}$ cluster at 0 and −1 charge states. SR represents various thiolates mentioned on *x*-axis. Reproduced with permission from ref.[122] Copyright 2017 Royal Society of Chemistry.

5.4.11 Photostability

Photostability is critical for nanosized materials for bioimaging and catalytic applications. It is known that NCs tend to sinter and grow to larger particles upon light irradiation. This is due to dissociation/cleavage of surface passivated ligands resulting in bare NC core with high surface energy followed by the agglomeration of NCs. To improve catalytic activities the loading of NCs onto solid support is commonly utilized which reduce these adverse effects. In most cases, even in the presence of solid support, coalescence of these NCs could not be avoided. Thus, the NC loaded catalyst substantially losses its photocatalytic activity in a reaction progress over time. For instance, the irradiation of high-energy electron beams on Au:SG-Pt/TiO_2 photocatalysts can lead to the aggregation of Au:SG NCs into larger Au NPs (~5 nm diameter) after 2 h of continuous visible light illumination ($\lambda > 420$ nm).[149] It has also been reported that the photogenerated electrons from Au:SG NCs or TiO_2 can be captured by Au(I) component on the outer layer of Au:SG. This results in the photocatalytic decomposition of –SG ligands from the Au NC surface which can also lead to the formation of metallic Au NPs. Thus, ligand dissociation/aggregation mechanism has been proposed to elucidate the photoinduced coalescence of Au NCs to larger metallic Au NPs at the Au/TiO_2 interface under illumination.

Although NCs exhibit limited photostability and the fluorescence intensity remains weaker than organic dyes, they still advantageous over quantum dots and organic dyes in view of their higher stokes-shift, low cytotoxicity, and better photostability. Note that the quantum yield of NCs ranging from 2% to 15%. Xavier et al.[150] performed a comparison study of photostability among the three prominent materials such as AuAg:SG NCs (SG: thiolate of glutathione), CdTe quantum dots and Rhodamine 6G. Photoirradiation effect of AuAg:SG NCs in water ($\lambda_{em} = 560$ nm), Rhodamine 6G (in 1 M NaOH; $\lambda_{em} = 560$ nm), and CdTe QD in water ($\lambda_{em} = 580$ nm) was tested by illuminating light with an intensity of 40 mW for

5 min. The results showed a strong resistance toward photobleaching in case of AuAg@SG (Fig. 15.24A). Its photostability behavior is similar to that of the CdTe quantum dots, while the fluorescence intensity of the organic dye experiences a drastically decrease during this illumination.

Another approach to improve photostability as well as photocatalytic efficiency is deposition of Au:SG NCs on SiO_2 sphere followed by the surface modification of this composite with branched poly-ethylenimine (BPEI).[151] In the presence of rich amine groups in BPEI, this polymer acts as an excellent surface charge controller, reducing agent, and stabilizing agent for SiO_2–Au:SG composition. Specifically, the size and structure of Au:SG can be well retained over 10 h under continuous visible light irradiation ($\lambda > 420$ nm) because of the high reductive ability of BPEI to inhibit the -SG oxidation process on Au:SG NCs. The photostability on both samples, SiO_2–Au:SG NCs-BPEI composites and SiO_2–Au:SG NCs have been carried out separately by exposing these samples to a continuous visible light irradiation ($\lambda > 420$ nm) for 10 h under ambient conditions. TEM analysis suggests that in case of SiO_2–Au:SG NCs-BPEI, the size of NCs remains similar size before and after photoirradiation (Fig. 15.24B and D), while NCs aggregates to 6 nm AuNPs for samples without BPEI composites after photoirradiation (Fig. 15.24C–E). Such new approaches would open up opportunities to improve the photocatalytic activities of NCs as well as their stability upon light irradiation.

15.5 Nomenclature of nanoclusters

In general, it is convenient to call these atomically precise few-atom clusters as "nanoclusters" or by various other names such as quantum clusters, nanomolecules, superatoms, faradaurates, etc. With rapid addition to the new family of NCs, one requires a model naming scheme to describe the atomic positions in the core as well as in the outer shells. In addition, it is necessary to recognize chemical compositions of NCs such as $Au_{24}Pd(SR_1)_{18-x}(SR_2)_x$ or different regioisomers, $Au_{38}(SR_1)_{23}(SR_2)_1$ by their name. Recognizing the chemical compositions by their nomenclature is well established for organic molecules as well as for several inorganic molecules such as in fullerene.

In early attempt to naming NCs, Knoppe et al.[153] used a terminology to differentiate chiral and achiral $Au_{38}(SR)_{24}$ NCs based on IUPAC stereochemical nomenclature: *A,A*-$Au_{38}(SR)_{24}$, *C,C*-$Au_{38}(SR)_{24}$, where *A* and *C* represents anticlockwise and clockwise rotation. Typically, this nomenclature is used for naming coordination compounds. In 2015, Ganapati et al. developed a unique way to name any NCs.[152] In this model, authors considered a Borromean ring diagram for the cluster with octahedral symmetry (Fig. 15.25), showing its topological configuration consisting of three interlocked (Au_8S_6)-rings. Note that three Au_8S_6 units equal to $Au_{24}S_{18}$ and the presence one central Au atom gives rise the complete $Au_{25}SR_{18}$ composition. This terminology is called as aspicule nomenclature, meaning shielded molecules. For developing the aspicule nomenclature, four points were considered: (i) symmetry of nanocluster, (ii) universality and ability to describe the structure and/or modifications of any aspicule, (iii) taking guidelines from the IUPAC nomenclature, and (iv) keep as simple as possible to recognize the complex structures.

So far, this nomenclature has been proposed for the three most common NCs, they are $Au_{25}(SR)_{18}$, $Au_{38}(SR)_{24}$, and $Au_{144}(SR)_{60}$, and may be extended further for other clusters. The

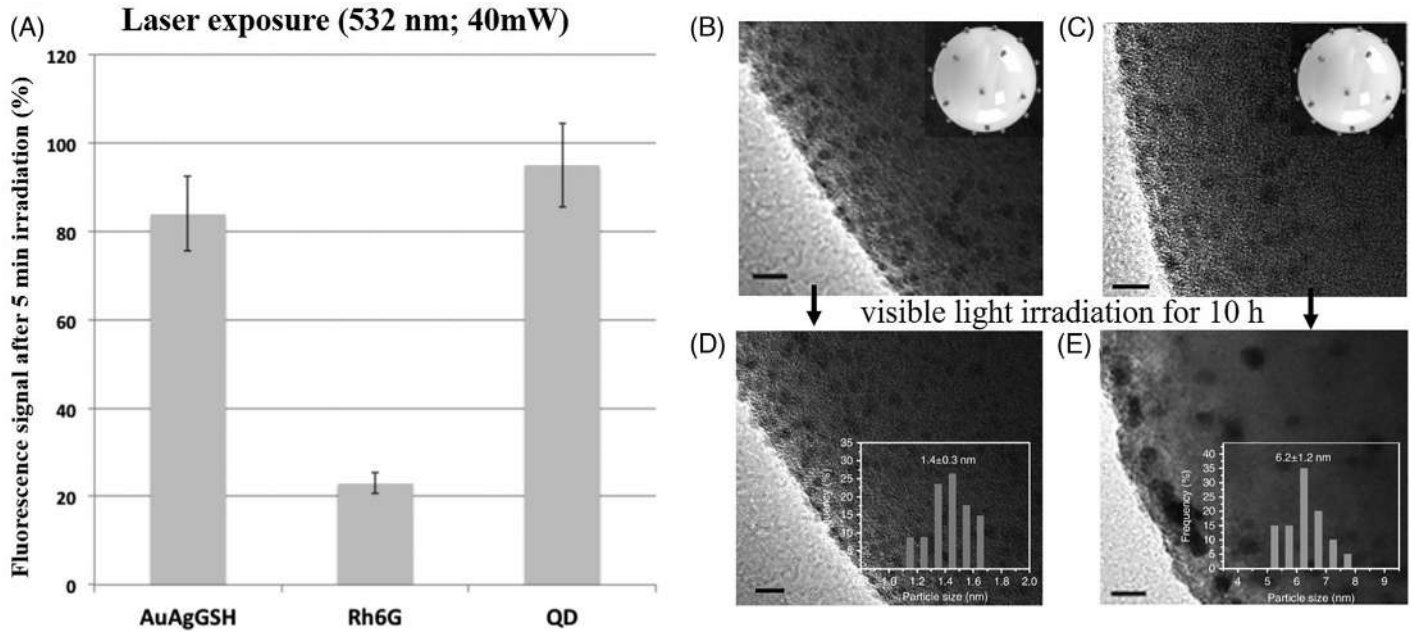

FIGURE 15.24 (A) Photobleaching measurements of AuAg:SG, rhodamine 6G (Rh6G), and CdTe solutions determined after laser exposure ($\lambda_{ex} = 532$ nm; 40 mW) for 5 min. Reproduced with permission from ref.[150] Copyright 2012 Royal Society of Chemistry. (B–E) TEM images of samples before and after photoirradiation. TEM analysis suggests that SiO_2–Au:SG NCs with BPEI composite maintain almost same size on the surface of SiO_2 spheres (B–D) whereas in case of SiO_2–Au:SG NCs, the ~1.4 nm sized NCs aggregate to ~6 nm AuNPs on SiO_2 surface after photoirradiation. Reproduced with permission from ref.[151]

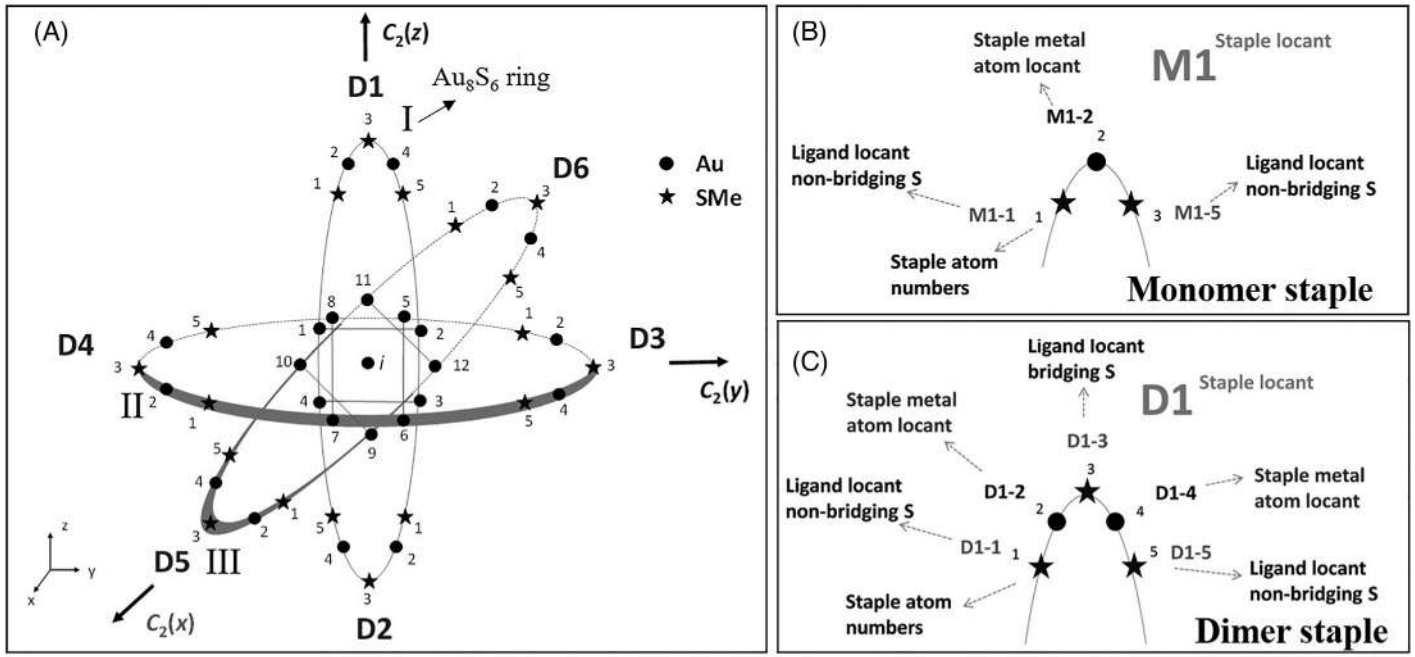

FIGURE 15.25 (A) Borromean-rings diagram of $Au_{25}(SMe)_{18}$. Three interlocked (Au_8S_6)-rings are labeled with I, II, and III. D1 to D6 are the dimer staples enlarged in Section C. (B) Assignments of ligand and staple metal atom locants in monomer and dimer staples, which are taken to be M_1 and D_1 in this example. Reproduced with permission from ref.[152] Copyright 2015 American Chemical Society.

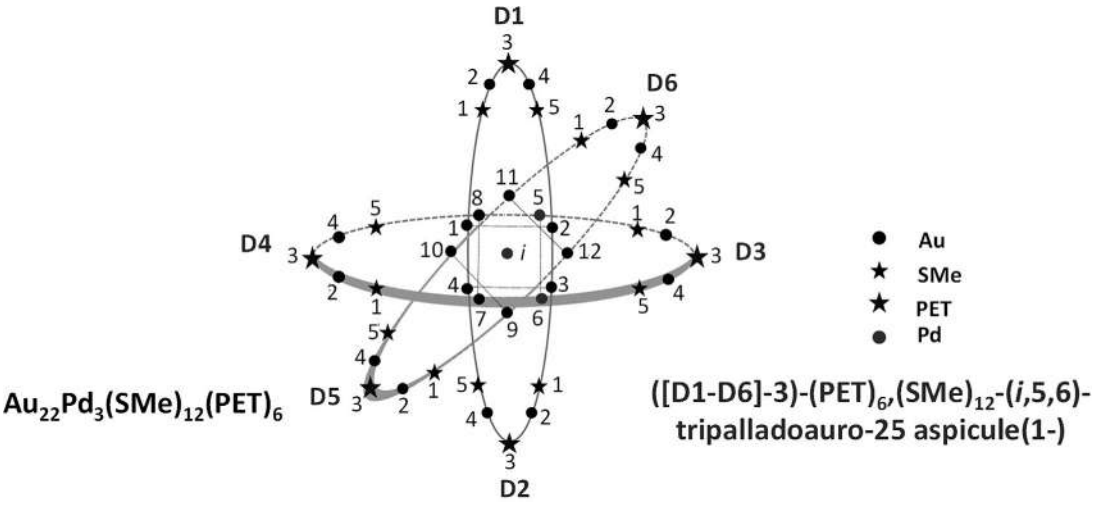

FIGURE 15.26 Borromean-rings diagram of $Au_{22}Pd_3(SMe)_{12}(PET)_6$. Reproduced with permission from ref.[152] Copyright 2015 American Chemical Society.

most common inner core for these NCs is icosahedral. The simplified structural representation in the form of a diagram (Fig. 15.25) includes unique positional labels (locants) for (i) the core atoms, (ii) the staples, (iii) the ligands, and (iv) the staple metal atoms.

The name for $Au_{25}(SMe)_{18}$ according to the "aspicule nomenclature" is 18(methylthiolato)-auro-25 aspicule(1−) or in its shortened form, $(SMe)_{18}$-auro-25 aspicule(1−). The name for $Au_{25}(SMe)_{17}(PET)_1$ is (D3-3)-(2-phenylethanethiolato),17-(methylthiolato)-auro-25 aspicule(1−) or, in its condensed form, (D3-3)-$(PET)_1$, $(SMe)_{17}$-auro-25 aspicule(1−). This naming is based on the position of the PET. In this particular example, PET ligand exchanged at the bridging position 3 on the D3 staple, that is, the 3 in D3 corresponds to the ligand exchanging position. Because of this reason the "(D3-3)-(2-phenylethanethiolato)" added in the beginning of nomenclature.

Similarly, an alloy cluster such as $Au_{22}Pd_3(SMe)_{12}(PET)_6$ can have its aspicule name (Fig. 15.26) as ([D1−D6]-3)-hexa (PET), dodeca(methylthiolato)-(i,5,6)-tripalladoauro-25 aspicule(1−) or, in its short form, ([D1−D6]-3)-$(PET)_6$,$(SMe)_{12}$-(i,5,6)-tripalladoauro-25 aspicule(1−). In the above example, totally six PET ligands are substituted from 18 of SMe ligands. The six PET locates on third position of all the dimer staples (D1 to D6). So, this is simplified by mentioning first and last staples separated by a hyphen, all are enclosed in square brackets, followed by the common position on each of the staples; for example [D1–D6]-3, stands for (D1-3, D2-3, D3-3, D4-3, D5-3, and D6-3). The positions of metal atom substituents are labeled by prefixing their locants based on the respective substituent metal name in a NC, for example, (i,2)-dipalladoauro represents substitution at the central position and the core atom 2. In case of the structure in Fig. 15.26, this system (i,5,6) represents positions of palladium, the substitution of the central and the core atom 5 and 6. In this way, a variety of isomers with various ligand and metal positions can be recognized by aspicule nomenclature.

15.6 Summary and future perspectives

This chapter provides an overview of Ag and Au clusters which includes variation in their properties while they undergo transformation from bulk to plasmonic nanoparticles further to atomically precise nanoclusters. Various types of nanoclusters with protecting agents such as thiols, biomolecules, polymers, and dendrimers are included. This section also contains early research of gas phase bare clusters. Electronic and geometric stability are discussed in detail in this chapter. The nature of solvent (polarity) and charge state plays an unexpected role in the stability of the NCs which is discussed in more details through $Au_{25}SR_{18}$ as case study. The structure of ligand is an important parameter contributing to the formation of stable NCs. Recent advancement in stabilizing clusters with unusual compositions (for ex. Au_{31}) is highly influenced by steric hindrance of bulky ligands. This has been realized by the recent successes in controlling Au NCs with all three (BCC, FCC, HCP) types of crystalline structures. The influence of external surroundings such as temperature and radiation on the nanocluster stability is also discussed here. A systematic naming to the $Au_{25}(SR)_{18}$, $Au_{38}(SR)_{24}$, $Au_{144}(SR)_{60}$, and their derivatives has been provided based on their topology and structure. This method of naming can be extended further to other NCs.

Despite significant progress, several issues pertaining to NCs remain unaddressed. In the case of water-soluble systems, (1) the relatively low quantum yield (QY) (below 10%) needs to be improved by suitable synthetic procedures and scaffolds. (2) Most of the water-soluble NCs lack fundamental understandings of metal–metal and metal–thiol interactions. So far, such understanding is mainly available for NCs dissolved in organic solvents, limiting their applications of water-soluble NCs in biomedical field. (3) Different crystalline phases, for example, $Au_{36}(SR)_{24}$– in FCC, $Au_{30}(SR)_{18}$ – in HCP, and $Au_{38}S_2(SR)_{20}$– in BCC, change their crystal structures based on their ligand environment. The role of ligands and their steric hindrance on the crystal structure needs to be studied further. Especially, there is a need to develop methods to input full ligands in computational methods. (4) There remains plenty of opportunities for developing better synthesis procedures for non-crystallographic structures (e.g., icosahedron) and crystallographic structures (FCC, HCP, and BCC). (5) There are still major challenges exists concerning Ag NC including lack of relevant crystal structures compared with Au NCs. Bridging the gap between rapidly growing Au NCs structural understanding and Ag NCs is essential for application viewpoint, which has begun recently.

List of abbreviation

LSPR- localized surface plasmon resonance ,
SR- alkane thiolate,
FCC- face centered cubic packing,
BCC- body centered cubic packing,
HCP- hexagonal cubic packing,
BSA- bovine serum albumin,
HOMO- highest occupied molecular orbital,
LUMO- lowest unoccupied molecular orbital,
PET- phenylethanethiolate,
TOA^{+-} tetrabutylammonium cation,
Adm- admantanethiolate,

MBT- methylbenzenethiol,
TBBT- tert-butylbenzenethiol,
MPA- mercaptopropionic acid,
SG- thiolate of glutathione

References

1. Schmid G. Large clusters and colloids. Metals in the embryonic state. *Chem Rev*. 1992;92:1709–1727.
2. Jimenez VL, Leopold MC, Mazzitelli C, Jorgenson JW, Murray RW. HPLC of monolayer-protected gold nanoclusters. *Anal Chem*. 2003;75:199–206.
3. Song Y, Heien MLAV, Jimenez V, Wightman RM, Murray RW. Voltammetric detection of metal nanoparticles separated by liquid chromatography. *Anal Chem*. 2004;76:4911–4919.
4. Wang G, Huang T, Murray RW, Menard L, Nuzzo RG. Near-IR luminescence of monolayer-protected metal clusters. *J Am Chem Soc*. 2005;127:812–813.
5. Guerrero AH, Fasoli HJ, Costa JL. Why gold and copper are colored but silver is not. *J Chem Educ*. 1999;76:200.
6. Jain PK, Huang X, El-Sayed IH, El-Sayed MA. Review of some interesting surface plasmon resonance-enhanced properties of noble metal nanoparticles and their applications to biosystems. *Plasmonics*. 2007;2:107–118.
7. Kreibig UVM. Optical Properties of Metal Clusters. Berlin: Springer; 1995.
8. Crasto D, Dass A. Green gold: $Au_{30}(S\text{-}t\text{-}C_4H_9)_{18}$ molecules. *J Phys Chem C*. 2013;117:22094–22097.
9. Lu HM, Li PY, Cao ZH, Meng XK. Size-, shape-, and dimensionality-dependent melting temperatures of nanocrystals. *J Phys Chem C*. 2009;113:7598–7602.
10. Schlexer P, Andersen AB, Sebok B, Chorkendorff I, Schiøtz J, Hansen TW. Size-dependence of the melting temperature of individual Au nanoparticles. *Part Part Syst Charact*. 2019;36.
11. Nealon GL, Donnio B, Greget R, Kappler J-P, Terazzi E, Gallani J-L. Magnetism in gold nanoparticles. *Nanoscale*. 2012;4:5244–5258.
12. Granja LP, Martínez ED, Troiani H, Sanchez C, Soler Illia GJAA. Magnetic gold confined in ordered mesoporous titania thin films: a noble approach for magnetic devices. *ACS Appl Mater Interf*. 2017;9:965–971.
13. Reich S, Leitus G, Feldman Y. Observation of magnetism in Au thin films. *Appl Phys Lett*. 2006;88.
14. Zhang P, Sham TK. X-ray studies of the structure and electronic behavior of alkanethiolate-capped gold nanoparticles: the interplay of size and surface effects. *Phys Rev Lett*. 2003;90.
15. Guerrero E, Muñoz-Márquez MA, García MA, et al. Surface plasmon resonance and magnetism of thiol-capped gold nanoparticles. *Nanotechnology*. 2008;19.
16. Crespo P, García MA, Fernández Pinel E, et al. Fe impurities weaken the ferromagnetic behavior in Au nanoparticles. *Phys Rev Lett*. 2006;97.
17. Yamamoto Y, Miura T, Suzuki M, et al. Direct observation of ferromagnetic spin polarization in gold nanoparticles. *Phys Rev Lett*. 2004;93.
18. Gréget R, Nealon GL, Vileno B, et al. Magnetic properties of gold nanoparticles: a room-temperature quantum effect. *Chem Phys Chem*. 2012;13:3092–3097.
19. Donnio B, García-Vázquez P, Gallani J-L, Guillon D, Terazzi E. Dendronized ferromagnetic gold nanoparticles self-organized in a thermotropic cubic phase. *Adv Mater*. 2007;19:3534–3539.
20. Zhu M, Aikens CM, Hendrich MP, et al. Reversible switching of magnetism in thiolate-protected Au_{25} superatoms. *J Am Chem Soc*. 2009;131:2490–2492.
21. Agrachev M, Antonello S, Dainese T, et al. Magnetic ordering in gold nanoclusters. *ACS Omega*. 2017;2:2607–2617.
22. Jadzinsky PD, Calero G, Ackerson CJ, Bushnell DA, Kornberg RD. Structure of a thiol monolayer-protected gold nanoparticle at 1.1 Å resolution. *Science*. 2007;318:430–433.
23. Heaven MW, Dass A, White PS, Holt KM, Murray RW. Crystal structure of the gold nanoparticle $[N(C_8H_{17})_4][Au_{25}(SCH_2CH_2Ph)_{18}]$. *J Am Chem Soc*. 2008;130:3754–3755.
24. Qian H, Eckenhoff WT, Zhu Y, Pintauer T, Jin R. Total structure determination of thiolate-protected Au_{38} nanoparticles. *J Am Chem Soc*. 2010;132:8280–8281.
25. Zeng C, Qian H, Li T, et al. Total structure and electronic properties of the gold nanocrystal $Au_{36}(SR)_{24}$. *Angew Chem Int Ed Engl*. 2012;51:13114–13118.

26. Higaki T, Liu C, Zeng C, et al. Controlling the atomic structure of Au_{30} nanoclusters by a ligand-based strategy. *Angew Chem Int Ed*. 2016;55:6694–6697.
27. Liu C, Li T, Li G, et al. Observation of body-centered cubic gold nanocluster. *Angew Chem Int Ed*. 2015;54:9826–9829.
28. Desireddy A, Conn BE, Guo J, et al. Ultrastable silver nanoparticles. *Nature*. 2013;501:399–402.
29. Joshi CP, Bootharaju MS, Alhilaly MJ, Bakr OM. $[Ag_{25}(SR)_{18}]-$: the "golden" silver nanoparticle. *J Am Chem Soc*. 2015;137:11578–11581.
30. Zhu M, Aikens CM, Hollander FJ, Schatz GC, Jin R. Correlating the crystal structure of a thiol-protected Au_{25} cluster and optical properties. *J Am Chem Soc*. 2008;130:5883–5885.
31. Ryogo Kubo. Electronic properties of metallic fine particles. *J Phys Soc Jpn*. 1962;17:975.
32. Ekardt W, Penzar Z. Collective excitations in open-shell metal clusters: the time-dependent local-density approximation applied to the self-consistent spheroidal jellium particle. *Phys Rev B*. 1991;43:1322–1330.
33. Jin R. Quantum sized, thiolate-protected gold nanoclusters. *Nanoscale*. 2010;2:343–362.
34. Sakthivel NA, Stener M, Sementa L, Fortunelli A, Ramakrishna G, Dass A. $Au_{279}(SR)_{84}$: the smallest gold thiolate nanocrystal that is metallic and the birth of plasmon. *J Phys Chem Lett*. 2018;9:1295–1300.
35. Negishi Y, Nobusada K, Tsukuda T. Glutathione-protected gold clusters revisited: bridging the gap between gold(I)−thiolate complexes and thiolate-protected gold nanocrystals. *J Am Chem Soc*. 2005;127:5261–5270.
36. Chakraborty I, Erusappan J, Govindarajan A, et al. Emergence of metallicity in silver clusters in the 150 atom regime: a study of differently sized silver clusters. *Nanoscale*. 2014;6:8024–8031.
37. Yang H, Wang Y, Chen X, et al. Plasmonic twinned silver nanoparticles with molecular precision. *Nat Commun*. 2016;7:12809.
38. Jin R. Atomically precise metal nanoclusters: stable sizes and optical properties. *Nanoscale*. 2015;7:1549–1565.
39. Zhou M, Higaki T, Li Y, Zeng C, Li Q, Sfeir MY, Jin R. Three-stage evolution from nonscalable to scalable optical properties of thiolate-protected gold nanoclusters. *J Am Chem Soc*. 2019;141:19754–19764.
40. Ozin GA, Huber H. Cryophotoclustering techniques for synthesizing very small, naked silver clusters Agn of known size (where n = 2-5). The molecular metal cluster-bulk metal particle interface. *Inorg Chem*. 1978;17:155–163.
41. Marcus RSN. Physics and Chemistry of Small Clusters. New York: Plenum Press; 1987.
42. Harbich W, Fedrigo S, Buttet J, Lindsay DM. Deposition of mass selected gold clusters in solid krypton. *J Chem Phys*. 1992;96:8104–8108.
43. Fedrigo S, Harbich W, Buttet J. Optical response of Ag_2, Ag_3, Au_2, and Au_3 in argon matrices. *J Chem Phys*. 1993;99:5712–5717.
44. Collings BA, Athanassenas K, Rayner DM, Hackett PA. Optical spectroscopy of Ag_7, Ag_{9+}, and Ag_9. A test of the photodepletion method. *Chem Phys Lett*. 1994;227:490–495.
45. Smalley RE. Laser studies of metal cluster beams. *Laser Chem*. 1983;2.
46. Mitchell SA, Ozin GA. Silver clusters in rare gas matrixes. Thermal and photochemical silver atom aggregation reactions. *J Phys Chem*. 1984;88:1425–1436.
47. Willey KF, Cheng PY, Yeh CS, Robbins DL, Duncan MA. Electronic spectroscopy of silver dimer rare gas complexes. *J Chem Phys*. 1991;95:6249–6256.
48. Fedrigo S, Harbich W, Buttet J. Soft landing and fragmentation of small clusters deposited in noble-gas films. *Phys Rev B*. 1998;58:7428–7433.
49. Ievlev D, Rabin I, Schulze W, Ertl G. Fluorescence spectroscopy of silver clusters formed in rare gas droplets. *Eur Phys J D - Atomic Mol Opt Plasma Phys*. 2001;16:157–160.
50. Rabin I, Schulze W, Ertl G. Light emission in matrix assisted cluster-cluster reactions. *Crystal Res Technol*. 1998;33:1075–1084.
51. Alameddin G, Hunter J, Cameron D, Kappes MM. Electronic and geometric structure in silver clusters. *Chem Phys Lett*. 1992;192:122–128.
52. Bao X, Muhler M, Pettinger B, Schlögl R, Ertl G. On the nature of the active state of silver during catalytic oxidation of methanol. *Catal Lett*. 1993;22:215–225.
53. Lefferts L, van Ommen JG, Ross JRH. The oxidative dehydrogenation of methanol to formaldehyde over silver catalysts in relation to the oxygen-silver interaction. *Appl Catal*. 1986;23:385–402.
54. Valden M, Lai X, Goodman DW. Onset of catalytic activity of gold clusters on titania with the appearance of nonmetallic properties. *Science*. 1998;281:1647–1650.

55. Peyser LA, Vinson AE, Bartko AP, Dickson RM. Photoactivated fluorescence from individual silver nanoclusters. *Science*. 2001;291:103–106.
56. Beer R, Calzaferri G, Li J, Waldeck B. Towards artificial photosynthesis: experiments with silver zeolites, part 2. *Coord Chem Rev*. 1991;111:193–200.
57. Ozin GA, Hugues F. Silver atoms and small silver clusters stabilized in zeolite Y: optical spectroscopy. *J Phys Chem*. 1983;87:94–97.
58. De Cremer G, Coutiño-Gonzalez E, Roeffaers MBJ, et al. Characterization of fluorescence in heat-treated silver-exchanged zeolites. *J Am Chem Soc*. 2009;131:3049–3056.
59. De Cremer G, Antoku Y, Roeffaers MBJ, et al. Photoactivation of silver-exchanged zeolite A. *Angew Chem Int Ed*. 2008;47:2813–2816.
60. De Cremer G, Sels BF, Hotta J-i, et al. Optical encoding of silver zeolite microcarriers. *Adv Mater*. 2010;22:957–960.
61. Watanabe Y, Namikawa G, Onuki T, Nishio K, Tsuchiya T. Photosensitivity in phosphate glass doped with Ag+ upon exposure to near-ultraviolet femtosecond laser pulses. *Appl Phys Lett*. 2001;78:2125–2127.
62. Bellec M, Royon A, Bourhis K, et al. 3D patterning at the nanoscale of fluorescent emitters in glass. *J Phys Chem C*. 2010;114:15584–15588.
63. Eichelbaum M, Rademann K, Hoell A, et al. Photoluminescence of atomic gold and silver particles in soda-lime silicate glasses. *Nanotechnology*. 2008;19.
64. Tikhomirov VK, Rodríguez VD, Kuznetsov A, Kirilenko D, Van Tendeloo G, Moshchalkov VV. Preparation and luminescence of bulk oxyfluoride glasses doped with Ag nanoclusters. *Opt Express*. 2010;18:22032–22040.
65. Hermerschmidt D, Haul R. ESR studies on the reduction process of silver zeolites. *Ber Bunsengesel Physik Chem*. 1980;84:902–907.
66. Royon A, Bourhis K, Bellec M, et al. Silver clusters embedded in glass as a perennial high capacity optical recording medium. *Adv Mater*. 2010;22:5282–5286.
67. Chakraborty I, Pradeep T. Atomically precise clusters of noble metals: emerging link between atoms and nanoparticles. *Chem Rev*. 2017;117:8208–8271.
68. Cowan MJ, Higaki T, Jin R, Mpourmpakis G. Understanding the solubility behavior of atomically precise gold nanoclusters. *J Phys Chem C*. 2019;123:20006–20012.
69. Nishida N, Yao H, Ueda T, Sasaki A, Kimura K. Synthesis and chiroptical study of d/l-penicillamine-capped silver nanoclusters. *Chem Mater*. 2007;19:2831–2841.
70. Yao H, Saeki M, Kimura K. Induced optical activity in boronic-acid-protected silver nanoclusters by complexation with chiral fructose. *J Phys Chem C*. 2010;114:15909–15915.
71. Wu Z, Lanni E, Chen W, Bier ME, Ly D, Jin R. High yield, large scale synthesis of thiolate-protected Ag_7 clusters. *J Am Chem Soc*. 2009;131:16672–16674.
72. Adhikari B, Banerjee A. Facile synthesis of water-soluble fluorescent silver nanoclusters and HgII sensing. *Chem Mater*. 2010;22:4364–4371.
73. Udayabhaskararao T, Pradeep T. New protocols for the synthesis of stable Ag and Au nanocluster molecules. *J Phys Chem Lett*. 2013;4:1553–1564.
74. Cathcart N, Kitaev V. Silver nanoclusters: single-stage scaleable synthesis of monodisperse species and their chirooptical properties. *J Phys Chem C*. 2010;114:16010–16017.
75. Habeeb Muhammed MA, Pradeep T. Aqueous to organic phase transfer of Au_{25} clusters. *J Clust Sci*. 2009;20:365–373.
76. Habeeb Muhammed MA, Ramesh S, Sinha SS, Pal SK, Pradeep T. Two distinct fluorescent quantum clusters of gold starting from metallic nanoparticles by pH-dependent ligand etching. *Nano Res*. 2008;1:333–340.
77. Yu Y, Luo Z, Yu Y, Lee JY, Xie J. Observation of cluster size growth in CO-directed synthesis of $Au_{25}(SR)_{18}$ nanoclusters. *ACS Nano*. 2012;6:7920–7927.
78. Miyata SMH, Kawasaki H, Yamamoto M, et al. Antimicrobial photodynamic activity and cytocompatibility of $Au_{25}(Capt)_{18}$ clusters photoexcited by blue LED light irradiation. *Int J Nanomed*. 2017;12:2716.
79. Mathew A, Pradeep T. Noble metal clusters: applications in energy, environment, and biology. *Part Part Syst Charact*. 2014;31:1017–1053.
80. Branham MR, Douglas AD, Mills AJ, Tracy JB, White PS, Murray RW. Arylthiolate-protected silver quantum dots. *Langmuir*. 2006;22:11376–11383.
81. Negishi Y, Arai R, Niihori Y, Tsukuda T. Isolation and structural characterization of magic silver clusters protected by 4-(tert-butyl)benzyl mercaptan. *Chem Commun*. 2011;47:5693–5695.

82. Bakr OM, Amendola V, Aikens CM, et al. Silver nanoparticles with broad multiband linear optical absorption. *Angew Chem Int Ed*. 2009;48:5921–5926.
83. Díez I, Ras RHA. Fluorescent silver nanoclusters. *Nanoscale*. 2011;3:1963–1970.
84. Xu H, Zeiger BW, Suslick KS. Sonochemical synthesis of nanomaterials. *Chem Soc Rev*. 2013;42:2555–2567.
85. Liu S, Lu F, Zhu J-J. Highly fluorescent Ag nanoclusters: microwave-assisted green synthesis and Cr^{3+} sensing. *Chem Commun*. 2011;47:2661–2663.
86. Santiago González B, Rodríguez MJ, Blanco C, et al. One step synthesis of the smallest photoluminescent and paramagnetic PVP-protected gold atomic clusters. *Nano Lett*. 2010;10:4217–4221.
87. Qu F, Li NB, Luo HQ. Transition from nanoparticles to nanoclusters: microscopic and spectroscopic investigation of size-dependent physicochemical properties of polyamine-functionalized silver nanoclusters. *J Phys Chem C*. 2013;117:3548–3555.
88. Díez I, Pusa M, Kulmala S, et al. Color tunability and electrochemiluminescence of silver nanoclusters. *Angew Chem Int Ed*. 2009;48:2122–2125.
89. Hu D, Jin S, Shi Y, et al. Preparation of hyperstar polymers with encapsulated $Au_{25}(SR)_{18}$ clusters as recyclable catalysts for nitrophenol reduction. *Nanoscale*. 2017;9:3629–3636.
90. Zheng J, Dickson RM. Individual water-soluble dendrimer-encapsulated silver nanodot fluorescence. *J Am Chem Soc*. 2002;124:13982–13983.
91. Zheng J, Petty JT, Dickson RM. High quantum yield blue emission from water-soluble Au_8 nanodots. *J Am Chem Soc*. 2003;125:7780–7781.
92. Triulzi RC, Micic M, Giordani S, Serry M, Chiou W-A, Leblanc RM. Immunoasssay based on the antibody-conjugated PAMAM-dendrimer–gold quantum dot complex. *Chem Commun*. 2006;48:5068–5070.
93. Choi S, Dickson RM, Lee J-K, Yu J. Generation of luminescent noble metal nanodots in cell matrices. *Photochem Photobiol Sci*. 2012;11:274–278.
94. Zhang Y, Hess EV, Pryhuber KG, Dorsey JG, Tepperman K, Elder RC. Gold binding sites in red blood cells. *Inorg Chim Acta*. 1995;229:271–280.
95. Petty JT, Zheng J, Hud NV, Dickson RM. DNA-templated Ag nanocluster formation. *J Am Chem Soc*. 2004;126:5207–5212.
96. Chandler M, Shevchenko O, Vivero-Escoto JL, Striplin CD, Afonin KA. DNA-templated synthesis of fluorescent silver nanoclusters. *J Chem Educ*. 2020;97:1992–1996.
97. O'Neill PR, Velazquez LR, Dunn DG, Gwinn EG, Fygenson DK. Hairpins with poly-C loops stabilize four types of fluorescent Agn:DNA. *J Phys Chem C*. 2009;113:4229–4233.
98. Latorre A, Lorca R, Zamora F, Somoza Á. Enhanced fluorescence of silver nanoclusters stabilized with branched oligonucleotides. *Chem Commun*. 2013;49:4950–4952.
99. Zhou R, Shi M, Chen X, Wang M, Chen H. Atomically monodispersed and fluorescent sub-nanometer gold clusters created by biomolecule-assisted etching of nanometer-sized gold particles and rods. *Chem –Eur J*. 2009;15:4944–4951.
100. Adhikari B, Banerjee A. Short-peptide-based hydrogel: a template for the in situ synthesis of fluorescent silver nanoclusters by using sunlight. *Chem –Eur J*. 2010;16:13698–13705.
101. Narayanan SS, Pal SK. Structural and functional characterization of luminescent silver−protein nanobioconjugates. *J Phys Chem C*. 2008;112:4874–4879.
102. Mathew A, Sajanlal PR, Pradeep T. A fifteen atom silver cluster confined in bovine serum albumin. *J Mater Chem*. 2011;21:11205–11212.
103. Le Guével X, Hötzer B, Jung G, Hollemeyer K, Trouillet V, Schneider M. Formation of fluorescent metal (Au, Ag) nanoclusters capped in bovine serum albumin followed by fluorescence and spectroscopy. *J Phys Chem C*. 2011;115:10955–10963.
104. Mathew A, Sajanlal PR, Pradeep T. Selective visual detection of TNT at the sub-zeptomole level. *Angew Chem Int Ed*. 2012;51:9596–9600.
105. Shang L, Dörlich RM, Trouillet V, Bruns M, Ulrich Nienhaus G. Ultrasmall fluorescent silver nanoclusters: protein adsorption and its effects on cellular responses. *Nano Res*. 2012;5:531–542.
106. Xie J, Zheng Y, Ying JY. Protein-directed synthesis of highly fluorescent gold nanoclusters. *J Am Chem Soc*. 2009;131:888–889.
107. Kawasaki H, Hamaguchi K, Osaka I, Arakawa R. ph-dependent synthesis of pepsin-mediated gold nanoclusters with blue green and red fluorescent emission. *Adv Funct Mater*. 2011;21:3508–3515.

108. Wen F, Dong Y, Feng L, Wang S, Zhang S, Zhang X. Horseradish peroxidase functionalized fluorescent gold nanoclusters for hydrogen peroxide sensing. *Anal Chem*. 2011;83:1193–1196.
109. Ledo-Suárez A, Rivas J, Rodríguez-Abreu CF, et al. Facile synthesis of stable subnanosized silver clusters in microemulsions. *Angew Chem Int Ed*. 2007;46:8823–8827.
110. Bootharaju MS, Dey R, Gevers LE, Hedhili MN, Basset J-M, Bakr OM. A new class of atomically precise, hydride-rich silver nanoclusters co-protected by phosphines. *J Am Chem Soc*. 2016;138:13770–13773.
111. Li G, Lei Z, Wang Q-M. Luminescent molecular Ag−S nanocluster $[Ag_{62}S_{13}(SBut)_{32}](BF_4)_4$. *J Am Chem Soc*. 2010;132:17678–17679.
112. Li B, Huang R-W, Qin J-H, et al. Thermochromic luminescent nest-like silver thiolate cluster. *Chem –Eur J*. 2014;20:12416–12420.
113. Sun D, Wang H, Lu H-F, et al. Two birds with one stone: anion templated ball-shaped Ag_{56} and disc-like Ag_{20} clusters. *Dalton Trans*. 2013;42:6281–6284.
114. Fenske D, Persau C, Dehnen S, Anson CE. Syntheses and crystal structures of the Ag–S cluster compounds $[Ag_{70}S_{20}(SPh)_{28}(dppm)_{10}]$ $(CF_3CO_2)_2$ and $[Ag_{262}S_{100}(StBu)_{62}(dppb)_6]$. *Angew Chem Int Ed*. 2004;43:305–309.
115. Fenske D, Anson CE, Eichhöfer A, et al. Syntheses and crystal structures of $[Ag_{123}S_{35}(StBu)_{50}]$ and $[Ag_{344}S_{124}(StBu)_{96}]$. *Angew Chem Int Ed*. 2005;44:5242–5246.
116. Manju CK, Chakraborty I, Pradeep T. Highly luminescent monolayer protected $Ag_{56}Se_{13}S_{15}$ clusters. *J Mater Chem C*. 2016;4:5572–5577.
117. Schaaff TG, Whetten RL. Controlled etching of Au:SR cluster compounds. *J Phys Chem B*. 1999;103:9394–9396.
118. Wang Y, Nieto-Ortega B, Bürgi T. Transformation from $[Au_{25}(SCH_2CH_2CH_2CH_3)_{18}]_0$ to $Au_{28}(SCH_2CH(CH_3)Ph)_{21}$ gold nanoclusters: gentle conditions is enough. *Chem Commun*. 2019;55:14914–14917.
119. Nimmala PR, Theivendran S, Barcaro G, et al. Transformation of $Au_{144}(SCH_2CH_2Ph)_{60}$ to $Au_{133}(SPh\text{-}tBu)_{52}$ nanomolecules: theoretical and experimental study. *J Phys Chem Lett*. 2015;6:2134–2139.
120. Ramasamy P, Guha S, Shibu ES, et al. Size tuning of Au nanoparticles formed by electron beam irradiation of Au_{25} quantum clusters anchored within and outside of dipeptide nanotubes. *J Mater Chem*. 2009;19:8456–8462.
121. Azubel M, Koh AL, Koyasu K, Tsukuda T, Kornberg RD. Structure determination of a water-soluble 144-gold atom particle at atomic resolution by aberration-corrected electron microscopy. *ACS Nano*. 2017;11:11866–11871.
122. Collins CB, Tofanelli MA, Crook MF, Phillips BD, Ackerson CJ. Practical stability of $Au_{25}(SR)_{18}-1/0/+1$. *RSC Adv*. 2017;7:45061–45065.
123. Hotze EM, Phenrat T, Lowry GV. Nanoparticle aggregation: challenges to understanding transport and reactivity in the environment. *J Environ Qual*. 2010;39:1909–1924.
124. Yuan X, Goswami N, Mathews I, Yu Y, Xie J. Enhancing stability through ligand-shell engineering: a case study with $Au_{25}(SR)_{18}$ nanoclusters. *Nano Res*. 2015;8:3488–3495.
125. Ghosh A, Pradeep T, Chakrabarti J. Coalescence of atomically precise clusters on graphenic surfaces. *J Phys Chem C*. 2014;118:13959–13964.
126. Higaki T, Zeng C, Chen Y, Hussain E, Jin R. Controlling the crystalline phases (FCC, HCP and BCC) of thiolate-protected gold nanoclusters by ligand-based strategies. *CrystEngComm*. 2016;18:6979–6986.
127. Das A, Li T, Nobusada K, Zeng C, Rosi NL, Jin R. Nonsuperatomic $[Au_{23}(SC_6H_{11})_{16}]-$ nanocluster featuring bipyramidal Au_{15} kernel and trimeric $Au_3(SR)_4$ motif. *J Am Chem Soc*. 2013;135:18264–18267.
128. Kurashige W, Yamaguchi M, Nobusada K, Negishi Y. Ligand-induced stability of gold nanoclusters: thiolate versus selenolate. *J Phys Chem Lett*. 2012;3:2649–2652.
129. Zeng C, Chen Y, Li G, Jin R. Magic size $Au_{64}(S\text{-}c\text{-}C_6H_{11})_{32}$ nanocluster protected by cyclohexanethiolate. *Chem Mater*. 2014;26:2635–2641.
130. Zeng C, Chen Y, Das A, Jin R. Transformation chemistry of gold nanoclusters: from one stable size to another. *J Phys Chem Lett*. 2015;6:2976–2986.
131. Jin R, Zeng C, Zhou M, Chen Y. Atomically precise colloidal metal nanoclusters and nanoparticles: fundamentals and opportunities. *Chem Rev*. 2016;116:10346–10413.
132. Rambukwella M, Sakthivel NA, Delcamp JH, Sementa L, Fortunelli A, Dass A. Ligand structure determines nanoparticles' atomic structure, metal-ligand interface and properties. *Front Chem*. 2018;6:330.
133. Zeng C, Liu C, Pei Y, Jin R. Thiol ligand-induced transformation of $Au_{38}(SC_2H_4Ph)_{24}$ to $Au_{36}(SPh\text{-}t\text{-}Bu)_{24}$. *ACS Nano*. 2013;7:6138–6145.

134. Chen Y, Zeng C, Liu C, et al. Crystal structure of barrel-shaped chiral Au_{130}(p-MBT)$_{50}$ nanocluster. *J Am Chem Soc*. 2015;137:10076–10079.
135. Zeng C, Chen Y, Kirschbaum K, Appavoo K, Sfeir MY, Jin R. Structural patterns at all scales in a nonmetallic chiral $Au_{133}(SR)_{52}$nanoparticle. *Sci Adv*. 2015;1.
136. Templeton AC, Chen S, Gross SM, Murray RW. Water-soluble, isolable gold clusters protected by tiopronin and coenzyme A monolayers. *Langmuir*. 1999;15:66–76.
137. Krommenhoek PJ, Wang J, Hentz N, et al. Bulky adamantanethiolate and cyclohexanethiolate ligands favor smaller gold nanoparticles with altered discrete sizes. *ACS Nano*. 2012;6:4903–4911.
138. Dameron AA, Charles LF, Weiss PS. Structures and displacement of 1-adamantanethiol self-assembled monolayers on Au{111}. *J Am Chem Soc*. 2005;127:8697–8704.
139. Shibu ES, Muhammed MAH, Tsukuda T, Pradeep T. Ligand exchange of $Au_{25}SG_{18}$ leading to functionalized gold clusters: spectroscopy, kinetics, and luminescence. *J Phys Chem C*. 2008;112:12168–12176.
140. Miles DT, Murray RW. Temperature-dependent quantized double layer charging of monolayer-protected gold clusters. *Anal Chem*. 2003;75:1251–1257.
141. Devadas MS, Bairu S, Qian H, Sinn E, Jin R, Ramakrishna G. Temperature-dependent optical absorption properties of monolayer-protected Au_{25} and Au_{38} clusters. *J Phys Chem Lett*. 2011;2:2752–2758.
142. Qin Z, Zhang J, Wan C, et al. Atomically precise nanoclusters with reversible isomeric transformation for rotary nanomotors. *Nat Commun*. 2020;11:6019.
143. Bauld R, Hesari M, Workentin MS, Fanchini G. Thermal stability of Au_{25} − molecular precursors and nucleation of gold nanoparticles in thermosetting polyimide thin films. *Appl Phys Lett*. 2012;101.
144. Tofanelli MA, Ackerson CJ. Superatom electron configuration predicts thermal stability of $Au_{25}(SR)_{18}$ nanoclusters. *J Am Chem Soc*. 2012;134:16937–16940.
145. Zhu Y, Qian H, Jin R. An atomic-level strategy for unraveling gold nanocatalysis from the perspective of Aun(SR)m nanoclusters. *Chem –Eur J*. 2010;16:11455–11462.
146. Remya KP, Udayabhaskararao T, Pradeep T. Low-temperature thermal dissociation of Ag quantum clusters in solution and formation of monodisperse Ag_2S nanoparticles. *J Phys Chem C*. 2012;116:26019–26026.
147. Kumar S, Jin R. Water-soluble $Au_{25}(Capt)_{18}$ nanoclusters: synthesis, thermal stability, and optical properties. *Nanoscale*. 2012;4:4222–4227.
148. Bhat S, Narayanan RP, Baksi A, et al. Detection of $[Au_{25}(PET)_{18}(O_2)n]-$ (n = 1, 2, 3) species by mass spectrometry. *J Phys Chem C*. 2018;122:19455–19462.
149. Chen Y-S, Kamat PV. Glutathione-capped gold nanoclusters as photosensitizers. Visible light-induced hydrogen generation in neutral water. *J Am Chem Soc*. 2014;136:6075–6082.
150. Le Guével X, Trouillet V, Spies C, et al. High photostability and enhanced fluorescence of gold nanoclusters by silver doping. *Nanoscale*. 2012;4:7624–7631.
151. Weng B, Lu K-Q, Tang Z, Chen HM, Xu Y-J. Stabilizing ultrasmall Au clusters for enhanced photoredox catalysis. *Nat Commun*. 2018;9:1543.
152. Natarajan G, Mathew A, Negishi Y, Whetten RL, Pradeep T. A unified framework for understanding the structure and modifications of atomically precise monolayer protected gold clusters. *J Phys Chem C*. 2015;119:27768–27785.
153. Knoppe S. On the Stereochemistry of Atomically Defined Gold Clusters*:* Synthesis, Size-Selection and Stereochemical Characterization of Thiolate-Protected Gold Clusters Ph.D. Thesis; 2012.
154. Jiang W, Bai Y, Li Q, et al. Steric and Electrostatic Control of the pH-Regulated Interconversion of Au16(SR)12 and Au18(SR)14 (SR: Deprotonated Captopril). *Inorg Chem*. 2020;59(8):5394–5404.

CHAPTER

16

Alloy nanoclusters

Esma Khatun[a] *and Thalappil Pradeep*[b]

[a] Department of Chemistry, DST Unit of Nanoscience (DST UNS) and Thematic Unit of Excellence (TUE), Indian Institute of Technology Madras, Chennai, India
[b] Deepak Parekh Institute Chair Professor and Professor of Chemistry, Department of Chemistry, Indian Institute of Technology Madras, Chennai, India

16.1 Introduction

16.1.1 General introduction of alloy

Alloys are mixtures of different metals or metals and nonmetals. Alloys are stronger than the pure metals, for example, steel is stronger than pure iron. This is due to the close-packed layer arrangements of atoms in pure metal which can slide over each other in the presence of an external force. Whereas in an alloy, different sized metals distort the regular structure and this makes the layers of atoms difficult to slide over each other as shown in Fig. 16.1.

16.1.2 Alloy nanotechnology from the ab initio perspective

The importance of metals and their alloys was understood in very ancient time. Prehistoric man used six metals; Au, Ag, Cu, Sn, Pd, and Fe. The first alloy was Bronze which was invented by the Sumerians in around 3000 BC. Bronze is mainly composed of Cu and Sn and it was used for making tools and weapons. This first age of material civilization is known as the Bronze Age. Around the same time brass was made by mixing of Cu with Zn. In 16th century BC, Persians invented carbon steel marking the beginning of the Iron Age and is used even today. Although Ag and Au were known then, these were mostly used for aesthetic purposes owing to their softness. Later, naturally occurring alloy of gold and silver, known as electrum was discovered and used as coinage metal. The ancient man controlled the number and configuration of nanocrystalline elements of copper. However, the term nanotechnology was not used then. The famous Lycurgus cup was invented by Roman glass workers in the fourth century AD which was a mixture of nanometer-sized Au, Ag, and Cu atoms. The Lycurgus cup attracted researchers due to its unique optical property. It shows three different colors, red, purple, and green. The red color is observed due to the absorption of light (~520 nm) by the smaller gold particles. The purple color is seen due to the absorption of light by the larger gold particles and the green color appears due to the scattering of light by colloidal dispersions of

Atomically Precise Metal Nanoclusters.
DOI: https://doi.org/10.1016/B978-0-323-90879-5.00012-3

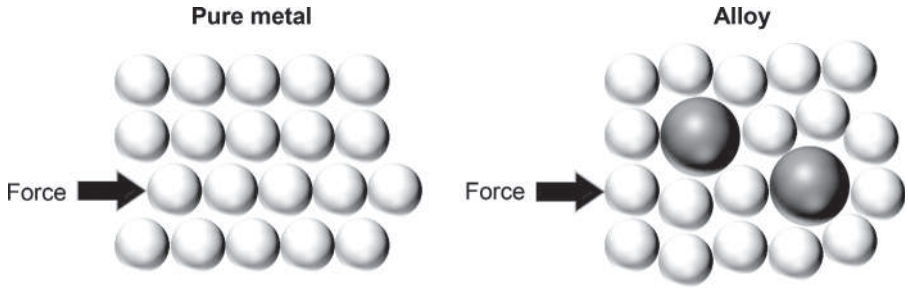

FIGURE 16.1 Schematic representation of atomic structures of a pure metal and an metal alloy which demonstrate why alloy is stronger than pure metal.

silver particles with size >40 nm. It is recognized as the oldest synthetic alloy nanocomposite, however, the scientific investigation did not begin until Michael Faraday's work in the mid-1850s. He first discovered that the ruby colored gold solution contains finely divided particles of gold. Since then the concept of nanotechnology started to flourish.

16.1.3 Alloy nanoparticles and nanoclusters

Multimetallic alloy NPs have gained immense attention in last two decades due to their wide range of applications. Their physical and chemical properties are highly dependent on their size, shape, and composition. Thus, depending on the size, shape, and composition, bimetallic alloy nanomaterials can be grouped into several types; (A) random alloy, (B) intermetallic, (C) subcluster, (D) core–shell, (E) multi shell–core, and (F) multi core–shell as shown in Fig. 16.2.[1]

Subnanometer sized atomically precise NPs are known as NCs. They are composed of various metal atoms and stabilized by different ligands. Higher surface to volume ratio and well-defined optical features differentiate them from NPs. They are represented by the number of metal atoms and ligand molecules present such as $Au_{25}(SR)_{18}$, $Ag_{25}(SR)_{18}$, etc., where –SR denotes thiolate ligand. Since last decade, the availability of single crystal X-ray structures of these NCs has drawn great attention from researchers as it helps to relate their properties with their structures. Alloying enriches physicochemical properties of NCs such as stability, luminescence, catalytic activity, chirality, etc. (see Section 16.4). These properties are strongly dependent on their structures, compositions, doping sites, and nature of the dopants. The compositions of alloy NCs are understood well by electrospray ionization mass spectrometry (ESI MS), the detailed description of what is given in Chapter 10. While the structures of these alloy NCs are determined by single crystal X-ray diffraction (explained in Section 16.3).

Depending on the doping sites of foreign metals, they can be categorized into three groups: (1) central-doped NCs such as $AuAg_{24}(2,4\text{-DMBT})_{18}$, where dopant Au atom occupies the central position,[3] (2) doping at icosahedral vertices such as $Au_{12}Ag_{32}(4\text{-FTP})_{30}$, where Au atoms occupy 12 vertex positions of the icosahedral core,[4] and (3) doping at outer shell such as $Cu_{12}Ag_{17}(1,3\text{-BDT})_{12}(PPh_3)_4$, where Cu atoms are doped at the outer staples.[5] The nature of dopants plays an important role in deciding the doping sites in alloy NCs. Pt, Pd, Ni, Cd prefer to occupy the central position while Ag, Au can occupy the central, vertex as well as

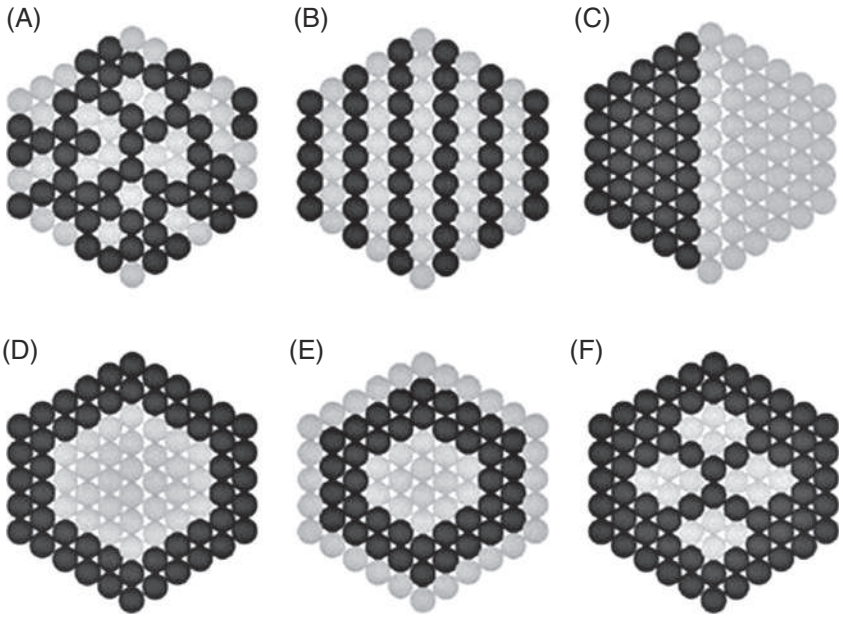

FIGURE 16.2 Pictorial representation of various bimetallic alloy NPs. Reprinted from ref.[1] Copyright 2020 Arora, Thangavelu, and Karanikolos.

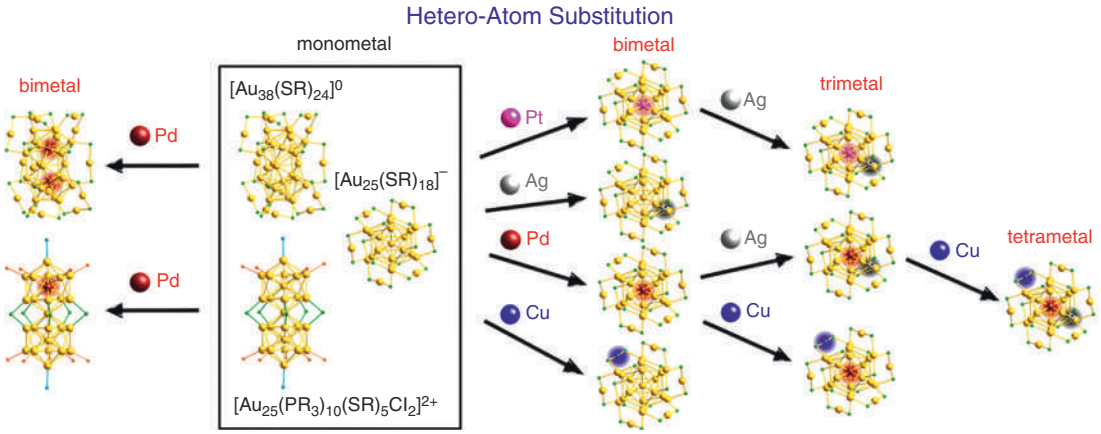

FIGURE 16.3 Schematic representation of possible dopant sites of different metals. Structures of spherical and rod-shaped NCs are shown here as model structure. Reprinted from ref.[2] Copyright 2018 American Chemical Society.

outer staple positions. Cu atom prefers to be in the outer staples. The doping site preferences of different metals are illustrated in Fig. 16.3 with the examples of two NCs having mono- and bi-icosahedral structures. By proper combination of different metals, several tri- and tetrametallic alloy NCs have been prepared. Although the number of tri- and tetrametallic NCs is

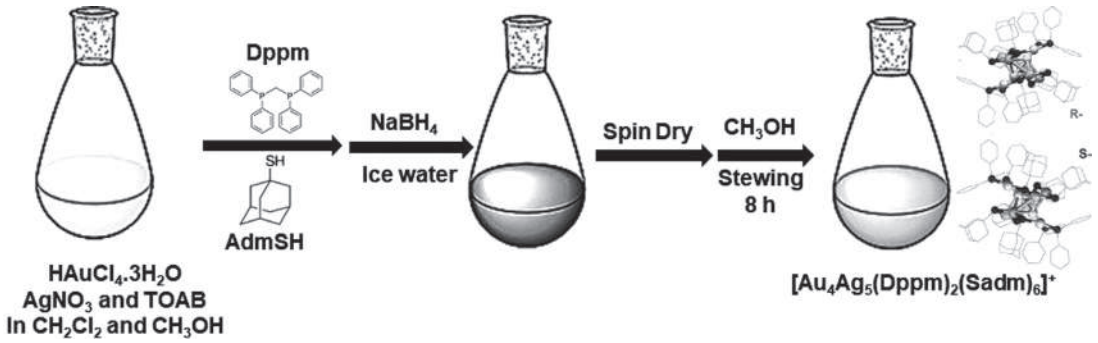

FIGURE 16.4 Schematic synthetic pathway of $[Au_4Ag_5(Dppm)_2(SAdm)_6]^+$. Reprinted from ref.[6] Copyright 2018 John Wiley and Sons.

less than the bimetallic NCs, this method enlighten the path to create multimetallic alloy NCs leading to high entropy alloy NCs.

16.2 Various synthetic methodologies

As the atomic precision is one of the most important factors to control various properties of NCs, their atom by atom designing is crucial. A large varities of NCs with precise number of atoms are successfully synthesized via some specific synthetic routes. Metals such as Au, Ag, Cu, Pt, Pd, Ir, etc. and ligands such as various types of thiols, phosphines, alkynyls, etc. are used to prepare NCs of exciting properties. The detailed synthetic methodologies to prepare homometallic NCs are given in Chapter 08. Here, different synthetic pathways of heterometallic alloy NCs, their opportunities and challenges are described briefly.

16.2.1 Co-reduction

Co-reduction of metal atoms is the earliest known and simplest method to prepare alloy NCs. Most of the alloy NCs are successfully synthesized by this direct in situ reduction process. However, the major disadvantage of this technique is poor control on their shapes and sizes. In this methodology, metal precursors are mixed with suitable protecting ligands and then the metal–ligand complexes are reduced using appropriate reducing agents. The synthetic process of $[Au_4Ag_5(Dppm)_2(SAdm)_6]^+$ (Au_4Ag_5) is presented schematically in Fig. 16.4.[6] To prepare Au_4Ag_5, $HAuCl_4$ and $AgNO_3$ metal precursors were mixed in a solvent mixture of methanol and DCM (DCM = dichloromethane). Then, tetraoctyl ammonium bromide (TOAB) was added to the mixture followed by the addition of protecting ligands, Dppm and HSAdm. In the next step, $NaBH_4$ solution in ice-cold water was used for the reduction of metal complexes. The reaction mixture was kept at room temperature for the complete formation of bright red colored Au_4Ag_5. In some synthesis, temperature control is highly needed as in the case of $NiAg_{24}$(2,4-DMBT)$_{18}$ which requires ice-cold temperature to be maintained throughout the reaction.[7]

The nature of metal precursor plays a crucial role in determining the composition and structures of NCs. Various metal salts such as $AgNO_3$, $HAuCl_4$, $AuPPh_3Cl$, K_2PtCl_4, $Pd(CH_3COO)_2$, $PdCl_2$, $Cu(CH_3COO)_2$, CuI, etc. are used during co-reduction synthesis. It was observed that the use of $AgSbF_6$ precursor resulted in the formation of cationic $[Au_{80}Ag_{30}(C{\equiv}CPh)_{42}Cl_9]Cl$ while, neutral $Au_{57}Ag_{53}(C{\equiv}CPh)_{40}Cl_{12}$ was formed when $AgC{\equiv}CPh$ was used.[8,9] Although the total number of metal atoms is same in both NCs, their compositions and structures are different. Both NCs have shell-by-shell arrangement but different architectures; $Au_{57}Ag_{53}$ adopts $Au_2M_3@Au_{34}@Ag_{51}@Au_{20}$ framework and $Au_{80}Ag_{30}$ has $Au_6@Au_{35}@Ag_{30}Au_{18}@Au_{21}$ arrangement. In the case of in situ synthesis of $Cu_{12}Ag_{17}(BDT)_{12}(PPh_3)_4$, copper(II) acetylacetonate ($Cu(C_5H_7O_2)_2$) salt is needed exclusively.[5] Several phosphine-protected bimetallic NCs such as $[(PPh_3)_{12}Au_{13}Ag_{12}Cl_6]^{m+}$, $[(Ph_3P)_{l0}Au_{13}Ag_{12}Br_8](PF_6)$, $[(p\text{-}Tol_3P)_{12}Au_{18}Ag_{20}Cl_{14}]$, $(Ph_3P)_{12}Au_{22}Ag_{24}Cl_{10}$, etc. were synthesized by co-reduction method during 1984–1992.[10–13] $AuPPh_3X$ and $[(Ph_3P)AgX]_4$ (X = Cl, Br) were used as metal precursors for the preparation of these NCs. Then in 1993, phosphine stabilized trimetallic $[MAu_{12}Ag_{12}(PPh_3)_{10}Cl_7]^+$ (M = Pt, Ni) NCs were synthesized. A large number of thiolate-protected alloy NCs were made among which $MAu_{24}(SR)_{18}$ and $MAg_{24}(SR)_{18}$ (M = Pd/Pt/Ni) are mostly studied in terms of their structures and properties.[7,14–17] Alloy nanoclusters with similar sized metal atoms such as $Ag_xAu_{25-x}(SR)_{18}$, $Cu_xAu_{25-x}(SR)_{18}$, $Au_xAg_{25-x}(SR)_{18}$, $Au_xAg_{29-x}(BDT)_{12}(PPh_3)_4$, $Au_xAg_{44-x}(SR)_{30}$, etc., were successfully made.[3,4,18–21] In these NCs, the number of doped metal atoms depends on the molar ratio of precursor salts. The use of 10% $AuPPh_3Cl$ against $AgNO_3$ resulted in the formation of $AuAg_{28}$ as the major product and the number of doped Au atoms increased with the increasing percentage of $AuPPh_3Cl$.[20] Smaller NCs such as $[Au_8M(PPh_3)_8](NO_3)_2$ (M = Pd/Pt) were synthesized using $Pd(PPh_3)_4$/$Pt(PPh_3)_3$ and $AuPPh_3NO_3$ precursors.[22] Mostly $NaBH_4$ is used as reducing agent, however, CO and H_2 are also used in some synthesis. For example, $[HPtAu_7(PPh_3)_8(NO_3)_2$ was prepared by bubbling H_2 through a THF solution of $AuPPh_3NO_3$ and $Pt(PPh_3)_3$.[23] $(PPh_3)_2CuBH_4$ was used as reducing agent during the preparation of bimetallic $AuCu_{14}(SR)_{12}(PPh_3)_6$, $Au_9Cu_2(PPh_3)_8Cl_2$, and $Ag_{25}Cu_4(PhC{\equiv}C)_{12}(PPh_3)_{12}Cl_6H_8$ NCs.[24]

16.2.2 Metal exchange

Incorporation of hetero-metal atoms in an already synthesized NC is an effective method to prepare alloy NCs. The alloy NCs, composed of metal atoms with larger difference in their redox potentials, are difficult to prepare by co-reduction method. This drawback of in situ reduction process can be overcome in metal exchange process. Most often, the number of constituent atoms of the metal core does not change during metal exchange. As a result, this reaction allows some of the atoms in a cluster to be replaced with other elements while preserving the original geometry and number of constituent atoms. For example, trimetallic $M_1Ag_xAu_{24-x}(SR)_{18}$ (M = Cd/Hg) were synthesized by two-step metal exchange method.[25] At first, bimetallic $Ag_xAu_{25-x}(SR)_{18}$ were prepared by the reaction between pure $Au_{25}(SR)_{18}$ and $Ag^{(I)}SR$ complex. Later, the formed bimetallic NC was reacted with $M^{(II)}SR$ (M = Cd/Hg) complex to make trimetallic $M_1Ag_xAu_{24-x}(SR)_{18}$ (M = Cd/Hg). Also, Negishi *et al.* synthesized $MAg_4Au_{20}(SR)_{18}$ by reacting $MAu_{24}(SR)_{18}$ with AgSR (M = Pd/Pt) complexes.[26] Precise doping of single Au atom in $Ag_{25}(SR)_{18}$ was observed during metal exchange process while a mixture of bimetallic NCs, $Au_xAg_{24-x}(SR)_{18}$ where x = 1–8, were obtained

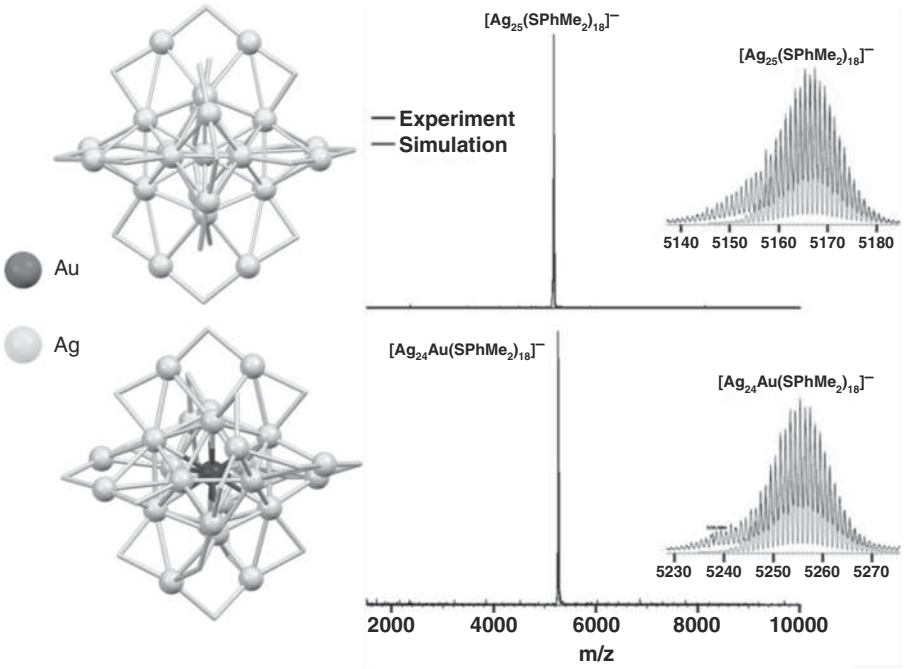

FIGURE 16.5 Lower panel shows ESI MS of $AuAg_{24}(SR)_{18}$ synthesized by metal exchange process from $Ag_{25}(SR)_{18}$ whose ESI MS is given in upper panel. Insets show the theoretical and experimental isotopic distribution matching for both the NCs and their structures. Reprinted from ref.[3] Copyright 2015 John Wiley and Sons.

during co-reduction process.[3] The atomically precise $AuAg_{24}(SR)_{18}$ was prepared by mixing of $AuPPh_3Cl$ with $Ag_{25}(SR)_{18}$. The formation of single product was confirmed by ESI MS measurement which showed only one peak corresponded to $[AuAg_{24}(SR)_{18}]^-$, as depicted in Fig. 16.5. The green colored $AuAg_{24}(SR)_{18}$ was then easily crystallized due to its purity which was not possible for the mixture of bimetallic NCs. Although the number of dopants in alloy NCs can be controlled during metal exchange, it is difficult for the metal atoms of similar size. Hence, the doping of Ag and Cu atoms in Au NCs is not easy to control. For example, $Ag_xAu_{25-x}(SR)_{18}$ (x = 1-24) and $Cu_xAu_{25-x}(SR)_{18}$ (x = 1-6) were formed by the reaction of $Au_{25}(SR)_{18}$ with Ag(SR) and $Cu(SR)_2$, respectively. However, the polydispersed NCs can be converted to monodispersed NCs by targeted metal exchange as in the case of $Pt_1Ag_{16-x}Cu_{12+x}(SR)_{18}(PPh_3)_4$.[27] The addition of a large amount of $AgPPh_3NO_3$ led to the formation of monodispersed $Pt_1Ag_{16}Cu_{12}(SR)_{18}(PPh_3)_4$ while the addition of excess $Cu(PPh_3)_2Cl$ generated $Pt_1Ag_{12}Cu_{16}(SR)_{18}(PPh_3)_4$. Similarly, by targeted metal exchange using AgBr in $Au_{18}(Dppm)_6Br_4$, bimetallic $Ag_xAu_{18-x}(Dppm)_6Br_4$ was obtained. In most of the cases, structure-retained metal exchange requires the presence of same ligand in NCs and metal complexes. Metal exchange reactions involving metal complexes with different ligands resulted in structural changes as demonstrated by Kang *et al.* They observed that the reaction of $PtAg_{24}(SR)_{18}$ with AuSR complex resulted the formation of structure-preserved trimetallic $PtAu_xAg_{24-x}(SR)_{18}$. On the other hand, the use of $Au(PPh_3)Br$ led to the synthesis

of rod-shaped trimetallic $Pt_2Au_{10}Ag_{13}(PPh_3)_{10}Br_7$ unlike spherical $PtAg_{24}(SR)_{18}$.[28] The metal exchange strategy of doping heteroatom in templated NCs using metal complexes and metal salts follows metal displacement reaction mechanism based on standard electrode potentials. These mechanisms can be categorized broadly in two reduction pathways: (1) galvanic exchange and (2) antigalvanic exchange.

16.2.2.1 *Galvanic exchange*

According to the classic galvanic theory, a metal ion in solution with a higher reduction potential reduces and replaces a metal atom in a material, which then joins the solution. Depending on the standard redox potential, the metal activity sequence is Fe (−0.77 V) > Cd (−0.40 V) >Co (−0.28 V) > Ni (−0.25 V) > Cu (+0.34 V) > Hg (+0.79 V) > Ag (+0.80 V) > Pd (+0.95 V) > Pt (+1.2 V) > Au (+1.50 V). Doping of Au in $Ag_{50}(Dppm)_6(SR)_{30}$ by the addition of Au(I)SR complex to make bimetallic $Au_xAg_{50-x}(Dppm)_6(SR)_{30}$ (x = 4–7) follow galvanic reduction process.[29] Here, the redox potential of Au (+1.50 V) is higher than that of Ag (+0.80 V) and hence, Au(I) easily replaces Ag(0) of NC, after reducing it to Ag(I). Similarly, $AuAg_{19}\{S_2P(O^nPr)_2\}_{12}$ forms from $Ag_{20}\{S_2P(O^nPr)_2\}_{12}$ template via galvanic exchange method.[30] To construct silver-rich multimetallic alloy NCs, various metal atoms were incorporated into Ag NCs using a galvanic exchange process. Bootharaju *et al.* introduced Au atoms in $PtAg_{24}(SR)_{18}$ using $AuPPh_3Cl$ salt to make trimetallic $PtAu_xAg_{24-x}(SR)_{18}$.[31]

Although galvanic reduction route has emerged as a highly successful metal exchange method of creating Ag-rich alloy NCs, the doping of Ag and Cu in Au NCs via metal exchange method goes against the classic galvanic theory. This reduction process is now known as antigalvanic reduction which is discussed below.

16.2.2.2 *Antigalvanic exchange*

The alloys of $Au_{25}(SR)_{18}$ are well studied due to their exciting physicochemical properties which has broadened their applications. The majority of the alloying or doping in $Au_{25}(SR)_{18}$ was done with Ag and Cu atoms. In 2012, Z. Wu performed thorough experiments on $Au_{25}(SR)_{18}$ and larger sized NPs with Ag and Cu ions and found that Au and Ag NPs below 3 nm exhibit a very different redox activity than the bulk.[32] In this size regime, metal NCs or NPs can reduce metal ions of lower reduction potential. This led Z. Wu to change the metal activity sequence to Fe > Cd > Co > Ni > Pb > [Au NCs] > Cu > Hg > Ag > Pd > Pt > Au and proposed the antigalvanic reduction. Zhu *et al.* showed doping of Ag and Cu in templated $Au_{25}(SR)_{18}$ NCs using M(I)SR (M = Ag/Cu) complexes which created bimetallic $M_xAu_{25-x}(SR)_{18}$ (M = Ag/Cu).[33] They also incorporated Cd and Hg into $Au_{25}(SR)_{18}$ to form $M_1Au_{24}(SR)_{18}$ (M = Cd/Hg) by M(II)SR. However, Yao *et al.* showed antigalvanic reduction reaction of $Cd(CH_3COO)_2$ with $Au_{25}(SR)_{18}$ led to the formation of $Au_{19}Cd_3(SR^2)_{18}$.[34] Doping of Ag and Cu in $Ag_{38}(SR)_{24}$, $Au_{36}(SR)_{24}$, and $Au_{144}(2\text{-PET})_{60}$ were also carried out.[18,35,36] The targeted metal exchange of $Pt_1Ag_{16-x}Cu_{12+x}(SR)_{18}(PPh_3)_4$ to $PtAg_{12}Cu_{16}(SR)_{18}(PPh_3)_4$ using $Cu(PPh_3)_2Cl$ occurred via antigalvanic exchange mechanism. Although Ag, Cu, Cd, Hg atoms were inserted successfully in Au NCs, the doping of Ni, Pd, and Pt in $Au_{25}(SR)_{18}$ was not obtained via this process.

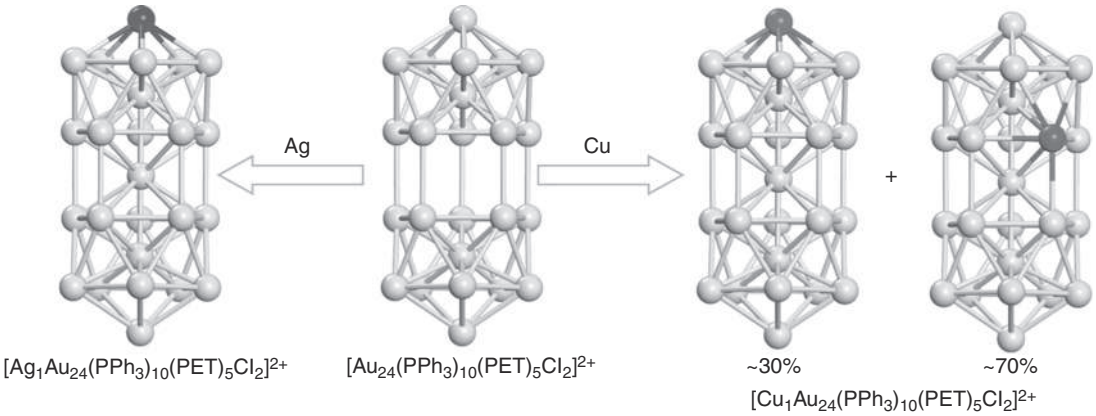

FIGURE 16.6 Deposition/addition of Ag/Cu atoms in $Au_{24}(PPh_3)_{10}(SC_2H_4Ph)_5Cl_2$ to form bimetallic Ag/$CuAu_{24}(PPh_3)_{10}(SC_2H_4Ph)_5Cl_2$. Reprinted from ref.[37] Copyright 2017 Springer Nature.

16.2.3 Metal deposition

One of the emerging alloying route is metal deposition, whereby foreign metal atoms are inserted into NCs. The composition of NCs is altered during this process, however, the structure of NCs remained unchanged after alloying. Wang *et al.* developed a new hollowing-and-refilling technique, in which a single Ag or Cu atom can easily fill a hole that has pre-formed inside the Au NCs. $Au_{24}(PPh_3)_{10}(SC_2H_4Ph)_5Cl_2$ composed of a hollow bi-icosahedral structure as shown in Fig. 16.6 which was transformed into a non-hollow bi-icosahedral $MAu_{24}(PPh_3)_{10}(SC_2H_4Ph)_5Cl_2$ (M = Ag/Cu) upon the addition of AgCl and CuCl.[37] The mechanism followed single atom shuttling which was driven by ligands and thermodynamics. During the hollowing process, the central Au atom squeezes the waist Au atom out of the NC and is trapped by excess PPh_3 in solution. Then, the surface ligands, Cl and SR, get attached to the Ag^+/ Cu^+ into the NC. Since AgCl has a stronger binding than AgSR, the Ag atom is doped at the apex of the NC, whereas since CuCl and CuSR have equal binding energies, the Cu atom is doped at both waist and apex positions. Similar metal shuttling is observed in $Au_2Ag_{25}(SR)_{18}$ which led to the formation of $AuAg_{24}(SR)_{18}$.[38] Here, two step atom diffusions were observed, involving self-metal exchange or intramolecular metal exchange in the first step, and metal stripping processes in the second step.

16.2.4 Ligand exchange

NCs with remarkable physicochemical properties can be synthesized by the reaction of an already synthesized metal NCs with foreign ligands. Such processes have been documented since 20 years back when Murray *et al.* used polydispersed $Au_n(SR)_m$ NCs to react with RSH.[39] Metal NCs can be converted to anothe NCs as a result of the reaction with foreign ligands. There are four types of conversions; (i) structure retained ligand exchange,[40] (ii) partial ligand exchange, (iii) ligand exchange leading to the change in the geometry of NCs without changing the composition, and (iv) ligand exchange-induced structural transformation (LEIST).

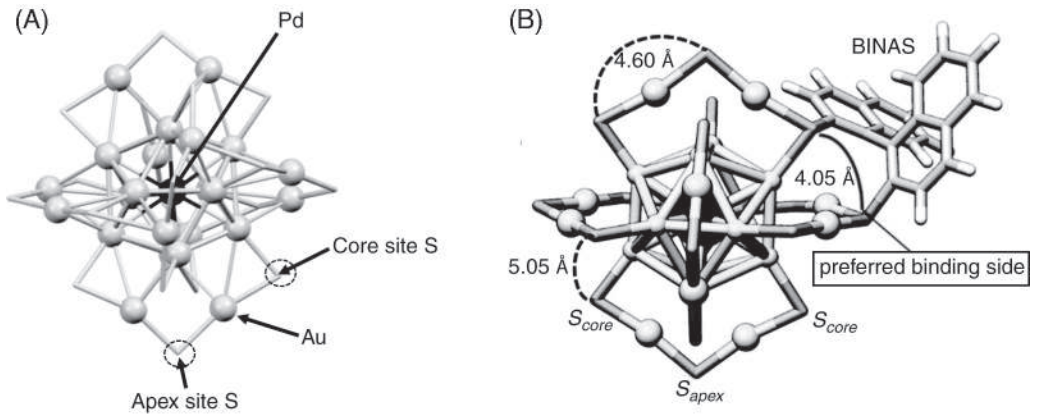

FIGURE 16.7 (A) Two sites of sulfur (S) in $PdAu_{24}(SR)_{18}$ shown here. The different reactivity of two different S atoms led partial ligand exchange. (B) Structure of the partial ligand exchanged $Au_{24}Pd(SC_2H_4Ph)_{16}$(BINAS) showing the binding sites of BINAS. Reprinted from ref.[46] Copyright 2017 American Chemical Society.

After the reaction with foreign ligands, some NCs undergo complete ligand exchange keeping the structure of precursor NCs preserved. Conversion of $Au_{24}Cd(SC_2H_4Ph)_{18}$ to $Au_{24}Cd(SCH_2Ph^tBu)_{18}$ in the presence of $HSCH_2Ph^tBu$ is a good example for this type of ligand exchange reaction.[41] The sole factor for the direction of ligand exchange reaction is the intrinsic stability of NCs. Also, it determines the possibility of complete ligand exchange.

Some of the NCs consist of heterogeneous ligand shell, wherein some of the sites on the ligand shell are inactive toward ligand exchange reaction, while others are comparatively reactive and participate in the exchange reaction. Such NCs undergo partial ligand exchange reactions. One such example is the partial ligand exchange of $Au_{24}Pd(SC_2H_4Ph)_{18}$ by $C_{12}H_{25}SH$, which led to the formation of structure retained $Au_{24}Pd(SC_2H_4Ph)_{18-x}(C_{12}H_{25}S)_x$ ($x = 1$–7).[42] $Au_{24}Pd(SC_2H_4Ph)_{18}$ composed of an icosahedral $Au_{12}Pd$ core surrounded by six $Au_2(SR)_3$ staples. Due to the symmetric structure, all $Au_2(SR)_3$ staples have identical environment. However, two kinds of thiolate ligands are present in the staple. One type of thiolate ligand (apex site) is connected to two staple Au atoms while, another type of thiolate ligand (core site) is bonded to one staple Au atom and one icosahedral Au atom (Fig. 16.7A). It was observed that the ligand exchange reactions started at the core site thiolate ligand. The exchange reaction followed an associative S_N2 like mechanism which was observed in the case of $Au_{25}(SR)_{18}$ and $Au_{38}(SR)_{24}$.[43,44] Partial ligand exchange was also observed during the reaction between $Au_{24}Pd(SC_2H_4Ph)_{18}$ and 1,10-binaphthalene-2,20-dithiol (H_2BINAS).[45,46] Two units of HSC_2H_4Ph ligands were replaced by one unit of BINAS resulting in the formation of $Au_{24}Pd(SC_2H_4Ph)_{18-2x}(BINAS)_x$. BINAS is attached to the core site of one staple and apex site of other. It is difficult to bind to the core and apex sites of same staple as shown in Fig. 16.7B. The structure of NCs produced after reaction remained unaltered.

The formation of isomeric structures after ligand exchange was observed by Jin *et al.* during the ligand exchange reaction of 4-tert-butylbenzenethiolate (TBBT) with $Au_{28}(CHT)_{20}$ (CHT = cyclohexanethiolate). To prepare isomeric alloy NCs, this ligand-induced isomerism

process was also used which helps in tailoring the performance of NCs. Conversion of $PtAg_{28}(SAdm)_{18}(PPh_3)_4$ to isomeric $PtAg_{28}(1,3\text{-BDT})_{12}(PPh_3)_4$ in the presence of 1,3-BDT is one such example.[47] Reversible conversion of $PtAg_{28}(SAdm)_{18}(PPh_3)_4$ to $PtAg_{28}(CHT)_{18}(PPh_3)_4$ is also a good example where structural transformation was observed keeping the composition unaltered.[48]

In addition to the structure, the composition and size of parent NCs can be changed during the ligand exchange reaction. The methodology of complete conversion of a NC system is generally known as ligand exchange-induced structural transformation (LEIST) and this term was introduced by Jin group. LEIST method is now widely used to make NCs with unprecedented properties. LEIST method was applied on $PtAg_{24}(DMBT)_{18}$ to make several new alloy NCs, such as, the addition of 1,3-BDT and PPh_3 yielded a more stable and strong red luminescent NC, $PtAg_{28}(BDT)_{12}(PPh_3)_4$.[7] After the reaction with $AuPPh_3Br$, bimetallic $PtAg_{24}(DMBT)_{18}$ converted to trimetallic $Pt_2Au_{10}Ag_{13}(DMBT)_{18}$.[28] Besides, the study of Kang *et al.* showed the formation of a highly luminescent $PtAg_{12}(Dppm)_5(DMBT)_2$ by the reaction between $PtAg_{24}(DMBT)_{18}$ and Dppm ligand.[49] They also found the transformation of $AgAu_{17}(CHT)_{14}$ in the presence of HSAdm yielded $AgAu_{16}(S\text{-}Adm)_{13}$. Luminescent bimetallic $[Au_4Cu_5(CHT)_6(Dppm)_2](BPh_4)$ was obtained by the reversible LEIST method starting from $[Au_4Cu_4(SAdm)_5(Dppm)_2]Br$.[50]

16.2.5 Interparticle reactions

Another efficient synthetic method is interparticle reaction, which is successfully used to obtain several bi- and trimetallic NCs. Intercluster reaction between a pure Ag NC, $Ag_{44}(SR)_{30}$ and a pure Au NC, $Au_{25}(SR)_{18}$ yielded a mixture of bimetallic NCs, $Ag_{44-x}Au_x(SR)_{30}$ and $Au_{25-x}Ag_x(SR)_{18}$.[51] Similarly, reaction between structurally analogous $Ag_{25}(DMBT)_{18}$ and $Au_{25}(PET)_{18}$ resulted in the formation of bimetallic $Ag_{25-x}Au_x(SR)_{18}$ ($x = 1$–24).[52] The details of these reactions and their mechanisms are given in Chapter 2. Au-doped bimetallic $Ag_{29-x}Au_x(1,3\text{-BDT})_{12}(PPh_3)_4$ ($x = 1$–13) were synthesized by intercluster reaction between $Ag_{29}(1,3\text{-BDT})_{12}(PPh_3)_4$ and $Au_{25}(PET)_{18}$.[7] Similarly, dithiol-protected $Ag_{51}(1,3\text{-BDT})_{19}(PPh_3)_3$ underwent metal exchange reaction in the presence of $Au_{25}(SR)_{18}$ to produce bimetallic $Ag_{51-x}Au_x(1,3\text{-BDT})_{19}(PPh_3)_3$.[53] Also, trimetallic $MAg_{28-x}Au_x(1,3\text{-BDT})_{12}(PPh_3)_4$ ($M = Pd/Pt/Ni$) ($x = 1$–12) were prepared via intercluster reactions between bimetallic $MAg_{28}(1,3\text{-BDT})_{12}(PPh_3)_4$ ($M = Pd/Pt/Ni$) and $Au_{25}(PET)_{18}$.[7] In these reactions, the metal exchange rate is highly dependent on the molar ratio of the precursor NCs. The highest rate was observed using 1:5 ratio of $MAg_{28}(1,3\text{-BDT})_{12}(PPh_3)_4$ ($M = Pd/Pt/Ni$) and $Au_{25}(PET)_{18}$. The time-dependent ESI MS of the reaction is shown in Fig. 16.8. This opens up the possibilities of making high-entropy alloy NCs through intercluster reaction.

Besides, NPs can react with NCs to create alloy NCs and this was first observed by Xia *et al.* They synthesized Cu-doped bimetallic $Au_{25-x}Cu_x(PET)_{18}$ by reacting $Au_{25}(PET)_{18}$ with Cu NPs. A similar observation of Ag doping in $Au_{25}(PET)_{18}$ NCs to form $Au_{25-x}Ag_x(PET)_{18}$ was made using polydispersed Ag NPs.[54] The extent of doping is largely dependent on the average size of Ag NPs. The number of doped Ag atoms was found to be inversely proportional to the average size of NPs, that is, reaction of NCs with smaller sized Ag NPs led to the incorporation of higher number of Ag atoms.

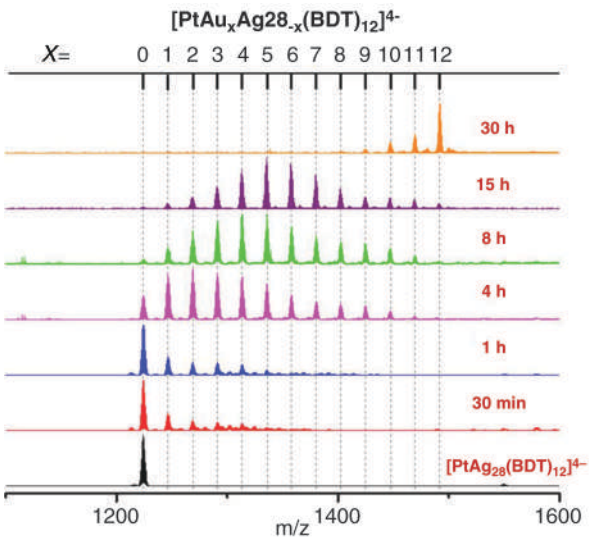

FIGURE 16.8 Time-dependent ESI MS of reaction between $PtAg_{28}(1,3\text{-}BDT)_{12}(PPh_3)_4$ and $Au_{25}(PET)_{18}$ leading to the formation of trimetallic $PtAg_{28-x}Au_x(1,3\text{-}BDT)_{12}(PPh_3)_4$. Reprinted from ref.[7] Copyright 2019 American Chemical Society.

16.2.6 Reaction of nanoclusters with bulk metal

In all of the above mentioned processes, various types of metal salts were used as precursor for heteroatom doping. In some study, metal NPs were also used as doping precursor, as mentioned in the above section. In 2019, Kazan *et al.* established a doping procedure wherein metal foils were used as precursor for doping reactions.[55] Ag, Cu, Cd foils were reacted with $Au_{25}(PET)_{18}$ and $Au_{38}(PET)_{24}$ NCs which led to the formation of bimetallic $Au_{25-x}Ag_x(PET)_{18}$, $Au_{25-x}Cu_x(PET)_{18}$, $Au_{38-x}Ag_x(PET)_{24}$, $Au_{38-x}Cu_x(PET)_{24}$, $Au_{24}Cd(PET)_{18}$, etc. The Ag foils pretreated with thiols showed higher reactivity than the untreated one. No doping reaction took place with untreated Cu and Cd foils. This study proved that the presence of prefunctionalized thiol is important as it helps to build metal ligand interface as shown in Fig. 16.9. Metal–ligand interface is thought to play a very crucial role in interparticle reactions. This observation provides important information about the reaction mechanism as well opens up opportunities of forming new heterometallic NCs.

16.3 Structures of alloy nanoclusters

The number and position of dopants have significant influence on the properties of alloy NCs. Although the precise number of dopants in alloy NCs can be identified by high resolution ESI MS, the distribution of heteroatoms can only be obtained from their crystal structures. Heteroatoms can be inserted into a monometallic NC keeping the structure of the parent cluster intact. This type of NCs is known as doped alloy NCs. However, there are many alloy NCs whose monometallic analogues are not known yet. To know whether an alloy NC is in the category of doped NC or not, we need to solve their crystal structures by X-ray crystallography. A plenty of crystal structures of alloy NCs are reported so far but the structural details of a few well-known alloy NCs are discussed here. In the absence of the diffractable single

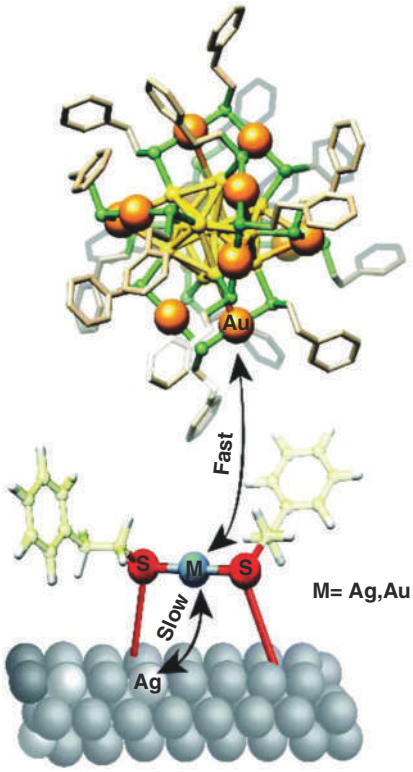

FIGURE 16.9 The reaction between prefactionalized Ag foil and $Au_{25}(PET)_{18}$ is shown schematically. Adapted with permission from ref.[55] Copyright 2019 Royal Society of Chemistry.

crystals, the structures can be determined with the help of computational study and tandem mass spectrometry. The details of these method of structural determination are discussed in Chapters 14 and 10.

16.3.1 Gold-rich alloys

Among Au NCs, $Au_{25}(SR)_{18}$ is the most studied one due to its easy synthesis, higher stability, easy functionalization, various photophysical properties and versatile applications. It is one of the earliest discovered NCs whose X-ray crystal structure was obtained. Researchers were eager to understand the effect of heteroatoms on the structure and properties of $Au_{25}(SR)_{18}$. The structural anatomy of $Au_{25}(SR)_{18}$ revealed that it consists of an Au_{13} icosahedral core which is protected by an outer shell made up of six $Au_2(SR)_3$ staples.[56,57] Kumara et al. obtained the X-ray crystal structure of $Au_{25-x}Ag_x(SR)_{18}$ ($x \sim 6$), where Ag atoms occupied the vertices of icosahedron (Fig. 16.10B).[58] Group 10 elements, that is, Pt/Pd replaces the central Au of icosahedral core to form Pt/Pd@Au_{12} kernel.[59] Similarly, single crystal structure unveiled that Cd atom form central-doped $Au_{25-x}Cd_x(SR)_{18}$ (Fig. 16.10A).[33] On the other hand, Cu atoms get incorporated in the outer staple motifs to make bimetallic NCs (Fig. 16.10C).[60] Ir atoms were incorporated in $Au_{25}(SR)_{18}$ to make bimetallic $Au_{22}Ir_3(SR)_{18}$. Although its crystal structure was not obtained, detailed density functional theory (DFT)

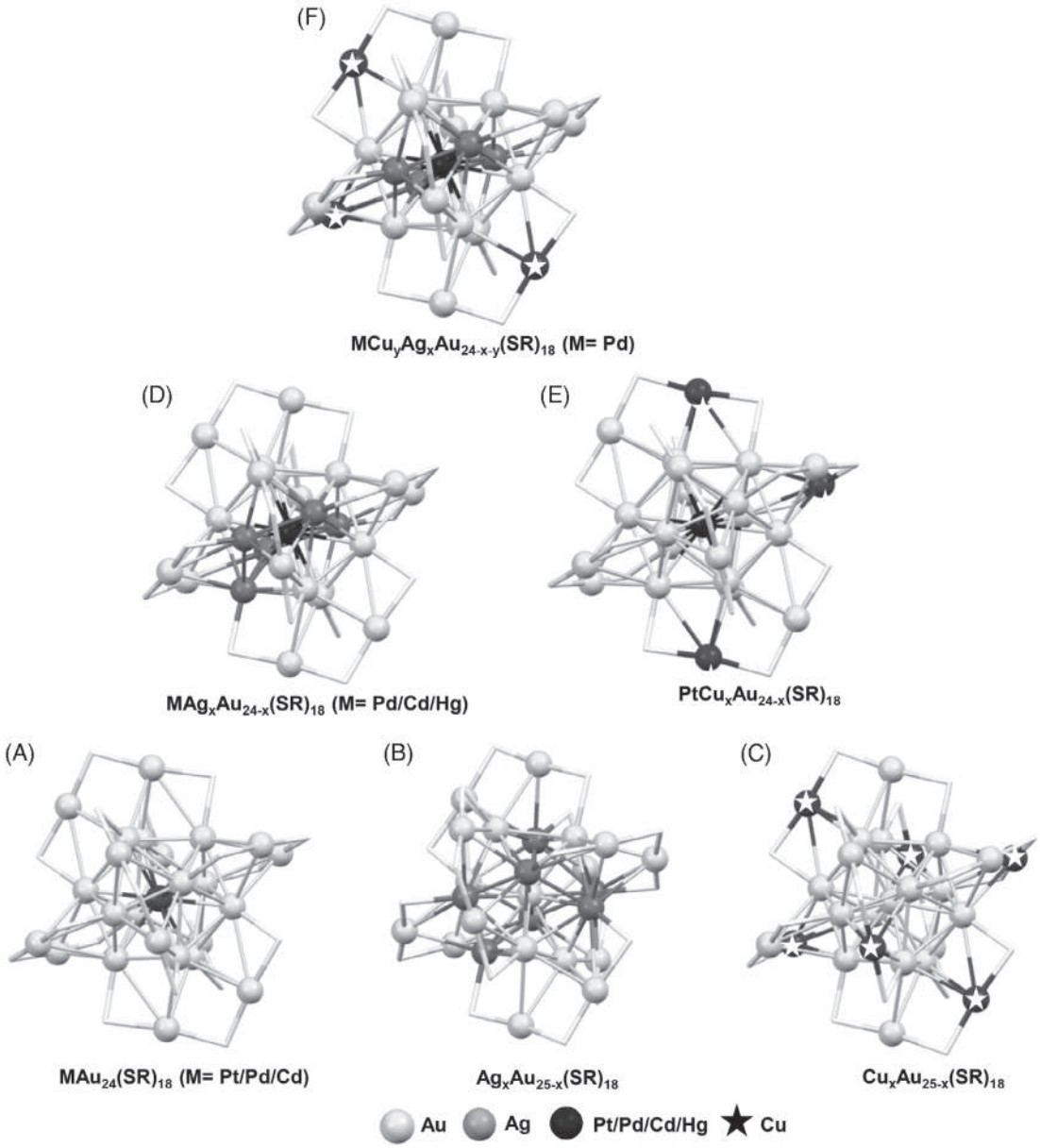

FIGURE 16.10 Geometric structures of thiolate-protected bi-, tri-, and tetrametallic alloy NCs of total 25 metal atoms having more Au atoms. (A–C) The crystal structures of bimetallic $MAu_{24}(SR)_{18}$ (M = Pt/Pd/Cd). (D) and (E) Present the structures of trimetallic $MAg_xAu_{24-x}(SR)_{18}$ (M = Pd/Pt/Cd/Hg) obtained from single crystal X-ray diffraction and theoretical studies and (F) denotes the structure of tetrametallic $PdCu_yAg_xAu_{24-x-y}(SR)_{18}$ estimated by EXAFS (extended X-ray absorption fine structure) study. Ligands are made in capped sticks and white colored so that different metal atoms can be seen unambiguously.

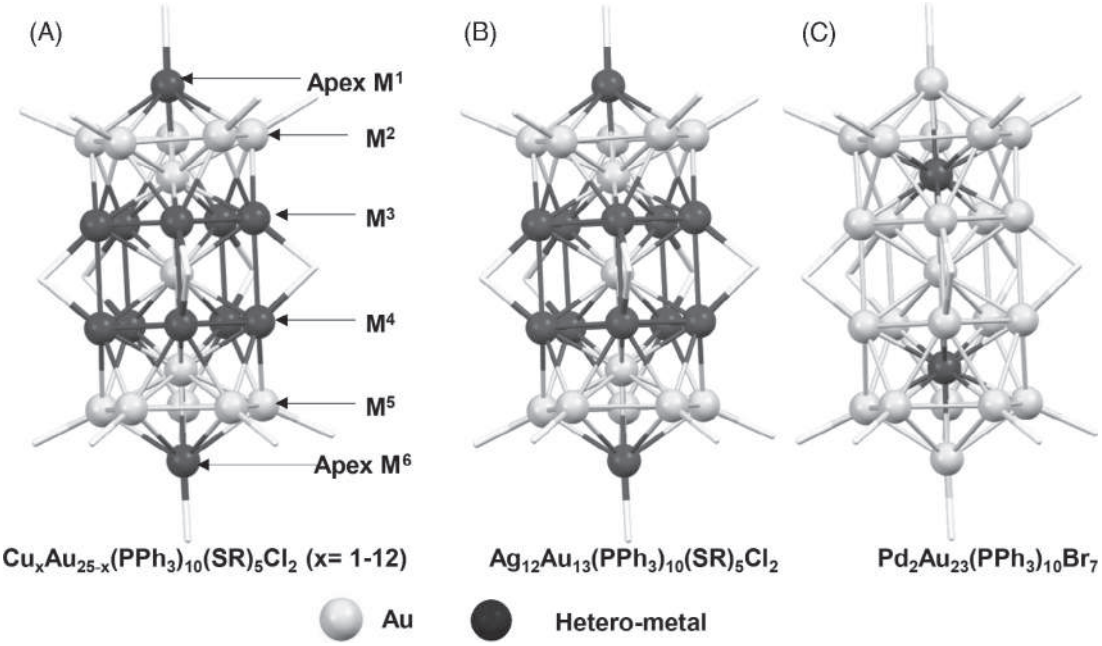

FIGURE 16.11 Geometric structures of rod-shaped bimetallic alloy NCs of total 25 metal atoms having more Au atoms. (A)–(C) denote structures of $Cu_xAu_{25-x}(PPh_3)_{10}(SR)_5Cl_2$, $Au_{13}Ag_{12}(PPh_3)_{10}(SR)_5Cl_7$ and $Pd_2Au_{23}(PPh_3)_{10}Br_7$. Ligands are drawn in capped sticks and white colored so that different metals atoms can be seen unambiguously.

calculation revealed that one Ir atom prefers to occupy the central position, and more than one Ir atoms occupy the icosahedral surface positions.[61]

Recently, Anderson *et al.* observed the formation of bimetallic $RhAu_{24}(SR)_{18}$ and characterized it using ESI MS. Due to its instability, the crystal structure was not obtained. However, according to the computational study, Rh atom is doped at the center of M_{13} core.[62] Using Ag atoms which can only substitute the Au atoms on the icosahedral surface and Cd/Hg which can only be placed in the center of the icosahedral core, trimetallic $M_1Ag_xAu_{24-x}(SR)_{18}$ (Cd/Hg) were prepared (Fig. 16.10D).[25] In a similar way, trimetallic $MAg_xAu_{24-x}(SR)_{18}$ (M = Pd/Pt) (Fig. 16.10D) and $PtCu_xAu_{24-x}(SR)_{18}$ (Fig. 16.10E) were prepared, where Pd/Pt atom replaced the central Au atom, Ag atoms occupied the icosahedral surface positions and Cu atoms were placed in the dimeric staple.[26,60] Using these four different types of metals which occupy four different positions in a NC, tetrametallic $PdCu_yAg_xAu_{24-x-y}(SR)_{18}$ was prepared (Fig. 16.10F) and the structure was investigated by EXAFS analysis.[63]

Contrary to the thiolate-protected $Au_{25}(SR)_{18}$, phosphine and thiol co-protected $Au_{25}(PPh_3)_{10}(SR)_5Cl_2$ exhibits a rod-shaped structure as shown in Fig. 16.11. The structure can be viewed as two vertex sharing icosahedral units whose apex/vertex metal atoms are bonded to Cl atoms. The two icosahedral units are clipped by five thiolate ligands (−SR). PPh_3 ligands occupy the top of the peripheral Au atoms. In this structure, four pentagonal layers are visible which are arranged in a staggered–eclipsed–staggered (M^2–M^3–M^4–M^5) fashion. In

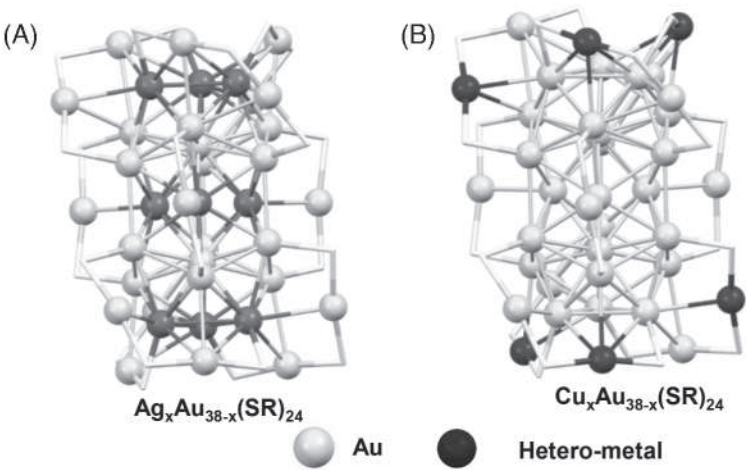

FIGURE 16.12 Geometric structures of bimetallic alloy NCs of total 38 metal atoms having more Au atoms. (A) and (B) denote structures of bimetallic $Ag_xAu_{38-x}(SR)_{18}$ and $Cu_xAu_{38-x}(SR)_{18}$. Ligands are drawn in capped sticks and white colored so that different metals atoms can be seen unambiguously.

the case of Cu-doped bimetallic $Cu_xAu_{25-x}(PPh_3)_{10}(SR)_5Cl_2$, the apex positions and M^3 and M^4 pentagonal layers are partially occupied by Au and Cu atoms (Fig. 16.11A).[64] Similarly, Ag atoms in bimetallic $Ag_xAu_{25-x}(PPh_3)_{10}(SR)_5Cl_2$, occupy M_1, M_3, and M_4 positions (Fig. 16.11B).[65] The center of bi-icosahedral kernel can be occupied randomly by Au and Ag atoms. At a higher Ag concentration, 13th Ag atom is doped and occupy the central position which significantly changed its photoluminescence property (described in Section 16.4.2). Crystal structure of hetero bi-icosahedral 25-atom NC, $PdAu_{24}(PPh_3)_{10}(SC_2H_4Ph)_5Cl_2$ was obtained in which the central atom of one icosahedral core was occupied by a Pd atom. Besides, all-phosphine-protected alloy NCs of 25 metal atoms exhibit rod-shaped structures. For example, $Pd_2Au_{23}(PPh_3)_{10}Br_7$ acquires similar structure to that of $Au_{25}(PPh_3)_{10}(SR)_5Cl_2$ (Fig. 16.11C).[66] Pd atoms are inserted in the center of icosahedral M_{13} kernel. Instead of –SR ligands, here, Br atoms act as the bridging ligand between two kernels. Apex Au atoms are also bonded to Br, and PPh_3 is attached to the peripheral Au atoms. Bimetallic $Au_{13}Ag_{12}(p\text{-}Tol_3P)_{10}Cl_7$ (p-Tol_3P = Tri(p-tolyl)phosphine) has similar structure as that of $Au_{13}Ag_{12}(PPh_3)_{10}(SR)_5Cl_7$.

Another well-studied NC is $Au_{38}(SR)_{24}$, due to its higher stability, interesting structure and chiral property. $Au_{38}(SR)_{24}$ consists of a bi-icosahedral Au_{23} core which is protected by three monomeric $Au(SR)_2$ and six dimeric $Au_2(SR)_3$ staples.[67] In bimetallic $Ag_xAu_{38-x}(SR)_{18}$, Ag atoms are doped at the surface of the bi-icosahedral core, preferentially at nine sites: (a) the two vertices, each with three atoms and a total of six atoms, and (b) the middle face-shared three-atom ring (see Fig. 16.12A).[68] In $Cu_xAu_{38-x}(SR)_{18}$, Cu atoms preferentially occupy the six outer dimeric staple motifs rather than the core (Fig. 16.12B).[69] Doping of two atoms of Pt/Pd in $Au_{38}(SR)_{24}$ was also observed by mass spectrometry. DFT calculation and EXAFS study indicated the occupation of Pt/Pd atoms at the center of two icosahedra.[70–72]

Soon after the synthesis and crystallization of bi-icosahedral $Au_{25}(PPh_3)_{10}(SR)_5Cl_2$, tri-icosahedral $Au_{37}(PPh_3)_{10}(SC_2H_4Ph)_{10}X_2$ (X = Cl/Br) was obtained.[73] Its core consists of a linear assembly of three M_{13} icosahedra which share the vertex metal atoms. Unlike

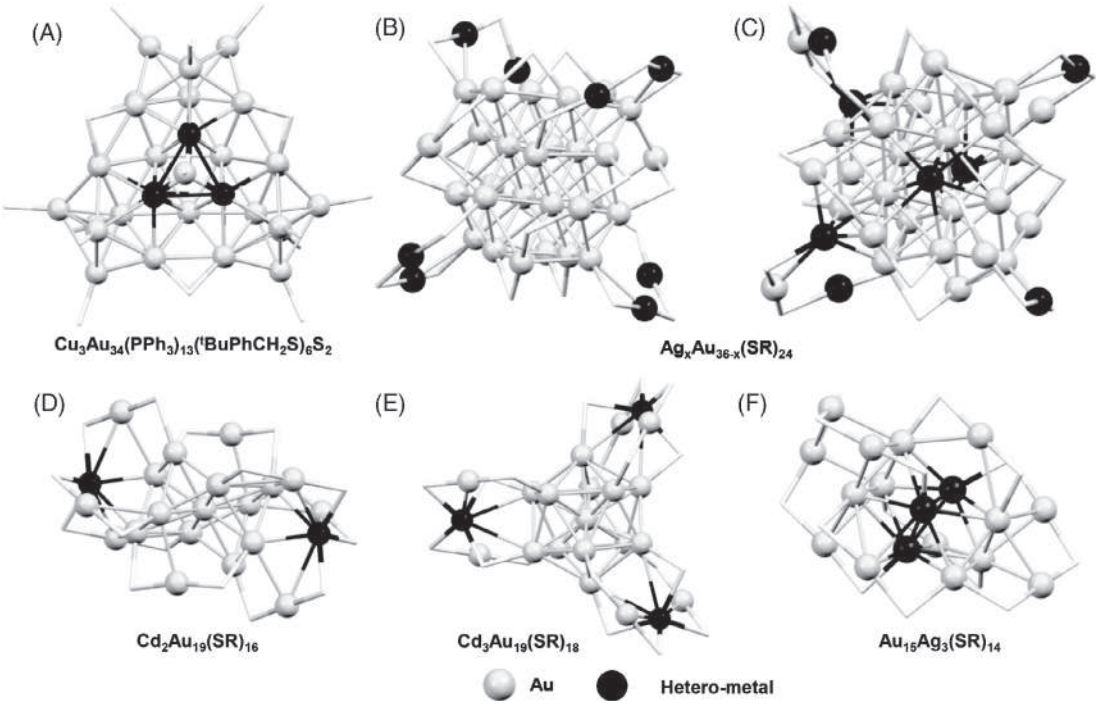

FIGURE 16.13 Structures of (A) $Cu_3Au_{34}(PPh_3)_{13}(^tBuPhCH_2S)6S_2$, (B) and (C) $Ag_xAu_{36-x}(SR)_{24}$, (D) $Au_{19}Cd_2(SR)_{16}$, (E) $Au_{19}Cd_3(SR)_{18}$, (F) $Au_{15}Ag_3(SR)_{14}$. Ligands are made in capped sticks and white colored so that different metals atoms can be seen unambiguously.

the mono- and bi-icosahedral structures, tri-icosahedral structure changes upon the incorporation of hetero-metal atoms. Such as $Cu_3Au_{34}(PPh_3)_{13}(^tBuPhCH_2S)_6S_2$ is a cyclic tri-icosahedral structure (Fig. 16.13A).[64] In this structure, the adjacent three M_{13} icosahedra share their three vertex atoms and form a cyclic shape. Hence, 13*3 − 3 = 36 metal atoms are present in this cycle. The remaining one Au atom is capped to one bare S atom and one PPh_3. Thiol-protected $Au_{36}(SR)_{24}$ acquires a completely different structure than Au_{37} and Au_{38}. It contains an Au_{28} FCC kernel surrounded by four dimeric $Au_2(SR)_3$ units.[74] Unlike Au_{25} and Au_{37}, the single crystal X-ray structure of $Ag_xAu_{36-x}(SR)_{24}$ revealed that Ag atoms occupy the four dimeric staples as shown in Fig. 16.13B.[75] However, another report evidenced the doping of Ag atoms at the icosahedral surface along with the staple (Fig. 16.13C).[76] Similar to Ag, Cu atoms can also occupy both icosahedral surface positions and staple motifs.[36] More than one Cd doping is observed in $Au_{23}(SR)_{16}$ which form bimetallic $Au_{23-x}Cd_x(SR)_{16}$ at a lower Au/Cd ratio. A structural reconstruction occurred at a higher Au/Cd ratio to form $Au_{19}Cd_2(SR)_{16}$.[77] Cd atoms were found to occupy the staple motifs forming $Cd(SR)_3$ paw-like structures (Fig. 16.13D). The ligand induced surface reconstruction of $Au_{25}(PET)_{18}$ resulted in the formation of bimetallic $Au_{19}Cd_3(SR)_{18}$ (SR = p-toluenethiol).[34] This unique bimetallic NC contains Au_{13} icosahedral core capped with three quadridentate $Au_2Cd(SR)_6$ staple units as presented in Fig. 16.13E.

Other than FCC and icosahedral structures, Au NCs obtain HCP structures such as $Au_{18}(SR)_{14}$ consisting of a bioctahedral HCP Au_9 core protected by three monomeric $Au(SR)_2$ units, one dimeric $Au_2(SR)_3$ and one tetrameric $Au_4(SR)_5$ unit (Fig. 16.13F). In Au_{18} template, till now Ag-doped bimetallic $Au_{15}Ag_3(SR)_{14}$ (HSR = DMBT, CHT) and $Au_{17}Ag_1(SR)_{14}$ (HSR = CHT) are known. In the case of $Au_{15}Ag_3(SR)_{14}$, three Ag atoms are located in the Au_9 kernel.[78] Among three trigonal M_3 planes of Au_9, the central layer is occupied by Ag heteroatoms forming Ag_3 trigonal plane.

Among thiolate-protected bigger sized alloy NCs, Ag-, Cu-, and Pd-doped $Au_{144}(SR)_{60}$ are important. Before obtaining the crystal structure of $Au_{144}(SR)_{60}$, its bimetallic alloys have been prepared. The structure of $Au_{144}(SR)_{60}$ contains a Au_{114} capped by 30 monomeric $Au(SR)_2$ staples.[79] The Au_{114} core is arranged in Au_{12} (M_1)-Au_{42} (M_2)-Au_{60} (M_3) configuration. ESI MS revealed the doping of ~53 Ag atoms whose theoretical doping positions are on the surface of Au_{114} kernel.[80] Cu atoms are theoretically predicted to occupy the M_1 ($Au_{12-x}Cu_x$) and M_2 ($Au_{42-x}Cu_x$) shell in the Au_{114} kernel and a maximum of ~23 Cu atom doping was observed from ESI MS.[18] Dass *et al.* reported the incorporation of seven Pd atoms to make bimetallic $Pd_xAu_{144-x}(SR)_{60}$ which shows maximum number of Pd doping (~7), not observed in any other NCs. Computational study indicated that Pd atoms are inserted in the inner most shell of the Au_{114} kernel ($Au_{12-x}Pd_x$).[81] Ag and Pd doping in $Au_{130}(SR)_{50}$ is also accomplished, however, single crystal structure of these alloys are not yet determined.[82]

Small-sized alloy NCs were also prepared, mainly protected by phosphine ligands. Some of them are $PdAu_8(PPh_3)_8$, $PdAu_{10}(PPh_3)_8Cl_2$, H-$Pt(X)_2(AuPPh_3)_8$ (X = $AgNO_3$ or CuCl), $Ag_4Au_9(PPh_3)_8Cl_4$, $Cu_4Au_9(PPh_3)_8Cl_4$, $Ag_3Au_8(PPh_3)_7Cl_3$, etc. In the case of $PdAu_8(PPh_3)_8$, Pd atom substitutes the central Au atom of crown-like Au_9.[22] Hydride-containing trimetallic alloys—H-$Pt(X)_2(AuPPh_3)_8$ and H-$Pt(AgNO_3)(AuPPh_3)_8$—were prepared, wherein Pt occupies the central position and Au, Ag/Cu atoms are placed on the surface.[83,84] Phosphine and hydride-protected trimetallic $HPdM_2Au_8(PPh_3)_8Cl_2$ (M = Ag/Cu) NCs were also synthesized, where Pd atom is placed in the center and Ag/Cu and Au occupy the surface positions.[85] Phosphine-protected bimetallic 13-atom alloy NCs, $Au_9M_4Cl_4(PMePh_2)_8][C_2B_9H_{12}]$ (M = Ag/Cu), were made, where dopants (Ag/Cu) are incorporated on the surface of the M_{13} icosahedron.[86] Nevertheless, thiolate and phosphine ligands having pyridyl groups resulted in the formation of a series of Au–Cu bimetallic NCs, $Au_{13}Cu_2(PPh_3)_6(SPy)_6$ (Py = 2-pyridyl), $Au_{13}Cu_4(PPh_2Py)_4(SC_6H_4\text{-tert-}C_4H_9)_8$ and $Au_{13}Cu_8(PPh_2Py)_{12}$.[87] According to X-ray crystal structures, these NCs have Au_{13} icosahedral core whose trigonal faces are capped by two, four, and eight Cu atoms. In $Au_{13}Cu_2(PPh_3)_6(SPy)_6$, two Cu atoms are capped on the icosahedral core in the orientation of one of the C_3 axes while four Cu atoms in $Au_{13}Cu_4(PPh_2Py)_4(SC_6H_4\text{-tert-}C_4H_9)_8$ are capped in a tetrahedral configuration. For $Au_{13}Cu_8(PPh_2Py)_{12}$, among eight Cu atoms, three Cu_2 dimers are capped equatorially and remaining two Cu atoms are placed in the opposite orientation across the Au_{13} core. Recently, Sun et al. have prepared two interesting Au–Ru bimetallic alloy NCs, $Au_4Ru_2(PPh_3)_2(PET)_8$ and $Au_5Ru_2(PPh_3)_2(PMeC_5)_2Cl_2$ ($PMeC_5$ = 1,2,3,4,5-pentamethylcyclopentadienyl) which are coprotected by thiol and phosphine ligands.[88] $Au_4Ru_2(PPh_3)_2(PET)_8$ is made up of a crown-like structure with Ru-$(PET)_4$-Au_4-$(PET)_4$-Ru arrangement. Two apical Ru atoms are bonded to PPh_3 ligands. While, $Au_5Ru_2(PPh_3)_2(PMeC_5)_2Cl_2$ has decahedral structure with a planar Au_5 pentagonal ring with two apex occupied by two Ru atoms.

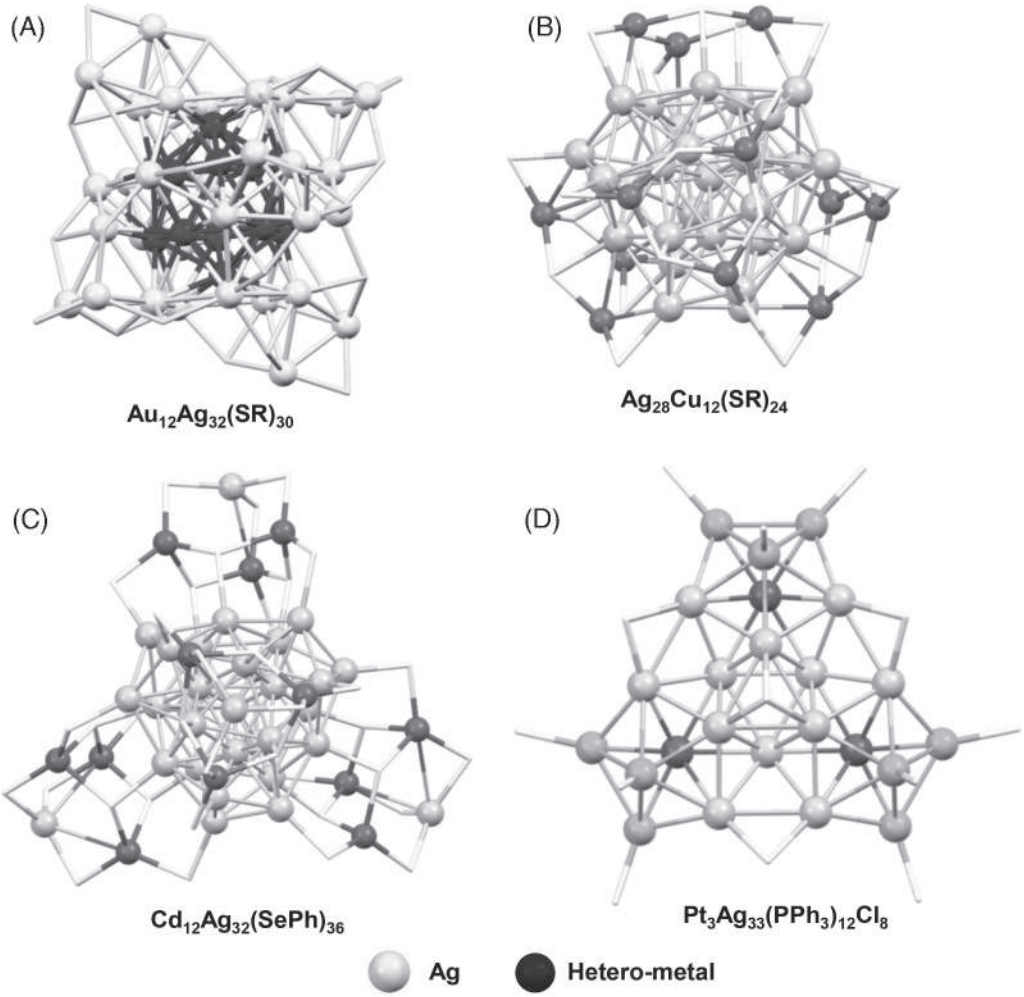

FIGURE 16.14 Geometric structures of (A) $Au_{12}Ag_{32}(SR)_{30}$, (B) $Ag_{28}Cu_{12}(SR)_{24}$, (C) $Cd_{12}Ag_{32}(SePh)_{36}$, and (D) $Pt_3Ag_{33}(PPh_3)_{12}Cl_8$. Ligands are drawn in capped sticks and white colored so that different metal atoms can be seen unambiguously.

16.3.2 Silver-rich alloys

Among Ag NCs, $Ag_{44}(SR)_{30}$ is one of the earliest synthesized and mostly studied one due to its higher stability than other reported Ag NCs till date. Its single crystal structure consists of an Ag_{12} hollow icosahedral which is covered by an inner Ag_{20} shell and the Ag_{32} kernel is capped by six dimeric $Ag_2(SR)_5$ units. This NC easily undergoes exchange reaction with Au atoms and forms bimetallic $Au_{12}Ag_{32}(SR)_{30}$, where inner M_{12} icosahedron is completely occupied by Au atoms (Fig. 16.14A).[89] When bimetallic NC containing Cu atoms was synthesized, it resulted in the formation of $Ag_{28}Cu_{12}(SR)_{24}$ (SR = 2,4-DCBT). It has Ag_{28} (Ag_4

tetrahedron@Ag_{24}) metal core shielded by four $Cu_3(SR)_6$ outer staples (Fig. 16.14B).[90] Synthesis of alloy NC containing Cd atoms resulted in the formation of bimetallic $Cd_{12}Ag_{32}(SePh)_{36}$.[91] Although the NC consists of a total of 44 metal atom, its structure resembles $Ag_{28}Cu_{12}(SR)_{24}$, rather than that of $Ag_{44}(SR)_{30}$. Similar to the $Ag_{28}Cu_{12}(SR)_{24}$, Ag_{28} (Ag_4 tetrahedron@Ag_{24}) metal kernel is observed to be surrounded by four $Cd_3Ag(SePh)_9$ moieties (Fig. 16.14C). Recently, Zhu et al. prepared chiral $Ag_{32}Cu_{12}(CH_3COO)_{12}(SAdm)_{12}(P(CH_3OPh)_3)_4$ having similar metal structure as that of $Ag_{28}Cu_{12}(SR)_{24}$ and the only difference is that in the presence of NC, each $Cu_3(SR)_6$ unit is further connected to Ag-PR_3 unit.[92] Similarly, the effort of doping Pt/Pd in $Ag_{44}(SR)_{30}$ altered the structure and composition and produced bimetallic Pt/Pd$Ag_{24}(SR)_{18}$ (SR = 2,4-DCBT) NCs.[17] Its monometallic analogue, $Ag_{25}(SR)_{18}$ (SR = 2,4-DMBT) is also reported and is of high importance as it is structurally similar to that of famous $Au_{25}(SR)_{18}$.[93]

Silver analogue has an Ag_{13} centered icosahedral core protected by six dimeric $Ag_2(SR)_3$ units. Among heteroatoms, Au, Ni, Pt, Pd atoms are successfully incorporated in $Ag_{25}(SR)_{18}$ to make bi- and trimetallic NCs. In bimetallic $MAg_{24}(SR)_{18}$ (M = Ni/Pd/Pt), Ni/Pd/Pt atoms occupy the center of M_{13} icosahedron.[17,94] Similarly, the preferred location of Au atom is the center of icosahedral core, however, when more than one Au atom is incorporated, they prefer to occupy icosahedral surface and further incorporation led to the doping in the outer staples.[3] Though both Pt and Au atoms prefers the central position, in trimetallic $PtAu_xAg_{24-x}(SR)_{18}$ (x = 1–2), Pt atom gets into the center, while Au atoms occupy the surface of icosahedron. This does not happen for Pd and Au combination as Au atoms readily replace Pd atoms from the central position and corresponding trimetallic cluster become unstable.[31] The addition of Dppm into $PtAg_{24}(SR)_{18}$ converts its structure to generate a sole-M_{13} center doped kernel $Pt_1Ag_{12}(Dppm)_5(SR)_2$.[49] Unlike Au_{25}, rod-shaped bi-icosahedral M_{25} homo-silver NC is not reported. However, silver-rich rod-shaped bi-icosahedral bimetallic $Pt_2Ag_{23}(PPh_3)_{10}Cl_7$ and trimetallic $Pt_2Au_{10}Ag_{13}(PPh_3)_{10}Br_7$ are known. Structures of $Pt_2Ag_{23}(PPh_3)_{10}Cl_7$ and $Pd_2Au_{23}(PPh_3)_{10}Cl_7$ resemble each other (Fig. 16.11C) wherein two Pt atoms are placed in the center of two icosahedra and remaining metal positions are occupied by Ag atoms.[95] In trimetallic $Pt_2Au_{10}Ag_{13}(PPh_3)_{10}Br_7$, Au atoms are doped in pentagonal M_2 and M_5 layers keeping Pt atoms at the two icosahedral centers.[28] Similar to bi-icosahedral building blocks, tri-icosahedral building blocks are also seen in silver-rich bimetallic $Pt_3Ag_{33}(PPh_3)_{12}Cl_8$ and trimetallic $Pt_3Au_{12}Ag_{21}(PPh_3)_{12}Cl_8$ NCs.[96] The cyclic tri-icosahedral structure is similar to that of $Cu_3Au_{34}(PPh_3)_{13}(^tBuPhCH_2S)_6S_2$ (Fig. 16.13A). In these NCs, three Pt atoms occupy the three icosahedral centers and for trimetallic one, Au atoms are selectively located at the top site of tri-icosahedral structure. Twelve Au atoms are bonded to 12 PPh_3 ligands while Ag atoms are connected to eight Cl atoms in the form of μ_2 and μ_3 Ag–Cl bonds (Fig. 16.14D). In addition to the M_{36} template, "cluster of clusters" category includes heavily doped bimetallic $Au_{18}Ag_{20}(PPh_3)_{12}Cl_{14}$ and $Au_{18}Ag_{19}(p\text{-}Tol_3P)_{12}Br_{11}$ having M_{37} and M_{38} templates.[10] Both bimetallic NCs acquire cyclic tri-icosahedral assembly, where the first one has one capping Ag atom, while second one contains two capping Ag atoms along with a pseudo C_3 axis.[97] $Ag_{44}(SR)_{30}$ (SR = p-MBA) transformed into $Ag_{50}(Dppm)_6(SR)_{30}$ after the reaction with Dppm ligand keeping the kernel structure intact. In the new structure, metal atoms accommodate Ag_{12}(hollow icosahedron)@Ag_{20}(dodecahedron)@6Ag$(SR)_2$@6$Ag_2(SR)_3$(dppm) arrangement.[29] Similar to $Au_{12}Ag_{32}(SR)_{30}$, M_{12} inner core is filled with Au atom in case of bimetallic $Au_xAg_{50-x}(dppm)_6(SR)_{30}$.

Among homo-silver NCs, thiol and phosphine coprotected $Ag_{29}(BDT)_{12}(PPh_3)_4$ is one of the most studied NCs due to its unique structure, interesting properties and very high stability.[98] The structure of Au-, Cu-, Ni-, Pd-, Pt-doped bi- and trimetallic NCs have been synthesized. The structural anatomy of $Ag_{29}(BDT)_{12}(PPh_3)_4$ showed the presence of Ag_{13}-centered icosahedral core capped by four $Ag_3(BDT)_3$ crown motifs and four $AgPPh_3$ motifs. One of the two S atoms of BDT ligand is connected to two Ag atoms of crown motifs and the other one is bonded to the Ag atoms of Ag-PPh_3 motif which is also bonded to the Ag atom of icosahedral core and one Ag atom of neighboring crown motif. Similarly, the dithiol and phosphine ligands form a very protective outer layer for Ag_{13} icosahedral core.[98] More than one Au atom is inserted to make bimetallic $Ag_{29}(BDT)_{12}(PPh_3)_4$ NCs, but crystal structure of multiple Au-doped ones is not yet obtained. Similar to $Au_xAg_{25-x}(SR)_{18}$, preferable doping site of single Au is the center of icosahedron. NMR study by Soldan et al. revealed that when more than one Au atoms are incorporated they prefer to replace the outer Ag atoms bonded to PPh_3.[20] Pt, Ni, and Pd are specifically located at the central position to form bimetallic $MAg_{28}(BDT)_{12}(PPh_3)_4$ (M = Pt/Ni/Pd), as revealed by their single crystal structures and DFT calculations.[7,47] In trimetallic $MAu_{12}Ag_{16}(BDT)_{12}(PPh_3)_4$ (M = Pt/Ni/Pd), 12 Au atoms prefer to occupy 12 vertices of icosahedral core.[7] Cu-doped bimetallic $Ag_{29}(BDT)_{12}(PPh_3)_4$ NCs showed incorporation of 12 Cu atoms at the four crown motifs to form $Ag_{17}Cu_{12}(BDT)_{12}(PPh_3)_4$ (Fig. 16.3A).[5] Co-reduction of Ag, Cu, and Au in the presence of BDT and PPh_3 ligands resulted in the formation of trimetallic $AuAg_{16}Cu_{12}(BDT)_{12}(PPh_3)_4$ with Au atom located at the center of the icosahedral core. This trimetallic NC can also be formed by the addition of Au(I) salt to $Ag_{17}Cu_{12}(BDT)_{12}(PPh_3)_4$.[5] Using HSAdm thiol instead of BDT, bi-, tri-, and tetrametallic $M_{29}(S\text{-}Adm)_{18}(PPh_3)_4$ NCs were prepared.[27] It has M_1(center)@M_{12}(core)@6$M_2(SR)_3$(staple motifs)@(M-$PPh_3)_4$(vertex motifs) configuration as shown in Fig. 16.15D. Au-, Pd-, Pt-doped bimetallic $MAg_{28}(S\text{-}Adm)_{18}(PPh_3)_4$ (M = Au/Pd/Pt) is composed of 28 Ag atoms and has one dopant at the center position.

Using Au, Pt, Cu atoms, a series of trimetallic NCs were prepared, that is, $PtCu_4Ag_{24}(S\text{-}Adm)_{18}(PPh_3)_4$ ($PtCu_4Ag_{24}$), $PtAu_4Ag_{24}(S\text{-}Adm)_{18}(PPh_3)_4$ ($PtAu_4Ag_{24}$), $PtAg_{12}Cu_{16}(S\text{-}Adm)_{18}(PPh_3)_4$, and $PtAg_{16}Cu_{12}(S\text{-}Adm)_{18}(PPh_3)_4$. In the case of $PtCu_4Ag_{24}$ and $PtAu_4Ag_{24}$, Au atoms occupy four M-PPh_3 motifs while Cu atoms prefers crown staples. Structure of $PtAg_{16}Cu_{12}(S\text{-}Adm)_{18}(PPh_3)_4$ is similar to that of $Ag_{17}Cu_{12}(BDT)_{12}(PPh_3)_4$, where Pt atom is placed at the center. In $PtAg_{12}Cu_{16}(S\text{-}Adm)_{18}(PPh_3)_4$, along with 12 Cu atoms are doped at four crown motifs, four remaining Cu atoms occupy four M-PPh_3 vertex positions. By the addition of $Au(PPh_3)Cl$, four Au atoms are placed in the vertex motifs of trimetallic $PtAg_{12}Cu_{16}(S\text{-}Adm)_{18}(PPh_3)_4$ to obtain tetrametallic $PtAu_4Ag_{12}Cu_{12}(S\text{-}Adm)_{18}(PPh_3)_4$. Hydrophilic thiol-protected bimetallic $AuAg_{28}(DHLA)_{12}$ comprises of a similar structure to that of $AuAg_{28}(BDT)_{12}(PPh_3)_4$ as evident from DFT calculation.[99] Recently, Cu-containing M_{29} bimetallic NC, $Ag_{25}Cu_4(PhC{\equiv}C)_{12}(PPh_3)_{12}Cl_6H_8$ has been reported by Shen *et al.* This contains an Ag_{13} icosahedral core which is capped by four $Ag_3Cu(PPh_3)_3(PhC{\equiv}C)_3$ motifs. Ag atoms of adjacent Ag_3Cu motifs are connected to each other by μ_2 Cl atoms.[24] A large-sized M_{70} Ag–Au bimetallic $[Ag_{46}Au_{24}(SR)_{32}](BPh_4)_2$ was formed, which does not have any monometallic analogue.[100] It has $Ag_2@Au_{18}@Ag_{20}@Ag_{24}Au_6(SR)_{32}$ arrangement, wherein Ag and Au locate together at the surface motifs. Similarly, Cu–Ag bimetallic $[Cu_{30}Ag_{61}(SAdm)_{38}S_3](BPh_4)$ with a shell-by-shell Ag_{13}(inner core)@$Cu_{30}@Ag_{48}(SAdm)_{38}S_3$ arrangement was synthesized. This

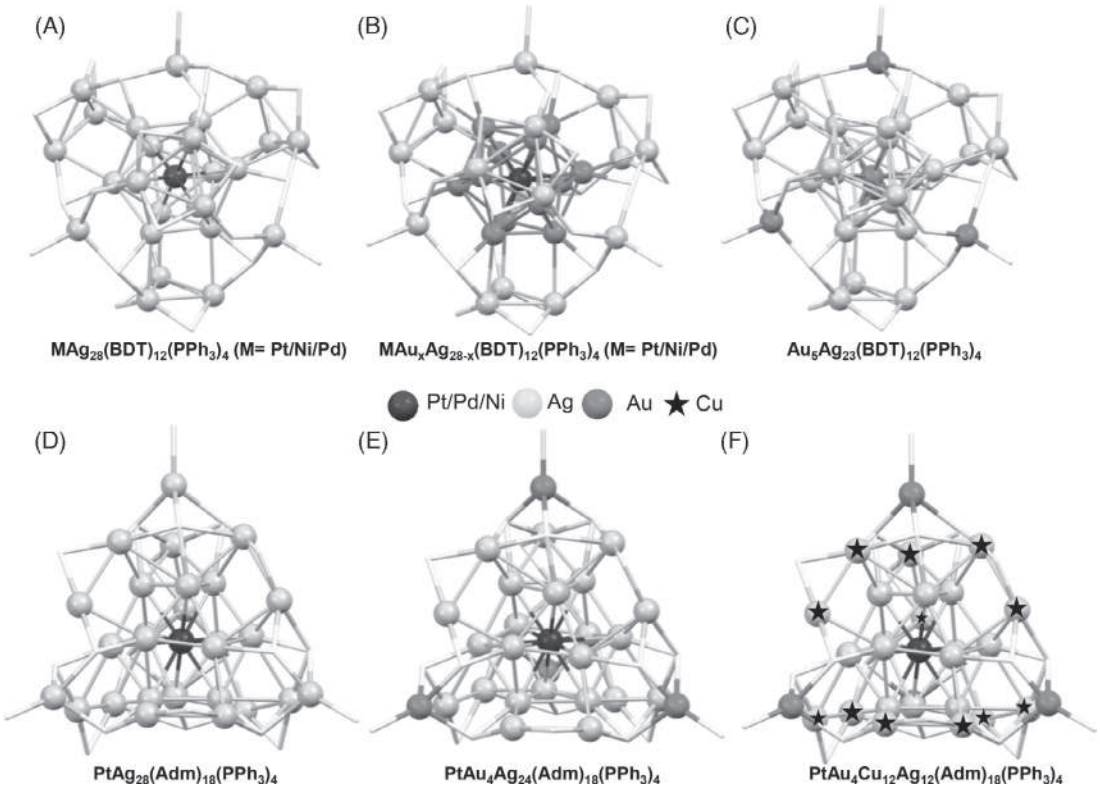

FIGURE 16.15 (A)–(C) Represent the structure of $MAg_{28}(BDT)_{12}(PPh_3)_4$ (M = Pt/Ni/Pd), $MAu_xAg_{28-x}(BDT)_{12}(PPh_3)_4$ (M = Pt/Ni/Pd) and bimetallic $Au_5Ag_{23}(BDT)_{12}(PPh_3)_4$. Ligands are drawn in capped sticks and white colored so that different metal atoms can be seen unambiguously.

is a unique NC, where Cu atoms are doped at the kernel rather than outer staples.[101] The largest alloy NC, $Ag_{267-x}Au_x(SR)_{80}$ was found by Yan et al. in 2018. In this buckyball-shaped NC, metals are distributed in $Ag_1@M_{12}$(1st-shell)@M_{42}(2nd-shell)@M_{92}(3rd-shell)@$Ag_{120}(SR)_{80}$(outer cage) (M = Au or Ag) fashion.[102]

16.3.3 Copper-rich alloys

Among Cu-rich alloy NCs, $Au_2Cu_6(SR)_6(PPh_3)_2$, $Au_7Cu_{12}(PPh_2Py)_6(SR)_6Br_4$, $AuCu_{24}H_{22}(PPh_3)_{12}$, $Au_{12+n}Cu_{32}(SPhCF_3)_{30+n}$,[103] $MCu_{12}(S_2CN^nBu_2)_6(C{\equiv}CR)_4$ (M = Au/Ag), $AuCu_{14}(SR)_{12}(BCPP)_6$, $Au_{52}Cu_{72}(SPh^pMe)_{55}$, etc. are well studied due to their strong emission properties. The superatom alloys , $MCu_{12}(S_2CN^nBu_2)_6(C{\equiv}CR)_4$ (M = Au/Ag) are obtained by galvanic reduction process using $Cu_{13}(S_2CN^nBu_2)_6(C{\equiv}CR)_4$ as template.[104] Unlike M_{13} system composed of Au and Ag atoms which accommodates central icosahedral structure, Cu_{13} possesses a central cuboctahedral core. Au and Ag atoms are specifically doped at the center of cuboctahedron to form MCu_{12} core. Among eight triangular faces, four

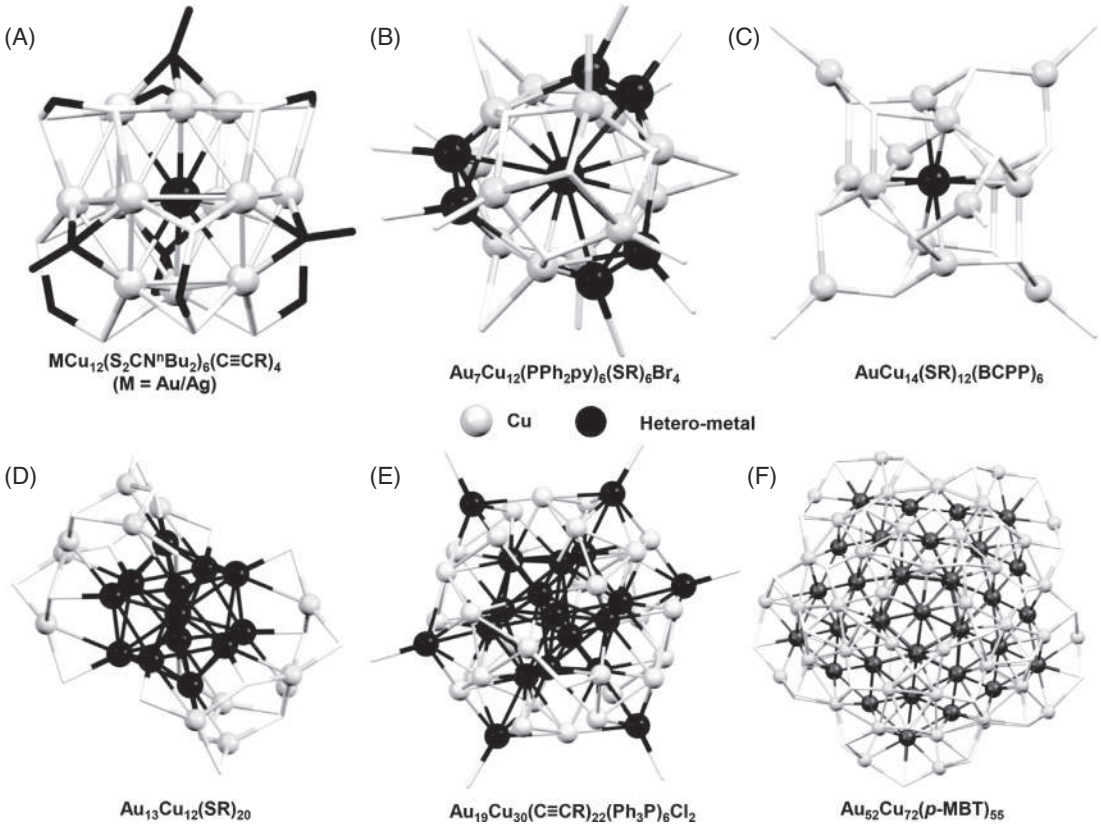

FIGURE 16.16 Crystal structure of Cu-rich bimetallic NCs; (A) $MCu_{12}(S_2CN^nBu_2)_6(C{\equiv}CR)_4$ (M = Au/Ag), (B) $Au_7Cu_{12}(PPh_2Py)_6(SR)_6Br_4$, (C) $AuCu_{14}(SR)_{12}(BCPP)_6$, (D) $Au_{13}Cu_{12}(SR)_{20}$, (E) $Au_{19}Cu_{30}(C{\equiv}CR)_{22}(Ph_3P)_6Cl_2$, and (F) $Au_{52}Cu_{72}(p\text{-MBT})_{55}$.

are capped by alkynyl groups while six square faces are connected to thiolate ligands (Fig. 16.16A). $Au_2Cu_6(SR)_6(PPh_3)_2$ comprises of benzenoid-like $Cu_6(SR)_6$ framework which is capped with two apical Au atoms connected to PPh_3 ligands.[105] Using PPh_2Py and HS-Ph^{t}Bu ligands, bimetallic $Au_7Cu_{12}(PPh_2Py)_6(SR)_6Br_4$ was prepared which is a combination of a fan-like Au_7Cu_6 kernel having six blades and two Cu_3S_3 staple motifs similar to tri-blade fan (Fig. 16.16B). The Au_7Cu_6 kernel is ring-shaped, which was not observed for any other M_{13} NC.[106] The highly luminescent $AuCu_{14}(SR)_{12}(BCPP)_6$ (BCPP = bis(2-cyanoethyl)-phenylphosphine; HSR = HSPh^{t}Bu) NC is made up of a single Au atom kernel protected by a large $Cu_{14}(SR)_{12}(BCPP)_6$ cage (Fig. 16.16C).[107] A series of thiol-protected bimetallic Au–Cu alloys, $Au_{12+n}Cu_{32}(SR)_{30+n}$ (n = 0, 2, 4, 6 and SR = $SPhCF_3$) were successfully made.[103] $Au_{12}Cu_{32}(SR)_{30}$ possesses exactly similar structure as that of $Au_{12}Ag_{32}(SR)_{30}$. It consists of Au_{12} (hollow icosahedron)@Cu_{20} (decahedron) kernel covered by a shell made up of six $Cu_2(SR)_5$ units. $Au_{14}Cu_{32}(SR)_{32}$, $Au_{16}Cu_{32}(SR)_{34}$, and $Au_{18}Cu_{32}(SR)_{36}$ NCs possess similar $Au_{12}@Cu_{20}$ core which are protected by different staple motifs. $Au_{14}Cu_{32}(SR)_{32}$ contains four $Cu_2(SR)_5$

and two $Cu_2Au(SR)_6$ staples, where one $Cu_2(SR)_5$ and four $Cu_2Au(SR)_6$ units are present in $Au_{16}Cu_{32}(SR)_{34}$. In $Au_{18}Cu_{32}(SR)_{36}$, M_{32} kernel is surrounded by six $Cu_2Au(SR)_6$ units.

$Au_{16}Cu_{32}(SR)_{34}$ degrades to form bimetallic $Au_{13}Cu_{12}(SR)_{20}$, whose crystal structure revealed the presence of a centered icosahedral core instead of a hollow Au_{12} core. Here, icosahedral Au_{13} core is protected by two $Cu_6(SR)_{10}$ staples (Fig. 16.16D). A large number of Cu NCs showed the incorporation of hydride to stabilize the NC system. Such an example is $Cu_{25}H_{22}(PPh_3)_{12}$ which has Cu_{13} icosahedral core capped by four $[Cu(PPh_3)]_3$ units and 22 hydride ligands. Chen *et al.* described that one Au atom preferentially occupies the center of icosahedron yielding bimetallic $AuCu_{24}H_{22}(PPh_3)_{12}$.[108] A larger-sized phosphine-alkynyl coprotected $Au_{19}Cu_{30}(C{\equiv}CR)_{22}(Ph_3P)_6Cl_2$(R = H_3C_4S-3) was reported by Wang *et al.*, which can be described as a multi shell NC with $Au@Au_{12}@Cu_{30}@Au_6$ configuration.[109] The icosahedral Au_{13} is surrounded by a unique icosidodecahedron Cu_{30} shell. The outer six Au atoms form a chair-like hexagon as shown in Fig. 16.16E. Thiol-protected bimetallic $Au_{52}Cu_{72}$(*p*-MBT)$_{55}$ occupies both Au and Cu atoms at the M_7 kernel (Au_5Cu_2) which is stabilized by a second shell of Au_{47} and outer cage of $Cu_{70}(SR)_{55}$ (Fig. 16.16F).[110] Pd, Ag, etc. can be doped in Cu-rich NCs such as $PdCu_{14}H_2$(dtc/dtp)$_6$($C{\equiv}CPh)_6$ (dtc = $S_2CN^nBu_2$; dtp = $S_2P(O^iPr)_2$), $AgCu_{12}(S_2CN^nBu_2)_6(C{\equiv}CR)_4$, etc.[111]

16.4 Properties of multimetallic nanoclusters

16.4.1 Optical properties

Substitution of hetero-metal atoms in NCs changes their electronic structures which is reflected in their optical absorption and emission properties. The precise structural determination of these NC enable to understand their structure–property relationships. A few such examples are discussed here. As mentioned in Section 16.3.1, different metal atoms such as Ag, Pd, Pt, Cd, Cu, etc. prefer to occupy different sites of $Au_{25}(SR)_{18}$ and hence they are having different effects on the optical properties. $Au_{25}(SR)_{18}$ exhibits four distinct absorption features at 400, 450, 670, and 780 nm. Doping of Pd weakens the peak at ~670 nm (~1.8 eV), whereas two new peaks emerge at ~620 (~2.0 eV) and ~1030 nm (~1.2 eV). Similarly, in $PtAu_{24}(SR)_{18}$, two absorption peaks at 1.1 and 2.1 eV are observed as shown in Fig. 16.17A. These significant changes are due to the presence of Pd and Pt atoms in the center of icosahedral core.[112] Blue-shifts of peaks at 400 and 780 nm to 380 and 615 nm occur upon Ag-doping at the vertices of icosahedral core. Central doped $CdAu_{24}(SR)_{18}$ exhibits blue-shifted absorption features at 650 and 770 nm. Two major peaks at 405 and 710 nm are observed in the absorption spectrum of $HgAu_{24}(SR)_{18}$. Doping of Cu atoms at the staple motifs red-shifts the optical absorption peak at 670–690 nm and eliminates the peak at 780 nm (Fig. 16.17B).[33] Rod-shaped $Au_{25}(PPh_3)_{10}(SR)_5Cl_2$ shows several UV–vis absorption peaks at ~380, 415, 430, and 670 nm. Absorption spectrum of one Cu-doped NC looks exactly similar to that of undoped one with a small blue-shift of the absorption maximum. But a significant change is seen after doping of Ag atoms.[37] The peak at ~670 nm experiences a blue shift and peak at 415 nm disappears. In 13 Ag atom-doped bimetallic NC, two intense peaks at ~370 and ~430 nm arise in addition to the blue shift of 670 nm peak to 635 nm (Fig. 16.17C).[65] Also, a visible color change of the cluster solution from brown to green is observed upon Ag doping. Not only absorption spectrum

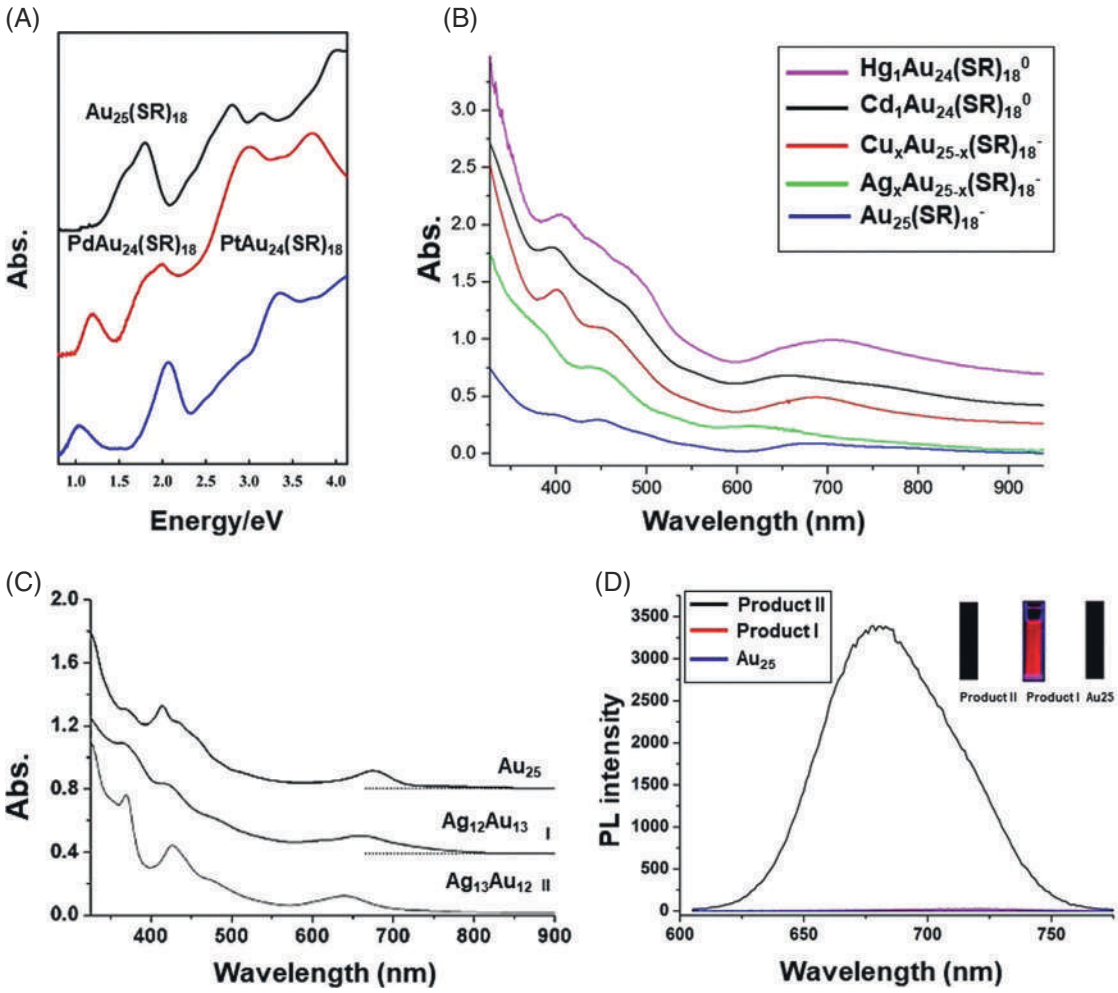

FIGURE 16.17 UV–vis absorption spectrum of (A) $Au_{25}(SR)_{18}$ and $MAu_{24}(SR)_{18}$ (M = Pt/Pd), (B) $MAu_{24}(SR)_{18}$ (M = Au, Cd, Hg, Ag, Cu), and (C) $Au_{25}(PPh_3)_{10}(SR)_5Cl_2$, $Ag_{12}Au_{13}(PPh_3)_{10}(SR)_5Cl_2$, and $Ag_{13}Au_{12}(PPh_3)_{10}(SR)_5Cl_2$. (D) Emission spectra of $Au_{25}(PPh_3)_{10}(SR)_5Cl_2$, $Ag_{12}Au_{13}(PPh_3)_{10}(SR)_5Cl_2$, and $Ag_{13}Au_{12}(PPh_3)_{10}(SR)_5Cl_2$. Reprinted from refs.[112,33,65] Copyright 2015 American Chemical Society and Copyright 2014 Wiley-VCH Verlag GmbH & Co. KGaA, Weinheim.

but the emission spectrum changes significantly after 13th Ag atom doping. It exhibits 200-fold enhanced luminescence with 40.1% quantum yield (QY). Also, the emission maximum blue-shifted to 680 nm (Fig. 16.17D). The structure of $Ag_{13}Au_{12}(PPh_3)_{10}(SR)_5Cl_2$ is discussed in Section 16.3.1. Due to the incorporation of 13th Ag atom in the center, a large perturbation to the electron dynamics occurs leading to the enhancement of the luminescence intensity. Similar to Au NCs, electronic structures of Ag NCs get affected by hetero-metal incorporation. A notable change occurs when the central Ag atoms of $Ag_{25}(SR)_{18}$ and $Ag_{29}(SR)_{12}(PPh_3)_4$

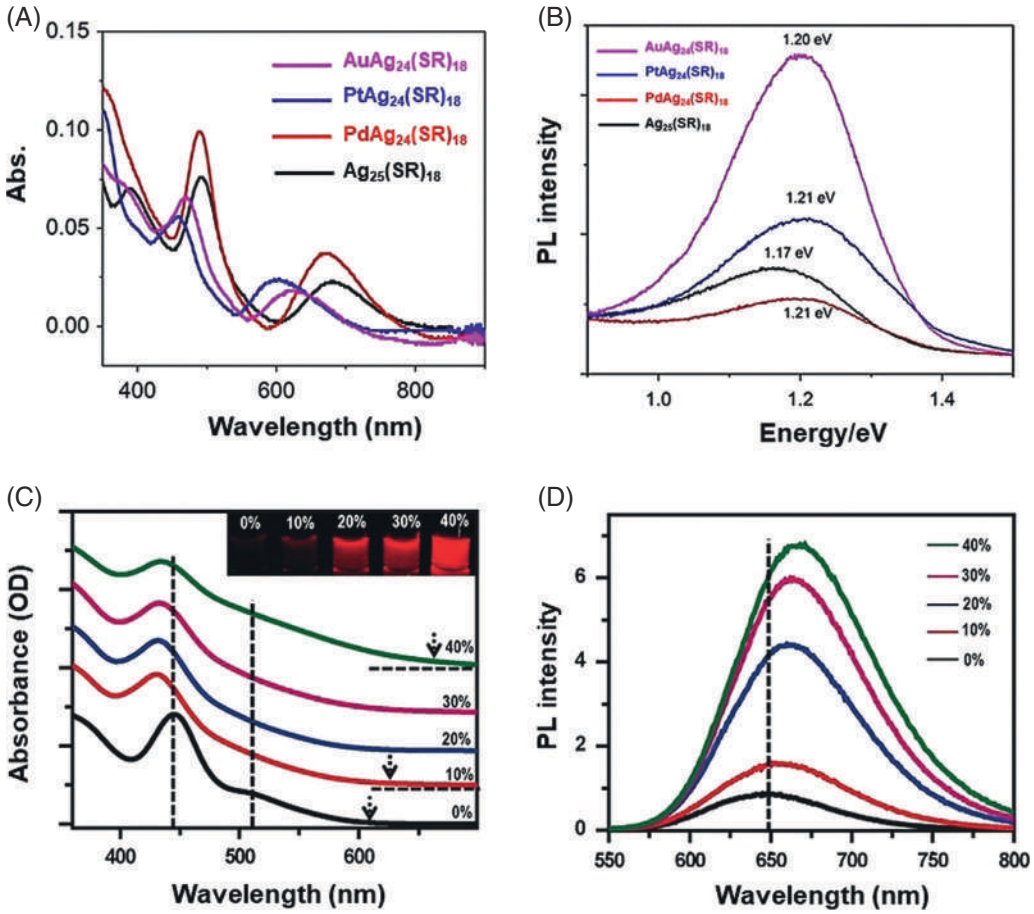

FIGURE 16.18 (A and B) Absorption and emission spectra of $MAg_{24}(SR)_{18}$ (M = Au/Pt/Pd). Reprinted from ref.[113] Copyright 2017 American Chemical Society. (C and D) Absorption and emission spectra of $Au_xAg_{29-x}(SR)_{12}(PPh_3)_4$. Reprinted from ref.[20] 2016 Wiley-VCH Verlag GmbH & Co. KGaA, Weinheim.

are replaced with Au/Pt/Pd/Ni (Fig. 16.18). The peaks at ~490 and 675 nm of $Ag_{25}(SR)_{18}$ shift to ~483 and 665 nm, respectively, upon insertion of Ni atom.[7] For $PdAg_{24}(SR)_{18}$, two major absorption features are observed at ~480 and 630 nm and $PtAg_{24}(SR)_{18}$ exhibits blue-shifted peaks at ~453 and 580 nm.[17] Crystal of $Ag_{25}(SR)_{18}$ possesses NIR luminescence with the emission maximum at ~1013 nm which is 23, 28, and 32 nm blue-shifted upon doping with Au, Pd, and Pt, respectively. Also, the emission intensities are increased by 270% and 80% for Au- and Pt-doped NCs while Pd doping lower the photoluminescence (PL) intensity by 40%.[113] Small blue-shifted peaks are observed due to the Au doping in $Ag_{29}(SR)_{12}(PPh_3)_4$. With the increasing amount of Au atoms, the main peak at ~447 nm broadens and the shoulder peak around 510 nm gradually flatten (Fig. 16.18C). On the other hand, up to 26-fold enhancement in emission QY is observed upon the incorporation of ~5 Au atoms.[20] The

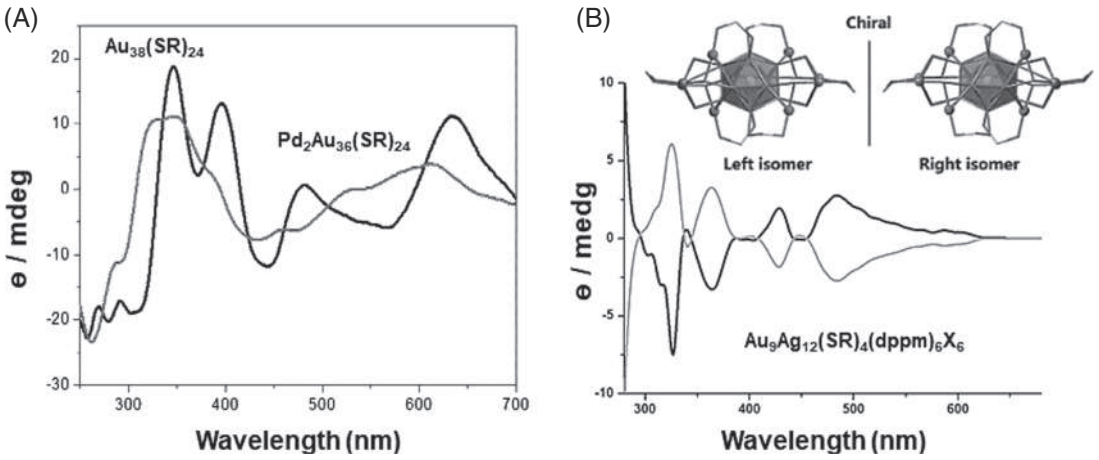

FIGURE 16.19 (A) Comparative CD spectra of $Pd_2Au_{36}(PET)_{24}$ and $Au_{38}(PET)_{24}$. Reprinted from ref.[116] Copyright 2014 American Chemical Society. (B) CD spectra of $Au_9Ag_{12}(SR)_4(dppm)_6X_6$. Inset shows the structure of its enantiomers. Reprinted from ref.[117] Copyright 2018 American Chemical Society.

emission maximum is red-shifted significantly (Fig. 16.18D) and it is due to the change in the higher wavelength range of the absorption spectrum which is shown by the dotted arrow in Fig. 16.18C. Central doping with Pt atom in $Ag_{29}(SR)_{12}(PPh_3)_4$ resulted in ~2.3-fold increment in the PL QY. Also, $PtAg_{28}(SR)_{12}(PPh_3)_4$ exhibits remarkable blue-shifted UV–vis absorption features at ~425 and 491 nm and the emission maximum is ~80 nm red-shifted.[114] Ni-doped bimetallic $NiAg_{28}(SR)_{12}(PPh_3)_4$ displays two absorption peaks at ~440 and 517 nm while $PdAg_{28}(SR)_{12}(PPh_3)_4$ manifests absorption peaks at ~444 and 518 nm.[7] Apart from the doped clusters, bimetallic alloy clusters such as $Au_{19}Cd_3(SR_2)_{18}$, $Au_2Cu_6(S\text{-}Adm)_6(PPh_2Py)_2$, etc. exhibit huge emission intensity than that of $Au_{25}(SR)_{18}$.[34,115] A maximum of 71.3% PL QY is observed in bimetallic $AuCu_{14}(SPh^tBu)_{12}(PPh(C_2H_4CN)_2)_6$.[107]

16.4.2 Chirality

Chirality of NCs could play an important role in the applications of NCs and NC-based materials, such as asymmetric catalysis, optical devices, chiral pharmaceuticals, etc. Alloying helps to control the chiral properties of NCs. Burgi *et al.* demonstrated significant impact of Pd doping in the intrinsic chiral property of $Au_{38}(PET)_{24}$. The circular dichroism (CD) spectra of $Pd_2Au_{36}(PET)_{24}$ and $Au_{38}(PET)_{24}$ show notable differences which display strong effect of doping on the electronic structure of the NC (see Fig. 16.19A).[116] Incorporation of Ag and Cu atoms in $Au_{38}(PET)_{24}$ change CD responses by changing the flexibility of the NC's surface.[118] Chirality in NCs has various origins which can be categorized in four types: (1) chiral outer ligands, (2) chiral metal–ligand interface/staples, (3) inherent/intrinsic chiral core, (4) chiral arrangement of ligands on the surface. Bimetallic NC, $Au_{13}Cu_2(2s,4s\text{-}BDPP)_3(SPy)_6$ (BDPP = (2r,4r)/(2s,4s)-2,4-bis(diphenylphosphino)pentane), shows chirality due to the presence of chiral ligand (BDPP).[119] This chiral NC exhibits a maximum anisotropic factor up to 1.2×10^{-3} at 360 nm. Ag–Cu bimetallic $Ag_{28}Cu_{12}(SR)_{24}$ acquires chirality due to

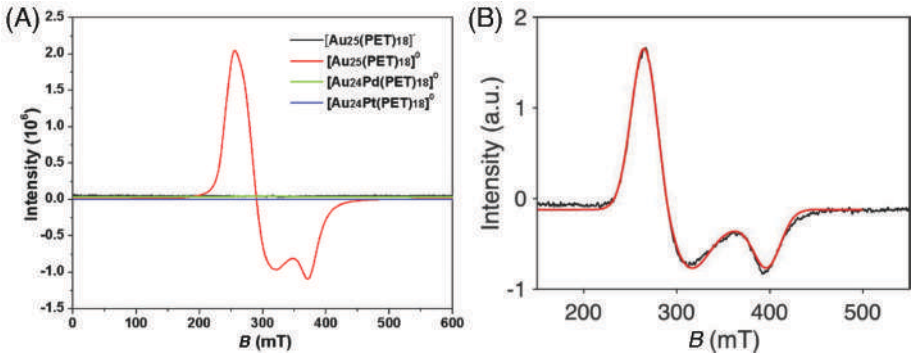

FIGURE 16.20 (A) EPR signals of $[Au_{25}(SR)_{18}]^{0/-1}$ and $[Pt/PdAu_{24}(SR)_{18}]^0$. (B) Theoretical (red) and experimental (black) EPR signals of $[PtAu_{24}(SR)_{18}]^-$. Reprinted from refs.[59,14] Copyright 2016 Royal Society of Chemistry. Copyright 2019 American Chemical Society.

the presence of chiral arrangement of Cu atoms of the four $Cu_3(SR)_6$ staples (structural details are given in Fig. 16.14B).[90] The anisotropic factor of this bimetallic alloy NC is 1×10^{-3}. Au–Ag bimetallic $Au_9Ag_{12}(SR)_4(dppm)_6X_6$ (SR = HSR = tert-butylmercaptan, X = Br/Cl) exhibits chirality due to the chiral arrangement of metal–ligand staples.[117] CD spectrum of this NC and the arrangement of staple motifs on the NC surface is shown in Fig. 16.19B.

16.4.3 Magnetism

Magnetism is one of the fascinating properties of NCs. It is due to the precise atomicity, the precise number of free electrons present in a NC can be calculated. Doping can alter their electronic configuration in turn affecting the magnetic properties. Pt and Pd doping modifies the electronic configuration of $[Au_{25}(SR)_{18}]^0$ which contains seven free electrons and hence exhibits paramagnetic property. $[Pt/PdAu_{24}(SR)_{18}]^0$ NCs on the other hand possess diamagnetism with six free electrons, as affirmed by their EPR spectra (Fig. 16.20A).[59] While $[PtAu_{24}(SR)_{18}]^0$ does not possess free electron, its monoanionic species $[PtAu_{24}(SR)_{18}]^{-1}$ contains an unpaired electron due to which it becomes paramagnetic. The EPR spectrum of $[PtAu_{24}(SR)_{18}]^{-1}$ is given in Fig. 16.20B which is similar to that of $[Au_{25}(SR)_{18}]^0$.[14]

16.5 Summary and future perspectives

To summarize, this chapter discussed various synthetic routes to prepare multimetallic NCs. Characterizations of these alloys by single crystal X-ray structural analysis and various interesting properties of alloy NCs such as optical properties, chirality, magnetism are demonstrated. The structural determination of alloy NC to understand their structure–property relationship is discussed. Structural determination also helps to understand the doping sites of various metals and hence, using the proper combination of metals,multimetallic NCs are prepared. Various metals such as Ru, Rh, Ir, Cd, Hg, Cu, Ni, Pt, Pd are incorporated to make alloy NCs, further extending the area of interest. Since last decade a large number of alloy NCs

have been prepared. However, there is a need to look into other aspects, such as, synthesis of alloy NCs containing Fe, Co, and lanthanides because of their magnetic and photophysical properties. Also, these alloy NCs may display multiple phenomena such as magneto fluorescence, circularly polarized luminescence, etc. Obtaining larger sized single crystals of alloy NCs will enable us to measure their bulk properties such as mechanical properties, electrical conductivity, etc. Though doping of four metals have been achieved, doping of more numbers of different metals will enable us to make high entropy alloy NCs which may unveil interesting catalytic properties. As the field of alloy NC is growing rapidly, a great amount of computational effort is required to elucidate their structure–property relationships.

List of abbreviation

BDT	benzenedithiolate
BINAS	1,10-binaphthalene-2,20-dithiolate
CHT	cyclohexanethiol
DCM	dichloromethane
DFT	density functional theory
DMBT	dimethylbenzenethiolate
Dppm	1,1-bis(diphenylphosphino)methane
EXAFS	extended X-ray absorption fine structure
FTP	fluorothiophenolate
NC	nanocluster
NP	nanoparticle
PET	phenylethanethiolate
p-Tol_3P	tri(p-tolyl)phosphine
SAdm	adamentanethiolate
TBBT	4-tert-butylbenzenethiolate

References

1. Arora N, Thangavelu K, Karanikolos GN. Bimetallic nanoparticles for antimicrobial applications. *Front Chem*. 2020;8:412.
2. Hossain S, Niihori Y, Nair LV, Kumar B, Kurashige W, Negishi Y. Alloy clusters: precise synthesis and mixing effects. *Acc Chem Res*. 2018;51:3114–3124.
3. Bootharaju MS, Joshi CP, Parida MR, Mohammed OF, Bakr OM. Templated atom-precise galvanic synthesis and structure elucidation of a $[Ag_{24}Au(SR)_{18}]^-$ nanocluster. *Angew Chem*. 2016;128:934–938.
4. Yang H, Wang Y, Huang H, et al. All-thiol-stabilized Ag_{44} and $Au_{12}Ag_{32}$ nanoparticles with single-crystal structures. *Nat Commun*. 2013;4:2422.
5. Kang X, Abroshan H, Wang S, Zhu M. Free valence electron centralization strategy for preparing ultrastable nanoclusters and their catalytic application. *Inorg Chem*. 2019;58:11000–11009.
6. Jin S, Liu W, Hu D, et al. Aggregation-induced emission (AIE) in Ag–Au bimetallic nanocluster. *Chem – Eur J*. 2018;24:3712–3715.
7. Khatun E, Chakraborty P, Jacob BR, et al. Intercluster reactions resulting in silver-rich trimetallic nanoclusters. *Chem Mater*. 2020;32:611–619.
8. Guan ZJ, Zeng JL, Yuan SF, Hu F, Lin YM, Wang QM. $Au_{57}Ag_{53}(C{\equiv}CPh)_{40}Br_{12}$: a large nanocluster with C1 symmetry. *Angew Chem – Int Ed*. 2018;57:5703–5707.
9. Zeng JL, Guan ZJ, Du Y, Nan ZA, Lin YM, Wang QM. Chloride-promoted formation of a bimetallic nanocluster $Au_{80}Ag_{30}$ and the total structure determination. *J Am Chem Soc*. 2016;138:7848–7851.
10. Teo BK, Zhang H, Shi X. Cluster of clusters: a modular approach to large metal clusters. structural characterization of a 38-atom cluster $[(p\text{-}Tol_3P)_{12}Au_{18}Ag_{20}Cl_{14}]$ based on vertex-sharing triicosahedra. *J Am Chem Soc*. 1990;112:8552–8562.

11. Teo BK, Keating K. Novel triicosahedral structure of the largest metal alloy cluster: $[(Ph_3P)_{12}Au_{13}Ag_{12}Cl_6]^{M+}$. *J Am Chem Soc*. 1984;106:2224–2226.
12. Teo BK, Zhang H, Shi X. Molecular architecture of a novel vertex-sharing biicosahedral cluster $[(p\text{-}Tol_3P)_{10}Au_{13}Ag_{12}Br_8](PF_6)$ containing a staggered-staggered-staggered configuration for the 25-atom metal framework. *Inorg Chem*. 1990;29:2083–2091. https://doi.org/10.1021/ic00336a011.
13. Haggin J. Illinois scientists synthesize huge cluster. *Chem Eng News Arch*. 1989;67:6.
14. Suyama M, Takano S, Nakamura T, Tsukuda T. Stoichiometric formation of open-shell $[PtAu_{24}(SC_2H_4Ph)_{18}]^-$ via spontaneous electron proportionation between $[PtAu_{24}(SC_2H_4Ph)_{18}]^{2-}$ and $[PtAu_{24}(SC_2H_4Ph)_{18}]^0$. *J Am Chem Soc*. 2019;141:14048–14051.
15. Negishi Y, Kurashige W, Niihori Y, Iwasa T, Nobusada K. Isolation, structure, and stability of a dodecanethiolate-protected Pd_1Au_{24} cluster. *Phys Chem Chem Phys*. 2010;12:6219–6225.
16. Fields-Zinna CA, Crowe MC, Dass A, Weaver JEF, Murray RW. Mass spectrometry of small bimetal monolayer-protected clusters. *Langmuir*. 2009;25:7704–7710.
17. Yan J, Su H, Yang H, et al. Total structure and electronic structure analysis of doped thiolated silver $[MAg_{24}(SR)_{18}]^{2-}$ (M = Pd, Pt) clusters. *J Am Chem Soc*. 2015;137:11880–11883.
18. Dharmaratne AC, Dass A. $Au_{144-x}Cu_x(SC_6H_{13})_{60}$ nanomolecules: effect of Cu incorporation on composition and plasmon-like peak emergence in optical spectra. *Chem Commun*. 2014;50:1722.
19. Kauffman DR, Alfonso D, Matranga C, Qian H, Jin R. A quantum alloy: the ligand-protected $Au_{25-x}Ag_x(SR)_{18}$ cluster. *J Phys Chem C*. 2013;117:7914–7923.
20. Soldan G, Aljuhani MA, Bootharaju MS, et al. Gold doping of silver nanoclusters: a 26-fold enhancement in the luminescence quantum yield. *Angew Chem Int Ed*. 2016;55:5749–5753.
21. Negishi Y, Munakata K, Ohgake W, Nobusada K. Effect of copper doping on electronic structure, geometric structure, and stability of thiolate-protected Au_{25} nanoclusters. *J Phys Chem Lett*. 2012;3:2209–2214.
22. Ito LN, Mueting BJJAM, Pignolet LH. Heterobimetallic Au-Pd phosphine cluster complexes. X-ray crystal and molecular structure of $[Au_8Pd(PPh_3)_8](N0_3)_2$. *Inorg Chem*. 1989;28:2028–2029.
23. Bour JJ, Kanters RPF, Schlebos PPJ, et al. Hetero-metallic clusters. Synthesis and characterization of $[PtAu_8(PPh_3)_8](NO_3)_2$ and $[HPtAu_7(PPh_3)_8](NO_3)_2$. *Recl Trav Chim Pays-Bas*. 1987;106:157–158.
24. Shen H, Han YZ, Wu Q, Peng J, Teo BK, Zheng N. Simple and selective synthesis of copper-containing metal nanoclusters using $(PPh_3)_2CuBH_4$ as reducing agent. *Small Methods*. 2021;5:2–8.
25. Yang S, Wang S, Jin S, Chen S, Sheng H, Zhu M. A metal exchange method for thiolate-protected tri-metal $M_1Ag_xAu_{24-x}(SR)_{18}{}^0$ (M = Cd/Hg) nanoclusters. *Nanoscale*. 2015;7:10005–10007.
26. Hossain S, Ono T, Yoshioka M, et al. Thiolate-protected trimetallic $Au_{\sim 20}Ag_{\sim 4}Pd$ and $Au_{\sim 20}Ag_{\sim 4}Pt$ alloy clusters with controlled chemical composition and metal positions. *J Phys Chem Lett*. 2018;9:2590–2594.
27. Kang X, Wei X, Jin S, et al. Rational construction of a library of M_{29} nanoclusters from monometallic to tetrametallic. *Proc Natl Acad Sci*. 2019;116:18834–18840.
28. Kang X, Xiong L, Wang S, et al. Shape-controlled synthesis of trimetallic nanoclusters: structure elucidation and properties investigation. *Chem – Eur J*. 2016;22:17145–17150.
29. Du W, Jin S, Xiong L, et al. $Ag_{50}(Dppm)_6(SR)_{30}$ and its homologue $Au_xAg_{50-x}(Dppm)_6(SR)_{30}$ alloy nanocluster: seeded growth, structure determination, and differences in properties. *J Am Chem Soc*. 2017;139:1618–1624.
30. Lin Y-R, Kishore PVVN, Liao J-H, et al. Synthesis, structural characterization and transformation of an eight-electron superatomic alloy, $[Au@Ag_{19}\{S_2P(OPr)_2\}_{12}]$. *Nanoscale*. 2018;10:6855–6860.
31. Bootharaju MS, Sinatra L, Bakr OM. Distinct metal-exchange pathways of doped Ag_{25} nanoclusters. *Nanoscale*. 2016;8:17333–17339.
32. Wu Z. Anti-galvanic reduction of thiolate-protected gold and silver nanoparticles. *Angew Chem Int Ed*. 2012;51:2934–2938.
33. Wang S, Song Y, Jin S, et al. Metal exchange method using Au_{25} nanoclusters as templates for alloy nanoclusters with atomic precision. *J Am Chem Soc*. 2015;137:4018–4021.
34. Yao C, Xu C, Park I, et al. Giant emission enhancement of solid-state gold nanoclusters by surface engineering. *Angew Chem*. 2020;132:8347–8353.
35. Kazan R, Zhang B, Bürgi T. $Au_{38}Cu_1(2\text{-}PET)_{24}$ nanocluster: synthesis, enantioseparation and luminescence. *Dalt Trans*. 2017;46:7708–7713.
36. Rao B, Zhao T, Yang S, et al. X-ray crystal structure and doping mechanism of bimetallic nanocluster $Au_{36-x}Cu_x(m\text{-}MBT)_{24}$ (x = 1–3). *Dalt Trans*. 2018;47:475–480.

37. Wang S, Abroshan H, Liu C, et al. Shuttling single metal atom into and out of a metal nanoparticle. *Nat Commun*. 2017;8:848.
38. Li Y, Chen M, Wang S, Zhu M. Intramolecular metal exchange reaction promoted by thiol ligands. *Nanomaterials*. 2018;8:1070.
39. Song Y, Huang T, Murray RW. Heterophase ligand exchange and metal transfer between monolayer protected clusters. *J Am Chem Soc*. 2003;125:11694–11701.
40. Abdulhalim LG, Kothalawala N, Sinatra L, Dass A, Bakr OM. Neat and complete: thiolate-ligand exchange on a silver molecular nanoparticle. *J Am Chem Soc*. 2014;136:15865–15868.
41. Yan N, Xia N, Wu Z. Metal nanoparticles confronted with foreign ligands: mere ligand exchange or further structural transformation? *Small*. 2020;2000609:1–9.
42. Niihori Y, Kikuchi Y, Kato A, Matsuzaki M, Negishi Y. Understanding ligand-exchange reactions on thiolate-protected gold clusters by probing isomer distributions using reversed-phase high-performance liquid chromatography. *ACS Nano*. 2015;9:9347–9356.
43. Fernando A, Aikens CM. Ligand exchange mechanism on thiolate monolayer protected $Au_{25}(SR)_{18}$ nanoclusters. *J Phys Chem C*. 2015;119:20179–20187.
44. Fernando A, Aikens CM. Deciphering the ligand exchange process on thiolate monolayer protected $Au_{38}(SR)_{24}$ nanoclusters. *J Phys Chem C*. 2016;120:14948–14961.
45. Sels A, Barrabés N, Knoppe S, Bürgi T. Isolation of atomically precise mixed ligand shell $PdAu_{24}$ clusters. *Nanoscale*. 2016;8:11130–11135.
46. Sels A, Salassa G, Pollitt S, et al. Structural investigation of the ligand exchange reaction with rigid dithiol on doped (Pt, Pd) Au_{25} clusters. *J Phys Chem C*. 2017;121:10919–10926.
47. Bootharaju MS, Kozlov SM, Cao Z, et al. Tailoring the crystal structure of nanoclusters unveiled high photoluminescence via ion pairing. *Chem Mater*. 2018;30:2719–2725.
48. Kang X, Huang L, Liu W, et al. Reversible nanocluster structure transformation between face-centered cubic and icosahedral isomers. *Chem Sci*. 2019;10:8685–8693.
49. Kang X, Xiong L, Wang S, Pei Y, Zhu M. De-assembly of assembled Pt_1Ag_{12} units: tailoring the photoluminescence of atomically precise nanoclusters. *Chem Commun (Cambridge, United Kingdom)*. 2017;53:12564–12567.
50. Zhou M, Jin S, Wei X, et al. Reversible Cu−S motif transformation and Au 4 distortion via thiol ligand exchange engineering. *J Phys Chem C*. 2020;124:7531–7538.
51. Krishnadas KR, Ghosh A, Baksi A, Chakraborty I, Natarajan G, Pradeep T. Intercluster reactions between $Au_{25}(SR)_{18}$ and $Ag_{44}(SR)_{30}$. *J Am Chem Soc*. 2016;138:140–148.
52. Krishnadas KR, Baksi A, Ghosh A, Natarajan G, Pradeep T. Structure-conserving spontaneous transformations between nanoparticles. *Nat Commun*. 2016;7:13447.
53. Ghosh A, Ghosh D, Khatun E, Chakraborty P, Pradeep T. Unusual reactivity of dithiol protected clusters in comparison to monothiol protected clusters: studies using $Ag_{51}(BDT)_{19}(TPP)_3$ and $Ag_{29}(BDT)_{12}(TPP)_4$. *Nanoscale*. 2017;9:1068–1077.
54. Bose P, Chakraborty P, Mohanty JS, et al. Atom transfer between precision nanoclusters and polydispersed nanoparticles: a facile route for monodisperse alloy nanoparticles and their superstructures. *Nanoscale*. 2020;12:22116–22128.
55. Kazan R, Müller U, Bürgi T. Doping of thiolate protected gold clusters through reaction with metal surfaces. *Nanoscale*. 2019;11:2938–2945.
56. Zhu M, Aikens CM, Hollander FJ, Schatz GC, Jin R. Correlating the crystal structure of a thiol-protected Au_{25} cluster and optical properties. *J Am Chem Soc*. 2008;130:5883–5885.
57. Heaven MW, Dass A, White PS, Holt KM, Murray RW. Crystal structure of the gold nanoparticle $[N(C_8H_{17})_4][Au_{25}(SCH_2CH_2Ph)_{18}]$. *J Am Chem Soc*. 2008;130:3754–3755.
58. Kumara C, Aikens CM, Dass A. X-ray crystal structure and theoretical analysis of $Au_{25-x}Ag_x(SCH_2CH_2Ph)_{18}^-$ alloy. *J Phys Chem Lett*. 2014;5:461–466.
59. Tian S, Liao L, Yao C, et al. Structures and magnetism of mono-palladium and mono-platinum doped $Au_{25}(PET)_{18}$ nanoclusters. *Chem Commun*. 2016;52:9873–9876.
60. Hossain S, Suzuki D, Iwasa T, et al. Determining and controlling Cu-substitution sites in thiolate-protected gold-based 25-atom alloy nanoclusters. *J Phys Chem C*. 2020;124(40):22304–22313.
61. Bhat S, Baksi A, Mudedla SK, Natarajan G, Subramanian V, Pradeep T. $Au_{22}Ir_3(PET)_{18}$: an unusual alloy cluster through intercluster reaction. *J Phys Chem Lett*. 2017;8:2787–2793.

62. Anderson ID, Riskowski RA, Ackerson CJ. Observable but not isolable: the $RhAu_{24}(PET)_{18}^{1+}$ nanocluster. *Small*. 2020;24:1–7.
63. Sharma S, Yamazoe S, Ono T, et al. Tuning the electronic structure of thiolate-protected 25-atom clusters by co-substitution with metals having different preferential sites. *Dalt Trans*. 2016;45:18064–18068.
64. Yang S, Chai J, Chen T, et al. Crystal structures of two new gold–copper bimetallic nanoclusters: $Cu_xAu_{25-x}(PPh_3)_{10}(PhC_2H_4S)_5Cl_2^{2+}$ and $Cu_3Au_{34}(PPh_3)_{13}(^tBuPhCH_2S)_6S_2^{3+}$. *Inorg Chem*. 2017;56:1771–1774.
65. Wang S, Meng X, Das A, et al. A 200-fold quantum yield boost in the photoluminescence of silver-doped Ag_xAu_{25-x} nanoclusters: the 13th silver atom matters. *Angew Chem Int Ed*. 2014;53:2376–2380.
66. Kang X, Xiang J, Lv Y, et al. Synthesis and structure of self-assembled $Pd_2Au_{23}(PPh_3)_{10}Br_7$ nanocluster: exploiting factors that promote assembly of icosahedral nano-building-blocks. *Chem Mater*. 2017;29:6856–6862.
67. Qian H, Eckenhoff WT, Zhu Y, Pintauer T, Jin R. Total structure determination of thiolate-protected Au_{38} nanoparticles. *J Am Chem Soc*. 2010;132:8280–8281.
68. Kumara C, Gagnon KJ, Dass A. X-ray crystal structure of $Au_{38-x}Ag_x(SCH_2CH_2Ph)_{24}$ alloy nanomolecules. *J Phys Chem Lett*. 2015;6:1223–1228.
69. Chai J, Lv Y, Yang S, et al. X-ray crystal structure and optical properties of $Au_{38-x}Cu_x(2,4\text{-}(CH_3)_2C_6H_3S)_{24}$ (x = 0–6) alloy nanocluster. *J Phys Chem C*. 2017;121:21665–21669.
70. Zhang B, Safonova OV, Pollitt S, et al. On the mechanism of rapid metal exchange between thiolate-protected gold and gold/silver clusters: a time-resolved in situ XAFS study. *Phys Chem Chem Phys*. 2018;20:5312–5318.
71. Toffoli D, Baseggio O, Fronzoni G, Stener M, Fortunelli A, Sementa L. Pd doping, conformational, and charge effects on the dichroic response of a monolayer protected $Au_{38}(SR)_{24}$ nanocluster. *Phys Chem Chem Phys*. 2019;21:3585–3596.
72. Muñoz-Castro A. Single, double, and triple intercluster bonds: analyses of $M_2Au_{36}(SR)_{24}$ (M = Au, Pd, Pt) as 14-, 12- and 10-ve superatomic molecules. *Chem Commun*. 2019;55:7307–7310.
73. Jin R, Liu C, Zhao S, et al. Tri-icosahedral gold nanocluster $[Au_{37}(PPh_3)_{10}(SC_2H_4Ph)_{10}X_2]^+$: linear assembly of icosahedral building blocks. *ACS Nano*. 2015;9:8530–8536.
74. Zeng C, Qian H, Li T, et al. Total structure and electronic properties of the gold nanocrystal $Au_{36}(SR)_{24}$. *Angew Chem – Int Ed*. 2012;51:13114–13118.
75. Fan J, Song Y, Chai J, et al. The solely motif-doped $Au_{36-x}Ag_x(SPh\text{-}^TBu)_{24}$ (x = 1–8) nanoclusters: X-ray crystal structure and optical properties. *Nanoscale*. 2016;8:15317–15322.
76. Sakthivel NA, Stener M, Sementa L, et al. Crystal structure of $Au_{36-x}Ag_x(SPh\text{-}^TBu)_{24}$ nanoalloy and the role of Ag doping in excited state coupling. *J Phys Chem C*. 2019;123:29484–29494.
77. Li Q, Lambright KJ, Taylor MG, et al. Reconstructing the surface of gold nanoclusters by cadmium doping. *J Am Chem Soc*. 2017;139:17779–17782.
78. Kang X, Silalai C, Lv Y, et al. $Au_{15}Ag_3(SPhMe_2)_{14}$ nanoclusters – crystal structure and insights into ligand-induced variation. *Eur J Inorg Chem*. 2017;2017:1414–1419.
79. Yan N, Xia N, Liao L, et al. Unraveling the long-pursued Au_{144} structure by x-ray crystallography. *Sci Adv*. 2018;4:eaat7259.
80. Kumara C, Dass A. $AuAg)_{144}(SR)_{60}$ alloy nanomolecules. *Nanoscale*. 2011;3:3064–3067.
81. Kothalawala N, Kumara C, Ferrando R, Dass A. $Au_{144-x}Pd_x(SR)_{60}$ nanomolecules. *Chem Commun*. 2013;49:10850.
82. Kumara C, Zuo X, Ilavsky J, Cullen D, Dass A. Atomic structure of $Au_{329}(SR)_{84}$ faradaurate plasmonic nanomolecules. *J Phys Chem C*. 2015;119:11260–11266.
83. Kappen TGMM, Schlebos PPJ, Bour JJ, et al. Cluster growth: some representative reactions. Crystal structures of $[Pt(H)(AgNO_3)(AuPPh_3)_8](NO_3)$ and $[Pt(H)(AgNO_3)_2(AuPPh_3)_8](NO_3)$. *Inorg Chem*. 1995;34:2121–2132.
84. Kappen TGMM, Schlebos PPJ, Bour JJ, et al. New hydride-containing mixed-metal-gold phosphine clusters. Crystal structures of $[Pt(H)(CuCl)(AuPPh_3)_8](NO_3)$ and $[Pt(H)(CuCl)_2(AuPPh_3)_8](NO_3)$. *Inorg Chem*. 1995;34:2133–2142.
85. Hirai H, Takano S, Tsukuda T. Synthesis of trimetallic $(HPd@M_2Au_8)^{3+}$ superatoms (M = Ag, Cu) via hydride-mediated regioselective doping to $(Pd@Au_8)^{2+}$. *ACS Omega*. 2019;4:7070–7075.
86. Copley RCB, Mingos DMP. Synthesis and characterization of the centred icosahedral cluster series $[Au_9MIB_4Cl_4(PMePh_2)_8][C_2B_9H_{12}]$, where MIB = Au, Ag or Cu. *J Chem Soc Dalt Trans*. 1996;4:491.
87. Yang H, Wang Y, Lei J, et al. Ligand-stabilized $Au_{13}Cu_x$ (x = 2, 4, 8) bimetallic nanoclusters: ligand engineering to control the exposure of metal sites. *J Am Chem Soc*. 2013;135:9568–9571.

88. Sun Y, Yang D, Zhang Y, et al. Ligand-protected Au_4Ru_2 and Au_5Ru_2 nanoclusters: distinct structures and implications for site-cooperation catalysis. *Chem Commun*. 2020;56:12833–12836.
89. Yang H, Wang Y, Huang H, et al. All-thiol-stabilized Ag_{44} and $Au_{12}Ag_{32}$ nanoparticles with single-crystal structures. *Nat Commun*. 2013;4:2422.
90. Yan J, Su H, Yang H, et al. Asymmetric synthesis of chiral bimetallic $[Ag_{28}Cu_{12}(SR)_{24}]^{4-}$ nanoclusters via ion pairing. *J Am Chem Soc*. 2016;138:12751–12754.
91. Bootharaju MS, Chang H, Deng G, et al. $Cd_{12}Ag_{32}(SePh)_{36}$: non-noble metal doped silver nanoclusters. *J Am Chem Soc*. 2019;141:8422–8425.
92. Chai J, Yang S, Chen T, Li Q, Wang S, Zhu M. Chiral inversion and conservation of clusters: a case study of racemic $Ag_{32}Cu_{12}$ nanocluster. *Inorg Chem*. 2021;60:9050–9056.
93. Joshi CP, Bootharaju MS, Alhilaly MJ, Bakr OM. $[Ag_{25}(SR)_{18}]^-$: the "golden" silver nanoparticle silver nanoparticle. *J Am Chem Soc*. 2015;137:11578–11581.
94. Kim M, Weerawardene KLDM, Choi W, et al. Insights into the metal-exchange synthesis of $MAg_{24}(SR)_{18}$ (M = Ni, Pd, Pt) nanoclusters. *Chem Mater*. 2020;32:10216–10226.
95. Bootharaju MS, Kozlov SM, Cao Z, et al. Doping-induced anisotropic self-assembly of silver icosahedra in $[Pt_2Ag_{23}Cl_7(PPh_3)_{10}]$ nanoclusters. *J Am Chem Soc*. 2017;139:1053–1056.
96. Yang S, Chai J, Lv Y, et al. Cyclic Pt_3Ag_{33} and $Pt_3Au_{12}Ag_{21}$ nanoclusters with M_{13} icosahedra as building-blocks. *Chem Commun*. 2018;54:12077–12080.
97. Teo BK, Hong MC, Zhang H, Huang DB. Cluster of clusters: structure of the 37-atom cluster $[(p\text{-}Tol_3P)_{12}Au_{18}Ag_{19}Br_{11}]^{2+}$ and a novel series of supraclusters based on vertex-sharing icosahedra. *Angew Chem Int Ed Engl*. 1987;26:897–900.
98. AbdulHalim LG, Bootharaju MS, Tang Q, et al. $Ag_{29}(BDT)_{12}(TPP)_4$: a tetravalent nanocluster. *J Am Chem Soc*. 2015;137:11970–11975.
99. Mishra D, Lobodin V, Zhang C, Aldeek F, Lochner E, Mattoussi H. Gold-doped silver nanoclusters with enhanced photophysical properties. *Phys Chem Chem Phys*. 2018;20:12992–13007.
100. Wang S, Jin S, Yang S, et al. Total structure determination of surface doping $[Ag_{46}Au_{24}(SR)_{32}](BPh_4)_2$ nanocluster and its structure-related catalytic property. *Sci Adv*. 2015;1.
101. Zou X, Li Y, Jin S, et al. Doping copper atoms into the nanocluster kernel: total structure determination of $[Cu_{30}Ag_{61}(SAdm)_{38}S_3](BPh_4)$. *J Phys Chem Lett*. 2020;11:2272–2276.
102. Yan J, Malola S, Hu C, et al. Co-crystallization of atomically precise metal nanoparticles driven by magic atomic and electronic shells. *Nat Commun*. 2018;9:1–8.
103. Yang H, Wang Y, Yan J, et al. Structural evolution of atomically precise thiolated bimetallic $[Au_{12+n}Cu_{32}(SR)_{30+n}]^{4-}$ (n = 0, 2, 4, 6) nanoclusters. *J Am Chem Soc*. 2014;136:7197–7200.
104. Silalahi RPB, Chakrahari KK, Liao JH, et al. Synthesis of two-electron bimetallic Cu–Ag and Cu–Au clusters by using $[Cu_{13}(S_2CN^nBu_2)_6(C{\equiv}CPh)_4]^+$ as a template. *Chem – Asian J*. 2018;13:500–504.
105. Kang X, Wang S, Song Y, et al. Bimetallic Au_2Cu_6 nanoclusters: strong luminescence induced by the aggregation of copper(I) complexes with gold(0) species. *Angew Chem Int Ed*. 2016;55:3611–3614.
106. Song Y, Weng S, Li H, Yu H, Zhu M. The structure of a Au_7Cu_{12} bimetal nanocluster and its strong emission. *Inorg Chem*. 2019;58:7136–7140.
107. Song Y, Li Y, Zhou M, et al. Ultrabright $Au@Cu_{14}$ nanoclusters: 71.3% phosphorescence quantum yield in non-degassed solution at room temperature. *Sci Adv*. 2021;7:eabd2091.
108. Chen A, Kang X, Jin S, Du W, Wang S, Zhu M. Gram-scale preparation of stable hydride $M@Cu_{24}$ (M = Au/Cu) nanoclusters. *J Phys Chem Lett*. 2019;10:6124–6128.
109. Wan X-K, Cheng X-L, Tang Q, et al. Atomically precise bimetallic $Au_{19}Cu_{30}$ nanocluster with an icosidodecahedral Cu_{30} shell and an alkynyl−Cu interface. *J Am Chem Soc*. 2017;139:16.
110. Song Y, Li Y, Li H, et al. Atomically resolved $Au_{52}Cu_{72}(SR)_{55}$ nanoalloy reveals marks decahedron truncation and penrose tiling surface. *Nat Commun*. 2020;11:478.
111. Chakrahari KK, Silalahi RPB, Chiu TH, et al. Synthesis of bimetallic copper-rich nanoclusters encapsulating a linear palladium dihydride unit. *Angew Chem – Int Ed*. 2019;58:4943–4947.
112. Kwak K, Tang Q, Kim M, Jiang D-E, Lee D. Interconversion between superatomic 6-electron and 8-electron configurations of $M@Au_{24}(SR)_{18}$ clusters (M = Pd, Pt). *J Am Chem Soc*. 2015;137:10833–10840.
113. Liu X, Yuan J, Yao C, et al. Crystal and solution photoluminescence of $MAg_{24}(SR)_{18}$ (M = Ag/Pd/Pt/Au)

nanoclusters and some implications for the photoluminescence mechanisms. *J Phys Chem C*. 2017;121:13848–13853.
114. Bootharaju MS, Kozlov SM, Cao Z, et al. Direct versus ligand-exchange synthesis of $[PtAg_{28}(BDT)_{12}(TPP)_4]^{4-}$ nanoclusters: effect of a single-atom dopant on the optoelectronic and chemical properties. *Nanoscale*. 2017;9:9529–9536.
115. Kang X, Li X, Yu H, et al. Modulating photo-luminescence of Au_2Cu_6 nanoclusters: via ligand-engineering. *RSC Adv*. 2017;7:28606–28609.
116. Barrabésbarrabés N, Zhang B, Bü T. Racemization of chiral $Pd_2Au_{36}(SC_2H_4Ph)_{24}$: doping increases the flexibility of the cluster surface. *J Am Chem Soc*. 2014;136(41):14361–14364.
117. Jin S, Xu F, Du W, et al. Isomerism in Au–Ag alloy nanoclusters: structure determination and enantioseparation of $[Au_9Ag_{12}(SR)_4(Dppm)_6X_6]^{3+}$. *Inorg Chem*. 2018;57:5114–5119.
118. Zhang B, Bürgi T. Doping silver increases the $Au_{38}(SR)_{24}$ cluster surface flexibility. *J Phys Chem C*. 2016;120:4660–4666.
119. Deng G, Malola S, Yan J, et al. From symmetry breaking to unraveling the origin of the chirality of ligated $Au_{13}Cu_2$ nanoclusters. *Angew Chem – Int Ed*. 2018;57:3421–3425.

CHAPTER

17

Naked clusters and ion chemistry of clusters

Madhuri Jash[a] *and Thalappil Pradeep*[b]

[a]Postdoctoral Researcher, Department of Applied Physics, KTH - Royal Institute of Technology, Stockholm, Sweden [b]Deepak Parekh Institute Chair Professor and Professor of Chemistry, Department of Chemistry, Indian Institute of Technology Madras, Chennai, India

17.1 Introduction

Nanoclusters (NCs) are aggregates of a countable number of particles which can exist in both condensed and gas phases. Gas phase unprotected clusters known as "naked clusters" are ensembles of atoms or molecules that do not have a stabilizing ligand shell. Whereas in the condensed phase, clusters are generally synthesized via a wet chemistry approach in the presence of protecting ligands or are embedded in a matrix. The main drawback of atomically precise ligand protected NCs is the difficulty of removing the ligand and sintering of the NCs into bigger particles during their catalytic applications.[1] Hence, unraveling the properties of isolated, atomically precise NCs is essential for an in-depth understanding of cluster science. In the case of gas phase naked clusters, the absence of ligands and stabilizing medium provides an opportunity to investigate the molecule-like properties and chemical reactivity of size-selected clusters. Typically, these clusters are extremely reactive under ambient conditions due to the absence of protecting ligands and cannot be stored in their free state. In a typical experiment, naked clusters are prepared in a vacuum or under an inert atmosphere where their properties are investigated and their characterization is performed.

Gas phase naked clusters are synthesized using different types of cluster sources. During the 1960s and 1970s, cluster sources based on high-temperature based techniques were developed, and clusters were analyzed using mass spectrometry. In addition to experiments, theoretical models (liquid drop model and jellium model) and computational methods have been employed to study several properties of gas phase clusters such as electronic and geometric shell structures, binding energies, cluster bonding types, etc.[2] In the above backdrop, this chapter provides a comprehensive understanding of different types of naked cluster sources, their detection, analysis, and ionization techniques. Further, the gas phase reactivity, catalysis, various characterization techniques, clusters supported on solids are discussed in detail.

DOI: https://doi.org/10.1016/B978-0-323-90879-5.00003-2

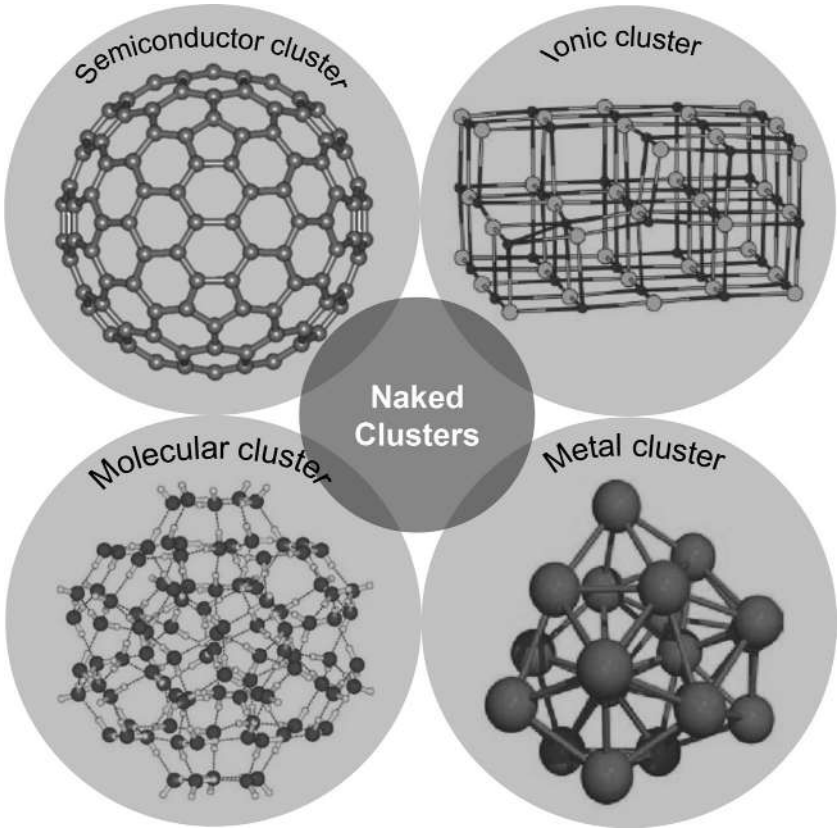

FIGURE 17.1 A few examples of naked clusters. In each category, there are many clusters. Among all the examples of naked clusters, fullerene (semiconductor cluster), sodium chloride cluster (ionic cluster), water cluster (molecular cluster), and sodium cluster (metal cluster) have been shown in this figure.

17.2 Types of naked clusters

Based on the composition and nature of bonding, naked clusters can be classified as metal clusters, semiconductor clusters, ionic clusters, rare gas clusters, and molecular clusters (Fig. 17.1).

17.2.1 Metal clusters

Metal clusters are composed of alkali and alkaline earth metals (s-block elements); and transition metals (d-block elements). Metal clusters can be either monometallic or bi-, tri-, or multimetallic. The alkali metal clusters show intense peaks in their mass spectra in comparison to their neighboring elements, which depend upon their nuclearity ($N = 2, 8, 20, 40, 58$, etc.). Knight et al. and Walt de Heer observed that the mass spectra of bare, gas phase Na clusters show abundances for certain nuclearity (known as magic numbers), as shown in Fig. 17.2.[3]

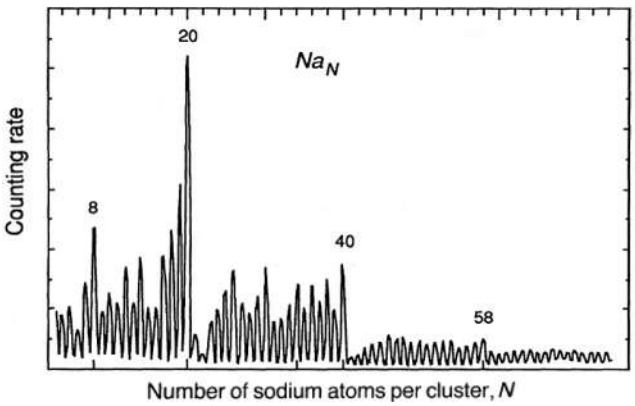

FIGURE 17.2 Mass spectrum of Na_N clusters. It shows the higher abundance for $N = 8$, 20, 40, etc., corresponding to electronically closed-shell clusters (reproduced with permission from ref.[3]).

These sodium clusters were generated by the ionization of sodium molecular beam, generated by supersonic nozzle technique. Then these clusters were mass-selected by a quadrupole mass analyzer and detected by an ion detection system having single-ion counting capability. The higher stability of magic numbered clusters was justified through the jellium model. Different kinds of metal clusters of sodium, aluminum, copper, silver, gold, zinc, cadmium, etc. are known, where their magic numbered nuclearity depends on the cluster's charge state, free-electron count, electron localizing effect, s–p hybridization, spin-pairing effect, etc. Thus, for the metal clusters, physical properties such as ionization energies and electron affinities as a function of size have been studied using theoretical models.[4] The stability of clusters is generally governed by either geometric and/or electronic shell structure, which depends on the electron configuration, electronic density of state (DOS), and cluster-melting temperature.

17.2.2 Semiconductor clusters

Semiconductor clusters are composed of group 14 elements like carbon, silicon, and germanium. These clusters are covalent in nature, and the formation of a cluster in equilibrium vapor is mainly due to the directional covalent binding between these elements. Carbon has a tendency to form clusters readily, and the bonding in these clusters has a higher covalent character than cluster composed of other elements. Carbon clusters were initially produced by the electric discharge method, then the method of laser vaporization of graphite rod was used. Fig. 17.3 represents a typical photoionization time of flight mass spectrum (PI-TOF-MS) of carbon clusters where as large as 120 atoms are shown.[5] After the historical discovery of C_{60} in 1985 by laser vaporization, there has been increased research interest in this field leading to the development of a number of novel clusters with unusual structures and properties.[6] In addition to carbon, silicon clusters have been studied significantly, and the mass spectrum of the first silicon cluster was reported in 1985.[7] The silicon clusters were produced by laser flash evaporation followed by quenching in a carrier gas and then the vapor was cooled by supersonic expansion. The higher abundance of Si_N^+ ($N = 6$, 10, 16, and 32) was revealed in their mass spectrum. The photofragmentation and reactivity of mass selected silicon clusters have been studied using ion trap mass analyzers.[8] Germanium clusters with a higher abundance of Ge_N^+, for $N = 6$, 10, 14, 15, and 18 were observed as in the case of silicon

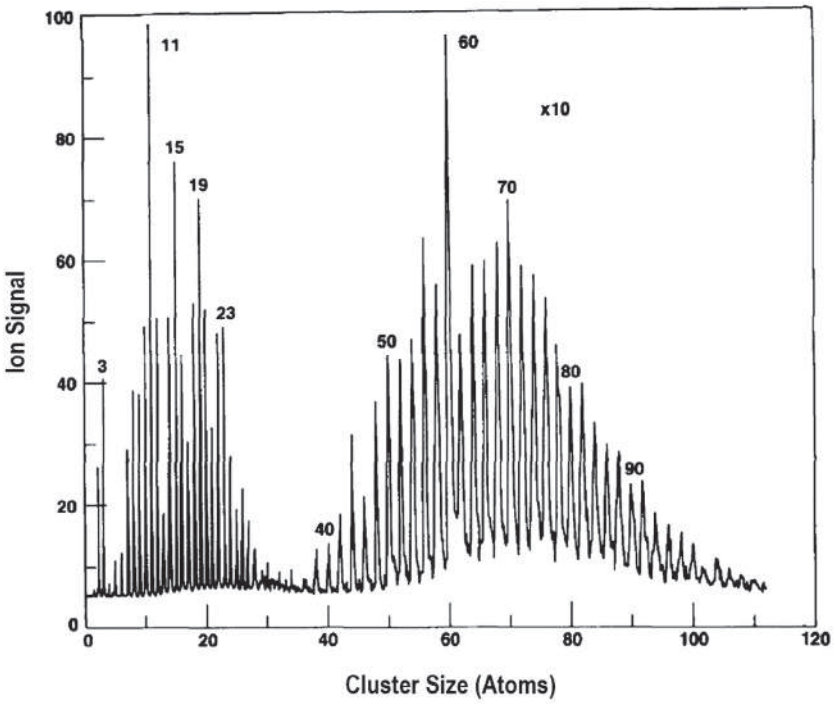

FIGURE 17.3 PI-TOF-MS of carbon clusters produced from a laser vaporization source using a Nd:YAG laser. Here the formation of carbon clusters with odd nuclearity, C_N were observed in the range of 1–30 atoms, whereas clusters with even nuclearity C_{2N+} were formed above around 40 atoms where, $20 \leq N \leq 50$ (reproduced with permission from ref.[5]).

clusters. Apart from elemental semiconductor clusters, compound semiconductor clusters like gallium arsenide clusters (Ga_xAs_y), indium phosphide clusters (In_xP_y); metal oxide (MoO_3, WO_3, MgO, FeO, LiO) and metal chalcogenide (MoS_2, WS_2, ZnS, FeS, Nb_2S_2) clusters have also been studied.[9] Although the bonding in A–B type compound semiconductor is mainly covalent, it can have more ionic character depending on the electronegativity differences of the constituent elements.

17.2.3 Ionic clusters

Ionic clusters are derived from ionic compounds composed of elements that exhibit considerable electronegativity differences. The nature of bonding in these clusters is ionic in nature. Ionic bonds exist between electropositive metals and electronegative nonmetals (e.g., the halides and oxides of alkali and alkaline earth metals). Alkali metal halide (NaCl, CsCl) clusters are perfect examples of this kind whereas, metal oxide clusters also exist.

In metal oxide clusters, the nature of bonding is affected by the anion polarization and covalent character. Generally, the heating or laser vaporization of ionic compounds has been followed to generate ionic clusters. Subsequently, the vapor is quenched in a stream of cold inert gas. Ionic clusters can be produced as positively or negatively charged clusters or neutral,

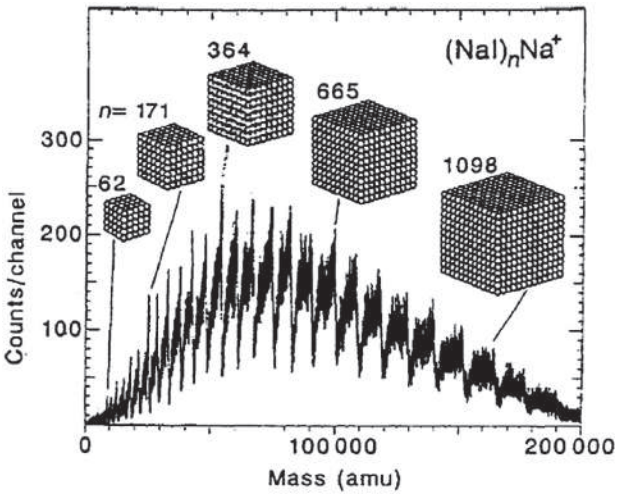

FIGURE 17.4 Mass spectrum of NaI clusters where the difference between two peaks represents the number of atoms needed to complete one face of a cuboid structure (reproduced with permission from ref.[10]).

depending on their stoichiometry. For NaI clusters ($(NaI)_nNa^+$), Fig. 17.4 shows the mass spectrum of the corresponding cuboidal clusters where the interval between minima refer to the number of atoms needed to cover one face of a cuboid.[10] The study of ionic clusters allows us to determine the size of the cluster at which it manifests bulk-like properties due to the changes in interionic bonding. At this stage, they may be called nanocrystalline and are stable due to exposure of only the lowest energy square surfaces in their structures.

17.2.4 Rare gas clusters

Rare gas clusters are the most widely studied clusters due to their ease of formation and low reactivity. In the early days, rare gas clusters were investigated in molecular beam experiments.[11] These clusters are bound by weak van der Waals forces, and their interatomic attraction increases with increasing atomic masses (from helium to radon). Supersonic expansion method is employed to create such clusters into a vacuum. They are detected in the mass spectrometer as cations where the ionization is carried out by electron bombardment or photoionization method. During ionization, fragmentation and evaporation of the clusters occur due to the transfer of 1–2 eV of energy to the cluster. Therefore, the abundances observed in the mass spectrum of rare gas clusters reflect the stabilities of the clusters toward evaporation. The magic number observed in the experimental mass spectrum is due to the size-dependency of the binding energy of the rare gas cluster cations, and it also depends on the fragmentation process that occurs during ionization. Whereas, for neutral clusters, magic numbers are different, and they can be understood in terms of cluster structures.

17.2.5 Molecular clusters

Molecular clusters are aggregates of an integer number of molecules. The homomolecular clusters, for example, $(H_2O)_N$, are composed of the same type of molecules, while

hetero-molecular clusters, for example, $(CH_3OH)_N(H_2O)_M$, are composed of molecules of different types. There are two different types of bonding in a molecular cluster: strong covalent bond between constituent molecules and much weaker intermolecular force between clusters. Types of forces found in molecular clusters are dispersion forces, multipolar induction forces and hydrogen bonding. A molecular cluster can be ionized through the ionization of a molecule of the cluster accompanied by molecular excitation. In general, water clusters are synthesized by evaporation, condensation and supersonic expansion into a molecular beam. The neutral water clusters are then ionized by electron impact or photoionization techniques for mass spectrometric measurements. Apart from water clusters, several experiments have been carried out on hydrogen bonded methanol and ammonia clusters and nonhydrogen bonded carbon dioxide clusters.

17.2.6 Cluster molecules

Cluster molecules exist as covalently bonded clusters or cages (P_4, $[B_{12}H_{12}]^{2-}$, $Os_6(CO)_{18}$). These species are mostly thermodynamically and/or kinetically stable and can exist in solid, liquid and gas phases. They are characterized using classical spectroscopic techniques like IR, NMR, XRD, etc.

17.3 Mass spectrometry as a primary characterization technique of naked clusters

Mass spectrometry is a primary technique for detecting and analyzing clusters in the gas phase, and it can provide important information about the composition, purity, structure, and stability. Mass spectrometry is one of the oldest techniques used in cluster science. The experimental studies on clusters are divided into three main stages: generation, investigation and detection of cluster. First, clusters are generated using various cluster sources, and the clusters so formed can exist as neutral, positively, or negatively charged entities. The development of the molecular beam technique has made it possible to study the "free" clusters or gas phase naked clusters in an interaction free environment (in the absence of ligands and solvents) by using mass spectrometry. Although measuring the physical properties of these gas phase free clusters is challenging, deposition of the size-selected clusters on a substrate can solve this issue partially. Physicists first introduced mass spectrometry in the late 1880s, and the first mass spectrometer was constructed in 1912. Later, it developed rapidly in conformance with the advancement of MS technologies. Mass spectrometry basically works on the principle of generating gas phase ions and detecting them based on their mass-to-charge ratio (m/z). The explication of mass spectral intensities and emergence of magic number clusters have been done based on the cluster stability, cluster type, and experimental set up.

17.3.1 Synthesis of naked clusters using various cluster sources

In all sources, cluster generation takes place in different stages: vaporization (atoms or molecules are produced in the gas phase), nucleation (early stage of condensation to form cluster nucleus), growth (addition of more atoms or molecules to the cluster nucleus), and

coalescence (formation of larger clusters by integrating smaller clusters). Depending on the nature and conditions of the cluster source, different size distributions of clusters can be produced. Among the variety of available sources, the most commonly used are described below with their most relevant characteristics. The following section discusses some of the most commonly used cluster sources (see Fig. 17.5).[2c]

17.3.1.1 Laser vaporization source

In this technique, metal vapor is produced by the pulsed laser ablation which generates small and medium-sized clusters (Fig. 17.5A).[6] Intense pulsed UV laser, for example, ND:YAG (neodymium-doped yttrium aluminum garnet) or excimer can be used. The laser is focused on the surface of a rod of target material wherein a 10 ns pulse vaporizes 10^{14}–10^{15} atoms per mm^2 of the target. A pulse of cold helium gas is allowed to flow through the vaporized material (a plasma with a temperature of around 10^4 K) that leads to cooling the metal vapor and produces clusters that are then ejected out of the nozzle. Since intense lasers cause ionization, the generated clusters can be neutral, cationic or anionic and do not require postionization, and can be conveniently analyzed using mass spectrometry. Size-distribution of clusters generated using this method depends on the source conditions and can typically contain several hundred to thousands of atoms. The pulsed source produces an immediate high intensity of clusters suitable for the TOF analysis in the mass spectrometer.

17.3.1.2 Pulsed arc cluster ion source

Pulsed arc cluster ion source (PACIS) is closely related to the vapor ionization source wherein the rod or the cluster precursor is vaporized by a powerful electric discharge instead of a laser beam (Fig. 17.5B).[12] Compared to laser vaporization source, cluster beam created using this source is more intense and less expensive as it does not require any laser. About 10% of the clusters generated by this technique are charged, facilitating mass spectrometric measurement possible without any postionization process.

17.3.1.3 Supersonic nozzle source

Supersonic nozzle sources are of two types: unseeded and seeded. In case of unseeded, clusters are formed without any carrier gas. While in the seeded, metal is vaporized (with the vapor pressure of 10–100 mbar $\approx 10^3$–10^4 Pa) in a hot oven, and the vapor is mixed with an inert carrier gas with a pressure of $\approx 10^5$–10^6 Pa, and at a temperature of 77–1500 K. The mixture of metal and inert gas is then ejected into the vacuum (10^{-1}–10^{-3} Pa) through a small nozzle, thereby creating a supersonic beam (Fig. 17.5C). The mean free path of particles is smaller than the diameter of the nozzle, resulting in numerous collisions during the expansion of the gas mixture. The adiabatic and isoenthalpic expansion into the vacuum cools the vapor resulting in supersaturation and condensation in the form of clusters.[13] These cluster sources generate intense cluster beams with narrow velocity distribution, and the generated clusters can contain few hundreds to thousands of atoms each. In the case of the seeded type, larger clusters are produced, while the absence of carrier gas results in smaller clusters (with fewer than 10 atoms), where cluster abundances entirely depend on the binding energies, which is a thermodynamic process.

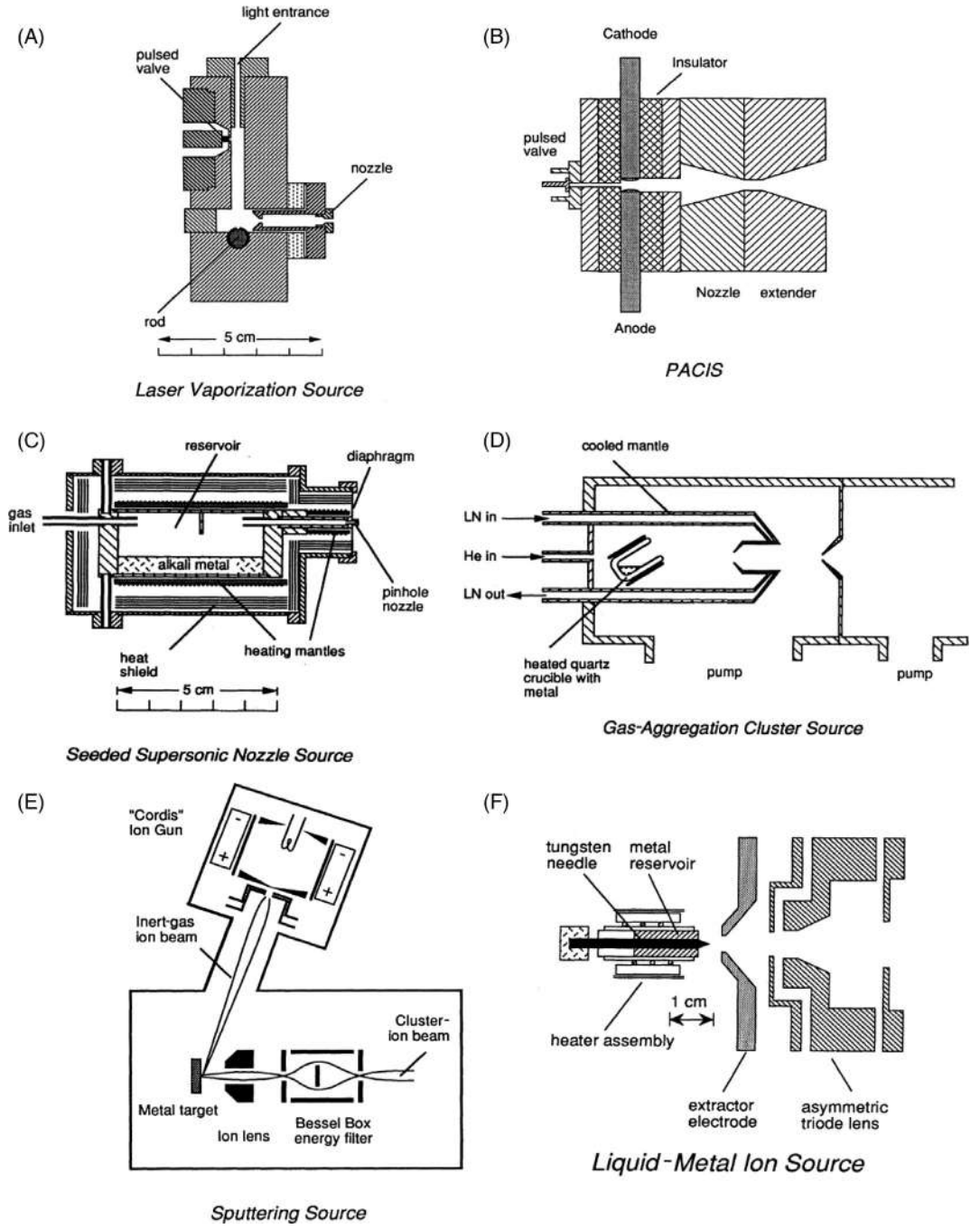

FIGURE 17.5 Various cluster sources (A) laser vaporization source, (B) PACIS, (C) seeded supersonic nozzle source, (D) gas-aggregation cluster source, (E) sputtering source, (F) liquid metal ion source (reproduced with permission from ref.[2c]).

17.3.1.4 Gas-aggregation or smoke sources

In this source, metal vapor is produced via evaporation or sputtering techniques and is introduced into a cold inert quench gas. The vapor becomes supersaturated and clusters aggregate (Fig. 17.5D).[14] This source generates a continuous cluster beam of low to medium boiling (<2000 K) metals, including noble metals. Here, the intensities of the cluster beam are much lower compared to the seeded supersonic nozzle source. However, a higher number of collisions with the cooling gases result in bigger sized clusters (>20,000 atoms each).

17.3.1.5 Ion sputtering source

In this source, clusters are formed by bombarding a target material with high energy inert gas ions (Fig. 17.5E). In contrast to the previously discussed sources, here cluster formation is independent of the condensation process in inert gas. Heavier inert gases (Kr or Xe) give the best results for cluster production, while bombardment energies range from 10 to 30 keV with currents up to 10 mA.[15] These sources typically generate small, singly ionized clusters, although mass selected clusters with hundreds of atoms can also be generated.

17.3.1.6 Magnetron sputtering source

Magnetron sputtering source is a modified type of ion sputtering source wherein a plasma is generated in argon by applying a DC or RF potential on a target material and is confined using a magnetic field.[16] Usually, this method produces small clusters (2–30 atoms each), and the intensity of clusters diminishes rapidly with an increase in cluster size. However, it is observed that a hybrid magnetron sputtering/condensation source can produce copper and silver clusters with sizes ranging from 2 to 70,000 atoms.

17.3.1.7 Liquid metal ion source

This source is used to create multiply charged clusters of metals with a low melting point. In this technique, a very high electric field is applied at the tip of the tungsten needle (Fig. 17.5F).[17] The desired metal heated above its melting point wets the needle along with an applied potential. The presence of high potential at the tip of the needle causes electrospray of the metal. The hot and multiply charged droplets generated through electrospray are then evaporated, which cause cooling of the droplets. When the Coulomb repulsion between the charged droplets becomes higher than the binding energy of the drop, the charged droplets undergo fission to create smaller clusters.

17.3.2 Cluster growth and generation of cluster ions

Cluster growth occurs in two stages: nucleation and growth. To explain the process of nucleation, a three-body collision is assumed to occur when the binding energy of the dimer is greater than the thermal energy of the beam leading to the formation of a dimeric nucleus. Here, the third body involved in the collision removes the excess internal energy of the dimer as kinetic energy. The dimer serves as a seed for further cluster growth. Subsequently, the coalescence between the smaller clusters leads to the formation of larger clusters.

To detect the cluster in mass spectrometer, it is necessary to segregate clusters according to their m/z value, and therefore it is essential to ionize the clusters after their growth. In case the

growth results in charged clusters, postionization experiments can be eliminated. However, postionization techniques like electron impact, photoionization, electric discharge, or electron transfer processes are employed to generate charged species from neutral clusters.

17.3.3 Synthesis of naked clusters from different precursors and ionization techniques

The production of gas phase naked clusters using different cluster sources including laser ablation, PACIS, supersonic nozzle sources, gas aggregation, ion and magnetron sputtering, liquid ion sources, etc. are reported, wherein adiabatic expansion of a gas into an evacuated chamber is the most commonly used technique to get a supersaturated and condensed form of clusters. In most of these cases, a rod of target material or bulk material is used to produce a molecular beam of clusters after irradiating with laser, electric discharge, high temperature, or ion bombardment. However, there is another important area of gas phase cluster science in which different types of precursors like solution phase atomically precise monolayer protected clusters, metal salts, etc. are employed to synthesize atomically precise naked gas phase clusters. Novel ionization techniques are developed with these new cluster sources to obtain a narrow size-distribution of the specific cluster. Some common examples are discussed below.

17.3.3.1 Electrospray ionization

Electrospray ionization (ESI) technique is a soft ionization technique discovered in 1989 to ionize biological supramolecules. ESI finds application in mass spectrometry to generate cluster ions from liquids and solutions. In this technique, the analyte dissolved in a solvent is injected through a needle in the presence of a high electric field and a carrier gas. The presence of very high potential at the tip of the needle leads to the formation of charged microdroplets of the analytes. The solvent continues to evaporate from the surface of the charged droplets until it reaches its Rayleigh limit. At the Rayleigh limit, the surface tension can no longer sustain the Coulomb force of repulsion between the like charges. This results in Coulomb fission, whereby several smaller and stable droplets are formed. The new droplets further undergo Coulomb fissions and solvent evaporation cycles until it contains an average single analyte molecule or less. Then further evaporation of the remaining solvent from the droplet generates the gas phase ions. These charged ions/clusters then enter into the analyzer of the mass spectrometer, which is maintained under a high vacuum. This method allows one to obtain gas phase solvated ions of complex or nonvolatile molecules. Several variants of ESI technique have been developed over the years, of which nanoelectrospray is the most popular, wherein a significantly less volume of sample is needed, and the flow rate of the sample is used as low as 20–50 nL/min.

17.3.3.1.1 Metal salts as precursors

Alkali metal halides and other alkali metal salts are commonly employed to produce cluster ions in electrospray ionization mass spectrometry (ESI MS). The ability of these salts to form gas phase metal cluster ions in ESI MS highly depends on the experimental conditions such as the choice of solvents, salt concentration, instrumental conditions, pH of the solution, type of cations and anions present in the salt and the stability of gas phase cluster ions. Mass

calibration of ESI MS can be achieved using various calibration compounds, which includes alkali metal salts as shown by Anacleto et al.[18] In their results, cluster formation was shown at an elevated salt concentration of (0.1 M) in water–acetonitrile mixture (50% v/v). Naked silver cluster cations (Ag_9^+) were also synthesized by ESI of a solution containing metal salt, tryptophan and is accomplished via multiple step collision-induced dissociation (CID). O'Hair and others showed the possibility of obtaining silver and silver hydride clusters through ESI of silver salt or silver–amino acid complexes. Cooks et al. have made notable contributions to the field of ESI techniques. They proposed a novel method for producing naked metal clusters in air from silver acetate and silver fluoride.[19] They reported the formation of naked cationic clusters, Ag_n^+ ($n = 2$–17), from electrospray silver acetate salt using a special technique (Fig. 17.6), wherein the electrosprayed salt is passed through a heated copper tube. They also generated anionic clusters of Ag_n^- ($n = 3$–18) from heated electrospray silver fluoride solution.

17.3.3.1.2 Collision-induced dissociation and thermal ligand desorption of ligand protected clusters

Atomically precise ligand protected nanoclusters can also be used as starting material to make gas phase naked clusters by stripping off the ligands from the protected clusters. Desorption of ligands from clusters can result in the formation of naked clusters. Various ligands such as thiols, phosphines, alkyne, etc. are used as protecting agents for clusters. Over the years, different methodologies have been developed to create naked clusters from ligand protected clusters in solution. In 1986, Schmid et al., for the first time, developed a methodology to create naked Au_{13} clusters by electrophoresis of protected $[Au_{55}(PPh_3)_{12}Cl_6]$ clusters in solution that reorganizes to form superclusters $(Au_{13})_{13}$ and microcrystallites $[(Au_{13})_{13}]_n$. One of the recent reports showed that the application of collision energy on ligand protected clusters could remove the ligands, and naked clusters can be generated in the gas phase. This method has been employed to create a series of naked clusters, Ag_n^+ ($n = 1$–17) from ligand-protected $[Ag_{18}H_{16}(TPP)_{10}]^{2+}$ clusters (Fig. 17.7A). Similarly, naked clusters Ag_{21}^+, Ag_{19}^+, Ag_{13}^+, and Ag_{25}^+ were obtained from $[Ag_{25}H_{22}(DPPE)_8]^{3+}$,$[Ag_{22}H_{19}(DPPE)_8]^{3+}$ (DPPE = 1,2-bis(diphenylphosphino)ethane), $[Ag_{15}H_{13}(DPPH)_5H_{13}]^{2+}$ (DPPH = 1,6-bis(diphenylphosphino)hexane), and $[Ag_{27}H_{22}(DPPB)_7]^{3+}$ (DPPB = 1,4-bis(diphenylphosphino) butane), respectively.[20] The formation of Ag_{17}^+ from $[Ag_{18}H_{16}(TPP)_{10}]^{2+}$ was also observed in air and outside the mass spectrometer by passing the electrosprayed clusters through a heated tube (Fig. 17.7B).[21] This single species or mass selected naked cluster can be stabilized using an appropriate substrate and has the potential in catalytic applications.

17.3.3.1.3 Photodissociation of ligand protected clusters

Photodissociation is a method to activate molecules leading to the breaking of the chemical bonds, which relies on the absorption of photons. Irradiation with UV photons is preferred owing to the very high energy deposition per photon. For a UV photon with a wavelength of 193 nm, the energy deposition per photon is 6.4 eV. Moreover, in the case of thiol protected gold clusters, laser irradiation has been efficient in stripping off the ligands by cleavage of the M–S (M = metal) bonds, as shown in Fig. 17.8. Using this method, naked gold clusters (Au_4^+ to Au_{20}^+) were prepared from Au_{25}(p-MBA)$_{18}$ and Au_{36}(p-MBA)$_{24}$ clusters in the gas phase.[22] ESI of the clusters was carried out in a mass spectrometer, wherein a 193 nm ArF excimer laser was coupled with the spectrometer for the photodissociation experiment. A pulsed laser

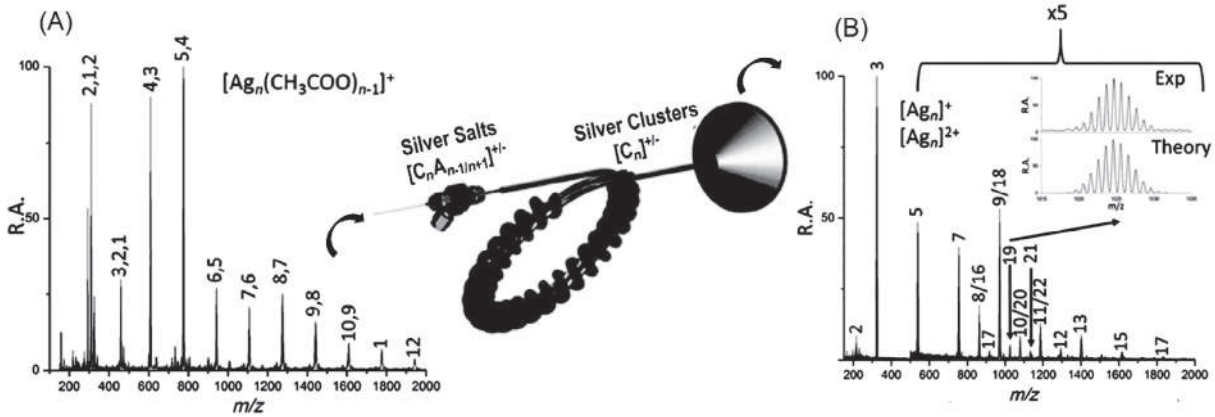

FIGURE 17.6 The ESI mass spectrum of (A) unheated and (B) heated electrosprayed silver acetate salt. Both spectra are collected in positive ion mode. When passing through a heated coiled copper tube outside the mass spectrometer, the electrosprayed salt produced naked metal clusters. In A, the number above the peak indicates the number of silver atoms (first number), ligands (second number), and water molecules (third number) present. In B, the number above the peak indicates the number of silver atoms (reproduced with permission from ref.[19]).

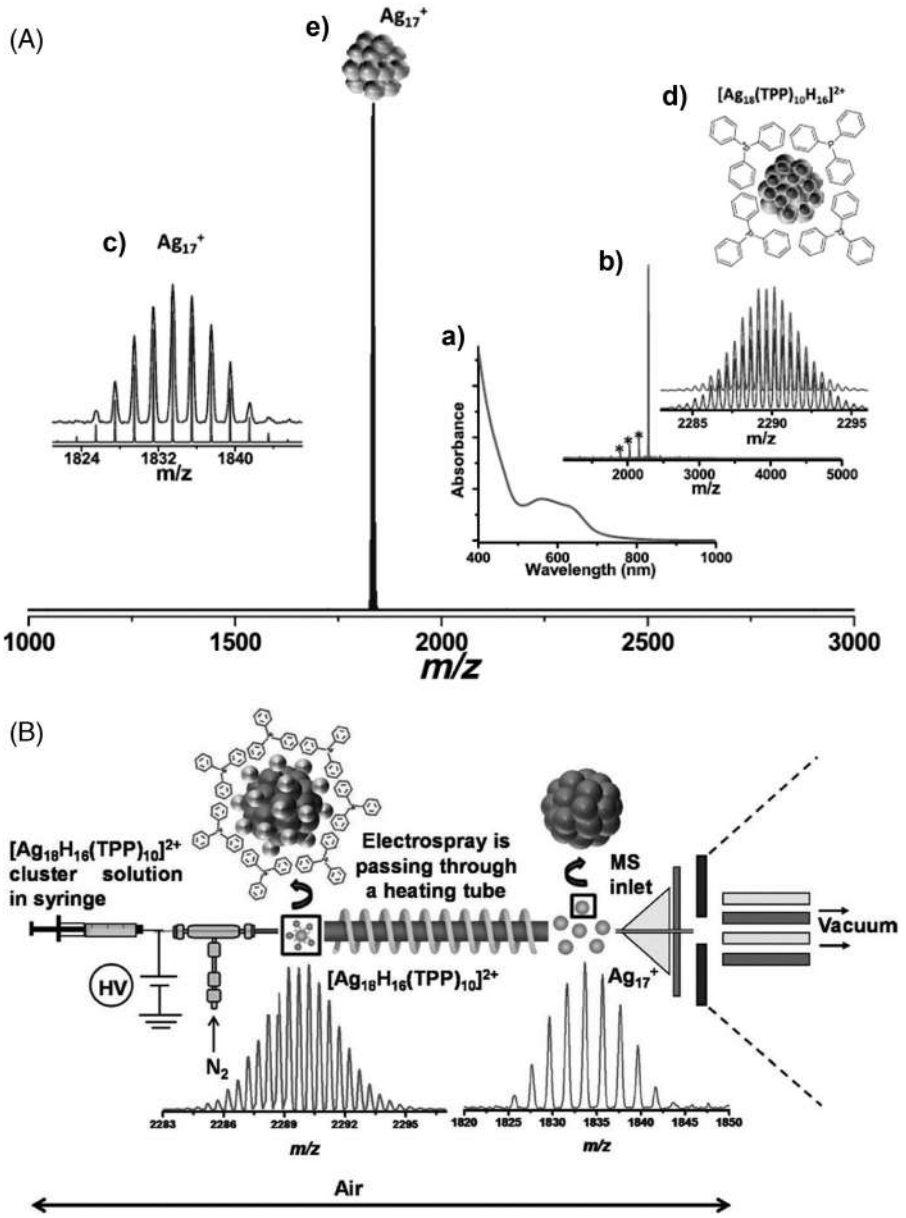

FIGURE 17.7 (A) ESI mass spectrum of naked cluster ion (Ag_{17}^+), which was produced by in situ fragmentation of parent cluster $[Ag_{18}(TPP)_{10}H_{16}]^{2+}$. a) Represents the UV−vis spectrum, and b) represents the full-range ESI MS spectrum of the parent cluster. c) Represents the calculated isotopic distribution of Ag_{17}^+. d) and e) are the schematic illustrations of the parent cluster and the naked cluster, respectively (reproduced with permission from ref.[20a]). (B) is the schematic representation of the experimental set-up, which is used to prepare the naked cluster Ag_{17}^+ from the protected cluster $[Ag_{18}(TPP)_{10}H_{16}]^{2+}$ in air (reproduced with permission from ref.[21]).

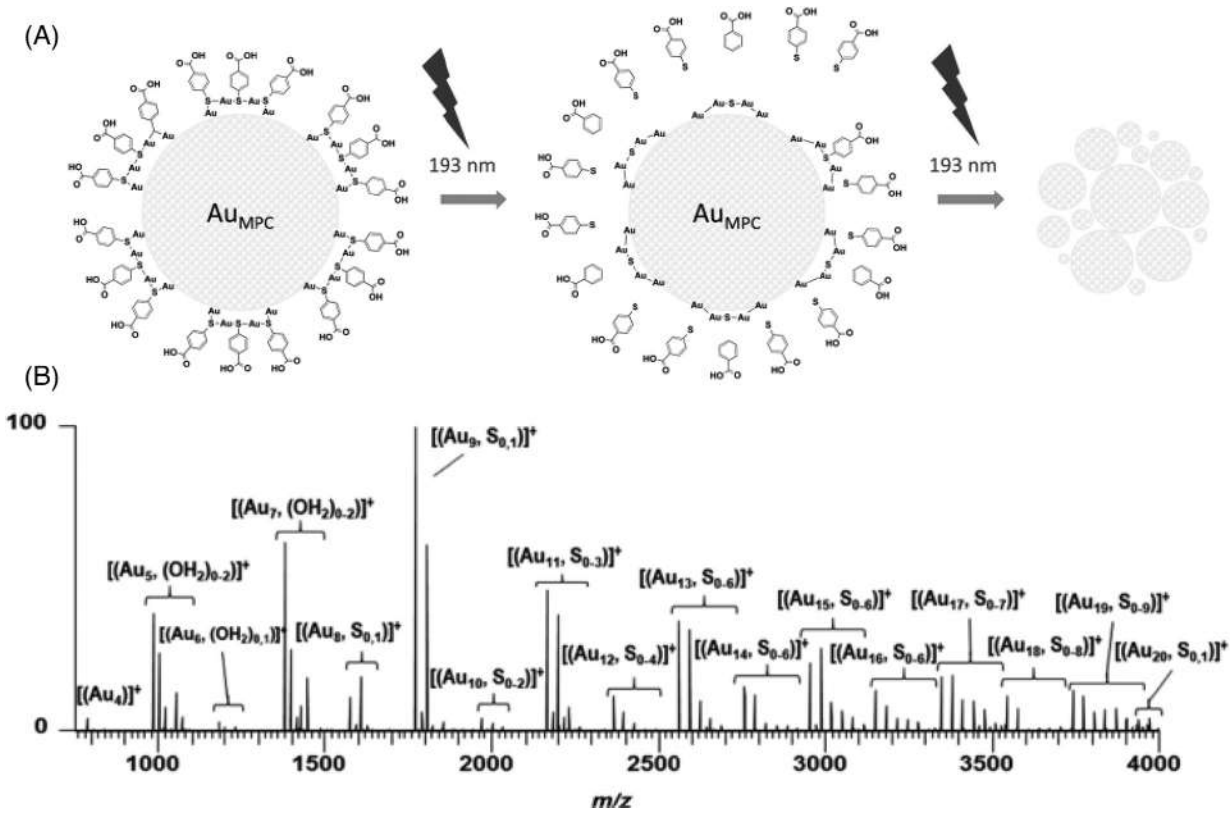

FIGURE 17.8 (A) Schematic representation of the formation of naked cluster from monolayer protected clusters by ultraviolet photodissociation (UVPD). (B) UVPD mass spectra of $[Au_{25}(pMBA)_{18} + 4NH_4]^{3+}$ acquired at 10 pulses, which shows the formation of naked clusters $(Au_nS_0)^+$ (reproduced with permission from ref.[22]).

was used in this experiment, and the photodissociation was conducted inside a high-pressure linear ion trap of the mass spectrometer.

17.3.3.2 Matrix-assisted laser desorption ionization from protein templates

Matrix-assisted laser desorption ionization (MALDI) is an ionization technique used in mass spectrometry. This technique enables the researchers to study biomolecules such as proteins, DNA, etc. MALDI and ESI were invented by Koichi Tanaka and John Fenn, respectively, and were awarded the 2002 Nobel Prize in chemistry. In MALDI mass spectrometry, the sample is dissolved in a suitable solvent and mixed with the solution of an appropriate matrix molecule. Subsequently, the mixture is drop casted on a MALDI plate and is dried under an ambient or inert atmosphere. During this process, cocrystallization of the sample with the matrix takes place.

By using a laser beam, the components of the mixture are transferred to the gas phase for mass spectrometric analysis. Generally, nitrogen laser, which has a wavelength of 337 nm is used for MALDI MS analysis. The matrix absorbs the irradiated laser energy in the sample-matrix cocrystal. The matrix then desorbs the energy and gets ionized by the addition of a proton. It then transfers the protons to the analyte, by which process the analyte becomes charged. The choice of the matrix depends on the nature of the analyte and ionization mode (whether positive or negative). MALDI MS is an important soft ionization tool for investigations of protein-protected clusters. However, the fragmentation of the S–C bond of the cluster core (for thiolate protected clusters) often occurs due to the laser desorption and ionization, which results in the formation of M_nS_m aggregates.

The formation of stable naked gas phase clusters with specific nuclearities has been achieved using a MALDI mass spectrometer.[23] The results showed the formation of protein-template-derived stable gas phase clusters of Au_{18}^+, Au_{25}^+, Au_{38}^+, and Au_{102}^+ (Fig. 17.9). The protein here serves as a confining growth environment which acts as an effective reservoir for dissipation of the cluster aggregation and stabilization energy.

17.3.4 Detection and analysis of naked clusters

Based on their m/z value, charged cluster ions can be easily selected and separated using a mass spectrometer. Below are a few analyzers that differ in their nature and analyzing techniques currently in use for the detection of clusters.

17.3.4.1 Wein filter

In the Wien filter, mass separation is carried out by homogenous electric (E) and magnetic fields (B). The two fields are aligned perpendicular to each other and are also perpendicular to the direction of the cluster beam. For a cluster with a charge z has mass m and velocity v, the net force on the cluster is $E = Bv$. By applying a voltage V, the cluster ions are accelerated to an energy of zV. In the Wien filter, clusters with a mass-to-charge ratio $(m/z) = 2V/(E/B)^2$ are undeflected and are selected (by collimators) and detected while other cluster ions with different m/z values undergo deflection and are lost. The resolution of the Wien filter depends on a number of factors such as the velocity spread of the cluster ions, the strength of the electric and magnetic fields and the collimator widths (Fig. 17.10A). Higher resolution can be obtained in the presence of high field strengths, narrow collimators, and large acceleration potential.

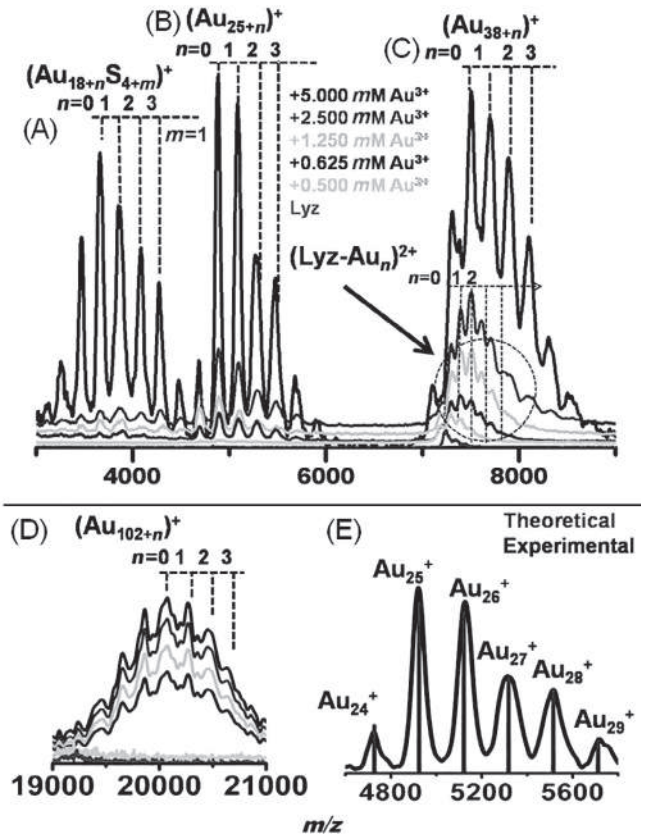

FIGURE 17.9 MALDI MS of Lyz–Au adduct, which shows the formation of Au clusters. All the spectra are collected in the positive ion mode. The formation of bare clusters are separately shown for (A) $Au_{18}S_4$, (B) Au_{25}, and (C) Au_{38}, and (D) Au_{102} (reproduced with permission from ref.[23]).

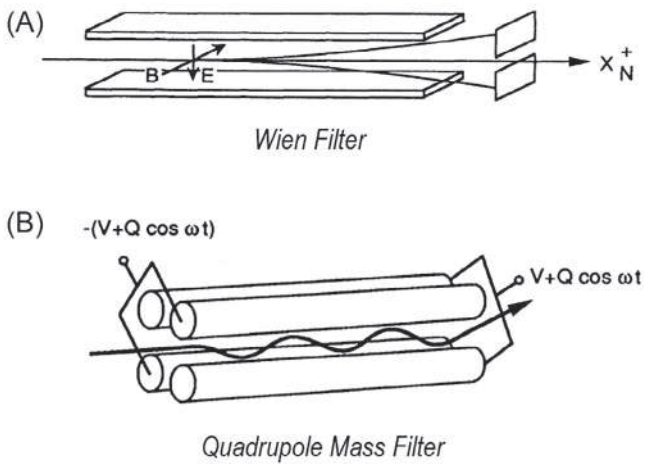

FIGURE 17.10 Schematic of (A) Wein filter and (B) quadrupole mass filter (reproduced with permission from ref.[2c]).

The obtained mass resolution ($\delta m/m$) of this filter is in the order of 10^{-2}, though for larger clusters, it is lesser than that. The practical mass range is 1–5000 amu, which is limited by field strengths.

17.3.4.2 *Quadrupole mass filter*

Quadrupole mass filter is the most widely used analyzer in mass spectrometry because of its ease-of-use, compactness, and low cost. In the quadrupole mass filter, four cylindrical metal rods are held in a square geometry, forming a quadrupole where an AC electric field is superimposed on a DC electric field. A time-dependent potential, $U + V\cos(\omega t)$, is applied to one pair of rods and $-[U + V\cos(\omega t)]$ to the other (Fig. 17.10B). The adjacent rods have equal voltage with opposite polarities, while the diagonally opposite rods have equal voltage with the same polarities. A stable ion trajectory of clusters through the filter is obtained by varying the field strengths (V_{DC} and V_{AC}) and the AC frequency (ω) applied to the rods. Mass resolution is affected by various factors such as field strength, cluster velocity, and the alignment of the rods. The ($\delta m/m$) of this filter is in the order of 10^{-3}, which is better than the mass resolution of the Wien filter. The typical mass range is up to 9000 amu, which can be achieved by using high voltages and lower AC frequencies.

A variation of the quadrupole mass filter called phase space compressor is also available. In phase space compressors, an inert gas such as He or Ar is used to fill the quadrupole region. In this region, the collisions between cluster ions and the buffer gas cause the cluster ions to lose internal energy and only the translational energy due to the fields remain. The advantages of a quadrupole mass filter are its good transmission, high scan speed, and wide acceptance angle, which facilitates high sensitivity. It is therefore coupled to several instruments such as gas chromatographs.

17.3.4.3 *Time of flight mass analyzer*

This analyzer comprises three main components, an ion gun, a field-free drift space and an ion detector (Fig. 17.11A). First, a pulsed UV laser or electron beam ionizes the neutral clusters. The ions are then accelerated by the ion gun, which fly through the flight tube (field-free drift space), finally impinging on the ion detector. The flight time of the ions is measured by a digital oscilloscope which provides an indirect estimation of the mass of the individual clusters. Essentially, the quantification of the mass actually represents the m/z of the cluster. The intrinsic characteristics (velocity, charge, etc.), the detection accuracy of the flight time, and the stability of the acceleration power supply govern the resolution of the TOF mass spectrometer. The resolution of the analyzer is mass independent ($\delta m/m \approx 10^{-4}$–$10^{-3}$), and it is almost the same throughout the mass range. The major disadvantage of this analyzer is that it detects only low ion intensities as it operates only on short cluster pulses.

The mass resolution of the TOF mass spectrometer can be improved through a reflectron scheme wherein the flight path of the cluster ions are increased by reflecting them using an electrostatic mirror (Fig. 17.11B). The electrostatic mirrors play an important role in segregating different clusters of different masses based on their velocities. This mirror, situated at the end of the tube, reduces the velocity of the ionized clusters and reverses its flight direction. Intuitively, the time required for a high velocity ionized cluster to reach the electrostatic mirror will be less than its slower counterparts. Interestingly, reversing the original path will be more

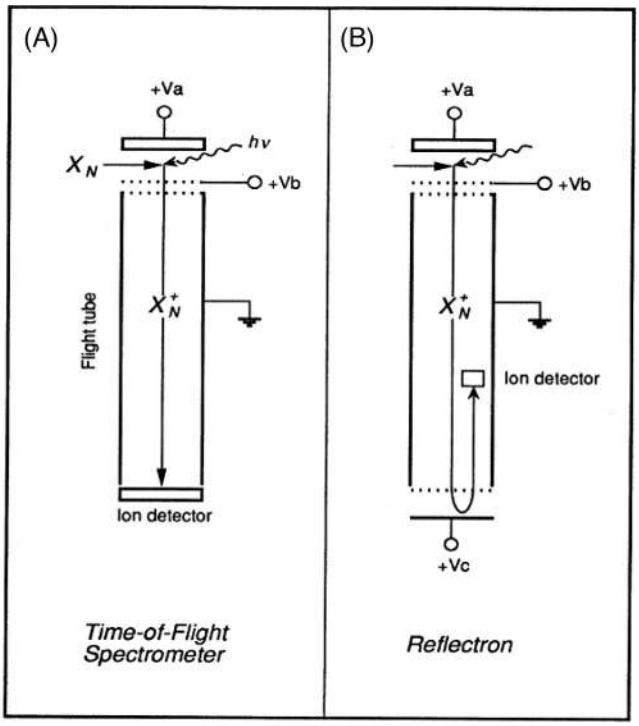

FIGURE 17.11 Schematic of TOF mass spectrometer. (A) Represents a standard linear configuration and (B) represents the TOF mass spectrometer with reflectron configuration (reproduced with permission from ref.[2c]).

time-consuming in the case of the high-speed clusters compared to the slower clusters. As a result, all the ionized clusters with a specific mass will assume almost similar velocities in their reverse flight, and they will reach the detector with a minimal time lag. The "add-in" reflectron TOF facility enables one to achieve enhanced mass resolution ($\delta m/m$) in the order of 10^{-5}, which is higher than the normal TOF mass spectrometer by almost an order of magnitude.

17.3.4.4 Ion cyclotron resonance

In this technique, the ionized clusters are trapped in a 3-D ion field. A static quadrupolar electric field in combination with a uniform magnetic field (B) is used for ion confinement. The magnetic field contributes to the cyclotron frequency ($\omega_c = zB/m$) of the ionized cluster. The confined ionized cluster is further excited using electric pulse, and then a Fourier analysis is performed on this resonating ion cloud in order to estimate the cyclotron resonance frequency or m/z value (Fig. 17.12).[24] When compared with the previously described TOF mass spectrometer, the mass resolution of the ICR spectrometry is established to be superior by an order of magnitude (in the order of 10^{-6}). Due to the superior resolution, possibility of combining with cluster sources, and extreme sensitivity, FT-ICR is the ideal technique for cluster mass spectrometry.

17.3.5 Reactivity of naked clusters in the gas phase

Reactivity of gas phase clusters has gained enormous interest since the discovery of strong cluster beam about three decades ago.[25] Studying the reactivity of gas phase clusters allows

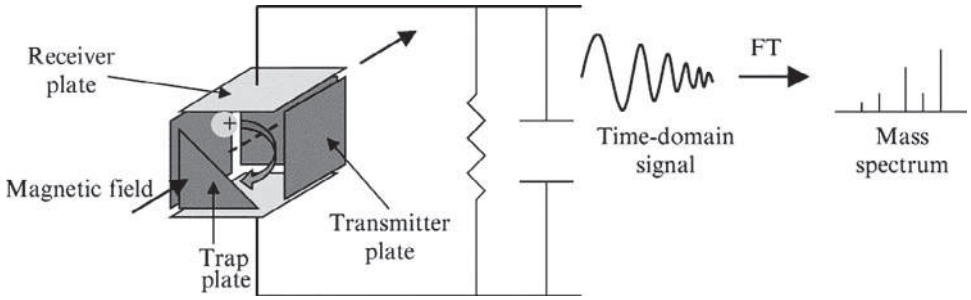

FIGURE 17.12 A schematic of Fourier-transform ion cyclotron resonance mass spectrometer (FT-ICR-MS) showing the ion trapping, detection, and signal generation (reproduced with permission from ref.[24]).

us to understand the reactivity of the materials in the absence of any protecting ligand and solvent medium. The physicochemical properties of clusters are often altered by changing a single atom in the cluster composition, and thus understanding their chemical behavior in the gas phase is essential to the field of catalysis, etching, and adsorption processes. It also provides information about their structure–reactivity relationships on metal surfaces. Sometimes unique reactivity and properties are obtained from certain sized clusters indicating the optimum methodology to generate efficient and selective catalysts for a specific reaction. It has been demonstrated that the reactivity of metal clusters depends strongly on cluster size, composition, and charge state. The correlation between the electronic structure and reactivity has been established through experimental and theoretical findings. The study of gas phase reaction kinetics enables one to understand the reaction mechanism and the energetics along the reaction pathway. Most of the cluster reactivity studies have been carried out with transition metals with unoccupied/partially occupied d orbitals. The interest in transition metal reactivity has helped to build an understanding of the fundamental processes involved in heterogeneous catalysis, as most of the catalysts are typically composed of transition metals or intermetallic compounds. Recently, there has been an increasing focus on the ion chemistry of noble metal (Au, Ag, Cu) clusters, whereby their catalytic activity has been controlled by tuning the cluster compositions. The investigations in this field not only help predict chemical properties of gas phase clusters but also have contributed to other interdisciplinary areas and provided new perspectives into the condensed matter and monolayer protected clusters. A discussion on the specific reactivity of the clusters is presented later.

17.3.5.1 Reaction apparatuses

Commonly used reaction apparatuses mainly consist of three parts with distinct functions such as cluster generation, cluster reaction, and ion detection. As mentioned earlier, there are various cluster sources available for cluster generation, such as laser vaporization, pulsed-arc discharge, magnetron sputtering, supersonic nozzle, ESI, etc. Laser vaporization is the most popular technique for cluster generation since it can easily generate clusters from a disk or rod of bulk components. Recently, magnetron sputtering has also gained increasing research interest due to its high efficiency and controllability. Gas phase cluster ions largely undergo photoexcited dissociation, CID and cluster molecule reactions. In the case of cluster molecule

reaction, the reaction occurs between gas phase clusters and reactive gas inside a chamber. The reactive gas is generally mixed with an inert gas. After the reaction, detection is carried out by mass spectrometry which provides information about the product formed during the reaction. In particular, the technological advancement and development of various commercial mass spectrometers have dominated the investigations of cluster chemistry during the past few decades.

17.3.5.1.1 Multiple-ions laminar flow tube

To investigate the cluster reaction in the gas phase, Castleman's group had developed a reaction apparatus which is called multiple-ions laminar flow tube.[26] In this apparatus, clusters generated by laser vaporization or magnetron sputtering source are passed through a reaction tube wherein different reagent gases can be introduced. To increase the laminar flow of the reactant/product molecules, a higher amount of carrier/inert gases are introduced inside the flow tube. This results in increased collisional reactions, and fast laminar flow assists the ions in reaching the quadrupole mass spectrometer after passing through a series of ion optics. This kind of apparatus is helpful for studying multiple collision reactivity, which is essential to probe the magic species of the clusters simply by checking their reactivity for oxygen-etching reactions.

17.3.5.1.2 Selected-ion flow tube

Inside this tube, mass selected cluster ions which are obtained from the cluster source, undergo collision reaction in gas phase. This technique was first introduced by Adams and Smith in 1976.[27] The combination of the selected-ion-flow tube with mass spectrometer has been widely used for the investigation of gas phase ion-molecule reactions of clusters. In this instrument, there are multiple ion sources that are used to obtain the subsequent mass selected cluster. After the mass selection is performed using a quadrupole mass filter, the clusters pass through a flow tube. The mass selected ions can be further guided toward a second quadrupole analyzer before they enter into a collision cell. Inside the collision cell, the mass selected ions react with the reagent gases, generating product ions. The ions that emerge from the collision cell pass through a final quadrupole and a mass spectrometer for mass analysis. The advantage of using a selected-ion flow tube system is that it allows one to study the reactivity of size-selected clusters in the gas phase.

17.3.5.1.3 Reaction/collision cells

Reaction cell or collision cell functions as a mini flow tube and is popular and convenient. By using the reaction cell, the cluster beam can be expanded to a longer path, whereby it comes in contact with a pure reagent gas or one that is diluted in inert gas.

17.3.5.1.4 Ion traps and tandem quadrupole reactors

Ion trap is a combination of electric field, and magnetic field wherein radio frequency (RF) is generated to capture charged particles or ions. Linear quadrupole ion traps can be two-dimensional or three-dimensional, which create an RF quadrupole field inside the mass spectrometer to store ions within a definite boundary. Ion traps in combination with tandem quadrupole reactors are used to trap the mass selected charged clusters during gas phase reactions of clusters. Inside the ion traps, clusters initially attain thermal equilibrium under

experimental conditions. The thermalized cluster is then mass selected and transferred to a quadrupole reactor or customized octupole ion trap wherein reactant gases together with buffer gas can be introduced. On completion of the reaction, reactants, intermediates, and products that emerge from the ion trap are analyzed by a mass spectrometer.

17.3.5.2 Reactivity of naked clusters with nonpolar molecules

The reaction between gas phase metal clusters with nonpolar gas molecules (e.g., O_2, N_2, H_2, halogens, and inert gases) has been studied to gain an insight into the stability and reactivity of the clusters. Most of these investigations are conducted by examining the ionic reaction products using a mass spectrometer.

17.3.5.2.1 Reactions with oxygen

Gas phase cluster–oxygen reaction has been widely investigated to identify magic species of the cluster. These magic species exhibit large HOMO−LUMO gaps, high atom-removal energies, spin excitation energies, and/or ionization energies. The oxygen etching effect was observed during the very early days of cluster reactivity studies. In 1986, Jarrold and Bower demonstrated the gas phase reaction of cationic aluminum clusters with oxygen, where Al_n^+ ($n = 4-25$) were produced by a laser vaporization source.[28] The ionized cluster was expanded into the vacuum system and mass selected using a quadrupole mass filter and finally passed into a cell where the reactant gas (oxygen) was introduced. Among all the generated clusters, Al_7^+ showed relatively more abundance in the mass spectrum which indicates its higher stability (Fig. 17.13A). After the gas phase reaction, no oxygen containing product was observed for any of the aluminum cluster cations, rather the mass selected clusters were fragmenting to smaller clusters. For example, Al_{16}^+ after reacting with oxygen leads to the fragmented products of Al_{12}^+ and Al_{11}^+. Using a similar cluster system, Castleman et al. demonstrated a reaction scheme of anionic aluminum clusters with oxygen. It was observed that the anionic clusters having up to 12 Al atoms reacted with oxygen while, some of the cluster anions having 13, 23, and 37 Al atoms demonstrated resistivity toward reaction with oxygen. The resistivity of these clusters is accounted for shell closings at 40, 70, and 112 electrons predicted by the jellium model. Such findings revealed that the activation of molecular oxygen requires the spin excitation from triplet to a singlet. This spin excitation of oxygen is linked to the HOMO–LUMO gap of the clusters, which creates an energy barrier during the reaction with oxygen. Similarly, aluminum–copper alloy, aluminum–magnesium alloy, and cobalt clusters also have been studied toward oxygen etching reaction.[29]

The odd–even selectivity of clusters also states that the clusters containing an even number of atoms react differently compared to the ones containing an odd number of atoms due to the effect of spin pairing. This behavior is revealed through the reaction with oxygen. For example, the reactivity of silver cluster anions with oxygen shows the magic nature of Ag_{13}^-, which is quite unusual despite having an odd electron molecular orbital structure.[30] Fig. 17.13B shows the mass spectra of Ag_n^- clusters with different amounts of oxygen. The experimental results showed that the clusters with an even number of silver atoms showed a decrease in intensity upon reaction. The odd number of silver atoms demonstrated reduced reactivity toward oxygen, and Ag_{13}^- appeared as a magic species after the reaction. From this result, it was concluded that the reactivity of Ag_n^- with oxygen corresponds to their spin excitation energy. In the case of Ag_{13}^-, the distorted geometry gives rise to D shell splitting, which contributes

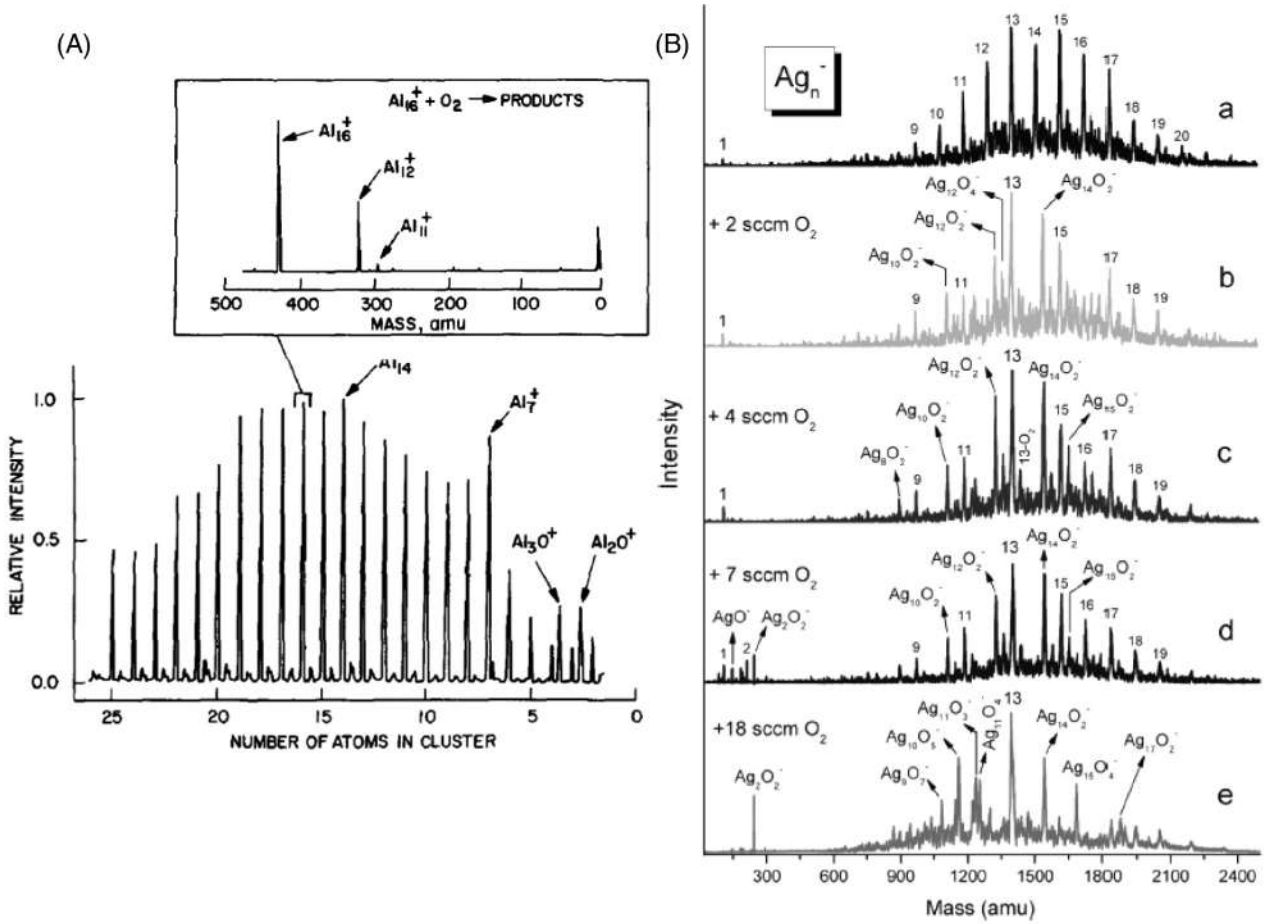

FIGURE 17.13 (A) The mass spectrum of aluminum cluster ions produced by laser vaporization method. The inset shows the mass spectrum of the reactant and product ions after the reaction between mass selected Al_{16}^+ and oxygen inside the reaction cell (reproduced with permission from ref.[28]). (B) Mass spectra of silver cluster anions (a) generated by magnetron sputtering source and (b–e) after reaction with different amounts of oxygen (reproduced with permission from ref.[30]).

to a higher electron detachment energy and HOMO–LUMO gap at the subshell level. These types of geometrically distorted clusters essentially provide stability through a crystal-field like the splitting of degenerated shells. These results further endorse the application of the near-free electron gas (NFEG) model (with closed shell $n = 2, 8, 20, 40\ldots$) to explain the electronic structure and the counterintuitive stability of the metal clusters. In addition to the oxygen etching reaction, oxygen addition reactions of metal clusters have been investigated for the past two decades. Considering the oxygen molecule as an electron-withdrawing group, the oxygen-addition reaction is favorable for noble metal clusters with unpaired electrons. Thus, the coinage metal clusters (Cu_n^-, Ag_n^-, and Au_n^-) along with cationic and anionic cobalt clusters have oxygen added or displacement products.[31] It has been observed that the adsorption of oxygen molecules on large-sized clusters causes dissociation of oxygen molecule resulting in a superoxo state of addition.[32] The activation of O–O bond on the surface of a cluster can result in the coexistence of superoxo and peroxo states.[33]

17.3.5.2.2 Reactions with halogens

Since halide compounds are useful intermediates during the synthesis of functional materials, understanding the reactivity of metal cluster with halogen can provide useful insights about such synthesis. Considering the filled d orbital and singly occupied valence s orbital of copper, silver, and gold, the reaction with halogen might be similar to the reactivity of alkali metals with halogens. The reactivity of copper clusters (Cu_n^-) with chlorine has been studied where Cu_n^- were produced by a magnetron sputtering source, and the reaction was performed inside a fast-flow reactor.[34] In presence of the reacting gas (chlorine), all the copper cluster anions diminished except Cu_7^-, owing to its closed electronic structure. $Cu_nCl_{n+1}^-$ ($n = 1$–6) species were obtained as products, with the abundance of $CuCl_2^-$ (Fig. 17.14A). Cu_n^- clusters react with chlorine molecule, generating CuCl and $CuCl_2^-$, which then undergo consecutive reactions to produce the final product $Cu_nCl_{n+1}^-$ with higher values of n. The experiment leads to the conclusion that the reaction of copper clusters with halogen preferentially follows the dissociative chemisorption pathway. Likewise, the reaction of silver clusters with chlorine produced $Ag_nCl_{n+1}^-$ species.[35] For the reaction between Al_n^- clusters with iodine molecule, Al_nI^- becomes the most energetically favored product, which forms due to the dissociative chemisorption of I_2 on aluminum clusters.[36]

17.3.5.2.3 Reactions with hydrogen and nitrogen

The reactivity of metal clusters with hydrogen has been studied mainly with iron (Fe), cobalt (Co), vanadium (V), and niobium (Nb) clusters. Several studies concluded that hydrogen chemisorption is the dominant reaction pathway. The positive charge on iron clusters (Fe_n^+) shows enhanced chemisorption of hydrogen molecules compared to the neutral iron clusters (Fe_n).[37] This behavior arises due to the electrostatic interactions between cationic iron clusters and hydrogen molecules. To study the influence of cluster size on the reactivity with hydrogen, a reaction between neutral aluminum clusters and hydrogen was conducted. The results display that hydrogen is more reactive toward clusters with unfilled shells compared to the clusters with filled electronic shells.[38] This result is also concurrent with metal cluster reactivity with other diatomic gas molecules. The rate of D_2 chemisorption also have been studied on Fe_n^+, V_n^+, Nb_n^+, and Co_n^+ clusters, where the kinetics of chemisorption and the maximum uptake of D_2 depend on the number of constituents, n in the clusters.[39]

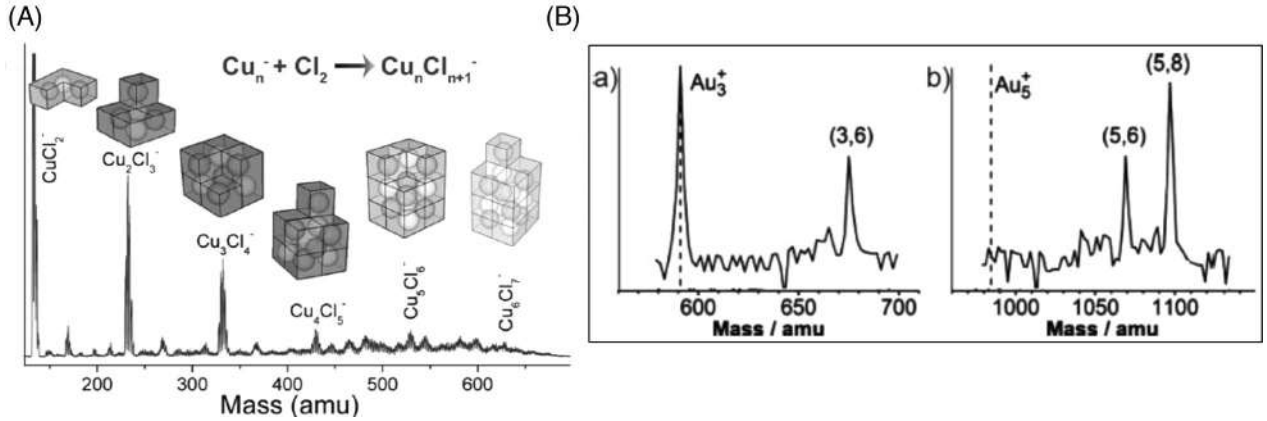

FIGURE 17.14 (A) Mass spectrum of the products, $Cu_nCl_{n+1}^-$ resulting from the reaction between copper cluster anions and chlorine. The insets of (A) show the structure of different species that make up the product crystal (reproduced with permission from ref.[34]). (B) Mass spectrum of (a) Au_3^+ and (b) Au_5^+ in the presence of nitrogen at a temperature of 200 K. The number above the peaks represents the stoichiometry of Au and N in the product ions ($Au_xN_y^+$) (reproduced with permission from ref.[40]).

Though nitrogen is the most stable diatomic molecule, it undergoes addition reactions with certain sized metal clusters. The reaction of small gold clusters Au_3^+ and Au_5^+ with nitrogen inside an octupole ion trap was studied by Lang and Bernhardt.[40] The low temperature reaction of mass selected Au_3^+ and Au_5^+ generates the product $Au_3N_6^+$ and $Au_5N_8^+$, and $Au_5N_6^+$, respectively (Fig. 17.14B). These observations indicate that the adsorption of nitrogen molecules on Au_n^+ clusters follows size-dependent selectivity. Clusters of metals such as cobalt, nickel, niobium, molybdenum also undergo chemisorption reactions with nitrogen molecules where the number of adsorbed N_2 depends on the cluster's size, charge, and reaction temperature.

17.3.5.2.4 Reactions with methane, ethane, and acetylene

The reactivity of metal clusters with hydrocarbons like CH_4, C_2H_2, and C_2H_4 has been carried out. Gas phase Pd clusters have been used to activate the methane molecule. Experimental results showed some exceptions, such as Pd_3 and Pd_4 do not react with methane compared to the other neutral palladium clusters (Pd_x, $x \leq 24$).[41] Apart from palladium clusters, small palladium oxides show size-dependent reactivity toward methane, resulting in methane dehydrogenation. The reactivity of cobalt cluster cations with CH_4, C_2H_2, and C_2H_4 have been studied, which indicate the cluster size-dependent reactivity toward CH_4 and C_2H_4.[42] However, Co_n^+ was found to be highly reactive with C_2H_2, irrespective of the cluster sizes. The reaction of silver cluster cation Ag_{17}^+, which was generated from a ligand protected cluster, has been investigated in the presence of C_2H_2. The reaction was conducted inside an ion trap of a mass spectrometer and in air outside the mass spectrometer. Inside the trap, there was polymerization of the $–C_2H$ group, which gives $–C_4H_{10}$ anchored to the Ag_{17}^+ peak in the mass spectrum (Fig. 17.15A).[43] Whereas, there was an adduct formation of Ag_{17}^+ with 2, 4, and 6 acetylene molecules after dehydrogenation in air (Fig. 17.15B).[44] Such studies foster our understanding of homologous metal and metal oxides, which are important catalysts in industrial processes, and the parameters and elementary reaction mechanisms involved in catalysis.

17.3.5.3 Reactivity of naked clusters with polar molecules

Understanding the effect of shape and size on the chemical reactivity of metal clusters with a specific reagent can be obtained from studying the reactivity of clusters toward various polar molecules.

17.3.5.3.1 Reactions with monoxides

Cluster oxides such as AgO, AuO, CeO_2, and FeO exhibiting oxygen atom transfer mechanism have been studied extensively in view of their pollutant removal property where carbon/nitrogen monoxides are reduced and generate the less-poisonous oxygen-rich products.[45] In comparison, there is a diminished interest in exploring the reactivity of bare metal clusters with these gases. There are few reports which discuss the adsorption of CO, N_2O and NO on metal or metal alloy clusters to yield information on their size, shape, and electronic structure and also the bonding mechanism during the pollutant removal in the environment.

17.3.5.3.2 Reactions with hydroxyl compounds

The reactivity of clusters with water has gained interest due to the possibilities for hydrogen evolution. A report on aluminum clusters demonstrated the generation of hydrogen from

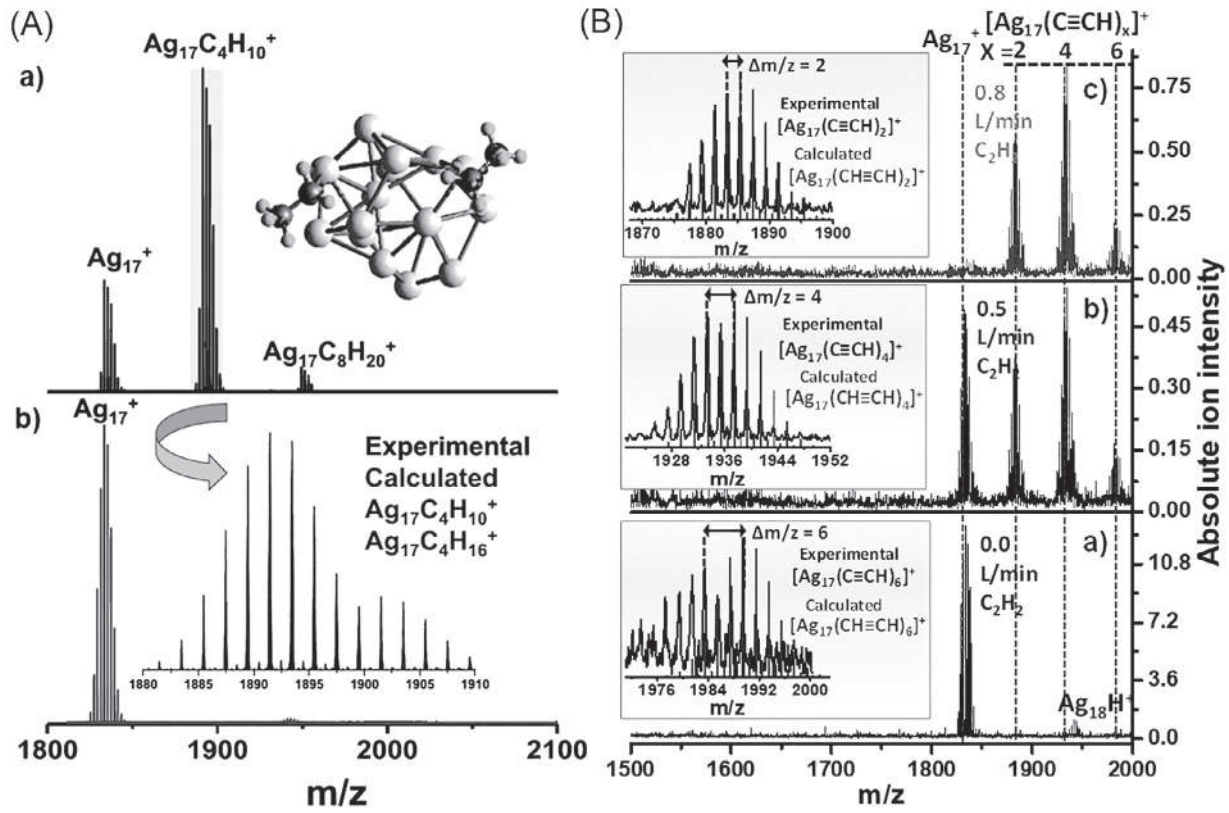

FIGURE 17.15 (A) Mass spectrum of Ag_{17}^+ after reaction with a) lower amount and b) higher amount of acetylene inside the trap. At a higher flow rate of acetylene, an intense peak was appeared along with Ag_{17}^+, which is denoted as the product $Ag_{17}C_4H_{10}^+$ (reproduced with permission from ref.[43]). (B) ESI mass spectrum (a) of Ag_{17}^+ and $Ag_{18}H^+$ created in the air, outside the mass spectrometer, (b and c) after the reaction between Ag_{17}^+ and different quantities of acetylene in air (reproduced with permission from ref.[44]).

water in the presence of Al_{16}^-, Al_{17}^-, and Al_{18}^-.[46] The reaction involves an initial nucleophilic attack of H_2O on the alumina surface followed by the breaking of the OH bond. The neighboring Al site acts as a Lewis base and helps in breaking this bond. The presence of neighboring pairs governed by the cluster geometry may result in the dissociation of H atoms that can combine to form H_2 molecule, leading to spontaneous hydrogen evolution.

It has been noticed that the reactivity of aluminum clusters is not limited to H_2O alone but is extended to other molecules with –OH functional groups, such as alcohols. However, it is found that alcohols have an etching effect toward aluminum clusters (except Al_{13}^-), which closely resembles the oxygen etching reaction where Al_{13}^- also exhibit resistivity toward oxygen etching reaction.[47]

17.3.5.3.3 Reactions with ammonia and hydrogen sulfide

There are several reports on the reactivity of metal clusters with ammonia. Interestingly Al_{12}^- exhibits high reactivity toward both NH_3 and H_2S.[48] This can be attributed to the position of prominent complementary active sites in the cluster, along with their low LUMO energy level and high binding energy. On the other hand, Al_{13}^- and Al_{20}^- show significant inertness toward NH_3 and H_2S compared with their proximal clusters. Thus, the reactivity of aluminum clusters toward S–H and N–H bonds of H_2S and NH_3 is similar to its reactivity with the O–H bond of H_2O.

17.3.5.3.4 Reactions with thiols

The gas phase reactivity studies of thiols with Al clusters were reported by Luo et al.[49]. The report explored the C−S bond activation, as shown in Fig. 17.16. During the course of the reaction, there will be the formation of two Al–S bonds between one S atom and two Al atoms, which results in the depletion of electron density between C and S atoms leading to the C–S bond dissociation. The reaction produces $Al_nS_m^-$ species as a major product and ethylene as a byproduct. In addition, ethanethiol also reacts with gas phase silver clusters and produces Ag_nSH^-, $Ag_nSH_2^-$ as major products and H_3S^-, $(H_3S)_2^-$ as the byproducts. This reaction helps to gain insights into the C−S bond-breaking mechanism, which is important in many chemical, environmental, and biological processes.

17.3.6 Catalysis in gas phase

The catalysis of gas phase cluster has been discussed in Chapter 5 and Chapter 20.

17.4 Other characterization methods of naked clusters

In addition to the mass spectrometric technique, other characterization methods (e.g., photoelectron spectroscopy, infrared spectroscopy, Raman spectroscopy) are utilized for gas phase clusters, which are already discussed in Chapter 8.

17.5 Solid-supported metal clusters/cluster assembled materials

Though the reactivity of gas phase clusters is interesting, but for commercial applications a large amount of cluster material is needed that can be stored and transported. Gas phase

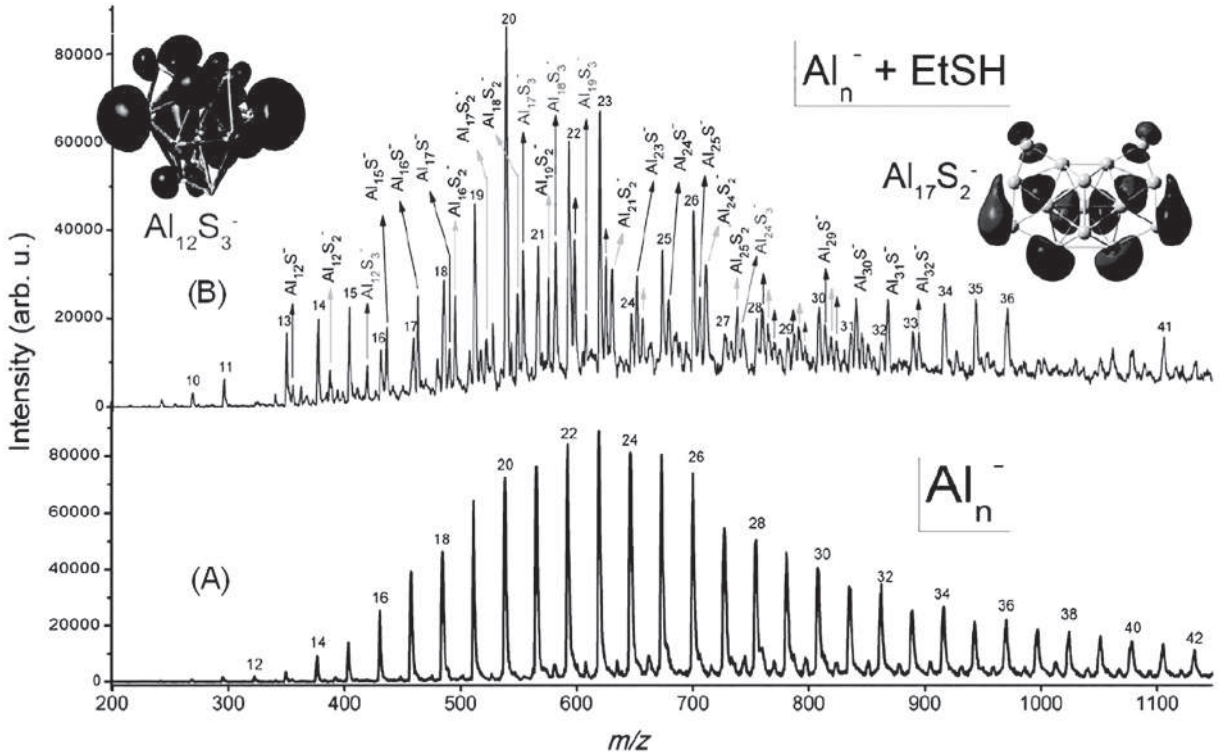

FIGURE 17.16 (A) The mass spectrum of aluminum cluster anions with different size distributions. (B) The mass spectrum of the same aluminum clusters after reaction with EtSH. The inset corresponds to the calculated HOMO profiles of $Al_{12}S_3^-$ and $Al_{17}S_2^-$ (reproduced with permission from ref. 49).

naked clusters are very unstable against coalescence, and they can easily agglomerate to form bulk material. So, for large-scale utilization of catalytic applications, it is important to stabilize them either by protecting them with ligands (colloidal particles) or by depositing them on an appropriate surface like graphite, oxides, zeolites, etc. (solid-supported clusters). To design supported clusters for catalytic applications, generally silica, alumina, titania are employed as support materials since they are inactive toward catalytic reactions. To prepare supported clusters, gas phase cluster beam is deposited onto the surface of a support. After deposition, the size of the cluster can vary due to different factors like impact energy, interaction with the substrate, coalescence, etc. Two methods are adopted for cluster deposition: low energy deposition and high energy deposition. In the low energy deposition, very low accelerating potential is used in between the cluster beam and the substrate so that there will be the generation of low impact energy after deposition. Due to the low impact energy, the possibility of fragmentation of the clusters will be less, and the surface morphology of the substrate will remain intact. This method is also called the soft-landing method. To produce size-selected cluster deposition without any change in their geometric and electronic structure, low energy deposition is much reliable than high energy deposition. This method can create supported clusters that show properties and reactivity, similar to gas phase reactivity. Notably, the deposited clusters are different from their gas phase counterparts, with a few exceptions. Woodward et al. successfully demonstrated soft-landed mass selected Al_7^- cluster on a self-assembled monolayer to create the cluster-assembled material (Fig. 17.17).[50] Thus, it is possible to make surface-bound small clusters that will be stable in ambient conditions using the low energy deposition or soft-landing technique.

To study the effect of high energy deposition of cluster, several experiments and theoretical calculations have been carried out. The effect on the cluster due to high energy deposition depends on factors like impact energy, surface material, composition of the cluster, etc. In the case of moderate impact energy generally, the cluster is spread on the surface, causing little surface damage. However, mixing between cluster atoms and substrates can occur. For high impact energy, the local temperature generated due to the deposition is very high, and crater forms on the surface. Apart from these methods, clusters can also be crystallized to form solid, different from their bulk counterpart, wherein cluster coalescence can be prevented. These materials are called cluster solids, and they will be discussed in Chapter 20.

17.6 Summary and future perspectives

Gas phase naked clusters bridge the gap between the molecules and materials by allowing the molecular level studies of their gas phase properties in the absence of ligands and solvent medium. The methods of preparation of a variety of naked clusters and various ionization and detection techniques have been discussed in this chapter. This reinforces the importance of choosing a proper synthesis method and ionization technique to generate a particular gas phase cluster. Mass spectrometry has been a vital tool to understand these naked clusters and their gas phase reactivity. The study of their reactivities helps in the exploration of catalysts in the newer system.

In this chapter, we also discuss the importance of making cluster assembled solids in the larger view of applications. However, a few issues such as the stability of clusters and

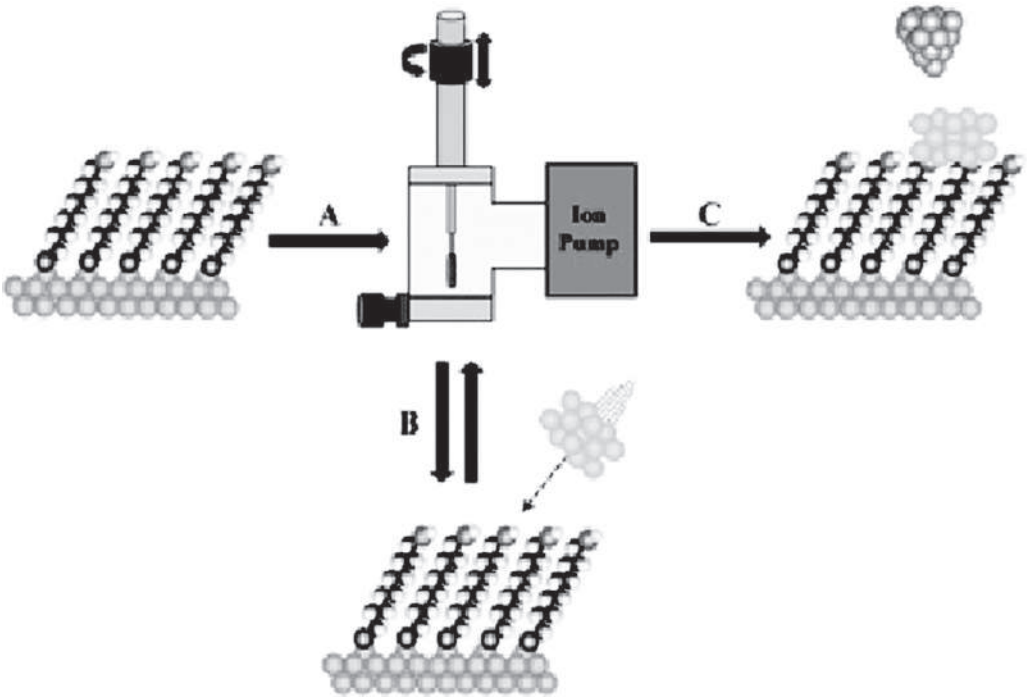

FIGURE 17.17 Schematic diagram of soft-landing deposition of Al_{17}^- cluster on a self-assembled monolayer. Here, size selected cluster was deposited on a hydroxyl-terminated self-assembled monolayer to obtain the cluster-assembled material. Scanning tunneling microscopy was used to characterize postdeposition material (reproduced with permission from ref.[50]).

experimental limitations, need to be addressed to execute the large-scale application of gas phase clusters. The stability of naked clusters should be improved against coalescence so that different types of experiments such as reactivity and catalytic studies, soft-landing, etc. can be performed without the change in the nuclearity of the clusters. In order to achieve this, various experimental conditions need to be analyzed to keep the cluster size intact. Along with that, novel starting materials and ionization techniques have to be explored further to ensure the cost-effective production of naked clusters.

List of abbreviation

AC	alternating current
CID	collision-induced dissociation
DC	direct current
DNA	deoxyribonucleic acid
DOS	density of state
DPPB	1,4-bis(diphenylphosphino)butane
DPPE	1,2-bis(diphenylphosphino)ethane
DPPH	1,6-bis(diphenylphosphino)hexane
ESI	electrospray ionization
HOMO	highest occupied molecular orbital

IR	infrared
Lyz	lysozyme
LUMO	lowest unoccupied molecular orbital
MALDI	matrix-assisted laser desorption ionization
MS	mass spectrometry
m/z	mass-to-charge ratio
NCs	nanoclusters
Nd:YAG	neodymium-doped yttrium aluminum garnet
NFEG	near-free electron gas
NMR	nuclear magnetic resonance
PACIS	pulsed arc cluster ion source
PI-TOF-MS	photoionization time of flight mass spectrum
pMBA	para-mercaptobenzoic acid
RF	radiofrequency
TEM	transmission electron microscopy
TOF	time of flight
TPP	triphenyl phosphine
XRD	X-ray diffraction
UVPD	ultraviolet photodissociation

References

1. Turner M, Golovko VB, Vaughan OPH, et al. Selective oxidation with dioxygen by gold nanoparticle catalysts derived from 55-atom clusters. *Nature*. 2008;454:981–983.
2. (a) Cohen ML, Chou MY, Knight WD, De Heer WA. Physics of metal clusters. *J Phys Chem C*. 1987;91:3141–3149; (b) Castleman AW, Khanna SN. Clusters, superatoms, and building blocks of new materials. *J Phys Chem C*. 2009;113:2664–2675; (c) de Heer WA. The physics of simple metal clusters: experimental aspects and simple models. *Rev Mod Phys*. 1993;65:611–676.
3. Knight WD, Clemenger K, De Heer WA, Saunders WA, Chou MY, Cohen ML. Electronic shell structure and abundances of sodium clusters. *Phys Rev Lett*. 1984;52:2141–2143.
4. (a) Seidl M, Perdew JP, Brajczewska M, Fiolhais C. Ionization energy and electron affinity of a metal cluster in the stabilized jellium model: size effect and charging limit. *J Chem Phys*. 1998;108:8182–8189; (b) Phung TVB, Hashimoto T, Nishikawa K, Nagao H. Theoretical studies on ionization potential of aluminum clusters. *Int J Quant Chem*. 2009;109:3602–3612.
5. Rohlfing EA, Cox DM, Kaldor A. Production and characterization of supersonic carbon cluster beams. *J Chem Phys*. 1984;81:3322–3330.
6. Kroto HW, Heath JR, O'Brien SC, Curl RF, Smalley RE. C60: Buckminsterfullerene. *Nature*. 1985;318:162–163.
7. Martin TP, Schaber H. Mass spectra of Si, Ge, and Sn clusters. *J Chem Phys*. 1985;83:855–858.
8. (a) Maruyama S, Kohno M, Inoue S. FT-ICR study of chemical reaction of silicon clusters. *Therm Sci Eng*. 1999;7:69–74; (b) Bloomfield LA, Freeman RR, Brown WL. Photofragmentation of mass-resolved $Si_{2\text{-}12}^{+}$ clusters. *Phys Rev Lett*. 1985;54:2246–2249.
9. (a) O'Brien SC, Liu Y, Zhang Q, et al. Supersonic cluster beams of III–V semiconductors: Ga_xAs_y. *J Chem Phys*. 1986;84:4074–4079; (b) Goacher RE, Luo H, Gardella JA. Formation of high-mass cluster ions from compound semiconductors using time-of-flight secondary ion mass spectrometry with cluster primary ions. *Anal Chem*. 2008;80:3261–3269.
10. Martin TP. Shells of atoms. *Phys Rep*. 1996;273:199–241.
11. Miehle W, Kandler O, Leisner T, Echt O. Mass spectrometric evidence for icosahedral structure in large rare gas clusters: Ar, Kr, Xe. *J Chem Phys*. 1989;91:5940–5952.
12. Siekmann HR, Lüder C, Faehrmann J, Lutz HO, Meiwes-Broer KH. The pulsed arc cluster ion source (PACIS). *Z Phys D Atoms Mol Clust*. 1991;20:417–420.
13. de Heer WA, Selby K, Kresin V, et al. Collective dipole oscillations in small sodium clusters. *Phys Rev Lett*. 1987;59:1805–1808.

14. Sattler K, Mühlbach J, Recknagel E. Generation of metal clusters containing from 2 to 500 atoms. *Phys Rev Lett*. 1980;45:821–824.
15. Begemann W, Meiwes-Broer KH, Lutz HO. Unimolecular decomposition of sputtered Al_n^+, Cu_n^+, and Si_n^+ clusters. *Phys Rev Lett*. 1986;56:2248–2251.
16. Luo Z, Woodward WH, Smith JC, Castleman AW. Growth kinetics of Al clusters in the gas phase produced by a magnetron-sputtering source. *Int J Mass Spectrom*. 2012;309:176–181.
17. Wagner A, Hall TM. Liquid gold ion source. *J Vacuum Sci Technol*. 1979;16:1871–1874.
18. Anacleto JF, Pleasance S, Boyd RK. Calibration of ion spray mass spectra using cluster ions. *Org Mass Spectrom*. 1992;27:660–666.
19. Wleklinski M, Sarkar D, Hollerbach A, Pradeep T, Cooks RG. Ambient preparation and reactions of gas phase silver cluster cations and anions. *Phys Chem Chem Phys*. 2015;17:18364–18373.
20. (a) Ghosh A, Bodiuzzaman M, Nag A, Jash M, Baksi A, Pradeep T. Sequential dihydrogen desorption from hydride-protected atomically precise silver clusters and the formation of naked clusters in the gas phase. *ACS Nano*. 2017;11:11145–11151; (b) Jash M, Khatun E, Chakraborty P, Sudhakar C, Pradeep T. $[Ag_{15}H_{13}(DPPH)_5]^{2+}$ and $[Ag_{27}H_{22}(DPPB)_7]^{3+}$: two new hydride and phosphine co-protected clusters and their fragmentation leading to naked clusters, $Ag^1{}_3{}^+$ and Ag_{25}^+. *J Phys Chem C*. 2020;124:20569–20577.
21. Jash M, Reber AC, Ghosh A, et al. Preparation of gas phase naked silver cluster cations outside a mass spectrometer from ligand protected clusters in solution. *Nanoscale*. 2018;10:15714–15722.
22. Black DM, Crittenden CM, Brodbelt JS, Whetten RL. Ultraviolet photodissociation of selected gold clusters: ultraefficient unstapling and ligand stripping of $Au_{25}(pMBA)_{18}$ and $Au_{36}(pMBA)_{24}$. *J Phys Chem Lett*. 2017;8:1283–1289.
23. Baksi A, Pradeep T, Yoon B, Yannouleas C, Landman U. Bare clusters derived from protein templates: Au_{25}^+, Au_{38}^+ and Au_{102}^+. *ChemPhysChem*. 2013;14:1272–1282.
24. Loo JA. The tools of proteomics. In: Smith RD, Veenstra TD, eds. *Adv Protein Chem*. Academic Press; 2003:25–56.
25. Luo Z, Castleman AW, Khanna SN. Reactivity of metal clusters. *Chem Rev*. 2016;116:14456–14492.
26. Roach PJ, Woodward WH, Castleman AW,Jr, Reber AC, Khanna SN. Complementary active sites cause size-selective reactivity of aluminum cluster anions with water. *Science (Washington, DC, US)*. 2009;323:492–495.
27. Adams NG, Smith D. The selected ion flow tube (SIFT), a technique for studying ion-neutral reactions. *Int J Mass Spectrom Ion Phys*. 1976;21:349–359.
28. Jarrold MF, Bower JE. The reactions of mass selected aluminum cluster ions, $Al^+{}_n$ (n = 4–25), with oxygen. *J Chem Phys*. 1986;85:5373–5375.
29. (a) Roach PJ, Woodward WH, Reber AC, Khanna SN, Castleman AW. Crystal field effects on the reactivity of aluminum-copper cluster anions. *Phys Rev B*. 2010;81; (b) Luo Z, Grover CJ, Reber AC, Khanna SN, Castleman AW. Probing the magic numbers of aluminum–magnesium cluster anions and their reactivity toward oxygen. *J Am Chem Soc*. 2013;135:4307–4313; (c) Kapiloff E, Ervin KM. Reactions of cobalt cluster anions with oxygen, nitrogen, and carbon monoxide. *J Phys Chem A*. 1997;101:8460–8469.
30. Luo Z, Gamboa GU, Smith JC, et al. Spin accommodation and reactivity of silver clusters with oxygen: the enhanced stability of Ag_{13}^-. *J Am Chem Soc*. 2012;134:18973–18978.
31. (a) Lee TH, Ervin KM. Reactions of copper group cluster anions with oxygen and carbon monoxide. *J Phys Chem*. 1994;98:10023–10031; (b) Florez E, Tiznado W, Mondragón F, Fuentealba P. Theoretical study of the interaction of molecular oxygen with copper clusters. *J Phys Chem A*. 2005;109:7815–7821.
32. Yoon B, Häkkinen H, Landman U. Interaction of O_2 with gold clusters: molecular and dissociative adsorption. *J Phys Chem A*. 2003;107:4066–4071.
33. Pal R, Wang L-M, Pei Y, Wang L-S, Zeng XC. Unraveling the mechanisms of O_2 activation by size-selected gold clusters: transition from superoxo to peroxo chemisorption. *J Am Chem Soc*. 2012;134:9438–9445.
34. Luo Z, Smith JC, Woodward WH, Castleman AW. The growth of ionic crystals based on the halogenation of copper cluster anions. *J Phys Chem A*. 2012;116:2012–2017.
35. Luo Z, Berkdemir C, Smith JC, Castleman AW. Cluster reaction of $[Ag_8]^-/[Cu_8]^-$ with chlorine: evidence for the harpoon mechanism? *Chem Phys Lett*. 2013;582:24–30.
36. Bergeron DE, Castleman AW,Jr, Morisato T, Khanna SN. Formation and properties of halogenated aluminum clusters. *J Chem Phys*. 2004;121:10456–10466.
37. Zakin MR, Brickman RO, Cox DM, Kaldor A. Dependence of metal cluster reaction kinetics on charge state. II. Chemisorption of hydrogen by neutral and positively charged iron clusters. *J Chem Phys*. 1988;88:6605–6610.

38. Khanna SN, Jena P. Reactivity of hydrogen with open and closed shell clusters. *Chem Phys Lett*. 1994;218:383–386.
39. (a) Liu K, Parks EK, Richtsmeier SC, Pobo LG, Riley SJ. Reactions of iron clusters with hydrogen. III. Laser-induced desorption of H_2 by multiphoton absorption. *J Chem Phys*. 1985;83:2882–2888; (b) Alford JM, Weiss FD, Laaksonen RT, Smalley RE. Dissociative chemisorption of molecular hydrogen on niobium cluster ions. A supersonic cluster beam FT-ICR experiment. *J Phys Chem*. 1986;90:4480–4482.
40. Lang SM, Bernhardt TM. Cooperative and competitive coadsorption of H_2, O_2, and N_2 on Au_x^+(x = 3,5). *J Chem Phys*. 2009;131.
41. Lang SM, Frank A, Bernhardt TM. Activation and catalytic dehydrogenation of methane on small Pd_x^+ and Pd_xO^+ clusters. *J Phys Chem C*. 2013;117:9791–9800.
42. Nakajima A, Kishi T, Sone Y, Nonose S, Kaya K. Reactivity of positively charged cobalt cluster ions with methane, nitrogen, hydrogen, ethylene, and acetylene. *Z Phys D: At. Mol Clust*. 1991;19:385–387.
43. Baksi A, Jash M, Bag S, et al. Mechanistic elucidation of the structure and reactivity of bare and hydride-protected Ag_{17}^+ clusters. *J Phys Chem C*. 2019;123:28494–28501.
44. Jash M, Methikkalam RRJ, Bodiuzzaman M, Paramasivam G, Pradeep T. Reaction between Ag_{17}^+ and acetylene outside the mass spectrometer: dehydrogenation in the gas phase. *Chem Commun*. 2020;56:15623–15626.
45. (a) Wang Z-C, Yin S, Bernstein ER. Catalytic oxidation of CO by N_2O conducted via the neutral oxide cluster couple VO_2/VO_3. *Phys Chem Chem Phys*. 2013;15:10429–10434; (b) Siu CK, Reitmeier SJ, Balteanu I, Bondybey VE, Beyer MK. Catalyst poisoning in the conversion of CO and N_2O to CO_2 and N_2 on Pt_4^- in the gas phase. *Eur Phys J D*. 2007;43:189–192; (c) Johnson GE, Tyo EC, Castleman AW. Oxidation of CO by aluminum oxide cluster ions in the gas phase. *J Phys Chem A*. 2008;112:4732–4735.
46. Roach PJ, Woodward WH, Castleman AW, Reber AC, Khanna SN. Complementary active sites cause size-selective reactivity of aluminum cluster anions with water. *Science*. 2009;323:492–495.
47. Luo Z, Smith JC, Woodward WH, Castleman AW. Reactivity of aluminum clusters with water and alcohols: competition and catalysis? *J Phys Chem Lett*. 2012;3:3818–3821.
48. Grubisic A, Li X, Gantefoer G, et al. Reactivity of aluminum cluster anions with ammonia: selective etching of Al_{11}^- and Al_{12}^-. *J Chem Phys*. 2009;131.
49. Luo Z, Smith JC, Berkdemir C, Castleman AW. Gas-phase reactivity of aluminum cluster anions with ethanethiol: carbon–sulfur bond activation. *Chem Phys Lett*. 2013;590:63–68.
50. Woodward WH, Blake MM, Luo Z, Weiss PS, Castleman AW. Soft-landing deposition of Al_{17}^- on a hydroxyl-terminated self-assembled monolayer. *J Phys Chem C*. 2011;115:5373–5377.

CHAPTER

18

Atomic precision in other nanocluster systems: Chalcogenides

Cheruvattil Koyitti Manju[a], *Anagha Jose*[a] *and Thalappil Pradeep*[b]

[a]DST Unit of Nanoscience and Thematic Unit of Excellence, Department of Chemistry, Indian Institute of Technology Madras, Chennai, India [b]Deepak Parekh Institute Chair Professor and Professor of Chemistry, Department of Chemistry, Indian Institute of Technology Madras, Chennai, India

18.1 Introduction

Ligand-protected atomically precise metal chalcogenide (ME, M = metal, E = S, Se, Te) nanoclusters (NCs) are interesting because these compounds allow the study of quantum confinement at lower size regime of typical quantum dots.[1] Polynuclear chalcogenide/chalcogenolate NCs can contain ten to hundreds of metal and chalcogen core atoms. They can be crystallized, and complete structural information can be obtained using single crystal XRD. Semiconductor chalcogenide NCs show size dependent electronic properties similar to their NPs. A systematic blue shift is observed in the optical absorption spectrum of CdSe NCs due to quantum confinement.[2]

The ability of chalcogenide (E^{2-}) and chalcogenolate (RE^{-}) ligands to form distinct bridging modes with most of the transition and post-transition metals is the key to the successful synthesis of metal chalcogenide NCs.[1b] The highly polarizable electrons and anionic nature of these ligands contribute to the bridging bond formation. Chalcogenide ligands most commonly show three (μ_3) and four (μ_4) coordination bridging, and higher coordination bridging is observed in high nuclearity clusters.[1b] The number of bridging coordination increases as we move down the group in periodic table due to the large size. Similarly, the RE^{-} ligands mostly bridge doubly to the metal atom. The size effect is observed in this case also.

This chapter describes the synthesis, structure, and properties of a variety of metal chalcogenide NCs. NCs gained prominent attention as building blocks for creating novel materials

Atomically Precise Metal Nanoclusters.
DOI: https://doi.org/10.1016/B978-0-323-90879-5.00015-9

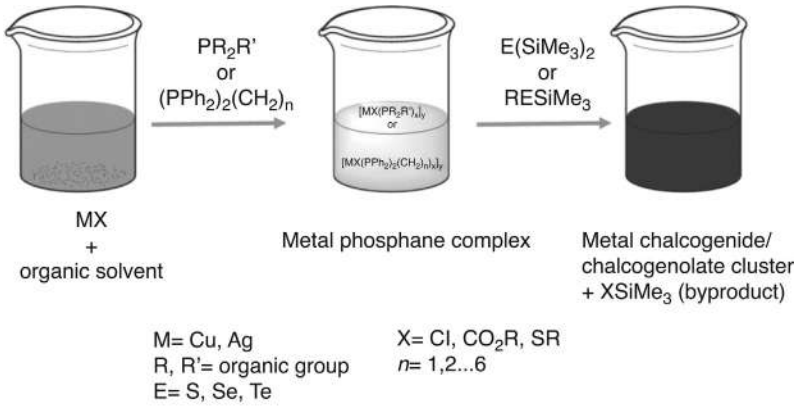

SCHEME 18.1 General synthetic route for chalcogenide NCs from silylated reagents.

with tailored properties owing to their unique combination of atomic precision, tunability, and functionality. The hybrid structures prepared using this building blocks are also discussed in this chapter. Finally, a discussion on the importance of mass spectrometry in understanding the chalcogenide NCs is presented.

18.2 Synthetic approaches for copper and silver chalcogenide NCs

18.2.1 Chalcogenide NCs from silylated chalcogenide sources

Most of the chalcogenide NCs reported are synthesized by the strategy shown in Scheme 18.1. In this approach, metal salt (MX) is reacted with silylated compounds such as $E(SiMe_3)_2$ or $RESiMe_3$ and phosphane to form chalcogenide NC.[1b] The counterion (X) of the metal salt and phosphanes (PR_2R' or $(PPh_2)_2(CH_2)_n$) is the essential parameters in this procedure. The addition of phosphanes determines the crystallization behavior of these compounds, and in some cases, the order of addition of reagents affects the product formation. Initially, a metal salt phosphane complex is formed by the reaction between MX and phosphane. Reactivity of these complexes can be controlled by the choice of X and the phosphanes. The success of this methodology is attributed to the formation of a thermodynamically stable $SiMe_3X$ byproduct. Different products were obtained on replacing the $E(SiMe_3)_2$ reagent with $RESiMe_3$, keeping all other parameters the same. Another essential feature of this strategy is the requirement of low temperature for the reaction. In comparison to the metal NCs, the majority of metal chalcogenide clusters show a +1 charge state for the metal atoms. The chalcogen is considered to be in a −2 charge state. However, a different trend is observed in the case of selenide and telluride NCs of copper, where mixed charge states (0 and +1 or +1 and +2) are favored.

18.2.1.1 Copper chalcogenide

The reactivity of the metal salt phosphane complexes ($[MX(PR_2R')x]y$) with silylated reagents determines the final product obtained through the method shown in Scheme 18.1.

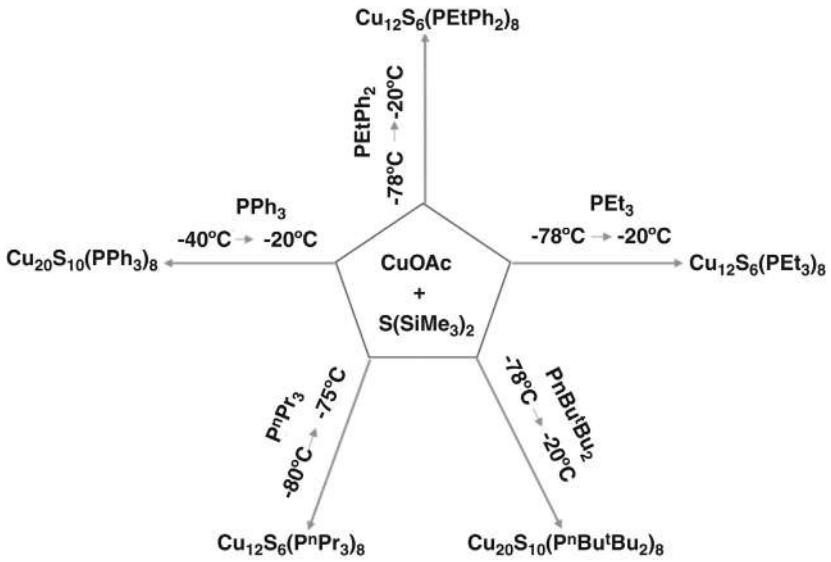

SCHEME 18.2 Synthesis of various copper sulfide NCs using different phosphanes.

If the reactivity of the complex formed is too high, it results in the precipitation of M_2E.[1b] In the case of copper sulfide NCs, the complex formed with metal halides reacts very fast with the silylated reagents. This problem was overcome by the use of metal carboxylates, which forms a less reactive complex. In contrast, the reactivity of $Se(SiMe_3)_2$ with metal halide phosphane complex is different and hence copper selenide NCs are possible with both metal halide and carboxylate.

Synthesis of $Cu_{24}S_{12}(PMe^iPr_2)_{12}$ involves the reaction of CuOAc with P^iPr_2Me and $S(SiMe_3)_2$ in diethylether.[3] The addition of phosphane makes CuOAc soluble in diethylether. Then the reaction mixture was cooled down to −78°C and $S(SiMe_3)_2$ was added. The color of the solution was turned to orange red after keeping for 3 days. Red crystals of the NCs were formed after increasing the temperature to −24°C. Mixture of $Cu_{28}S_{14}(P^tBu_2Me)_{12}$ and $Cu_{50}S_{25}(P^tBu_2Me)_{16}$ was formed after changing the phosphane in the above reaction condition.[3] Other copper sulfide NCs like $Cu_{12}S_6(PEt_3)_8$, $Cu_{12}S_6(PE^tPh_2)_8$, $Cu_{12}S_6(P^nPr_3)_8$, $Cu_{20}S_{10}(PPh_3)_8$, and $Cu_{20}S_{10}(P^nBu^tBu_2)_8$ were synthesized by adding different phosphanes and changing the ratio of reagents (Scheme 18.2).[4] A few copper sulfide NCs protected with both phosphane and thiolates was also made by this route.

There is a rich variety of copper selenide NCs reported using the above mentioned strategy.[1b, 5] These include NCs protected with phosphane, phosphane and selenolate, phosphane and thiolates etc. $Cu_{73}Se_{35}(SePh)_3(P^iPr_3)_{21}$ NC was obtained when CuCl, $PhSeSiMe_3$, P^iPr_3, and $Se(SiMe_3)_2$ were reacted in 2.50:1.25:5.00:0.64 mmol ratio.[6] A clear yellow solution was formed when $PhSeSiMe_3$ was added to a mixture of CuCl and P^iPr_3 in Et_2O. Then the mixture was cooled to −70°C and $Se(SiMe_3)_2$ was added. The yellow color changed to brown and then to black on warming the mixture to room temperature. Black crystals are grown within several weeks at room temperature. When the phosphane was changed to PEt_3 (3.2 mmol) a new

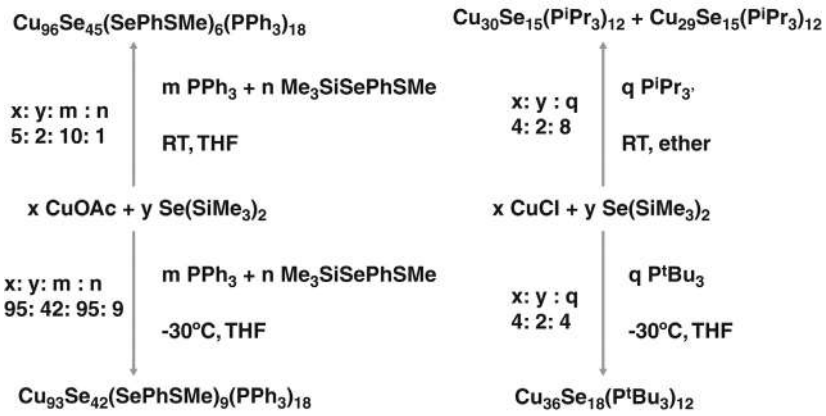

SCHEME 18.3 Scheme for the synthesis of various copper selenide NCs.

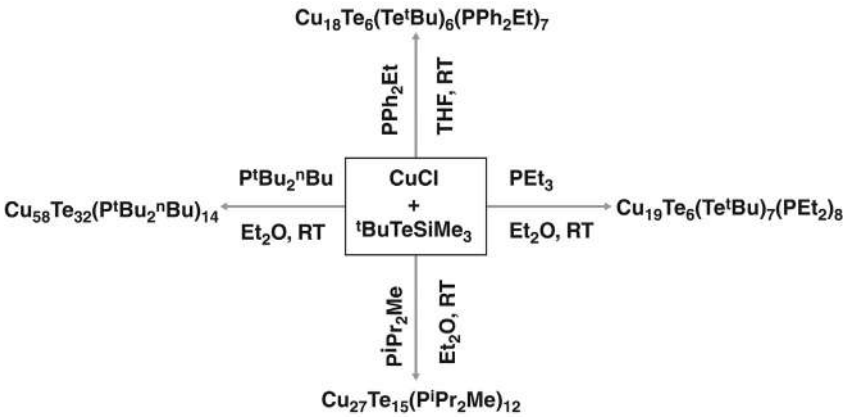

SCHEME 18.4 Synthesis of different copper telluride NCs by adding various phosphane to CuCl and ^{t}BuTeSiMe$_3$ (1:1) mixture.

NC, $Cu_{140}Se_{70}(PEt_3)_{34}$ was obtained. Scheme 18.3 describes the synthesis of various copper selenide NCs.

The copper telluride NCs reported using this strategy (Scheme 18.1) can be divided into four categories as (i) containing only Te^{2-} bridges, (ii) containing additional Te–Te bonds, (iii) containing additional TeR^1 ligands, and (iv) mixed valence NCs. Similar to the synthesis of copper selenide NCs, copper telluride NCs are also produced by the reaction of copper chloride or carboxylate with silylated tellurium sources and phosphanes.[1b,5] In addition, some of the NCs are prepared using smaller copper telluride NCs as precursor. The reaction of CuCl with ^{t}BuTeSiMe$_3$ with various phosphanes produced NCs with different nuclearity (Scheme 18.4). $[Cu_{50}Te_{17}(TePh)_{20}(PEtPh_2)_8][PEtPh_3]$ was formed when a smaller NC, $Cu_6(TePh)_6(PEtPh_2)_5$ dissolved in benzene was exposed to light.[1b] Initially, $Cu_6(TePh)_6(PEtPh_2)_5$ was synthesized

by the reaction of CuCl, $PEtPh_2$, and $Te(Ph)SiMe_3$ in THF/Et_2O mixture. Benzene solution of this cluster is yellow in color. Upon exposure to light the solution turned gradually to brown.

18.2.1.2 Silver chalcogenide clusters

Selection of metal precursor is crucial in the case of silver chalcogenide NC synthesis as well. Reaction of metal halide with silylated reagents always resulted in the precipitation of Ag_2E (E = S, Se).[1b] This issue can be tackled by the use of metal carboxylates, which gives stable NC after reacting with chalcogen sources. The largest chalcogenide NC synthesized and characterized till date is a combination of silver and sulfur. In an alternate method, silver thiolates react with silylated reagent and diphosphanes to give silver sulfide/selenide NC. In this method the use of diphosphane was necessary for the formation of the NC. But the diphosphane was not present as protecting ligand always. It was also observed that the synthesis of silver telluride clusters were successful with both silver halide and silver carboxylate.

The reaction of CH_3COOAg and 1,1,1-tris((diphenylphosphanyl)methyl)ethane (triphos) with a mixture of $S(Ph)SiMe_3$ and $S(SiMe_3)_2$ at −20°C in diglyme produced red needle-like crystals of $[Ag_{70}S_{16}(PhS)_{34}(PhCO_2)_4(triphos)_4]$.[7] Another cluster $[Ag_{70}S_{20}(PhS)_{28}(dppm)_{10}](CF_3CO_2)_2$ was obtained by the reaction of CF_3CO_2Ag with bis(diphenylphosphanyl)methane (dppm), $PhS(SiMe_3)$ and $S(SiMe_3)_2$ at −40°C in dimethoxyethane.[8] A deep red solution was obtained after warming up the reaction mixture to room temperature. This solution was layered with hexane, and red crystals were formed within several days. $Ag_{65}S_{13}(SPhNMe_2)_{39}(dppm)_5$ cluster was formed by the reaction of silver benzoate and dppm in THF with $S(SiMe_3)_2$ and $(Me_2N)C_6H_4(SSiMe_3)$ at low temperature.[9] The yellow solution formed was warmed to room temperature slowly. Yellow crystals were obtained by layering the solution with diethyl ether. Several larger silver sulfide/thiolates clusters, $[Ag_{123}S_{35}(^tBuS)_{50}]$,[10] $[Ag_{188}S_{94}(P^nPr_3)_{20}]$,[7] $[Ag_{262}S_{100}(^tBuS)_{62}(dppb)_6]$,[8] $[Ag_{320}S_{130}(^tBuS)_{60}(dppp)_{12}]$,[11] $[Ag_{344}S_{124}(^tBuS)_{96}]$,[10] $[Ag_{352}S_{128}(^tC_5H_{11}S)_{96}]$,[11] and $[Ag_{490}S_{188}(^t C_5H_{11}S)_{114}]$[11] are also synthesized and characterized.

Solution phase studies on silver sulfide clusters synthesized using this method remained challenging until the report of $[Ag_{115}S_{34}(SCH_2C_6H_4{}^tBu)_{47}(dpph)_6]$.[12] In this case, the insolubility issue of silver sulfide clusters was overcome by using 4-*tert*-butylbenzyl mercaptan as a capping agent. In a typical synthesis, $S(SiMe_3)_2$ was added to a mixture of $[AgSCH_2C_6H_4{}^tBu]$ and 1,6-(diphenylphosphino)hexane (dpph) in toluene. Initially, the mixture was colorless, slowly it changed to yellow then red and finally to green. Dark green crystals were obtained within a few days from a heptane solution of the cluster.

NCs of silver selenides were mainly synthesized by the reaction of silver carboxylate and mono silylated selenium reagent. NCs such as $Ag_{14}Se(SePh)_{12}(PR_3)_8$,[13] $Ag_{28}Se_6(Se^nBu)_{16}(dppp)_4$,[14] $Ag_{30}Se_8(Se^tBu)_{14}(P^nPR_3)_8$,[15] $Ag_{90}Se_{38}(Se^tBu)_{14}(PEt_3)_{22}$,[15] $Ag_{112}Se_{32}(Se^nBu)_{48}(P^tBu_3)_{12}$,[15] $Ag_{114}Se_{34}(Se^nBu)_{46}(P^tBu_3)_{14}$,[15] $Ag_{124}Se_{57}(SeP^tBu_2)_4C_{l6}(P^tBu_2(CH_2)_3)_{12}$,[14] and $Ag_{172}Se_{40}(Se^nBu)_{92}(dppp)_4$,[15] have been obtained by this route. Orange crystals of $Ag_{30}Se_8(Se^tBu)_{14}(P^nPR_3)_8$ were formed by the reaction of silver benzoate with P^nPR_3 and $^tBuSeSiMe_3$ in pentane at −30°C.[15] By changing the phosphane and temperature, a new NC, $Ag_{90}Se_{38}(Se^tBu)_{14}(PEt_3)_{22}$ was obtained. In this case, temperature was set as −20°C and a slight increase in temperature resulted in the precipitation of Ag_2Se. The reaction of silver laurate with $^nBuSeSiMe_3$ and bis(diphenylphosphanyl)propane (dppp) afforded $Ag_{172}Se_{40}(Se^nBu)_{92}(dppp)_4$. The change of diphoshane to P^tBu_3 gave $Ag_{114}Se_{34}(Se^nBu)_{46}(P^tBu_3)_{14}$.[15]

As mentioned earlier, synthesis of silver telluride NCs was successful using silver halide precursor. The addition of $^{n}BuTeSiMe_3$ to a mixture of 1:1 ratio of AgCl:PEt_3 gave rise to $Ag_{32}Te_7(Te^{n}Bu)_{18}(PEt_3)_6$.[16] The reaction was performed at −40°C in pentane. A completely different product, $Ag_{48}Te_{12}(Te^{n}Bu)_{24}(PEt_3)_{14}$, was formed if the ratio of AgCl:PEt_3 is maintained as 1:2.[16] In another case the reaction of 1:2:0.5:0.25 ratio of AgCl:PEt_2R:$Te(SiMe_3)_2$:$TePhSiMe_3$ afforded to $Ag_{30}Te_9(TePh)_{12}(PEt_2Ph)_{12}$.[17] An analogous reaction using bulkier Te(Mes)$SiMe_3$ reagent produced $Ag_{46}Te_{17}(TeMes)_{12}(PEt_3)_{16}$.[17]

18.2.2 CS_2 as chalcogen source

Insertion reactions of CS_2 into M–S bond (M = Cu, Ag, Cd) were mainly observed at by Tang and coworkers.[18] They found that the mono insertion product $M(PPh_3)_2(CS_2SR)$ (M = Ag, Cu) formed by the reaction of M(SR)n with PPh_3 and CS_2, reacts readily with solvents to form $Ag_{14}(\mu_6\text{-}S)(SPh)_{12}(PPh_3)_8{\cdot}4CH_3OH{\cdot}13H_2O_5$ and $Cu_{14}(\mu_2\text{-}S)(SPh)_{12}(PPh_3)_6$. A larger NC, $[Ag_{50}S_7(SC_6H_4{}^{t}Bu\text{-}4)_{40}{\cdot}2CS_2{\cdot}6C_3H_6O]$ $[HNEt_3]_4$ was formed when 4-*tert*-butylthiophenolate, the silver anionic complex, reacted with CS_2 in acetone.[19] In this synthesis, a solution of 4-$^{t}BuC_6H_4SH$ and Et_3N in ethanol was added dropwise to a solution of $AgNO_3$ in ACN and stirred for overnight under N_2 atmosphere. After evaporation, the resultant yellow powder was dissolved in 1:1 CS_2: acetone mixture. Red colored crystals suitable for diffraction were obtained after several days of evaporation at room temperature. The slow release of S^{2-} occurred by the reaction of CS_2 with solvents.

Thermochromic luminescent NCs, $[Ag_{33}S_3(S^{t}Bu)_{16}(CF_3COO)_9(NO_3)(CH_3CN)_2](NO_3)$ (NC 1) and $[Ag_{31}S_3(S^{t}Bu)_{16}(NO_3)_9]_n$ (NC 2) were synthesized by the addition of CS_2 to $AgS^{t}Bu$ and $CF_3COOAg/AgNO_3$.[20] $AgS^{t}Bu$ was first prepared by the reaction of an equivalent amount of Ag_2O and $^{t}BuSH$ in Et_3N. Then the thiolate was dissolved in a mixture of methanol and acetonitrile. Addition of a mixture of CF_3COOAg, $AgNO_3$, and CS_2 into the above solution resulted in NC 1. NC 2 was formed in the absence of CF_3COOAg.

18.2.3 Chalcogen release by the C–S bond cleavage

Sulfur (S^{2-}) release can be facilitated by the cleavage of the C–S bond of thiol. NCs like $Ag_{62}S_{13}(S^{t}Bu)_{32}{}^{4+}$ and $Ag_{62}S_{12}(S^{t}Bu)_{32}{}^{2+}$ were produced by this route.[21] A mixture of $AgBF_4$, NH_2–NH_2, and Ag–$S^{t}Bu$ was heated in methanol at 65°C which lead to the isolation of $Ag_{62}S_{13}(S^{t}Bu)_{32}{}^{4+}$. The cluster $Ag_{62}S_{12}(S^{t}Bu)_{32}{}^{2+}$ was synthesized by a different method, which involves two steps. In the first step, glutathione (GSH)-protected NC was prepared by reducing the solution of GSH and $AgNO_3$ in NaOH using $NaBH_4$. The $Ag_n(SG)_m$ formed was used as a precursor for the two-phase ligand exchange reaction in the second step. An aqueous solution of $Ag_n(SG)_m$ was allowed to react with $^{t}BuSH$ in dichloromethane under vigorous stirring. The NC was completely transferred into organic layer after 10h of stirring. Then the solvent was evaporated and purified by DCM/MeOH mixture. To get better crystals the anion was replaced by adding the required amount of $NaBPh_4$.

Nan et al. monitored the growth of Ag–S NCs by crystallizing the intermediates formed.[22] In this study the slow release of S^{2-} by the cleavage of C–S bond helped in isolation and crystallization of the intermediates. In a typical reaction, $AgS^{t}Bu$ was added to methanolic solution of CF_3COOAg and sonicated to get a suspension. After the addition of

acetonitrile to this suspension, a clear solution was obtained. The resultant colorless solution was kept undisturbed. The solution color was changed to yellow to orange to red as time passed. Different colored solutions gave different NC crystals. Yellowish solution gave $Ag_{31}S_3(S^tBu)_{10}(CF_3COO)_8(MeCN)_4$, orange solution gave $Ag_{45}S_7(S^tBu)_{24}(CF_3COO)_7$, and red solution gave $[Ag_{62}S_{13}(S^tBu)_{32}(CF_3COO)_2](CF_3COO)_2$.

In addition to the synthetic methods described above, there were efforts to make chalcogenide NCs using chalcogen (S, Se) powder as chalcogen source.[23] These reactions were carried out at a lower reaction temperature than the conventional quantum dot synthesis using chalcogen powder. These NCs are highly soluble in organic solvents and hence the solution phase properties were studied in detail.

18.3 Structure and properties of copper and silver chalcogenide clusters

18.3.1 Structure

Determining the crystal structure of NCs is important to understand their properties in detail. The importance of molecular structure was quoted by Francis Crick, "If you want to understand function, study structure." Single crystal X-ray crystallography (XRD) is the widely accepted method for structural analysis. Most of the copper and silver chalcogenide NCs reported are characterized using single crystal XRD. This section describes a few of the reported structures.

Owing to the different coordination affinity of Cu^{+1} (trigonal or tetrahedral) and Ag^{+1} (linear or trigonal), chalcogenide NCs of copper and silver shows various structures. When the chalcogenide is changed, the bridging mode also changes and thus the structure. NCs of copper chalcogenide and silver selenide shows a clear tendency to approach bulk structural pattern, whereas in silver sulfide this was not visible. The structural determination of larger silver chalcogenide (number of metal atoms greater than 120) clusters was problematic due to the low translational order in the lattice and hence only an idealized formulae was assigned to them.

The structure of copper chalcogenide NCs can be classified as small, middle sized and large depending on their tendency to show similarity with their bulk Cu_2E phase. Spherical shaped smaller clusters show similarity with the bulk phase in local coordination environment. Larger NCs show similarity with the bulk in layered arrangement of copper and chalcogen atoms. Middle sized NCs show characteristics of both. Smaller and middle sized NCs are known for copper sulfides and all the three category are reported for the copper selenides. In contrast to this, copper telluride NCs show a tendency to form nonstoichiometric systems.

The structure of $Cu_{12}S_6(PEt_2Ph)_8$ consists of an S_6 octahedron interpenetrated by an Cu_{12} cuboctahedron.[4b] The phosphane ligands are connected to the copper atoms and hence the cuboctahedron is distorted.[24a] A structural isomer is formed when a different phosphane (P^nPr_3) is bound to the $Cu_{12}S_6$ core.[4a] In the former NC, eight phosphorus ligands are arranged in a cubic manner around the cluster surface, and in the latter cluster a P_8-delta dodecahedron is observed. A distorted cubic close packing (fcc) sulfur substructure was found in $Cu_{136}S_{56}(SCH_2C_4H_3O)_{24}(dpppt)_{10}$ (Fig. 18.1A).[24a] This can be considered as a distorted portion of cubic copper(1)sulfide phases. Some of the copper positions are only partially filled

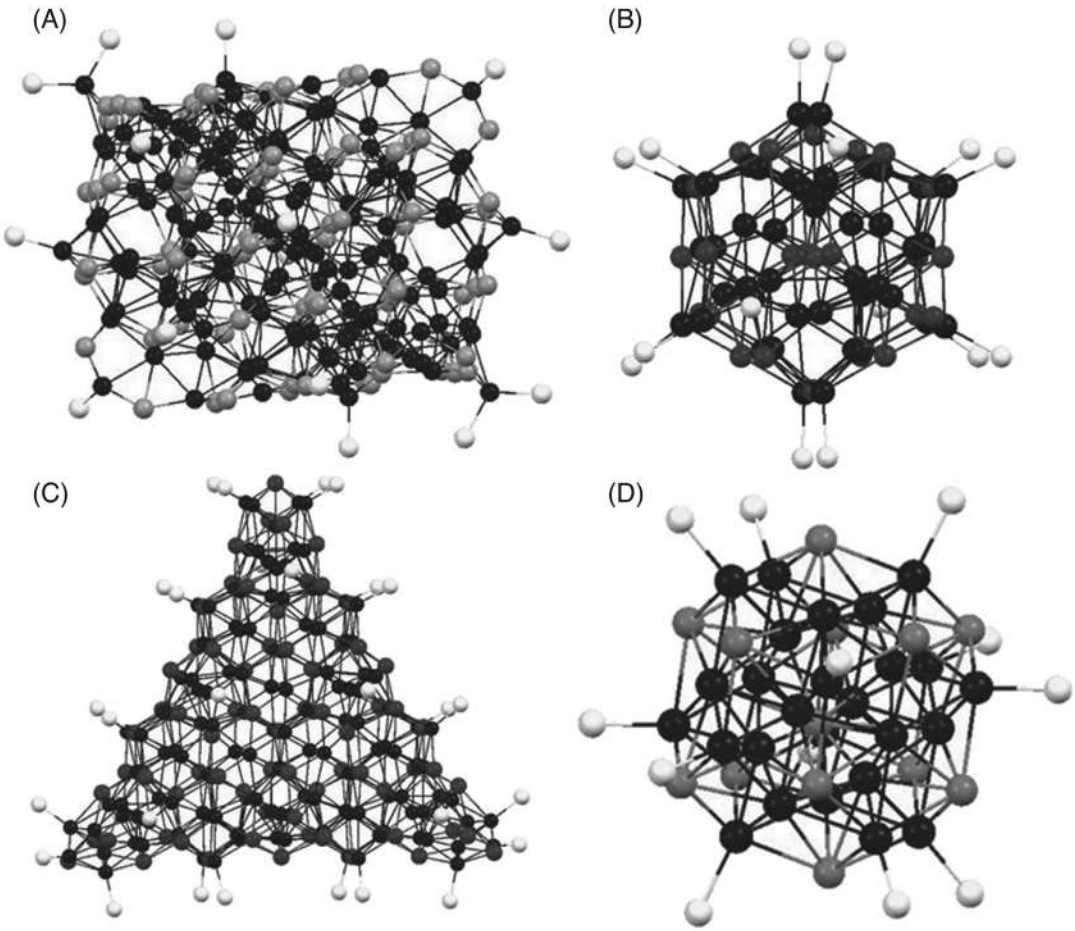

FIGURE 18.1 Crysral structure of $Cu_{136}S_{56}(SCH_2C_4H_3O)_{24}(dpppt)_{10}$ (A), $Cu_{44}Se_{22}(PEt_2Ph)_{18}$ (B), $Cu_{140}Se_{70}(PEt_3)_{34}$ (C), and $Cu_{23}Te_{13}(PEt_3)_{12}$ (D) without organic group. Cu: ●, S: ●, Se: ●, Te: ●, P: ●. Adapted with permission from ref.[24] Copyright 1994 and 2010, Wiley-VCH for (B) and (A). Adapted with permission from refs.[6, 25] Copyright 1996 and 1999, The Royal Society of Chemistry for (D) and (C).

in this cluster. Sulfur atom of the thiol group shows μ_3 or μ_4 coordination and the sulfide group are μ_5 or μ_6 coordinated.

Copper selenide NCs with 12 copper atoms fall under the category of smaller NC and those containing 20–59 copper atoms under middle sized NCs. A structural change is evident when the number of copper atoms is larger than 59 and these are considered larger NCs.[1b] $Cu_{12}Se_6(PR_2R')$ ($PR_2R' = PEt_2Ph$, P^nPR_3) have structure identical to their sulfur analogues. The middle sized NC $Cu_{44}Se_{22}(PEt_2Ph)_{18}$ has a 20 selenium atom consisting of deltohedron selenium frame work (Fig. 18.1B).[24b] There are two selenium atoms at the center and no bonding interactions exist between the selenium atoms. This can also be viewed as two hexagonal antiprisms joined by a hexagonal face with two selenium atoms capping the free hexagonal face. Among the 44 copper atoms 18 are arranged above and 18 are below the

triangles of the deltohedron. The 18 PEt_2Ph ligands are connected to the copper atoms which are arranged above the polyhedron. The remaining eight copper atoms form two trigonal prisms linked by a triangular face inside the cluster. An isomeric Cu–Se framework is observed in $Cu_{44}Se_{22}(P^nBu^tBu_2)_{12}$.[24b]

The larger copper selenide NCs display A–B–A hexagonal type packing of selenium layer. The metal atoms occupy either the tetrahedral or the trigonal holes. This layer type arrangement is similar to the one observed in bulk materials. $Cu_{140}Se_{70}(PEt_3)_{34}$ NC comprises of hexagonal layers containing 21-28-21 numbers of selenium (Fig. 18.1C).[6] There are 86 tetrahedral holes and 15 pairs of octahedral holes present in this layer. Of the 140 copper atoms, 85 occupy tetrahedral holes, 40 occupy in octahedral holes. The remaining 15 copper atoms are found at the three corners. The spherical NC $Cu_{23}Te_{13}(PEt_3)_{12}$ comprises four Cu–Te layers with a central tellurium atom (Fig. 18.1D).[25] There are 12 Cu-PEt_3 protecting the cluster core. This can also be viewed as a body centered icosahedron of tellurium with 12 faces covered with $CuPEt_3$ group.

A core–shell type $Ag_{65}S_{13}(SPhNMe_3)_{39}(dppm)_5$ was characterized by Chitsaz et al.[9] The cluster contains an inner S_{13} core. Sulfur atoms are arranged in an ABAC (double hexagonal close pack) pattern (Fig. 18.2A). Three S atoms form A layer, six S atoms form B layer, and three S atoms form another A layer, and a single S atoms forms C layer. This inner S_{13} core is surrounded by 39 shell S atoms, and 65 silver atoms are incorporated into the sulfur substructure. A shell-like sulfur substructure consisting of an inner S_8 hexagonal bipyramid and an outer S_{40} polyhedron is observed in $[Ag_{70}S_{20}(PhS)_{28}(dppm)_{10}](CF_3CO_2)_2$[8]. The S_8 structure is highly distorted and are μ_5 bridged to silver atoms (Fig. 18.2B). The outer S_{40} polyhedron is formed by the 28 sulfur atoms of thiophenol ligand and 12 sulfur atoms of S^{2-}. These sulfur atoms are μ_3, μ_4, and μ_6 bridged to silver. Alternatively, the structure can be viewed as edge shared or corner shared building blocks consisting of 22 linear S–Ag–S groups, 24 distorted trigonal planar AgS_3 units, four distorted AgS_4 polyhedra, and 20 AgS_3P polyhedra.

The structure of $Ag_{90}Se_{38}(Se^tBu)_{14}(PEt_3)_{22}$ is formed by a torus-shaped polyhedron of Se atoms and distorted polyhedra of Ag atoms (Fig. 18.2C).[15] The Se atoms of the Se^tBu group are arranged at the surface of the polyhedron, which is having a D_{6h} symmetry. Se^{2-} form two layers, inner layer contains 18 Se^{2-} atoms alone and in the outer layer Se^{2-} is arranged along with the Se^-. The inner Se^{2-} forms five to eight bonds with Ag atoms. Outer Se^{2-} are μ_4 or μ_5 coordinated. Of the 90 Ag atoms, 68 are only bonded to Se^{2-} atoms. Among this 20 are bonded to two Se^{2-} in a distorted linear fashion, 28 are connected in distorted trigonal arrangement, and remaining 20 have distorted tetrahedral arrangement. This NC is spherical in shape and shows no similarity with the bulk counterpart. Another NC, $Ag_{114}Se_{34}(Se^nBu)_{46}(P^tBu_3)_{14}$ has a structure which can be described as cross section of bulk Ag_2Se (Fig. 18.2D).[15] Silver atoms in this NC are coordinated to Se atom in a trigonal and tetrahedral fashion similar to the bulk Ag_2Se coordination.

18.3.2 Optical properties

NCs gained enormous research interest in the recent years due to the unique optical absorption and emission properties, which make them useful for the applions such as sensing and biolabeling.[26] The important characteristic of a NC is the appearance of step-like features

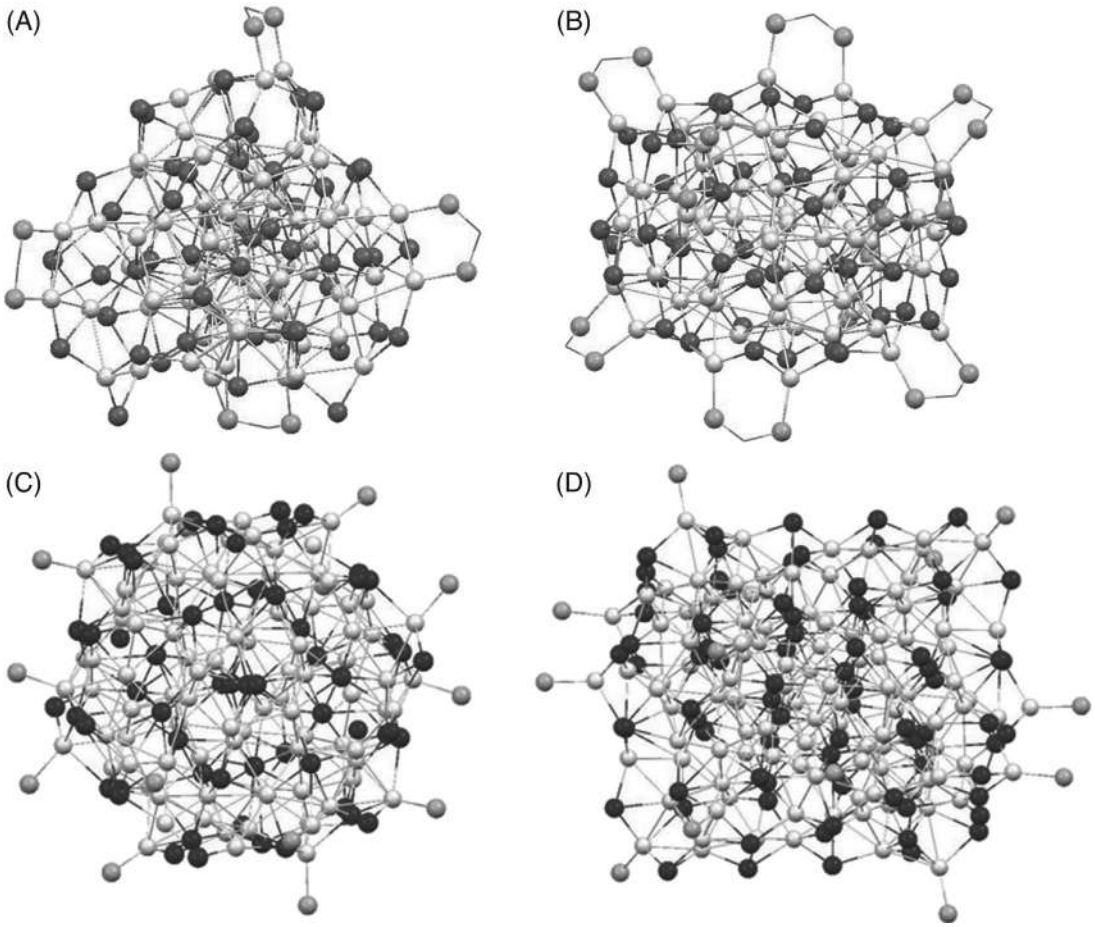

FIGURE 18.2 Crystal structure of $Ag_{65}S_{13}(SPhNMe_3)_{39}(dppm)_5$ (A), $[Ag_{70}S_{20}(PhS)_{28}(dppm)_{10}](CF_3CO_2)_2$ (B), $Ag_{90}Se_{38}(Se^tBu)_{14}(PEt_3)_{22}$ (C), and $Ag_{114}Se_{34}(Se^nBu)_{46}(PtBu_3)_{14}$ (D) without organic group. Ag: ●, S: ●, Se: ●, P: ●. Adapted with permission from refs.[8,9,15] Copyright 1998, 2004, and 2006, Wiley VCH.

in the optical absorption spectrum. In semiconductor NCs, the absorption band is blue shifted to higher energy compared to their larger NPs.

Optical absorption spectrum of some of the reported copper selenide NCs are studied using solid state absorption spectroscopy.[1b] The solid-state absorption spectra of $Cu_{26}Se_{13}(PEt_2Ph)_{14}$, $Cu_{44}Se_{22}(PEt_2Ph)_{18}$, $Cu_{70}Se_{35}(PEt_2Ph)_{23}$, and $Cu_{140}Se_{70}(PEt_3)_{34}$ are compared in this study. These clusters showed larger band gap compared to the bulk Cu_2Se. As the cluster size increases, the onset of absorption shifted to higher wavelength region. The clusters showed weak photoluminescence in the NIR region and the emission intensity increased at lower temperature. Size dependency was also visible in photoluminescence spectra of these clusters.

Jin et al. reported drastic changes in the optical properties of silver sulfide NCs as the number of sulfur atoms present in the cluster core varied.[21b] $Ag_{62}S_{13}(S^tBu)_{32}^{4+}$ (NC-1) contain one extra sulfur atom at the center compared to the $Ag_{62}S_{12}(S^tBu)_{32}^{2+}$ (NC-11). NC-1 shows

three absorption features at 330, 370, and 543 nm whereas NC-11 shows peaks at 420 and 520 nm (Fig. 18.3A). NC-1 was highly red luminescent both in the solution ($\lambda_{em}{}^{max} = 613$ nm) and in the solid state ($\lambda_{em}{}^{max} = 621$ nm), while the NC-11 was nonluminescent. The emission of NC-1 has been assigned to the ligand to metal charge transfer (LMCT) (S 3p to Ag 5s). From the femtosecond transient absorption spectra, the difference in luminescence features was attributed to the availability of free electrons in case of the latter NC. All of the silver atoms in NC-1 do not have valence electrons of silver leading to triplet LMCT with emission. In the case of NC-11, there are four delocalized valence electrons which prevents the charge transfer from ligand to the metal core and hence results in luminescence quenching.

Optical properties of silver sulfide NCs synthesized using silylated reagents are not well studied due to their low solubility. In 2017, an organic soluble $[Ag_{115}S_{34}(SCH_2C_6H_4{}^tBu)_{47}(dpph)_6]$ was reported by Bestgen et al.[12] The cluster showed a broad absorption features in the range 550–650 nm. A highly red luminescent mixed chalcogenide silver NC $Ag_{56}Se_{13}S_{15}$ protected by 4-*tert* butylbenzyl mercaptan was reported by Manju et al.[23b] The optical absorption spectrum of this cluster showed three prominent features at 370, 445, and 570 nm. When excited at 440 nm, the cluster exhibits an emission band at around 625 nm (Fig. 18.3B). The photoluminescence quantum yield (QY) of this cluster was calculated to be 21% percentage. If a substance changes its emission color in response to the temperature, it is known as thermochromic luminescent. NCs $[Ag_{33}S_3(S^tBu)_{16}(CF_3COO)_9(NO_3)(CH_3CN)_2](NO_3)$ and $[Ag_{31}S_3(S^tBu)_{16}(NO_3)_9]_n$ show a color change from yellow to orange when the temperature changed from 273 to 77 K, and the phenomenon was reversible.[20]

Density functional theory (DFT) calculations were carried out to correlate the structure and electronic properties of $Ag_{62}S_{13}(S^tBu)_{32}{}^{4+}$ (NC-1) and $Ag_{62}S_{12}(S^tBu)_{32}{}^{2+}$ (NC-11). The main difference in electronic properties of these NCs is that in the case of NC-1 the HOMO electron density is concentrated on inner $Ag_{14}S_{13}$ kernel and LUMO electron density is concentrated in outer AgS shell. Whereas NC-11 showed a reverse electron density distribution. The electron density of NC-11 LUMO is distributed on inner $Ag_{14}S_{12}$ kernal. This difference in electron density makes these two clusters behave differently during electronic excitation. The Kohn–Sham (KS) molecular orbital energy diagram of NC-1 and NC-11 (Fig. 18.4) shows that the NC-1 has larger HOMO–LUMO gap compared to NC-11.

18.3.3 Thermal properties

Thermogravimetric investigations of copper selenide NCs points to the formation of copper selenide nanoparticles by losing phosphane ligands. Phosphane ligands are lost at temperatures between 60 and 200°C.[1b] The exact temperature depends on the cluster size, type of ligand, and other experimental conditions. Thermal properties of NCs such as $Cu_{26}Se_{13}(PEt_2Ph)_{14}$, $Cu_{44}Se_{22}(PEt_2Ph)_{18}$, $Cu_{70}Se_{35}(PEt_2Ph)_{23}$, $Cu_{26}S_{13}(PEt_3)_{14}$, $Cu_{70}Se_{35}(PEt_3)_{23}$, and $Cu_{140}Se_{70}(PEt_3)_{34}$ were monitored in vacuum and in helium atmosphere. The desorbed species PEt_3 and PEt_2Ph were confirmed from the mass spectrometric measurements. There was a good agreement with the calculated and experimental weight loss of the clusters. Thermal analysis under helium atmosphere showed stepwise desorption of ligands but in vacuum only single step was observed. The analysis also showed a difference in the onset temperature for the ligand cleavage under the two experimental conditions. Lower temperature was required in vacuum than in helium. The cluster protected with PEt_3 desorbed at

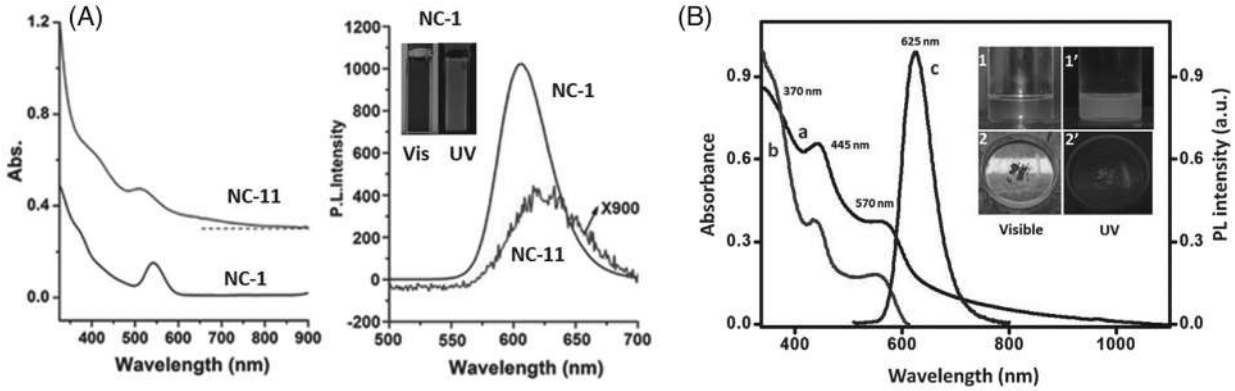

FIGURE 18.3 UV–Vis and emission spectra of $Ag_{62}S_{13}(S^tBu)_{32}^{4+}$(NC-1) and $Ag_{62}S_{12}(S^tBu)_{32}^{2+}$ (A). Inset of emission spectra shows the photograph of NC-1 under UV and visible light. UV–Vis (A), excitation (B), and emission (C) spectra of $Ag_{56}Se_{13}S_{15}$ NC. Inset shows the photograph of the NC under UV and visible light both in solid and solution state. Reproduced with permission from ref.[21] Copyright 2010 and 2014, American Chemical Society for (A). Reproduced with permission from ref.[23b] Copyright 2016, The Royal Society of Chemistry for (B).

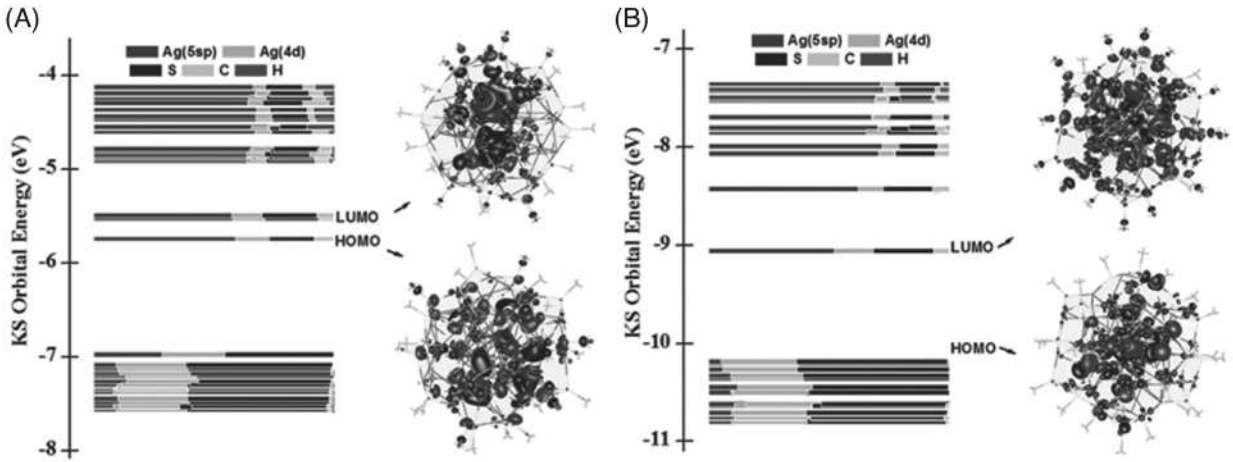

FIGURE 18.4 Kohn–Sham (KS) molecular orbital energies and molecular orbital populations of NC-11 (A) and NC-1 (B). Electron densities of HOMO and LUMO of both NCs are also shown. Reproduced with permission from ref.[21b] Copyright 2014, American Chemical Society.

a reduced temperature than the cluster protected with PEt_2Ph. This is due to the stronger Cu–P bond in the case of PEt_2Ph. To confirm the formation of Cu_2Se particles, powder X-ray diffraction (P-XRD) was performed using the black residue formed. P-XRD patterns clearly show the formation of nano Cu_2Se. Thermal analysis of diphoshane and thiol-protected NC, $[Ag_{115}S_{34}(SCH_2C_6H_4{}^tBu)_{47}(dpph)_6]$ demonstrated the onset of ligand desorption from 160°C.[12] Complete desorption of ligands occurred at around 600°C with a total weight loss of 47%. The experimental weight loss was comparable with the calculated mass.

18.4 Tetrahedral nanoclusters of cadmium and zinc

Tetrahedral chalcogenide/chalcognolate NCs with distinct molecular structures and exceptional properties attracted research interest because they display a clear structural association with the bulk materials. Chalcogenides/chalcognolates of main group elements (In, Ga, Sn, Ge) and transition elements (Cd, Zn, Hg, Fe, Co, Mn) forms tetrahedral NCs.[27] Majority of these clusters consist of adamantoid and barrelanoid frameworks, the same structural units were observed in bulk. Larger homologs of these clusters are formed by the combination of these cages via side sharing. This section discusses the tetrahedral NCs of Cd, Zn, and their assemblies.

18.4.1 Series of tetrahedral nanoclusters

Three different categories of tetrahedral NCs are known.[27] Supertetrahedral NC, denoted as T_n (n designates the number of individual ME_4 tetrahedron along each side), is tetrahedral shaped fragments of cubic, adamantoid ZnS type lattice. Larger NCs of this series are formed by the fusion of adamantoid cages only. In this series, T_2 to T_6 clusters are known. T_1 is a simple tetrahedron, and T_2 consists of four corner connected tetrahedra. Chalcogenide NCs T_3, T_4, T_5, and T_6 are formed by 10, 20, 35, and 56 corner-linked tetrahedra, respectively. In a T_n NC, the number of E sites is equivalent to the number of M sites in the next larger T_{n+1} NC. The second category, pentasupertetrahedral NC (P_n), can be viewed as four T_n clusters coupled to the faces of an antisupertetrahedral cluster of the same order. Here, the M and E positions of the central antisupertetrahedral unit are exchanged in comparison to the regular one. Capped supertetrahedral, C_n, the third member of this family consist of cubic ZnS type lattice core, together with four corner barrelanoid (hexagonal) cages capping the vertices. Similar to T_n NC the number of E sites in C_n NCs are equivalent to the number of M sites in the next larger C_{n+1} in the series. The hexagonal units at the vertex can be rotated independently by 60° resulting in isomerism. This series is denoted as $C_{n,m}$, where m denotes the number of corners that have been rotated from the original positions in the parent C_n NC.

18.4.2 Synthesis and crystallization

The fusion chemistry of adamantoid and barrelanoid cages was understood after the successful synthesis of $[M_{10}E_4(SPh)_{16}]^{4-}$ (M = Cd, Zn; E = S, Se) using the reaction of elemental sulfur or selenium with $M_4(SPh)_{10}{}^{2-}$.[28] Initially $M_4(SPh)_{10}{}^{2-}$ was synthesized by adding a methanolic solution of metal nitrate to a mixture of benzenethiol (PhSH) and triethylamine

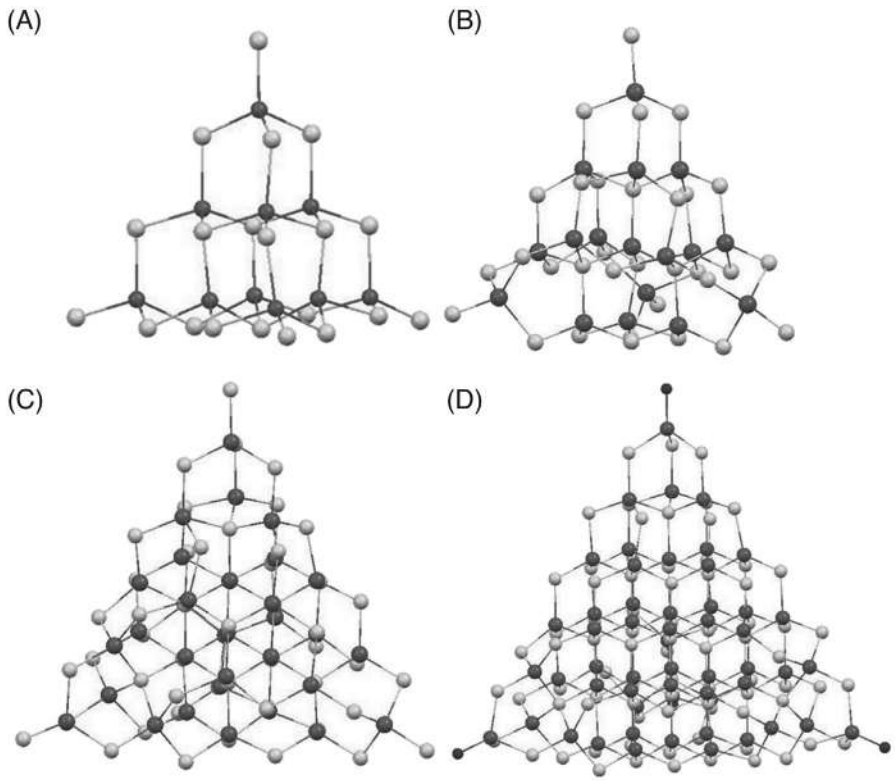

FIGURE 18.5 Crystal structure of $Zn_{10}S_4(SPh)_{16}^{4-}$ (A), $Cd_{17}S_4(SPh)_{26}^{2-}$ (B), $Cd_{32}S_{14}(SPh)_{40}^{4-}$ (C), $Cd_{52}S_{32}(SPh)_{48}(H_2O)_4^{4-}$ (D) without organic group. S: ●, Cd, Zn: ●, H_2O: ●. Adapted with permission from refs.[28,29,31] Copyright 1984, 1988, and 2005, American Chemical Society.

in MeOH, followed by the addition of tetramethylammonium chloride. Colorless crystals of $M_4(SPh)_{10}^{2-}$ were obtained after keeping the reaction mixture at 0°C. $M_{10}E_4S_{16}$ core of these NCs is a macrotetrahedral fragment of cubic zinc blend lattice (Fig. 18.5A). An inner octahedron is formed by six metal ions. Four of its faces are capped by triply bridging chalcogenide ion. Remaining four metal atom are arranged as a larger outer tetrahedron. Each inner metal atom is coordinated to two triply bridging chalcogenide ion and two doubly bridging SPh ligand and each outer metal atom is connected to three doubly bridging SPh and one terminal SPh groups.

$[Cd_{17}S_4(SPh)_{28}]^{2-}$, the first member of C_n series was reported subsequently by the reaction of Na_2S, PhSH, and $Cd(NO)_2$ in ACN.[29] The structure consists of a central cadmium atom connected to four S^{2-} groups. All of these four S^{2-} is connected to three cadmium atoms, which are part of a cuboctahedron. Four faces and 12 edges of cuboctahedron are internally covered by μ_4-S^{2-} groups. The remaining 12 edges are doubly connected to SPh ligands. These 12 SPh ligands can be viewed as a tetratruncated tetrahedron. Four of the eight faces connected to μ_4-S^{2-} groups are also connected to external cadmium atoms via SPh ligands. There are four external cadmium atoms connected to three bridging SPh and one terminal SPh group (Fig. 18.5B). A double-diamond superlattice network of neutral $Cd_{17}S_4(SCH_2CH_2OH)_{26}$ was

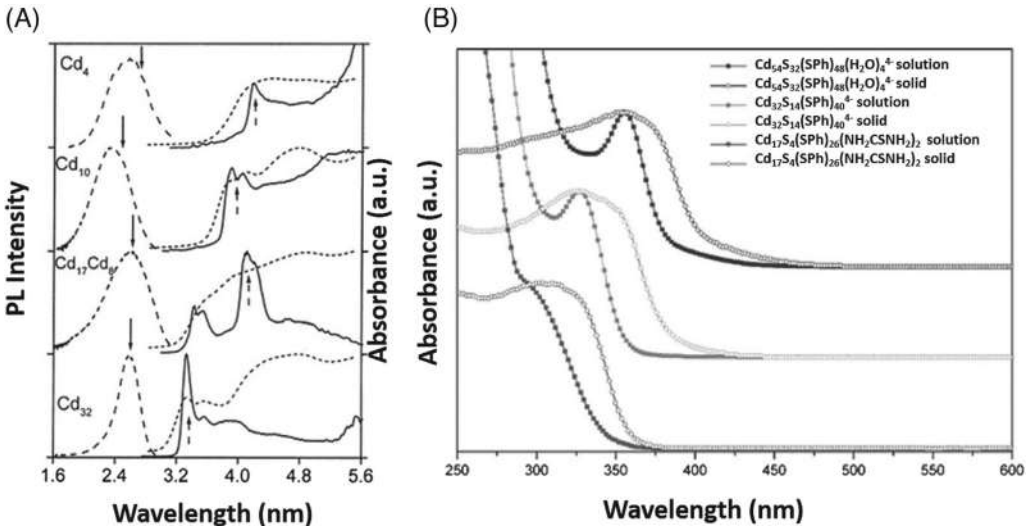

FIGURE 18.6 UV–Vis spectra (dotted lines), excitation spectra (solid lines), and emission spectra (dashed lines) of CdSe NCs (A). Solution and solid state UV–Vis spectra of $Cd_{54}S_{32}(SPh)_{48}(H_2O)_4{}^{4-}$, $Cd_{32}S_{14}(SPh)_{40}{}^{4-}$, and $Cd_{17}S_4(SPh)_{26}(NH_2CSNH_2)_2$(B). Reproduced with permission from refs.[2,31] Copyright 2001 and 2005, American Chemical Society for (A) and (B).

observed in another study.[30] This structure was similar to the anionic cluster described above. In the case of negatively charged $[Cd_{17}S_4(SPh)_{28}]^{2-}$ cluster, all the vertices are capped by thiolates ligands whereas two terminal ligands are absent in the superlattice, and each cluster is connected to four neighboring clusters by sharing its vertices.

Larger NCs of C_n series $Cd_{32}S_{14}(SPh)_{36}.DMF_4$,[32] $Cd_{32}S_{14}(SPh)_{40}{}^{4-}$ (C2,2),[31] $Cd_{54}S_{32}(SPh)_{48}(H_2O)^{4-}$ (C3,4)[31], and $Cd_{54}S_{28}(SPh)_{52}(L)_4$ (L = solvent)[33] have also been crystallized in independent works (Fig. 18.5C and D). $Cd_{32}S_{14}(SPh)_{36}.DMF_4$ and $Cd_{54}S_{28}(SPh)_{52}(L)_4$ were crystallized from a pyridine solution of $Cd_{10}S_4(SPh)_{12}$, the intermediate product of thermal decomposition of $Cd_{10}S_4(SPh)_{16}{}^{4-}$, by the addition of coordinating solvents.[32,33] Similar to the CdS clusters, formation of CdSe clusters such as $Cd_{10}Se_4(SePh)_{12}(PnPr_3)_4$, $[Cd_{17}Se_4(SPh)_{28}]_{2-}$, $Cd_{32}Se_{14}(SePh)_{36}(PPh_3)_4$, and $Cd_{54}Se_{32}(SPh)_{48}(H_2O)_4{}^{4-}$ are also reported. It was also shown that thiophenolate complexes, $Cd(EPh)_4(NMe)_4$ (E = S, Se) could also be used as a starting material for larger CdS/Se clusters.[34]

18.4.3 Optical properties

Tetrahedral NCs are an excellent example for studying the size dependent optical properties. Soloviev et al. studied the systematic blue shift in the optical properties of CdSe tetrahedral NCs.[2] They investigated the room temperature UV–Vis and low temperature emission spectra of CdSe NCs with 4, 8, 10, 17, 32 metal atoms as depicted in Fig. 18.6A. Absorption onset was red shifted as the NC size increased. The double diamond shaped $Cd_{17}S_4(SCH_2CH_2OH)_{26}$ NC dissolved in solvents such as water, DMF, and DMSO exhibit pronounced absorption features at 290 nm.[30] Solid state films of these NCs grown by spin

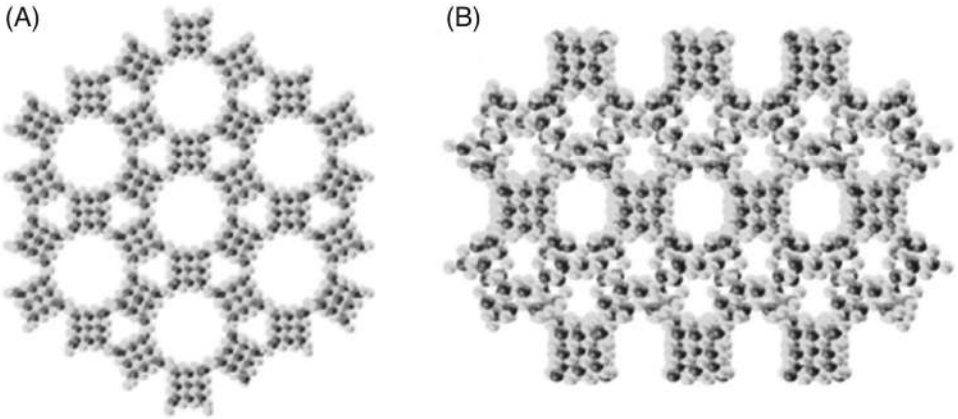

FIGURE 18.7 3-D frameworks of $Cd_{17}S_4(SPhMe\text{-}3)_{26}$ (A) and $[Cd_8S_4(SPhMe\text{-}3)_{14}]$ $[Cd_{17}S_4(SPhMe\text{-}3)_{26}]$ (B). Organic ligands are omitted for clarity. Reproduced with permission from ref.[35] Copyright 2007, American Chemical Society.

coating showed similar absorption spectrum with small red shift. The NC emits both in solution ($\lambda_{em} = 400$ nm) and in solid state ($\lambda_{em} = 412$ nm). The next homolog in the series $Cd_{32}S_{14}(SPh)_{36}.DMF_4$ shows absorption peak at 358 nm and emits around 500 nm.[32] In comparison, the charged NC $Cd_{32}S_{14}(SPh)_{40}^{4-}$ synthesized by Zang et al. absorbs around 325 nm.[31] They have also reported $Cd_{54}S_{32}(SPh)_{48}(H_2O)_4^{4-}$ and $Cd_{17}S_4(SPh)_{26}(NH_2CSNH_2)_2$ with 353 and 291 nm absorption features, respectively (Fig. 18.6B).

18.4.4 Hybrid materials based on tetrahedral NCs

Hybrid materials, fabricated from covalently bonded organic and inorganic moieties are an important class of solid state materials.[27a] The combination of different organic and inorganic groups provides materials with novel properties. Well-defined NCs serve as a promising building block for hybrid materials. Such cluster-based networks show distinct optical and electronic properties. The porosity of these networks can be utilized for the sensing of different solvent and gas molecules. Hybrid materials can be classified into two categories as extended inorganic hybrids, structures formed by the side sharing interaction of protecting ligands and coordination polymer or metal–organic frameworks (MOFs), structures formed through organic linker connectivity.

Tetrahedral chalcogenide NCs are attractive building units for both kinds of networks.[35,36] Chiral frameworks of P1 NC, $Cd_8S_4(SPhMe\text{-}3)_{14}$, and C1 NC $Cd_{17}S_4(SPhMe\text{-}3)_{26}$ were obtained by the reaction of CS_2 with $Cd(SPhMe\text{-}3)_2$ at room temperature or solvothermal conditions.[35] These frameworks adopted β-quartz topology (Fig. 18.7A). Materials containing both P1 and C1 NC having moganite topology was also formed under solvothermal conditions (Fig. 18.7B). Formation of a novel 3D architecture of $Cd_{17}S_4(SPhMe\text{-}3)_{26}^{2-}$ NC was described by Zhang et al.[36a] This superlattice with boracite topology consists of alternating three and four connected centers. The framework formed also showed interesting photoelectric properties.

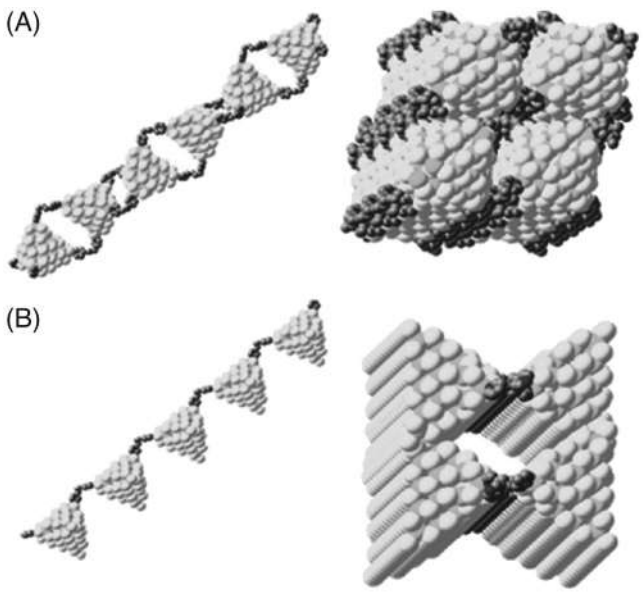

FIGURE 18.8 1-D assembly of $Cd_{32}S_{14}(SPh)_{36}L_4$ (A) and $Cd_{32}S_{14}(SPh)_{38}L_2^{2-}$ (B), (L = TMDPy). In (A) neighboring C2,1 CdS clusters are combined together through two TMDPy ligands. In (B) a negatively charged chain is formed through the connection of each C2,2 CdS cluster with one TMDPy ligand. Figures at the left side show the 3D arrangements of chains. Reproduced from ref.[36b] Copyright 2005, American Chemical Society.

Pyridyl-based ligands are mainly used for the formation of MOF structures of tetrahedral NCs. Zheng et al. reported the 1-D assembly of CdS NCs using 4,4′-trimethylenedipyridine (TMDPy) and 4,4′-bipyridine (BPy).[36b] In the case of $Cd_{32}S_{14}(SPh)_{36}L_4$ (L = TMDPy) assembly the NCs are joined together through two TMDPy into a doubly bridged chain, whereas $Cd_{32}S_{14}(SPh)_{38}L_2^{2-}$ NC formed a singly bridged assembly using one TMDPy (Fig. 18.8). NCs $Cd_{17}S_4(SPh)_{26}L_2$, $Cd_{17}Se_4(SPh)_{26}L_2$ (L = BPy), and $Cd_8S(SPh)_{14}L_2$ (L = TMDPy) also forms 1D assembly. 1D zig-zag chains of $Zn_8S(SPh)_{14}L_2$ (L = 1,2-bis(4-pyridyl)ethylene) have been prepared by Xie et al.[37] A 2-D assembly of $Cd_{32}S_{14}(SPh)_{36}L_4$ NC was observed with 4,4′-trimethylenedipyridine and 1,2-bis(4-pyridyl)ethane.[36c]

18.5 Amine-protected magic sized nanoclusters

18.5.1 Synthesis and properties

Mass selected magic sized nanoclusters (MSCs) of 12–16 chalcogenides with stoichiometric composition identical to their bulk solids were first reported by Kasuya et al.[38] Prior to this report, formation of CdSe particles of size below 2 nm was observed in Murray's method and its modifications for semiconductor nanoparticle synthesis.[39] Kasuya et al. synthesized $(CdSe)_n$ ($n = 33, 34$) NCs by reverse micelles method wherein a mixture of $CdSO_4$ and sodium nitrilotriacetic acid in water was added to decylamine ($CH_3(CH_2)_9NH_2$) surfactant. Cadmium ions bind with the nitrogen of the surfactant molecule. Aqueous solution of sodium selenosulfate (Na_2SeSO_3), which releases Se^{2-} in alkaline condition, was used as Se^{2-} precursor. Further, toluene was added to this mixture, which results in a reverse micelle wherein the (CdSe)*n* NCs are formed. Nuclearity of the NCs formed were determined using mass spectrometry. Optical absorption spectrum of the cluster solution showed sharp peak at 415 nm along with small

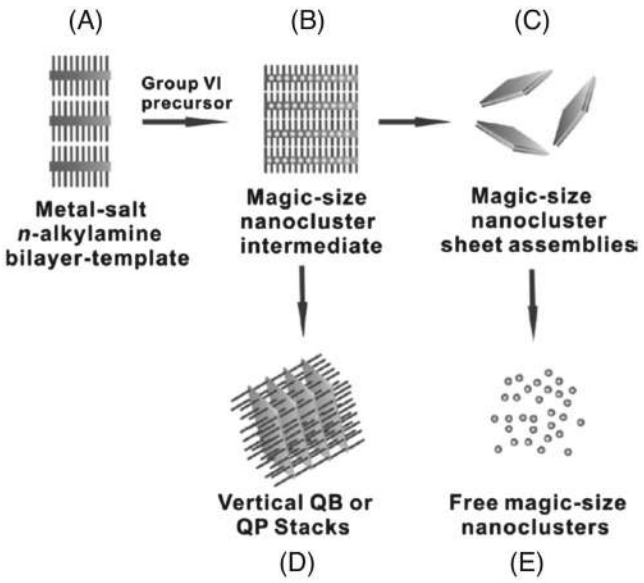

FIGURE 18.9 Schematic representation of the synthesis of magic-sized nanoclusters using bilayer assembly method. Reproduced with permission from ref.[40] Copyright 2015, American Chemical Society.

peaks at 382 nm and 352 nm which is largely blue shifted from the bulk value. This sharp features indicate the formation of specific sized species in the solution. Absorption spectrum was red shifted by keeping the peak at 415 nm when the temperature of the reaction was raised from 45°C to 80°C. This shows the stability of clusters formed even under the conditions favoring cluster growth.

Subsequent work on the synthesis of CdSe nanoribbon, nanoplatelets, nanosheets, and quantum belts demonstrated that MSCs act as an intermediates during their formation.[41] Fig. 18.9 represents the general scheme for the synthesis and separation of MSCs. Isolation of discrete $(CdSe)_{13}$ clusters, the intermediate of CdSe quantum belts was first accomplished by Wang et al.[42] In a typical synthesis, cadmium acetate dihydrate $(Cd(OAc)_2(H_2O)_2)$ was reacted with selenourea (NH_2CSeNH_2) in *n*-octylamine at room temperature and produced $(CdSe)_{13}$ NCs. The mechanism of the reaction is as follows; the combination of CdX_2 (X = halide, acetate) and *n*-octylamine results in a lamellar mesophase, wherein CdX_2 layers are separated by amine bilayers. Addition of selenourea to this mixture gives rise to MSCs. Formation of $(CdSe)_{13}$ was confirmed from the UV–Vis spectrum of this material in toluene with three peaks at 312, 335, and 350 nm (Fig. 18.10A). Absence of absorption peaks at 363, 389, and 413 nm which are assigned for $(CdSe)_{19}$, $(CdSe)_{33}$, and $(CdSe)_{34}$ establishes the purity of $(CdSe)_{13}$ formed.

Synthesis of atomically precise $(CdSe)_{34}$ cluster in gram scale was described by Dolai et al.[43] The cluster showed blue emission with a quantum yield (QY) of 5.7%. Here, the chalcogenide source was prepared by dissolving Se powder in a mixture of hexanethiol (HT) and octylamine (OA) under argon atmosphere. Then the mixture was added to a Cd-OA complex formed by dissolving cadmium acetate $(Cd(OAc)_2{\cdot}2H_2O)$ in OA. The Cd-OA complex was diluted with toluene before the addition of Se precursor. Absorption spectrum of the cluster in toluene exhibited a sharp peak at 418 nm and additional peaks at 353 and 382 nm (Fig. 18.10B). The cluster emitted in the blue region with an emission maxima at 440 nm when excited at 380 nm (Fig. 18.10B). Further, the emission QY was enhanced by surface ligand modification with

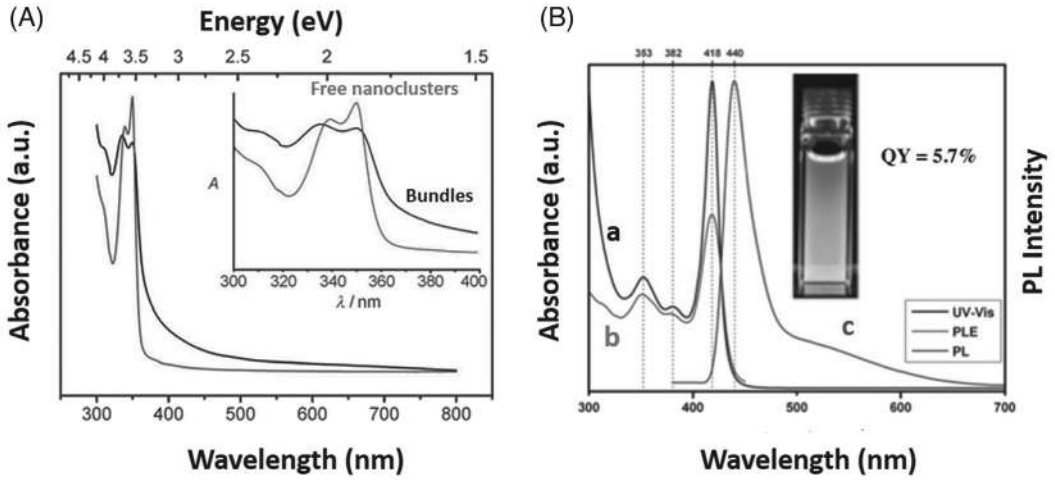

FIGURE 18.10 UV–Vis spectra of $(CdSe)_{13}$(*n*-octylamine)$_{13}$ bundles (black) and free $(CdSe)_{13}$(oleylamine)$_{13}$ NCs (red) (A). Absorption features are expanded in the inset to show the changes in spectral features. UV–Vis absorption (a), excitation (b), and emission (c) spectra of $(CdSe)_{34}$ NC. Inset shows the NC emission under UV light (B). Reproduced from ref.[42] Copyright 2012, Wiley-VCH for (A). Reproduced from ref.[43] Copyright 2014, American Chemical society.

triphenyl phosphine (TPP). QY was increased to 24% after the postsynthetic treatment. The core composition of CdSe NC was confirmed by LDI MS. Following the bilayer assembly method described above (Fig. 18.9) mixed amine-protected NCs such as $(CdSe)_{34}$(*n*-octylamine)$_{18}$(di-*n*-pentylamine)$_2$, $(CdS)_{34}$(*n*-butylamine)$_{18}$, $(ZnS)_{34}$(*n*-butylamine)$_{34}$, $(ZnSe)_{13}$(*n*-butylamine)$_{13}$, $(CdTe)_{13}$(*n*-propylamine)$_{13}$, and $(ZnTe)_{13}$(*n*-butylamine)$_{13}$, etc. were also synthesized.[40]

Properties of NCs can be tuned by metal ion doping or alloying. Yang et al. reported the smallest doped MSC, $Cd_{13-x}Mn_xSe_{13}$ ($x = 1, 2$). The synthesis involves the addition of octylammonium selenocarbamate to the oleylamine solution containing $CdCl_2$ and $MnCl_2$.[44a] Octylammonium selenocarbamate was prepared by bubbling CO gas into selenium powder containing octylamine solution. Before the addition of selenium precursor the metal ion precursor was heated for 2 h at 120°C and cooled down to room temperature. After the addition of selenium precursor, the mixture was kept for 40 h at room temperature for the complete conversion to product NC. Doped NC showed optical absorption features at around 350 nm which is blue shifted from bulk CdSe nanoparticles. The intense emission observed at 600 nm is assigned to the Mn^{2+} ($^4T_1$–$^6A_1$) transition (Fig. 18.11A, C). The undoped $(CdSe)_{13}$ NC emission at 365 nm was not observed in the doped NC. Magnetic circular dichroism (MCD) measurement of the doped NC gave pronounced signals indicating a strong coupling between the charge carriers of the dopants and the host material. Subsequent work of Yang et al. explained the formation of $ZnxCd_{13}$-*x*Se ($x = 0$–13) alloy NC.[44b] The composition of alloy cluster was controlled by changing the ratio of the metal ion precursor. Optical absorption features of these alloys were in between those of $(CdSe)_{13}$ and $(ZnSe)_{13}$ (Fig. 18.11D). Absorption peaks of $(ZnSe)_{13}$ were red shifted with increase in the amount Cd content.

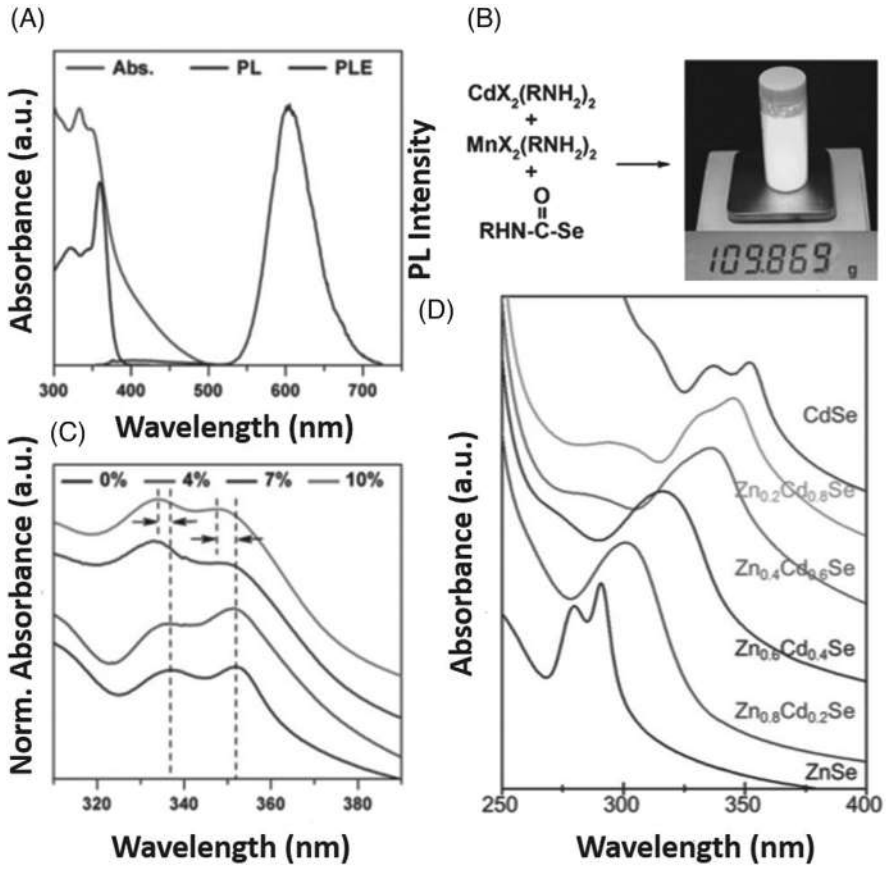

FIGURE 18.11 UV–Vis spectra, excitation spectra, and emission spectra of Mn^{2+} doped $(CdSe)_{13}$ NC (A). Reagents used for the doping reaction and photograph of doped NC under UV light (B). UV–Vis spectra of $(CdSe)_{13}$ cluster with different concentration of Mn^{2+} (C). UV–Vis spectra of Zn*x*Cd_{13}-*x*Se (x = 0–13) alloy NCs synthesized by varying the concentration of metal ions (D). Reproduced with permission from ref.[44] Copyright 2015 and 2017, American Chemical society.

18.5.2 Structure

Resolving the crystal structure of NC is important to understand their properties in detail. In the case of MSCs there are no reports on their single crystal structure. The difficulty in crystal growth is mainly due to the weak bond between the NC and protecting amine ligands. The MSCs reported till date are either protected by amine or phosphane. However, there are theoretical predictions on the structure of MSCs using first principles calculations.[38] First principles calculations showed that (CdSe)*n* has a cage like polyhedron with sp3 like zigzag networks of alternately connected Cd and Se ions forming four- and six-membered rings (highly puckered) structure. This cage is stabilized by filling a core connected to the cage. In order to retain a stable tetrahedral-like 3D network, the choice of highly symmetric cage with

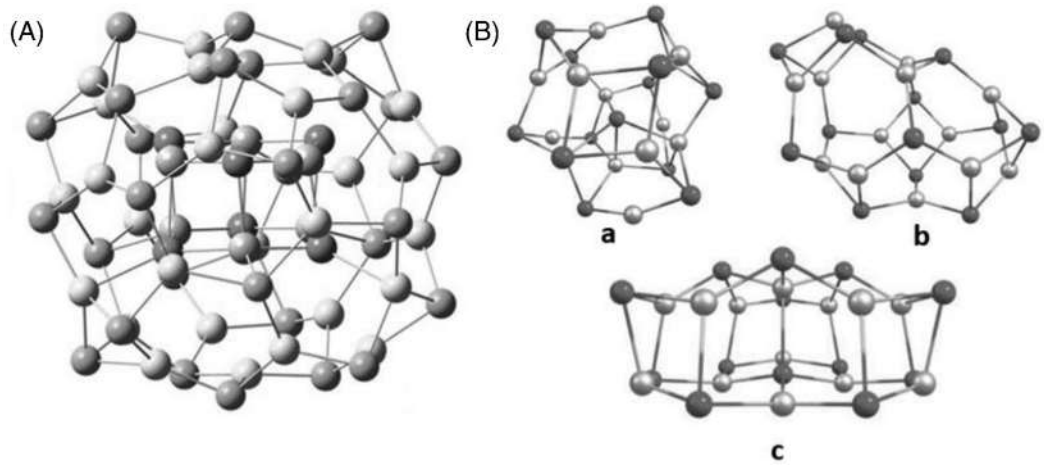

FIGURE 18.12 Optimized structure of $(CdSe)_{34}$ with $(CdSe)_6$ core inside $(CdSe)_{28}$ cage (A). Optimized structure of gas phase isomer of $(CdSe)_{13}$ NCs, (A) $Se@(Cd_{13}Se_{12})$ core@cage isomer, (B) fullerene-like isomer, (C) wurtzite-like isomer (B). Reproduced with permission from refs.[45,46] Copyright 2013 and 2014, The Royal Society of Chemistry.

the right size of core is important. The structure of $(CdSe)_{34}$ is formed by $(CdSe)_6$ core and $(CdSe)_{28}$ cage according to Kasuya et al.[38] The structure of $(CdSe)_{34}$ is shown in Fig. 18.12A.[45] Azpiroz et al. studied the structure of $(CdSe)_{13}$ using DFT calculations and showed that the most stable isomer is core@cage structure $Se@Cd_{13}Se_{12}$ compared to the fullerene like and wurtzite like isomers both in bare and ligand-protected state (Fig. 18.12B).[46] The favorable structure of $(CdSe)_{19}$ was found to be $(CdSe)_1$ core inside a $(CdSe)_{18}$ cage. The core@cage configuration $(CdSe)_3@(CdSe)_{16}$ was unfavorable due to the small inner space available.[38]

18.6 Nanoclusters of Co, Ni, and Mn chalcogenides

The NCs of Co, Ni, and Mn chalcogenides are remarkable because of their redox activity, electrochemical stability, and unique magnetic properties. They fall apart from the above discussed metal chalcogenide NCs.[47] Synthesis and structure determination of these classes of NCs were known since the 1980s. Building structures with these classes of NCs instead of atoms offers the opportunity of new hierarchical solids with collective properties. They gained significant attention as unique building blocks for novel functional materials which find applications in catalysis, energy storage, and sensing. These materials provide a new dimension to atomically precise metal chalcogenide NCs.

18.6.1 Solution-phase synthesis of NCs

The most commonly employed synthetic method for NCs of Co, Ni, and Mn chalcogenide is the solution phase synthesis.[48] This bottom-up approach requires milder conditions, the reaction of a metal ion source with a chalcogenide ion source. This method can be classified

into two. One approach involves the self-assembly of metal cations and chalcogenide anions in the presence of protecting ligands that result in the formation of the NC. The second approach combines a low valent organometallic complex and a functionally low valent chalcogen (typically a phosphine chalcogenide). By tuning the ratio of the reagents, NCs with different core structures can be synthesized. The synthesis of specific examples of Co, Ni, and Mn chalcogenide NCs are discussed below.

$Co_6E_8L_6$ (E = S, Se, Te; L = Ligand)
$Co_6E_8L_6$ is a relevant class of NCs because of a straightforward preparation, scalability, and flexibility to a variety of phosphine ligands, which make it a relevant class of cluster. There are two synthetic approaches for this NC. The first approach uses $E(SiMe_3)_2$ (E = S, Se) as the chalcogen source.[49] Metal chloride complex $CoCl_2(P^nBu_3)_6$ reacts with $E(SiMe_3)_2$ (E = S, Se) in toluene to produce $Co_6E_8L_6$ NC. The second method uses a low-valent organometallic complex $Co_2(CO)_8$ with various phosphine chalcogenides.[50] The trialkylphosphine chalcogenides (R_3PE, E = S, Se, Te) are the stable and soluble source of chalcogen and are milder reagents to handle than H_2E.

$Ni_9Te_8L_6$ (L = Ligand)
High nuclearity nickel selenide and telluride NCs have been synthesized using R_3PE (E = Se, Te) or $E(SiMe_3)_2$ (E = S, Se) as the chalcogen reagent. Nickel sulfide NCs could not be synthesized using R_3PS due to the inherent stability of P=S bond. Reagents like Na_2S were proven to be a good sulfur source. The preparation of $Ni_9Te_8(PEt_3)_8$ involves the reaction of $Ni(COD)_2$ (cyclooctadiene = COD), $TePEt_3$, and PEt_3 in a 2:1:22 molar ratio in heptane.[51] This nickel chalcogenide NC can be considered as the metal filled analogue of $M_6E_8L_6$.

$[MnTe]_n$ (n = 4, 6, 8)
In the case of $[MnTe]_n$ NCs, the choice of metal ion precursor and ligand has a significant role in deciding the structure of the formed NC.[52] The reaction of metal halide phosphane complex with $Te(SiMe^tBu)_2$ resulted in an amorphous insoluble product. Synthesis was successful with the combination of organometallic complex Mn(η^4-butadiene)PMe_3 and $^iPr_3PTe$. The mixture in THF was refluxed with an excess of $PiPr_3$ for 2 h. Crystals of cubane type $Mn_4Te_4(PiPr_3)_4$ was obtained while cooling the mixture to −35°C. Prismane type $Mn_6Te_6L_6$ was formed with less bulky ligand PMe_3. Ligand PEt_3 with intermediate sizes give rise to mixture of cubane and prismane NCs. A dicubane structure, $Mn_8Te_8L_8$, was obtained when *N*-heterocyclic carbine (NHC) was used as protecting ligand.

18.6.2 Structural characterization

The chalcogenide NCs described above are characterized using single crystal XRD. Structural understanding of NCs is vital to correlate their properties as mentioned previously.

18.6.2.1 Cluster core

The common cluster core observed in above mentioned metal chalcogenide NCs is an M_6E_8 octahedron and M_4E_4 cubane (M = metal; E = chalcogen) as shown in Fig. 18.13.[47] Mn chalcogenides also show another core structure, prismane, which is different from the commonly observed ones. In the case of NCs, the cluster core generally determines its electronic, optical,

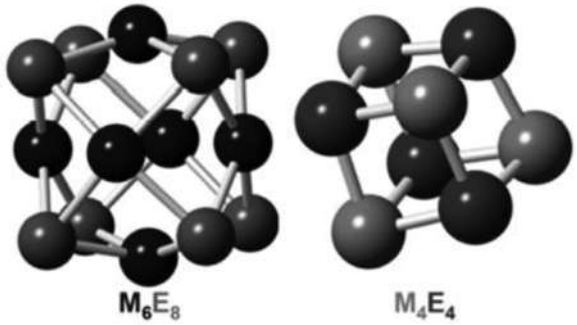

FIGURE 18.13 Structure of commonly observed M_6E_8 and M_4E_4 core. Reproduced with permission from ref.[47] Copyright 2018, American chemical Society.

and magnetic properties. The cluster cores formed by different metal chalcogenide NCs and their structural features will be discussed below.

M_4E_4

NCs of formula M_4E_4 have a cubane structure, which consists of metal and chalcogen on alternate vertices of a cube. This type of core structure is abundant in biological systems such as iron−sulfur proteins. The redox-active Fe_4S_4 core catalyzes a variety of transformations. Mn chalcogenides form NCs of the type $Mn_4Te_4L_4$ with bulky ligands such as L = P^iPr_3 or PCy_3.[52] The structure of Mn_4E_4 NC consists of a tetrahedron of Mn atoms (Fig. 18.14A). Te atoms are arranged on the faces of this tetrahedron, forming another larger tetrahedron. Each Mn atom is bound to four phosphine ligands in a tetrahedral fashion.

M_6E_8

Structurally, the M_6E_8 core comprises an octahedron of metal atoms (M_6) concentric with a cube of face capping chalcogen atoms (E_8).[50, 53] The passivating ligand, generally phosphines, coordinate with each metal atom, to yield $M_6E_8L_6$. Though $Co_6E_8L_6$ (Fig. 18.14B) clusters were known since 1980s, they gained significant relevance as potential building units of novel materials only recently. They exhibit desirable properties such as redox activity, large magnetic moments, and luminescence. These clusters are electron rich and tunable by the modification of the phosphine ligands a property that can be utilized to direct the assembly into a solid state. $Ni_9Te_8L_6$ (Fig. 18.14C) is considered as a metal filled analogue of $M_6E_8L_6$.[51] The cluster core consists of a single central Ni atom surrounded by an octahedron of six Te atoms and a cube of eight Ni atoms. Each exterior Ni atom is capped with a single phosphine ligand. The cluster $Ni_9Te_6(PEt_3)_8$ is electron-donating and have sizable magnetic moments at high temperature which quenches upon cooling.[54]

$Mn_6Te_6L_6$

$Mn_6Te_6L_6$ (Fig. 18.14D) is the first example of a neutral prismane cluster.[52] The cylindrical prismane core of the NC is formed by two face sharing hexagonal Mn_3Te_3 puckered rings. The Mn and Te atoms are situated at alternating vertices with each Mn atom coordinated to one ligand.

18.6.2.2 Ligand shell

The NC core is passivated by a ligand shell that provides both stability and solubility. The size of the capping ligand controls the structure of the inorganic core in case of Mn–Te

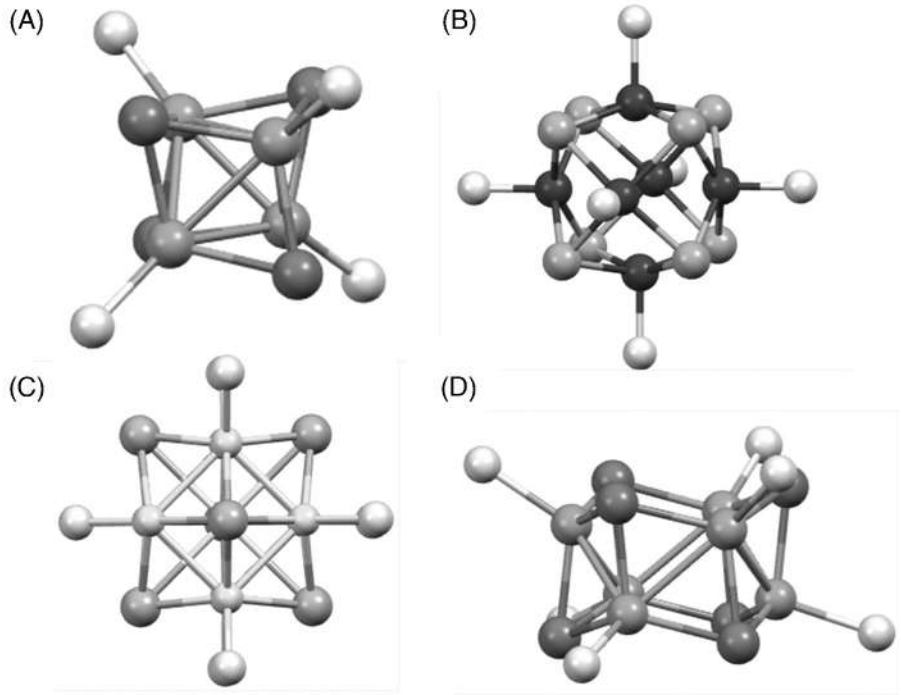

FIGURE 18.14 Structure of $Mn_4Te_4L_4$ (A), $Co_6E_8L_6$ (E = S, Se, Te) (B), $Ni_9Te_8L_8$ (C), and $Mn_6Te_6L_6$ (D) (L = ligand). Mn: ●, Co: ●, Ni: ●, Te: ●, Te: ●, L: ●. Adapted with permission from refs.[52–54] Copyright 1991, 2014 and 2015, American Chemical Society.

nanocluster. Ligand plays a significant role in controlling the communication between neighboring clusters. They assist in the self-assembly of NCs into hierarchical solids. Decorating the cluster core with ligands containing various functional group can find applications in electronic, thermal, and magnetic studies. The properties of materials formed by the assembly of NC units can be modified by exchanging their ligands.[47,48]

The synthesis and crystal structure of this class of NCs were known long back from the work of Fenske, Steigerwald, and others.[49,50] The application of these NCs as building blocks of superatomic crystals (SAC) is a recent development. The following section discusses some examples of SAC and their properties.

18.6.3 Assembly of NCs into hierarchical solids

Superatomic solids are three-dimensional periodic arrays of NCs which are independently prepared. Until recently, the use of NCs as building blocks to create hierarchical solids was dormant. The careful selection of chalcogenide NC is a powerful strategy for the bottom up creation of hierarchical solids with tailored chemical and physical properties. The resulting assembly is stabilized by electrostatic interactions. There are several approaches to obtain

superatomic solids, of which we will be mainly focusing on (1) charge transfer (2) molecular recognition.[47,48,55]

18.6.3.1 Charge transfer

The straightforward approach for creating superatomic solids is via charge transfer between neutral NCs.[47,48] The driving force for the coassembly and crystallization is the intercluster electrostatic attraction between NCs. The electron rich metal chalcogenide NCs combine with structurally and electronically complementary electron-accepting NCs in solution to form binary solids (Fig. 18.15). There occurs an electron transfer between these electrically neutral NCs in solutions with no alteration in the internal structure of the constituent NC. Various superatomic solids can be designed by simple alteration of ligands. The resulting solid state compound can be characterized by single crystal XRD. These superatomic solids are structurally analogous to ionic compounds like NaCl, CsCl, and CdI_2.

Fig. 18.15 shows a library of superatomic solids that can be formed via charge transfer interactions between electron-donating and electron-accepting NCs. The superatomic solid $[Co_6Te_8(PEt_3)_6][Fe_8O_4pz_{12}Cl_4]$ is formed when the electron-donating $Co_6Te_8(PEt_3)_6$ and electron-accepting $Fe_8O_4pz_{12}Cl_4$ is combined in solution.[55a] SCXRD reveals that its structure is analogue to that of CsCl. Fullerenes (C_{60}, C_{70}) are another kind of electron-accepting cluster which can be used for assembly formation. Fullerenes have the ability to mediate electronic coupling by accepting electrons than the $Fe_8O_4pz_{12}Cl_4$. Roy et al. have taken advantage of this property of C_{60} to create SACs $[Cr_6Te_8(PEt_3)_6][C_{60}]_2$, $[Co_6Se_8(PEt_3)_6][C_{60}]_2$, and $[Ni_9Te_6(PEt_3)_8][C_{60}]$.[55b] $[Co_6Se_8(PEt_3)_6][C_{60}]_2$ and $[Ni_9Te_6(PEt_3)_8][C_{60}]$ are structurally analogous to ionic compounds CdI_2 and NaCl, respectively.

18.6.3.2 Molecular recognition

Molecular recognition is an effective method for the synthesis of organized hierarchical solids.[47,48] Apart from simple charge transfer, the synthetic flexibility of NCs can be utilized for guiding assembly formation. The noncovalent interactions of these building block act as the driving force for the assembly. The use of building blocks, that is, NC with preorganized nanostructures can direct the assembly into superatomic solids. The ligands used in the cluster synthesis are highly tunable and molecular recognition moieties can be incorporated to direct the assembly into desired solids. Choi et al. reported that $Co_6Se_8(PEt_2phen)_6$ forms hierarchical solids with C_{60}.[55c] The molecular cluster acts as structure director, diethyl(9-ethynylphenanthrene)phosphine (PEt_2phen) in the ligand sphere provides only weak van der Waals interactions with C_{60}. The ligands on the cluster core undergo reorganization to thermodynamically stable unit that is complementary to C_{60} resulting in the formation of van der Waals solids such as $[Co_6Se_8(PEt_2phen)_6][C_{60}]_5$.

18.6.4 Collective properties

The cluster assembled solids formed by the assembly of NCs exhibit exciting properties such as electronic transport, thermal transport, and magnetic ordering owing to their atomic precision. These properties can be tuned by judicious choice of NC as the building block. The electrical resistivity measurements were carried out on hierarchical solids of $[Cr_6Te_8(PEt_3)_6][C_{60}]_2$ and $[Co_6Se_8(PEt_3)_6][C_{60}]_2$ to determine their electronic properties.[55b]

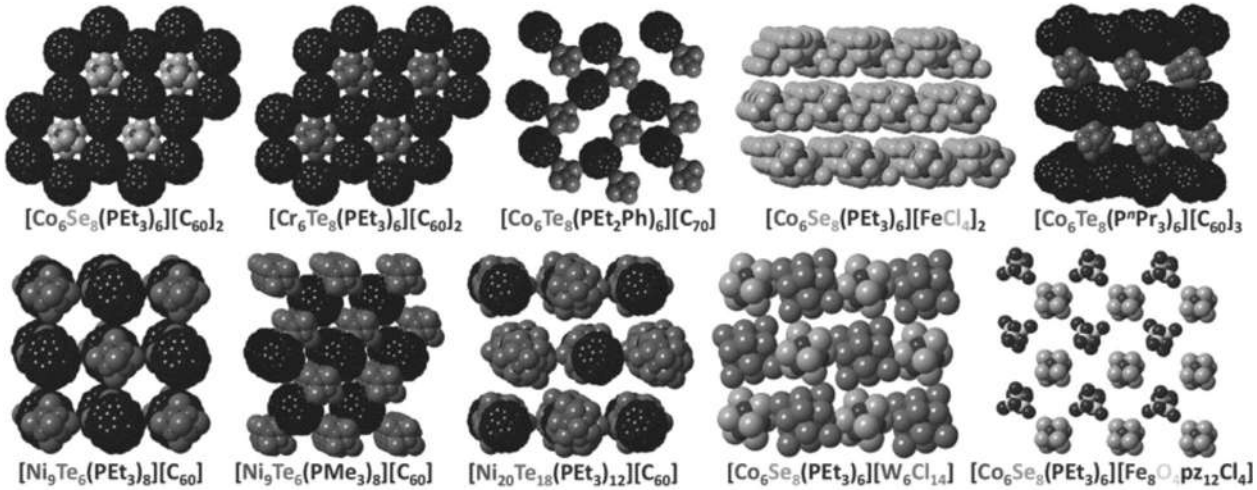

FIGURE 18.15 Superatomic crystals formed by the combination of electron rich nanoclusters and electron accepting clusters. Reproduced with permission from ref.[47] Copyright 2018, American Chemical Society.

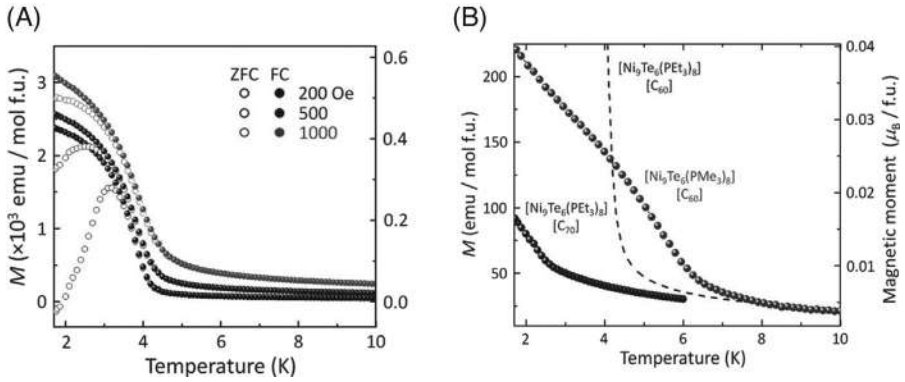

FIGURE 18.16 Temperature ZFC and FC magnetic ordering of SAC $[Ni_9Te_6(PEt_3)_8][C_{60}]$ in different magnetic fields applied (A). Comparison of magnetization temperature of $[Ni_9Te_6(PEt_3)_8][C_{60}]$, $[Ni_9Te_6(PEt_3)_8][C_{70}]$, and $[Ni_9Te_6(PMe_3)_8][C_{60}]$ (B). Reproduced with permission from ref.[54] Copyright 2014, American Chemical Society.

This study showed that these materials exhibit active electronic transport with activation energies of 100–150 meV. The superatomic solids contain various intra and inter NC interaction which can lead to unpredicted thermal transport properties. For example, the SAC $[Co_6Se_8(PEt_3)_6][C_{60}]$ exhibits surprising thermal transport property at nearly 200 K due to the transition from amorphous to crystalline state. In these superatomic solids, the localized spin centers interact resulting in long range cooperative magnetic properties such as ferromagnetism and antiferromagnetism. The bulk magnetically ordered phases are generally not seen even though nanoclusters possess large magnetic moment because of their weak interactions. Superconducting quantum interference device (SQUID) and muon-spin relaxation measurements on SAC $[Ni_9Te_6(PEt_3)_8][C_{60}]$ confirmed the ferromagnetic ground state at low temperature (below 4 K).[54] The temperature dependence of zero field cooled (ZFC) and field cooled (FC) magnetizations of $[Ni_9Te_6(PEt_3)_8][C_{60}]$ is given in Fig. 18.16A. In contrast, the analogues $[Ni_9Te_6(PEt_3)_8][C_{70}]$ and $[Ni_9Te_6(PMe_3)_8][C_{60}]$ display lower and higher magnetic ordering temperature, respectively (Fig. 18.16B).

18.7 Understanding of chalcogenide NCs through mass spectrometry

Mass spectrometry (MS) has evolved as an essential analytical tool for understanding NCs.[56] Ionization techniques such as electrospray ionization (ESI) and matrix-assisted laser desorption ionization (MALDI) have been used extensively to understand the bare, and monolayer-protected clusters in gas phase. Advancements in mass spectrometry enabled detailed understanding of clusters using MS/MS studies, ion mobility separation, etc. Details of the ionization methods and instrumentation are described in Chapter 10. This section discusses the use of MS to understand the chalcogenide NCs.

MS of chalcogenide clusters is less explored comparison to the case of metal NCs. Some of the issues are the reduced solubility of the reported clusters, less stability under the MS conditions, formation of neutral NC species etc. Fenske et al. measured the MALDI MS

spectrum of the $Ag_{344}S_{124}(S^tBu)_{96}$ NC synthesized using silylated reagent.[10] The spectrum showed a series of peaks with peak maxima at m/z 49,446, 93,104, 135,586, 176,572, and 216,487 (Fig. 18.17A). The peak at m/z 49,446 was in good agreement with the molecular weight of the cluster (49,645 kDa). Other peaks observed in the mass spectra were assigned to the aggregation of the NCs in the gas phase. The difference between the individual peak maxima is approximately 41.5 kDa and this mass can be assigned to $Ag_{344}S_{124}^+$. The NC $Ag_{344}S_{124}(S^tBu)_{96}$ can lose S^tBu ligands under the conditions of MS and gives rise to $Ag_{344}S_{124}^+$ fragments. The matrix used in this case was nitroanthracene. MALDI MS spectrum of the largest silver sulfide cluster, $Ag_{490}S_{188}(S^tC_5H_{11})_{114}$ was analyzed using 2-hydroxy benzoic acid by Anson et al.[11] Mass spectrum of this NC also shows cluster fragment aggregation in the gas phase. $Cu_{136}S_{56}(SCH_2C_4H_3O)_{24}(dpppt)_{10}$ also shows similar behavior.

Choice of the matrix is important to acquire a good MALDI mass spectrum. In 2008, Dass et al. introduced a new matrix, trans-2-[3-(4-tert-butylphenyl)-2-methyl-propenylidine] malononitrile (DCTB) for NC.[57] The use of DCTB reduced fragmentation of NC compared to many other matrices in the case of gold and silver NCs. Manju et al. reported the MS of chalcogenide NCs without any ligand desorption using DCTB matrix.[23a] Growth of silver sulfide NCs at various temperatures (60°C, 70°C, 80°C, and 90°C) were studied using MALDI MS. The clusters synthesized at 60°C and 70°C showed two peaks in the MALDI MS spectrum. TLC separation of the NC and the MALDI MS measurements of the separated bands proved that these two peaks were not due to cluster aggregation in the gas phase and was because of multiple NC population.

LDI MS has been employed extensively for the assignment of the nuclearity of MSCs when crystal structures are not available. Mass spectrum of stoichiometric MSCs was first reported by Kasuya et al. in 2004.[38] Mass spectrum of the NCs formed showed prominent peaks for clusters with nuclearities (n) 13, 33, and 34. MS measurements at higher laser power showed increased intensity of NCs of $n < 33$, indicating that the $n = 33, 34$ are mainly formed in solution and the smaller NCs may be formed by the fragmentation of larger clusters. The stability of these clusters with specific nuclearities was also confirmed by the laser ablation of bulk crystalline samples of CdSe, CdS, and ZnS. The predominant species formed in this case were of $n = 13$, 33, and 34.

Wang et al. confirmed the formation of isolated $(CdSe)_{13}$(n-octylamine)$_{13}$ NC using LDI MS.[42] The base peak at m/z 2488.57 in the LDI MS spectrum was assigned to $(CdSe)_{13}$ (Fig. 18.17B). This also indicates that the ligand n-octylamine is desorbed under the MS conditions. Mass spectrum also showed peaks which attributed to $(CdSe)_{19}$, $(CdSe)_{33}$, and $(CdSe)_{34}$. One possible reason for this is the gas phase growth of $(CdSe)_{13}$ into larger ones. Exclusive formation of $(CdSe)_{34}$ was shown by Dolai et al.[43] They observed an intense peak at m/z 6506.5 which is in good agreement with the calculated mass of $(CdSe)_{34}$ (Fig. 18.17C). The peaks in the lower mas range corresponding to $(CdSe)_{33}$ and $(CdSe)_{19}$ were also present in the mass spectrum. LDI MS measurements at different laser power demonstrated that smaller NCs are formed due to the fragmentation of $(CdSe)_{34}$. In this case cluster growth was not observed. Mono and di doping of Mn^{2+} into $(CdSe)_{13}$ (Fig. 18.17D) and formation of ZnxCd_{13}-xSe ($x = 0$–13) alloy NC was described by Yang et al. using LDI MS.[44]

Lover et al. studied the fragmentation, metal and chalcogen exchange, and ligand exchange of tetrahedral NCs of cadmium and zinc.[58] Thiophenol capped tetrahedral NCs like

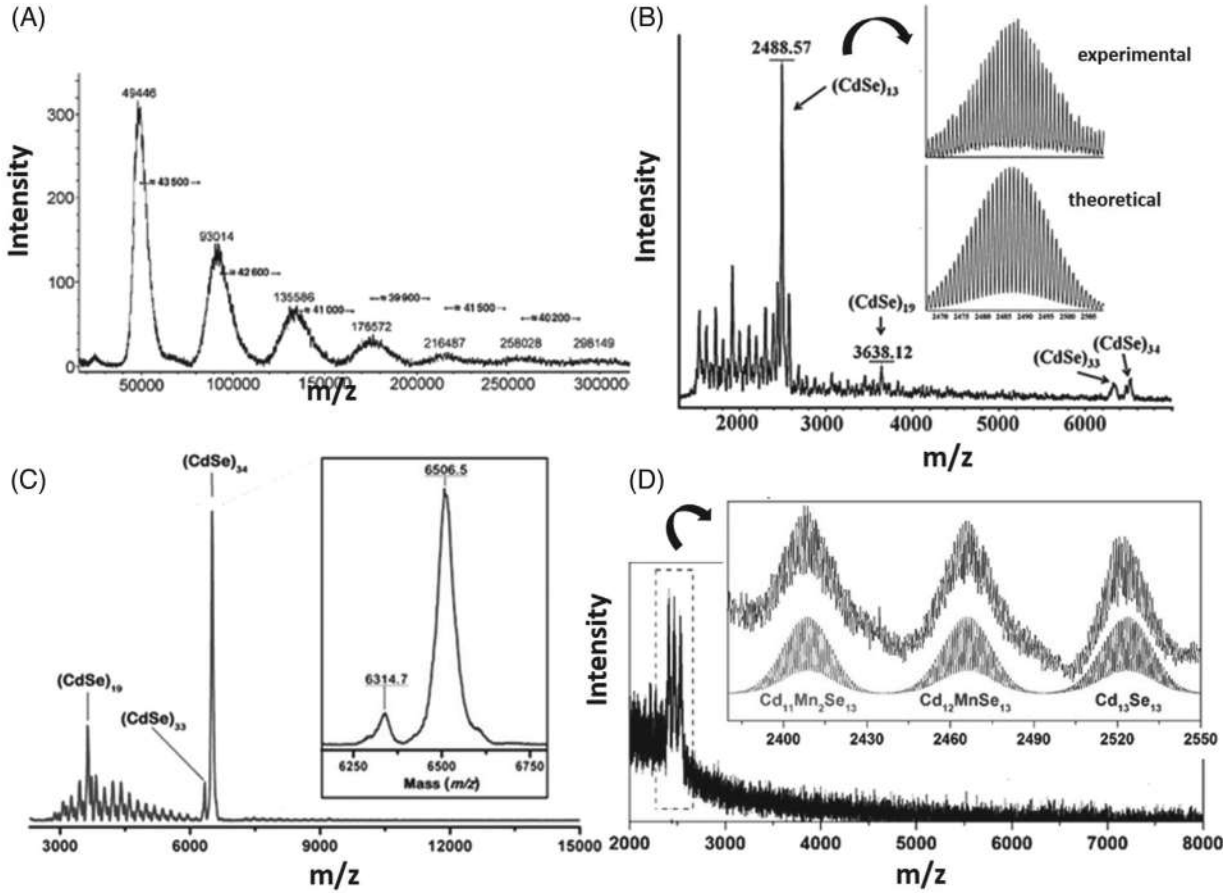

FIGURE 18.17 MALDI TOF spectrum of $Ag_{344}S_{124}(S^tBu)_{96}$ (A), LDI MS spectrum of $(CdSe)_{13}$(n-octylamine)$_{13}$ peak at m/z 2488.27 is expanded and compared with isotopic pattern in the inset (B). LDI MS spectrum of $(CdSe)_{34}$. Peak at m/z 6506.5 is expanded in inset (C). LDI MS spectrum of doped $(CdSe)_{13}$. Mono and di Mn-doped peaks are expanded and compared with isotopic pattern in the inset (D). Reproduced with permission from refs.[10,42] Copyright 2005 and 2012, Wiley-VCH for (A) and (B). Reproduced with permission from refs.[43,44] Copyright 2014 and 2015, American Chemical Society.

$Cd_{10}S_4(SPh)_{16}^{4-}$, $Cd_{10}Se_4(SPh)_{16}^{4-}$, $Zn_{10}S_4(SPh)_{16}^{4-}$, and $Cd_{17}S_4(SPh)_{28}^{2-}$ were used in this study. The NCs $M_{10}E_4(SPh)_{16}^{4-}$ (M = Cd, Zn E = S, Se) and $Cd_{17}S_4(SPh)_{28}^{2-}$ dissociates by the loss of $M(SPh)_3^-$ in the first step. $M_{10}E_4(SPh)_{16}^{4-}$ (M = Cd, Zn E = S, Se) NCs show similar fragmentation pattern (Fig. 18.18A). At higher cone voltage (20 V), the $M(SPh)_3^-$ ions are dominant. Intact molecular ions were observed at lower cone voltage (5 V). Peaks corresponding to the $^+NMe_4$ (counter ions) adducts were also observed in the mass spectrum. In the case of $Cd_{17}S_4(SPh)_{28}^{2-}$ the dominant species was intact molecular ion observed at m/z 2548 (Fig. 18.18B). Singly charged ions are formed at higher cone voltages by the loss of neutral $M(SPh)_2$ groups. This results in almost complete removal of ligands. Fragmentation of $(EM)_n$ core occurs only at higher voltages. It was also observed that the cadmium chalcogenide clusters were more resistant to fragmentation compared to the zinc analogues.

Gaumet et al. used ESI MS and ESI MS/MS to analyze $Cd_{32}S_{14}(SPh)_{36}$ DMF_4.[60] The parent ion was absent in the mass spectra as the cluster was neutral (molecular mass 8268.6). A pseudo parent ion was observed at m/z 2830.5. This peak was assigned to a composition $[Cd_{32}S_{14}(SPh)_{36}$ DMF+ DMF_3-$3H^+]^-$. Other peaks observed in the mass spectrum belong to three categories: (i) $[Cd_n(SPh)_{2n+1}]^-$, where n = 1–3, (ii) $Cd_{17}S_4(SPh)_{28}^{2-}$, and (iii) $[Cd_nS_4(SPh)_{2n-7}]^{2-}$ where n is between 16 and 11. MS/MS studies on the pseudo parent ion showed that the NC fragments into $Cd_{17}S_4(SPh)_{28}^{2-}$ along the lattice planes. ESI FT ICR MS spectrum of a neutral NC $Cd_{32}Se_{14}(SPh)_{36}L_4$ was measured after ligand exchange with various anionic ligands.

Recently, Ranjbar et al. studied the atom-by-atom substitution of Ni and Fe into $[Co_6S_8(PEt_3)_6]^+$ NC using ESI MS.[59] Ni gave mono substituted product in contrast to Fe which resulted in multisubstitution up to six atoms into the core Co_6S_8. ESI MS spectrum of parent cluster, $[Co_6S_8(PEt_3)_6]^+$ showed a strong peak at m/z 1317.922 due to singly charged NC and a small peak at m/z 658.484 due to doubly charged ion. Upon Ni substitution, a new peak was observed at m/z 1316.929 which was assigned to the formula, $[Co_5NiS_8(PEt_3)_6]^+$ (Fig. 18.18C). In the case of Fe doping, singly charged species were observed for 1–3 atom substitution and doubly charged species for more than three atom doping (Fig. 18.18D).

18.8 Summary and future perspectives

Metal chalcogenide NCs exhibit promising optical, electrical, thermal, and magnetic properties. It fueled an explosion of research interest on these NCs. This chapter presented a more profound understanding about their solution phase synthesis, structure, and properties. The solid state materials synthesized using the NC building blocks opened new avenues. Such materials exhibit photoelectric properties, unusual electric transport, and magnetic ordering, making them potential materials for applications. Mass spectrometry served as an indispensable tool in understanding the composition of atomically precise chalcogenide NCs, especially of amine-protected MSCs, for which no crystal structure is available. Looking forward, judicious design and tuning of amine ligand of MSCs may help to develop better crystallization strategies. This helps in achieving the structure–property relationship. Substantial development has happened in the area of hydrid structures composed of metal chalcogenide NCs. Designing new materials with novel collective properties and understanding their structure property relationship opens up new horizons.

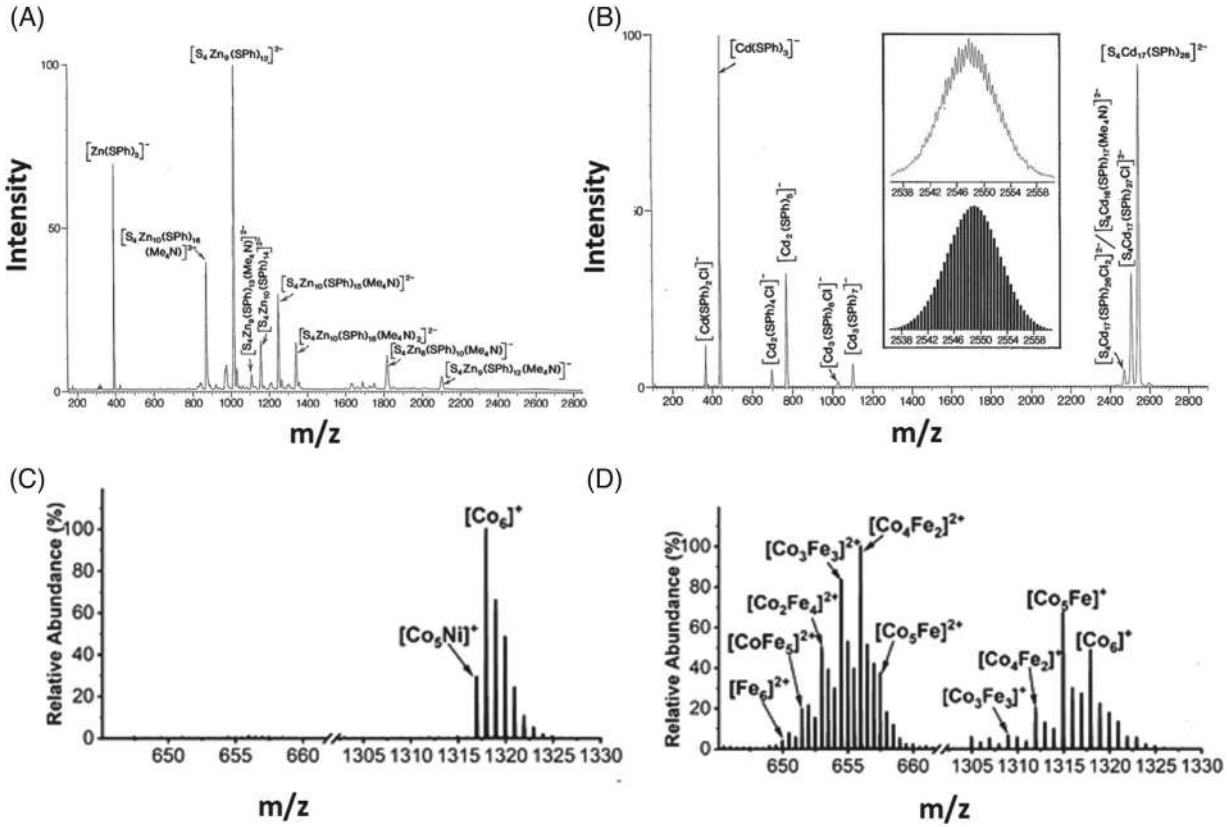

FIGURE 18.18 ESI MS spectrum of $Zn_{10}S_4(SPh)_{16}{}^{4-}$ at a cone voltage of 20 V (A) and $Cd_{17}S_4(SPh)_{26}{}^{2-}$ at a cone voltage of 90V (B). ESI MS spectrum of Ni (C) and Fe (D) doped $[Co_6S_8(PEt_3)_6]^+$ NC. Reproduced with permission from ref.[58] Copyright 1997, American Chemical Society. Reproduced with permission from ref.[59] Copyright 2020, Wiley-VCH.

List of abbreviation

BPy	4,4′-bipyridine
DCTB	trans-2-[3-(4-tert-butylphenyl)-2-methyl-propenylidine] malononitrile
DFT	density functional theory
dppb	1,4-bis(diphenylphosphino)butane
dpph	1,6-(diphenylphosphino)hexane
dppm	bis(diphenylphosphanyl)methane
dppp	1,3-bis(diphenylphosphino)propane
Dpppt	1,5-bis(diphenylphosphino)pentane
ESI FT ICR MS	electrospray ionization Fourier transform ion cyclotron resonance mass spectrometry
ESI MS	electrospray ionization mass spectrometry
FC	field cooled
LDI MS	laser desorption/ionization mass spectrometry
LMCT	ligand to metal charge transfer
MALDI MS	matrix assisted laser desorption ionization mass spectrometer
MOF	metal–organic frameworks
MSCs	magic sized nanoclusters
NC	nanoclusters
PEt_2phen	diethyl(9-ethynylphenanthrene)phosphine
P-XRD	powder X-ray diffraction
QY	quantum yield
SAC	superatomic crystals
SQUID	Superconducting quantum interference device
TMDPy	4,4′-trimethylenedipyridine
UV/Vis	ultraviolet−visible spectroscopy
XRD	X-ray diffraction
ZFC	zero field cooled

References

1. (a) Corrigan JF, Fuhr O, Fenske D. Metal chalcogenide clusters on the border between molecules and materials. *Adv Mater*. 2009;21:1867–1871; (b) Fuhr O, Dehnen S, Fenske D. Chalcogenide clusters of copper and silver from silylated chalcogenide sources. *Chem Soc Rev*. 2013;42:1871–1906.
2. Soloviev VN, Eichhöfer A, Fenske D, Banin U. Size-dependent optical spectroscopy of a homologous series of CdSe cluster molecules. *J Am Chem Soc*. 2001;123:2354–2364.
3. Dehnen S, Fenske D. $[Cu_{24}S_{12}(PMeiPr_2)_{12}]$, $[Cu_{28}S_{14}(PtBu_2Me)_{12}]$, $[Cu_{50}S_{25}(PtBu_2Me)_{16}]$, $[Cu_{70}Se_{35}(PtBu_2Me)_{21}]$, $[Cu_{31}Se_{15}(SeSiMe_3)(PtBu_2Me)_{12}]$ and $[Cu_{48}Se_{24}(PMe_2Ph)_{20}]$: new sulfur- and selenium-bridged copper clusters. *Chem – Eur J*. 1996;2:1407–1416.
4. (a) Dehnen S, Fenske D, Deveson AC. $[Cu_{12}S_6(PnPr_3)_8]$ and $[Cu_{20}S_{10}(PnBu_1Bu_2)_8]$: two sulfur bridged copper clusters with Cu-s cluster cores of known compositions but new structures. *J Cluster Sci*. 1996;7:351–369; (b) Dehnen S, Schäfer A, Fenske D, Ahlrichs R. New sulfur- and selenium-bridged copper clusters, ab initio calculations on $[Cu_2nSen(PH_3)m]$ clusters. *Angew Chem Int Ed Engl*. 1994;33:746–749.
5. Dehnen S, Eichhöfer A, Fenske D. Chalcogen-bridged copper clusters. *Inorg Chem.Eur J Inorg Chem*. 2002;2002:279–317.
6. Zhu N, Fenske D. Novel Cu–Se clusters with Se–layer structures: $[Cu_{32}Se_7(SenBu)_{18}(PiPr_3)_6]$, $[Cu_{50}Se_{20}(SetBu)_{10}(PiPr_3)_{10}]$, $[Cu_{73}Se_{35}(SePh)_3(PiPr_3)_{21}]$, $[Cu_{140}Se_{70}(PEt_3)_{34}]$ and $[Cu_{140}Se_{70}(PEt_3)_{36}]$. *J Chem Soc Dalt Trans*. 1999;7:1067–1076.
7. Wang X-J, Langetepe T, Persau C, Kang B-S, Sheldrick GM, Fenske D. Syntheses and crystal structures of the new Ag–S clusters $[Ag_{70}S_{16}(SPh)_{34}(PhCO_2)_4(triphos)_4]$ and $[Ag_{188}S_{94}(PR_3)_{30}]$. *Angew Chem Int Ed*. 2002;41:3818–3822.
8. Fenske D, Persau C, Dehnen S, Anson CE. Syntheses and crystal structures of the Ag–S cluster compounds $[Ag_{70}S_{20}(SPh)_{28}(dppm)_{10}]$ $(CF_3CO_2)_2$ and $[Ag_{262}S_{100}(StBu)_{62}(dppb)_6]$. *Angew Chem Int Ed*. 2004;43:305–309.

9. Chitsaz S, Fenske D, Fuhr O. Silver chalcogenide clusters with dimethylanilinomercapto ligands: syntheses and crystal structures of $[Ag_{65}S_{13}(SC_6H_4NMe_2)_{39}(dppm)_5]$, $[Ag_{76}Se_{13}(SC_6H_4NMe_2)_{50}(PPh_3)_{6.5}]$, and $[Ag_{88}Se_{12}(SC_6H_4NMe_2)_{63}(PPh_3)_6]$. *Angew Chem Int Ed*. 2006;45:8055–8059.
10. Fenske D, Anson CE, Eichhöfer A, et al. Syntheses and crystal structures of $[Ag_{123}S_{35}(StBu)_{50}]$ and $[Ag_{344}S_{124}(StBu)_{96}]$. *Angew Chem Int Ed*. 2005;44:5242–5246.
11. Anson CE, Eichhöfer A, Issac I, et al. Synthesis and crystal structures of the ligand-stabilized silver chalcogenide clusters $[Ag_{154}Se_{77}(dppxy)_{18}]$, $[Ag_{320}(StBu)_{60}S_{130}(dppp)_{12}]$, $[Ag_{352}S_{128}(StC_5H_{11})_{96}]$, and $[Ag_{490}S_{188}(StC_5H_{11})_{114}]$. *Angew Chem Int Ed*. 2008;47:1326–1331.
12. Bestgen S, Fuhr O, Breitung B, et al. $[Ag_{115}S_{34}(SCH_2C_6H_4tBu)_{47}(dpph)_6]$: synthesis, crystal structure and NMR investigations of a soluble silver chalcogenide nanocluster. *Chem Sci*. 2017;8:2235–2240.
13. Nayek HP, Massa W, Dehnen S. Presence or absence of a central Se atom in silver selenide/selenolate clusters with halite topology: syntheses and properties of $[(Ph_3PAg)_8Ag_6(\mu 6\text{-}Se)1-x/2(SePh)_{12}]x+$ (x = 0, 1). *Inorg Chem*. 2010;49:144–149.
14. Fenske D, Langetepe T. Synthesis and structures of silver–selenide cluster complexes $[Ag_4(SeiPr)_4(dppm)_2]$, $[Ag_8(SeEt)_8(dppp)]\infty$, $[Ag_{28}Se_6(SenBu)_{16}(dppp)_4]$, and $[Ag_{124}Se_{57}(SePtBu_2)_4Cl_6(tBu_2P(CH_2)_3PtBu_2)_{12}]$. *Angew Chem Int Ed*. 2002;41:300–304.
15. Fenske D, Zhu N, Langetepe T. Synthesis and structure of new Ag−Se clusters: $[Ag_{30}Se_8(SetBu)_{14}(PnPr_3)_8]$, $[Ag_{90}Se_{38}$ $(SetBu)_{14}(PEt_3)_{22}]$, $[Ag_{114}Se_{34}(SenBu)_{46}(PtBu_3)_{14}]$, $[Ag_{112}Se_{32}(SenBu)_{48}(PtBu_3)_{12}]$, and $[Ag_{172}Se_{40}$ $(SenBu)_{92}(dppp)_4]$. *Angew Chem Int Ed*. 1998;37:2639–2644.
16. Corrigan JF, Fenske D. Butyltellurolate ligands in cluster synthesis: molecular structure of Ag_6Te_6, $Ag_{32}Te_{25}$ and $Ag_{48}Te_{36}$ complexes. *Chem Commun*. 1996;8:943–944.
17. Corrigan FJ. Mono- and bis-silylated tellurium reagents in silver–telluride cluster synthesis: characterisation of $Ag_{30}Te_{21}$ and $Ag_{46}Te_{29}$ complexes. *Chem Commun*. 1997;19:1837–1838.
18. Jin X, Tang K, Liu W, et al. Formation and X-ray structure of a novel tetradecanuclear silver cluster complex, $Ag_{14}(\mu_6\text{-}S)(SPh)_{12}(PPh_3)_8 \cdot {}_4CH_3OH \cdot {}_{13}H_2O$. *Polyhedron*. 1996;15:1207–1211.
19. Tang K, Xie X, Zhang Y, Zhao X, Jin X. Synthesis and crystal structure of a novel pentaconta-nuclear silver anionic cluster complex $[HNEt_3]_4[Ag_{50}S_7(SC_6H_4But\text{-}4)_{40}]\cdot 2CS_2\cdot 6C_3H_6O$. *Chem Commun*. 2002;10:1024–1025.
20. Li B, Huang R-W, Qin J-H, et al. Thermochromic luminescent nest-like silver thiolate cluster. *Chem – Eur J*. 2014;20:12416–12420.
21. (a) Li G, Lei Z, Wang Q-M. Luminescent molecular Ag−S nanocluster $[Ag_{62}S_{13}(SBut)_{32}](BF_4)_4$. *J Am Chem Soc*. 2010;132:17678–17679; (b) Jin S, Wang S, Song Y, et al. Crystal structure and optical properties of the $[Ag_{62}S_{12}(SBut)_{32}]^{2+}$ nanocluster with a complete face-centered cubic kernel. *J Am Chem Soc*. 2014;136:15559–15565.
22. Nan Z-A, Xiao Y, Liu X-Y, et al. Monitoring the growth of Ag–S clusters through crystallization of intermediate clusters. *Chem Commun*. 2019;55:6771–6774.
23. (a) Manju CK, Mohanty JS, Sarkar D, Chennu S, Pradeep T. Towards atomically precise luminescent Ag_2S clusters separable by thin layer chromatography. *J Mater Chem C*. 2018;6:5754–5759; (b) Manju CK, Chakraborty I, Pradeep T. Highly luminescent monolayer protected $Ag_{56}Se_{13}S_{15}$ clusters. *J Mater Chem C*. 2016;4:5572–5577.
24. (a) Fu M-L, Issac I, Fenske D, Fuhr O. Metal-rich copper chalcogenide clusters at the border between molecule and bulk phase: the structures of $[Cu_{93}Se_{42}(SeC_6H_4SMe)_9(PPh_3)_{18}]$, $[Cu_{96}Se_{45}(SeC_6H_4SMe)_6(PPh_3)_{18}]$, and $[Cu_{136}S_{56}(SCH_2C_4H_3O)_{24}(dpppt)_{10}]$. *Angew Chem Int Ed*. 2010;49:6899–6903; (b) Dehnen S, Fenske D. $[Cu_{44}Se_{22}(PEt_2Ph)_{18}]$ and $[Cu_{44}Se_{22}(PnButBu_2)_{12}]$: synthesis and structure of two copper clusters with isomeric Cu–Se frameworks. *Angew Chem Int Ed Engl*. 1994;33:2287–2289.
25. Corrigan JF, Balter S, Fenske D. Synthesis and structural characterisation of new copper–tellurium clusters: $TeBun(SiMe_3)$ as a source of RTe- and Te_2- ligands. *J Chem Soc Dalt Trans*. 1996;5:729–738.
26. (a) Chakraborty I, Pradeep T. Atomically precise clusters of noble metals: emerging link between atoms and nanoparticles. *Chem Rev*. 2017;117:8208–8271; (b) Jin R, Zeng C, Zhou M, Chen Y. Atomically precise colloidal metal nanoclusters and nanoparticles: fundamentals and opportunities. *Chem Rev*. 2016;116:10346–10413; (c) Kang X, Zhu M. Tailoring the photoluminescence of atomically precise nanoclusters. *Chem Soc Rev*. 2019;48:2422–2457.
27. (a) Vaqueiro P. Hybrid materials through linkage of chalcogenide tetrahedral clusters. *Dalt Trans*. 2010;39:5965–5972; (b) Feng P, Bu X, Zheng N. The interface chemistry between chalcogenide clusters and open framework chalcogenides. *Acc Chem Res*. 2005;38:293–303.
28. Dance IG, Choy A, Scudder ML. Syntheses, properties, and molecular and crystal structures of

$(Me_4N)_4[E_4M_{10}(SPh)_{16}]$ (E = sulfur or selenium, M = zinc or cadmium): molecular supertetrahedral fragments of the cubic metal chalcogenide lattice. *J Am Chem Soc*. 1984;106:6285–6295.
29. Lee GSH, Craig DC, Ma I, Scudder ML, Bailey TD, Dance IG. $[S_4Cd_{17}(SPh)_{28}]_{2-}$, the first member of a third series of tetrahedral [SWMX(SR)y]z- clusters. *J Am Chem Soc*. 1988;110:4863–4864.
30. Vossmeyer T, Reck G, Katsikas L, Haupt ET, Schulz B, Weller H. A "double-diamond superlattice" built up of $Cd_{17}S_4(SCH_2CH_2OH)_{26}$ clusters. *Science*. 1995;267:1476–1479.
31. Zheng N, Bu X, Lu H, Zhang Q, Feng P. Crystalline superlattices from single-sized quantum dots. *J Am Chem Soc*. 2005;127:11963–11965.
32. Herron N, Calabrese JC, Farneth WE, Wang Y. Crystal structure and optical properties of $Cd_{32}S_{14}(SC_6H_5)_{36}$. DMF_4, a cluster with a 15 Angstrom CdS core. *Science*. 1993;259:1426–1428.
33. Bendova M, Puchberger M, Schubert U. Characterization of "$Cd_{10}S_4(SPh)_{12}$", the thermal decomposition product of $(NMe_4)_4[Cd_{10}S_4(SPh)_{16}]$: synthesis of a neutral Cd_{54} sulfide cluster and of a polymeric chain of thiolate-bridged Cd_{17} sulfide clusters. *Eur J Inorg Chem*. 2010;2010:3299–3306.
34. (a) Levchenko TI, Kübel C, Khalili Najafabadi B, et al. Luminescent CdSe superstructures: a nanocluster superlattice and a nanoporous crystal. *J Am Chem Soc*. 2017;139:1129–1144; (b) Levchenko TI, Kübel C, Wang D, Khalili Najafabadi B, Huang Y, Corrigan JF. Controlled solvothermal routes to hierarchical 3D superparticles of nanoscopic CdS. *Chem Mater*. 2015;27:3666–3682.
35. Zhang Q, Bu X, Zhang J, Wu T, Feng P. Chiral semiconductor frameworks from cadmium sulfide clusters. *J Am Chem Soc*. 2007;129:8412–8413.
36. (a) Zhang Q, Liu Y, Bu X, Wu T, Feng P. A rare (3,4)-connected chalcogenide superlattice and its photoelectric effect. *Angew Chem Int Ed*. 2008;47:113–116; (b) Zheng N, Bu X, Lu H, Chen L, Feng P. One-dimensional assembly of chalcogenide nanoclusters with bifunctional covalent linkers. *J Am Chem Soc*. 2005;127:14990–14991; (c) Zheng N, Bu X, Lauda J, Feng P. Zero- and two-dimensional organization of tetrahedral cadmium chalcogenide clusters with bifunctional covalent linkers. *Chem Mater*. 2006;18:4307–4311.
37. Xie J, Bu X, Zheng N, Feng P. One-dimensional coordination polymers containing penta-supertetrahedral sulfide clusters linked by dipyridyl ligands. *Chem Commun*. 2005;39:4916–4918.
38. Kasuya A, Sivamohan R, Barnakov YA, et al. Ultra-stable nanoparticles of CdSe revealed from mass spectrometry. *Nat Mater*. 2004;3:99–102.
39. Murray CB, Norris DJ, Bawendi MG. Synthesis and characterization of nearly monodisperse CdE (E = sulfur, selenium, tellurium) semiconductor nanocrystallites. *J Am Chem Soc*. 1993;115:8706–8715.
40. Wang Y, Zhou Y, Zhang Y, Buhro WE. Magic-size II–VI nanoclusters as synthons for flat colloidal nanocrystals. *Inorg Chem*. 2015;54:1165–1177.
41. Liu Y-H, Wang F, Wang Y, Gibbons PC, Buhro WE. Lamellar assembly of cadmium selenide nanoclusters into quantum belts. *J Am Chem Soc*. 2011;133:17005–17013.
42. Wang Y, Liu Y-H, Zhang Y, et al. Isolation of the magic-size CdSe nanoclusters $[(CdSe)_{13}$(n-octylamine)$_{13}]$ and $[(CdSe)_{13}$(oleylamine)$_{13}]$. *Angew Chem Int Ed*. 2012;51:6154–6157.
43. Dolai S, Nimmala PR, Mandal M, et al. Isolation of bright blue light-emitting CdSe nanocrystals with 6.5 kDa core in gram scale: high photoluminescence efficiency controlled by surface ligand chemistry. *Chem Mater*. 2014;26:1278–1285.
44. (a) Yang J, Fainblat R, Kwon SG, et al. Route to the smallest doped semiconductor: Mn^{2+}-doped $(CdSe)_{13}$ clusters. *J Am Chem Soc*. 2015;137:12776–12779; (b) Yang J, Muckel F, Baek W, et al. Chemical synthesis, doping, and transformation of magic-sized semiconductor alloy nanoclusters. *J Am Chem Soc*. 2017;139:6761–6770.
45. Sigalas MM, Koukaras EN, Zdetsis AD. Size dependence of the structural, electronic, and optical properties of (CdSe)n, n = 6–60, nanocrystals. *RSC Adv*. 2014;4:14613–14623.
46. Azpiroz JM, Matxain JM, Infante I, Lopez X, Ugalde JM. A DFT/TDDFT study on the optoelectronic properties of the amine-capped magic $(CdSe)_{13}$ nanocluster. *Phys Chem Chem Phys*. 2013;15:10996–11005.
47. Pinkard A, Champsaur AM, Roy X. Molecular clusters: nanoscale building blocks for solid-state materials. *Acc Chem Res*. 2018;51:919–929.
48. Doud EA, Voevodin A, Hochuli TJ, Champsaur AM, Nuckolls C, Roy X. Superatoms in materials science. *Nat Rev Mater*. 2020;5:371–387.
49. Fenske D, Ohmer J, Hachgenei J, Merzweiler K. New transition metal clusters with ligands from main groups five and six. *Angew Chem Int Ed Engl*. 1988;27:1277–1296.
50. Stuczynski SM, Kwon YU, Steigerwald ML. The use of phosphine chalcogenides in the preparation of cobalt chalcogenides. *J Organomet Chem*. 1993;449:167–172.

51. Brennan JG, Siegrist T, Stuczynski SM, Steigerwald ML. The transition from molecules to solids: molecular syntheses of $Ni_9Te_6(PEt_3)_8$, $Ni_{20}Te_{18}(PEt_3)_{12}$ and NiTe. *J Am Chem Soc*. 1989;111:9240–9241.
52. Choi B, Paley DW, Siegrist T, Steigerwald ML, Roy X. Ligand control of manganese telluride molecular cluster core nuclearity. *Inorg Chem*. 2015;54:8348–8355.
53. Steigerwald ML, Siegrist T, Stuczynski SM. Octatelluridohexakis(triethylphosphine)hexacobalt and a connection between Chevrel clusters and the NiAs structure. *Inorg Chem*. 1991;30:2256–2257.
54. Lee C-H, Liu L, Bejger C, et al. Ferromagnetic ordering in superatomic solids. *J Am Chem Soc*. 2014;136:16926–16931.
55. (a) Turkiewicz A, Paley DW, Besara T, et al. Assembling hierarchical cluster solids with atomic precision. *J Am Chem Soc*. 2014;136:15873–15876; (b) Roy X, Lee C-H, Crowther AC, et al. Nanoscale atoms in solid-state chemistry. *Science*. 2013;341:157; (c) Choi B, Yu J, Paley DW, et al. van der Waals solids from self-assembled nanoscale building blocks. *Nano Lett*. 2016;16:1445–1449.
56. (a) Bhat S, Chakraborty I, Baksi A, Narayanan RP, Pradeep T. Evolution of atomically precise clusters through the eye of mass spectrometry. In: *Professor Paul O'Brien and Dr John Thomas, Nanoscience: Volume 3*. The Royal Society of Chemistry, London, United Kingdom; 2016:343–385; (b) Chakraborty P, Pradeep T. *The emerging interface of mass spectrometry with materials*; 2019 *NPG Asia Mater*;11:48.
57. Dass A, Stevenson A, Dubay GR, Tracy JB, Murray RW. Nanoparticle MALDI-TOF mass spectrometry without fragmentation: $Au_{25}(SCH_2CH_2Ph)_{18}$ and mixed monolayer $Au_{25}(SCH_2CH_2Ph)_{18-x}(L)x$. *J Am Chem Soc*. 2008;130:5940–5946.
58. Løver T, Henderson W, Bowmaker GA, Seakins JM, Cooney RP. Electrospray mass spectrometry of thiophenolate-capped clusters of CdS, CdSe, and ZnS and of cadmium and zinc thiophenolate complexes: observation of fragmentation and metal, chalcogenide, and ligand exchange processes. *Inorg Chem*. 1997;36:3711–3723.
59. Gholipour-Ranjbar H, Fang H, Guan J, et al. Designing new metal chalcogenide nanoclusters through atom-by-atom substitution. *Small*. 2021;17.
60. Gaumet JJ, Khitrov GA, Strouse GF. Mass spectrometry analysis of the 1.5 nm sphalerite−CdS core of $[Cd_{32}S_{14}(SC_6H_5)_{36}{\cdot}DMF_4]$. *Nano Lett*. 2002;2:375–379.

CHAPTER

19

Other metal nanoclusters

Indranath Chakraborty[a] *and Thalappil Pradeep*[b]

[a] School of Nano Science and Technology, Indian Institute of Technology Kharagpur, Kharagpur, India [b] Deepak Parekh Institute Chair Professor and Professor of Chemistry, Department of Chemistry, Indian Institute of Technology Madras, Chennai, India

19.1 Significance of other metal nanoclusters (OMNCs)

Atomically precise noble metal nanoclusters (NCs) are novel nanomaterials with particle sizes less than 2 nm.[1,2] They are typically composed of a few to tens of metal atoms protected with ligand shells and can be considered as molecules.[1,2] The strong quantum confinement in these ultrasmall-sized materials renders them physical and chemical properties such as photoluminescence,[3–5] quantized charging,[1,2] molecular magnetism,[6–9] optical chirality,[10–13] surface chemistry,[5,14] and catalytic performance,[1,15] which are all distinct from their bulk and larger nanocrystal counterparts. For instance, the surface plasmon resonance usually observed around 520 nm (depending on particle size) for gold (Au) nanoparticles (NPs) disappear in the subnanometer size regime due to the presence of discrete energy states.[16] The physicochemical properties of metal NCs can be tuned in a controlled and predictable manner to meet the requirements of a specific application.[1,2,15] The properties of metal NCs depend on their size, composition, surface, structure, and chemical environment.[1,2,15] A slight change in these parameters can lead to NCs with remarkably different properties. The molecule-like properties of metal NCs have been explored for optoelectronics,[17,18] bioimaging,[19,20] sensing,[21] and catalysis,[15] among others.

Au and Ag NCs have attracted tremendous interest from the scientific community due to their applicability in single-molecule studies, sensing, bioimaging, etc.[1,2] As a result, reports on Au and Ag dominate the field of NCs.[1,2] For example, as per the web of science data on NC research, 51% and 26% of the reported publications in 2020 were on Au and Ag NCs, respectively (Fig. 19.1A).

However, there have been reports on Cu NCs in 2020, which contributed to 20% of the publications on NC research; this indicates the increasing interest in exploring OMNCs (Fig. 19.1B). The total number of publications in 2020 on OMNCs, especially for Cu, Pd, Pt, and Ir, are plotted in Fig. 19.1B. Despite the limited number of reports (compared to Au and

Atomically Precise Metal Nanoclusters.
DOI: https://doi.org/10.1016/B978-0-323-90879-5.00006-8

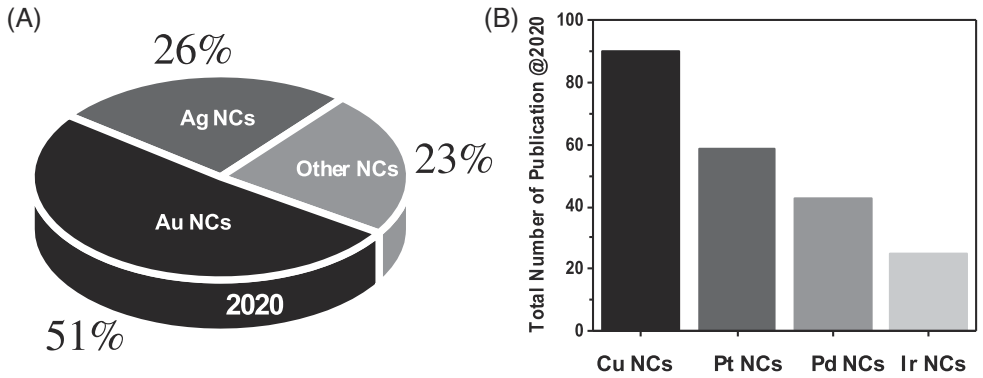

FIGURE 19.1 (A) Percentage of papers published on Au NCs, Ag NCs, and other metal NCs in the year 2020 (data obtained from the web of science). (B) The total number of publications reported 2020 (from the web of science with topic searching word <metal nanoclusters> or <M nanoclusters> where metal refers to copper, platinum, palladium, and iridium and M refers to Cu, Pt, Pd, and Ir, respectively).

Ag, in total ~77%), this chapter will look into the significance of OMNCs, their synthesis, and some select properties.

The bulk properties, such as resistance to oxidation and corrosion of noble metals, like palladium (Pd), platinum (Pt), and iridium (Ir), are similar to Au and Ag. Despite this, there was not much interest in applying these metals in NC research. It, therefore, becomes necessary to understand the reasons behind the pointed interest in Au and Ag. First, both Au and Ag exhibit exciting properties (optical, catalytic, chiral, etc.) when their sizes are reduced to the nanoscale. Furthermore, since the crystal structure of several NC has been solved, correlating structure with properties has become feasible. Therefore, the exciting properties and extensive understanding have attracted significant attention toward Au and Ag. Furthermore, in-depth knowledge (see Chapter 5 for more details about Au and Ag NCs) about metal–ligand interactions, metal–metal bonding, and interfacial properties has lead researchers to look into materials beyond Au and Ag.

The tendency of most of the metals to undergo oxidation under ambient conditions, limited researchers from considering metals other than Au and Ag during the early days of investigation. Palladium (Pd), platinum (Pt), ruthenium (Ru), rhodium (Rh), and copper (Cu) are known for their high efficacy in catalysis. Cu is cost-effective (as compared to Au, Pt, Ag, and other noble metals). The standard electrode potential of various metals listed in Table 19.1 suggests that these metals can also be effectively reduced to form NCs following or by modifying the reported synthesis protocol of Au and Ag NCs. An increasing number of reports on the synthesis and properties of other metal NCs indicate that "there are a plethora of opportunities."

19.2 Diverse synthetic strategies for OMNCs

OMNCs can be chemically synthesized following the standard approach of mixing the metal precursor with some suitable organic ligands followed by chemical reduction (a general

TABLE 19.1 Standard reduction potentials of noble metals (including Cu). The accuracies reported are different.

Atomic number (*Z*)	Metals	Reaction	Standard reduction potential (*V*)
29	Copper	$Cu^{2+} + 2\,e^- \rightarrow Cu$	0.339
44	Ruthenium	$Ru^{3+} + 3\,e^- \rightarrow Ru$	0.6
45	Rhodium	$Rh^{3+} + 3\,e^- \rightarrow Rh$	0.8
46	Palladium	$Pd^{2+} + 2\,e^- \rightarrow Pd$	0.915
47	Silver	$Ag^{+} + e^- \rightarrow Ag$	0.7993
76	Osmium	$OsO_2 + 4\,H^+ + 4\,e^- \rightarrow Os + 2\,H_2O$	0.85
77	Iridium	$Ir^{3+} + 3\,e^- \rightarrow Ir$	1.16
78	Platinum	$Pt^{2+} + 2\,e^- \rightarrow Pt$	1.2
79	Gold	$Au^{3+} + 3\,e^- \rightarrow Au$	1.5

scheme is shown in Fig. 19.2A) using reducing agents. Depending on the choice of the ligand, solvents, and reducing agents, and other physical parameters, the synthesis protocols are of different types, such as solid-state route (Fig. 19.2B),[22] protein-directed route,[23] etc., and a detailed discussion about such routes can be found in Chapter 2. These methods only differ in the choice of the metal precursor and, in some cases, the choice of ligands. For example, Chakraborty et al. have synthesized 11 atom Pt NCs via solid-state route using 4-(tert-butyl)benzyl mercaptan as a ligand.[24] Ganguly et al. have synthesized 2-pehnylethanethiol protected Cu NCs through a solid-state route.[22] Ghosh et al. have synthesized and solved the crystal structure of tert-butyl thiolated Cu_{61} NCs.[25]

Apart from these colloidal routes for synthesizing OMNCs, the templated route is becoming popular and mainly applicable to catalytically active metals. In this method, solid and porous materials are used as templates, and the pore size is used to control the NC's size. Metal–organic frameworks (MOFs) are the apt choice for the template, and there are numerous reports on the synthesis of metal NCs in MOF-template. For example, Kratzl et al. have adopted a multistep synthetic approach (Fig. 19.3) to synthesize atomically precise Pt NCs.[26] First, the Pt-carbonyl cluster was integrated into the ZIF-8 structure. Then decarbonylation was carried out to remove the carbonyl (CO) ligands, to produce ligand-free Pt NCs in the ZIF-8 template. A major drawback of this method is the multistep approach which takes a much longer time to make the final NCs, and the chemicals used are expensive. Chen et al. adapted a rapid template-guided ligand-free PtNC synthesis using ZIF-8 as a template.[27] In the report, common Pt precursor (chloroplatinic acid) was reduced in the presence of ZIF-8 using sodium borohydride, resulting in the rapid formation of PtNCs on the outer surface of the MOFs. The concentration of precursor solution was key in controlling the particle size. Apart from the solid template, biotemplates are also used in synthesizing NCs, wherein NCs are formed in the cavity of proteins. Rajamanikandan et al. have shown bovine serum albumin (BSA) protein as a biotemplate to synthesize fluorescent Cu NCs.[23] Soft-templates such as hydrogel network,[28] egg shell membrane,[29] etc. have also been utilized in Cu NC synthesis.

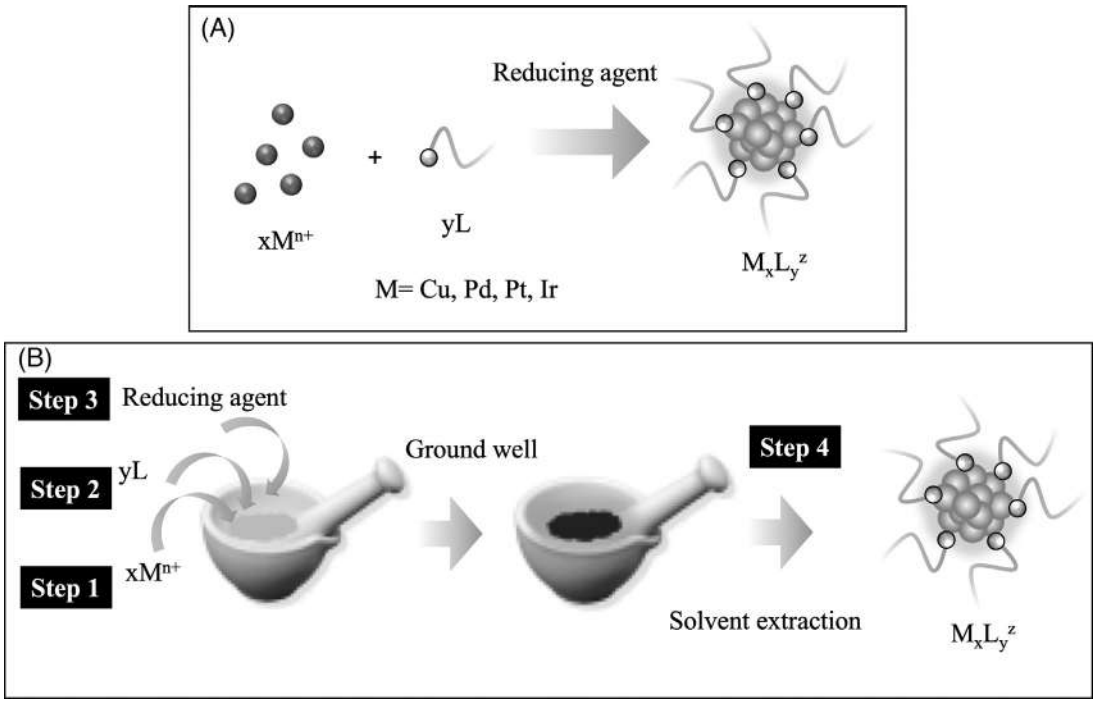

FIGURE 19.2 (A) General scheme of other metal NC synthesis following a chemical reduction in solution. (B) Scheme of the paste-based synthesis route for other metal NCs.

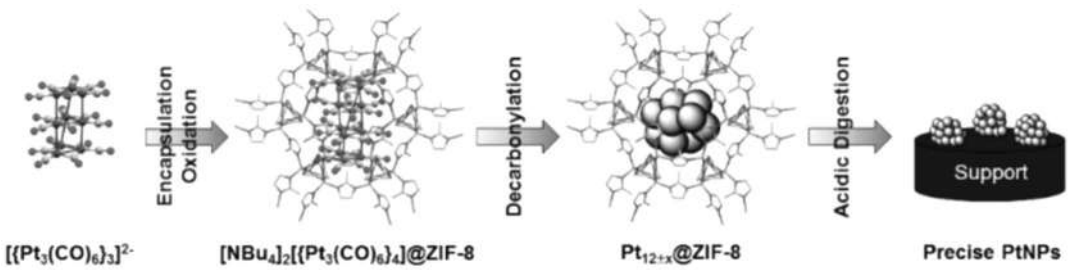

FIGURE 19.3 Scheme of the multistep Pt NC synthesis following a templated route. Adapted with permission from ref.[26] Copyright 2019, American Chemical Society.

19.3 Selected properties of OMNCs

There are numerous interesting optical, structural, and catalytic properties of OMNCs, making them one of the promising areas in "material research." In the following section, properties and characterizations of some of the OMNC will be discussed.

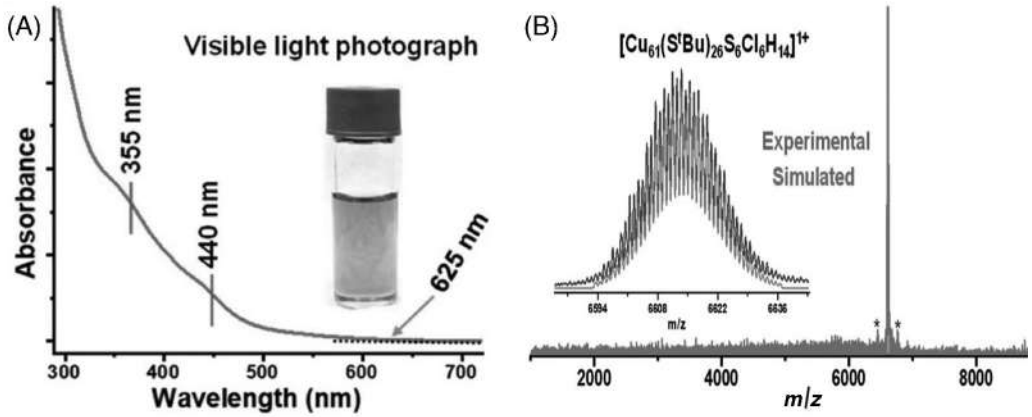

FIGURE 19.4 (A) UV–vis spectrum of the toluene solution of the $Cu_{61}(S^tBu)_{26}S_6Cl_6H_{14}$ NCs. Inset shows the photograph of the NC in the toluene solution. (B) Positive-mode ESI MS spectrum of the $[Cu_{61}(S^tBu)_{26}S_6Cl_6H_{14}]^+$ NCs. Inset shows agreement between experimental and simulated isotopic distribution. Adapted with permission from ref.[25] Copyright 2019, American Chemical Society.

19.3.1 Cu nanoclusters

Cu NCs are the third most reported NCs in literature,[30–34] but only a handful of them have solved crystal structures.[35–43] However, synthesizing Cu (0) NCs is complicated because of the instability of Cu(0), which is prone to oxidation ($E°_{Cu(I)/Cu(0)=} = 0.52$ V). Hence it is challenging to synthesize Cu(0) NCs in solution, especially in the aqueous medium. Different physicochemical parameters (such as ligands, solvents, temperature, polymeric matrix, etc.) are optimized to synthesize CuNCs with core (Cu(0))–shell (Cu(I)) structures.

Bakr group has reported one such Cu(0)-containing core–shell NCs, $[Cu_{61}(S^tBu)_{26}S_6Cl_6H_{14}]^+$ ($-S^tBu$; *tert*-butyl thiolate), which shows distinct absorption peaks (Fig. 19.4A) and well-defined mass spectral features (Fig. 19.4B).[25] The NC contains a quasi-elongated triangular gyrobicupola Cu_{19} core and a giant $Cu_{42}(StBu)_{26}S_6Cl_6$ shell (Fig. 19.5). Such 19-atom core was also seen in AgNCs but with different symmetry and structure.[44,45] The shell is composed of a pair of tricorne-like caps, $Cu_{15}(S^tBu)_{13}Cl_3$, and a ring-like macrocycle or belt $(Cu_2S)_6$, which resembles "18-crown-6." Bakr group has also reported high-nuclearity Cu NC with a molecular formula, $[Cu_{81}(PhS)_{46}(^tBuNH_2)_{10}(H)_{32}]^{3+}$ which has an entirely different core and shell structure than Cu_{61} NCs.[42] Notably, along with differences in core structures of reported CuNCs, there are also reports of comparable core structures with Au and Ag NCs; for example, $[Cu_{25}H_{22}(PPh_3)_{12}]Cl$ NC[39] has icosahedral M_{13} core similar to $Au_{25}(SR)_{18}$[46,47] and $Ag_{25}(SR)_{18}$ NCs.[48] Hence, a direct comparison of the Au and Ag system with a handful of solved structures of Cu NCs is not appropriate.

Although noticeable photoluminescence (PL) is not observed in most structurally solved CuNCs with partial Cu(0), a few reports exist with structurally unsolved CuNCs (except recent report of Cu_{15} NC[40] with a photoluminescence quantum yield of 0.1%). Patra's group reported Cu NCs with tunable PL properties synthesized via a top-down approach from bigger-sized Cu NPs.[49] By varying the temperature and time of the etching process in presence

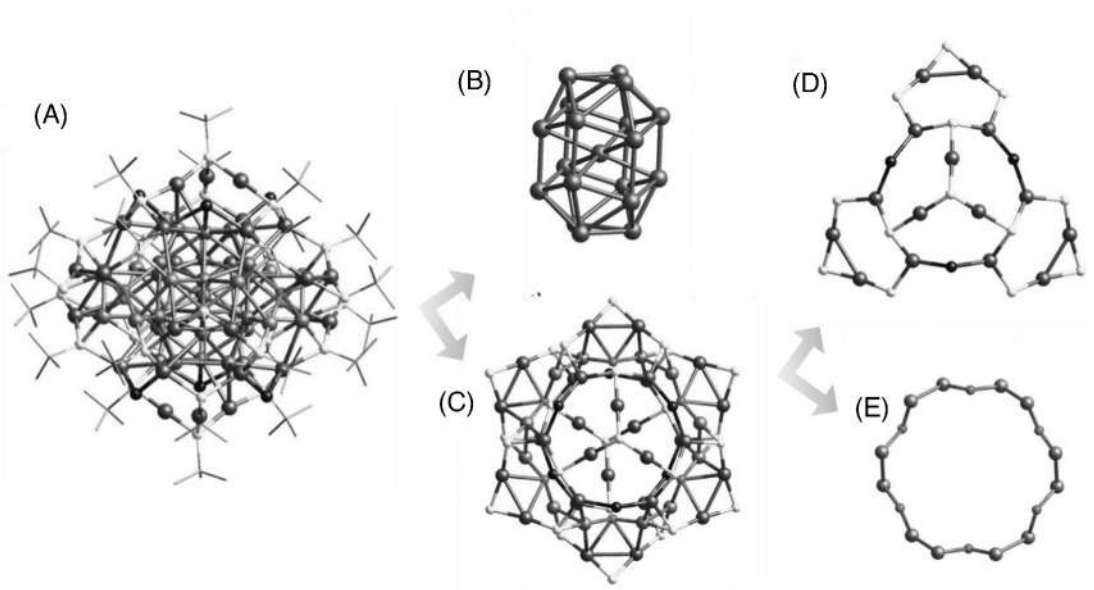

FIGURE 19.5 (A) Molecular structure of the $Cu_{61}(S^tBu)_{26}S_6Cl_6H_{14}$ NC. Hydrogen atoms are omitted for clarity. (B) Side-view of Quasi-J_{36} Cu_{19} core. (C) Top-view of metal–ligand shell, $Cu_{42}(S^tBu)_{26}S_6Cl_6$. (D) Tricorne-like cap, $Cu_{15}(StBu)_{13}Cl_3$. (E) Metal sulfide macrocycle or belt, $(Cu_2S)_6$, which resembles the structure of "18-crown-6." Adapted with permission from ref.[25] Copyright 2019, American Chemical Society.

of glutathione (GSH), a weak red-emitting $Cu_{34–32}(SG)_{16–13}$ NC, and a bright blue-emitting $Cu_{25}(SG)_{20}$ NC were synthesized. Additionally, they reported that the PL intensity could be enhanced by 36 times for $Cu_{34–32}(SG)_{16–13}$ NCs (Fig. 19.6A) via aggregation-induced emission (AIE) in presence of ethanol.[49]

The average lifetime increased from 115.9 ns to 239.5 ns upon aggregation (Fig. 19.6B).[49] They proposed a ligand to metal charge transfer (LMCT) mechanism for the NC's emission, and upon aggregation, solvent polarity alters the charge transfer process, which affects their PL. The shift in PL emission peak upon aggregation was attributed to the presence of different triplet states. While these aggregations are uncontrolled, there are numerous reports of CuNC's controlled assembly to tune their PL properties via the AIE mechanism.[49] The Zhang group has discussed this in detail in their perspective article.[50] In another report, they found a decisive role of ligands in the resultant PL properties of CuNC, supporting the LMCT mechanism.[51] The experiment was conducted by replacing the alkyl thiol with aromatic thiols with different para-substituted functionalities ($-OCH_3$, $-CH_3$, $-Br$, $-Cl$, and $-F$). The emission peak shift can be correlated with the trend in substituent groups' electron-withdrawing ability. On the other hand, the substituent groups' steric hindrance controls the rigidity of NC's and the PL QY.[51] Due to the broad emission color tunability, emission stability, and excitation wavelength independence, these self-assembled CuNCs can be employed to fabricate light-emitting diodes (LEDs) (Fig. 19.7).

Cu(0) and Cu(I) are both prone to oxidation, and hence CuNCs can be utilized as an electrochemical sensor for detecting oxidizers. Gao et al. have synthesized smaller-sized six atom Cu

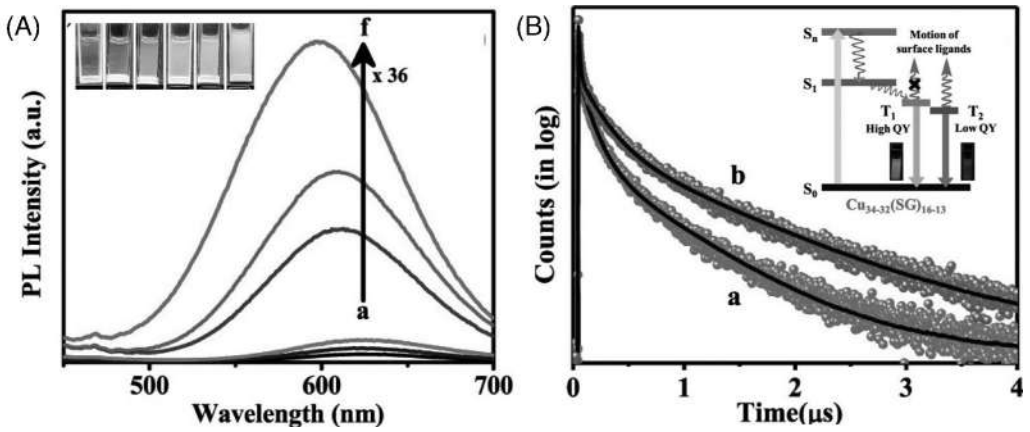

FIGURE 19.6 (A) Photoluminescence spectra of $Cu_{34–32}(SG)_{16–13}$ NCs with (a) 0%, (b) 20%, (c) 40%, (d) 60%, (e) 80%, and (f) 90% ethanol. Inset shows the corresponding photograph of the colloids under daylight. (B) Time-resolved decay curves of $Cu_{34–32}(SG)_{16–13}$ NCs in water–EtOH mixture with f_v of (a) 0% and (b) 40%. Inset shows a schematic of decay dynamics and origin of emission. Adapted with permission from ref.[49] Copyright 2019, American Chemical Society.

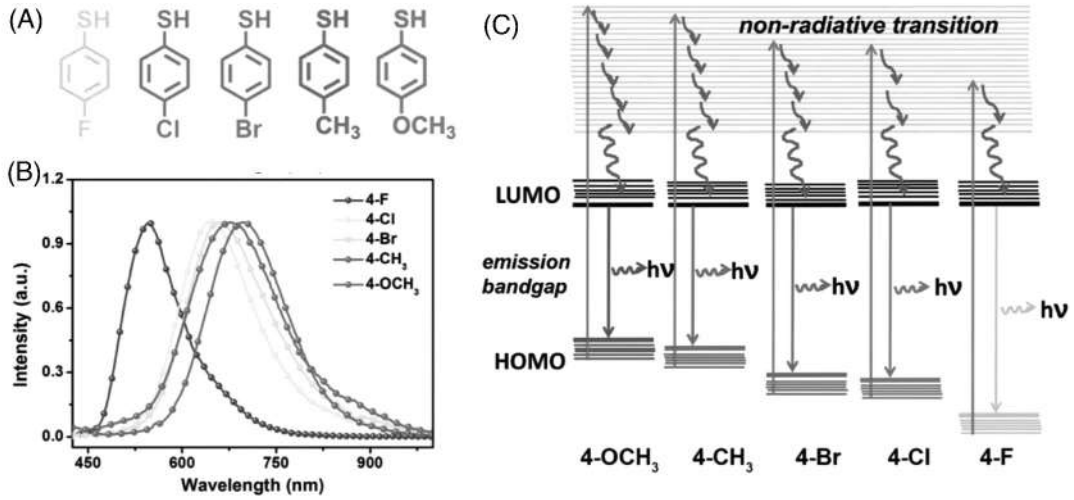

FIGURE 19.7 (A) Chemical structures of the capping ligands. (B) PL emission spectra of the self-assembled architectures composed of Cu NCs capped with different ligands. (C) Schematic of energy levels of the self-assembled architectures composed of the NCs capped with different ligands. Adapted with permission from ref.[51] Copyright 2017, Royal Society of Chemistry.

NCs with mercaptobenzoxazole as a protecting ligand.[52] The crystal structure revealed that two copper atoms present at the opposite vertices of the octahedron were exposed and were useful for the electrochemical detection of H_2O_2. Furthermore, the concentration-dependent CV data (Fig. 19.8A) suggest a linear detection response for H_2O_2 (Fig. 19.8B).[52]

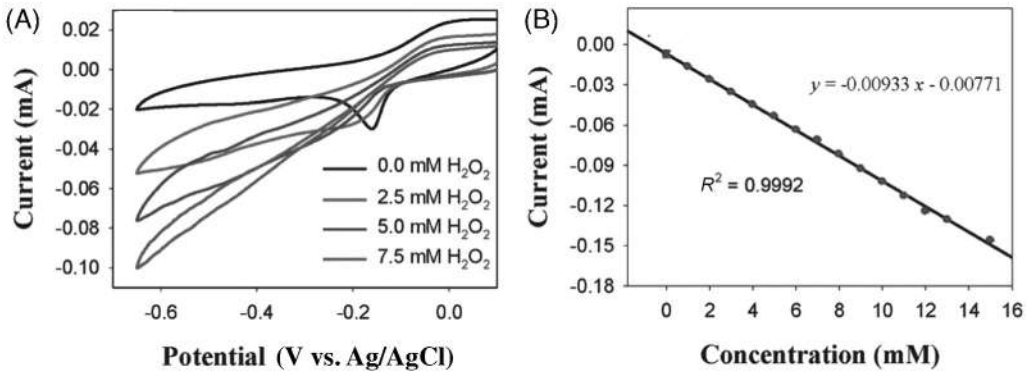

FIGURE 19.8 (A) CVs of the Cu_6 clusters in 0.1 m PBS in the absence and presence of H_2O_2 at different concentrations of 2.5×10^{-3}, 5×10^{-3}, and 7.5×10^{-3} m (scan rate: 100 mV/s). (C) The linear relationship between responding current and concentration of H_2O_2. Adapted with permission from ref.[52] Copyright 2016, John Wiley & Sons.

The limit of detection (LOD) attained was 1.8×10^{-6} M for H_2O_2. Since the detection is based on redox principle, the sensing is very specific, and H_2O_2 can be detected even in the presence of glucose, ascorbic acid (AA), dopamine (DA), uric acid (UA), and NaCl. Apart from this report, Zhao et al. demonstrated electrochemiluminescence (ECL) behavior of GSH protected Cu NCs.[52] Using the ECL probe, dopamine has been detected with a LOD as low as 3.5×10^{-13} M. Tashkhourian et al. have also reported detecting dopamine using CuNCs conjugated with SiNPs.[53] In this case, the electrode was designed as a CuNCs/SiO_2 NPs/carbon paste composite, and the detection was investigated by cyclic voltammetry and differential pulse voltammetry.[53]

While it is known that ligands can mask the catalytic sites of NCs, it relies on several other factors such as ligand density, ligands orientation, etc.[15] Hence, removal of the ligand is not necessary for catalysis applications and this has been demonstrated in numerous reports of NC-based homogenous catalysis. Lee et al. have shown that thiolated Cu_{32} NC is an excellent catalyst for the reaction of carbonylation of anilines to produce carbamates).[43] Cu_{32} NCs also accelerate carbonylation of aniline, methyl-, and halide-substituted aniline through C–N bond formation (Fig. 19.9). The NC catalyst can be reused multiple times; however, a slight reduction in selectivity is observed.

CuNCs are also known for their effective sensing and bioimaging capability, owing to their reduced cytotoxicity. An et al. in a recent review article have presented a comprehensive discussion on the sensing and bioimaging capabilities of all CuNCs reported so far.[30] For instance, Liu et al. have developed a CuNC-based ratiometric sensor for real-time sensing and imaging of Ca^{2+} in neurons (Fig. 19.10).[54] The Ca^{2+} capturing, in this case, was performed via ligand engineering of the CuNCs.[54] Furthermore, Heo et al. have shown radiolabeling (^{64}Cu) in CuNCs which can be employed for accurate in vivo tumor imaging.[54] Thus, numerous examples of the application of CuNCs in bioimaging can be found in literature, highlighting the potential of Cu NCs in future imaging and therapeutics.[30]

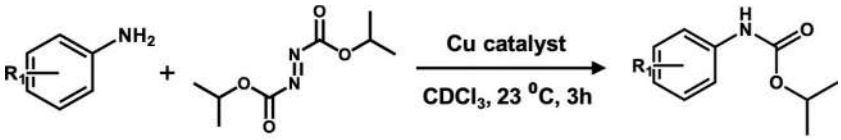

Catalyst	R_1	Product	Isolated Yield (%)
$Cu_{32}NC$	H	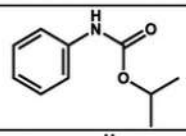	60.5
$Cu_{32}NC$	*p*-CH_3	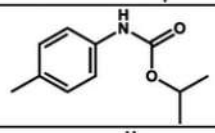	47.4
$Cu_{32}NC$	*p*-Br	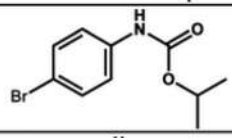	46.7
$Cu_{32}NC$	H	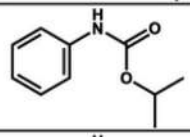	42.7[a]
CuPET thiolate	H	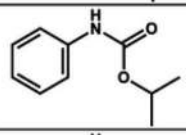	6.1
CuI salt	H	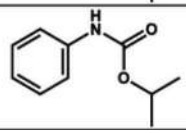	3.0

FIGURE 19.9 Scheme of carbonylation of anilines using Cu NCs. Examples of C−N Bond formation during carbonylation of anilines together with their yields. Adapted with permission from ref.[43] Copyright 2020, American Chemical Society.

19.3.2 Pt nanoclusters

While Cu has emerged as the center of interest in recent years, a few reports exist on ligand protected Pt NCs despite their catalytic properties. This is mainly because of the high cost and low relative abundance of the Pt metal. Our previous review article on atomically precise NCs had highlighted this topic briefly.[1] Here we emphasize mostly on PtNCs of size less than 2 nm. There are plenty of reports on bigger-sized particles used in applications, including catalysis

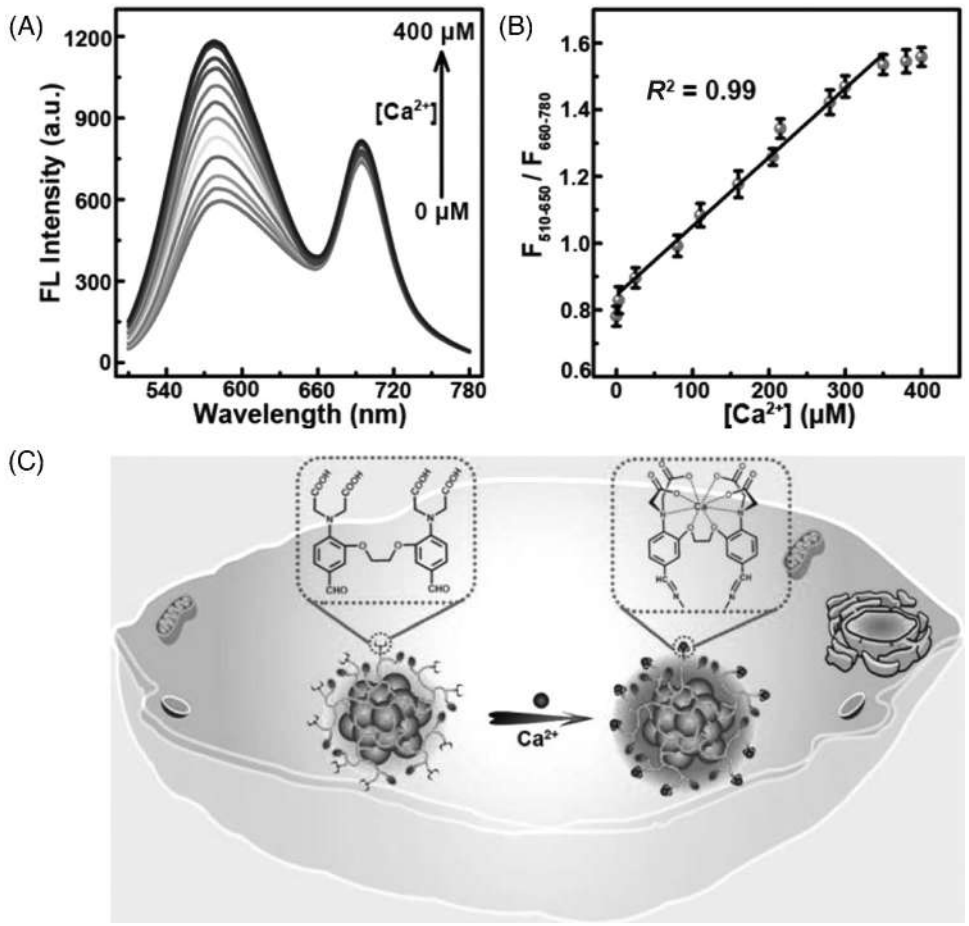

FIGURE 19.10 (A) Fluorescence response of CuNC (90 μg/mL) in the presence of various concentrations of Ca^{2+} (0, 2, 25, 80, 110, 160, 205, 215, 280, 300, 350, 380, 400 μM) in a cell lysis buffer. (B) Calibration curve between $F_{510–650}/F_{660–780}$ and various concentrations of Ca^{2+}. (C) Schematic of ratiometric biosensing of Ca^{2+} ions in neurons by CuNCs. Adapted with permission from ref.[54] Copyright 2019, American Chemical Society.

and medicine.[55,56] Pt NCs can be synthesized using numerous methods such as templated-method, solid-state route, and solution-phase synthesis.[57]

Kawasaki et al. have synthesized four to six atom surfactant-free PtNCs and carried out characterization by MALDI MS using 2-mercapto-benzothiazole (MBT) as a matrix.[58] The mass spectral data showed (Fig. 19.11) matrix incorporated four to six atom PtNCs. Chakraborty et al. synthesized 11 atom Pt NCs protected by 4-(tert-butyl)benzyl mercaptan and characterized it with ESI and MALDI MS. Fischer's group prepared atomically precise Pt carbonyl NCs using ZIF-8-templates, which exhibited enhanced electrocatalytic properties.[26,59] In addition to ligand-protected PtNCs, there is an increasing trend toward synthesizing ligand-free PtNCs owing to their catalytic activities. There are numerous reports

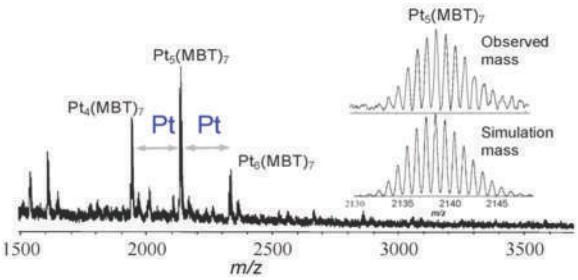

FIGURE 19.11 MALDI mass spectrum of MBT-protected Pt NCs in the negative ion mode, obtained for DMF-protected Pt NCs by ligand exchange with 2-mercapto-benzothiazole (MBT). Adapted with permission from ref.[58] Copyright 2010, Royal Society of Chemistry.

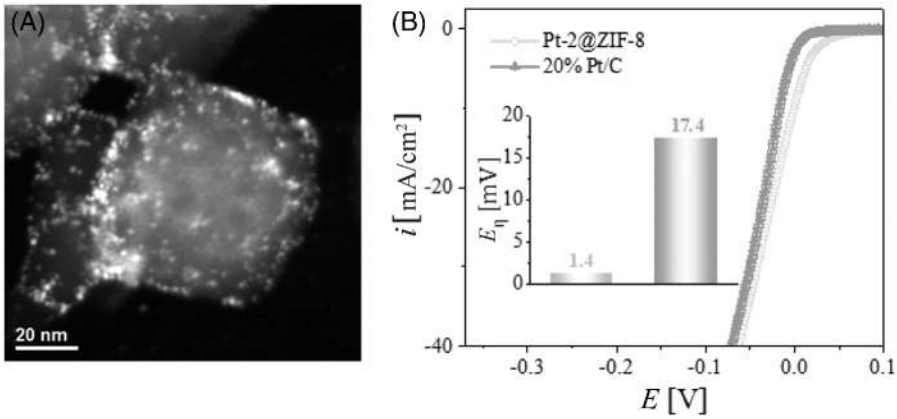

FIGURE 19.12 (A) HAADF-STEM image of Pt NCs@ZIF-8. (B) HER polarization curves of Pt NCs@ZIF-8 (4 μg Pt/cm^2) and 20% commercial Pt/C (32 μg Pt/cm^2) catalysts in N_2-saturated 0.1 M $HClO_4$. The inset shows the overpotential E_η at a current density of $j = 10$ mA/cm^2. The current density j is plotted versus the applied potential E, which has been converted in reference to the potential of an RHE. The scan rate was 5 mV/s. Adapted with permission from ref.[27] Copyright 2021, John Wiley & Sons.

on supported PtNCs with an average size between 1 and 2 nm.[57] Chen et al. reported ZIF-8-templated PtNCs (Fig. 19.12A), which show high catalytic activity for the hydrogen evolution reaction (HER).[60] Under identical conditions, the HER performance of PtNCs@ZIF-8 was found to be better than the commercially available 20% Pt/C catalysts (Fig. 19.12B). Extensive reports on catalytic properties of PtNCs are summarized in a review article by Zhu et al.[15]

There are a few reports on fluorescent Pt NCs, and they can also be utilized for bioimaging.[61–63] For example, Tanaka et al. demonstrated effective bioimaging of ultrasmall five atom Pt NCs.[61] First, they conjugated the Pt_5 NCs with a protein via 1-[(3-dimethylamino)-propyl]-3-ethylcarbodiimide hydrochloride (EDC) coupling reaction. Then, an anti-chemokine receptor antibody (anti-CXCR4-Ab) was attached to the protein conjugated PtNCs for specificity.

The antibody-bound PtNCs were then introduced into HeLa cells for fluorescence imaging (Fig. 19.13A), showing a bright blue color as chemokine receptors are highly expressed in tumor (HeLa) cells. These Pt NCs were also biocompatible, as evidenced from their cytotoxicity analysis (Fig. 19.13B), and are superior to toxic organic dyes or semiconductor QDs.[59]

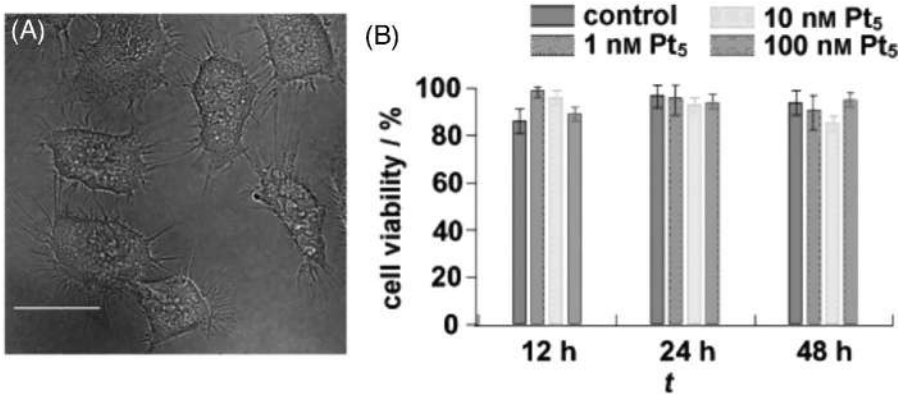

FIGURE 19.13 (A) Confocal fluorescence microscopic images (in grayscale) merged with differential interference contrast (DIC) images of living HeLa cells labeled with $Pt_5(MAA)_8$-(protein A)-(anti-CXCR4-Ab). The scale bar is 20 μm. (B) Cell viability of HeLa cells. Cells were incubated with 1, 10, and 100 nM Pt_5 NCs at 37°C. Left bars show the cell viability of the control sample in the absence of Pt_5 NCs. Adapted with permission from ref.[61] Copyright 2011, John Wiley & Sons.

19.3.3 Pd nanoclusters

The reports on Pd NCs are even fewer than the Pt NCs. Most of the reported PdNCs are protected using π-accepting ligands such as carbon monoxide (CO), substituted phosphine (PR_3) isocyanides, tropylium cation ($C_7H_7^+$), ketimide ligand ($R_2C{=}N^-$), etc. which helps in stabilizing the low-valent Pd.[64–71] Cook et al. have reported one such ketimide protected Pd NC with a hexagonal aromatic Pd_7 core (Fig. 19.14A).[71] The mass spectral data confirmed the NC's assignment as $Pd_7(N{=}C^tBu_2)_6$ (Fig. 19.14B). This was an exciting and rare example of an all-metal aromatic NC with hexagonal symmetry.[71] Interestingly, in mass spectral characterization, Pd shows broader envelopes than other noble metal NCs with identical atomicity due to their six stable isotopes, ^{102}Pd, ^{104}Pd, ^{105}Pd, ^{106}Pd, ^{108}Pd, and ^{110}Pd.

PdNCs are commonly used in heterogeneous catalysis of organic reactions, especially hydrogenation and cross-coupling reactions. Confined PdNCs are preferred for catalysis applications. Zhu et al. have made PdNCs confined in a core–shell metal–organic frameworks@covalent organic polymer (PdNCs@MOF@COP).[72] High stability, abundant porosity, and large surface area render them useful for catalytic applications. The experimental observation suggests the "condensation pathway" mechanism for hydrogenation of nitrobenzene, based on which a possible reaction mechanism was proposed, which is presented in Fig. 19.15.

In another report, Hyotanishi et al. synthesized surfactant-free Pd NCs with excellent catalytic activity in Suzuki–Miyaura cross-coupling and Mizoroki–Heck reactions.[73] The catalytic performance of the PdNCs in Suzuki–Miyaura was verified with the reaction between various aryl iodides (1) and aryl boronic acids (2), as mentioned in Fig. 19.16 with turnover numbers greater than 5. Thus, these NCs can be reused at least five times without compromising their catalytic performances.[73] Many other interesting catalytic properties of PdNCs can be found in the review article by Liu and Corma.[74]

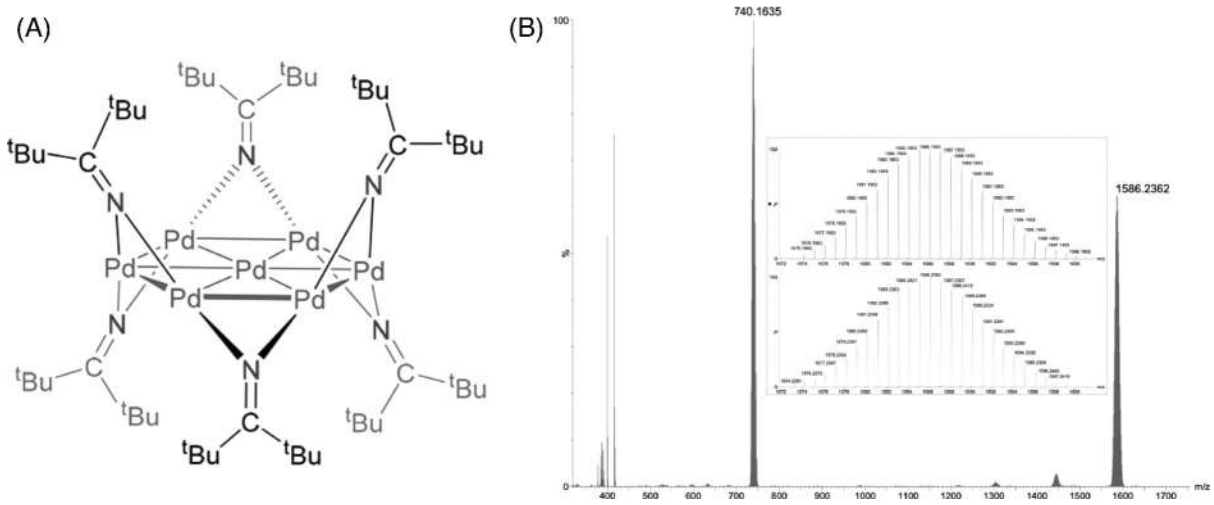

FIGURE 19.14 (A) Structure of $[Pd_7(N{=}C^tBu_2)_6]$ NC. (B) ESI-MS of $Pd_7(N{=}C^tBu_2)_6$ in THF. The peak at m/z 1586.2362 can be assigned to the $[M]^+$ ion, whereas the peak at m/z 740.1635 can be associated with the $[Pd_3(N{=}C^tBu_2)_3]^+$ fragment. Inset: Experimental (bottom) and calculated (top) peaks assignable to the $[M]^+$ ion. Adapted with permission from ref.[71] Copyright 2020, American Chemical Society.

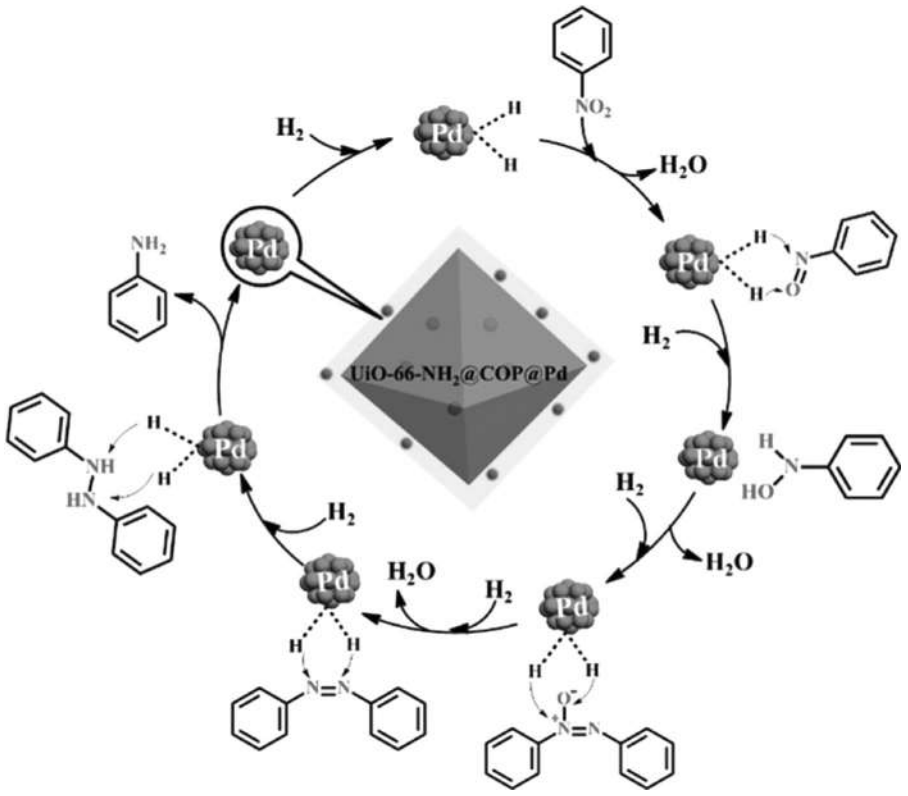

FIGURE 19.15 Possible reaction mechanism of catalytic hydrogenation of nitrobenzene to aniline with UiO-66-NH_2@COP@Pd. Adapted with permission from ref.[72] Copyright 2020, American Chemical Society.

19.3.4 Ir nanoclusters

Iridium is known for its excellent catalytic and electrocatalytic properties, including hydrogenations, hydrogen evolution reaction (HER), and anodic oxygen evolution reaction.[75,76] Xu et al., in 1994, compared the catalytic performances of bare Ir_4 and Ir_6 clusters supported on porous metal oxides.[77] They performed hydrogenation reactions of hydrocarbons and found that the catalytic performances are different in each case, and more importantly, both are superior to the corresponding bulk Ir. Later in 2003, Argo et al. reported that the rate of hydrogenation of ethane is much faster for Ir_4 than the Ir_6 cluster supported on γ-Al_2O_3.[78] The catalyst's reactivity depends on the size and structure of the reactant, as revealed from their systematic study with propene and toluene. Aydin et al. have used aberration-corrected scanning electron microscopy to capture the high-resolution image of Ir_6 clusters.[79] In another report, Kerpal et al. studied the CO gas adsorption on neutral and atomically precise Ir clusters of 3–21 atoms.[80] These are a few studies of gas-phase or supported atomically precise Ir clusters. Notably, thiol, which forms a stronger bond with Au/Ag, was not found to be very common in these Ir NC syntheses except the report by Bhat et al. in which a paste-based route

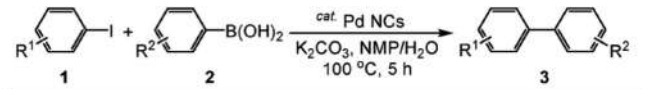

Entry	1 (R^1 =)		2 (R^2 =)		Yield[b] (%)		TON[c] ($\times 10^4$)
1	*p*-CH_3O	**1b**	H	**2a**	>99 (93)	**3b**	>5.0
2	*p*-CF_3	**1c**	H	**2a**	97 (94)	**3c**	4.8
3	*p*-NH_2	**1d**	H	**2a**	>99 (87)	**3d**	>5.0
4		**1e**	H	**2a**	87 (75)	**3e**	4.6
5		**1f**	H	**2a**	82 (69)	**3f**	4.7
6	*p*-CH_3	**1a**	*p*-Cl	**2b**	87 (79)	**3g**	4.5
7	*p*-CH_3	**1a**	*p*-CH_3O	**2c**	>99 (88)	**3h**	>5.0
8	*p*-CH_3	**1a**	*m*-NO_2	**2d**	75 (73)	**3i**	3.8

FIGURE 19.16 Pd-NCs-catalyzed Suzuki–Miyaura cross-coupling reaction of aryl iodides (1) with various arylboronic acids (2). Adapted with permission from ref.[73] Copyright 2011, Royal Society of Chemistry.

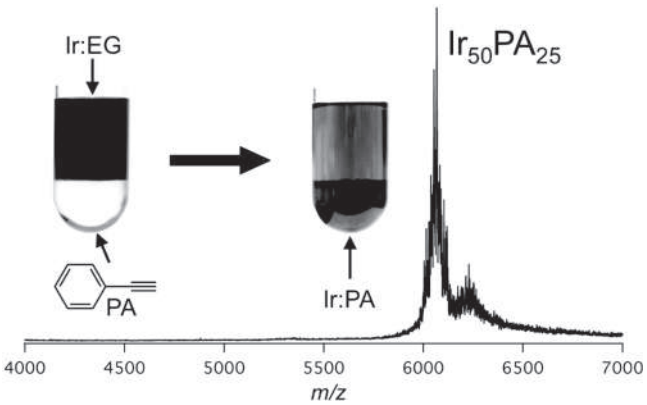

FIGURE 19.17 ESI-FT-ICR mass spectra of Ir NC. Inset shows the photographs of the biphasic layers before and after the ligand exchange. Adapted with permission from ref.[82] Copyright 2017, American Chemical Society.

was used to synthesize 2-phenylethanthiolate (PET) protected atomically precise $Ir_9(PET)_6$ NCs.[81] In 2017 Yamamoto et al. have reported atomically precise Ir NCs with phenylacetylene (PA) as ligand.[82] Mass spectral data confirmed the composition of the clusters as $Ir_{50}(PA)_{25}$ NCs (Fig. 19.17).

Apart from such atomically precise clusters, some reports also exist on Ir NPs of size 1–3 nm. For example, dodecanethiolate protected magnetic Ir nanoparticles of size around 1.2 ± 0.3 nm were synthesized by Gavia et al. via the modified Brust–Schiffrin method.[83] Yee et al. have reported octadecanethiol functionalized Ir NPs using superhydride as a reducing agent.[84] Wang et al. in 2020 reported the synthesis of ultrasmall Ir NCs of size 1.55 nm embedded on N, S-doped graphene.[85] These graphene-supported Ir NCs show efficient and robust electrocatalysis performances for both HER and OER at all pH conditions. They also demonstrated the practical applications of water splitting owing to the favorable mesoporous morphology, surface electronic structure, coordination environment, and pH universality of graphene-supported Ir NCs.[85] For this purpose, a two-electrode water electrolysis cell was constructed by loading the Ir NC catalyst on carbon fiber paper (CFP) as both the anode and cathode, and studied the linear sweep voltammograms (LSVs) (Fig. 19.18) in 0.1 M $HClO_4$,

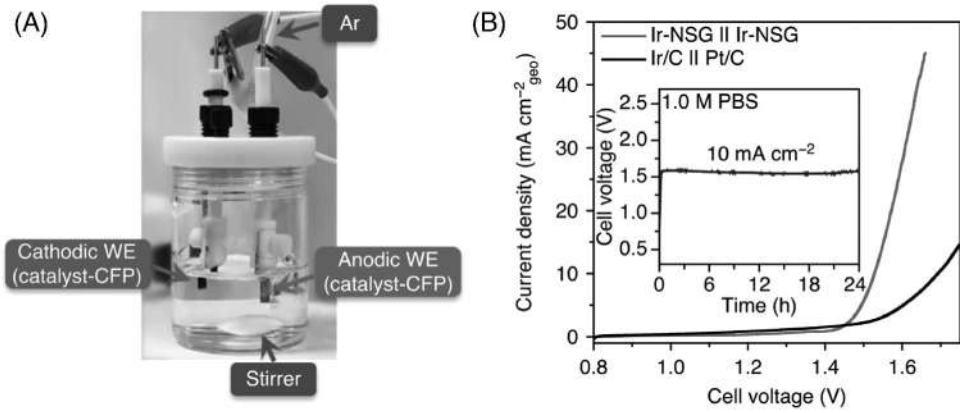

FIGURE 19.18 (A) Digital photograph of the homemade two-electrode cell for water splitting. WE working electrode, CFP carbon fiber paper, and Ar pure argon gas (99.99%). (B) LSV curves of Ir-NSG and Ir/C-Pt/C coupled water electrolysis cell at a scan rate of 5 mV/s in 1 M PBS. Inset shows the corresponding chronopotentiometric curves at 10 mA/cm^2. Catalyst loading: 73.3 $\mu g_{metal}/cm^2$. All measurements were conducted in Ar-saturated electrolytes and corrected for i–R drop. Adapted with permission from ref.[85] Copyright 2020, Springer Nature Limited.

1 M PBS, and 1 M KOH solutions. The cell with Ir NC anode and cathode shows remarkable electrocatalysis performances, which required only 1.53, 1.42, and 1.45 V to reach a current density of 10 mA/cm^2 in acidic, neutral, and alkaline electrolyzers, respectively.[85] Apart from the catalytic activities of such clusters, Vankayala et al. have reported 2,2′-binapthol protected Ir clusters for bioimaging.[86] These ~2 nm-sized and bluish green-emitting Ir NCs exhibited good biocompatibility (IC_{50} value of ~100 μg/mL).[86]

19.4 Summary and future perspectives

This chapter briefly summarizes OMNCs, their synthesis, and select properties, including some applications. Among OMNCs, major contribution comes from Cu followed by Pt, Pd, and Ir, which also suggest the plethora of opportunities, especially in this direction, to enhance the diversity and variety in OMNCs. Looking into the future, unprecedented growth is evident in multiple research directions, from synthesis to application. As pointed in the above sections, control in the synthesis of OMNCs is still in its infancy. More effort is needed to find the right synthetic conditions for atomic and molecular engineering of OMNCs. Especially, finding out the most suitable ligand is utmost important to tune their atomicity in a controllable manner. Despite the report of a few OMNC with mass spectral characterization, crystallization has not been achieved in most cases (except a few Cu NCs). This could be one of the most important future directions to understand OMNCs in more detail, which will be immensely beneficial for expanding their applications. Only limited computational support has been reported on this, which also has a potential future direction to explore their properties. Most of the applications of OMNCs focused on catalysis, but structure–prediction can help expand these applications in multiple avenues.

List of abbreviation

NCs	nanoclusters
OMNCs	other metal nanoclusters
NPs	nanoparticles
MOFs	metal–organic frameworks
ZIF	zeolitic imidazole framework
BSA	bovine serum albumin
-S^{t}Bu	tert-butyl thiolate
E^0	standard reduction potential
PPh_3	triphenylphosphine
^{t}BuNH$_2$	t-butylamine
PL	photoluminescence
GSH	glutathione
LMCT	ligand to metal charge transfer
AIE	aggregation-induced emission
QY	quantum yield
LEDs	light-emitting diodes
LOD	limit of detection
AA	ascorbic acid
DA	dopamine
UA	uric acid
ECL	electrochemiluminescence
CV	cyclic voltammetry
PET	phenylethanethiolate
MBT	2-mercapto-benzothiazole
ESI	electrospray ionization
MALDI	matrix-assisted laser desorption ionization
HAADF-STEM	high-angle annular dark-field scanning transmission electron microscopy
HER	hydrogen evolution reaction
RHE	reversible hydrogen electrode
EDC	1-[(3-dimethylamino)-propyl]-3-ethylcarbodiimide hydrochloride
anti-CXCR4-Ab	anti-chemokine receptor antibody
MAA	mercaptoacetic acid
THF	tetrahydrofuran
COP	covalent organic polymer
ESI-FT-ICR	electrospray ionization Fourier transform ion cyclotron resonance
CFP	carbon fiber paper
LSV	linear sweep voltammograms
PBS	phosphate-buffered saline

References

1. Chakraborty I, Pradeep T. Atomically precise clusters of noble metals: emerging link between atoms and nanoparticles. *Chem Rev*. 2017;117(12):8208–8271.
2. Jin R, Zeng C, Zhou M, Chen Y. Atomically precise colloidal metal nanoclusters and nanoparticles: fundamentals and opportunities. *Chem Rev*. 2016;116:10346–10413.
3. Kang X, Zhu M. Tailoring the photoluminescence of atomically precise nanoclusters. *Chem Soc Rev*. 2019;48:2422–2457.
4. Zeng Y, Havenridge S, Gharib M, et al. Impact of ligands on structural and optical properties of Ag_{29} nanoclusters. *J Am Chem Soc*. 2021;143:9405–9414.
5. Zhu L, Zeng Y, Teubner M, et al. Surface engineering of gold nanoclusters protected with 11-mercaptoundecanoic acid for photoluminescence sensing. *ACS Appl Nano Mater*. 2021;4:3197–3203.

6. Zhu M, Aikens CM, Hendrich MP, et al. Reversible switching of magnetism in thiolate-protected Au_{25} superatoms. *J Am Chem Soc*. 2009;131:2490–2492.
7. Antonello S, Perera NV, Ruzzi M, Gascón JA, Maran F. Interplay of charge state, lability, and magnetism in the molecule-like $Au_{25}(SR)_{18}$ cluster. *J Am Chem Soc*. 2013;135:15585–15594.
8. Tian S, Liao L, Yuan J, et al. Structures and magnetism of mono-palladium and mono-platinum doped $Au_{25}(PET)_{18}$ nanoclusters. *Chem Commun*. 2016;52:9873–9876.
9. Agrachev M, Antonello S, Dainese T, et al. Magnetic ordering in gold nanoclusters. *ACS Omega*. 2017;2:2607–2617.
10. Zhu M, Qian H, Meng X, Jin S, Wu Z, Jin R. Chiral Au_{25} nanospheres and nanorods: synthesis and insight into the origin of chirality. *Nano Lett*. 2011;11:3963–3969.
11. Zeng C, Li T, Das A, Rosi NL, Jin R. Chiral structure of thiolate-protected 28-gold-atom nanocluster determined by X-ray crystallography. *J Am Chem Soc*. 2013;135:10011–10013.
12. Lopez-Acevedo O, Tsunoyama H, Tsukuda T, Hakkinen H, Aikens CM. Chirality and electronic structure of the thiolate-protected Au_{38} nanocluster. *J Am Chem Soc*. 2010;132:8210–8218.
13. Knoppe S, Bürgi T. Chirality in thiolate-protected gold clusters. *Acc Chem Res*. 2014;47:1318–1326.
14. Zheng K, Setyawati MI, Leong DT, Xie J. Surface ligand chemistry of gold nanoclusters determines their antimicrobial ability. *Chem Mater*. 2018;30:2800–2808.
15. Du Y, Sheng H, Astruc D, Zhu M. Atomically precise noble metal nanoclusters as efficient catalysts: a bridge between structure and properties. *Chem Rev*. 2020;120:526–622.
16. Zhou M, Zeng C, Chen Y, et al. Evolution from the plasmon to exciton state in ligand-protected atomically precise gold nanoparticles. *Nat Commun*. 2016;7:13240.
17. Galchenko M, Black A, Heymann L, Klinke C. Field effect and photoconduction in Au_{25} nanoclusters films. *Adv Mater*. 2019;31.
18. Yuan P, Zhang R, Selenius E, et al. Solvent-mediated assembly of atom-precise gold–silver nanoclusters to semiconducting one-dimensional materials. *Nat Commun*. 2020;11:2229.
19. Zhang L, Wang E. Metal nanoclusters: new fluorescent probes for sensors and bioimaging. *Nano Today*. 2014;9:132–157.
20. Xiao Y, Wu Z, Yao Q, Xie J. Luminescent metal nanoclusters: biosensing strategies and bioimaging applications. *Aggregate*. 2021;2:114–132.
21. Mathew A, Pradeep T. Noble metal clusters: applications in energy, environment, and biology. *Particle Particle Syst Charact*. 2014;31:1017–1053.
22. Ganguly A, Chakraborty I, Udayabhaskararao T, Pradeep T. A copper cluster protected with phenylethanethiol. *J Nanopart Res*. 2013;15:1522.
23. Rajamanikandan R, Ilanchelian M. Protein-protected red emittive copper nanoclusters as a fluorometric probe for highly sensitive biosensing of creatinine. *Analyt Meth*. 2018;10:3666–3674.
24. Chakraborty I, Bhuin RG, Bhat S, Pradeep T. Blue emitting undecaplatinum clusters. *Nanoscale*. 2014;6:8561–8564.
25. Ghosh A, Huang R-W, Alamer B, et al. $[Cu_{61}(StBu)_{26}S_6C_{16}H_{14}]+$: a core–shell superatom nanocluster with a quasi-J36 Cu_{19} core and an "18-Crown-6" metal-sulfide-like stabilizing belt. *ACS Mater Lett*. 2019;1:297–302.
26. Kratzl K, Kratky T, Günther S, et al. Generation and stabilization of small platinum clusters $Pt_{12}\pm x$ inside a metal–organic framework. *J Am Chem Soc*. 2019;141:13962–13969.
27. Chen L, Azeem S, Ruan M, et al. Rapid template-guided ligand-free synthesis of ultrasmall Pt nanoclusters with efficient hydrogen evolution reaction activity and their versatile release. *Nano Select*. 2021;2:758–767.
28. Shen J-S, Chen Y-L, Wang Q-P, et al. In situ synthesis of red emissive copper nanoclusters in supramolecular hydrogels. *J Mater Chem C*. 2013;1:2092–2096.
29. Li L, Huang M, Liu X, Sun D, Shao C. In situ generation of fluorescent copper nanoclusters embedded in monolithic eggshell membrane: properties and applications. *Materials*. 2018;11:1913.
30. An Y, Ren Y, Bick M, et al. Highly fluorescent copper nanoclusters for sensing and bioimaging. *Biosens Bioelectron*. 2020;154:112078.
31. Han S, Zhao YH, Zhang ZC, Xu GB. Recent advances in electrochemiluminescence and chemiluminescence of metal nanoclusters. *Molecules*. 2020;25:5208.
32. Chen TX, Xue Q, Leung KC, Lo BTW. Recent advances of precise Cu nanoclusters in microporous materials. *Chem-Asian J*. 2020;15:1819–1828.
33. Zhao ZY, Li YT. Developing fluorescent copper nanoclusters: synthesis, properties, and applications. *Colloids Surf B-Biointerf*. 2020;195:111244.

34. Gawande MB, Goswami A, Felpin F-X, et al. Cu and Cu-based nanoparticles: synthesis and applications in catalysis. *Chem Rev*. 2016;116:3722–3811.
35. Dong C, Huang R-W, Chen C, et al. $[Cu_{36}H_{10}(PET)_{24}(PPh_3)_6Cl_2]$ reveals surface vacancy defects in ligand-stabilized metal nanoclusters. *J Am Chem Soc*. 2021;143:11026–11035.
36. Cook AW, Jones ZR, Wu G, Scott SL, Hayton TW. An organometallic Cu_{20} nanocluster: synthesis, characterization, immobilization on silica, and "click" chemistry. *J Am Chem Soc*. 2018;140:394–400.
37. Dhayal RS, van Zyl WE, Liu CW. Polyhydrido copper clusters: synthetic advances, structural diversity, and nanocluster-to-nanoparticle conversion. *Acc Chem Res*. 2016;49:86–95.
38. Nguyen T-AD, Goldsmith BR, Zaman HT, Wu G, Peters B, Hayton TW. Synthesis and characterization of a Cu_{14} hydride cluster supported by neutral donor ligands. *Chem –Eur J*. 2015;21:5341–5344.
39. Nguyen T-AD, Jones ZR, Goldsmith BR, et al. A Cu_{25} nanocluster with partial Cu(0) character. *J Am Chem Soc*. 2015;137:13319–13324.
40. Nematulloev S, Huang R-W, Yin J, et al. $[Cu_{15}(PPh_3)_6(PET)_{13}]_2$+: a copper nanocluster with crystallization enhanced photoluminescence. *Small*. 2021;17.
41. Huang R-W, Yin J, Dong C, et al. $[Cu_{23}(PhSe)_{16}(Ph_3P)_8(H)_6]$·BF4: atomic-level insights into cuboidal polyhydrido copper nanoclusters and their quasi-simple cubic self-assembly. *ACS Mater Lett*. 2021;3:90–99.
42. Huang R-W, Yin J, Dong C, et al. $[Cu_{81}(PhS)_{46}(tBuNH_2)_{10}(H)_{32}]_3$+ reveals the coexistence of large planar cores and hemispherical shells in high-nuclearity copper nanoclusters. *J Am Chem Soc*. 2020;142:8696–8705.
43. Lee S, Bootharaju MS, Deng G, et al. $[Cu_{32}(PET)_{24}H_8Cl_2](PPh_4)_2$: a copper hydride nanocluster with a bisquare antiprismatic core. *J Am Chem Soc*. 2020;142:13974–13981.
44. Ren L, Yuan P, Su H, et al. Bulky surface ligands promote surface reactivities of $[Ag_{141} \times {}_{12}(S\text{-}Adm)_{40}]_3$+ (X = Cl, Br, I) nanoclusters: models for multiple-twinned nanoparticles. *J Am Chem Soc*. 2017;139:13288–13291.
45. Liu J-Y, Alkan F, Wang Z, et al. Different silver nanoparticles in one crystal: $Ag_{210}(iPrPhS)_{71}(Ph_3P)_5Cl$ and $Ag_{211}(iPrPhS)_{71}(Ph3P)_6Cl$. *Angew Chem Int Ed*. 2019;58:195–199.
46. Heaven MW, Dass A, White PS, Holt KM, Murray RW. Crystal structure of the gold nanoparticle $[N(C_8H_{17})_4][Au_{25}(SCH_2CH_2Ph)_{18}]$. *J Am Chem Soc*. 2008;130:3754–3755.
47. Zhu M, Aikens CM, Hollander FJ, Schatz GC, Jin R. Correlating the crystal structure of a thiol-protected Au_{25} cluster and optical properties. *J Am Chem Soc*. 2008;130:5883–5885.
48. Joshi CP, Bootharaju MS, Alhilaly MJ, Bakr OM. $[Ag_{25}(SR)_{18}]-$: the "golden" silver nanoparticle. *J Am Chem Soc*. 2015;137:11578–11581.
49. Maity S, Bain D, Patra A. Engineering atomically precise copper nanoclusters with aggregation induced emission. *J Phys Chem C*. 2019;123:2506–2515.
50. Yang TQ, Peng B, Shan BQ, et al. Origin of the photoluminescence of metal nanoclusters: from metal-centered emission to ligand-centered emission. *Nanomaterials (Basel)*. 2020;10:261.
51. Ai L, Jiang W, Liu Z, et al. Engineering a red emission of copper nanocluster self-assembly architectures by employing aromatic thiols as capping ligands. *Nanoscale*. 2017;9:12618–12627.
52. Gao X, He S, Zhang C, et al. Single crystal sub-nanometer sized $Cu_6(SR)_6$ clusters: structure, photophysical properties, and electrochemical sensing. *Adva Sci*. 2016;3.
53. Tashkhourian J, Sheydaei O, Nami-Ana SF. Copper nanoclusters conjugated silica nanoparticles modified on carbon paste as an electrochemical sensor for the determination of dopamine. *Appl Organomet Chem*. 2018;32: e4196.
54. Heo GS, Zhao Y, Sultan D, et al. Assessment of copper nanoclusters for accurate in vivo tumor imaging and potential for translation. *ACS Appl Mater Inter*. 2019;11:19669–19678.
55. Jeyaraj M, Gurunathan S, Qasim M, Kang M-H, Kim J-H. A comprehensive review on the synthesis, characterization, and biomedical application of platinum nanoparticles. *Nanomaterials*. 2019;9:1719.
56. Bratlie KM, Lee H, Komvopoulos K, Yang P, Somorjai GA. Platinum nanoparticle shape effects on benzene hydrogenation selectivity. *Nano Lett*. 2007;7:3097–3101.
57. Huang X, Li Z, Yu Z, Deng X, Xin Y. Recent advances in the synthesis, properties, and biological applications of platinum nanoclusters. *J Nanomater*. 2019;2019.
58. Kawasaki H, Yamamoto H, Fujimori H, Arakawa R, Inada M, Iwasaki Y. Surfactant-free solution synthesis of fluorescent platinum subnanoclusters. *Chem Commun*. 2010;46:3759–3761.
59. Garlyyev B, Kratzl K, Rück M, et al. Optimizing the size of platinum nanoparticles for enhanced mass activity in the electrochemical oxygen reduction reaction. *Angew Chem Int Ed*. 2019;58:9596–9600.

60. Chen L, Azeem S, Ruan M, et al. In: Feliu N, Mews A, ParakW,Weller H, eds. AFacile and One-pot Synthesis of Ligand-free Noble Metal Nanoclusters Catalysts on Zeolitic Imidazolate Frameworks Supports – abstract NaNaX 9 – Nanoscience with Nanocrystals, Hamburg; 2019.
61. Tanaka S-I, Miyazaki J, Tiwari DK, Jin T, Inouye Y. Fluorescent platinum nanoclusters: synthesis, purification, characterization, and application to bioimaging. *Angew Chem Int Ed*. 2011;50:431–435.
62. Chen D, Zhao C, Ye J, et al. In situ biosynthesis of fluorescent platinum nanoclusters: toward self-bioimaging-guided cancer theranostics. *ACS Appl Mater Inter*. 2015;7:18163–18169.
63. Tanaka S-i, Wadati H, Sato K, Yasuda H, Niioka H. Red-fluorescent Pt nanoclusters for detecting and imaging HER2 in breast cancer cells. *ACS Omega*. 2020;5:23718–23723.
64. Erickson JD, Mednikov EG, Ivanov SA, Dahl LF. Isolation and structural characterization of a Mackay 55-metal-atom two-shell icosahedron of pseudo-Ih symmetry, $Pd_{55}L_{12}(\mu_3\text{-}CO)_{20}$ (L = PR3, R = Isopropyl): comparative analysis with interior two-shell icosahedral geometries in capped three-shell Pd_{145}, Pt-centered four-shell Pd–Pt M_{165}, and four-shell Au_{133} nanoclusters. *J Am Chem Soc*. 2016;138:1502–1505.
65. Moiseev II, Stromnova TA, Vargaftig MN, Mazo GJ, Kuz'Mina LG, Struchkov YT. New palladium carbonyl clusters: X-ray crystal structure of $[Pd_4(CO)_4(OAc)_4]\cdot(AcOH)_2$. *J Chem Soc, Chem Commun*. 1978;1:27–28.
66. Mednikov EG, Eremenko NK, Mikhailov VA, Gubin SP, Slovokhotov YL, Struchkov YT. New palladium cluster compounds. X-ray crystal structure of $Pd_{10}(CO)_{12}(PBu_3n)_6$. *J Chem Soc, Chem Commun*. 1981;19:989–990.
67. Wei J, Kahlal S, Halet J-F, Saillard J-Y. Elucidating the electronic structure of the ligated cuboctahedral palladium cluster $[Pd_{13}(\mu_4\text{-}C_7H_7)_6]_2+$. *J Cluster Sci*. 2019;30:1227–1233.
68. Mednikov EG, Jewell MC, Dahl LF. Nanosized $(\mu_{12}\text{-}Pt)Pd_{164}\text{-}xPtx(CO)_{72}(PPh_3)_{20}$ ($x \approx 7$) containing Pt-centered four-shell $_{165}$-atom Pd−Pt core with unprecedented intershell bridging carbonyl ligands: comparative analysis of icosahedral shell-growth patterns with geometrically related $Pd_{145}(CO)x(PEt_3)_{30}$ ($x \approx 60$) containing capped three-shell Pd_{145} core. *J Am Chem Soc*. 2007;129:11619–11630.
69. Teramoto M, Iwata K, Yamaura H, et al. Three-dimensional sandwich nanocubes composed of 13-atom palladium core and hexakis-carbocycle shell. *J Am Chem Soc*. 2018;140:12682–12686.
70. Dart JW, Lloyd MK, Mason R, McCleverty JA, Williams J. Properties of isocyanide ligands in metal complexes. Characterisation and voltammetric properties of bis(tertiary phosphine)tris(iso-nitrile)cobalt(I) complexes. *J Chem Soc, Dalton Trans*. 1973;17:1747–1751.
71. Cook AW, Hrobárik P, Damon PL, Wu G, Hayton TW. A ketimide-stabilized palladium nanocluster with a hexagonal aromatic Pd_7 core. *Inorg Chem*. 2020;59:1471–1480.
72. Zhu Y, Wang WD, Sun X, Fan M, Hu X, Dong Z. Palladium nanoclusters confined in MOF@COP as a novel nanoreactor for catalytic hydrogenation. *ACS Appl Mater Inter*. 2020;12:7285–7294.
73. Hyotanishi M, Isomura Y, Yamamoto H, Kawasaki H, Obora Y. Surfactant-free synthesis of palladium nanoclusters for their use in catalytic cross-coupling reactions. *Chem Commun*. 2011;47:5750–5752.
74. Liu L, Corma A. Metal catalysts for heterogeneous catalysis: from single atoms to nanoclusters and nanoparticles. *Chem Rev*. 2018;118:4981–5079.
75. Reier T, Oezaslan M, Strasser P. Electrocatalytic oxygen evolution reaction (OER) on Ru, Ir, and Pt catalysts: a comparative study of nanoparticles and bulk materials. *ACS Catal*. 2012;2:1765–1772.
76. Li C, Baek J-B. Recent advances in noble metal (Pt, Ru, and Ir)-based electrocatalysts for efficient hydrogen evolution reaction. *ACS Omega*. 2020;5:31–40.
77. Xu Z, Xiao FS, Purnell SK, et al. Size-dependent catalytic activity of supported metal clusters. *Nature*. 1994;372:346–348.
78. Argo AM, Odzak JF, Gates BC. Role of cluster size in catalysis: spectroscopic investigation of $\gamma\text{-}Al_2O_3$-supported Ir_4 and Ir_6 during ethene hydrogenation. *J Am Chem Soc*. 2003;125:7107–7115.
79. Aydin C, Lu J, Browning ND, Gates BC. A "smart" catalyst: sinter-resistant supported iridium clusters visualized with electron microscopy. *Angew Chem Int Ed*. 2012;51:5929–5934.
80. Kerpal C, Harding DJ, Meijer G, Fielicke A. CO adsorption on neutral iridium clusters. *Eur Phys J D*. 2011;63:231–234.
81. Bhat S, Chakraborty I, Baksi A, Narayanan RP, Pradeep T. Evolution of atomically precise clusters through the eye of mass spectrometry. In: *Nanoscience: Volume 3*. The Royal Society of Chemistry, Thomas Graham House, Science Park, Milton Road,Cambridge CB4 0WF, UK; 2016:343–385.
82. Yamamoto H, Maity P, Takahata R, et al. Monodisperse iridium clusters protected by phenylacetylene: implication for size-dependent evolution of binding sites. *J Phys Chem C*. 2017;121:10936–10941.

83. Gavia DJ, Do Y, Gu J, Shon Y-S. Mechanistic insights into the formation of dodecanethiolate-stabilized magnetic iridium nanoparticles: thiosulfate vs thiol ligands. *J Phys Chem C*. 2014;118:14548–14554.
84. Yee CK, Jordan R, Ulman A, et al. Novel one-phase synthesis of thiol-functionalized gold, palladium, and iridium nanoparticles using superhydride. *Langmuir*. 1999;15:3486–3491.
85. Wang Q, Xu C-Q, Liu W, et al. Coordination engineering of iridium nanocluster bifunctional electrocatalyst for highly efficient and pH-universal overall water splitting. *Nat Commun*. 2020;11:4246.
86. Vankayala R, Gollavelli G, Mandal BK. Highly fluorescent and biocompatible iridium nanoclusters for cellular imaging. *J Mater Sci Mater Med*. 2013;24:1993–2000.

CHAPTER

20

Thiols as ligands and structural control of nanoclusters

Edakkattuparambil Sidharth Shibu[a] *and Thalappil Pradeep*[b]

[a]Department of Nanoscience and Technology, University of Calicut, Kerala, India
[b]Deepak Parekh Institute Chair Professor and Professor of Chemistry, Department of Chemistry, Indian Institute of Technology Madras, Chennai, India

20.1 Introduction

The self-assembled monolayers (SAMs) of organic moieties on 2D bulk metal surfaces became the foundation for many metal-based nanostructures.[1–3] Over the last few decades, the effective chemisorption of thiol molecules on coinage metal (Au, Ag, and Cu) surfaces has evolved significantly. At the beginning of 1990s, researchers developed a protocol for the fabrication of thiol stabilized metal nanoparticles by the simultaneous anchoring of protecting moieties on growing nuclei.[4–8] The strong metal–thiol interaction could help to prevent oxidation and metal atom agglomeration. Among the coinage metals, the thiol-protected gold nanosystems received notable attention and were considered as the model system. To create thiol-stabilized gold nanoparticles, a two-phase chemical reduction approach was performed, in which inorganic gold salts and organic functional thiol units were mixed in presence of a phase transferring catalyst. The thiol functionalized organic molecules form a 3D self-assembled monolayer around the metallic core during reduction, resulting in gold NPs. Following their footsteps, silver and copper NPs have also been explored in detail. Nevertheless, coinage metal NPs encountered some basic barriers such as poor size dispersity (or atomic precision) and complex metal core/ligand interfaces. Researchers attempted to deduce the total structure of nanoparticles with atomic precision to overcome such fundamental limitations. In the late 2000s, atomically precise nanoclusters of coinage metals were made[9–12] owing to the simple synthetic protocol and high stability under aerobic conditions, gold nanoclusters were extensively used for various applications. Compared to gold nanoclusters, those of silver and copper were readily oxidizable in air. Nevertheless, recent research activities identified several potential nanoclusters of them with improved stability.[13] The structure of thiolate-protected

Atomically Precise Metal Nanoclusters.
DOI: https://doi.org/10.1016/B978-0-323-90879-5.00004-4

gold nanoclusters typically has a metal core with Au-Au bonds and surface $[Au_n(SR)_{n+1}]$ ($n = 1, 2$) staple motifs. But, the surface motifs of silver and copper are more complicated or distinct than those of gold nanoclusters. A comparative study of geometrical structures of coinage metal nanoclusters showed that the gold core consisting of fewer gold atoms ($n = 3$–12) tends to form 2D planar structures, whereas 3D geometrical designs are created when $n \geq 13$. On the other hand, silver and copper nanoclusters can form 3D structures even with five atoms. Furthermore, electronic charges also could influence the geometrical structures of coinage metals.[14] These functionally rich thiol-protected precision coinage metal nanoclusters are an exciting piece of science due to their tunable optoelectronic properties. This chapter will discuss the origin of precision nanoclusters, the role of thiols on their structural control, and the evolution of interesting photophysical, electrochemical, and catalytic properties due to surface functionalization. The enhanced optical properties resulting from the periodic self-organization of functional nanoclusters via different methods will be discussed toward the end of this chapter.

20.2 Origin of monolayer thiol-protected precision nanoclusters

20.2.1 Thiol-protected gold nanoclusters

The synthesis of monolayer-thiol-protected gold nanoclusters received a tremendous boost after the development of the two-phase Brust–Schiffrin method in 1994.[4] The synthesis typically involves two steps, in which an aqueous solution of Au^{3+} ions ($HAuCl_4{\cdot}3H_2O$) was phase-transferred into an organic (toluene) layer using tetraoctylammonium bromide (TOABr) as the phase transfer agent. Subsequently, the Au(I)-thiolates were prepared by reducing the phase-transferred Au^{3+} ions with long chain-alkyl thiols added at a molar ratio of 1:1. The freshly prepared Au(I)-alkyl thiolates were reduced at the oil–water interface using an aqueous solution of excess sodium borohydride ($NaBH_4$) to yield nanoparticles soluble in organic medium. Further, the gold to thiol molar ratio was slightly modified (1:3) to produce small-sized organic-soluble gold nanoclusters stabilized with various alkyl thiols.[8] The precipitation of the as-prepared nanoclusters by adding excess ethanol or acetone harvested the black crystalline nanocluster powder. Successively, a series of stable magic number nanoclusters were separated and identified from the above-prepared black powder with core masses ca. 8, 14, 22, and 29 kDa using laser desorption ionization mass spectrometry (LDI-MS).[5,15] A modified chemical reduction strategy was used to demonstrate the formation of water-soluble nanoclusters stabilized with biologically relevant and ecofriendly tripeptide, L-γ-glutamyl-L-cysteinyl-glycine (glutathione; GSH).[16] In a typical synthesis, the chemical reduction of Au(I)-SG thiolates prepared in water by mixing Au^{3+} ions and GSH at a molar ratio of 1:3, using excess $NaBH_4$ resulted in [Au@SG] nanoclusters. The nanoclusters were purified and separated using the polyacrylamide gel electrophoresis (PAGE) method. The molecular composition of the most abundant species, $[Au_{28}(SG)_{16}]$, was confirmed by mass spectrometry. Later, Negishi et al. demonstrated the size-selective synthesis, separation, and identification of water-soluble $[Au_n(SG)_m]$ magic number nanoclusters, including $[Au_{10}(SG)_{10}]$, $[Au_{15}(SG)_{13}]$, $[Au_{18}(SG)_{14}]$, $[Au_{22}(SG)_{16}]$, $[Au_{22}(SG)_{17}]$, $[Au_{25}(SG)_{18}]$, $[Au_{29}\ (SG)_{20}]$, $[Au_{33}(SG)_{22}]$, and $[Au_{39}(SG)_{24}]$.[17,18] The formation of mixed nanoclusters and low synthetic yield were the major

drawbacks of the above-mentioned methods. Later, a variety of new protocols were introduced to synthesize size-specific nanoclusters in large quantities. Among these, the gram-scale synthesis of $[Au_{25}(SG)_{18}]$ from $[Au_{11}(PPh_3)_8Cl_3]$ nanocluster (undecagold) by a ligand-exchange reaction with excess GSH was found to be promising.[19] In this synthesis route, the precursor, $[Au_{11}(PPh_3)_8Cl_3]$ was prepared by reducing $[AuCl(PPh_3)]$ in ethanol using $NaBH_4$ under N_2 atmosphere. Vigorous stirring of a mixture of $[Au_{11}(PPh_3)_8Cl_3]$ in chloroform and GSH in water resulted in a highly monodisperse $[Au_{25}(SG)_{18}]$ nanocluster via ligand exchange followed by a core-ripening method. Further, the core-etching reaction of a mixture of [Au@SG] nanoclusters with excess GSH at elevated temperature (70–80°C) resulted in the selective formation of $[Au_{25}(SG)_{18}]$.[20] The greater affinity of thiols toward gold could control the core reduction (or addition) during the core-etching (or core-ripening) reactions. A two-phase Brust–Schiffrin method was adopted using 2-phenylethanethiol (PET) for the size-selective synthesis of $[Au_{25}(PET)_{18}]$ nanoclusters in toluene.[20] In this method, control over the reaction temperature resulted in better yield of nanoclusters. The reduction of Au(I)-thiolates at 0°C produced large quantities of nanoclusters compared to the room temperature procedure. To avoid the difficulties encountered during the two-phase reduction protocol, a modified Brust–Schiffrin one-pot procedure was proposed by replacing toluene with tetrahydrofuran (THF).[21] Later, the protection–deprotection strategy was proposed for the ultrafast synthesis of Au_{25} nanoclusters.[22] In this method, a surfactant molecule (cetyltrimethylammonium bromide; CTAB) was initially introduced into the reaction mixture to protect Au(I)-Cys thiolate (Cys = L-cysteine) during the reduction process. Later, CTAB was detached from the surface of the CTAB-capped $[Au_{25}(Cys)_{18}]$ nanocluster through dissolution in toluene. This method helped to harvest highly pure $[Au_{25}(Cys)_{18}]$ nanoclusters within a short time frame. Parallelly, a slow reduction method for the selective synthesis of $[Au_{25}(Cys)_{18}]$ nanoclusters was demonstrated.[23] In this method, the reduction rate of the Au(I)-thiolate complex was controlled by replacing the traditional $NaBH_4$ solution with CO gas. Here, NaOH was added to an aqueous solution of gold precursor and Cys to maintain the pH (~11), followed by saturating the reaction solution with CO gas (1 bar) for 2 min. The slow reduction of Au(I)-thiolates in the presence of CO gas under a sealed condition produced $[Au_{25}(Cys)_{18}]$ nanoclusters within 24 h. Notably, size-selected nanoclusters were formed when the pH of the reaction mixture was optimized. For example, $[Au_{10–12}(SG)_{10–12}]$, $[Au_{15}(SG)_{13}]$, $[Au_{18}(SG)_{14}]$, and $[Au_{25}(SG)_{18}]$ were selectively produced when the pH of the reaction mixture was set at 7, 9, 10, and 11, respectively in the presence of CO gas.[24] Later, gram-scale production of water-soluble size-selected nanoclusters was reported by NaOH-mediated $NaBH_4$ reduction.[25] NaOH was initially introduced into an aqueous mixture of gold precursor and thiol, which helped to control the rate of formation of gold(I)-thiolate complexes in the reaction mixture. Successive addition of aqueous $NaBH_4$ into the above solution resulted in Au_{25} nanoclusters in large quantities.

20.2.2 Thiol-protected silver nanoclusters

Despite tremendous progress in producing various gold nanoclusters, the evolution of precision silver nanoclusters was delayed due to the stability issues resulting from their surface oxidation. The thiol-protected silver nanoclusters were first reported in 2006,[26] wherein the two-step Brust–Schiffrin protocol was adopted to synthesize 4-(*tert*-butyl)benzyl mercaptan

(BBSH)-stabilized silver nanoclusters with mixed molecular masses, ca. 15.8 and 28.2 kDa. Later, the cyclic reduction approach under oxidative conditions was introduced to reduce the surface oxidation of the silver core.[27] In this method, chemical ($NaBH_4$) reduction of silver salt ($AgNO_3$) in the presence of water-soluble monothiol (captopril; Capt), hydrogen peroxide, and citric acid produced size-selected silver nanoclusters. Hydrogen peroxide and citric acid served as the oxidizing agent and charge-stabilizing ligand, respectively. The core-etching reaction of bigger nanoparticles in the presence of excess thiols was also employed to produce size-selected silver nanoclusters.[28] The interface chemistry has great potential to control the core size of nanoclusters. Such chemistry has been utilized to synthesize Ag_7 and Ag_8 nanoclusters by the core-etching of MSA (MSA = mercaptosuccinic acid) capped silver nanoparticles using an aqueous/organic solvent mixture.[29,30] Briefly, the room temperature stirring of previously prepared water-soluble MSA-capped nanoparticles (water) in the presence of excess MSA (toluene) for 48 h resulted in orange-colored nanoclusters in the aqueous phase. The etching happens at the solvent–water interface. Sometimes, the interaction of nanoclusters with specific thiol molecules has the potential to direct the ripening of smaller nanoclusters into bigger ones. For example, incubation of $[Ag_{140}(SBB)_{53}]$ nanoclusters with neat BBSH (without any solvents) at elevated temperature (60°C) produced $[Ag_{280}(SBB)_{120}]$ nanoclusters.[31] In some cases, the neat chemical reactions help to achieve better control over size-selected nanoclusters. Concurrent with this, the solid-state route developed for the selective production of Ag_9 nanoclusters[32] was found to be straightforward and precise compared to the traditional solution-phase chemical reduction method. Here, a mixture of solid $AgNO_3$ and MSA (1:5 molar ratio) was initially ground well until an orange-colored silver-thiolate was formed. The addition of solid $NaBH_4$ into the above thiolate with constant grinding resulted in a brownish-black powder. At this point, the compounds were mixed well, followed by the addition of water over a period of 1 min. Nanoclusters were precipitated upon addition of excess ethanol, purified by PAGE, and the molecular composition ($[Ag_9(H_2MSA)_7]$) was determined by ESI-MS. Furthermore, dithiols, rather than monothiols, were discovered to provide better stability to silver nanoclusters. One such example is the formation of $[Ag_7(DMSA)_4]$ nanoclusters by the chemical reduction of an ethanolic solution of $AgNO_3$ and DMSA (DMSA = 2,3-dimercaptosuccinic acid) at 0°C by the slow addition of $NaBH_4$ powder.[33] Later, the role of bulky thiols on size-selective production of nanoclusters was investigated. To address the importance of the bulky substitutions on the thiol skeleton, two different thiols, viz, 2,4-dimethylbenzenethiol ($HSPhMe_2$) and 2,4-difluorobenzenethiol ($HSPhF_2$) were taken.[34] The $NaBH_4$ reduction of $AgNO_3$ in the presence of $HSPhMe_2$ resulted in the formation of precision $[Ag_{25}(SPhMe_2)_{18}]^-$ nanoclusters. On the other hand, a similar reaction with $HSPhF_2$ directed the formation of $[Ag_{44}(SPhF_2)_{30}]$ nanoclusters. The influence of bulky thiols on the size-focused synthesis of nanoclusters was studied in detail.[35] Three ligands, (I) small alkanethiol (6-mercaptohexanoic acid; MHA), (II) medium-sized aromatic-thiol (*p*-mercaptobenzoic acid; *p*-MBA), and (III) a bulky thiol (GSH), were selected to demonstrate the synthesis of water-soluble silver nanoclusters using a modified NaOH-mediated $NaBH_4$ reduction method[25] under similar experimental conditions. The reaction of $AgNO_3$ with MHA, *p*-MBA, and GSH generated $[Ag_{25}(MHA)_{18}]$, $[Ag_{9–15}(SG)_{5–10}]$, and $[Ag_{44}(p\text{-MBA})_{30}]$ nanoclusters, respectively. It is evident from the above two sets of experiments that the bulky substituted thiols always direct the formation of smaller-sized nanoclusters compared to the simple thiols owing to former's larger steric hindrance.

20.3 Surface functionalization of nanoclusters via ligand replacement reaction

The in situ fabrication of size-selected nanoclusters protected with every functional thiol is impossible due to restricted factors such as steric hindrance, solubility, polarity, etc. However, the postsynthetic method, especially the ligand replacement reaction, helped to impart the required functionalities on the nanocluster surface. Constant stirring of a mixture of nanocluster solution and the desired functional thiol at a certain temperature for a specific time frame could harvest functional nanoclusters via the ligand replacement reaction. Such reactions in monolayer thiol-protected nanoclusters were known since 1996.[6,36–38] Later, the ligand-exchange reactions of $[Au_{25}(SG)_{18}]$ nanoclusters with 3-mercapto-2-butanol (MB) were studied in detail.[39] The in situ replacement of bound-SG with MB was observed in the time-dependent ^1H nuclear magnetic resonance (NMR) spectra. The unaltered binding energies of Au_{25} nanoclusters in the X-ray photoelectron spectra (XPS) before and after the ligand-exchange reaction proved their core stability. Though the ligand-exchange reaction is straightforward and convenient, a complete replacement of ligands could not be realized. A two-phase ligand exchange protocol was introduced to address the complete ligand replacement.[40] The addition of cyclohexylthiol (in dichloromethane; DCM) into an aqueous solution of $[Au_{18}(SG)_{14}]$ nanoclusters followed by constant stirring at 313 K resulted in the complete replacement of GSH. The final product, $[Au_{18}(SC_6H_{11})_{14}]$ nanocluster, was automatically phase-transferred into DCM due to its preferential solubility in the organic solvent. The interaction of nanoclusters with externally added thiols sometimes leads to core reduction or expansion, resulting in the production of smaller or bigger-sized nanoclusters. In such cases, the parent nanocluster will act as a sacrificial template to initiate the reaction. For example, the room temperature ligand-exchange attempt on $[Au_{25}(SG)_{18}]$ with porphyrin thiol at the water–toluene interface produced Au_{22} nanoclusters via a core-reduction followed by ligand-exchange process.[41] However, constant stirring of a mixture of $[Au_{25}(PET)_{18}]$ nanoclusters with excess 4-*tert*-butylbenzenthiol (TBBT) at 80°C resulted in the formation of $[Au_{28}(TBBT)_{20}]$ nanoclusters via core-ripening followed by ligand-exchange process.[42] The above-mentioned core-reduction and core-expansion methods are irreversible. As a result, the new nanoclusters formed via the ligand-exchange reaction cannot revert to the initial size/shape. The reversible transformation of nanoclusters can be achieved by an appropriate selection of thiol molecules. For example, the reversible core conversion between $[Ag_{44}(SPhF)_{30}]$ and $[Ag_{25}(SPhMe_2)_{18}]$ nanoclusters was reported by stirring the nanoclusters with excess $HSPhMe_2$ and HSPhF, respectively, at room temperature.[43,44] The switchable core conversion was evident from their temporal optical absorption (Fig. 20.1) and ESI-MS spectra.

20.4 Surface modification of nanoclusters via functional transformation chemistry

Another possible way to functionalize the nanocluster surface is through chemical transformation reactions. The well-practiced chemical transformation reactions that have been efficiently used to functionalize nanocluster surfaces are (i) carbodiimide crosslinking chemistry (EDC or DCC coupling) and (ii) click reaction.

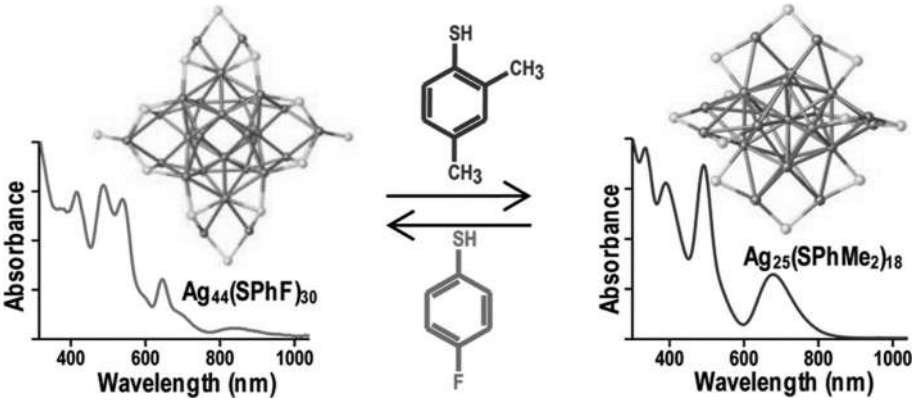

FIGURE 20.1 Switchable optical absorption and crystal structure of $[Ag_{44}(SPhF)_{30}]$ and $[Ag_{25}(SPhMe_2)_{18}]$ nanoclusters in the presence of $HSPhMe_2$ and HSPhF. Reproduced with permission from ref.[43] Copyright 2016 American Chemical Society.

20.4.1 EDC/DCC coupling

The carbodiimide crosslinking chemistry is one of the most versatile and popular methods used to crosslink the carboxylic acid terminated nanosurface with the desired molecules holding primary amine. The easily available carbodiimides are EDC (1-ethyl-3-(3-dimethylaminopropyl)carbodiimide; water-soluble) for aqueous crosslinking and DCC (*N*, *N*′-dicyclohexylcarbodiimide; organic-soluble) for nonaqueous crosslinking reactions. Both EDC or amines via amide bond formation. The reaction of EDC or DCC with carboxylic acid groups results in an active unstable intermediate (O-acylisourea), which could easily be replaced by a nucleophilic attack using the primary amine. Finally, the by-product (urea derivative) was removed via filtration or extraction, depending on its solubility. The addition of *N*-hydroxysuccinimide (NHS) or their water-soluble analog (sulfo-NHS) during the reaction could enhance the reactivity of EDC/DCC coupling. The NHS/sulfo-NHS can immediately react with unstable O-acylisourea to form a stable NHS/sulfo-NHS ester derivative, which allows an efficient conjugation with a primary amine to form the final product. EDC/DCC reactions have been extensively used to conjugate the peptides or small protein molecules on the nanocluster surface.[45–53]

20.4.2 Click reaction

Click reaction has been successfully employed to conjugate the nanocluster surface with desired molecules. The classic click reaction involves the copper(I) catalyzed conjugation reaction between azide and alkyl terminated molecules to form a five-membered heteroatom ring (triazole ring), and is known as copper(I)-catalyzed azide-alkyne cycloaddition reaction (CuAAC). To accomplish such reactions, nanosurface is prefunctionalized with azide or alkyl terminating groups. This can be done by either directly synthesizing nanoprobes with azide/alkyl terminated thiols or the ligand-exchange reaction with corresponding thiols. Though CuAAC has been used to conjugate the nanoparticle surface, it was not successful in nanoclusters due to their poor stability in the presence of Cu(I) ions. To circumvent

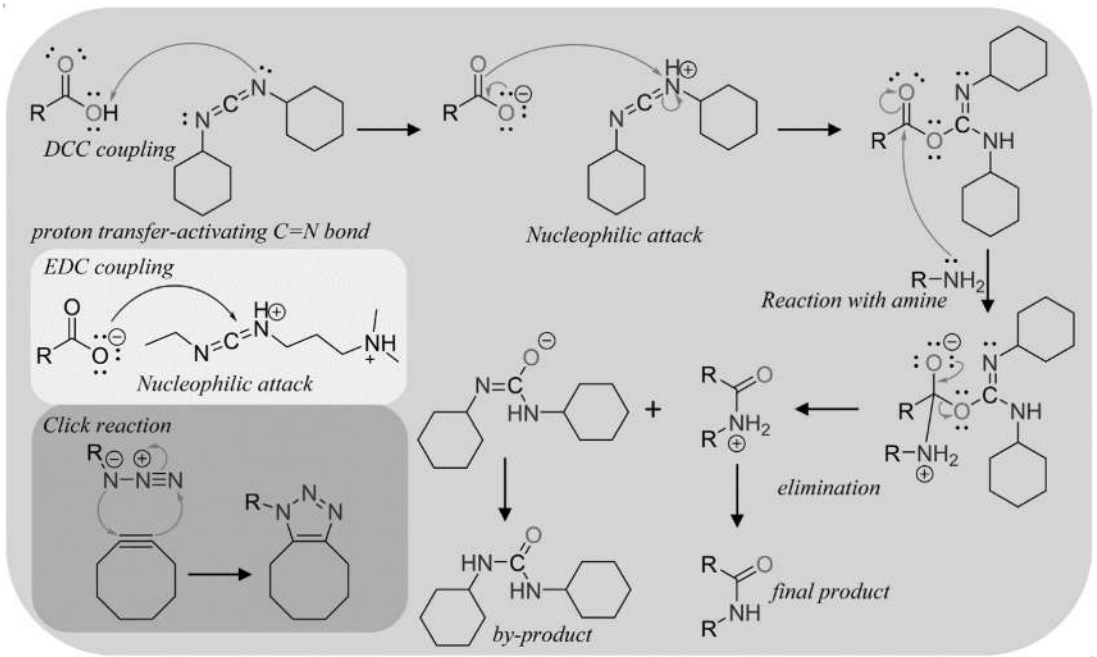

SCHEME 20.1 This scheme represents the mechanism for DCC and EDC coupling and SPAAC reaction.

this issue, the catalyst-free, strain-promoted azide-alkyne cycloaddition reaction (SPAAC) was introduced on the nanocluster surface by carefully choosing the functional thiols.[54] To demonstrate SPAAC, Au_{25} nanocluster was initially synthesized using the azide-terminated alkyl thiol ($HSCH_2CH_2$-*p*-C_6H_4-N_3). The addition of a symmetrical strained-cyclooctyne to the purified azide-terminated Au_{25} nanoclusters resulted in the conjugated product (triazole) within 5 min, irrespective of the solvents used. SPAAC has been further demonstrated on [$Au_{28}(SPhN_3)_{20}$] nanocluster surface.[55] Since the metal-free SPAAC is unique and fast, such reactions have found numerous applications, especially in live-cell labeling. The mechanisms for DCC and EDC coupling and SPAAC are shown in Scheme 20.1.

20.5 Chemistry of surface ligands

The previous section discussed in detail the route to modify nanocluster surfaces without altering their photophysical properties. Such functionally rich nanoclusters can be considered as unique materials to investigate different surface chemistry, including photochemistry, electrochemistry, optical chirality, catalysis, etc. This section will cover the chemistry of the nanocluster surface, resulting from the bound functional moieties.

20.5.1 Photochemistry

The different photochemical events, such as energy transfer, electron transfer, photoisomerization, and photosensitization of nanocluster surfaces, will be discussed in this section.

20.5.1.1 Energy transfer

To demonstrate the energy transfer process on the nanocluster surface, suitable chromophores should be integrated into them. For example, successful Förster resonance energy transfer (FRET) from a chromophore to water-soluble Au_{25} nanoclusters was demonstrated by carefully conjugating dansyl molecules on the surface of $[Au_{25}(SG)_{18}]$ nanoclusters.[56] Dansyl moieties were tethered on the nanocluster surface by both direct reaction with dansyl chloride and by replacing the bound –SG with presynthesized dansyl-GSH molecules. In the direct method, the dansyl moieties were anchored on the presynthesized $[Au_{25}(SG)_{18}]$ nanocluster surface by the addition of dansyl chloride in the presence of NaOH. For the ligand exchange reaction, dansyl-GSH molecules were synthesized by reacting the oxidized GSH and dansyl chloride under alkaline pH (~9) conditions. The overlap integral between the emission spectrum of the dansyl chromophore and the excitation spectrum of the nanocluster was well adapted for dansyl chromophore to act as a donor (D) and the nanocluster as an acceptor (A) in the energy transfer process. FRET from dansyl to Au_{25} core was evident from the drastic decrease in the excited state lifetime of dansyl moiety and corresponding fluorescence quenching. The calculated Förster distance (d_0; the distance between D and A at which the FRET efficiency is 50%) was found to be 41 Å, and was calculated using the equation given below.

$$d_0 = 0.211\,[\kappa^2\, n^{-4}\, Q_D J(\lambda)]^{\frac{1}{6}}\,(\text{Å})$$

where κ^2 is the orientation factor (in space) between the transition dipoles of D and A, n is the refractive index of the medium, and Q_D is the quantum yield of D.

The overlap integral, $J(\lambda)$, can be calculated using the equation shown below.

$$J(\lambda) = \int_0^\infty (F_D(\lambda)\varepsilon\ (\lambda)\ \lambda^4\ d\lambda) \Big/ \int_0^\infty (F_D(\lambda)\ d\lambda)$$

$F_D(\lambda)$ is the fluorescence intensity of D, $\varepsilon(\lambda)$ is the extinction coefficient of A.

The efficiency of energy transfer (E_{FRET}) is calculated using the equation

$$E_{\text{FRET}} = \left(1 - \frac{\tau_{DA}}{\tau_D}\right)$$

$\boldsymbol{\tau}_{\text{DA}}$ and τ_{D} are the average lifetime of **D** in the presence and absence of **A**, respectively.

An efficient FRET from nanocluster to the chromophore[43] occurs although the reverse process was also reported. To address such unexpected FRET, a pH-responsive chromophore, aminofluorescein (AF), was conjugated on the surface of previously synthesized $[Au_{22}(SG)_{18}]$ nanoclusters[57] via the EDC coupling reaction. The primary amine group in GSH was initially protected with benzyl chloroformate, which avoided the coupling among GSH units. The transient absorption measurements of AF-conjugated Au_{22} nanoclusters showed two ultrafast relaxation processes; (i) nonthermalized energy transfer from Au_{22} to AF and (ii) intracore-state relaxation. Surprisingly, FRET from Au_{22} to AF was found to vary by changing the pH. As a result, the FRET rate increased with increasing pH due to improved overlap of spectral integral between **D** (Au_{22}) and **A** (AF). Notably, the fluorescence from AF increased up to 160-fold when the pH changed from 4.3 to 7.8. The pH-dependent emission was originated from the acid dissociation and spirocycle ring-opening processes. The dianionic form of AF generated at higher pH was responsible for the better fluorescence and ultrafast FRET (Fig. 20.2).

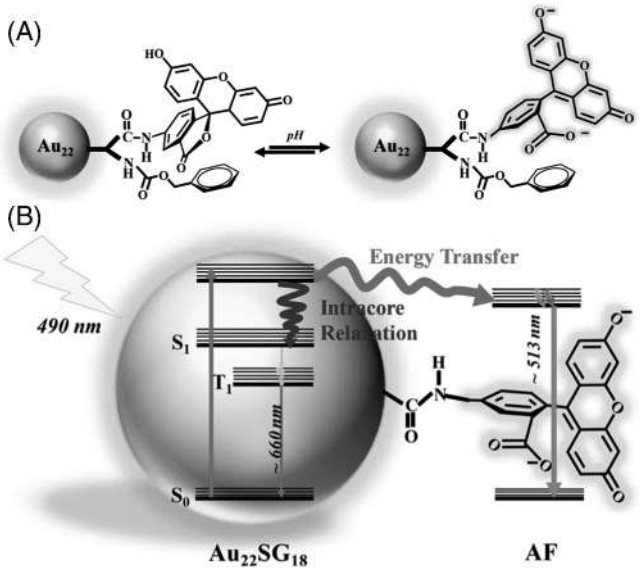

FIGURE 20.2 (A and B) represent the spirocycle ring-opening process in AF conjugated Au_{22} nanoclusters and the nonthermalized FRET from Au_{22} to AF in AF conjugated Au_{22} nanoclusters. Reproduced with permission from ref.[52] Copyright 2018 American Chemical Society.

20.5.1.2 Electron transfer

The energy transfer and electron transfer are two competing processes in well-defined **D**–**A** dyads. However, one could control the rate of energy transfer and electron transfer by suitably selecting **D** and **A**. An efficient electron transfer from Au_{25} core to the covalently conjugated chromophore was reported in $[Au_{25}(SC_6)_{17}(SPy)_1]$ nanoclusters.[58] To address the electron transfer process in Au_{25} nanoclusters, a single pyrenethiol (PySH) was carefully tethered on the surface of $[Au_{25}(SC_6)_{18}]$ nanoclusters via the ligand-exchange reaction to yield $[Au_{25}(SC_6)_{17}(SPy)_1]$. The unaltered optical absorption spectrum of $[Au_{25}(SC_6)_{17}(SPy)_1]$ nanoclusters compared to the parent $[Au_{25}(SC_6)_{18}]$ and PySH ruled out the ground-state interactions between Au_{25} core and pyrene in $[Au_{25}(SC_6)_{17}(SPy)_1]$ hybrid. However, the strong excited-state interactions were evident from the drastic fluorescence quenching of pyrene in the hybrid nanoclusters. As a result of electron/energy transfer process, the fluorescence quantum yield of pyrene decreased from 54% to 0.8% in the hybrid system. The photoexcited electron/energy transfer process in $[Au_{25}(SC_6)_{17}(SPy)_1]$ hybrid system was well studied using the excited state absorption spectra. The mismatch in the transient absorption spectrum of $[Au_{25}(SC_6)_{17}(SPy)_1]$ with the parent $[Au_{25}(SC_6)_{18}]$ nanoclusters and PySH ruled out the feasibility of the energy transfer process. Nevertheless, an efficient electron transfer in $[Au_{25}(SC_6)_{17}(SPy)_1]$ was obvious due to the presence of pyrene radical anion in the transient absorption spectrum.

Free energy of the electron transfer process was estimated using the Rehm–Weller equation shown below.

$$\Delta G = e\left[E_{\frac{D}{D+}} - E_{\frac{A}{A-}}\right] - E_{00} + w_p$$

$E_{D/D+}$ and $E_{A/A-}$ are the oxidation and reduction potentials of **D** and **A**, E_{00} is the excitation energy of the photoexcited species, and w_p is the Coulombic interaction term (insignificant

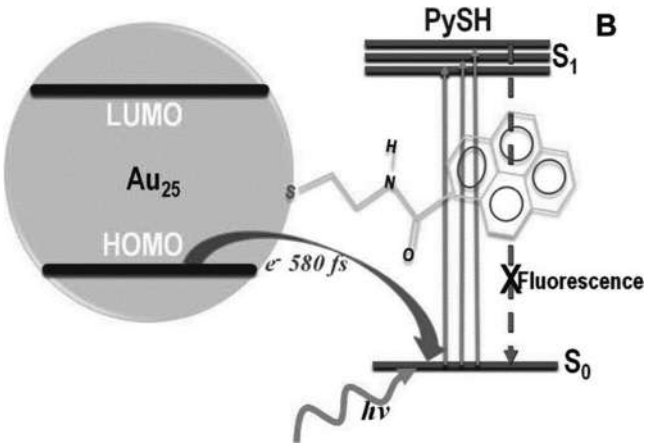

FIGURE 20.3 Schematic shows the photoinduced directional electron transfer from Au_{25} core to pyrene. Reproduced with permission from ref.[58] Copyright 2010 American Chemical Society.

in polar media). The estimated free energies of the electron transfer process from (i) Au_{25} to the excited pyrene and (ii) excited pyrene to Au_{25} are −1.37 and −0.16 eV, respectively. The free energy calculations have shown that the electron transfer from the HOMO of Au_{25} to the HOMO of the photoexcited pyrene is more feasible due to the higher negative ΔG value (Fig. 20.3).

20.5.1.3 Photoisomerization

Another possible photochemistry explored on the nanocluster surface is photoswitchable isomerization under a defined spectrum of light. The photoisomers of nanoclusters could be obtained by smartly tailoring the photoswitchable ligands on the nanocluster surface. Azobenzene and spiropyran are two prominent photoisomerizing chromophores used to demonstrate photoisomerization on nanosurfaces.[59,60] These molecules can change their conformation when irradiated with a particular wavelength of light. Two geometrical isomers (*cis* and *trans*) can be distinctly isolated on irradiation with UV and visible light, respectively. To demonstrate the photoswitchable isomerization in nanoclusters, azobenzene alkyl monothiol (C_3-AMT) tethered Au_{25} nanoclusters[61] were synthesized using the modified one-pot Brust–Schiffrin method.[21] Energy-minimized structures of $[Au_{25}(C_3\text{-AMT})_{18}]^-$ nanoclusters optimized using density functional theory (DFT) have shown two well-distinguished photoisomers (Fig. 20.4A). The *trans* isomers of C_3-AMT and $[Au_{25}(C_3\text{-AMT})_{18}]^-$ showed optical absorption maximum in the UV region (λ_{max} = 345 nm), while the corresponding *cis* isomers exhibit greater absorption in the visible (λ_{max} = 435 nm) region. Photoisomerization of $[Au_{25}(C_3\text{-AMT})_{18}]^-$ nanoclusters using visible (435 nm) and ultraviolet (345 nm) illumination showed changes in their optical absorption (Fig. 20.4B) and NMR spectra. Photoisomerization of nanoclusters using spiropyran molecule is also known.[62] Spiropyran is a well-studied photochromic molecule in which the ring-opening/closing process triggers photoisomerization. The chromophore was tethered on the surface of Au_{25} nanoclusters via a ligand-exchange reaction. The spiropyran-bound Au_{25} nanoclusters showed reversible photoisomerization when exposed to UV and visible light, similar to $[Au_{25}(C_3\text{-AMT})_{18}]^-$.

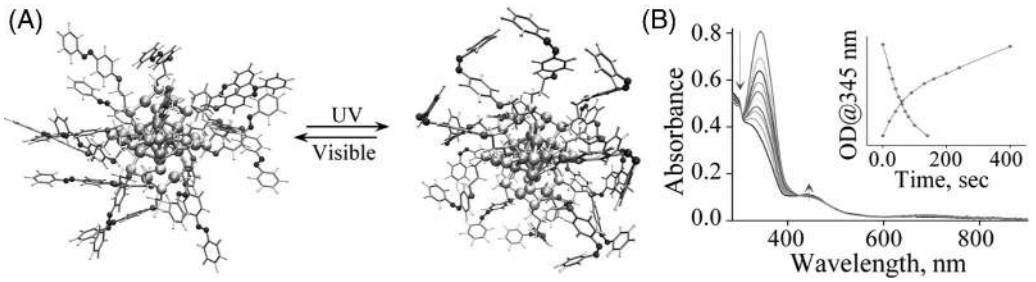

FIGURE 20.4 (A) Schematic representation showing the photoisomerization of $[Au_{25}(C_3\text{-}AMT)_{18}]^-$ nanocluster under UV and visible light. (B) Temporal-absorption spectra of $[Au_{25}(AMT)_{18}]^-$ under 345 nm illumination. A plot of OD (ca. 345 nm) versus illumination time under ultraviolet and visible light is shown in the inset. Reproduced with permission from ref.[61] Copyright 2020 American Chemical Society.

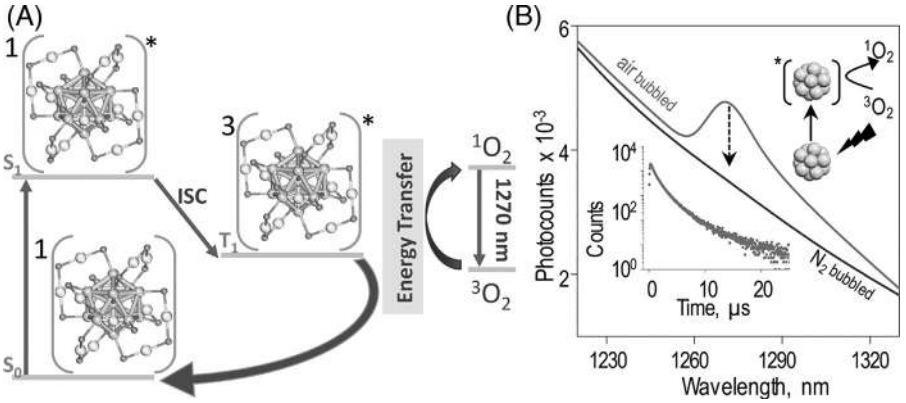

FIGURE 20.5 (A) Mechanism for the photosensitized production of $^1O_2$. (B) Fluorescence spectra of $^1O_2$ generated by nanoclusters. Inset shows PL decay profile of $^1O_2$ produced by NCs. Reproduced with permission from ref. [63] Copyright 2013 Wiley-VCH.

20.5.1.4 Photosensitization

It is known since 2013 that gold nanoclusters are suitable probes to produce singlet oxygen ($^1O_2$) by a photosensitized mechanism.[63] The photoactivation of nanoclusters into the excited singlet (S1) state is followed by a relaxation to the triplet (T1) state via intersystem crossing. Finally, the energy transfer between photoactivated nanoclusters (T1) and molecular oxygen ($^3O_2$) results in the formation of $^1O_2$ (Fig. 20.5A). The $^1O_2$ emits 1270 nm, which is direct evidence of the formation of $^1O_2$ (Fig. 20.5B). The $^1O_2$ scavengers such as singlet oxygen sensitized green dye (SOSG) or 1,3-diphenylisobenzofuran (DPBF) could be utilized for the selective detection of $^1O_2$ during photosensitization. The enhanced green emission during the photoactivation of nanoclusters in the presence of SOSG confirms the formation of endoperoxide through the trapping of $^1O_2$ in the anthracene moiety of SOSG. The quantum yield of $^1O_2$ can be estimated using a relative method.

$$\tau(^1O_2)s = \tau(^1O_2)r(m^s F^r/m^r F^s)$$

Here, s and r represent the sample and reference (porphyrin), τ is quantum yield, F is optical absorption correction factor ($1–10^{-OD}$), and m is the slope measured from the plot of OD versus irradiation time of $^1O_2$ scavenger (DPBF) during the photoactivation of sample or reference in the presence of DPBF. The efficiency of $^1O_2$ production is mostly dependent on the structure of bound ligands.[64] The role of ligands on $^1O_2$ production was investigated in $[Au_{25}(SC_3H_7)_{18}]^-$, $[Au_{25}(SC_4H_9)_{18}]^-$, and $[Au_{25}(PET)_{18}]^-$ nanoclusters synthesized by the chemical reduction method. The $^1O_2$ lifetime was found to be in the order of $[Au_{25}(SC_2H_4Ph)_{18}]^- > [Au_{25}(SC_3H_7)_{18}]^- > [Au_{25}(SC_4H_9)_{18}]^-$, which exactly follows the positive oxidation potential values (E^0) of nanoclusters (from higher to lower). The higher $^1O_2$ production from $[Au_{25}(SC_2H_4Ph)_{18}]^-$ nanocluster is due to their larger HOMO–LUMO band gap (1.3 eV). Such information will be beneficial in the development of nanocluster-based probes for photodynamic therapy.

20.5.2 Electrochemistry

The nature of ligands is important to manipulate the redox potential and optical bandgap of precision nanoclusters. The substituent effects on formal potentials were investigated in detail by having various X in $[Au_{38}(SPhX)_{24}]$ such as NO_2, Br, H, CH_3, and OCH_3 via ligand-exchange reaction.[65] To demonstrate the role of substituents on the formal potential of nanoclusters, Osteryoung square wave voltammetry (OSWV) was performed by dispersing substituted nanoclusters in 0.1 M Bu_4NClO_4/CH_2Cl_2 solution using Pt as working electrode, Pt foil as a counter electrode, and Ag wire as a quasi-reference electrode (ferrocene was used as an internal reference). The OSWV recorded from $[Au_{38}(SPhX)_{24}]$ nanoclusters with different substituents (Fig. 20.6A) showed a considerable peak shift toward more positive potentials relative to ferrocene when the X was replaced from electron-donating (OCH_3) to electron-withdrawing groups (NO_2). The shift is due to the changes in the polarization of nanoclusters and charge distribution among the ligands. As a result, the electron-withdrawing groups favor reduction, and electron-donating groups favor oxidation. The observed shift in the HOMO–LUMO energies is because electron-withdrawing substituents push the formal potential for oxidation of a molecular electron donor to further positive values. A similar trend was observed in $[Au_{25}(SPhX)_{18}]$ nanoclusters when substituted with different electron-withdrawing groups.[66] Notably, the substituents have great control over the stability of nanoclusters. This could be explained by considering the electrochemical and thermodynamic stability of ligands. To address the importance of ligands on the stability of nanoclusters, a variety of nanoclusters such as $[Au_{25}(SX)_{18}]^-$, $[Au_{38}(SX)_{24}]$, and $[Au_{102}(SX)_{44}]$ (X = CH_3, C_6H_{13}, CH_2CH_2Ph, Ph, PhF, and PhCOOH) were synthesized using standard procedures.[67] The Au_n nanoclusters stabilized with PhCOOH ligands exhibited better stability than other ligands due to the higher bond strength of Au-SPhCOOH and larger solvent stabilization energy (Fig. 20.6B) of $Au_n(SPhCOOH)_m$. The order of stability follows $C_6H_{13} < CH_3 \sim CH_2CH_2Ph \sim Ph \sim PhF < PhCOOH$.

20.5.3 Optical chirality

Optical chirality is a well-studied phenomenon in chemical/biological sciences owing to its significance in developing asymmetric drugs, catalysts, chiroptical sensors, etc. The

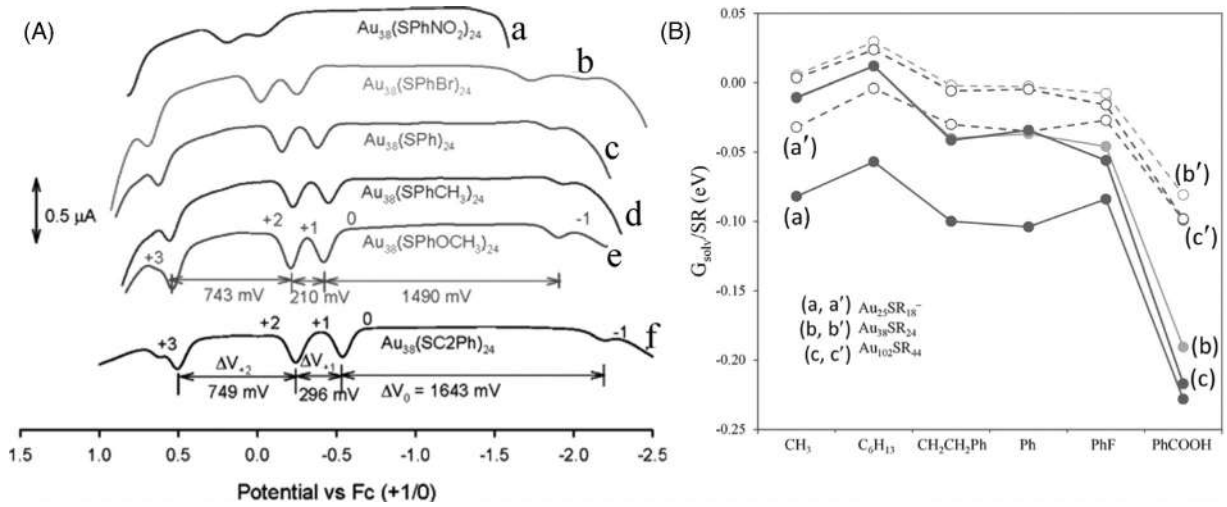

FIGURE 20.6 (A) Osteryoung square wave voltammograms (positive-going scan only) of different nanoclusters recorded at 11°C in 0.1 M Bu_4NClO_4/CH_2Cl_2. Reproduced with permission.[65] Copyright 2005, American Chemical Society. (B) Stabilization of different nanoclusters due to bulk solvent with $\varepsilon = 5$ (open circles) and 50 (filled circles). Reproduced with permission from ref.[67] Copyright 2012 The Royal Society of Chemistry.

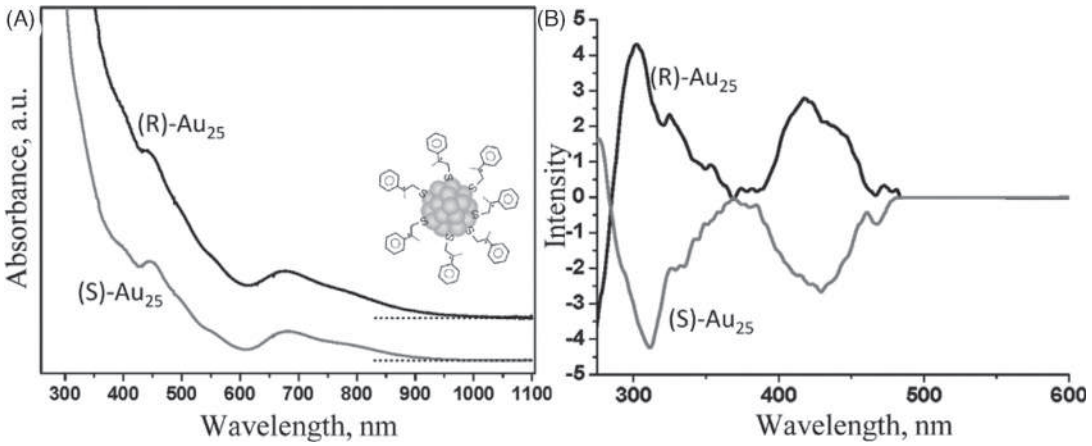

FIGURE 20.7 (A) UV/Vis absorption, (B) CD spectra of R- and S-[$Au_{25}(PET)^*_{18}$] nanoclusters. Reproduced with permission from ref.[70] Copyright 2011 American Chemical Society.

optical chirality in thiolate-protected nanoclusters could originate in different ways which include (i) protection with chiral thiolates, (ii) asymmetry originated due to the arrangement of ligands on the cluster surface, and (iii) inherent chirality of nanocluster core. The optical chirality of nanoclusters resulting from the protecting chiral thiolates will be discussed in this section. The ability of a chiral molecule to rotate circularly polarized light in the left or right direction determines the sign of the Cotton signal in the circular dichroism (CD) spectrum. The CD spectrum is represented in molar ellipticity, $[\theta]$, a measure of the ellipticity of the polarization,

$$\text{Molar ellipticity, } [\theta] = (3298^* \Delta\varepsilon) \text{ degree } M^{-1}\ m^{-1}$$
$$\text{From the extended Beer–Lambert law, } \Delta\varepsilon = \Delta A c l = (A_L - A_R) c l$$

$\Delta A = A_L - A_R$; A_L and A_R are the absorbances of left and right circularized polarized light, c is the molar concentration of the sample (M), and l is the sample pathlength (m).

The sign of the Cotton signal will be positive when A_L is higher than A_R, or vice versa.

Early stages of optically active D- or L-penicillamine (D-Pen and L-Pen) tethered gold nanocluster enantiomers were reported in 2005. The mirror image correlation between D-Pen and L-Pen stapled gold nanoclusters confirmed their optical chirality. Notably, the optical activity and anisotropy factors gradually decreased with increasing core diameter of nanoclusters.[68] The effect of temperature on the optical chirality was studied in detail by recording and analyzing the CD spectra from different pairs of gold nanocluster enantiomers at 20°C and 40°C.[69] The intensity of the Cotton signal was found to decrease with increasing temperature due to the fluctuating population of two conformational isomers at higher temperatures. Later, the enantioselective synthesis and purification of R- and S-[$Au_{25}(PET)^*_{18}$],[70] [$Au_{38}(PET)^*_{24}$], and [$Au_{25}(Capt)_{18}$] nanoclusters were demonstrated.[71] This one-pot method received considerable attention due to the purity of two distinct enantiomers, which was evident from the clean optical absorption, ESI-MS, and CD spectra recorded from the R- and S-[$Au_{25}(PET)^*_{18}$] nanoclusters (Fig. 20.7A and B).

20.5.4 Catalysis

The breakthrough invention on the low-temperature oxidation of CO using the nanogold opened a new platform for plasmonic nanoparticles in the field of catalysis.[72] A better understanding of their catalytic properties helped to study various chemical transformations, including oxidation, hydrogenation, and coupling reactions.[73–76] This section will discuss the effect of ligands on the catalytic properties of nanoclusters. The ligand landscape, functional moieties, and chain length of the protective ligands anchored to the nanocluster surface offer excellent control over the catalytic activities for a specific reaction. For example, the specific arrangements of the protective ligands regulate and limit the exposure area of active sites on the nanocluster surface during the catalytic reaction.[77] To address the role of ligand landscape on the nanocluster surface, $[Au_{25}(p\text{-MBA})_{18}]$ is chosen as a model system owing to its novel geometric structure and well-defined active sites. $[Au_{25}(p\text{-MBA})_{18}]$ nanocluster has an icosahedral core with one atom at the center and is surrounded by six (Au_2-SR_3) staple motifs. Such a geometric configuration results in twenty triangular-like structures of Au_3 in Au_{25} nanoclusters. Among these, twelve are face-capped by ligands. Hence, eight faces are available as active sites for adsorption and chemical reactions. The hydrogenation of 4-nitrophenol with $NaBH_4$ in presence of $[Au_{25}(p\text{-MBA})_{18}]$ nanocatalyst showed a different reaction route with the formation of azobenzene intermediate, by adsorbing two 4-nitrophenols and one BH_4^- ion on the cluster surface. The formation of a 4,4′-dihydroxyazobenzene intermediate was identified using optical absorption and ESI-MS spectroscopy. A similar catalytic reaction in the presence of different chain length thiolates tethered-Au_{25} nanoclusters showed a difference in the rate of catalytic conversion.[78] To study the ligand-length effects, Au_{25} nanoclusters stabilized with different chain length thiolates, including C_3-mercaptopropanoic acid (MPA), C_6-mercaptohexanoic acid (MHA), C_8-mercaptooctanoic acid (MOA), and C_{11}-mercaptoundecanoic acid (MUA) were synthesized and purified using the standard protocol. The catalytic conversion rate of 4-nitrophenol into 4-aminophenol decreased when the chain length increased from C_3 to C_{11} due to the lower accessibility of active sites to adsorb and perform chemical reactions (Fig. 20.8A). The functional moieties present on the protecting ligands also affect the rate of catalytic conversion. For example, Au_{25} nanoclusters stabilized with MPA (carboxyl group), L-cysteine (L-Cys; one carboxyl and one amine group), and *p*-MBA (*p*-mercaptobenzoic acid) have shown the difference in their performance during the hydrogenation of 4-nitrophenol. Among the three, $[Au_{25}(MPA)_{18}]$ showed a better conversion rate compared to $[Au_{25}(p\text{-MBA})_{18}]$ nanocatalyst (Fig. 20.8B). However, the introduction of amine functionalities on $[Au_{25}(MPA)_{18}]$ nanocatalyst ($[Au_{25}(MPA/Cysm)_{18}]$) using mixed ligands (MPA and cysteamine = Cysm) during the synthesis showed negative effects on the catalytic activity due to the mixed-effects arising from steric hindrance and electronic modifications of the gold core (Fig. 20.8C). Though the aromatic ligands enhance the accessibility of active sites via strong $\pi-\pi$ stacking between the *p*-MBA and reactants, the rate of formation of the desired products was slightly lower due to the relatively greater difficulty in the dissociation of the final products from the gold active sites. Generally, the presence of aromatic ligands on the nanocatalyst could enhance the accessibility of active sites and it was evident from the Ullmann hetero-coupling reaction between 4-methyliodobenzene and 4-nitro-iodobenzene using $[Au_{25}(SNap)_{18}]^-$ $[TOA]^+$ (SNap = 1-naphthalenethiolate) nanocatalyst.[79] The conversion rate and selectivity of heterocoupling reaction were more in the presence

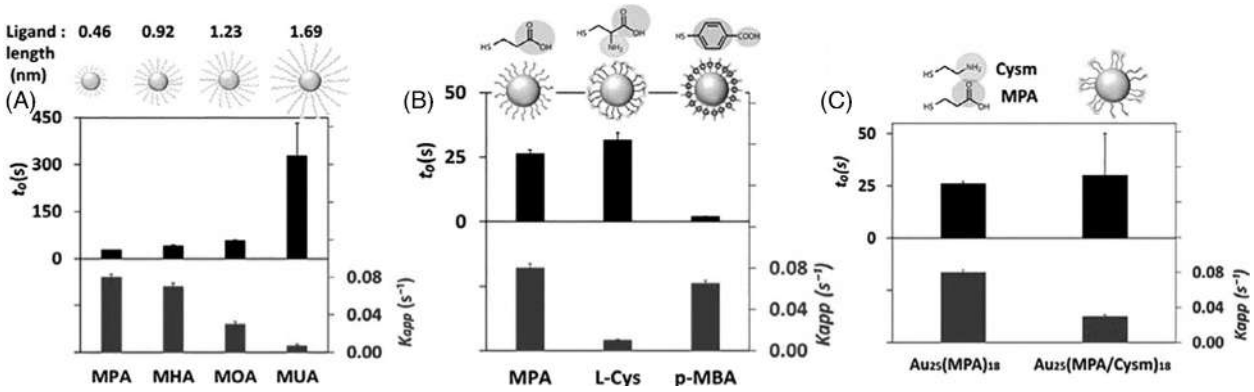

FIGURE 20.8 Effects of (A) ligand chain length and (B and C) functional groups on the accessibility and catalytic activity of Au_{25} nanoclusters. Reproduced with permission from ref.[78] Copyright 2016 Wiley-VCH.

of $[Au_{25}(SNap)_{18}]^{-}$ $[TOA]^{+}$ nanoclusters supported on CeO_2 compared to $[Au_{25}(SC_6H_{13})_{18}]^{-}$, $[Au_{25}(SCH_2CH_2Ph)_{18}]^{-}$, and $[Au_{25}(SPh)_{18}]^{-}$ on CeO_2.

20.6 Long-range colloidal assembly

Functionally rich monolayer thiol-protected nanoclusters could act as nanoscale building blocks for fabricating three-dimensional (3D) architectures via colloidal self-assembly. The nanoscale surface forces created by the functional moieties tethered on the nanocluster surface play an important role in self-organize the nanoclusters. The self-assembled superstructures help to harvest the enhanced and collective optical and electronic properties from the surrounding nanoclusters in the assembly. Such enhanced photophysical properties are certainly helpful to develop precision devices. Several advantages associated with nanoclusters—highly monodisperse structures, covalently bound ligands with different functional moieties, patchy ligand distributions, and inevitable dispersion behavior—aid in self-assembly in solution. During the spontaneous organization of nanoclusters, the free energy of the system will be reduced. However, due to their smaller size, the fluctuation in the thermal energy of the surroundings is similar to internanocluster interactions. Hence, it is necessary to balance the thermodynamic forces and nanoscale molecular forces before the onset of self-assembly. The nanoscale driving forces include hydrogen bonding, electrostatic interactions, van der Waals interactions, C–H$\cdots\pi/\pi$ $\cdots\pi$ interactions, amphiphilicity, light-triggered dipole-induced attractions, metal chelation, and template-assisted attractions originating from the functional thiolates have been used to address the colloidal self-assembly in nanoclusters. A detailed discussion of each method is given below.

20.6.1 Hydrogen bonding and electrostatic interactions

The basic criteria for a nanocluster to self-assemble via hydrogen bonding or electrostatic interaction are the presence of free −COOH terminated groups on the surface. Hydrogen bonding-induced superlattice formation was reported in $[Na_4Ag_{44}(p\text{-MBA})_{30}]$ nanoclusters.[80] During the storage of $[Na_4Ag_{44}(p\text{-MBA})_{30}]$ in N,N′-dimethylformamide (DMF) solution, the –COOH moieties of the bound ligands protonated entirely resulting in the dissolution of nanoclusters in DMF. The free carboxylic acid group on the nanocluster surface produced dimers or trimers through hydrogen bonding, which resulted in rhombus-shaped self-assembled crystals. The coexistence of hydrogen bonds and electrostatic interactions could also play a key role in the self-assembly of nanoclusters due to the charges on the bound ligands. The strong attraction or repulsion between two oppositely charged ions is known as electrostatic interactions. To establish the self-assembly in nanoclusters via electrostatic interactions, one could create charge separation between the neighboring participants by employing nanoclusters possessing opposite charges or introducing the counterions in monocharged nanoclusters. $[Ag_{44}(p\text{-MBA})_{30}]^{4-}$ nanoclusters were cleverly assembled via electrostatic interactions under highly alkaline conditions.[81] The complete deprotonation of ligands followed by the addition of cesium (Cs^{+}) counterions in dimethylsulfoxide (DMSO)/water system helped in the formation of superstructures of $[Ag_{44}(p\text{-MBA})_{30}]^{4-}$ nanoclusters. The addition of Cs^{+} counterions resulted in the packing of deprotonated $[Ag_{44}(p\text{-MBA})_{30}]^{4-}$ nanoclusters into

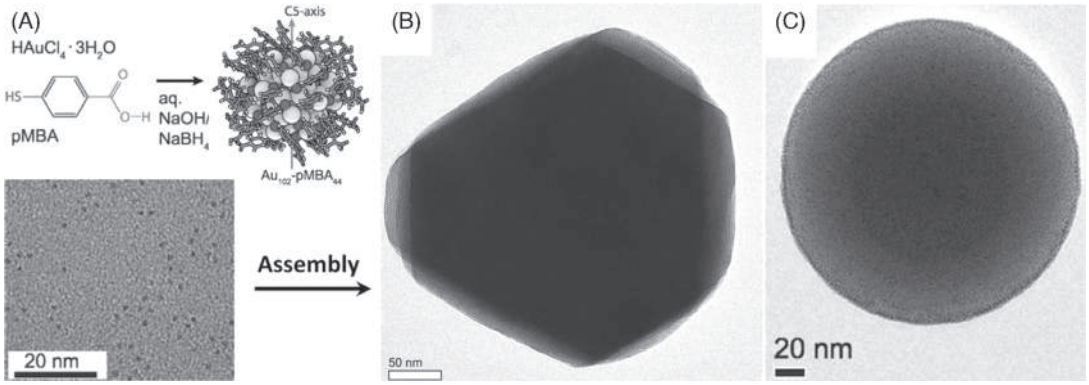

FIGURE 20.9 (A) Synthetic route for $[Au_{102}(p\text{-MBA})_{44}]$ nanoclusters, internal structure extracted from the solid-state structure, and TEM image dispersed in water. TEM images of (B) 2D nanosheets and (C) spherical capsids fabricated from $[Au_{102}(p\text{-MBA})_{44}]$ nanoclusters via (B) hydrogen bonding and (C) electrostatic interactions. Reproduced with permission from ref.[82] Copyright 2016 Wiley-VCH.

polymorphic octahedral single crystals via electrostatic interactions through the removal of existing directional hydrogen bonds. Further addition of Cs^+ ions produced a charge screening in $[Ag_{44}(p\text{-MBA})_{30}]^{4-}$ nanoclusters, which produced concave octahedral-shaped crystals. Highly uniform self-assembly of nanoclusters into colloidal crystals and spherical capsids were reported for $[Au_{102}(p\text{-MBA})_{44}]$ via partial hydrogen bond formation.[82] The purified $[Au_{102}(p\text{-MBA})_{44}]$ nanoclusters (Fig. 20.9A) were initially dispersed in sodium hydroxide (NaOH) solution to achieve partial deprotonation. The subsequent solvent exchange of nanoclusters from water to methanol via dialysis resulted in self-assembled nanosheets (Fig. 20.9B). The anisotropic and patchy distribution of ligands helped in the formation of 2D crystals. The authors could switch the crystallization kinetics via the electrostatic interactions by replacing the dialysis method with the direct addition of methanol into nanocluster dispersion. As a result, spherical capsids were formed (Fig. 20.9C) instead of the assembled nanosheets. In another example, the spherical self-assembly of $[Au_{22}(SG)_{18}]$ nanoclusters were established, which exactly mimicked the capsid protein self-assembly.[83] To address the self-assembly of $[Au_{22}(SG)_{18}]$, DMSO was initially introduced into the system, which hindered the active hydrogen bonding network between the nanoclusters and water molecules. Successive replacement of the hydrated water molecules around the nanoclusters via evaporation hindered the hydrogen bonding network between the adjacent nanoclusters. To address the larger assembly of $[Au_{22}(SG)_{18}]$ nanoclusters, the dialysis method was implemented using water–DMSO or water–DMF binary solvent systems. The higher dielectric constant of the water–DMSO cosolvent system helped to create larger assemblies due to the efficient screening from the repulsive electrostatic forces between negatively charged nanoclusters. Such a capsid-like mimicking strategy will be highly useful in understanding the protein self-assembly mechanism.

20.6.2 Van der Waals interactions

Distance-dependent weak electrostatic attractions or repulsions are known as van der Waals interactions. Three different types of van der Waals attractions viz Keesom, Debye, and

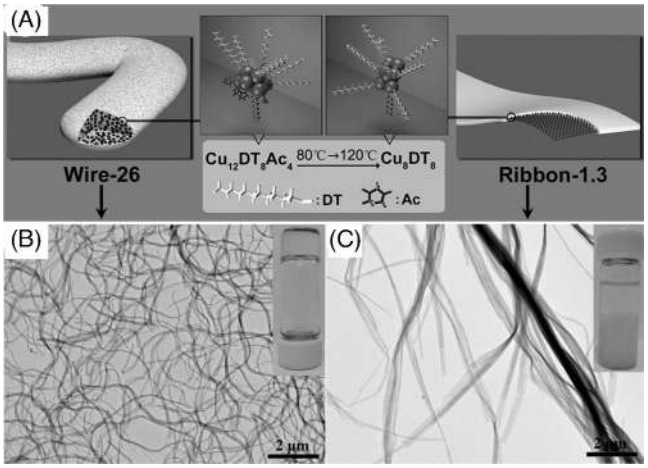

FIGURE 20.10 (A) Schematic illustration shows the evolution of $[Cu_{12}(DT)_8Ac_4]$ nanocluster self-assembly architectures from nanowire to nanoribbon. (B and C) TEM images of nanowires and nanoribbons. Photographs of nanowire and nanoribbon dispersions are shown in inset B and C, respectively. Reproduced with permission from ref.[85] Copyright 2013 Wiley-VCH.

London forces are known based on the nature of interactions. Such van der Waals forces have resulted from:

1. The interaction between two permanent dipoles (Keesom).
2. The polarizable molecule produces an induced dipole (Debye).

Dipoles arise when fluctuating electron clouds induce a charge redistribution between molecules that hold zero dipole moments (London).

Nanoclusters functionalized with long-chain alkyl moieties tend to self-assemble into microstructures at high temperatures due to the attractive hydrophobic van der Waals interactions between the alkyl chains ligands. Such assembly was reported in 1-dodecane thiol (DT)-tethered gold nanoclusters (Au_{15}). When the temperature was increased above 140°C (vacuum), Au_{15} nanocluster dispersion (liquid paraffin/dibenzyl ether) was self-assembled into nanosheets.[84] At high temperatures, the lamellar interface of solvent microphase separation could act as a soft template to initiate the assembly. Hydrophobic attractions between the ligands from the assembled nanoclusters were calculated to be $7\,k_BT$, where k_B is the Boltzmann constant, and T is the absolute temperature. Sometimes, the presence of multiple ligands also helps to assemble nanoclusters via different interactions. One such example is the self-assembly of $[Cu_{12}(DT)_8Ac_4]$ (Ac = acetylacetonate) via van der Waals interactions, attributed to DT ligands, and dipolar attractions originating from the permanent dipole of nanocluster core due to the Ac moiety.[85] In this particular case, due to the combined dipolar and van der Waals interactions, $[Cu_{12}(DT)_8Ac_4]$ initially self-assembled into long nanowires. However, such nanowires were self-organized into nanoribbons at elevated temperatures due to permanent van der Waals interactions. At high temperatures, the Ac moieties were removed from the nanocluster surface, which eventually quenched the overall dipole moment of the system. As a result, at high temperatures, van der Waals interactions control the assembly (Fig. 20.10).

20.6.3 C–H$\cdots\pi/\pi\cdots\pi$ interactions

The C–H$\cdots\pi$ interactions are weak attractions between the C–H bond and the delocalized π electrons.[86] Similar interactions between the delocalized π electrons are known as

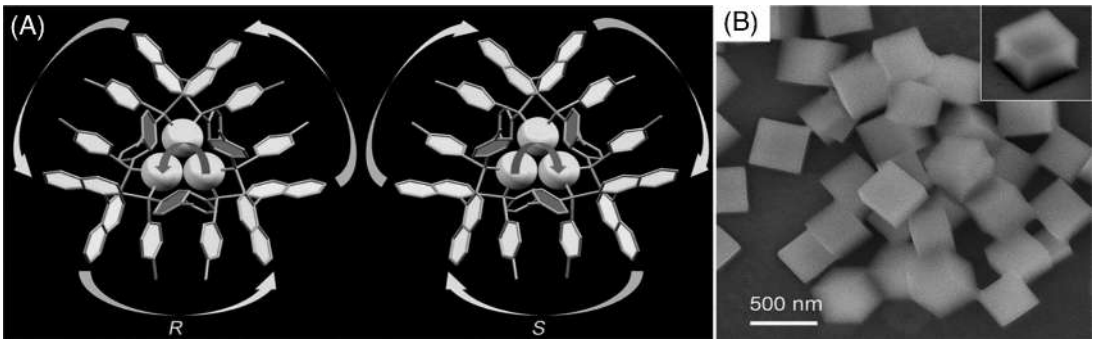

FIGURE 20.11 (A) Chiral $[Au_3\{(R)\text{-Tol-BINAP}\}_3Cl]$ and $[Au_3\{(S)\text{-Tol-BINAP}\}_3Cl]$ nanoclusters. (B) SEM image of $[Au_3\{(R)\text{-Tol-BINAP}\}_3Cl]$ nanocluster assembly fabricated in DCM with 70% *n*-hexane. Reproduced with permission from ref.[87] Copyright 2017 Wiley-VCH.

$\pi\cdots\pi$ interactions. The colloidal assembly of nanoclusters via the C–H$\cdots\pi$ /$\pi\cdots\pi$ interactions could be demonstrated by choosing appropriate functional moieties on the surfaces. The nanoclusters covalently bonded to the delocalized π electrons rings are expected to display colloidal assembly via the C–H$\cdots\pi$ interactions. A long-range self-assembly from the smallest chiral $[Au_3\{(R)\text{-Tol-BINAP}\}_3Cl]$ and $[Au_3\{(S)\text{-Tol-BINAP}\}_3Cl]$ nanoclusters was reported via the dominating C–H$\cdots\pi$ interactions (BINAP = 2,2′-bis(di-*p*-tolylphosphino)-1,1′-binaphthyl).[87] To address such an assembly, chiral $[Au_3\{(R)\text{-Tol-BINAP}\}_3Cl]$ and $[Au_3\{(S)\text{-Tol-BINAP}\}_3Cl]$ nanoclusters were separately synthesized using R- and S-BINAP ligands. The mirror image-Cotton signals in the CD spectra proved the enantiomeric characteristics of $[Au_3\{(R)\text{-Tol-BINAP}\}_3Cl]$ and $[Au_3\{(S)\text{-Tol-BINAP}\}_3Cl]$ nanoclusters. Drop-wise addition of *n*-hexane (antisolvent) into the nanocluster solution (DCM) induced strong intermolecular C–H$\cdots\pi$ interactions among BINAPs bound to the nanocluster surface. An orange color emission was observed from the nanocluster solution when the concentration of *n*-hexane reaches up to 40%. The intensity of photoluminescence was increased with increasing concentration of the antisolvent. Enhanced photoluminescence indicated the formation of assembled nanoclusters via strong C–H$\cdots\pi$ interactions (Fig. 20.11). Microscopic investigations of the organized nanocluster solution showed a cube-shaped assembly. The intermolecular interactions between the BINAPs bounded on nanocluster surface improved the circularly polarized photoluminescence and chiral responses from the assembled superstructures, due to their restricted movements.

The efficient $\pi\cdots\pi$ stacking between the aromatic rings terminated-bound ligands also could lead to assembly of nanoclusters. One such example is the colloidal self-assembly of $[Au_{25}(p\text{-MBA})_{18}]^-$ nanoclusters via $\pi\cdots\pi$ interactions. The primary stage of the assembly in this system was triggered by the aurophilic (Au–Au) interactions. The noncovalent attractions between the closed-shells (d^{10}, s^2) or pseudoclosed-shell (d^8) of metal cations are known as metallophilic (M–M) interactions.[88] To demonstrate the self-assembly, $[Au_{25}(p\text{-MBA})_{18}]^-$ nanoclusters synthesized by the pH-adjusted chemical reduction method were subjected to the cyclic dialysis process, which reduced the pH of the nanocluster solution.[89] During this process, the parent $[Au_{25}(p\text{-MBA})_{18}]^-$ nanoclusters transformed into the surface-motif reconstructed nanoclusters having Au^1 centers with d^{10} electronic configuration. The self-assembled nanoribbons formed when the nanocluster solution was incubated overnight due to the

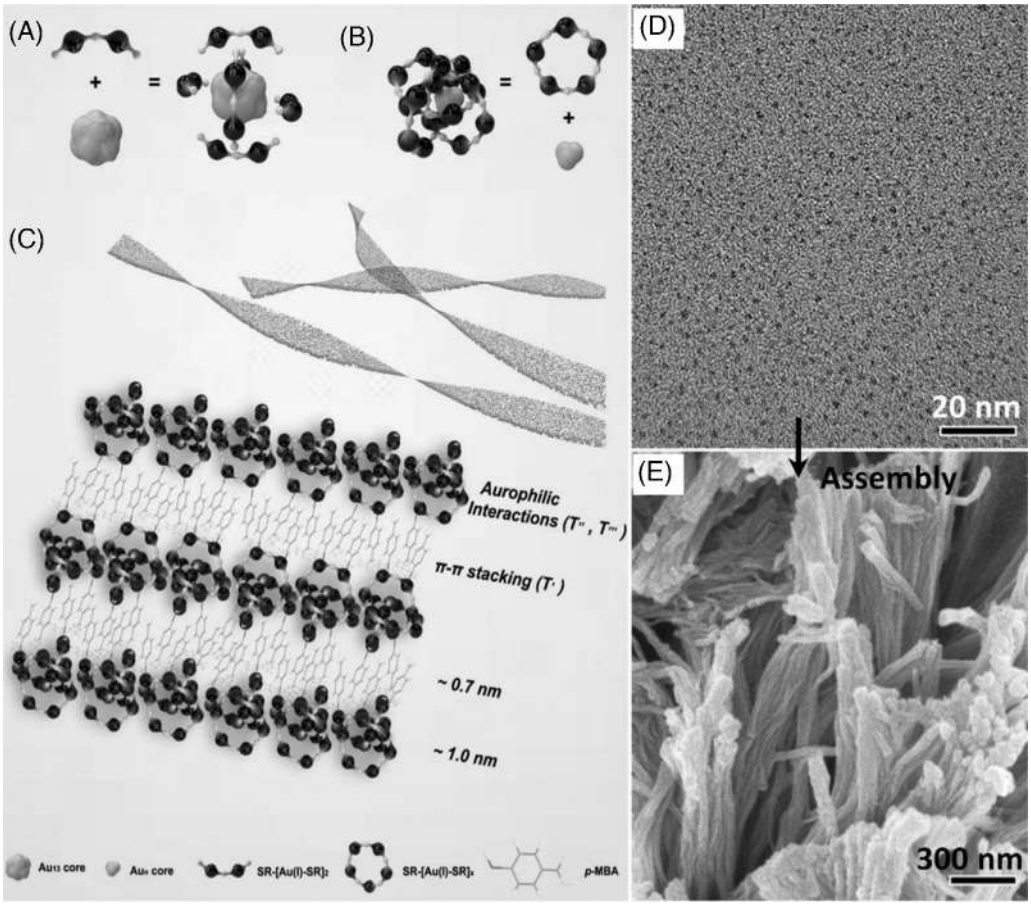

FIGURE 20.12 Schematic showing the evolution of $[Au_{25}(p\text{-MBA})_{18}]^-$ nanoclusters into well-defined self-assembled nanoribbons. The cartoon illustrates the structure of (A) $[Au_{25}(p\text{-MBA})_{18}]^-$ nanoclusters and (B) the as-evoked smaller nanoclusters, and (C) their spatial arrangement within nanoribbons. (D) TEM image of $[Au_{25}(p\text{-MBA})_{18}]^-$ nanoclusters, and (E) SEM images of the nanoribbons. Reproduced with permission from ref.[89] Copyright 2019 American Chemical Society.

surface-motif reconstruction of nanoclusters from the short SR-$[Au^1\text{-SR}]_2$ moieties into long SR-$[Au^1\text{-SR}]_x$ ($x > 2$) staples followed by the structural reorganization of intrinsic Au_{13} kernel. The presence of rich Au^1 centers and short-range $Au^1 \cdots Au^1$ interactions in the initial stage of assembly drive the nanoclusters into 1D nanowires. However, the strong $\pi \cdots \pi$ stacking between *p*-MBA ligands from the adjacent nanowires resulted in the formation of nanoribbons from 1D nanowires, and was evident from the reduced internanowire distance (Fig. 20.12).

20.6.4 Amphiphilicity

The ability to possess both hydrophobic and hydrophilic properties on the same surface is known as amphiphilicity. Creating such surface properties on nanoclusters offers new routes to demonstrate their colloidal self-assembly. Periodic organization of amphiphilic molecular

level surfactant or block-copolymers into various nanostructures such as micelle, vesicles, or bilayers by tuning the hydrophobic–hydrophilic compositions is well-established. The in situ creation of such hydrophobic–hydrophilic patterns on the nanocluster surface is challenging. However, one could functionalize the nanocluster surface with a suitable combination of hydrophobic and hydrophilic molecules via the ligand replacement reaction. Amphiphilicity was demonstrated in Au_{25} nanoclusters using the "surfactant-mimicking" protocol.[90] For this, the hydrophilic $[Au_{25}(MHA)_{18}]$ nanoclusters were initially synthesized by the NaOH-mediated $NaBH_4$ reduction method, followed by the introduction of 50% hydrophobic cations (cetyltrimethylammonium, CTA^+) via the phase-transfer driven ion-pairing reaction. The electrostatic interactions between the positively charged CTA^+ ions and carboxylate anion from the bound MHA form amphiphilic $[Au_{25}(MHA)_{18}@xCTA]$ ($x = 6$–9) nanoclusters. Since only one half of the MHA were replaced, a mixture of flexible hydrophilic MHA and hydrophobic MHA···CTA ligands could coexist on the nanocluster surface. When the amphiphilic Au_{25} nanocluster solution evaporated slowly from the DMSO–ethanol mixture, a thin film of the self-assembled superstructures was formed at the air–liquid interface with exactly stacked bilayers (Fig. 20.13). Such assembled superstructures exactly mimic the lyotropic liquid crystalline phases shown by the molecular surfactants.

20.6.5 Light-triggered assembly

The reversible assembly of nanoclusters using a defined spectrum of light could be achieved by tailoring their surface with photoswitchable ligands such as thiolated azobenzene[61,91] and spiropyran.[62] Light-assisted reversible self-assembly of Au_{25} nanoclusters using two different spectra of lights was demonstrated in this perspective.[61] To address such switchable assembly, photoswitchable $[Au_{25}(C_3\text{-AMT})_{18}]^-$ nanoclusters were synthesized using azobenzene alkyl monothiols. When $[Au_{25}(C_3\text{-AMT})_{18}]^-$ nanocluster solution (in DCM) was illuminated with UV (345 nm) and visible light (435 nm) separately, the bound chromophores underwent photoisomerization. Under UV light, the azobenzene moieties bound to the nanocluster surface switch to the *cis* geometry with a net dipole moment. The attractive dipole-dipole interactions between the nearby nanoclusters in the *cis* arrangement initiate self-organization. However, the null dipole moment between the assembled nanoclusters under *trans* geometry in the presence of visible light disassembles them into individual nanoclusters. Notably, the assembly and disassembly of nanoclusters can be tuned multiple times through modulation of the excitation wavelength. Microscopic investigations showed the formation of disc-like superstructures during the light-induced assembly (Fig. 20.14).

20.6.6 Coordination-assisted assembly

Coordination of functionally rich nanoclusters with suitable metal ions could initiate the formation of nanocluster-based inorganic frameworks. For example, a highly luminescent gold nanocluster framework (GNCF) was formed on mixing [Au@SG] nanoclusters and divalent cations due to the efficient chelation of metal ions with carboxylate anions present on the nanocluster surface.[92] To demonstrate the formation of GNCFs, luminescent [Au@SG] nanoclusters were initially synthesized by the chemical reduction of Au(I)–SG thiolates. A sevenfold enhancement in photoluminescence was observed when Sn^{2+} ions were injected

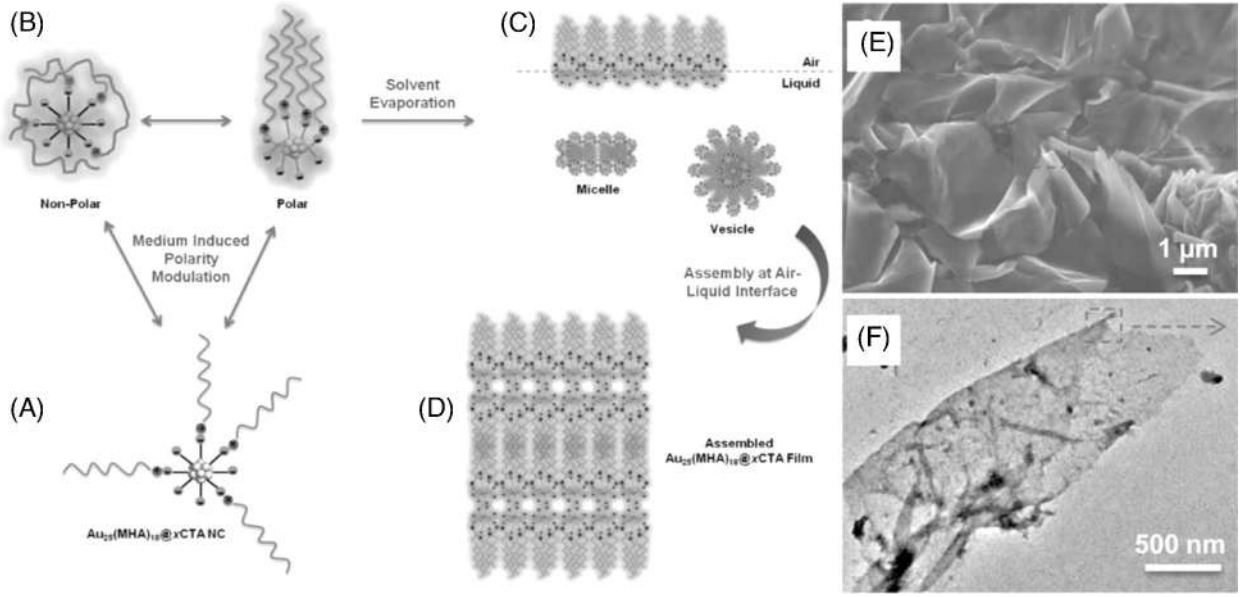

FIGURE 20.13 (A–D) Schematic shows the self-assembly of $[Au_{25}(MHA)_{18}@xCTA]$ nanoclusters. (E) FESEM and (F) TEM images of assembled $[Au_{25}(MHA)_{18}@xCTA]$ nanoclusters at the air–liquid interface. Reproduced with permission from ref.[90] Copyright 2015 American Chemical Society.

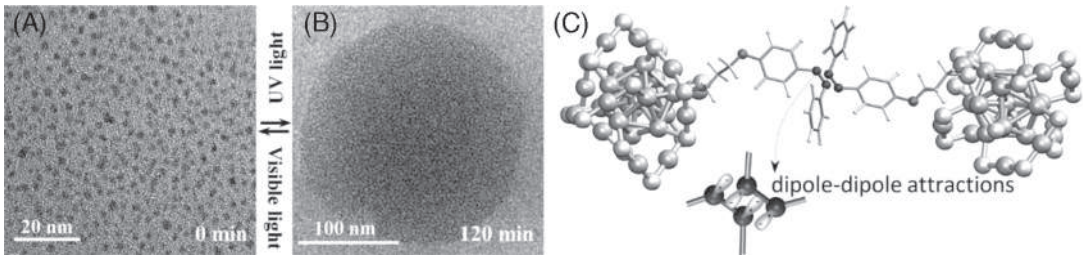

FIGURE 20.14 TEM images of (A) *trans* $[Au_{25}(C_3\text{-AMT})_{18}]^-$ nanoclusters and (B) *cis* $[Au_{25}(C_3\text{-AMT})_{18}]^-$ nanocluster assembly captured after (B) 120 min of light illumination (345 nm). (C) Cartoon representation of dipole-induced self-assembly in $[Au_{25}(C_3\text{-AMT})_{18}]^-$ nanocluster. Reproduced with permission from ref.[61] Copyright 2020 American Chemical Society.

into the as-prepared [Au@SG] nanoclusters. The efficient coordination of negatively charged carboxylate group from the bound SG with divalent Sn^{2+} cations resulted in coordination complexes among the nanoclusters, which eventually expanded into 3D self-assembled superstructures (Fig. 20.15).

20.6.7 Template-assisted assembly

Template molecules such as polymers or DNA could act as an active scaffold to induce self-organization in nanoclusters. The pH-dependent self-organization of [Au@SG] nanoclusters in the presence of cationic polymers such as poly(allylamine hydrochloride) is known.[93] Efficient electrostatic interactions between the amine groups (positively charged) of polymer and carboxylate moiety (negatively charged) of nanocluster results in self-assembled [Au@SG-PAH] spheres. Another template that has been efficiently used to self-organize nanoclusters is DNA. One such example includes the self-assembly of copper nanoclusters using DNA-nanoribbon templates.[94] The thermal annealing method has been efficiently employed to prepare different DNA-nanoribbon templates (C-DNR) composed of multiple single-strand DNA units. Subsequently, copper nanoclusters were prepared on the surface of C-DNRs by mixing copper sulfate ($CuSO_4$) with presynthesized C-DNR solution in a mixture of NaCl and MOPS (3-(N-morpholino)propane sulfonic acid) buffer. Addition of sodium ascorbate into the above-prepared solution followed by keeping them at room temperature for 30 min resulted in the self-organization of nanoclusters on C-DNR templates (Fig. 20.16).

20.7 Summary and future perspectives

In this chapter, we have outlined aspects of (i) surface functionalization of nanoclusters via ligand replacement and transformation chemistry, (ii) the role of thiols on the stability and structural control of nanoclusters, (iii) evolution of photophysical, electrochemical, and catalytic properties due to surface functionalization, and (iv) tuning of enhanced photophysical properties via long-range periodic self-organization. Enhanced optoelectronic properties originating from the assembled superstructures will be useful to develop next-generation precision devices.

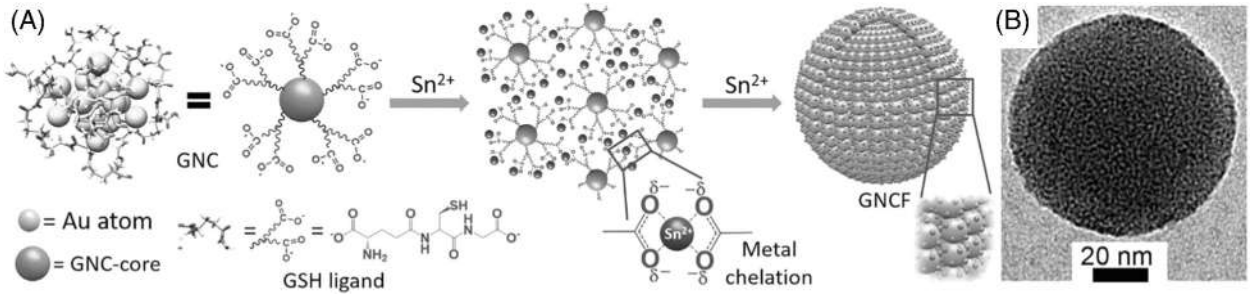

FIGURE 20.15 (A) Representation of a luminescent [Au@SG] nanocluster, possible interactions between the metal ions and COO^{-} groups of the ligand over nanoclusters through chelation, and schematic illustration for the formation of GNCFs. (B) HR-TEM micrograph of GNCF-100 dispersed in water. Reproduced with permission from ref.[92] Copyright 2019 Wiley-VCH.

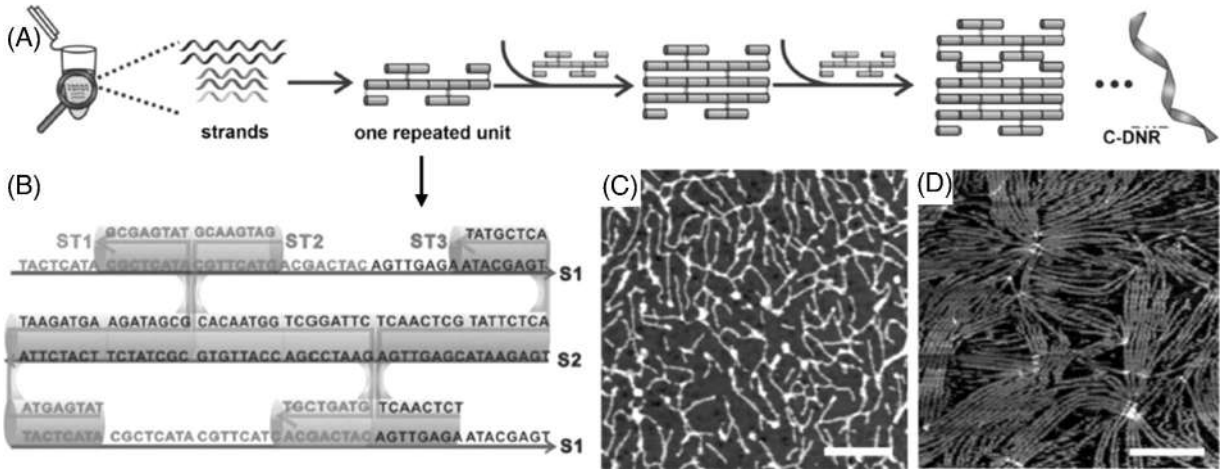

FIGURE 20.16 (A) Formation scheme of C-DNRs. (B) Sequence of repeating units in C-DNR. AFM images of C-DNR1 under (C) tapping mode in air and (D) in liquid. Reproduced with permission from ref.[94] Copyright 2020 Wiley-VCH.

List of abbreviation

SAM	self-assembled monolayer
TOABr	tetraoctylammonium bromide
LDI-MS	laser desorption ionization mass spectrometry
GSH	glutathione
PAGE	polyacrylamide gel electrophoresis
CTAB	cetyltrimethylammonium bromide
Cys	L-cysteine
BBSH	4-(*tert*-butyl)benzyl mercaptan
$AgNO_3$	silver nitrate
Capt	captopril
MSA	mercaptosuccinic acid
$HSPhMe_2$	2,4-dimethylbenzenethiol
$HSPhF_2$	4-difluorobenzenethiol
MHA	6-mercaptohexanoic acid
p-MBA	*p*-mercaptobenzoic acid
MB	3-mercapto-2-butanol
DCM	dichloromethane
TBBT	4-*tert*-butylbenzenthiol
EDC	1-ethyl-3-(3-dimethylaminopropyl)carbodiimide
DCC	N, N′-dicyclohexylcarbodiimide
NHS	*N*-hydroxysuccinimide
CuAAC	copper(I)-catalyzed azide-alkyne cycloaddition reaction
SPAAC	strain-promoted azide-alkyne cycloaddition reaction
FRET	Förster resonance energy transfer
AF	aminofluorescein
PySH	pyrenethiol
C_3-AMT	azobenzene alkyl monothiol
DPBF	diphenylisobenzofuran
SOSG	singlet oxygen sensitized green dye
CD	circular dichroism
D-Pen and L-Pen	D- or L-penicillamine
MPA	mercaptopropanoic acid
MHA	mercaptohexanoic acid
Cysm	cysteamine
SNap	1-naphthalenethiolate
DMF	N,N′-dimethylformamide
DMSO	dimethylsulfoxide
NaOH	sodium hydroxide
Ac	acetylacetonate
BINAP	2,2′-bis(di-*p*-tolylphosphino)-1,1′-binaphthyl
CTA^+	cetyltrimethylammonium
GNCF	gold nanocluster framework
C-DNR	DNA-nanoribbon template
$CuSO_4$	copper sulfate
MOPS	3-(N-morpholino)propane sulfonic acid

References

1. Bain CD, Troughton EB, Tao YT, Evall J, Whitesides GM, Nuzzo RG. Formation of monolayer films by the spontaneous assembly of organic thiols from solution onto gold. *J Am Chem Soc*. 1989;111:321–335.
2. Laibinis PE, Parikh AN, Nuzzo RG. Comparison of the structures and wetting properties of self-assembled monolayers of n-alkanethiols on the coinage metal surfaces, copper, silver, and gold. *J Am Chem Soc*. 1991;113:7152–7167.

3. Love JC, Estroff LA, Kriebel JK, Nuzzo RG, Whitesides GM. Self-assembled monolayers of thiolates on metals as a form of nanotechnology. *Chem Rev*. 2005;105:1103–1170.
4. Brust M, Walker M, Bethell D, Schiffrin DJ, Whyman R. Synthesis of thiol-derivatised gold nanoparticles in a two-phase liquid-liquid system. *J Chem Soc Chem Commun*. 1994:801–802.
5. Whetten RL, Khoury JT, Alvarez MM, et al. Nanocrystal gold molecules. *Adv Mater*. 1996;8:428–433.
6. Hostetler MJ, Green SJ, Stokes JJ, Murray RW. Monolayers in three dimensions: synthesis and electrochemistry of ω-functionalized alkanethiolate-stabilized gold cluster compounds. *J Am Chem Soc*. 1996;118:4212–4213.
7. Alvarez MM, Khoury JT, Schaaff TG, Shafigullin M, Vezmar I, Whetten RL. Critical sizes in the growth of Au clusters. *Chem Phys Lett*. 1997;266:91–98.
8. Schaaff TG, Shafigullin MN, Khoury JT, et al. Isolation of smaller nanocrystal Au molecules: robust quantum effects in optical spectra. *J Phys Chem B*. 1997;101:7885–7891.
9. Jadzinsky PD, Calero G, Ackerson CJ, Bushnell DA, Kornberg RD. Structure of a thiol monolayer-protected gold nanoparticle at 1.1 A resolution. *Science*. 2007;318:430–433.
10. Zhu M, Lanni E, Garg N, Bier ME, Jin R. Kinetically controlled, high-yield synthesis of Au_{25} clusters. *J Am Chem Soc*. 2008;130:1138–1139.
11. Kumar S, Bolan MD, Bigioni TP. Glutathione-stabilized magic-number silver cluster compounds. *J Am Chem Soc*. 2010;132:13141–13143.
12. Desireddy A, Conn BE, Guo J, et al. Ultrastable silver nanoparticles. *Nature*. 2013;501:399–402.
13. Udayabhaskararao T, Pradeep T. New protocols for the synthesis of stable Ag and Au nanocluster molecules. *J Phys Chem Lett*. 2013;4:1553–1564.
14. Yin B, Luo Z. Coinage metal clusters: from superatom chemistry to genetic materials. *Coord Chem Rev*. 2021;429.
15. Whetten RL, Shafigullin MN, Khoury JT, et al. Crystal structures of molecular gold nanocrystal arrays. *Acc Chem Res*. 1999;32:397–406.
16. Schaaff TG, Knight G, Shafigullin MN, Borkman RF, Whetten RL. Isolation and selected properties of a 10.4 kDa gold:glutathione cluster compound. *J Phys Chem B*. 1998;102:10643–10646.
17. Negishi Y, Takasugi Y, Sato S, Yao H, Kimura K, Tsukuda T. Magic-numbered Au*n* clusters protected by glutathione monolayers ($n = 18, 21, 25, 28, 32, 39$): isolation and spectroscopic characterization. *J Am Chem Soc*. 2004;126:6518–6519.
18. Negishi Y, Nobusada K, Tsukuda T. Glutathione-protected gold clusters revisited: bridging the gap between gold(I)-thiolate complexes and thiolate-protected gold nanocrystals. *J Am Chem Soc*. 2005;127:5261–5270.
19. Shichibu Y, Negishi Y, Tsukuda T, Teranishi T. Large-scale synthesis of thiolated Au_{25} clusters via ligand exchange reactions of phosphine-stabilized Au_{11} clusters. *J Am Chem Soc*. 2005;127:13464–13465.
20. Shichibu Y, Negishi Y, Tsunoyama H, Kanehara M, Teranishi T, Tsukuda T. Extremely high stability of glutathionate-protected Au_{25} clusters against core etching. *Small*. 2007;3:835–839.
21. Wu Z, Suhan J, Jin R. One-pot synthesis of atomically monodisperse, thiol-functionalized Au_{25} nanoclusters. *J Mater Chem*. 2009;19:622–626.
22. Yuan X, Yu Y, Yao Q, Zhang Q, Xie J. Fast synthesis of thiolated Au_{25} nanoclusters via protection-deprotection method. *J Phys Chem Lett*. 2012;3:2310–2314.
23. Yu Y, Luo Z, Yu Y, Lee JY, Xie J. Observation of cluster size growth in CO-directed synthesis of $Au_{25}(SR)_{18}$ nanoclusters. *ACS Nano*. 2012;6:7920–7927.
24. Yu Y, Chen X, Yao Q, Yu Y, Yan N, Xie J. Scalable and precise synthesis of thiolated $Au_{10–12}$, Au_{15}, Au_{18}, and Au_{25} nanoclusters via pH controlled CO reduction. *Chem Mater*. 2013;25:946–952.
25. Yuan X, Zhang B, Luo Z, et al. Balancing the rate of cluster growth and etching for gram-scale synthesis of thiolate-protected Au_{25} nanoclusters with atomic precision. *Angew Chem Int Ed*. 2014;53:4623–4627.
26. Branham MR, Douglas AD, Mills AJ. Arylthiolate-protected silver quantum dots. *Langmuir*. 2006;22:11376–11383.
27. Cathcart N, Mistry P, Makra C, et al. Chiral thiol-stabilized silver nanoclusters with well-resolved optical transitions synthesized by a facile etching procedure in aqueous solutions. *Langmuir*. 2009;25:5840–5846.
28. Dhanalakshmi L, Udayabhaskararao T, Pradeep T. Conversion of double layer charge-stabilized Ag@citrate colloids to thiol passivated luminescent quantum clusters. *Chem Commun*. 2012;48:859–861.
29. Mrudula KV, Bhaskara Rao TU, Pradeep T. Interfacial synthesis of luminescent 7 kDa silver clusters. *J Mater Chem*. 2009;19:4335–4342.
30. Udaya Bhaskara Rao T, Pradeep T. Luminescent Ag_7 and Ag_8 clusters by interfacial synthesis. *Angew Chem Int Ed*. 2010;49:3925–3929.

31. Negishi Y, Arai R, Niihori Y, Tsukuda T. Isolation and structural characterization of magic silver clusters protected by 4-(*tert*-butyl)benzyl mercaptan. *Chem Commun*. 2011;47:5693–5695.
32. Rao TUB, Nataraju B, Pradeep T. Ag_9 quantum cluster through a solid-state route. *J Am Chem Soc*. 2010;132:16304–16307.
33. Wu Z, Lanni E, Chen W, Bier ME, Ly D, Jin R. High yield, large scale synthesis of thiolate-protected Ag_7 clusters. *J Am Chem Soc*. 2009;131:16672–16674.
34. Joshi CP, Bootharaju MS, Alhilaly MJ, Bakr OM. $[Ag_{25}(SR)_{18}]^-$: the "golden"silver nanoparticle silver nanoparticle. *J Am Chem Soc*. 2015;137:11578–11581.
35. Zheng K, Yuan X, Xie J. Effect of ligand structure on the size control of mono- and bi-thiolate-protected silver nanoclusters. *Chem Commun*. 2017;53:9697–9700.
36. Ingram RS, Hostetler MJ, Murray RW. Poly-hetero-ω-functionalized alkanethiolate-stabilized gold cluster compounds. *J Am Chem Soc*. 1997;119:9175–9178.
37. Hostetler MJ, Templeton AC, Murray RW. Dynamics of place-exchange reactions on monolayer-protected gold cluster molecules. *Langmuir*. 1999;15:3782–3789.
38. Song Y, Huang T, Murray RW. Heterophase ligand exchange and metal transfer between monolayer protected clusters. *J Am Chem Soc*. 2003;125:11694–11701.
39. Shibu ES, Muhammed MAH, Tsukuda T, Pradeep T. Ligand exchange of $Au_{25}SG_{18}$ leading to functionalized gold clusters: spectroscopy, kinetics, and luminescence. *J Phys Chem C*. 2008;112:12168–12176.
40. Chen S, Wang S, Zhong J, et al. The structure and optical properties of the $[Au_{18}(SR)_{14}]$ nanocluster. *Angew Chem Int Ed*. 2015;54:3145–3149.
41. Shibu ES, Radha B, Verma PK, et al. Functionalized Au_{22} clusters: synthesis, characterization, and patterning. *ACS Appl Mater Interfaces*. 2009;1:2199–2210.
42. Zeng C, Li T, Das A, Rosi NL, Jin R. Chiral structure of thiolate-protected 28-gold-atom nanocluster determined by X-ray crystallography. *J Am Chem Soc*. 2013;135:10011–10013.
43. Bootharaju MS, Joshi CP, Alhilaly MJ, Bakr OM. Switching a nanocluster core from hollow to nonhollow. *Chem Mater*. 2016;28:3292–3297.
44. Bootharaju MS, Burlakov VM, Besong TMD, et al. Reversible size control of silver nanoclusters via ligand-exchange. *Chem Mater*. 2015;27:4289–4297.
45. Muhammed MAH, Verma PK, Pal SK, et al. Bright, NIR-emitting Au_{23} from Au_{25}: characterization and applications including biolabeling. *Chem Eur J*. 2009;15:10110–10120.
46. Lin C-AJ, Yang T-Y, Lee C-H, et al. Synthesis, characterization, and bioconjugation of fluorescent gold nanoclusters toward biological labeling applications. *ACS Nano*. 2009;3:395–401.
47. Wang Y, Chen J, Irudayaraj J. Nuclear targeting dynamics of gold nanoclusters for enhanced therapy of $HER2^+$ breast cancer. *ACS Nano*. 2011;5:9718–9725.
48. Vankayala R, Kuo C-L, Nuthalapati K, Chiang C-S, Hwang KC. Nucleus-targeting gold nanoclusters for simultaneous in vivo fluorescence imaging, gene delivery, and NIR-light activated photodynamic therapy. *Adv Funct Mater*. 2015;25:5934–5945.
49. Pyo K, Thanthirige VD, Yoon SY, Ramakrishna G, Lee D. Enhanced luminescence of $Au_{22}(SG)_{18}$ nanoclusters via rational surface engineering. *Nanoscale*. 2016;8:20008–20016.
50. Pyo K, Ly NH, Yoon SY, et al. Highly luminescent folate-functionalized Au_{22} nanoclusters for bioimaging. *Adv Healthcare Mater*. 2017;6.
51. Ding C, Xu Y, Zhao Y, Zhong H, Luo X. Fabrication of BSA@AuNC-based nanostructures for cell fluoresce imaging and target drug delivery. *ACS Appl Mater Interfaces*. 2018;10:8947–8954.
52. Pyo K, Ly NH, Han SM, et al. Unique energy transfer in fluorescein-conjugated Au_{22} nanoclusters leading to 160-fold pH-contrasting photoluminescence. *J Phys Chem Lett*. 2018;9:5303–5310.
53. Marjomaki V, Lahtinen T, Martikainen M, et al. Site-specific targeting of enterovirus capsid by functionalized monodisperse gold nanoclusters. *Proc Natl Acad Sci U.S.A*. 2014;111:1277–1281.
54. Gunawardene PN, Corrigan JF, Workentin MS. Golden opportunity: a clickable azide-functionalized $[Au_{25}(SR)_{18}]^-$ nanocluster platform for interfacial surface modifications. *J Am Chem Soc*. 2019;141:11781–11785.
55. Kang X, Ren M, Zhu M, Zhang K. Azide-functionalized nanoclusters via a ligand-induced rearrangement. *Chem Mater*. 2020;32:6736–6743.
56. Muhammed MAH, Shaw AK, Pal SK, Pradeep T. Quantum clusters of gold exhibiting FRET. *J Phys Chem C*. 2008;112:14324–14330.

57. Pyo K, Thanthirige VD, Kwak K, Pandurangan P, Ramakrishna G, Lee D. Ultrabright luminescence from gold nanoclusters: rigidifying the Au(I)–thiolate shell. *J Am Chem Soc*. 2015;137:8244–8250.
58. Devadas MS, Kwak K, Park J-W, et al. Directional electron transfer in chromophore-labeled quantum-sized Au_{25} clusters: Au_{25} as an electron donor. *J Phys Chem Lett*. 2010;1:1497–1503.
59. Klajn R, Bishop KJM, Grzybowski BA. Light-controlled self-assembly of reversible and irreversible nanoparticle suprastructures. *Proc Natl Acad Sci U.S.A*. 2007;104:10305–10309.
60. Klajn R, Stoddart JF, Grzybowski BA. Nanoparticles functionalised with reversible molecular and supramolecular switches. *Chem Soc Rev*. 2010;39:2203–2237.
61. Rival JV, Nonappa, Shibu ES. Light-Triggered Reversible Supracolloidal Self-Assembly of Precision Gold Nanoclusters. *ACS Appl Mater Interfaces*. 2020;12:14569–14577.
62. Udayabhaskararao T, Kundu PK, Ahrens J, Klajn R. Reversible photoisomerization of spiropyran on the surfaces of Au_{25} nanoclusters. *Chem Phys Chem*. 2016;17:1805–1809.
63. Shibu ES, Sugino S, Ono K, et al. Singlet-oxygen-sensitizing near-infrared-fluorescent multimodal nanoparticles. *Angew Chem Int Ed*. 2013;52:10559–10563.
64. Agrachev M, Fei W, Antonello S, et al. Understanding and controlling the efficiency of $Au_{24}M(SR)_{18}$ nanoclusters as singlet-oxygen photosensitizers. *Chem Sci*. 2020;11:3427–3440.
65. Guo R, Murray RW. Substituent effects on redox potentials and optical gap energies of molecule-like $Au_{38}(SPhX)_{24}$ nanoparticles. *J Am Chem Soc*. 2005;127:12140–12143.
66. Parker JF, Kacprzak KA, Lopez-Acevedo O, Häkkinen H, Murray RW. Experimental and density functional theory analysis of serial introductions of electron-withdrawing ligands into the ligand shell of a thiolate-protected Au_{25} nanoparticle. *J Phys Chem C*. 2010;114:8276–8281.
67. Jung J, Kang S, Han Y-K. Ligand effects on the stability of thiol-stabilized gold nanoclusters: $Au_{25}(SR)_{18}^{-}$, $Au_{38}(SR)_{24}$, and $Au_{102}(SR)_{44}$. *Nanoscale*. 2012;4:4206–4210.
68. Yao H, Miki K, Nishida N, Sasaki A, Kimura K. Large optical activity of gold nanocluster enantiomers induced by a pair of optically active penicillamines. *J Am Chem Soc*. 2005;127:15536–15543.
69. Yao H, Fukui T, Kimura K. Chiroptical responses of D-/L-penicillamine-capped gold clusters under perturbations of temperature change and phase transfer. *J Phys Chem C*. 2007;111:14968–14976.
70. Zhu M, Qian H, Meng X, Jin S, Wu Z, Jin R. Chiral Au_{25} nanospheres and nanorods: synthesis and insight into the origin of chirality. *Nano Lett*. 2011;11:3963–3969.
71. Xu Q, Kumar S, Jin S, Qian H, Zhu M, Jin R. Chiral 38-gold-atom nanoclusters: synthesis and chiroptical properties. *Small*. 2014;10:1008–1014.
72. Haruta M, Yamada N, Kobayashi T, Iijima S. Gold catalysts prepared by coprecipitation for low-temperature oxidation of hydrogen and of carbon monoxide. *J Catal*. 1989;115:301–309.
73. Liu L, Corma A. Metal catalysts for heterogeneous catalysis: from single atoms to nanoclusters and nanoparticles. *Chem Rev*. 2018;118:4981–5079.
74. Fang J, Zhang B, Yao Q, Yang Y, Xie J, Yan N. Recent advances in the synthesis and catalytic applications of ligand-protected, atomically precise metal nanoclusters. *Coord Chem Rev*. 2016;322:1–29.
75. Yamazoe S, Koyasu K, Tsukuda T. Nonscalable oxidation catalysis of gold clusters. *Acc Chem Res*. 2014;47:816–824.
76. Li G, Jin R. Atomically precise gold nanoclusters as new model catalysts. *Acc Chem Res*. 2013;46:1749–1758.
77. Nasaruddin RR, Chen T, Li J, et al. Ligands modulate reaction pathway in the hydrogenation of 4-nitrophenol catalyzed by gold nanoclusters. *ChemCatChem*. 2018;10:395–402.
78. Li J, Nasaruddin RR, Feng Y, Yang J, Yan N, Xie J. Tuning the accessibility and activity of $Au_{25}(SR)_{18}$ nanocluster catalysts through ligand engineering. *Chem Eur J*. 2016;22:14816–14820.
79. Li G, Abroshan H, Liu C, et al. Tailoring the electronic and catalytic properties of Au_{25} nanoclusters *via* ligand engineering. *ACS Nano*. 2016;10:7998–8005.
80. Yoon B, Luedtke WD, Barnett RN, et al. Hydrogen-bonded structure and mechanical chiral response of a silver nanoparticle superlattice. *Nat Mater*. 2014;13:807–811.
81. Yao Q, Yu Y, Yuan X, et al. Counterion-assisted shaping of nanocluster supracrystals. *Angew Chem Int Ed*. 2015;54:184–189.
82. Nonappa, Lahtinen T, Haataja JS, Tero T-R, Häkkinen H, Ikkala O. Template-free supracolloidal self-assembly of atomically precise gold nanoclusters: from 2D colloidal crystals to spherical capsids. *Angew Chem Int Ed*. 2016;55:16035–16038.

83. Zhang C, Zhang A, Hou W, et al. Mimicking pathogenic invasion with the complexes of $Au_{22}(SG)_{18}$-engineered assemblies and folic acid. *ACS Nano*. 2018;12:4408–4418.
84. Wu Z, Dong C, Li Y, et al. Self-assembly of Au_{15} into single-cluster-thick sheets at the interface of two miscible high-boiling solvents. *Angew Chem Int Ed*. 2013;52:9952–9955.
85. Wu Z, Li Y, Liu J, Lu Z, Zhang H, Yang B. Colloidal self-assembly of catalytic copper nanoclusters into ultrathin ribbons. *Angew Chem Int Ed*. 2014;53:12196–12200.
86. Tsuzuki S. CH/π interactions. *Annu Rep Prog Chem Sect C: Phys Chem*. 2012;108:69–95.
87. Shi L, Zhu L, Guo J, et al. Self-assembly of chiral gold clusters into crystalline nanocubes of exceptional optical activity. *Angew Chem Int Ed*. 2017;56:15397–15401.
88. Sculfort S, Braunstein P. Intramolecular d^{10}-d^{10} interactions in heterometallic clusters of the transition metals. *Chem Soc Rev*. 2011;40:2741–2760.
89. Wu Z, Du Y, Liu J, et al. Aurophilic interactions in the self-assembly of gold nanoclusters into nanoribbons with enhanced luminescence. *Angew Chem Int Ed*. 2019;58:8139–8144.
90. Yao Q, Yuan X, Yu Y, Yu Y, Xie J, Lee JY. Introducing amphiphilicity to noble metal nanoclusters via phase-transfer driven ion-pairing reaction. *J Am Chem Soc*. 2015;137:2128–2136.
91. Negishi Y, Kamimura U, Ide M, Hirayama M. A photoresponsive Au_{25} nanocluster protected by azobenzene derivative thiolates. *Nanoscale*. 2012;4:4263–4268.
92. Chandra S, Nonappa, Beaune G, et al. Highly luminescent gold nanocluster frameworks. *Adv Opt Mater*. 2019;7.
93. Yahia-Ammar A, Sierra D, Mérola F, Hildebrandt N, Le Guével X. Self-assembled gold nanoclusters for bright fluorescence imaging and enhanced drug delivery. *ACS Nano*. 2016;10:2591–2599.
94. Ouyang X, Wang M, Guo L, et al. DNA nanoribbon-templated self-assembly of ultrasmall fluorescent copper nanoclusters with enhanced luminescence. *Angew Chem Int Ed*. 2020;59:11836–11844.

CHAPTER

21

Hydrides, alkynyls, phosphines, and amines as ligands for nanoclusters

Megalamane S. Bootharaju[a] *and Thalappil Pradeep*[b]

[a] Seoul National University, South Korea [b] Deepak Parekh Institute Chair Professor and Professor of Chemistry, Department of Chemistry, Indian Institute of Technology Madras, Chennai, India

21.1 Introduction

Atomically precise clusters (APCs) of the coinage and transition metals as well as the main group elements exhibit unusual structural diversity and potential applications in catalysis, energy conversion, sensing, and bioimaging.[1] High monodispersity and well-defined molecular structures have rendered APCs promising materials for correlating structures with properties. APCs are large molecules composed of various components, because of which their rational chemical synthesis remains challenging. Significant advancements in the synthetic approaches have produced a giant library of APCs with well-defined geometric and electronic structures.[2] The capping ligands, one of the most important components, provide not only stability but also influence the formation of APCs. Distinctly sized and structurally well-defined APCs are indeed essential for various purposes; however, their synthesis is largely influenced by the choice of ligands and preparative protocols. Notably, thiolates (–SR, R: alkyl or aryl group) are widely employed as protecting ligands for coinage metal APCs. Others, including, phosphines (PR_3), carbenes ($:CR_2$), halides (X^-, X: Cl or Br), carbonyls (CO), amines (RNH_2), hydrides (H^-), alkynyls ($RC{\equiv}C^-$), and/or their combinations have also been considered to be potential size and structure modulators.[2–6]

The role of the ligands in controlling the size, structure, and growth mechanisms of APCs remains unclear. However, the steric and electronic constraints of the ligands are found to significantly affect the overall cluster size. Metal–ligand interfaces in the structurally characterized APCs have intriguing implications on optical, structural, and catalytic properties. Particularly, when the ligands exhibit diverse coordination modes with metals, the size,

DOI: https://doi.org/10.1016/B978-0-323-90879-5.00011-1

structure, and properties of the resultant clusters will be greatly modified, as compared to ligands which exhibit only a limited number of surface anchoring modes. In addition to size and structural control of APCs, the ligands play pivotal roles in self-assembly and photophysical properties through strong noncovalent interactions, including, hydrogen bonding, and aromatic π–π and alkyl/aryl CH-π interactions.[7] The ligands also affect catalytic activity; for example, alkynylated Au clusters are found to efficiently catalyze semihydrogenation of alkynes as compared to thiolated ones of identical size.[8] The surface charge and the functional groups of the ligands of APCs (for example, $-COO^-$ groups of mercaptocarboxylic acids) are further useful for postsynthetic surface functionalization and catalysis by capturing metal ions.[9] In this chapter, we provide a brief overview of the bonding, characterization, and unique properties of coinage metal APCs, particularly, with phosphines, hydrides, alkynyls, and nitrogen donors as well as their combinations as protecting ligands.

21.1.1 Hydrides

Hydrides, the anions of hydrogen, possess unit negative charge and are represented as H^-. Each hydride contains one proton in the nucleus and two electrons surrounding it. It is the smallest closed-shell spherical anion known until now. Metal hydrides (e.g., NaH, $LiAlH_4$) are known to be strong bases and reducing agents in organic and nanomaterials synthesis. Importantly, hydrides in the metal hydride clusters can be transformed to reactive neutral (H^0) atoms and ions (H^+), which are often highly desirable in catalytic cycles.[3]

The coinage metals (Cu, Ag, and Au) form hydrides through the interactions between metal and hydrogen atoms. The d-subshells of these metals are fully occupied in their common monovalent state. However, the d-electrons of coinage metals are still energetically accessible, enabling their unusual reactivity and bonding. The nature of bonding between hydrogen and metals is largely covalent due to low electropositivity of the latter. Theoretical analyses suggested planar cyclic structures for coinage metal hydrides owing to the reduced dipole moment and small charge separation between metal and hydrogen.[10] In contrast, group 1 and group 11 metal hydrides, with greater ionic bonding character, prefer a cubic tetrameric structure for $[MH]_4$ clusters. The lower half reduction potential for Cu^I/Cu^0 (0.52 V) makes it challenging to prepare Cu° clusters. As a result, numerous Cu^I APCs with high nuclearities are realized. On the other hand, relatively high half reduction potential for M^I/M^0 (M = Ag and Au; 0.8 and 1.69 V, respectively) has resulted only a limited number of hydride-containing Ag and Au clusters. Interestingly, in small clusters, hydrogen is found to behave as a metal atom and it mimics coinage metals, particularly Au, as the metallic affinity increases in the order of Cu < Ag < Au. The hydride is found to exhibit a variety of coordination modes, including bridging (μ_2-H), capping (μ_3-H) and interstitial (μ_{4-6}-H), as shown in Fig. 21.1.

21.1.2 Alkynyls

Inspired by the chemisorption of alkynes onto the surface of gold nanoparticles, ligand-engineering has been further extended to prepare coinage metal clusters using alkynes as ligands. The alkynyls are monoanionic species ($RC{\equiv}C^-$) similar to widely used thiolates (RS^-) for metal clusters. Furthermore, they are unsaturated hydrocarbons with a triple bond (one σ and two π bonds) between two *sp* hybridized carbon atoms. The proton bound to alkynyl

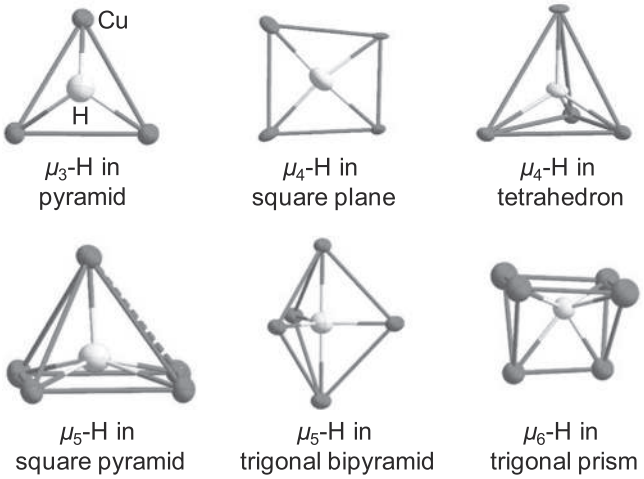

FIGURE 21.1 Different coordination modes observed for hydride in copper hydride clusters. Color legends: gray, Cu; white, H. Reproduced with permission from ref.[5] Copyright 2016 American Chemical Society.

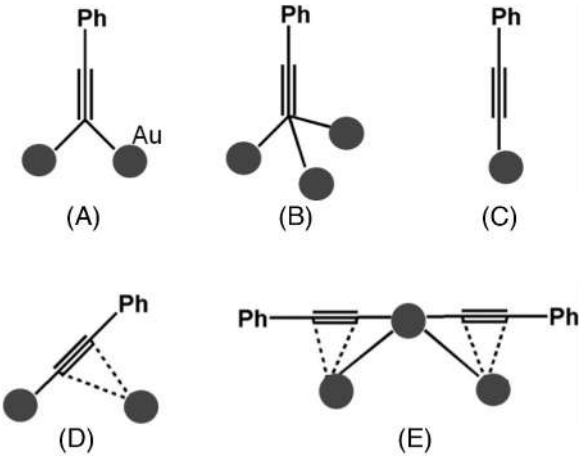

FIGURE 21.2 Various surface coordination modes (motifs A–E) of PhC≡C$^-$ observed on the surface of gold APCs. Filled gray circles indicate Au atoms. Reproduced with permission from ref.[6] Copyright 2018 American Chemical Society.

carbon, which has 50% *s* character with high electronegativity, is sufficiently acidic and can readily interact with coinage metals through a strong metal–carbon bond formation. For example, the Cu and Ag ions are well known to form corresponding metal acetylides. In addition to terminal alkynyl carbanion, the C≡C bond can also interact with metal surface through both σ and π bonding.

Those interactions resulted in several intriguing metal–alkynyl interfacial structures, such as linear, L-shaped and V-shaped staple motifs as shown in Fig. 21.2.[6] The motifs A and B represent the μ_2- and μ_3-coordinated alkynyl ligands with Au atoms, respectively, while C is the simple terminal binding mode forming an Au–C σ-bond. The motif D is observed on bridging of two Au atoms of two different Au icosahedrons. The complex motif E represents an energetically favored linear PhC≡C–Au–C≡CPh unit with π interactions between C≡C and Au atoms. The extended conjugation to ligands through the metal–alkynyl bond may

enable the direct electronic interactions with the metal core, modifying the total electronic and geometric structures as well as the optical absorption, photoluminescence, and catalytic properties of the APCs. The V- and L-shaped motifs resemble RS-$(AuSR)_n$ (n =1 or 2) staples in thiolated Au clusters. However, the L-shaped motifs differ significantly from each other. The triple bond in alkynes can orient perpendicularly or horizontally due to flexibility in the coordination modes, whereas the thiolates normally interact with Au atoms via Au−S σ-bond. The metal–ligand interfaces play major role in dictating the size and structure of the APCs. The electronic and steric constraints of the ligand's tail groups also influence the coordination modes of ligands on the metal surface.

21.1.3 Phosphines and amines

The phosphine and amine ligands are charge-neutral, while thiolates, hydrides and alkynyls are singly charged anions. Both the binding sites, P and N, of phosphines and amines belong to the group 15 of the periodic table. The lone pair of electrons on these atoms can readily form coordinate bonds with the metal atoms. While the phosphines are found to form a wide range of coinage metal clusters,[11] the amines are found only in a limited number of cases,[12,13] probably due to the soft cationic nature of coinage metals. However, other forms of N binding ligands/groups such as amido is frequently observed in APCs.[14,15] The triphenylphosphine (TPP or PPh_3; Ph = phenyl) is the commonly used bulky phosphine ligand either solely or as a coligand in the preparation of APCs. As it binds with metals only through terminal binding mode, the resulting metal clusters will possess, exclusively, metal framework (inorganic core), and surrounding ligands (organic shell), unlike other cases containing metal core and metal–ligand–shell.[11]

While monophosphine-protected APCs have been widely explored, the use of multiphosphine ligands for the synthesis of APCs has just begun. Different orientations of multiphosphines offer clusters with intriguing features of intrinsic chirality and uncoordinated metal sites. The monophosphine ligands often results in clusters with closed polyhedral geometries. However, multidentate ligands occasionally form exceptional metal structures containing polyhedral cores with extra metal atoms surrounding them, denoted as [core + *exo*]-type clusters (Fig. 21.3A). In such clusters, the highest occupied molecular orbitals (HOMOs) are distributed over core and the lowest unoccupied molecular orbitals (LUMOs) are centered on *exo* metal atoms, resulting in a single electronic transition in their absorption spectrum.[11] The monoanionic dipyridylamido (dpa) ligand, deprotonated dipyridylamine (Hdpa), forms all-nitrogen-donor-protected Ag nanoclusters $[Ag_{21}(dpa)_{12}]^+$ and $[Ag_{22}(dpa)_{12}]^{2+}$ with the coordination modes as depicted in Fig. 21.3B.[15] The flexibility in the dpa arrangement enables reversible interconversion between these two clusters due to the differences in their solubility.

21.2 Atomic precision in labile ligand protected clusters

Steric constraints such as the presence of bulky alkyl or aryl groups within the ligand moiety are one of the important variables to tailor the size and geometric structure as well as the ligand exchange chemistry of the APCs.[16] However, the bulky ligands are thought to block and deactivate the catalytic activity of metal sites. In order to overcome this issue, the use of simple and

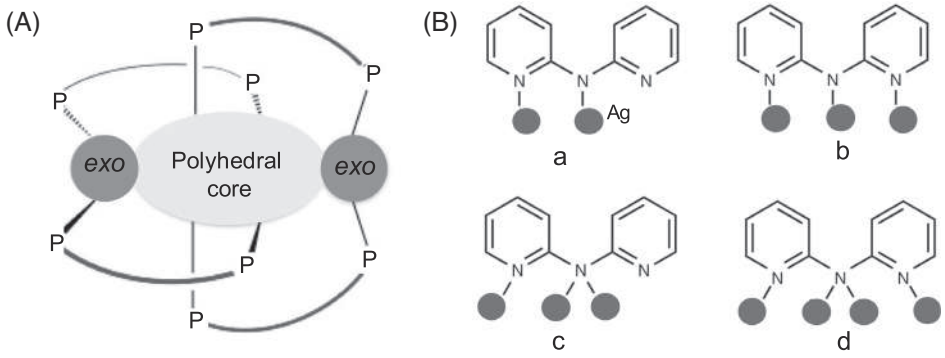

FIGURE 21.3 (A) Schematic of a [core + *exo*]-type cluster; *exo* Au atoms (gray) and the polyhedral Au core are bridged by diphosphine ligands. Reproduced with permission from ref.[11] Copyright 2018 American Chemical Society. (B) Various surface coordination modes (motifs a–d) of dipyridylamido (dpa) ligand observed on the surface of Ag clusters. Filled gray circles indicate Ag atoms. Redrawn with permission from the ref.[15] Copyright 2019 Nature Publishing Group.

labile ligands, such as hydrides, halides, and phosphines or their combination is suggested. Employing such ligands, various atomically precise materials, including simple clusters, self-assembled nanostructures (i.e., clusters of clusters), and APCs with uncoordinated sites are generated. In the following sections, we show-case specific examples for each category of these materials.

21.2.1 Simple clusters

The hydride-containing coinage metal clusters are commonly found to be coprotected with secondary ligands, including phosphines, halides, dithiophosphates, and thiolates. The small size of the hydrides, compared to coinage metal ions, hindered the formation of stable metal clusters protected solely by hydrides. The usual sources of hydrides, such as $NaBH_4$ or silanes, are typically used in the synthesis of hydride-protected APCs. The Cu-hydride cluster $[CuH(PPh_3)]_6$ is well known as the Stryker's reagent as well as the catalyst for various reduction reactions.[10] Its structure consists of a distorted octahedron of six copper atoms, wherein each of them is bound to one PPh_3 molecule. The hydrides are described as face-bridging (μ_3-H) on the basis of single crystal X-ray diffraction. However, the single crystal neutron diffraction and theoretical calculations of its analogue revealed that the hydrides are actually the edge-bridging (μ_2-H).[17] A four-coordinate hydride is observed in the $[Cu_7(H)(S_2C(aza\text{-}15\text{-}crown\text{-}5)_6]$ cluster. Its X-ray structure identified an elongated tricapped pyramidal Cu_7 framework, as shown in Fig. 21.4A. On the other hand, the neutron diffraction data reveal a tricapped distorted tetrahedron Cu_7H framework with the central position occupied by one hydride (μ_4-H) (Fig. 21.4B). The neutron diffraction is a more reliable technique to locate hydrides and their bonding in metal clusters since the electron density on hydrides is not adequate for X-ray diffraction. Liu and coworkers reported the presence of capping (eight μ_3-H), truncating (four μ_5-H and two μ_6-H), and interstitial hydrides (one μ_4-H) simultaneously within the rhombicuboctahedral $[Cu_{28}(H)_{15}(S_2CNR)_{12}]PF_6$ cluster.[5]

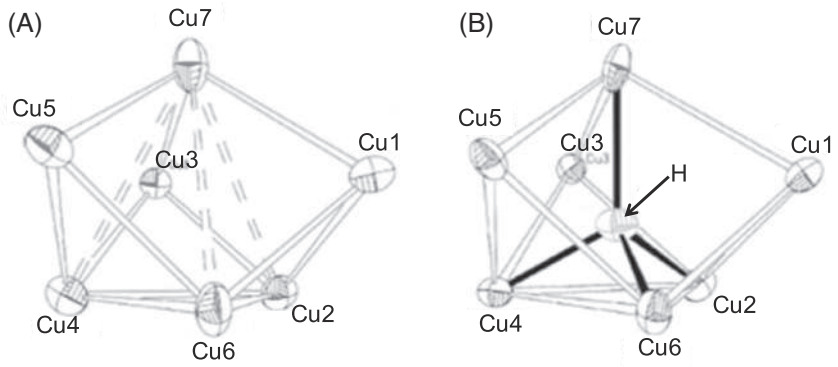

FIGURE 21.4 The single crystal X-ray (A) and neutron (B) diffraction structures of $[Cu_7(H)(S_2C(aza\text{-}15\text{-}crown\text{-}5)_6]$ clusters. For clarity, only Cu_7 and Cu_7H frameworks are shown. Reproduced with permission from ref.[5] Copyright 2016 American Chemical Society.

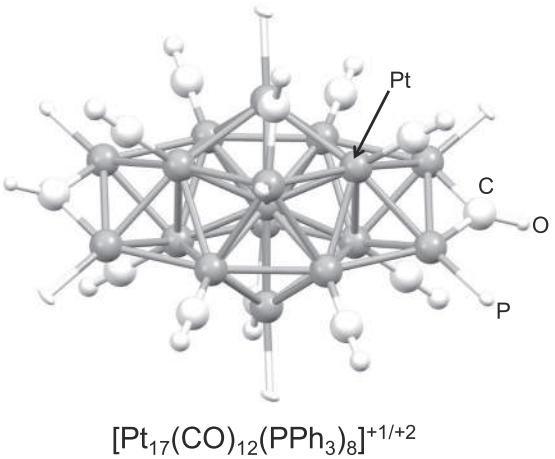

FIGURE 21.5 The single crystal X-ray structure of $[Pt_{17}(CO)_{12}(PPh_3)_8]^+$ cluster. Reproduced with permission from ref.[18] Copyright 2017 American Chemical Society.

Phosphine-protected metal clusters have a rich literature owing to the binding ability of phosphines with a variety of metals. Among them, Pt- and Au-based clusters are important as they serve as miniaturized fuel-cell redox catalysts. The $[Pt_{17}(CO)_{12}(PPh_3)_8]$ is a notable cluster, which exists in both +1 and +2 charge states, that is, $[Pt_{17}(CO)_{12}(PPh_3)_8]^{n+}$, $(n = 1, 2)$.[18] Despite different charges, the overall ellipsoid-like structure is apparent in both clusters. Such a structure is also observed in a neutral $[Pt_{17}(CO)_{12}(PEt_3)_8]$ cluster with a different phosphine. They all comprise a Pt_{13} icosahedron core stabilized by eight terminal CO, two bridging μ_2-CO, four PPh_3 and two capping $Pt_2(\mu_2\text{-}CO)(PPh_3)_2$ units (Fig. 21.5). The charge-states are found to modify electronic properties similar to those in $[Au_{25}(SR)_{18}]^{+1/0/-1}$ clusters. Furthermore, the $[Pt_{17}(CO)_{12}(PPh_3)_8]^{n+}$ clusters ($n = 1, 2$) exhibit photoluminescence in the near-infrared region.

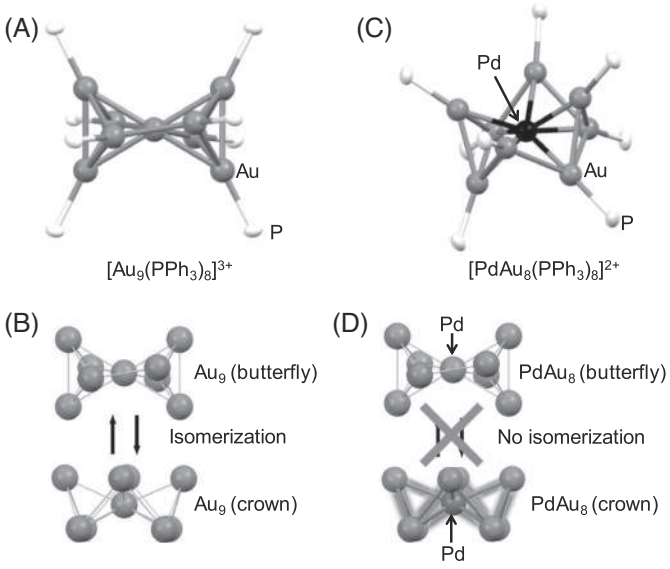

FIGURE 21.6 The single crystal X-ray structures of (A) $[Au_9(PPh_3)_8]^{3+}$ and (C) $[PdAu_8(PPh_3)_8]^{2+}$ clusters. Representation of (B) isomerization of $[Au_9(PPh_3)_8]^{3+}$ clusters and (D) its isomerization suppression upon Pd doping. Adapted with permission from ref.[20] Copyright 2017 American Chemical Society.

The $[Au_9(PPh_3)_8]^{3+}$ is an important example of all-phosphine-ligated gold clusters. Its X-ray crystal structure revealed the presence of an icosahedron-derived crystallographic D_2 and approximate molecular D_{2h} skeletal symmetries.[19] In other words, the Au_9 framework is obtained by removing a rectangle of four gold atoms from the centered Au_{13} icosahedron. The Au_9 framework in $[Au_9(PPh_3)_8](NO_3)_3$ cluster can be visualized as butterfly shaped (Fig. 21.6A), denoted as Au_9 (butterfly). However, in the presence of a different counterion such as $[PMo_{12}O_{40}]^{3-}$, this cluster crystallizes in crown shape, denoted as Au_9 (crown).[20] This demonstrates that $[Au_9(PPh_3)_8]^{3+}$ can have both butterfly and crown isomers, depending on the counter anions and the physical state of the cluster (i.e., solution- and solid-state) (Fig. 21.6B). It is interesting to note that in $[Au_9(PPh_3)_8]^{3+}$, one of the Au atoms can be replaced by a Pd atom to form the $[PdAu_8(PPh_3)_8]^{2+}$ cluster. Its crystal structure revealed that the Pd atom is located at the center (Fig. 21.6C).[19,21] The overall structure appears to be crown, which is the original structure to begin with in the solution-state. This indicates that the isomerization has been suppressed after Pd doping (Fig. 21.6D). Tsukuda and coworkers showed that the energy difference between isomers of Au_9^{3+} is comparable to that between isomers of $PdAu_8^{2+}$. This suggests that relative stabilities of the isomers may not be the primary reason for the isomerization suppression.[20] The X-ray absorption fine-structure analysis of $PdAu_8$ crown cluster reveals that its metal–metal bonds are stiffer than the corresponding bonds in Au_9 crown. Particularly, radial Au–Pd and lateral Au–Au bonds of $PdAu_8$ crown are more stiff owing to the increase in the ionic nature and decrease in electrostatic repulsion between the surface Au atoms, respectively. Instead of Pd, Pt could also be incorporated to produce $[PtAu_8(PPh_3)_8]^{2+}$.[22] This similar site-elective-doping may be due to the similar electronic structures of Pd and Pt (i.e., outermost electronic configuration).

The silver–phosphine clusters are also an equally important topic of current study, particularly with respect to structural and size correlations. Instead of simple phosphines, the use of

polyphosphines may provide clusters of unusual molecular structures. A tripodal polyphosphine ligand, tris((diphenylphosphino)methyl)amine, denoted as (N-triphos), is employed to prepare a silver cluster with the formula $[Ag_{15}(N\text{-triphos})_4(Cl_4)](NO_3)_3$.[23] Its crystal structure comprises a hexacapped body-centered cubic (bcc) framework, which is further stabilized by four N-triphos and four Cl^- ligands. This cluster has both geometric and electronic shell closures with eight valence-free electrons.

21.2.2 Clusters of clusters

The second mode of APCs that can be generated by the engineering of surface ligands is "clusters of clusters" containing several cluster monomers that are self-assembled uniquely. The word "cluster of clusters" was first coined by Teo and coworkers for the $Au_{25-x}M_x$ clusters (M = Ag, Pt, Pd) in the 1980s.[24] These materials are highly desirable since they provide mechanistic insights into structural- and size-growth modes. The centered M_{13} icosahedron (M = Au, Ag, and Cu) is a primary building block frequently encountered in a large number of APCs. Assembling of such icosahedra in a linear or cyclic fashion produces this subclass of clusters with the formula $(M_{13})_n$. Experimentally, only the Au_{13}, Au_{25}, and Au_{37} and analogous doped clusters have been observed through the vertex-sharing pattern. The $[Au_{13}(PPh_3)_{10}Cl_2]^{3+}$ monomer contains two Cl^- ions on the two apical Au sites and remaining 10 Au atoms are connected to 10 PPh_3 ligands. The Au_{13} dimer, $[Au_{25}(PPh_3)_{10}Cl_7]^{2+}$ is still unavailable due to the challenges in overcoming of the instability of Au–halogen bonds. However, corresponding heteroatom doped clusters could be obtained through the formation of stable heteroatom–halogen bonds. For example, the strong Ag-halide bonding enables the synthesis of $[Au_{12}Ag_{13}(PPh_3)_{10}X_7]^{2+}$ cluster.[25] The top and bottom pentagonal positions occupied by 10 Au atoms are stabilized by 10 PPh_3 ligands. The top and bottom apical positions and 10 waist positions (in the middle of the M_{25} rod) are occupied by 10 Ag atoms. The waist Ag atoms are bridged by five Cl atoms to complete the $[Au_{12}Ag_{13}(PPh_3)_{10}X_7]^{2+}$ structure. The icosahedron center and the vertex sharing atom are Au and Ag, respectively. The Pt-doped Ag counterpart $[Pt_2Ag_{23}(PPh_3)_{10}Cl_7]$ has shown similar structure with the two Pt atoms at the center of icosahedrons.[26]

Although synthesis of $[Au_{25}(PPh_3)_{10}Cl_7]^{2+}$ cluster has remained a challenge, a combination of thiol, PPh_3 and halide (X = Cl or Br) provides both bi-icosahedral $[Au_{25}(PPh_3)_{10}(SC_2H_4Ph)_5X_2]^{2+}$ and tri-icosahedral $[Au_{37}(PPh_3)_{10}(SC_2H_4Ph)_{10}X_2]^+$ clusters.[27] Their crystal structures are shown in Fig. 21.7, revealing the vertex sharing linear self-assembly of icosahedra. The optical absorption features sequentially red-shift to near-infrared region with increasing number of building blocks. Especially, the absorption peaks for HOMO–LUMO transitions in mono-, bi-, and tri-icosahedral clusters appear at 500, 670, and 1230 nm, respectively. Consequently, optical band-gap also correspondingly decreases, indicating that free electrons are delocalized in the one-dimensional quantum box. Furthermore, the tri-icosahedral clusters showed better catalytic activity for CO oxidation compared to bi-icosahedral clusters due to the increased number of side atoms. The driving force for the assembly of Au_{13} icosahedra is not fully understood yet. However, the experimental observations indicate that enhanced stability of clusters through synergistic effects between metal atoms guide their assembly. For example, the bi-icosahedral $Pd_2Au_{23}(PPh_3)_{10}Br_7$ could be synthesized by overcoming the weak Au–halogen bonding through PdAu synergistic interactions.[28] In the absence of Pd, the synthesized product is only $[Au_{11}(PPh_3)_8Br_2]^+$. Alternatively,

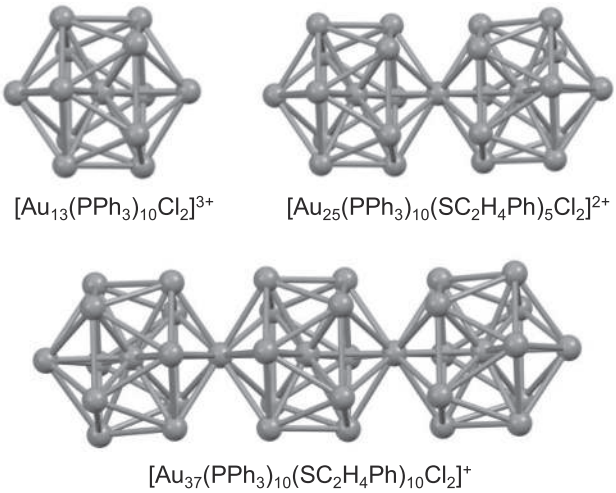

FIGURE 21.7 Structures of nanoclusters comprising mono-, bi-, and tri-icosahedron units. Color labels: gray = Au atoms. Atoms of the ligands are not shown for clarity. Redrawn with permission from ref.[27] Copyright 2015 American Chemical Society.

synergy between ligands (thiol, halide, and phosphine) resulted in the bi-icosahedral linear assembly in $[Au_{25}(PPh_3)_{10}(SR)_5X_2]^{2+}$ cluster.

In addition to linear assembly, the icosahedrons are found to assemble in cyclic manner as well. The $[Pt_3Ag_{33}(PPh_3)_{12}Cl_8]^+$ cluster is found to have three Pt-centered Ag icosahedra (i.e., $PtAg_{12}$), which are connected in a cyclic manner by vertex sharing.[29] This icosahedral assembly is further manifested in their optical properties. Compared to mono- and bi-icosahedral $PtAg_{12}$ units, $[Pt_3Ag_{33}(PPh_3)_{12}Cl_8]^+$ exhibits red-shifted absorption and photoluminescence features. Furthermore, a trimetallic $[Pt_3Au_{12}Ag_{21}(PPh_3)_{12}Cl_8]^+$ cluster with such a cyclic assembly could also be obtained by metal exchange method.[29] The Au atoms preferably occupy the Ag sites connected to phosphine ligands.

21.2.3 APCs with uncoordinated sites

One of the long-standing goals of the cluster science is to develop synthetic protocols for producing stable metal clusters which can serve as model catalysts as well as building blocks to design functional materials. Pioneering work by Haruta and coworkers[30] on catalytic CO oxidation by gold nanoparticles has stimulated a wide range of interests in APCs. The ligands are absolutely necessary for the synthesis and stabilization of APCs. The presence of ligands generally results in the low catalytic activity of APCs. The removal of ligands by thermal treatment may cause aggregation of clusters and the loss of the original structure of the cluster. To overcome this problem, the synthesis of APCs with uncoordinated surface metal sites is suggested.

The tetrahedral (T_d) Au_{20} pyramidal cluster, denoted as T_d-Au_{20}, is found to be highly stable in the gas phase.[31] The simulated structure is found to have four Au(111) faces with all the gold atoms on the surface (Fig. 21.8A) mimicking a small piece of the bulk gold. The hypothesis of the capping of four Au atoms at the tetrahedral corners with four phosphine ligands creates uncoordinated 16 Au atoms (Fig. 21.8B). The chemical synthesis of this cluster with different phosphine and other ligands will open a new direction in cluster science for catalysis. Only a little success has been achieved in the solution-phase synthesis and

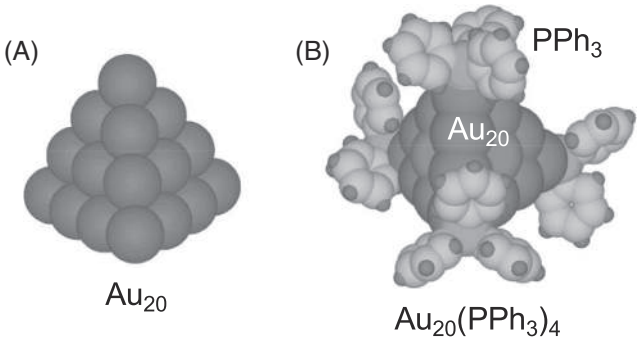

FIGURE 21.8 Computed structures of (A) Au_{20} and (B) $Au_{20}(PPh_3)_4$ clusters. Adapted with permission from ref.[33] Copyright 2018 American Chemical Society.

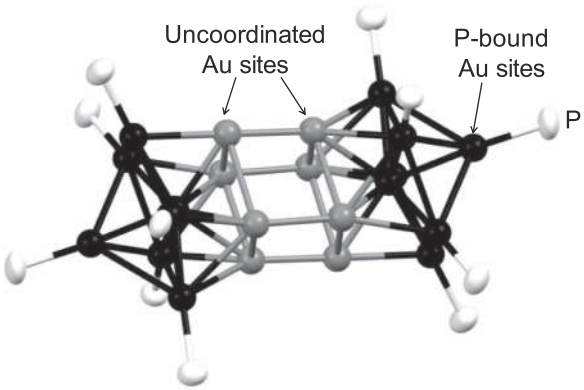

FIGURE 21.9 Structure of $Au_{22}(dppo)_6$ nanocluster. Color labels: white: P atom of dppo ligand; black: Au atoms binding with P; gray: uncoordinated Au atoms. Redrawn with permission from ref.[34] Copyright 2014 American Chemical Society.

mass spectrometric identification of a dicationic $[Au_{20}(PPh_3)_4]^{2+}$ cluster with 18 free valence electrons.[32] However, its crystal structure is still unavailable due to lack of synthetic methods to produce pure clusters with high yield. Theoretical calculations predict that the T_d-Au_{20} cluster is energetically stable, but the four central atoms on the four Au(111) faces are pushed outward. Even if these four Au atoms are involved in bonding with ligands, at least 12 Au atoms are left uncoordinated.

The phosphines are envisioned to be ideal ligands to maintain the pyramidal structure of the T_d-Au_{20} cluster. Various multidentate phosphines of the type $[(Ph)_2P(CH_2)_nP(Ph)_2$, n =1, 2,….] are explored with the aim of producing T_d-Au_{20} cluster. However, steric and electronic constraints need to be appropriate to obtain clusters of desired sizes and structures, which is very challenging. After repeated trials by using diphosphines of different carbon chain lengths, $Au_{22}(L^8)_6$ clusters, L = 1,8-bis(diphenylphosphino)octane or dppo, are synthesized and their structure is determined. Surprisingly, its structure contains two Au_{11} units bridged by a total of six dppo ligands, leaving a total of eight Au atoms uncoordinated (Fig. 21.9).[34] The overall structure resembles a rod of 1.4 nm length. Specifically, the uncoordinated Au atoms participate in the bridging of two Au_{11} units. This cluster is the first example of ligand protected APCs to contain unprotected metal sites.

The flexibility in the carbon chain of the diphosphine ligand is explored to deduce the difference in the cluster's size. By using bis[(2-diphenylphosphino)ethyl]ether (or dppee), a polymorphic cluster with the composition $[Au_{22}(dppee)_7H_3]^{3+}$ is obtained.[33] Its distinct optical properties compared to that of $Au_{22}(L^8)_6$ indicate that the molecular structure would be different from each other. With the hypothesis that the C_3-axis of the tetrahedral Au_{20} cluster may be experimentally achieved by using a tetraphosphine ligand, tris[2-(diphenylphosphino)ethyl]phosphine (PP_3) with a threefold symmetry is employed. Surprisingly, the synthesized cluster is $[Au_{20}(PP_3)_4]Cl_4$. Unfortunately, the single crystal structure showed that it does not have the tetrahedral geometry. Instead, it comprises Au_{13} icosahedron core, on which a seven atom Au layer is arranged in a propeller fashion. This arrangement induces intrinsic chirality to the cluster with all 16 surface Au atoms being coordinated with ligands.

The uncoordinated Au sites in the $Au_{22}(L^8)_6$ cluster are exploited as catalysts for the oxidation of CO to CO_2 on reducible metal oxide supports such as TiO_2 and CeO_2. Indeed, without thermal treatment, that is, without ligand desorption, the $Au_{22}(L^8)_6$ clusters show catalytic activity at low temperatures.[35] On the contrary, Au_{25} clusters with all surface metal sites being ligated do not show any activity. Furthermore, theoretical calculations show that that the eight uncoordinated Au sites of $Au_{22}(L^8)_6$ cluster can chemisorb both CO and O_2 and catalyze the formation of CO_2 by activating CO and O_2. It is recently revealed that gold nanohydride cluster $[Au_{22}H_4(dppo)_6]^{2+}$ is the actual product during the synthesis of $Au_{22}(dppo)_6$.[36] During the slow crystallization, the hydrides are desorbed. The $[Au_{22}H_4(dppo)_6]^{2+}$ cluster would become a model cluster compound to demonstrate the hydrogen transformation reactions including, hydrogen evolution and proton (H^+) and hydride (H^-) release.

The steric repulsion between two ligands can produce clusters with open metal sites. The simultaneous use of bulky phosphine Ph_3P and planar dipyridyl amine (Hdpa) for the gold cluster synthesis provides $[Au_{23}(Ph_3P)_{10}(dpa)_2Cl](SO_3CF_3)_2$.[37] Interestingly, this cluster comprises eight uncoordinated gold atoms in the shape of a distorted bicapped triangular prism. These eight gold atoms are found to be available for coordination as revealed by a quantitative luminescence titration with 2-naphthalenethiol. The $[Au_{23}(Ph_3P)_{10}(dpa)_2Cl]^{2+}$ cluster exhibits excellent catalytic activity for selective oxidation of benzyl alcohol to benzaldehyde without the loss of its characteristics due to the protection by negatively charged multidentate dpa ligand.

21.3 Characterization

The ligand-protected metal clusters are characterized by various analytical techniques, including, single crystal X-ray diffraction (SCXRD), UV–vis spectroscopy, vibrational spectroscopy, photoelectron spectroscopy as well as the mass spectrometry. However, in addition to the SCXRD, the APCs stabilized by the ligands discussed in this chapter need other analytical tools, such as the neutron diffraction, electrospray ionization mass spectrometry (ESI MS), infrared (IR) spectroscopy, and nuclear magnetic resonance (NMR) spectroscopy.

21.3.1 Single crystal neutron diffraction (SCND)

The SCXRD is a very useful method to determine atomic arrangements containing medium to heavy elements with high electron densities. However, characterizing light elements

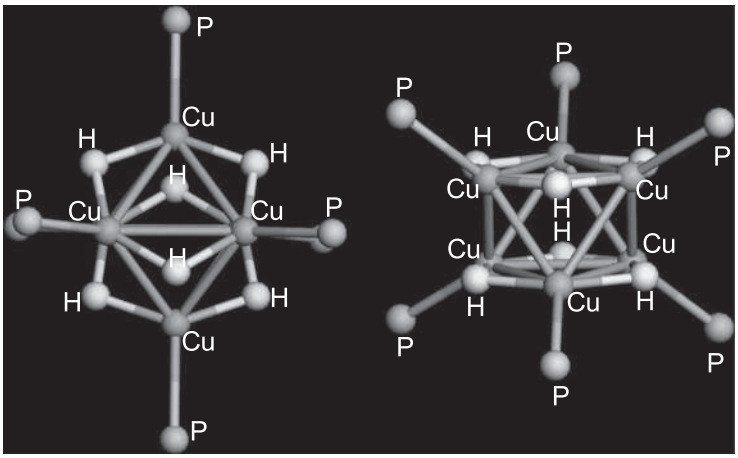

FIGURE 21.10 Different views of the $[HCuP]_6$ framework of Stryker's reagent. The hydrides appear to be triply bridging and edge bridging, left and right view, respectively. Adapted with permission from ref.[17] Copyright 2014 American Chemical Society.

using SCXRD is highly challenging. Especially, hydrides require alternative characterization methods such as neutron scattering. However, high-quality single crystals with larger size is a prerequisite condition for a successful SCND measurement. The accurate measurement of metal–hydrogen distances is critical for establishing the binding modes of hydrides with metals. The metal–hydrogen bond distances, for example, Cu–H in $[HCuP]_6$ core of Stryker's reagent, can be directly obtained via the radial distribution function (rdf), $g(R)$, which is generated from the neutron diffraction data.[17] Typically, hydrogen (^{1}H) possesses negative scattering lengths, while copper, deuterium, phosphorus, and carbon atoms possess positive scattering lengths. Here, the negative scattering length indicates that the neutron experiences a 180° phase shift upon scattering. Therefore, negative-going features are indicative of the distances involving hydrogen. For example, the negative-going and positive-going signals are observed at 1.09 Å for phenyl C–H in $[HCu(P(C_6H_5)_3)]_6$ and phenyl C–D in $[DCu(P(C_6D_5)_3)]_6$, respectively. However, the phenyl C–C signal at 1.40 Å is positive-going both in $[HCu(P(C_6H_5)_3)]_6$ and $[DCu(P(C_6D_5)_3)]_6$. The two different Cu–H distances appear through two negative-going signals at 1.67 and 1.92 Å for $[HCu(P(C_6H_5)_3)]_6$; similarly, two positive-going peaks are observed for Cu–D at 1.75 and 1.89 Å in $[DCu(P(C_6D_5)_3)]_6$. The Cu–H distances in $[HCu(P(C_6H_5)_3)]_6$ are very close to those observed in the P(*p*-tolyl)$_3$ derivative, confirming the presence of edge-bridging of hydrides in both (Fig. 21.10).

21.3.2 Infrared spectroscopy

Infrared (IR) spectroscopy provides information related to the presence and nature of metal–hydride bonding. The presence of other organic ligands, such as PPh_3, which exhibits a large number of infrared bands, complicates the analysis of metal–hydride bonds. Typically, the Cu–H stretching frequency appears in the range of 880–950 cm^{-1}.[10] The presence of hydrides should be confirmed by measuring the IR spectrum of deuteride-incorporated compounds. The deuterated samples exhibit red-shifted stretching frequencies due to increase in atomic mass. The gold hydride asymmetric stretching mode of $[Au_{22}H_4(dppo)_6]^{2+}$ appears around 1260 cm^{-1}.[36] The carbonyl group binds with metals in terminal (1940–1975 cm^{-1}) and

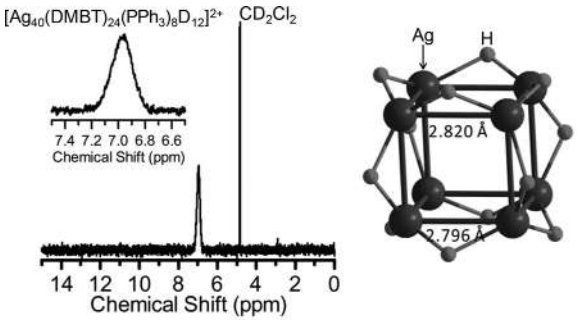

FIGURE 21.11 ^{2}H NMR spectrum (left) and molecular structure of innermost Ag_8H_{12} part of the $[Ag_{40}(DMBT)_{24}(PPh_3)_8D_{12}]^{2+}$ nanoclusters. Adapted with permission from ref.[38] Copyright 2019 American Chemical Society.

bridging (~1740 cm^{-1}) modes.[18] The alkynes (–C≡CH) exhibit various IR features. Generally, after formation of metal–alkyne bond, the C–H stretching and bending vibrations of ≡C–H at ~3324 and ~630 cm^{-1}, respectively disappear. The C≡C stretching peak at ~2120 cm^{-1} remains, however, with some shifts.

21.3.3 NMR spectroscopy

The proton NMR spectroscopy provides information on the types and the number of hydrides. Especially, it establishes the chemical environment around hydrides, which is very useful for structural optimization and property characterization. As the metal hydrides are generally metastable, irradiation with radiofrequencies during NMR measurements can cause liberation of H_2 gas, which typically appears at ~4.6 ppm. In such cases, low-temperature measurements would be helpful. Typically, coinage metal hydrides appear in ^{1}H NMR spectrum around 16 to −3 ppm. Similar to IR spectra, the ^{1}H NMR spectra are also highly complex due to the presence of several types of protons from other ligands. The ^{1}H NMR spectrum of $[Au_{22}H_4(dppo)_6]^{2+}$ clusters show four discrete peaks in 15.3–18.8 ppm range.[36] The complexity of ^{1}H NMR for hydrides can be simplified by performing ^{2}H NMR of deuterated samples. For example, $[Ag_{40}(DMBT)_{24}(PPh_3)_8D_{12}]^{2+}$ shows a single broad peak centered at ~7 ppm in the 0–15 ppm range (Fig. 21.11).[38] The single peak suggests that all hydrides are of one-type, that is, they are in the same chemical environment. The ^{31}P NMR spectra are usually recorded to support the binding of phosphines with the cluster surface. Upon binding with the cluster, the phosphine peaks become broad and shift downfield. The ^{31}P peak of PPh_3 at −5.4 ppm shifted to 2.83 ppm after formation of $[Pt_2Ag_{23}Cl_7(PPh_3)_{10}]$ cluster.

21.3.4 ESI mass spectrometry

Among various ionization methods available in mass spectrometry, the electrospray ionization (ESI) is the most important for nanoclusters. Since the single crystal X-ray structure cannot determine the complete formula of the metal-hydride clusters, the ESI MS is absolutely necessary. Importantly, the number of hydrides can be easily determined by performing deuterated experiments. The increase in mass to charge ratio and comparison between simulated and experimental mass spectra clarify the number of hydrides. For example, $[Ag_{40}(DMBT)_{24}(PPh_3)_8H_{12}]^{2+}$ cluster peak shifts to higher mass side by 6 on deuteration

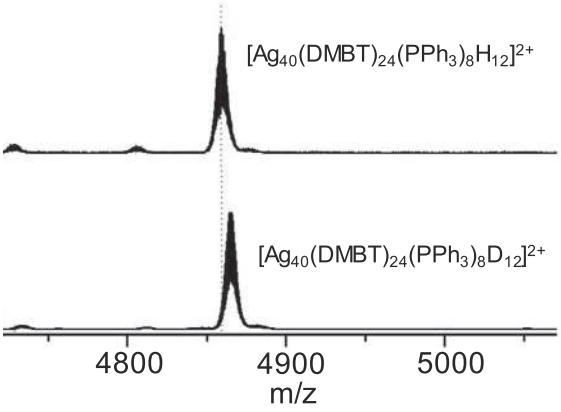

FIGURE 21.12 Mass spectrometric identification of hydrides. ESI mass spectra of $[Ag_{40}(DMBT)_{24}(PPh_3)_8H_{12}]^{2+}$ and $[Ag_{40}(DMBT)_{24}(PPh_3)_8D_{12}]^{2+}$ nanoclusters. A clear shift of peak toward high-mass after incorporating deuterides indicates the presence of hydrides. Adapted with permission from ref.[38] Copyright 2019 American Chemical Society.

(Fig. 21.12).[38] Since the charge-state of the cluster is 2, the total mass thus increased is 12 (2*6) Da. Therefore, the cluster originally has 12 hydrides. When the charge of the cluster is neutral, they can be detected as the adduct containing Cs^+ ions. The Cs^+-containing adducts can be identified in the mass spectrum in the positive ion mode. The ESI MS is also useful for determining the correct charge state of the clusters. The counterions cannot be located in the single crystal structure due to disorder or poor quality of the single crystals. For example, the $[Ag_{29}(BDT)_{12}(PPh_3)_4]^{3-}$ has 3^- core-charge.[39] However, it also appears as 2^- ion in the mass spectrum. The high intensity for 3^- state mass signal suggests that 3^- state is the actual charge, which is also in line with the electron close shell rule.

The lability of the ligands in metal clusters is an important aspect. However, experimental identification of this parameter is challenging. The mass spectrometry could help in this regard. The lability of ligands has importance in homogenous catalysis and synthesis of novel nanostructured materials. For example, the $[Ag_{29}(BDT)_{12}(PPh_3)_4]^{3-}$ cluster has four PPh_3 ligands in its solid-state structure.[39] The mass spectrum of its solution contains five peaks, wherein each is separated by a mass/charge ratio corresponding to one PPh_3 (Fig. 21.13). This suggests that the interactions between cluster surface and PPh_3 are rather weak compared to thiolates. This establishes a dynamic equilibrium between PPh_3 association and dissociation in solution. It is important to note that not all phosphine-containing clusters exhibit such lability. For example, $[PtAg_{28}(S\text{-}Adm)_{18}(PPh_3)_4]^{2+}$ cluster shows only one mass peak containing all four PPh_3 ligands.[40] This demonstrates the importance of mass spectrometry in detecting the lability of ligands.

21.4 Chemical and photophysical properties

In general, metal clusters are metastable and they exhibit unusual reactivity depending on the reaction conditions. Particularly, they can undergo ligand and metal exchange reactions to produce clusters with different size and structure as well as properties.[29] The APCs can serve as readily available precursors to rationally design functional materials through bottom-up approach. The oblate-shaped $[Au_9(PPh_3)_8]^{3+}$ cluster is found to react with the reducing

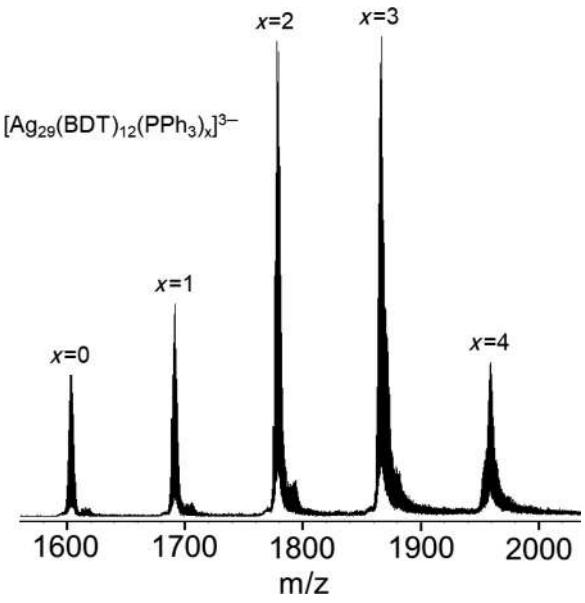

FIGURE 21.13 Mass spectrometric identification of phosphines. A sequential loss of PPh_3 ligands is clearly seen. Adapted with permission from ref.[39] Copyright 2015 American Chemical Society.

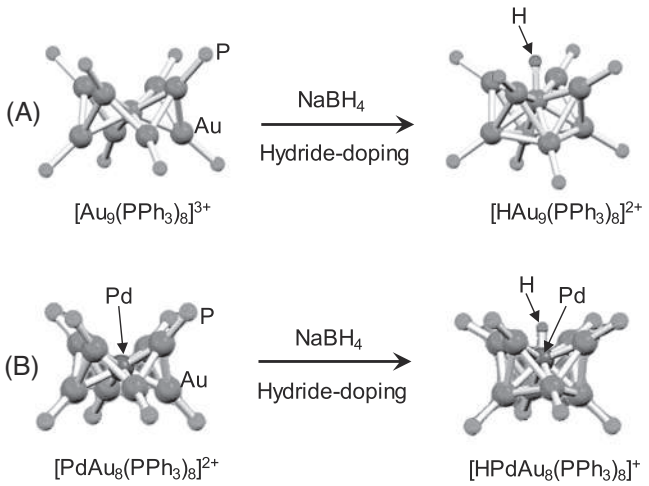

FIGURE 21.14 Hydride-doping pathways of (A) Au-phosphine and (B) Pd-doped Au-phosphine clusters. Adapted with permission from ref.[41] Copyright 2018 American Chemical Society. Adapted with permission from ref.[42] Copyright 2018 American Chemical Society.

agents such as sodium borohydride to produce a hydride-doped $[HAu_9(PPh_3)_8]^{2+}$ cluster.[41] The $[Au_9(PPh_3)_8]^{3+}$ cluster is a six-electron superatom containing a coordinatively unsaturated metal site at the center (Fig. 21.14A). The theoretical calculations suggested that the hydride binds with the central Au atom, making the resulting structure nearly spherical. More interestingly, this hydride behaves as a metal atom and contributes its 1*s* electron to the superatomic electron count. The $[HAu_9(PPh_3)_8]^{2+}$ cluster carries 8 (1 + 9 − 2) free valence electrons, which is a stable closed shell electronic configuration. This cluster further reacts with AuCl to form $[Au_{11}(PPh_3)_8Cl_2]^+$ through an intermediate of $[Au_{10}(PPh_3)_8Cl]^+$. These transformations of

clusters involving nucleophilic addition of two Au(I)Cl units can be represented as shown below.

$$[HAu_9(PPh_3)_8]^{2+} + AuCl \rightarrow [Au_{10}(PPh_3)_8Cl]^{+} + H^{+}$$

$$[Au_{10}(PPh_3)_8Cl]^{+} + AuCl \rightarrow [Au_{11}(PPh_3)_8Cl_2]^{+}$$

A similar hydride-doping is also observed in case of an oblate $(Pd@Au_8)^{2+}$ superatomic cluster $[PdAu_8(PPh_3)_8]^{2+}$. The hydride in the $[HPdAu_8(PPh_3)_8]^{+}$ cluster is found to bind with the Pd atom which is at the center being coordinatively unsaturated (Fig. 21.14B). This cluster further undergoes transformation to $[HPdAu_{10}(PPh_3)_8Cl_2]^{+}$ cluster via addition of two units of Au(I)Cl.[42] In contrast to the formation of $[Au_{11}(PPh_3)_8Cl_2]^{+}$ with the loss of hydride by the release of proton, the hydride is preserved in $[HPdAu_{10}(PPh_3)_8Cl_2]^{+}$ after the size-growth. Due to the presence of the hydride, core of the $[HPdAu_{10}(PPh_3)_8Cl_2]^{+}$ is significantly distorted. These observations suggest that the Pd dopant has unique role in the controlled growth of the bimetallic $(Pd@Au_8)^{2+}$ superatom to the hydride-doped $(HPd@Au_{10})^{3+}$ superatom.

The hydride-doped clusters are particularly important as they react with a wide variety of thiolate and alkynyl ligands to produce doped gold clusters with novel characteristics as well as high product yields (>50%) up to few hundreds of milligrams. The high yield of the cluster product is attributed to the well-controlled stoichiometric transformation of hydride-doped gold-phosphine clusters.[43] The yields of the final clusters, especially for gold, are generally poor, as gold produces a wide variety of cluster sizes and structures with the same ligand. Importantly, the product selectivity in ligand-exchange-induced transformation can be tuned by varying the structure of the incoming ligand as well as other factors, including solvent and metal precursors. While the neutral doped clusters with $(M@Au_{12})^{6+}$ (M = Pd or Pt) core are produced with thiols, the dianionic clusters comprising $(M@Au_{12})^{4+}$ core is formed by using alkynyls. This difference is ascribed to the stronger electron withdrawing character of alkynyls than thiolates, increasing the number of valence-free electrons from 6 to 8. The hydride-mediated doping is also observed in silver clusters as well.[26] The $[Ag_{18}H_{16}(PPh_3)_{10}]^{2+}$ clusters react with Pt precursor to form a rod-shaped, red-emitting $[Pt_2Ag_{23}Cl_7(PPh_3)_{10}]$ cluster.

The dynamics of the ligands on the cluster surface influence significantly the photophysical processes in solution. When the ligands are labile, they undergo association and dissociation at the cluster surface. Lowering the temperature to well below 0 °C may restrict to some extent the dissociation of ligands. But this prevents the room-temperature applications based on photoluminescence (PL). Improving the PL of metal clusters is one of the important topics in cluster science. Aggregation induced emission has been frequently used to achieve this through electrostatic attractions as well as weak nonspecific interactions. The former is generally possible if the cluster is charged. A new type of aggregation-enhanced emission is observed for $[Ag_{29}(BDT)_{12}(PPh_3)_4]^{3-}$ clusters. When the PPh_3 ligands of the cluster are in equilibrium with the solvent molecules, the PL of the cluster is found to be weak (PL quantum yield, PLQY: 0.9%). The addition of a large excess of PPh_3 to a dimethylformamide (DMF) solution of $[Ag_{29}(BDT)_{12}(PPh_3)_4]^{3-}$ cluster leads to a dramatic PLQY enhancement (11.7%).[40] The excess PPh_3 ligand in the solution not only shifts the equilibrium toward undissociated clusters but also rigidifies the surface of the cluster, which eventually reduces the nonradiative recombination relaxation pathways of the excited states of clusters. While the heteroatom Pt doping also caused PL enhancement in a compositionally and structurally

similar $[PtAg_{28}(BDT)_{12}(PPh_3)_4]^{4-}$ through synergistic effects, the restricted dissociation of PPh_3 ligands from its surface further increased the PLQY to 18.9%. A similarly sized $[PtAg_{28}(S\text{-}Adm)_{18}(PPh_3)_4]^{2+}$ cluster is seen to have inherently nondissociative PPh_3 ligands. The addition of the excess PPh_3 to this cluster does not affect the PL intensity. This strongly indicates that the cluster should have dissociative ligands in order to apply this surface treatment for the PL enhancement.

The surface rigidification through specific interactions is another pathway to improve PL of metal clusters. Although the cluster needs to be charged in order to execute electrostatic attraction-induced surface rigidification, the surface structure is also found to play a pivotal role in PL enhancement. The strong electrostatic attraction between $[PtAg_{28}(BDT)_{12}(PPh_3)_4]^{4-}$ clusters with added tetraoctylammonium cations leads to high PL enhancement through suppression of nonradiative relaxations by ligand–shell rigidification.[44] The surface of this cluster is relatively accessible to bulky cations compared to nonaccessible $[Ag_{44}(SR)_{30}]^{4-}$ clusters. Furthermore, the appropriate bulkiness of the counter cation is also found to be critical in guiding the strength of cluster–counterion interactions and the PL enhancement.

21.5 Significance of hydrogen, phosphines, and alkynyls

Hydrogen is often observed in catalytic steps of numerous important reactions, including water splitting as well as CO_2 and N_2 reduction. The moderate electronegativity (2.2) and the small size (Van der Waals radius: 120 pm) make hydrogen to potentially interact with active sites on metal clusters and nanoparticles. More importantly, depending on its electronic and chemical environment, the hydrogen fluctuates among positively charged proton, negatively charged hydride, and simple hydrogen atom, enabling its disproportionation during catalysis.[45] The binding strength of hydrogen, the descriptor of the chemical and catalytic properties, can be effectively modified by tunable electronic and geometric structures of metal clusters. Although hydrogen is mostly observed as hydrides on silver and copper clusters, it appears as hydrogen atom on gold. In fact, the gold-hydride cluster compounds are scarce. The hydrogen atom when bound to cluster contributes its 1*s* electron toward free electron count in superatomic clusters. For example, the extraordinary hydrogen evolution reaction (HER) activity of $[PtAu_{24}(SR)_{18}]$ can be explained by the formation of $[H_2PtAu_{24}(SR)_{18}]$ cluster based on its stable close-shell superatomic electronic configuration.[46,47] Specifically, the endothermic hydrogen binding on $Au_{25}(SR)_{18}$ of 0.539 eV shifts to a thermodynamically neutral binding energy of −0.059 eV on $[PtAu_{24}(SR)_{18}]$. The precisely known structures of metal clusters allow DFT calculations to predict hydrogen adsorption-free energies and thereby predicting potential dopants to optimize their catalytic activity.

One of the ways to increase hydrogen interaction is to prepare clusters with weakly coordinating ligands and uncoordinated metal (open) sites. As previously discussed, the $[Au_9(PPh_3)_8]^{3+}$ cluster captures one hydride to form $[HAu_9(PPh_3)_8]^{2+}$ through hydride coordination with the central Au atom.[41] Here, this hydride acts as a metal atom by contributing its 1*s* electron and turns it to a superatom, indicating $[Au_9(PPh_3)_8]^{3+}$ cluster may have promising catalytic activity in hydrogen-related reactions. The Au-phosphine cluster $Au_{22}(dppo)_6$, with eight uncoordinated sites, is estimated to have strong hydrogen adsorption by bridging two

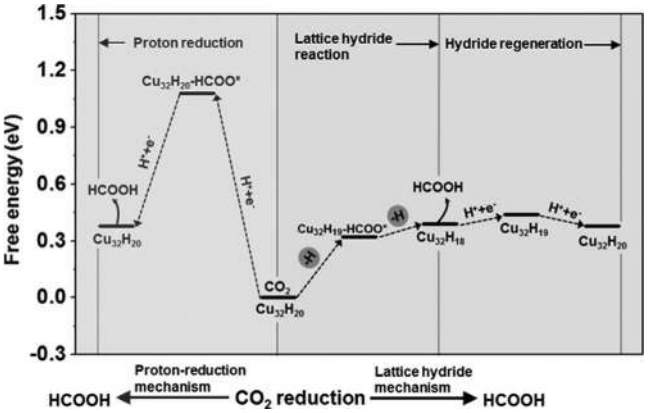

FIGURE 21.15 A reaction scheme for CO_2 electroreduction on $Cu_{32}H_{20}L_{12}$ cluster, forming HCOOH via the proton-reduction channel (left) and the lattice-hydride channel (right). L_{12} is not shown for clarity. Reproduced with permission from ref.[50] Copyright 2017 American Chemical Society.

adjacent Au atoms.[48] Here, the hydrogen is found to be a hydride, rather than the atomic hydrogen as in the case of thiolated gold cluster. This is due to the fact that phosphines are electron-rich and they promote charge transfer from gold core to hydrogen. The stronger bonding of H, up to six H, with this cluster than that of Pt can make $Au_{22}(dppo)_6$ highly active HER catalyst as the Gibbs adsorption-free energy (ΔG_H) is close to zero.

The hydride ligands in copper and silver clusters are particularly relevant to the reduction reactions.[49] The well-controlled metal sites and electronic structure may open new avenues to overcome the competitive HER at low overpotentials during the electrochemical CO_2 reduction. Importantly, structurally characterized copper-hydride clusters can provide important mechanistic insights into the product selectivity and catalyst activity. The negatively charged hydrides in a prototypical cluster, $Cu_{32}H_{20}L_{12}$ ($L = S_2P(OiPr)_2$), are found to facilitate the formation of HCOOH over CO during the electroreduction of CO_2.[50] The theoretical results predicted that a lattice-hydride mechanism of CO_2 reduction is preferred to the common proton-reduction mechanism (Fig. 21.15). The two hydrides of the clusters are sequentially transferred to adsorbed CO_2 to form formic acid. However, the two consumed hydrides are subsequently regenerated from proton reduction. The HER and CO formation paths are predicted to be kinetically unfavorable due to significant reaction barriers.

The capping ligands of the metal clusters are often thought to be barriers for the progress of the catalytic reactions. To understand precisely the role of ligands, clusters with identical size and structure need to be prepared with the structure of the ligands as the only variable. Two isostructural Au_{38} clusters, $[Au_{38}(L)_{20}(PPh_3)_4]^{2+}$ (L = alkynyl or thiolate) with unprecedented face-centered cubic (fcc)-type Au_{34} kernel was prepared. These clusters were loaded onto reducible support TiO_2 and their catalytic activity was compared for semihydrogenation of akynes.[8] The alkynylated clusters exhibit alkynes to alkene conversion, whereas thiolated ones show no activity. This indicates that the activation of H_2 on these clusters depends on the nature of the ligands. The significant H_2 activation by alkynyl-protected gold clusters is attributed to the electronic mixing of alkynyl triple bond with the kernel of gold cluster. Interestingly, an intermetallic $Au_{34}Ag_{28}(C{\equiv}CPh)_{34}$ cluster shows enhanced catalysis for hydrolytic oxidation of organosilanes to silanols.[51] The alkynyl ligands enhance the catalytic activity of this cluster, while their partial or complete removal decreases the activity. Although the

exact reason for the ligand-promoted catalysis is unknown, this study will encourage future mechanistic investigations on the role of other ligands in catalysis.

21.6 Summary and future perspectives

In summary, this chapter provides an overview of the coinage metal clusters stabilized with hydrides, alkynyls, phosphines, and nitrogen-donor ligands. The metal clusters of different size and molecular structures are extremely important for establishing the structure–property correlations. However, it is still challenging to rationally design desired nanoclusters with required characteristics. The differences in the binding modes of surface ligands with metals can tune the overall geometric and electronic structures of clusters. The hydrides are found in majority of the silver and copper clusters due to high electropositivity of these metals. Hydrogen in copper and silver clusters exists as anionic hydride, while in gold clusters, it exists either as neutral atom or anionic hydride depending on the electronic structure and stability conditions. The phosphine ligands of certain metal clusters are labile, indicating new possibilities in homogenous catalytic applications. Metal clusters are used as promising precursors to synthesize novel clusters through ligand exchange. Gold, silver, and their alloy clusters have been constructed with self-assembled icosahedral building blocks, exhibiting unusual optical properties, including broad absorption extending from UV–visible to near infrared. Gold clusters with uncoordinated sites display high catalytic activity. Essential tools for the characterization of metal clusters ligated by hydrides and phosphines have also been discussed.

Undoubtedly, the past few decades have witnessed great advancements in the cluster science of coinage metals, including synthetic strategies and unraveling the atomic structures as well as uncovering new properties. The nitrogen-donor ligands have been less explored compared to thiolates and others for metal clusters. The metal cluster systems with nitrogen ligands are particularly important for addressing challenges in CO_2 conversion. Another revolutionary class of clusters is those with uncoordinated metal sites. There are only two types of gold clusters in this category and much efforts are needed in preparing this class of materials. Although the clusters of clusters represent miniaturized cluster assembly, they are still small in size compared to other supramolecular systems. Efficient cluster assembled materials need to be developed to realize advanced applications in energy, catalysis, and medicine.

List of abbreviation

APCs	atomically precise clusters
HOMOs	highest occupied molecular orbitals
LUMOs	lowest unoccupied molecular orbitals
dpa	monoanionic dipyridylamido
Hdpa	deprotonated dipyridylamine
TPP or PPh_3	triphenylphosphine
Ph	phenyl
RS^- or RS	thiolate
$RC{\equiv}C^-$ or RC≡C	alkynyl
RNH_2	amine

H^- or H	hydride
CO	carbonyl
X^- or X	halide
R	alkyl
$RCOO^-$	carboxylate
μ	mu (indicates bridging)
Et	ethyl
S_2CNR	dithiocarbamate
PF_6 or PF_6^-	hexafluorophosphate
L	ligand
NO_3 or NO_3^-	nitrate
N-triphos	tris((diphenylphosphino)methyl)amine
T_d	tetrahedral
dppo	1,8-bis(diphenylphosphino)octane
dppee	bis[(2-diphenylphosphino)ethyl]ether
PP_3	tris[2-(diphenylphosphino)ethyl]phosphine
SCXRD	single crystal X-ray diffraction
ESI MS	electrospray ionization mass spectrometry
IR	infrared
NMR	nuclear magnetic resonance
SCND	single crystal neutron diffraction
DMBT	dimethylbenzenethiolate
BDT	benzenedithiolate
D	deuteride
S-Adm	adamantanethiolate
PL	photoluminescence
PLQY	photoluminescence quantum yield
DMF	dimethylformamide
HER	hydrogen evolution reaction
DFT	density functional theory
eV	electron volt
ΔG_H	Gibbs adsorption-free energies for hydrogen

References

1. Du Y, Sheng H, Astruc D, Zhu M. Atomically precise noble metal nanoclusters as efficient catalysts: a bridge between structure and properties. *Chem Rev*. 2020;120:526–622.
2. Chakraborty I, Pradeep T. Atomically precise clusters of noble metals: emerging link between atoms and nanoparticles. *Chem Rev*. 2017;117:8208–8271.
3. Sun C, Teo BK, Deng C, et al. Hydrido-coinage-metal clusters: rational design, synthetic protocols and structural characteristics. *Coord Chem Rev*. 2021;427.
4. Narouz MR, Takano S, Lummis PA, et al. Highly luminescent Au_{13} superatoms protected by N-heterocyclic carbenes. *J Am Chem Soc*. 2019;141:14997–15002.
5. Dhayal RS, van Zyl WE, Liu CW. Polyhydrido copper clusters: synthetic advances, structural diversity, and nanocluster-to-nanoparticle conversion. *Acc Chem Res*. 2016;49:86–95.
6. Lei Z, Wan X-K, Yuan S-F, Guan Z-J, Wang Q-M. Alkynyl approach toward the protection of metal nanoclusters. *Acc Chem Res*. 2018;51:2465–2474.
7. Chakraborty P, Nag A, Chakraborty A, Pradeep T. Approaching materials with atomic precision using supramolecular cluster assemblies. *Acc Chem Res*. 2019;52:2–11.
8. Wan X-K, Wang J-Q, Nan Z-A, Wang Q-M. Ligand effects in catalysis by atomically precise gold nanoclusters. *Sci Adv*. 2017;3.
9. Cui X, Wang J, Liu B, Ling S, Long R, Xiong Y. Turning Au nanoclusters catalytically active for visible-light-driven CO_2 reduction through bridging ligands. *J Am Chem Soc*. 2018;140:16514–16520.

10. Jordan AJ, Lalic G, Sadighi JP. Coinage metal hydrides: synthesis, characterization, and reactivity. *Chem Rev*. 2016;116:8318–8372.
11. Konishi K, Iwasaki M, Shichibu Y. Phosphine-ligated gold clusters with core+exo geometries: unique properties and interactions at the ligand–cluster interface. *Acc Chem Res*. 2018;51:3125–3133.
12. Huang R-W, Yin J, Dong C, et al. $[Cu_{81}(PhS)_{46}(t\text{BuNH}_2)_{10}(H)_{32}]^{3+}$ reveals the coexistence of large planar cores and hemispherical shells in high-nuclearity copper nanoclusters. *J Am Chem Soc*. 2020;142:8696–8705.
13. Wan X-K, Tang Q, Yuan S-F, Jiang D-e, Wang Q-M. Au_{19} nanocluster featuring a V-shaped alkynyl–gold motif. *J Am Chem Soc*. 2015;137:652–655.
14. Nguyen T-AD, Jones ZR, Leto DF, Wu G, Scott SL, Hayton TW. Ligand-exchange-induced growth of an atomically precise Cu_{29} nanocluster from a smaller cluster. *Chem Mater*. 2016;28:8385–8390.
15. Yuan S-F, Guan Z-J, Liu W-D, Wang Q-M. Solvent-triggered reversible interconversion of all-nitrogen-donor-protected silver nanoclusters and their responsive optical properties. *Nat Commun*. 2019;10:4032.
16. Parrish KA, King M, Ligare MR, Johnson GE, Hernández H. Role of sterics in phosphine-ligated gold clusters. *Phys Chem Chem Phys*. 2019;21:1689–1699.
17. Bennett EL, Murphy PJ, Imberti S, Parker SF. Characterization of the hydrides in stryker's reagent: $[HCu(P(C_6H_5)_3)]_6$. *Inorg Chem*. 2014;53:2963–2967.
18. Nair LV, Hossain S, Wakayama S, et al. $[Pt_{17}(CO)_{12}(PPh_3)_8]^{n+}$ (n = 1, 2): synthesis and geometric and electronic structures. *J. Phys. Chem. C*. 2017;121:11002–11009.
19. Wen F, Englert U, Gutrath B, Simon U. Crystal structure, electrochemical and optical properties of $[Au_9(PPh_3)_8](NO_3)_3$. *Eur J Inorg Chem*. 2008;2008:106–111.
20. Yamazoe S, Matsuo S, Muramatsu S, Takano S, Nitta K, Tsukuda T. Suppressing isomerization of phosphine-protected Au_9 cluster by bond stiffening induced by a single Pd atom substitution. *Inorg Chem*. 2017;56:8319–8325.
21. Matsuo S, Takano S, Yamazoe S, Koyasu K, Tsukuda T. Selective and high-yield synthesis of oblate superatom $[PdAu_8(PPh_3)_8]^{2+}$. *Chem. Electro. Chem*. 2016;3:1206–1211.
22. Kang X, Li Y, Zhu M, Jin R. Atomically precise alloy nanoclusters: syntheses, structures, and properties. *Chem Soc Rev*. 2020;49:6443–6514.
23. Shen X-T, Ma X-L, Ni Q-L, et al. $[Ag_{15}(\text{N-triphos})_4(Cl_4)](NO_3)_3$: a stable Ag–P superatom with eight electrons (N-triphos = tris((diphenylphosphino)methyl)amine). *Nanoscale*. 2018;10:515–519.
24. Teo BK, Zhang H. Cluster of clusters (C_2) model for electron counting of supracluster based on smaller cluster units. *Inorg. Chim. Acta*. 1988;144:173–176.
25. Teo BK, Zhang H. Polyicosahedricity: icosahedron to icosahedron of icosahedra growth pathway for bimetallic (Au-Ag) and trimetallic (Au-Ag-M, M = Pt, Pd, Ni) supraclusters, synthetic strategies, site preference, and stereochemical principles. *Coord. Chem. Rev*. 1995;143:611–636.
26. Bootharaju MS, Kozlov SM, Cao Z, et al. Doping-induced anisotropic self-assembly of silver icosahedra in $[Pt_2Ag_{23}Cl_7(PPh_3)_{10}]$ nanoclusters. *J Am Chem Soc*. 2017;139:1053–1056.
27. Jin R, Liu C, Zhao S, et al. Tri-icosahedral gold nanocluster $[Au_{37}(PPh_3)_{10}(SC_2H_4Ph)_{10}X_2]^+$: linear assembly of icosahedral building blocks. *ACS Nano*. 2015;9:8530–8536.
28. Kang X, Xiang J, Lv Y, et al. Synthesis and structure of self-assembled $Pd_2Au_{23}(PPh_3)_{10}Br_7$ nanocluster: exploiting factors that promote assembly of icosahedral nano-building-blocks. *Chem Mater*. 2017;29:6856–6862.
29. Yang S, Chai J, Lv Y, et al. Cyclic Pt_3Ag_{33} and $Pt_3Au_{12}Ag_{21}$ nanoclusters with M_{13} icosahedra as building-blocks. *Chem Commun*. 2018;54:12077–12080.
30. Masatake H, Tetsuhiko K, Hiroshi S, Nobumasa Y. Novel gold catalysts for the oxidation of carbon monoxide at a temperature far below 0°C. *Chem Lett*. 1987;16:405–408.
31. Li J, Li X, Zhai H-J, Wang L-S. Au_{20}: a tetrahedral cluster. *Science*. 2003;299:864–867.
32. Zhang H-F, Stender M, Zhang R, Wang C, Li J, Wang L-S. Toward the solution synthesis of the tetrahedral Au_{20} cluster. *J. Phys. Chem. B*. 2004;108:12259–12263.
33. Zhang Q-F, Chen X, Wang L-S. Toward solution syntheses of the tetrahedral Au_{20} pyramid and atomically precise gold nanoclusters with uncoordinated sites. *Acc Chem Res*. 2018;51:2159–2168.
34. Chen J, Zhang Q-F, Bonaccorso TA, Williard PG, Wang L-S. Controlling gold nanoclusters by diphospine ligands. *J Am Chem Soc*. 2014;136:92–95.
35. Wu Z, Hu G, Jiang D-e, et al. Diphosphine-protected Au_{22} nanoclusters on oxide supports are active for gas-phase catalysis without ligand removal. *Nano Lett*. 2016;16:6560–6567.

36. Dong J, Gao Z-H, Zhang Q-F, Wang L-S. The synthesis, bonding, and transformation of a ligand-protected gold nanohydride cluster. *Angew Chem Int Ed*. 2021;60:2424–2430. http://doi.org/10.1002/anie.202011748.
37. Yuan S-F, Lei Z, Guan Z-J, Wang Q-M. Atomically precise preorganization of open metal sites on gold nanocluster with high catalytic performance. *Angew Chem Int Ed*. 2021;60:5225–5229. http://doi.org/10.1002/anie.202012499.
38. Yuan X, Sun C, Li X, et al. Combinatorial identification of hydrides in a ligated Ag_{40} nanocluster with noncompact metal core. *J Am Chem Soc*. 2019;141:11905–11911.
39. AbdulHalim LG, Bootharaju MS, Tang Q, et al. $Ag_{29}(BDT)_{12}(TPP)_4$: a tetravalent nanocluster. *J Am Chem Soc*. 2015;137:11970–11975.
40. Kang X, Wang S, Zhu M. Observation of a new type of aggregation-induced emission in nanoclusters. *Chem Sci*. 2018;9:3062–3068.
41. Takano S, Hirai H, Muramatsu S, Tsukuda T. Hydride-doped gold superatom $(Au_9H)^{2+}$: synthesis, structure, and transformation. *J Am Chem Soc*. 2018;140:8380–8383.
42. Takano S, Hirai H, Muramatsu S, Tsukuda T. Hydride-mediated controlled growth of a bimetallic $(Pd@Au_8)^{2+}$ superatom to a hydride-doped $(HPd@Au_{10})^{3+}$ superatom. *J Am Chem Soc*. 2018;140:12314–12317.
43. Takano S, Ito S, Tsukuda T. Efficient and selective conversion of phosphine-protected $(MAu_8)^{2+}$ (M = Pd, Pt) superatoms to thiolate-protected $(MAu_{12})^{6+}$ or alkynyl-protected $(MAu_{12})^{4+}$ superatoms via hydride doping. *J Am Chem Soc*. 2019;141:15994–16002.
44. Bootharaju MS, Kozlov SM, Cao Z, et al. Tailoring the crystal structure of nanoclusters unveiled high photoluminescence via ion pairing. *Chem Mater*. 2018;30:2719–2725.
45. Fung V, Hu G, Wu Z, Jiang D-e. Hydrogen in nanocatalysis. *J Phys Chem Lett*. 2020;11:7049–7057.
46. Kwak K, Choi W, Tang Q, et al. A molecule-like $PtAu_{24}(SC_6H_{13})_{18}$ nanocluster as an electrocatalyst for hydrogen production. *Nat Commun*. 2017;8:14723.
47. Hu G, Tang Q, Lee D, Wu Z, Jiang D-e. Metallic hydrogen in atomically precise gold nanoclusters. *Chem Mater*. 2017;29:4840–4847.
48. Hu G, Wu Z, Jiang D-e. Stronger-than-Pt hydrogen adsorption in a Au_{22} nanocluster for the hydrogen evolution reaction. *J. Mater. Chem. A*. 2018;6:7532–7537.
49. Sun C, Mammen N, Kaappa S, et al. Atomically precise, thiolated copper–hydride nanoclusters as single-site hydrogenation catalysts for ketones in mild conditions. *ACS Nano*. 2019;13:5975–5986.
50. Tang Q, Lee Y, Li D-Y, et al. Lattice-hydride mechanism in electrocatalytic CO_2 reduction by structurally precise copper-hydride nanoclusters. *J Am Chem Soc*. 2017;139:9728–9736.
51. Wang Y, Wan X-K, Ren L, et al. Atomically precise alkynyl-protected metal nanoclusters as a model catalyst: observation of promoting effect of surface ligands on catalysis by metal nanoparticles. *J Am Chem Soc*. 2016;138:3278–3281.

CHAPTER

22

Clusters for biological applications

Debasmita Ghosh[a] *and Thalappil Pradeep*[b]

[a] **ARNA Laboratory, Inserm U1212, CNRS5320, Université de Bordeaux, France**
[b] **Deepak Parekh Institute Chair Professor and Professor of Chemistry, Department of Chemistry, Indian Institute of Technology Madras, Chennai, India**

22.1 Introduction

Ultrasmall metal NCs, with size ~1 nm, are materials of future interest in medicine and healthcare.[1–3] They have wide-ranging applications due to their well-defined structures, simple surface functionalization, unique physicochemical properties, and biocompatibility. In this chapter, we first describe the biological consideration of clusters in their design and then discuss their important contributions in biosensing, bioimaging, drug delivery, and therapeutic applications (shown in Fig. 22.1).[4]

22.2 Selection of the nanoclusters for biological application

Clusters with certain basic features are useful for biological applications. Size, structure, composition, and surface chemistry determine the application of clusters in biological systems. Although these properties were investigated to a considerable extent for the nanoparticles, they are poorly explored in the context of clusters. Thus, designing these functional nanomaterials with desired properties is essential for biological applications. Here, we discuss the important considerations of the clusters for biological applications.

22.2.1 Interactions of NCs with biological systems

Generally, proteins adsorbed on the surface of NPs in the biological media forms a protein corona,[5] but ultrasmall clusters interact differently in biological media. They undergo molecular interactions with proteins.[6] Ligands can control the association rate constant for cluster–protein interactions. Clusters with the same surface charge and core size but different protecting ligand (MBA vs. GSH) shows different association rate constants.[7] Fast diffusion-limited adsorption with larger association rate constant was observed for MBA-protected clusters, while GSH-protected clusters showed slow, reaction-limited adsorption. Thus, dynamic reversible interactions of Au@GSH clusters with serum proteins preserve the

DOI: https://doi.org/10.1016/B978-0-323-90879-5.00020-2

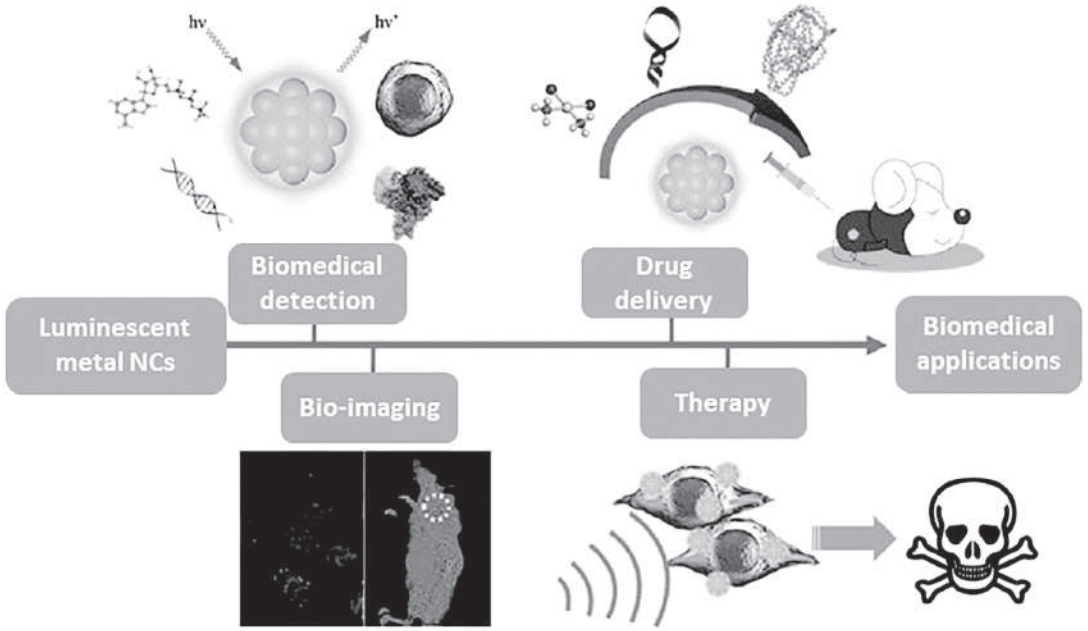

FIGURE 22.1 Different applications of the NCs in biology. Reproduced with permission.[4]

hydrodynamic diameter of clusters in blood plasma. This ligand-dependent behavior is due to the hydrophobicity and changes in the surface charge distribution of the clusters. As a consequence, MBA-protected clusters are accumulated in the liver and spleen for long time, but Au@GSH excreted fast via renal clearance pathway.[8]

22.2.2 Cellular uptake and in vivo distribution

Understanding the cellular uptake mechanism of clusters and their interactions at cellular and subcellular level is needed for biomedical applications. This determines their performance as theranostic or therapeutic agents. PEGylation of inorganic NPs (charge neutral) has been carried out to improve blood circulation time. Intracellular uptake and in vivo distribution depend on the surface charge. Surface chemistry of the thiol-protected Au NCs determines cellular uptake and intracellular redox signaling. Au@MPA showed higher cellular internalization than Au@GSH, for the clusters with same atomicity.

In addition to hydrodynamic diameter and net surface charge, hydrophobic surface area and surface charge density determine the biodistribution, pharmacokinetics, and excretion of clusters.[9] The optimum hydrophilic/hydrophobic balance of the metal cluster surface can prevent the corona formation and determine its insertion into the phospholipid membrane and the cellular uptake. Unlike NPs, smaller (less than 2 nm in size) NCs form small aggregates on the surface of cell membrane to begin the endocytic pathway to facilitate insertion of NCs into the cell. This provides better circulation time and cellular internalization.[10]

22.2.3 Renal clearance

Molecular nanoprobes show increased renal clearance with strong enhanced permeability and retention (EPR) effect than small molecular probes or conventional probes. Zwitterionic GSH-protected clusters showed exceptional renal clearance.[11] A few atom differences in Au NCs showed notable changes in the renal clearance profile. A few-atom decrease in cluster size results in a nearly one order reduction in renal clearance. Du et al. reported that $Au_{10–11}$, Au_{15}, and Au_{18} NCs retained in the glomerular glycocalyx for a longer time compared to Au_{25} NCs.[12] Here, glomerular barrier acts as a size band pass filter rather than a size cut-off filter for subnanometer NCs. Not only differences in their nuclearity, surface ligand composition and surface charge also decide renal clearance. Ning et al. studied the effect of ligand length on efficiency of renal clearance of peptide-protected Au NCs.[13]

Zhang et al. showed that BSA-protected gold nanoclusters have low-efficient renal clearance and only 1% of gold can be cleared, but the GSH-protected gold nanoclusters have high-efficient renal clearance and 36% of gold can be cleared after 24 h.[14] The biodistribution further revealed that 94% of gold can be metabolized for the GSH-protected nanoclusters, but only less than 5% of gold can be metabolized for the BSA-protected nanoclusters after 28 days. These studies showed that the GSH-protected gold nanoclusters have small size and can be metabolized by renal clearance and thus the toxicity can be significantly decreased.

22.3 Biomedical applications

22.3.1 Biomolecular sensing

22.3.1.1 Detection of ions

The exposure of heavy metals such as Hg^{2+}, Pb^{2+}, Cu^{2+}, Cr^{3+}, and toxic anions is a threat to organisms due to accumulation in the body. Thus, the identification and eradication of toxic components are extremely important. Metal NCs are ideal choice for sensing of different hazardous analytes due to their high sensitivity and selectivity. The mechanism of sensing could be explained by different phenomenon like photoinduced electron transfer, analyte-induced aggregation of cluster core, chemiluminescence, and fluorescence resonance energy transfer, etc.[15]

Quenching of luminescence of the Au_{25}@BSA by Hg^{2+} was observed by Xie et al.[16] Strong metallophilic interaction between Hg^{2+}–Au^{1+} in the NCs quenched the luminescence and was recovered partially by adding strong reducing agent like sodium borohydride. Excellent selectivity toward Hg^{2+} in the presence of other metal ions was observed as a result of the high specificity of Hg^{2+}–Au^{1+} interactions. Very low concentrations such as 0.5 nM of Hg^{2+} was detected using Au_{25}@BSA. Various protein-protected clusters like Au@Lyz, Au@Pepsin, Ag@BSA NCs were used as Hg^{2+} sensor.[17–19] Pu et al. reported a hybrid nanoprobe based on fluorescence energy transfer (FRET) to detect Hg^{2+} both in solution and in cells.[20] The oppositely charged blue fluorescent conjugated-oligomer-substituted polyhedral oligomeric silsesquioxane (POSSFF) and red fluorescent Au@BSA was used to make the dual emissive pink fluorescent hybrid material. They showed FRET between the blue emissive POSSFF and red emissive Au@BSA. Addition of Hg^{2+} quenched the red fluorescence of the cluster and it

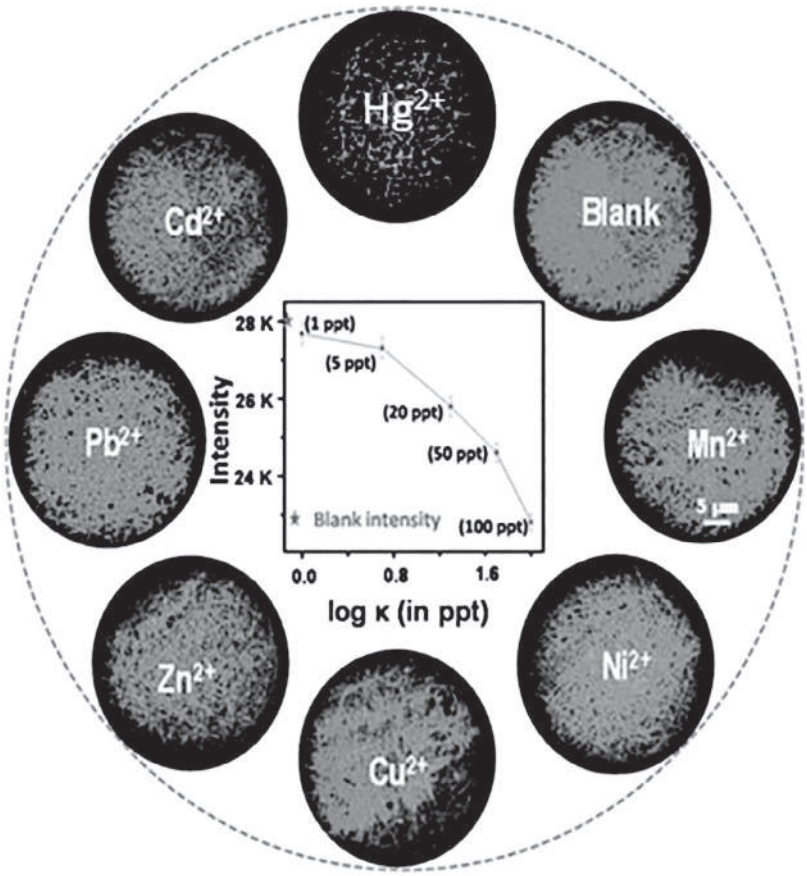

FIGURE 22.2 The images of sensing experiment showing the specificity of cluster–nanofiber composites toward Hg^{2+} ions. Reproduced with permission.[23]

exhibited only blue fluorescence. This study established a new way to develop metal NCs based intracellular nanosensor for qualitative and quantitative measurements. Paramanik et al. developed a single optical probe made of Au_{25}@BSA-tripeptide-capped CdTe quantum dots nanocomposite for luminescence turn off–on detection of toxic Hg^{2+} and F^- ion.[21] This new probe can be employed to sense nanomolar concentration of these hazardous ions. They have estimated the limit of detection (LOD) value for both Hg^{2+} and F^- concentration as 9 and 117 nM, respectively. Both values are within the safety limit in drinking water set by United States Environment Protection Agency. Hg^{2+} sensing was done using electrospun fibers of Au@BSA, shown in Fig. 22.2.[22, 23] The quenching of the green luminescence of 11-mercaptoundecanoic acid (MUA)-protected Au clusters upon addition of Hg^{2+} ions was observed.[24] DHLA-protected Ag NCs have been utilized as sensor for selective and ultrasensitive detection of Hg^{2+} ions in water, at subnanomolar concentrations.[25]

The sensing of Cu^{2+} ions by BSA-protected Au NCs in live cells was reported by Durgadas et al.[26] They proposed that the quenching mechanism by Cu^{2+} ions is different than that of Hg^{2+} ions. Unlike the metal–metal interaction, Cu^{2+} interacted with BSA in the NCs and quenched the luminescence. In the presence of other metal ions such as Pb^{2+}, Cd^{2+}, Mn^{2+}, Zn^{2+}, Fe^{2+}, Co^{2+}, selective quenching of luminescence of NCs can be attained. Spectroscopic data clearly showed that the paramagnetic nature of the Cu^{2+} bound BSA, promoted the intersystem crossing (ISC) of the excited electrons from the Au NCs and quenched the luminescence. The addition of Cu^{2+} chelator such as glycin recovered fluorescence up to 72%. Hg^{2+} and Cu^{2+} interaction with Au NCs was studied thoroughly by Yu et al. using spectroscopic techniques such as steady-state, time-resolved luminescence, and transient absorption measurements.[27] For the first time, they reported a novel triplet electron transfer process via Hg^{2+}–Au^{1+} metallophilic bonds and quenching of the delayed fluorescence of the Au_{25}@BSA, however, Cu^{2+} did not show any change in the delayed fluorescence due to the absence of metal–metal interaction. They also suggested that this phenomenon occurred through the Au^{1+}–S semiring interactions and, as a result, the fluorescence of Au_8@BSA and Au_{10}@His was not quenched. The detection of Cu^{2+} ions was also done using Au_{38}@BSA, Au@Lf, Ag@Au@BSA.[28–30] Su et al. developed a simple method to make a reusable fluorescent off–on Cu^{2+} sensor with high selectivity.[31] They mixed the Au@BSA with polyelectrolytes, that is, positively charged polydiallyldimethylammonium (PDDA) and negatively charged polystyrenesulfonate (PSS) and then coated the luminescent composite on a glass substrate. When this modified glass substrate was immersed in Cu^{2+} solution, fluorescence disappeared but reappeared on immersing in the ethylene diamine tetra acetic acid solution. They repeated this experiment several times and proved that this process could be repeated at least for 15 cycles. DNA-protected Cu/Ag NCs detected Cu^{2+} ions with high selectivity in the presence of mercaptopropionic acid and the LOD for Cu^{2+} ions was 2.7 nM.[32]

Presence of silver ions was detected by fluorescence enhancement of the Au_{16}@BSA by Wu and coworkers.[33] Upon addition of Ag^{1+} ions in the Au_{16}@BSA solution, the red emission at 604 nm was blue shifted to the 567 nm and enhancement was observed at 567 nm due to the formation of alloy species.

Goswami et al. demonstrated sensing of Pb^{2+} ions using blue-emitting $Cu_{5,13}$@BSA.[34] The blue luminescence quenched due to aggregation induced by Pb^{2+} ions. Electrochemiluminescence or electrogenerated chemiluminescence (ECL), that is, luminescence resulted from high energy electron transfer reactions, has a higher sensitivity than fluorescence and chemiluminescence. Although semiconductor quantum dots (QDs) were known to have ECL,[35–38] Fang et al. reported ECL from Au NCs for the first time.[39] It was observed that ECL of Au@BSA clusters could detect the Pb^{2+} ions, using triethylamine as coreactant.

It is necessary to sense toxic anions, in addition to cations, which can affect human health. Liu et al. detected cyanide (CN^-) by Au@BSA and proposed a possible mechanism, shown in Fig. 22.3.[40] The authors hypothesized that the probable interaction of Au NCs and CN^- formed gold–cyanide complex, which quenched the luminescence. Earlier studies showed that cyanide could interact with Au(0) through strong covalent bond and formed a stable $Au(CN)_2^-$ complex.[41] This sensor showed high selectivity in the presence of different cations and anions. This can be explained by the etching of cluster core to Au ions by CN^-.

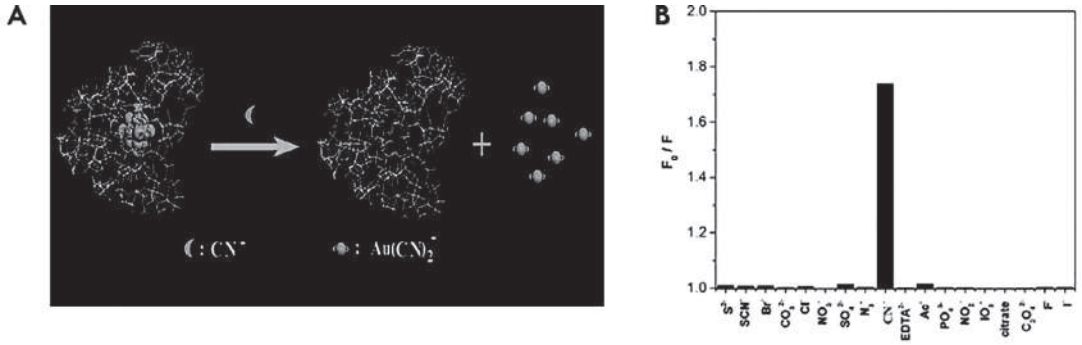

FIGURE 22.3 (A) Schematic for CN^- sensing by Au NCs; (B) Specificity for CN^- sensing of Au NCs sensor over other anions. Reproduced with permission.[40]

Liu et al. developed an environmentally friendly sensor using Cu^{2+}chelated-Au@BSA for detection of pyrophosphate ($P_2O_7^{4-}$).[42] Upon addition of Cu^{2+} to Au@BSA, fluorescence was quenched due to the chelation of Cu^{2+} with glycine residue present in the BSA. When $P_2O_7^{4-}$ was added to the solution, fluorescence was recovered due to the chelation of the $P_2O_7^{4-}$ with Cu^{2+}. They showed high selectivity and sensitivity of this sensor toward pyrophosphate sensing.

Au@BSA as a nitrite sensor was first designed by Liu et al. but the limitation was the interference from Hg^{2+}, Cu^{2+}, etc. Later Unnikrishnan et al. reported the detection of nitrite by fluorescence quenching of Au@BSA and explained the mechanism.[43] They detected nitrite in urine samples. Most importantly, they solved the interference issues from Cu^{2+} and Hg^{2+} by using masking agents such as ethylene diamine tetraacetic acid and borohydride. Protein-protected, red luminescent Au NCs were used to detect nitrite, however, when coupled with blue emissive graphene oxide (GO), the ratiometric probe could detect the nitrite ion in the solution. This dual emissive nanoprobe was used for qualitative and quantitative detection of nitrite. This simple, on-site, rapid, and sensitive method of sensing was developed by Xu et al.[44] In the presence of the nitrite ions, red emission from NCs was decreased, but the intensity of blue emission remained constant. As a result, the fluorescence changed from red to blue gradually. Using this ratiometric detection method, they established a detection limit of 46 nM.

22.3.1.2 Detection of small biomolecules

Small biomolecules, for example, biothiol, ascorbic acid, adenosine triphosphate (ATP), vitamin B1, reactive oxygen species (ROS) have important roles in biological system. Sensing of small biomolecules by metal clusters is discussed briefly in this section.

Cysteine is a semiessential thiol-containing aminoacid. Presence of cysteine could quench the fluorescence of Ag@PMAA NCs.[45] Cysteine directly interacts with NCs via strong Ag–S interaction and results in the oxidation of Ag by oxygen. This is a sensitive and selective fluorescence probe. Strong red fluorescence of Ag@GSH could be efficiently quenched due to the high affinity of the thiol–Ag interaction. This was used for highly sensitive detection of Cys with LOD of <3 nM as shown in Fig. 22.4.[46] Various biothiols like cysteine, homocysteine,

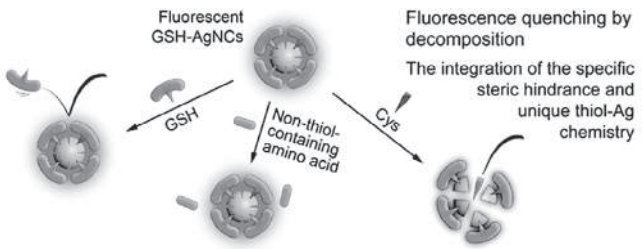

FIGURE 22.4 Detection of Cys by fluorometric and colorimetric probes using Ag@GSH NCs. Reproduced with permission.[46]

glutathione could be detected in human plasma samples with single-stranded and double-stranded DNA-protected metal NCs by similar principle.[47,48] Fluorescent enhancement was observed for Au@BSA NCs in the presence of cysteine. This may be due to the fact that surface defects of the NCs might be reduced in presence of cysteine, which helped in fluorescence enhancement of the NCs.[49] Graphene oxide-Au@BSA nanocomposite was used to make an electrochemical biosensor for L-cysteine analysis. It was made through electrostatic interaction between GO and Au@BSA.[50]

Detection of glutathione in a single drop of blood was done by Lyz-stabilized Au NCs. As a result of the core etching in presence of small amount of GSH, the blue-emitting Au_8 NCs was quenched.[51] Sensing of glutathione in living cells was done using Au@BSA.[52]

An ascorbic acid sensor was developed considering that Au(I) can be reduced to Au(0) by ascorbic acid. Change in the oxidation state of the surface Au(I) of NCs could lead to the quenching of NC fluorescence. Wang et al. developed a turn-off fluorescent probe to detect ascorbic acid by controlling the oxidation state of the Au NCs of Au@BSA.[53]

Cu@ovalbumin NCs were used for vitamin B1 and doxycycline sensing based on both fluorescence quenching and enhancement.[54] Small drug molecules such as ibuprofen, warfarin, phenytoin, and sulfanilamide have a wide range of binding affinities toward HSA and BSA. These could be sensed by monitoring the formation kinetics of fluorescent HSA–Au NCs and BSA–Au NCs when loaded with small drugs.[55] Vitamin B_{12} was detected by Samari et al. by using Au@BSA.[56] Sensing of uric acid was done using Au@BSA.[57]

Dopamine (DA) is one of the most of important neurotransmitters and plays several important roles in the body. Li et al. developed a simple label-free probe, where Au_{25}@BSA immobilized indium tin oxide (ITO) electrodes were used for the detection of dopamine.[58] They carried out a detailed study on the ECL phenomenon and proposed a probable mechanism. The high energy electrons from the conduction band of the ITO are transferred to the Au NCs. This Au@BSA combined ITO served as a good sensor with high selectivity toward dopamine detection. The fluorescence intensity of Cu@dsDNA was quenched in the presence of dopamine due to the photoinduced electron transfer process.[59]

Histidine detection was also done using Au@BSA NCs. The mechanism of sensing was the same as in the case of pyrophosphate detection which was discussed earlier. Electrochemical methods were used for dopamine detection, however, it suffered from the interference from ascorbic acid due to their similar oxidation potential. To overcome this, Aswathy et al. demonstrated the use of Cu^{2+} modified Au@BSA for sensing of dopamine.[60] Similarly, Ni^{2+} modified Au@BSA was used to detect histidine in urine samples by He et al.[61] Acetyl cholinesterase activity was detected by denatured Au@BSA.[62]

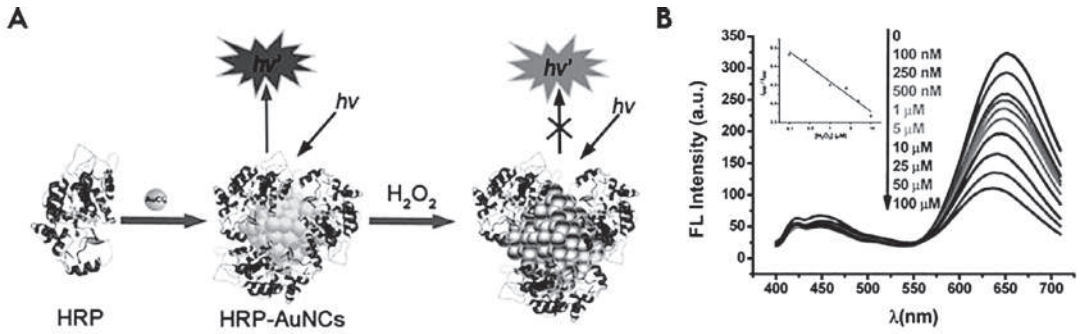

FIGURE 22.5 (A) Schematic representation of H_2O_2 sensing by Au@HRP NCs. (B) Fluorescence quenching of NCs. Reproduced with permission.[64]

Glucose is used as energy source in most of the organisms, from bacteria to humans. However, the excess amount of glucose in the blood indicates diabetes and hypoglycemia. Therefore, a selective and sensitive glucose sensor is needed in biomedical research and food analysis. The oxidation of glucose releases H_2O_2 in the presence of glucose oxidase.

$$\text{Glucose} + O_2 + H_2O \rightarrow \text{Gluconicacid} + H_2O_2$$

The concentration of glucose can be estimated from the amount of enzymatically generated H_2O_2. Fluorescence detection of H_2O_2 and glucose were done using Au NCs.[63] The ligand on the surface of NCs was oxidized by H_2O_2 and formed disulfide products. As a consequence, the fluorescence of NCs was quenched. Combination of GOD with Au NCs helped in detection of glucose. The LOD was 1 μM for the 11-MUDA-protected cluster, and for BSA-protected Au NCs, the LOD was 5 μM for glucose detection.

Wen et al. synthesized Au NCs using horseradish peroxidase (HRP) as a template wherein the ligand assisted in the formation of NCs and this functional NCs helped in the detection of H_2O_2.[64] They showed that H_2O_2 could quench the luminescence of the Au NCs and the LOD was 30 nM as shown in Fig. 22.5. The quenching occurred due to the aggregation of Au NCs. They have also used this nanoprobe to detect the ROS species. Another nanocomposite based on Au@BSA-silica nanoparticle was developed by Wu et al., which showed acceptable sensitivity toward hydrogen peroxide sensing.[65] This is an example of a stable, less toxic, solid-state ECL sensor. In addition to gold, Cu@BSA was also used as peroxidase mimic to detect the H_2O_2 and glucose by Hu et al.[66] The luminol–H_2O_2 system through Au@BSA NCs in alkaline medium can be employed for sensing of H_2O_2.[67] Enhanced chemiluminescence was achieved. The enhancement was observed mainly due to the luminol oxidation in alkaline medium in the presence of H_2O_2, initiated with the decomposition of H_2O_2, catalyzed by Au@BSA.

22.3.1.3 *Detection of proteins*

Concanavalin A (ConA), a carbohydrate-binding protein, was detected using mannose-stabilized Au NCs.[68] This work was based on the aggregation-induced fluorescence quenching. The same sensor can be used for *E. coli* detection because NCs can bind to the bacteria. The LOD for Con A is 75 pM and for *E. coli* is 7.20×10^5 cells/mL.

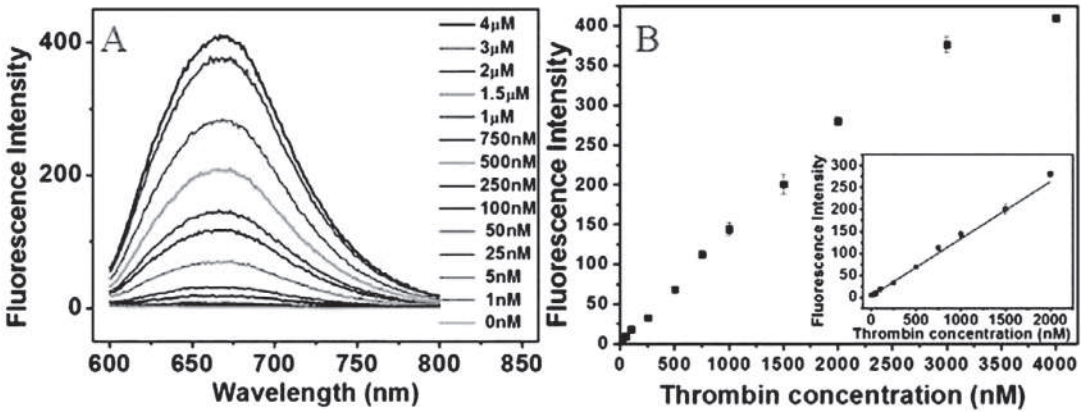

FIGURE 22.6 (A) Fluorescence spectra from the assay for thrombin. (B) Emission intensity (at 669 nm) increases with the concentration of human α-thrombin. Reproduced with permission.[74]

Poly(amidoamine) or (PAMAM)-protected Au NCs were used as a probe for the detection of human IgG antigen.[69] This work was based on the fluorescence quenching. Protein A-modified Au NCs was used as a sensor for sensing of human immunoglobulin G (hIgG) in a homogeneous solution.

For detection of ciprofloxacin and proteases, Au@BSA was used by Chen et al.[70] and Wang et al.[71] Hu et al. developed a probe based on Au@BSA to detect proteases for the first time.[72] The protein-protected NCs were stabilized by bulky protein like BSA, which contains 59 lysine and 24 arginine groups. Presence of trypsin could cleave these residues and decompose NCs. The change in the surface structure of the cluster led to the formation of aggregates and quenched the fluorescence.

Thrombin was detected by Ag@DNA (cytosin-rich) clusters using strong recognition chemistry of DNA aptamers.[73] Clusters were conjugated with an antithrombin aptamer sequence to recognize the thrombin. Similarly, Ag clusters with guanine-rich DNA sequence was used to detect human α-thrombin as shown in Fig. 22.6.[74]

22.3.1.4 Detection of nucleic acids

DNA-protected metal NCs were used broadly for sensing of nucleic acids. Intense luminescence, excellent photostability, and complementary base pairing rendered them as fast and reliable sensor.

DNA-protected Cu nanoclusters are very sensitive to the base type located in the major groove. The fluorescence detection of mismatch type in a specific DNA sequence was possible using DNA-protected Cu NCs, shown in Fig. 22.7. The sensitivity of the fluorescent NCs to the base type allowed mix and measure type detection.[75] Fluorescent Ag NC probe discriminates single-nucleotide variants by emission color.[76]

22.3.2 Bioimaging (in vitro and in vivo)

Biolabeling of proteins with metal clusters began in 1980s[77] using undecagold clusters. They are known as immunogold:protein conjugates. In immunogold labeling, protected small

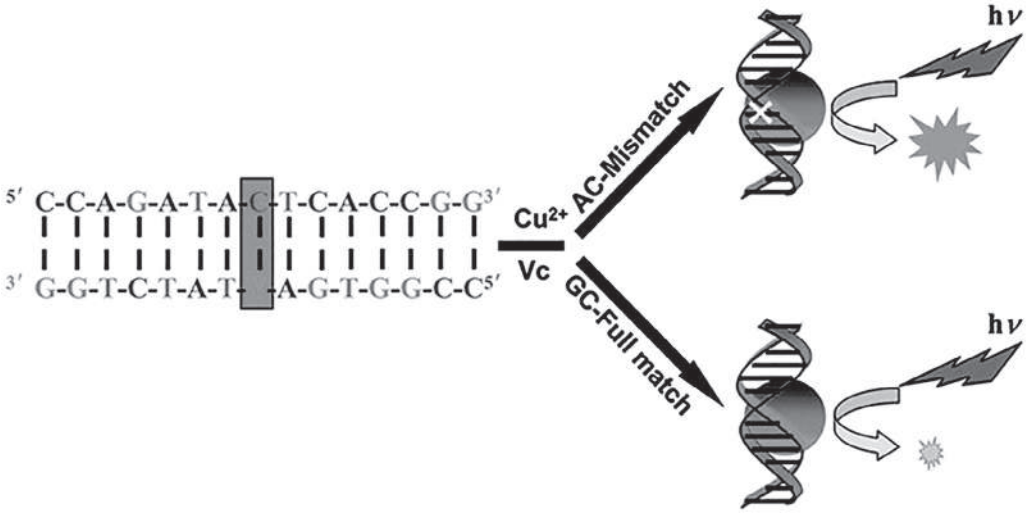

FIGURE 22.7 Schematic representation of the detection of nucleic acids by Cu NCs. Reproduced with permission.[75]

gold clusters are attached to secondary antibodies, which in turn are attached to primary antibodies to specifically bind an antigen or a cell component. Those small Au-conjugated antibody labels improved the resolution of electron microscopic investigations,[78] and helped in several studies, for example, the visualization of the biotin-binding site on avidin.[77] The technique has been in use for several decades and is quite well known in electron microscopy.[79–81] These probes are commercially available now. Small gold cluster-protein conjugates were used as TEM contrast agents. However, nowadays, fluorescent molecules are used in optical imaging for live systems. Organic dyes[82] and fluorescent quantum dots[83,84] have been used extensively for optical imaging of biosystems for the past few decades. Though quantum dots are superior to organic dyes, because of their stable luminescence and photostability, toxicity prevented their application in biology. Researchers wanted to develop a biocompatible, nontoxic nanoprobe for high-quality optical imaging. In 2009, when the first atomically precise NCs were reported, researchers tried to use these materials in biology because of their biocompatible scaffold, intense and stable luminescence, and solubility in water. The intense NIR fluorescence of NCs eliminated the involvement of autofluorescence and scattering light from the tissues of a biological media. They were used for targeting and imaging (in vitro and in vivo), drug delivery, therapeutic applications, etc. Their versatile applications in biomedical fields to date are discussed here.

22.3.2.1 Targeting and imaging

Functional NCs allow us to targeting and selective labeling for the detection of biomolecules. Retnakumari et al. reported targeted imaging of cancer cells based on molecular-receptor (Fig. 22.8). They used Au_{25}@BSA NCs conjugated with folic acid.[85] For targeting cancer cell, folic acid conjugation is a very important aspect. This is because certain cancer cells overexpressed the folate receptor (FR), and endocytosis in case of cancer cells usually

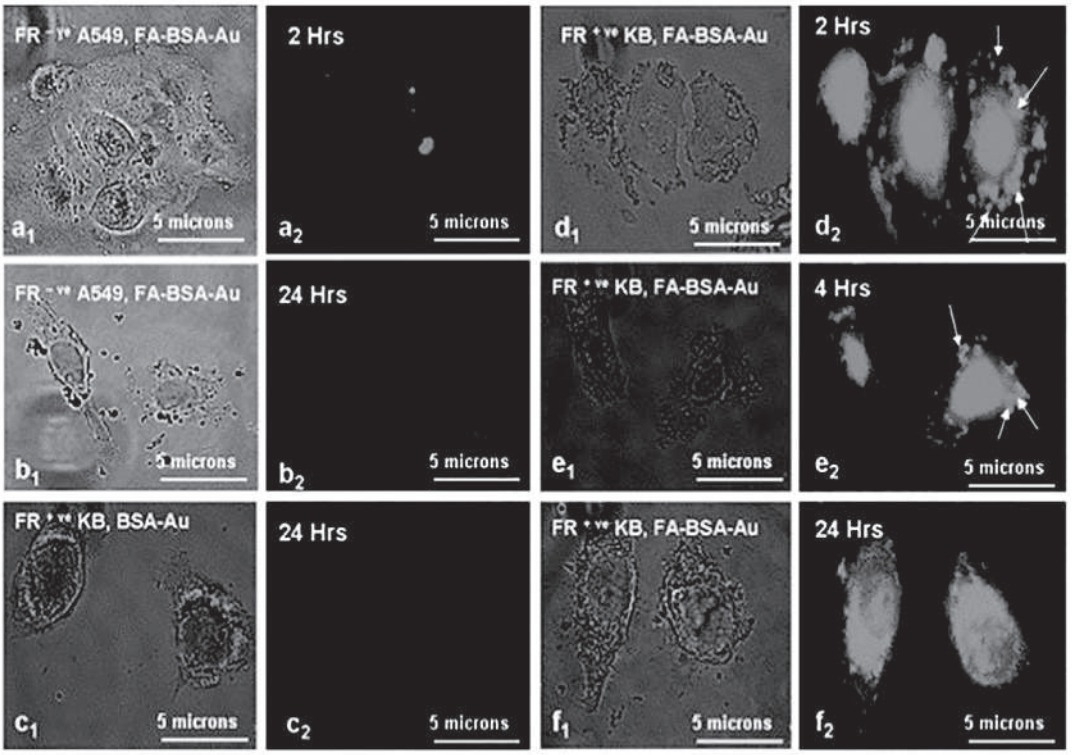

FIGURE 22.8 Targeted cancer cell fluorescence imaging of FA conjugated Au@BSA NCs in different types of cell lines at different time intervals. It showed that internalization of the FA conjugated cluster was greater in FR^{+ve} cells than that in FR^{-ve} cells. Reproduced with permission.[85]

happens through FR. First, they confirmed the stability of the conjugated clusters in a wide pH range from 4 to 14 and also fluorescence at pH 7.4 in phosphate buffer saline. Also, the cell viability results, and ROS toxicity studies confirmed that the bioconjugate is nontoxic and during cell–cluster interaction, the highly stable intense broad fluorescence in NIR range could be retained. The folate targeted cancer cell imaging was demonstrated using FR^{+ve} oral squamous cell carcinoma (KB) and breast adenocarcinoma cell MCF-7 and also on FR^{-ve} lung carcinoma cell lines (A549). In this study, they observed that internalization of the folic acid conjugated cluster was greater in FR^{+ve} cells compared to that in FR^{-ve} cells. Muhammed et al. made Au_{38}@BSA NCs, conjugated with folic acid and demonstrated bioimaging in oral carcinoma (KB) cells, based on the same principle.[28] Later Ghosh et al. showed the cellular uptake of as-synthesized Ag_{18}@BSA NCs without any conjugation or special purification.[86]

Qiao et al. designed a nanohybrid system by conjugating Au@Ova NCs with folic acid (FA) and then a homopolymer, N-acryloxysuccinimide (PNAS).[87] They used NCs as the fluorescent probe, FA as the targeting ligand, PNAS as the linker. Au@Ova-FA-PNAS hybrid material was used to demonstrate the specific staining of the HeLa cells.

When transferrin functionalized Au NCs were fabricated with graphene oxide by Wang et al., a turn-on fluorescent probe for bioimaging was developed.[88] This hybrid nanocomposite

was used to image cancer cells and small animals. Ligand Tf acted as a reducer, stabilizer, and helped in specific targeting of the transferrin receptor (TfR). Initially, the interaction of GO with Au@Tf NCs quenched the fluorescence, but was restored in the presence of TfR. This turn-on fluorescence was observed because the specificity of Tf with TfR was greater compared to that of GO in the Tf-Au NCs/GO hybrid material. Excellent stability, biocompatibility, intense fluorescence, and negligible cytotoxicity allowed this material to be used as a turn-on fluorescent bioimaging probe for cancer cells and small animals.

Lin et al. reported nuclear targeting and intracellular imaging by luminescent Au@MUDA NCs.[89] Clusters were functionalized with a specific peptide, SV40 (PKKKRKV), for nuclear-localization signal (NLS). This was studied using HeLa cell lines. NCs were easily internalized and distributed in the nucleus and cytoplasm. Muhammed et al. shown the labeling of HepG2, cancerous cells, with NIR emitting Au_{23}@SG NCs.[90] Clusters were conjugated with streptavidin. Since cancerous cells contain excess biotin, strong binding of streptavidin with biotin helped in imaging of the cells.

Hu et al. developed a ^{64}Cu-doped chelator-free Au@HSA NCs for dual-mode in vitro and in vivo imaging of animals.[91] This nontoxic hybrid NCs was used to do PET and NIR imaging. This self-illuminating material converted short wavelengths of Cerenkov radiation into longer wavelengths. Thus, imaging was done based on Cerenkov resonance energy transfer (CRET).

Gao et al. introduced an ultrasmall [^{64}Cu]Cu@BSA NCs for targeting orthotopic lung tumors.[92] Here, they used positron emission tomography (PET) imaging, which is more sensitive, accurate, and deeply penetrating than NIR fluorescence imaging. Generally, ^{64}Cu is used as a PET agent through macrocyclic chelators, but that can misapprehend the results due to detachment and transchelation of ^{64}Cu. This was the first report, whereby authors made chelator-free radioactive Cu NCs for PET imaging. They have preconjugated the BSA molecules with tumor target peptide luteinizing hormone releasing hormone (LHRH) and prepared [^{64}Cu]Cu@BSA-LHRH for in vitro and in vivo PET imaging.

Ding et al. developed a biosensor for specific imaging of cancer cells and for ratiometric determination of intracellular pH, in a wide range from 6.0 to 7.8 with a pKa at 6.84.[93] Monitoring intracellular pH by ratiometric fluorescence sensor, wherein the Au@BSA NCs acted as a reference fluorophore and fluorescein-isothiocyanate (FITC) worked as the response for pH. They performed targeted imaging of FR^{+ve} HeLa cells by conjugating NCs with folic acid and monitored the pH changes in the HeLa cells.

Zhou et al. developed a hybrid material using blue emissive Au@BSA NCs and red emissive Au@DHLA NCs, whereby an enhancement in fluorescence was observed due to efficient FRET, shown in Fig. 22.9.[94] In this material, the polymer-like shielding layers throughout the Au core made it ultrastable in living cells. Thus, this can be used as a fluorescent label for long-term imaging, especially in ROS species containing cells.

Wu et al. have shown that Au@BSA NCs conjugated with FITC can be used as a fluorescent probe for simultaneous pH (6–9) and temperature (1–71°C) sensing.[95] With the increase in temperature, fluorescence was quenched due to the reduction of charge transfer from protein to clusters. This FITC-Au@BSA probe was sensitive to the change in pH, temperature, and trypsin concentration, enabling them to construct two and three-input AND logic gates. They monitored the variation in temperature and pH in the HeLa cells via fluorescence imaging with this probe.

Au NCs capped with N-acetyl-L-cysteine (NAC-CS) could be used for long time imaging.[96] They were insensitive to hydrogen peroxide and trypsin unlike protein-protected metal

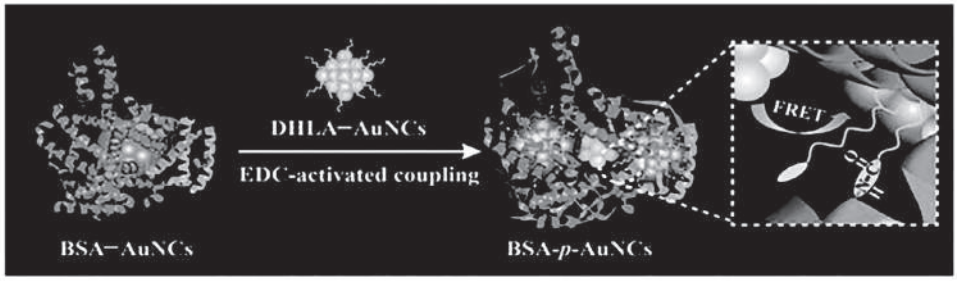

FIGURE 22.9 Schematic representation of the synthetic strategy of combining blue emissive Au@BSA NCs and red emissive Au@DHLA NCs. Reproduced with permission.[94]

clusters. This allows them to image for long time (strong fluorescence was observed up to 4 h) in HeLa cells.

22.3.2.2 *In vivo imaging*

In vivo bioimaging is more challenging than imaging of cell-lines or in vitro studies. Interaction of clusters with animal models increased complexity of the system such as the interaction with various biomolecules and possible loss of luminescence, less transmission of visible light through tissues, etc. However, NCs are potential candidates for in vivo imaging for their unique properties, biocompatibility, NIR emission, photothermal stability, etc.

Li et al. demonstrated the preparation of Au NCs/PPI NPs, where PPI is pea protein isolate, which was successfully fused into the RBC membrane, shown in Fig. 22.10.[97] It showed increased blood circulation with enhanced tumor locating capability. This material provided a new strategy that could be used in biomedicine for excellent in vivo and in vitro imaging.

Liu et al. synthesized insulin-protected Au NCs. They conducted two-photon fluorescence in vivo imaging. The versatility of this NCs was displayed by fluorescence imaging and X-ray computed tomography (CT).[98]

Sun et al. developed a new technique of targeting specific organs for in vitro and in vivo imaging.[99] It is well known that cells in human colorectal carcinoma cell line, Caco-2, express a ferritin receptor on their plasma membrane. For in vivo kidney targeting, they assembled a pair of Au NCs in apoferritin nanoreactor. Here the protein, horse spleen apoFt acts as a template to the NCs as well as it functionalized the pair of NCs formed inside this scaffold. Hep G2, a human hepatoma cell line, was used as a negative control because it does not express a ferritin receptor on the plasma. First, they did in vitro imaging using paired far-red Au NCs wherein receptor-mediated binding and cellular uptake was observed in Caco-2 cells, but no cellular uptake was observed in the case of Hep G2. This proved that the cellular uptake was mainly driven by the ferritin receptor. Whole-body in vivo fluorescence imaging with specifically targeting the kidney was done using this nanoprobe which is effective in targeting certain cells that express ferritin receptors. Later from the same research group, multiple Au NCs within an apo H-ferritin nanocage was designed, which was used as a NIR fluorescent nanoprobe for live animals.[100] The ultimate specificity of this material was proved by the observation of 10 times higher accumulation in kidney than in other organs like liver, spleen, which are common organs for nanoparticle accumulation.

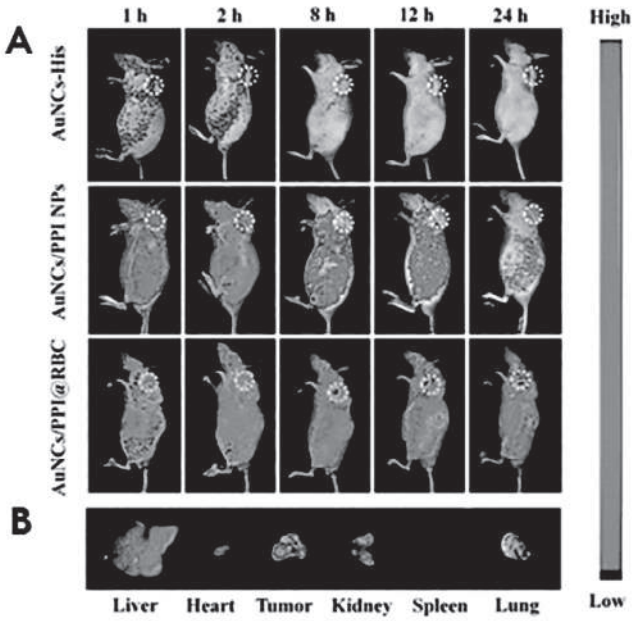

FIGURE 22.10 Time-dependent real-time in vivo fluorescence images of tumor-bearing mice, lower panel shows the ex vivo tissue images. Reproduced with permission.[97]

22.3.2.3 *Multimodal imaging*

Triple modal NIRF/CT/MRI in vivo imaging was performed using hybrid gold–gadolinium NCs protected by albumin.[101] In the biomedical field, multimodal imaging is very useful because it can provide complementary information from each mode of imaging with accuracy. Ultrasmall, stable, biocompatible hybrid NCs were injected intravenously, and they accumulated in tumor tissues and was excreted quickly from the body. The information about the heterostructure of the solid tumor was obtained using this hybrid NC. Thus, the hybrid NCs effectively acted as a nanoprobe in cancer targeted bioimaging and diagnosis accurately in vivo.

Sun et al. fabricated a hybrid nanoprobe for multimodal imaging using a one-step mild synthesis route as shown in Fig. 22.11.[102] They have used multifunctional BSA-Gd_2O_3/Au NCs for NIR fluorescence and magnetic resonance imaging (MRI). They bioconjugated this hybrid material with arginine–glycine–aspartic acid peptide for in vivo targeted tumor imaging.

Shibu et al. developed QCs-based hybrid nanoprobe, which can provide a triple modality for live-cell imaging.[103] They prepared the hybrid material by conjugating biotinylating Au@BSA clusters with streptavidin-functionalized Fe_3O_4 NPs and followed it by uncaging of fluorescein by $^1O_2$ in the methylanthracene-fluorescein-caged conjugate. For the first time, they showed that the QC based hybrid materials can be used for NIR fluorescence, MRI contrast and $^1O_2$-sensitized intracellular fluorescence modalities for bioimaging.

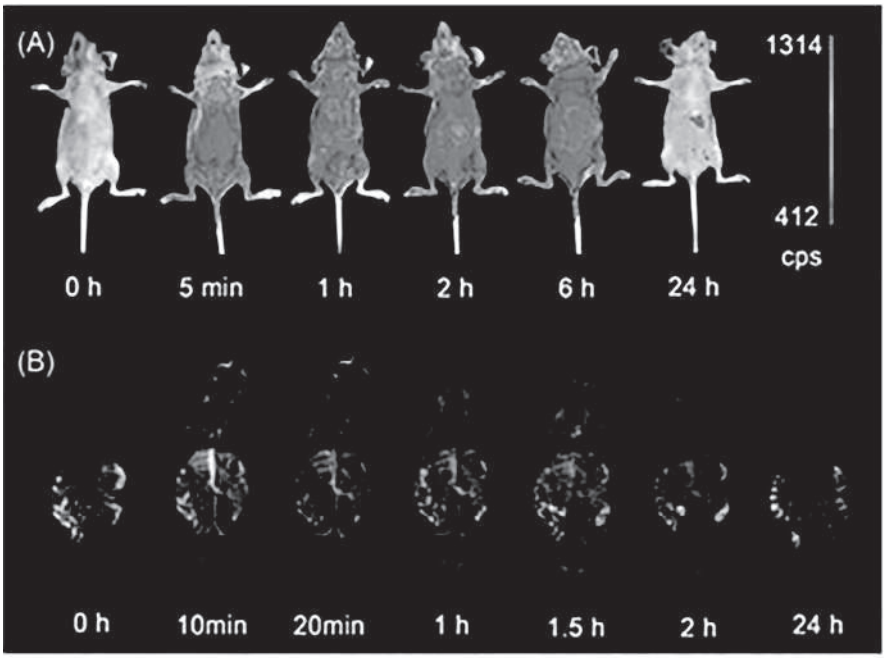

FIGURE 22.11 Multimodal in vivo imaging using BSA-Gd_2O_3/Au nanoprobe (A) NIR fluorescent imaging, (B) magnetic resonance imaging. Reproduced with permission.[102]

22.4 Therapeutic applications

Nanoclusters have been integrated into molecular medicine and made significant advances in diagnostics and therapy. Chen et al. introduced two kinds of multifunctional nanocarriers, where Au@BSA was in the core and in the shell FA-conjugated amphiphilic hyperbranched block copolymer based on poly(L-lactide) (PLA) was used as inner arm and FA-conjugated sulfated polysaccharide (GPPS-FA) as outer arm in the hybrid Au NCs-PLA-GPPS-FA.[104] Anticancer drug camptothecin (CPT) was used for drug delivery. The slow and steady release of the drug made it very promising in drug delivery and treatment of cancer.

Efficiency of NCs for therapeutic applications depends on the powerful nuclear drug delivery vehicles to help transport of the drugs from the cytoplasm to the nucleus. Wang et al. demonstrated specific nuclear targeting of Au@BSA-Herceptin hybrid material for enhanced therapy of HER2+ breast cancer.[105] Because of the conjugation of Au@BSA with Herceptin, which has high targeting specificity and nuclear localization capability, simultaneous fluorescence imaging and enhanced cancer therapy was possible. Due to the small size, it escaped the endolysosomal pathway and penetrated the nucleus. The hybrid material showed enhanced anticancer therapeutic efficiency compared to only Herceptin which is mainly due to the DNA damage.

An anticancer drug, Doxorubicin (DOX) was used to make a hybrid material with FA conjugated Au NCs. Prodrug Au-FA-DOX was synthesized for therapeutic applications. Chen

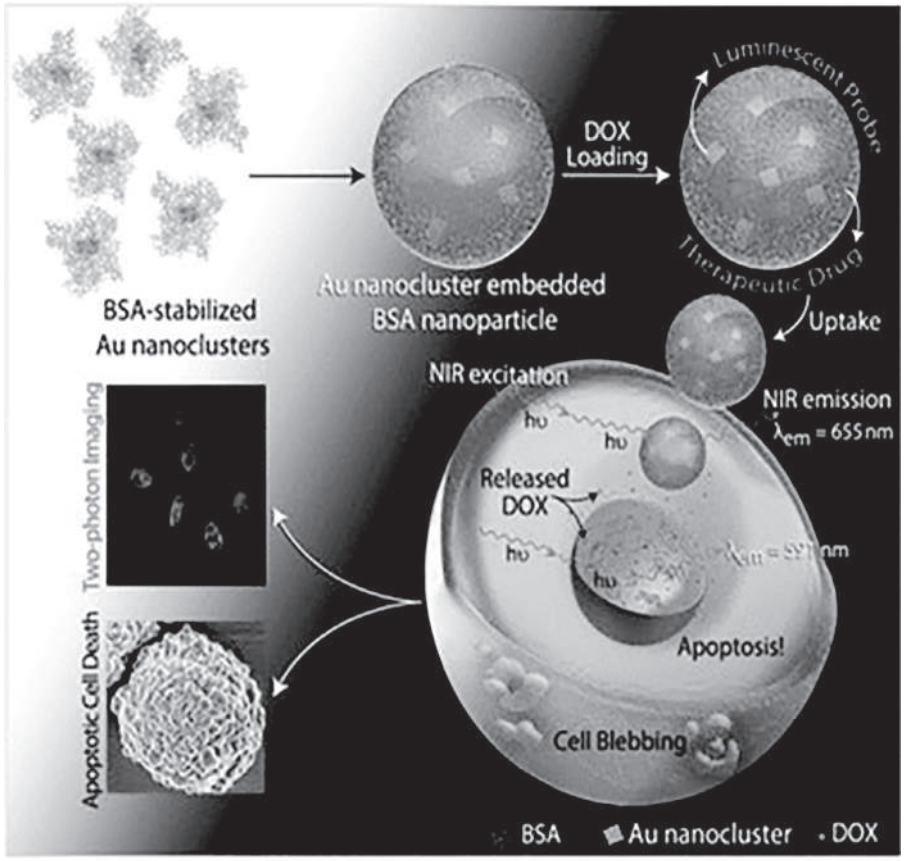

FIGURE 22.12 Therapeutic applications using PPCs and hybrid materials based on PPC. The formation of luminescent therapeutic drug, that is, DOX loaded Au NCs embedded in BSA NPs, and the fate of the DOX inside the HeLa cells is shown. Reproduced with permission.[106]

et al. showed that it has high tumor-targeting activity and high antitumor efficacy in FR-positive cells.[107]

Khandelia et al. fabricated a hybrid anticancer, nontoxic, biocompatible agent based on Au@BSA NCs embedded BSA nanoparticles conjugated with DOX as shown in Fig. 22.12.[102,106] They reported that this composite released the DOX to the cancer cells and as a result, apoptotic cell death occurred. The luminescence of the Au NCs probed the uptake of the nanoparticles by the cancer cells and the luminescence of DOX tracked the intracellular release of the drug. They performed two-photon fluorescence imaging of HeLa cells with this composite.

Protein-protected Cu NCs were also used for theranostic purpose in a similar fashion by conjugation with DOX.[108] Blue luminescent Cu@Tf NCs was conjugated with DOX by electrostatic interactions, and as a result, the red luminescent hybrid material, Tf-Cu NC-DOX NPs was formed. This nanodrug has shown its potential in targeting and therapeutic

efficacy by cellular uptake of the drug in TfR overexpressed HeLa and MCF-7 cells than the normal healthy cells. The cellular uptake and the release of the drug from the hybrid material was observed by FRET-assisted imaging. After internalization of the NPs in the cancer cells, blue luminescence of the NCs was restored and the red luminescence from within the nucleus monitored the release of DOX. In vivo experiments were performed using this NP on TfR positive Daltons lymphoma ascites-bearing mice which showed significant inhibition of tumor growth in the mice for prolonged survival.

22.5 Other applications

22.5.1 Self-vaccine

Tao et al. reported smart self-vaccines based on Au NCs for enhanced immune response and cell imaging.[109] They have shown that the antigen protein ovalbumin (OVA) conjugated with CpG oligodeoxynucleotides (ODNs) could be used as a template to form luminescent Au NCs. This is the first report wherein Au NCs were used as effective vaccines. It acted as smart self-vaccines through the dual delivery of the protein antigen and CpG ODNs.

22.5.2 Intrauterine device

Mathew et al. made a hybrid material which can act as an intrauterine device as shown in Fig. 22.13.[110] It was composed of gluten-protected Cu NCs conjugated with polyurethane (PU) polymer. For contraceptive applications, they quantified the release of Cu(II) ions. Cu(II) ions released slowly compared to intrauterine device and also the release rate can be tuned by varying the material composition.

22.5.3 Cancer biomarker detection

Peng et al. introduced a different hybrid material which was used to detect a cancer biomarker namely, neuron-specific enolase (NSE).[111] Au@BSA NCs were loaded into $CaCO_3$ spheres via electrostatic interaction. They used this porous, biocompatible material, $CaCO_3$/AuNCs as a template to conjugate horseradish peroxidase/antibody and made a versatile immunosensor ($CaCO_3$/AuNCs/HRP-Ab_2). The fluorescence-based and electrochemical detection limits of this hybrid sensor were 2.0 and 0.1 pg/mL, respectively.

22.5.4 Anticancer activity

Lystvet et al. have shown the anticancer activity from the Au@LA NCs.[112] The conformational change in LA during clusters formation has made it lethal to HeLa cells.

22.5.5 Antimicrobial agent

Chen et al. have shown that pathogenic bacteria like gram-positive, gram-negative bacteria could be labeled by Au@Lyz clusters.[113] It can be used as antimicrobial agents to prevent the cell growth of antibiotic-resistant bacteria. Au@Lyz was used to detect bacteria by Chan et al. using mass spectrometry.[114]

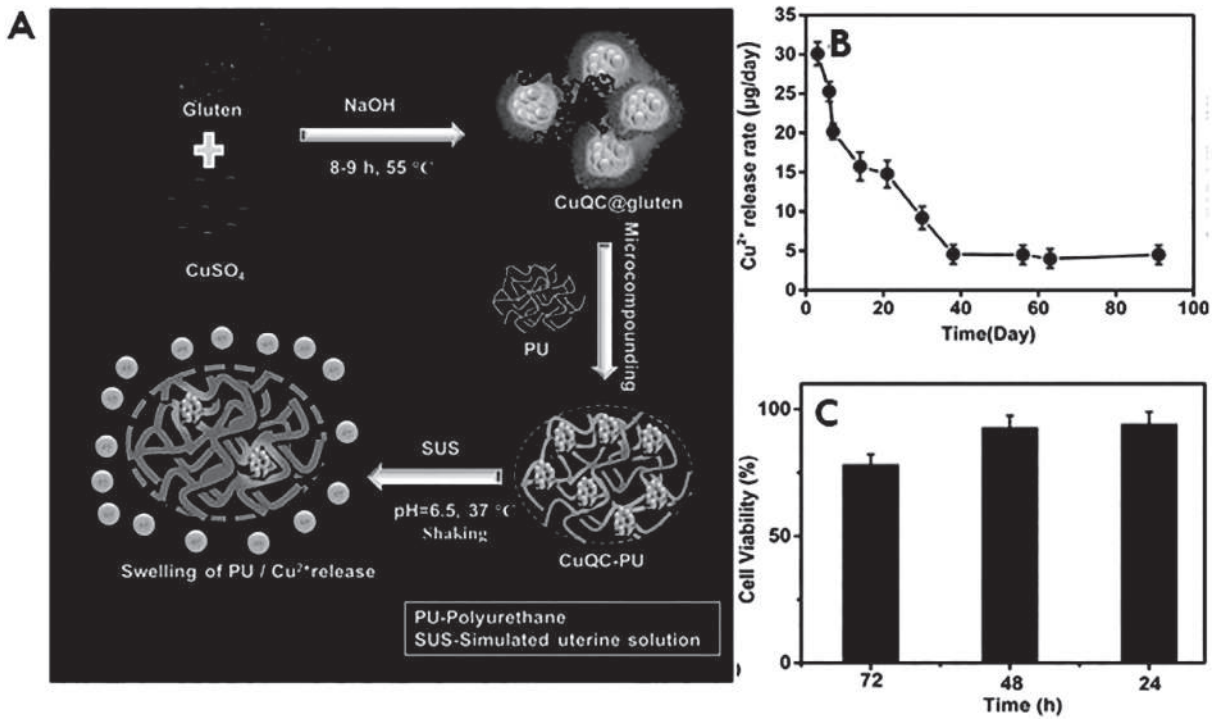

FIGURE 22.13 Synthesis scheme of the hybrid material and release of Cu^{2+} from the material (A); kinetics of the release of Cu^{2+} ions from the composite (B); cell viability (in vitro) experiment of L929 cells with composite (C). Reproduced with permission.[110]

22.5.6 Enzymatic activity

Graphene oxide (GO)-Au@Lyz NCs hybrid (GA) reported by Tao et al. has shown excellent peroxidase-like activity over a broad pH range, even at physiological pH range of 5–7.4.[115] Electrostatic interaction of NCs and GO made this hybrid GA, which can serve as peroxidase enzyme mimics. The catalytic activity of GA was examined with peroxidase substrate 3,3′,5,5′-tetramethylbenzidine (TMB) in the presence of H_2O_2. A deep blue color was observed as a result of the oxidation reaction. They have tested this oxidation reaction at different pH for parent and the hybrid material, whereby they observed that GA showed excellent catalytic property at neutral pH, unlike the parent material. This is due to the synergistic effect between Au NCs and the GO. They compared the activity with HRP and proposed that both mechanisms are similar, when the active sites are close to the substrate. They combined the GA with folic acid (GFA) and made a robust nanoprobe for quantitative, selective, and fast colorimetric detection of cancer cells.

22.6 Summary and future perspective

This chapter discussed the applications of NCs in biology. The first part of this chapter focused on the consideration of NCs for biomedical applications. Different applications of clusters in sensing, imaging, therapeutic, etc. were discussed afterward. Unique properties, biocompatibility, simple surface functionalization of clusters made them potential for the biomedical applications. Random selection of ligands as a template to synthesize clusters involved single function in metal NCs. Now the goal is to make multifunctional NCs for advanced applications in biology. Although this research was carried out by different groups for a long time, very little is known till now. This is a real challenge to know about how these templates can be rationally designed to tune the optical and physicochemical properties of metal NCs and how it can be combined with functionalities of the ligands to develop multi-functional theranostic agents. For synthesizing multifunctional metal NC, rational design of the template at the molecular level by combining suitable components is needed. This is going to be a step forward for future nanomedicine.

List of abbreviation

FRET	fluorescence energy transfer
LOD	limit of detection
MUA	mercaptoundecanoic acid
GSH	glutathione
MBA	mercaptobenzoic acid
ECL	electrochemiluminescence or electrogenerated chemiluminescence
QDs	quantum dots
ROS	reactive oxygen species
ATP	adenosine triphosphate
FA	folic acid
CRET	Cerenkov resonance energy transfer
PET	positron emission tomography
MRI	magnetic resonance imaging
POSSFF	polyhedral oligomeric silsesquioxane
DOX	doxorubicin

References

1. Jin R, Zeng C, Zhou M, Chen Y. Atomically precise colloidal metal nanoclusters and nanoparticles: fundamentals and opportunities. *Chem Rev*. 2016;116:10346–10413.
2. Chakraborty I, Pradeep T. Atomically precise clusters of noble metals: emerging link between atoms and nanoparticles. *Chem Rev (Washington, DC, US)*. 2017;117:8208–8271.
3. Genji Srinivasulu Y, Yao Q, Goswami N, Xie J. Interfacial engineering of gold nanoclusters for biomedical applications. *Mater Horizons*. 2020;7:2596–2618.
4. Su Y, Xue T, Liu Y, Qi J, Jin R, Lin Z. Luminescent metal nanoclusters for biomedical applications. *Nano Res*. 2019;12:1251–1265.
5. Casals E, Pfaller T, Duschl A, Oostingh GJ, Puntes V. Time evolution of the nanoparticle protein corona. *ACS Nano*. 2010;4:3623–3632.
6. Kopp M, Kollenda S, Epple M. Nanoparticle–protein interactions: therapeutic approaches and supramolecular chemistry. *Acc Chem Res*. 2017;50:1383–1390.
7. Lira AL, Ferreira RS, Torquato RJS, et al. Binding kinetics of ultrasmall gold nanoparticles with proteins. *Nanoscale*. 2018;10:3235–3244.
8. Zhou C, Long M, Qin Y, Sun X, Zheng J. Luminescent gold nanoparticles with efficient renal clearance. *Angew Chem Int Ed*. 2011;50:3168–3172 S3168/1-S3168/15.
9. Wong OA, Hansen RJ, Ni TW, et al. Structure–activity relationships for biodistribution, pharmacokinetics, and excretion of atomically precise nanoclusters in a murine model. *Nanoscale*. 2013;5:10525–10533.
10. Yuan H, Li J, Bao G, Zhang S. Variable nanoparticle-cell adhesion strength regulates cellular uptake. *Phys Rev Lett*. 2010;105.
11. Du B, Yu M, Zheng J. Transport and interactions of nanoparticles in the kidneys. *Nat Rev Mater*. 2018;3:358–374.
12. Du B, Jiang X, Das A, et al. Glomerular barrier behaves as an atomically precise bandpass filter in a sub-nanometre regime. *Nat Nanotechnol*. 2017;12:1096–1102.
13. Ning X, Peng C, Li ES, et al. Physiological stability and renal clearance of ultrasmall zwitterionic gold nanoparticles: ligand length matters. *APL Mater*. 2017;5: 053406.
14. Zhang X-D, Wu D, Shen X, Liu P-X, Fan F-Y, Fan S-J. In vivo renal clearance, biodistribution, toxicity of gold nanoclusters. *Biomaterials*. 2012;33:4628–4638.
15. Li H, Zhu W, Wan A, Liu L. The mechanism and application of the protein-stabilized gold nanocluster sensing system. *Analyst (Cambridge, UK)*. 2017;142:567–581.
16. Xie J, Zheng Y, Ying JY. Highly selective and ultrasensitive detection of Hg^{2+} based on fluorescence quenching of Au nanoclusters by Hg^{2+}–Au^{+} interactions. *Chem Commun (Cambridge, UK)*. 2010;46:961–963.
17. Lin Y-H, Tseng W-L. Ultrasensitive sensing of Hg^{2+} and CH_3Hg_+ based on the fluorescence quenching of lysozyme type VI-stabilized gold nanoclusters. *Anal Chem (Washington, DC, US)*. 2010;82:9194–9200.
18. Kawasaki H, Hamaguchi K, Osaka I, Arakawa R. pH-dependent synthesis of pepsin-mediated gold nanoclusters with blue green and red fluorescent emission. *Adv Funct Mater*. 2011;21:3508–3515.
19. Guo C, Irudayaraj J. Fluorescent Ag clusters via a protein-directed approach as a Hg(II) ion sensor. *Anal Chem (Washington, DC, US)*. 2011;83:2883–2889.
20. Pu K-Y, Luo Z, Li K, Xie J, Liu B. Energy transfer between conjugated-oligoelectrolyte-substituted POSS and gold nanocluster for multicolor intracellular detection of mercury ion. *J Phys Chem C*. 2011;115:13069–13075.
21. Paramanik B, Bhattacharyya S, Patra A. Detection of Hg^{2+} and F^{-} ions by using fluorescence switching of quantum dots in an Au-cluster-CdTe QDs nanocomposite. *Chem - Eur J*. 2013;19:5980–5987.
22. Cai Y, Yan L, Liu G, Yuan H, Xiao D. In-situ synthesis of fluorescent gold nanoclusters with electrospun fibrous membrane and application on Hg (II) sensing. *Biosens Bioelectron*. 2013;41:875–879.
23. Ghosh A, Jeseentharani V, Ganayee MA, et al. Approaching sensitivity of tens of ions using atomically precise cluster-nanofiber composites. *Anal Chem (Washington, DC, US)*. 2014;86:10996–11001.
24. Huang C-C, Yang Z, Lee K-H, Chang H-T, Synthesis of highly fluorescent gold nanoparticles for sensing mercury(II). Angew Chem Int Ed. 2007;46:6824–6828.
25. Adhikari B, Banerjee A. Facile synthesis of water-soluble fluorescent silver nanoclusters and HgII sensing. *Chem Mater*. 2010;22:4364–4371.
26. Durgadas CV, Sharma CP, Sreenivasan K. Fluorescent gold clusters as Nanosensors for copper ions in live cells. *Analyst (Cambridge, UK)*. 2011;136:933–940.
27. Yu P, Wen X, Toh Y-R, Huang J, Tang J. Metallophilic bond-induced quenching of delayed fluorescence in Au_{25}@BSA nanoclusters. *Part Part Syst Charact*. 2013;30:467–472.

28. Habeeb Muhammed MA, Verma PK, Pal SK, et al. Luminescent quantum clusters of gold in bulk by albumin-induced core etching of nanoparticles: metal ion sensing, metal-enhanced luminescence, and biolabeling. *Chem - Eur J*. 2010;16:10103–10112 S10103/1-S10103/8.
29. Xavier PL, Chaudhari K, Verma PK, Pal SK, Pradeep T. Luminescent quantum clusters of gold in transferrin family protein, lactoferrin exhibiting FRET. *Nanoscale*. 2010;2:2769–2776.
30. Liu H-Y, Zhang X, Wu X-M, Jiang L-P, Burda C, Zhu J-J. Rapid sonochemical synthesis of highly luminescent non-toxic AuNCs and Au@AgNCs and Cu (II) sensing. *Chem Commun (Cambridge, UK)*. 2011;47:4237–4239.
31. Su L, Shu T, Wang Z. Immobilization of bovine serum albumin-protected gold nanoclusters by using polyelectrolytes of opposite charges for the development of the reusable fluorescent Cu^{2+}-sensor. *Biosens Bioelectron*. 2013;44:16–20.
32. Su Y-T, Lan G-Y, Chen W-Y, Chang H-T. Detection of copper ions through recovery of the fluorescence of DNA-templated copper/silver nanoclusters in the presence of mercaptopropionic acid. *Anal Chem*. 2010;82:8566–8572.
33. Yue Y, Liu T-Y, Li H-W, Liu Z, Wu Y. Microwave-assisted synthesis of BSA-protected small gold nanoclusters and their fluorescence-enhanced sensing of silver(I) ions. *Nanoscale*. 2012;4:2251–2254.
34. Goswami N, Giri A, Bootharaju MS, Xavier PL, Pradeep T, Pal SK. Copper quantum clusters in protein matrix: potential sensor of Pb^{2+} ion. *Anal Chem (Washington, DC, US)*. 2011;83:9676–9680.
35. Myung N, Ding Z, Bard AJ. Electrogenerated chemiluminescence of CdSe nanocrystals. *Nano Lett*. 2002;2:1315–1319.
36. Zou G, Ju H. Electrogenerated chemiluminescence from a CdSe nanocrystal film and its sensing application in aqueous solution. *Anal Chem*. 2004;76:6871–6876.
37. Myung N, Bae Y, Bard AJ. Effect of surface passivation on the electrogenerated chemiluminescence of CdSe/ZnSe nanocrystals. *Nano Lett*. 2003;3:1053–1055.
38. Fang Y-M, Sun J-J, Wu A-H, Su X-L, Chen G-N. Catalytic electrogenerated chemiluminescence and nitrate reduction at CdS nanotubes modified glassy carbon electrode. *Langmuir*. 2009;25:555–560.
39. Fang Y-M, Song J, Li J, et al. Electrogenerated chemiluminescence from Au nanoclusters. *Chem Commun (Cambridge, UK)*. 2011;47:2369–2371.
40. Liu Y, Ai K, Cheng X, Huo L, Lu L. Gold-nanocluster-based fluorescent sensors for highly sensitive and selective detection of cyanide in water. *Adv Funct Mater*. 2010;20:951–956.
41. Wang X-B, Wang Y-L, Yang J, Xing X-P, Li J, Wang L-S. Evidence of significant covalent bonding in $Au(CN)_2$. *J Am Chem Soc*. 2009;131:16368–16370.
42. Liu J-M, Cui M-L, Jiang S-L, et al. BSA-protected gold nanoclusters as fluorescent sensor for selective and sensitive detection of pyrophosphate. *Anal Meth*. 2013;5:3942–3947.
43. Unnikrishnan B, Wei S-C, Chiu W-J, Cang J, Hsu P-H, Huang C-C. Nitrite ion-induced fluorescence quenching of luminescent BSA-Au_{25} nanoclusters: mechanism and application. *Analyst (Cambridge, UK)*. 2014;139:2221–2228.
44. Xu H, Zhu H, Sun M, et al. Graphene oxide supported gold nanoclusters for the sensitive and selective detection of nitrite ions. *Analyst (Cambridge, UK)*. 2015;140:1678–1685.
45. Shang L, Dong S. Sensitive detection of cysteine based on fluorescent silver clusters. *Biosens Bioelectron*. 2009;24:1569–1573.
46. Yuan X, Tay Y, Dou X, Luo Z, Leong DT, Xie J. Glutathione-protected silver nanoclusters as cysteine-selective fluorometric and colorimetric probe. *Anal Chem*. 2013;85:1913–1919.
47. Han B, Wang E. Oligonucleotide-stabilized fluorescent silver nanoclusters for sensitive detection of biothiols in biological fluids. *Biosens Bioelectron*. 2011;26:2585–2589.
48. Hu Y, Wu Y, Chen T, Chu X, Yu R. Double-strand DNA-templated synthesis of copper nanoclusters as novel fluorescence probe for label-free detection of biothiols. *Anal Meth*. 2013;5:3577–3581.
49. Cui M-L, Liu J-M, Wang X-X, et al. Selective determination of cysteine using BSA-stabilized gold nanoclusters with red emission. *Analyst*. 2012;137:5346–5351.
50. Ge S, Yan M, Lu J, et al. Electrochemical biosensor based on graphene oxide-Au nanoclusters composites for L-cysteine analysis. *Biosens Bioelectron*. 2012;31:49–54.
51. Chen T-H, Tseng W-L. Lysozyme type VI)-stabilized Au_8 clusters: synthesis mechanism and application for sensing of glutathione in a single drop of blood. *Small*. 2012;8:1912–1919.
52. Tian D, Qian Z, Xia Y, Zhu C. Gold nanocluster-based fluorescent probes for near-infrared and turn-on sensing of glutathione in living cells. *Langmuir*. 2012;28:3945–3951.

53. Wang X, Wu P, Hou X, Lv Y. An ascorbic acid sensor based on protein-modified Au nanoclusters. *Analyst (Cambridge, UK)*. 2013;138:229–233.
54. Yang K, Wang Y, Lu C, Yang X. Ovalbumin-directed synthesis of fluorescent copper nanoclusters for sensing both vitamin B1 and doxycycline. *J Lumin*. 2018;196:181–186.
55. Yu Y, New SY, Xie J, Su X, Tan YN. Protein-based fluorescent metal nanoclusters for small molecular drug screening. *Chem. Commun. (Cambridge, UK)*. 2014;50:13805–13808.
56. Samari F, Hemmateenejad B, Rezaei Z, Shamsipur M. A novel approach for rapid determination of vitamin B12 in pharmaceutical preparations using BSA-modified gold nanoclusters. *Anal. Meth*. 2012;4:4155–4160.
57. Zhao H, Wang Z, Jiao X, Zhang L, Lv Y. Uricase-based highly sensitive and selective spectrophotometric determination of uric acid using BSA-stabilized Au nanoclusters as artificial enzyme. *Spectrosc Lett*. 2012;45:511–519.
58. Li L, Liu H, Shen Y, Zhang J, Zhu J-J. Electrogenerated chemiluminescence of Au nanoclusters for the detection of dopamine. *Anal. Chem. (Washington, DC, US)*. 2011;83:661–665.
59. Wang H-B, Zhang H-D, Chen Y, Huang K-J, Liu Y-M. A label-free and ultrasensitive fluorescent sensor for dopamine detection based on double-stranded DNA templated copper nanoparticles. *Sens Actuat B: Chem*. 2015;220:146–153.
60. Aswathy B, Sony G. Cu^{2+} modulated BSA-Au nanoclusters: a versatile fluorescence turn-on sensor for dopamine. *Microchem J*. 2014;116:151–156.
61. He Y, Wang X, Zhu J, Zhong S, Song G. Ni^{2+}-modified gold nanoclusters for fluorescence turn-on detection of histidine in biological fluids. *Analyst (Cambridge, UK)*. 2012;137:4005–4009.
62. Li H, Guo Y, Xiao L, Chen B. Selective and sensitive detection of acetylcholinesterase activity using denatured protein-protected gold nanoclusters as a label-free probe. *Analyst (Cambridge, UK)*. 2014;139:285–289.
63. Shiang Y-C, Huang C-C, Chang H-T. Gold nanodot-based luminescent sensor for the detection of hydrogen peroxide and glucose. *Chem Commun*. 2009;23:3437–3439.
64. Wen F, Dong Y, Feng L, Wang S, Zhang S, Zhang X. Horseradish peroxidase functionalized fluorescent gold nanoclusters for hydrogen peroxide sensing. *Anal. Chem. (Washington, DC, US)*. 2011;83:1193–1196.
65. Wu Y, Huang J, Zhou T, Rong M, Jiang Y, Chen X. A novel solid-state electrochemiluminescence sensor for the determination of hydrogen peroxide based on an Au nanocluster-silica nanoparticle nanocomposite. *Analyst (Cambridge, UK)*. 2013;138:5563–5565.
66. Hu L, Yuan Y, Zhang L, Zhao J, Majeed S, Xu G. Copper nanoclusters as peroxidase mimetics and their applications to H_2O_2 and glucose detection. *Anal. Chim. Acta*. 2013;762:83–86.
67. Deng M, Xu S, Chen F. Enhanced chemiluminescence of the luminol-hydrogen peroxide system by BSA-stabilized Au nanoclusters as a peroxidase mimic and its application. *Anal. Meth*. 2014;6:3117–3123.
68. Huang C-C, Chen C-T, Shiang Y-C, Lin Z-H, Chang H-T. Synthesis of fluorescent carbohydrate-protected Au nanodots for detection of concanavalin A and *Escherichia coli*. *Anal Chem*. 2009;81:875–882.
69. Triulzi RC, Micic M, Giordani S, Serry M, Chiou W-A, Leblanc RM. Immunoasssay based on the antibody-conjugated PAMAM-dendrimer–gold quantum dot complex. *Chem Commun*. 2006;48:5068–5070.
70. Chen Z, Qian S, Chen J, Cai J, Wu S, Cai Z. Protein-templated gold nanoclusters based sensor for off-on detection of ciprofloxacin with a high selectivity. *Talanta*. 2012;94:240–245.
71. Wang Y, Wang Y, Zhou F, Kim P, Xia Y. Protein-protected Au clusters as a new class of nanoscale biosensor for label-free fluorescence detection of proteases. *Small*. 2012;8:3769–3773.
72. Hu L, Han S, Parveen S, Yuan Y, Zhang L, Xu G. Highly sensitive fluorescent detection of trypsin based on BSA-stabilized gold nanoclusters. *Biosens Bioelectron*. 2012;32:297–299.
73. Sharma J, Yeh H-C, Yoo H, Werner JH, Martinez JS. Silver nanocluster aptamers: in situ generation of intrinsically fluorescent recognition ligands for protein detection. *Chem Commun*. 2011;47:2294–2296.
74. Li J, Zhong X, Zhang H, Le XC, Zhu J-J. Binding-induced fluorescence turn-on assay using aptamer-functionalized silver nanocluster DNA probes. *Anal Chem*. 2012;84:5170–5174.
75. Jia X, Li J, Han L, Ren J, Yang X, Wang E. DNA-hosted copper nanoclusters for fluorescent identification of single nucleotide polymorphisms. *ACS Nano*. 2012;6:3311–3317.
76. Yeh H-C, Sharma J, Shih I-M, Vu DM, Martinez JS, Werner JH. A fluorescence light-up Ag nanocluster probe that discriminates single-nucleotide variants by emission color. *J Am Chem Soc*. 2012;134:11550–11558.
77. Safer D, Hainfeld J, Wall JS, Reardon JE. Biospecific labeling with undecagold: visualization of the biotin-binding site on avidin. *Science*. 1982;218:290–291.

78. Hainfeld JF. A small gold-conjugated antibody label: improved resolution for electron microscopy. *Science*. 1987;236:450–453.
79. Hyatt AD, Eaton B. *Immuno-Gold Electron Microscopy in Virus Diagnosis and Research*. CRC Press: Taylor & Francis; 1992.
80. Safer D. Undecagold cluster labeling of proteins at reactive cysteine residues. *J Struct Biol*. 1999;127:101–105.
81. Jahn W. Review: chemical aspects of the use of gold clusters in structural biology. *J Struct Biol*. 1999;127:106–112.
82. Guo Z, Park S, Yoon J, Shin I. Recent progress in the development of near-infrared fluorescent probes for bioimaging applications. *Chem Soc Rev*. 2014;43:16–29.
83. Wegner KD, Hildebrandt N. Quantum dots: bright and versatile in vitro and in vivo fluorescence imaging biosensors. *Chem Soc Rev*. 2015;44:4792–4834.
84. Michalet X, Pinaud FF, Bentolila LA, et al. Quantum dots for live cells, in vivo imaging, and diagnostics. *Science (Washington, DC, US)*. 2005;307:538–544.
85. Retnakumari A, Setua S, Menon D, et al. Molecular-receptor-specific, non-toxic, near-infrared-emitting Au cluster-protein nanoconjugates for targeted cancer imaging. *Nanotechnology*. 2010;21 055103/1-055103/12.
86. Ghosh D, Bodiuzzaman M, Som A, et al. Internalization of a preformed atomically precise silver cluster in proteins by multistep events and emergence of luminescent counterparts retaining bioactivity. *J Phys Chem C*. 2019;123:29408–29417.
87. Qiao J, Mu X, Qi L, Deng J, Mao L. Folic acid-functionalized fluorescent gold nanoclusters with polymers as linkers for cancer cell imaging. *Chem Commun. (Cambridge, UK)*. 2013;49:8030–8032.
88. Wang Y, Chen J-T, Yan X-P. Fabrication of transferrin functionalized gold nanoclusters/graphene oxide nanocomposite for turn-on near-infrared fluorescent bioimaging of cancer cells and small animals. *Anal Chem. (Washington, DC, US)*. 2013;85:2529–2535.
89. Lin S-Y, Chen N-T, Sum S-P, Lo L-W, Yang C-S. Ligand exchanged photoluminescentgold quantum dots functionalized with leading peptides for nuclear targeting and intracellular imaging. *Chem Commun*. 2008;39:4762–4764.
90. Muhammed MAH, Verma PK, Pal SK, et al. Bright, NIR-emitting Au_{23} from Au_{25}: characterization and applications including biolabeling. Chem Eur J. 2009;15:10110–10120.
91. Hu H, Huang P, Weiss OJ, et al. PET and NIR optical imaging using self-illuminating ^{64}Cu-doped chelator-free gold nanoclusters. *Biomaterials*. 2014;35:9868–9876.
92. Gao F, Cai P, Yang W, et al. Ultrasmall [^{64}Cu]Cu nanoclusters for targeting orthotopic lung tumors using accurate positron emission tomography imaging. *ACS Nano*. 2015;9:4976–4986.
93. Ding C, Tian Y. Gold nanocluster-based fluorescence biosensor for targeted imaging in cancer cells and ratiometric determination of intracellular pH. *Biosens Bioelectron*. 2015;65:183–190.
94. Zhou W, Cao Y, Sui D, Guan W, Lu C, Xie J. Ultrastable BSA-capped gold nanoclusters with a polymer-like shielding layer against reactive oxygen species in living cells. *Nanoscale*. 2016;8:9614–9620.
95. Wu Y-T, Shanmugam C, Tseng W-B, Hiseh M-M, Tseng W-L. A gold nanocluster-based fluorescent probe for simultaneous pH and temperature sensing and its application to cellular imaging and logic gates. *Nanoscale*. 2016;8:11210–11216.
96. Duan Y, Duan R, Liu R, et al. Chitosan-stabilized self-assembled fluorescent gold nanoclusters for cell imaging and biodistribution in vivo. *ACS Biomater Sci Eng*. 2018;4:1055–1063.
97. Li Z, Peng H, Liu J, et al. Plant protein-directed synthesis of luminescent gold nanocluster hybrids for tumor imaging. *ACS Appl. Mater. Interfaces*. 2018;10:83–90.
98. Liu C-L, Wu H-T, Hsiao Y-H, et al. Insulin-directed synthesis of fluorescent gold nanoclusters: preservation of insulin bioactivity and versatility in cell imaging. *Angew Chem Int Ed*. 2011;50:7056–7060 S7056/1-S7056/8.
99. Sun C, Yang H, Yuan Y, et al. Controlling assembly of paired gold clusters within apoferritin nanoreactor for in vivo kidney targeting and biomedical imaging. *J Am Chem Soc*. 2011;133:8617–8624.
100. Sun C, Yuan Y, Xu Z, et al. Fine-tuned H-ferritin nanocage with multiple gold clusters as near-infrared kidney specific targeting nanoprobe. *Bioconjug Chem*. 2015;26:193–196.
101. Hu D-H, Sheng Z-H, Zhang P-F, et al. Hybrid gold-gadolinium nanoclusters for tumor-targeted NIRF/CT/MRI triple-modal imaging in vivo. *Nanoscale*. 2013;5:1624–1628.
102. Sun S-K, Dong L-X, Cao Y, Sun H-R, Yan X-P. Fabrication of multifunctional Gd_2O_3/Au hybrid nanoprobe via a one-step approach for near-infrared fluorescence and magnetic resonance multimodal imaging in vivo. *Anal Chem. (Washington, DC, US)*. 2013;85:8436–8441.

103. Shibu ES, Sugino S, Ono K, et al. Singlet-oxygen-sensitizing near-infrared-fluorescent multimodal nanoparticles. *Angew Chem Int Ed*. 2013;52:10559–10563.
104. Chen T, Xu S, Zhao T, et al. Gold nanocluster-conjugated amphiphilic block copolymer for tumor-targeted drug delivery. *ACS Appl Mater Interfaces*. 2012;4:5766–5774.
105. Wang Y, Chen J, Irudayaraj J. Nuclear targeting dynamics of gold nanoclusters for enhanced therapy of HER2+ breast cancer. *ACS Nano*. 2011;5:9718–9725.
106. Khandelia R, Bhandari S, Pan UN, Ghosh SS, Chattopadhyay A. Gold nanocluster embedded albumin nanoparticles for two-photon imaging of cancer cells accompanying drug delivery. *Small*. 2015;11:4075–4081.
107. Chen H, Li S, Li B, et al. Folate-modified gold nanoclusters as near-infrared fluorescent probes for tumor imaging and therapy. *Nanoscale*. 2012;4:6050–6064.
108. Goswami U, Dutta A, Raza A, et al. Transferrin-copper nanocluster-doxorubicin nanoparticles as targeted theranostic cancer nanodrug. *ACS Appl Mater Interfaces*. 2018;10:3282–3294.
109. Tao Y, Ju E, Li Z, Ren J, Qu X. Engineered CpG-antigen conjugates protected gold nanoclusters as smart self-vaccines for enhanced immune response and cell imaging. *Adv Funct Mater*. 2014;24:1004–1010.
110. Mathew MS, Davis J, Joseph K. Green synthesis of a plant-derived protein protected copper quantum cluster for intrauterine device application. *Analyst (Cambridge, UK)*. 2018;143:3841–3849.
111. Peng J, Feng L-N, Zhang K, Li X-H, Jiang L-P, Zhu J-J. Calcium carbonate-gold nanoclusters hybrid spheres: synthesis and versatile application in immunoassays. *Chem. - Eur. J*. 2012;18:5261–5268 S5261/1-S5261/4.
112. Lystvet SM, Volden S, Singh G, et al. Anticancer activity from gold-α-lactalbumin nanoconstructs? *J Phys Chem C*. 2013;117:2230–2238.
113. Chen W-Y, Lin J-Y, Chen W-J, Luo L, Wei-Guang Diau E, Chen Y-C. Functional gold nanoclusters as antimicrobial agents for antibiotic-resistant bacteria. *Nanomedicine (London, UK)*. 2010;5:755–764.
114. Chan P-H, Wong S-Y, Lin S-H, Chen Y-C. Lysozyme-encapsulated gold nanocluster-based affinity mass spectrometry for pathogenic bacteria. *Rapid Commun Mass Spectrom*. 2013;27:2143–2148.
115. Tao Y, Lin Y, Huang Z, Ren J, Qu X. Incorporating graphene oxide and gold nanoclusters: a synergistic catalyst with surprisingly high peroxidase-like activity over a broad pH range and its application for cancer cell detection. *Adv Mater (Weinheim, Ger.)*. 2013;25:2594–2599.

CHAPTER

23

Atomically precise clusters: What next?

Thalappil Pradeep

Deepak Parekh Institute Chair Professor and Professor of Chemistry, Department of Chemistry, Indian Institute of Technology Madras, Chennai, India

Several aspects presented in previous pages make it clear that APCs are molecules. The categorization also captures the direction of growth this branch of science would invariably possess. Let us try to capture these directions under the following heads.

Variety: This suggests expansion of APCs along the chemical variety possible. One obvious direction is along the axes of increasing size and structural complexity, leading to new cluster systems. This path can only be infinite as clusters can be prepared with arbitrary nuclearity and complexity and are composed of different metals and ligands. However, beyond a particular cluster size, the properties are likely to be nearly identical and so, at some point in size, single component clusters will not offer many new possibilities in terms of structure and functions. However, there are numerous alloys and their arbitrary combinations. Thus, expanding the clusters from A_mL_n to $A_{m-x}B_xL_{n-y}M_y$, with or without charges, where A, B and L, M are metals and ligands, respectively, and further extending to multimetallic and multiligand combinations would present infinite possibilities.

Besides, these variations could present distinct structural varieties and each structure of the kind A_mL_n and $A_{m-x}B_xL_{n-y}M_y$ could present distinct building blocks. Thus, it is clear that compositional and structural explorations of these systems and methods to create them will be the preoccupation of several research groups.

A particularly new direction in variety is the creation of different types of solids as several A_mL_n clusters would be similar in the periphery, making it possible for them to crystallize together. This produces cocrystals of clusters.[1] This offers many possibilities as the building blocks expand. This expansion would make binary, ternary, and other cocrystals and also in each of them many stoichiometric combinations (X:Y) are possible, corresponding to the number of units of each cluster possible in the lattice of the cocrystal.

The variety naturally will expand to other APCs of oxides, chalcogenides, pnictides, and others. Recently, new properties are found in cluster crystals of $Cr_6Te_8L_6$, $Co_6E_8L_6$, and

DOI: https://doi.org/10.1016/B978-0-323-90879-5.00016-0

$Ni_9Te_6L_6$.[2–4] These APCs are an attractive set of building blocks for solid state materials like $[Cr_6Te_8L_6][C_{60}]_2$, $[Co_6E_8L_6][C_{60}]_2$, and $[Ni_9Te_6(PEt_3)_8][C_{60}]$ with exciting properties.[5] Some of these cluster systems are interesting in view of their magnetic and semiconducting characteristics. There are reports of $Re_6Se_8Cl_2$ showing superconductivity under 8 K and upper critical field exceeding 30 T, by the process of charge injection.[6] It is the first demonstration of superconductivity in a van der Waals superatomic crystal. These make APCs of such kinds new materials of study.

APCs of noble metals are increasingly made in proteins and DNA matrices. Although only a handful of these systems have been crystallized so far, it is clear that numerous such systems are likely. Coupled with properties such as near-infrared luminescence and water solubility they possess, along with stability and possibility of conjugation, along with biological activity, these new systems may be used for labeling and therapy. The current problem in the applicability of these systems is their lack of precision, although compositional precision has been established. There is a need to ensure structural precision in materials to understand properties and to establish the specific advantages of each APC.

Properties: The variety they present in molecular properties is another aspect. Besides the properties which make each one of these systems distinct, allowing them to be identified and characterized, it is also clear that unique properties are likely to be manifested in several of them due to their chemical, electronic, photophysical, magnetic, and other properties. It is likely that the capacity to make new cluster systems and to create millimeter sized cluster crystals of several of them will produce many new properties. These properties are likely to be centered around their unique catalytic, electrical transport, and magnetic properties. Suggestions of unusual charge transport and even superconductivity in clusters[6] and also magnetic ordering[7] in them will offer new possibilities. For example, room temperature ferromagnetism in such systems would produce renewed interest in molecular magnets.

Supramolecular aspects: As molecular science expands further, it is clear that the expanding boundaries will cross the limits of molecules. This is evident in conventional molecules and there is no reason why this will not expand to APCs. Initial signs of those expansions are available in the literature. However, the way such science has expanded into soft materials, supramolecular gels and related systems suggest that many properties are beginning to evolve in such areas using APCs. The capacity to use many soft chemistry techniques leading to functionalized cluster systems will limit the growth of these materials.

Current limitations: Understanding each of the aspects above would need unique capabilities in several areas as listed below.

Mass spectrometry: Analyzing compositions and structures of large clusters would need new capabilities in mass spectrometry. One important development would be the capability in analyzing masses in the megadalton range with reasonable resolution to ensure that compositions are exact. The current instrumental capabilities in the commercial space are not adequate to examine them routinely. While kilodalton mass spectrometry allows the study of clusters in the few hundred atom range, larger clusters in the several hundreds to thousands of atoms for heavier elements such as gold would require new mass spectrometric capabilities. Developments in charge detection mass spectrometry[8] would make such analysis very much possible.

Besides such analysis, it will also be necessary to study their dissociation and mobility as well. New methods of stable, intact ionization have to be developed. It will also be necessary to create methods to standardize the masses at very high mass ranges, especially in the negative ion mode, as most clusters are negative ions. While developments in mass spectrometry are promising, these methods have to be available to ensure that cluster science expands.

Computational capabilities: This will be a major limiting factor in evaluating the properties and understanding clusters in greater detail. As the number of atoms increase, computational complexities will expand further as well. This would need the development of new methods to treat such megaclusters effectively within the computational limitations, yet offering realistic matches with experiments. Developments in parameterization enabling such studies were discussed in Chapter 14.

Experimental limitations: As clusters become large, the problems that are faced by macromolecular science will become important here as well. These relate to the structural complexities and the many degrees of freedom available to them, which make these systems difficult to crystallize. This will limit the application of computational methods, as structure is an essential requirement to predict properties. The complexity will expand to crystallization, structure elucidation, realistic estimation of properties, and eventually to appreciate the data in detail.

Despite such limitations, the directions of this research appear to be exciting for many more years. Intense excitement and more research attracting greater number of researchers will happen when unique properties are discovered in cluster systems.

References

1. Bodiuzzaman M, Dar WA, Pradeep T. Cocrystals of atomically precise noble metal nanoclusters. *Small*. 2020;2003981:1–15.
2. Hessen B, Siegrist T, Palstra T, Tanzler SM, Steigerwald ML. $Cr_6Te_8(PEt_3)_6$ and a molecule-based synthesis of Cr_3Te_4. *Inorg Chem*. 1993;32:5165–5169.
3. Fenske D, Ohmer J, Hachgenei J, Merzweiler K. New transition metal clusters with ligands from main groups five and six. *Angew Chem Int Ed*. 1988;27:1277–1296.
4. Brennan JG, Siegrist T, Stuczynski SM, Steigerwald ML. The transition from molecules to solids: molecular syntheses of $Ni_9Te_6(PEt_3)_8$, $Ni_{20}Te_{18}(PEt_3)_{12}$, and NiTe. *J Am Chem Soc*. 1989;111:9240–9241.
5. Roy X, Lee C-H, Crowther AC, et al. Nanoscale atoms in solid-state chemistry. *Science*. 2013;341:157−160.
6. Telford EJ, Russell JC, Swann JR, et al. Doping-induced superconductivity in the van Der Waals superatomic crystal $Re_6Se_8Cl_2$. *Nano Lett*. 2020;20:1718–1724.
7. Lee CH, Liu L, Bejger C, et al. Ferromagnetic ordering in superatomic solids. *J Am Chem Soc*. 2014;136:16926–16931.
8. Keifer DZ, Pierson EE, Jarrold MF. Charge detection mass spectrometry: weighing heavier things. *Analyst*. 2017;142:1654–1671.

Appendix

TABLE 1 A summary of atomically precise nanoclusters synthesized so far (as on May 4, 2022, using web of science). Unprotected or naked clusters are not included. The list is alphabetical and in ascending order of nuclearity of clusters. Alloy clusters, listed separately, are arranged in ascending order of total nuclearity. For each nuclearity, an alphabetical order is followed.

Core	Ligand	Composition	Focus	Synthesis method	References
Ag_4	Se^iPr, 1,1-bis(diphenylphosphino) methane, SeEt,	$[Ag_4(Se^iPr)_4(dppm)_2]$	Characterization	Solution phase	1
Ag_8	1,1-bis(diphenylphosphino) propane	$[Ag_8(SeEt)_8(dppp)]$			
Ag_5	TePh, 1,1-bis(diphenylphosphino) ethane	$[Ag_5(TePh)_6(dppe)(Ph_2P(CH_2)_2PPh_3)]$	Characterization	Solution phase	2
Ag_7	2,3-Dimercaptosuccinic acid	$Ag_7(DMSA)_4$	Characterization	Solution phase	3
Ag_7	Mercaptosuccinic acid	$Ag_7(H_2MSA)_7$	Characterization	Interfacial method	4
Ag_8		$Ag_8(H_2MSA)_8$			
Ag_{1-9}	Naked clusters	Ag_{1-9} NCs	Spectroscopic study	Gas phase	5
Ag_9	Mercaptosuccinic acid	$Ag_9(H_2MSA)_7$	Characterization	Solid state route	6
Ag_9	1,2-Benzenedithiolate	$[Ag_9(1,2\text{-}BDT)_6]^{3-}$	Crystal structure	Solution phase	7
Ag_{9-15}	Glutathione	$Ag_{9\text{-}15}(SR)_{5\text{-}10}$	Crystal structure	Solution Phase	8
Ag_9	Diethylphenylphosphine, TePh,	$[Ag_9(TePh)_9(PEt_2Ph)_6]$	Characterization	Solution phase	9
Ag_{10}	Trimethylphosphine	$[Ag_{10}(TePh)_{10}(PMe_3)_2]$			
$Ag_{14}Te$		$[Ag_{14}Te(TePh)_{12}(PMe_3)_8]$			
Ag_{11}	Glutathione	$[Ag_{11}(SG)_7]$	Characterization	Solution phase	10
Ag_{12}	Tert-butylthiol, Trifluoroacetate	$Ag_{12}(TBT)_6(TFA)_6(pyz)_6].2CH_3CN$	Crystal structure	Solution phase	11
		$Ag_{12}S_2(TBT)_8(TFA)_4(bpy)_8].bpy$			
Ag_{12}	Metallothionein	Ag_{12}-MT	Luminescence	Solution phase	12
Ag_{14}	3,4-Difluoro-benzenethiol, Triphenylphosphine	$Ag_{14}(SC_6H_3F_2)_{12}(PPh_3)_8$	Crystal structure	Solution phase	13
Ag_{14}	Fluorobenzenethiol, Triphenylphosphine	$Ag_{14}(SC_6H_4X)_{12}(PPh_3)_8$ (X = F, Cl, Br)	Luminescence	Solution phase	14
Ag_{14}	N1, N2 -bis(pyridin-3-ylmethylene)cyclohexane-1,2-diamine	$[Ag_{14}(SPh(CF_3)_2)_{12}(PPh_3)_4(LR)_2]$	Crystal structure	Solution phase	15
$Ag_{14}Se$	SePh, 1,1-bis(diphenylphosphino) methane	$[Ag_{14}Se(SePh)_{12}(PR_3)_8]$	Characterization	Solution phase	16
$Ag_{14}S$	Triphenylphosphine	$[Ag_{14}S(SPh)_{12}(PPh_3)_8]$	Characterization	Solution phase	17
$Ag_{14}S$	Triphenylphosphine (HSC_6H_4CN)	$[Ag_{14}S(SC_6H_4CN)_{12}(PPh_3)_8]$	Characterization	Solution phase	18
		$[Ag_{23}S_2(SC_6H_4OSiMe_3)_{15}(SC_6H_4OH)_3(PPh_3)_8]$			
Ag_{15}	BVA	Ag_{15}@BVA	Characterization	Modified Xie method	19
Ag_{15}	1,6-Bis(diphenylphosphino) hexane,	$[Ag_{15}H_{13}(DPPH)_5]^{2+}$	Characterization	Solution phase	20
Ag_{27}	1,4-bis(diphenylphosphino) butane	$[Ag_{27}H_{22}(DPPB)_7]^{3+}$			
Ag_{15}	Glutathione	$Ag_{31}(SG)_{19}$	Characterization	Cyclic reduction method	21
Ag_{31}		$Ag_{15}(SG)_{11}$			
Ag_{16}	1,2-Bis(diphenylphosphino) ethane,	$Ag_{16}(DPPE)_4(SC_6H_3F_2)_{14}$	Crystal structure	Two-step solution phase	22
Ag_{32}	3,4-difluorothiophenol, 4-(trifluoromethyl)thiophenol	$[Ag_{32}(DPPE)_5(SC_6H_3F_2)_{24}]^{2-}$			

(*continued on next page*)

TABLE 1 A summary of atomically precise nanoclusters synthesized so far (as on May 4, 2022, using web of science). Unprotected or naked clusters are not included. The list is alphabetical and in ascending order of nuclearity of clusters. Alloy clusters, listed separately, are arranged in ascending order of total nuclearity. For each nuclearity, an alphabetical order is followed—cont'd

Core	Ligand	Composition	Focus	Synthesis method	References
Ag_{16}	Tert-butylthiol, Trifluoroacetate	$[Ag_{16}(TBT)_8(TFA)_7(CH_3CN)_3Cl]$	Crystal structure	Intercluster reaction	23
Ag_{17}		$[Ag_{17}(TBT)_8(TFA)_7(CH_3CN)_3Cl]$			
Ag_{17}	1-(Naphthalen-4-yl)ethyl)prop-2-yn-1-amine	$[Ag_{17}(NYA)_{12}]^{3+}$	Crystal structure	Solution phase	24
Ag_{18}	Triphenylphosphine,	$[Ag_{18}H_{16}(TPP)_{10}]^{2+}$	Characterization	Solution phase	25
Ag_{25}	1,2-bis(diphenylphosphino) ethane,	$[Ag_{25}H_{22}(DPPE)_8]^{3+}$			
Ag_{26}	Tris(4-fluorophenyl) phosphine	$[Ag_{26}H_{22}(TFPP)_{13}]^{2+}$			
Ag_{18}	1,1-Bis(diphenylphosphino) propane,	$[Ag_{18}Te(TePh)_{15}Cl(dppp)_3]$	Characterization	Solution phase	26
Ag_{38}	1,1-bis(diphenylphosphino) ethane	$[Ag_{38}Te_{13}(TetBu)_{12}(dppe)_3]$			
Ag_{19}	1,2-Bis(diphenylphosphino) methane, phenylacetylene	$[Ag_{19}(dppm)_3(PhC{\equiv}C)_{14}](SbF_6)_3$	Crystal structure	Solution phase	27
Ag_{20}	Dithiophosphate	$[Ag_{20}[S_2P(O^iPr)_2]_{12}]$	Crystal structure	Solution phase	28
Ag_{21}	Dithiophosphate	$[Ag_{21}[S_2P(O^iPr)_2]_{12}]^+$	Crystal structure	Solution phase	29
Ag_{21}	*p-tert*-butylthiacalix[4]arene (H_4BTCA), 1-ethylnyl-3,5-dimethoxybenzene	$[Ag_{21}\text{-}(H_2BTCA)_3(O_2PPh_2)_6]SbF_6$ $[Ag_{21}(C{\equiv}CC_6H_3{-}3,5\text{-}R_2)6{-}(O_2PPh_2)_{10}]SbF_6$	Crystal structure	Solution phase	30
Ag_{21}	9-SH meta-carboranethiol	$[Ag_{21}(MCT)_{12}(TPP)_2]^+$	Crystal structure	Solution phase	31
Ag_{22}	1,2-Bis(diphenylphosphino) ethane, 2,5-Dimethylbenzenethiol	$Ag_{22}(dppe)_4(2,5\text{-}DMBT)_{12}Cl_4]^{2+}$	Crystal structure	Solution phase	32
Ag_{22}	Thiophenol	$[Ag_{22}(SPh)_{10}Cl(O_2CPh)_{11}(dmf)_3]$	Characterization	Solution phase	33
Ag_{23}	Phenylethanethiol, Triphenylphosphine	$Ag_{23}(PPh_3)_8(SC_2H_4Ph)_{18}$	Crystal structure	Solution phase	34
Ag_{24}	Tert-butylthiol, Proline	$Ag_{24}(S^tBu)_{10}(L/D{-}proline)_8(NO_3)_4(H_2O)$	Luminescence	Solution phase	35
Ag_{25}	Dimethylbenzenethiol	$Ag_{25}(DMBT)_{18}(PPh_4)^+$	Crystal structure	Solution phase	36
Ag_{27}	Tert-butylthiol	$[Ag_{27}S_2(^tBuS)_{14}]$	Crystal structure	Solution phase	37
$Ag_{28}Se_6$	1,1-Bis(diphenylphosphino) propane	$[Ag_{28}Se_6(SenBu)_{16}(dppp)_4]$	Characterization	Solution phase	38
Ag_{29}	1,3-Benzenedithiol	$Ag_{29}(BDT)_{12}(TPP)_4$	Crystal structure	Solution phase	39
Ag_{29}	1,3-Benzenedithiol, Fullerene	$[Ag_{29}(BDT)_{12}(C_{60})_n]^{3-}$	Characterization	Solution phase	40
Ag_{29}	Dihydrolipoic acid, 1,3-Benzenedithiol	$Ag_{29}(BDT)_{12-x}(DHLA)_x$ $(x=1{-}6)$	Characterization	Solution phase	41
Ag_{29}	1,3-Benzenedithiol, 1,2-bis(diphenylphosphino) alkane	$Ag_{29}(BDT)_{12}(P)_4$ (P = dppm, dppe, dppp)	Crystal structure	Solution phase	42
Ag_{29}	Lipoic acid	$Ag_{29}(LA)_{19}$	Characterization	Solution phase	43
Ag_{30}	Captopril	$Ag_{30}(Capt)_{18}$	Characterization	Solution phase	44
$Ag_{30}Te_9$	1,1-Bis(diphenylphosphino) ethane, TePh,	$[Ag_{30}Te_9(TePh)_{12}(PEt_3)_{12}]$	Characterization	Solution phase	45
$Ag_{46}Te_{17}$	TeMes	$[Ag_{46}Te_{17}(TeMes)_{12}(PEt_3)_{16}]$			
$Ag_{30}Se_8$	1,1-Bis(diphenylphosphino) ethane, Se^tBu	$[Ag_{30}Se_8(Se^tBu)_{14}(PnPr_3)_8]$	Characterization	Solution phase	46
$Ag_{90}Se_{38}$		$[Ag_{90}Se_{38}(Se^tBu)_{14}(PEt_3)_{22}]$			
Ag_{31}	Glutathione	$Ag_{31}(SG)_{19}$	Characterization	Solution phase	47
Ag_{15}		$Ag_{15}(SG)_{11}$			
Ag_{32}	Glutathione	$Ag_{32}(SG)_{19}$	Characterization	Solution phase	48
Ag_{32}	N-(2-mercaptopropionyl)glycine	$Ag_{32}(SG)_{19}$	NMR	Solid state route	49
	Glutathione	$Ag_{32}(MPG)_{19}$			
Ag_{33}	Phenylethanethiol, Tert-butylthiol, Triphenylphosphine	$Ag_{33}(SCH_2CH_2Ph)_{24}(PPh_3)_4$ $Ag_{33}S_3(StBu)_{16}(CF_3COO)_9{-}(NO_3)(CH_3CN)_2](NO_3)$	Crystal structure	Solution phase	50
Ag_{34}	3,3-Dimethyl-1-butyne, 4-tert-butylthiacalix[4] arene	$[Ag_{34}(TCA)_3(C{\equiv}CH)_9(tfa)_4]^+$	Crystal structure	Solution phase	51
Ag_{34}	4-tert-butylbenzyl mercaptan (BBSH)	$Ag_{34}S_3SBB_{20}(CF_3COO)_6{}^{2+}$	Characterization	Solution phase	52
Ag_{35}	3,3-Dimethyl-1-butyne, 4-tert-butylthiacalix[4]arene	$[Ag_{35}(H_2L)_2(L)(C{\equiv}CBut)_{16}]^{3+}$	Crystal structure	Solution phase	53
Ag_{37}	Trifluoroacetate, Tert-butylbenzenethiol	$[Ag_{37}S_4(SC_6H_4\ tBu)_{24}(CF_3COO)_6(H_2O)_{12}]^-$	Crystal structure	Solution phase	54

(*continued on next page*)

TABLE 1 A summary of atomically precise nanoclusters synthesized so far (as on May 4, 2022, using web of science). Unprotected or naked clusters are not included. The list is alphabetical and in ascending order of nuclearity of clusters. Alloy clusters, listed separately, are arranged in ascending order of total nuclearity. For each nuclearity, an alphabetical order is followed—cont'd

Core	Ligand	Composition	Focus	Synthesis method	References
Ag_{38}	Difluorobenzenethiol	$[Ag_{38}(SPhF_2)_{26}(PR'_3)_8]$	Crystal structure	Solution phase	55
Ag_{39}	Pentafluorobenzenethiol, Triphenylphosphine	$[Ag_{39}(PFBT)_{24}(TPP)_8]^{2-}$	Crystal structure	Solution Phase	56
Ag_{40}	2,4-Dimethylbenzenethiol	$[Ag_{40}(2,4\text{-}DMBT)_{24}(PPh_3)_8]$	Crystal structure	Solution phase	57
Ag_{40}	Dimethylbenzenethiol, Triphenylphosphine	$[Ag_{40}(SPhMe_2)_{24}(PPh_3)_8](NO_3)_2$	Crystal structure	Solution phase	58
Ag_{46}		$[Ag_{46}(SPhMe_2)_{24}(PPh_3)_8](NO_3)_2$			
Ag_{42}	o-Carborane-1,2-dithiol, Triphenylphosphine	$[Ag_{42}(CBDT)_{15}(TPP)_4]^{2-}$	Crystal structure	Solution phase	59
Ag_{44}	4-Fluorothiophenol or 2-naphthalenethiol	$[Ag_{44}(SR)_{30}]^{4-}$	Characterization	Multiple temperature controlled process	60
Ag_{44}	5-Mercapto-2-nitrobenzoic acid	$[Ag_{44}(MNBA)_{30}]^{4-}$	Scalable synthesis	One pot solution phase	61
Ag_{44}	5-Mercapto-2-nitrobenzoic acid	$[Ag_{44}(MNBA)_{30}]^{4-}$	Surface modification	One pot solution phase	62
Ag_{44}	3,4-Difluorothiophenol, 4-(trifluoromethyl)thiophenol, 4-flurothiophenol	$[Ag_{44}(SR)_{30}]^{4-}$	Crystal structure	One step solution phase	63
Ag_{44}	4-Mercaptobenzoic acid	$Na_4Ag_{44}(MBA)_{30}$	Crystal structure	Three step solution phase	64
Ag_{44}	2-Ethylbenzenethiolate, Triphenylphosphine	$Ag_{44}(EBT)_{26}(TPP)_4$	Crystal structure	Solution phase	65
Ag_{44}	Benzeneselenol	$[Ag_{44}(SePh)_{30}]^{4-}$	Characterization	Solid state route	66
Ag_{44}	Benzeneselenol	$[Ag_{44}(SePh)_{30}]^{4-}$	Reversibility	Solution phase	67
Ag_{44}	4-Mercaptobenzoic acid	$M_4Ag_{44}(MBA)_{30}$	Stability and optical properties	Three-step solution phase	68
Ag_{44}	4-Mercaptobenzoic acid	$M_4Ag_{44}(MBA)_{30}$	Orthogonal assembly of Ag_{44}-TeNW composite	Three-step solution phase	69
Ag_{44}	4-Mercaptobenzoic acid	$M_4Ag_{44}(MBA)_{30}$	Janus cluster	Three step solution phase	70
Ag_{44}	3,4-Difluorobenzenethiolate	$[Ag_{44}(SC_6H_3F_2)_{30}]^{4-}$	DFT analysis	Solution phase	71
Ag_{44}	4-Fluorothiophenol, Glutathione	$Ag_{44}(4\text{-}FTP)_{30}$, $Ag_{35}(SG)_{18}$	Ligand exchange	Solid state route	72
Ag_{35}					
Ag_{40}	4-tert-butylbenzylmercaptan	$Ag_{40}(C_6H_5COO)_{13}(SR)_{19}(CH_3CN)$	Crystal structure	Solution phase	73
Ag_{45}		$Ag_{45}(C_6H_5COO)_{13}(SR)_{22}Cl_2$			
Ag_{46}	Dimethylbenzenethiol	$[Ag_{46}S_7(SPhMe_2)_{24}]NO_3$	Characterization	Solution phase	74
Ag_{47}	3,3-Dimethyl-1-butyne, L-/D-valine, L-/D-isoleucine	$[Ag_{47}L_{12}(C{\equiv}C^tBu)_{16}]BF_4$	Crystal structure	Solution phase	75
Ag_{48}	3,3-Dimethyl-1-butyne	$[Ag_{48}(C{\equiv}C^tBu)_{20}(CrO_4)_7]$	Characterization	Solution phase	76
Ag_{48}	1,2-Bis(diphenylphosphino) propane, 1-adamantanethiol	$Ag_{48}Cl_{14}(S\text{-}Adm)_{26}(S\text{-}c\text{-}C_6H_{11})_4$,	Characterization	Solution phase	77
Ag_{50}		$Ag_{50}C_{116}(S\text{-}Adm)_{28}(dppp)_2$			
Ag_{50}	1,2-Bis(diphenylphosphino) methane	$Ag_{50}(dppm)_6(SR)_{30}$	Characterization	Solution phase	78
Ag_{55}	4-Tert-butylbenzyl mercaptan, Phenylethanethiol	$Ag_{55}(BBS)_{31}$, $Ag_{55}(PET)_{31}$	Characterization	Solid state route	79
Ag_{58}	Trifluoroacetic acid, $_i$PrC$_6$H$_4$SH	$Ag_{58}(_iPrC_6H_4S)_{40}(CF_3COO)_6(H_2O)_{10}$	Crystal structure	Solution phase	80
Ag_{59}	2,5-Dichlorobenzenethiol	$[Ag_{59}(2,5\text{-}DCBT)_{32}]^{3-}$	Characterization	Solution phase	81
Ag_{60}	Tert-butylthiol	$[Ag_{60}(^tBuS)_{20}(o\text{-}CH_3OPhCOO)_{16}(H_2O)_4(Cl)_2]$	Crystal structure	Solution phase	82
Ag_{61}	Dipyridylamine	$Ag_{61}(dpa)_{27}(SbF_6)_4$	Crystal structure	Solution phase	83
Ag_{62}	Tert-butylthiol	$[Ag_{62}S_{13}(^tSBu)_{32}](BF_4)_4$	Crystal structure	Solution phase	84

(*continued on next page*)

TABLE 1 A summary of atomically precise nanoclusters synthesized so far (as on May 4, 2022, using web of science). Unprotected or naked clusters are not included. The list is alphabetical and in ascending order of nuclearity of clusters. Alloy clusters, listed separately, are arranged in ascending order of total nuclearity. For each nuclearity, an alphabetical order is followed—cont'd

Core	Ligand	Composition	Focus	Synthesis method	References
Ag_{64}	Tributylphosphine	$Ag_{64}(PnBu_3)_{16}Cl_6$	Crystal structure	Solution phase	85
$Ag_{65}S_{13}$	1,1-Bis(diphenylphosphino) methane, $SC_6H_4NMe_2$	$[Ag_{65}S_{13}(SC_6H_4NMe_2)_{28}(dppm)_5]$	Characterization	Solution phase	86
Ag_{67}	2,4-Dimethylbenzenethiol, Triphenylphosphine	$[Ag_{67}(SPhMe_2)_{32}(PPh_3)_8]^{3+}$	Crystal structure	Solution phase	87
Ag_{68}	4-Tert-butylbenzylmercaptan	$Ag_{68}(SBB)_{34}$	Characterization	Miscibility principle	88
$Ag_{70}S_{16}$	Thiophenol	$[Ag_{70}S_{16}(SPh)_{34}(O_2CPh)_4(triphos)_4]$	Characterization	Solution phase	89
$Ag_{70}S_{20}$	1,1-Bis(diphenylphosphino) methane	$[Ag_{70}S_{20}(SPh)_{28}(dppm)_{10}](O_2CCF_3)_2$	Characterization	Solution phase	90
Ag_{71}	1,2-Bis-(diphenylphosphino) methane, tert-butylthiol	$[Ag_{71}(S\text{-}Bu)_{31}(dppm)](SbF_6)_2$	Crystal structure	Solution phase	91
Ag_{74}	Phenylacetylene	$Ag_{74}(C{\equiv}CPh)_{44}$	Characterization	Solution phase	92
Ag_{75}	Glutathione	$Ag_{75}(SG)_{40}$	Characterization	Solution phase	93
$Ag_{76}Se_{13}$	Triphenylphosphine	$[Ag_{76}Se_{13}(SC_6H_4NMe_2)_{50}(PPh_3)_5]$	Characterization	Solution phase	94
$Ag_{88}Se_{12}$		$[Ag_{88}Se_{12}(SC_6H_4NMe_2)_{63}(PPh_3)_6]$			
Ag_{78}	1,2-Bis-(diphenylphosphino) methane	$[Ag_{78}(^{i}PrPhS)_{30}(dppm)_{10}Cl_{10}]^{4+}$	Crystal structure	Solution phase	95
Ag_{84}	Isopropylthiol	$[Ag_{84}S_2(^{i}PrS)_{40}(^{n}PrCOO)_{18}]$	Crystal structure	Solution phase	96
Ag_{88}	p-tert-butylthiacalix[4]arene (H_4TC4A)	$Ag_{88}(TC4A)_8(EtS)_{32}(OAc)_8(CH_3CN)$	Crystal structure	Solvothermal reaction	97
Ag_{90}	Tert-butylthiol	$Ag_{90}(^{t}BuS)_{24}(PhPO_3)_{18}$	Crystal structure	Solution phase	98
Ag_{94}	1-Adamantanethiol,	$[Ag_{94}S_{34}(SAd)_{26}(dpppt)_6]$	Crystal structure	Solution phase	99
Ag_{58}	Furan-2-ylmethanethiol	$[Ag_{58}S_{13}(SAd)_{32}]$			
Ag_{190}		$[Ag_{190}S_{58}(SCH_2Fur)_{74}(dpppt)_8]$			
Ag_{112}	3,5-$(CF_3)_2$PhC≡CH	$[Ag_{112}Cl_6(3,5\text{-}(CF_3)_2PhC{\equiv}C)_{51}]^{3-}$	Crystal structure	Direct reduction	100
$Ag_{112}Se_{32}$	1,1-Bis(diphenylphosphino) propane, ($Se^{n}Bu$)	$[Ag_{112}Se_{32}(Se^{n}Bu)_{48}(PtBu_3)_{12}]$	Characterization	Solution phase	101
$Ag_{114}Se_{34}$		$[Ag_{114}Se_{34}(Se^{n}Bu)_{46}(PtBu_3)_{14}]$			
$Ag_{172}Se_{40}$		$[Ag_{172}Se_{40}(Se^{n}Bu)_{92}(dppp)_4]$			
$Ag_{123}S_{35}$	tert-butyl thiol	$[Ag_{123}S_{35}(StBu)_{50}]$	Characterization	Solution phase	102
$Ag_{124}Se_{57}$	tert-butyl thiol	$[Ag_{124}Se_{57}(SePtBu_2)_4Cl_6(tBu_2P(CH_2)_3PtBu_2)_{12}]$	Characterization	Solution phase	103
Ag_{136}	4-tert-butylbenzenethiolate	$[Ag_{136}(SR)_{64}Cl_3Ag_{0.45}]^{-}$	Crystal structure	Two-step solution phase	104
Ag_{374}		$[Ag_{374}(SR)_{113}Br_2Cl_2]$			
Ag_{140}	4-tert-butylbenzyl mercaptan	$Ag_{140}BBT_{53}$	Characterization	Brust method	105
Ag_{146}	4-Isopropylbenzenethiolate	$Ag_{146}Br_2(SR)_{80}$	Characterization	Solution phase	106
Ag_{152}	Phenylethanethiol	$Ag_{152}(SCH_2CH_2Ph)_{60}$	Characterization	Solid state route	107
Ag_{152}	Phenylethanethiol	$Ag_{152}(SCH_2CH_2Ph)_{60}$	SERS	Solid state route	108
$Ag_{188}S_{94}$	tert-butyl thiol	$[Ag_{188}S_{94}(PnPr_3)_{20}]$	Characterization	Solution phase	109
Ag_{210}	^{i}PrPhSH	$Ag_{210}(^{i}PrPhS)_{71}(Ph_3P)_5Cl$	Crystal structure	Solution phase	110
Ag_{211}	Triphenylphosphin	$Ag_{211}(^{i}PrPhS)_{71}(Ph_3P)_6Cl$			
$Ag_{262}S_{100}$	Tert-butyl thiol	$[Ag_{262}S_{100}(StBu)_{62}(dppb)_6]$	Characterization	Solution phase	111
Ag_{280}	4-(tert-butyl)benzyl mercaptan	$\sim Ag_{280}(SBB)_{120}$	Characterization	Brust method	112
Ag_{307}	$SPh^{t}Bu$	$[Ag_{307}Cl_{62}(SPh^{t}Bu)_{110}]$	Crystal structure	Solution phase	113
$Ag_{344}S_{124}$	Tert-butyl thiol	$[Ag_{344}S_{124}(S^{t}Bu)_{96}]$	Characterization	Solution phase	114
$Ag_{320}S_{130}$	1,1-Bis(diphenylphosphino) propane, tert-butyl thiol	$[Ag_{320}S_{130}(S^{t}Bu)_{60}(dppp)_{12}]$	Characterization	Solution phase	115
$Ag_{352}S_{128}$		$[Ag_{352}S_{128}(S^{t}C_5H_{11})]$			
$Ag_{490}S_{188}$		$[Ag_{490}S_{188}(S^{t}C_5H_{11})_{114}]$			
Au_2	Bis(diphenylphosphino)methane	$[Au_2(Ph_2P)_2CH]_2$	Crystal structure	Solution phase	116

(*continued on next page*)

TABLE 1 A summary of atomically precise nanoclusters synthesized so far (as on May 4, 2022, using web of science). Unprotected or naked clusters are not included. The list is alphabetical and in ascending order of nuclearity of clusters. Alloy clusters, listed separately, are arranged in ascending order of total nuclearity. For each nuclearity, an alphabetical order is followed—cont'd

Core	Ligand	Composition	Focus	Synthesis method	References
Au_2	Triphenylphosphine	$[Au_2(Ph_3P)_2]$	DFT study	Solution phase	117
Au_4	Triphenylphosphine	$[Au_4(PPh_3)_4(\mu\text{-}2\text{-}SnCl_3)_2]$	Crystal structure	Solution phase	118
Au_4	Triphenylphosphine, iodide	$[Au_4(\mu\text{-}I)_2(PPh_3)_4]$	Crystal structure	Solution phase	119
Au_5	1,2-Bis(diphenylphosphino) methane, nitrate	$[Au_5(dppmH)_3(dppm)](NO_3)_2$	Crystal structure	Solution phase	120
Au_5	Triphenylphosphine	$[Au_5(PPh_3)_5]^+$	Characterization	Solution phase	121
Au_{12}		$[Au_{12}(PPh_3)_9HCl]^{2+}$			
Au_{15}		$[Au_{15}(PPh_3)_9Cl]^{2+}$			
Au_{16}		$[Au_{16}(PPh_3)_{10}Cl_2]^{2+}$			
Au_{17}		$[Au_{17}(PPh_3)_{11}]^{3+}$			
Au_5	1,2-Bis(diphenylphosphino) methane	$[Au_5(DPPMH)_3(DPPM)](NO_3)_2$	Crystal structure	Solution phase	122
Au_{13}		$[Au_{13}(DPPMH)_6](NO_3)N$			
Au_6	Triphenylphosphine, nitrate	$[Au_6(PPh_3)_6]\ (NO_3)_2{\cdot}3CH_2Cl_2$	Crystal structure	Solution phase	123,124
Au_6	1,3-Bis(diphenylphosphino) propane	$[Au_6(dppp)_4]^{2+}\ [Au_{11}(dppp)_5]^{3+}$	Characterization	Magnetron sputtering method	125
Au_{11}					
Au_6	N-heterocyclic carbene	$[Au_6(NHC\text{-}S)_4]^{2+}$	DFT analysis	Solution phase	126
Au_6	Biotin	$Au_6(S\text{-}PEG_{70}\text{-}biotin)_6$	Characterization	Solution phase	127
Au_7		$Au_7(S\text{-}PEG_{70}\text{-}biotin)_7$			
Au_{10}		$Au_{10}(S\text{-}PEG_{70}\text{-}biotin)_{10}$			
Au_7	Triphenylphosphine	$[Au_7(PPh_3)_7]^+$	Crystal structure	Solution phase	128
Au_8	Triphenylphosphine	$[Au_8(PPh_3)_8](PF_6)_2$	Crystal structure	Solution phase	129
Au_8	Triphenylphosphine	$[Au_8(PPh_3)_8](NO_3)_2$	Crystal structure	Solution phase	130
Au_9	Tris(-p-methylphenyl)phosphine	$[Au_9(P(C_6H_4\text{-}p\text{-}Me)_3)_8]\ [PF_6]_3$	Crystal structure	Solution phase	131
Au_9	Tris(-p-methylphenyl)phosphine	$[Au_9(P(C_6H_4\text{-}p\text{-}Me)_3)_8]\ [BF_4]_3$	Crystal structure	Solution phase	132
Au_9	Triphenylphosphine	$[Au_9(PPh_3)_8]X_3\ (X = NO_3^-, ClO_4^-)$	Magnetic circular dichroism	Solution phase	133
Au_9	Triphenylphosphine	$[Au_9(PPh_3)_8]^{3+}$	Reactivity of cluster	Solution phase	134
Au_8		$[Au_8(PPh_3)_7]^{2+}$			
Au_9	Dibenzimidazolium salt	$[Au_9(NHC)_4Br]Br_2$	Crystal structure	Solution phase	135
Au_{10}		$[Au_{10}(NHC)_4Br_2](O_2CCF_3)_2$			
Au_{10}	Dicyclohexylphenylphosphine, chloride	$[Au_{10}Cl_3(PCy_2Ph)_6](NO_3)$	Crystal structure	Solution phase	136
Au_{10}	Triphenylphosphine	$[Au_{10}(PPh_3)_7(S_2C_2(CN)_2)_2]$	Crystal structure	Solution phase	137
Au_{10}	Pentafluorobenzenethiol	$[Au_{10}(C_6F_5)_4(PPh_3)_5]$	Crystal structure	Solution phase	138
	Triphenylphosphine				
Au_{10}	1,3-di(2,4,6-trimethylbenzyl)benzimidazolium halide	$[Au_{10}(^{MesCH2}Bimy)_6X_3]$ (X = Cl, Br, I)	Crystal structure	Solution phase	139
Au_{25}		$[Au_{25}(^{MesCH2}Bimy)_{10}Br_8$			
Au_{11}	Triphenylphosphine	$Au_{11}(PPh_3)_{10}(SCN)_3$	Crystal structure	Solution phase	140
Au_{11}	Tris(-p-chlorophenyl)phosphine, Iodide	$Au_{11}I_3[P(C_6H_4\text{-}p\text{-}Cl)_3]_7$	Crystal structure	Solution phase	141
Au_{11}	Tris(-p-fluorophenyl)phosphine, iodide	$Au_{11}I_3[P(C_6H_4\text{-}p\text{-}F)_3]_7$	Crystal structure	Solution phase	142
Au_{11}	3-Mercaptopropionic acid	$Au_{11}(SCH_2CH_2COOH)_7(TOA)_7$	Luminescence	Brust method	143
Au_{11}	3-Mercaptopropionic acid	$Au_{11}(SCH_2CH_2COO\text{-})_7(TOA)_7$	Thermal stability	Brust method	144
Au_{11}	Triphenylphosphine, Chloride	$Au_{11}(PPh_3)_7Cl_3$	Spectral diffusion in STM	Hutchison method	145
Au_{11}	DPEphos, Xantphos	$[Au_{11}(DPEphos)_4Cl_2]Cl$ $[Au_{11}(Xantphos)_4Cl_2]Cl$	Characterization	Solution phase	146

(*continued on next page*)

TABLE 1 A summary of atomically precise nanoclusters synthesized so far (as on May 4, 2022, using web of science). Unprotected or naked clusters are not included. The list is alphabetical and in ascending order of nuclearity of clusters. Alloy clusters, listed separately, are arranged in ascending order of total nuclearity. For each nuclearity, an alphabetical order is followed—cont'd

Core	Ligand	Composition	Focus	Synthesis method	References
Au_{11}	Diphosphine	$[Au_{11}(DP)_4L_2]^+$	Characterization	Solution phase	147
Au_{13}	Dimethylphenylphosphine	$[Au_{13}(PMe_2Ph)_{10}Cl_2](PF_6)_3$	Crystal structure	Solution phase	148
Au_{13}	1,2-Bis(diphenylphosphino) ethane, Chloride	$[Au_{13}(dppe)_5Cl_2]Cl_3$	Crystal structure	Solution phase	149
Au_{13}	Triphenylphosphine, 4-mercaptobenzoic acid	$Au_{13}(PPh_3)_8(p\text{-}MBA)_3$	DFT analysis	Solution phase	150
Au_{13}	1,3-Disubstituted benzimidazolium chloride (NHC)	$[Au_{13}(NHC)_{10}Cl_2]^{3+}$	Crystal structure	Solution phase	151
Au_{13}	1,3-Disubstituted benzimidazolium chloride (NHC)	$[Au_{13}(NHC)_5Cl_2]Cl_3$	Crystal structure	Solution phase	152
Au_{14}	Triphenylphosphine, Nitrate	$[Au_{14}(PPh_3)_8(NO_3)_4]$	Crystal structure	Solution phase	153
Au_n(n = 10, 15, 18, 22, 25, 29, 33, 39)	Glutathione	$Au_{10}(SG)_{10}$, $Au_{15}(SG)_{13}$, $Au_{18}(SG)_{14}$, $Au_{22}(SG)_{16}$, $Au_{22}(SG)_{17}$, $Au_{25}(SG)_{18}$, $Au_{29}(SG)_{20}$, $Au_{33}(SG)_{22}$, $Au_{39}(SG)_{24}$	Characterization	Solution phase	154
Au_{15}	Glutathione, Cyclodextrin	Au_{15}@CD	Characterization	Solution phase	155
Au_{15}	Glutathione	$Au_{15}(SG)_{13}$	Luminescence probing	Solution phase	156
Au_{15} Au_{18}	Glutathione	$Au_{15}(SG)_{13}$ $Au_{18}(SG)_{14}$	Characterization	Two-phase solution phase	157
Au_{16}	1-Adamantanethiol	$Au_{16}(S\text{-}Adm)_{12}$	Crystal structure	Solution phase	158
Au_{18}	Glutathione	$Au_{18}(SG)_{14}$	Characterization	Solution phase	159
Au_{18}	Cyclohexanethiol	$Au_{18}(SC_6H_{11})_{14}$	Crystal structure	Two-phase ligand exchange	160
Au_{18}	2,4,6-Triisopropylbenzylmercaptan	$Au_{18}S_2\text{-}(STipb)_{12}$	Crystal structure	Solution phase	161
Au_{18}	$HSC_2H_4CO_2H$	$Au_{18}(SC_2H_4CO_2H)_{14}$	Characterization	One pot synthesis	162
Au_{19}	N,N-bis(diphenylphosphino)amine), Phenylacetylene	$[Au_{19}(PhC{\equiv}C)_9(Hdppa)_3](SbF_6)_2$	Crystal structure	Solution phase	163
Au_{19}	Phenylethanethiol	$Au_{19}(SC_2H_4Ph)_{13}$	Characterization	Solution phase	164
Au_{20}	Phenylethanethiol	$Au_{20}(SCH_2CH_2Ph)_{16}$	Characterization	Brust method	165
Au_{20}	Tert-butylbenzenethiol	$Au_{20}(TBBT)_{16}$	Crystal structure	Ligand exchange	166
Au_{20}	Triphenylphosphine	$[Au_{20}(PPh_3)_4]$	Crystal structure	Solution phase	167
Au_{20}	Tris(2-(diphenylphosphino) ethyl)phosphine	$[Au_{20}(PP_3)_4]Cl_4$	Crystal structure	Two-step solution phase	168
Au_{20}	Tris(2-(diphenylphosphino)ethyl)phosphine	$[Au_{20}(PP_3)_4]Cl_4$	Hyperpolarizability	Two-step solution phase	169
Au_{21}	Adamantanethiol	$Au_{21}(S\text{-}Adm)_{15}$	Crystal structure	Two-step solution phase	170
Au_{22}	Glutathione, porphyrin	$Au_{22}[(SG)_{15}(SAOPPTH_2)_2]$	Characterization	Three step solution phase	171
Au_{22}	1,8-Bis-(diphenylphosphino)octane	$Au_{22}(L)_6$	Crystal structure	Solution phase	172
Au_{22}	Glutathione	$Au_{22}(SG)_{18}$	Characterization	COdirected	173
Au_{22}	3-Ethynylthiophene, Phenylacetylene, 3-ethynyltoluene, 3-ethynylanisole	$Au_{22}(C{\equiv}CPh)_{18}$	Crystal structure	Solution phase	174
Au_{23}	Glutathione	$Au_{23}(SG)_{18}$	NIR emission	Two-step solution phase	175
Au_{23}	Cyclohexanethiol	$[Au_{23}(SC_6H_{11})_{16}]^-$	Crystal structure	Solution phase	176
Au_{23}	3,3-Dimethyl-1-butyne	$Au_{23}(C{\equiv}CtBu)_{15}$	Crystal structure	Direct reduction method	177
Au_{23}	Phenylethanethiol, 4-*tert*-butylbenzenethiol	$Au_{23}(SPh^tBu)_{17}$	Characterization	Solution phase	178
Au_{24}	Phenylethanethiol, Triphenylphosphine	$[Au_{24}(PPh_3)_{10}(SC_2H_4Ph)_5X_2]^+$	Crystal structure	Modified Brust method	179

(*continued on next page*)

TABLE 1 A summary of atomically precise nanoclusters synthesized so far (as on May 4, 2022, using web of science). Unprotected or naked clusters are not included. The list is alphabetical and in ascending order of nuclearity of clusters. Alloy clusters, listed separately, are arranged in ascending order of total nuclearity. For each nuclearity, an alphabetical order is followed—cont'd

Core	Ligand	Composition	Focus	Synthesis method	References
Au_{24}	Benzeneselenol	$Au_{24}(SePh)_{20}$	Crystal structure	Modified Brust method	180
Au_{24}	Adamantanethiol	$Au_{24}(SAdm)_{16}$	Crystal structure	Three step solution phase	181
Au_{24}	Polyvinyl 2-pyrrolidone (PVP)	$Au_{24}Cl_x$ ($x = 0$–3)	Characterization	Solution phase	182
Au_{25}	Glutathione	$Au_{25}(SG)_{18}$	Solid state emission	Three step solution phase	183
Au_{25}	Glutathione	$Au_{25}(SG)_{18}$	Ligand etching	Two-step solution phase	184
Au_{25}	Glutathione	$Au_{25}(SG)_{18}$	Phase transfer	Two-step solution phase	185
Au_{25}	(*R*)-5,5′,6,6′,7,7′,8,8′-octafluoro-[1,1′-binaphthalene]-2,2′-dithiol	$Au_{25}(R\text{-}BINAS)_{18}$	Stereo-electronic effects	Solution phase	186
Au_{25}	Glutathione	$Au_{25}(SG)_{18}$	Silica embedding	Two-step solution phase	187
Au_{25}	$PPh_3/C_nH_{(2n+1)}SH$	$Au_{25}(PPh_3)_{10}(SC_nH_{2n+1})_5Cl_2^{2+}$	Crystal structure	Hutchison method	188
Au_{25}	Phenylethanethiol	$Au_{25}(SCH_2CH_2Ph)_{18}$	CO oxidation	Two-step solution phase	189
Au_{25}	Phenylethanethiol	$Au_{25}(SCH_2CH_2Ph)_{18}^{-}$	Air oxidation	Two-step solution phase	190
Au_{25}	Phenylethanethiol	$Au_{25}(SCH_2CH_2Ph)_{18}$	Crystal structure	Solution phase	191
Au_{25}	Phenylethanethiol	$[N(C_8H_{17})_4][Au_{25}(SCH_2CH_2Ph)_{18}]$	Crystal structure	Brust method	192
Au_{25}	Phenylethanethiol	$[Au_{25}(PET)_{18}(O_2)_n]^{-}$	Mass spectrometry	Solution phase	193
Au_{25}	Hexanethiol/Pyr-SH	$Au_{25}(C_6S)_{17}PyS$	Electron transfer	Brust method	194
Au_{25}	Phenylethanethiol	$Au_{25}(SCH_2CH_2Ph)_{18}$	NMR	Brust method	195
Au_{25}	Phenylethanethiol	$Au_{25}(SCH_2CH_2Ph)_{18}$	Electrochemical sensing	Brust method	196
Au_{25}	Hexanethiol	$Au_{25}(SC_6H_{13})_{18}$	Electrochemistry	Brust method	197
Au_{25}	Glutathione	$[Au_{25}(SG)_{18}\text{-}6H]^{7-}$	Electron emission	Solution phase	198
Au_{25}	Phenylethanethiol	$[Au_{25}(SCH_2CH_2Ph)_{18}]^{0/1-}$	Electron self-exchange dynamics	Modified Brust method	199
Au_{25}	Dodecanethiol	$Au_{25}(SC_{12}H_{25})_{18}$	Alcohol oxidation	Brust method	200
Au_{25}	Glutathione	$Au_{25}(SG)_{18}$	Core etching	Solution phase	201
Au_{25}	Phenylethanethiol	$Au_{25}(SCH_2CH_2Ph)_{18}$	Dithiol crosslinking	Brust method	202
Au_{25}	Phenylethanethiol	$[Au_{25}(SCH_2CH_2Ph)_{18}]^{-}$	Mass spectrometry	Brust method	203
Au_{25}	Dioctyl diselenide	$Au_{25}(SeC_8H_{17})_{18}$	Characterization	Brust method	204
Au_{25}	Phenylethanethiol	$Au_{25}(SCH_2CH_2Ph)_{18}$	High yield synthesis	Solution phase	205
Au_{25}	Glutathione	$Au_{25}(SG)_{18}$	Ligand exchange	Hutchison method	206
Au_{25}	Phenylethanethiol	$Au_{25}(SCH_2CH_2Ph)_{18}$	Ligand exchange	Solution phase	207
Au_{25}	Fluorobenzenethiol	$Au_{25}(F\text{-}Ph)_{18}$	Ligand exchange	Solution phase	208
Au_{25}	Phenylethanethiol	$Au_{25}(SCH_2CH_2Ph)_{18}$	Size evolution	Solution phase	209
Au_{25}	Cysteine	$Au_{25}(Cys)_{18}$	COdirected synthesis	Solution phase	210
Au_{25}	Phenylethanethiol	$Au_{25}(SCH_2CH_2Ph)_{18}$	Magnetic circular dichroism	Two-step solution phase	211
Au_{25}	Glutathione	$Au_{25}(SG)_{18}$	Size dependent properties	Solution phase	212

(*continued on next page*)

TABLE 1 A summary of atomically precise nanoclusters synthesized so far (as on May 4, 2022, using web of science). Unprotected or naked clusters are not included. The list is alphabetical and in ascending order of nuclearity of clusters. Alloy clusters, listed separately, are arranged in ascending order of total nuclearity. For each nuclearity, an alphabetical order is followed—cont'd

Core	Ligand	Composition	Focus	Synthesis method	References
Au_{25}	Hexanethiol	$Au_{25}(SC_6H_{13})_{18}$	Origin of magic stability	Schiffrin method	213
Au_{25}	Glutathione	$Au_{25}(SG)_{18}$	Characterization	Solution phase	214
Au_{25}	Glutathione	$Au_{25}(SG)_{18}$	FRET	Two-step solution phase	215
Au_{25}	Glutathione	$Au_{25}(SG)_{18}$	Reactivity	Two-step solution phase	216
Au_{25}	Phenylethanethiol	$Au_{25}(SCH_2CH_2Ph)_{18}$	EPR	Two-step solution phase	217
Au_{25}	Glutathione	$Au_{25}(SG)_{18}$	NMR	One step solution phase	218
Au_{25}	BSA	Au_{25}@BSA	Luminescence	Solution phase	219
Au_{25}	Hexanethiol	$Au_{25}(SC_6H_{13})_{18}$	Temperature-dependent absorbance	Brust method	220
Au_{25}	Phenylethanethiol	$Au_{25}(SCH_2CH_2Ph)_{18}$	EXAFS	Brust method	221
Au_{25}	Glutathione, Hexanethiol	$Au_{25}(SG)_{18}$ $Au_{25}(SC_6H_{13})_{18}$	Luminescence	Brust method	222
Au_{25}	Phenylethanethiol	$Au_{25}(SCH_2CH_2Ph)_{18}$	^{1}HNMR	Modified Brust method	223
Au_{25}	Glutathione	$Au_{25}(SG)_{18}$	Mass spectrometry	Two-step solution phase	224
Au_{25}	6-Mercaptohexanoic Acid	$Au_{25}(MHA)_{18}$	Self-assembly	Solution phase	225
Au_{25} Au_4	2-Methacryloyloxyethyl, Phosphorylcholine	$Au_{25}(MPC)_{18}$ $Au_4(MPC)_4$	Optical properties	Solution phase	226
Au_{25}	Phenylethanethiol, Butanethiol	$Au_{25}(SCH_2CH_2Ph)_{18}$ $Au_{25}(BT)_{18}$	TLC	Solution phase	227
Au_{25}	4-(tert-butyl)-benzyl mercaptan	$Au_{25}(SBB)_{18}$	Luminescence	Solution phase	228
Au_{25}	4-Mercapto-n-butoxy)calix[4]arene	$[Au_{25}(Calix\text{-}4S)_{18}]$	Characterization	Solution phase	229
Au_{28}	Glutathione	$Au_{28}(SG)_{14}$	Optical properties	Solution phase	230
Au_{28}	Glutathione	$Au_{28}(SG)_{14}$	Isolation	Solution phase	231
Au_{28}	Glutathione	$Au_{28}(SG)_{14}$	Luminescence	Solution phase	232
Au_{28}	4-Tert-butylbenzenethiol	$Au_{28}(TBBT)_{20}$	Crystal structure	Solution phase	233
Au_{28}	1,3-Benzenedithiolate, Triphenylphosphine	$[Au_{28}(BDT)_4(TPP)_9]^{2+}$	Characterizatio	Solution phase	234
Au_{28}	*N*,*N*′-diphenylformamidinate	$[Au_{28}(Ph{-}form)_{12}](OTf)_2$	Crystal structure	Solution phase	235
Au_{28}	9-HC≡C-*closo*-1,2-$C_2B_{10}H_{11}$, Tetrahydrothiophene	$[Au_{28}(C_4B_{10}H_{11})_{12}(tht)_8]^{3+}$	Crystal structure	Solution phase	236
Au_{28}	Tert-butylbenzenethiol	$Au_{28}(SCH_2Ph\text{-}^tBu)_{22}$	Crystal structure	Solution phase	237
Au_{29}	Glutathione	$Au_{29}(SG)_{18}$	Characterization	COdirected	238
Au_{30}	1-Adamantanethiol,	$Au_{30}(SAd)_{18}$	Characterization	Modified Brust method	239
Au_{65}	Cyclohexanethiol	$Au_{65}(SCy)_{30}$			
Au_{30}	Tert-butanethiol, 1-adamantanethiol	$Au_{30}(S\text{-}^tC_4H_9)_{18}$ $Au_{30}(SAd)_{18}$	Characterization	Two-step solution phase	240
Au_{30}	Tert-butanethiol	$Au_{30}S(S\text{-}^tBu)_{18}$	Crystal structure	On pot THF method	241
Au_{32}	Triethylphosphine, Chloride	$Au_{32}(Et_3P)_{12}Cl_8$	Crystal structure	Solution phase	242
Au_{54}		$Au_{54}(Et_3P)_{18}Cl_{12}$			
Au_{32}	Trialkylphosphine	$Au_{32}(R_3P)_{12}Cl_8$	Crystal structure	Solution phase	243

(*continued on next page*)

TABLE 1 A summary of atomically precise nanoclusters synthesized so far (as on May 4, 2022, using web of science). Unprotected or naked clusters are not included. The list is alphabetical and in ascending order of nuclearity of clusters. Alloy clusters, listed separately, are arranged in ascending order of total nuclearity. For each nuclearity, an alphabetical order is followed—cont'd

Core	Ligand	Composition	Focus	Synthesis method	References
Au_{32}	Trialkylphosphine, Chloride	$Au_{32}(R_3P)_{12}Cl_8$	DFT study	Solution phase	244
Au_{33}		$Au_{33}(R_3P)_{12}Cl_5$			
Au_{36}	Thiophenol	$Au_{36}(SPh)_{23}$	Characterization	Solution phase	245
Au_{36}	4-tert-butylbenzenethiol	$Au_{36}(SPh\text{-}^tBu)_{24}$	Crystal structure	Two-step solution phase	246
Au_{36}	2,4-Dimethylbenzenethiol	$Au_{36}(DMBT)_{24}$	Crystal structure	Solution phase	247
Au_{37}	Triphenylphosphine, Chloride	$[Au_{37}(PPh_3)_{10}(SR)_{10}Cl_2]^+$	Detecting cis-platin	Solution phase	248
Au_{38}	Adamantanethiol	$Au_{38}(SAd)_{20}S_2$	Crystal structure	Two-step solution phase	249
Au_{38}	Dodecanethiol	$Au_{38}(SC_{12}H_{25})_{24}$	Photoemission	Two-step solution phase	250
Au_{38}	Butanethiol, Hexanethiol, Octanethiol, Decanethiol, Ddecanethiol	$Au_{38}(SR)_{24}$	Characterization	Modified Brust method	251
Au_{38}	Butanethiol, Hexanethiol, Octanethiol, Decanethiol, Dodecanethiol, Hexadecanethiol	$Au_{38}(SR)_{24}$	Characterization	Modified Brust method	252
Au_{38}	Dodecanethiol	$Au_{38}(SC_{12}H_{25})_{24}$	Characterization	Solution phase	253
Au_{38}	Phenylethanethiol	$Au_{38}(SCH_2CH_2Ph)_{24}$	Ligand exchange	Solution phase	254
Au_{40}		$Au_{40}(SCH_2CH_2Ph)_{24}$			
Au_{38}	Phenylethanethiol	$Au_{38}(SCH_2CH_2Ph)_{24}$	Oxidative electron charging	Brust method	255
Au_{38}	Phenylethanethiol	$Au_{38}(SCH_2CH_2Ph)_{24}$	Electron transfer	Brust method	256
Au_{38}	Phenylethanethiol	$Au_{38}(SCH_2CH_2Ph)_{24}$	Pd-doping	Solution phase	257
Au_{38}	Phenylethanethiol	$Au_{38}(SCH_2CH_2Ph)_{24}$	Reactivity with PPh_3	Brust method	258
Au_{38}	Phenylethanethiol	$Au_{38}(SCH_2CH_2Ph)_{24}$	Isolation through size exclusion chromatography	Two-step solution phase	259
Au_{40}		$Au_{40}(SCH_2CH_2Ph)_{24}$			
Au_{38}	Phenylethanethiol	$Au_{38}(SCH_2CH_2Ph)_{24}$	Electrochemical properties	Ligand exchange	260
Au_{38}	Phenylethanethiol	$Au_{38}(SCH_2CH_2Ph)_{24}$	Structure and bonding	Solution phase	261
Au_{38}	Hexanethiol	$Au_{38}(SC_6H_{13})_{24}$	Solvent dependent stability	Brust–Schiffrin method	262
Au_{38}	Phenylethanethiol	$Au_{38}(SCH_2CH_2Ph)_{24}$	Crystal structure	Modified Brust method	263
Au_{38}	X-benzenethiol, X = nitro/bromo/hydroxy	$Au_{38}(SPhX)_{24}$	Substituent effects	Ligand exchange	264
Au_{38}	Phenylethanethiol	$Au_{38}(SCH_2CH_2Ph)_{24}$	Characterization	Brust two-phase method	265
Au_{38}	Hexanethiol	$Au_{38}(SC_6H_{13})_{22}$	Characterization	Brust-Schiffrin method	266
Au_{38}	Dodecanethiol	$Au_{38}(SC_{12}H_{25})_{24}$	Catalysis	Modified Brust method	267
Au_{38}	Hexanethiol	$Au_{38}(SC_6H_{13})_{22}$	Temperature dependent emission	Brust-Schiffrin method	268
Au_{39}	Triphenylphosphine	$[(Ph_3P)_{14}Au_{39}Cl_6]_2$	Crystal structure	Modified Hutchison method	269
Au_{40}	Phenylethanethiol	$Au_{40}(SCH_2CH_2Ph)_{24}$	Isolation	Solution phas	270
Au_{40}	Phenylethanethiol	$Au_{40}(SCH_2CH_2Ph)_{24}$	Enantiomers separation	Solution phase	271
Au_{40}	2-methylbenzenethiol	$Au_{40}(o\text{-}MBT)_{24}$	Crystal structure	Solution phase	272

(*continued on next page*)

TABLE 1 A summary of atomically precise nanoclusters synthesized so far (as on May 4, 2022, using web of science). Unprotected or naked clusters are not included. The list is alphabetical and in ascending order of nuclearity of clusters. Alloy clusters, listed separately, are arranged in ascending order of total nuclearity. For each nuclearity, an alphabetical order is followed—cont'd

Core	Ligand	Composition	Focus	Synthesis method	References
Au_{41}	S-Eind	$Au_{41}(S\text{-}Eind)_{12}$	Binding motif	Modified Brust method	273
Au_{42}	4-tert-butylbenzenelthiol	$Au_{42}(Ph^tBu)_{26}$	Crystal structure	Ion induction method	274
Au_{42}	$HC{\equiv}CC_6H_4\text{-}2\text{-}CF_3$	$Au_{42}(C{\equiv}CC_6H_4\text{-}2\text{-}CF_3)_{22}$	Crystal structure	Direct reduction	275
Au_{50}	$HC{\equiv}CC_6H_4\text{-}3\text{-}F$	$Au_{50}(C{\equiv}CC_6H_4\text{-}3\text{-}F)_{26}$			
Au_n (n = 43, 46, 52, 54, 59, 71, 90, 94, 101, 110)	Phenylacetylene	$Au_{43}L_{22}$, $Au_{46}L_{24}$, $Au_{52}L_{26}$, $Au_{54}L_{26}$, $Au_{59}L_{27}$, $Au_{71}L_{32}$, $Au_{90}L_{36}$, $Au_{94}L_{38}$, $Au_{101}L_{38}$, $Au_{110}L_{40}$	Characterization	Ligand exchange	276
Au_{44}	Thiophenol	$Au_{44}(SPh)_{28}$	Characterization	Solution phase	277
Au_{44}	4-tert-butylbenzenelthiol, 2,4-dimethylbenzenethiol	$Au_{44}(TBBT)_{28}$ $Au_{44}(2,4\text{-}DMBT)_{26}$	Single crystal	Modified Brust method	278
Au_{44} Au_{36}	Phenylacetylene	$Au_{44}(C{\equiv}CPh)_{28}$ $Au_{36}(C{\equiv}CPh)_{24}$	Crystal structure	Direct reduction	279
Au_{49}	2,4-Dimethylbenzenethiol	$Au_{49}(2,4\text{-}DMBT)_{27}$	Crystal structure	Modified Brust method	280
Au_{52}	4-tert-butylbenzenethiol	$Au_{52}(TBBT)_{32}$	Crystal Structure	Two-step solution phase	281
Au_{54}	Phenylacetylene	$Au_{54}(C{\equiv}CPh)_{26}$	Characterization	Ligand exchange	282
Au_{54}	Phenylacetylene	$Au_{54}(C{\equiv}CPh)_{26}$	Characterization	Solution phase	283
Au_{55}	Octadencanethiol	$Au_{55}(SC_{18})_{32}$	Isolation	Brust method	284
Au_{55}	Triphenylphosphine	$Au_{55}(PPh_3)_{12}C1_6$	Application in microelectronics	Schmid method	285
Au_{55}	Triphenylphosphine	$Au_{55}(PPh_3)_{12}C1_6$	Interfacial synthesis	Schmid method	286
Au_{55}	Triphenylphosphine	$Au_{55}(PPh_3)_{12}C1_6$	Characterization	Schmid method	287
Au_{55}	Triphenylphosphine	$Au_{55}(PPh_3)_{12}C1_6$	Ligand exchange	Schmid method	288
Au_{55}	Triphenylphosphine	$Au_{55}(PPh_3)_{12}C1_6$	STM study	Schmid method	289
Au_{55}	Triphenylphosphine	$Au_{55}(PPh_3)_{12}C1_6$	Direct Atomic Imaging	Schmid method	290
Au_{55}	Triphenylphosphine	$Au_{55}(PPh_3)_{12}C1_6$	Double layer formation on silicon wafer barrier film	Schmid method	291
Au_{55}	Triphenylphosphine	$Au_{55}(PPh_3)_{12}C1_6$	Electrical properties	Schmid method	292
Au_{55}	Triphenylphosphine	$Au_{55}(PPh_3)_{12}C1_6$	3D assembly and electrical properties	Schmid method	293
Au_{55}	Triphenylphosphine	$Au_{55}(PPh_3)_{12}C1_6$	Superstructure property	Schmid method	294
Au_{55}	Triphenylphosphine	$Au_{55}(Ph_2PC_6H_4SO_3H)_{12}Cl_6$	2D monolayer formation	Schmid method	295
Au_{55}	Triphenylphosphine	$Au_{55}(PPh_3)_{12}C1_6$	Oxidation resistant property	Schmid method	296
Au_{55}	Triphenylphosphine	$Au_{55}(PPh_3)_{12}C1_6$	Quasi 1 D arrangement	Schmid method	297
Au_{55}	Triphenylphosphine	$Au_{55}(PPh_3)_{12}C1_6$	Metallic properties	Schmid method	298
Au_{55}	Triphenylphosphine	$Au_{55}(PPh_3)_{12}C1_6$	Temperature dependent impedance study	Schmid method	299
Au_{55}	Phenylethanethiol	$Au_{55}(SCH_2CH_2Ph)_{31}$	Characterization	Two-step solution phase	300

(*continued on next page*)

TABLE 1 A summary of atomically precise nanoclusters synthesized so far (as on May 4, 2022, using web of science). Unprotected or naked clusters are not included. The list is alphabetical and in ascending order of nuclearity of clusters. Alloy clusters, listed separately, are arranged in ascending order of total nuclearity. For each nuclearity, an alphabetical order is followed—cont'd

Core	Ligand	Composition	Focus	Synthesis method	References
Au_{55}	Triphenylphosphine	$Au_{55}(PPh_3)_{12}C1_6$	Application as quantum dots	Schmid method	301
Au_{55}	Triphenylphosphine	$Au_{55}(PPh_3)_{12}C1_6$	Diode behavior	Schmid method	302
Au_{55}	Triphenylphosphine	$Au_{55}(PPh_3)_{12}C1_6$	Electronic interaction	Schmid method	303
Au_{55}	Triphenylphosphine	$Au_{55}(PPh_3)_{12}C1_6$	TEM and SAXD study	Schmid method	304
Au_{55}	4-Methylbenzenethiolate, Triphenylphosphine	$[Au_{55}(p\text{-}MBT)_{24}(Ph_3P)_6](SbF_6)_3$	Crystal structure	Co reduction	305
Au_{60}	Triphenylphosphine, Benzeneselenol	$[Au_{60}Se_2(Ph_3P)_{10}(SeR)_{15}]^+$	Crystal structure	Modified Brust method	306
Au_{64}	Cyclohexanethiol	$Au_{64}(S\text{-}c\text{-}C_6H_{11})_{32}$	Characterization	Solution phase	307
Au_{67}	Phenylethanethiol, Hexanethiol	$Au_{67}(SR)_{35}$	Characterization	Three step solution phase method	308
Au_{68}	Phenylethanethiol	$Au_{68}(SCH_2CH_2Ph)_{34}$	Characterization	Solution phase	309
Au_{69}	Triphenylphosphine, Chloride	$Au_{69}(Ph_3)_{20}Cl_{12}$	DFT study	Theoretical	310
Au_{70}	Triphenylphosphine	$Au_{70}S_{20}(PPh_3)_{12}$	DFT study	Theoretical	311
Au_{75}	Hexanethiol	$Au_{75}(SC_6H_{13})_{40}$	Characterization	Thiol exchange process	312
Au_{76}	4-(2-mercaptoethyl)benzoic acid	$Au_{76}(4\text{-}MEBA)_{44}$	Characterization	Solution phase	313
Au_{92}	4-tert-butylbenzenethiol	$Au_{92}(TBBT)_{44}$	Crystal structure	Solution phase	314
Au_{99}	$2,4\text{-}F_2C_6H_3C{\equiv}CH$	$Au_{99}(C{\equiv}CC_6H_3\text{-}2,4\text{-}F_2)_{40}$	Crystal structure	Direct reduction	315
Au_{101}	Triphenylphosphine	$Au_{101}(PPh_3)_{21}Cl_5$	Ligand Exchange	Hutchison method	316
Au_{102}	p-Mercaptobenzoic acid	$Au_{102}(p\text{-}MBA)_{44}$	Crystal structure	One step solution phase	317
Au_{103}	Naphthalenethiol	$Au_{103}S_2(S\text{-}Nap)_{41}$	Crystal structure	Solution phase	318
Au_{103}	Phenylethanethiol	$Au_{103}(CH_2CH_2Ph)_{45}$	Characterization	Solution phase	319
Au_{104}		$Au_{104}(CH_2CH_2Ph)_{45}$			
Au_{105}		$Au_{104}(CH_2CH_2Ph)_{46}$ $Au_{105}(CH_2CH_2Ph)_{46}$			
Au_{106}	$3,5\text{-}(CF_3)_2C_6H_3C{\equiv}CH$	$[HNEt_3]_4[Au_{106}L_{40}Cl_{12}]$	Crystal structure	Direct reduction	320
Au_{108}	Triphenylphosphine	$Au_{108}S_{24}(PPh_3)_{16}$	Crystal structure	Solution phase	321
Au_{110}	$p\text{-}CF_3C_6H_4C{\equiv}CH$	$[Au_{110}(p\text{-}CF_3C_6H_4C{\equiv}C)_{48}]\ [HNEt_3]_2$	Crystal structure	Direct reduction	322
Au_{130}	4-Methylbenzenethiol	$Au_{130}(p\text{-}MBT)_{50}$	Crystal structure	Two-step size focusing	323
Au_{130}	4-Bromothiophenol	$Au_{130}(SPh\text{-}Br)_{50}$	Characterization	Brust method	324
Au_{133}	4-tert-butylbenzenethiol	$Au_{133}(SPh\text{-}tBu)_{52}$	Crystal structure	Three step solution phase	325
Au_{137}	Phenylethanethiol	$Au_{137}(SC_{12}H_{25})_{56}$	Characterization	Brust method	326
Au_{130}	Dodecanethiol	$Au_{130}(SC_{12}H_{25})_{50}$	Characterization	Brust method	327
Au_{187}		$Au_{187}(SC_{12}H_{25})_{68}$			
$Au_{144-146}$	Butanethiol, hexanethiol, dodecanethiol, benzylthiol	$Au_{144\text{-}146}(SR)_{50\text{-}60}$	Characterization	Brust method	328
Au_{144}	$2\text{-}FC_6H_4C{\equiv}CH$	$Au_{144}(2\text{-}FC_6H_4C{\equiv}C)_{60}$	Crystal structure	Direct reduction	329
Au_{144}	$C_nH_{2n+1}SH\ (n=48)$	$Au_{144}(SR)_{60}$	Characterization	Two-step solution phase	330
Au_{25}	Phenylethanethiol	$Au_{25}(SCH_2CH_2Ph)_{18}$	FT IR	Modified Brust methods	331

(*continued on next page*)

TABLE 1 A summary of atomically precise nanoclusters synthesized so far (as on May 4, 2022, using web of science). Unprotected or naked clusters are not included. The list is alphabetical and in ascending order of nuclearity of clusters. Alloy clusters, listed separately, are arranged in ascending order of total nuclearity. For each nuclearity, an alphabetical order is followed—cont'd

Core	Ligand	Composition	Focus	Synthesis method	References
Au_{38}		$Au_{38}(SCH_2CH_2Ph)_{24}$,			
Au_{144}		$Au_{144}(SCH_2CH_2Ph)_{60}$			
Au_{25}	Phenylethanethiol	$Au_{25}(SCH_2CH_2Ph)_{18}$	Far-infrared spectroscopy	Modified Brust methods	332
Au_{38}		$Au_{38}(SCH_2CH_2Ph)_{24}$			
Au_{40}		$Au_{40}(SCH_2CH_2Ph)_{24}$			
Au_{145}	n-butylthiol, n-pentylthiol	$Au_{145}(SR)_{60}X$ (X = Br, Cl)	Mass spectrometry	Brust method	333
Au_{156}	4-$CF_3C_6H_4C{\equiv}CH$	$Au_{156}(4\text{-}CF_3C_6H_4C{\equiv}C)_{60}$	Crystal structure	Direct reduction	334
Au_{191}	4-tert-butylbenzenethiol (TBBT)	$Au_{191}(TBBT)_{66}$	Crystal structure	Brust method	335
Au_{225}	Hexanethiol	$Au_{225}[S(CH_2)_5CH_3]_{75}$	Characterization	Brust method	336
Au_{246}	p-MBT	$Au_{246}(pMBT)_{80}$	Crystal structure	Brust method	337
Au_{246}	p-MBT	$Au_{246}(pMBT)_{80}$	Metallicity	Brust method	338
Au_{279}	4-tert-butylbenzenethiol (TBBT)	$Au_{279}(TBBT)_{84}$	Crystal structure	Brust method	339
Au_{329}	Phenylethanethiol	$Au_{329}(SCH_2CH_2Ph)_{84}$	Characterization	Brust method	340
Au_{333}	Phenylethanethiol	$Au_{333}(SCH_2CH_2Ph)_{79}$	Characterization	Brust method	341
Au_{500}	Phenylethanethiol	$Au_{\sim500}(SR)_{\sim120}$	Characterization	Modified Brust method	342
$Au_{\sim940\pm20}$	Phenylethanethiol	$Au_{\sim940\pm20}(SR)_{\sim160\pm4}$	Characterization	Modified Brust method	343
$Au_{\sim1400}$	Hexanethiol	$Au_{\sim1400}(SR)_{\sim240}$	Characterization	Modified Brust method	344
$Au_{\sim2000}$	Hexanethiol	$Au_{\sim2000}(SR)_{\sim290}$	Characterization	Modified Brust method	345
Cu_2	1,1-Bis(diphenylphosphino)	$[Cu_2(SePh)_2(dppb)_3]$	Characterization	Solution phase	346
$Cu_{16}Se_4$	Butane, SePh	$[Cu_{16}Se_4(SePh)_8(dppb)_4]$			
$Cu_4(Te_2)_2$	Triisopropylphosphine	$[Cu_4(Te_2)_2(P^iPr_3)_4]$	Characterization	Solution phase	347
Cu_5	Triethylphosphine, TePh	$[PEt_3Ph][Cu_5(TePh)_6(PEt)_3]$	Characterization	Solution phase	348
Cu_6	2-Mercaptobenzoxazole	$Cu_6(SR)_6$	Crystal structure	Solution phase	349
Cu_6	Triphenylphosphine, SePh	$[Cu_6(SePh)_6(PPh_3)_3(4,4'\text{-bpy})]$	Characterization	Solution phase	350
Cu_6	Dithiophosphinate	$Cu_6[\mu_3\text{-}S_2P(OEt)_2]_6$	Crystal structure	Solution phase	351
Cu_6	Diphenylethylphosphine, TePh	$[Cu_6(TePh)_6(PEtPh_2)_5]$	Characterization	Solution phase	352
$Cu_{50}Te_{17}$		$[PEtPh_3]_4[Cu_{50}Te_{17}(TePh)_{20}(PEtPh_2)_8]$			
Cu_8Te_4	Triphenylphosphine	$[Cu_8Te_4(PPh_3)_7]$	Characterization	Solution phase	353
$Cu_{12}Te_6$		$[Cu_{12}Te_6(PPh_3)_8]$			
$Cu_{16}Te_9$		$[Cu_{16}Te_9(PPh_3)_8]$			
$Cu_{23}Te_{13}$		$[Cu_{23}Te_{13}(PPh_3)_{10}]$			
Cu_{11}	N,N′-Di(5-trifluoromethyl-2-pyridyl)formamidinate, Hydride	$Cu_{11}H_3(Tf\text{-}dpf)_6(OAc)_2$	Crystal structure	Solution phase	354
Cu_{12}		$[Cu_{12}H_3(Tfdpf)_6(OAc)_2]OAc$			
$Cu_{12}Te_3$	Triethylphosphine	$[Cu_{12}Te_3(TePh)_6(PEt_3)_6]$	Characterization	Solution phase	355
$Cu_{12}S_6$	Triethylphosphine, Triphenylphosphine	$[Cu_{12}S_6(PEt_3)_8]$	Characterization	Solution phase	356
$Cu_{20}S_{10}$		$[Cu_{20}S_{10}(PPh_3)_8]$			
Cu_{15}	Phenylethanethiol, Triphenylphosphine	$[Cu_{15}(PPh_3)_6(PET)_{13}]^{2+}$	Characterization	Solution phase	357
$Cu_{20}Se_4$	Triphenylphosphine, SePh	$[Cu_{20}Se_4(SePh)_{12}(PPh_3)_6]$	Characterization	Solution phase	358
$Cu_{31}Se_{15}$		$[Cu_{31}Se_{15}(SeSiMe_3)(P^tBu_2Me)_{12}]$			
Cu_{23}	Triphenylphosphine	$[Cu_{23}(PhSe)_{16}(Ph_3P)_8(H)_6]\cdot BF_4$	Characterization	Solution phase	359
$Cu_{24}S_{12}$	Diisopropyl(methyl)phosphine,	$[Cu_{24}S_{12}(PMe^iPr_2)_{12}]$	Characterization	Solution phase	360
$Cu_{48}Se_{24}$	Dimethylphenylphosphine,	$[Cu_{48}Se_{24}(PMe_2Ph)_{20}]$			
$Cu_{50}S_{25}$	Dibutylmethylphosphine	$[Cu_{50}S_{25}(P^tBu_2Me)_{16}]$			

(*continued on next page*)

TABLE 1 A summary of atomically precise nanoclusters synthesized so far (as on May 4, 2022, using web of science). Unprotected or naked clusters are not included. The list is alphabetical and in ascending order of nuclearity of clusters. Alloy clusters, listed separately, are arranged in ascending order of total nuclearity. For each nuclearity, an alphabetical order is followed—cont'd

Core	Ligand	Composition	Focus	Synthesis method	References
Cu_{25}	Triphenylphosphine	$[Cu_{25}H_{22}(PPh_3)_{12}]Cl$	Characterization	Solution phase	361
$Cu_{25}Te_6$	1,1-Bis(diphenylphosphino)alkane	$[Cu_{25}Te_{6(}TeBu)_{13}(dppa)_6]$	Characterization	Solution phase	362
$Cu_{26}Se_{13}$	Triethylphosphine	$[Cu_{26}Se_{13}(PEt_3)_{14}]$	Characterization	Solution phase	363
$Cu_{26}Te_{12}$	Diethylphenylphosphine	$[Cu_{26}Te_{12}(PEt_2Ph)_{12}]$	Characterization	Solution phase	364
$Cu_{29}Te_9$	Triethylphosphine, TePh	$[PEt_3Ph][Cu_{29}Te_9(TePh)_{12}(PEt_3)_8]$	Characterization	Solution phase	365
$Cu_{29}Se_{15}$ $Cu_{30}Se_{15}$	Triisopropylphosphine	$[Cu_{29}Se_{15}(P^iPr_3)_{12}]$ $[Cu_{30}Se_{15}(P^iPr_3)_{12}]$	Characterization	Solution phase	366
Cu_{32}	Phenylethanethiol, Triphenylphosphine	$[Cu_{32}(PET)_{24}H_8Cl_2](PPh_4)_2$	Characterization	Solution phase	367
$Cu_{32}Se_{16}$ $Cu_{52}Se_{26}$ $Cu_{72}Se_{36}$	Triphenylphosphine	$[Cu_{32}Se_{16}(PPh_3)_{12}]$ $[Cu_{52}Se_{26}(PPh_3)_{16}]$ $[Cu_{72}Se_{36}(PPh_3)_{20}]$	Characterization	Solution phase	368
Cu_{34-32}	Phenylethanethiol	$Cu_{34-32}(SG)_{16-13}$	Characterization	Solution phase	369
$Cu_{38}Se_{13}$ $Cu_{58}Se_{16}$	1,1-Bis(diphenylphosphino)butane	$[Cu_{38}Se_{13}(SePh)_{12}(dppb)_6]$ $[Cu_{58}Se_{16}(SePh)_{24}(dppa)_6]$	Characterization	Solution phase	370
$Cu_{44}Se_{22}$	Diethylphenylphosphine	$[Cu_{44}Se_{22}(PEt_2Ph)_{18}]$	Characterization	Solution phase	371
$Cu_{44}Te_{23}$	Triphenylphosphine	$[Cu_{44}Te_{23}(PPh_3)_{15}]$	Characterization	Solution phase	372
$Cu_{58}Te_{32}$	Triphenylphosphine	$[Cu_{58}Te_{32}(PPh_3)_{16}]$	Characterization	Solution phase	373
$Cu_{59}Se_{30}$	Tricyclohexylphosphine	$[Cu_{59}Se_{30}(PCy_3)_{15}]$	Characterization	Solution phase	374
Cu_{61}	tert-butylbenzenethiol	$Cu_{61}(S^tBu)_{26}S_6Cl_6H_{14}$	Characterization	Solution phase	375
$Cu_{70}Se_{35}$	Triethylphosphine	$[Cu_{70}Se_{35}(PEt_3)_{22}]$	Characterization	Solution phase	376
Cu_{81}	tert-butylbenzenethiol	$[Cu_{81}(PhS)_{46}(^tBuNH_2)_{10}(H)_{32}]^{3+}$	Characterization	Solution phase	377
$Cu_{93}Se_{42}$ $Cu_{96}Se_{45}$	Triphenylphosphine	$[Cu_{93}Se_{42}(SeC_6H_4SMe)_9(PPh_3)_{18}]$ $[Cu_{96}Se_{45}(SeC_6H_4SMe)_6(PPh_3)_{18}]$	Characterization	Solution phase	378
$Cu_{146}Se_{73}$	Triphenylphosphine	$[Cu_{146}Se_{73}(PPh_3)_{30}]$	Characterization	Solution phase	379
Ir_4 Ir_6	Carbon monoxide	$Ir_4(CO)_{12}$ $[Ir_6(CO)_{15}]^{2-}$	Characterization	Solution phase	380
Ir_9	Phenylethanethiol	$Ir_9(PET)_6$	Characterization	Solution phase	381
Ir_{50}	Phenylacetylene	$Ir_{50}(PA)_{25}$	Characterization	Solution phase	382
Ni_8 Ni_{10}	2-Mercapto-5-amino-1,3,4-thiadiazole, (Hydroxymethyl)methylglycine	$Ni_8O(H_3thmmg)_6{\cdot}2NO_3$ $Ni_{10}O(OH)_2(H_3thmmg)_4(mat)_8$	Crystal structure	Solution phase	383
Ni_{30}	Triethylphosphine	$[Ni_{30}S_{16}(PEt_3)_{11}]$	Crystal structure	Solution phase	384
Pd_4	Acetate, Carbon monoxide	$[Pd_4(CO)_4(OAc)_4]{\cdot}(AcOH)_2$	Characterization	Solution phase	385
Pd_7	$N{=}C^tBu_2$	$Pd_7(N{=}C^tBu_2)_6$	Characterization	Solution phase	386
Pd_{10}	PBu_3n, Carbon monoxide	$Pd_{10}(CO)_{12}(PBu_3n)_6$	Characterization	Solution phase	387
Pd_{13}	Cycloheptadiene	$[Pd_{13}(\mu_4\text{-}C_7H_7)_6]^{2+}$	Characterization	Solution phase	388
Pd_{21} Pd_{38}	Phenylethanethiol	$Pd_{21}(SCH_2CH_2Ph)_{18}$ $Pd_{38}(SCH_2CH_2Ph)_{21}S_2$	Characterization	Solution phase	389
Pd_{55}	(L = PR_3, R = Isopropyl)	$Pd_{55}L_{12}[Pd_{13}(\mu_4\text{-}C_7H_7)_6]^{2+}$ $(\mu_3\text{-}CO)_{20}$	Characterization	Solution phase	390
Pt_6	Glutathione	Pt_6NCs	Hydrogen electro-oxidation	Solution phase	391
Pt_8	($L = C_2H_2O_2S$)	$Pt_8(C_2H_2O_2S)_8$	Characterization	Solution phase	392
Alloy clusters					
Ag_4Ni_2	Dimercaptosuccinic acid	$Ag_4Ni_2(DMSA)_4$	Mass spectrometry	Coreduction	393
Ag_4Pd_2	Dimercaptosuccinic acid	$Ag_4Pd_2(DMSA)_4$	Crystal structure	Coreduction	394
Ag_4Pt_2	Dimercaptosuccinic acid	$Ag_4Pt_2(DMSA)_4$	Mass spectrometry	Coreduction	395
Au_4Pd_2	Phenylethanethiol	$Au_4Pd_2(PET)_8$	Crystal structure	Coreduction	396

(*continued on next page*)

TABLE 1 A summary of atomically precise nanoclusters synthesized so far (as on May 4, 2022, using web of science). Unprotected or naked clusters are not included. The list is alphabetical and in ascending order of nuclearity of clusters. Alloy clusters, listed separately, are arranged in ascending order of total nuclearity. For each nuclearity, an alphabetical order is followed—cont'd

Core	Ligand	Composition	Focus	Synthesis method	References
Au_4Pt_2	Phenylethanethiol	$Au_4Pt_2(PET)_8$	Crystal structure	Coreduction	397
Au_2Cu_6	1,2-Diphenylpyridinephosphine, Adamantanethiol	$Au_2Cu_6(S\text{-}Adm)_6(PPh_2Py)_2$	Crystal structure	Coreduction	398
Au_4Cu_4	1,1-Bis(diphenylphosphino) methane, Adamantanethiol	$[Au_4Cu_4(Dppm)_2(SAdm)_5]Br$	Crystal structure	Coreduction	399
Ag_5Au_4	1,1-Bis(diphenylphosphino)methane, Adamantanethiol	$[Au_4Ag_5(dppm)_2(SAdm)_6]^+$	Crystal structure	Coreduction	400
Au_4Cu_5	1,1-Bis(diphenylphosphino)methane, Cyclohexanethiol	$[Au_4Cu_5(C_6H_{11}S)_6(Dppm)_2](BPh_4)$	Crystal structure	Ligand exchange	401
Au_8Pd_1 Au_8Pt_1	Triphenylphosphine	$[PdAu_8(PPh_3)_8]^{2+}$ $[PtAu_8(PPh_3)_8]^{2+}$	Mass spectrometry	Coreduction	402
Au_8Pt_1	Triphenylphosphine	$PtAu_8(PPh_3)_8](NO_3)_2$	Crystal structure	Coreduction	403
Ag_9Pt_1	tris(4-fluorophenyl)phosphine	$Pt_1Ag_9[P(Ph\text{-}F)_3]_7Cl_3$	Crystal structure	Coreduction	404
Au_8Ag_3	Triphenylphosphine	$Au_8Ag_3(PPh_3)_7Cl_3$	Crystal structure	Coreduction	405
$Au_{10}Ag_2$	2-pyridylethynyl, 2-pyridyldiphenylphosphine	$[Au_{10}Ag_2(2\text{-}py{-}C{\equiv}C)_3(dppy)_6](BF_4)_5$	Crystal structure	Coreduction	406
Ag_7Au_6	Mercaptosuccinic acid	$Ag_7Au_6(H_2MSA)$	Mass spectrometry	Galvanic exchange	407
$Ag_{12}Pt_1$	1, 1-Bis(diphenylphosphino) methane, 2,4-dimethylbenzenethiol	$Pt_1Ag_{12}(dppm)_5(SPhMe_2)_2$	Mass spectrometry	Ligand exchange	408
Au_9M_4 (M = Ag, Cu)	Diphenylmethylphosphine	$[Au_9M_4Cl_4(PMePh_2)_8][C_2B_9H_{12}]$ $\cdot CH_2Cl_2$ (M = Ag, Cu)	FAB mass spectrometry	Anti-galvanic exchange	409
$Au_{13}Cu_x$ ($x = 2, 4, 8$)	Pyridine-2-thiol, Triphenylpyridine, 4-*ter*-butylbenzenethiol, Pyridinediphenylphosphine	$[Au_{13}Cu_2(PPh_3)_6(Spy)_6]^+$ $[Au_{13}Cu_4(PPh_2Py)_4(SC_6H_4\text{-}tert\text{-}C_4H_9)_8]^+$ $[Au_{13}Cu_8(PPh_2Py)_{12}]^+$	Crystal structure	Coreduction	410, 411
$Au_{14}Cd_1$	Tert-butylthiol	$Cd_1Au_{14}(S^tBu)_{12}$	Crystal structure	Coreduction	412
Ag_9Au_7	1,1′-Bis(diphenylphosphino) ferrocene	$[Au_7Ag_9(dppf)_3(CF_3CO_2)_7BF_4]_n$	Crystal structure	Coreduction	413
$AgAu_{16}$	Adamantanethiol	$[Au_{16}Ag(S\text{-}Adm)_{13}]$	Crystal structure	Ligand exchange	414
$Ag_{16}Au$	Tert-butylbenzenethiol	$(TOA)_3AuAg_{16}(TBBT)_{12}$	Crystal structure	Coreduction	415
$AgAu_{17}$	Hexanethiol	$AgAu_{17}(HT)_{14}$	Crystal structure	Anti-galvanic exchange	416
Ag_3Au_{15}	2,4-Dimethylbenzenethiol	$Au_{15}Ag_3(SPhMe_2)_{14}$	Crystal structure	Anti-galvanic exchange	417
$Ag_{19}Au$	O,O-Diisopropyl dithiophosphate	$[AuAg_{19}\{S_2P(O^nPr)_2\}_{12}]$	Crystal structure	Coreduction	418
$Ag_{12}Au_9$	1,1-Bis(diphenylphosphino) methane, adamantanethiol, tert-butylmercaptan	$[Au_9Ag_{12}(SR)_4(dppm)_6X_6]^{3+}$	Crystal structure	Coreduction	419
$Ag_{20}M$	$E_2(PH_2)_{12}$ (E = S, Se)	$[MAg_{20}(E_2PH_2)_{12}]$ (E = S, Se) M = Au, Pt, Pd, Cu	DFT analysis	Solution phase	420
$Au_{21-x}Ag_x$ $Au_{21-x}Cu_x$	tert-butylthiol	$Au_{21-x}Ag_x(SR)_{15}$ ($x = 4{-}8$) $Au_{21-x}Cu_x(SR)_{15}$ ($x = 0, 1$) $Au_{21-x}Cu_x(SR)_{15}$ ($x = 2{-}5$)	Crystal structure	Coreduction, Ligand exchange	421
Ag_xAu_{23-x}	Cyclohexanethiol	$Au_{23-x}Ag_x(S\text{-}Adm)_{16}$	Crystal structure	Coreduction	422
$Ag_{22}Au_1$	Adamantanethiol	$[Au_1Ag_{22}(S\text{-}Adm)_{12}]^{3+}$	Crystal structure	Ligand exchange	423
Ag_xAu_{24-x}	Tert-butylbenzylmercaptan	$Au_{24-x}Ag_x(TBBM)_{20}$	Crystal structure	Ligand exchange	424
$Ag_xAu_{24-x}M_1$	Phenylethanethiol	$M_1Ag_xAu_{24-x}(SR)_{18}$ (M = Cd/Hg)	Mass spectrometry	Anti-galvanic exchange	425
$Ag_xAu_{24-x-y}Cu_yPd$	1-dodecanethiol	$Au_{24-x-y}Ag_xCu_yPd(SC_{12}H_{25})_{18}$	Mass spectrometry	Anti-galvanic exchange	426

(*continued on next page*)

TABLE 1 A summary of atomically precise nanoclusters synthesized so far (as on May 4, 2022, using web of science). Unprotected or naked clusters are not included. The list is alphabetical and in ascending order of nuclearity of clusters. Alloy clusters, listed separately, are arranged in ascending order of total nuclearity. For each nuclearity, an alphabetical order is followed—cont'd

Core	Ligand	Composition	Focus	Synthesis method	References
$Ag_{24-x}Au_x$	2,4-dichlorobenzenethiol	$(PPh_4)_2[Ag_{25-x}Au_x(SR)_{18}]$	Crystal structure	Coreduction, Galvanic exchange	427
	2,4-dimethylbenzenethiol				
Ag_xAu_{25-x} ($x = 6$–8)	Phenylethanethiol	$[Au_{25-x}Ag_x(PET)_{18}]$	Crystal structure	Coreduction	428,429
Ag_5Au_{20}	Captopril	$Au_{20}Ag_5(Capt)_{18}$	Mass spectrometry	Intercluster reaction	430
Ag_6Au_{19}	Triphenylphosphine	$[Au_{19}Ag_6(MeOPhS)_{17}(PPh_3)_6]^{2+}$	Crystal structure	Solution phase	431
	MeOPhSH				
$Ag_{12}Au_{12}Ni$	Hexafluroantimonate, Triphenylphosphine	$[Au_{12}Ag_{12}Ni(PPh_3)_{10}Cl_7][SbF_6]$	Crystal structure	Coreduction	432
$Ag_{12}Au_{12}Pt$		$[Au_{12}Ag_{12}Pt(PPh_3)_{10}Cl_7]Cl$			
$Ag_{13}Au_{12}$	Diphenylmethylphosphine	$(MePh_2P)_{10}Au_{12}Ag_{13}Br_9$	Crystal structure	Coreduction	433
$Ag_{13}Au_{12}$	Triphenylphosphine, Phenylethanethiol	$[Ag_{13}Au_{12}(PPh_3)_{10}(SR)_5Cl_2]^{2+}$	Crystal structure	Ligand exchange	434
$Ag_{23}Au_2$	2-Ethylbenzenethiol	$[Ag_{23}Au_2(2\text{-}EBT)_{18}Ag_{22}Au_3(2\text{-}EBT)_{18}]^{2-}[2(PPh_4)]^{2+}$	Cocrystallization	Solution phase	435
$Ag_{22}Au_3$					
$Ag_{23}Pd_2$	Triphenylphosphine	$[Ag_{23}Pd_2(PPh_3)_{10}Cl_7]$	Crystal structure	Solution Phase	436
$Ag_{23}Pt_2$	Triphenylphosphine	$[Pt_2Ag_{23}Cl_7(PPh_3)_{10}]$	Crystal structure	Coreduction	437
$Ag_{24}Au$	1,1-Bis(diphenylphosphino)methane	$[AuAg_{24}(dppm)_3(SR)_{17}]^{2+}$	Crystal structure	Coreduction	438
$Ag_{24}Au$	6-Mercaptohexanoic acid	$AuAg_{24}(MHA)_{18}$	Mass spectrometry	Galvanic exchange	439
$Ag_{24}Au$	2,4-Dimethylbenzenethiol	$[Ag_{24}Au(SR)_{18}]^-$	Crystal structure	Galvanic exchange	440
$Ag_{24}Pd$	2,4-Dichlorobenzenethiol	$(PPh_4)_2[Ag_{24}Pd(SR)_{18}]$	Crystal structure	Coreduction	441
$Ag_{24}Pt$		$(PPh_4)_2[Ag_{25-x}Pt_x(SR)_{18}]$			
$Au_{22}Ir_3$	Phenylethanethiol	$Au_{22}Ir_3(SC_2H_4Ph)_{18}$	Mass spectrometry	Intercluster reaction	442
$Au_{24}Ag$	Phenylethanethiol, Triphenylphosphine	$[AgAu_{24}(PPh_3)_{10}(PET)_5Cl_2]^{2+}$	Crystal structure	Metal-deposition	443
$Au_{24}Cu$		$[CuAu_{24}(PPh_3)_{10}(PET)_5Cl_2]^{2+}$			
$Au_{24}Cd$	Phenylethanethiol	$Au_{24}Cd(SC_2H_4Ph)_{18}$	Characterization	Antigalvanic exchange	444
$Au_{24}Hg$		$Au_{24}Hg(SC_2H_4Ph)_{18}$			
$Au_{24}Pd$	Phenylethanethiol	$[Au_{24}Pd(PET)_{18}]^-$	Crystal structure	Coreduction	445
$Au_{24}Pt$	Phenylethanethiol	$[Au_{24}Pt(PET)_{18}]$	Crystal structure	Coreduction	446,447
$Au_{24}Pt$	3,5-$(CF_3)_2C_6H_3C{\equiv}CH$	$[MAu_{24}(C{\equiv}CR)_{18}]^{2-}$ (M = Pt, Pd)	DFT analysis	Coreduction	448
$Au_{24}Pd$					
$Au_{25-x}Cu_x$	Phenylethanethiol	$[Au_{25-x}Cu_x(PET)_{18}]$	Mass spectrometry	Coreduction	449
$Au_{24}Cd_2$	1,1-Bis(diphenylphosphino) propane, 1-Adamantanethiol	$Au_{24}Cd_2(SAdm)_{12}(dppp)_2Cl_2$	Crystal structure	Solution phase	450
Ag_2Au_{25}	Phenylethanethiol	$Ag_2Au_{25}(SR)_{18}$	Mass spectrometry	Metal-deposition	451
$Ag_{23}Au_4$	1,1′-Bis(diphenylphosphino) ferrocene, tert-butylalkynyl	$[Au_4Ag_{23}(C{\equiv}CBut)_{10}Cl_7(dppf)_4]^{2+}$	Crystal structure	Coreduction	452
$Ag_{26}Au$	2-Ethylbenzenethiol	$[Ag_{26}Au(2\text{-}EBT)_{18}(PPh_3)_6]^+$	Crystal structure	Galvanic exchange	453
$Au_{26}Pd$	Phenylethanethiol	$Au_{26}Pd(SPh^tBu)_{20}$	Characterization	Solution phase	454
$Ag_{26}Pt$	2-Ethylbenzenethiol	$Ag_{26}Pt(2\text{-}EBT)_{18}(PPh_3)_6$	Crystal structure	Coreduction	455
$Au_{27}Cd_1$	1,1′-Bis(diphenylphosphino) ferrocene, Adamantanethiol	$Au_{27}Cd_1(SAdm)_{14}(DPPF)Cl$	Crystal structure	Solution phase	456

(*continued on next page*)

TABLE 1 A summary of atomically precise nanoclusters synthesized so far (as on May 4, 2022, using web of science). Unprotected or naked clusters are not included. The list is alphabetical and in ascending order of nuclearity of clusters. Alloy clusters, listed separately, are arranged in ascending order of total nuclearity. For each nuclearity, an alphabetical order is followed—cont'd

Core	Ligand	Composition	Focus	Synthesis method	References
$Ag_{12}Cu_{12}Au_4Pt$	Adamantanethiol	$Pt_1Ag_{12}Cu_{12}Au_4(S\text{-}Adm)_{18}(PPh_3)_4$	Mass spectrometry	Galvanic reduction	457
$Ag_{16}Au_{13}$	Hydroxybenzonitrile, 3-Bromoprop-1-yne	$[Au_{13}Ag_{16}(C_{10}H_6NO)_{24}]^{3-}$	Crystal structure	Solution phase	458
$Ag_{17}Au_{12}$	1,3-Benzenedithiol, Triphenylphosphine	$Au_{12}Ag_{17}(BDT)_{12}(PPh_3)_4$	Mass spectrometry	Intercluster reaction	459
$Ag_{17}Cu_{12}$	1,3-Benznedithiol, Triphenylphosphine	$Ag_{17}Cu_{12}(SR)_{12}(PPh_3)_4$	Crystal structure	Coreduction	460
$Ag_{25}Cu_4$	Phenylacetylene, Triphenylphosphine	$[Ag_{25}Cu_4H_8Br_6(C{\equiv}CPh)_{12}(PPh_3)_{12}]^{3+}$	Crystal structure	Solution phase	461
$Ag_{28}Ni$	1,3-Benzenedithiol,	$NiAg_{28}(BDT)_{12}(PPh_3)_4$	Mass spectrometry	Coreduction	462
$Ag_{28}Pd$	Triphenylphosphine	$PdAg_{28}(BDT)_{12}(PPh_3)_4$			
$Ag_{28}Pt$	Adamantanethiol, Triphenylphosphine	$Pt_1Ag_{28}(SR)_{18}(PPh_3)_4$	Crystal structure	Ligand exchange	463
$Ag_{28-x}MAu_x$	1,3-Benzenedithiol, Triphenylphosphine	$MAu_xAg_{28-x}(BDT)_{12}(PPh_3)_4$ (M = Ni/Pd/Pt)	Mass spectrometry	Intercluster reaction	464
$Au_{24}Cu_6$	Tert-butylbenzenethiol	$Au_{24}Cu_6(TBBT)_{22}$	Crystal structure	Coreduction	465
$Ag_{20}Cu_{12}$	2,4-Dimethylbenzenethiol, 1,1-bis(diphenylphosphino) methane	$[Ag_{20}Cu_{12}(SR)_{14}(Dppm)_6Br_8]^{2+}$	Crystal structure	Coreduction	466
$Au_{34}Rh$	Poly vinyl 2-pyrrolidone (PVP)	$Au_{34}Rh_1Cl^-$	Mass spectrometry	Solution phase	467
Ag_xAu_{36-x}	Tert-butylbenzenethiol	$Au_{36-x}Ag_x(SPh\text{-}^tBu)_{24}$	Mass spectrometry	Coreduction	468
$Cu_{34}Pt_2$	Phenylethanethiol	$[Pt_2Cu_{34}(PET)_{22}Cl_4]^{2-}$	Crystal structure	Metal exchange	469
Ag_xAu_{38-x}	Phenylethanethiol	$Ag_xAu_{38-x}(SR)_{24}$	Crystal structure	Coreduction	470
$Ag_{20}Au_{18}$	Tri(p-tolyl)phosphine	$[(p\text{-}Tol_3P)_{12}Au_{18}Ag_{20}Cl_{14}]$	Crystal structure	Coreduction	471
$Au_{36}Pd_2$	Phenylethanethiol	$Au_{36}Pd_2(SC_2H_4Ph)_{24}$	Mass spectrometry	Coreduction	472
$Au_{37}Pd$	Phenylethanethiol	$Au_{37}Pd_1(SC_2H_4Ph)_{24}$	Mass spectrometry	Coreduction	473
$Au_{38-x}Cu_x$	2,4-Dimethylbenzenethiol	$Au_{38-x}Cu_x(2,4\text{-}(CH_3)_2C_6H_3S)_{24}$ ($x = 0$–6)	Crystal structure	Coreduction	474
$Ag_{37}Cu_2$	Pentafluorobenzenethiol, Triphenylphosphine	$[Ag_{37}Cu_2(PFBT)_{24}(TPP)_8]^{2-}$	Crystal structure	Solution Phase	475
$Ag_{28}Cu_{12}$	2,4-Dichlorobenzenethiol	$[Ag_{28}Cu_{12}(SR)_{24}]^{4-}$	Crystal structure	Coreduction	476
$Ag_{38}Au_3$	Phenylethanethiol	$[Au_3Ag_{38}(SCH_2Ph)_{24}X_5]^{2-}$ (X = Cl, Br)	Crystal structure	Coreduction	477
$Ag_{20}Au_{24}$	Phenylalkynyl, 2-pyridylthiol	$Au_{24}Ag_{20}(2\text{-}Spy)_4(PhC{\equiv}C)_{20}Cl_2$	Crystal structure	Coreduction	478
$Ag_{32}Au_{12}$	Fluorobenzenethiol	$[Ag_{32}Au_{12}(SR)_{30}]^{4-}$	Crystal structure	Intercluster reaction	479,480
$Ag_{32}Cd_{12}$	Phenylselenolate	$Cd_{12}Ag_{32}(SePh)_{36}$	Crystal structure	Solution phase	481
$Ag_{32}Cu_{12}$	Tris(4-methoxyphenyl)phosphine, Adamantanethiol	$[Ag_{32}Cu_{12}(CH_3COO)_{12}(SAdm)_{12}(P(CH_3OPh)_3)_4]$	Crystal structure	Solution phase	482
$Au_{12}Cu_{32}$	4-(trifluoromethyl)thiophenol	$Au_{12+n}Cu_{32}(SR)_{30+n}]^{4-}$ ($n = 0, 2, 4, 6$)	Crystal structure	Coreduction	483
$Ag_{24}Au_{22}$	Triphenylphosphine	$[(Ph_3P)_{12}Au_{22}Ag_{24}Cl_{10}]$	Crystal structure	Coreduction	484
$Au_{19}Cu_{30}$	3-Ethynylthiophene, ethynylbenzene	$[Au_{19}Cu_{30}(C{\equiv}CR)_{22}(Ph_3P)_6Cl_2]$	Crystal structure	Coreduction	485
$Ag_{50-x}Au_x$	1,1-Bis(diphenylphosphino)methane, Tert-butylbenzylmercaptan	$Au_xAg_{50-x}(dppm)_6(SR)_{30}$ R = TBBM	Crystal structure	Galvanic exchange	486
$Ag_{43}Au_{16}$	2,4-Dichlorobenzenethiol	$[Au_{16}Ag_{43}H_{12}(SPhCl_2)_{34}]^{5-}$	Crystal structure	Solution phase	487
$Ag_{28}Au_{34}$	Phenylacetylene	$Au_{34}Ag_{28}PhC{\equiv}C)_{34}$	Crystal structure	Coreduction	488
$Ag_{55}Au_8$	1,3-Bis(diphenylphosphino) propane, cyclohexanethiol	$[Au_8Ag_{55}(Dppp)_4(C_6H_{11}S)_{34}](BPh_4)_2$	Crystal structure	Ligand exchange	489
$Ag_{57}Au_8$	1,3-Bis(diphenylphosphino) propane, cyclohexanethiol	$[Au_8Ag_{57}(Dppp)_4(C_6H_{11}S)_{32}Cl_2]Cl$	Crystal structure	Coreduction	490

(*continued on next page*)

TABLE 1 A summary of atomically precise nanoclusters synthesized so far (as on May 4, 2022, using web of science). Unprotected or naked clusters are not included. The list is alphabetical and in ascending order of nuclearity of clusters. Alloy clusters, listed separately, are arranged in ascending order of total nuclearity. For each nuclearity, an alphabetical order is followed—cont'd

Core	Ligand	Composition	Focus	Synthesis method	References
$Ag_{46}Au_{24}$	Tert-butylthiol	$Ag_{46}Au_{24}(TBHP)_{32}]^{2+}$	Crystal structure	Coreduction	491
$Ag_{38}Au_{43}$	Dodecanethiol	$Au_{43}Ag_{38}(C_{12}H_{13})_{36}Cl$	Characterization	Solution phase	492
$Ag_{61}Cu_{30}$	Adamantanethiol	$[Cu_{30}Ag_{61}(SAdm)_{38}S_3](BPh_4)$	Crystal structure	Coreduction	493
$Ag_{30}Au_{80}$	Phenylacetylene	$[Au_{80}Ag_{30}$ $(PhC{\equiv}C)_{42}Cl_9]Cl$	Crystal structure	Coreduction	494
$Ag_{53}Au_{57}$	Phenylacetylene	$[Au_{57}Ag_{53}(PhC{\equiv}C)_{40}Br_{12}]$	Crystal structure	Coreduction	495
Ag_xAu_{130-x}	Tert-butylbenzenethiol	$Au_{130-x}Ag_x(TBBT)_{55}$	Crystal structure	Coreduction	496
$Ag_{60}Au_{74}$	Phenylacetylene	$[Au_{74}Ag_{60}(PhC{\equiv}C)_{40}Br_{12}]$	Crystal structure	Coreduction	497
$Ag_{66}Au_{78}$		$[Au_{78}Ag_{66}(PhC{\equiv}C)_{48}Cl_8]$			
$(Ag–Au)_{144}$	Phenylethanethiol	$(Ag–Au)_{144}(PET)_{60}$	Mass spectrometry	Coreduction	498
$Au_{144-x}Cu_x$	Hexanethiol	$Au_{144-x}Cu_x(SC_6H_{13})_{60}$	Mass spectrometry	Coreduction	499
$Pd_{164-x}Pt_x$	Triphenylphosphine	$Pd_{164-x}Pt_x(CO)_{72}(PPh_3)_{20}$ $(x \approx 7)$	Characterization	Solution phase	500

References

1. Fenske D, Langetepe T. Synthesis and structures of silver-selenide cluster complexes $[Ag_4(Se^iPr)_4(Dppm)_2]$, $[Ag_8(Set)_8(Dppp)_3]$, $[Ag_{28}Se_6(SenBu)_{16}(Dppp)_4]$, and $[Ag_{124}Se_{57}(SePtBu_2)_4Cl_6(^tBu_2P(CH_2)_3P^tBu_2)_{12}]$. *Angew Chem Int Ed Engl*. 2002;41:300–304.
2. Langetepe T, Fenske DN. Silver-telluride cluster stabilized with phosphines: synthesis and structure of $[Ag_5(TePh)_6(Ph_2P(CH_2)_2PPh_3)](Ph_2P(CH_2)_2PPh_2)\infty$, $[Ag_{18}Te(TePh)_{15}(Ph_2P(CH_2)_3PPh_2)_3Cl]$ and $[Ag_{38}Te_{13}(TetBu)_{12}(Ph_2P(CH_2)_2PPh_2)_3]$. *Z Anorg Allg Chem*. 2001;627:820–826.
3. Wu Z, Lanni E, Chen W, Bier ME, Ly D, Jin R. High yield, large scale synthesis of thiolate-protected Ag_7 clusters. *J Am Chem Soc*. 2009;131:16672–16674.
4. Udaya Bhaskara Rao T, Pradeep T. Luminescent Ag_7 and Ag_8 clusters by interfacial synthesis. *Angew Chemie Int Ed*. 2010;49:3925–3929.
5. Lecoultre S, Rydlo A, Buttet J, Félix C, Gilb S, Harbich W. Ultraviolet-visible absorption of small silver clusters in neon: Ag_n (n = 1-9). *J Chem Phys*. 2011;134.
6. Rao TUB, Nataraju B, Pradeep T. Ag_9 quantum cluster through a solid-state route. *J Am Chem Soc*. 2010;132:16304–16307.
7. Alamer BJ, Bootharaju MS, Kozlov SM, et al. $[Ag_9(1,2\text{-}BDT)_6]^{3-}$: how square-pyramidal building blocks self-assemble into the smallest silver nanocluster. *Inorg Chem*. 2021;60:4306–4312.
8. Zheng K, Yuan X, Xie J. Effect of ligand structure on the size control of mono- and bi-thiolate-protected silver nanoclusters. *Chem Commun (Camb)*. 2017;53:9697–9700.
9. Corrigan JF, Fenske D, Power WP. Silver-tellurolate polynuclear complexes: from isolated cluster units to extended polymer chains. *Angew Chem Int Ed Engl*. 1997;36:1176–1179.
10. Baksi A, Bootharaju MS, Chen X, Häkkinen H, Pradeep T. $Ag_{11}(SG)_7$: a new cluster identified by mass spectrometry and optical spectroscopy. *J Phys Chem C*. 2014;118(37):21722–21729.
11. Dar A, Jana A, Sugi KS, et al. Molecular engineering of atomically precise silver clusters into 2D and 3D framework solids. *Chem. Mater*. 2022;34(10):4703–4711.
12. Stillman MJ, Zelazowski AJ, Gasyna Z. Luminescent Ag_{12}-metallothionein: dependence of emission intensity on silver-thiolate cluster formation. *FEBS Lett*. 1988;240:159–162.
13. Yang H, Lei J, Wu B, et al. Crystal structure of a luminescent thiolated Ag nanocluster with an octahedral Ag_{14}^{+} core. *Chem Commun*. 2012;49:300–306.
14. Das AK, Mekkat R, Maity S, et al. Role of ligand on photophysical properties of nanoclusters with Fcc kernel: a case study of $Ag_{14}(SC_6H_4X)_{12}(PPh_3)_8$ (X = F, Cl, Br). *Inorg Chem*. 2021;60:19270–19277.

15. Deng G, Teo BK, Zheng N. Assembly of chiral cluster-based metal-organic frameworks and the chirality memory effect during their disassembly. *J Am Chem Soc*. 2021;143:10214–10220.
16. Nayek HP, Massa W, Dehnen S. Presence or absence of a central Se atom in silver selenide/selenolate clusters with halite topology: syntheses and properties of $[(Ph_3PAg)_8Ag_6(Mu_6\text{-}Se)(1\text{-}x/2)(SePh)_{12}]^{X+}$ (x = 0, 1). *Inorg Chem*. 2010;49:144–149.
17. Jin X, Tang K, Liu W, et al. Formation and X-ray structure of a novel tetradecanuclear silver cluster complex, $Ag_{l4}(M_6\text{-}S)(SPh)_{12}(PPh_3)_8{\cdot}4CH_3OH\ 13H_2O$. *Polyhedron*. 1996;15:1207–1211.
18. Langer R, Breitung B, Wünsche L, Fenske D, Fuhr O. Functionalised silver chalcogenide clusters. *Z Anorg Allg Chem*. 2011;637:995–1006.
19. Mathew A, Sajanlal PR, Pradeep T. A fifteen atom silver cluster confined in bovine serum albumin. *J Mater Chem*. 2011;21:11205–11212.
20. Jash M, Khatun E, Chakraborty P, Sudhakar C, Pradeep T. $[Ag_{15}H_{13}(DPPH)_5]^{2+}$ and $[Ag_{27}H_{22}(DPPB)_7]^{3+}$: two new hydride and phosphine co-protected clusters and their fragmentation leading to naked clusters, Ag_{13}^{+} and Ag_{25}^{+}. *J Phys Chem C Nanomater Interfaces*. 2020;124:20569–20577.
21. Bertorelle F, Hamouda R, Rayane D, et al. Synthesis, characterization and optical properties of low nuclearity liganded silver clusters: $Ag_{31}(SG)_{19}$ and $Ag_{15}(SG)_{11}$. *Nanoscale*. 2013;5:5637–5643.
22. Yang H, Wang Y, Zheng N. Stabilizing subnanometer Ag(0) nanoclusters by thiolate and diphosphine ligands and their crystal structures. *Nanoscale*. 2013;5:2674–2677.
23. Dar WA, Bodiuzzaman M, Ghosh D, et al. Interparticle reactions between silver nanoclusters leading to product cocrystals by selective cocrystallization. *ACS Nano*. 2019;13:13365–13373.
24. Zhang M-M, Dong X-Y, Wang Z-Y, et al. Alkynyl-stabilized superatomic silver clusters showing circularly polarized luminescence. *J Am Chem Soc*. 2021;143:6048–6053.
25. Bootharaju MS, Dey R, Gevers LE, Hedhili MN, Basset J-M, Bakr OM. A new class of atomically precise, hydride-rich silver nanoclusters co-protected by phosphines. *J Am Chem Soc*. 2016;138:13770–13773.
26. Langetepe T, Fenske D. Neue silver-telluride cluster stabilized with phosphines: synthesis and structure of $[Ag_5(TePh)_6(Ph_2P(CH_2)_2PPh_3)](Ph_2P(CH_2)_2PPh_2)\infty$, $[Ag_{18}Te(TePh)_{15}(Ph_2P(CH_2)_3PPh_2)_3Cl]$ and $[Ag_{38}Te_{13}(TetBu)_{12}(Ph_2P(CH_2)_2PPh_2)_3]$. *Z Anorg Allg Chem*. 2001;627:820–826.
27. Yuan S, Pei L, Qing, T, De-en, J, Wang QM. Alkynyl-protected silver nanoclusters featuring an anticuboctahedral kernel. *Nanoscale*. 2017;9:11405–11410.
28. Dhayal RS, Lin Y-R, Liao J-H, et al. $[Ag_{20}\{S_2P(OR)_2\}_{12}]$: a superatom complex with a chiral metallic core and high potential for isomerism. *Chemistry*. 2016;22:9943–9947.
29. Dhayal RS, Liao J-H, Liu Y-C, et al. $[Ag_{21}\{S_2P(O^iPr)_2\}_{12}]^{+}$: an eight-electron superatom. *Angew Chemie Int Ed*. 2015;54:3702–3706.
30. Guan Z-J, He R-L, Yuan S-F, et al. Ligand engineering toward the trade-off between stability and activity in cluster catalysis. *Angew Chem Int Ed Engl*. 2022;61.
31. Jana A, Unnikrishnan P, Poonia A, et al. Carborane-thiol protected propeller-shaped photoresponsive silver nanomolecule. *Inorg Chem*. 2022;61(23):8593–8603.
32. Khatun E, Bodiuzzaman M, Sugi KS, et al. Confining an Ag_{10} core in an Ag_{12} shell: a four-electron superatom with enhanced photoluminescence upon crystallization. *ACS Nano*. 2019;13:5753–5759.
33. Wang X-J, Langetepe T, Fenske D, Kang B-S. Synthesis and structure of polymeric silver-complexes $[Ag_2Cl_2(Dppbp)_3]\infty$, $[Ag_2(SPh)_2(Dppe)_3]\infty$ and $[Ag_2(SPh)_2(Triphos)]\infty$ and silver-chalkogenide-cluster $[Ag_7(SPh)_7(Dppm)_3]$, $[Ag_7(TePh)_7(Dppp)_3]_2(Dppp)$ and $[Ag_{22}Cl(SPh)_{10}(PhCOO)_{11}(Dmf)_3]\infty$. *Z Anorg Allg Chem*. 2002;628:1158.
34. Liu C, Li T, Abroshan H, et al. Chiral Ag_{23} nanocluster with open shell electronic structure and helical face-centered cubic framework. *Nat Commun*. 2018;9:744–748.
35. Li S, Dong X-Y, Qi K-S, Zang S-Q, Mak TCW. Full-color tunable circularly polarized luminescence induced by the crystal defect from the co-assembly of chiral silver (I) clusters and dyes. *J Am Chem Soc*. 2021;143:20574–20578.
36. Joshi CP, Bootharaju MS, Alhilaly MJ, Bakr OM. $[Ag_{25}(SR)_{18}]^{-}$: The "golden" silver nanoparticle. *J Am Chem Soc*. 2015;137:11578–11581.
37. Zhao M, Huang S, Fu Q, et al. Ambient chemical fixation of CO_2 using a robust Ag_{27} cluster-based two-dimensional metal-organic framework. *Angew Chem Int Ed Engl*. 2020;59:20031–20036.
38. Fenske D, Langetepe T. Synthesis and structures of silver-selenide cluster complexes $[Ag_4(SeiPr)_4(Dppm)_2]$, $[Ag_8(SeEt)_8(Dppp)]_3$, $[Ag_{28}Se_6(SenBu)_{16}(Dppp)_4]$, and $[Ag_{124}Se_{57}(SePtBu_2)_4Cl_6(TBu_2P(CH_2)_3P^tBu_2)_{12}]$. *Angew Chem Int Ed Engl*. 2002;41:300–304.

39. AbdulHalim LG, Bootharaju MS, Tang Q, et al. $Ag_{29}(BDT)_{12}(TPP)_4$: a tetravalent nanocluster. *J Am Chem Soc*. 2015;137(37):11970–11975.
40. Chakraborty P, Nag A, Paramasivam G, Natarajan G, Pradeep T. Fullerene-functionalized monolayer-protected silver clusters: $[Ag_{29}(BDT)_{12}(C_{60})_n]^{3-}$ (n = 1–9). *ACS Nano*. 2018;12:2415–2425.
41. Zeng Y, Havenridge S, Gharib M, et al. Impact of ligands on structural and optical properties of Ag_{29} nanoclusters. *J Am Chem Soc*. 2021;143:9405–9414.
42. Khatun E, Ghosh A, Chakraborty P, et al. A thirty-fold photoluminescence enhancement induced by secondary ligands in monolayer protected silver clusters. *Nanoscale*. 2018;10:20033–20042.
43. Van der Linden M, Barendregt A, van Bunningen AJ, et al. Characterisation, degradation and regeneration of luminescent Ag_{29} clusters in solution. *Nanoscale*. 2016;8:19901–19909.
44. Xia N, Yang J, Wu Z. Fast, high-yield synthesis of amphiphilic Ag nanoclusters and the sensing of Hg^{2+} in environmental samples. *Nanoscale*. 2015;7:10013–10020.
45. Corrigan FJ. Mono- and bis-silylated tellurium reagents in silver–telluride cluster synthesis: characterization of $Ag_{30}Te_{21}$ and $Ag_{46}Te_{29}$ complexes. *Chem Commun (Camb.)*. 1997;19:1837.
46. Fenske D, Zhu N, Langetepe T. Synthesis and structure of new Ag-Se clusters: $[Ag_{30}Se_8(SetBu)_{14}(PnPr_3)_8]$, $[Ag_{90}\ Se_{38}\ (SetBu)_{14}(PEt_3)_{22}]$, $[Ag_{114}Se_{34}(SenBu)_{46}(P^tBu_3)_{14}]$, $[Ag_{112}Se_{32}(SenBu)_{48}(P^tBu_3)_{12}]$, and $[Ag_{172}Se_{40}(SenBu)_{92}(Dppp)_4]$. *Angew Chem Int Ed Engl*. 1998;37:2639–2644.
47. Bertorelle F, Hamouda R, Rayane D, et al. Synthesis, characterization and optical properties of low nuclearity liganded silver clusters: $Ag_{31}(SG)_{19}$ and $Ag_{15}(SG)_{11}$. *Nanoscale*. 2013;5:5637–5643.
48. Guo J, Kumar S, Bolan M, Desireddy A, Bigioni TP, Griffith WP. Mass spectrometric identification of silver nanoparticles: the case of $Ag_{32}(SG)_{19}$. *Anal Chem*. 2012;84:5304–5308.
49. Udayabhaskararao T, Bootharaju MS, Pradeep T. Thiolate-protected Ag_{32} clusters: mass spectral studies of composition and insights into the Ag-thiolate structure from NMR. *Nanoscale*. 2013;5:9404–9411.
50. Tian F, Chen R. Pd-mediated synthesis of Ag_{33} chiral nanocluster with core-shell structure in T point group. *J Am Chem Soc*. 2019;141:7107–7114.
51. Li B, Huang R-W, Qin J-H, et al. Thermochromic luminescent nest-like silver thiolate cluster. *Chemistry*. 2014;20:12416–12420.
52. Manju CK, Ghosh D, Bodiuzzaman M, Pradeep T. Formation of an NIR-emitting $Ag_{34}S_3SBB_{20}(CF_3COO)_6^{2+}$ cluster from a hydride-protected silver cluster. *Dalton Trans*. 2019;48:8664–8670.
53. Guan Z-J, Zeng J-L, Nan Z-A, Wan X-K, Lin Y-M, Wang Q-M. Thiacalix[4]arene: new protection for metal nanoclusters. *Sci Adv*. 2016;2 e1600323.
54. Li X-Y, Su H-F, Yu K, et al. A platonic solid templating archimedean solid: an unprecedented nanometre-sized Ag_{37} cluster. *Nanoscale*. 2015;7:8284–8288.
55. Yang H, Yan J, Wang Y, et al. Embryonic growth of face-center-cubic silver nanoclusters shaped in nearly perfect half-cubes and cubes. *J Am Chem Soc*. 2017;139:31–34.
56. Ma X-H, Si Y, Luo L-L, Wang Z-Y, Zang S-Q, Mak TCW. Directional doping and cocrystallizing an open-shell Ag_{39} superatom via precursor engineering. *ACS Nano*. 2022;16(4):5507–5514.
57. Chai J, Yang S, Lv Y, et al. A unique pair: Ag_{40} and Ag_{46} nanoclusters with the same surface but different cores for structure–property correlation. *J Am Chem Soc*. 2018;140:15582–15585.
58. Bodiuzzaman M, Ghosh A, Sugi KS, et al. Camouflaging structural diversity: co-crystallization of two different nanoparticles having different cores but the same shell. *Angew Chem Int Ed Engl*. 2019;58:189–194.
59. Jana A, Jash M, Poonia AK, et al. Light-activated intercluster conversion of an atomically precise silver nanocluster. *ACS Nano*. 2021;15:15781–15793.
60. Harkness KM, Tang Y, Dass A, et al. $Ag_{44}(SR)_{30}^{4-}$: a silver-thiolate superatom complex. *Nanoscale*. 2012;4:4269–4274.
61. AbdulHalim LG, Ashraf S, Katsiev K, et al. A scalable synthesis of highly stable and water dispersible $Ag_{44}(SR)_{30}$ nanoclusters. *J Mater Chem A*. 2013;1:10148–10154.
62. AbdulHalim LG, Hooshmand Z, Parida MR, et al. pH-induced surface modification of atomically precise silver nanoclusters: an approach for tunable optical and electronic properties. *Inorg Chem*. 2016;55(21):11522–11528.
63. Yang H, Wang Y, Huang H, et al. All-thiol-stabilized Ag_{44} and $Au_{12}Ag_{32}$ nanoparticles with single-crystal structures. *Nat Commun*. 2013;4:2422.
64. Desireddy A, Conn BE, Guo J, et al. Ultrastable silver nanoparticles. *Nature*. 2013;501:399–402.

65. Bootharaju MS, Lee S, Deng G, et al. $Ag_{44}(EBT)_{26}(TPP)_4$ nanoclusters with tailored molecular and electronic structure. *Angew Chem Int Ed Engl*. 2021;60:9038–9044.
66. Chakraborty I, Kurashige W, Kanehira K, et al. $Ag_{44}(SeR)_{30}$: a hollow cage silver cluster with selenolate protection. *J Phys Chem Lett*. 2013:3351–3355.
67. Chakraborty I, Pradeep T. Reversible formation of Ag_{44} from selenolates. *Nanoscale*. 2014;6:14190–14194.
68. Conn BE, Desireddy A, Atnagulov A, et al. $M_4Ag_{44}(p\text{-}MBA)_{30}$ molecular nanoparticles. *J Phys Chem C*. 2015;119:11238–11249.
69. Som A, Chakraborty I, Maark TA, Bhat S, Pradeep T. Cluster-mediated crossed bilayer precision assemblies of 1D nanowires. *Adv Mater*. 2016;28:2827–2833.
70. Chakraborty I, Som A, Adit Maark T, Mondal B, Sarkar D, Pradeep T. Toward a janus cluster: regiospecific decarboxylation of $Ag_{44}(4\text{-}MBA)_{30}$@Ag nanoparticles. *J Phys Chem C*. 2016;120:15471–15479.
71. Tasaka Y, Nakamura K, Malola S, et al. Electron binding in a superatom with a repulsive coulomb barrier: the case of $[Ag_{44}(SC_6H_3F_2)_{30}]^{4-}$ in the gas phase. *J Phys Chem Lett*. 2020;11:3069–3074.
72. Bootharaju MS, Burlakov VM, Besong TMD, et al. Reversible size control of silver nanoclusters via ligand-exchange. *Chem Mater*. 2015;27:4289–4297.
73. Du W, Deng S, Chen S, et al. Anisotropic evolution of nanoclusters from Ag_{40} to Ag_{45}: halogen- and defect-induced epitaxial growth in nanoclusters. *J Phys Chem Lett*. 2021;12:6654–6660.
74. Liu X, Chen J, Yuan J, et al. A silver nanocluster containing interstitial sulfur and unprecedented chemical bonds. *Angew Chem Int Ed Engl*. 2018;57:11273–11277.
75. Liu W, Wang J, Yuan S, Chen X, Wang Q. Chiral superatomic nanoclusters Ag_{47} induced by the ligation of amino acids. *Angew Chem Weinheim Bergstr Ger*. 2021;133:11531–11536.
76. Zhang S-S, Alkan F, Su H-F, Aikens CM, Tung C-H, Sun D. $[Ag_{48}(C{\equiv}C\ TBu)_{20}(CrO_4)_7]$: an atomically precise silver nanocluster co-protected by inorganic and organic ligands. *J Am Chem Soc*. 2019;141:4460–4467.
77. Wei X, Shen H, Xu C, et al. Ag_{48} and Ag_{50} nanoclusters: toward active-site tailoring of nanocluster surface structures. *Inorg Chem*. 2021;60:5931–5936.
78. Du W, Jin S, Xiong L, et al. $Ag_{50}(Dppm)_6(SR)_{30}$ and its homologue $Au_xAg_{50-x}(Dppm)_6(SR)_{30}$ alloy nanocluster: seeded growth, structure determination, and differences in properties. *J Am Chem Soc*. 2017;139:1618–1624.
79. Chakraborty I, Mahata S, Mitra A, De G, Pradeep T. Controlled synthesis and characterization of the elusive thiolated Ag_{55} cluster. *Dalton Trans*. 2014;43:17904–17907.
80. Wang Z, Li M-D, Shi J-Y, et al. In situ capture of a ternary supramolecular cluster in a 58-nuclei silver supertetrahedron. *CCS Chem*. 2021;4:1788–1795.
81. Khatun E, Ghosh A, Ghosh D, et al. $[Ag_{59}(2,5\text{-}DCBT)_{32}]$: A1 new cluster and a precursor for three well-known clusters. *Nanoscale*. 2017;9:8240–8248.
82. Su Y-M, Li X-Y, Wang Z, et al. Structural rearrangement of Ag_{60} nanocluster endowing different luminescence performances. *J Chem Phys*. 2021;155.
83. Yuan S-F, Xu C-Q, Liu W-D, Zhang J-X, Li J, Wang Q-M. Rod-shaped silver supercluster unveiling strong electron coupling between substituent icosahedral units. *J Am Chem Soc*. 2021;143:12261–12267.
84. Li G, Lei Z, Wang Q-M. Luminescent molecular Ag-S nanocluster $[Ag_{62}S_{13}(SBut)_{32}](BF_4)_4$. *J Am Chem Soc*. 2010;132:17678–17679.
85. Diecke M, Schrenk C, Schnepf A. Synthesis and characterization of the highly unstable metalloid cluster $Ag_{64}(PnBu_3)_{16}Cl_6$. *Angew Chem Int Ed Engl*. 2020;59:14418–14422.
86. Chitsaz S, Fenske D, Fuhr O. Silver chalcogenide clusters with dimethylanilinomercapto ligands: syntheses and crystal structures of $[Ag_{65}S_{13}(SC_6H_4NMe_2)_{39}(Dppm)_5]$, $[Ag_{76}Se_{13}(SC_6H_4NMe_2)_{50}(PPh_3)_{6.5}]$, and $[Ag_{88}Se_{12}(SC_6H_4NMe_2)_{63}(PPh_3)_6]$. *Angew Chem Int Ed Engl*. 2006;45:8055–8059.
87. Alhilaly MJ, Bootharaju MS, Joshi CP, et al. $[Ag_{67}(SPhMe_2)_{32}(PPh_3)_8]^{3+}$: synthesis, total structure, and optical properties of a large box-shaped silver nanocluster. *J Am Chem Soc*. 2016;138(44):14727–14732.
88. Ghosh A, Pradeep T. Synthesis of atomically precise silver clusters by using the miscibility principle. *Eur J Inorg Chem*. 2014;2014:5271–5275.
89. Wang X-J, Langetepe T, Persau C, Kang B-S, Sheldrick GM, Fenske D. Syntheses and crystal structures of the new Ag-S clusters $[Ag_{70}S_{16}(SPh)_{34}(PhCO_2)_4(Triphos)_4]$ and $[Ag_{188}S_{94}(PR_3)_{30}]$. *Angew Chem Int Ed Engl*. 2002;41:3818–3822.
90. Fenske D, Persau C, Dehnen S, Anson CE. Syntheses and crystal structures of the Ag[Bond]S cluster compounds $[Ag_{70}S_{20}(SPh)_{28}(Dppm)_{10}](CF_3CO_2)_2$ and $[Ag_{262}S_{100}(StBu)_{62}(Dppb)_6]$. *Angew Chem Int Ed Engl*. 2004;43:305–309.

91. Zhou M, Bao Y, Jin S, Wen S, Chen S, Zhu M. $[Ag_{71}(S\text{-}tBu)_{31}(dppm)](SbF_6)_2$: an intermediate-sized metalloid silver nanocluster containing a building block of Ag_{64}. *Chem Commun (Camb)*. 2021;57:10383–10386.
92. Qu M, Li H, Xie L-H, et al. Bidentate phosphine-assisted synthesis of an all-alkynyl-protected Ag_{74} nanocluster. *J Am Chem Soc*. 2017;139:12346–12349.
93. Chakraborty I, Udayabhaskararao T, Pradeep T. High temperature nucleation and growth of glutathione protected [similar]Ag_{75} clusters. *Chem Commun*. 2012;48:6788–6790.
94. Chitsaz S, Fenske D, Fuhr O. Silver chalcogenide clusters with dimethylanilinomercapto ligands: syntheses and crystal structures of $[Ag_{65}S_{13}(SC_6H_4NMe_2)_{39}(Dppm)_5]$, $[Ag_{76}Se_{13}(SC_6H_4NMe_2)_{50}(PPh_3)_{6.5}]$, and $[Ag_{88}Se_{12}(SC_6H_4NMe_2)_{63}(PPh_3)_6]$. *Angew Chem Int Ed Engl*. 2006;45:8055–8059.
95. Zhang W-J, Liu Z, Song K-P, et al. A 34-electron superatom Ag_{78} cluster with regioselective ternary ligands shells and its 2D rhombic superlattice assembly. *Angew Chem Int Ed Engl*. 2021;60:4231–4237.
96. Wang Z, Sun H-T, Kurmoo M, et al. Carboxylic acid stimulated silver shell isomerism in a triple core-shell Ag_{84} nanocluster. *Chem Sci*. 2019;10:4862–4867.
97. Wang Z, Su H-F, Gong Y-W, et al. A hierarchically assembled 88-nuclei silver-thiacalix[4]arene nanocluster. *Nat Commun*. 2020;11:308.
98. Su Y-M, Wang Z, Schein S, Tung C-H, Sun D. A Keplerian Ag_{90} nest of platonic and archimedean polyhedra in different symmetry groups. *Nat Commun*. 2020;11:3316.
99. Bestgen S, Yang X, Issac I, Fuhr O, Roesky PW, Fenske D. Adamantyl- and furanyl-protected nanoscale silver sulfide clusters. *Chemistry*. 2016;22:9933–9937.
100. Hu F, Li J-J, Guan Z-J, Yuan S-F, Wang Q-M. Formation of an alkynyl-protected Ag_{112} silver nanocluster as promoted by chloride released in situ from CH_2Cl_2. *Angew Chem Int Ed Engl*. 2020;59:5312–5315.
101. Fenske D, Zhu N, Langetepe T. Synthesis and structure of new Ag-Se clusters: $[Ag_{30}Se_8(SetBu)_{14}(PnPr_3)_8]$, $[Ag_{90}Se_{38}(SetBu)_{14}(PEt_3)_{22}]$, $[Ag_{114}Se_{34}(SenBu)_{46}(PtBu_3)_{14}]$, $[Ag_{112}Se_{32}(SenBu)_{48}(PtBu_3)_{12}]$, and $[Ag_{172}Se_{40}(SenBu)_{92}(Dppp)_4]$. *Angew Chem Int Ed Engl*. 1998;37:2639–2644.
102. Fenske D, Anson CE, Eichhöfer A, et al. Syntheses and crystal structures of $[Ag_{123}S_{35}(StBu)_{50}]$ and $[Ag_{344}S_{124}(StBu)_{96}]$. *Angew Chem Int Ed Engl*. 2005;44:5242–5246.
103. Fenske D, Langetepe T. Synthesis and structures of silver-selenide cluster complexes $[Ag_4(SeiPr)_4(Dppm)_2]$, $[Ag_8(SeEt)_8(Dppp)]_\infty$, $[Ag_{28}Se_6(SenBu)_{16}(Dppp)_4]$, and $[Ag_{124}Se_{57}(SeP^tBu_2)_4Cl_6(^tBu_2P(CH_2)_3P^tBu_2)_{12}]$. *Angew Chem Int Ed Engl*. 2002;41:300–304.
104. Yang H, Wang Y, Chen X, et al. Plasmonic twinned silver nanoparticles with molecular precision. *Nat Commun*. 2016;7:12809.
105. Branham MR, Douglas AD, Mills AJ, Tracy JB, White PS, Murray RW. Arylthiolate-protected silver quantum dots. *Langmuir*. 2006;22:11376–11383.
106. Song Y, Lambright K, Zhou M, et al. Large-scale synthesis, crystal structure, and optical properties of the $Ag_{146}Br_2(SR)_{80}$ nanocluster. *ACS Nano*. 2018;12:9318–9325.
107. Chakraborty I, Govindarajan A, Erusappan J, et al. The superstable 25 kDa monolayer protected silver nanoparticle: measurements and interpretation as an icosahedral $Ag_{152}(SCH_2CH_2Ph)_{60}$ cluster. *Nano Lett*. 2012;12:5861–5866.
108. Chakraborty I, Bag S, Landman U, Pradeep T. Atomically precise silver clusters as new SERS substrates. *J Phys Chem Lett*. 2013;4:2769–2773.
109. Wang X-J, Langetepe T, Persau C, Kang B-S, Sheldrick GM, Fenske D. Syntheses and crystal structures of the new Ag-S clusters $[Ag_{70}S_{16}(SPh)_{34}(PhCO_2)_4(Triphos)_4]$ and $[Ag_{188}S_{94}(PR_3)_{30}]$. *Angew Chem Int Ed Engl*. 2002;41:3818–3822.
110. Liu J-Y, Alkan F, Wang Z, et al. Different silver nanoparticles in one crystal: $Ag_{210}(iPrPhS)_{71}(Ph_3P)_5Cl$ and $Ag_{211}(iPrPhS)_{71}(Ph_3P)_6Cl$. *Angew Chem Int Ed Engl*. 2019;58:195–199.
111. Fenske D, Persau C, Dehnen S, Anson CE. Syntheses and crystal structures of the Ag[Bond]S cluster compounds $[Ag_{70}S_{20}(SPh)_{28}(Dppm)_{10}](CF_3CO_2)_2$ and $[Ag_{262}S_{100}(StBu)_{62}(Dppb)_6]$. *Angew Chem Int Ed Engl*. 2004;43:305–309.
112. Negishi Y, Arai R, Niihori Y, Tsukuda T. Isolation and structural characterization of magic silver clusters protected by 4-(tert-butyl)benzyl mercaptan. *Chem Commun*. 2011;47:5693–5695.
113. Ma M-X, Ma X-L, Liang G-M, et al. A nanocluster $[Ag_{307}Cl_{62}(SPhtBu)_{110}]$: chloride intercalation, specific electronic state, and superstability. *J Am Chem Soc*. 2021;143:13731–13737.
114. Fenske D, Anson CE, Eichhöfer A, et al. Syntheses and crystal structures of $[Ag_{123}S_{35}(S^tBu)_{50}]$ and $[Ag_{344}S_{124}(S^tBu)_{96}]$. *Angew Chem Int Ed Engl*. 2005;44:5242–5246.

115. Anson CE, Eichhöfer A, Issac I, et al. Synthesis and crystal structures of the ligand-stabilized silver chalcogenide clusters $[Ag_{154}Se_{77}(Dppxy)_{18}]$, $[Ag_{320}(StBu)_{60}S]$, $[Ag_{352}S_{128}(S^tC_5H_{11})_{96}]$, and $[Ag_{490}S_{188}(S^tC_5H_{11})_{114}]$. *Angew Chem Int Ed Engl*. 2008;47:1326–1331.
116. Briant OE, Hall KP, Mingos DMP. Unusual degradation reaction of icosahedral cluster compounds of gold with chelating diphosphanes and the X-ray structure of dis(dephenylphosphino)methanido-digold(I), $\{Au(Ph_2P)_2CH\}_2$. *J Organomet Chem*. 1982;229:C5–C8.
117. Schwerdtfeger P, Boyd PDW. Role of phosphine ligands in gold cluster chemistry. Relativistic SCF calculations on Au_2 and $Au_2(Ph_3)_2$. *Inorg Chem*. 1992;31:327–329.
118. Mingos DMP, Powell HR, Stolberg TL. Synthesis and structural characterization of the tetrahedral cluster $[Au_4(PPh_3)_4(M_2\text{-}SnCl_3)_2]$. *Transit Met Chem*. 1992;17:334–337.
119. Demartin F, Manassero M, Naldini L, Ruggeri R, Sansoni M. Synthesis and X-ray characterization of an iodine-bridged tetranuclear gold cluster, di-[small micro]-iodo-tetrakis(Triphenylphosphine)-tetrahedro-tetragold. *J Chem Soc Chem Commun*. 1981;5:222–223.
120. Van der Velden JWA, Bour JJ, Vollenbroek FA, Beurskens PT, Smits JMM. Synthesis of a new pentanuclear gold cluster by metal evaporation. Preparation and X-ray structure determination of [tris{bis(diphenylphosphino)methane}][bis(diphenylphosphino)methanido]pentagold dinitrate. *J Chem Soc Chem Commun*. 1979;24:1162–1163.
121. Hewitt MA, Hernández H, Johnson GE. ESI-MS identification of the cationic phosphine-ligated gold clusters $Au_{1\text{-}22}$: insight into the gold-ligand ratio and abundance of larger clusters. *J Am Soc Mass Spectrom*. 2021;32:237–246.
122. Van der Velden JWA, Vollenbroek FA, Bour JJ, Beurskens PT, Smits JMM, Bosnian WP. Gold clusters containing bidentate phosphine ligands. Preparation and X-ray structure investigation of $[Au_5(DppmH)_3(Dppm)](NO_3)_2$ and $[Au_{13}(DppmH)_6](NO_3)$n. *Recl Trav Chim Pays Bas*. 1981;100:148–152.
123. Briant CE, Hall KP, Mingos DMP. Synthesis and structural characterisation of $[Au_6(pph_3)_6]^{\cdot}(NO_3)_2{\cdot}3CH_2Cl_2$, an edge-shared bitetrahedral gold cluster. *J Organomet Chem*. 1983;254:C18–C20.
124. Briant CE, Hall KP, Mingos DMP, Wheeler AC. Synthesis and structural characterisation of hexakis(triphenyl phosphine)hexagold(2+) nitrate, $[Au_6(PPh_3)_6][NO_3]_2$, and related clusters with edgesharing bitetrahedral geometries. *J Chem Soc Dalton Trans*. 1986;3:687–692.
125. Ren X, Fu J, Lin X, et al. Cluster-to-cluster transformation among Au_6, Au_8 and Au_{11} nanoclusters. *Dalton Trans*. 2018;47:7487–7491.
126. Sabooni Asre Hazer M, Malola S, Häkkinen H. Isomer dynamics of the $[Au_6(NHC\text{-}S)_4]^{2+}$ nanocluster. *Chem Commun (Camb)*. 2022;58:3218–3221.
127. Moreaud L, Prasad J, Mazères S, et al. Facile one-pot synthesis of white emitting gold nanocluster solutions composed of red, green and blue emitters. *J Mater Chem C Mater Opt Electron Devices*. 2022;10:2263–2270.
128. Van der Velden JWA, Beurskens PT, Bour JJ, et al. Intermediates in the formation of gold clusters. Preparation and x-ray analysis of $[Au_7(PPh_3)_7]^+$ and synthesis and characterization of $[Au_8(PPh_3)_6I]PF_6$. *Inorg Chem*. 1984;23:146–151.
129. Vollenbroek FA, Bosman WP, Bour JJ, Noordik JH, Beurskens PT. Reactions of gold-phosphine cluster compounds. Preparation and X-ray structure determination of octakis(triphenylphosphine)octa-gold bis(hexafluorophosphate). *J Chem Soc Chem Commun*. 1979;9:387–388.
130. Van der Velden JWA, Bour JJ, Bosman WP, Noordik JH. Synthesis and X-ray crystal structure determination of the cationic gold cluster compound $[Au_8(PPh_3)_7](NO_3)_2$. *Chem Commun*. 1981;23:1218–1219.
131. Bellon PL, Cariati F, Manassero M, Naldini L, Sansoni M. Novel gold clusters. Preparation, properties, and X-ray structure determination of salts of octakis(triarylphosphine)enneagold, $[Au_9L_8]X_3$. *J Chem Soc D: Chem Commun*. 1971;22:1423–1424.
132. Hall KP, Theoblad BRC, Gilmour DI, Mingos DMP, Welch AJ. Synthesis and structural characterization of $[Au_9\{P(p\text{-}C_6H_4OMe)_3\}_8](BF_4)_3$, a cluster with a centred crown of gold atoms. *J Chem Soc Chem Commun*. 1982;10:528–530.
133. Jaw HRC, Mason WR. Magnetic circular dichroism spectra for the octakis(triphenylphosphino)nonagold(3+) ion. *Inorg Chem*. 1991;30:275–278.
134. Bos W, Bour JJ, Van der Velden JWA, Steggerda JJ, Casalnuovo AL, Pignolet LH. Gold clusters. Reactivity of $[Au_9(PPh_3)_8]^{3+}$ and $[Au_8(PPh_3)_7]^{2+}$ towards isopropyl isocyanide. *J Organomet Chem*. 1983;253:C64–C66.

135. Man RWY, Yi H, Malola S, et al. Synthesis and characterization of enantiopure chiral bis NHC-stabilized edge-shared Au_{10} nanocluster with unique prolate shape. *J Am Chem Soc*. 2022;144:2056–2061.
136. Briant CE, Hall KP, Wheeler AC, Mingos DMP. Structural characterisation of $[Au_{10}Cl_3(PCy_2Ph)_6](NO_3)$(Cy = cyclohexyl) and the development of a structural principle for high nuclearity gold clusters. *J Chem Soc Chem Commun*. 1984;4:248–250.
137. Cheetham GMT, Harding MM, Haggitt JL, Mingos DMP, Powell HR. Synthesis and microcrystal structure determination of $[Au_{10}(PPh_3)_7(S_2C_2(CN)_2)_2]$ with monochromatic synchrotron-radiation. *J Chem Soc Chem Commun*. 1993;12:1000–1001.
138. Laguna A, Laguna M, Gimeno MC, Jones PG. Synthesis and X-ray characterization of the neutral organometallic gold cluster $[Au_{10}(C_6F_5)_4(PPh_3)_5]$. *Organometallics*. 1992;11:2759–2760.
139. Lummis PA, Osten KM, Levchenko TI, et al. NHC-stabilized Au_{10} nanoclusters and their conversion to Au_{25} nanoclusters. *JACS Au*. 2022;2:875–885.
140. McPartlin M, Mason R, Malatesta L. Novel cluster complexes of gold(0)-gold(I). *J Chem Soc D: Chem Commun*. 1969;7:334.
141. Albano VG, Bellon PL, Manassero M, Sansoni M. Intermetallic pattern in metal-atom clusters. Structural studies on $Au_{11}X_3(PR_3)_7$ species. *J Chem Soc D: Chem Commun*. 1970;18:1210–1211.
142. Bellon P, Manassero M, Sansoni M. Crystal and molecular structure of tri-iodoheptakis(tri-p-fluorophenylphosphine)undecagold. *J Chem Soc Dalton Trans*. 1972;14:1481–1487.
143. Wang Z, Cai W, Sui J. Blue luminescence emitted from monodisperse thiolate-capped Au_{11} clusters. *Chem Phys Chem*. 2009;10:2012–2015.
144. Wang Z, Wu L, Cai W, Jiang Z. Luminescent Au_{11} nanocluster superlattices with high thermal stability. *J Mater Chem*. 2012;22:3632–3636.
145. Smith RK, Nanayakkara SU, Woehrle GH, et al. Spectral diffusion in the tunneling spectra of ligand-stabilized undecagold clusters. *J Am Chem Soc*. 2006;128:9266–9267.
146. Huang T-H, Zhao F-Z, Hu Q-L, et al. Bisphosphine-stabilized gold nanoclusters with the crown/birdcage-shaped Au_{11} cores: structures and optical properties. *Inorg Chem*. 2020;59:16027–16034.
147. Shinjo N, Takano S, Tsukuda T. Effects of Π-electron systems on optical activity of Au_{11} clusters protected by chiral diphosphines. *Bull Korean Chem Soc*. 2021;42:1265–1268.
148. Briant CE, Theobald BRC, White JW, Bell LK, Mingos DMP, Welch AJ. Synthesis and X-ray structural characterization of the centred icosahedral gold cluster compound $[Au_{13}(PMe_2Ph)_{10}Cl_2](PF_6)_3$, the realization of a theoretical prediction. *J Chem Soc Chem Commun*. 1981;5:201–202.
149. Shichibu Y, Suzuki K, Konishi K. Facile synthesis and optical properties of magic-number Au_{13} clusters. *Nanoscale*. 2012;4:4125–4129.
150. Takano S, Yamazoe S, Tsukuda T. A gold superatom with 10 electrons in $Au_{13}(PPh_3)_8(p\text{-}SC_6H_4CO_2H)_3$. *APL Mater*. 2017;5.
151. Narouz MR, Takano S, Lummis PA, et al. Highly luminescent Au_{13} superatoms protected by N-heterocyclic carbenes. *J Am Chem Soc*. 2019;141:14997–15002.
152. Yi H, Osten KM, Levchenko TI, et al. Synthesis and enantioseparation of chiral Au_{13} nanoclusters protected by bis-N-heterocyclic carbene ligands. *Chem Sci*. 2021;12:10436–10440.
153. Gutrath BS, Oppel IM, Presly O, Beljakov I, Meded V, Wenzel W, Simon U. $[Au_{14}(PPh_3)_8(NO_3)_4]$: an example of a new class of $Au(NO_3)$-ligated superatom complexes. *Angew Chem Int Ed*. 2013;52:3529–3532.
154. Negishi Y, Nobusada K, Tsukuda T. Glutathione-protected gold clusters revisited: bridging the gap between gold(I) thiolate complexes and thiolate-protected gold nanocrystals. *J Am Chem Soc*. 2005;127:5261–5270.
155. Shibu ES, Pradeep T. Quantum clusters in cavities: trapped Au_{15} in cyclodextrins. *Chem Mater*. 2011;23:989–999.
156. Combes GF, Fakhouri H, Moulin C, et al. Functionalized Au_{15} nanoclusters as luminescent probes for protein carbonylation detection. *Commun Chem*. 2021;4:497–507.
157. Yao Q, Yu Y, Yuan X, Yu Y, Xie J, Lee JY. Two-phase synthesis of small thiolate-protected Au_{15} and Au_{18} nanoclusters. *Small*. 2013;9:2696–2701.
158. Yang S, Chen S, Xiong L, et al. Total structure determination of Au_{16}(S-Adm)$_{12}$ and $Cd_1Au_{14}(StBu)_{12}$ and implications for the structure of $Au_{15}(SR)_{13}$. *J Am Chem Soc*. 2018;140:10988–10994.
159. Ghosh A, Udayabhaskararao T, Pradeep T. One-step route to luminescent $Au_{18}SG_{14}$ in the condensed phase and its closed shell molecular ions in the gas phase. *J Phys Chem Lett*. 2012;3:1997–2002.
160. Chen S, Wang S, Zhong J, et al. The structure and optical properties of the $[Au_{18}(SR)_{14}]$ nanocluster. *Angew Chem Int Ed*. 2015;54:3145–3149.

161. Shigeta T, Takano S, Tsukuda T. A face-to-face dimer of Au_3 superatoms supported by interlocked tridentate scaffolds formed in $Au_{18}S_2(SR)_{12}$. *Angew Chem Int Ed Engl*. 2022;61.
162. Itteboina R, Madhuri UD, Ghosal P, et al. Efficient one-pot synthesis and pH-dependent tuning of photoluminescence and stability of $Au_{18}(SC_2H_4CO_2H)_{14}$ cluster. *J Phys Chem A*. 2018;122:1228–1234.
163. Wan X-K, Tang Q, Yuan S-F, Jiang DE, Wang QM. Au_{19} nanocluster featuring a V-shaped alkynyl–gold motif. *J Am Chem Soc*. 2015;137:652–655.
164. Wu Z, MacDonald MA, Chen J, Zhang P, Jin R. Kinetic control and thermodynamic selection in the synthesis of atomically precise gold nanoclusters. *J Am Chem Soc*. 2011;133:9670–9673.
165. Tsunoyama H, Negishi Y, Tsukuda T. Chromatographic isolation of "missing"Au_{55} clusters protected by alkanethiolates. *J Am Chem Soc*. 2006;128:6036–6037.
166. Zeng C, Liu C, Chen Y, Rosi NL, Jin R. Gold–thiolate ring as a protecting motif in the $Au_{20}(SR)_{16}$ nanocluster and implications. *J Am Chem Soc*. 2014;136:11922–11925.
167. Zhang Q-F, Chen X, Wang L-S. Toward solution syntheses of the tetrahedral Au_{20} pyramid and atomically precise gold nanoclusters with uncoordinated sites. *Acc Chem Res*. 2018;51:2159–2168.
168. Chen J, Zhang Q-F, Williard PG, Wang L-S. Synthesis and structure determination of a new Au_{20} nanocluster protected by tripodal tetraphosphine ligands. *Inorg Chem*. 2014;53:3932–3934.
169. Knoppe S, Zhang Q-F, Wan X-K, Wang Q-M, Wang L-S, Verbiest T. Second-order nonlinear optical scattering properties of phosphine-protected Au_{20} clusters. *Ind Eng Chem Res*. 2016;55:10500–10506.
170. Chen S, Xiong L, Wang S, et al. Total structure determination of Au_{21}(S-Adm)$_{15}$ and geometrical/electronic structure evolution of thiolated gold nanoclusters. *J Am Chem Soc*. 2016;138:10754–10757.
171. Shibu ES, Radha B, Verma PK, et al. Functionalized Au_{22} clusters: synthesis, characterization, and patterning. *ACS Appl Mater Interfaces*. 2009;1:2199–2210.
172. Chen J, Zhang Q-F, Bonaccorso TA, Williard PG, Wang L-S. Controlling gold nanoclusters by diphospine ligands. *J Am Chem Soc*. 2014;136:92–95.
173. Yu Y, Luo Z, Chevrier DM, et al. Identification of a highly luminescent $Au_{22}(SG)_{18}$ nanocluster. *J Am Chem Soc*. 2014;136:1246–1249.
174. Ito S, Takano S, Tsukuda T. Alkynyl-protected $Au_{22}(C{\equiv}CR)_{18}$ clusters featuring new interfacial motifs and R-dependent photoluminescence. *J Phys Chem Lett*. 2019;10:6892–6896.
175. Muhammed MAH, Verma PK, Pal SK, et al. NIR-emitting Au_{23} from Au_{25}: characterization and applications including biolabeling. *Chem – Eur J*. 2009;15:10110–10120.
176. Das A, Li T, Nobusada K, Zeng C, Rosi NL, Jin R. Nonsuperatomic $[Au_{23}(SC_6H_{11})_{16}]^-$ nanocluster featuring bipyramidal Au_{15} kernel and trimeric $Au_3(SR)_4$ motif. *J Am Chem Soc*. 2013;135:18264–18267.
177. Guan ZJ, Hu F, Li JJ, Wen ZR, Lin Y-M, Wang Q-M. Isomerization in alkynyl-protected gold nanoclusters. *J Am Chem Soc*. 2020;142:2995–3001.
178. Negishi Y, Horihata H, Ebina A, et al. Selective formation of $[Au_{23}(SPh^tBu)_{17}]^0$, $[Au_{26}Pd(SPh^tBu)_{20}]^0$ and $[Au_{24}Pt(SC_2H_4Ph)_7(SPh^tBu)_{11}]^0$ by controlling ligand-exchange reaction. *Chem Sci*. 2022;13(19):5546–5556.
179. Das A, Li T, Nobusada K, Zeng Q, Rosi NL, Jin R. Total structure and optical properties of a phosphine/thiolate-protected Au_{24} nanocluster. *J Am Chem Soc*. 2012;134:20286–20289.
180. Song Y, Wang S, Zhang J, et al. Crystal structure of selenolate-protected $Au_{24}(SeR)_{20}$ nanocluster. *J Am Chem Soc*. 2014;136:2963–2965.
181. Crasto D, Barcaro G, Stener M, Sementa L, Fortunelli A, Dass A. $Au_{24}(SAdm)_{16}$ nanomolecules: X-ray crystal structure, theoretical analysis, adaptability of adamantane ligands to form $Au_{23}(SAdm)_{16}$ and $Au_{25}(SAdm)_{16}$, and its relation to $Au_{25}(SR)_{18}$. *J Am Chem Soc*. 2014;136:14933–14940.
182. Hasegawa S, Takano S, Harano K, Tsukuda T. New magic Au_{24} cluster stabilized by PVP: selective formation, atomic structure, and oxidation catalysis. *JACS Au*. 2021;1:660–668.
183. Shibu ES, Pradeep T. Photoluminescence and temperature-dependent emission studies of Au_{25} clusters in the solid state. *Int J Nanosci*. 2009;08:223–226.
184. Habeeb Muhammed M, Ramesh S, Sinha S, Pal S, Pradeep T. Two distinct fluorescent quantum clusters of gold starting from metallic nanoparticles by pH-dependent ligand etching. *Nano Res*. 2008;1:333–340.
185. Habeeb Muhammed MA, Pradeep T. Aqueous to organic phase transfer of Au_{25} clusters. *J Cluster Sci*. 2009;20:365–373.
186. Wang Y, Bürgi T. Evidence for stereoelectronic effects in ligand exchange reactions on Au_{25} nanoclusters. *Nanoscale*. 2022;14:2456–2464.

187. Habeeb Muhammed MA, Pradeep T. Au_{25}@SiO_2: quantum clusters of gold embedded in silica. *Small*. 2010;7:204–208.
188. Shichibu Y, Negishi Y, Watanabe T, Chaki NK, Kawaguchi H, Tsukuda T. Biicosahedral gold clusters $[Au_{25}(PPh_3)_{10}(SC_nH_{2n+1})_5Cl_2]^{2+}$: a stepping stone to cluster-assembled materials. *J Phys Chem C*. 2007;111:7845–7847.
189. Nie X, Qian H, Ge Q, Xu H, Jin RCO. Oxidation catalyzed by oxide-supported $Au_{25}(SR)_{18}$ nanoclusters and identification of perimeter sites as active centers. *ACS Nano*. 2012;6:6014–6022.
190. Zhu M, Eckenhoff WT, Pintauer T, Jin R. Conversion of anionic $[Au_{25}(SCH_2CH_2Ph)_{18}]^-$ cluster to charge neutral cluster via air oxidation. *J Phys Chem C*. 2008;112:14221–14224.
191. Zhu M, Aikens CM, Hollander FJ, Schatz GC, Jin R. Correlating the crystal structure of A thiol-protected Au_{25} cluster and optical properties. *J Am Chem Soc*. 2008;130:5883–5885.
192. Heaven M, Dass A, White P, Holt K, Murray R. Crystal structure of the gold nanoparticle $[N(C_8H_{17})_4][Au_{25}(SCH_2CH_2Ph)_{18}]$. *J Am Chem Soc*. 2008;130:3754.
193. Bhat S, Narayanan RP, Baksi A, et al. Detection of $[Au_{25}(PET)_{18}(O_2)_n]^-$ (n = 1, 2, 3) species by mass spectrometry. *J Phys Chem C Nanomater Interfaces*. 2018;122:19455–19462.
194. Devadas MS, Kwak K, Park J-W, et al. Directional electron transfer in chromophore-labeled quantum-sized Au_{25} clusters: Au_{25} as an electron donor. *J Phys Chem Lett*. 2010;1:1497–1503.
195. Venzo A, Antonello S, GascoÌn JA, et al. Effect of the charge state (z = -1, 0, +1) on the nuclear magnetic resonance of monodisperse $Au_{25}[S(CH_2)_2Ph]_{18}$ clusters. *Anal Chem*. 2011;83:6355–6362.
196. Kumar SS, Kwak K, Lee D. Electrochemical sensing using quantum-sized gold nanoparticles. *Anal Chem*. 2011;83:3244–3247.
197. GarciÌa-Raya D, MaduenÌƒo R, BlaÌzquez M, Pineda T. Electrochemistry of molecule-like Au_{25} nanoclusters protected by hexanethiolate. *J Phys Chem C*. 2009;113:8756–8761.
198. Hamouda R, Bellina B, Bertorelle F, et al. Electron emission of gas-phase $[Au_{25}(SG)_{18}–6H]^{7-}$ gold cluster and its action spectroscopy. *J Phys Chem Lett*. 2010;1:3189–3194.
199. Parker JF, Choi J-P, Wang W, Murray RW. Electron self-exchange dynamics of the nanoparticle couple $[Au_{25}(SC_2Ph)_{18}]^{0/1-}$ by nuclear magnetic resonance line-broadening. *J Phys Chem C*. 2008;112:13976–13981.
200. Xie S, Tsunoyama H, Kurashige W, Negishi Y, Tsukuda T. Enhancement in aerobic alcohol oxidation catalysis of Au_{25} clusters by single Pd atom doping. *ACS Catal*. 2012;2:1519–1523.
201. Shichibu Y, Negishi Y, Tsunoyama H, Kanehara M, Teranishi T, Tsukuda T. Extremely high stability of glutathionate-protected Au_{25} clusters against core etching. *Small*. 2007;3:835–839.
202. Jupally VR, Kota R, Dornshuld EV, et al. Interstaple dithiol cross-linking in $Au_{25}(SR)_{18}$ nanomolecules: a combined mass spectrometric and computational study. *J Am Chem Soc*. 2011;133:20258–20266.
203. Angel LA, Majors LT, Dharmaratne AC, Dass A. Ion mobility mass spectrometry of $Au_{25}(SCH_2CH_2Ph)_{18}$ nanoclusters. *ACS Nano*. 2010;4:4691–4700.
204. Negishi Y, Kurashige W, Kamimura U. Isolation and structural characterization of an octaneselenolate-protected Au_{25} cluster. *Langmuir*. 2011;27:12289–12292.
205. Zhu M, Lanni E, Garg N, Bier ME, Jin R KC. High-yield synthesis of Au_{25} clusters. *J Am Chem Soc*. 2008;130:1138–1139.
206. Shichibu Y, Negishi Y, Tsukuda T, Teranishi T. Large-scale synthesis of thiolated Au_{25} clusters via ligand exchange reactions of phosphine-stabilized Au_{11} clusters. *J Am Chem Soc*. 2005;127:13464–13465.
207. Si S, Gautier C, Boudon J, Taras R, Gladiali S, Bürgi T. Ligand exchange on Au_{25} cluster with chiral thiols. *J Phys Chem C*. 2009;113:12966–12969.
208. Wang S, Tang L, Cai B, et al. Ligand modification of Au_{25} nanoclusters for near-infrared photocatalytic oxidative functionalization. *J Am Chem Soc*. 2022;144:3787–3792.
209. Dharmaratne AC, Krick T, Dass A. Nanocluster size evolution studied by mass spectrometry in room temperature $Au_{25}(SR)_{18}$ synthesis. *J Am Chem Soc*. 2009;131:13604–13605.
210. Yu Y, Luo Z, Yu Y, Lee JY, Xie J. Observation of cluster size growth in CO-directed synthesis of $Au_{25}(SR)_{18}$ nanoclusters. *ACS Nano*. 2012;6:7920–7927.
211. Yao H. On the electronic structures of $Au_{25}(SR)_{18}$ clusters studied by magnetic circular dichroism spectroscopy. *J Phys Chem Lett*. 2012;3:1701–1706.
212. Wu Z, Chen J, Jin R. One-pot synthesis of $Au_{25}(SG)_{18}$ 2- and 4-nm gold nanoparticles and comparison of their size-dependent properties. *Adv Funct Mater*. 2012;21:177–183.

213. Negishi Y, Chaki NK, Shichibu Y, Whetten RL, Tsukuda T. Origin of magic stability of thiolated gold clusters: a case study on $Au_{25}(SC_6H_{13})_{18}$. *J Am Chem Soc*. 2007;129:11322–11323.
214. Wu Z, Gayathri C, Gil RR, Jin R. Probing the structure and charge state of glutathione-capped $Au_{25}(SG)_{18}$ clusters by NMR and mass spectrometry. *J Am Chem Soc*. 2009;131:6535–6542.
215. Muhammed MAH, Shaw AK, Pal SK, Pradeep T. Quantum clusters of gold exhibiting FRET. *J Phys Chem C*. 2008;112:14324–14330.
216. Habeeb Muhammed MA, Pradeep T. Reactivity of Au_{25} clusters with Au^{3+}. *Chem Phys Lett*. 2007;449:186–190.
217. Zhu M, Aikens CM, Hendrich MP, et al. Reversible switching of magnetism in thiolate-protected Au_{25} superatoms. *J Am Chem Soc*. 2009;131:2490–2492.
218. Wu Z, Jin R. Stability of the two Au-S binding modes in $Au_{25}(SG)_{18}$ nanoclusters probed by NMR and optical spectroscopy. *ACS Nano*. 2009;3:2036–2042.
219. Wen X, Yu P, Toh Y-R, Tang J. Structure-correlated dual fluorescent bands in BSA-protected Au_{25} nanoclusters. *J Phys Chem C*. 2012;116:11830–11836.
220. Devadas MS, Bairu S, Qian H, Sinn E, Jin R, Ramakrishna G. Temperature-dependent optical absorption properties of monolayer-protected Au_{25} and Au_{38} clusters. *J Phys Chem Lett*. 2011;2:2752–2758.
221. MacDonald MA, Chevrier DM, Zhang P, Qian H, Jin R. The structure and bonding of $Au_{25}(SR)_{18}$ nanoclusters from EXAFS: the interplay of metallic and molecular behavior. *J Phys Chem C*. 2011;115:15282–15287.
222. Devadas MS, Kim J, Sinn E, Lee D, Goodson T, Ramakrishna G. Unique ultrafast visible luminescence in monolayer-protected Au_{25} clusters. *J Phys Chem C*. 2010;114:22417–22423.
223. GarciÌa-Raya D, MaduenÌ*f*o R, BlaÌzquez M, Pineda T. Electrochemistry of molecule-like Au_{25} nanoclusters protected by hexanethiolate. *J Phys Chem C*. 2009;113:8756–8761.
224. Angevine CE, Chavis AE, Kothalawala N, Dass A, Reiner JE. Enhanced single molecule mass spectrometry via charged metallic clusters. *Anal Chem*. 2014;86:11077–11085.
225. Yao Q, Yuan X, Yu Y, Yu Y, Xie J, Lee JY. Introducing amphiphilicity to noble metal nanoclusters via phase-transfer driven ion-pairing reaction. *J Am Chem Soc*. 2015;137:2128–2136.
226. Yoshimoto J, Sangsuwan A, Osaka I, et al. Optical properties of 2-methacryloyloxyethyl phosphorylcholine-protected Au_4 nanoclusters and their fluorescence sensing of C-reactive protein. *J Phys Chem C*. 2015;119:14319–14325.
227. Ghosh A, Hassinen J, Pulkkinen P, Tenhu H, Ras RHA, Pradeep T. Simple and efficient separation of atomically precise noble metal clusters. *Anal Chem*. 2014;86:12185–12190.
228. Mathew A, Varghese E, Choudhury S, Pal SK, Pradeep T. Efficient red luminescence from organic-soluble Au_{25} clusters by ligand structure modification. *Nanoscale*. 2015;7:14305–14315.
229. Hassinen J, Pulkkinen P, Kalenius E, Pradeep T, Tenhu H, Häkkinen H. Ras RHA mixed-monolayer-protected Au_{25} clusters with bulky calix[4]arene functionalities. *J Phys Chem Lett*. 2014;5:585–589.
230. Schaaff TG, Whetten RL. Giant gold glutathione cluster compounds: intense optical activity in metal-based transitions. *J Phys Chem B*. 2000;104:2630–2641.
231. Schaaff TG, Knight G, Shafigullin MN, Borkman RF, Whetten RL. Isolation and selected properties of a 10.4 kDa gold: glutathione cluster compound. *J Phys Chem B*. 1998;102:10643–10646.
232. Link S, Beeby A, FitzGerald S, El-Sayed MA, Schaaff TG, Whetten RL. Visible to infrared luminescence from a 28-atom gold cluster. *J Phys Chem B*. 2002;106:3410–3415.
233. Zeng C, Li T, Das A, Rosi NL, Jin R. Chiral structure of thiolate-protected 28-gold-atom nanocluster determined by X-ray crystallography. *J Am Chem Soc*. 2013;135:10011–10013.
234. AbdulHalim LG, Bootharaju MS, Tang Q, et al. $Ag_{29}(BDT)_{12}(TPP)_4$: a tetravalent nanocluster. *J Am Chem Soc*. 2015;137:11970–11975.
235. Yuan S-F, He R-L, Han X-S, Wang J-Q, Guan Z-J, Wang Q-M. Robust gold nanocluster protected with amidinates for electrocatalytic CO_2 reduction. *Angew Chem Int Ed Engl*. 2021;60:14345–14349.
236. Wang J, Wang Z-Y, Li S-J, Zang S-Q, Mak TCW. Carboranealkynyl-protected gold nanoclusters: size conversion and UV/Vis-NIR optical properties. *Angew Chem Int Ed Engl*. 2021;60:5959–5964.
237. Dong J, Gan Z, Gu W, et al. Synthesizing photoluminescent $Au_{28}(SCH_2Ph\text{-}^tBu)_{22}$ nanoclusters with structural features by using a combined method. *Angew Chem Int Ed Engl*. 2021;60:17932–17936.
238. Yu Y, Yao Q, Cheng K, Yuan X, Luo Z, Xie J. Solvent controls the formation of $Au_{29}(SR)_{20}$ nanoclusters in the CO-reduction method. *Part Part Syst Charact*. 2014;31:652–656.

239. Krommenhoek PJ, Wang J, Hentz N, et al. Bulky adamantanethiolate and cyclohexanethiolate ligands favor smaller gold nanoparticles with altered discrete sizes. *ACS Nano*. 2012;6:4903–4911.
240. Crasto D, Dass A. Green gold: $Au_{30}(S\text{-}t\text{-}C_4H_9)_{18}$ molecules. *J Phys Chem C*. 2013;117:22094–22097.
241. Crasto D, Malola S, Brosofsky G, Dass A, Häkkinen H. Single crystal XRD structure and theoretical analysis of the chiral $Au_{30}S(S\text{-}t\text{-}Bu)_{18}$ cluster. *J Am Chem Soc*. 2014;136:5000–5005.
242. Kenzler S, Schrenk C, Schnepf A. $Au_{54}(Et_3P)_{18}Cl_{12}$: a structurally related cluster to $Au_{32}(Et_3P)_{12}Cl_8$ gives insight into the formation process. *Dalton Trans*. 2020;49:10765–10771.
243. Kenzler S, Fetzer F, Schrenk C, et al. Synthesis and characterization of three multi-shell metalloid gold clusters $Au_{32}(R_3P)_{12}$ Cl_8. *Angew Chem Int Ed Engl*. 2019;58:5902–5905.
244. Wang Q, Halet J-F, Kahlal S, Muñoz-Castro A, Saillard J-Y. Electron count and electronic structure of bare icosahedral Au_{32} and Au_{33} ionic nanoclusters and ligated derivatives. Stable models with intermediate superatomic shell fillings. *Phys Chem Chem Phys*. 2020;22:20751–20757.
245. Nimmala PR, Dass A. $Au_{36}(SPh)_{23}$ nanomolecules. *J Am Chem Soc*. 2011;133:9175–9177.
246. Zeng C, Qian H, Li T, et al. Total structure and electronic properties of the gold nanocrystal $Au_{36}(SR)_{24}$. *Angew Chem*. 2012;51(52):13114–13118.
247. Liu Xu, Wen Xu, Xinyu H, et al. The novel design of $Au_{36}(SR)_{24}$ nanoclusters. *Nat Commun*. 2020;11:3349–3355.
248. Liu C, Li T, Li G, et al. Observation of body-centered cubic gold nanocluster. *Angew Chem Int Ed Engl*. 2015;54:9826–9829.
249. Palacios-Álvarez O, Tlahuice-Flores A. Tri-icosahedral Au_{37} cluster as a carrier/detector for anti-cancer cisplatin drug. *J Raman Spectrosc*. 2019;50:52–62.
250. Losovyj YB, Li S-C, Lozova N, et al. Evidence for sp3d hybridization in Au_{38} clusters. *J Phys Chem C*. 2012;116:5857–5861.
251. Kim J, Lema K, Ukaigwe M, Lee D. Facile preparative route to alkanethiolate-coated Au_{38} nanoparticles: post synthesis core size evolution. *Langmuir*. 2007;23:7853–7858.
252. Stellwagen D, Weber A, Bovenkamp GL, Jin R, Bitter JH, Kumar CSSR. Ligand control in thiol stabilized Au_{38} clusters. *RSC Adv*. 2011;2:2276–2283.
253. Qian H, Zhu M, Andersen UN, Jin RF. Large-scale synthesis of dodecanethiol-stabilized Au_{38} clusters. *J Phys Chem A*. 2009;113:4281–4284.
254. Knoppe S, Dharmaratne AC, Schreiner E, Dass A, Burgi T. Size ligand exchange reactions on Au_{38} and Au_{40} clusters: a combined circular dichroism and mass spectrometry study. *J Am Chem Soc*. 2010;132:16783–16789.
255. Song Y, Harper AS, Murray RW. Ligand heterogeneity on monolayer-protected gold clusters. *Langmuir*. 2005;21:5492–5500.
256. Antonello S, Holm AH, Instuli E, Maran F. Molecular electron-transfer properties of Au_{38} clusters. *J Am Chem Soc*. 2007;129:9836–9837.
257. Negishi Y, Igarashi K, Munakata K, Ohgake W, Nobusada K. Palladium doping of magic gold cluster $Au_{38}(SC_2H_4Ph)_{24}$: formation of $Pd_2Au_{36}(SC_2H_4Ph)_{24}$ with higher stability than $Au_{38}(SC_2H_4Ph)_{24}$. *Chem Commun (Camb)*. 2012;48:660–662.
258. Wang W, Murray RW. Reaction of triphenylphosphine with phenylethanethiolate-protected Au_{38} nanoparticles. *Langmuir*. 2005;21:7015–7022.
259. Knoppe S, Boudon J, Dolamic I, Dass A, Burgi T. Size exclusion chromatography for semipreparative scale separation of $Au_{38}(SR)_{24}$ and $Au_{40}(SR)_{24}$ and larger clusters. *Anal Chem*. 2011;83:5056–5061.
260. Qian H, Zhu Y, Jin R. Size-focusing synthesis, optical and electrochemical properties of monodisperse $Au_{38}(SC_2H_4Ph)_{24}$ nanoclusters. *ACS Nano*. 2009;3:3795–3803.
261. MacDonald MA, Zhang P, Chen N, Qian H, Jin R. Solution phase structure and bonding of $Au_{38}(SR)_{24}$ nanoclusters from X-ray absorption spectroscopy. *J Phys Chem C*. 2011;115:65–69.
262. Toikkanen O, Carlsson S, Dass A, Ronnholm G, Kalkkinen N, Quinn BM. Solvent-dependent stability of monolayer-protected Au_{38} clusters. *J Phys Chem Lett*. 2009;1:32–37.
263. Qian H, Eckenhoff WT, Zhu Y, Pintauer T, Jin R. Total structure determination of thiolate-protected Au_{38} nanoparticles. *J Am Chem Soc*. 2010;132:8280–8281.
264. Guo R, Murray RW. Substituent effects on redox potentials and optical gap energies of molecule-like $Au_{38}(SPhX)_{24}$ nanoparticles. *J Am Chem Soc*. 2005;127:12140–12143.
265. Donkers RL, Lee D, Murray RW. Synthesis and isolation of the molecule-like cluster $Au_{38}(PhCH_2CH_2S)_{24}$. *Langmuir*. 2004;20:1945–1952.

266. Toikkanen O, Ruiz V, Roĺˆnnholm G, Kalkkinen N, Liljeroth P, Quinn BM. Synthesis and stability of monolayer-protected Au_{38} clusters. *J Am Chem Soc*. 2008;130:11049–11055.
267. Gaur S, Miller JT, Stellwagen D, Sanampudi A, Kumar CSSR, Spivey JJ. Synthesis, characterization, and testing of supported Au catalysts prepared from atomically-tailored $Au_{38}(SC_{12}H_{25})_{24}$ clusters. *Phys Chem Chem Phys*. 2012;14:1627–1634.
268. Wijngaarden JTV, Toikkanen O, Liljeroth P, Quinn BM, Meijerink A. Temperature-dependent emission of monolayer-protected Au_{38} clusters. *J Phys Chem C*. 2010;114:16025–16028.
269. Teo BK, Shi X, Zhang H. Pure gold cluster of 1:9:9:1:9:9:1 layered structure: a novel 39-metal-atom cluster $[(Ph_3P)_{14}Au_{39}Cl_6]Cl_2$ with an interstitial gold atom in a hexagonal antiprismatic cage. *J Am Chem Soc*. 1992;114:2743–2745.
270. Qian H, Zhu Y, Jin R. Isolation of ubiquitous $Au_{40}(SR)_{24}$ clusters from the 8 kDa gold clusters. *J Am Chem Soc*. 2010;132:4583–4585.
271. Knoppe S, Dolamic I, Dass A, Bürgi T. Separation of enantiomers and CD spectra of $Au_{40}(SCH_2CH_2Ph)_{24}$: spectroscopic evidence for intrinsic chirality. *Angew Chemie – Int Ed*. 2012;51:7589–7591.
272. Zeng C, Chen Y, Liu C, Nobusada K, Rosi NL, Jin R. Gold tetrahedra coil up: Kekulé-like and double helical superstructures. *Sci Adv*. 2015;1:425–430.
273. Nishigaki J-i, Tsunoyama R, Tsunoyama H, et al. A new binding motif of sterically demanding thiolates on a gold cluster. *J Am Chem Soc*. 2012;134:14295–14297.
274. Zhuang S, Liao L, Yuan J, et al. Fcc versus non-Fcc structural isomerism of gold nanoparticles with kernel atom packing dependent photoluminescence. *Angew Chem Int Ed Engl*. 2019;58:4510–4514.
275. Guan Z-J, Hu F, Li J-J, Liu Z-R, Wang Q-M. Homoleptic alkynyl-protected gold nanoclusters with unusual compositions and structures. *Nanoscale*. 2020;12:13346–13350.
276. Maity P, Tsunoyama H, Yamauchi M, Xie S, Tsukuda T. Organogold clusters protected by phenylacetylene. *J Am Chem Soc*. 2011;133:20123–20125.
277. Price RC, Whetten RL. All-aromatic, nanometer-scale, gold-cluster thiolate complexes. *J Am Chem Soc*. 2005;127:13750–13751.
278. Liao L, Zhuang S, Yao C, et al. Structure of chiral $Au_{44}(2,4\text{-DMBT})_{26}$ nanocluster with an 18-electron shell closure. *J Am Chem Soc*. 2016;138:10425–10428.
279. Wan X-K, Guan Z-J, Wang Q-M. Homoleptic alkynyl-protected gold nanoclusters: $Au_{44}(PhC{\equiv}C)_{28}$ and $Au_{36}(PhC{\equiv}C)_{24}$. *Angew Chem Int Ed Engl*. 2017;56:11494–11497.
280. Liao L, Zhuang S, Wang P, et al. Quasi-dual-packed-kerneled $Au_{49}(2,4\text{-DMBT})_{27}$ nanoclusters and the influence of kernel packing on the electrochemical gap. *Angew Chem Int Ed Engl*. 2017;56:12644–12648.
281. Zeng C, Chen Y, Liu C, Nobusada K, Rosi NL, Jin R. Gold tetrahedra coil up: Kekulé-like and double helical superstructures. *Sci Adv*. 2015;1:425–430.
282. Maity P, Wakabayashi T, Ichikuni N, et al. Selective synthesis of organogold magic clusters $Au_{54}(C{\equiv}CPh)_{26}$. *Chem Commun (Camb)*. 2012;48:6085–6087.
283. Maity P, Tsunoyama H, Yamauchi M, Xie S, Tsukuda T. Organogold clusters protected by phenylacetylene. *J Am Chem Soc*. 2011;133:20123–20125.
284. Tsunoyama R, Tsunoyama H, Pannopard P, Limtrakul J, Tsukuda T. MALDI mass analysis of 11 kDa gold clusters protected by octadecanethiolate ligands. *J Phys Chem C*. 2010;114:16004–16009.
285. Schon G, Simon U. A fascinating new field in colloid science: small ligand-stabilized metal clusters and their possible application in microelectronics. *Colloid Polym Sci*. 1995;273:202–218.
286. Schmid G, Beyer N. A new approach to well-ordered quantum dots. *Eur J Inorg Chem*. 2000;20:835–837.
287. Schmid G, Pfeil R, Boese R, et al. $Au_{55}[P(C_6H_5)_3]_{12}Cl_6$ — ein Goldcluster ungewöhnlicher Größe. *Chem Ber*. 1981;114:3634–3642.
288. Schmid G, Pugin R, Meyer-Zaika W, Simon U. Clusters on clusters: closo-dodecaborate as a ligand for Au_{55} clusters. *Eur J Inorg Chem*. 1999;1999:2051–2055.
289. Zhang H, Hartmann U, Schmid G. Energy-level splitting of ligand-stabilized Au_{55} clusters observed by scanning tunneling spectroscopy. *Appl Phys Lett*. 2004;84:1543–1545.
290. Wang ZW, Palmer RE. Experimental evidence for fluctuating, chiral-type Au_{55} clusters by direct atomic imaging. *Nano Lett*. 2012;12:5510–5514.
291. Reuter T, Neumeier S, Schmid G, Koplin E, Simon U. Generation and characterization of multilayer systems consisting of $Au_{55}(PPh_3)_{12}Cl_6$ double layers and SiO_2 barrier films. *Eur J Inorg Chem*. 2005;2005:3670–3678.

292. Schmid G, Reuter T, Simon U, et al. Generation and electrical contacting of gold quantum dots. *Colloid Polym Sci*. 2008;286:1029–1037.
293. Schmid G, Simon U. Gold nanoparticles: assembly and electrical properties in 1-3 dimensions. *Chem Commun*. 2005;6:697–710.
294. Schmid G, Meyer-Zaika W, Pugin R, et al. Naked Au_{55} clusters: dramatic effect of a thiol-terminated dendrimer. *Chem – Eur J*. 2000;6:1693–1697.
295. Schmid G, Bäumle M, Beyer N. Ordered two-dimensional monolayers of Au_{55} clusters. *Angew Chemie – Int Ed*. 2000;39:181–183.
296. Boyen HG, Weigl F, Koslowski B, et al. Oxidation-resistant gold-55 clusters. *Science*. 2002;297:1533–1536.
297. Schmid Gn, Liu Y-P, Schumann M, Raschke T, Radehaus C. Quasi one-dimensional arrangements of $Au_{55}(PPh_3)_{12}Cl_6$ clusters and their electrical properties at room temperature. *Nano Lett*. 2001;1:405–407.
298. Zhang H, Schmid Gn, Hartmann U. Reduced metallic properties of ligand-stabilized small metal clusters. *Nano Lett*. 2003;3:305–307.
299. Torma V, Schmid G, Simon U. Structure–property relations in Au_{55} cluster layers studied by temperature-dependent impedance measurements. *Chem Phys Chem*. 2001;2:321–325.
300. Qian H, Jin R. Synthesis and electrospray mass spectrometry determination of thiolate-protected $Au_{55}(SR)_{31}$ nanoclusters. *Chem Commun*. 2011;47:11462–11464.
301. Simon U, Schön G, Schmid G. The application of Au_{55} clusters as quantum dots. *Angew Chemie Int Ed Engl*. 1993;32:250–254.
302. Torma V, Reuter T, Vidoni O, Schumann M, Radehaus C, Schmid G. The diode behavior of asymmetrically ordered Au_{55} clusters. *Chem Phys Chem*. 2001;2:546–548.
303. Neumeier S, Reuter T, Schmid G. The electronic interaction between $Au_{55}(PPh_3)_{12}Cl_6$ monolayers through SiO_2 films. *Eur J Inorg Chem*. 2005;2005:3679–3682.
304. Schmid G, Pugin R, Sawitowski T, Simon U, Marler B. Transmission electron microscopic and small angle X-ray diffraction investigations of $Au_{55}(PPh_3)_{12}Cl_6$ microcrystals[dagger]. *Chem Commun*. 1999;14:1303–1304.
305. Wan X-K, Wang J-Q, Wang Q-M. Ligand-protected Au_{55} with a novel structure and remarkable CO_2 electroreduction performance. *Angew Chem Weinheim Bergstr Ger*. 2021;133:20916–20921.
306. Song Y, Fu F, Zhang J, et al. The magic Au_{60} nanocluster: a new cluster-assembled material with five Au_{13} building blocks. *Angew Chemie Int Ed*. 2015;54:8430–8434.
307. Zeng C, Chen Y, Li G, Jin R. Magic size $Au_{64}(S\text{-}c\text{-}C_6H_{11})_{32}$ nanocluster protected by cyclohexanethiolate. *Chem Mater*. 2014;26:2635–2641.
308. Nimmala PR, Yoon B, Whetten RL, Landman U, Dass A. $Au_{67}(SR)_{35}$ nanomolecules: characteristic size-specific optical, electrochemical, structural properties and first-principles theoretical analysis. *J Phys Chem A*. 2013;117:504–517.
309. Dass A. Mass spectrometric identification of $Au_{68}(SR)_{34}$ molecular gold nanoclusters with 34-electron shell closing. *J Am Chem Soc*. 2009;131:11666–11667.
310. Burgess RW, Keast VJ. TDDFT study of the optical absorption spectra of bare and coated Au_{55} and Au_{69} clusters. *J Phys Chem C Nanomater Interfaces*. 2011;115:21016–21021.
311. Tian Z, Xu Y, Cheng L. New perspectives on the electronic and geometric structure of $Au_{70}S_{20}(PPh_3)_{12}$ cluster: superatomic-network core protected by novel $Au_{12}(M_3\text{-}S)_{10}$ staple motifs. *Nanomaterials (Basel)*. 2019;9:1132.
312. Balasubramanian R, Guo R, Mills AJ, Murray RW. Reaction of $Au_{55}(PPh_3)_{12}Cl_6$ with thiols yields thiolate monolayer protected Au_{75} clusters. *J Am Chem Soc*. 2005;127:8126–8132.
313. Takano S, Yamazoe S, Koyasu K, Tsukuda T. Slow-reduction synthesis of a thiolate-protected one-dimensional gold cluster showing an intense near-infrared absorption. *J Am Chem Soc*. 2015;137:7027–7030.
314. Zeng C, Liu C, Chen Y, Rosi NL, Jin R. Atomic structure of self-assembled monolayer of thiolates on a tetragonal Au nanocrystal. *J Am Chem Soc*. 2016;138:8710–8713.
315. Li J-J, Liu Z, Guan Z-J, Han X-S, Shi W-Q, Wang Q-M. A 59-electron non-magic-number gold nanocluster $Au_{99}(C{\equiv}CR)_{40}$ showing unexpectedly high stability. *J Am Chem Soc*. 2022;144:690–694.
316. Kuo C-T, Yu J-Y, Huang M-J, Chen C-h. On the size evolution of gold-monolayer-protected clusters by ligand place-exchange reactions: the effect of headgroup on gold interactions. *Langmuir*. 2010;26:6149–6153.
317. Jadzinsky PD, Calero G, Ackerson CJ, Bushnell DA, Kornberg RD. Structure of a thiol monolayer-protected gold nanoparticle at 1.1 Ã… resolution. *Science*. 2007;318:430–433.

318. Higaki T, Liu C, Zhou M, Luo T-Y, Rosi NL, Jin R. Tailoring the structure of 58-electron gold nanoclusters: $Au_{103}S_2(S\text{-}Nap)_{41}$ and its implications. *J Am Chem Soc*. 2017;139:9994–10001.
319. Dass A, Nimmala PR, Jupally VR, Kothalawala N. $Au_{103}(SR)_{45}$, $Au_{104}(SR)_{45}$, $Au_{104}(SR)_{46}$ and $Au_{105}(SR)_{46}$ nanoclusters. *Nanoscale*. 2013;5:12082–12085.
320. Li J-J, Guan Z-J, Yuan S-F, Hu F, Wang Q-M. Enriching structural diversity of alkynyl-protected gold nanoclusters with chlorides. *Angew Chem Int Ed Engl*. 2021;60:6699–6703.
321. Kenzler S, Schrenk C, Schnepf A. $Au_{108}S_{24}(PPh_3)_{16}$: a highly symmetric nanoscale gold cluster confirms the general concept of metalloid clusters. *Angew Chem Int Ed Engl*. 2017;56:393–396.
322. Wang J-Q, Shi S, He R-L, et al. Total structure determination of the largest alkynyl-protected Fcc gold nanocluster Au_{110} and the study on its ultrafast excited-state dynamics. *J Am Chem Soc*. 2020;142:18086–18092.
323. Chen Y, Zeng C, Liu C, et al. Crystal structure of barrel-shaped chiral $Au_{130}(p\text{-}MBT)_{50}$ nanocluster. *J Am Chem Soc*. 2015;137:10076–10079.
324. Ren X, Fu X, Lin X, Liu C, Huang J, Yan J. Highly efficient synthesis of $Au_{130}(SPh\text{-}Br)_{50}$ nanocluster. *Chem Res Chin Univ*. 2018;34:719–722.
325. Dass A, Theivendran S, Nimmala PR, et al. $Au_{133}(SPh\text{-}tBu)_{52}$ nanomolecules: X-ray crystallography, optical, electrochemical, and theoretical analysis. *J Am Chem Soc*. 2015;137:4610–4613.
326. Negishi Y, Nakazaki T, Malola S, et al. A critical size for emergence of nonbulk electronic and geometric structures in dodecanethiolate-protected Au clusters. *J Am Chem Soc*. 2015;137:1206–1212.
327. Negishi Y, Sakamoto C, Ohyama T, Tsukuda T. Synthesis and the origin of the stability of thiolate-protected Au_{130} and Au_{187} clusters. *J Phys Chem Lett*. 2012;3:1624–1628.
328. Schaaff TG, Shafigullin MN, Khoury JT, Vezmar I, Whetten RL. Properties of a ubiquitous 29 kDa Au:SR cluster compound. *J Phys Chem B*. 2001;105:8785–8796.
329. Lei Z, Li J-J, Wan X-K, Zhang W-H, Wang Q-M. Isolation and total structure determination of an all-alkynyl-protected gold nanocluster Au_{144}. *Angew Chem Int Ed Engl*. 2018;57:8639–8643.
330. Qian H, Jin R. Ambient synthesis of $Au_{144}(SR)_{60}$ nanoclusters in methanol. *Chem Mater*. 2011;23:2209–2217.
331. Farrag M, Tschurl M, Dass A, Heiz U. Infra-red spectroscopy of size selected Au_{25}, Au_{38} and Au_{144} ligand protected gold clusters. *Phys Chem Chem Phys: PCCP*. 2013;15:12539–12542.
332. Dolamic I, Varnholt B, Burgi T. Far-infrared spectra of well-defined thiolate-protected gold clusters. *Phys Chem Chem Phys*. 2013;15:19561–19565.
333. Dainese T, Antonello S, Bonacchi S, et al. Isolation of the $Au_{145}(SR)_{60}X$ compound (R = n-Butyl, n-Pentyl, X = Br, Cl): novel gold nanoclusters that exhibit properties subtly distinct from the ubiquitous icosahedral $Au_{144}(SR)_{60}$ compound. *Nanoscale*. 2021;13:15394–15400.
334. Hu F, Guan Z-J, Yang G, et al. Molecular gold nanocluster Au_{156} showing metallic electron dynamics. *J Am Chem Soc*. 2021;143:17059–17067.
335. Sakthivel NA, Shabaninezhad M, Sementa L, et al. The missing link: $Au_{191}(SPh\text{-}TBu)_{66}$ janus nanoparticle with molecular and bulk-metal-like properties. *J Am Chem Soc*. 2020;142:15799–15814.
336. Wolfe RL, Murray RW. Analytical evidence for the monolayer-protected cluster $Au_{225}[(S(CH_2)_5CH_3)]_{75}$. *Anal Chem*. 2006;78:1167–1173.
337. Zhou M, Zeng C, Song Y, et al. On the non-metallicity of 2.2 Nm $Au_{246}(SR)_{80}$ nanoclusters. *Angew Chem Weinheim Bergstr Ger*. 2017;129:16475–16479.
338. Higaki T, Zhou M, Lambright KJ, Kirschbaum K, Sfeir MY, Jin R. Sharp transition from nonmetallic Au_{246} to metallic Au_{279} with nascent surface plasmon resonance. *J Am Chem Soc*. 2018;140:5691–5695.
339. Sakthivel NA, Theivendran S, Ganeshraj V, Oliver AG, Dass A. Crystal structure of faradaurate-279: $Au_{279}(SPh\text{-}TBu)_{84}$ plasmonic nanocrystal molecules. *J Am Chem Soc*. 2017;139:15450–15459.
340. Kumara C, Zuo X, Ilavsky J, Cullen D, Dass A. Atomic structure of $Au_{329}(SR)_{84}$ faradaurate plasmonic nanomolecules. *J Phys Chem C*. 2015;119:11260–11266.
341. Qian H, Zhu Y, Jin R. Atomically precise gold nanocrystal molecules with surface plasmon resonance. *Proc Natl Acad Sci*. 2012;109:696–700.
342. Kumara C, Zuo X, Ilavsky J, Chapman KW, Cullen DA, Dass A. Super-stable, highly monodisperse plasmonic faradaurate-500 nanocrystals with 500 gold atoms: $Au_{\sim 500}(SR)_{\sim 120}$. *J Am Chem Soc*. 2014;136:7410–7417.
343. Kumara C, Zuo X, Cullen DA, Dass A. Faradaurate-940: synthesis, mass spectrometry, electron microscopy, high-energy X-ray diffraction, and X-ray scattering study of $Au_{\sim 940\pm 20}(SR)_{\sim 160\pm 4}$ nanocrystals. *ACS Nano*. 2014;8:6431–6439.

344. Kumara C, Hoque MM, Zuo X, Cullen DA, Whetten RL, Dass A. Isolation of a 300 KDa, $Au_{\sim 1400}$ gold compound, the standard 3.6 Nm capstone to a series of plasmonic nanocrystals protected by aliphatic-like thiolates. *J Phys Chem Lett*. 2018;9:6825–6832.
345. Vergara S, Santiago U, Kumara C, et al. Synthesis, mass spectrometry, and atomic structural analysis of $Au_{\sim 2000}(SR)_{\sim 290}$ nanoparticles. *J Phys Chem C Nanomater Interfaces*. 2018;122:26733–26738.
346. Semmelmann M, Fenske D, Corrigan JF. Copper-chalcogenide clusters stabilised with linear bidentate phosphine ligands. *J Chem Soc Dalton Trans*. 1998;15:2541–2546.
347. Fenske D, Steck JC. New Cu-Te clusters. *Angew Chem Int Ed Engl*. 1993;32:238–242.
348. DeGroot MW, Cockburn MW, Workentin MS, Corrigan JF. Trialkylphosphine-stabilized copper-phenyltellurolate complexes: from small molecules to nanoclusters via condensation reactions. *Inorg Chem*. 2001;40:4678–4685.
349. Gao X, He S, Zhang C, et al. Single crystal sub-nanometer sized $Cu_6(SR)_6$ clusters: structure, photophysical properties, and electrochemical sensing. *Adv Sci (Weinh*. 2016;3.
350. Fu M-L, Fenske D, Weinert B, Fuhr O. One-dimensional coordination polymers containing polynuclear (selenolato)copper complexes linked by bipyridine ligands. *Eur J Inorg Chem*. 2010;2010:1098–1102.
351. Avdeef A, Fackler Jr JP. Studies of the cubane cluster of copper(I). A modified self-consistent charge and configuration molecular orbital investigation of the cluster containing the $[Cu_8S_{12}]^{4-}$ core. *Inorg Chem*. 1978;17:2182–2187.
352. Corrigan JF, Fenske D. New copper telluride clusters by light-induced tellurolate–telluride conversions. *Angew Chem Int Ed Engl*. 1997;36:1981–1983.
353. Eichhöfer A, Corrigan JF, Fenske D, Tröster E. New copper telluride cluster – synthesis, crystal structure and optical spectrum. *Z Anorg Allg Chem*. 2000;626:338–348.
354. Liu C-Y, Yuan S-F, Wang S, Guan Z-J, Jiang D-E, Wang QM. Structural transformation and catalytic hydrogenation activity of amidinate-protected copper hydride clusters. *Nat Commun*. 2022;13:2082.
355. DeGroot MW, Cockburn MW, Workentin MS, Corrigan JF. Trialkylphosphine-stabilized copper-phenyltellurolate complexes: from small molecules to nanoclusters via condensation reactions. *Inorg Chem*. 2001;40:4678–4685.
356. Dehnen S, Schäfer A, Fenske D, Ahlrichs R. New sulfur- and selenium-bridged copper clusters, ab initio calculations on $[Cu_{2n}Se_n(PH_3)_m]$ clusters. *Angew Chem Int Ed Engl*. 1994;33:746–749.
357. Nematulloev S, Huang R-W, Yin J, et al. $[Cu_{15}(PPh_3)_6(PET)_{13}]^{2+}$: a copper nanocluster with crystallization enhanced photoluminescence. *Small*. 2021;17.
358. Cuthbert HL, Wallbank AI, Taylor NJ, Corrigan JF. Synthesis and structural characterization of $[Cu_{20}Se_4(\mu^3\text{-}SePh)_{12}(PPh_3)_6]$ and $[Ag(SePh)]_\infty$. *Z Anorg Allg Chem*. 2002;628:2483–2488.
359. Huang R-W, Yin J, Dong C, et al. $[Cu_{23}(PhSe)_{16}(Ph_3P)_8(H)_6]\cdot BF_4$: atomic-level insights into cuboidal polyhydrido copper nanoclusters and their quasi-simple cubic self-assembly. *ACS Mater Lett*. 2021;3:90–99.
360. Dehnen S, Fenske D. $[Cu_{24}S_{12}(PMeiPr_2)_{12}]$, $[Cu_{28}S_{14}(PtBu_2Me)_{12}]$, $[Cu_{50}S_{25}(PtBu_2Me)_{16}]$, $[Cu_{70}Se_{35}(PtBu_2Me)_{21}]$, $[Cu_{31}Se_{15}(SeSiMe_3)(PtBu_2Me)_{12}]$ and $[Cu_{48}Se_{24}(PMe_2Ph)_{20}]$: new sulfur- and selenium-bridged copper clusters. *Chemistry*. 1996;2:1407–1416.
361. Nguyen T-AD, Jones ZR, Goldsmith BR, et al. A Cu_{25} nanocluster with partial Cu(0) character. *J Am Chem Soc*. 2015;137:13319–13324.
362. Semmelmann M, Fenske D, Corrigan JF. Copper-chalcogenide clusters stabilised with linear bidentate phosphine ligands. *J Chem Soc Dalton Trans*. 1998;15:2541–2546.
363. Cave D, Corrigan JF, Eichhöfer A, et al. Investigation of the thermal properties of a series of copper selenide cluster molecules. *J Cluster Sci*. 2007;18:157–172.
364. Ahlrichs R, Besinger J, Eichhöfer A, Fenske D, Gbureck A. Synthesis, crystal structure, and binding properties of the mixed valence clusters $[Cu_{32}As_{30}(Dppm)_8]$ and $[Cu_{26}Te_{12}(PEt_2Ph)_{12}]$. *Angew Chem Int Ed Engl*. 2000;39:3929–3933.
365. DeGroot MW, Cockburn MW, Workentin MS, Corrigan JF. Trialkylphosphine-stabilized copper-phenyltellurolate complexes: from small molecules to nanoclusters via condensation reactions. *Inorg Chem*. 2001;40:4678–4685.
366. Fenske D, Krautscheid H, Balter S. Synthesis and structure of novel Cu-clusters: $[Cu_{30-x}Se_{15}(PiPr_3)_{12}]$ (X = 0,1) and $[Cu_{36}Se_{18}(PtBu_3)_{12}]$. *Angew Chem Int Ed Engl*. 1990;29:796–799.
367. Lee S, Bootharaju MS, Deng G, et al. $[Cu_{32}(PET)_{24}H_8Cl_2](PPh_4)_2$: a copper hydride nanocluster with a bisquare antiprismatic core. *J Am Chem Soc*. 2020;142:13974–13981.

368. Eichhöfer A, Fenske D. Syntheses and structures of new copper(I) selenide clusters $[Cu_{32}Se_{16}(PPh_3)_{12}]$, $[Cu_{52}Se_{26}(PPh_3)_{16}]$ and $[Cu_{72}Se_{36}(PPh_3)_{20}]$. *J Chem Soc Dalton Trans*. 1998;18:2969–2972.
369. Maity S, Bain D, Patra A. Engineering atomically precise copper nanoclusters with aggregation induced emission. *J Phys Chem C Nanomater Interfaces*. 2019;123:2506–2515.
370. Bettenhausen M, Eichhöfer A, Fenske D, Semmelmann M. Synthese und Strukturen neuer selenido- und selenolatoverbrückter Kupfercluster: $[Cu_{38}Se_{13}(SePh)_{12}(dppb)_6]$ (1), $[Cu(dppp)_2][Cu_{25}Se_4(SePh)_{18}(dppp)_2]$ (2), $[Cu_{36}Se_5(SePh)_{26}(dppa)_4]$ (3), $[Cu_{58}Se_{16}(SePh)_{24}(dppa)_6]$ (4) und $[Cu_3(SeMes)_3(dppm)]$ (5). *Z Anorg Allg Chem*. 1999;625:593–601.
371. Dehnen S, Fenske D. $[Cu_{44}Se_{22}(PEt_2Ph)_{18}]$ and$[Cu_{44}Se_{22}(PnButBu_2)_{12}]$: synthesis and structure of two copper clusters with isomeric Cu-Se frameworks. *Angew Chem Int Ed Engl*. 1994;33:2287–2289.
372. Eichhöfer A, Corrigan JF, Fenske D, Tröster E. New copper telluride cluster - synthesis, crystal structure and optical spectrum. *Z Anorg Allg Chem*. 2000;626:338–348.
373. Corrigan JF, Balter S, Fenske D. Synthesis and structural characterization of new copper–tellurium clusters: $TeCu_n(SiMe_3)$ as a source of RTe–and Te_2–ligands. *J Chem Soc Dalton Trans*. 1996;5:729–738.
374. Deveson A, Dehnen S, Fenske D. Syntheses and structures of four new copper(I)–selenium clusters: size dependence of the cluster on the reaction conditions. *J Chem Soc Dalton Trans*. 1997;23:4491–4498.
375. Ghosh A, Huang R-W, Alamer B, et al. $[Cu_{61}(S^tBu)_{26}S_6Cl_6H_{14}]^+$: a core–shell superatom nanocluster with a quasi-J36 Cu_{19} core and an "18-Crown-6" metal-sulfide-like stabilizing belt. *ACS Mater Lett*. 2019;1:297–302.
376. Fenske D, Krautscheid H. New copper clusters containing Se and PEt_3 as ligands: $[Cu_{70}Se_{35}(PEt_3)_{22}]$ and $[Cu_{20}Se_{13}(PEt_3)_{12}]$. *Angew Chem Int Ed Engl*. 1990(29):1452–1454.
377. Huang R-W, Yin J, Dong C, et al. $[Cu_{81}(PhS)_{46}(TBuNH_2)_{10}(H)_{32}]^{3+}$ reveals the coexistence of large planar cores and hemispherical shells in high-nuclearity copper nanoclusters. *J Am Chem Soc*. 2020;142:8696–8705.
378. Fu M-L, Issac I, Fenske D, Fuhr O. Metal-rich copper chalcogenide clusters at the border between molecule and bulk phase: the structures of $[Cu_{93}Se_{42}(SeC_6H_4SMe)_9(PPh_3)_{18}]$, $[Cu_{96}Se_{45}(SeC_6H_4SMe)_6(PPh_3)_{18}]$, and $[Cu_{136}S_{56}(SCH_2C_4H_3O)_{24}(Dpppt)_{10}]$. *Angew Chem Int Ed Engl*. 2010;49:6899–6903.
379. Krautscheid H, Fenske D, Baum G, Semmelmann M. A new copper selenide cluster with PPh3 ligands: $[Cu_{146}Se_{73}(PPh_3)_{30}]$. *Angew Chem Int Ed Engl*. 1993;32:1303–1305.
380. Uzun A, Dixon DA, Gates BC. Prototype supported metal cluster catalysts: Ir_4 and Ir_6. *Chem Cat Chem*. 2011;3:95–107.
381. Bhat S, Chakraborty I, Maark TA, Mitra A, De G, Pradeep T. Atomically precise and monolayer protected iridium clusters in solution. *RSC Adv*. 2016;6:26679–26688.
382. Yamamoto H, Maity P, Takahata R, et al. Monodisperse iridium clusters protected by phenylacetylene: implication for size-dependent evolution of binding sites. *J Phys Chem C Nanomater Interfaces*. 2017;121:10936–10941.
383. Zou Y, Gao Q, Sun N, Han S, Li X, Wang G. Ligand-regulated unusual nickel clusters: a centrosymmetric dicubane Ni and a tetrahedral Ni cluster. *Chin Chem Lett*. 2022;22:8417–8425.
384. Touchton AJ, Wu G, Hayton TW. $[Ni_{30}S_{16}(PEt_3)_{11}]$: an open-shell nickel sulfide nanocluster with a "metal-like" core. *Chem Sci*. 2022;13:5171–5175.
385. Moiseev I, Tatiana S, Michail V, Yuri S. New palladium carbonyl clusters: *X*-ray crystal structure of $[Pd_4(CO)_4(OAc)_4]\cdot(AcOH)_2$. *J Chem Soc Chem Commun*. 1978;10:27–28.
386. Cook AW, Hrobárik P, Damon PL, Wu G, Hayton TW. A ketimide-stabilized palladium nanocluster with a hexagonal aromatic Pd_7 core. *Inorg Chem*. 2020;59:1471–1480.
387. Mednikov EG, Eremenko NK, Mikhailov VA, Gubin SP, Slovokhotov YL, Struchkov YT. New palladium cluster compounds. X-ray crystal structure of $Pd_{10}(CO)_{12}(PBu_3)_6$. *J Chem Soc Chem Commun*. 1981;19:989.
388. Wei J, Kahlal S, Halet J-F, Saillard J-Y. Elucidating the electronic structure of the ligated cuboctahedral palladium cluster $[Pd_{13}(M4\text{-}C_7H_7)_6]^{2+}$. *J Cluster Sci*. 2019;30:1227–1233.
389. Eswaramoorthy SK, Dass A. Atomically precise palladium nanoclusters with 21 and 38 Pd atoms protected by phenylethanethiol. *J Phys Chem C Nanomater Interfaces*. 2022;126:444–450.
390. Wei J, Marchal R, Astruc D, Saillard J-Y, Halet J-F, Kahlal S. Theoretical analysis of the Mackay icosahedral cluster $Pd_{55}(PiPr_3)_{12}(M3\text{-}CO)_{20}$: an open-shell 20-electron superatom. *Chemistry*. 2020;26:5508–5514.
391. Wang X, Zhao L, Li X, et al. Atomic-precision Pt_6 nanoclusters for enhanced hydrogen electro-oxidation. *Nat Commun*. 2022;13:1596.
392. Tanaka S-I, Aoki K, Muratsugu A, Ishitobi H, Jin T, Inouye Y. Synthesis of green-emitting Pt_8 nanoclusters for biomedical imaging by pre-equilibrated Pt/PAMAM (G4-OH) and mild reduction. *Opt Mater Express*. 2013;3:157.

393. Biltek SR, Mandal S, Sen A, Reber AC, Pedicini AF, Khanna SN. Synthesis and structural characterization of an atom-precise bimetallic nanocluster, Ag_4Ni_2 $(DMSA)_4$. *J Am Chem Soc*. 2013;135:20.
394. Liu X, Yuan J, Chen J, Yang J, Wu Z. The synthesis of chiral $Ag_4Pd_2(SR)_8$ by nonreplaced galvanic reaction. *Part Part Syst Charact*. 2019;36.
395. Biltek SR, Sen A, Pedicini AF, Reber AC, Khanna SN. Isolation and structural characterization of a silver–platinum nanocluster, $Ag_4Pt_2(DMSA)_4$. *J Phys Chem A*. 2014;118:8314–8319.
396. Chen J, Liu L, Liu X, et al. Gold-doping of double-crown Pd nanoclusters. *Chem Eur J*. 2017;23:18187–18192.
397. Khatun E, Chakraborty P, Jacob BR, et al. Intercluster reactions resulting in silver-rich trimetallic nanoclusters. *Chem Mater*. 2020;32:611–619.
398. Kang X, Li X, Yu H, et al. Modulating photo-luminescence of Au_2Cu_6 nanoclusters: via ligand-engineering. *RSC Adv*. 2017;7:28606–28609.
399. Zhou M, Jin S, Wei X, et al. Reversible Cu−S motif transformation and Au_4 distortion via thiol ligand exchange engineering. *J Phys Chem C*. 2020;124:7531–7538.
400. Jin S, Liu W, Hu D, et al. Aggregation-induced emission (AIE) in Ag-Au bimetallic nanocluster. *Chem Eur J*. 2018;24:3712–3715.
401. Zhou M, Jin S, Wei X, et al. Reversible Cu−S motif transformation and Au_4 distortion via thiol ligand exchange engineering. *J Phys Chem C*. 2020;124:7531–7538.
402. Emori S, Takano S, Koyasu K, Tsukuda T. Chemical transformations of $[MAu_8(PPh_3)_8]^{2+}$ (M = Pt, Pd) and $[Au_9(PPh_3)_8]^{3+}$ in methanol induced by irradiation of atmospheric pressure plasma. *J Chem Phys*. 2021;155.
403. Bour JJ, Kanters RPF, Schlebos PPJ, et al. Hetero-metallic clusters. Synthesis and characterization of $[PtAu_8(PPh_3)_8](NO_3)_2$ and $[HPtAu_7(PPh_3)_8](NO_3)_2$. *Recl Trav Chim Pays-Bas*. 1987;106:157–158.
404. Sun W, Jin S, Du W, et al. Total structure determination of the $Pt_1Ag_9[P(Ph\text{-}F)_3]_7Cl_3$ nanocluster. *Eur J Inorg Chem*. 2020;2020:590–594.
405. Qin Z, Zhao D, Zhao L, et al. Tailoring the stability, photocatalysis and photoluminescence properties of Au_{11} nanoclusters via doping engineering. *Nanoscale Adv*. 2019;1:2529–2536.
406. Aguiar SRMM, Öztopcu Ö, Stöger B, et al. Synthesis and reactivity of coordinatively unsaturated halocarbonyl molybdenum PNP pincer complexes. *Dalton Trans*. 2014;43:14669–14679.
407. Udayabhaskararao T, Sun Y, Goswami N, Pal SK, Balasubramanian K, Pradeep T. Ag_7Au_6: a 13-atom alloy quantum cluster. *Angew Chem Int Ed*. 2012;51:2155–2159.
408. Kang X, Xiong L, Wang S, Pei Y, Zhu M. De-assembly of assembled Pt_1Ag_{12} units: tailoring the photoluminescence of atomically precise nanoclusters. *Chem Commun*. 2017;53:12564–12567.
409. Copley RCB, Mingos DMP. Synthesis and characterization of the centred icosahedral cluster series $[Au_9MIB_4Cl_4(PMePh_2)_8][C_2B_9H_{12}]$, where MIB = Au, Ag or Cu. *J Chem Soc Dalt Trans*. 1996;4:491.
410. Deng G, Malola S, Yan J, et al. From symmetry breaking to unraveling the origin of the chirality of ligated $Au_{13}Cu_2$ nanoclusters. *Angew Chem Int Ed*. 2018;57:3421–3425.
411. Yang H, Wang Y, Lei J, et al. Ligand-stabilized $Au_{13}Cu_x$ (x = 2, 4, 8) bimetallic nanoclusters: ligand engineering to control the exposure of metal sites. *J Am Chem Soc*. 2013;135:9568–9571.
412. Yang S, Chen S, Xiong L, et al. Total structure determination of $Au_{16}(S\text{-}Adm)_{12}$ and $Cd_1Au_{14}(StBu)_{12}$ and implications for the structure of $Au_{15}(SR)_{13}$. *J Am Chem Soc*. 2018;140:10988–10994.
413. Wen Z-R, Guan Z-J, Zhang Y, Lin Y-M, Wang Q-M. $[Au_7Ag_9(Dppf)_3(CF_3CO_2)_7BF_4]_n$: a linear nanocluster polymer from molecular Au_7Ag_8 clusters covalently linked by silver atoms. *Chem Commun*. 2019;55:12992–12995.
414. Kang X, Xiong L, Wang S, Pei Y, Zhu M. Combining the single-atom engineering and ligand-exchange strategies: obtaining the single-heteroatom-doped $Au_{16}Ag_1(S\text{-}Adm)_{13}$ nanocluster with atomically precise structure. *Inorg Chem*. 2018;57:335–342.
415. Conn BE, Atnagulov A, Yoon B, Barnett RN, Landman U, Bigioni TP. Confirmation of a de novo structure prediction for an atomically precise monolayer-coated silver nanoparticle. *Sci Adv*. 2016;2.
416. Xia N, Wu Z. Doping Au_{25} nanoparticles using ultrasmall silver or copper nanoparticles as the metal source. *J Mater Chem C*. 2016;4:4125–4128.
417. Kang X, Silalai C, Lv Y, et al. $Au_{15}Ag_3(SPhMe_2)_{14}$ nanoclusters – crystal structure and insights into ligand-induced variation. *Eur J Inorg Chem*. 2017;2017:1414–1419.
418. Lin Y-R, Kishore PVVN, Liao J-H, et al. Synthesis, structural characterization and transformation of an eight-electron superatomic alloy, $[Au@Ag_{19}\{S_2P(OPr)_2\}_{12}]$. *Nanoscale*. 2018;10:6855–6860.

419. Jin S, Xu F, Du W, et al. Isomerism in Au–Ag alloy nanoclusters: structure determination and enantioseparation of $[Au_9Ag_{12}(SR)_4(Dppm)_6X_6]^{3+}$. *Inorg Chem*. 2018;57:5114–5119.
420. Gam F, Chantrenne I, Kahlal S, et al. Alloying dichalcogenolate-protected Ag_{21} eight-electron nanoclusters: a DFT investigation. *Nanoscale*. 2021;14:196–203.
421. Yang S, Chai J, Song Y, et al. In situ two-phase ligand exchange: a new method for the synthesis of alloy nanoclusters with precise atomic structures. *J Am Chem Soc*. 2017;139:5668–5671.
422. Liu C, Ren X, Lin F, et al. Structure of the $Au_{23-x}Ag_x(S\text{-}Adm)_{15}$ nanocluster and its application for photocatalytic degradation of organic pollutants. *Angew Chemie - Int Ed*. 2019;58:11335–11339.
423. Chen S, Du W, Qin C, et al. Assembly of the thiolated $[Au_1Ag_{22}(S\text{-}Adm)_{12}]^{3+}$ superatom complex into a framework material through direct linkage by SbF_6 anions. *Angew Chemie Int Ed*. 2020;59:7542–7547.
424. Li Q, Taylor MG, Kirschbaum K, et al. Site-selective substitution of gold atoms in the $Au_{24}(SR)_{20}$ nanocluster by silver. *J Colloid Interface Sci*. 2017;505:1202–1207.
425. Yang S, Wang S, Jin S, Chen S, Sheng H, Zhu M. A metal exchange method for thiolate-protected tri-metal $M_1Ag_xAu_{24-x}(SR)_{180}$ (M = Cd/Hg) nanoclusters. *Nanoscale*. 2015;7:10005–10007.
426. Sharma S, Yamazoe S, Ono T, et al. Tuning the electronic structure of thiolate-protected 25-atom clusters by co-substitution with metals having different preferential sites. *Dalt Trans*. 2016;45:18064–18068.
427. Bootharaju MS, Joshi CP, Parida MR, Mohammed OF, Bakr OM. Templated atom-precise galvanic synthesis and structure elucidation of a $[Ag_{24}Au(SR)_{18}]^-$ nanocluster. *Angew Chem Int Ed*. 2016;128:934–938.
428. Kumara C, Aikens CM, Dass A. X-ray crystal structure and theoretical analysis of $Au_{25\text{-}X}Ag_x(SCH_2CH_2Ph)_{18}$ alloy. *J Phys Chem Lett*. 2014;5:461–466.
429. Kauffman DR, Alfonso D, Matranga C, Qian H, Jin R. A quantum alloy: the ligand-protected $Au_{25\text{-}X}Ag_x(SR)_{18}$ cluster. *J Phys Chem C*. 2013;117:7914–7923.
430. Xia N, Wu Z. Doping Au_{25} nanoparticles using ultrasmall silver or copper nanoparticles as the metal source. *J Mater Chem C*. 2016;4:4125–4128.
431. Shi W-Q, Guan Z-J, Li J-J, Han X-S, Wang Q-M. Site-specified doping of silver atoms into Au_{25} nanocluster as directed by ligand binding preference. *Chem Sci*. 2022;13:5148–5154.
432. Teo BK, Zhang H, Shi X. Site preference in vertex-sharing polyicosahedral supraclusters containing groups 10 and 11 metals and their bonding implications: syntheses and structures of the first Au-Ag-M (M = Pt, Ni) biicosahedral clusters $[(Ph_3P)_{10}Au_{12}Ag_{12}PtCl_7]Cl$ and $[(Ph_3P)_{10}Au_1$. *Inorg Chem*. 1994;33:4086–4097.
433. Teo BK, Dang H, Campana CF, Zhang H. Synthesis, structure, and characterization of $(MePh_2P)_{10}Au_{12}Ag_{13}Br_9$: the first example of a neutral Bi-icosahedral Au-Ag cluster with a novel seven-membered satellite ring of bridging ligands. *Polyhedron*. 1998;17:617–621.
434. Wang S, Meng X, Das A, et al. A 200-fold quantum yield boost in the photoluminescence of silver-doped $Ag_xAu_{25\text{-}x}$ nanoclusters: the 13th silver atom matters. *Angew Chem Int Ed*. 2014;53:2376–2380.
435. He L, He X, Wang J, Fu C, Liang J. $Ag_{23}Au_2$ and $Ag_{22}Au_3$: a model of cocrystallization in bimetal nanoclusters. *Inorg Chem*. 2021;60:8404–8408.
436. Hossain S, Miyajima S, Iwasa T, et al. $[Ag_{23}Pd_2(PPh_3)_{10}Cl_7]$: a new family of synthesizable Bi-icosahedral superatomic molecules. *J Chem Phys*. 2021;155.
437. Bootharaju MS, Kozlov SM, Cao Z, et al. Doping-induced anisotropic self-assembly of silver icosahedra in $[Pt_2Ag_{23}Cl_7(PPh_3)_{10}]$ nanoclusters. *J Am Chem Soc*. 2017;139:1053–1056.
438. Li Y, Zhou M, Jin S, et al. Total structural determination of $[Au_1Ag_{24}(Dppm)_3(SR)_{17}]^{2+}$ comprising an open icosahedral Au_1Ag_{12} core with six free valence electrons. *Chem Commun*. 2019;55:6457–6460.
439. Zheng K, Fung V, Yuan X, Jiang DE, Xie J. Real time monitoring of the dynamic intracluster diffusion of single gold atoms into silver nanoclusters. *J Am Chem Soc*. 2019;141:18977–18983.
440. Bootharaju MS, Joshi CP, Parida MR, Mohammed OF, Bakr OM. Templated atom-precise galvanic synthesis and structure elucidation of a $[Ag_{24}Au(SR)_{18}]^-$ nanocluster. *Angew Chem Int Ed Engl*. 2016;55:922–926.
441. Yan J, Su H, Yang H, et al. Total structure and electronic structure analysis of doped thiolated silver $[MAg_{24}(SR)_{18}]^{2-}$ (M = Pd, Pt) clusters. *J Am Chem Soc*. 2015;137:11880–11883.
442. Bhat S, Baksi A, Mudedla SK, Natarajan G, Subramanian V, Pradeep T. $Au_{22}Ir_3(PET)_{18}$: an unusual alloy cluster through intercluster reaction. *J Phys Chem Lett*. 2017;8:2787–2793.
443. Wang S, Abroshan H, Liu C. Shuttling single metal atom into and out of a metal nanoparticle. *Nat Commun*. 2017;8:848.

444. Wang S, Song Y, Jin S, et al. Metal exchange method using Au_{25} nanoclusters as templates for alloy nanoclusters with atomic precision. *J Am Chem Soc*. 2015;137:4018–4021.
445. Fields-Zinna CA, Crowe MC, Dass A, Weaver JEF, Murray RW. Mass spectrometry of small bimetal monolayer-protected clusters. *Langmuir*. 2009;25:7704–7710.
446. Tian S, Liao L, Yao C, et al. Structures and magnetism of mono-palladium and mono-platinum doped $Au_{25}(PET)_{18}$ nanoclusters. *Chem Commun*. 2016;52:9873–9876.
447. Suyama M, Takano S, Nakamura T, Tsukuda T. Stoichiometric formation of open-shell $[PtAu_{24}(SC_2H_4Ph)_{18}]^-$ via spontaneous electron proportionation between $[PtAu_{24}(SC_2H_4Ph)_{18}]^{2-}$ and $[PtAu_{24}(SC_2H_4Ph)_{18}]^0$. *J Am Chem Soc*. 2019;141:14048–14051.
448. Ito S, Koyasu K, Takano S, Tsukuda T. Collision-induced reductive elimination of 1,3-diynes from $[MAu_{24}(C{\equiv}CR)_{18}]^{2-}$ (M = Pd, Pt) yielding clusters of superatoms. *J Phys Chem C Nanomater Interfaces*. 2020;124:19119–19125.
449. Negishi Y, Munakata K, Ohgake W, Nobusada K. Effect of copper doping on electronic structure, geometric structure, and stability of thiolate-protected Au_{25} nanoclusters. *J Phys Chem Lett*. 2012;3:2209–2214.
450. Zhou J, Li T, Li Q, et al. Insight into the effects of chiral diphosphine ligands on the structure and optical properties of the $Au_{24}Cd_2$ nanocluster. *Inorg Chem*. 2022;61(17):6493–6499.
451. Li Y, Chen M, Wang S, Zhu M. Intramolecular metal exchange reaction promoted by thiol ligands. *Nanomaterials*. 2018;8:1070.
452. Du Y, Guan Z-J, Wen Z-R, Lin Y-M, Wang Q-M. Ligand-controlled doping effects in alloy nanoclusters Au_4Ag_{23} and Au_5Ag_{24}. *Chem Eur J*. 2018;24:16029–16035.
453. He L, Gan Z, Xia N, Liao L, Wu Z. Alternating array stacking of $Ag_{26}Au$ and $Ag_{24}Au$ nanoclusters. *Angew Chem*. 2019;131:10002–10006.
454. Negishi Y, Horihata H, Ebina A, et al. Selective formation of $[Au_{23}(SPh^tBu)_{17}]^0$, $[Au_{26}Pd(SPh^tBu)_{20}]^0$ and $[Au_{24}Pt(SC_2H_4Ph)_7(SPh^tBu)_{11}]^0$ by controlling ligand-exchange reaction. *Chem Sci*. 2022;13(19):5546–5556.
455. He L, Yuan J, Xia N, et al. Kernel tuning and nonuniform influence on optical and electrochemical gaps of bimetal nanoclusters. *J Am Chem Soc*. 2018;140:3487–3490.
456. Xu L, Li Q, Li T, Chai J, Yang S, Zhu M. Construction of a new $Au_{27}Cd_1(SAdm)_{14}(DPPF)Cl$ nanocluster by surface engineering and insight into its structure–property correlation. *Inorg Chem Front*. 2021;8:4820–4827.
457. Kang X, Wei X, Jin S, et al. Rational construction of a library of M_{29} nanoclusters from monometallic to tetrametallic. *Proc Natl Acad Sci*. 2019;116:18834–18840.
458. Qin Z, Sharma S, Wan C-Q, et al. A homoleptic alkynyl-ligated $[Au_{13}\ Ag_{16}L_{24}]^{3-}$ cluster as a catalytically active eight-electron superatom. *Angew Chem Int Ed Engl*. 2021;60:970–975.
459. Khatun E, Chakraborty P, Jacob BR, et al. Intercluster reactions resulting in silver-rich trimetallic nanoclusters. *Chem Mater*. 2020;32:611–619.
460. Kang X, Abroshan H, Wang S, Zhu M. Free valence electron centralization strategy for preparing ultrastable nanoclusters and their catalytic application. *Inorg Chem*. 2019;58:11000–11009.
461. Mikami K, Hui S, Kubo K, Kume S, Mizuta T. The $[Ag_{25}Cu_4H_8Br_6(CCPh)_{12}(PPh_3)_{12}]^{3+}$: $Ag_{13}H_8$ silver hydride core protected by $[CuAg_3(CCPh)_3(PPh_3)_3]^+$ motifs. *Dalton Trans*. 2021;50:5659–5665.
462. Khatun E, Chakraborty P, Jacob BR, et al. Intercluster reactions resulting in silver-rich trimetallic nanoclusters. *Chem Mater*. 2020;32:611–619.
463. Kang X, Zhou M, Wang S, et al. The tetrahedral structure and luminescence properties of bi-metallic $Pt_1Ag_{28}(SR)_{18}(PPh_3)_4$ nanocluster. *Chem Sci*. 2017;8:2581–2587.
464. Hossain S, Imai Y, Motohashi Y, et al. Understanding and designing one-dimensional assemblies of ligand-protected metal nanoclusters. *Mater Horiz*. 2020;7:796.
465. Chai J, Yang S, Lv Y, Chong H, Yu H, Zhu M. Exposing the delocalized Cu−S π bonds on the $Au_{24}Cu_6(SPhtBu)_{22}$ nanocluster and its application in ring-opening reactions. *Angew Chem Int Ed*. 2019;58:15671–15674.
466. Zou X, Jin S, Wang S, Zhu M, Jin R. Tailoring the structure of 32-metal-atom nanoclusters by ligands and alloying. *Nano Fut*. 2018;2.
467. Hasegawa S, Takano S, Yamazoe S, Tsukuda T. Prominent hydrogenation catalysis of a PVP-stabilized Au_{34} superatom provided by doping a single Rh atom. *Chem Commun (Camb)*. 2018;54:5915–5918.
468. Theivendran S, Chang L, Mukherjee A, et al. Principles of optical spectroscopy of aromatic alloy nanomolecules: $Au_{36-x}Ag_x(SPh\text{-}tBu)_{24}$. *J Phys Chem C*. 2018;122:4524–4531.

469. Takano S, Tsukuda T. Chemically modified gold/silver superatoms as artificial elements at nanoscale: design principles and synthesis challenges. *J Am Chem Soc*. 2021;143:1683–1698.
470. Kumara C, Gagnon KJ, Dass AX-R. Crystal structure of $Au_{38-X}Ag_x(SCH_2CH_2Ph)_{24}$ alloy nanomolecules. *J Phys Chem Lett*. 2015;6:1223–1228.
471. Teo BK, Zhang H, Shi X. Cluster of clusters: a modular approach to large metal clusters. Structural characterization of a 38-atom cluster $[(p\text{-}Tol_3P)_{12}Au_{18}Ag_{20}Cl_{14}]$ based on vertex-sharing triicosahedra. *J Am Chem Soc*. 1990;112:8552–8562.
472. Negishi Y, Igarashi K, Munakata K, Ohgake W, Nobusada K. Palladium doping of magic gold cluster $Au_{38}(SC_2H_4Ph)_{24}$: formation of $Pd_2Au_{36}(SC_2H_4Ph)_{24}$ with higher stability than $Au_{38}(SC_2H_4Ph)_{24}$. *Chem Commun*. 2012;48:660–662.
473. Huifeng Q, Barry Ellen Z, Yan JR. Doping 25-atom and 38-atom gold nanoclusters with palladium. *Acta Phys Chim Sin*. 2011;27:513–519.
474. Chai J, Lv Y, Yang S, et al. Crystal structure and optical properties of $Au_{38-x}Cu_x(2,4\text{-}(CH_3)_2C_6H_3S)_{24}$ ($x = 0$–6) alloy nanocluster. *J Phys Chem C*. 2017;121:21665–21669.
475. Ma X-H, Si Y, Luo L-L, Wang Z-Y, Zang S-Q, Mak TCW. Directional doping and cocrystallizing an open-shell Ag_{39} superatom via precursor engineering. *ACS Nano*. 2022;16(4):5507–5514.
476. Yan J, Su H, Yang H, et al. Asymmetric synthesis of chiral bimetallic $[Ag_{28}Cu_{12}(SR)_{24}]^{4-}$ nanoclusters via ion pairing. *J Am Chem Soc*. 2016;138:12751–12754.
477. Wang Z, Senanayake R, Aikens CM, Chen W-M, Tung C-H, Sun D. Nanoscale gold-doped silver nanocluster $[Au_3Ag_{38}(SCH_2Ph)_{24}X_5]^{2-}$ ($X = Cl$ or Br). *Nanoscale*. 2016;8:18905.
478. Wang Y, Su H, Xu C, et al. An intermetallic $Au_{24}Ag_{20}$ superatom nanocluster stabilized by labile ligands. *J Am Chem Soc*. 2015;137:4324–4327.
479. Yang H, Wang Y, Huang H, et al. All-thiol-stabilized Ag_{44} and $Au_{12}Ag_{32}$ nanoparticles with single-crystal structures. *Nat Commun*. 2013;4:2422.
480. Krishnadas KR, Baksi A, Ghosh A, Natarajan G, Pradeep T. Manifestation of geometric and electronic shell structures of metal clusters in intercluster reactions. *ACS Nano*. 2017;11:6015–6023.
481. Bootharaju MS, Chang H, Deng G, et al. $Cd_{12}Ag_{32}(SePh)_{36}$: non-noble metal doped silver nanoclusters. *J Am Chem Soc*. 2019;141:8422–8425.
482. Chai J, Yang S, Chen T, Li Q, Wang S, Zhu M. Chiral inversion and conservation of clusters: a case study of racemic $Ag_{32}Cu_{12}$ nanocluster. *Inorg Chem*. 2021;60:9050–9056.
483. Yang H, Wang Y, Yan J, et al. Structural evolution of atomically precise thiolated bimetallic $[Au_{12+n}Cu_{32}(SR)_{30+n}]$ ($n = 0$, 2, 4, 6) nanoclusters. *J Am Chem Soc*. 2014;136:7197–7200.
484. Haggin J. Illinois scientists synthesize huge cluster. *Chem Eng News Arch*. 1989;67:6.
485. Wan X-K, Cheng X-L, Tang Q, et al. Atomically precise bimetallic $Au_{19}Cu_{30}$ nanocluster with an icosidodecahedral Cu_{30} shell and an alkynyl−Cu interface. *J Am Chem Soc*. 2017;139:9451–9454.
486. Du W, Jin S, Xiong L, et al. $Ag_{50}(Dppm)_6(SR)_{30}$ and its homologue $Au_xAg_{50-x}(Dppm)_6(SR)_{30}$ alloy nanocluster: seeded growth, structure determination, and differences in properties. *J Am Chem Soc*. 2017;139:1618–1624.
487. Wei X, Kang X, Duan T, et al. $[Au_{16}Ag_{43}H_{12}(SPhCl_2)_{34}]^{5-}$: an Au-Ag alloy nanocluster with 12 hydrides and its enlightenment on nanocluster structural evolution. *Inorg Chem*. 2021;60:11640–11647.
488. Wang Y, Wan X-K, Ren L, et al. Atomically precise alkynyl-protected metal nanoclusters as a model catalyst: observation of promoting effect of surface ligands on catalysis by metal nanoparticles. *J Am Chem Soc*. 2016;138:3278–3281.
489. Jin S, Zhou M, Kang X, et al. Three-dimensional octameric assembly of icosahedral M 13 units in $[Au_8Ag_{57}(Dppp)_4(C_6H_{11}S)_{32}Cl_2]Cl$ and its $[Au_8Ag_{55}(Dppp)_4(C_6H_{11}S)_{34}][BPh_4]_2$ derivative. *Angew Chem*. 2020;132:3919–3923.
490. Jin S, Zhou M, Kang X, et al. Three-dimensional octameric assembly of icosahedral M 13 units in $[Au_8Ag_{57}(Dppp)_4(C_6H_{11}S)_{32}Cl_2]Cl$ and its $[Au_8Ag_{55}(Dppp)_4(C_6H_{11}S)_{34}][BPh_4]_2$ derivative. *Angew Chem*. 2020;132:3919–3923.
491. Wang S, Jin S, Yang S, et al. Total structure determination of surface doping $[Ag_{46}Au_{24}(SR)_{32}](BPh_4)_2$ nanocluster and its structure-related catalytic property. *Sci Adv*. 2015;1.
492. Xu J, Xiong L, Cai X, et al. Evolution from superatomic $Au_{24}Ag_{20}$ monomers into molecular-like $Au_{43}Ag_{38}$ dimeric nanoclusters. *Chem Sci*. 2022;13:2778–2782.

493. Zou X, Li Y, Jin S, et al. Doping copper atoms into the nanocluster kernel: total structure determination of $[Cu_{30}Ag_{61}(SAdm)_{38}S_3](BPh_4)$. *J Phys Chem Lett*. 2020;11:2272–2276.
494. Zeng JL, Guan ZJ, Du Y, Nan ZA, Lin YM, Wang QM. Chloride-promoted formation of a bimetallic nanocluster $Au_{80}Ag_{30}$ and the total structure determination. *J Am Chem Soc*. 2016;138:7848–7851.
495. Guan Z-J, Zeng J-L, Yuan S-F, Hu F, Lin Y-M, Wang Q-M. $Au_{57}Ag_{53}(C{\equiv}CPh)_{40}Br_{12}$: a large nanocluster with C1 symmetry. *Angew Chem Int Ed Engl*. 2018;57:5703–5707.
496. Higaki T, Liu C, Morris DJ, et al. $Au_{130-x}Ag_x$ nanoclusters with non-metallicity: a drum of silver-rich sites enclosed in a marks-decahedral cage of gold-rich sites. *Angew Chem - Int Ed*. 2019;58:18798–18802.
497. Yuan X, Malola S, Deng G, et al. Atomically precise alkynyl- and halide-protected AuAg nanoclusters $Au_{78}Ag_{66}(C{\equiv}CPh)_{48}Cl_8$ and $Au_{74}Ag_{60}(C{\equiv}CPh)_{40}Br_{12}$: the ligation effects of halides. *Inorg Chem*. 2021;60:3529–3533.
498. Jensen KMØ, Juhas P, Tofanelli MA, et al. Polymorphism in magic-sized $Au_{144}(SR)_{60}$ clusters. *Nat Commun*. 2016;7:11859.
499. Dharmaratne AC, Dass A. $Au_{144-x}Cu_x(SC_6H_{13})_{60}$ nanomolecules: effect of Cu incorporation on composition and plasmon-like peak emergence in optical spectra. *Chem Commun*. 2014;50:1722.
500. Mednikov EG, Jewell MC, Dahl LF. Nanosized $Pd_{164-X}Pt_x(CO)_{72}(PPh_3)_{20}$ containing Pt-centered four-shell 165-atom Pd-Pt core with unprecedented intershell bridging carbonyl ligands: comparative analysis of icosahedral shell-growth patterns with geometrically related $Pd_{145}(CO)_x(PEt_3)_{30}$ containing capped three-shell Pd_{145} core. *J Am Chem Soc*. 2007;129:11619–11630.

Index

Page numbers followed by "*f*" and "*t*" indicate, figures and tables respectively.

N

ATOMICALLY PRECISE METAL NANOCLUSTERS

A comprehensive guide to nanoparticles at molecular length scale

Edited By

Thalappil Pradeep

Atomically Precise Metal Nanoclusters belongs to an expanding area of molecular materials, which can be better utilized with a solid understanding of their diverse variety, structures, and properties. This book delves into the foundational chemistry of the key cluster systems, and provides guidance on the principal approaches employed to examine them in more detail.

Under the guidance of its expert editor, *Atomically Precise Metal Nanoclusters* draws together the knowledge of an experienced and active team of contributors.

Key Features

- Comprehensive guide combining key knowledge, approaches, and types of metal nanoclusters at one place
- Supports understanding of important phenomena using clear figures
- Highlights future needs and prospects for the field

About the Editor

Thalappil Pradeep is an Institute Professor at the Indian Institute of Technology Madras, Chennai, India. He is the Deepak Parekh Institute Chair Professor and is also a Professor of Chemistry. He studied at the University of Calicut, Indian Institute of Science, UC Berkeley, and Purdue. His research interests are in molecular and nanoscale materials and he develops instrumentation for such studies. In addition to the work on advanced materials, he is involved in the development of affordable technologies for drinking water purification and some of them have been commercialized. Visit https://pradeepresearch.org/ for more information.

ISBN 978-0-323-90879-5

9 780323 908795

ELSEVIER

elsevier.com/books-and-journals